

# Fundamentals of Aircraft and Airship Design

## Volume I — Aircraft Design



**Leland M. Nicolai**

Lockheed Martin Aeronautics Company  
Advanced Development Programs (Skunk Works)  
Palmdale, California

**Grant E. Carichner**

Lockheed Martin Aeronautics Company  
Advanced Development Programs (Skunk Works)  
Palmdale, California



**EDUCATION SERIES**

**Joseph A. Schetz**

**Editor-in-Chief**

Virginia Polytechnic Institute and State University  
Blacksburg, Virginia

*Published by*

AMERICAN INSTITUTE OF AERONAUTICS AND ASTRONAUTICS, INC.  
1801 ALEXANDER BELL DRIVE, RESTON, VA 20191-4344

American Institute of Aeronautics and Astronautics, Inc., Reston, Virginia  
1 2 3 4 5

**Library of Congress Cataloging-in-Publication Data**

Nicolai, Leland M. (Leland Malcolm)

Fundamentals of aircraft and airship design / Leland M. Nicolai, Grant Carichner.

p. cm. — (AIAA educational series)

Rev. and expanded ed. of: Fundamentals of aircraft design / Leland M. Nicolai. 1975.

Includes bibliographical references and index.

ISBN 978-1-60086-751-4 (alk. paper)

1. Airplanes—Design and construction—History. 2. Airships—Design and construction—History. 3. Aeronautics—Pictorial works. I. Carichner, Grant. II. Nicolai, Leland M. (Leland Malcolm). Fundamentals of aircraft design. III. Title.

TL671.2.N5 2010

629.134'1—dc22

2010012955

Skunk Works® is a registered trademark of the Lockheed Martin Corporation.

Photographs of Lockheed Martin aircraft on the first page of Chapters 4, 12, 13, 19, and Appendices C and K, as well as in Figures 8.9, 9.33, 12.1, 12.3, 12.10, 19.3, F.6 and Color Plates 1 and 10 are provided courtesy of Lockheed Martin Corporation. Images on the first page of Chapters 3, 11, 16, 17, 23, and Appendices B and F, as well as in Figures 2.15, 4.9a, and 12.2 are from the private collection of the authors. Unattributed photographs are held in the public domain and are from either the U.S. Department of Defense or Wikipedia.

Copyright © 2010 by Leland M. Nicolai and Grant E. Carichner. Published by the American Institute of Aeronautics and Astronautics, Inc. with permission. Printed in the United States of America. No part of this publication may be reproduced, distributed, or transmitted, in any form or by any means, or stored in a database or retrieval system, without the prior written permission.

Data and information appearing in this book are for informational purposes only. The authors and the publisher are not responsible for any injury or damage resulting from use or reliance, nor do they warrant that use or reliance will be free from privately owned rights.

## LIST OF COLOR PLATES

	Pilot's Prayer	cp1
	F-18 Vortices (NASA, Dryden Water Tunnel Facility)	cp2
<b>Fig. 10.1</b>	B-767 with Trailing Vortices (courtesy of Ray Nicolai)	cp2
<b>Fig. 2.14</b>	Vortices Shedding from F-18 LEX and F-22 Wing Leading Edge	cp3
<b>Ch. 2</b>	F-14 with Shock Condensation @ $M = 0.9$	cp3
<b>Fig. 1.8</b>	DC-3—Timeless Elegance	cp4
<b>Appen. G.</b>	Cessna 172 Skyhawk—Classic Design	cp4
<b>Ch. 5</b>	YF-16 and YF-17—LWF Competition Finalists	cp5
<b>Fig. 1.9</b>	YF-22 and YF-23—ATF Competitors	cp5
<b>Fig. 1.11</b>	X-32 and X-35—JSF Competitors	cp5
<b>Appen. H</b>	F-16 Fighting Falcon—Configured for Air-to-air Mission	cp6
	F-18—Powered Approach to Aircraft Carrier (courtesy of John Stratton)	cp6
<b>Fig. 15.13b</b>	A Variety of Inlet Designs for Supersonic Missions	cp7
<b>Ch. 3</b>	SR-71—Kelly Johnson's Crowning Achievement	cp8
<b>Ch. 16</b>	Transonic $C_{D_0}$ of the SR-71—A Surprise when Compared to Predictions	cp8
<b>Fig. 9.31</b>	V/STOL Aircraft Summary (1970s)	cp9
	AV-8B Harrier Performs a Hover Maneuver	cp9
<b>Fig. 9.32</b>	V/STOL Aircraft Summary (2008)	cp10
	F-35B Transitions from Level Flight to Vertical Mode	cp10
<b>Ch. 23</b>	Canadian Geese Make STOL Landing	cp11
<b>Appen. C</b>	F-35B Lightning II Prepares for Vertical Landing	cp11
<b>Ch. 12</b>	F-117A and the "Father of Stealth" Ben Rich	cp12
<b>Ch. 13</b>	F-22 and F-117—Two Generations of Stealth	cp12
<b>Fig. F.6</b>	Polecat Unmanned Aircraft	cp13
<b>Ch. 19</b>	F-117—Built in Secrecy in Burbank, California	cp13
<b>Fig. 18.5</b>	Solar Energy Radiated to Earth	cp14
<b>Fig. 18.8</b>	Diurnal Energy Balance—Stationkeeping Over Moscow and Miami	cp15
<b>Fig. 10.14</b>	Mig 31, F-15, B-1B, and L1011—Takeoffs	cp16
<b>Fig. G.1</b>	High-Subsonic Drag Polars—Flight Test Data	cp17
	Boeing 747-400—Boeing's Gamble Pays Off (early 1970s)	cp17

<b>Fig. G.4</b>	Drag Polars for Fighter Aircraft—Flight Test Data	cp18
<b>Fig. G.5</b>	$C_{D_{\min}}$ vs Mach Number—Flight Test Data	cp19
<b>Fig. G.8</b>	Max. $L/D$ Correlation Curve—Flight Test Data	cp20
<b>Fig. G.9</b>	Subsonic Wing Efficiency vs Aspect Ratio	cp21
<b>Ch. 21</b>	Sopwith Camel—A Highly Maneuverable WWI Fighter	cp22
<b>Ch. 18</b>	Nemesis—A Formula One A-Class Racer	cp22
<b>Fig. 18.10</b>	Daedalus—Record Holder for Human-powered Distance	cp23
<b>Appen. I</b>	Eta Glider—With Today’s Highest Maximum $L/D$ of 73	cp23
<b>Fig. 19.16</b>	Wing Structural Configurations	cp24

## PREFACE

Volume I is an update and expansion of the 1975 text *Fundamentals of Aircraft Design*. The updated material includes designing for survivability (stealth), solar power aircraft systems, and very high altitude operation with air breathing propulsion. The added material is a discussion of both the science and art of aircraft design and includes a new chapter on materials and structural design. The art of design is captured in the history, the lessons learned, the facts and stories appearing in blue boxes, and the case studies, as well as in the four-color section found at the back of the book. The DC-3 and the F-35B on the title page portray the blend of art and science in aircraft design. The DC-3 represents the *art of design* ingeniously displayed by Donald Douglas in creating an airplane of timeless elegance that set the standard for air transportation in 1935. The F-35B represents the *science of design* in applying the latest in methodology and technology to “create that which never was” (Theodore von Kármán). This work is the result of the collaboration of two practicing engineers with a combined 80 years of design experience. The projects cover aircraft from fast to slow, high to low, big to small. The design of airships is the central theme of Volume II.

The aerospace industry has changed the way it designs aircraft and has expanded the spectrum of vehicle types. Beginning in the late 1970s stealth (RF and IR) became a big part of the aircraft design process. This single technology has enabled the United States of America to have air superiority over every nation for the last 25 years. Volume I includes the unclassified details of incorporating stealth into a viable design. The authors have lived it and now you can read and learn about it.

The text is aimed at upper-level undergraduate and graduate students as well as at practicing engineers. It contains comprehensive treatment of the conceptual design phase, treating civil and military aircraft equally. The book covers all phases of conceptual design, from consideration of user needs to the decision to iterate the design one more time. The book is complete in that the reader should not have to go outside the text for additional information.

The text is structured to lead the reader through one iteration of the conceptual design cycle loop. It can also be used as a convenient reference book for practicing engineers to give them up-to-date methodology in

aerodynamics, propulsion, performance, structures and materials, weights, stability and control, and life cycle costing. It can also be used by technical managers to better understand and appreciate the fundamental parameters driving the design of an aircraft and their interplay. It has a rich set of appendixes that puts pertinent data at the designer's fingertips.

The main theme of the text is that the aircraft is only a dust cover. The point being that the designer needs to remember that the aircraft is only a mechanism for transporting the payload (people, cargo, bombs, sensors, and so on). All design decisions must consider the needs of the payload first. The text emphasizes that the aircraft design process is always a compromise and that there is no right answer; however, there is always a best answer based on existing requirements and available technologies. But the best design answer today will probably be different from that of tomorrow.

Chapter 19 about material selection and structural arrangement is completely new. It is written by Walter Franklin, a Lockheed Martin Fellow and practicing structures engineer. It is a wonderful addition to the book as it thoroughly covers the material and structural issues associated with aircraft design. At the end of this chapter is a complete wing design example.

Using design examples throughout the book, the authors guide your journey through the design process as it would happen in the actual design environment. Using color, historical design facts, and case studies, the authors make the journey a real life experience in one of the most important engineering inventions of modern time. Students, practicing engineers, and engineering managers alike will find Volume 1 of *Fundamentals of Aircraft and Airship Design* an indispensable resource and a pleasure to read.

A special thanks to Pat DuMoulin, our AIAA editor, for her consistent efforts to make this book as good as it possibly could be. Thanks also to Becky Rivard and Mike Baden-Campbell for assistance with proof checking.

**Leland M. Nicolai**  
**Grant E. Carichner**  
June 2010

# CONTENTS

List of Color Plates	xix
Preface	xxi
<b>Chapter 1</b> Introduction	1
<b>1.1</b> Aeronautics—The Beginning	2
<b>1.2</b> Aircraft Design—A Compromise	3
<b>1.3</b> Overall Design Requirements	6
<b>1.4</b> Unmanned Aerial Vehicle	16
<b>1.5</b> Specifications, Standards, and Regulations	21
<b>1.6</b> Aircraft Design Phases	23
<b>1.7</b> Scope of the Text	27
References	30
<b>Chapter 2</b> Review of Practical Aerodynamics	33
<b>2.1</b> Introduction	34
<b>2.2</b> Drag	37
<b>2.3</b> Boundary Layers and Skin Friction Drag	38
<b>2.4</b> Incompressible Airfoil Section Theory	40
<b>2.5</b> Subsonic Compressibility Corrections	43
<b>2.6</b> Finite Wing Corrections	43
<b>2.7</b> Sweep Correction	44
<b>2.8</b> Combined Effects	45
<b>2.9</b> Nonlinear Wing Lift and Moment	46
<b>2.10</b> Total Aircraft Subsonic Aerodynamics	48
<b>2.11</b> Transonic Flow and Its Effects	54
<b>2.12</b> Wing Thickness Ratio	56
<b>2.13</b> Wing Sweep	57
<b>2.14</b> Supercritical Wing	59
<b>2.15</b> Wing–Body Combinations for Transonic Flight	61
<b>2.16</b> Mach Wave	62
<b>2.17</b> Subsonic and Supersonic Leading Edge	63
<b>2.18</b> Supersonic Skin Friction	63
<b>2.19</b> Supersonic Lift and Wave Drag	64
<b>2.20</b> Correction for Three-Dimensional Effects	66

<b>2.21</b>	Sanity Check	67
	References	70
<b>Chapter 3</b>	Aircraft Performance Methods	71
<b>3.1</b>	Introduction	72
<b>3.2</b>	Level Unaccelerated Flight	72
<b>3.3</b>	Minimum Drag and Maximum $L/D$	75
<b>3.4</b>	Variation of $T_R$ with Weight, Configuration, and Altitude	77
<b>3.5</b>	Endurance or Loiter	78
<b>3.6</b>	Range	83
<b>3.7</b>	Level Constant Velocity Turn	89
<b>3.8</b>	Energy-State Approximation (Energy Maneuverability)	90
<b>3.9</b>	Energy Maneuverability for Air Combat Assessment	93
<b>3.10</b>	Rate of Climb and Descent	97
<b>3.11</b>	Summary for Maximum Range and Endurance	100
	References	100
<b>Chapter 4</b>	Aircraft Operating Envelope	101
<b>4.1</b>	Flight Envelope	102
<b>4.2</b>	Minimum Dynamic Pressure	103
<b>4.3</b>	Maximum Thrust Limit	104
<b>4.4</b>	Maximum Dynamic Pressure	104
<b>4.5</b>	Aerodynamic Heating	105
<b>4.6</b>	Sonic Boom	108
<b>4.7</b>	Noise and Pollution Limits	108
<b>4.8</b>	Propulsion Limits	112
<b>4.9</b>	Optimal Trajectories	112
	References	121
<b>Chapter 5</b>	Preliminary Estimate of Takeoff Weight	123
<b>5.1</b>	Introduction	124
<b>5.2</b>	Fixed Weight	124
<b>5.3</b>	Empty Weight	124
<b>5.4</b>	Fuel Weight	126
<b>5.5</b>	Determining $W_{TO}$	132
<b>5.6</b>	Range- or Payload-Dominated Vehicles	140
<b>5.7</b>	High Altitude Atmospheric Research Platform	146
	Reference	149



<b>Chapter 6</b>	Estimating the Takeoff Wing Loading	151
6.1	Introduction	152
6.2	Range-Dominated Vehicle (Cruise Efficiency)	152
6.3	Endurance or Loiter	156
6.4	Landing and Takeoff	157
6.5	Air-to-Air Combat and Acceleration	159
6.6	High Altitude	163
6.7	High Altitude, Long Endurance	165
6.8	Low-Altitude Ride Quality	168
<b>Chapter 7</b>	Selecting the Planform and Airfoil Section	171
7.1	Introduction	172
7.2	Effect of Airfoil: Maximum Thickness Ratio	173
7.3	Effect of Airfoil: Location of Maximum Thickness	174
7.4	Effect of Airfoil: Leading Edge Shape	175
7.5	Effect of Airfoil: Camber	178
7.6	Effect of Planform: Aspect Ratio	180
7.7	Effect of Planform: Sweep	182
7.8	Effect of Planform: Taper Ratio	186
7.9	Variable Geometry	186
7.10	Summary	194
	References	194
<b>Chapter 8</b>	Preliminary Fuselage Sizing and Design	195
8.1	Fuselage Volume	196
8.2	Fuselage Fineness Ratio	213
8.3	Fuselage Shapes	214
8.4	Transonic and Supersonic Area-Ruling	217
	References	220
<b>Chapter 9</b>	High-Lift Devices	221
9.1	Introduction	222
9.2	Mechanical High-Lift Devices: Trailing Edge Flaps	222
9.3	Mechanical High-Lift Devices: Separation Delay Devices	223
9.4	Methods for Determining Maximum Subsonic $C_L$ of Mechanical Lift Devices	230
9.5	Subsonic Drag Due to Flap Deflection	242
9.6	Powered High-Lift Devices for STOL	242
9.7	Powered High-Lift Devices for V/STOL	248
	References	253

<b>Chapter 10</b>	Takeoff and Landing Analysis	255
10.1	Introduction	256
10.2	Ground Effects	257
10.3	Takeoff Analysis	260
10.4	Landing Analysis	267
10.5	Aircraft Retardation Devices	270
10.6	Critical Field Length (Balanced Field Length)	273
10.7	Comparison of Analytical Estimates With L-1011 Flight Test	273
10.8	Airport Operations	281
	References	282
<b>Chapter 11</b>	Preliminary Sizing of the Vertical and Horizontal Tails	283
11.1	Tail Volume Coefficient Approach	284
11.2	Sizing the Vertical Tail	284
11.3	Sizing the Horizontal Tail (Aft Tailplane)	286
11.4	Horizontal Tail (Canard)	290
11.5	Tailless	291
11.6	Vertical Location of the Aft Horizontal Tail	291
11.7	Horizontal Location of the Vertical Tail References	291 292
<b>Chapter 12</b>	Designing for Survivability (Stealth)	293
12.1	Putting Things in Perspective	294
12.2	Designing for Reduced Vulnerability	295
12.3	Designing for Reduced Susceptibility	297
12.4	Radar Cross Section (RCS) Signatures	300
12.5	Infrared	313
12.6	Visual Signature	317
12.7	Acoustic Signature	317
12.8	Case Study—AGM-129A Advanced Cruise Missile References	319 320
<b>Chapter 13</b>	Estimating Wing–Body Aerodynamics	323
13.1	Linear Lift Curve Slope	325
13.2	Drag-Due-to-Lift	331
13.3	Zero-Lift Drag Coefficient	336
13.4	Combined Vehicle Aerodynamics References	353 353

<b>Chapter 14</b>	Propulsion System Fundamentals	355
14.1	Introduction	356
14.2	Operation of Propeller Systems	357
14.3	Operation of Turbine Systems	363
14.4	Ramjet Engine Operation	373
14.5	Rocket Operation	375
	References	382
<b>Chapter 15</b>	Turbine Engine Inlet Design	383
15.1	Introduction	384
15.2	Pressure Recovery and Inlet Types	385
15.3	Capture-Area Ratio or Mass-Flow Ratio (Supersonic Flow)	395
15.4	Variable-Geometry Inlets	397
15.5	Quality of the Airflow—Distortion and Turbulence	399
15.6	Weight and Cost	401
15.7	Inlet Sizing and Design	402
	References	412
<b>Chapter 16</b>	Corrections for Turbine Engine Installation	413
16.1	Introduction	414
16.2	Total Pressure Recovery	414
16.3	Engine Bleed Requirements	416
16.4	Inlet Flow Distortion	416
16.5	Inlet Drag	416
16.6	Additive (or Spillage) Drag	417
16.7	Boundary Layer Bleed Drag	422
16.8	Bypass Drag	425
16.9	Boundary Layer Diverter Drag	425
16.10	Nozzle–Airframe Interference Effects	427
	References	434
<b>Chapter 17</b>	Propeller Propulsion Systems	435
17.1	Introduction	436
17.2	Why Propellers?	436
17.3	Theory	437
17.4	Preliminary Design	448
17.5	Shaft Engine Characteristics	459
	References	464

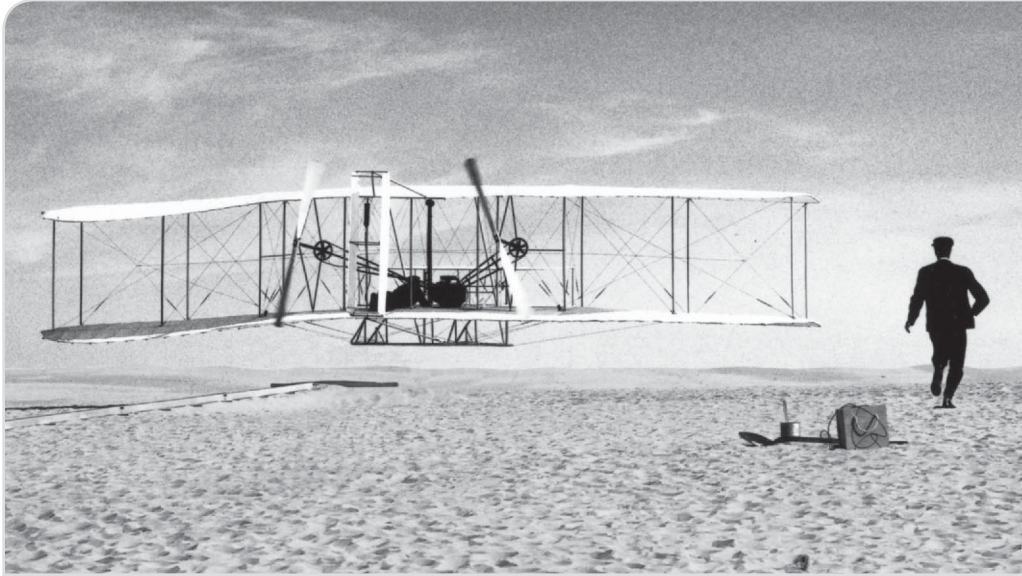
<b>Chapter 18</b>	<b>Propulsion System Thrust Sizing</b>	467
18.1	Introduction	468
18.2	Turbine Engine Scaling	468
18.3	Turbine Engines Sized for Cruise Efficiency	469
18.4	Energy Maneuverability (Air-to-Air Combat)	471
18.5	Engine Sizing for Acceleration	472
18.6	Turbine Engine Sizing for Takeoff	473
18.7	Solar Power	477
18.8	Sizing Solar-Powered Aircraft	480
18.9	Piston Engine Sizing—HAARP	486
18.10	Human-Powered Aircraft—Daedalus	487
18.11	Rocket Engine Sizing	488
	References	490
<b>Chapter 19</b>	<b>Structures and Materials</b>	491
19.1	Introduction	492
19.2	Structural Design Criteria and External Loads	493
19.3	Stress Analysis	500
19.4	Finite Element Modeling	507
19.5	Structural Joints	510
19.6	Durability and Damage Tolerance	513
19.7	Mass Properties	514
19.8	Flutter and Dynamics	516
19.9	Structural Layout	517
19.10	Material Selection	525
19.11	Composite Materials	527
19.12	Sandwich Structure	529
19.13	Structural Testing	531
19.14	Summary	550
	References	550
<b>Chapter 20</b>	<b>Refined Weight Estimate</b>	551
20.1	Introduction	552
20.2	Weight-Estimation Methods	553
20.3	Determining Center of Gravity and Moments of Inertia	572
	References	574
<b>Chapter 21</b>	<b>Static Stability and Control</b>	575
21.1	Introduction	576
21.2	Federal Regulations	578
21.3	Static Stability and Control Considerations	579

<b>21.4</b>	Static Longitudinal Stability and Control	580
<b>21.5</b>	Static Lateral Stability and Control	587
<b>21.6</b>	Static Directional (Weathercock) Stability and Control	594
<b>21.7</b>	Aft Tail Location for Reduced Pitch-Up	597
	References	600
<b>Chapter 22</b>	Trim Drag and Maneuvering Flight	601
<b>22.1</b>	Neutral Point and Static Margin	602
<b>22.2</b>	Aft Tail Deflection to Trim $n = 1$ Flight	603
<b>22.3</b>	Canard Deflection for Trim at $n = 1$	607
<b>22.4</b>	Control of a Tailless Aircraft at $n = 1$	608
<b>22.5</b>	Aft Tail Deflection for Maneuvering Flight—Pull-Up Maneuver	610
<b>22.6</b>	Canard Deflection for Maneuvering Flight—Pull-Up Maneuver	611
<b>22.7</b>	Elevon Deflection for a Tailless Aircraft in Maneuvering Flight—Pull-Up Maneuver	611
<b>22.8</b>	Control Deflection for Level Turn Maneuvering Flight	611
	References	612
<b>Chapter 23</b>	Control Surface Sizing Criteria	613
<b>23.1</b>	Government Regulations Require Static Stability	614
<b>23.2</b>	Center of Gravity Location	615
<b>23.3</b>	Sizing the Horizontal Surface	618
<b>23.4</b>	Sizing the Vertical Tail	620
<b>23.5</b>	Sizing the Ailerons	623
	References	624
<b>Chapter 24</b>	Life Cycle Cost	625
<b>24.1</b>	Life Cycle Cost	626
<b>24.2</b>	DT&E and Acquisition—Production Costs	629
<b>24.3</b>	Operations and Maintenance Phase	644
<b>24.4</b>	O&M Costs	647
<b>24.5</b>	Design for Reduced Cost	648
	References	650
<b>Chapter 25</b>	Trade Studies and Sizing	651
<b>25.1</b>	Introduction	652
<b>25.2</b>	Carpet Plots and Knotholes	653
<b>25.3</b>	Design Trades	660
<b>25.4</b>	Mission Trades	660

25.5	Technology Trades	661
25.6	Risk Analysis	662
25.7	Now We Are Done	665
25.8	Kelly Johnson's 14 Rules of Management	665
	References	668
<b>Appendix A</b>	Conversions	669
A.1	Unit Conversions	670
A.2	Temperature Conversions	678
A.3	Gases and Liquids	679
<b>Appendix B</b>	Atmospheric Data	681
<b>Appendix C</b>	Isentropic Compressible Flow Functions	689
C.1	One-Dimensional Isentropic Compressible Flow Functions for a Perfect Gas with Constant Specific Heat and Molecular Weight, $\gamma = 1.4$	690
<b>Appendix D</b>	Normal Shock Functions for a Perfect Gas	697
D.1	One-Dimensional Normal Shock Functions for a Perfect Gas with Constant Specific Heat and Molecular Weight, $\gamma = 1.4$	698
<b>Appendix E</b>	Plane Oblique and Conical Shocks	703
E.1	Perfect Gas with Constant Specific Heat and Molecular Weight, $\gamma = 1.4$	704
	Reference	713
<b>Appendix F</b>	NACA Airfoil Nomenclature and Data	715
F.1	Introduction	716
F.2	NACA Airfoil Nomenclature and Characteristics	716
F.3	Selecting an Airfoil	729
	Reference	731
<b>Appendix G</b>	Aerodynamic Data of Real Aircraft	733
G.1	How To Use Aerodynamic Data	734
G.2	How to Estimate Subsonic Drag Polar	741
	Reference	743
<b>Appendix H</b>	Aerodynamics of Wing–Body Combinations	745
	Reference	757

<b>Appendix I</b>	Aircraft Weights Data	759
<b>I.1</b>	Introduction	760
<b>I.2</b>	Empty-Weight Trends for Conventional Metal Structure	760
<b>I.3</b>	Adjustment Factors for Advanced Composite Structure	777
<b>I.4</b>	Development of the Sailplane and Weight Trends	783
<b>I.5</b>	Square–Cube Law	784
	Reference	784
<b>Appendix J</b>	Propulsion Data	785
<b>J.1</b>	Design Tasks and Propulsion Data	786
<b>J.2</b>	Gas Turbine Engines	786
<b>J.3</b>	Piston, Turboprop, and Turbofan Engines	786
<b>Appendix K</b>	Miscellaneous Data	823
<b>K.1</b>	General Scientific Data	824
<b>K.2</b>	City Populations and Capital Cities	830
<b>K.3</b>	Airports	841
	Index	867

# Chapter 1 Introduction



- There Is Never a Right Answer
- Requirements—Requirements Pull & Technology Push
- Always Question the Requirements
- Measure of Merit
- UAVs
- Specs, Standards, & Regulations
- Design Phases
- Scope of Text

First manned, powered controlled flight at Kitty Hawk on 17 December 1903. This photo shows Wilbur running alongside, with Orville at the controls. The flight lasted 12 seconds and covered 120 feet. Three more flights were made that day, with the last one traveling 852 feet!

*It's only a dust cover!*

Leland Nicolai (1975)



## 1.1 Aeronautics—The Beginning

**A**eronautics is a relatively new engineering discipline that is little more than 100 years old. However, serious thoughts about how people could fly have been on the minds of laymen and scholars over the last 500 years. Leonardo da Vinci designed many variations of machines that would allow people to fly. However, serious aeronautical analysis and experimentation did not happen until the early 19th century when Sir George Cayley first started applying the basic laws of flight and the scientific method to the development of manned flight. Cayley's work would influence airplane designers for the next 50 years. He was the first to identify the four fundamental forces of thrust, lift, drag, and weight and their interrelationship in flight mechanics. In particular, he correctly understood and documented that wings should be responsible for lift and engines responsible for thrust. Cayley was also the first to understand and incorporate the concept of cambering to change the lift of a wing. His close observation of bird flight was directly responsible for adding camber to his earliest flying models. He also correctly predicted that continued manned flight could not happen until the development of an engine with a high thrust-to-weight ratio. It would take another 50 years for that engine to be developed. Although history has highlighted the importance of work by Samuel Langley and the Wright brothers, it was Cayley who designed and built the glider that carried the first human aloft. It would take over four decades for someone else to equal this accomplishment.

In the late 1800s many people were attempting to develop efficient gliders to better understand the fundamental principles of flight. Glider designers such as Otto Lilienthal (who would lose his life in a glider accident) and Octave Chanute contributed greatly to the body of knowledge that Langley and the Wrights would use in their pursuit of powered manned flight. Even though December 1903 is heralded as the beginning of powered manned flight, many evolutionary efforts had incrementally led up to this historic event.

As the Wright brothers continued to improve on their design, it created an opportunity for a new engineering discipline—aeronautics. Past efforts had been performed by people who designed, analyzed, and experimentally verified their ideas. Soon, brilliant scholars and teachers such as Ludwig Prandtl and Theodore von Kármán would emerge as pillars of aeronautical thought and principles. At this time, the fluid mechanics principles of Daniel Ber-

*"It's only a dust cover."* This is not meant to trivialize the external shape of an aircraft design. It is merely a reminder to the designer that protecting and delivering the payload is crucial for mission success. Adding features not related to the payload always results in a more expensive design.

Sir George Cayley's coachman was actually the first person to successfully fly in a glider. This event took place in England in 1853 and the flight covered a distance of approximately 900 feet. It was the only time the coachman flew.

noëlli were used by these analytical pioneers as the foundation of the formal engineering discipline *aeronautical engineering*. Prandtl concentrated on subsonic flow and was the first to postulate the existence of the boundary layer and its influence on flow separation. Von Kármán is reknowned for his contributions to the understanding of supersonic and hypersonic flight regimes.

## 1.2 Aircraft Design—A Compromise

The design of an aircraft is a large undertaking requiring the team efforts of many engineers having expertise in the areas of aerodynamics, propulsion, structures, flight control, performance, and weights. As the design takes shape, specialists are called in to design such components as the crew station, landing gear, interior layout, armament location, and equipment installation. The completed aircraft design is a compromise of the best efforts of many talented engineers. The different design groups they represent must work together to produce the most efficient flight vehicle. It should be clear that the design process is a very involved integration effort, requiring the pulling together and blending of many engineering disciplines. The key element in the design process is the design team leader, or Chief Designer, who acts as the integrator and referee. The Chief Designer is usually one who understands and appreciates all of the various disciplines involved in the design process and is often called upon to negotiate compromises between the design groups. For example, the propulsion group might propose an inlet arrangement that aggravates the clean configuration of the aerodynamics group. At the same time, the structures group might recommend a wing thickness ratio of 8% while the aerodynamics group might choose 2%. The flight control group might complicate matters by putting an aft tail on the design and insisting that the wing be moved forward for better balance. The Chief Designer will pull the design groups together to bring about the best compromise toward the design goal. The Chief Designer must prevent any one design group from driving the design, which might otherwise produce one of the designs shown in Fig. 1.1.

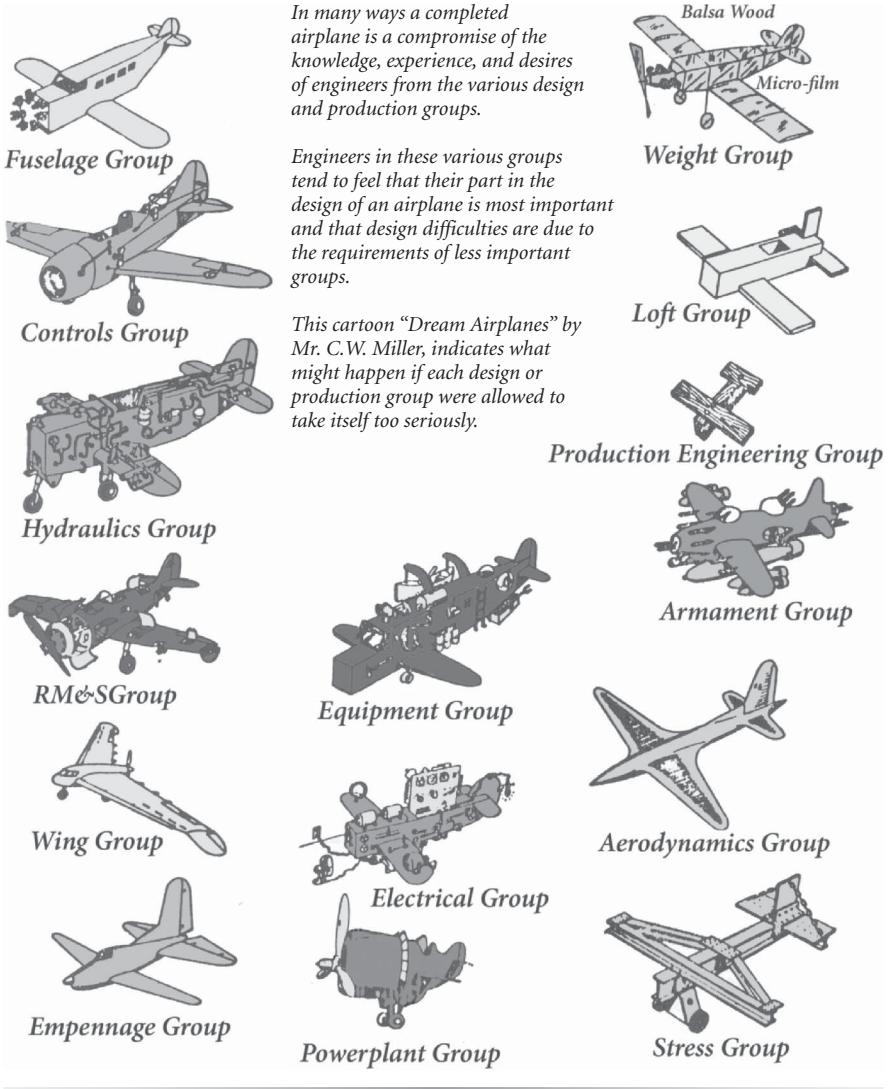
### 1.2.1 Performance vs Cost

Prior to the 1970s, the performance of the aircraft was paramount. All design efforts were

Let us hope that the advent of a successful flying machine, now only dimly foreseen and nevertheless thought to be possible, will bring nothing but good into the world; that it shall abridge distance, make all parts of the globe accessible, bring men into closer relation with each other, advance civilization, and hasten the promised era in which there shall be nothing but peace and goodwill among all men.

*Octave Chanute, circa 1895*

Bernoulli's complex book was titled "Hydrodynamica." As a favor, his close friend and famed mathematician Leonhard Euler rewrote the book to be more understandable. The basis of the Bernoulli principle is established in this work.



**Figure 1.1** Resulting aircraft design if one group is dominant.

focused to produce a vehicle displaying maximum performance for a given aircraft weight or a minimum weight for a specified level of performance. Cost was a consideration after the aircraft design was "locked in." In the late 1960s, the government and the aircraft industry became extremely cost-conscious. The acquisition cost of aircraft systems was skyrocketing and the measure of merit became minimum acquisition cost. The A-10A Thunderbolt II was designed in the late 1960s for an acquisition cost of \$3

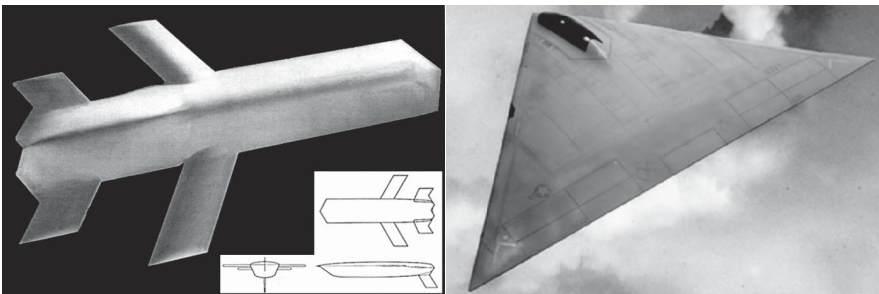
million. The Lightweight Fighter competition in the early 1970s had a unit cost requirement of \$5 million and led to the F-16 and F-18. This cost metric later changed to life cycle cost (LCC; the sum of the development cost, acquisition cost, and operation and support cost) in the late 1970s. This emphasis on design-to-cost [1] brought two new players into the design team: the cost analyst and the manufacturing expert, who were installed in the design team with full voting rights. The cost and performance trade study results have become key considerations in design decisions.

Aircraft program costs spiraled out of control in the 1990s and led to the cancellation of the U.S. Navy A-12 Avenger and TSSAM/AGM-137 Tri-Service Standoff Attack Missile, shown in the photograph (Fig. 1.2). It was at this point in time that the principle of cost as an independent variable (CAIV) was introduced as a legitimate design criterion. The U.S. government instituted the CAIV principle as part of its acquisition regulation for military systems DoD 5000.1 [2], which states that cost must be considered to be equal in importance with performance and that programs must show the cost gradient with respect to performance. Essentially, CAIV is the government equivalent of commercial best business practices.

In many ways a completed airplane is a compromise of the knowledge, experience, and desires of engineers from the various design and production groups.

Engineers in these various groups tend to feel that their part in the design of an airplane is most important and that design difficulties are due to the requirements of less important groups.

The cartoon “Dream Airplanes,” by Mr. C. W. Miller, (Fig. 1.1) indicates what might happen if each design or production group were allowed to take itself too seriously.



**Figure 1.2** A-12 and TSSAM; both programs were cancelled by the Navy due to cost growth.

## 1.2.2 There Is Never a Right Answer

In the design of an aircraft there is never a right answer—only a best answer at a point in time. The reason is that the design of an aircraft is a balance between the following competing requirements:

- **Technical.** Performance, survivability
- **Signature.** Survivability, appearance
- **Economic.** Cost, LCC
- **Political.** Policy, payback, risk, and so on
- **Schedule.** When needed? The need to be first to market
- **Environmental.** Limited energy source, noise, hydrocarbon emissions

Also, the priorities of these requirements change with time. An aircraft might be designed to certain technical and economic requirements, but if the government administration changes, then the priority requirement becomes political or environmental. The advice to the designer is to remain flexible and develop as robust a design as possible so that it will survive as the requirements change over time. The watchwords are *compromise*, *balance*, and *flexibility*.

## 1.3 Overall Design Requirements

Before designing a building, an architect must first establish who and how many will occupy the building, what is its purpose, what are its scale and cost level, and so on. The design of an aircraft is similar in that the aircraft designer must have requirements established before a design can proceed. The requirements define the following: (1) what mission the aircraft will be called upon to perform, (2) how much the aircraft should cost, (3) how the aircraft should be maintained and supported, and (4) the schedule for the aircraft.

### 1.3.1 Mission Requirements

The mission requirements identify the following:

- **Purpose.** Commercial transport; air-to-air fighter, air-to-ground fighter, bomber; general aviation; intelligence, surveillance, and reconnaissance (ISR); trainer, and so on
- **Crew.** Manned or unmanned
- **Payload.** Passengers, cargo, weapons, sensors, and so on
- **Speed.** Cruise, maximum, loiter, landing, and so on
- **Distance.** Range or radius
- **Duration.** Endurance or loiter (time-on-station)

- **Field length.** Vertical, short, or conventional takeoff and landing (VTOL, STOL, CTOL)
- **Signature level.** Radar cross section (RCS); infrared (IR); visual; and acoustic (noise)

In 2007 for a typical airline seat, 5% of the ticket went to pay for aircraft maintenance; 25% for taxes and fees; 30% for salaries; 30% for fuel; and 10% miscellaneous.

### 1.3.2 Cost Requirements

Cost requirements encompass the following:

- Development cost
- Acquisition cost
- Operation and support (O&S) cost
- Life cycle cost (LCC), which is the sum of development, acquisition, and O&S
- Cost as an independent variable (CAIV) for government programs

### 1.3.3 Maintenance and Support Requirements

The maintenance and support requirements are as follows:

- Maintenance man-hours per flight hour (MMH/FH)
- Ground support equipment (GSE)
- Maintenance levels (i.e., organizational, intermediate, and depot)
- Integrated logistics support (ILS) plan
- Contractor support or user support

### 1.3.4 Scheduling Requirements

The schedule requirements identify the following:

- Development and test scheduling
- Product availability, that is, when the aircraft should be available for deployment [initial operational capability (IOC)] to the warfighter or the commercial customer

### 1.3.5 Where Do the Design Requirements Come From?

In the case of a commercial program, the requirements are usually established by the aircraft supplier, such as Boeing, Lockheed Martin, Northrop-Grumman, Gulfstream, Cessna. The aircraft companies perform market analyses to determine what the public's needs or desires will be in the near future. Projections are made for

For military aircraft ~67% of the LCC is for O&S costs.

future passenger travel, air freight needs, and general aviation aircraft demands. The commercial program is kicked off when a customer steps up and shows serious intent to buy the production airplane. A down payment usually entitles the customer to influence some of the requirements.

The Boeing 777 airliner was a cultural change for Boeing as they invited eight airlines (called the “Gang of Eight”) to develop the requirements for the B777 in the early 1990s. It is recommended that the reader review the Boeing 777 Case Design Study in Volume 2.

Careful thought and research must go into establishing the requirements because if they are inappropriate, then the aircraft (if it is even built) may not find a customer or keep its initial customers. Aircraft companies have lost large sums of money because they followed a bad or inappropriate set of requirements. American millionaire Howard Hughes decided in 1942 that the world needed a large plywood flying boat capable of carrying 700 passengers. The U.S. government agreed (initially) but changed its mind and Mr. Hughes was left with one wooden aircraft giant that made one flight of only six seconds. Today, it is generally felt that the technical design of the Hughes Hercules aircraft was sound, but the mission requirements were about 25 years ahead of their time.

Sometimes the requirements are established by a military user such as the U.S. Air Force (USAF), U.S. Navy and Marines (USN), or U.S. Army. These requirements are usually developed to fill a military need (shortfall) or to replace an obsolete system. Such requirements are termed a *requirements pull* because the military need “pulls” the requirements.

Figure 1.3 is an example of an early military requirement for an aircraft. The mission requirements were pretty demanding, in that they required a payload of 350 lb, a top speed of 40 mph, and that the aircraft had to be easily transportable in an Army wagon. This procurement was sole-sourced to two brothers in Dayton, Ohio, named Wilbur and Orville Wright. It is interesting to note that the contract for the heavier-than-air flying machine was for \$25,000 and called for delivery in seven months. The photograph (Fig. 1.4) shows a Wright brothers design for Specification 486.

A more modern example of a requirement that met both a military and a commercial requirement was the Request for Proposal (RFP) in the mid-1950s for a utility jet transport. In August of 1956, the USAF addressed an RFP to industry expressing a requirement for a “Twin Jet Aircraft (UTX) to fulfill utility and pilot readiness missions.” The letter also stated: “It appears that commercial requirements for such utility and transport aircraft are realistic. ...” In accordance with the USAF’s RFP, industry was to develop a prototype for evaluation without government compensation because “... there is a potential commercial market for these aircraft” and the “... estimated costs of development programs of this type are within the capability

## SIGNAL CORPS SPECIFICATION, NO. 486

## ADVERTISEMENT AND SPECIFICATION FOR A HEAVIER-THAN-AIR FLYING MACHINE

## TO THE PUBLIC:

Sealed proposals, in duplicate, will be received at this office until 12 o'clock noon on February 1, 1908, on behalf of the Board of Ordnance and Fortification for furnishing the Signal Corps with a heavier-than-air flying machine. All proposals received will be turned over to the Board of Ordnance and Fortification at its first meeting after February 1 for its official action.

Persons wishing to submit proposals under this specification can obtain the necessary forms and envelopes by application to the Chief Signal Officer, United States Army, War Department, Washington, D. C. The United States reserves the right to reject any and all proposals.

Unless the bidders are also the manufacturers of the flying machine they must state the name and place of the maker.

*Preliminary.*—This specification covers the construction of a flying machine supported entirely by the dynamic reaction of the atmosphere and having no gas bag.

*Acceptance.*—The flying machine will be accepted only after a successful trial flight, during which it will comply with all requirements of this specification. No payments on account will be made until after the trial flight and acceptance.

*Inspection.*—The Government reserves the right to inspect any and all processes of manufacture.

## GENERAL REQUIREMENTS.

The general dimensions of the flying machine will be determined by the manufacturer, subject to the following conditions:

1. Bidders must submit with their proposals the following:

- (a) Drawings to scale showing the general dimensions and shape of the flying machine which they propose to build under this specification.
- (b) Statement of the speed for which it is designed.
- (c) Statement of the total surface area of the supporting planes.
- (d) Statement of the total weight.
- (e) Description of the engine which will be used for motive power.
- (f) The material of which the frame, planes, and propellers will be constructed. Plans received will not be shown to other bidders.

2. It is desirable that the flying machine should be designed so that it may be quickly and easily assembled and taken apart and packed for transportation in army wagons. It should be capable of being assembled and put in operating condition in about one hour.

3. The flying machine must be designed to carry two persons having a combined weight of about 350 pounds, also sufficient fuel for a flight of 125 miles.

4. The flying machine should be designed to have a speed of at least forty miles per hour in still air, but bidders must submit quotations in their proposals for cost depending upon the speed attained during the trial flight, according to the following scale:

40 miles per hour, 100 per cent.
39 miles per hour, 90 per cent.
38 miles per hour, 80 per cent.
37 miles per hour, 70 per cent.
36 miles per hour, 60 per cent.
Less than 36 miles per hour rejected.
41 miles per hour, 110 per cent.
42 miles per hour, 120 per cent.
43 miles per hour, 130 per cent.
44 miles per hour, 140 per cent.

5. The speed accomplished during the trial flight will be determined by taking an average of the time over a measured course of more than five miles, against and with the wind. The time will be taken by a flying start, passing the starting point at full speed at both ends of the course. This test subject to such additional details as the Chief Signal Officer of the Army may prescribe at the time.

6. Before acceptance a trial endurance flight will be required of at least one hour during which time the flying machine must remain continuously in the air without landing. It shall return to the starting point and land without any damage that would prevent it immediately starting upon another flight. During this trial flight of one hour it must be steered in all directions without difficulty and at all times under perfect control and equilibrium.

7. Three trials will be allowed for speed as provided for in paragraphs 4 and 5. Three trials for endurance as provided for in paragraph 6, and both tests must be completed within a period of thirty days from the date of delivery. The expense of the tests to be borne by the manufacturer. The place of delivery to the Government and trial flights will be at Fort Myer, Virginia.

8. It should be so designed as to ascend in any country which may be encountered in field service. The starting device must be simple and transportable. It should also land in a field without requiring a specially prepared spot and without damaging its structure.

9. It should be provided with some device to permit of a safe descent in case of an accident to the propelling machinery.

10. It should be sufficiently simple in its construction and operation to permit an intelligent man to become proficient in its use within a reasonable length of time.

11. Bidders must furnish evidence that the Government of the United States has the lawful right to use all patented devices or appurtenances which may be a part of the flying machine, and that the manufacturers of the flying machine are authorized to convey the same to the Government. This refers to the unrestricted right to use the flying machine sold to the Government, but does not contemplate the exclusive purchase of patent rights for duplicating the flying machine.

12. Bidders will be required to furnish with their proposal a certified check amounting to ten per cent of the price stated for the 40-mile speed. Upon making the award for this flying machine these certified checks will be returned to the bidders, and the successful bidder will be required to furnish a bond, according to Army Regulations, of the amount equal to the price stated for the 40-mile speed.

13. The price quoted in proposals must be understood to include the instruction of two men in the handling and operation of this flying machine. No extra charge for this service will be allowed.

14. Bidders must state the time which will be required for delivery after receipt of order.

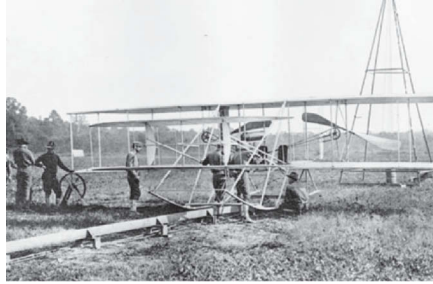
JAMES ALLEN,

Brigadier General, Chief Signal Officer of the Army.

SIGNAL OFFICE,  
WASHINGTON, D. C., December 23, 1907.

Figure 1.3 First published mission requirement for a military aircraft, 20 January 1908.





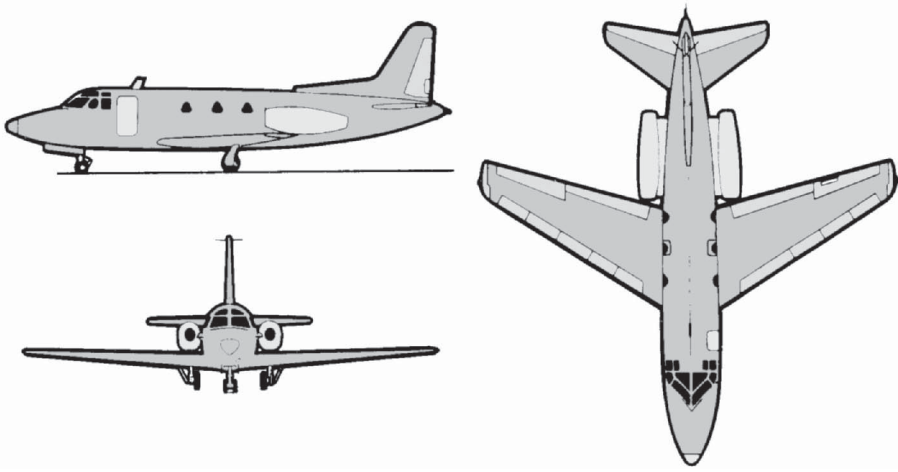
**Figure 1.4** Wright Brothers’ design for Specification 486.

of industry.” The Air Force estimated that the flyaway cost of these aircraft would be about \$200,000 each.

The letter was accompanied by a General Design Requirement document that described the requirements of the aircraft in detail. Some of the more pertinent requirements were as follows:

Range	1500 nautical miles
Maximum cruise ceiling	45,000 ft
Service ceiling (one-engine)	15,000 ft
Critical field length	5000 ft
Landing roll (1/2 fuel)	2500 ft
Cruise speed	0.76 Mach
Payload	2 crew, 4 passengers, 240 lb of baggage
Escape	Inflight escape provisions
Fueling	Single point, pressure refueling
Instrumentation	Military-type instruments and avionics
Certification	Suitable for certification by the Federal Aviation Administration (FAA)

North American Rockwell had actually initiated UTX design work in the spring of 1952 so they were more than ready in August of 1956. They firmed up their baseline design and pressed into fabrication of their prototype Sabreliner. The prototype aircraft was completed and the first flight of the Sabreliner was accomplished in September 1958. North American Rockwell won the UTX competition and was awarded a contract in January 1959 for seven flight test aircraft. The aircraft that resulted from the UTX mission requirement is designated the USAF T-39 and is shown in Fig. 1.5. The characteristics of the T-39 are shown in Table 1.1. North American Rockwell has produced several very successful commercial derivatives of the T-39: the Sabreliner Series 40, Series 50, Series 60, and Series 75. All of the Sabreliner series have similar configuration geometry but incorporate different interior arrangements, special mission features, uprated propulsion units, and different equipment.



**Figure 1.5** North American Rockwell T-39 Sabreliner.

**Table 1.1** Characteristics of the U.S. Air Force T-39

Wing span	44 ft 4 in.
Length	43 ft 9 in.
Maximum takeoff weight	19,000 lb
Empty weight	9805 lb
Fuel weight	7122 lb
Crew	2
Payload	9 passengers or 2100 lb
High speed at 41,000 ft	Mach 0.76
Cruise speed at 42,000 ft	Mach 0.7
Service ceiling (one engine)	21,500 ft
Range	2060 miles
Critical field length	4900 ft
Landing distance	2190 ft
Engines	Two JT12A
W/S at takeoff	55 psf
Wing sweep ( $\frac{1}{4}$ chord)	28°33'
Wing aspect ratio	5.77
Number built	149 for USAF; 42 for USN

Sometimes a new technology will push the requirements for a new aircraft (termed a *technology push*). The jet engine in the early 1940s, stealth technology in the mid-1970s, and the high-energy airborne laser in the early 1990s are examples of technology push requirements that led to the XP-80, the Have Blue/F-117, and the YAL-1/ABL, respectively.

The requirements usually come with a document called a Concept of Operations, or ConOps for short. The ConOps describes how the aircraft will be deployed, operated, maintained, and supported—essentially all the information the designer needs to complete the design. The ConOps is helpful for a commercial aircraft but is essential for a military aircraft. For example, the military aircraft designer needs to know if the threat defenses will be “up and in-place” or rolled back, if fuel tankers will be available, and what the maintenance concept will be: organization, intermediate, depot, contractor logistics support, and so on.

### 1.3.6 Need to Question the Requirements

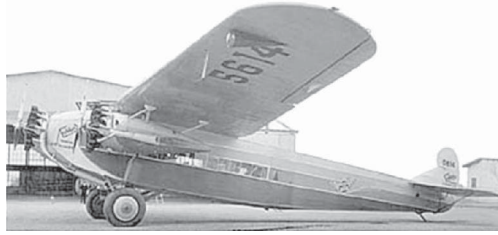
When the requirements arrive, the designer *must* study them, understand them, evaluate them, and question them—and if necessary negotiate them with the customer—because a designer who does not agree with the requirements must walk away. Disagreement with the fundamental requirements will sap the designer’s passion and commitment, which are necessary to generate a successful conceptual design that will ultimately be selected to proceed into preliminary design.

Even when the customer tries very hard to generate a credible set of requirements, sometimes they are flawed. History is filled with flawed requirements. Some flawed requirements are discovered and changed, some flawed requirements prevail and designs are produced, and some flawed requirements are ignored (this one is always risky). Three examples of flawed requirements are the following:

- 1932 Transcontinental and Western Air, Inc. (TWA) replacement of Fokker F-10A
- 1985 USAF Advanced Tactical Fighter (ATF)
- 1995 USAF Joint Air-to-Surface Standoff Missile (JASSM)

#### TWA Specification—1932

In the late 1920s and early 1930s, the flagship of the TWA commercial transport fleet was the three-engine Fokker F-10A Trimotor. In 1931 an F-10A crashed, taking the life of Knute Rockne, the famed Notre Dame football coach [see the photograph (Fig. 1.6)]. Inspectors blamed moisture inside the wooden wing that caused the wing structure of the F-10A to separate. The Aeronautics Branch, Department of Commerce (predecessor to



**Figure 1.6** Fokker F-10A.

the FAA), suspended the airworthiness certificate of the F-10A, grounding a major part of the TWA fleet. In August 1932 TWA issued the specification for a modern luxury transport airplane shown in Fig. 1.7. Although the TWA document specified an all-metal three-engine aircraft, the contract winner was the two-engine DC-1. Donald Douglas took a risk and offered up a two-engine design. The TWA specs were an extreme challenge for the time, but were met and exceeded by the DC-1, predecessor to the famous DC-3 and World War II C-47 [see the photograph (Fig. 1.8)]. Even though only one DC-1 was built, and 218 DC-2s, the Douglas Aircraft Company turned out 13,300 DC-3s. The fact that DC-3s are still flying today is a testament to the design genius of Donald Douglas.

### USAF ATF Specification—1985

In 1985 the USAF issued an RFP for a new air-to-air advanced tactical fighter to replace the F-15. The RFP requirements called for “supermaneuver” and “supercruise” [the ability to cruise at supersonic speeds on dry power (without afterburners)]—and a modest signature level. The Lockheed Skunk Works challenged the requirements and convinced the USAF that the radar cross section (RCS) levels in their signature requirement

- All Metal Trimotor Monoplane
- Payload : 12 passengers
- Range: 1000 miles
- Crew: 2
- Top Speed, Sea Level: 185 mph
- Cruising Speed, Sea Level: 145 mph
- Landing Speed: 65 mph
- Service Ceiling: 21000 ft
- Rate of climb, Sea Level: 1200 fpm
- Maximum Gross Weight: 14200 lb
- Passenger compartment must have ample room for comfortable seats, miscellaneous fixtures and conveniences
- Airplane must have latest radio equipment, flight instruments and navigational aids for night flying

**Figure 1.7** TWA specification for a new transport aircraft (August 1932).

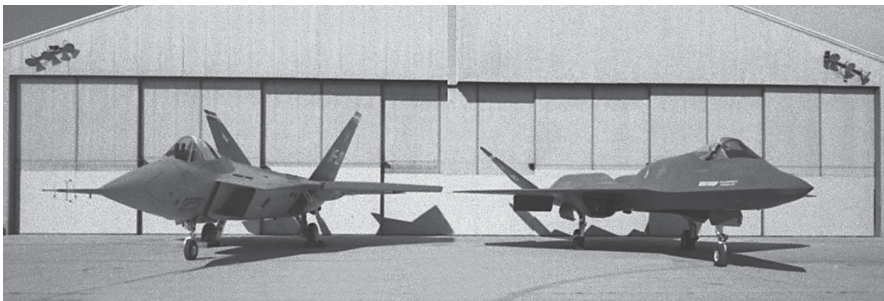


**Figure 1.8** DC-3—timeless elegance (courtesy of Gary Shepard).

should be lowered to be a true 21st-century fighter. The USAF agreed and recalled the RFP and reissued it in February 1986 with superstealth as a requirement. Lockheed (YF-22) and Northrop (YF-23) [see the photograph (Fig. 1.9)] won contracts to build two prototypes each and have a fly-off. The rest is history.

### USAF JASSM Specification—1995

In the spring of 1995 the Department of Defense (DoD) canceled the stealthy air-launched cruise missile named Tri-Service Standoff Attack Missile (TSSAM/AGM-137) because of excessive unit cost. The mission need for the TSSAM still existed so a draft RFP was issued to industry in the fall of 1995 for JASSM. The JASSM requirements were the same performance as TSSAM but a higher signature (RCS). The unit cost requirement was \$400,000—the same as TSSAM. The USAF concluded that the only way to meet the unit cost requirement was to ask for a derivative of an existing cruise missile (forcing the increase in the signature requirement). The 1995 RFP specified a derivative missile. Lockheed Martin questioned the requirements. The Skunk Works convinced the USAF that they could have the same performance, signature, and unit cost as TSSAM with



**Figure 1.9** YF-22 and YF-23—ATF competitors.



**Figure 1.10** B-2 launching a JASSM/AGM-158.

a clean-sheet design. The JASSM RFP was issued in the winter of 1996 asking for a derivative or clean-sheet design with a lower signature. Lockheed Martin and McDonnell Douglas both won contracts, with clean-sheet designs, for further work. Lockheed Martin won the production contract for the AGM-158 [shown in the photograph (Fig. 1.10) being dropped from a B-2] and is now building over 2000 cruise missiles.

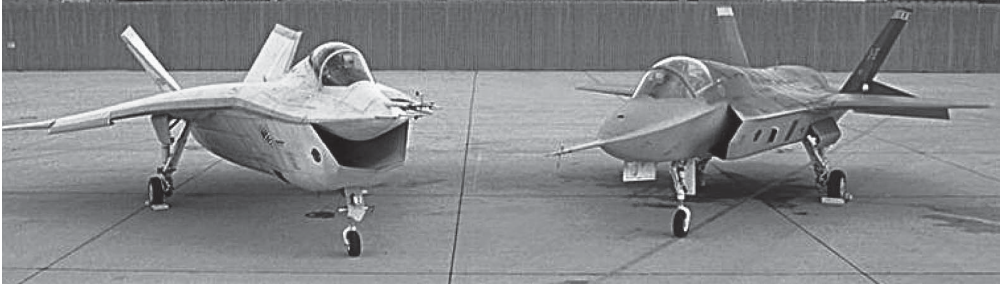
### 1.3.7 Measure of Merit

To be acceptable to the customer, the aircraft design must meet (or exceed) the stated requirements. Meeting the requirements is a necessary condition for being a candidate to proceed to the next phase. If there is a requirement that the designer cannot meet or thinks is unrealistic, then the designer needs to petition the customer for a waiver.

The *Measure of Merit* (MoM; sometimes called figure of merit) is similar to a requirement except that it is initially known only to the customer and is not overtly specified. The MoM is important to the customer and will be used as a “tie breaker” in selecting the winning design. It is often said that meeting the requirements gets you invited to the dance, but meeting the MoM gets you out on the dance floor.

Because the MoM is initially unspecified, the designer (or someone in the design group) must do the homework to understand what the customer is really looking for. Sometimes the MoM is simply that the design must be aesthetically pleasing. This seemed to be a MoM in the selection of the Lockheed Martin X-35 over the Boeing X-32 [see the photograph (Fig. 1.11)] in the Joint Strike Fighter competition. More often, however, the MoM is more substantive and is learned by developing a close rapport with the customer. It goes without saying that developing a design to the wrong MoM will lose the contract.

In the ATF competition mentioned previously, Lockheed determined that what the USAF really wanted was a fighter pilot’s airplane with supercruise and superstealth. So Lockheed made “maneuver with reckless



**Figure 1.11** X-32 and X-35—JSF competitors.

abandon” their MoM. This MoM actually compromised the supercruise Mach number and RCS, but still met the requirements. The addition of pitch thrust vectoring (not required) added weight and cost to the YF-22 but gave the airplane high angle-of-attack maneuvering that was unprecedented. This feature was demonstrated during the fly-off between the YF-22 and Northrop’s YF-23, although it was not required. The YF-23 was a beautiful airplane and actually beat the YF-22 in supercruise Mach and RCS, but the fighter pilots preferred the maneuverability of the YF-22. The F-22A is now operational with the USAF.

## 1.4 Unmanned Aerial Vehicle

The DoD defines an *unmanned aerial vehicle* (UAV) [3] as a powered aerial vehicle that does not carry a human operator, uses aerodynamic forces to provide vehicle lift, can fly autonomously or be piloted remotely, can be expendable or recoverable, and can carry a lethal or nonlethal payload. With this definition cruise missiles and aerial targets qualify as UAVs. As indicated by Table 1.2, UAVs come in all shapes and sizes [4] [see the photograph (Fig. 1.12)].

The design of unmanned and manned aircraft is the same in that they must obey the same laws of physics, but there the similarity ends. Each has advantages over the other. We should use unmanned aircraft where they have an advantage over their manned counterparts and vice versa.

The main disadvantage of the unmanned aircraft system (and hence the manned aircraft advantage) is that it cannot think for itself and cope with unforeseen or dynamically changing events. No amount of autonomy and artificial intelligence can address all the uncertainties of war. Because of this shortcoming, unmanned aircraft systems will always have off-board human operators in the loop. This means that the unmanned aircraft system must have additional sensors and data-link capability onboard to make the off-board human operator aware of the situation at all times [5].

Table 1.2 Categories of UAVs<sup>a</sup>

UAV Class	Weight Class	Current Vehicles
Micro	Several pounds	DARPA Organic Air Vehicle (Army)
Mini	<100 lb	FPASS (USAF), Pointer (Army), Dragon Eye (USMC)
Aerial target	<2500 lb	BQM-74E (Chukar), BQM-34S (Firebee), MQM-107E, BQM-167 (Skeeter)
Tactical ISR	<2000 lb	RQ-2A (Pioneer), Shadow 200, MQ-5C (E-Hunter), RQ-8A (Fire Scout)
Theater ISR and UAV	>2000 lb	RQ-1/MQ-1 (Predator), RQ-4A (Global Hawk), MQ-9 (Reaper), X-45A (USAF), X-47 (USN)
Cruise missiles	>1000 lb	AGM-84 (Harpoon), AGM-109 (Tomahawk), AGM-129 (Advanced Cruise Missile), AGM-158 (JASSM)

<sup>a</sup>See [3].

The advantages of the unmanned aircraft system are as follows [6]:

1. The design of the unmanned system is not limited by the requirement to carry a human onboard and accommodate human frailties.
2. No human is at risk of capture.
3. No infrastructure is required to recover the crew if the aircraft crashes.
4. The unmanned aircraft does not need to fly for the unmanned system to train or stay proficient.

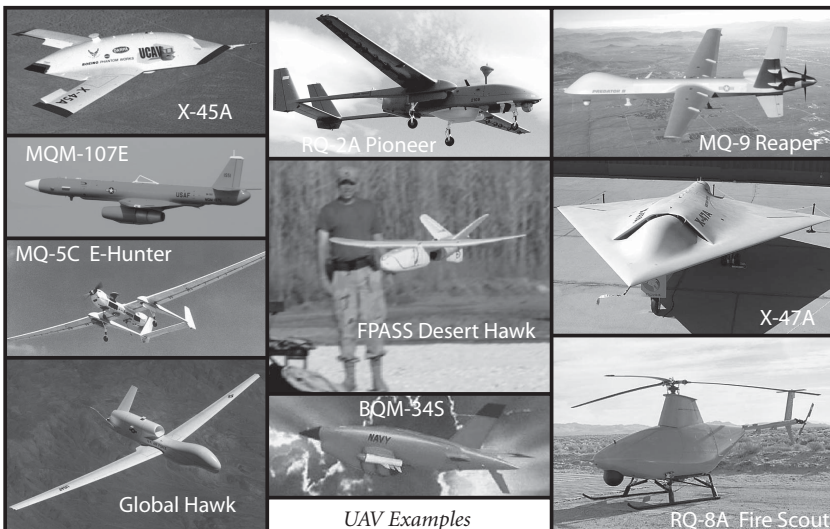


Figure 1.12 Miscellaneous UAVs.



### 1.4.1 Design Limitations—Human Operator

Unmanned operation has both plusses and minuses. On the plus side the unmanned vehicle does not have to accommodate a crew station, which gives greater design freedom in locating the inlet, engine, subsystems, and payload. The elimination of the crew station also shortens the aircraft (about 7.5 ft for a single seat and 11 ft for a tandem two seat fighter) and reduces the empty weight by eliminating the crew equipment items, such as seat, cockpit controls, instruments and Environmental Control System (ECS), and the structure for the crew station. Because we buy aircraft by the pound of empty weight (to the first order), the unit cost reduction would be by about the same percentage as the weight reduction. The design freedom that results from not having a crew station in a fighter-size aircraft is very real and should produce a more efficient utilization of internal volume, but it is hard to quantify in terms of weight or cost savings. This advantage, however, diminishes with increasing aircraft size because the crew station weight and volume becomes an ever decreasing portion of larger aircraft, as shown in Fig. 1.13.

Based upon the information in Fig. 1.13 a transport UAV does not make any sense. A transport is a large aircraft and would not have an appreciable empty weight reduction due to eliminating the crew. In addition it does not qualify for any of the UAV advantages because its cargo might be people and it is making revenue flights all the time like an ISR vehicle. On the other

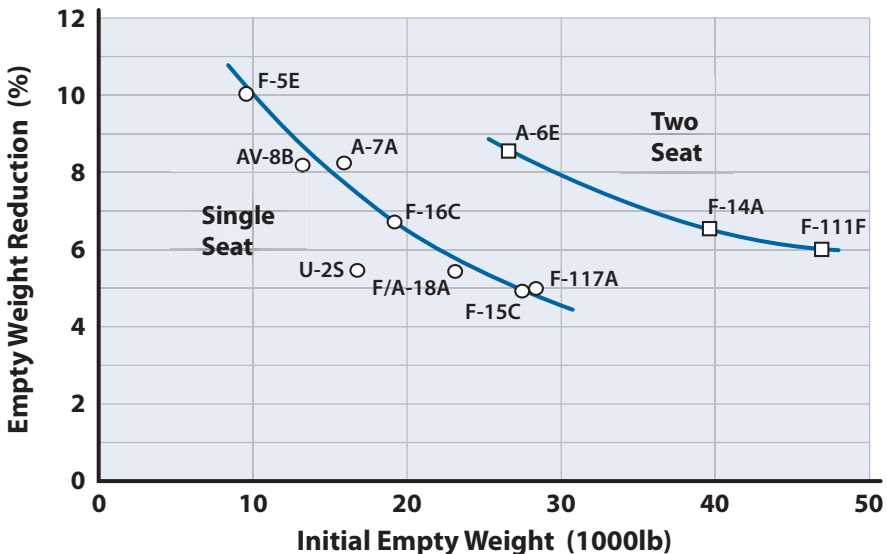


Figure 1.13 Empty weight reduction by eliminating all crew station equipment and shortening fuselage.

hand, an unmanned long range strike (LRS) vehicle may make sense as it qualifies for all the advantages.

Not having to “man-rate” the aircraft will simplify the design and development of the unmanned UAV somewhat. There will be a cost savings due to not having to man-rate the engine (engine testing) and due to the elimination of a crew escape system, canopy, and crew survival equipment (design and testing). Reducing the aircraft factor-of-safety (FS) from 1.5 to 1.25 will let the materials be worked more efficiently in structural design. In addition the safety of flight design criteria can be relaxed and the systems redundancy reduced from quadruple to dual.

Not having to man-rate the aircraft will also open the door for capabilities not available to manned aircraft. For example, the maneuver  $g$  and altitude are limited by the mechanical systems, and the endurance is limited by the size, weight, and cost of the unmanned system. This means the maneuver limit load factor can exceed  $9 g$  for a UAV and can have persistence well in excess of 12 hours for an ISR vehicle. In addition, micro-UAVs (weight on the order of a pound) and mini-UAVs (weight on the order of 500 lb) are feasible for limited surveillance missions.

However, the downside to not having a human onboard is the requirement to recover pilot functionality by having an off-board operator who has complete situational awareness. This means increasing the software development for autonomous flight, adding sensors and data links, and of course adding a ground station to the overall system development cost.

The consensus of knowledgeable aerospace professionals is that all of the plusses and minuses together will give only a modest cost reduction in the development and acquisition cost of an unmanned UAV relative to a manned aircraft [7,8]. Many advantages of UAVs tend to be political and will be discussed in the following subsections.

### 1.4.2 Risk to Human Operator

Because a human pilot is not onboard the UAV, loss of life is not a concern. Thus, the UAV could be assigned missions deemed too risky for its manned counterpart. Examples are the suppression of enemy air defenses (SEAD) mission and the employment of high-powered microwave weapons.

### 1.4.3 Elimination of Search and Rescue

The elimination of the infrastructure to search for and rescue downed crew members is a real opportunity for cost saving. In addition, the attention given a downed crew results in a significant resource shift away from combat operations. Because the crew has been eliminated from the vehicle,

the political sensitivity of the UAV mission is reduced as there is no one to be held hostage and identified with a country (e.g., Gary Powers). In an extreme case, a country could deny ownership of a “laundered” UAV.

#### **1.4.4 Training and Proficiency**

The fundamental premise is that the unmanned aircraft does not need to fly for the unmanned system to train or stay proficient. The human operator is off-board and trains by simulation. This means that when the UAV aircraft flies it should be for a revenue flight. A revenue flight for the UAV happens during wartime. During peacetime the vehicle is in some type of “flyable” storage. On the other hand, the ISR UAV flies all the time because its revenue flights are for the purpose of gathering continuous intelligence on target countries. Critics accept this premise but argue that the UAV needs to fly during peacetime as well. As part of a combined arms team, the UAVs have to operate with the manned aircraft as the humans train. This argument fails when the capability of modern air combat simulators is recognized. This notion of no (or at least minimal) peacetime flying presents a tremendous cost-saving opportunity for the UAV.

If we assume four 30-day wars over a 20-year period (typical fighter aircraft system life), the cumulative flying time (and hence design life) for the UAV is less than 1000 hours [9]. This is contrasted with manned fighter aircraft, which are designed for 8000 hours because they have to fly during peacetime. This reduced design life should result in reduced design, development, and production costs.

Design of a UAV with a design life of less than 1000 hours is different than for a manned aircraft with 8000 hours. For starters the UAV does not need to worry about material fatigue. The structure can be designed for strength instead of durability, which yields a lighter structure. In addition, equipment items could be selected with a mean flight time between unscheduled maintenance actions (MFTBUMA) of 1000 hours. The wartime maintenance would be minimal, with the turnaround actions being “refuel, rearm, and go” (true pit stop scenario). There would be a reduced number of access panels with their associated structural cutout penalties. It may be possible for the engine not to need removal during the life of the UAV. The engine removal time on commercial jets is well past 1000 hours. Because equipment items can be “stacked” more than two deep the density of the fuselage would be much greater (better utilization of available volume) than for a manned aircraft. This cost saving for the reduced design life is often difficult to quantify.

The elimination of peacetime flying (or at most minimal flying) would result in a large operation and support (O&S) cost saving relative to a manned fighter squadron. This feature is examined in more detail in

Chapter 24 as part of the discussion on life cycle cost. For the moment suffice it to say that the saving in a UAV squadron O&S costs is on the order of 80% of an equivalent manned aircraft squadron.

The unmanned ISR aircraft, on the other hand, provides continuous (24/365) coverage of a target area during peacetime and war and needs a design life of 90,000 hours over a 20-year life. The U-2S, which has a similar mission scenario, has a design life of 75,000 hours. The annual O&S cost for an unmanned ISR unit would be similar to that for a manned unit.

## 1.5 Specifications, Standards, and Regulations

The U.S. government regulates the operation of all aircraft in the United States by a system of specifications, standards, and regulations. An aircraft designer must not only meet (or exceed) the requirements discussed earlier, but must also comply with all the appropriate aircraft specifications, standards, and regulations if the aircraft is to be operated in the United States. The regulation of military aircraft is administered by the Department of Defense through the Department of Defense Specifications and Standards System (DODSSS); regulation of civil commercial aircraft is administered by the Department of Transportation through the Federal Aviation Regulations (FAR).

Specifications are procurement documents that describe the essential and technical requirements for aircraft items, materials, or services, including the procedures by which it will be determined that the requirements have been met. Standards establish engineering and technical limitations and applications for items, materials, processes, methods, designs, and engineering practices.

Table 1.3 lists some of the documents in the DODSSS, and [10,11] give a numerical index of the U.S. Government Specifications and Standards. Reading these specifications and standards can be overwhelming because there are over 2500 documents appropriate to a military aircraft and its associated avionics gear. Some of the more important specifications and standards in the DODSSS with which an aircraft designer should be familiar are listed in Table 1.4.

The documentation of the airworthiness standards for civil and commercial aircraft is reported in the Federal Aviation Regulations, Parts 23 and 25 [11]. Part 23 pertains to normal, utility, and acrobatic aircraft; Part 25 considers transport aircraft. The noise standards for these categories are detailed in Part 36. Civilian helicopters are regulated by Parts 27 and 29; moored balloons and kites are considered in Part 101. Parts 23 and 25 are quite thorough in that they set reasonable standards for the performance, stability, control, structure, design, construction, powerplant, equipment, and operating limits for civil and commercial aircraft.

**Table 1.3** Documents in the DoD Specification and Standards System

Military specifications	Military handbooks
Military standards	Federal handbooks
Federal specifications	Air Force–Navy aeronautical standards
Federal standards	Air Force–Navy aero design standards
Qualified products list	Air Force–Navy aeronautical specifications
Industry documents	USAF specifications
Aerospace Industries Association (AIA)	Air Force–Navy aeronautical bulletins
Aerospace materials specifications (AMS)	USAF specifications bulletins
American National Standards Institute (ANSI)	USAF regulations
American Society for Testing and Materials (ASTM)	DoD manuals
American Welding Society (AWS)	USAF manuals
Magnetic Materials Products Association (MMPA)	Navy manuals
Tech orders	USAF Systems Command design handbooks

**Table 1.4** Partial Listing of Military Specifications and Standards—Aircraft Design

Document Number	Title
MIL-HDBK-1797	Flying Qualities of Piloted Airplanes (replaced MIL-F-8785C)
MIL-F-83300	Flying Qualities of Piloted V/STOL Aircraft
MIL-F-9490	Flight Control Sys-Design, Installation and Test of Piloted Aircraft
MIL-S-8369	Stall/Post-Stall/Spin Flight Test Demonstration Reqs for Airplanes
MIL-C-18244	Control and Stabilization Systems: Automatic, Piloted Aircraft
MIL-D-8708	Demonstration Requirements for Airplanes
MIL-A-8860-64, 70	Airplane Strength and Rigidity
MIL-I-8700	Installation and Test of Electronics Equipment in Aircraft
MIL-P-26366	Propellers, Type Test of
MIL-S-18471	Seat System, Ejectable, Aircraft
MIL-W-25140	Weight and Balance Control Data
MIL-STD-850	Aircrew Station Vision Req. for Military Aircraft
MIL-STD-757	Reliability Evaluation from Demonstration Data
MIL-C-5011	Charts; Standard Aircraft Characteristics and Performance
MIL-STD-881	Work Breakdown Structure (WBS)
MIL-STD-499B	Systems Engineering
MIL-HDBK-516B	Airworthiness Certification—U.S. Tri-Service

It is a fact that the specifications and standards for military aircraft far outnumber the regulations for civil and commercial aircraft. For example, the entire FAR Parts 23 and 25 together form a document about two inches thick, whereas MIL-HDBK-1797, Flying Qualities of Piloted Airplanes, plus its supplement, is over two inches thick alone. It has been asserted that the military specifications and standards are excessive and are part of the reason for the high cost of military aircraft systems. Aircraft companies spend considerable time and money in military “spec” compliance. The authors will remain neutral in this matter but suggest that the reader examine this issue and become involved.

## 1.6 Aircraft Design Phases

Aircraft design is the name given to the activities that span the creation of a new flight vehicle. It starts as a vision and finishes as metal is being bent or as prepreg cloth for composites is being cut to conform to detail design drawings. It is the most important time in the life cycle of an aircraft as all the features both good and bad are locked in at this point. The design process is usually divided into the following three phases:

- Conceptual design
- Preliminary design
- Detail design

Although the specific activities during these three phases vary from one design group to another, they are generally formed as shown in Fig. 1.14.

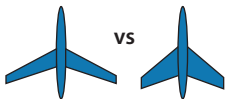
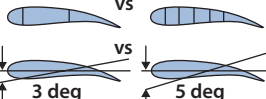
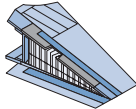
	Phase 1 Conceptual Design	Phase 2 Preliminary Design	Phase 3 Detail Design				
							
Known	Basic Mission Requirements Range, Altitude, & Speed Basic Material Properties $\sigma/\rho$ $E/\rho$ $\$/lb$	Aeroelastic Requirements Fatigue Requirements Flutter Requirements Overall Strength Requirements	Local Strength Requirements Producibility Functional Requirements				
Results	<table border="1" style="width: 100%;"> <tr> <th>Geometry</th> <th>Design Objectives</th> </tr> <tr> <td>Airfoil Type R t/c <math>\lambda</math> <math>\Delta</math></td> <td>Drag Level Weight Goals Cost Goals</td> </tr> </table>	Geometry	Design Objectives	Airfoil Type R t/c $\lambda$ $\Delta$	Drag Level Weight Goals Cost Goals	Basic Internal Arrangement Complete External Configuration <i>Camber &amp; Twist Distribution</i> <i>Local Flow Problems Solved</i> Major Loads, Stresses, Deflections	Detail Design <i>Mechanisms</i> <i>Joint Fittings and Attachments</i> Design Refinements as Result of Testing
Geometry	Design Objectives						
Airfoil Type R t/c $\lambda$ $\Delta$	Drag Level Weight Goals Cost Goals						
Output	Feasible Design	Mature Design	Shop Designs				
TRL	2 – 3	4 – 5	6 – 7				

Figure 1.14 The three phases or levels of aircraft design [12].

### Conceptual Design Phase

The conceptual design phase determines the feasibility of meeting the requirements with a credible aircraft design. The conceptual design process is shown schematically in Fig. 1.15 and discussed next. The general size and configuration of the aircraft, the inboard profile, and most of the major subsystems are determined during this phase.

The first task is to study, evaluate, understand, question, and if necessary negotiate the requirements (or at least ask for a waiver). The requirements are flowed down to the design group in a document called Design Guidelines. The Design Guidelines lay out the ground rules for the design study along with sensitive information about the MoMs, program strategy, selection criteria, significant design decisions, and assumptions about technologies. The Design Guidelines document is a living document and is changed or updated when appropriate.

It is a good idea at the very beginning to have a brainstorming session to identify all possible solutions to the design problem. This session needs

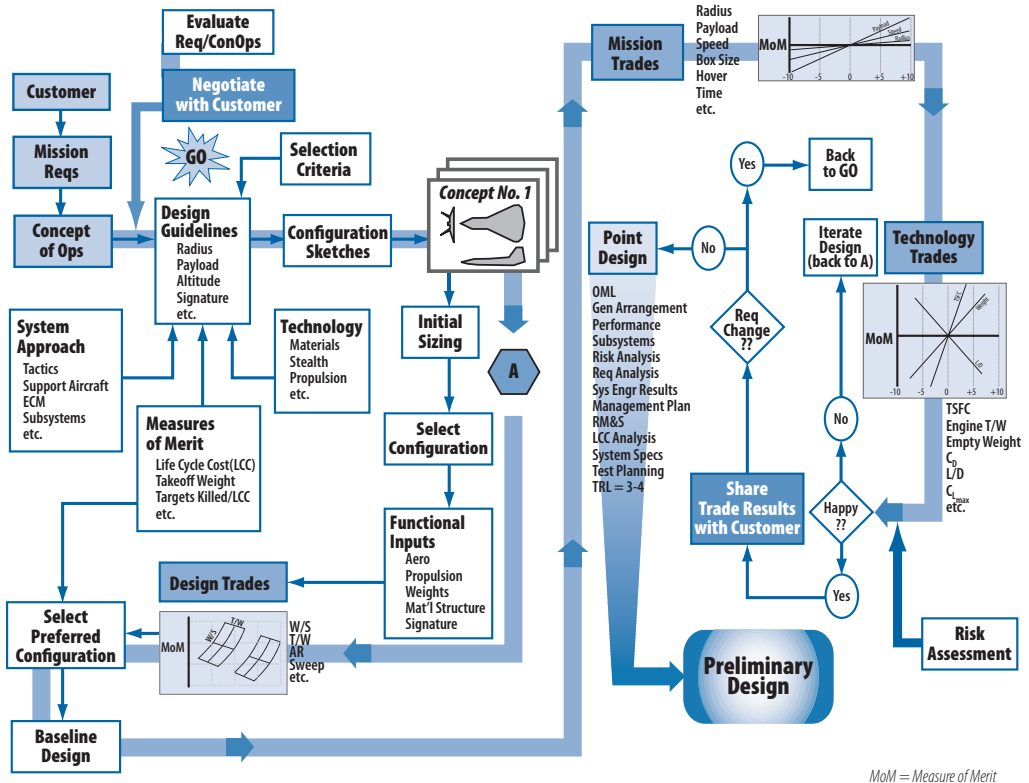


Figure 1.15 The conceptual design process.

to be a wide-open exploration of any and all concepts. Both left- and right-brain thinkers should attend as well as any person who will touch the design, for example, engineers and maintenance, manufacturing, and cost personnel.

*Design trade* studies are conducted around the more promising concepts using preliminary estimates of aerodynamics and weights to converge on the best wing loading, wing sweep, aspect ratio, thickness ratio, and general wing–body–tail configuration. Different engines are considered and thrust loading approaches explored to find the best airframe–engine match. The control surfaces are sized based upon the static stability and control considerations of a rigid aircraft. The performance requirements are varied (called *mission trades*) to determine the impact of each performance item on the aircraft size, weight, and cost. This information is then shared with the customer to make sure the customer is comfortable with the penalty each requirement imparts to the design. The technologies being considered in the design are examined (called *technology trades*) and estimates made of their “maturity” (probability of success) and the consequence of their not meeting the required maturity level. The results of the technology trades form the design risk analysis (discussed further in Chapter 25). The first look at cost and manufacturing is made at this time. Only gross structural aspects are considered during the conceptual design phase as resources are usually limited and the design is changing weekly. The ability of the design to accomplish the given set of requirements is established during this phase, but the details of the configuration are subject to change. Most of the work done during this phase is on paper and the manpower varies between 15 and 40 people over a year. It should be emphasized that the cost of making a design change is small during conceptual design but is extremely large during detail design.

### Preliminary Design Phase

The best configuration in terms of cost and performance from the conceptual design phase is now fine tuned through wind tunnel parametric testing. This fine tuning is accomplished with an expensive wind tunnel model capable of representing the general configuration, with provision for minor variations in wing and tail planform and location. The engine is selected and inlet–engine–airframe problems are considered in detail. If the inlet arrangement is complex, an inlet component wind tunnel test might be warranted. Major loads, stresses, and deflections are determined along with considerable structural design. Aeroelastic, fatigue, and flutter analyses are conducted. Some structural components might be built and tested.

Refined weight estimates are made and a more thorough performance analysis conducted. Dynamic stability and control analysis influences are determined and six-degrees-of-freedom (6-DOF) rigid aircraft simulations



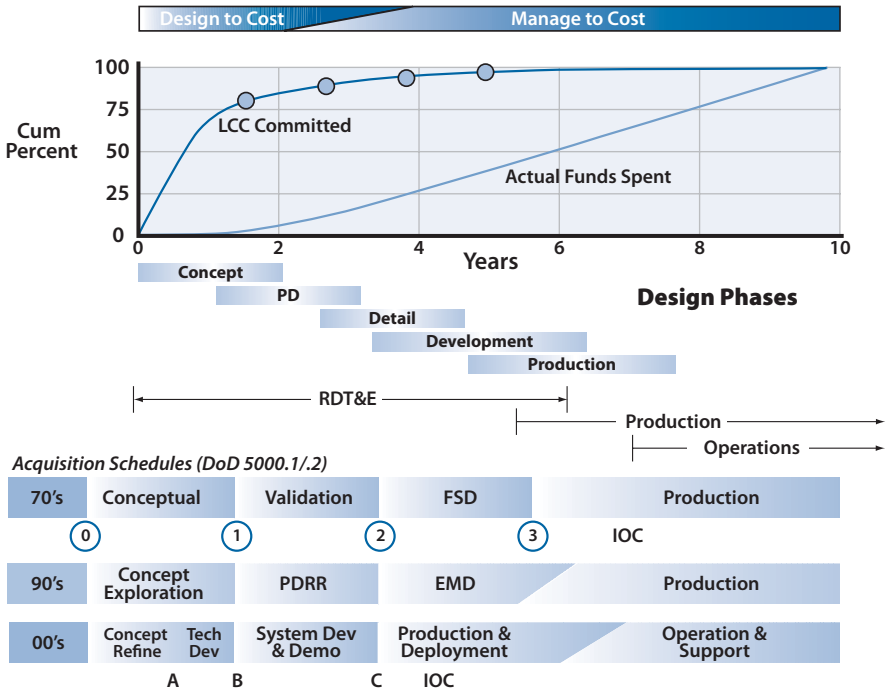
are conducted to establish flight control requirements and handling quality levels. If the aircraft is highly flexible (such as a high aspect ratio wing, a high fineness ratio fuselage, low fuselage damping), the simulation might require consideration of more than six degrees of freedom in order to examine the coupling of the rigid aircraft modes and the flexible aircraft modes. The three trade studies (design, mission, and technology) started in the conceptual design phase are continued but with more vigor.

The design is given serious manufacturing consideration with preliminary plans for jigs, tooling, and production breaks. Refined cost estimates are made. Clearly the resources for the preliminary design phase are greater than for the conceptual phase and personnel typically number 100 or more people over several years.

### Detail Design Phase

In the detail design phase, the configuration is “frozen” and the decision has been made to build the aircraft. Detailed structural design is completed. All of the detail design and shop drawings of the mechanisms, joints, fittings, and attachments are accomplished. Interior layout is detailed with respect to location and mounting of equipment, hydraulic lines, ducting, control cables, and wiring bundles. Sometimes component mock-ups are built to aid in the interior layout. The drawings for the jigs, tooling, and other production fixtures are done at this time. A detailed cost estimate based upon work breakdown structure (WBS) is made. All equipment and hardware items are specified. Often, system mock-ups (such as fuel system, landing gear, ECS, engine-inlet, and a hardware-in-the-loop flight control system called an iron bird) will be designed, built, and tested during this phase. It is important that from this point on the design changes be kept to a minimum because the cost of making a change is large once the drawing hits the shop floor. The next step is ordering all the equipment items (called Bill of Materials) and the fabrication and assembly of the prototype (usually at least two prototypes are built). Often, the fabrication of some components will be started during this phase as soon as their shop drawings are released.

Figure 1.16 shows the three phases of design in a typical government program acquisition according to DoD 5000.1 [2]. The years shown are extremely optimistic because there are always breaks in the schedule while the government issues a Request for Proposal, industry submits proposals, and the government evaluates the proposals, selects a winner, and gets its funding in place. Commercial programs move much faster because the aircraft builder controls the tempo and funding of the program. Typical times from the decision to build the aircraft [Milestone 1 or B for the government; the start of preliminary design (PD) for commercial] to production is about 10 years for the government and 5 years for commercial.



**Figure 1.16** Design phases integrated into the entire government program.

Figure 1.16 also shows the importance of the conceptual design phase in that over 70% of the design features that drive life cycle cost (LCC) are selected during that phase. Because it all started with gliders, a number of early examples are shown in Fig. 1.17.

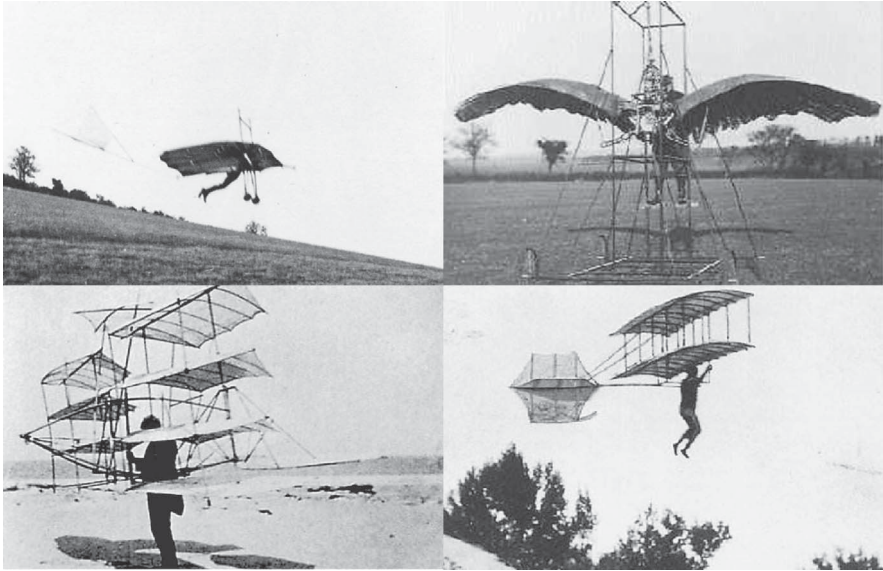
## 1.7 Scope of the Text

The text is in two volumes:

- Volume 1, Aircraft Design
- Volume 2, Airship Design, Aircraft Design Case Studies, and Photo Gallery

Volume 1 considers the conceptual design phase of the aircraft design process. It is self-contained, and the chapters and appendices lead the reader through one iteration of the conceptual design process. Volume 1 will give the reader an understanding and appreciation of how the different disciplines must blend together to produce an effective aircraft.

Volume 2 is also written as a stand-alone volume and uses rewritten introductory material from Volume 1 that is focused on the unique design



*Unpowered gliders of all shapes and sizes were the forerunners of manned powered flight. Otto Lilienthal was the most famous glider designer, builder, and pilot of all. He made over 2000 flights in the 1890s and with his brother Gustav measured lift and drag. Otto would die in a crash of one of his designs in 1896.*

**Figure 1.17** Various unpowered glider designs.

issues of airships, hybrid airships, and high-altitude balloons. Actual design case studies are also included for both aircraft and airship programs.

In Volume 1 the conceptual design process is shown schematically in Fig. 1.15 and proceeds as follows (this order will be followed throughout the remainder of Volume 1):

1. **Critical requirements.** The mission requirements are studied to identify the requirement that drives the design. For example, will the aircraft be range-dominated, field-length constrained, or required to operate supersonically for extended periods? An early assessment of the driving requirement can help in the proper selection of the wing planform shape and size. The applicable specifications, standards, and regulations should be identified and met throughout the design process.
2. **Initial aircraft sizing.** At this point, the aircraft takeoff gross weight (TOGW) is estimated. If this is the first time through the design loop, many assumptions will have to be made to get started. A first estimate of the fuel weight is made at this point also.
3. **Takeoff wing loading,  $(W/S)_{TO}$ .** Here the aircraft wing is sized. One or more of the following criteria will size the wing area:
  - Landing and takeoff
  - Operational or intercept altitude and speed (i.e., a low- $q$  or high- $q$  vehicle?)

- Air combat (maneuverability)
- Efficient cruise
- Efficient loiter

**4. Airfoil section and planform shape.** The following items are selected:

- Airfoil—section,  $t/c$ , camber, nose shape
- Planform—aspect ratio, taper, sweep, fixed versus variable geometry

This is a major design decision and is not an easy task. The importance of low-speed performance, maximum lift coefficient  $C_{L_{\max}}$ , and other related issues must be determined.

- 5. Fuselage sizing and shape.** The fuselage is sized to meet the volume requirements of crew, payload (passengers, bombs, or cargo), engines (external or internal), fuel (in fuselage, wings, or external tanks), avionics, and so on. The fuselage fineness ratio,  $l/d$  (ratio of length to maximum diameter), is estimated based on whether the primary requirement of the mission is subsonic, supersonic, or mixed.
- 6. Estimation of tail size.** A rough layout of the aircraft is prepared and the wing is positioned on the fuselage. A decision must be made whether the aircraft will be an aft tail, canard, or tailless configuration. The designer will use tail volume coefficients and historical data to prepare an initial estimate of tail sizes.
- 7. Configuration aerodynamics.** The designer must estimate the aircraft zero-lift drag  $C_{D0}$ , lift curve slope  $C_{L\alpha}$ , and drag-due-to-lift factor  $K$  versus Mach number using the best available methodology. It is important to double-check initial aerodynamic estimates by comparing them with existing aircraft (“sanity check”).
- 8. Sizing of engines.** The type and number or size (in the case of “rubber” engines) of the engines are determined. The engine thrust-to-weight ratio  $(T/W)_{TO}$  is an important design parameter and will be driven by one or more of the following criteria:
- Efficient cruise or loiter
  - Takeoff
  - Air combat
  - Minimum time to intercept
  - Service ceiling
- 9. Design and sizing inlets.** Inlets are located and designed to match engine requirements. Pressure recovery, thrust data corrections, bypass drag, and spillage drag are determined.
- 10. Refined fuel estimate.** A refined fuel estimate is made and compared with the original estimate made in step 2.
- 11. Component weights and c.g. location.** The fuel is located in the aircraft and a refined estimate of the aircraft component weights is made. The aircraft is balanced and the c.g. travel during the mission is

checked. The updated TOGW is compared with the original estimate made in step 2.

12. **Sizing of tail and control surfaces and determination of trim drags.** A static stability and control analysis (longitudinal, directional, and lateral) is performed to size the control surfaces to meet acceptable requirements. The cruise and maneuver trim drags are determined.
13. **Refined performance analysis.** A refined performance analysis is conducted and compared with the mission requirements.
14. **Cost estimate.** Estimates are made of the prototype and production aircraft costs. If enough information exists, an estimate of operation and maintenance costs should be made to give an indication of the life cycle cost (LCC) for the aircraft.
15. **Design iteration.** At this point, a review of the entire design process is performed, changing and updating design features and results until the design team is satisfied or funds run out, whichever comes first.

Numerous texts dealing with aircraft design are listed at the end of this chapter [12–27]. Corning [14] is a good text dealing with transport design in the early 1950s. Wood [13,15] is a general design text full of design information, including a section on seaplane hull design. Perkins and Hage [16] is an excellent text on performance, stability, and control, but unfortunately it is badly outdated. Stinton [17] gives the aircraft design picture with a British flavor. Torenbeek [18] is an excellent text for transport design, with numerous weight equations. Roskam [22] is an excellent eight-volume series written by a practicing engineer and design professor at the University of Kansas (over 35 years, see [28]). Raymer [23] is a design text used by some U.S. universities. Thomas [26] is an easy-to-read, authoritative text on sailplane design written by a practicing engineer at DLR, Braunschweig, Germany, and a World-class sailplane pilot. Newberry [25] is filled with copies of landmark design papers from the years 1941–1991. The remaining referenced texts and articles are also recommended.

## References

- [1] “Design to Cost,” DoD Directive 5000.28, U.S. Department of Defense, U.S. Government Printing Office, Washington, DC, 2009.
- [2] “Acquisition of Major Defense Systems,” DoD Directive 5000.1, U.S. Department of Defense, U.S. Government Printing Office, Washington, DC, 2009.
- [3] Wilson, J. R., “Unmanned Aerial Vehicles: Background and Issues for Congress,” report for Congress, Congressional Research Service Rept. RL31872, 25 April 2003, pp. 30–37.
- [4] “2007 UAV Worldwide Roundup,” *Aerospace America*, May 2007.
- [5] Clough, B., “UAVs—You Want Affordability and Capability? Get Autonomy!”, Association of Unmanned Vehicle Systems International paper, 14–17 July 2003, Baltimore, MD.

- [6] “Matching Resources with Requirements Is Key to the Unmanned Combat Air Vehicle Program’s Success,” report to the Subcommittee on Tactical Air and Land Forces, Committee on Armed Services, House of Representatives, General Accounting Office Rept. 03-598, June 2003, p. 3.
- [7] Brown, R., “Enhancing UAV Affordability,” briefing to the Air Force Scientific Advisory Board, ASC/FB, 19 March 2002.
- [8] Brown, R., “DoD Juggles Affordability, Capability as UAV Costs, Budgets Rise” *Aerospace Daily, Aviation Week & Space Technology*, 2 Jan. 2003, p. 7.
- [9] “UAV Technologies and Combat Operations,” *Panel Reports*, Vol. 2, U.S. Air Force Scientific Advisory Board, SAB-TR-96-01, Dec. 1996, pp. 3–49.
- [10] *Department of Defense Index of Specifications and Standards*, U.S. Government Printing Office, Washington, DC, 2009.
- [11] “Airworthiness Standards: Part 23—Normal, Utility, Acrobatic, and Commuter Category Airplanes; Part 25—Transport Category Airplanes,” *Federal Aviation Regulation*, Vol. 3, U.S. Department of Transportation, U.S. Government Printing Office, Washington, DC, 2009.
- [12] Nicolai, L. M., *Fundamentals of Aircraft Design*, METS Inc., San Jose, CA, 2009.
- [13] Wood, K. D., *Airplane Design*, Univ. of Colorado, CO, 1947.
- [14] Corning, G., *Supersonic and Subsonic Airplane Design*, Edwards Bros., Ann Arbor, MI, 1953 (revised 1964).
- [15] Wood, K. D., *Aircraft Design*, Johnson Publ., Boulder, CO, 1966.
- [16] Perkins, C. D., and Hage, R. E., *Airplane Performance, Stability and Control*, Wiley, New York, 1949.
- [17] Stinton, D., *The Anatomy of the Aeroplane*, American Elsevier, New York, 1966.
- [18] Torenbeek, E., *Synthesis of Subsonic Aircraft Design*, Delft Univ. Press, The Netherlands, 1976.
- [19] Goodmanson, L. T., and Gratzler, L. B., “Recent Advances in Aerodynamics for Transport Aircraft, Part 1,” *Astronautics and Aeronautics*, Vol. 11, No. 12, Dec. 1973, p. 30.
- [20] Goodmanson, L. T., and Gratzler, L. B., “Recent Advances in Aerodynamics for Transport Aircraft, Part 2,” *Astronautics and Aeronautics*, Vol. 12, No. 1, Jan. 1974, p. 52.
- [21] Kuchemann, D., *The Aerodynamic Design of Aircraft*, Pergamon, New York, 1978.
- [22] Roskam, J., *Aircraft Design*, Pts. 1–8, Roskam Aviation and Engineering Corp., Lawrence, KS, 1985. [Available via [www.darcorp.com](http://www.darcorp.com) (accessed 31 Oct 2009).]
- [23] Raymer, D. P., *Aircraft Design: A Conceptual Approach*, AIAA Education Series, AIAA, Washington, DC, 1989.
- [24] Whitford, R., *Design for Air Combat*, Jane’s Publ., London, 1987.
- [25] Newberry, C. F., *Perspectives in Aerospace Design*, AIAA Education Series, AIAA, Washington, DC, 1991.
- [26] Thomas, F., *Fundamentals of Sailplane Design*, College Park Press, College Park, MD, 1999.
- [27] Corke, C. C., *Design of Aircraft*, Prentice Hall, Pearson Education, Upper Saddle River, NJ, 2003.
- [28] Roskam, J., *Roskam’s Airplane War Stories*, DARcorp., Lawrence, KS, 2002.

## Chapter 2

# Review of Practical Aerodynamics



- Lift & Drag
- Boundary Layers & Skin Friction
- Wings & Bodies
- Subsonic & Supersonic
- Drag Polar
- Transonic Effects
- Finite-Wing Effects
- Swept-Wing Effects

An F-14 flies on a humid day near Mach 0.9 with shock condensation on the top of the wing and canopy. The flow decelerates from supersonic to subsonic through a normal shock with a jump in static pressure that can cause the water vapor in the air to condense into a cloud trailing behind the aircraft.

*Eagles don't flock. You have to find them one at a time.*

Ross Perot

## 2.1 Introduction

An aircraft is a unique machine because it lifts itself from the ground. This lift is generated by air flowing over a wing; it is then balanced by smaller amounts of lift (up or down) being generated at the aft end (front end for a canard) and at each wingtip. The cross section of the wing (looking down the span), called an *airfoil section*, is uniquely shaped (see Fig. 2.1). As the air flows over the wing (because the wing is being pushed through the air, as in flight, or because air is being blown over a static wing, as in a wind tunnel; see Fig. 2.2) it accelerates over the upper and lower surfaces so that it meets at the trailing edge (called the *Kutta condition*). This acceleration of the air particles causes the static pressure on the surfaces to drop below the static pressure in the freestream. There is one streamline of air particles (called the *dividing streamline*) that slams into the airfoil leading edge and comes to a stop. This point on the airfoil is called the *stagnation point*, and the pressure at this location is equal to the freestream static pressure plus the dynamic pressure. At this point the reader should review the airfoil appendix, Appendix F.

Lift and drag data for an aircraft throughout the Mach number range of its flight envelope are necessary ingredients for any performance analysis. Moment data about all three axes, as shown in Fig. 2.3, are necessary for stability and control analysis. This chapter will review the fundamental aerodynamic concepts relative to lift, drag, and moment methods. The working equations and methodology for estimating lift and drag are pre-

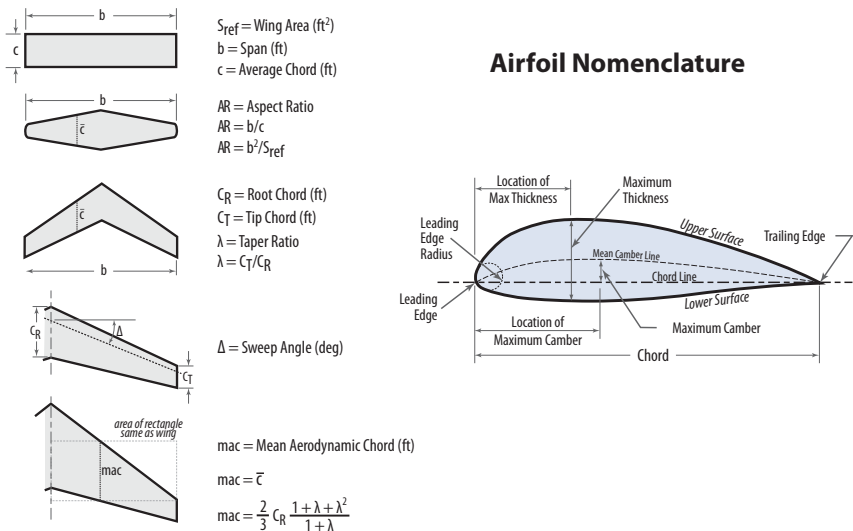


Figure 2.1 Wing geometry and nomenclature.



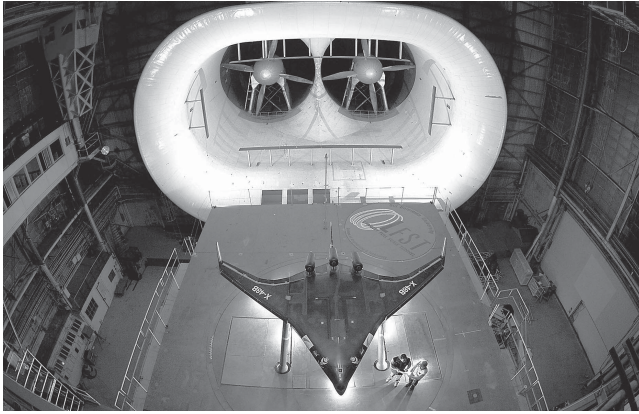
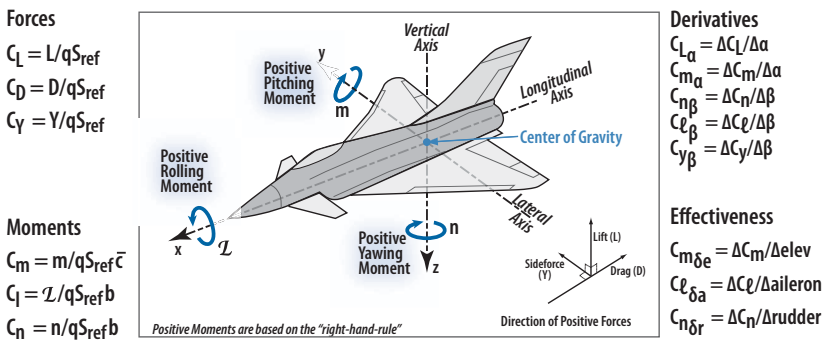


Figure 2.2 Langley 30 x 60-ft wind tunnel with the X-48B in the test section.

sented in Chapter 13; those for stability and control analysis, in Chapters 21–23.

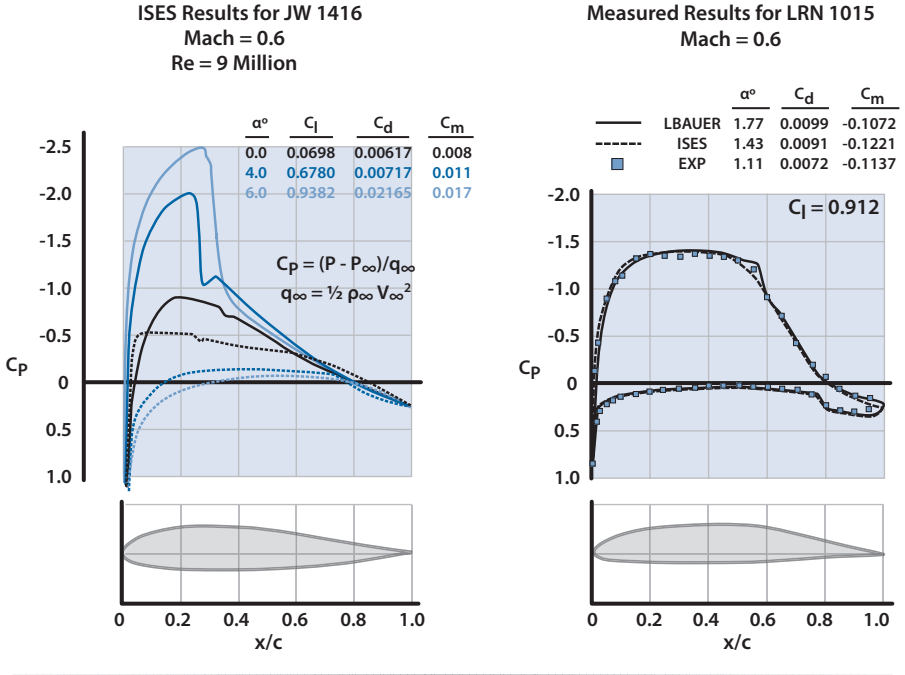
The pressure distribution over the upper and lower surfaces of an airfoil designed for long endurance missions is shown in Fig. 2.4. The pressure distribution is usually expressed as the pressure coefficient  $C_p$  as defined in Fig. 2.4. The shaping of the airfoil is such that there is more suction on the upper surface than on the lower, and a force normal to the

**Nondimensionalization Permits Comparison of Forces and Moments Between Dissimilar Vehicles**



$q = \text{Dynamic Pressure} = \frac{1}{2}\rho V^2$   
 Reference Areas and Lengths Are Just That — *References*

Figure 2.3 Major nondimensional aerodynamic parameters and sign convention.



**Figure 2.4** Wing surface pressure distributions for airfoil designed for long endurance.

freestream is generated called *lift*. This lift will increase as the angle-of-attack  $\alpha$  (the angle between the airfoil chord line and the freestream) is increased until  $\alpha$  reaches a value where the flow on the upper surface separates, greatly reducing the lift, and the airfoil stalls. This pressure distribution also produces a pressure drag parallel to the freestream and a pitching moment (usually taken about the quarter chord or aerodynamic center). The *aerodynamic center* (a.c.) is the point on the airfoil at which the value of the pitching moment does not change as the angle-of-attack changes. The aerodynamic coefficients discussed in this chapter are defined as follows:

$$C_L = \frac{L}{qS_{ref}} \tag{2.1}$$

$$C_D = \frac{D}{qS_{ref}} \tag{2.2}$$

$$C_{MA} = \frac{M_A}{qS_{ref}\bar{c}} \tag{2.3}$$

The aerodynamicist usually furnishes the data in coefficient form as a function of Mach number ( $M$ ), and sometimes Reynolds number ( $Re$ ). The coefficients of interest are shown in Fig. 2.3, where  $q = \frac{1}{2}\rho V_\infty^2$  (dynamic pressure),  $\bar{c}$  is the mean aerodynamic chord, and the moments are about a specified point (usually the wing quarter chord, aerodynamic center, or center-of-gravity). Notice that the coefficients are referenced to  $S_{\text{ref}}$ , which is usually the wing total planform area as shown in Fig. 2.1. The aerodynamic coefficients for three-dimensional bodies (wings, bodies, and combinations) are denoted by capital subscripts; for two-dimensional airfoils, by lowercase subscripts.

## 2.2 Drag

In aerodynamics, lift is very good, moment is useful, and drag is horrid. Designers spend most of their time trying to maximize the lift, control the moment, and minimize the drag. The *drag* is the aerodynamic force resolved in the direction of the freestream due to (1) viscous shearing stresses, (2) the integrated effect of the static pressures acting normal to the surfaces, and (3) the influence of the wing trailing vortices on the aerodynamic center of the configuration.

- **Skin friction drag.** The drag on a body resulting from viscous shearing stresses over its wetted surface.
- **Pressure drag (or form drag).** The drag on a body resulting from the integrated effect of the static pressure acting normal to its surface resolved in the drag direction.
- **Profile drag.** Usually defined as the sum of the skin friction drag and the pressure drag for a two-dimensional airfoil.
- **Viscous drag-due-to-lift.** The drag that results due to the integrated effect of the static pressure acting normal to its surface (resolved in the drag direction) when the airfoil angle-of-attack is increased to generate lift. (Note: It is present without vortices.)
- **Inviscid drag-due-to-lift (or induced drag).** The drag that results from the influence of a trailing vortex (downstream of a lifting surface of finite aspect ratio) on the wing aerodynamic center. (Note: It is present with or without viscosity).
- **Interference drag.** The increment in drag resulting from bringing two bodies into proximity to each other; for example, the total drag of a wing–fuselage combination will usually be greater than the sum of the wing drag and fuselage drag independent of one another.
- **Trim drag.** The increment in drag resulting from the aerodynamic forces required to trim the aircraft about its center of gravity; usually this takes the form of added drag-due-to-lift on the horizontal tail.

- **Base drag.** The specific contribution to the pressure drag attributed to a blunt afterbody.
- **Wave drag.** Only exists with supersonic flow; this is a pressure drag resulting from noncanceling static pressure components on either side of a shock wave acting on the surface of the body from which the wave is emanating.
- **Excrescence drag (or protuberance drag).** The drag associated with antennas, total pressure probes (part of the air data system), and other protrusions above the exterior of the aircraft; external fuel tanks, missiles, and bombs are also considered excrescence drag items.
- **Cooling drag.** The drag resulting from the momentum lost by the air that passes through the powerplant installation (i.e., the heat exchanger) for cooling the engine, oil, and so on.
- **Ram drag.** The drag resulting from the momentum lost by the air as it slows down to enter an inlet.

## 2.3 Boundary Layers and Skin Friction Drag

Air molecules flow over a body in layers called *streamlines*. The air molecules in the streamline next to the body surface actually interact with the molecular structure of the surface and come to a stop. This is the “no slip condition” that makes up the foundation of boundary layer theory and is shown in Fig. 2.5. As the streamlines move away from the surface the air molecules speed up, giving an increasing velocity gradient  $dv/dz$ . At a distance  $\delta$  (called the *boundary layer thickness*) from the surface the velocity gradient is zero.

The boundary layer composed of many streamlines can take one of three forms as shown in Fig. 2.5: (1) if the streamlines are smoothly flowing, it is *laminar*; (2) if the streamlines are chaotic and vortical, it is *turbulent*; and (3) if the streamlines are separated from the surface ( $dv/dz = 0$  at  $z = 0$ ), it is called a *separated boundary layer*. The character of the separated boundary layer is such that the flow near the surface can actually reverse direction and flow upstream. The shearing action between the streamlines creates a friction force in the streamline direction. At the surface ( $z = 0$ ) this friction force is equal to  $\mu dv/dz$  times the surface area, where  $\mu$  is the fluid coefficient of viscosity and acts parallel to the surface. Notice that the velocity gradient  $dv/dz$  at the surface is smaller for the laminar boundary layer than the turbulent boundary layer, giving a lower skin friction drag. Notice also that in the separated region  $dv/dz = 0$  at the surface there is nearly zero skin friction drag, but at the same time there is a large increase in static pressure, pressure drag, and loss of lift.

The character of the boundary layer is dependent upon a nondimensional parameter called the *Reynolds number*,  $Re_x = \rho Vx/\mu$ , which is a ratio

Friction force  $\sim \mu dv/dz$  (area) where  $\mu$  is the fluid coefficient of viscosity and  $dv/dz$  is the velocity gradient evaluated at  $z=0$ . This force acts parallel to the surface.

Boundary layer starts out laminar and transitions to turbulent at

$Re_x \approx 5 \times 10^5$  where  $Re_x = \text{local Reynold's Number} = \rho v x / \mu$

Laminar thickness  $\delta_L = 5.2x/Re_x^{0.5}$  and turbulent thickness

$\delta_T = 0.37x/Re_x^{0.2}$

Flow separates when  $dv/dz = 0$  at the surface.

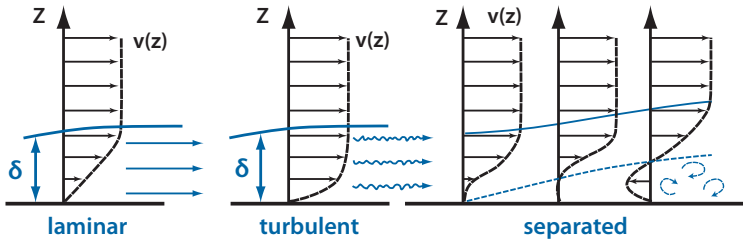


Figure 2.5 Boundary layer profile: three flow conditions.

of the inertia forces in the boundary layer to the friction forces. The boundary layer starts out laminar and transitions to turbulent at a local  $Re_x \approx 5 \times 10^5$ . The laminar boundary layer is extremely delicate and will transition early if it encounters surface disturbances or increasing pressure gradient. The thickness of the boundary layer is given by the following expressions:

Laminar Thickness:

$$\delta_L = 5.2x / Re_x^{0.5}$$

Turbulent Thickness:

$$\delta_T = 0.37x / Re_x^{0.2}$$

The averaged skin friction coefficient  $C_F$  acting on a square unit of the aircraft surface is shown in Fig. 2.6 as a function of Reynolds number, where  $L$  is a characteristic dimension of the aircraft such as fuselage length or wing mean aerodynamic chord. The solid lines in Fig. 2.6 assume the boundary layer to be completely laminar or completely turbulent, with the dashed line in the middle denoting a situation of transition. The skin friction drag force of the aircraft component is calculated as follows:

$$\text{Skin friction drag force} = C_F (\text{surface area}) (\text{dynamic pressure})$$

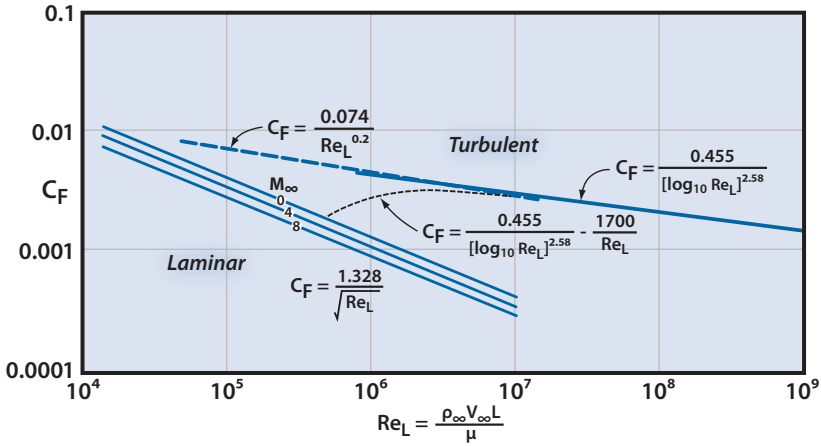


Figure 2.6 Skin friction coefficient over a flat plate.

## 2.4 Incompressible Airfoil Section Theory

Subsonic thin airfoil theory (incompressible and inviscid) predicts the section lift and moment coefficients quite well for airfoil shapes up to moderate angles-of-attack below stall. The theory predicts (see [1], page 73, and [2], page 34)

$$\frac{dC_l}{d\alpha} = m_0 = 2\pi \text{ per radian}$$

Aerodynamic center location = quarter chord =  $\frac{1}{4}\bar{c}$

$$\alpha_{ol} = -\frac{1}{\pi} \int_0^\pi \left( \frac{dz}{dx} \right) (\cos\theta - 1) d\theta \tag{2.4}$$

$$C_{m_{a.c.}} = -\frac{1}{2} \int_0^\pi \left( \frac{dz}{dx} \right) (\cos 2\theta - \cos\theta) d\theta \tag{2.5}$$

where  $dz/dx$  is the local slope of the camber line,  $\theta$  is the change of variable  $x = c/2(1 - \cos \theta)$ , and  $c$  is the chord of the airfoil section.

Typical section data are shown in Figs 2.7 and 2.8. References [1], [3], and [4] report experimental section data on many airfoil shapes. Appendix F discusses airfoil nomenclature and presents section data on the more popular airfoil sections.

The  $C_{m_{a.c.}}$  is constant with changing  $C_l$  or  $\alpha$  by definition of the *aerodynamic center* (a.c.). The section lift data up through moderate angles (i.e., the linear lift region) is expressed as

$$C_l = m_0(\alpha - \alpha_{0l})$$

Notice that  $\alpha_{0l}$  is zero for symmetric or uncambered sections (i.e.,  $dz/dx = 0$ ) such as the NACA 0012 airfoil shown in Fig. 2.7.

The drag coefficient for an airfoil section pretty much has a parabolic behavior with the lift coefficient, except at large  $\alpha$ . This parabolic behavior is expressed as

$$C_d = C_{d_{\min}} + k''(C_l - C_{l_{\min}})^2 \tag{2.6a}$$

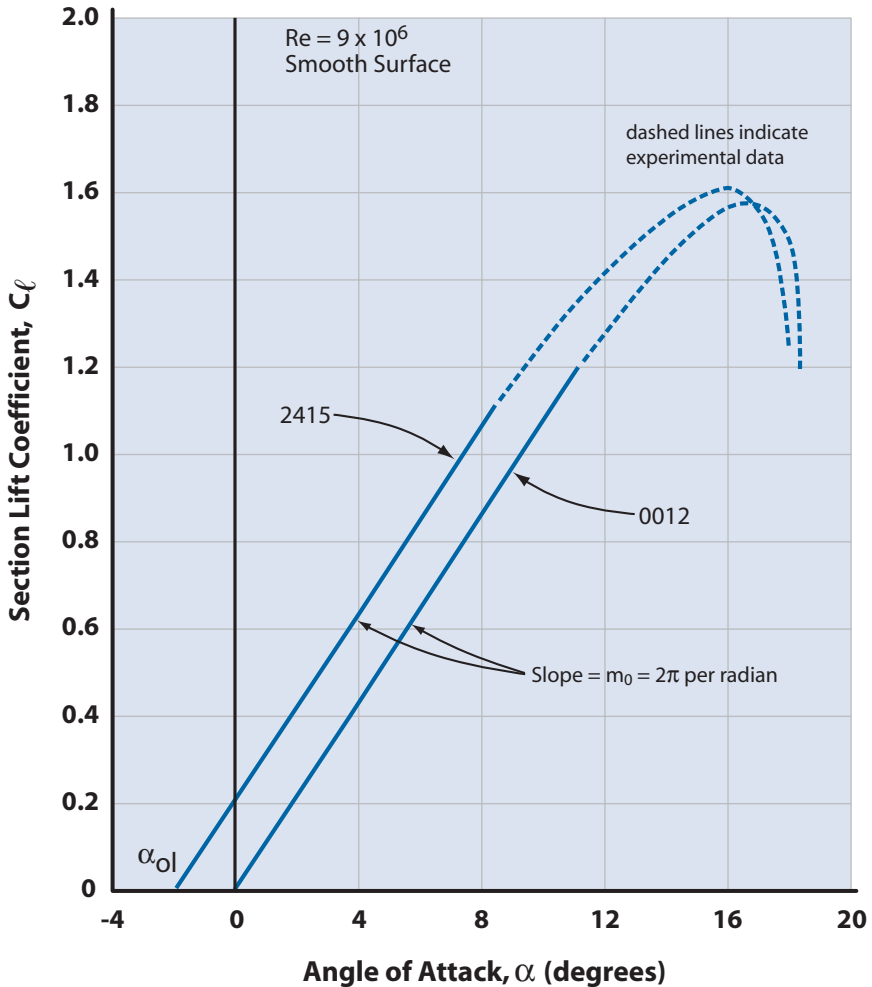


Figure 2.7 Section lift data (from [3]).

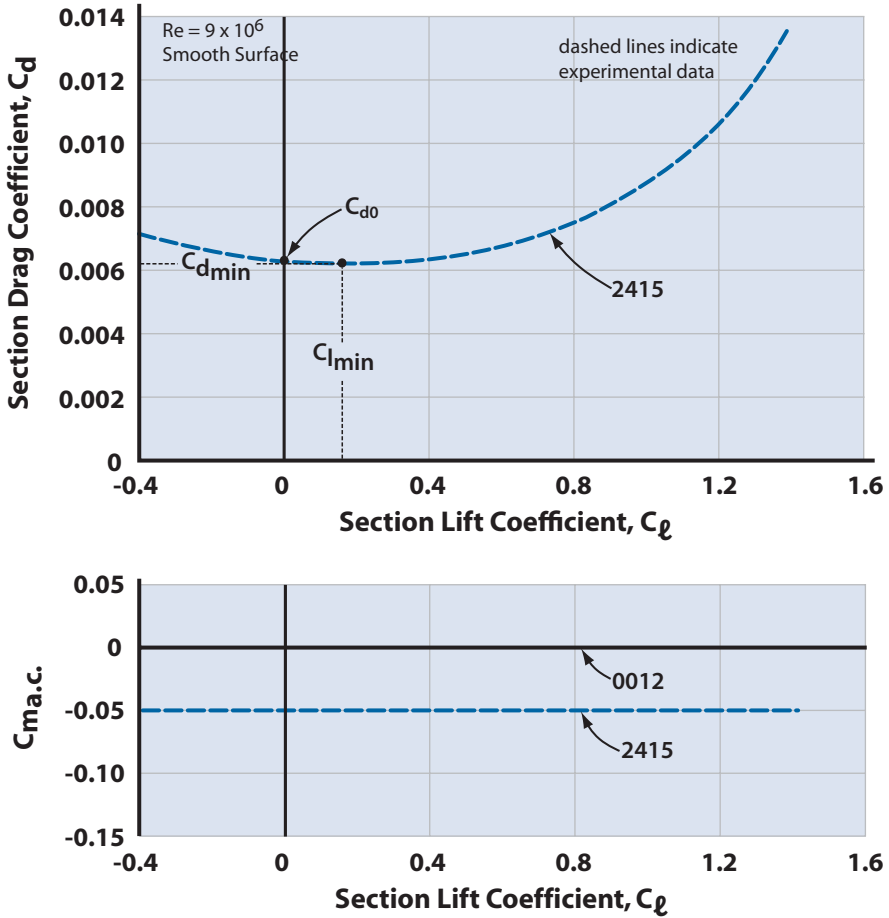


Figure 2.8 Section  $C_d$  and  $C_{m_{a.c.}}$  data (from [3]).

where  $C_{d_{min}}$  is the minimum value of  $C_d$  (see Fig. 2.8),  $C_{l_{min}}$  is the  $C_l$  value for  $C_{d_{min}}$ , and  $k'' = \Delta(C_d - C_{d_{min}})/\Delta(C_l - C_{l_{min}})^2$  is called the viscous drag due to the lift factor. Symmetric sections have  $C_{l_{min}} = 0$  such that the  $C_d$  is expressed as

$$C_d = C_{d_0} + k''C_l^2 \tag{2.6b}$$

where  $C_{d_0}$  is called the *zero-lift drag coefficient* and is due to separation and skin friction drag at  $C_l = 0$ . Appendix F shows that the NACA 24XX family of airfoils has a  $k'' \sim 0.0047$  at  $Re = 3 \times 10^6$ .

Thin airfoil theory is an inviscid theory and thus cannot predict section characteristics due to viscous effects (drag and stall characteristics). Results from thin airfoil theory are indicated by solid lines in Figs. 2.7 and 2.8.



The section data shown in Fig. 2.7 must be corrected for Mach number (compressibility), wing sweep, and finite wing effects and are discussed in the next section.

## 2.5 Subsonic Compressibility Corrections

The subsonic compressibility correction factor is known as the Prandtl–Glauert transformation. Essentially it transforms the compressible flow problem into an equivalent incompressible flow problem. The correction for lift curve slope is as follows:

$$(m_0)_{M \neq 0} = \frac{(m_0)_{M=0}}{\sqrt{1-M^2}} \quad (2.7)$$

The effect of compressibility is to increase the section lift curve slope. Theoretical and experimental values usually agree well for  $0 < M < 0.8$ . Beyond  $M = 0.8$  the agreement breaks down.

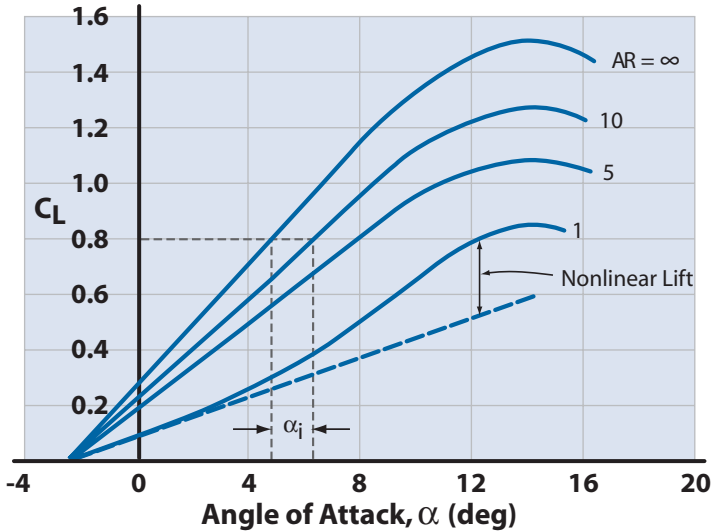
## 2.6 Finite Wing Corrections

When the airfoil has a finite span (i.e., a wing) the differential pressure on the top and bottom surfaces causes a circular motion of the air about the wingtips. This circular or vortex motion of the air (counterclockwise on the right wing and clockwise on the left wing as you look forward) trails behind the wingtips as trailing vortices. These trailing vortices, called *wake turbulence*, are what forces airports to impose separation distances behind airplanes that are landing and taking off. The trailing vortices induce a downwash at the wing aerodynamic center, which gives a lower effective angle-of-attack and an induced drag. This drag has nothing to do with viscosity and is an inviscid drag-due-to-lift. This decrease in the effective angle-of-attack is shown in Fig. 2.9. Notice that, for a finite wing of aspect ratio = 10, the  $\alpha$  must be increased by an amount  $\alpha_i$  to give the same lift coefficient as an airfoil of infinite aspect ratio. Finite wing theory (see [1], page 109) gives the following results:

$$\alpha_i = \text{induced angle-of-attack} = \frac{C_L}{\pi AR} (1 + \tau) \quad (2.8)$$

$$m = \frac{dC_L}{d\alpha} = \frac{m_0}{1 + \left[ m_0 (1 + \tau) / (\pi AR) \right]} \quad (2.9)$$

$$C_{D_{L_i}} = \text{induced drag} = \frac{C_L^2 (1 + \delta)}{\pi AR} = K' C_L^2 \quad (2.10)$$



**Figure 2.9** Effect of finite span on the lift characteristics of a NACA 65-410 airfoil (Appendix F).

where  $AR$  is the *aspect ratio* and  $\tau$  and  $\delta$  are correction factors to account for deviations from an elliptical lift distribution. The  $\tau$  and  $\delta$  are dependent upon  $AR$  and taper ratio and are shown in Fig. 2.10. The  $K'$  is called the inviscid drag-due-to-lift factor.

## 2.7 Sweep Correction

The finite wing correction depends solely on aspect ratio and taper ratio and is based upon the freestream velocity being perpendicular to the quarter chord line. If the wing is swept, the component of velocity perpendicular to the quarter chord establishes the pressure distribution over the wing, and the tangential component flows spanwise along the wing and does not influence the pressure distribution. This is shown in Fig. 2.11.

Empirical data indicates the following corrections for the lift curve slope of swept wings:

$$m = (m)_{\Delta=0} \cos \Delta, \quad \text{for } AR > 6 \quad (2.11)$$

$$m = (m)_{\Delta=0} \sqrt{\cos \Delta}, \quad \text{for } AR < 6 \quad (2.12)$$

where  $\Delta$  is the sweep of the quarter chord or maximum thickness line. Although wing sweep is advantageous for high-speed flight (discussed in the next section) it creates problems for low-speed flight. A swept-wing

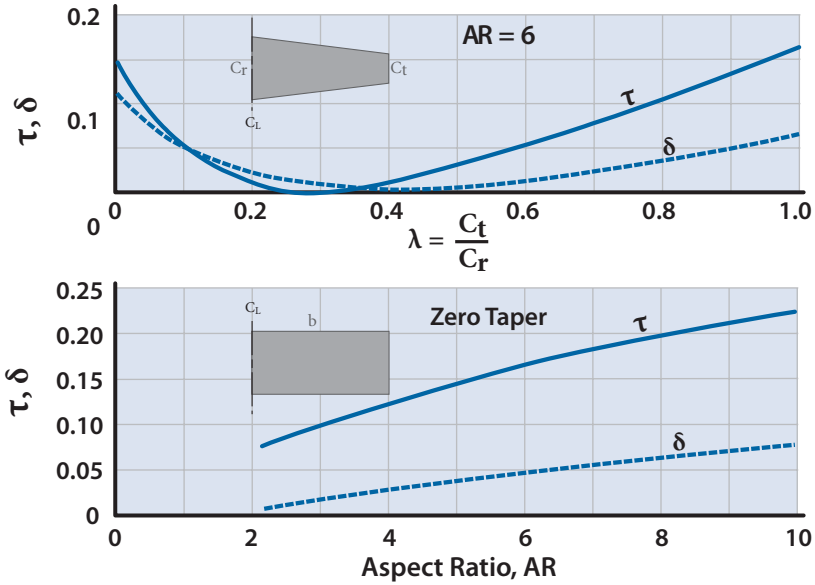


Figure 2.10 Correction factors for nonelliptic lift distribution (data from [4]).

aircraft will be required to land and take off at higher angles-of-attack than a straight-wing aircraft of the same aspect ratio because it has a lower  $C_{L\alpha}$ .

## 2.8 Combined Effects

The effects of sweep, finite span, and compressibility may be combined into the following useful equation for subsonic lift curve slope:

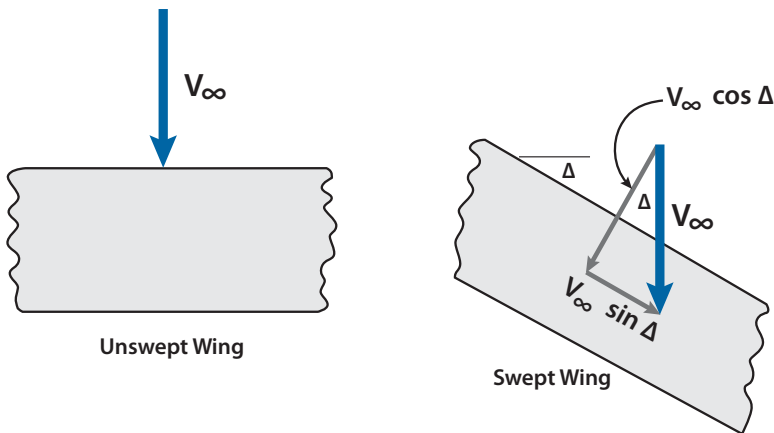


Figure 2.11 Normal component of  $V_\infty$  establishes the pressure distribution over wing station.

$$\frac{dC_L}{d\alpha} = C_{L\alpha} = \frac{2\pi AR}{2 + \sqrt{4 + AR^2 \beta^2 (1 + [(\tan^2 \Delta)/\beta^2])}} \quad (2.13)$$

where  $AR = \text{aspect ratio} = (\text{span})^2/\text{wing area}$

$$\beta = \sqrt{1 - M^2}$$

$\Delta = \text{sweep of the maximum thickness line}$

## 2.9 Nonlinear Wing Lift and Moment

Usually the wing  $C_L$  is thought to be linear in  $\alpha$ , that is,

$$C_L = \left( \frac{dC_L}{d\alpha} \right) \alpha$$

However, this is an approximation and is only accurate for high-AR wings. Actually the wing  $C_L$  is more correctly written as

$$C_L = \left( \frac{dC_L}{d\alpha} \right)_{\alpha=0} \alpha + C_1 \alpha^2 \quad (2.14)$$

where  $(dC_L/d\alpha)_{\alpha=0}$  is the wing lift curve slope evaluated at  $\alpha = 0$  (or close to it) using Eq. (2.13), and  $C_1$  is the nonlinear lift factor. A pronounced nonlinear relationship between aerodynamic coefficients and  $\alpha$  is typical of nearly all planforms when  $AR$  is less than approximately 3. The usual lifting surface theories (linear theories) predict linear relationships that underestimate the lift for low- $AR$  wings as shown in Fig. 2.9.

Nonlinear dependence of lift and pitching moment on the angle-of-attack is extremely significant for slender bodies and wings of small aspect ratio. This is because the flow past a slender body or low- $AR$  wing is completely different from the flow past a classic unswept wing of large  $AR$ . The characteristic feature of the flow past such a slender body or low- $AR$  wing is the strong cross flow that leads to separation of the flow at the sides of the body or wing edges and to the formation of free vortices on the upper surface, as shown in Fig. 2.12. This formation of free vortices on the upper surface of the low- $AR$  wing or slender body is the reason for the nonlinear relationship between lift and pitching moment and angle-of-attack,  $\alpha$ . The nonlinear behavior becomes more pronounced with decreasing  $AR$ , and with  $AR = 1$  the nonlinear part is of the same order of magnitude as the linear part, as shown in Fig. 2.9.

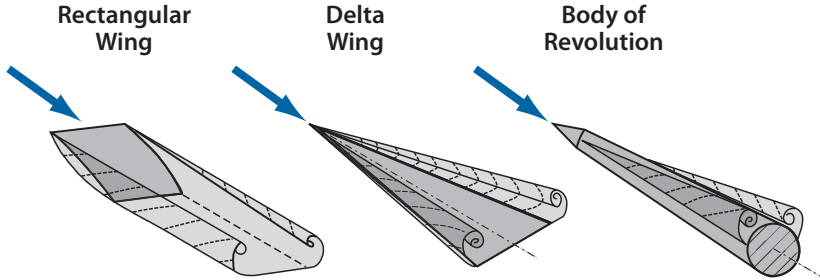


Figure 2.12 Vortex configurations past slender bodies.

The vortex flow pattern is initiated by the flow separation at the edge of the wing and is highly dependent upon the shape of the wing edge. A sharp edge precipitates separation sooner and more cleanly than a rounded edge. Thus, the nonlinear lift and moment contribution from sharp edges are about twice those from round edges. For delta wings the planform tip edges and leading edge are the same; thus, it is logical to assume that the nonlinear behavior is a function of planform (i.e., rectangular, swept, or delta) as well as AR. This nonlinear lift theory is developed in [2,5–8].

The wing  $C_L$  is given by

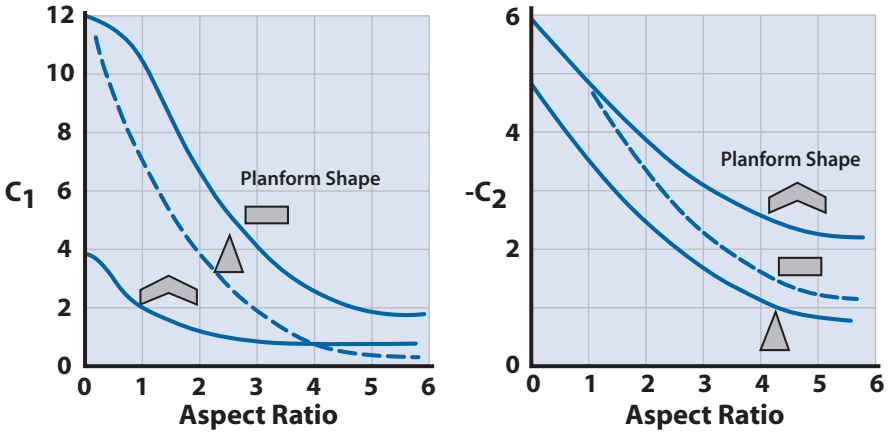
$$C_L = \left( \frac{dC_L}{d\alpha} \right)_{\alpha=0} \alpha + C_1 \alpha^2 \quad (2.14)$$

for  $\alpha$  in radians. The moment coefficient about the wing apex is similarly given by

$$C_M = \left( \frac{dC_M}{d\alpha} \right)_{\alpha=0} \alpha + C_2 \alpha^2 \quad (2.15)$$

for  $\alpha$  in radians, where the values for  $C_1$  and  $C_2$  are obtained from Fig. 2.13 for sharp-edged wings, and  $0.5C_1$  and  $0.45C_2$  are used for round leading edges.

This vortex formation and control over low-AR bodies is the reason for the use of fuselage strakes (SR-71 and F-16) and wing leading edge fuselage extensions (F-5, YF-17, and F-18). The strakes and leading edge extensions (LEX) are very low aspect ratio devices and form powerful vortices at moderate angles-of-attack that then reverse course over the top surface of the main wing, sweeping high-energy air into the boundary layer and delaying flow separation. Figure 2.14 visually illustrates the vortex rollup created by the low-AR forebody strakes. Notice also how the “V” tails have been positioned such that these vortices do not impinge on the tail surfaces. The



**Figure 2.13** Values of  $C_1$  and  $C_2$  for various planform shapes and aspect ratios.

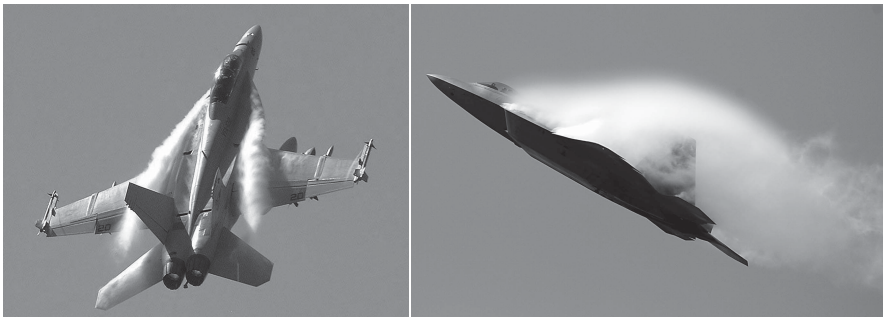
curved shape of the strake tends to tighten the vortex and thus reduce its influence on other parts of the vehicle.

## 2.10 Total Aircraft Subsonic Aerodynamics

The total wing subsonic drag coefficient is a combination of section and finite wing effects. The wing  $C_D$  can be expressed as

$$C_D = C_{D0} + C_{DLv} + C_{DLi} \quad (2.16)$$

where  $C_{DLv}$  is the viscous drag-due-to-lift and  $C_{DLi}$  is the induced (inviscid) drag-due-to-lift. For a cambered wing, Eq. (2.16) is written as



**Figure 2.14** a) F-18 in high- $g$  maneuver showing vortices rolling up over the LEX, and b) F-22 showing vortex shedding from its LEX and the leading edge of its swept back wing.

## Tigershark Wing Rock Fix

In 1983 the Northrop F-20A Tigershark (shown in Fig. 2.15) was in flight testing. The aircraft exhibited wing rock at  $\sim 18$  deg angle-of-attack due to asymmetric flow separation at the wingtips. Because the F-20A was to be an air-to-air fighter with guns and IR missiles this was unacceptable. The normal fix would be to twist the wing, with the LE down, so that the wing root stalls before the tips. This would have been expensive because the wing tools were already fabricated and in place. Because the F-20A always flew with wingtip missile rails, a small LE extension was put on the rails that created a vortex over the wingtip upper surface, which delayed flow separation until about 25 deg.

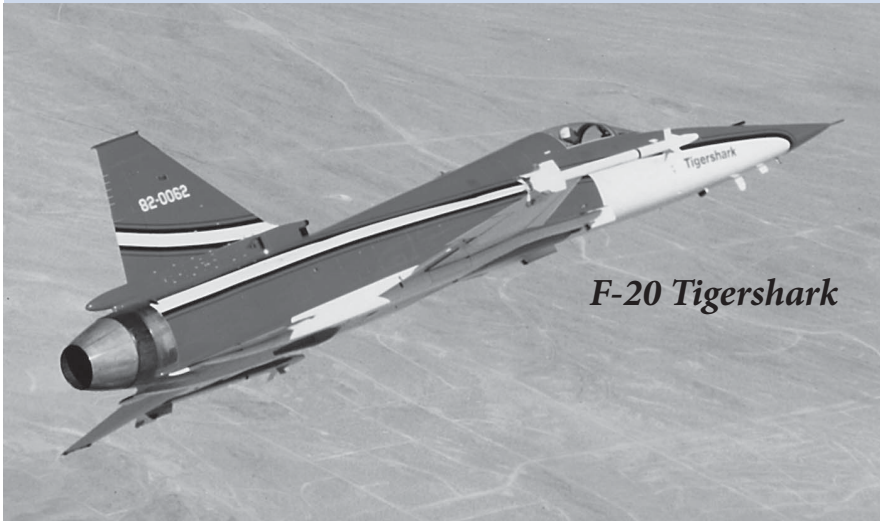


Figure 2.15

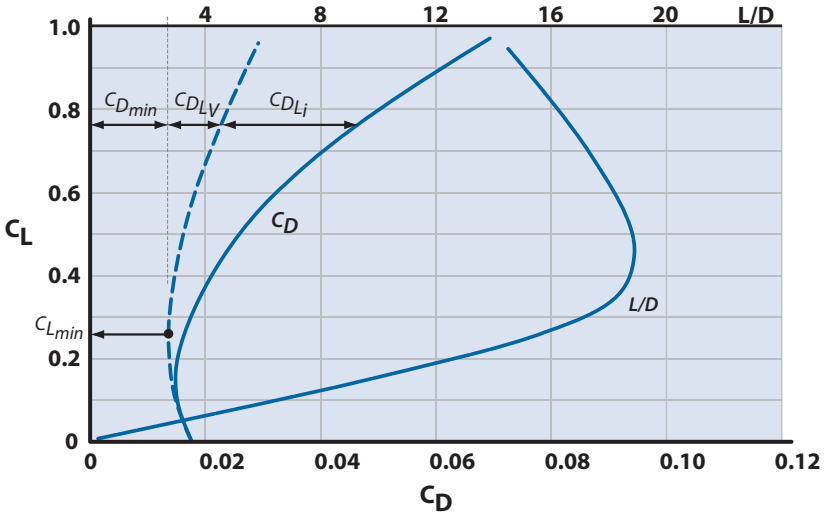


Figure 2.16 Low-speed drag polar ( $M \leq 0.4$ ) for C-141, clean configuration.

$$C_D = C_{D_{min}} + K''(C_L - C_{\ell_{min}})^2 + K'C_L^2 \quad (2.17)$$

where  $C_{\ell_{min}}$  is the  $C_{\ell}$  for  $C_{d_{min}}$  from the airfoil drag polar (see Fig. 2.8).

Equation (2.17) is illustrated in Fig. 2.16, which presents the experimental low-speed drag polar for the Lockheed C-141A. The C-141A uses a symmetric airfoil (average section is an NACA 0011) but the wing is at an average +3.2-deg angle of incidence to the fuselage, giving the entire vehicle an effective camber as evidenced by  $C_{\ell_{min}}$  being nonzero.

The wing aspect ratio is 7.9, sweep is 25 deg, and the taper ratio is 0.374, giving a low-speed  $C_{L\alpha} = 0.084$  per degree. For a zero fuselage angle-of-attack, the wing is at a  $C_L = 0.27 = C_{\ell_{min}}$ , which results in  $C_{D_{min}} = 0.016$  (see Fig. 2.16). The values for  $K''$  and  $K'$  are estimated from the methodology in Chapter 13 to be 0.02 and 0.0407, respectively. Inserting these values into Eq. (2.17) gives a  $C_D = 0.0252$  at  $C_L = 0.5$ , which agrees well with the experimental data. In this example, the  $C_{D_{min}}$  is made up of contributions from the wing, fuselage, tail, engine pods, and pylons; however, the aircraft  $C_{DL}$  is composed primarily of wing drag-due-to-lift. If the wing or entire aircraft is effectively uncambered, then  $C_{\ell_{min}} = 0$  and the expression is simplified to

$$C_D = C_{D_0} + K''C_L^2 + K'C_L^2 = C_{D_0} + KC_L^2 \quad (2.18)$$

Sometimes, early in the design when very little is known about the aircraft configuration, the expression for  $K$  will be approximated by



$$K = \frac{1}{\pi AR e}$$

where  $e$  is a wing planform efficiency factor (see Fig. G.9).

Equation (2.18) is illustrated in Fig. 2.17. The McDonnell F-4C Phantom II is effectively an uncambered wing aircraft, as shown in Fig. 2.17. The value for  $K$  is estimated from Chapter 13 to be 0.169. Figure 2.17 also highlights an interesting drag polar behavior for low-AR aircraft at high angles-of-attack. Aircraft display a parabolic behavior of  $C_D$  with  $C_L$  up to a lift coefficient  $C_{L_B}$ , called the *break  $C_L$* . Above  $C_{L_B}$  the  $C_D$  departs from classical parabolic behavior. This deviation from parabolic behavior is discussed in more detail in Chapter 13. The symmetric aircraft  $C_D$  at large  $\alpha$  can be expressed as

$$C_D = C_{D_0} + KC_L^2 + K_B (C_L - C_{L_B})^2 \tag{2.19a}$$

where  $K_B$  is called the *break drag-due-to-lift factor* and

$$\begin{aligned} K_B &= 0 & \text{for } C_L \leq C_{L_B} \\ K_B &> 0 & \text{for } C_L > C_{L_B} \end{aligned} \tag{2.19b}$$

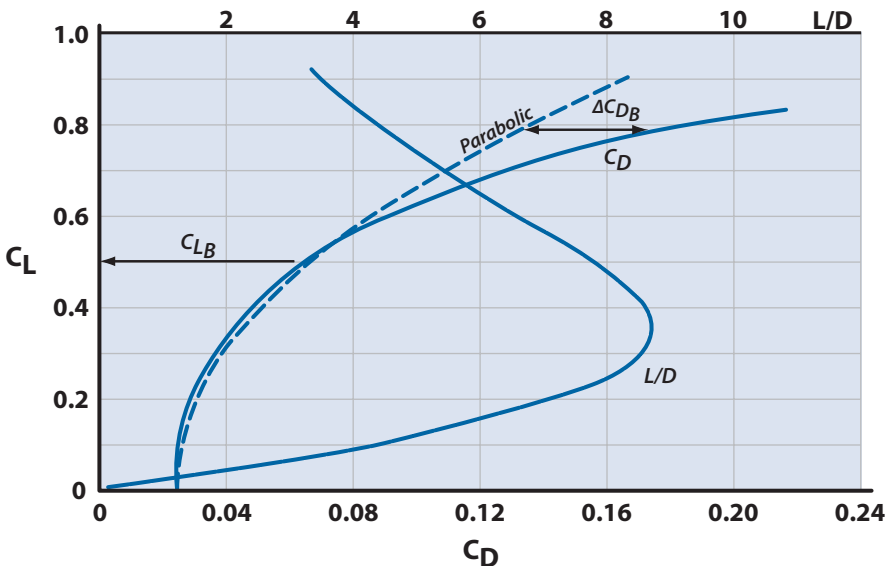


Figure 2.17 F-4C Aerodynamics at Mach 0.8 AR = 2.82,  $\lambda = 0.236$ ,  $t/c = 5\%$ , Series 64A,  $\Delta = 45$  deg.

Other fighter aircraft, such as the F-15 Eagle, have carefully tailored wings, resulting in  $C_{L_B}$  being very close to the buffet  $C_L$  with small values of  $K_B$ .

The wing  $C_{D_0}$  or  $C_{D_{\min}}$  is the same for section and finite wing and is given by

$$C_{D_0} = C_{D_{P_{\min}}} + C_{DF} \quad (2.20)$$

where  $C_{D_{P_{\min}}}$  = pressure drag due to viscous separation (experimentally determined) and small compared to  $C_{DF}$ .

$C_{DF}$  = skin friction drag coefficient

$$C_{DF} = C_F \frac{S_{\text{wet}}}{S_{\text{ref}}}$$

where  $S_{\text{wet}}$  is the wetted area of the exposed surface.

If the flow over the wing is laminar, that is,  $Re_\ell = \rho V_\infty \bar{c} / \mu < 5 \times 10^5$ , use

$$C_F = \frac{1.328}{\sqrt{Re_\ell}} \quad (2.21)$$

If the flow over the wing is turbulent, that is,  $Re_\ell > 5 \times 10^5$ , use

$$C_F = \frac{0.455}{[\log_{10} Re_\ell]^{2.58}} \quad (2.22)$$

Equations (2.21) and (2.22) are plotted in Fig. 2.6. For thin wings (i.e., thickness ratios of 20% and less) and streamlined bodies, the  $C_{D_0}$  is 70% to 80% skin friction. Thus, a good rule of thumb for subsonic  $C_{D_0}$  is

$$C_{D_0} \approx 1.2 C_{DF}$$

The fuselage and tail surfaces will contribute significant amounts to the aircraft  $C_{D_0}$ . As stated above the total aircraft  $C_{D_0}$  will be 70% to 80% skin friction with about 5% for mutual interference (adverse pressure gradients due to the interference of the wing on the body and vice versa). The skin friction of each aircraft component is determined and then added together; then a 5% mutual interference factor is added, to give the total aircraft  $C_{D_0}$ . The aircraft is broken down as shown in Fig. 2.18.

The  $C_F$  is determined for each aircraft component using, for laminar flow,

$$C_F = \frac{1.328}{\sqrt{Re_\ell}} \tag{2.21}$$

and for turbulent flow,

$$C_F = \frac{0.455}{[\log_{10} Re_\ell]^{2.58}} \tag{2.22}$$

and the  $C_F$  is always based upon the wetted area of the component. Each component is considered to be a flat plate of equivalent wetted area. The nose of the aircraft is treated as a cone and we use the result

$$C_{F_{\text{cone}}} = \frac{2}{\sqrt{3}} C_{F_{\text{flat plate}}}$$

The total skin friction coefficient of the vehicle is

$$(C_{DF})_{a/c} = C_{F_{\text{fuse}}} \frac{S_F}{S_{\text{ref}}} + C_{F_{\text{nose}}} \frac{S_N}{S_{\text{ref}}} + C_{F_{\text{wing}}} \frac{S_W}{S_{\text{ref}}} + C_{F_{\text{tail}}} \frac{S_T}{S_{\text{ref}}} \tag{2.23}$$

where  $S_{\text{ref}}$  is the reference area for the  $C_L$  and  $C_D$  and is usually the total wing planform area.

Finally the total aircraft  $C_{D_0}$  is

$$(C_{D_0})_{a/c} = 1.25(C_{DF})_{a/c} \tag{2.24}$$

where we have included a 5% mutual interference effect. This is to be regarded as a rule of thumb for early design estimates. The more accurate methodology of Chapter 13 is recommended for later design work.

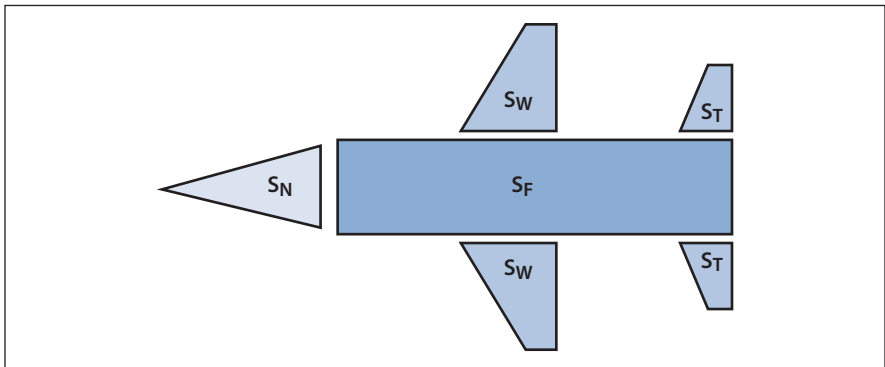


Figure 2.18 Aircraft components for skin friction estimation.

## 2.11 Transonic Flow and Its Effects

A body is considered to be in the *transonic flow* regime when sonic flow (Mach number greater than 1.0) first occurs somewhere on the body surface. The lower limit of transonic flow is for some  $M_\infty$  less than unity and depends upon the thickness of the wing or body. The upper limit is generally considered to be  $M_\infty \approx 1.3$  where all surface flows are supersonic.

A conventional subsonic airfoil shape is shown in Fig. 2.19. If this airfoil is at a flight Mach number of 0.50 and a slight positive angle-of-attack, the maximum local velocity on the surface will be greater than the flight speed but most likely less than sonic speed. Assume that an increase in flight Mach to 0.72 would produce the first evidence of local sonic flow. This condition would be the highest flight speed possible without supersonic flow and is termed the “critical Mach number.” Thus, critical Mach number is the boundary between subsonic and transonic flow and is an important point of reference for all compressible effects encountered in transonic flight.

As critical Mach number is exceeded, an area of supersonic flow is created on the wing surface. The acceleration of the airflow from subsonic to supersonic is smooth and unaccompanied by any shock waves. However, the transition from supersonic to subsonic occurs through a shock wave and because there is no change in direction of the flow the wave formed is a normal shock wave.

One of the principal effects of the normal shock wave is to produce a large increase in the static pressure of the airstream behind the wave. If the shock wave is strong, the boundary layer may not have sufficient kinetic energy to withstand the large adverse pressure gradient and separation will occur. At speeds only slightly beyond the critical Mach number the shock wave formed is not strong enough to cause separation or any noticeable change in the aerodynamic force coefficients. However, an increase in speed sufficiently above the critical Mach number to cause a strong shock wave will produce separation and yield a sudden change in the force coefficients. Such a flow condition is shown in Fig. 2.19 by the flow pattern for  $M = 0.77$ . Notice that a further increase in Mach number to 0.82 can enlarge the supersonic area on the upper surface and form an additional area of supersonic flow and a normal shock wave on the lower surface.

As the flight speed approaches the speed of sound, the areas of supersonic flow enlarge and the shock waves become stronger and move nearer the trailing edge (Fig. 2.20). When the flight speed exceeds the speed of sound, the “bow” wave forms at the leading edge as illustrated in Fig. 2.19 for  $M = 1.05$ . If the speed is increased to some higher supersonic value, all oblique portions of the wave incline more greatly and the detached normal shock portion of the bow shock wave moves closer to the leading edge.

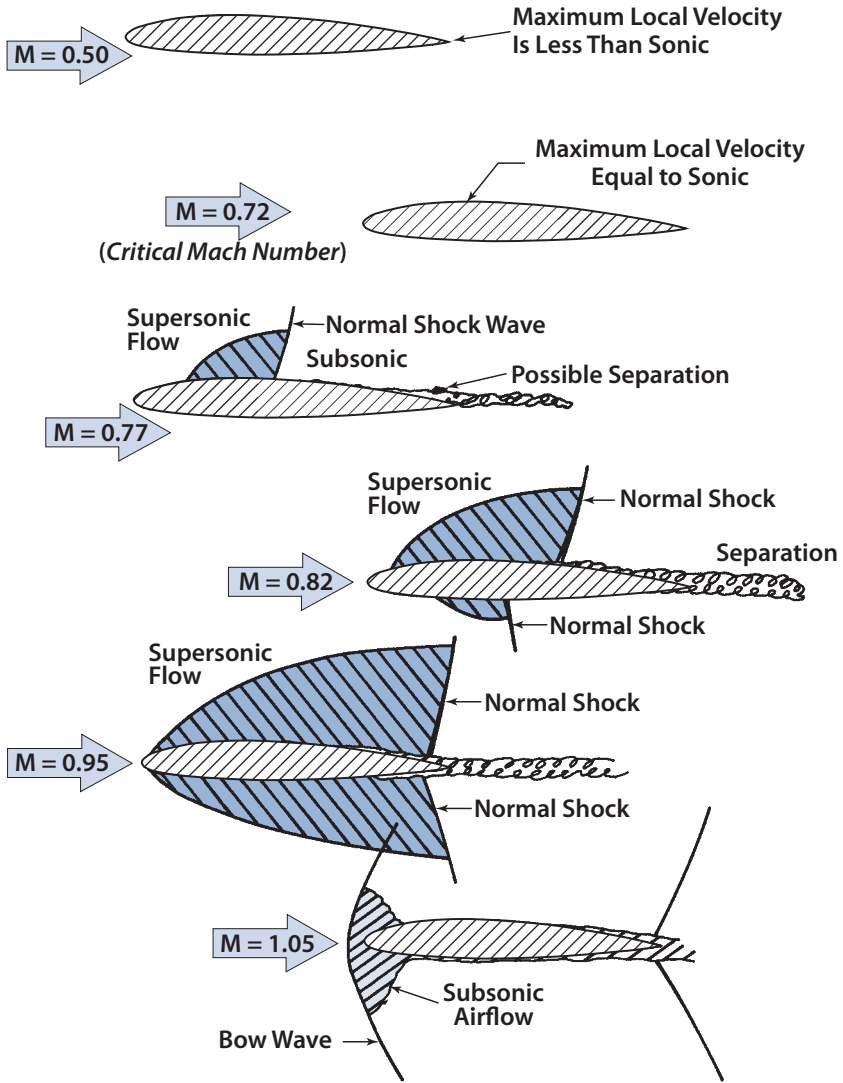


Figure 2.19 Flow patterns around an airfoil in transonic flow.

The airflow separation induced by the shock wave formation can create significant variations in the aerodynamic force coefficients. Some typical effects are an increase in the section drag coefficient and a decrease in the section lift coefficient for a given angle-of-attack. Accompanying the variations in  $C_l$  and  $C_d$  is a change in the pitching moment coefficient.

The Mach number that produces a large increase in the drag coefficient is termed the *force divergence Mach number* and for most airfoils exceeds



**Figure 2.20** F-14 at  $M \sim 0.95$  with condensation at trailing edge normal shock.

the critical Mach number by 5% to 10%. This condition is also referred to as *drag divergence* or *drag rise*.

Associated with the transonic drag rise are buffet, trim, and stability changes, and a decrease in the effectiveness of control surfaces. Conventional aileron, rudder, and elevator surfaces subjected to this high-frequency buffet may “buzz” and changes in moments may produce undesirable control forces. Also, when airflow separation occurs on the wing due to shock wave formation, there will be a loss of lift and subsequent loss of downwash aft of the affected area. If the wings shock unevenly due to physical shape differences or sideslip, a rolling moment may be created and can contribute to control difficulty. If the shock-induced separation occurs symmetrically near the wing root, the resulting decrease in downwash on the horizontal tail will create a diving moment and the aircraft will “tuck under.”

Because most of the difficulties of transonic flight are associated with shock wave induced flow separation, any means of delaying or alleviating this separation will improve the aerodynamic characteristics of an aircraft. Thus, it is important to seek ways to increase the critical Mach number  $M_{CR}$  of the aircraft.

The critical Mach number can be increased by the following:

- Decreasing wing thickness ratio
- Increasing leading edge sweep
- Decreasing aspect ratio
- Using a supercritical airfoil

## 2.12 Wing Thickness Ratio

It is clear from Fig. 2.19 that a smaller thickness ratio will give an increase in  $M_{CR}$ . Thus, supersonic aircraft will have small thickness ratios,

usually 5% or less, whereas subsonic aircraft will have thicker wings of perhaps up to 18%. Structural considerations prohibit wings of less than 3%. Figure 2.23b (see Section 2.14) and Fig. 7.7 (see Chapter 7) show how  $M_{CR}$  increases with decreasing thickness ratio.

### 2.13 Wing Sweep

One of the most effective means of delaying and reducing the effects of shock wave induced flow separation is the use of sweep. Generally the effect of wing sweep will apply either to sweepback or sweep forward. Although the sweep-forward wing has been used in rare instances, sweepback has been found to be more practical for ordinary applications.

A method of visualizing the effect of sweepback is shown in Fig. 2.21. The swept wing shown has the streamwise velocity vector resolved into components perpendicular and parallel to the leading edge. The component parallel to the leading edge may be visualized as moving across constant sections and thus does not contribute to the pressure distribution in the wing. The component perpendicular to the leading edge ( $V_\infty \cos \Delta$ ) is less than freestream velocity and it is this component that determines the magnitude of the pressure distribution and the aerodynamic force coefficients.

Hence, sweep of a surface in high-speed flight produces a beneficial effect, because higher flight speeds may be obtained before components of velocity perpendicular to the leading edge produce critical conditions on the wing. Thus, sweepback will increase the critical Mach number, the force divergence Mach number, and the Mach number at which the drag rise will peak. In other words, sweep will delay the onset of compressibility effects. The critical Mach number  $M_{CR}$  is increased by  $(M_{CR})_{\Delta=0} / \cos \Delta$ .

In addition to delaying the onset of compressibility effects, sweepback will reduce the magnitude of the changes in force coefficients due to compressibility. Because the component of velocity perpendicular to the leading edge is less than freestream velocity, the magnitude of all pressure forces on the wing will be reduced (approximately by the square of the sweep angle). Because compressibility force divergence occurs due to change in pressure distribution, the use of sweepback will “soften” the force divergence. This effect is illustrated qualitatively by the graph of Fig. 2.21, which shows the typical variation of drag coefficient with Mach number for various sweepback angles. The straight wing shown begins drag rise at about  $M = 0.90$ , reaches a peak near  $M = 1.1$ , and begins a continual drop past  $M = 1.1$ . Note that use of sweepback then delays the drag rise to some higher Mach number and reduces the magnitude of the rise in drag coefficient. It is evident from the figure that small angles of sweep provide little benefit. If sweep is to be used at all, at least 35–45 deg should be used.

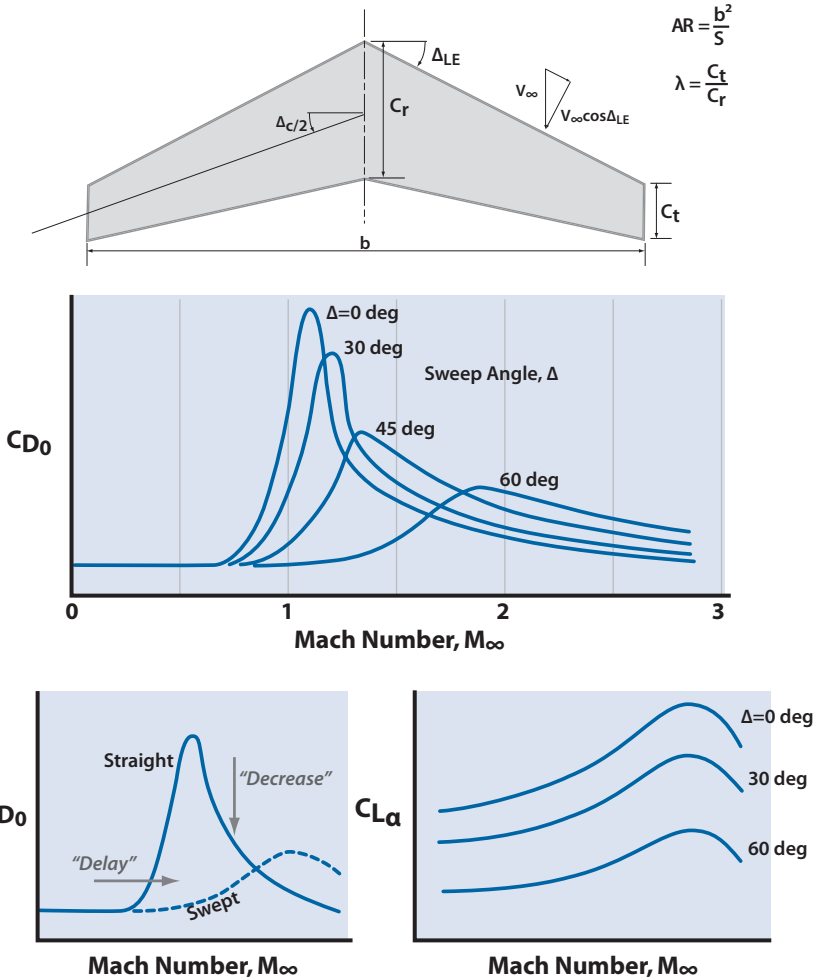


Figure 2.21 General effects of wing sweepback.

A disadvantage of wing sweep is the decrease in wing lift curve slope. This effect can be shown to be

$$\left( \frac{dC_L}{d\alpha} \right)_\Delta = \left( \frac{dC_L}{d\alpha} \right)_{\Delta=0} \cos \Delta$$

This means that a swept-wing aircraft will have to land and take off at higher angles-of-attack than a straight-wing aircraft.



Other disadvantages to wing sweep are a reduction in  $C_{L_{max}}$  and tip stall. Early flow separation at the tip is due to spanwise flow causing a thickening of the boundary layer near the tips and hastening flow separation.

### 2.14 Supercritical Wing

Another way of delaying the drag rise due to shock wave induced separation is by using an airfoil shape called a supercritical section. The supercritical section is shown in Fig. 2.22 compared with a conventional NACA 64A series section. The supercritical section has a much flatter shape on the upper surface that reduces both the extent and strength of the normal shock, as well as the adverse pressure rise behind the shock, with corresponding reductions in drag. To compensate for the reduced lift on the upper surface of the supercritical airfoil resulting from the reduced curvature, the airfoil has increased camber near the trailing edge.

The advantage of the supercritical airfoil section is shown in Fig. 2.22 and its geometry is shown in Fig. 2.23a. For a given thickness ratio, the critical Mach number stays the same but the divergence Mach number can be delayed as shown in Fig. 2.23b. Most high-subsonic aircraft will cruise near the divergence Mach number. The Boeing Airplane Company engineers were considering the application of a supercritical wing on their 707-320B and they had the choice of cruising at the same Mach number (about Mach 0.82) with an increase in the supercritical wing thickness to 13% or keeping the same thickness and cruising at a higher Mach number. Figure 2.23c shows the savings in wing weight as the wing is made thicker.

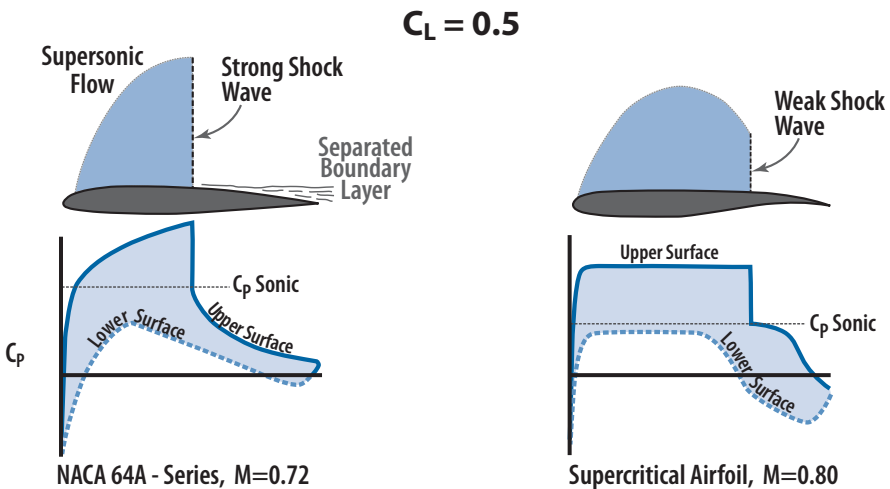


Figure 2.22 Supercritical airfoil flow phenomena.

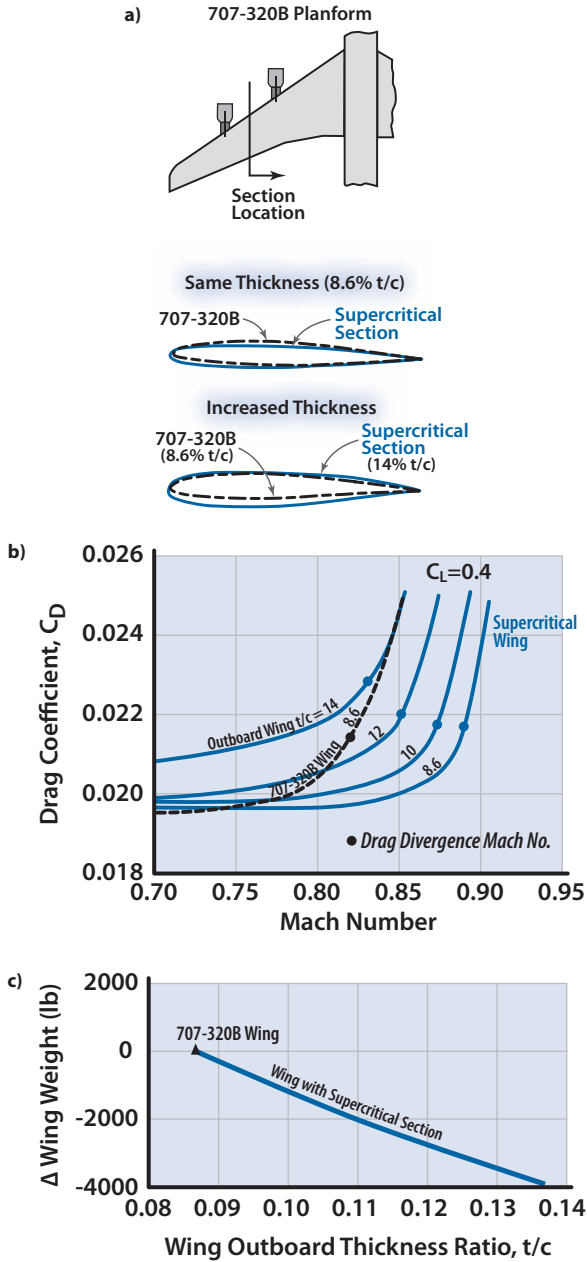


Figure 2.23 Supercritical section, a) geometry comparison, b) thickness effect on drag, and c) wing weight reduction with  $t/c$ .

## 2.15 Wing-Body Combinations for Transonic Flight

The zero-lift drag coefficient,  $C_{D_0}$ , of the fuselage will peak about Mach = 1.2. A typical fuselage  $C_{D_0}$  curve is shown in Fig. 2.24. The designer should observe the relative magnitude of the body  $C_{D_0}$  (referenced to wing area) compared to the wing  $C_{D_0}$  [9].

The  $C_{D_0}$  of a wing and a body can be added directly (for comparison purposes) to give the wing-body combination drag curve. Notice that the additional drag due to interference is not taken into account. From Fig. 2.24 we can see the advantage of having the wing drag rise occur at a higher

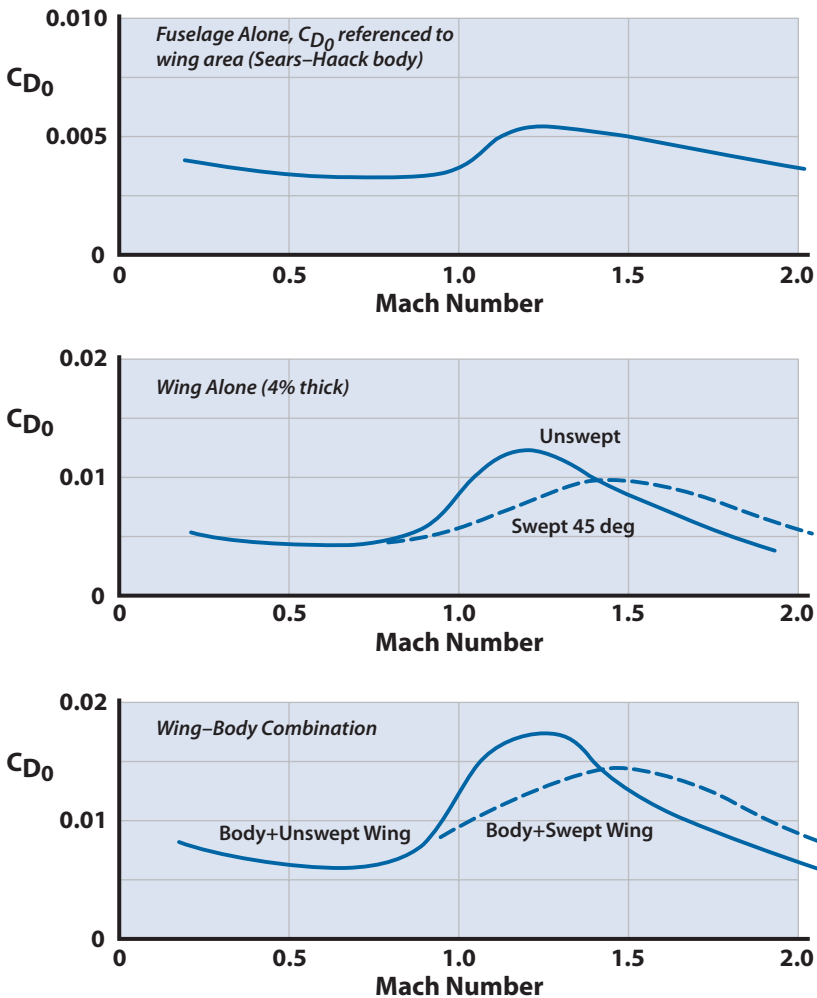


Figure 2.24 Wing, body, and wing-body  $C_{D_0}$  vs Mach number.

Mach number. This “adding together” of a wing and a body is shown in the same figure.

The swept-wing–body combination results in a lower drag coefficient and hence lower drag in the critical transonic flight regime. For many propulsion units the thrust around Mach = 1.0 increases more slowly than the drag increases and it is possible for the excess thrust ( $T-D$ ) to be marginal in the transonic region where the aircraft suffers a thrust pinch. There are several design methods to alleviate the thrust pinch. The designer could increase the size of the engines; however, this adds weight and may oversize the engines for other parts of the operating envelope. The wings could be swept as discussed previously and/or made thinner (lower thickness ratio). Another good design practice is to area-rule the aircraft (discussed in detail in Chapter 8 [10]).

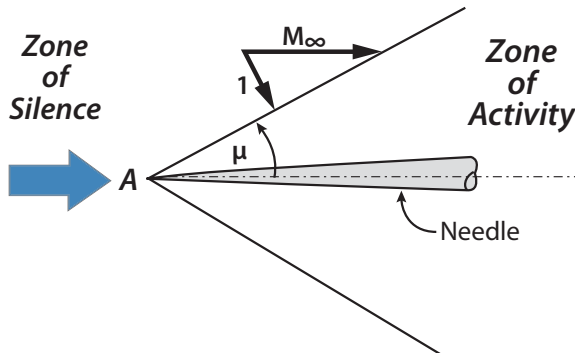
## 2.16 Mach Wave

A *Mach wave* is defined as the locus of all wave fronts from an infinitesimal pressure disturbance. An infinitesimal pressure disturbance propagates at the speed of sound  $a = \gamma RT$ . A *Mach cone* (three-dimensional Mach wave) is shown in Fig. 2.25.

The angle  $\mu$  is called the *Mach angle* and is equal to

$$\sin \mu = \frac{1}{M_\infty}, \quad \mu = \arcsin\left(\frac{1}{M_\infty}\right)$$

because the flow normal to the Mach wave is  $M = 1$ . The infinitesimal pressure disturbance at point  $A$  can influence every point inside its Mach cone, called the *zone of activity*. Similarly, the disturbance at point  $A$  will not be felt anywhere outside the Mach cone, called the *zone of silence*.



**Figure 2.25** Mach cone from an infinitesimal pressure disturbance.

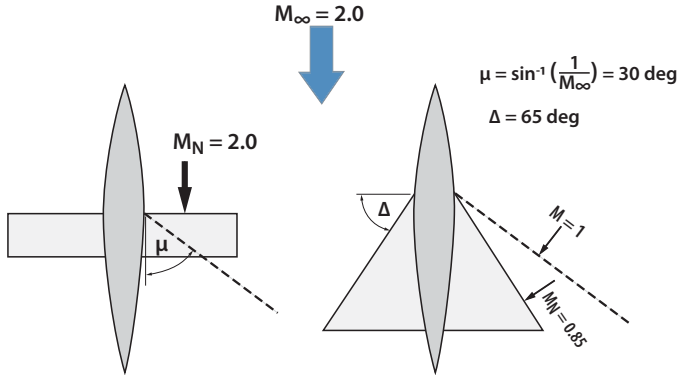


Figure 2.26 Straight and swept wing aircraft in Mach-2 flight.

## 2.17 Subsonic and Supersonic Leading Edge

Figure 2.26 shows both straight- and swept-wing aircraft where the freestream Mach number ( $M_\infty$ ) is 2.0 and the Mach angle ( $\mu$ ) is 30 deg. The normal Mach number at the leading edge of the straight wing is 2.0 (supersonic) and of the swept wing is 0.85 (subsonic). As was discussed earlier, the pressure distribution over the wing is established by the flow normal to the leading edge. Thus, the wing of the straight-wing aircraft is experiencing supersonic flow. The straight-wing aircraft is said to have a “supersonic leading edge,” and the leading edge must be sharp and the section thin for low wave drag, whereas the swept-wing aircraft is said to have a “subsonic leading edge” and its leading edge can be round or blunt and the section fairly thick.

Thus, if  $\Delta > (90 - \mu)$ , the leading edge is subsonic, and if  $\Delta < (90 - \mu)$ , the leading edge is supersonic.

The wave drag coefficient for a wing will peak at the  $M_\infty$  where the normal Mach  $\approx 1.2$ . This explains the  $C_D$  behavior in Figs. 2.24 and 2.29 (see Section 2.20). The F-111 has a round leading edge, characteristic of subsonic leading edges, and the sweep schedule for its variable-sweep wing is such that the normal Mach number is always subsonic, that is,  $\Delta > (90 - \mu)$ .

Because the lift curve slope decreases with wing sweep, it is not desirable to sweep a wing more than is necessary. Thus, a good rule of thumb for a swept wing with a subsonic leading edge is to sweep it 5 deg behind the Mach line.

## 2.18 Supersonic Skin Friction

The supersonic flow over a vehicle is very likely turbulent ( $Re_\ell > 5 \times 10^5$ ) so that the skin friction is given by the turbulent skin friction expression

[Eq. (2.22)] corrected for compressibility. The incompressible flat plate turbulent skin friction is given by (for one side of the flat plate)

$$C_{F_i} = \frac{0.455}{[\log_{10} Re_\ell]^{2.58}} \tag{2.22}$$

Equation (2.22) is plotted in Fig. 2.6. The compressibility correction is given in [11] as

$$C_F = \frac{C_{F_i}}{(1 + 0.144 M_\infty^2)^{0.65}} \tag{2.25}$$

The method for determining the total aircraft skin friction is the same as discussed earlier with the exception of correcting  $C_{F_i}$  for compressibility.

### 2.19 Supersonic Lift and Wave Drag

If the local flow inclination over a body in a supersonic stream is small, then the pressure coefficient at each point is given by the following linear theory result:

$$C_p = \frac{P - P_\infty}{\frac{1}{2} \rho V_\infty^2} = \frac{P - P_\infty}{\frac{1}{2} \gamma P_\infty M_\infty^2} = \frac{2\theta}{\sqrt{M_\infty^2 - 1}}$$

where  $\theta$ , in radians, is positive for compression regions and negative for expansion regions.

The supersonic section lift and wave drag coefficients are given by supersonic thin airfoil theory (linear theory [12]):

$$C_\ell = \frac{4\alpha}{\sqrt{M_\infty^2 - 1}} \tag{2.26}$$

$$C_{d_w} = \frac{4\alpha}{\sqrt{M_\infty^2 - 1}} \left[ \overline{\alpha^2 + \alpha_c(x)^2} + \left( \overline{\frac{dh}{dx}} \right)^2 \right] \tag{2.27}$$

where  $\alpha$  is the angle-of-attack (radians),  $\alpha_c(x)^2$  is the mean square of the camber line

$$\overline{\alpha_c(x)^2} = \frac{1}{c} \int_0^c \alpha_c(x)^2 dx \tag{2.28}$$

and  $\left( \overline{dh/dx} \right)^2$  is the mean square of the thickness distribution.

**Table 2.1** Section Parameters for Wave Drag

Shape	$\bar{\alpha}_c^2$	$(dh/dx)^2$
Flat plate	0	0
Double wedge	0	$t/c^a$
Biconvex	0	$\frac{4}{3} \frac{t}{c}$

<sup>a</sup> $t/c$  is the max thickness ratio of the section.

$$\left(\overline{\frac{dh}{dx}}\right)^2 = \frac{1}{c} \int_0^c \left(\frac{dh}{dx}\right)^2 dx \tag{2.29}$$

We observe that the supersonic  $C_{d_w}$  is made up of drag-due-to-lift, drag due to camber, and drag due to thickness. Table 2.1 gives values of  $\bar{\alpha}_c^2$  and  $(dh/dx)^2$  for several basic supersonic airfoil sections.

Equation (2.27) is usually rewritten as

$$C_d = C_{d_0} + KC_\ell^2 \tag{2.30}$$

where

$$C_{d_0} = C_{DF} + \frac{4}{\sqrt{M_\infty^2 - 1}} \left[ \frac{-2}{\alpha_c} + \left(\overline{\frac{dh}{dx}}\right)^2 \right] + C_{dB} \left( \frac{S_B}{S_{ref}} \right) \tag{2.31}$$

$$K = \frac{\sqrt{M_\infty^2 - 1}}{4} \tag{2.32}$$

$C_{dB}$  = base drag due to flow separation over a blunt base

$S_B$  = base area

At the rear of a wing with a blunt base in supersonic flow, the flow tries to expand 90 deg. Inviscid flow theory would predict that the base pressure  $P_B$  would be zero. However, in a viscous fluid the base pressure is not zero but is some value less than ambient pressure  $p_\infty$ . This is due to the boundary layer bleeding into the separated flow region at the base, giving a turbulent wake and  $0 < P_B < P_\infty$ . Experimental values of base pressure coefficients  $C_{pB}$  for two- and three-dimensional bodies are shown in Fig. 2.27. Notice that the  $C_{dB}$  of Eq. (2.31) is equal to the negative of  $C_{pB}$  and is referenced to the base area,  $S_B$ .

Equation (2.27) assumes that the shock is an attached oblique shock. If the shock is a detached normal shock, an additional drag term due to nose

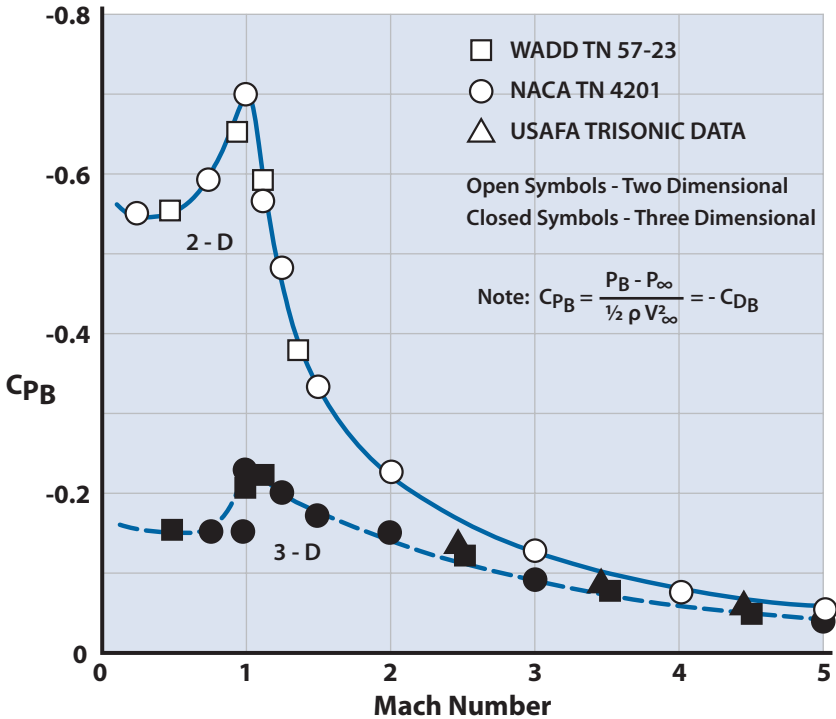


Figure 2.27 Experimental values of base pressure coefficient.

bluntness,  $C_{d_{LE}}$ , is added to Eq. (2.31). This bluntness term  $C_{d_{LE}}$  is discussed more fully in Chapter 13, Fig. 13.13, but it should be pointed out that  $C_{d_{LE}} = f[M_\infty, r_{LE}, \cos \Delta_{LE}]$ , where  $r_{LE}$  is the radius of the leading edge. Thus, for low wave drag at a given  $M_\infty$ , the best scenario is a wing with small thickness ratio, a small leading edge radius, a low aspect ratio, and lots of sweep. These ideas should be kept in mind when the airfoil and wing planform are selected (see Chapter 7).

## 2.20 Correction for Three-Dimensional Effects

A fuselage can be approximated by a cone-cylinder. The supersonic wave drag from a cone can be determined using the conical shock charts of Appendix E. The pressure coefficient on the surface of a cone is equal to the wave drag coefficient referenced to the cross-sectional area of the cone. If the cone is blunted, there will be a detached normal shock, and a drag coefficient due to nose bluntness must be determined. This nose bluntness term will be discussed in Chapter 13.



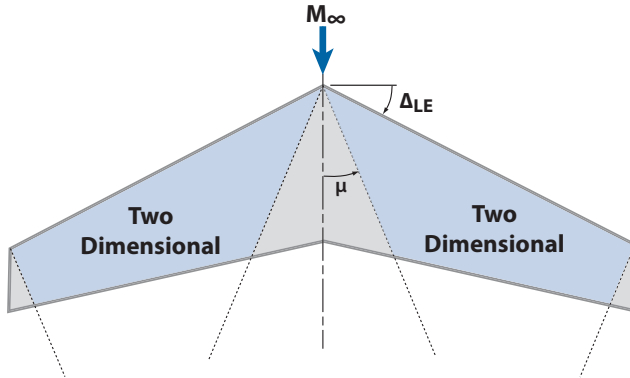


Figure 2.28 Finite span wing in supersonic flow.

The flow field around finite wings is made up of two parts: (1) the region within the Mach cones, and (2) the regions outside the Mach cones where the flow is two-dimensional. This flow pattern is shown in Fig. 2.28.

The analysis of a finite span wing is the determination of the field of three-dimensional flow and its influence on the rest of the wing. The lift and wave drag coefficients for the regions of two-dimensional flow are given by Eqs. (2.26) and (2.27). The three-dimensional wing lift uses supersonic thin airfoil theory and finite wing theory reported in [11–16] and is plotted in Fig. 13.2 for different wing taper ratios. Methods for determining wing–body supersonic  $C_{D_0}$  and drag-due-to-lift are discussed in Chapter 13, Sections 13.2.2 and 13.3.6. Figure 2.29 shows a comparison of wind tunnel data and theory for  $C_{D_0}$  vs Mach Number for varying 50% chord sweepback angles.

## 2.21 Sanity Check

It is always a good idea to get a sanity check on any analytical results or estimates (aero, weights, performance, etc.) before using them in the next part of the design process. In industry the sanity check might be performed by the group lead engineer double-checking the numbers. Or it might be done by comparing the estimates with real-world aircraft data. Appendix G contains the measured aerodynamics of many military and commercial aircraft.

The aircraft maximum  $L/D$  is a major design parameter as it indicates the aerodynamic efficiency of the configuration. It is important that the  $(L/D)_{\max}$  be checked with as many sources as possible before moving into the next stage of design. A correlation factor for  $(L/D)_{\max}$  is developed next.

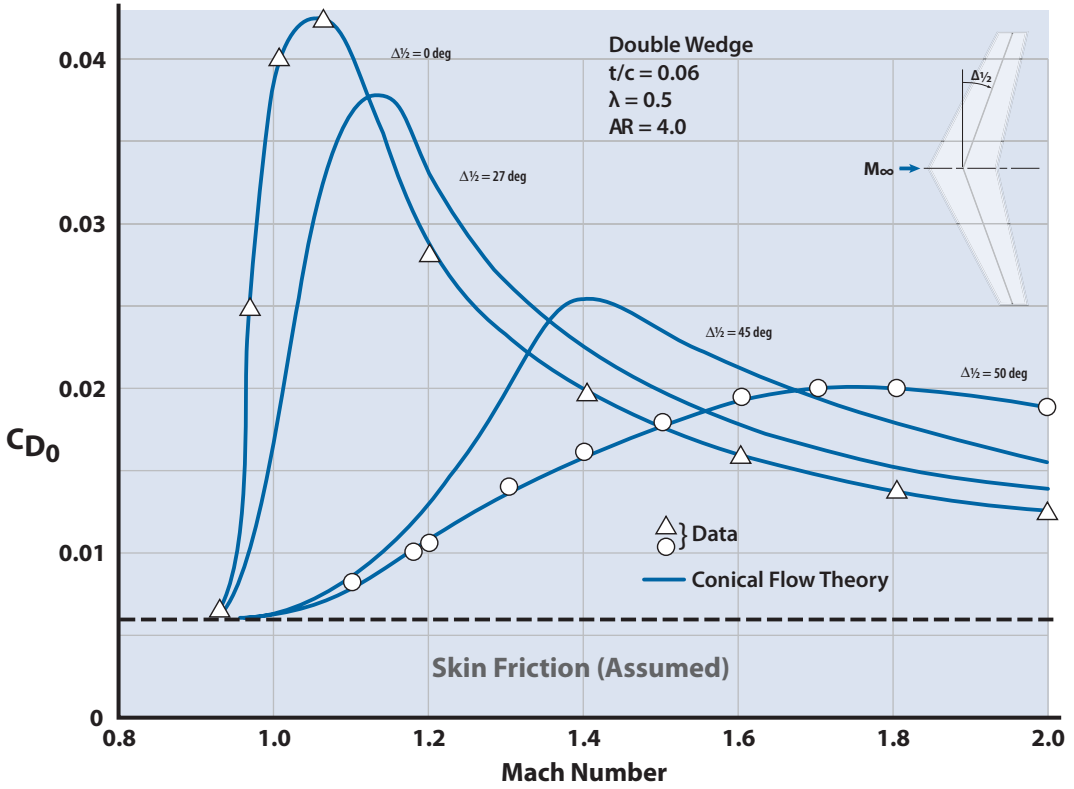


Figure 2.29 Effect of wing sweep on  $C_{D0}$ .

Assume the aircraft wing is uncambered so that the drag coefficient can be expressed as

$$C_D = C_{D0} + KC_L^2 \text{ [see Eq. (2.18)]}$$

where  $K = 1/\pi AR e$  and aspect ratio  $AR = b^2/S_{ref}$ .

The  $(L/D)_{max}$  is then expressed as

$$(L/D)_{max} = 1/\sqrt{4C_{D0}K}$$

[which is developed in Chapter 3 as Eq. (3.10a)]. As discussed in Section 2.10, the  $C_{D0}$  is *friction + form + interference + excrescence* drag, and the subsonic

$$C_{D0} \approx 1.25C_{DF} = 1.25C_F \frac{S_{wet}}{S_{ref}} \text{ [see Eq. (2.24)]}$$

where  $S_{\text{wet}}$  is defined as the aircraft wetted area and is the total area that would get wet if the aircraft were submerged in water. The correlation of subsonic  $C_{D_0}$  with  $S_{\text{wet}}/S_{\text{ref}}$  is shown in the aero data appendix in Fig. G.7. Finally, we can express a correlation factor for subsonic maximum  $L/D$  as

$$(L/D)_{\text{max}} \sim b/\sqrt{S_{\text{wet}}} \quad (2.33)$$

This correlation of  $(L/D)_{\text{max}}$  with  $b/(S_{\text{wet}})^{1/2}$  is shown in the aero data appendix in Fig. G.8. The world's aircraft can be plotted on this figure and will fall between the  $e/C_f$  lines shown. The lines of  $e/C_f$  represent a ratio of wing efficiency to skin friction. Most sailplanes fall on the upper curve because they have high aero efficiency and low friction drag, and zero interference or excrescence drag is essential for world competition. The lower line represents the “nominal” operational aircraft featuring good wing design but turbulent boundary layers, normal surface roughness, and some excrescence drag.

### Life of a Test Pilot (Tongue in Cheek)

Captain Buzz Jetspeed surveyed the sleek, shiny new prototype XRA-5C. This was it—the first flight of the new supersonic fighter. The engine start, taxi, takeoff, and climb to altitude were normal. The excitement grew as Buzz accelerated through Mach 1 to supersonic Mach = 1.6. He knew that he had to be careful here because he was in the region of decreasing minimum  $C_D$  (see the drag curve for the RA-5C in Fig. G.5a). If he were to accelerate to Mach = 2, he might not have enough drag to decelerate back through Mach = 1.0 into subsonic flight. But life was good—and so was Buzz. As he started to relax, his knee bumped the throttle and the XRA-5C started accelerating toward Mach = 2.0. He immediately reversed the engines, popped the speed brakes, and deployed the landing gear to generate enough drag to decelerate through the “drag rise.” The aircraft was starting to shudder, glow red hot, and melt. The entropy in the engines was decreasing and flowing out of the inlet. The usually cool and collected Buzz Jetspeed was starting to come unglued. Ever so slowly the XRA-5C began inching back toward Mach 1—1.6, 1.5, 1.4, 1.3, 1.2. When the airplane got to Mach = 1.1 the normal shock blew it through Mach 1 to Mach = 0.85 and eventual safety. When Buzz got back to the flight line the XRA-5C was not shiny and sleek anymore; it was bent, with a melted nose and burned leading edges. The floor of the cockpit was covered with a gooey liquid thought to be entropy. Buzz never talked about it.

## References

- [1] McCormick, B. W., *Aerodynamics, Aeronautics and Flight Mechanics*, Wiley, New York, 1995.
- [2] Kuethe, A. M., and Schetzer, J. D., *Foundations of Aerodynamics*, Vol. 2, Wiley, New York, 1959.
- [3] Abbott, I. H., Von Doenhoff, A. E., and Stivers, L., Jr., "Summary of Airfoil Data," NACA TR 824, 1945.
- [4] Abbott, I. H., and Von Doenhoff, A. E., *Theory of Wing Sections*, Dover, New York, 1959.
- [5] Gersten, K., "Calculation of Non-Linear Aerodynamic Stability Derivatives for Airplanes," AGARD Rept. No. 342, 1960.
- [6] Gersten, K., "Nonlinear Airfoil Theory for Rectangular Wings in Incompressible Flow," NASA RE-3-2-59W, 1959.
- [7] Lawrence, H. R., "Wing-Body Interference at Subsonic and Supersonic Speeds," *Journal of the Aeronautical Sciences*, Vol 21, No. 5, 1954, pp. 289–324.
- [8] Gersten, K., "A Nonlinear Lifting Surface Theory for Low Aspect Ratio Wings," *AIAA Journal*, Vol 1, No. 4, April 1963, pp. 924–925.
- [9] Mirels, H., "Aerodynamics of Slender Wings and Wing–Body Combinations Having Swept Trailing Edges," NACA TN-3105, 1954.
- [10] Whitcomb, R. T., "Supercritical Wing Technology—A Progress Report on Flight Evaluations," NASA Flight Research Center, Edwards, CA, 29 Feb. 1972.
- [11] Hayes, W. D., and Probstein, R. F., *Hypersonic Flow Theory*, Academic Press, New York, 1959.
- [12] Liepmann, H. W., and Roshko, A., *Elements of Gasdynamics*, Wiley, New York, 1957.
- [13] Eshbach, O. W., *Handbook of Engineering Fundamentals*, 3rd ed., Wiley, New York, 1974.
- [14] Jones, R. T., "Properties of Low-Aspect-Ratio Pointed Wings at Speeds Below and Above the Speed of Sound," NACA TR-835, 1946.
- [15] Harmon, S. M., and Jeffreys, I., "Theoretical Lift and Damping in Roll of Thin Wings with Arbitrary Sweep and Taper at Supersonic Speeds, Supersonic Leading and Trailing Edges," NACA TN-2114, 1950.
- [16] Malvestuto, F. S., Margolis, K., and Ribner, H. S., "Theoretical Lift and Damping in Roll at Supersonic Speeds of Thin Sweptback Tapered Wings with Streamwise Tips, Subsonic Leading Edges, and Supersonic Trailing Edges," NACA TR-970, 1950.

## Chapter 3

# Aircraft Performance Methods



- Optimum Flight Speed
- Breguet Range & Endurance Equation
- Maximum Range & Endurance
- Turning Performance
- Energy Maneuverability
- Climb & Descent

The SR-71 still holds the world speed record for manned air-breathing operational aircraft set in 1976 at 2194 mph. I was privileged to work on the SR-71, and later on the M-21/D-21 drone-carrying version of the M-21; I remember those times fondly.

*Grant Carichner*

*Good enough is not enough.  
It is ever the enemy of the best.*

### 3.1 Introduction

This chapter will consider steady-state and accelerated performance methods. A large portion of an aircraft's mission profile can be considered as *steady-state* (equilibrium) or a series of near-steady-state conditions. The landing and takeoff phases, the climb–acceleration phase, and the combat phase are not equilibrium conditions and are considered as *accelerated performance* problems. The landing and takeoff analysis is discussed in Chapter 10.

For the discussions in this chapter, the aircraft will be considered as a point mass system with horizontal and vertical translation degrees of freedom and subject to aerodynamic, propulsive, and gravity forces. The force diagram for the aircraft is shown in Fig. 3.1, where the lift and drag forces are normal and parallel to the freestream velocity  $V_\infty$ , respectively;  $i_T$  is the angle (usually small) between the wing chord line (WCL) and thrust vector; and  $\gamma$  is the flight path angle.

### 3.2 Level Unaccelerated Flight

During level unaccelerated flight, the flight path angle  $\gamma$  is zero and all external forces acting on the aircraft are in balance. Thus, adding forces normal and parallel to  $V_\infty$  (the wind axis) yields the following results:

$$L + T \sin(\alpha + i_T) = W \cos \gamma \quad (3.1)$$

$$T \cos(\alpha + i_T) = W \sin \gamma + D \quad (3.2)$$

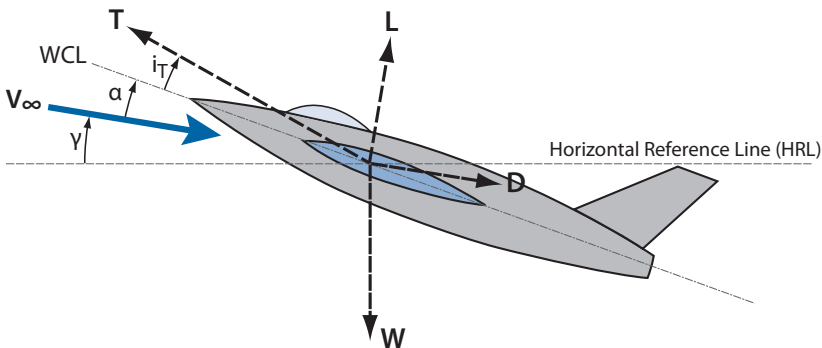


Figure 3.1 Forces acting on aircraft:

Because  $\gamma = 0$  and  $(\alpha + i_T)$  is usually small during this flight condition, the scalar equations representing level unaccelerated flight for a symmetric (uncambered,  $C_{L_{\min}} = 0$ ) aircraft are as follows:

$$W \approx L = C_L qS \quad (3.3)$$

$$T \approx D = (C_{D0} + KC_L^2)qS \quad (3.4)$$

where  $q = \frac{1}{2}\rho_\infty V_\infty^2$  is the *dynamic pressure* and  $S$  is the *reference area* for  $C_L$  and  $C_D$  (usually the total wing planform area). Because  $L = W$  the  $C_L$  at which the aircraft must fly at is expressed as

$$C_L = W/qS$$

From Eq. (3.4) the drag determines the *thrust required*  $T_R$ :

$$T_R = D = C_{D0}qS + KW^2/qS \quad (3.5)$$

The first term on the right-hand side of Eq. (3.5) is the *zero-lift drag*, and the second term is the *drag-due-to-lift* during level unaccelerated flight. For a given aircraft, altitude, weight, and aircraft configuration, the drag or thrust required can be plotted against velocity as shown in Fig. 3.2a.

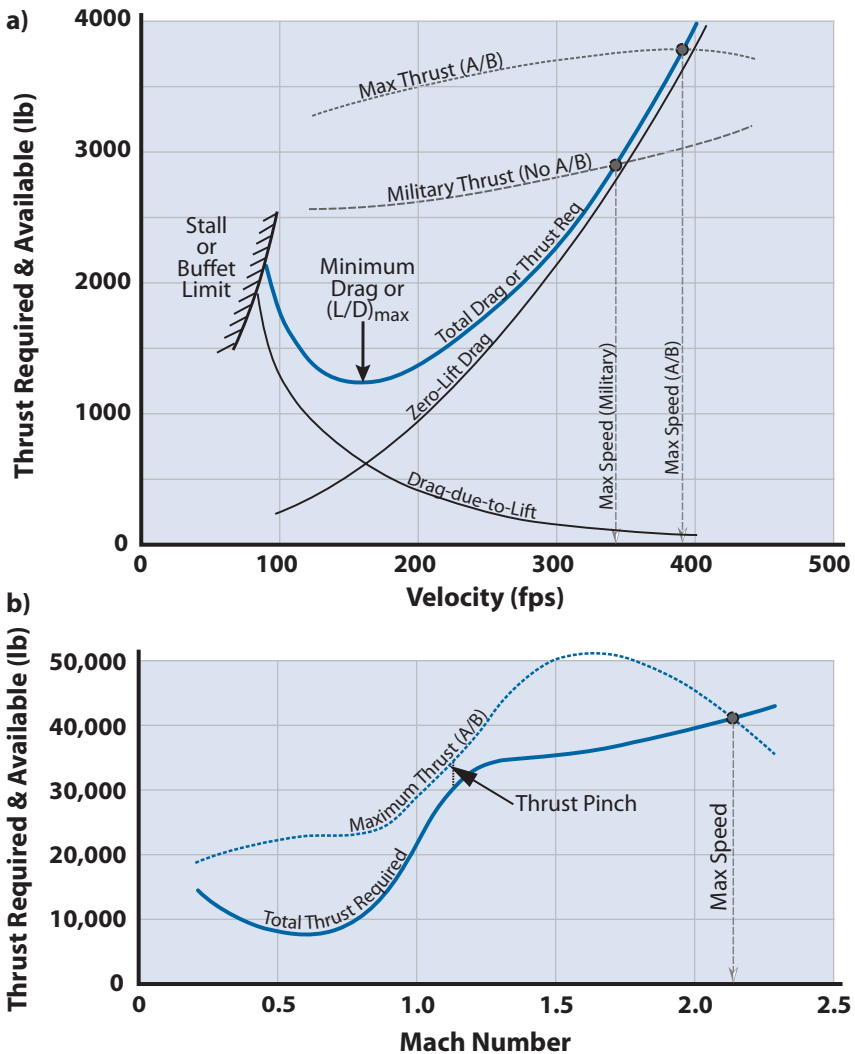
The *minimum velocity* point for the thrust-required curve in Fig. 3.2a is either stall speed or a minimum control speed. Flight below this speed is not relevant. The intersection of the thrust-available curve (either maximum thrust or military thrust) with the thrust-required curve is the *maximum speed* for the aircraft at that particular power condition ( $V_{\max}$ ). Notice that for speeds less than  $V_{\max}$  we do not have  $T = D$  and the aircraft will accelerate. If the pilot desires to fly at the minimum drag point on the  $T_R$  curve, for example, the engine must be throttled back until the available thrust equals  $T_R$  for minimum drag. The “thrust pinch point” shown in Fig. 3.2b can be a design challenge as the  $T-D$  can become so small that too much fuel is used in accelerating through  $M = 1$ . The SR-71 (see the SR-71 design case study in Volume 2) had a small  $T-D$  near  $M = 1$  and had to perform a dive maneuver to accelerate efficiently past  $M = 1$ .

The point of minimum drag is an interesting flight condition as it represents the velocity for maximum loiter or endurance for a turbine-powered aircraft. At this condition the aircraft’s *lift-to-drag ratio*  $L/D$  is at maximum, as will be shown in the next section.

The *power required* for a propeller aircraft is given by

$$P_R = DV = T_R V = (C_{D0} + KC_L^2) \frac{W}{C_L} \sqrt{\frac{2W}{\rho C_L S}} \quad (3.6)$$

Power-required curves can be constructed from thrust-required curves and are useful when analyzing reciprocating-engine propeller aircraft. The reciprocating engine fuel flow rate is proportional to power output rather than thrust output as for a jet engine. The power-required curve is constructed similarly to the thrust-required curve. A typical power-required curve is shown in Fig. 3.3. A useful conversion factor that the designer should remember is from horsepower to foot-pounds per second: 1 hp = 550 ft · lb/s.



**Figure 3.2** Thrust-required and thrust-available curves for typical jet aircraft: **a)** subsonic aircraft at constant altitude, and **b)** supersonic aircraft flying a minimum-time trajectory.



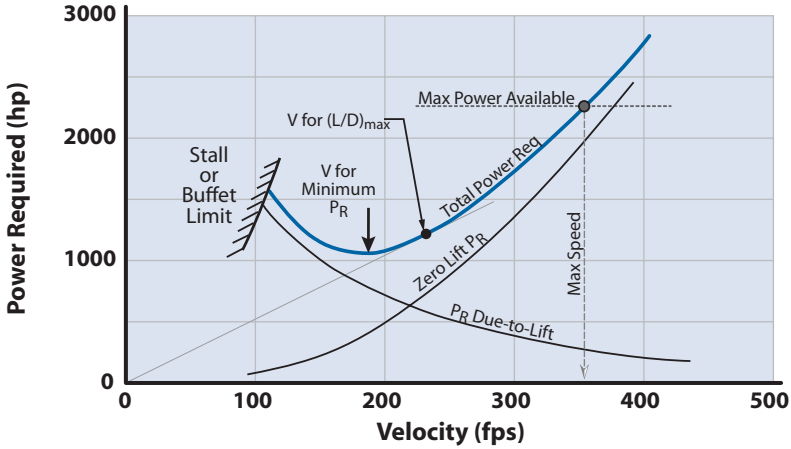


Figure 3.3 Power required for typical reciprocating-engine aircraft at constant altitude.

### 3.3 Minimum Drag and Maximum L/D

The total drag coefficient for an uncambered aircraft may be expressed as

$$C_D = C_{D0} + KC_L^2$$

and the total drag from Eq. (3.4) as

$$D = (C_{D0} + KC_L^2)qS$$

We seek to find the  $C_L$  that minimizes the total drag. In other words, the following operation is performed:

$$\frac{\partial D}{\partial C_L} = 0 \tag{3.7}$$

with  $q = (W/S) (1/C_L)$ . Performing the operation denoted in Eq. (3.7) (the details are left as an exercise for the reader) gives

$$C_{D0} = KC_L^2$$

or the zero-lift drag is equal to the drag-due-to-lift. From this relationship, we get the  $C_L$  for *minimum drag* (called the optimum  $C_L$ ) as

$$C_{Lopt} = \sqrt{\frac{C_{D0}}{K}} \tag{3.8a}$$

It is also of interest to find the value of the  $C_L$  that maximizes  $L/D$  or  $C_L/C_D$ . In other words, when the following operation is performed

$$\frac{\partial(C_L/C_D)}{\partial C_L} = 0 \tag{3.9}$$

it is determined that the  $C_L$  for *maximum*  $L/D$  is

$$C_{L_{opt}} = \sqrt{\frac{C_{D_0}}{K}} \tag{3.8a}$$

the same as for minimum drag. This gives the expression for  $(L/D)_{max}$  as

$$(L/D)_{max} = 1 / (2\sqrt{C_{D_0}K}) \tag{3.10a}$$

Equation (3.10a) illustrates how the aircraft  $(L/D)_{max}$  is dependent only upon the aircraft aerodynamics. The velocity for maximum  $L/D$  or minimum drag is expressed as

$$V_{(L/D)_{max}} = \sqrt{\frac{2W}{\rho C_{L_{opt}} S}} = \sqrt{\frac{2W}{\rho S} \sqrt{\frac{K}{C_{D_0}}}} \tag{3.11}$$

[shown in Figs. 3.2a and 3.7 (see Section 3.5)].

The total drag coefficient for a cambered airfoil where  $C_{\ell_{min}} \neq 0$  is expressed as

$$C_D = C_{D_{min}} + K'C_L^2 + K''(C_L - C_{\ell_{min}})^2 \tag{2.17}$$

The  $C_L$  for maximum  $L/D$  or minimum drag is

$$C_{L_{opt}} = \sqrt{\frac{C_{D_{min}} + K''C_{\ell_{min}}^2}{K' + K''}} \tag{3.8b}$$

and the expression for maximum  $L/D$  is

$$(L/D)_{max} = \frac{1}{\sqrt{4(C_{D_{min}} + K''C_{\ell_{min}}^2)(K' + K'') - 2K''C_{\ell_{min}}}} \tag{3.10b}$$

The velocity for minimum power required is a useful flight condition for propeller aircraft. The  $P_R$  is given by Eq. (3.6) and the goal is to find the value of  $C_L$  that minimizes  $P_R$ , that is,

$$\frac{\partial P_R}{\partial C_L} = 0$$

The result is

$$3C_{D_0} = KC_L^2$$

which means that the aircraft should fly at that flight condition where the zero-lift drag is one-third of the drag-due-to-lift. This gives the required value for  $C_L$  as

$$C_{L_{\min P_R}} = \sqrt{\frac{3C_{D_0}}{K}}$$

and the velocity for minimum  $P_R$  as

$$V_{\min P_R} = \sqrt{\frac{2W}{\rho S}} \sqrt{\frac{K}{3C_{D_0}}} \quad (3.12)$$

which is 24% less than the speed for maximum  $L/D$  as shown in Fig. 3.3.

### 3.4 Variation of $T_R$ with Weight, Configuration, and Altitude

The effect of changing aircraft weight, configuration (for example, changing the  $C_{D_0}$  by lowering the landing gear), and altitude is shown in Figs. 3.4, 3.5, and 3.6, respectively.

The aircraft *load factor*  $n$  is defined as

$$n = L/W \quad (3.13)$$

with *level flight* being the condition when  $n = 1$ . It should be noted that the weight change shown in Fig. 3.4 is equivalent to increasing the load factor from  $n = 1$  to  $n = 1.5$  for the 15,000-lb aircraft.

The configuration change shown in Fig. 3.5 represents a change in  $C_{D_0}$  that comes about when the landing gear or flaps are lowered or external stores are put on a fighter aircraft.

The altitude variation shown in Fig. 3.6 comes about because of the decrease in density  $\rho$  with altitude. Notice that the velocity for  $(L/D)_{\max}$  is increased with altitude, but  $T_R$  does not change. This is an interesting behavior that should be confirmed by close examination of Eq. (3.5).

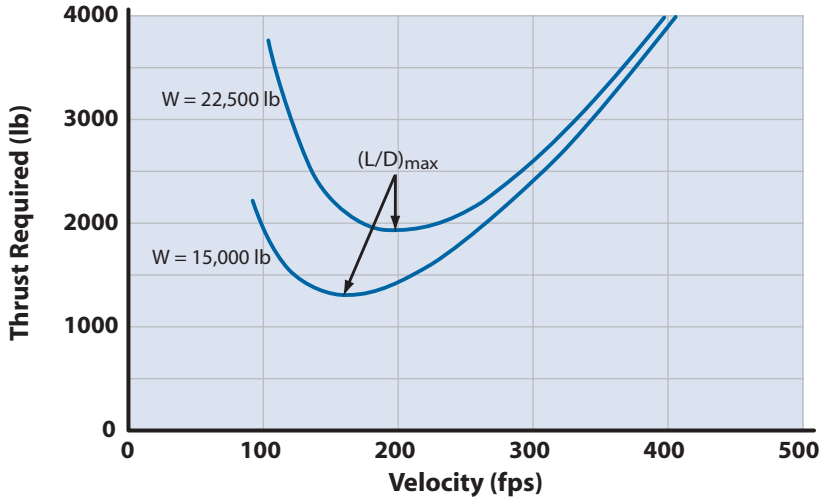


Figure 3.4 Effect on  $T_R$  of changing aircraft weight.

### 3.5 Endurance or Loiter

The aircraft *endurance* or *loiter* can be expressed as

$$E = \int_{t_i}^{t_f} dt = \int_{W_i}^{W_f} \frac{1}{dW/dt} dW \quad (3.14)$$

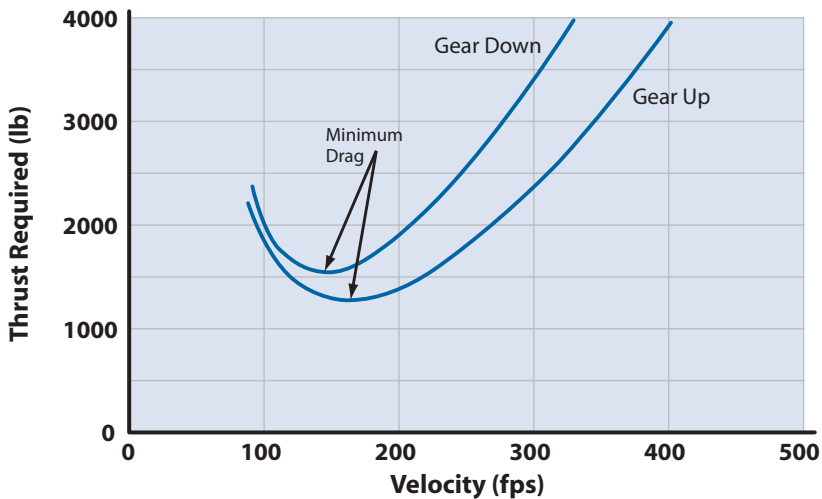


Figure 3.5 Effect on  $T_R$  of changing aircraft configuration.

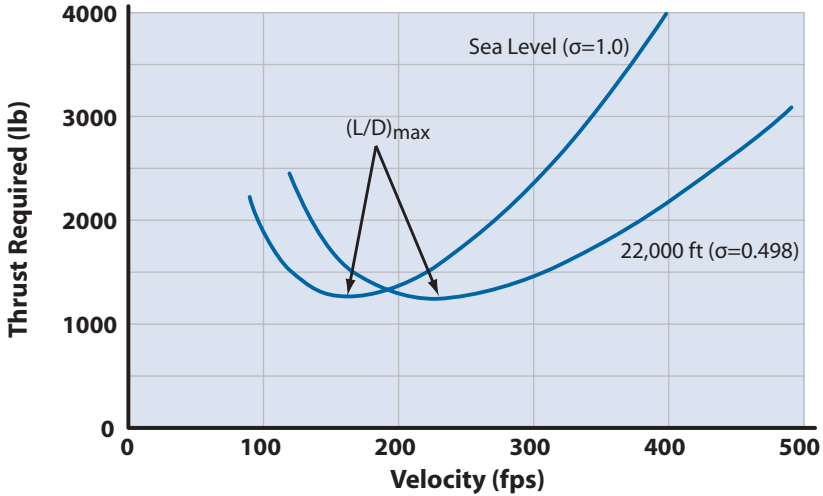


Figure 3.6 Effect on  $T_R$  of changing aircraft altitude ( $0 = \rho/\rho_{SL}$ ).

where  $dW/dt$  is the rate of change of aircraft weight due to burning fuel and the subscripts are initial and final conditions.

For a turbojet or turbofan aircraft, the  $dW/dt$  is *negative* and is expressed as the product of the engine thrust  $T$  and the thrust specific fuel consumption  $C$  as follows:

$$dW/dt = -T(\text{lb})C \left( \frac{\text{lb of fuel}}{\text{lb of thrust} \cdot \text{hour}} \right) \tag{3.15}$$

Putting Eq. (3.15) into Eq. (3.14) gives

$$E = - \int_{w_i}^{w_f} \frac{1}{TC} dW = \int_{w_f}^{w_i} \frac{W}{TCW} dW$$

Because  $L = W$  and  $T = D$  for the loiter condition, we can express the relation for  $E$  as

$$E = \int_{w_i}^{w_f} \frac{L}{D} \frac{1}{C} \frac{dW}{W} \tag{3.16}$$

For flight at a fixed altitude and Mach number,  $L/D$  and  $C$  are constant with respect to  $W$  so that the expression for the endurance of a jet aircraft (in hours) is given by

$$E = \frac{L}{D} \frac{1}{C} \ln \left[ \frac{W_i}{W_f} \right] \tag{3.17}$$

From Eq. (3.17), it is observed that, to obtain maximum endurance for a given weight change (i.e., given amount of fuel), the jet aircraft should fly at that altitude and Mach number such that the endurance parameter  $(L/D)(1/C)$ , which is often referred to as Range Factor, is a maximum. This usually means flying at or near  $(L/D)_{\max}$  in the tropopause, where  $C$  is a minimum. The designer will normally plot  $(L/D)(1/C)$  against Mach number and find the altitude and Mach number that make this endurance parameter a maximum (see Fig. 3.7, for example). It should be emphasized that maximum endurance does not necessarily occur at the velocity for  $(L/D)_{\max}$  because  $C$  is dependent upon maximum Mach number and altitude (see Chapter 14) and a different velocity could give a larger value for  $(L/D)(1/C)$ . However, the velocity for  $(L/D)_{\max}$  is close (within 10%) to the velocity for maximum endurance, as illustrated in Fig. 3.7. (The aerodynamic data for Fig. 3.7 are given in Table 3.1.)

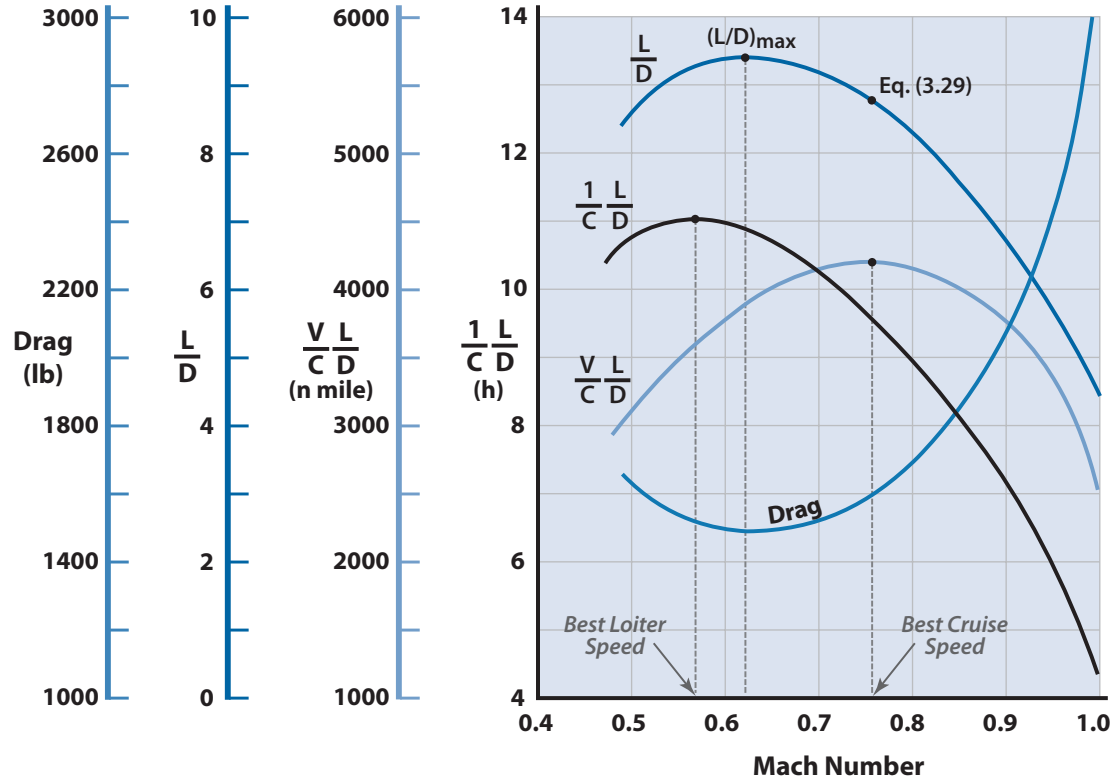
The thrust specific fuel consumption (per hour) is sometimes expressed as *specific impulse*  $I_{sp}$  (in seconds) as follows:

$$I_{sp} = \frac{3600}{C} \tag{3.18}$$

**Table 3.1** Composite Lightweight Fighter Aerodynamic Data for Fig. 3.7 (from Section 5.6, Composite LWF Example)

$W_{T0}$	15,000 lb	$T/W_{T0}$	1.2 installed	
$S_{ref}$	349 ft <sup>2</sup>	Wing	AR 3.0	
$W/S_{T0}$	43 psf	$\Delta_{LE}$	40 deg	
Engine	One F-100-PW-100 <sup>a</sup>	$\lambda$	0 deg	
<b>Cruise and loiter at 36,000 ft and <math>W/S = 40</math></b>				
Mach	$C_{D0}$	K	$C_D$	$C$ (lb of fuel/lb of thrust-h)
0.5	0.0167	0.17	0.056	0.80
0.6	0.0167	0.17	0.035	0.85
0.7	0.0167	0.17	0.027	0.888
0.8	0.0167	0.17	0.023	0.92
0.9	0.0180	0.17	0.022	0.933
1.0	0.0243	0.18	0.027	1.025

<sup>a</sup>see Chapter 14.



**Figure 3.7** Cruise and loiter performance of composite lightweight fighter at 36,000 ft and  $W/S_{ref} = 40$  psf (see Table 3.1).

The jet aircraft endurance equation becomes

$$E = I_{sp} \frac{L}{D} \ln \left[ \frac{W_i}{W_f} \right] \quad (3.19)$$

(in seconds). The endurance equation for reciprocating-engine aircraft is determined in the same fashion as the jet aircraft expression using Eq. (3.14). The  $dW/dt$  is expressed in the parameters appropriate to propeller aircraft. The *required horsepower*  $hp_R$  for the aircraft is given by

$$hp_R = \frac{P_R}{\eta} = \frac{DV}{\eta}$$

where  $\eta$  is the *propulsive efficiency* (see Chapter 14). The required fuel flow rate in pounds of fuel per hour is obtained as follows:

$$-\frac{dW}{dt} = \frac{\text{pounds of fuel}}{\text{hour}} = (C)H_{pR} = C \frac{P_R}{\eta} = \frac{DVC}{\eta} \quad (3.20)$$

where  $C$  is the *brake specific fuel consumption* in pounds per horsepower-hour (lb/hp · h). Equation (3.20) is put into Eq. (3.14) and rearranged as follows:

$$\begin{aligned} E &= -\int_{W_i}^{W_f} \frac{\eta}{DVC} dW = \int_{W_f}^{W_i} \frac{\eta}{C} \frac{L}{DV} \frac{dW}{W} \\ E &= \int_{W_f}^{W_i} \frac{\eta}{C} \frac{C_L}{C_D} \sqrt{\frac{\rho C_L S}{2W}} \frac{dW}{W} \\ E &= \int_{W_f}^{W_i} \frac{\eta}{C} \frac{C_L^{3/2}}{C_D} \frac{\sqrt{\rho S}}{\sqrt{2W_i}} \frac{dW}{W^{3/2}} \end{aligned} \quad (3.21)$$

During loiter or cruise,  $\eta$  and  $C$  are considered constant for cruising speeds and corresponding engine power. This assumption is valid for a first approximation, as this type of engine usually operates at maximum loiter or range at a constant power with a relatively constant variation in  $C$  between 50% and 65% of the normal rated power output of the engine. For corresponding loiter and cruise speeds, the propulsive efficiency is constant within 1% or 2%. If we assume constant altitude and constant  $C_L$  and  $C_D$ , then Eq. (3.21) becomes

$$E = 26.8 \frac{\eta}{C} \frac{C_L^{3/2}}{C_D} \sqrt{\frac{2\sigma S}{W_i}} \left[ \left( \frac{W_i}{W_f} \right)^{0.5} - 1 \right] \quad (3.22)$$



(in hours), where  $\sigma = \rho/\rho_{SL}$  and  $C =$  brake specific fuel consumption (BSFC) in pounds of fuel per brake horsepower-hour.

Because  $\eta$  and  $C$  are relatively constant with velocity, it should be clear from Fig. 3.3 that maximum endurance for a reciprocating engine aircraft will occur at minimum  $P_R$ . The velocity for this flight condition is given by Eq. (3.12).

### 3.6 Range

The *specific range* is defined as the distance traveled per pound of fuel consumed:

$$R_s = \frac{dR}{dW_{fuel}} = \frac{dR}{dt} \frac{dt}{dW_{fuel}} = \frac{V}{dW/dt}$$

The *total range* is determined by integrating the specific range over the weight change, that is,

$$R = \int_{w_i}^{w_f} \frac{V}{dW/dt} dW \tag{3.23}$$

As discussed before with the endurance equation, the final form of the range equation depends upon the form of  $dW/dt$ .

For jet aircraft, Eq. (3.15) is used in Eq. (3.23) and the following is obtained:

$$R = \int_{w_f}^{w_i} \frac{V}{TC} dW = \int_{w_f}^{w_i} \frac{V}{C} \frac{W}{T} \frac{dW}{W} \tag{3.24}$$

During cruise flight  $T = D$  and  $L = W$ , so Eq. (3.24) becomes

$$R = \int_{w_f}^{w_i} \frac{V}{C} \frac{L}{D} \frac{dW}{W} = \frac{V}{C} \frac{L}{D} \int_{w_f}^{w_i} \frac{dW}{W} \tag{3.25}$$

If we assume that the aircraft cruises at nearly a constant velocity and that during the weight change the  $C$  and  $L/D$  are fairly constant, the total weight change can be broken into small weight-change increments in which the assumptions of constant  $C$  and  $L/D$  are valid; the range increments can then be summed to give the total range. The jet aircraft range equation (called the *Breguet range equation*) is expressed as

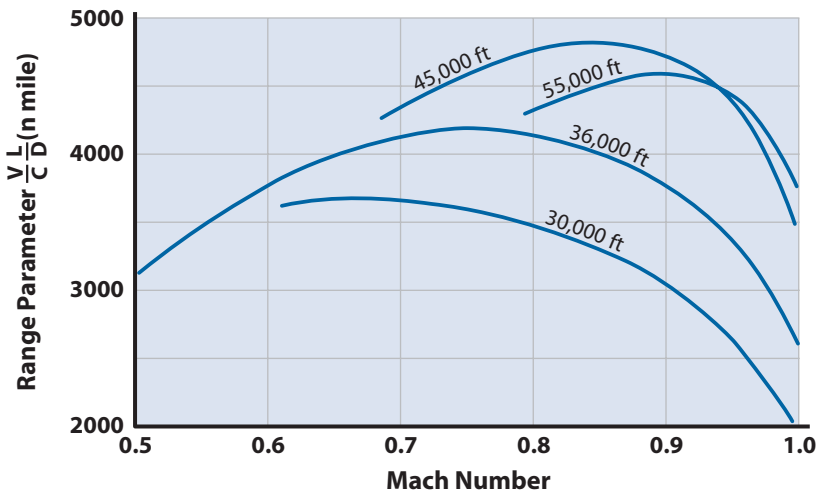
The Breguet range equation is named after Louis Charles Breguet, the record-setting aviation designer and builder. Breguet pioneered the development of the helicopter and built the first piloted vertical-ascent aircraft.

$$R = \frac{V}{C} \frac{L}{D} \ln \left[ \frac{W_i}{W_f} \right] \quad (3.26a)$$

$$R = VI_{sp} \frac{L}{D} \ln \left[ \frac{W_i}{W_f} \right] \quad (3.26b)$$

These equations assume flight at constant speed and  $C_L$  and change dramatically for propeller powered flight at constant speed and altitude (see Volume 2, “Buoyant Vehicle Design Basics”).

Equations (3.26) indicate that the jet aircraft should fly at that altitude and velocity condition such that the range parameter  $(V/C)(L/D)$  (often referred to as the *range factor*) is a maximum. This is done by determining the  $C$  for the engine when the thrust equals the cruise drag and calculating the value of  $(V/C)(L/D)$ . This is done for several velocities and altitudes with the weight equal to an average weight during the cruise weight-change increment. The results are plotted as  $(V/C)(L/D)$  against Mach number as shown in Fig. 3.8, and the cruise conditions for maximum range are determined. Notice in Fig. 3.8 that, as the cruise altitude is increased, the velocity for maximum range increases. It will be shown later that the altitude for optimum cruise increases as wing loading decreases. Normal range-dominated vehicles will have a wing loading around 120 psf and their optimum cruise altitude is around 36,000 ft. As fuel is burned and the wing loading decreases, the aircraft should climb in altitude to keep optimum



**Figure 3.8** Range factor vs Mach number for composite lightweight fighter at  $W/S = 40$  psf.

cruise conditions (i.e., constant  $C_L$ ). This is the familiar “cruise climb” schedule that aircraft follow as fuel is burned.

Further insight into the optimum range conditions can be obtained by examining Eq. (3.24), which can be rewritten as

$$R = \int_{W_f}^{W_i} \frac{a}{C} M \frac{L}{D} \frac{dW}{W} \tag{3.24a}$$

If we substitute

$$\begin{aligned} a &= (\gamma R' \theta)^{0.5} \\ T &= D = C_D (\gamma/2) P M^2 S \\ T &\approx T_{SL} \frac{P}{P_{SL}} \frac{\theta_{SL}}{\theta} \end{aligned}$$

(the approximate expression for thrust; see Chapter 14) into Eq. (3.24a), where  $\theta$  = static absolute temperature ratio,  $R'$  = gas constant,  $P$  = static pressure,  $\gamma$  = ratio of specific heats ( $\gamma = 1.44$  for air), and the subscript SL denotes conditions at sea level, we obtain the approximate expression

$$R \approx \sqrt{\frac{2R'\theta_{SL}}{SP_{SL}}} \int_{W_f}^{W_i} \frac{\sqrt{T_{SL}}}{C} \frac{C_L}{C_D^{3/2}} \frac{dW}{W}$$

If it is assumed that thrust setting and  $\alpha$  are constant, the expression for range is

$$R \approx \sqrt{\frac{2R'\theta_{SL}}{SP_{SL}}} \frac{\sqrt{T_{SL}}}{C} \frac{C_L}{C_D^{3/2}} \ln \left[ \frac{W_i}{W_f} \right] \tag{3.27}$$

Equation (3.27) indicates that, for efficient cruise, the aircraft should cruise-climb at a constant thrust level and at an angle-of-attack corresponding to maximum  $C_L/C_D^{3/2}$ . The condition on  $C_L$  for maximum ( $C_L/C_D^{3/2}$ ) is

$$C_{D0} = 2KC_L^2 \tag{3.28a}$$

$$C_L = \sqrt{\frac{C_{D0}}{2K}} \tag{3.28b}$$

which gives the  $L/D$  for maximum ( $C_L/C_D^{3/2}$ ) as

$$L/D = 0.943(L/D)_{\max} \tag{3.29}$$

(see Section 3.11). Equations (3.28) and (3.29) offer some useful “rules of thumb” for determining efficient cruise conditions during the early design phases. One rule is the following:

Efficient cruise will occur near  $L/D = 0.943(L/D)_{\max}$ , which is the velocity and altitude where the zero-lift drag is twice the drag-due-to-lift.

This rule is demonstrated in Fig. 3.9 for the C-141 and F-111A, where the cruise  $C_L$  region corresponds to Eq. (3.28a).

### Example 3.1

Find the speed for maximum range at 37,000 ft for the composite lightweight fighter shown in Table 3.1.

From Table 3.1,  $C_D = 0.0167$ ,  $K = 0.17$ , and  $W/S = 40.0$ . Using Eqs. (3.29) and (3.28b), the cruise  $L/D = 0.943(L/D)_{\max} = 8.87$  and the required cruise  $C_L = 0.222$ . From

$$V = \sqrt{\frac{W}{S} \frac{2}{\rho C_L}} = 714 \text{ fps}$$

the cruise Mach number is 0.74. These values are consistent with the more involved analysis depicted in Figs. 3.7 and 3.8.

The term  $V/TC$  in the integrand of Eq. (3.24) has the units of distance per pound of fuel. Aircraft companies will often present their range information as shown in Fig. 3.10. This presentation is useful because the total range can be determined from initial and final weight conditions as shown in Fig. 3.10b. Notice that Fig. 3.10 is for one altitude, and a user flying a cruise climb schedule would have to use several charts like Fig. 3.10 for different altitudes in order to develop Fig. 3.10b. Normally, air traffic control requires airlines to fly at constant altitudes so that a single altitude chart is sufficient. The reader should observe that the term  $V/TC$  could replace the range parameter in developing Fig. 3.8 to determine cruise conditions.

The range equation for a reciprocating engine aircraft is developed in the same manner as for the jet aircraft. Equation (3.20) is combined with Eq. (3.23) to give

$$R = \int_{W_f}^{W_i} \frac{\eta}{DC} dW = \int_{W_f}^{W_i} \frac{\eta}{C} \frac{L}{D} \frac{dW}{W}$$

Following the same arguments as for the loiter case we can assume  $V$ ,  $C$ , and  $L/D$  constant over the weight-change increment. Thus, the Breguet range equation for reciprocating-engine aircraft is expressed by

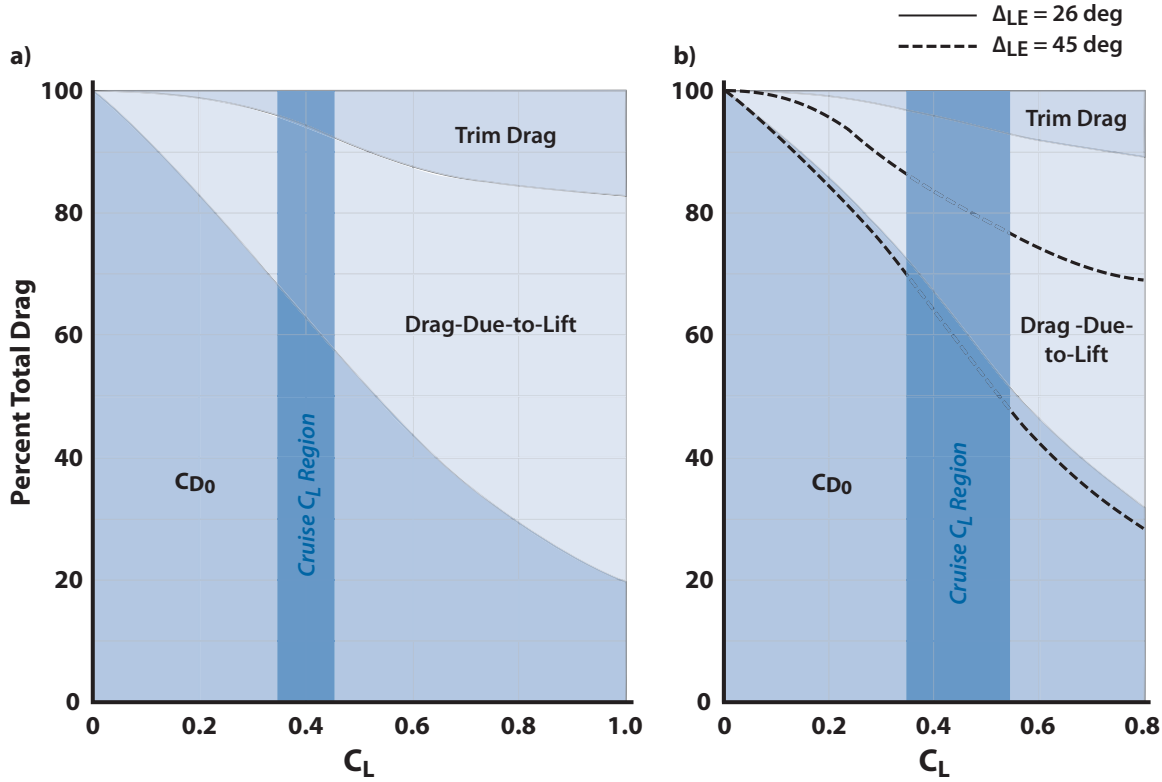
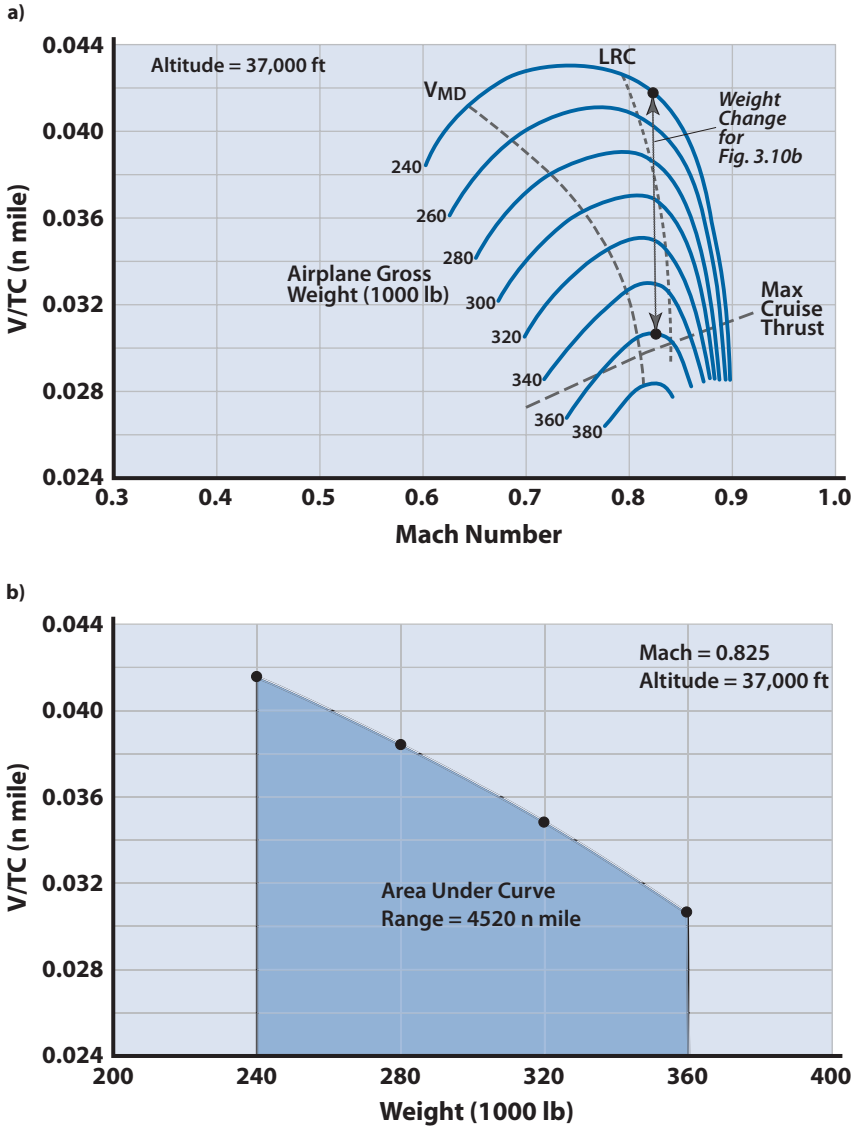


Figure 3.9 Cruise drag for cargo and fighter aircraft: a) C-141 at Mach =0.75, and b) F-111A.



**Figure 3.10** Range parameter for Lockheed L-1011 TriStar with Rolls Royce RB 211-22B engines (data from [1]), where  $V_{MD}$  is velocity for minimum drag and LRC is the velocity for long-range cruise; for **a)** weight and Mach variation, and **b)** weight change at constant Mach.

$$R = 326 \frac{\eta}{C} \frac{L}{D} \ln \left[ \frac{W_i}{W_f} \right] \quad (3.30)$$

(for range in nautical miles). For a reciprocating engine, assuming  $\eta/C$  constant, the maximum range occurs at that velocity for

maximum  $L/D$  [Eq. (3.11)] as shown in Fig. 3.3. This velocity can be found graphically by constructing a straight line through the origin and tangent to the  $P_R$  curve. Proof is left as an exercise for the reader.

### 3.7 Level Constant Velocity Turn

An aircraft turns by banking and using a component of the wing lift force to turn the aircraft [2,3]. This is shown schematically in Fig. 3.11. The aircraft can also turn with its wings level by deflecting the rudder, but this is inefficient as the vertical tail is not designed to provide rapid heading changes.

If the turn is to be a level turn, it is clear from Fig. 3.11 that the weight  $W$  of the aircraft must equal the vertical component of the lift,  $nW \cos \phi$ . Thus, the angle of bank  $\phi$  for a level turn of  $n g$  can be approximated by the following (neglecting small thrust component):

$$\phi = \arccos(1/n) \tag{3.31a}$$

The radius of the turn is then determined as

$$\text{Radius} = \frac{V^2}{n g \sin \phi} = \frac{V^2}{g \sqrt{n^2 - 1}} \tag{3.31b}$$

and the time to turn  $\psi$  degrees is given by

$$t_\psi = \frac{\text{Radius} (\Psi/57.3)}{V} \tag{3.31c}$$

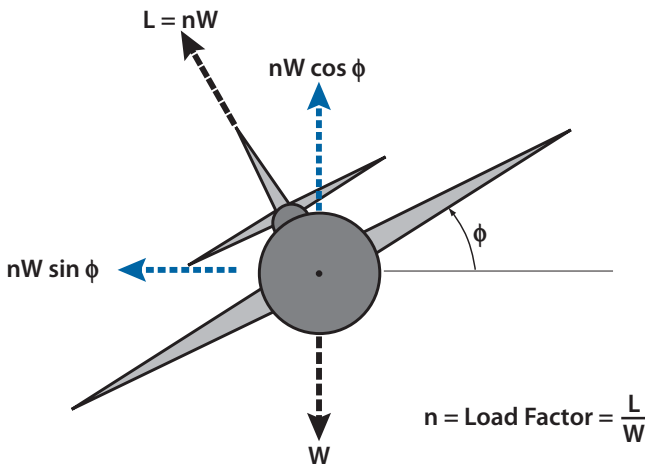


Figure 3.11 Forces acting on an aircraft in banked flight.

The turn rate in degrees/sec is dependent upon the load factor  $n$  as follows:

$$\dot{\psi} = \frac{g\sqrt{n^2 - 1}}{V} \quad (3.32)$$

A check should be made to see if the aircraft has enough thrust to overcome the drag while maneuvering at  $n$  gs so that the turn is at constant velocity. That is,

$$T_{\text{req}} = qS \left[ C_{D0} + K \left( \frac{nW}{qS} \right)^2 \right] + D_{\text{trim}} \leq T_{\text{max}} \quad (3.33)$$

where  $D_{\text{trim}}$  is the trim drag for a load factor of  $n$  (see Chapter 22). If we neglect the trim drag, Eq. (3.33) can be rewritten to express the *maximum sustained load factor*

$$n_{\text{MS}} = \frac{q}{W/S} \sqrt{\frac{1}{K} \left( \frac{T_{\text{max}}}{qS} - C_{D0} \right)} \quad (3.34)$$

Putting Eq. (3.34) into Eq. (3.32) will yield the *maximum sustained turn rate*,  $\psi_{\text{MS}}$ .

### 3.8 Energy-State Approximation (Energy Maneuverability)

The preceding discussions have considered the aircraft to be in a steady-state or near-steady-state condition. The forces on the aircraft were balanced and the system was not accelerating. This point of view was adequate for aircraft cruise, loiter, steady-state turn, and maximum speed.

The remainder of this chapter deals with the aircraft as an accelerating system. Normally for an accelerating system we should consider the governing aircraft equations of motion. These nonlinear, coupled, second-order differential equations are difficult to work with and require the use of high-speed computers. The approach taken in this chapter will be to consider an approximation to the accelerating problem that will give extremely good information without using a computer.

The approach is to cast the non-steady-state accelerating problem into a steady-state problem representing the balance that must exist between the potential and kinetic energy change of the aircraft, the energy dissipated against drag, and the energy derived from the fuel. Thus, we take a different perspective on our accelerating problem and it becomes a steady-state performance problem again [4–6].



The *total energy* of an aircraft in space is its kinetic energy (KE), due to velocity and rotation, and its potential energy (PE), due to its altitude  $h$  above mean sea level. The rate of change of the total energy  $E$  is the rate at which an aircraft can climb and/or accelerate. *Energy maneuverability* is the name given to an aircraft's ability to change its energy state. It is assumed that the aircraft rotation is zero,  $\dot{\gamma} = 0$ . The total energy at a point in velocity–altitude space is given by

$$E = Wh + \frac{1}{2} \frac{W}{g} V^2 \quad (3.35)$$

and the *specific energy*  $h_e$  (or energy height) is expressed as

$$h_e = \frac{E}{W} = h + \frac{1}{2} \frac{V^2}{g} \quad (3.36)$$

The specific energy has the units of feet and represents the theoretical height (altitude) that an aircraft could reach if all of its KE were converted to PE (i.e., a zoom climb to zero air speed). An aircraft at Mach 2.2 and 70,000 ft would have a specific energy of 140,000 ft. If there were no drag on the aircraft, it could zoom to an altitude of 140,000 ft or dive to sea level (PE = 0) and reach a velocity of 3000 fps. Figures 4.8 and 4.9 in Chapter 4 show the contours of specific energy.

To consider the accelerated performance of an aircraft we need to know the rate at which the aircraft can change its specific energy (i.e., its energy state). This rate of change of  $h_e$  is given by

$$\frac{dh_e}{dt} = \frac{dh}{dt} + \frac{V}{g} \frac{dV}{dt} \quad (3.37)$$

The first term on the right-hand side of Eq. (3.37) is the aircraft's rate of climb and the term  $dV/dt$  is its acceleration. From Fig. 3.1 the accelerating force is

$$m \frac{dV}{dt} = T \cos(\alpha + i_T) - D - W \sin \gamma \quad (3.38)$$

where  $m$  is the mass of the aircraft,  $W/g$ . If we multiply Eq. (3.38) by  $V$ , divide by  $W$ , and rearrange, we have

$$\frac{m}{W} V \frac{dV}{dt} = \frac{T \cos(\alpha + i_T)}{W} - \frac{DV}{W} - V \sin \gamma$$

The term  $V \sin \gamma$  is the rate of climb  $dh/dt$ . Thus,

$$\frac{V}{g} \frac{dV}{dt} + \frac{dh}{dt} = \frac{V [T \cos(\alpha + i_T) - D]}{W} \quad (3.39)$$

Comparing Eqs. (3.37) and (3.39) gives the expression for the rate of change of specific energy (sometimes called *specific excess power* or *specific power*,  $P_s$ ) with units of feet per second (fps):

$$P_s = \frac{dh_e}{dt} = \frac{V [T \cos(\alpha + i_T) - D]}{W} \quad (3.40)$$

Equation (3.40) is the basis for the examination of acceleration performance. The  $P_s$  value for an aircraft in space represents its ability to accelerate and/or climb. When  $P_s = 0$  the thrust is equal to the drag and we have the situation discussed in Section 3.2. When  $P_s$  is negative, the aircraft is slowing down and/or losing altitude. Notice that Eq. (3.40) explains the performance of the aircraft at a point in time along the velocity axis. What the aircraft is doing normal to the velocity axis is expressed through the lift term by the load factor. In other words, using

$$C_L = \frac{nW}{qS}$$

and assuming an uncambered aircraft ( $C_{l_{\min}} = 0$ ) the drag is

$$D = qS(C_{D_0} + KC_L^2) = C_{D_0}qS + \frac{K}{q}n^2 \frac{W^2}{S} \quad (3.41)$$

we get [assuming  $\cos(\alpha + i_T) \approx 1$ ]

$$P_s = \frac{dh_e}{dt} = V \left[ \frac{T}{W} - \frac{qC_{D_0}}{W/S} - \frac{K}{q}n^2 \frac{W}{S} \right] \quad (3.42)$$

Thus, the value of  $P_s$  at a point in space is dependent upon the aircraft's load factor  $n$ .

An aircraft's capabilities can be determined at a point in space by calculating its value of  $P_s$ . For example, the F-104G at  $n = 1$ , Mach = 0.8 (829 fps) at 20,000 ft has a maximum thrust of 10,000 lb and a drag of 2086 lb. For a weight of 18,000 lb and  $\cos(\alpha + i_T) \approx 1$  we have

$$\frac{dh_e}{dt} = P_s = \frac{(10,000 - 2086)829}{18,000} = 364 \text{ fps}$$

as shown in Fig. 4.8a. The F-104G has an instantaneous rate of climb of 364 fps for this initial point of level flight at  $n = 1$ . If the F-104F were to perform a level acceleration where  $dh/dt = 0$ , it could accelerate at

$$\frac{dV}{dt} = \frac{gP_S}{V} = \frac{(32.2)(364)}{829} = 14.1 \text{ ft/s}^2$$

A pilot of the F-104G wanting to cruise at Mach = 0.8 and 20,000 ft would have to throttle back or increase drag until  $P \approx 0$ .

### 3.9 Energy Maneuverability for Air Combat Assessment

The performance of an aircraft over its entire operating envelope can be displayed by plotting contours of its  $P_S$  for constant load factor values. The  $P_S$  contours for the F-104G are shown in Fig. 4.8a and a composite lightweight fighter design in Fig. 4.9a.

$P_S$  plots for  $n > 1$  are useful in assessing an aircraft's combat maneuverability. For example, the  $P_S$  plots at  $n = 5$  for two competing aircraft can be laid one over the other and regions of advantage and disadvantage are immediately obvious [7]. Typical  $P_S$  charts are shown in Fig. 3.12 for air-

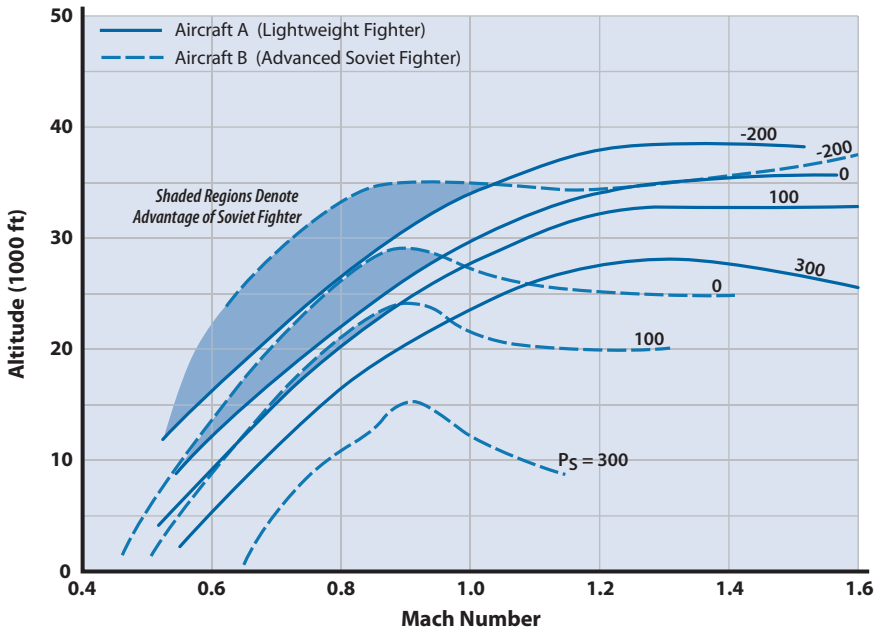


Figure 3.12  $P_S$  contours for aircraft A and B at  $n = 5$  g.

craft A and B at  $n = 5$ . Figure 3.12 shows regions of advantage and disadvantage for the two aircraft. Aircraft B is superior to [i.e., has an energy maneuverability (EM) advantage over] aircraft A at high subsonic speeds above 25,000 ft. The present-day combat arena is around Mach = 0.9 and below 30,000 ft [8]. Thus, aircraft A would appear to be the better air combat fighter based upon the performance comparison at  $n = 5$ .

Turn rate performance is the primary measure of an aircraft's air-to-air combat effectiveness [8,9] as it indicates the capability of the aircraft to gain a firing position advantage. A value of  $P_S = 0$  for  $n > 1$  indicates a certain level of maximum sustained turn rate. Thus,  $P_S = 0$  contours for  $n > 1$  indicate an aircraft's turning performance. The relation between  $P_S = 0$  and the maximum sustained load factor is given as follows [solving Eq. (3.42) for  $n$  with  $P_S = 0$ ]:

$$n_S = \frac{q}{W/S} \sqrt{\frac{1}{K} \left( \frac{T}{qS} - C_{D0} \right)} = \frac{q}{\sqrt{W/S}} \sqrt{\frac{1}{K} \left( \frac{T}{W} \frac{1}{q} - \frac{C_{D0}}{W/S} \right)} \quad (3.43)$$

and, for the maximum instantaneous load factor,

$$n_{\max} = \frac{q C_{L_{\max}}}{W/S}$$

where

$$\dot{\psi} = \frac{g \sqrt{n^2 - 1}}{V} \quad (3.32)$$

(the turn rate in radians per second). An evaluation of the relative turn performance of two aircraft can be made by comparing their respective  $P_S$  vs turn rate curves as shown in Fig. 3.13. Three useful reference points are indicated in Fig. 3.13. The  $n = 1$  energy rate ( $P_S$  at  $\dot{\psi} = 0$ ) provides a measure of the acceleration or climb performance. The turn rate at  $P_S = 0$  is that which can be sustained without energy loss. The maximum instantaneous turn rate corresponds to the maximum usable aerodynamic lift available, or *structural limit*, but is normally accompanied by a high energy loss rate. By having a margin in turn rate at all energy rates, the F-5E is assured a combat advantage. Reference [8] concludes that a desired turn rate margin over a threat aircraft is about two degrees per second. Thus, from Fig. 3.13 we observe that the F-5E should quickly attain a tail aspect relative to the F-5A and gain firing opportunities. The most significant region in the combat hassle occurs at zero to negative energy rates as this is where the majority of the time is spent during a hard turning air-to-air engagement. Even if the F-5A had an energy rate advantage at low turn rates (which it doesn't)

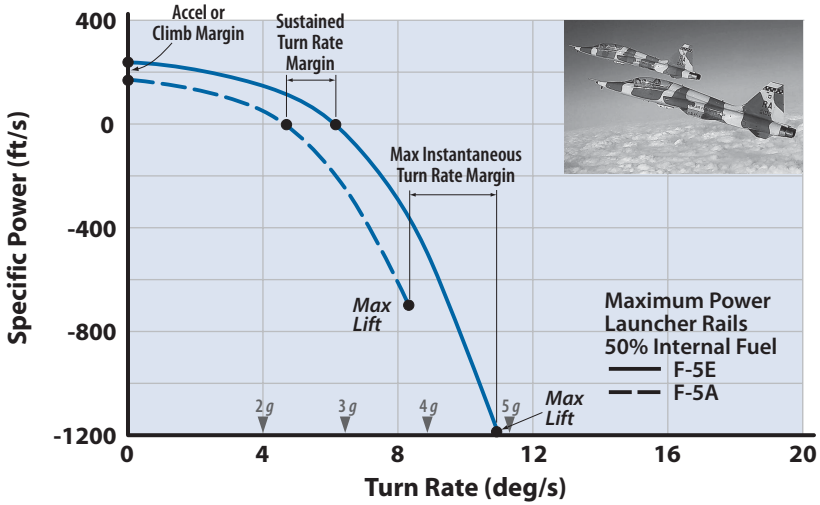


Figure 3.13 Specific power vs turn rate for the F-5A and F-5E at 30,000 ft and Mach = 0.8 (data from [10]).

and chose to disengage the combat, the F-5E could use its higher turn rate capability to gain a missile firing opportunity before sufficient separation distance could be attained.

The effect of speed on turn performance for constant altitude is illustrated in Fig. 3.14 for the F-5A and F-5E. Notice that the F-5A has an instantaneous turn rate advantage at Mach 1.6 due to its higher design load

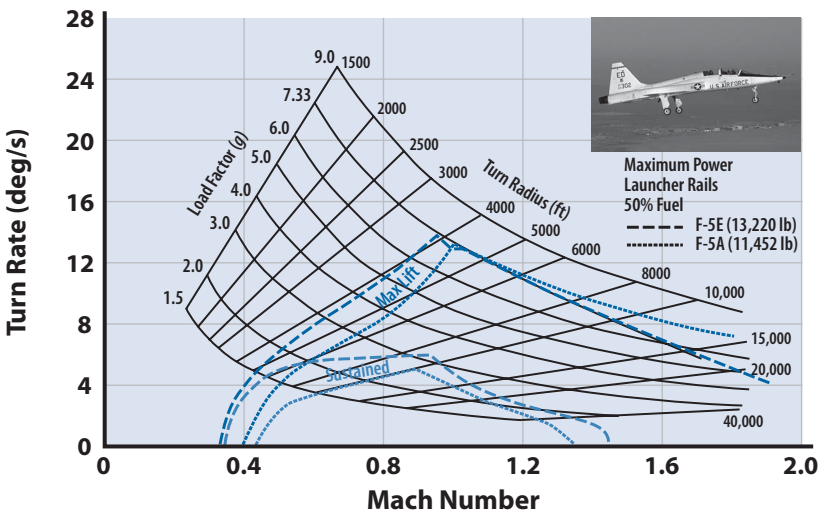


Figure 3.14 Turn performance at 30,000 ft for F-5A and F-5E (data from [10]).

## John Boyd: Father of Energy Maneuverability

The energy maneuverability (EM) presented in Sections 3.8 and 3.9 was developed by USAF officer John Boyd. Boyd entered the Air Force in 1951 with a degree in economics and an Air Force ROTC commission. He was an outstanding fighter pilot with an uncanny ability to visualize aerial combat maneuvering in four dimensions (X, Y, Z, and time). While on the faculty at the Air Force Fighter Weapons School (FWS), Nellis AFB, Boyd developed an aerial combat tactics manual that was used in the USAF, USN, US Marine Corps, and most foreign air forces. Boyd moved aerial combat from an art with a “bag of tricks” to a skill. His flying skills were legendary and it is reported that he never lost a “dog fight” in peace-time training or war-time fighting. When Boyd finished his tour at the Air Force FWS he was awarded the Legion of Merit, most unusual for a captain.

In 1960 Boyd entered Georgia Tech to study engineering. He needed the mathematics and physical sciences to put his aerial combat maneuvers on a solid footing and to quantify the positional advantage (expressed as excess specific energy) of one aircraft over another. He graduated three years later and was assigned to Eglin AFB, where he started developing the EM theory presented in this chapter. The development of the full EM theory would consume his free time for the next decade. For the first time the USAF had a tool that could quantify the aerial capability of one aircraft against another. The results of an evaluation of the F-4 against the MIG-25 showed the F-4 at a significant disadvantage and hastened its replacement. John Boyd’s EM theory was used to develop the requirements for the A-10 and F-15 in the late 1960s. In 1970 Boyd received a second Legion of Merit for “developing the most powerful evaluative tool for fighter aircraft analysis known to date and providing industry with one of the most effective tools generated in the history of aeronautical engineering” [7].

John was disappointed in the F-15; in his view it was a Cadillac when the Air Force really needed a Corvette. In the late 1960s he formed the “Fighter Mafia” and promoted the development of a small, low-cost, lightweight fighter, once again using his EM theory to develop the requirements. The Lightweight Fighter (LWF) program was initiated in 1971 with funds to build two prototypes. The RFP was issued in January 1972 and called for a 20,000 lb class fighter (half the weight of the F-15) optimized for air combat at speeds of Mach 0.6–1.6 and altitudes of 30,000–40,000 feet. The result was the F-16 for the USAF and the F-18 for the USN. I met John in 1972 when I was a major at Wright-Patterson AFB. For Boyd there were two types of people: fighter pilots and pukes (bomber pukes, desk pukes—it didn’t matter to John). I was a design puke and privileged to be a minor member of the “Fighter Mafia.”

In June 1975 Colonel Boyd was awarded the Harold Brown Award for the development of the F-16, the highest scientific award granted by the Air Force. In September 1975 John Boyd retired from the Air Force as a colonel. He spent the next twenty years developing the EM theory for land combat. His ideas were embraced by the US Marines and the US Army. The May 6, 1991, issue of *US News & World Report* featured an article about the innovative tactics that won the Gulf War. Credit is given to John Boyd.

*Leland Nicolai*

factor. However, Mach = 1.6 is well outside the combat arena and this region of advantage would not be very useful. In the combat arena, Mach = 0.7 to 0.9, the F-5E has a decided advantage. The F-5E performance gain is due largely to the incorporation of the J85-GE-21 turbojet engines, which provide 22% more thrust than the J85-GE-13 engines in the F-5A [10].

### 3.10 Rate of Climb and Descent

The rate of climb for an aircraft is given by  $dh/dt = V \sin \gamma$ . The expression for  $P_S$  is expressed as

$$P_S = \frac{dh}{dt} + \frac{V}{g} \frac{dV}{dt} = \frac{dh}{dt} + \frac{V}{g} \frac{dV}{dh} \frac{dh}{dt}$$

which gives

$$\frac{dh}{dt} = V \sin \gamma = \frac{P_S}{1 + (V/g)(dV/dh)} \tag{3.44}$$

Values for  $P_S$  can be found using Eq. (3.40) along a specified trajectory (i.e., plot of altitude vs velocity; see Chapter 4). Values for  $dV/dh$  can be determined because they are the inverse of the slope at any point on the trajectory. Thus, the aircraft rate of climb can be found using the energy state approximation. Notice that if the portion of the trajectory under consideration is for a constant-speed climb, then  $dV/dh$  is zero and the rate of climb expression is

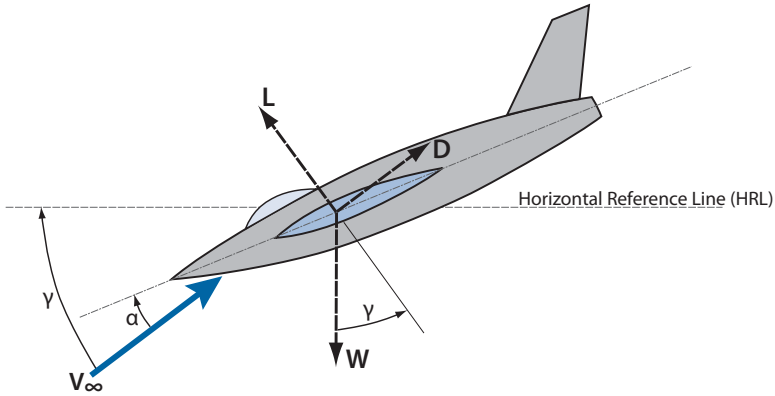
$$\frac{dh}{dt} = V \sin \gamma = \frac{V [T \cos(\alpha + i_T) - D]}{W} \tag{3.45}$$

Equation (3.45) with  $n = 1$  is quite valid for most subsonic climb situations. However, if the aircraft is a high-performance vehicle capable of accelerating during the climb, then Eq. (3.44) should be used.

When  $P_S$  is negative the aircraft is losing airspeed and/or altitude. The pilot usually wants to fly a constant airspeed descent ( $dV/dh = 0$ ) so that Eq. (3.45) is exact. In gliding flight the thrust is zero and the glide is usually a near-equilibrium situation at constant airspeed and  $n \approx 1$ . Thus, Eq. (3.45) represents the gliding descent quite well.

Figure 3.15 shows the force diagram on an aircraft during gliding flight [11]. The flight path angle during gliding flight is given by

$$\gamma = \arcsin(-D/W) \tag{3.46}$$



**Figure 3.15** Force diagram on aircraft in gliding flight.

and

$$\gamma = \arctan(-D/L) \tag{3.47}$$

For maximum range during the glide descent (i.e., stretching the glide) the aircraft should be flown at minimum  $\gamma$ , which means flying at  $(L/D)_{\max}$ . The velocity for maximum gliding range is given by Eq. (3.11)

$$V_{(L/D)\max} = \sqrt{\frac{2W}{\rho S}} \sqrt{\frac{K}{C_{D0}}}$$

The condition for minimum rate of descent (maximum endurance) is different than the condition for maximum range. Assuming that  $\gamma$  is small such that  $\sin \gamma \approx \tan \gamma$ , the *rate of descent* (ROD) can be expressed as

$$\text{ROD} = V \tan \gamma = -\frac{DV}{L} = -\frac{C_D}{C_L} \sqrt{\frac{2W}{\rho C_L S}} \tag{3.48}$$

The  $C_L$  that minimizes Eq. (3.48) is

$$C_L = \sqrt{\frac{3C_{D0}}{K}} \tag{3.49}$$

so that the velocity for minimum ROD is

$$V_{\text{RODmin}} = \sqrt{\frac{2W}{\rho S}} \sqrt{\frac{K}{3C_{D0}}} \tag{3.50}$$



**Table 3.2** Values of  $C_L$  for Maximum Range and Endurance

<b>Uncambered Wing</b>			
<b>Mission</b>	<b>Condition</b>	<b>Maximize</b>	<b>Value of <math>C_L^{(a)}</math></b>
Range—jet	Constant altitude	$C_L^{1/2}/C_D$	$\sqrt{C_{D_0}/3K}$
Range—jet	Constant throttle	$C_L/C_D^{3/2}$	$\sqrt{C_{D_0}/2K}$
Range—propeller	Constant altitude	$C_L/C_D$	$\sqrt{C_{D_0}/K}$
Range—sailplane	Minimum glide angle	$C_L/C_D$	$\sqrt{C_{D_0}/K}$
Endurance—sailplane	Minimum rate of sink	$C_L^{3/2}/C_D$	$\sqrt{3C_{D_0}/K}$
Endurance—propeller	Minimum power required	$C_L^{3/2}/C_D$	$\sqrt{3C_{D_0}/K}$
Endurance—jet	Minimum thrust required	$C_L/C_D$	$\sqrt{C_{D_0}/K}$
Use $C_D = C_{D_0} + KC_L^2$ to find $L/D$ or $C_L/C_D$ and $(L/D)_{\max} = 1/(2\sqrt{C_{D_0}/K})$			
Maximum jet range, constant throttle	$\frac{L}{D} = \frac{\sqrt{C_{D_0}/2K}}{C_{D_0} + KC_{D_0}/2K} = \sqrt{\frac{2}{9C_{D_0}K}} = \sqrt{\frac{8}{9}} (L/D)_{\max} = 0.943(L/D)_{\max}$		
Maximum jet range, constant altitude	$\frac{L}{D} = \frac{\sqrt{C_{D_0}/3K}}{C_{D_0} + KC_{D_0}/3K} = \sqrt{\frac{9}{48C_{D_0}K}} = \sqrt{\frac{3}{4}} (L/D)_{\max} = 0.866(L/D)_{\max}$		
Maximum propeller endurance	$\frac{L}{D} = \frac{\sqrt{3C_{D_0}/K}}{C_{D_0} + K3C_{D_0}/K} = \sqrt{\frac{3}{16C_{D_0}K}} = \sqrt{\frac{3}{4}} (L/D)_{\max} = 0.866(L/D)_{\max}$		
<b>Cambered Wing</b>			
Use $C_D = C_{D_0} + K'C_L^2 + K''(C_L - C_{L_{\min}})^2$			
$A = C_{D_{\min}} + K''C_{L_{\min}}^2$		$B = K'C_{L_{\min}}$	$K = K' + K''$
<b>Mission</b>	<b>Condition</b>	<b>Value of <math>C_L^{(a)}</math></b>	
Range—Jet	Constant Altitude	$\sqrt{A/3K} - B/3K$	
Range—Jet	Constant Throttle	$\sqrt{A/2K} - B/2K$	
Range—Prop	Constant Altitude	$\sqrt{A/K}$	
Range—Sailplane	Minimum Glide Angle	$\sqrt{A/K}$	
Endurance—Sailplane	Minimum Rate of Sink	$\sqrt{3A/K} - B/K$	
Endurance—Prop	Minimum Power Required	$\sqrt{3A/K} - B/K$	
Endurance—Jet	Minimum Thrust Required	$\sqrt{A/K}$	

<sup>a</sup>Fly at prescribed  $C_L$  for max range and endurance! Use value of  $C_L$  to size wing for the range or endurance phase of the mission.

which is about 23% less than the velocity for maximum gliding range. Notice that the velocity for minimum ROD is the same as for minimum power required, Eq. (3.12).

### 3.11 Summary for Maximum Range and Endurance

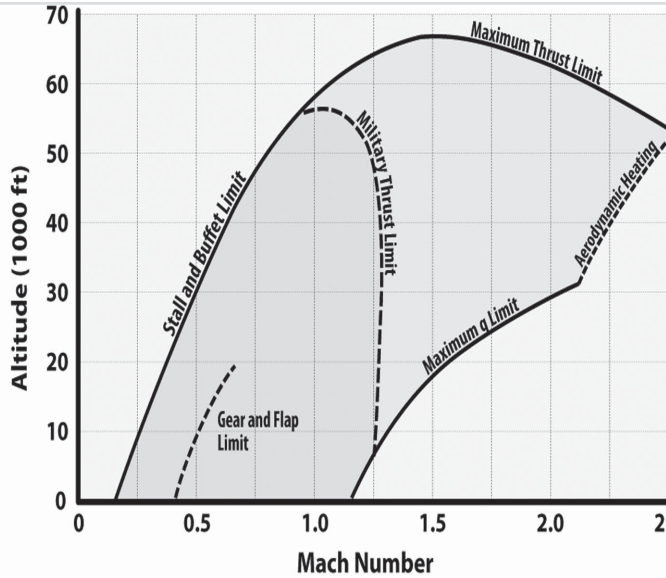
Aircraft  $C_L$  is the parameter that is varied to enable flight at a condition of maximum range or maximum endurance. This is because of the direct relationship between lift and drag. The pilot flies at a specific  $C_L$  by trimming the aircraft at a specific angle-of-attack.

Table 3.2 shows the values of  $C_L$  at which the airplane (jet, propeller, or sailplane) should fly to achieve maximum range or endurance. Notice that the  $C_L$  values are different for aircraft with uncambered vs cambered wings. For an uncambered jet aircraft flying a maximum-range mission at constant altitude, the  $L/D = 0.866(L/D)_{\max}$  and flying at constant throttle (cruise climb) the  $L/D = 0.943(L/D)_{\max}$ .

### References

- [1] "L-1011-2 Flight Performance with Rolls-Royce RB. 211-22B Engines," Lockheed Rept. LR 23973, Lockheed-California Co., Burbank, CA, Oct. 5, 1970.
- [2] Perkins, C. D., and Hage, R. E., *Airplane Performance Stability, and Control*, Wiley, New York, 1949.
- [3] Dommasch, D. O., Sherby, S. S., and Connolly, T. F., *Airplane Aerodynamics*, Pitman, New York, 1961.
- [4] Rutowski, E. S., "Energy Approach to the General Aircraft Performance Problem," *Journal of the Aeronautical Sciences*, Vol. 21, No. 3, March 1954, pp. 187-195.
- [5] Bryson, A. E., Desai, M. N., and Hoffman, W. C., "Energy-State Approximation in Performance Optimization of Supersonic Aircraft," *Journal of Aircraft*, Vol. 6, No. 6, Dec. 1969, p. 481.
- [6] Bryson, A. E., and Denham, W. F., "A Steepest Ascent Method for Solving Optimum Programming Problems," *Journal of Applied Mathematics*, Vol. 29, No. 6, June 1962, p. 286.
- [7] Coram, Robert, *Boyd: The Fighter Pilot Who Changed the Art of War*, Back Bay Books, Little, Brown, New York, 2002.
- [8] Fellers, W. E., and Patierno, J., "Fighter Requirements and Design for Superiority over Threat Aircraft at Low Cost," AIAA Paper No. 70-516, AIAA Fighter Aircraft Conf., St. Louis, MO., March 1970.
- [9] Bratt, R. W., and Patierno, J., "Design Criteria for Fighter Aircraft," AGARD Fluid Dynamics Panel on Aerodynamic Design and Criteria, London, England, Sept. 1971.
- [10] "F-5E Technical Description," Northrop Rept. NB 71-20, Aircraft Div., Northrop Corp., Hawthorne, CA, July 1973.
- [11] McCormick, B. W., *Aerodynamics, Aeronautics and Flight Mechanics*, Wiley, New York, 1995.

## Chapter 4

Aircraft  
Operating  
Envelope

- Stall & Buffet Limits
- Heating & Material Limits
- Thrust &  $Q$  Limits
- Propulsion System Limits
- Minimum Time & Fuel Climb
- Optimum Energy Profiles
- FAA Noise Regulations

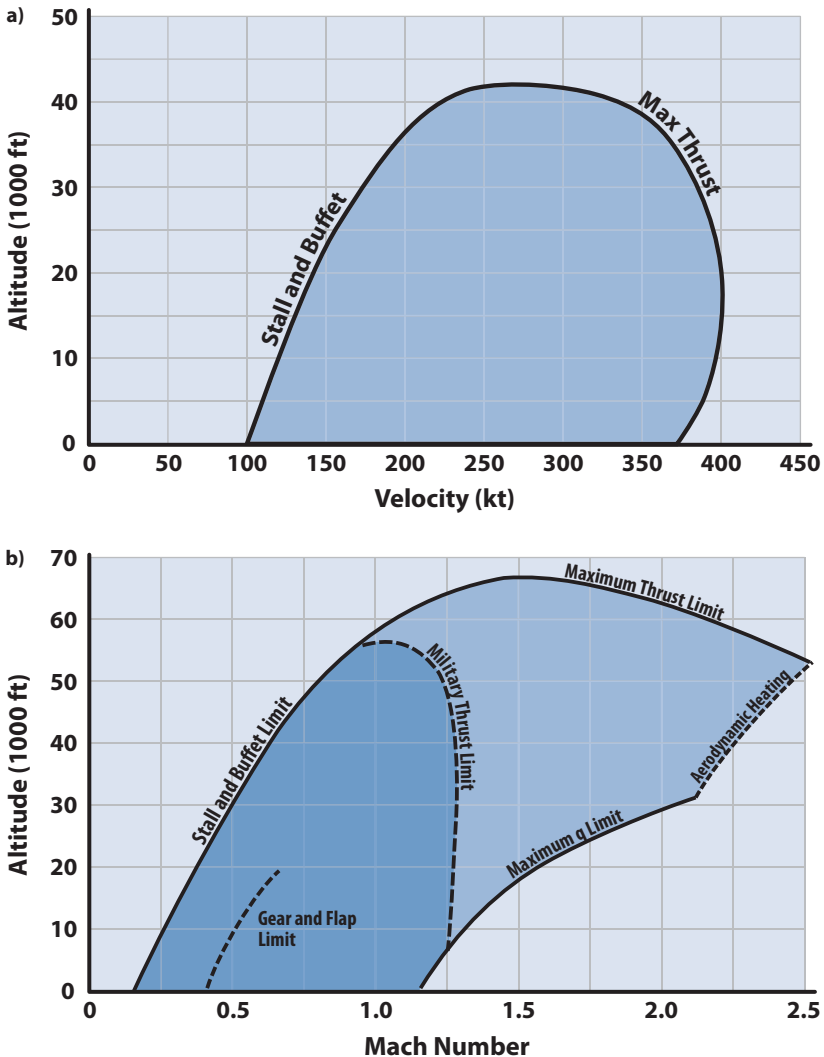
The F-22 rockets through 30,000 feet, well below its operational ceiling of 65,000 feet.

*Time is nature's way of keeping everything from happening at once.*

Woody Allen

## 4.1 Flight Envelope

The aircraft is not free to meander at will in its atmospheric environment. It is constrained to operate within a corridor in space called the *flight envelope* (Fig. 4.1). Mission requirements will usually define where in the airspace the aircraft must operate. The designer must be aware of the potential flight envelope limitations and design accordingly. This operating envelope is determined by aircraft limitations (such as minimum/maximum dynamic pressure and aerodynamic heating) and



**Figure 4.1** Typical aircraft flight envelopes: **a)** subsonic aircraft (Fairchild-Republic A-10),  $W_{TO} = 30,344$  lb with four Mk 82s, and **b)** supersonic aircraft.

operational limitations (such as sonic boom, noise, and air pollution). In addition, engine limitations (such as insufficient thrust, intolerable fuel consumption, and internal pressure and temperature limitations) mold part of the envelope.

## 4.2 Minimum Dynamic Pressure

The left side of the flight envelopes shown in Fig. 4.1 is determined by the stall and buffet characteristics of the aircraft. *Stall* is the loss of lift from the wing due to the sudden separation of the flow from the wing upper surface, which usually defines the low-speed part of the envelope. This stall boundary is sensitive to aircraft weight and the flap configuration on the aircraft. *Buffet* is caused by the turbulence of the airflow separation shaking some part of the aircraft (usually the wing or horizontal tail). Buffet precedes stall and is more noticeable at higher speeds. An arbitrary assessment of where the buffet becomes objectionable to the pilot is the basis for the buffet limit boundary. The designer can translate this buffet limit boundary to the left (to lower flight speeds) by selecting a lower wing loading, maneuver flaps, and careful tail-plane location. To develop the stall and buffet boundary, the designer needs information on the maximum usable  $C_L$  versus Mach number for the aircraft as shown in Figs. 4.2 and 6.6.

The F-22 Raptor is a single-seat, twin-engine, fifth-generation fighter; its survivability depends on high speed, maneuverability, and a very low signature (stealth). It has an empty weight of 43,430 lb, an air combat mission weight of 64,460 lb, and a max TO weight of 83,500 lb. The propulsion is two PWA F119-PW-100 turbofan engines at 35,000-lb TSLs each (in afterburner and uninstalled), giving an air combat mission thrust/weight of 1.08. The F-22 has a max speed of Mach 2.25, a supercruise (level flight in dry power) speed of Mach 1.82, and a range of 1600 nm.

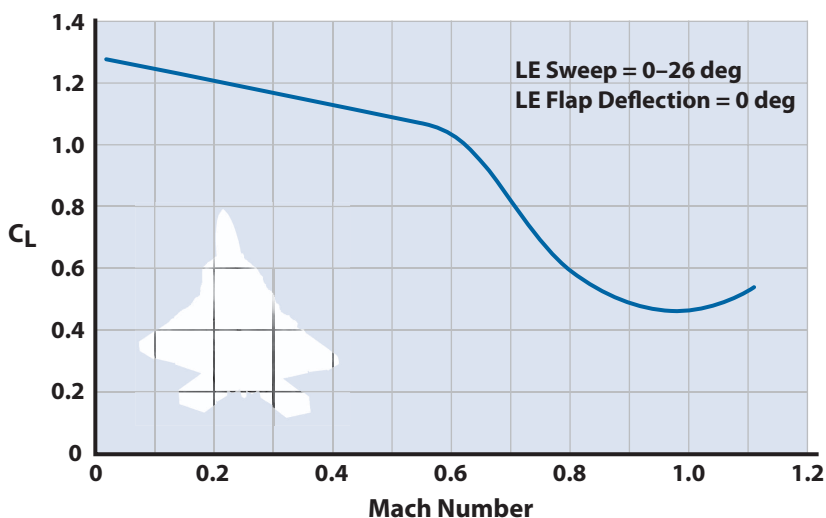


Figure 4.2 Typical variation of the maximum usable  $C_L$  with Mach number.

At low speeds this maximum usable  $C_L$  is usually close to the  $C_{L_{\max}}$  of the aircraft. As speed increases and maximum buffet becomes more pronounced, the maximum usable  $C_L$  decreases until, in the transonic region, it may drop to one-half or one-third of its low-speed value (review Section 2.11).

### 4.3 Maximum Thrust Limit

The top and part of the right side of the flight envelope are determined by the engines' maximum thrust. This boundary is where the thrust available equals the thrust required, as discussed in Section 3.2. The maximum altitude that can be reached is called the *absolute ceiling* of the aircraft. Remember that the absolute ceiling and the remainder of the thrust limit line are dependent upon the weight and external store configuration of the aircraft. The operational ceiling is where the rate of climb is 100 ft/min.

### 4.4 Maximum Dynamic Pressure

The maximum dynamic pressure limit for an aircraft is a structural limitation. Flight at high dynamic pressures introduces aeroelastic problems of flutter and engine inlet static pressure (for more information about aeroelasticity and flutter, see [1,2]). The designer must be well aware of the structural limitations involved in the aircraft's operating envelope and give them due consideration in the preliminary design phase. Current aircraft are generally designed for maximum  $q$  limits of about 1800 psf. Figure 4.3 shows the variation of  $q$  with altitude and velocity. There are both advantages and disadvantages to increasing the dynamic pressure limit of an aircraft. One advantage of a high  $q$  limit is increased survivability for a military aircraft. The high- $q$  aircraft could penetrate an enemy's defenses at a low altitude and high velocity and avoid early radar detection. Also, the high- $q$  aircraft could operate in a region (altitude and velocity) that would be denied to low- $q$  aircraft. The main disadvantage to a high  $q$  limit is that the aircraft structural and propulsion weights increase significantly, which decreases performance through an increase in  $W_{\text{TO}}$ . An aircraft can operate at any desired  $q$  provided that it is designed for that condition. The flight dynamic pressure  $q$  is given by

$$q = \frac{1}{2} \rho_{\infty} V_{\infty}^2 = (\gamma/2) P_{\infty} M_{\infty}^2 \quad (4.1)$$

where gamma is the ratio of specific heats (1.4 for air). The freestream total pressure is given by the isentropic relation (see Appendix C):

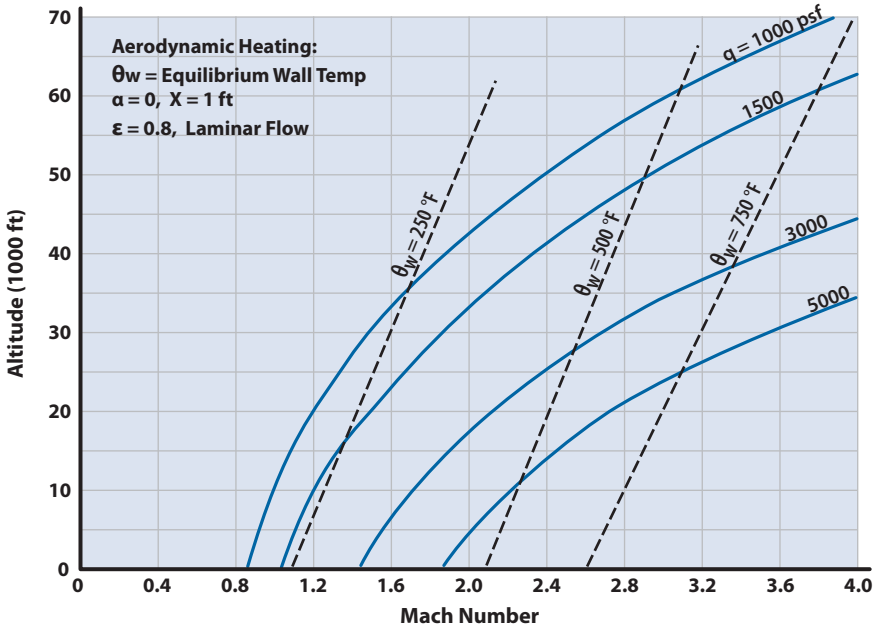


Figure 4.3 Trajectory limits of dynamic pressure and aerodynamic heating.

$$P_{0\infty} = P_{\infty} \left[ 1 + \frac{\gamma - 1}{2} M_{\infty}^2 \right]^{\gamma/(\gamma - 1)} \tag{4.2}$$

As the airflow is decelerated in the engine inlet to approximately Mach = 0.4 at the compressor face, the static pressure of the air increases. The static pressure at the compressor face can be many times greater than the ambient static pressure  $P_{\infty}$  if  $q_{\infty}$  is large. For example, consider a level flight at 25,000 ft at dynamic pressures of 1700 psf and 5000 psf. Assume the total pressure recovery for the inlet (see Chapter 16) is 90% for  $q = 1700$  psf ( $M_{\infty} = 1.75$ ) and 75% for  $q = 5000$  psf ( $M_{\infty} = 3.0$ ). The resulting static pressure at the compressor face is shown in Table 4.1. An inlet designed for the  $p_c$  associated with a  $q$  of 1700 psf would be blown apart by the static pressure associated with a  $q$  of 5000 psf.

### 4.5 Aerodynamic Heating

An aircraft flying at high Mach numbers (i.e., 2.0 or greater) heats up due to the conversion of the kinetic energy of the air into thermal energy. This thermal energy represents an elevated temperature, and heat is transferred to the aircraft by convection. The critical regions on an aircraft are

**Table 4.1** Inlet Static Pressures for Different Dynamic Pressure Conditions

$q$ (psf)	Altitude (ft)	Mach	$P_{\infty}^a$ (psf)	$P_{0_{\infty}}$ (psf)	$P_c^b$ (psf)
1700	25,000	1.75	786.3	4,180	3,360
5000	25,000	3.0	786.3	28,900	19,300

<sup>a</sup>From Appendix A.

<sup>b</sup> $P_c$  is the static pressure at the compressor face where the Mach number is 0.4.

the stagnation points and lower surfaces. The limiting skin temperatures of the aircraft vary with the material used. At temperatures above 250°F the aluminum alloys display a rapid degradation in mechanical properties [3], and the designer should consider other materials. The temperature limits for other aircraft materials are shown in Table 4.2.

### 4.5.1 Stagnation Point Heating on Nose and Swept Wing Leading Edge

The expression for heating rate [in British thermal units per square foot per second (Btu/ft<sup>2</sup>·s)] is

$$\dot{q}_{\text{conv}} = 15 \left( \frac{\rho_{\infty}}{R_0} \right)^{0.5} \left( \frac{V_{\infty}}{1000} \right)^3 (\cos \Delta)^{1.5} \tag{4.3}$$

where  $\rho_{\infty}$  is the density [in slugs per cubic foot (slug/ft<sup>3</sup>)],  $V_{\infty}$  is freestream velocity (in feet per second),  $R_0$  is the radius of the nose or leading edge (in feet), and  $\Delta$  is the sweep of the leading edge ( $\Delta = 0$  for body nose).

We assume a heat balance such that

$$\dot{q}_{\text{conv}} = \dot{q}_{\text{radiated}}$$

or

$$\theta_w = \left[ \frac{\dot{q}_{\text{conv}}}{\varepsilon v_{\text{SB}}} \right]^{1/4} \tag{4.4a}$$

where  $\varepsilon$  is the emissivity of the surface (approximately 0.8),  $v_{\text{SB}}$  is the Stephan–Boltzmann constant ( $0.481 \times 10^{-12}$  Btu/ft<sup>2</sup>·s·°R), and  $\theta_w$  is the equilibrium wall temperature (in °R).

### 4.5.2 Lower Surface Heating

This analysis is based upon the Reynolds analogy between skin friction and heat transfer. The local surface heat transfer can be approximated by



**Table 4.2** Properties of Metals at Room Temperature [3]

		Room Temperature Properties				Temperature Limitation (°F)	
	Condition	Ultimate Tensile Strength (ksi)	Yield Tensile Strength (ksi)	Compression Modulus (10 <sup>6</sup> psi)	Density (lb/in. <sup>3</sup> )	Primary Structure	Secondary Structure
Beryllium	SR	78	57	42.0	0.066	1000	1350
Ti-6Al-5Zr-4Mo-1Cu-0.2Si	STA	200	177	16.5	0.164	800	800
Ti-6Al-6V-2Sn	STA	170	160	16.5	0.164	800	800
Ti-8Mo-8V-2Fe-3Al	STA	180	165	16.6	0.175	600	600
Ti-6Al-2Sn-4Zr-6Mo	TA	170	160	16.5	0.169	1000	1000
Ti-6Al-4V	STA	157	143	16.4	0.160	800	900
Ti-6Al-6V-2Sn	A	155	145	15.0	0.164	800	800
PH 14-8Mo	STA	240	225	28.0	0.278	1000	1000
Ti-8Al-1Mo	STA	133	121	18.0	0.156	1000	1100
Ti-6Al-4V	A	134	126	16.4	0.160	1000	1000
Inco's "1000°F Alloy"	STA	228	19.1	29.0	0.267	1000	1000
Ti-5Al-2.5Sn	A	120	113	15.5	0.161	900	1100
Inconel 718	STA	210	185	29.0	0.297	1300	1800
Rene' 41	STA	184	145	31.9	0.298	1550	1800
2219-T81 (Aluminum)	STA	60	45	10.8	0.102	400	500
L-605 (Cobalt)	CR	185	145	32.6	0.330	1800	2000
TD NiC	SR	138	94	21.9	0.306	2200	2400
Haynes Alloy No. 188	A	130	67	34.5	0.333	2000	2000
Hastelloy X	A	114	55	28.6	0.297	2000	2100
TZM (Molybdenum)	SR	140	117	40.0	0.369	3200	3400
B66 (Columbium)	A	106	81	14.6	0.305	2600	2800
TDNi	SR	85	68	22.0	0.322	2000	2200
Cb-752 (Columbium)	A	81	70	17.0	0.326	2400	2800
T-222	A	120	110	29.0	0.605	3000	3400

SR, stress relieved; A, annealed; DA, duplex annealed; TA, triplex annealed; STA, solution treated and aged; CR, cold-rolled.

$$\dot{q}_{\text{surf}} = 3.21 \times 10^{-4} C_f \rho V_\infty^3 \quad (4.5)$$

where  $C_f$  is the local laminar skin friction coefficient at a distance  $x$  feet from the leading edge. Normally  $x$  is taken as 1.0 ft. The other quantities in Eq. (4.5) are the same as for Eq. (4.3).

As before, we assume a balance between the reradiated heat and the local surface heat transfer so that the equilibrium wall temperature is given by

$$\theta_w = \left[ \frac{\dot{q}_{\text{surf}}}{\varepsilon V_{\text{SB}}} \right]^{1/4} \quad (4.4b)$$

Figure 4.3 shows some lines of constant lower surface equilibrium temperatures for  $\varepsilon = 0.8$  and  $x = 1$  ft.

## 4.6 Sonic Boom

An aircraft flying at supersonic speed will create pressure waves on the ground associated with its shock system. If the aircraft altitude is low and/or the Mach number is large (greater than 2.5), this pressure on the ground (called *overpressure*) can cause discomfort and damage [4,5]. To avoid this ground overpressure from becoming excessive, a minimum altitude at which the aircraft may fly at supersonic speeds must be fixed. The supersonic transports (SSTs), Concorde and TU-144, were never able to negotiate these operating limits with those countries they overflew.

## 4.7 Noise and Pollution Limits

In 1969, the FAA found it necessary to establish the FAR-36 regulations [6] concerning noise. The rules limit the engine and aircraft noise, expressed in terms of effective perceived noise level in decibels (EPNdB), allowed at three reference locations shown in Fig. 4.4. On approach the measuring point is 1 nautical mile (n mile) before touchdown. When approaching on a 3-deg glide slope, the aircraft at this point has an altitude of 370 ft. Steeper glide slopes can reduce the noise measured at this point. On takeoff, the measuring point is 3.5 n mile from the point of brake release. Altitude at this point depends upon the particular aircraft and flight procedures used. The third measuring location is the sideline after liftoff at a distance of 0.35 n mile for four-engine aircraft and 0.25 n mile for three-engine aircraft. The FAR-36 specifies the permissible noise levels at each of these points as a function of aircraft gross weight. These permissible levels are shown in Fig. 4.5.

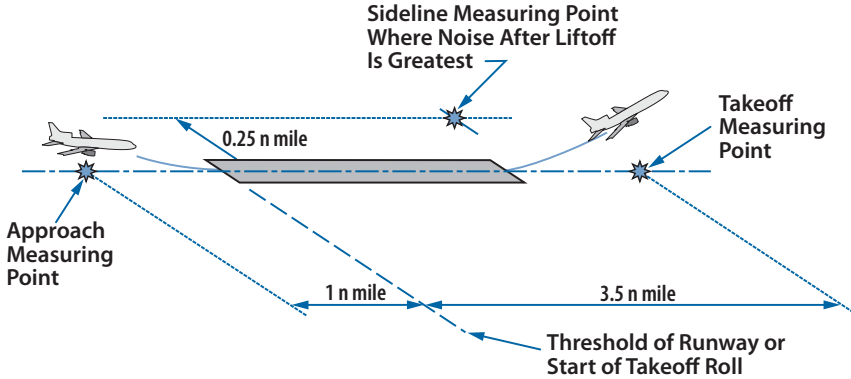


Figure 4.4 Noise measuring locations for FAR Part 36.

### 4.7.1 Regulations

Noise regulations in FAR Part 36 Stage 3 include restrictions on noise under three conditions. The *takeoff noise* (Fig. 4.5c) is defined as the noise measured at a distance of 21,325 ft (6500 m) from the start of the takeoff roll, directly under the airplane. The *sideline noise* (Fig. 4.5b) is measured 1476 ft (450 m) from the runway centerline at a point where the noise level after liftoff is greatest. The *approach noise* (Fig. 4.5a) is measured under the airplane when it is at a distance of 6562 ft (2000 m) from the runway thresh-

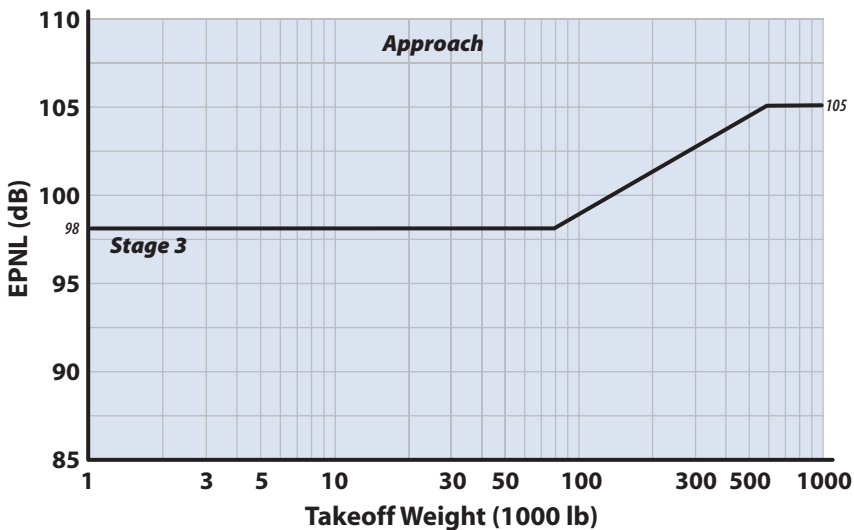


Figure 4.5a Maximum noise limits—approach.

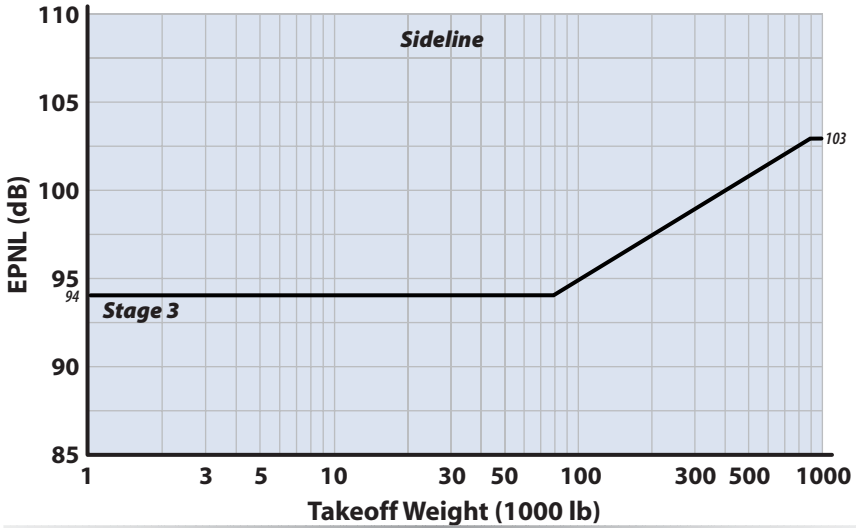


Figure 4.5b Maximum noise limits—sideline.

old. For each of these conditions the maximum noise level is a function of maximum takeoff gross weight; for the takeoff case the limits depend also on the number of engines.

Stage 4 noise regulations are applicable to new-type designs introduced after 1 January 2006. Existing aircraft will be able to operate under Stage 3 regulations. This new standard will be “Chapter 4” in the International

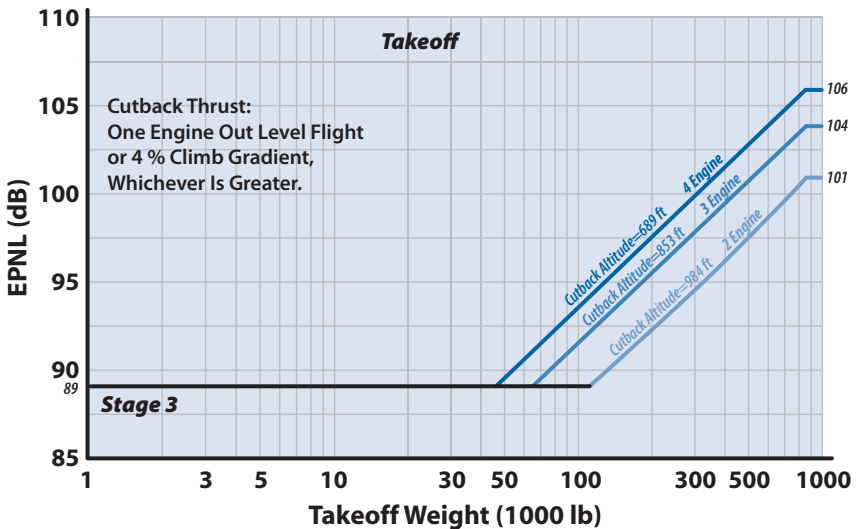


Figure 4.5c Maximum noise limits—takeoff.

Civil Air Organization (ICAO) Annex 16 and is related to the Stage 3/Chapter 3 regulations as follows:

- There is a cumulative margin of 10 dB relative to Chapter 3.
- There is a minimum sum of 2 dB at any two conditions.
- No trades are allowed

### 4.7.2 Estimating Aircraft Noise for Advanced Design

We start with a measurement of the noise due to a known engine at a known distance away. For example, a 25,000-lb thrust [sea level static (SLS) takeoff thrust] turbofan engine with a bypass ratio of 6 produces a noise of about 101 EPNdB at a distance of 1000 ft. This assumes some level of noise suppression (about 5 EPNdB).

Most of the internal noise comes from the high-speed rotating blades and is commonly called *turbomachinery* noise [7]. External noise arises from shear and eddy phenomena during mixing of the high-velocity jets with the ambient air. The fan noise can be effectively suppressed by acoustical treatment added to the engine nacelles, but the jet noise is hard to suppress. One alternative is to transfer a larger portion of the engine energy into the fan stream. This means larger bypass ratio turbofan engines. When the tradeoffs are made between noise suppression, engine efficiency over the mission profile, and inlet or nacelle drag, the optimum bypass ratio comes out around 5.5 [7].

The takeoff and sideline noise levels are established by the engine. However, the approach level is defined by the aircraft. During landing the engines are at low power and actually generate less noise than the turbulence from the aircraft flaps, landing gear, and wheel wells.

Although pollution regulations do not presently exist for aircraft, it is reasonable to assume that they will come into force in the future. These regulations will specify limits on engine emissions with emphasis on operation in the airport area and in the stratosphere. The airport area is of principal environmental concern because of its proximity to large population centers. Engine pollutants during idle result from inefficient combustion during off-design operation of a relatively simple combustor that cannot adapt to large changes in overall fuel–air ratios. The high-power condition during takeoff is another problem for the engine designer. Although hydrocarbon and carbon monoxide emissions can be currently brought to acceptable levels, the nitrogen oxide emission will plague engine designers for some time [7–10].

The operation of fleets of SSTs in the stratosphere could substantially reduce the ozone layer around the earth [9]. It has been concluded that a

reduction in the ozone layer would increase the incidence of skin cancer. The reduction of the ozone is due mainly to the introduction of nitric oxide from engine exhaust into the stratosphere. So, once again, the engine designer, with help from the aircraft designer, has the responsibility to produce better, more efficient engine and aircraft designs [9].

## 4.8 Propulsion Limits

The aircraft designer has nine propulsion devices from which to choose. Seven of these devices are shown in Fig. 4.6 [scramjet and pulse detonation engine (PDE) are not shown]. The decision of which propulsion device to use is not difficult as each device has its own preferred operating regime. The measure of merit for a propulsion device is its *thrust per engine weight* ( $T/W$ ) and its *thrust specific fuel consumption* (TSFC). As shown in Fig. 4.7, it is hard to beat the reciprocating-engine–propeller combination at low speeds (Mach = 0.5 and less). At higher subsonic speeds the turboprop engine is optimum but is limited to propeller tip speeds less than Mach = 1.0. At high subsonic speeds the turbofan is the best but loses out to the turbojet at low supersonic speeds because of the increased drag of the fan. At speeds around Mach 2 the turbojet engine has to have its thrust augmented by afterburning. Above Mach 3 the ramjet is very efficient [11]. If an effective coupling of a ramjet and a turbojet engine could be achieved (called a *turbo-ramjet*), the best of two worlds could be obtained. At speeds below Mach 2 the turbojet would operate with the inlet to the ramjet closed. Between Mach 2 and 3 both ramjet and turbojet would operate, and above Mach 3 the operation would be on ramjet with the inlet to the turbojet closed.

Because of the self-contained nature of the rocket, it does not care whether it is at Mach 0 or Mach 10. Thus, its characteristics are constant, as shown in Fig. 4.7. Figure 4.7 shows a TSFC of 16 for the rocket, which is typical of current solid-fuel rocket motors. Liquid-fuel rocket motors, such as the boost stages for the Space Shuttle and other spacecraft, use liquid hydrogen and oxygen and have TSFCs on the order of 9 (for more about rockets, see Section 18.12).

## 4.9 Optimal Trajectories

The *optimal trajectory*, that is, the one that minimizes time or fuel burned, can be determined using the methods of calculus of variations [12] or gradient [13]. These methods yield optimal path solutions but require large complex computer programs and high operator familiarity. The energy-state approximation, discussed in Chapter 3, Section 3.8, yields rapid useful results that agree well with the exact results of the calculus of variations.

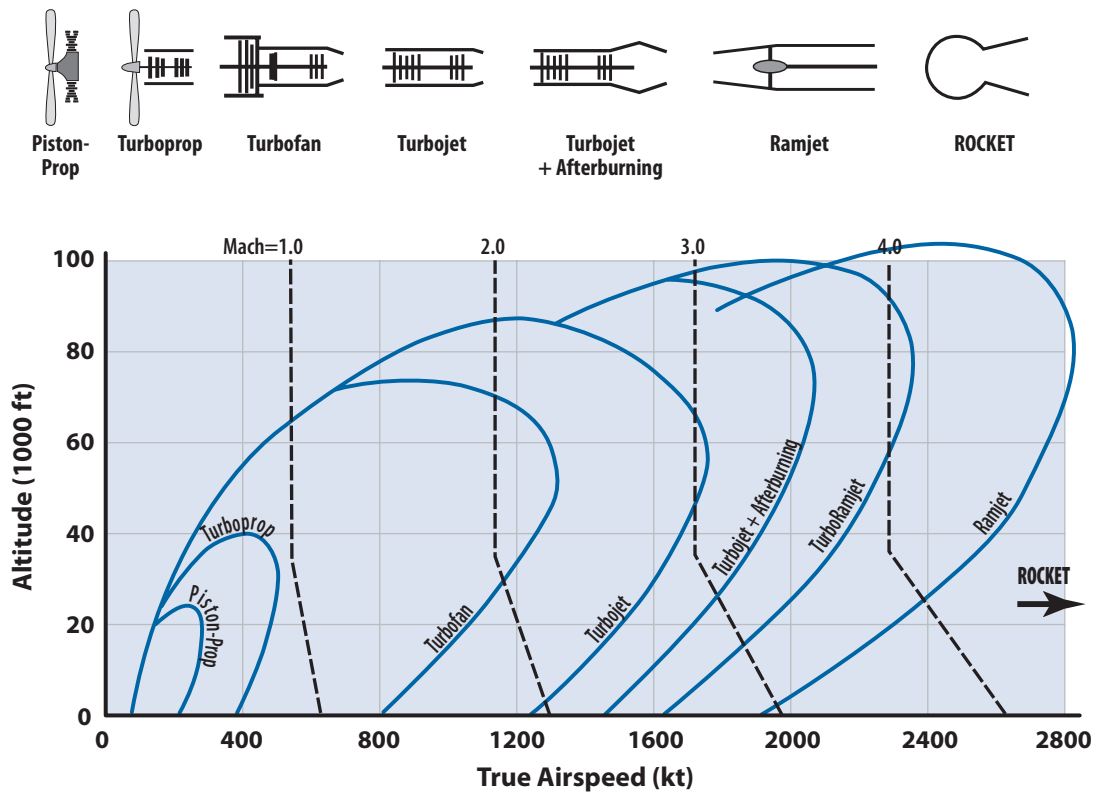
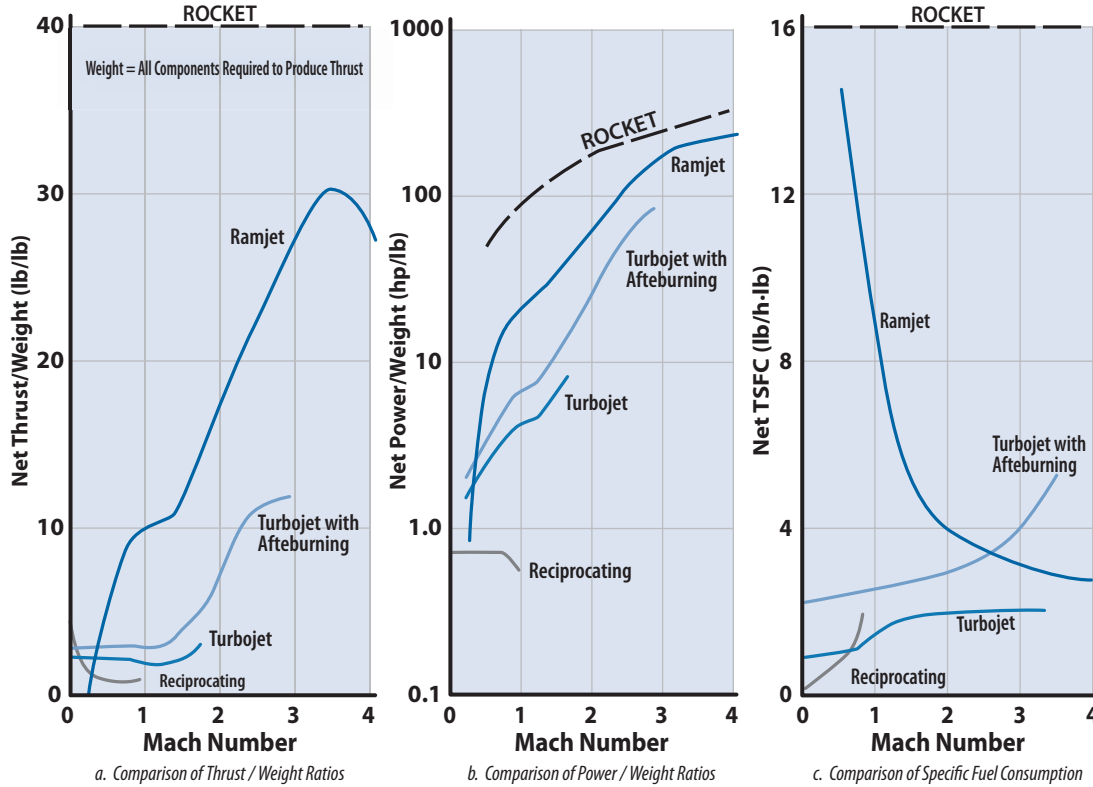


Figure 4.6 Level-flight propulsion options.



**Figure 4.7** Comparison of design characteristics of different propulsion engines as a function of flight Mach number. Each point on the graphs represents an engine design point with a structure that is critical at that point for pressure loads.



From Chapter 3, Section 3.8, the excess specific power  $P_S$  (in feet per second) is given by Eq. (3.40),

$$P_S = \frac{dh_e}{dt} = \frac{V(T \cos \alpha - D)}{W} \quad (3.40)$$

and expresses the rate of change of the aircraft's specific energy

$$h_e = h + \frac{V^2}{2g} \quad (3.36)$$

where  $h$  is the altitude above mean sea level. The quantity

$$f_S = \frac{dh_e}{dW_f} = \frac{dh_e/dt}{TC} \quad (4.6)$$

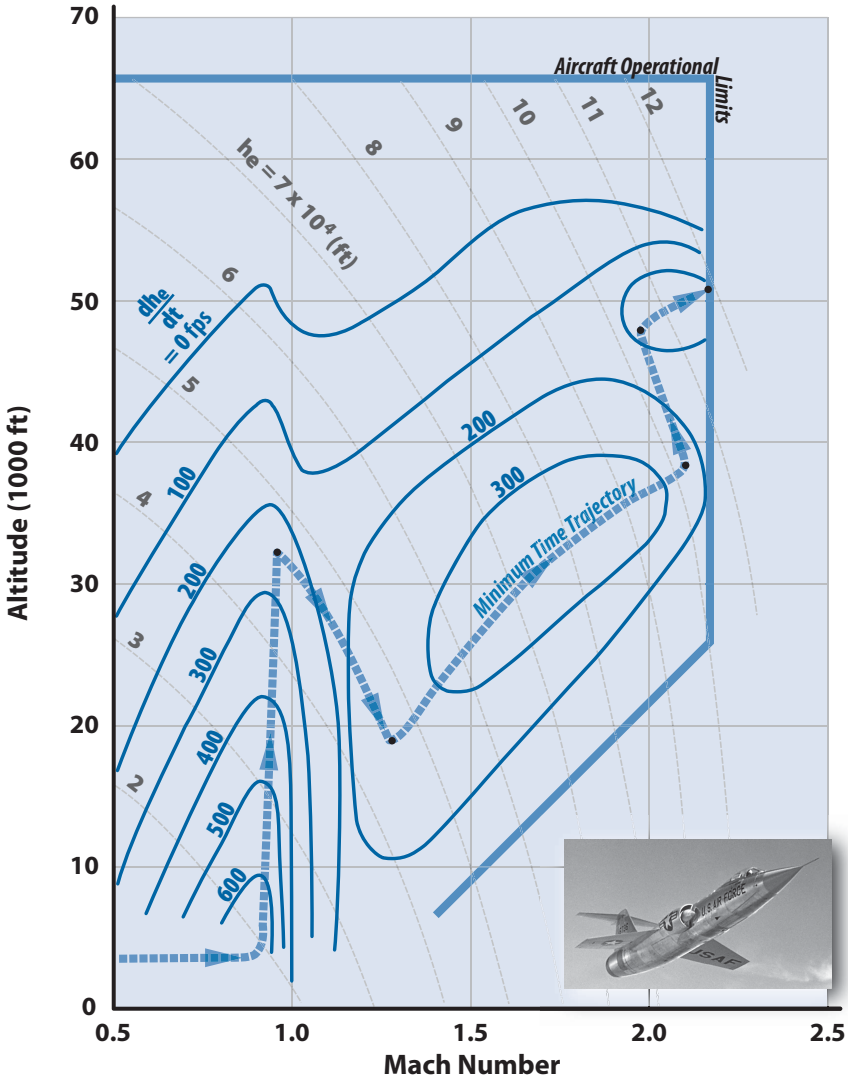
where  $T$  is the thrust and  $C$  is the specific fuel consumption, expresses (in feet per pound) the change of specific energy with respect to a change in fuel weight. Figure 4.8a shows a plot of constant  $h_e$  that is independent of the aircraft-propulsion system. Figure 4.8 a and b shows plots of constant  $P_S$  and  $f_S$ , respectively, for the supersonic F-104G at a load factor of 1. Figure 4.9 shows the  $P_S$  and  $f_S$  curves for an advanced fighter (composite lightweight fighter). Notice that the F-104G is typical of supersonic aircraft in the 1960–1970 time period and displays a thrust pinch (marginal excess power) around Mach 1.0. This characteristic results in the curves of constant  $P_S$  being closed loops in some regions and discontinuous in others, as shown in Fig. 4.8a. Modern propulsion systems and high  $(T/W)_{TO}$  eliminate this thrust pinch, and the curves of constant  $P_S$  are as shown in Fig. 4.9a. We shall see later that this difference results in two very different optimal trajectories for minimum time. For reference, Table 4.3 shows the data for the constant energy lines ( $h_e$ ).

The time for an aircraft to move from one point of altitude and velocity to another point (i.e., to change its energy state  $h_e$ ) along a trajectory A is given by the line integral

$$\Delta t = \int_{h_{e1}}^{h_{e2}} \frac{1}{P_S} dh_e \quad (4.7)$$

Similarly, the fuel burned along trajectory A from  $h_{e1}$  to  $h_{e2}$  is

$$\Delta W_f = \int_{h_{e1}}^{h_{e2}} \frac{1}{f_S} dh_e \quad (4.8)$$



**Figure 4.8a** Excess specific power,  $P_s = dh_e/dt$ , for the F-104G at  $n = 1$ , 18,000 lb, and maximum power [ $W_{TO} = 26,000$  lb,  $(W/S)_{TO} = 133$ , one J79-GE-11A at  $T_{SLS} = 15,800$  lb,  $(T/W)_{TO} = 0.61$ , maximum Mach = 2.2].

During a climb–acceleration, the aircraft load factor  $n$  varies. However, [14] concludes that the average value of the load factor during a climb–acceleration maneuver is such that the  $P_s$  and  $f_s$  in Eqs. (4.7) and (4.8), respectively, should be for 1 g.

From Eq. (4.7) it follows that the minimum time path for maximum energy change will be the one in which, at each value of specific energy, the

aircraft flies at that combination of velocity and altitude that gives the maximum rate of change of specific energy in the direction of changing  $h_e$  [15]. Thus, the optimal path for maximum energy change is the locus of the points at which the lines of constant  $h_e$  are tangent to lines of constant 1-g  $P_s$ . This minimum time path is shown in Fig. 4.8a for the F-104 and in Fig. 4.9a for an advanced fighter aircraft of high  $(T/W)_{TO}$ . It must be pointed out that this method for finding optimal trajectories by establishing the path

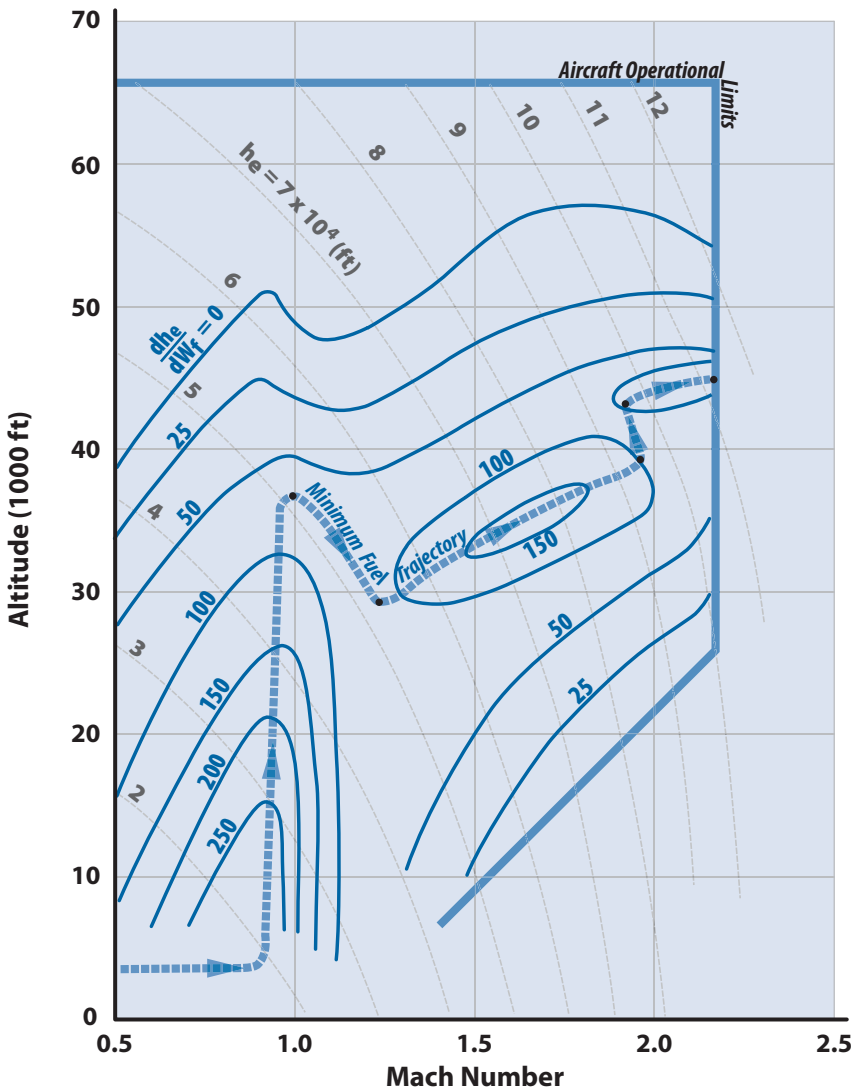
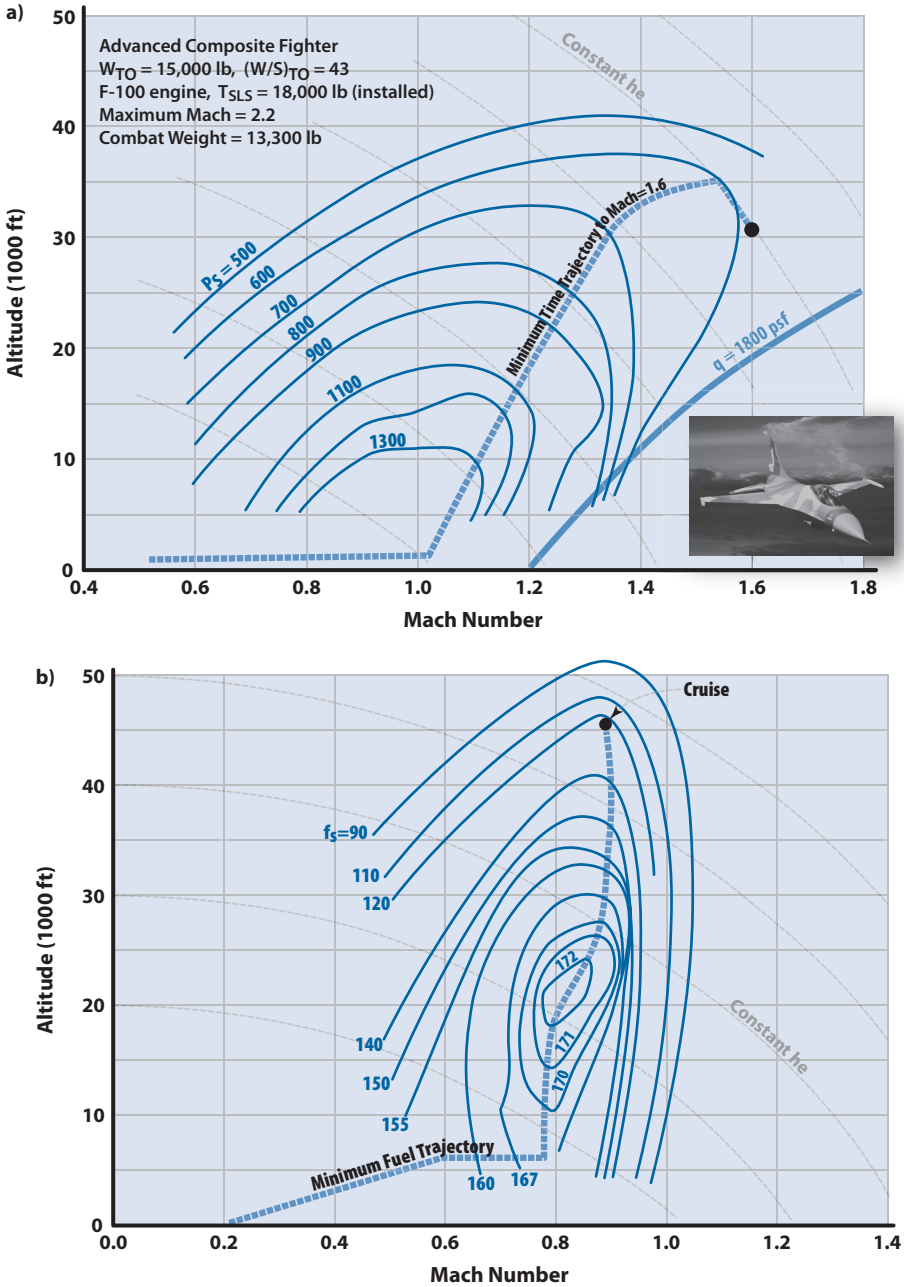


Figure 4.8b Contours of constant  $f_s = dh_e/dW_f$  for the F-104G at  $n = 1$  and maximum power.



**Figure 4.9** **a)** Excess specific power,  $P_s = dh_e/dt$ , for the LWF at  $n = 1$  and maximum power (afterburner) with  $W/S = 38.1 \text{ psf}$ , and **b)** contours of constant  $f_s = dh_e/dW_f$  for the LWF at  $n = 1$  and military power with  $W/S = 48.1 \text{ psf}$ .

**Table 4.3** Altitudes for Constant Energy Contours (1976 U.S. Standard Atmosphere)

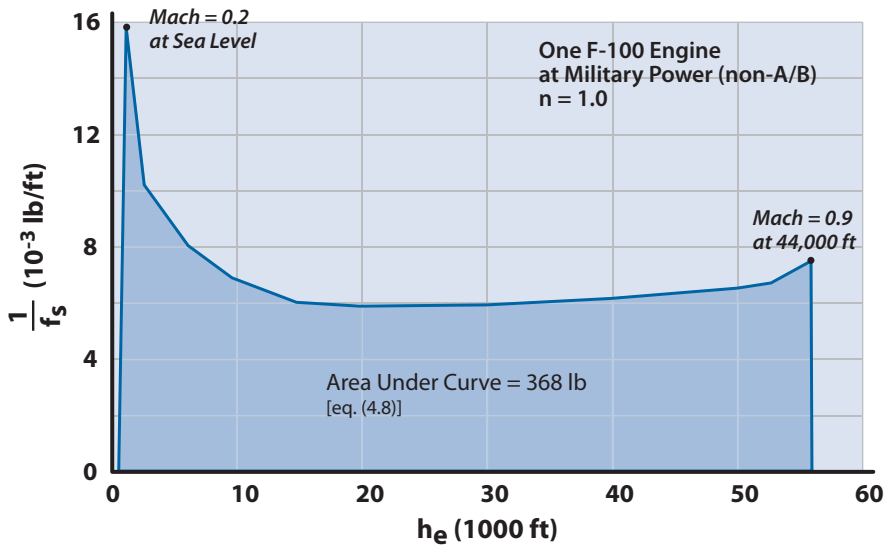
Mach	$h_e$ (ft)											
	10,000	20,000	30,000	40,000	50,000	60,000	70,000	80,000	90,000	100,000	110,000	120,000
0	10,000	20,000	30,000	40,000	50,000	60,000	70,000	80,000	90,000	100,000	110,000	120,000
0.1	9,819	19,833	29,846	39,854	49,854	59,854	69,853	79,851	89,849	99,847	109,844	119,838
0.2	9,275	19,328	29,382	39,417	49,417	59,417	69,414	79,406	89,398	99,390	109,375	119,352
0.3	8,357	18,478	28,599	38,689	48,689	58,689	68,684	78,665	88,647	98,628	108,598	118,547
0.4	7,051	17,269	27,486	37,670	47,670	57,670	67,663	77,630	87,598	97,565	107,517	117,426
0.5	5,335	15,679	26,024	36,359	46,359	56,359	66,355	76,304	86,253	96,202	106,141	115,999
0.6	3,179	13,683	24,186	34,690	44,757	54,757	64,757	74,690	84,617	94,544	104,470	114,275
0.7	544	11,242	21,940	32,638	42,864	52,864	62,864	72,792	82,692	92,593	102,493	112,264
0.8		8,311	19,243	30,175	40,679	50,679	60,679	70,613	80,484	90,355	100,225	109,979
0.9		4,831	16,040	27,249	38,203	48,203	58,203	68,161	77,998	87,834	97,671	107,436
1.0		726	12,263	23,799	35,336	45,436	55,436	65,436	75,239	85,038	94,837	104,636
1.1			7,822	19,743	31,664	42,377	52,377	62,377	72,214	81,972	91,730	101,488
1.2			2,606	14,979	27,352	39,028	49,028	59,028	68,930	78,643	88,357	98,070
1.3				9,373	22,278	35,183	45,387	55,387	65,387	75,060	84,725	94,390
1.4				2,752	16,285	29,817	41,454	51,454	61,454	71,229	80,843	90,457
1.5					9,162	23,440	37,231	47,231	57,231	67,160	76,719	86,278
1.6					624	15,797	30,971	42,716	52,716	62,716	72,362	81,864
1.7						6,534	22,791	37,910	47,910	57,910	67,782	77,223
1.8							12,734	30,325	42,812	52,812	62,812	72,364
1.9							139	19,399	37,424	47,424	57,424	67,299
2.0								5,388	26,789	41,744	51,744	61,744
2.1									11,088	35,321	45,772	55,772
2.2										17,576	39,510	49,510
2.3											25,485	42,956
2.4												36,111

with the most favorable gradient does not take into account the possibility of increasing performance on one portion of the trajectory by decreasing performance along another segment. Allowing for this possibility might result in a net improvement in performance.

Fortunately, the exact solution and the energy-state approximation for optimal trajectories are quite close [15]. A very important point is that the exact solution is often not available to the designer. The difficulty, time, and expense involved in obtaining the exact solution may not warrant solving the problem. When this is the case, solution by the energy-state approximation is satisfactory and very valuable.

The minimum fuel trajectory is determined in the same manner as the minimum time trajectory, that is, the locus of the points where the constant  $h_e$  lines are tangent to lines of constant  $f_s$ . The engine power setting for minimum climb–acceleration fuel performance is usually something less than the maximum power condition, whereas, for the minimum time, the aircraft should be at maximum power. The advanced fighter depicted in Fig. 4.9 uses military (continuous) power for minimum climb–acceleration fuel performance but maximum power (afterburner operation) for minimum-time climb–acceleration.

The time to climb and fuel burned can be calculated on a hand calculator to surprising accuracy by graphically integrating Eqs. (4.7) and (4.8). A typical plot of  $1/(dh_e/dW_f)$  versus  $h_e$  is shown in Fig. 4.10; the area under the



**Figure 4.10** Plot of  $1/f_s$  vs  $h_e$  for composite LWF along minimum fuel trajectory from Mach = 0.2 to Mach = 0.9 (see Fig. 4.9b).



**Figure 4.11** F-16 with fuel tanks, sensors, and missiles.

curve between  $h_{e1}$  and  $h_{e2}$  is the fuel burned during a climb–acceleration from  $h_{e1}$  to  $h_{e2}$ . This operation is expressed as

$$\Delta W_f \approx \sum_{j=1}^h \left[ \frac{1}{dh_e/dW_f} (h_{ei} - h_{ef}) \right]_j \quad (4.9)$$

where  $h_{ei}$  and  $h_{ef}$  are the initial and final values of specific energy for the  $j$ th interval. If small intervals are considered ( $\Delta h_e \leq 1000$ ), the results using Eq. (4.9) compare quite well with computer results. The LWF ultimately became the F-16; Fig. 4.11 shows a modern F-16 with missiles, fuel tanks, and sensors.

The energy approximation method is not valid for trajectories along constant  $h_e$  contours as Eqs. (4.7) and (4.8) would yield zero time and zero fuel to move from one point of velocity and altitude to another.

## References

- [1] Fung, Y. C., *An Introduction to the Theory of Aeroelasticity*, Wiley, New York, 1955.
- [2] Bisplinghoff, R. L., Ashley, H., and Hoffman, R. L., *Aeroelasticity*, Addison Wesley, Reading, MA, 1957.

- [3] "Military Standardization Handbook, Metallic Materials and Elements for Aerospace Vehicle Structures," MIL-HDBK-5B, Superintendent of Documents, U.S. Government Printing Office, Washington, DC, 1 Sept. 1971.
- [4] Henshaw, J. T., *Supersonic Engineering*, Wiley, New York, 1962.
- [5] "Aircraft Engine Noise and Sonic Boom," *AGARD Conference Proceedings No. 42*, Clearinghouse for Federal Scientific and Technical Information (CFSTI), Springfield, VA, May 1969.
- [6] "Noise Standards: Aircraft Type Certification," *Federal Aviation Regulations*, Vol. 1, Pt. 36, U.S. Government Printing Office, Washington, DC, Dec. 2009.
- [7] Beheim, M. A., Anti, R. J., and Povolny, J. H., "Advanced Propulsion, Cleaner and Quieter," *Astronautics and Aeronautics*, Vol. 10, No. 8, Aug. 1972, p. 37.
- [8] Jackson, R. P., "Putting All Our Noise Technology to Work," *Astronautics and Aeronautics*, Vol. 12, No. 1, Jan. 1974, p. 48.
- [9] Johnson, F. S., "SST's, Ozone and Skin Cancer," *Astronautics and Aeronautics*, Vol. 11, No. 7, July 1973, p. 16.
- [10] "Conference on Aircraft and the Environment," Society of Automotive Engineers, New York, 1971.
- [11] Harned, M., "The Ramjet Power Plant," *Aero Digest*, July 1954, p. 38.
- [12] Elsgolc, L. E., *Calculus of Variations*, Addison Wesley, Reading, MA, 1962.
- [13] Bryson, A. E., and Denham, W. F., "A Steepest Ascent Method for Solving Optimum Programming Problems," *Journal of Applied Mathematics*, Vol. 29, No. 6, June 1962, pp. 4–21.
- [14] Nash, R. C., "Analytical and Experimental Investigation of Optimum Fighter Aircraft Maneuvers," U.S. Air Force Flight Dynamics Laboratory Technical Rept. 73–145, Wright–Patterson AFB, OH, July 1974.
- [15] Bryson, A. E., Desai, M. N., and Hoffman, W. C., "Energy-State Approximation in Performance Optimization of Supersonic Aircraft," *Journal of Aircraft*, Vol. 6, No. 6, Dec. 1969, p. 481.



## Chapter 5

# Preliminary Estimate of Takeoff Weight



- Predicting Empty-Weight Fraction
- Estimating Mission Segment Fuel Fraction
- Predicting Takeoff Weight
- Examples

LWF competition finalists General Dynamics YF-16 and Northrop YF-17 fly side-by-side in 1975. The YF-16 was a conventional metal design with an empty weight of 12,500 lb and a mission weight of 18,500 lb. If the YF-16 had been designed using advanced composites, the mission weight could have been reduced (see Example 5.1).

*If you can find a path with no obstacles,  
it probably doesn't lead anywhere.*

Frank A. Clark

## 5.1 Introduction

The design process begins with the estimate of the *takeoff weight*  $W_{TO}$ . The  $W_{TO}$  is a very important design parameter as it sizes the vehicle. If this is the first iteration, that is, the first time through the design loop, the designer knows very little about the aircraft except for the requirements. The designer must decide what propulsion system will be used: this does not necessarily mean the size of the engine(s), but specific fuel consumption data are needed. In addition, the designer must select the material type (i.e., conventional metal structure, advanced composites, etc.).

Many people have difficulty getting started at this point because they must make some assumptions based upon very little information. Perhaps the best rule here is to “assume something even if it’s wrong” because the process cannot really begin until an estimate of the  $W_{TO}$  is made.

It is important to remember that the conceptual phase is actually a looping or iterative process in which the assumptions are refined on subsequent passes through the design loop and the design converges to a feasible baseline point. Aircraft companies have the material in the text computerized, so that they can loop through the conceptual phase in a matter of seconds and quickly “home in” on a baseline point design.

We consider the *takeoff gross weight* (TOGW), or  $W_{TO}$ , to be

$$W_{TO} = W_{\text{fuel}} + W_{\text{fixed}} + W_{\text{empty}} \quad (5.1)$$

## 5.2 Fixed Weight

The *fixed weight*  $W_{\text{fixed}}$  (usually called *payload*) consists of the following:

1. Nonexpendable
  - Crew plus equipment
  - Sensors
2. Expendable
  - Bombs
  - Missiles
  - Cannon plus ammunition
  - Passengers
  - Baggage and/or cargo
  - Food and drink

## 5.3 Empty Weight

The *empty weight* ( $W_{\text{empty}}$ ) of the aircraft includes structure, propulsion, subsystems, avionics, instruments, and so on.

**Table 5.1** Summary of Empty-Weight Trend Line Equations

Aircraft Type	Constant	XX
Fighter		
Air-to-air or developmental	1.2	0.947
Multipurpose	0.911	0.947
Air-to-ground	0.774	0.947
Bomber and transport	0.911	0.947
Light general aviation	0.911	0.947
Composite sailplane	0.911	0.947
Military jet trainer	0.747	0.993
High-altitude ISR	0.75	0.947
Unmanned air vehicles		
Propeller, endurance > 12 h	1.66	0.815
Propeller, endurance < 12 h	2.18	0.815
Turbine ISR	2.78	0.815
Turbine maneuver UCAV	3.53	0.815
Air-launch cruise missiles and targets	1.78	0.815

The designer will soon discover that this preliminary estimation of the aircraft empty weight is the weakest part of the conceptual design analysis and it has tremendous leverage on the aircraft takeoff weight. It is almost impossible to estimate the empty weight of something that has not been built (usually with new subsystems and structural materials) with any degree of accuracy. However, it is important to press on or the aircraft will never be designed.

The empty weight is determined at this point by using historical data and trends. Appendix I contains the historical weight trends that we will use in our preliminary estimate of takeoff weight. The empty weight data in Appendix I are presented by class of aircraft: fighters (broken out by type): general aviation; bombers and transports; jet trainers; intelligence, surveillance, and reconnaissance (ISR) aircraft; unmanned (combat) aerial vehicles (UAVs and UCAVs); air-launch cruise missiles; aerial targets; and sailplanes. Each aircraft has a trend line given by an equation of the type  $W_{\text{empty}} = (\text{constant})(W_{\text{TO}})^{xx}$ , with the data points making up the plotted trend line. A summary of the Appendix I weight-trend charts is given in Table 5.1. At this point Appendix I should be studied to appreciate the importance of having good historical weights data. Appendix I has weight summaries of many existing aircraft so that it can be seen how the compo-

ment weights roll up into the empty weight. Later in the design process, as more information is available on the aircraft, the empty weight will be determined by estimating the component weights using weight-estimating relationships (see Chapter 20).

## 5.4 Fuel Weight

The mission is divided into the eight phases shown in Fig. 5.1. The approach will be to determine the *fuel fraction* (ratio of the final to initial weight,  $W_{n+1}/W_n < 1$ , where  $n$  is the number of the phase) for each phase and then multiply them together to get the fuel fraction for the entire mission. If a specific mission does not have one or more of the phases shown in Fig. 5.1, the fuel fraction for the missing phase is set equal to 1. Also, the phases can be put in any order (e.g., phase 7 ahead of phase 6) and repeated as needed to fit the mission profile.

### Phase 1. Engine Start and Takeoff

In this phase, the fuel fraction for the start of the engines, taxi, takeoff, and climb out is determined. A reasonable first estimate is to assume that this phase burns about 2.5% to 3% of the takeoff weight in fuel. In other words,

$$\frac{W_2}{W_1} = 0.97 - 0.975$$

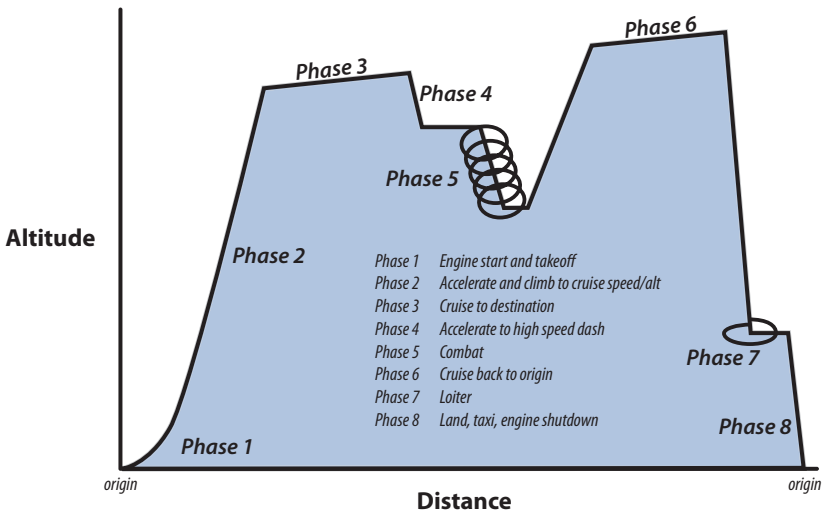


Figure 5.1 Typical military mission profile.

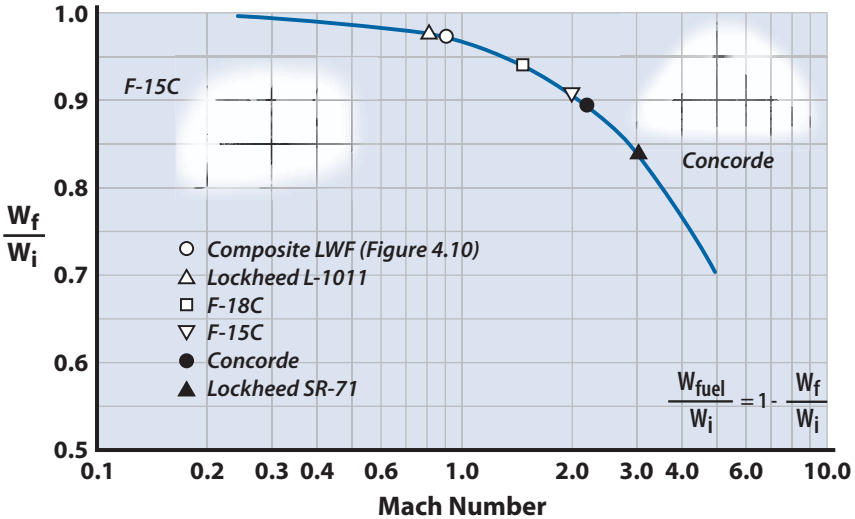


Figure 5.2 Weight fractions for climb-acceleration phase.

### Phase 2. Climb and Accelerate to Cruise Conditions

Fuel is used during this phase to increase both the kinetic and the potential energies of the aircraft. If the aircraft is a low-performance aircraft, cruising at less than Mach = 0.4, the fuel burned during this phase is not significant for the first iteration. If the aircraft cruises at speeds greater than Mach = 0.4 and/or altitudes greater than 10,000 ft, then the fuel burned in climbing and accelerating to cruise altitude and Mach number is significant. Figure 5.2 shows the ratio of  $W_3/W_2$  for typical high-performance aircraft. Because propulsion and climb-acceleration trajectories are similar for a wide variety of aircraft, it is possible to collapse the data onto a single curve as shown in Fig. 5.2. The use of Fig. 5.2 is recommended during the first iteration. Subsequent iterations can use a more refined method such as the energy-state approximation discussed in Chapter 4.

### Phase 3. Cruise Out

For this phase the designer needs to estimate the cruise speed and altitude, the configuration aspect ratio and wing sweep, and the cruise fuel consumption (for turbojet or turbofan aircraft or for propeller aircraft).

The fuel fraction for phase 3 is determined using the Breguet range expressions presented in Chapter 3. The expression for a turbojet or turbofan aircraft is

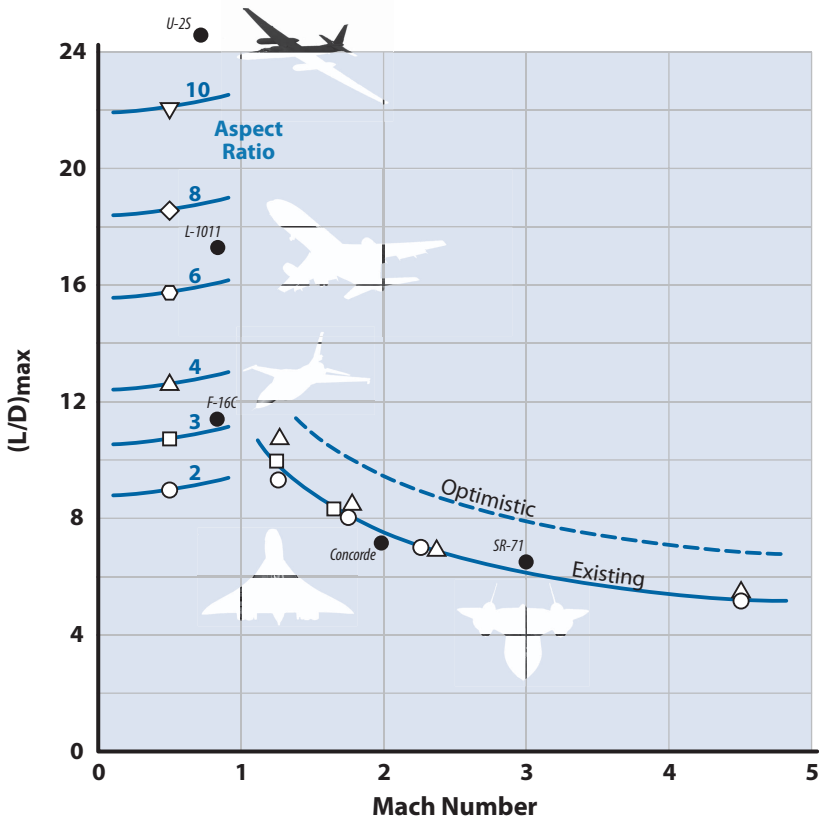


Figure 5.3  $(L/D)_{\max}$  vs Mach number for typical cruise aircraft.

$$R = \frac{V}{C} \frac{L}{D} \ln \left[ \frac{W_3}{W_4} \right] \quad (5.2)$$

and for a propeller aircraft (piston or turboshaft) is

$$R = \frac{\eta}{C} \frac{L}{D} \ln \left[ \frac{W_3}{W_4} \right] \quad (5.3)$$

Equation (5.2) or (5.3) is solved for the weight ratio  $W_3/W_4$ . For maximum range for a turbojet or turbofan aircraft, the cruise  $L/D$  will be close to (but less than) the value for  $(L/D)_{\max}$ . For a constant altitude cruise the  $L/D$  would be 86.6% of  $(L/D)_{\max}$  and for a cruise climb the  $L/D$  would be 94% of  $(L/D)_{\max}$  from Chapter 3, Table 3.2. Values for the *thrust specific fuel consumption* (TSFC) should be determined from appropriate engine data (see Chapter 14 or Appendix J). The subsonic turbojet or turbofan will cruise most efficiently above 30,000 ft and at a partial power setting of 75%

to 100% of normal rated thrust. If there is enough information on the aircraft, the designer should develop a chart similar to Fig. 3.8 to determine the optimum cruise condition and maximum value for the range factor  $VL/D$ .

For maximum range the propeller aircraft cruise  $L/D$  will be  $(L/D)_{\max}$ . The propulsive efficiency  $\eta$  can be obtained from Chapter 18 or assumed to be 0.85 for preliminary sizing. Values of the *brake specific fuel consumption* (BSFC) should be determined from appropriate engine data. The value for  $\eta/C$  is fairly constant such that maximum range occurs at the velocity for maximum  $L/D$ . Thus, the propeller aircraft would prefer to cruise at the velocity given by the expression (from Chapter 3)

$$V_{\max L/D} = \left( \frac{W}{S} \frac{2}{\rho} \right)^{1/2} \left( \frac{K}{C_{D0}} \right)^{1/4} \tag{3.11}$$

The  $(L/D)_{\max}$  can be estimated several different ways. The first way is to select a wing aspect ratio and obtain an historical value for  $(L/D)_{\max}$  from Fig. 5.3. The subsonic cruise  $L/D$  can also be estimated by using the expression for  $(L/D)_{\max}$  for a symmetrical aircraft:

$$(L/D)_{\max} = \frac{1}{2\sqrt{C_{D0}K}} \tag{5.4}$$

A value for the subsonic cruise  $C_{D0}$  can be estimated from Table 5.2 or by looking at data for similar aircraft in Appendix G. An estimate for the subsonic *drag-due-to-lift factor*  $K$  can be obtained from the expression

**Table 5.2** Representative Values for Subsonic  $C_{D0}$

Aircraft Type	Subsonic $C_{D0}$
High-subsonic jet transport	0.014–0.02
Supersonic fighter aircraft	0.014–0.022
Blended wing–body (tailless) jet aircraft	0.008–0.014
Large turboprop aircraft	0.018–0.024
Low-altitude subsonic cruise missile (high $W/S$ )	0.03–0.04
Small single-engine propeller aircraft	
Retractable gear	0.022–0.030
Fixed gear	0.026–0.04
Agricultural aircraft	
With spray system	0.07–0.08
Without spray system	0.06
High-performance sailplane	0.006–0.01

$$K = \frac{1}{\pi AR e} \quad (5.5)$$

where  $e$  is the wing efficiency factor obtained from Fig. G.9. During subsequent iterations, the designer can reduce the cruise range by the distance covered during the climb–acceleration to cruise (phase 2) if this distance is known. Also, the range can be broken into smaller segments (as discussed in Chapter 3) for more refined range segment fuel fractions.

### Phase 4. Acceleration to High Speed

The weight fraction for acceleration from a cruise condition to a high-speed dash can be estimated from Fig. 5.2. For example, assume we want the weight fraction for an acceleration from a cruise at Mach = 0.9 to a dash at Mach = 2.5. From Fig. 5.2 we have

$$\frac{W_f}{W_i}(M = 0.1 - 0.9) = 0.975, \quad \frac{W_f}{W_i}(M = 0.1 - 2.5) = 0.91$$

Thus,

$$\frac{W_5}{W_4} = \frac{W_f}{W_i}(M = 0.9 - 2.5) = \frac{0.91}{0.975} = 0.933$$

### Phase 5. Combat

The mission requirements for the combat phase usually specify one (or both) of the following:

1. Specified number of minutes at maximum power and a particular Mach number and altitude
2. Specified number of turns at maximum power and a particular load factor, Mach number, and altitude

Both of these requirements translate into a loiter time condition at maximum power. [From Chapter 3, equation 3.32,

$$\text{Turn rate} = \frac{g\sqrt{n^2 - 1}}{V}$$

(in radians per second), where  $n$  = load factor and  $g = 32.174 \text{ ft/s}^2$ ; time = (number of turns) (360 deg)/(turn rate).]

Then, the combat fuel is determined using



$$\text{Combat fuel} = (\text{TSFC})(\text{maximum thrust})(\text{time})$$

where TSFC is the maximum-power thrust specific fuel consumption. The mission requirements only size the fuel that must be available for combat. The performance level of an aircraft with this given amount of fuel is determined much later in the design cycle.

Generally, equations will use  $C$  to represent either “thrust specific fuel consumption” (TSFC) for turbine engines or “brake specific fuel consumption” (BSFC) for propeller engines. Context is usually sufficient to determine which term  $C$  represents.

### Phase 6. Cruise Back

The fuel fraction for this phase may be treated in the same way as the cruise out, phase 3. The return cruise altitude will probably be higher than cruise-out altitude because the aircraft is lighter. Also, if the aircraft dropped external weapons or tanks, the return cruise  $L/D$  will be slightly higher than the cruise-out case.

### Phase 7. Loiter

Once a loiter is established, the fuel-weight fraction may be found using the endurance equation of Chapter 3 for jet or propeller aircraft. The *endurance equation* for jet aircraft is given by Eq. (3.17):

$$E = \frac{1}{C} \frac{L}{D} \ln \left[ \frac{W_7}{W_8} \right] \tag{5.6}$$

where  $E$  is the endurance (or loiter time) in hours and  $C$  is the thrust specific fuel consumption in pounds of fuel per hour per pound of thrust [(lb of fuel)/(lb of thrust·h)]. The maximum endurance will occur at the flight condition where  $(L/D)/C$  is a maximum. This is usually less than but near the velocity for  $(L/D)_{\max}$  so the designer can use loiter  $L/D \sim (L/D)_{\max}$ . If loiter flight conditions are specified it is very probable that the aircraft will not be operating at  $(L/D)_{\max}$  and/or minimum  $C$ . Thus, conservative estimates for  $L/D$  and  $C$  should be made. The endurance equation for propeller aircraft is given by Eq. (3.22) in Chapter 3. This equation calls for a fair amount of detail to be available on the aircraft. If this is the first iteration, this detail may not be known and a more simple form of Eq. (3.22) is preferred. Thus, the following expression for propeller aircraft endurance is recommended:

$$E = \frac{\eta}{C} \frac{L}{D} \frac{1}{V} \ln \left[ \frac{W_3}{W_4} \right] \tag{5.7}$$

Again, the designer estimates the parameters with the highest accuracy possible.

### Phase 8. Reserve and Trapped Fuel

Mission requirements will often specify a reserve fuel. This fuel, normally 5% of the fuel required for the mission, is strictly for reserve and cannot be used for any part of the mission.

There is usually a small fraction of the oil and fuel that is trapped in lines and pumps and is really not available as fuel or lubricant. This trapped oil and fuel usually amounts to about 1% of the mission fuel.

## 5.5 Determining $W_{TO}$

The  $W_{fuel}$  is determined as a fraction of the takeoff weight, that is,

$$\left[ \frac{W_{final}}{W_{TO}} \right] = \left[ \frac{W_8}{W_1} \right] = \left[ \frac{W_2}{W_1} \right] \left[ \frac{W_3}{W_2} \right] \dots \left[ \frac{W_8}{W_7} \right] \quad (5.8)$$

$$W_{fuel} = \left( 1 + \text{reserve} + \text{trapped} \right) \left( 1 - \frac{W_8}{W_1} \right) W_{TO} \quad (5.9)$$

If there are any weight discontinuities (such as bombs dropped or missiles fired) and/or fuel phases that cannot be expressed as a weight fraction (such as combat fuel) during the mission, then Eq. (5.9) must be solved in segments. Example 5.1 will demonstrate this situation. The  $W_{fixed}$  is determined by the requirements of the mission and will be a fixed number independent of  $W_{TO}$ . A value of  $W_{TO}$  is assumed and the available empty weight determined using the expression

$$\left( W_{empty} \right)_A = W_{TO} - W_{fuel} - W_{fixed}$$

The required empty weight,  $\left( W_{empty} \right)_R$ , is determined from the empty-weight figures in Appendix I with appropriate adjustments for advanced materials and/or concepts. An iteration on  $W_{TO}$  ensues until  $\left( W_{empty} \right)_A$  and  $\left( W_{empty} \right)_R$  are close.

Usually the iteration continues until

$$\left| \left( W_{empty} \right)_A - \left( W_{empty} \right)_R \right| \leq 0.01 \left( W_{empty} \right)_R$$

This iteration for  $W_{TO}$  is illustrated in Fig. 5.4, which shows the empty-weight fraction and fixed-weight fraction as monotonic functions of  $W_{TO}$ . The fuel-weight fraction is independent of  $W_{TO}$  as depicted in Fig. 5.4

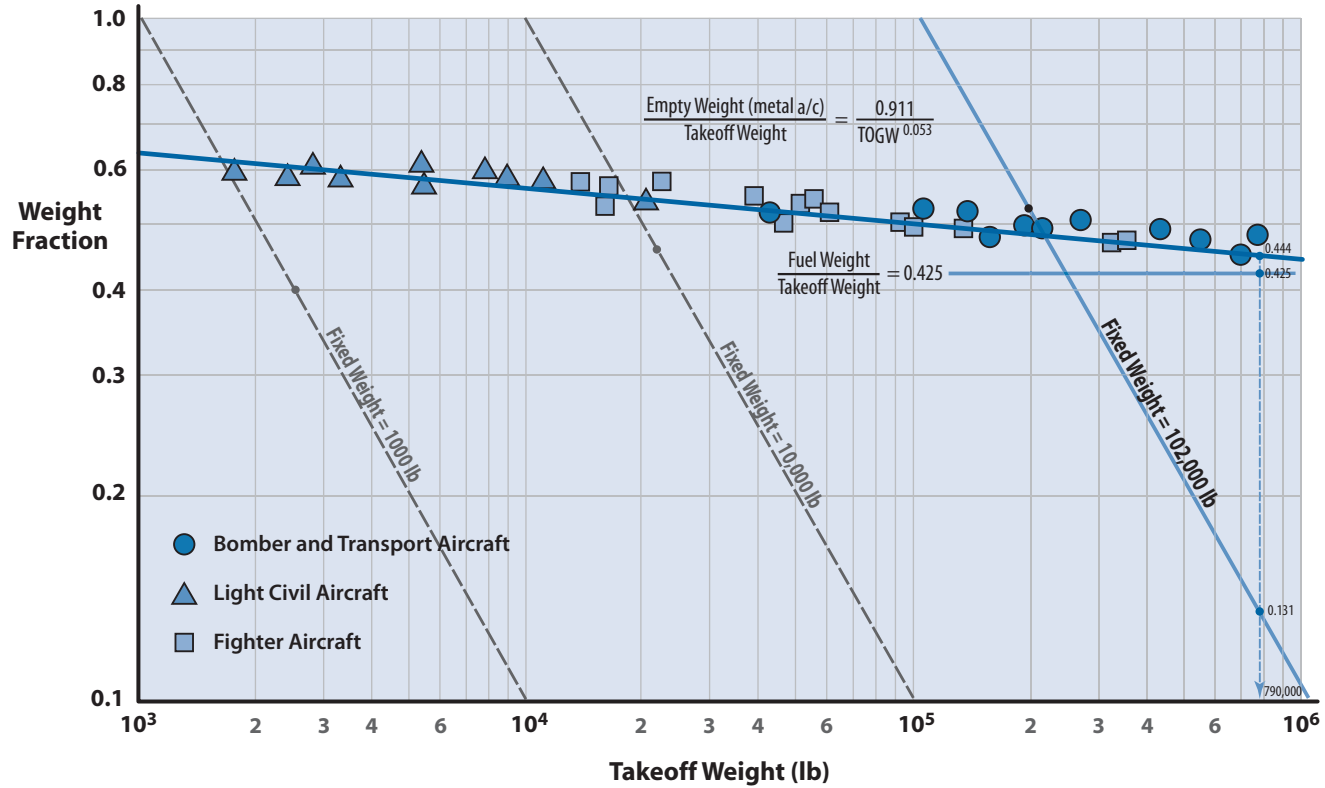


Figure 5.4 Empty-weight fraction for current aircraft (fighters, bombers, and light aircraft).

(0.425, which is the fuel-weight fraction from Example 5.2). The solution is found where the three fractions  $W_{\text{fuel}}$ ,  $W_{\text{empty}}$ , and  $W_{\text{fixed}}$  all sum to 1.0.

The selection of an initial estimate for  $W_{\text{TO}}$  must include the gross assumptions inherent in the first iteration. Subsequent iterations refine these assumptions and converge on a refined  $W_{\text{TO}}$ . However, this initial estimate of  $W_{\text{TO}}$  should be close to the final value, because a great deal of work will be done based upon this initial  $W_{\text{TO}}$ .

## USAF Invites Competition for LWF

As a result of the pressure brought about by John Boyd's "Fighter Mafia," the USAF launched an LWF program in 1972. The LWF was to be a low-cost F-15 20,000-lb class day fighter with good turn rate, acceleration and range, and optimized for air combat at speeds of Mach 0.6–1.6 and altitudes of 30,000–40,000 ft.

Competition finalists were General Dynamics' YF-16 (single F100-PW-100 afterburning turbofan at 23,000 lb TSLs) and Northrop's YF-17 (two YJ101-GE-100 turbofans at 14,400 lb TSLs each). The YF-16 was selected: the USAF liked its maneuverability, and the LCC for a single-engine fighter was less than that of a twin-engine craft. General Dynamics/Lockheed Martin has produced over 4500 F-16 Fighting Falcons. Meanwhile, the Navy liked the two-engine performance of the YF-17; it became the basis for the carrier capable F-18 Hornet. McDonnell/Boeing has produced over 1500 F-18s.

### Example 5.1 Advanced Composite Lightweight Fighter

Determine the initial weight estimate for an advanced composite lightweight fighter (LWF). The LWF is a good choice for an example as its mission profile involves every phase shown in Fig. 5.1.

USAF LWF Mission Requirements	
Purpose	Lightweight, low-cost, air-superiority, day fighter
Radius (internal fuel only)	250 n mile
Maximum speed	Above Mach 1.6
Cruise condition	Not specified
Combat fuel sizing	One acceleration from Mach = 0.9 to Mach = 1.6 at 30,000 ft Four minutes of maximum afterburner (A/B) operation at Mach = 0.9 30,000 ft
Loiter	Sea level at Mach = 0.35 for 20 min
Reserve	5% of fuel
Crew	One

Weapons	Two AIM 9 missiles One 20-mm M-61 cannon
Engine	One F100 (see Chapter 14) or two YJ-101 afterburning turbofan engines
Structures	Limit load factor of 7.33 at 80% internal fuel with missiles and full ammunition load Placard structural and flutter limit Mach = 1.1 at sea level Advanced composites used throughout the vehicle where applicable
<b>LWF Fixed Weights</b>	
Pilot plus gear	200 lb
2 AIM 9 missiles plus racks	472 lb
M-61 cannon plus accessories	485 lb
560 rounds of 20-mm shells	320 lb
Total	1477 lb
$W_{\text{fixed}}$	1500 lb

The LWF fuel fraction followed the mission profile shown in Fig. 5.1.

### Phase 1. Takeoff and Climb Out

Assume fuel burned during this phase to be 2.5% of  $W_{\text{TO}}$ ,

$$\frac{W_2}{W_1} = \frac{W_2}{W_{\text{TO}}} = 0.975$$

### Phase 2. Climb–Acceleration to Cruise

Assume cruise is near the tropopause at Mach = 0.9. From Fig. 5.2, the following fuel fraction is obtained:

$$\frac{W_3}{W_2} = 0.975$$

### Phase 3. Cruise Out 250 n Mile

Assume cruise is between 36,000 ft and 45,000 ft at Mach = 0.9. (This can be checked later when aerodynamic data are available and this weight fraction refined during subsequent iterations.) From the F100 engine data in Chapter 14 (Fig. 14.7 d and e), it may be observed that a reasonable estimate for the TSFC is 0.93. Because our aircraft is a fighter with the requirement to go supersonic, our fixed wing (another

assumption!) aspect ratio will be low. Assuming an  $AR = 3$  gives an  $(L/D)_{\max} \sim 10$  from Fig. 5.3. Thus, a realistic cruise  $L/D$  is about 9. This estimate for cruise  $L/D$  can be checked by using Eqs. (5.4) and (5.5). From Table 5.2 or Fig. G.6 we obtain an estimate of  $C_{D0} = 0.016$ . Using  $AR = 3$  and  $e = 0.8$  (from Fig. G.9) in Eq. (5.5) gives  $K = 0.1326$ . Finally Eq. (5.4) gives  $(L/D)_{\max} = 10.8$  (checks with the F-16 in Fig. G.3). Thus, a cruise  $L/D$  of 9 is conservative but realistic.

Using the Breguet range equation gives our weight fraction as

$$\begin{aligned} \frac{W_i}{W_f} &= \frac{W_3}{W_4} = \exp \left[ \frac{\text{Radius} \times C}{V \times L/D} \right] \\ &= \exp \left[ \frac{(250)(0.93)}{(516.24)(9)} \right] = 1.05 \end{aligned}$$

#### Phase 4. Combat Acceleration at 30,000 ft

The fuel fraction for the acceleration from Mach = 0.9 to Mach = 1.6 can be determined from Fig. 5.2 or using an energy-state approximation discussed in Section 4.8. Using Fig. 5.2 gives

$$\left( \frac{W_f}{W_i} \right)_{\text{to } M=0.9} = 0.975, \quad \left( \frac{W_f}{W_i} \right)_{\text{to } M=1.6} = 0.952$$

Thus,

$$\frac{W_5}{W_4} = \frac{0.952}{0.975} = 0.976$$

#### Phase 5. Combat Turns at Maximum Power

The fuel burned during the four minutes of combat at 30,000 ft cannot be expressed as a fuel fraction. From the F100 engine data in Chapter 14 (Fig. 14.7b), the thrust and TSFC for Mach 0.9 and 30,000 ft are

$$\text{Thrust} = 12,000 \text{ lb} \quad \text{TSFC} = 2.17$$

Thus, the weight of fuel burned during 4 minutes at maximum power is given by

$$\text{Combat } W_{\text{fuel}} = (\text{Thrust})(\text{TSFC})(\text{Time}) = 1740 \text{ lb}$$

### Phase 6. Cruise Back 250 n mile

Assume that the cruise back is similar to the cruise out (this is not really true because the aircraft will be lighter and will cruise at a higher altitude) and use the same fuel-weight fraction:

$$\frac{W_6}{W_7} = 1.05$$

Notice that the fuel expended for climb to cruise is not taken into account nor is the distance traveled during this climb. This is an approximation but is still within the noise level of this initial estimate.

### Phase 7. Loiter at Sea Level, Mach = 0.35

The 20-minute loiter at sea level uses the Breguet endurance equation. The F100 partial power data yield an estimated TSFC = 0.84. Assuming a loiter  $L/D = 8.7$  gives a fuel fraction of

$$\frac{W_f}{W_i} = \exp \left[ \frac{\text{Endurance} \times C}{L/D} \right] = \exp \left[ \frac{(20)(60)(0.84)}{(8.7)(3600)} \right] = 1.033$$

### Iterate for $W_{TO}$

The determination of  $W_{TO}$  is an iterative process whereby the available empty weight obtained from the fuel-weight fractions is balanced by the required empty weight obtained from Fig. I.1 using the upper trend line.

Assume

$$W_{TO} = W_1 = 13,000 \text{ lb}$$

The weight at beginning of combat,  $W_5$ , is

$$W_5 = \left( \frac{W_2}{W_1} \frac{W_3}{W_2} \frac{W_4}{W_3} \frac{W_5}{W_4} \right) W_1 = (0.8839)(13,000) = 11,491 \text{ lb}$$

Subtract the following:

- Missiles, 348 lb
- 20-mm ammo, 320 lb
- 4 minutes of combat fuel, 1740 lb
- Total = 2408 lb

from  $W_5$  to get the weight at beginning of cruise back,  $W_6$ .

$$W_6 = 9083 \text{ lb}$$

The weight at landing,  $W_8$ , is

$$W_8 = \left( \frac{W_7}{W_6} \frac{W_8}{W_7} \right) W_6 = 8379 \text{ lb}$$

The fuel weight required for the mission is

$$(W_{\text{fuel}})_{\text{mission}} = W_{\text{TO}} - W_8 - \text{missiles} - \text{ammo} = 3953 \text{ lb}$$

and the total fuel is the fuel required plus the reserve fuel (5%) and trapped fuel (1%). Thus,

$$W_{\text{fuel}} = 1.06 (W_{\text{fuel}})_{\text{mission}} = 4190 \text{ lb}$$

Now the available empty weight is

$$(W_{\text{empty}})_A = W_{\text{TO}} - W_{\text{fuel}} - W_{\text{fixed}} = 13,000 - 4190 - 1500 = 7309 \text{ lb}$$

Because advanced composites are being used, it is assumed that the conventional metal empty weights from Appendix I may be reduced by 16% (this assumption is very important and, right or wrong, it needs to be documented with the rationale used). The required empty weight is obtained from Fig. I.1 using the trend line for high- $(T/W)_{\text{TO}}$  and low- $(W/S)_{\text{TO}}$  fighter aircraft [i.e.,  $W_{\text{empty}} = 1.2(W_{\text{TO}})^{0.947}$ ] reduced by 16%. Thus,

$$(W_{\text{empty}})_R = 7932 \text{ lb}$$

The conclusion is that a  $W_{\text{TO}} = 13,000$  lb solution cannot accomplish the required mission because the available empty weight is 623 lb less than required. The next iterations would increase the  $W_{\text{TO}}$  until the difference between the available and required empty weights is within a specified limit such as  $0.01(W_{\text{empty}})_R$ . This iteration process is shown in Fig. 5.5. From Fig. 5.5, we observe that the initial estimate of  $W_{\text{TO}}$  to perform the LWF mission is 15,400 lb. (Note: further refinements decreased the  $W_{\text{TO}}$  to 15,000 lb, which is the value used in Table 3.1.)

### Mission Trades—Influence of Payload and Radius on $W_{\text{TO}}$

It is useful at this point to ask some “What if” questions about the mission requirements. What would the impact be on  $W_{\text{TO}}$  if the



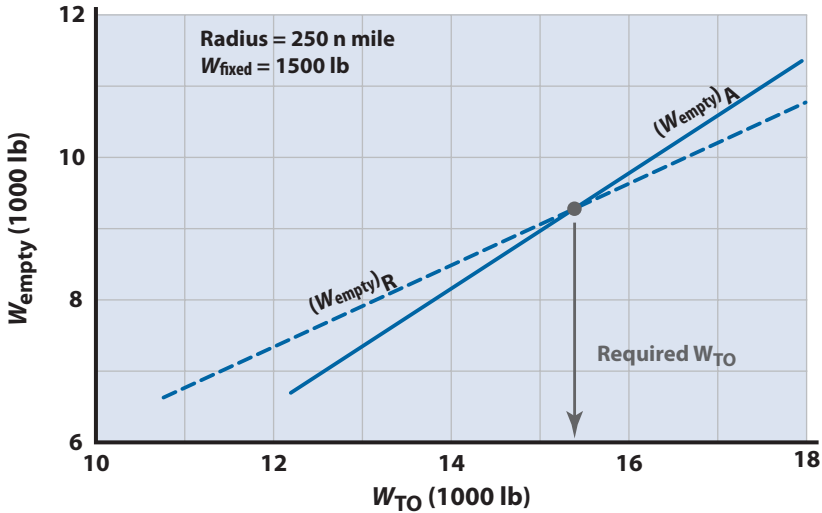


Figure 5.5 Determination of required  $W_{TO}$  for composite LWF.

payload weight or mission radius were changed? The answers to these types of questions are called *mission trades*, one of three very important trades studies that should be done during conceptual design (the other two are design trades and technology trades; see Fig. 1.15).

The iteration scheme just discussed can now be used to examine the influence of payload and radius variations on the required  $W_{TO}$ . First, consider increasing the payload (i.e., fixed weight) by 500 and 1000 lb. This could be expendable ordnance, increased avionics gear, or merely a fixed-weight increase in components or structure. The influence on  $W_{TO}$  due to changing the fixed weight (or payload) is shown in Fig. 5.6. Notice that an increase in fixed weight of 500 lb results in a  $W_{TO}$  increase of 1900 lb, or a weight sensitivity ratio of 3.8/1.0. This is because the extra 500 lb requires additional fuel to carry it out and back (or carry it out and drop it), and this extra fuel requires structure to contain it, which requires more fuel, and so on. Thus, the designer, especially the structural designer, must be aware that an extra pound of component or structure is magnified to obtain the new takeoff weight.

The weight sensitivity ratio is often called the *aircraft growth factor* because it reflects how the aircraft takeoff weight increases as the payload increases. The growth factor is defined as  $\Delta(\text{TOGW})/\Delta(\text{payload weight})$  and depends primarily on the character of the mission and the payload fraction (the larger the payload fraction, the larger the growth factor). For example, a growth factor of 3.5 to 4.0 is typical for fighter aircraft with payload fractions of 10% to 15%. For

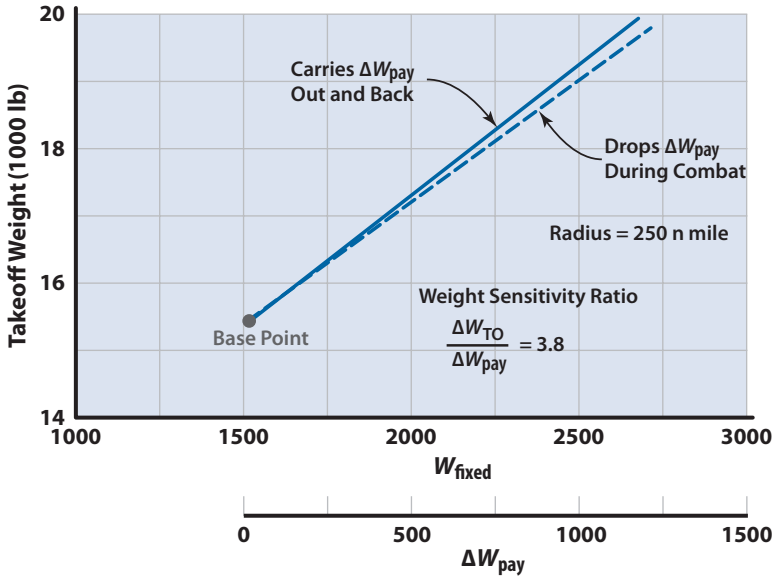


Figure 5.6 Influence of  $W_{fixed}$  on  $W_{TO}$  for composite LWF.

an air-launched cruise missile the payload fraction is typically 15% or more and the growth factor is approximately 4. For long endurance ISR aircraft (such as the RQ-4A Global Hawk) the payload fraction is less than 10% and the growth factor is approximately 2.5. The influence on  $W_{TO}$  of changing radius can be examined by determining new values for  $W_3/W_4$  and  $W_6/W_7$  and performing the iteration process. The result of changing mission radius is shown in Fig. 5.7. An additional 50 n mile in radius will cost an extra 1000 lb in takeoff weight.

## 5.6 Range- or Payload-Dominated Vehicles

Aircraft that have long range (or endurance) requirements and/or large payload requirements will be large in size. This is because a long range requirement (over 3000 n mile, for example) results in a large fuel fraction and a large payload (over 50,000 lb, for example) directly results in a large fixed-weight fraction. These two large fractions result in a large  $W_{TO}$ .

As  $W_{TO}$  increases, the empty-weight fraction decreases, as shown in Fig. 5.4. This behavior is welcome because without it long-range, high-payload missions would not have a solution. Empty-weight fraction improves for larger aircraft for two reasons. First, structural efficiency of larger vehicles is better (lower structural-weight fraction); second, many systems and components (such as avionics, hydraulic, actuators, and

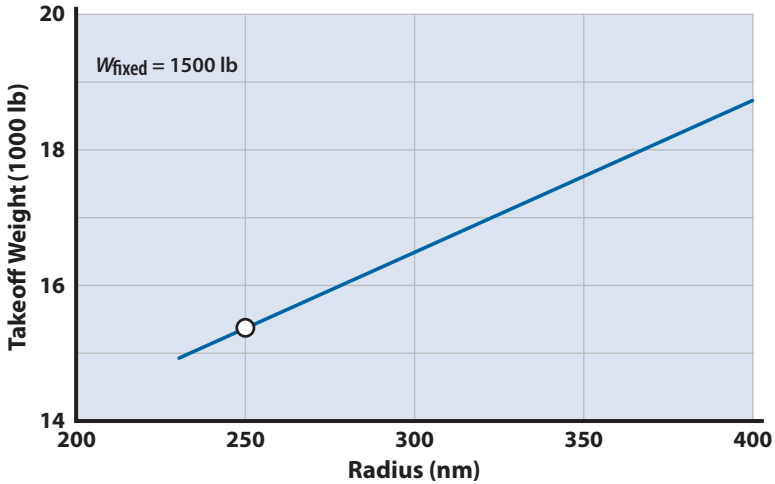


Figure 5.7 Influence of mission radius on  $W_{TO}$  for composite LWF.

control units) do not scale with weight and thus become a smaller fraction of the total aircraft weight. Figure 5.4 shows the empty-weight fraction decreasing from an average value 0.63 at  $W = 1000$  lb to about 0.44 at  $10^6$  lb takeoff weight for conventional metal structures. Advanced materials and structural concepts provide an even greater decrease.

**Example 5.2 Extended Range or Payload Aircraft**

Consider the following:

Mission Requirements	
Purpose	Long-range transport aircraft
Range (unrefueled)	6000 n mile
Payload	100,000 lb
Crew	Nine
Cruise	Subsonic
Maximum speed	Subsonic
Field length	Not specified
Service ceiling	Not specified
Reserve	5% of mission fuel
Assume 2000 lb for crew and equipment	gives a $W_{fixed} = 102,000$ lb
Assume high-bypass turbofan	gives cruise specific fuel consumption of 0.6 at Mach = 0.8 and 36,000 ft (see Tables 5.3, 14.8, and J.1)
Assume AR = 7	gives approximate $(L/D)_{max}$ from Fig. 5.3 of about 18 and a cruise $L/D$ of 17

**Table 5.3** Information on 747 and C-5 Aircraft

Aircraft	$W_{T0}$ (lb)	Range (n mile)	Payload (lb)	Engine Type	Cruise TSFC (Table J.1)
747-200	775,000	3744	200,000	JT9D-7	0.62
C-5A	728,000	3050	220,000	TF39-GE-1	0.582
C-5A	728,000	5500	112,600	TF39-GE-1	0.582

## Phase 1

Assume  $W_2/W_1 = 0.97$

## Phase 2. Weight Fraction

From Fig. 5.2 the weight fraction for climb–acceleration to Mach = 0.8 is

$$W_3/W_2 = 0.978$$

## Phase 3. Cruise Fuel Fraction

From the preceding assumptions, the cruise fuel fraction is

$$\frac{W_3}{W_4} = \exp \left[ \frac{(6000)(0.6)}{(459)(17)} \right] = 1.583$$

## Phases 4 through 7

These phases are not appropriate for this aircraft; thus

$$\frac{W_5}{W_4} = \frac{W_6}{W_5} = \frac{W_7}{W_6} = \frac{W_8}{W_7} = 1.0$$

## Fuel Fraction

The ratio of landing weight to takeoff weight is

$$\frac{W_8}{W_1} = (0.97)(0.978) \frac{1}{1.583} = 0.599$$

The resulting fuel fraction, considering reserve and trapped fuel, is

$$\frac{W_{\text{fuel}}}{W_{T0}} = 1.06 \left[ 1 - \frac{W_8}{W_1} \right] = 0.425$$

### Iteration for $W_{TO}$

The iteration for  $W_{TO}$  proceeds as described in Section 5.5: Assume

$$W_{TO} = 790,000 \text{ lb}$$

From Fig. 5.4 the empty-weight fraction is approximately 0.444. Thus,

$$(W_{\text{empty}})_A = 790,000 (1 - 0.425) - 102,000 = 352,250 \text{ lb}$$

$$(W_{\text{empty}})_R = (0.444)(790,000) = 350,760 \text{ lb}$$

The difference is within 1% so that 790,000 lb is a good estimate for the aircraft takeoff weight. Thus, a takeoff weight of 790,000 lb is a realistic design solution for the requirement of 6000 n mile range with 102,000 lb of payload. This range can be traded for additional payload as shown in Fig. 5.8. There is usually some upper payload limit resulting from fuselage volume constraints and/or floor load bearing limits. A payload limit of 250,000 lb is assumed for this example. The results of this example agree well with published weight and performance for the Boeing 747-200 Freighter and the Lockheed C-5A Galaxy. Information on these two jumbo jet aircraft is given in Table 5.3. Figure 5.8 shows good agreement between Example 5.2 and C-5A Ops Planning data.

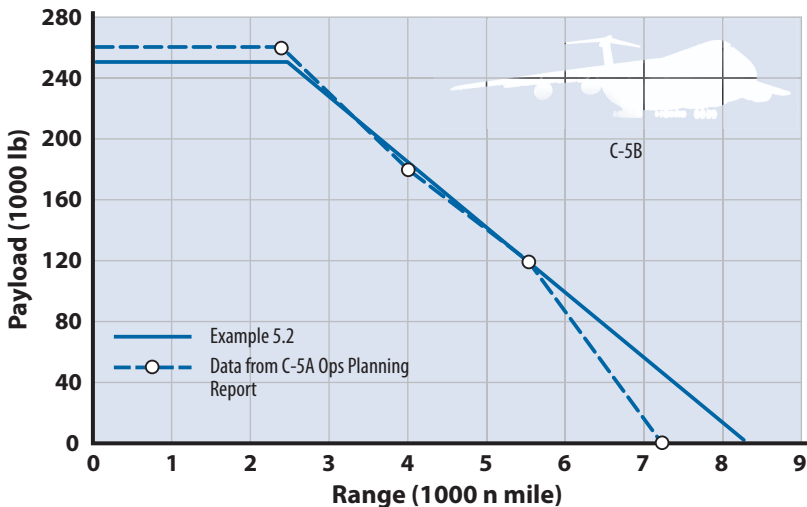


Figure 5.8 Variation of payload with range for large transport aircraft.

**Example 5.3 Low-Altitude, Subsonic Cruise Missile**

The driving requirements for cruise missiles are long range and high penetration survivability. To minimize the probability of being detected by enemy defenses, the cruise missile will be designed for stealth (low observables) and to cruise at low altitude so that it can take advantage of the decreased horizon range, terrain masking, and background clutter necessary to defeat enemy radar and other threat sensors. Flight at high altitude does not have these advantages and the detection problem is relatively simple for enemy defenses. Low altitude is a poor flight condition for efficient long-range cruise as turbofan engines operate best (low TSFC) at altitudes above 30,000 ft.

Cruise Missile Mission Requirements	
Range	1900 n mile
Payload	W-80 nuclear warhead, 300 lb
Speed	Mach 0.7 at 200 ft above ground level (AGL)
Engine	Williams F 107 turbofan (Fig. 5.9)
Profile	Terrain follow at Mach 0.7 and 200 ft AGL with limit load factor $n = +1.8, -0.5 g$
TSFC	1.15 (average installed value bet. cruise and max. thrust from Fig. 5.9)
$C_{D_0}$	0.035 (from Table 5.2)
Wing AR	6 with zero sweep
$K$	0.059 for an $e = 0.9$ (from Fig. G.9)
$(L/D)_{max}$	$1/(4C_{D_0}K)^{1/2} = 11$

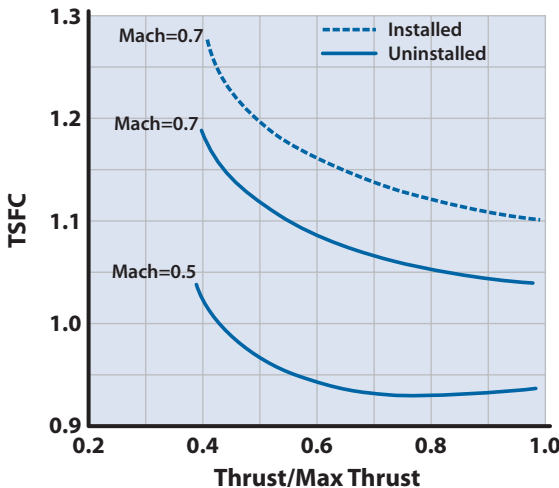


Figure 5.9 F-107 turbofan engine at sea level.

From Table 3.2 for a constant-altitude cruise the  $C_L$  for maximum range is

$$C_L = (C_{D0} / 3K)^{1/2} = 0.44$$

$$\text{Cruise } L/D = 0.866 (L/D)_{\max} = 9.5$$

In determining the TOGW, the only factor to be considered is the fuel fraction for the cruise out (phase 3), because all other fuel-weight fractions are equal to 1. The phase 3 fuel-weight fraction is determined using the Breguet range equation (5.2),

$$W_3/W_4 = \exp[(1900)(1.15)/(463)(9.5)] = \exp(0.497) = 1.644 \quad (5.10)$$

Assume a launch weight  $W_L = W_3 = 1800$  lb:

$$W_{\text{fuel}} = W_3 - (W_4/W_3)W_3 = 1800 - 1095 = 705 \text{ lb}$$

$$(W_{\text{empty}})_A = W_3 - W_{\text{payload}} - W_{\text{fuel}} = 795 \text{ lb}$$

Using Fig. I.7,

$$(W_{\text{empty}})_R = 801 \text{ lb}$$

Thus, an 1800-lb cruise missile can accomplish the mission!

At this point our design should be given a sanity check by comparing it with other existing nuclear, low-altitude, subsonic cruise missiles. The Convair/Raytheon AGM-109A Tomahawk has the following characteristics:

Range	1900 n mile
Engine	Williams F107 turbofan
Payload	W-80 warhead at 300 lb
Launch weight	2860 lb
Fuel weight	1200 lb
Empty weight	1350 lb
Wing AR	6 with zero sweep
Wing area	12 ft <sup>2</sup>
$C_{D0}$	0.035
$K$	0.059

When the 1800 lb estimated launch weight is compared to the actual Tomahawk missile weight of 2860 lb from the preceding list, the question is: Why? Actually, the design analysis has a fundamental flaw in it that will be discussed in more detail in Chapter 6.

## 5.7 High Altitude Atmospheric Research Platform

In the late 1980s, the world was concerned about the depletion of the ozone layer over the South Pole. The details of the depletion were not understood and there was no evidence that the action could be reversed. In situ measurements needed to be made at altitudes up to 120,000 feet. The U-2S could take measurements up to 70,000 feet and the Condor up to 66,000 feet. In 1990, the Lockheed Skunk Works was commissioned by NASA to develop a manned aircraft that could make atmospheric measurements at 100,000 feet worldwide. That program was referred to as the High Altitude Atmospheric Research Platform (HAARP) and will be used here as an unmanned-aircraft example [1].

### Example 5.4 HAARP Requirements

The HAARP mission objective was to conduct atmospheric research over the South Pole using an unmanned aircraft. The mission profile is shown in Fig. 5.10. The other requirements were as follows:

Range	6000 n mile with 5000 n mile at 100,000 ft and Mach = 0.6
Payload	2500 lb at 500 watts
Propulsion	Turbocharged piston engine(s)
Aerodynamics	Efficient wing design at flight $Re < 1.0 \times 10^6$
Structure	Metal [for sizing use $W_{empty} = 0.911$ (TOGW) <sup>0.947</sup> ]
BSFC	0.42 lb of fuel per hour/hp
Propeller efficiency @100,000 ft/Mach = 0.6	0.90
Engine start, takeoff, climb, and acceleration weight fraction	$W_3/W_1 = 0.93$
Aspect ratio	25
Span	< 150 ft for operability at airports worldwide

The BSFC = 0.42 is a realistic value for available piston engines operating at sea level (14.7 psia pressure). At 100,000 ft, the static pressure is 0.158 psia. Thus, a turbocharger is needed that will boost the pressure by a (surprisingly large) factor of 93. Whatever the turbocharger design, there will be considerable heating of the air, which will need to be cooled before it goes into the engine. Thus, we will assume wing-mounted, ram air heat exchangers, which will decrease the aircraft  $L/D$  by 22%.

The HAARP configuration is shown in Fig. 5.11. The aerodynamics for the aircraft are as follows:



Airfoil (generated using ISES airfoil design code from MIT)	
Maximum $t/c$	12.2% and located at 50% chord
$C_{l_{min}}$	0.4
Camber	4%
$K''$	0.006
$K'$	$1/AR e\pi = 0.013$ for $e = 0.97$ (from Fig. 13.5)
$C_{D_{min}}$	0.014
Maximum $L/D$	27 [from Eq. (3.10b) with 22% penalty]
Cruise $C_L$	0.89 [ $C_{L_{opt}}$ from Eq. (3.8b)]
Cruise-out Weight Fraction	
$W_3/W_4 = \exp[(5000)(0.42)/(326)(0.9)(27)] = 1.3$	
$W_6/W_1$	$(0.93)/(1/1.3) = 0.72$
$W_{fuel}/W_{TO}$	$1.06(1.0 - 0.72) = 0.30$
Assume TOGW	16,000 lb
$(W_{empty})_A$	$16,000 - 4800 - 2500 = 8700$ lb
$(W_{empty})_R$	$0.911 (TOGW)^{0.947} = 8726$ lb
Difference	< 1%

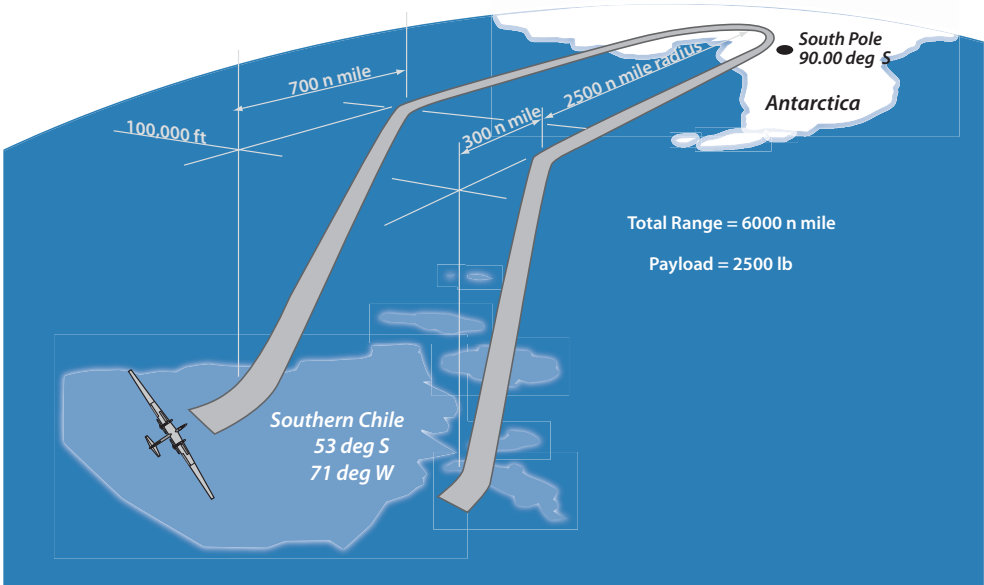


Figure 5.10 HAARP mission profile.

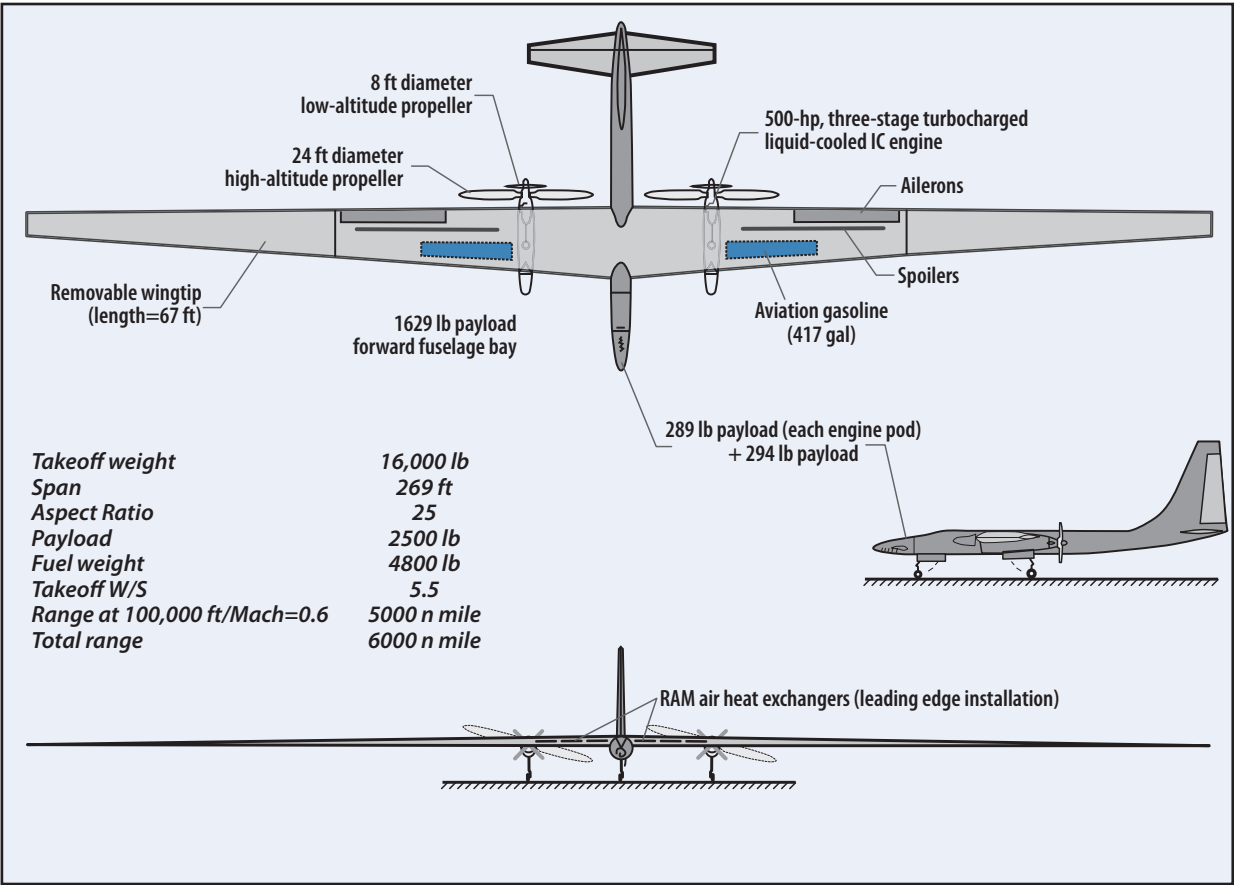


Figure 5.11 HAARP configuration.

The HAARP aircraft will be carried as an example through the following chapters:

- Chapter 6 (Section 6.6.1) for estimating the wing loading
- Chapter 14 (Section 14.2.1) for a discussion of turbocharger design
- Chapter 18 (Section 18.10) for piston engine sizing
- Chapter 19 (Section 19.14) for wing structural design

### *Reference*

- [1] “Global Stratospheric Change—Requirements for a Very High Altitude Aircraft for Atmospheric Research,” workshop report Truckee, CA, 15–16 July 1989, NASA Conf. Publ. No. CP-10041, 1989.

## Chapter 6

# Estimating the Takeoff Wing Loading



- Wing Sizing
- Takeoff & Landing W/S
- Air–Air Combat W/S
- Long-Endurance W/S
- High-Altitude W/S
- Examples

Built in the late 1940s, the USAF Boeing B-47 and the RAF Avro Vulcan B-1 were both designed for the same mission—long-range interception of Soviet manned bombers, but with noticeably different configurations and wing loadings. Both aircraft achieved a high cruise L/D as detailed in Example 6.3.

*Nothing in this world can take the place of persistence.*

Calvin Coolidge

## 6.1 Introduction

The *takeoff wing loading*  $(W/S)_{TO}$  is a very important design parameter as it sizes the wing and locks in the dominant performance features of the aircraft. It is determined by considering the following mission requirements:

1. Range (cruise efficiency)
2. Endurance (loiter efficiency)
3. Landing and takeoff
4. Air-to-air combat (maneuverability)
5. Air intercept (minimum acceleration time)
6. High altitude
7. High altitude, long endurance
8. Low-altitude ride quality

Here the designer faces a real dilemma as these mission requirements are in conflict with one another. For example, good cruise efficiency usually drives the  $(W/S)_{TO}$  to high values (i.e., in excess of 100 psf), whereas good combat maneuverability requires low  $(W/S)_{TO}$ . Thus, the designer must consider the  $(W/S)_{TO}$  needed to meet the different mission requirements and then decide upon an appropriate compromise. Remember that there is no right answer and what is appropriate for today might not be appropriate for tomorrow. It is important for the designer to give due priority to the dominant mission phase but also to look at the entire mission to assure that the performance features are acceptable in all phases. An example of a poor design compromise would be a highly swept Mach 3 transport that had fantastic cruise efficiency but required the entire length of the San Diego freeway for takeoff. Table 6.1 shows the wing loading trends for different mission requirements.

## 6.2 Range-Dominated Vehicle (Cruise Efficiency)

It is important to select the  $(W/S)_{TO}$  so that the aircraft can fly at conditions for maximum range for a given amount of fuel, or for a given range with a fuel load such that the aircraft weight (and cost) will be minimized.

Turbine aircraft flying at maximum cruise efficiency should fly at conditions where  $(V/C)(L/D)$  is a maximum [see Eq. (3.26a)]. At this maximum cruise condition, the cruise  $L/D$  is close to but less than  $(L/D)_{max}$  (87% for constant altitude cruise and 94% for a cruise climb; see Fig. 3.2).

The condition for maximum range for a propeller aircraft is to fly at conditions such that  $(1/C)(L/D)$  is a maximum [see Eq. (3.30)]. Thus, the propeller aircraft would fly at conditions for  $(L/D)_{max}$  as indicated by Table 3.2.

Table 6.1 Takeoff Wing Loading Trends

Dominant Mission Requirement	$(W/S)_{T0}$	Example
High-altitude, long-endurance solar-powered ISR <sup>a</sup>	0.5–3.0	Helios
Competition sailplanes	7–12	ASW 17
Light civil aircraft with short range and field length	10–30	C-172
High-altitude, long-endurance hydrocarbon-powered ISR	25–50	RQ-4A
STOL <sup>b</sup> and utility transports	40–90	C-130
Short or intermediate range with moderate field length	50–90	Learjet 35
Long-range transports and bombers (>3000 n mile)	110–150	B 747
Fighter, high-altitude	30–60	F-106
Fighter, air-to-air	50–80	F-15A
Fighter, close air support	65–90	A-10A
Fighter, strike interdiction	90–130	F-4E
Fighter, interceptor	120–150	F-104G
Low-altitude subsonic cruise missiles	200–240	AGM-109

<sup>a</sup>Intelligence, surveillance, and reconnaissance.

<sup>b</sup>Short takeoff and landing.

For a turbine airplane the cruise altitude should be around 35,000 ft, where the TSFC is near minimum (see Chapter 14). If the airplane is dominated by a long range requirement, its fuel fraction will be about 0.4. This means that its wing loading will change (decrease) approximately 40%. If the flight profile is at constant altitude, the aircraft will have to slow down to keep  $(W/S)/q$  a constant so that the  $C_L = (C_{D0}/3K)^{1/2}$  according to Fig. 3.2. It is instructive to return to the air-launched cruise missile example of Chapter 5.

### Example 6.1 Air-Launched Cruise Missile

Why does a cruise missile design that closed with a launch weight of 1800 lb do the same mission as the Tomahawk missile, which weighs 2860 lb?

The cruise missile and Tomahawk designs are very similar: same wing aspect ratio (AR), missile  $C_{D0}$ ,  $K$ , payload, engine, and empty-weight trends. Flying at maximum range at constant altitude gives a constant  $C_L = (C_{D0}/3K)^{1/2} = 0.44$ , which results in a wing loading at launch of  $W/S = qC_L = (725)(0.44) = 319$  psf, and a 5.64-ft<sup>2</sup> wing.

The  $(L/D)_{max} = 11$  at  $C_L = 0.77$  yields a cruise  $L/D = (0.866)(11) = 9.5$ . The  $L/D$  vs  $C_L$  relationship is shown in Fig. 6.1. Notice that  $C_L$  at launch for  $L = W$  is 0.44 and the  $L/D$  is indeed 9.5. However, as fuel is burned, the  $C_L$  must decrease for  $L = W$  so that at the end of the mission  $C_L = 0.27$  and  $L/D = 6.9$  at Mach = 0.7 and 200 ft.

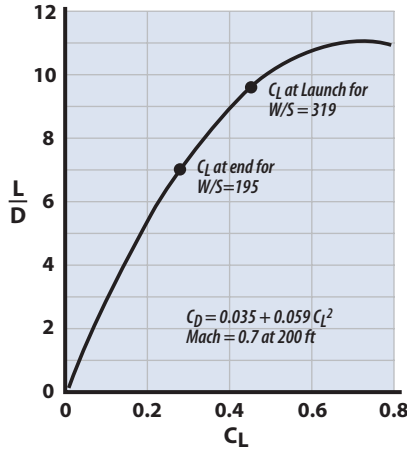


Figure 6.1 Cruise missile L/D throughout the entire  $C_L$  range.

Because slowing down or climbing is not permitted (for survivability),  $C_L$  and  $L/D$  decrease as shown in Fig. 6.1. Thus, in this exercise, the mistake was assuming in Eq. (5.10) that  $L/D = 9.5$  for the entire 1900 n mile. If the average  $L/D$  of 8.2 had been used, the vehicle would have sized out near the Tomahawk launch weight of 2860 lb.

### Example 6.2 Long-Range Subsonic Transport

Determine the best  $(W/S)_{TO}$  for a turbine-powered, long-range subsonic transport with a fuel fraction of 0.4. Assume a cruise climb (constant throttle setting) flight profile and

Start of cruise	Mach = 0.8 and 30,000 ft
$C_{D_0}$	0.018 (from Fig. G.1)
AR	7.25 wing with 25-deg sweep (from Fig. G.9, $e = 0.8$ )
$K$	0.0549
$(L/D)_{max}$	16
cruise $L/D$	15
cruise $C_L$	$(C_{D_0}/2K)^{1/2} = 0.41$ (from Table 3.2)
$q$	282 psf
start-of-cruise $W/S$	$qC_L = 116$ psf
$(W/S)_{TO}$	$\approx 120$ psf

The question is, what is the altitude at the end of cruise? The wing loading at end of cruise would be approximately  $(120)(1 - 0.4) = 72$  psf;  $C_L$  should still be 0.41 (i.e.,  $C_{D_0}$  and  $K$  have not changed). Thus,

$q = (W/S)(1/C_L) = 175$  psf. The altitude at which  $q = 175$  psf and Mach = 0.8 is 40,000 ft, which is a reasonable altitude for the end of cruise.

Note, the aircraft would like to climb at a constant Mach cruise as the fuel burns off and the wing loading decreases. However, the air traffic control regulations restrict airliners to constant even or odd 1000-ft altitude corridors. Thus, the actual long-range cruise climb profile would resemble stair steps of constant-altitude segments and 2000-ft climb segments.

From these two examples it would appear that range-dominated aircraft always have high wing loadings, as indicated in Tables 6.1 and 6.2.

There are two rules that must be learned in the design of aircraft:

1. There are no right answers, only a best answer.
2. There are no rules.

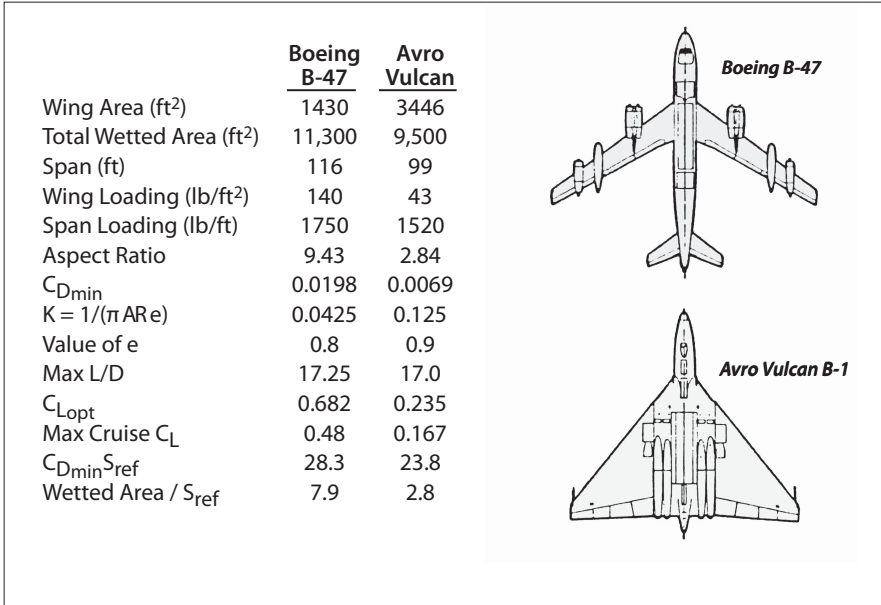
**Example 6.3 Boeing B-47 and Avro Vulcan B-1 Comparison**

In the early 1950s both the United States and the United Kingdom built bomber aircraft for strategic nuclear missions into the USSR. The result of their different design approaches is shown in Fig. 6.2. Both the USAF B-47 and the Royal Air Force (RAF) Vulcan B-1 were designed for high cruise efficiency, which meant high cruise  $L/D$ . The B-47 was designed as a high wing loading, high aspect ratio, wing/body/tail configuration to fly high subsonic at 30,000–40,000 feet. The B-1 also had the requirement to penetrate at high altitude to survive against the Soviet fighters. The Vulcan B-1 was designed as a low wing loading, low aspect ratio, blended wing/body tailless configuration to fly high subsonic at 50,000 feet. A low  $W/S$  leads to a

**Table 6.2** Takeoff Wing Loading and Fuel Fraction for Various Cruise-Dominant Aircraft

Aircraft	$(W/S)_{TO}$	$W_{fuel} / W_{TO}$
C-5A	117	0.417
KC-135	124	—
B 747	141	0.428
L-1011	124	0.352
DC-10	153	0.42
B-52G	122	0.62
C-17	152	0.34
B-1B	244	0.47
Tomahawk	213	0.47





**Figure 6.2** Design characteristics comparison—Boeing B-47 vs Avro Vulcan B-1.

large wing, which can mean a large  $C_{D0}$  due to skin friction unless the wing is blended with the fuselage to reduce the configuration wetted area. Notice that the Vulcan B-1 is a blended wing–fuselage configuration with a low-AR wing (high value for  $K$ ) but a low wetted area relative to  $S_{ref}$  (low  $C_{D0}$ ; see Fig. G.7). Thus, the Vulcan B-1 achieved a high maximum  $L/D$  by having a low  $C_{D0}$  in spite of the high  $K$ . The B-47 was the more traditional approach with a high-AR wing attached to a fuselage, giving a higher  $C_{D0}$  but low  $K$ . The  $(L/D)_{max}$  for both aircraft was almost the same.

### 6.3 Endurance or Loiter

For maximum loiter efficiency the turbine aircraft should fly at conditions for maximum  $L/D$  and the propeller aircraft for maximum  $(L/D)/V$ . The conditions on  $C_L$  are given in Table 3.2.

#### Example 6.4 High-Altitude, Long-Endurance ISR

Find the  $(W/S)_{TO}$  for the RQ-4A Global Hawk starting loiter at Mach 0.6 and 55,000 ft. The Global Hawk has a very highly cambered airfoil identified as the LRN 1015 (shown in Fig. 2.2). The aero data for the Global Hawk is as follows:

Wing AR	25 with 8-deg sweep
$C_{D_{\min}}$	0.019 (from Fig. G.2)
$C_{L_{\min}}$	0.3
$K = K' + K''$	0.0165 (the $e = 0.77$ from Fig. G.9)
$k''$	0.01 (from Fig. 13.6)

Because the Global Hawk wing is highly cambered we need to use the  $C_{L_{\text{opt}}}$  and  $(L/D)_{\text{max}}$  for a cambered aircraft [see Eqs. (3.8b) and (3.10b)]. Using these equations we get  $C_{L_{\text{opt}}} = 0.91$  and  $(L/D)_{\text{max}} \approx 36$ , which agrees with the data in Fig. G.4.

At Mach = 0.6 and 55,000 ft,  $q = 48$  psf. This gives a start-of-loiter  $W/S = 43.7$  psf. Global Hawk weighs 25,600 lb at takeoff and has a 540-ft<sup>2</sup> wing, giving a  $(W/S)_{\text{TO}} = 47$  psf. It continuously climbs during loiter, reaching altitudes above 60,000 ft.

## 6.4 Landing and Takeoff

If landing and/or takeoff are important mission requirements, the reader would do well to become familiar with the material in Chapters 9 and 10 before going on.

The wing loading of the aircraft influences the landing and takeoff distances through the stall speed

$$V_{\text{stall}} = \sqrt{\frac{W}{S} \frac{2}{\rho C_{L_{\text{max}}}}} \tag{6.1}$$

Takeoff is the distance required for an aircraft to accelerate from  $V = 0$  to  $V = 1.2V_{\text{stall}}$  and climb over a 50-ft obstacle. Landing is the horizontal distance required for an aircraft to clear a 50-ft obstacle at an approach speed of  $1.3V_{\text{stall}}$ , touch down at  $V_{\text{TD}} = 1.15V_{\text{stall}}$ , and brake to a complete stop.

The takeoff distance is dependent upon the *takeoff parameter* (TOP):

$$\text{TOP} = \frac{W}{S} \frac{1}{C_{L_{\text{max}}}} \frac{1}{T/W} \frac{1}{\sigma} \tag{6.2}$$

where  $\sigma = \rho/\rho_{\text{SL}}$ . This takeoff parameter is shown in Fig. 6.3. The takeoff distance can be estimated at this point in the design by using the approximate expression (in feet)

$$S_{TO} = 20.9 \frac{W/S}{\sigma C_{L_{max}} (T/W)} + 69.6 \sqrt{\frac{W/S}{\sigma C_{L_{max}}}} \tag{6.3}$$

or by using Fig. 6.3. It should be clear that a short takeoff distance can be achieved with a high wing loading if  $C_{L_{max}}$  and  $T/W$  are large.

The landing distance is dependent upon the *landing parameter* (LP):

$$LP = \frac{W/S}{\sigma C_{L_{max}}} \tag{6.4}$$

The landing distance for conventional takeoff and landing (CTOL) aircraft can be estimated from the approximate expression

$$S_L = 79.4 \frac{W/S}{\sigma C_{L_{max}}} + 50/\tan \theta_{app} \tag{6.5}$$

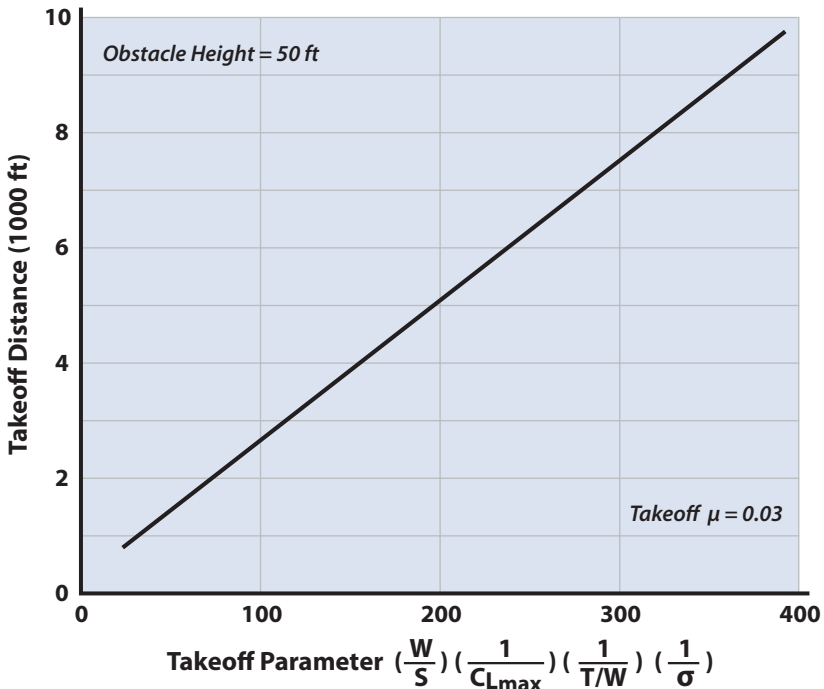


Figure 6.3 Takeoff distance vs the takeoff parameter (TOP).

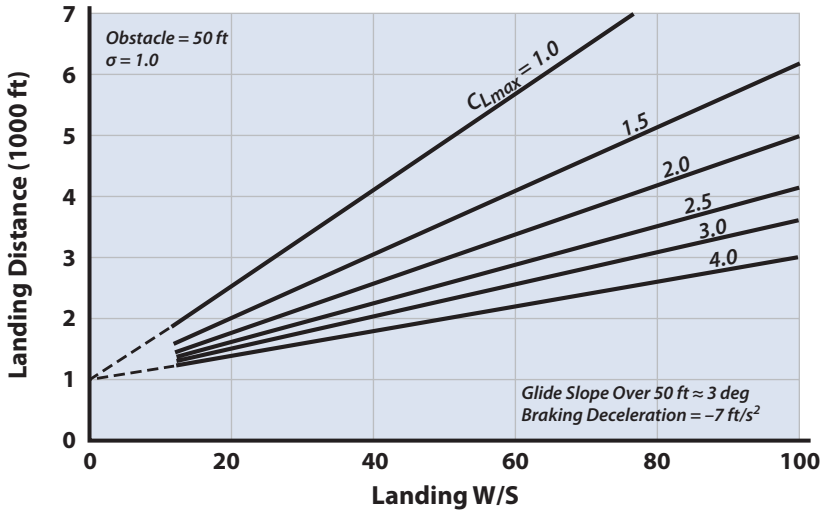


Figure 6.4 Landing distance for CTOL aircraft.

where  $S_L$  is in feet. Equation (6.5), shown in Fig. 6.4, assumes a glide slope over 50 ft of approximately 3 deg ( $\sim 950$  ft) and a braking deceleration of  $-7$  ft/s<sup>2</sup>.

Short takeoff and landing (STOL) aircraft approach at steeper angles (on the order of 7 deg) and employ thrust reversers and other ground braking devices to shorten the landing field distance. Figure 6.5 shows the impact of landing  $W/S$  and approach  $C_L$  ( $0.8C_{L_{\max}}$ ) on landing field distance.

Mechanical high-lift devices have an upper  $C_{L_{\max}}$  limit of about 4.0 (see Fig. 9.7), with powered lift devices extending up to about 12.0 (Chapter 9, Section 9.6). If STOL is a dominant feature of the mission requirements, the designer should give considerable thought to the expected performance from high-lift devices because  $W/S$  and  $C_{L_{\max}}$  are partners in the landing and takeoff problem. Selecting a takeoff  $W/S$  without due consideration of  $C_{L_{\max}}$ , and even  $T/W$ , may lead to an impossible design later.

## 6.5 Air-to-Air Combat and Acceleration

The ability of a fighter aircraft to accelerate at a point in space is given by its value of excess specific power  $P_S$ , for  $n = 1$ , and to maneuver by its  $P_S$  for  $n > 1$ . Thus, fighter aircraft should have their design parameters selected to maximize the value of  $P_S$  for critical mission phases. From Chapter 3, the expression for  $P_S$  [assuming  $\cos(\alpha + i_T) \sim 1$ ] is given by

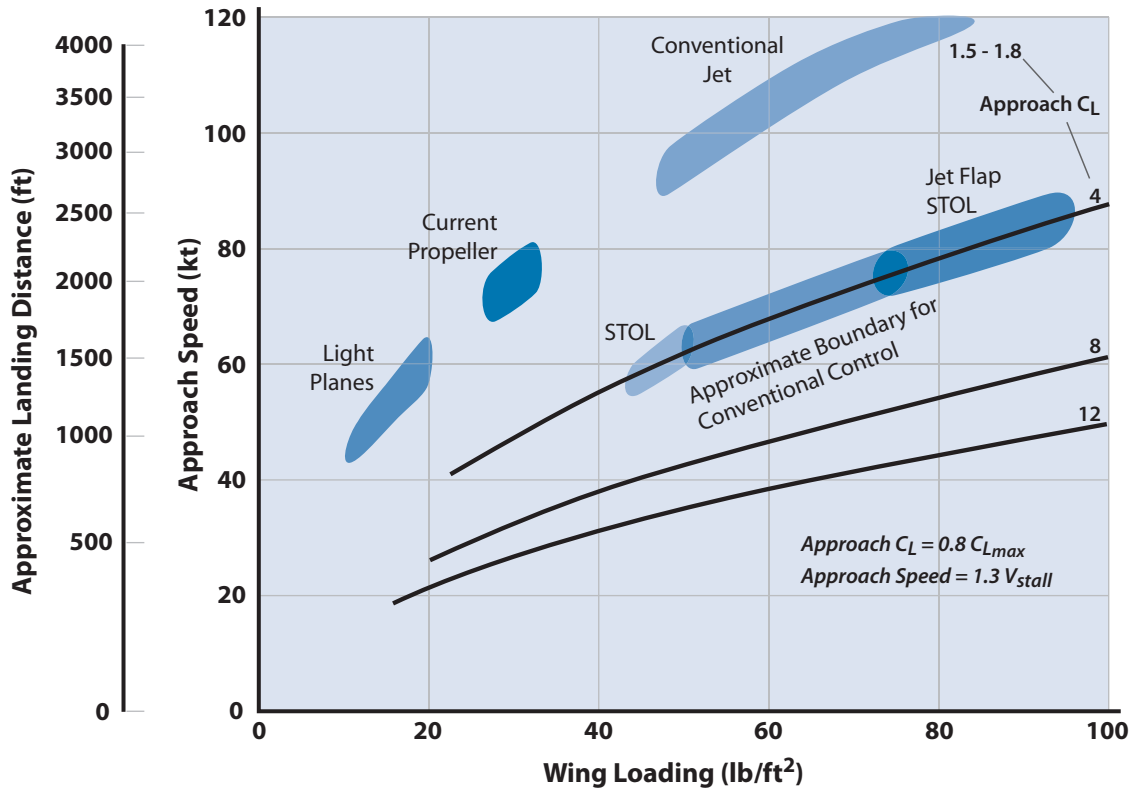


Figure 6.5 Effect of landing wing loading and approach C<sub>L</sub> on STOL landing distances.

$$P_S = V \left[ \frac{T}{W} - \frac{D}{W} \right] \quad (6.6)$$

For a certain  $T/W$ , the value for  $P_S$  can be maximized by finding the conditions for minimum  $D/W$ . It is of interest to find the *wing loading*  $W/S$  that will minimize  $D/W$ . Using\*

$$D = qS_{\text{ref}} \left[ C_{D_0} + KC_L^2 \right] \quad (6.7)$$

and

$$C_L = \frac{W}{S} \frac{n}{q} \quad (6.8)$$

we find the condition for  $W/S$  that sets  $\partial(D/W)/\partial(W/S) = 0$ . This condition is expressed as

$$\frac{W}{S} = \frac{q}{n} \sqrt{\frac{C_{D_0}}{K}}$$

where the reader should recognize  $(C_{D_0}/K)^{1/2}$  as the  $C_L$  for minimum drag or  $(L/D)_{\text{max}}$  from Chapter 3. Thus, Eq. (6.8) expresses the condition on  $W/S$  that gives maximum  $P_S$  at a point in velocity–altitude space for a given  $T/W$  and load factor.

Chapter 4 pointed out that during a minimum-time trajectory (an acceleration) the load factor  $n$  is close to 1. Thus, Eq. (6.8) with  $n = 1$  expresses the best wing loading for acceleration-dominated aircraft.

### Example 6.5 Acceleration-Dominated Aircraft

Find the best wing loading for a fighter interceptor at Mach = 0.8 and 25,000 ft using the aerodynamics of the F-4C shown in Fig. 2.15.

At Mach = 0.8 and 25,000 ft,  $q = 352$  psf. From Fig. 2.15 the result is  $C_{D_0} = 0.022$ ,  $K = 0.169$ , and  $K_B = 0$  because  $C_L < 0.5$  (check later).

Using Eq. (6.8) gives

$$\frac{W}{S} = \frac{352}{1} \sqrt{\frac{0.022}{0.169}} = 127 \text{ psf}$$

\* It is valid to assume  $K_B$  from Eq. (2.19), Chapter 2, is equal to zero, as will be shown later.

Thus, a high wing loading is very desirable for acceleration. The required  $C_L = 0.378$  is less than  $C_{L_B}$  from Fig. 2.15, so that indeed  $K_B = 0$ .

Example 6.5 points out that the requirement for minimum acceleration leads to a high wing loading. This should be clear because the goal is to minimize the drag at  $n = 1$ , and the skin friction is a large part of this drag at all Mach numbers. Thus, decreasing the aircraft wetted area by decreasing the wing area gives a decrease in the zero-lift drag.

### Example 6.6 Air-to-Air-Combat Aircraft

Here the issue is to find the best wing loading for an air-to-air fighter at Mach = 0.8 and 25,000 ft and for  $n = 5$  using the aerodynamics for the F-4C from Fig. 2.15.

Once again,  $q = 352$  psf,  $C_{D_0} = 0.022$ ,  $K = 0.169$ , and assume  $K_B = 0$ . Using Eq. (6.8) with  $n = 5$  gives  $W/S = 27$  psf. Thus, the mission requirement is low wing loading for air-to-air combat. The required  $C_L = 0.378$  is less than the  $C_L$  for buffer onset,  $C_{L_B}$ ,  $C_{L_B}$  so that the assumption of  $K_B = 0$  was valid.

Example 6.6 points out that low wing loading is desired for an air combat fighter, just the opposite of the result for the air interceptor. For air combat,  $n > 1$ , the drag-due-to-lift is the major part of the drag and it goes as the square of the required  $C_L$ . The required  $C_L$  is decreased for a given load factor by decreasing the wing loading. Previous research concludes that it is more efficient in terms of  $W_{TO}$  to improve the  $P_S$  at  $n > 1$  (i.e., improve the turn rate,  $\dot{\psi}$ ) of an aircraft by decreasing the wing loading rather than increasing the thrust-to-weight ratio. Because air-to-air combat is a series of hard turning maneuvers and accelerations (to gain back the energy lost during the hard turns), the air combat fighter will have low wing loading for turning flight and high  $T/W$  for the accelerations.

The result from Example 6.6 is unconstrained and does not take into consideration the large wing weight and the relatively poor cruise performance associated with a low  $W/S$ . For these (and other) reasons the designer would probably select a somewhat higher value of wing loading than is indicated by Eq. (6.8). It is important for the designer to select the wing loading only after giving due consideration to all phases of the mission profile.

Another consideration is that air-to-air combat usually takes place in the transonic regime and altitudes from 10,000 to 35,000 ft. The maximum usable transonic lift coefficient is limited by the onset of buffet and, thus,  $C_{L_{\max}} < 1$  is typical for transonic maneuvering. Figure 6.6 shows maximum  $C_{L,S}$  due to buffet obtained during flight tests.

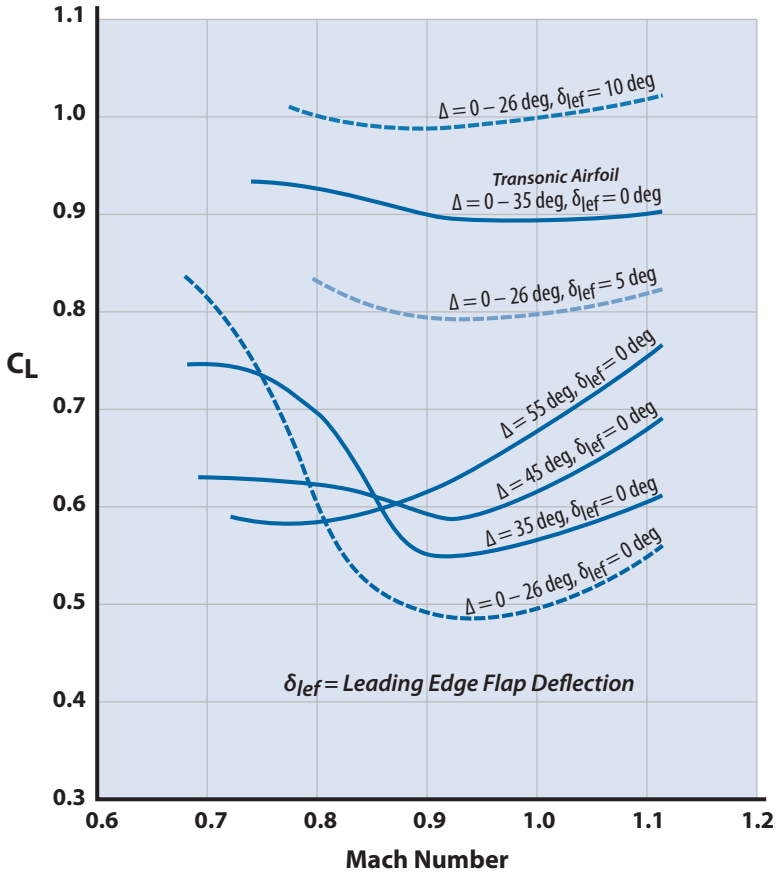


Figure 6.6 Maximum  $C_L$  due to buffet.

Therefore, an estimate of combat wing loading can be obtained from

$$\frac{W}{S} = \frac{qC_{L_{max}}}{n} \tag{6.9}$$

where the  $n$  is that load factor required for a particular turn rate. The desired maximum sustained turn rate  $\dot{\psi}_{MS}$  should be about 2 deg/s better than the enemy aircraft.

## 6.6 High Altitude

The wing loading for a high-altitude reconnaissance aircraft can be determined from



$$\frac{W}{S} = C_L q$$

Usually the altitude and velocity are specified (hence  $q$  is fixed), and realistic estimates of the maximum usable lift coefficient can be made so that the required  $W/S$  can be determined. The requirement for high altitude drives the  $(W/S)_{TO}$  to low values.

### 6.6.1 HAARP Wing Loading

The HAARP vehicle discussed in Section 5.8 and shown in Fig. 5.11 will have a wing loading driven by the requirement to fly 5000 n mile at 100,000 ft and Mach = 0.6. The aerodynamics for the HAARP are shown in Fig. 6.7. The aircraft has a maximum  $L/D = 27$  over a  $C_L$  range of 0.75–0.9. The wing area will be sized for a start-of-cruise  $C_L = 0.9$ . This gives an  $S_w = S_{Ref} = 2884 \text{ ft}^2$  and a takeoff  $W/S = 5.5 \text{ lb/ft}^2$ . With the 30% fuel fraction the aircraft wing loading at end of the mission is  $3.88 \text{ lb/ft}^2$ . During the 5000 n mile cruise at 100,000 ft the  $C_L$  will be reduced to 0.75 and the altitude increased to 102,000 ft in order to keep the cruise  $L/D = 27$ .

The aspect ratio is 25, giving a span of 268 ft. Notice that a wing span less than 150 ft is desired, to facilitate operation from airports worldwide. HAARP will have 67-ft detachable outer wing panels, which will reduce the wing span to 134 ft. The detachable outer wing panels will result in a

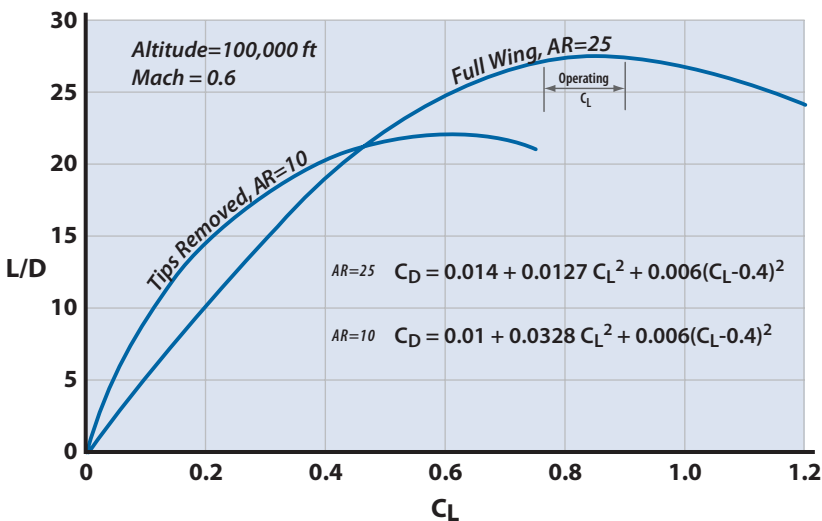


Figure 6.7 HAARP aircraft aerodynamics.

heavier wing than if the wing were continuous from tip to tip. The outer wing panels do not have any control surfaces or carry any fuel.

Removing the outer wing panels gives HAARP an  $S_w = 1789 \text{ ft}^2$ , an aspect ratio of 10 and a maximum  $L/D = 22.3$ . The aerodynamics for the short-wing HAARP are shown in Fig. 6.7. With the 4800 lb of fuel in HAARP, the short-wing version can fly 5500 n mile at 45,000 ft and Mach = 0.6. The concept of operations would be to transport the outer wing panels to the deployment area in a transport airplane. The short-wing HAARP would fly to the deployment area, attach the outer wing panels, and then conduct the atmospheric collection over the South Pole at 100,000 ft.

The design of the HAARP three-stage turbocharger will be discussed in Chapter 14.2.1.

## 6.7 High Altitude, Long Endurance

The requirement for high altitude and long endurance is especially challenging because not only is low wing loading (large wing) a requirement, but the fuel fraction must be large as well. The Global Hawk has an endurance of one-and-a-half days above 55,000 ft and requires a fuel fraction of 57%.

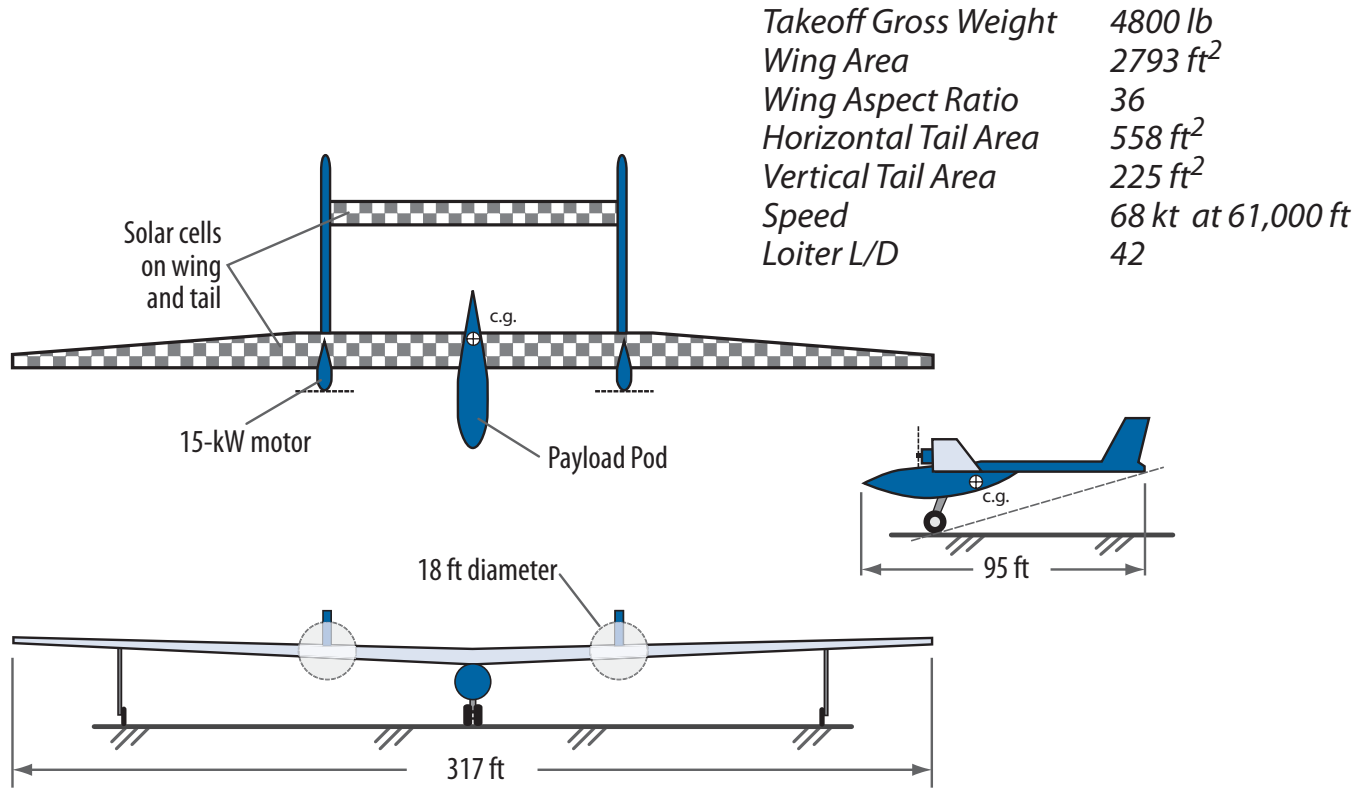
An endurance of several weeks or more will require frequent resupply of fuel or a propulsion system that can regenerate itself. The sun is a fine source of energy for aircraft: sunlight can be converted into electrical energy through photovoltaic cells (28% efficiency in 2010; discussed more in Chapter 14). However, the sun can only provide energy during the daytime. Thus, solar energy must be collected during daytime and stored to be used to support the aircraft during the night. The next example will examine a solar-powered ISR aircraft.

Example 6.7 considers solar power with storage. The solar energy is collected by thin-film photovoltaic cells covering the external surface of the airplane. Excess solar energy is collected during the daytime and stored in hydrogen–oxygen fuel cells or rechargeable batteries (discussed in Chapter 14) to be used to operate the aircraft during the night.

### Example 6.7 High-Altitude, Long-Endurance Solar-Powered ISR

Determine the wing loading and required power for the Solar Snooper. The configuration is the wing–body–tail design shown in Fig. 6.8.

The requirement for this aircraft is 4 weeks at 65,000 ft, in mid-latitudes during the summer conducting ISR. The payload is 500 lb at



**Figure 6.8** Solar Snoop configuration.

1 kW. The 4-week endurance immediately eliminates hydrocarbon (gasoline) propulsion systems. The propulsion candidates are solar power with storage and nuclear power.

The political issues connected with flying a nuclear-powered airplane in the atmosphere over another country are overwhelming and politically unacceptable.

It is assumed that the cruise speed at 64,000 feet is 68 kt (115 ft/s, Mach 0.12) and the TOGW equals 4800 lb. The assumed 4800 lb TOGW will be validated in Chapter 18. The solar powered aircraft has the following characteristics:

Wing aspect ratio	36 with zero sweep (similar to the Boeing Condor, which is discussed in Appendix G.2), shown in Fig. 6.9
$C_{D_{min}}$	0.0085 (assumed)
$C_{L_{min}}$	1.0 (assumed)
Wing efficiency $e$	0.60 (from Fig. G.9)
$K$	0.0147 ( $K = 1/\pi AR e$ )
$K''$	0.002 (assumed)
$K' = K - K''$	0.0147 - 0.002 = 0.0127
Maximum $L/D$	48 [using Eq. (3.10b) @ $C_L = 0.845$ ]
Best loiter $L/D$	42 at $C_L = 1.33$ (from Table 3.2)
Propeller efficiency, $\eta_p$	0.85 (assumed, based on Helios report)
Electric motor efficiency, $\eta_{EM}$	0.97 (vendor data)

The power required is given by

$$\text{Power required} = [\text{drag (lb)}][\text{speed (ft/s)}](0.745/550)/(\eta_p \eta_{EM}) \quad (6.10)$$

where the 550 converts foot-pounds per second into horsepower and the 0.745 converts horsepower into kilowatts. Using  $\text{drag} = \text{TOGW}/(L/D) = 4800/42 = 114 \text{ lb}$  in Eq. (6.10) gives a propulsion power required of 21.6 kW during loiter.

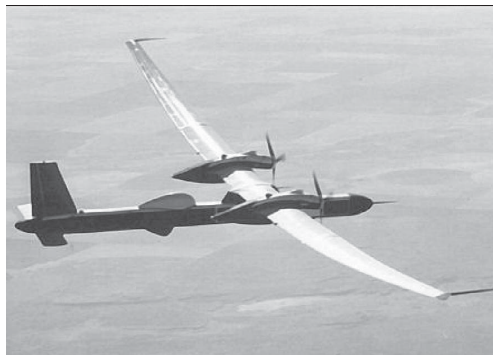


Figure 6.9 Condor (courtesy of The Boeing Company).

The total power required is then

- Propulsion (electric motors), 22 kW
- Payload, 1 kW
- Aircraft operation, 1 kW
- Total = 24 kW

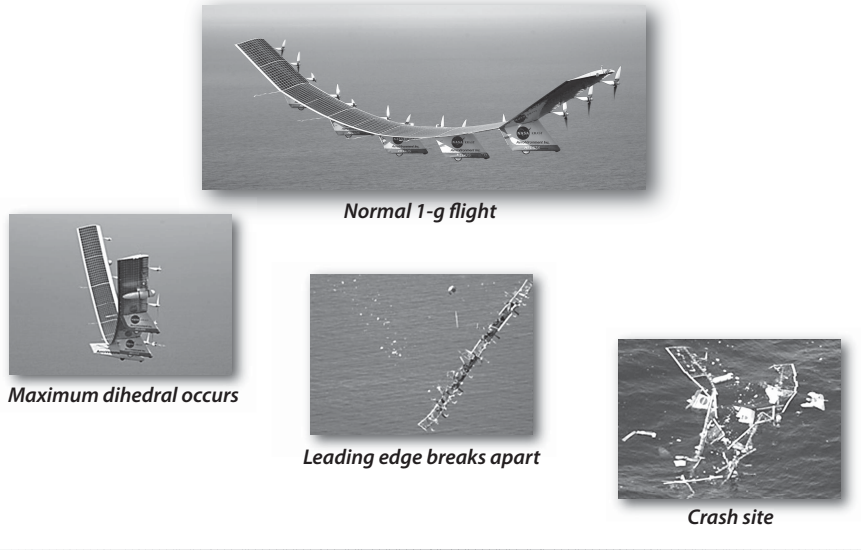
The problem is to find the  $W/S$  that will let us fly at 115 ft/s. The dynamic pressure  $q = 1.29$  psf (pretty low), such that  $W/S = qC_L = (1.29)(1.33) = 1.72$  and the wing area  $S_w = 2793$  ft<sup>2</sup>. The electric motors will be derated 25% for reliability, resulting in two 15-kW motors.

The design challenge from here is to install the solar cells onto a very lightweight 2793-ft<sup>2</sup> wing, integrate the energy storage and payload into a very lightweight fuselage, and install the engines—all within 4800 lb. Also, we need to check that there are enough solar cells to collect enough solar energy during daylight to operate at night. We will return to the Solar Snooper in Chapters 14 and 18 when we discuss propulsion concepts and engine sizing.

As a sanity check, we will look at the AeroVironment Helios solar-powered UAV. Helios is a flying wing (span loader) with a wing span of 247 ft, aspect ratio of 31, wing area of 1976 ft<sup>2</sup>, and weight 2048 lb, giving it a wing loading of 1.04 psf. At 90,000 ft, its speed is 148 kt, or Mach = 0.25 ( $q = 1.58$  psf). It flies at  $C_L = 0.5$  because it does not have a tail to trim out the pitching moment from a higher  $C_L$ . The solar cells (19% efficiency) are on the upper surface of the wing. On a bright sunny day Helios collects approximately 37 kW. It needs less than 20 kW to fly and stores the rest. In June 2003 Helios was on a path to demonstrate “24/7” flight using fuel cell storage when, on its second flight, it encountered turbulence at 3000 ft and broke up in midair over Kauai, Hawaii (see Fig. 6.10). The mishap investigation team concluded that when Helios encountered the turbulence it morphed into an unexpected, persistent, high-dihedral configuration. The aircraft became unstable in a very divergent pitch mode with airspeed excursions from nominal flight speed doubling every oscillation. The aircraft’s design speed was exceeded and the resulting high dynamic pressures caused the wing leading edge secondary structure on the outer wing panels to fail and the solar cells and skin on the upper surface to rip off.

## 6.8 Low-Altitude Ride Quality

Flight at low altitude is bumpy due to the gusts encountered close to the ground. If the flight speed is greater than 250 kt, the ride can be very uncomfortable and make the passengers sick. This is a problem that special operations forces (SOF) troops would have flying low and fast to evade



**Figure 6.10** Helios crash sequence.

detection. It is often said that the thing astronauts and SOF troops have in common is that they both get sick going to work.

Government specification MIL-F-9490D defines a discomfort index  $D_V$  and specifies the time duration for different  $D_V$  levels. The ride quality is strongly related to wing loading and lift curve slope  $C_{L\alpha}$ . The design features to meet this requirement are high wing loading (above 100 psf) and low AR and/or wing sweep to reduce the  $C_{L\alpha}$ .

## Chapter 7

# Selecting the Planform and Airfoil Section



- Measure of Merit
- Maximum Thickness Ratio
- Location of Maximum Thickness
- Camber
- Wing Aspect Ratio
- Wing Sweep
- Wing Taper Ratio
- Compromise

The forward swept wing on the DARPA/Grumman/USAF X-29 demonstrates high subsonic/transonic, high angle of attack maneuvering, and positive control for a fighter aircraft. This type of wing design is compared with other planform candidates in this chapter (see Section 7.7).

*It is better to beg forgiveness than ask permission.*

Skunk Works slogan

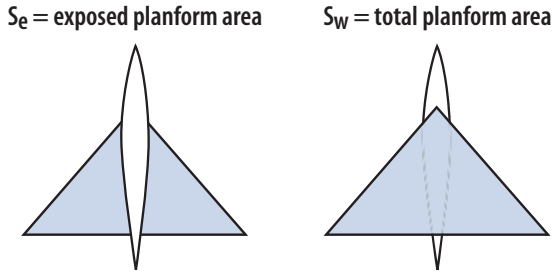


Figure 7.1 Definition of wing reference area.

## 7.1 Introduction

The *planform* of a vehicle means collectively the sweep of the leading edge ( $\delta$ ), the aspect ratio ( $AR$ ), the taper ratio ( $\lambda$ ), and the general shape of the top view of the wing. These *planform parameters* are defined in Fig. 2.1. The airfoil is selected when we decide upon the series designation (e.g., NACA 2415) or determine the maximum thickness ratio ( $t/c$ ), the location of the maximum thickness ratio, the leading-edge radius ( $r_{LE}$ ), and the camber (usually expressed in percent chord). Appendix F discusses airfoil nomenclature and presents section data on many popular airfoils. References [1–3] are also very useful in selecting an airfoil.

Planform selection is especially important as it influences vehicle aerodynamics significantly and gives the aircraft its characteristic shape. Both the airfoil and planform selection are strictly dependent upon the aircraft mission requirements. Figure 7.1 shows the two most popular methods of computing reference wing area,  $S_{ref}$ . (At the end of this chapter Fig. 7.11a–c presents a large selection of planforms for comparison.)

At this point in the design we select the general shape of the wing planform and select the airfoil section, keeping in mind that subsequent design iterations will refine the selection. Generally, an airfoil section and planform are selected to give the following design measures of merit:

- High
  - $C_{L\alpha}$
  - $C_{L_{max}}$
  - Wing fuel volume
- Low
  - $C_{D0}$
  - $K'$
  - Wing weight

The designer quickly learns that this design is impossible because of conflicting conditions. For example, a low  $K'$  means a high  $AR$ , but low wing



weight requires a low AR. Thus, the selection of the airfoil and planform is a compromise of the priorities established by the mission requirements.

## 7.2 Effect of Airfoil: Maximum Thickness Ratio

At low speed the  $t/c$  influences the maximum lift coefficient with the  $C_{\ell_{\max}}$  increasing as  $t/c$  increases. This behavior is shown in Fig. 7.2. The subsonic zero-lift drag coefficient increases slightly as  $t/c$  increases (see Fig. H.6).

The critical Mach number  $M_{CR}$  usually represents the maximum speed attainable for high-subsonic aircraft due to the increase in thrust required for flight past  $M_{CR}$ . Thus, a subsonic vehicle strives to push this upper speed limit as far as possible. A supersonic aircraft also has a large wing  $M_{CR}$ , or more correctly, larger than the fuselage  $M_{CR}$ . All of the vehicle components have a  $M_{CR}$ , and flight past this limit is accompanied by a large drag rise. The individual component drag rises are additive for the most part. Their sum at any Mach number represents the minimum thrust required for a vehicle to accelerate past that Mach number. By having the wing and fuselage drag rises peak at different Mach numbers, the thrust requirement to accelerate past  $M = 1$  is lessened. An example of this is shown in Fig. 2.20.

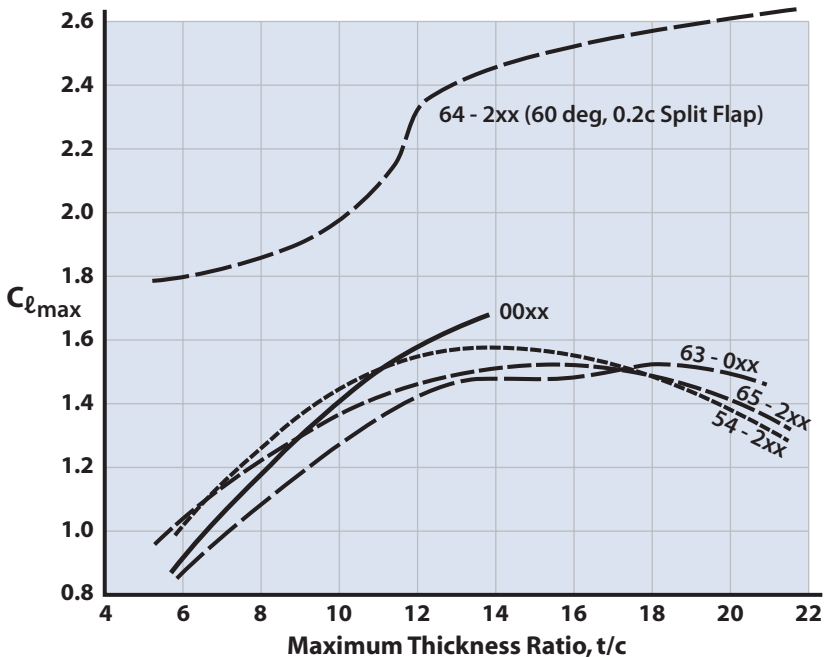


Figure 7.2 Maximum lift coefficient vs airfoil thickness ratio (data from [2]).

The  $t/c$  influences  $M_{CR}$  as shown in Figs. 2.23b and 7.9 (see Section 7.7). As the  $t/c$  increases, the  $M_{CR}$  decreases as supersonic flow occurs earlier on the upper surface, leading to the presence of a normal shock and flow separation (see Fig. 2.19).

In supersonic flight the wave drag increases approximately as the square of the  $t/c$  [see Eq. (2.31)]. This behavior is illustrated in Fig. H.6. If the aircraft will spend much of its mission at supersonic speeds, the  $t/c$  should be small (from 4% to 6%). A value of 3% for an airfoil is attractive from the wave-drag viewpoint; however, 3% represents a lower bound for  $t/c$  as it results in a heavy wing with little wing volume available for fuel. The B-58 Hustler supersonic bomber had a NACA 0003 airfoil and had to carry a large external fuel pod to get to the target. The fuel pod also housed the nuclear weapon and was dropped over the target. Figure 7.10 (see Section 7.7) shows a comparison of wing volume available for fuel relative to  $t/c$ .

Low wing weight is just as important as low wing drag. A relative comparison of wing weight versus  $t/c$  is shown in Figs. 2.23c and 7.10. Chapter 20 presents empirical equations for estimating the wing weight for fighter, bomber–transport, and general aviation aircraft. A quick examination of Eqs. (20.1), (20.2) and (20.69) reveals that  $t/c$  is in the denominator of the wing weight equations and has a significant effect on wing weight.

As  $t/c$  increases the wing volume available for fuel, landing gear, surface control actuators, and so on, also increases (as shown in Fig. 7.10).

### 7.3 Effect of Airfoil: Location of Maximum Thickness

The location of the maximum  $t/c$  determines the end of the favorable pressure gradient (decreasing pressure) and the start of the adverse pressure gradient as the static pressure increases to match the freestream pressure at the trailing edge. A laminar boundary layer cannot tolerate an increasing pressure and will transition to a turbulent boundary layer at the maximum thickness point (if not before, due to surface roughness or other disturbances). The further back the maximum  $t/c$ , the longer the boundary layer is apt to be laminar, thus producing lower skin friction drag. This behavior is shown in Fig. F.3 for the front-loaded NACA 63<sub>2</sub>-015 and the aft-loaded laminar NACA 66<sub>2</sub>-015 airfoil. The NACA 64, 65, and 66 series represent the families of laminar airfoils.

The location of the maximum  $t/c$  (along with camber) also determines whether the section pitching moment coefficient will be negative (nose down) or positive (nose up). If the maximum  $t/c$  is forward of the airfoil aerodynamic center (a.c.; about 25% chord), it is termed a *front-loaded section* and will produce a nose-up pitching moment. If the maximum  $t/c$  is aft of the a.c., it is called an *aft-loaded section* and produces a nose-down pitching moment. The selection of the maximum  $t/c$  location is important



**Figure 7.3** Global Hawk.

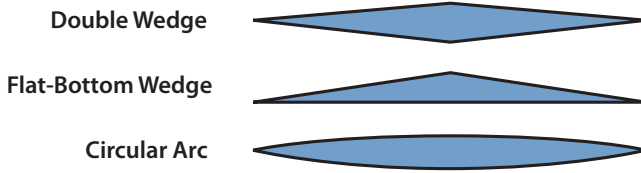
to the designer when the decision is made as to how the aircraft will be trimmed. For example, an aft-loaded airfoil (nose-down  $C_m$ ) on a tailless airplane will need to be trimmed with a down load at the trailing edge, reducing overall lift.

Figure 2.3 shows two airfoils designed for intelligence, surveillance, and reconnaissance (ISR) aircraft. They are about the same thickness (16% for the JW 1416 and 15% for the LRN 1015) but very different locations for maximum  $t/c$ . The JW 1416 was designed for low positive  $C_m$  at  $C_l \approx 0.9$  and was used on a high-AR, swept-wing tailless airplane called Polecat and built by Lockheed Martin in 2004. The LRN 1015 was designed for a laminar boundary layer back to about 55% chord at  $C_l \approx 0.9$  and used on the RQ-4A Global Hawk (Fig. 7.3), which has an aft horizontal tail (so that the negative  $C_m$  could be trimmed out without affecting overall lift). The two airfoils worked well on their respective aircraft, with the JW 1416 having low positive  $C_m$  and the LRN 1015 having low drag at the required high section lift coefficients. Each designed for its specific mission.

## 7.4 Effect of Airfoil: Leading Edge Shape

The leading edge (LE) shape can vary from sharp ( $r_{LE} = 0$ ) to round. Some popular sharp leading edge airfoils, designed primarily for supersonic flight, are shown in Fig. 7.4.

These airfoils have poor low-speed characteristics. However, the sharp leading edge airfoils can have their low-speed performance improved by



**Figure 7.4** Sharp leading edge airfoils.

the use of high-lift devices such as trailing edge (TE) or leading edge flaps. Experimental data in Fig. 7.5 shows the double wedge airfoil with deflected leading and trailing edge flaps. Notice that the basic airfoil section  $C_{l_{max}}$  is about 0.83.

The round-nosed airfoils exhibit much better low-speed characteristics than the sharp-nosed airfoils. The general trend is an increase in  $C_{l_{max}}$  for the larger  $r_{LE}$ . All of the airfoils in Appendix F are round-nosed airfoils. A quick examination shows that practically all the airfoils in Appendix F have a higher  $C_{l_{max}}$  than the double wedge. The round-nosed airfoils can also be fitted with slots, slats, and leading and trailing edge flaps to improve their low-speed characteristics (discussed in Chapter 9).

Subsonic  $C_{D_0}$  is primarily skin friction and is not influenced by the nose shape of the airfoil section. The subsonic viscous drag-due-to-lift is influenced by  $r_{LE}$  in that the smaller leading edge radius promotes earlier flow separation (i.e., more LE separation drag at angle-of-attack). Thus, the aircraft subsonic viscous drag-due-to-lift factor  $K''$  is slightly higher for the smaller  $r_{LE}$  (discussed in Section 13.2.1).

In supersonic flight the *wave drag coefficient* is expressed as:

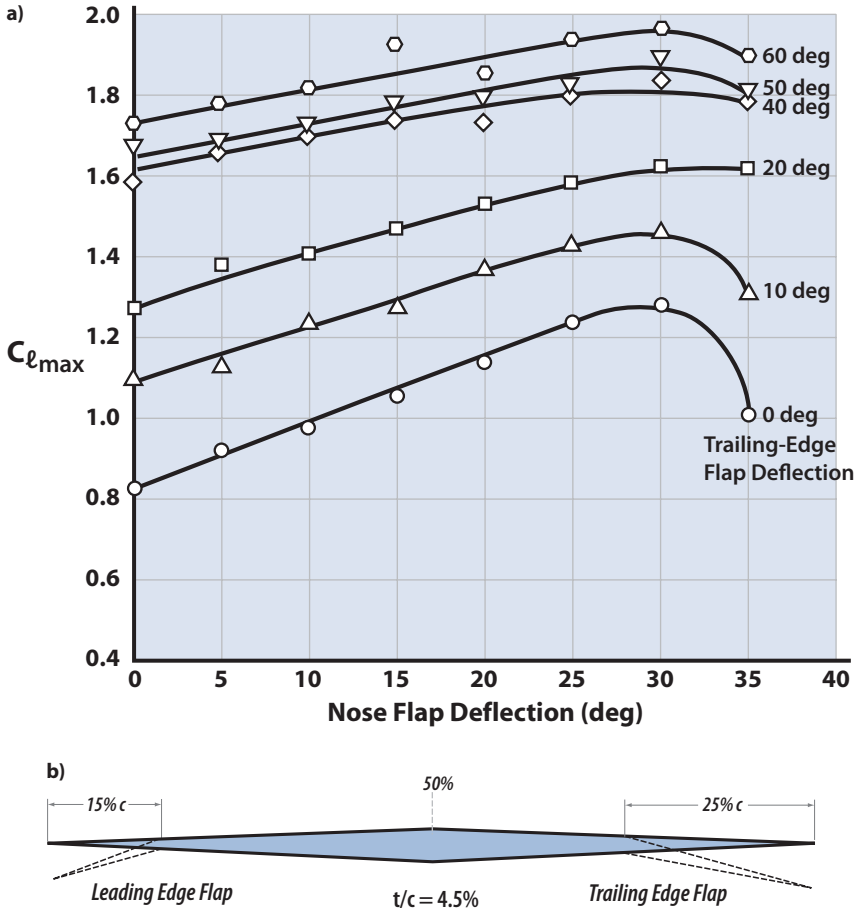
$$C_{DW} = C_{D_{LE}} + \frac{B}{\beta} \left( \frac{t}{c} \right)^2 \tag{7.1}$$

where

$$\beta = \sqrt{M^2 - 1}$$

$B$  = constant, dependent upon thickness distribution (discussed in Chapter 13)

The  $C_{D_{LE}}$  is the *leading edge bluntness* term introduced in Chapter 2. The expression for  $C_{D_{LE}}$  is (from [4])



**Figure 7.5** 4.5% double-wedge airfoil: **a)** variation of  $C_{\ell_{max}}$  with nose and TE flap deflections (data from [5]), and **b)** cross-section showing LE and TE flap deflection.

$$C_{D_{LE}} = \frac{2.56}{b} \left[ \frac{r_{LE} AR \cos^2 \Delta}{1 + [1/(M_\infty^3 \cos^3 \Delta)]} \right] \quad (7.2)$$

where  $b$  is the span of the wing and  $C_{D_{LE}}$  is referenced to the exposed planform area of the wing. The effect of  $r_{LE}$  on  $C_{D_{LE}}$  is readily apparent from Eq. (7.2). If the LE is supersonic (swept ahead of the Mach line such that  $M_\infty \cos \Delta > 1$ ) the LE radius should be small. Typical LE radii for a supersonic leading edge vary from 0 to about 0.25% of the chord. An example is the F-104 with  $\Delta_{LE} = 0$  and  $r_{LE} = 0$ .

The supersonic drag-due-to-lift factor  $K$  is expressed as [6]

$$K = \frac{1}{C_{L\alpha}} - \Delta N \quad (7.3)$$

where  $C_{L\alpha}$  is the wing lift curve slope and  $\Delta N$  is the leading edge suction parameter;  $\Delta N = 0$  for supersonic leading edges. For subsonic leading edges  $\Delta N > 0$  and increases as  $r_{LE}$  increases. Thus, the supersonic  $K$  decreases slightly as  $r_{LE}$  increases.

If  $M_\infty > 2.5$ , aerodynamic heating will have to be considered. Aerodynamic heating will dictate a larger  $r_{LE}$  than desired, to accommodate the heat inputs at the stagnation point on the wing LE. If flight speeds will exceed Mach = 2.5, the reader should examine the discussion on aerodynamic heating in Chapter 4.

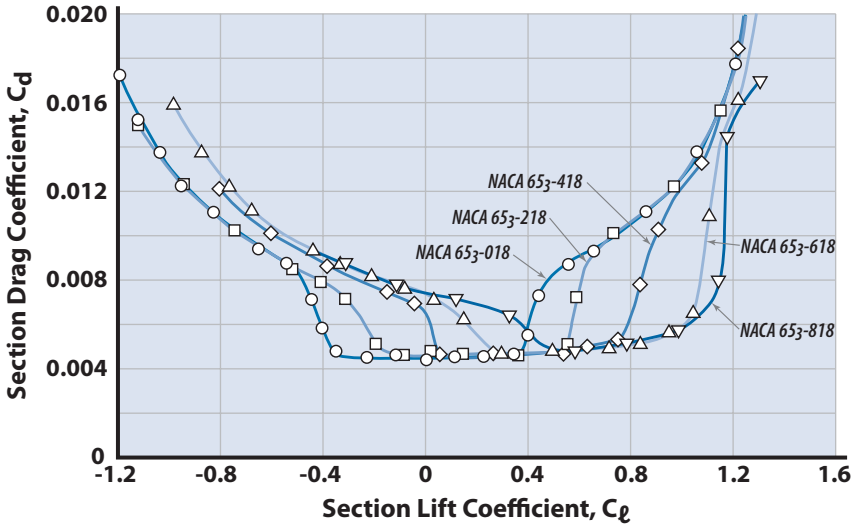
## 7.5 Effect of Airfoil: Camber

*Camber* is the amount (in percent chord) that a line equidistant from the upper and lower surface varies from the chord line (positive camber is shown in Fig. 2.1). Deflecting a trailing edge flap is the same as putting aft camber in the airfoil. Aft camber has a powerful effect on changing the lift of an airfoil at a specific angle-of-attack. Positive camber will shift the  $C_{L\alpha}$  curve to the left. Camber at the leading edge has almost no effect on changing the lift. The primary purpose of LE camber (i.e., deflecting a LE flap) is to delay flow separation over the forward part of the airfoil, producing higher maximum lift coefficients.

All subsonic low speed airfoil sections have about the same lift curve slope of  $2\pi$  per radian. The amount of camber determines the value of the angle for zero lift,  $\alpha_{0L}$ . The zero-camber airfoil, or symmetric airfoil, has  $\alpha_{0L} = 0$ . Airfoils with positive camber have negative values of  $C_{m_{a.c.}}$ , whereas a symmetric section has  $C_{m_{a.c.}} = 0$ . If the wing must have positive  $C_{m_{a.c.}}$ , such as a tailless design for static longitudinal stability, then the camber must be negative. The B-58 Hustler has a swooped-up trailing edge, called *inverse camber* or *reflexed trailing edge*, to give it negative camber and a positive  $C_{m_{a.c.}}$ .

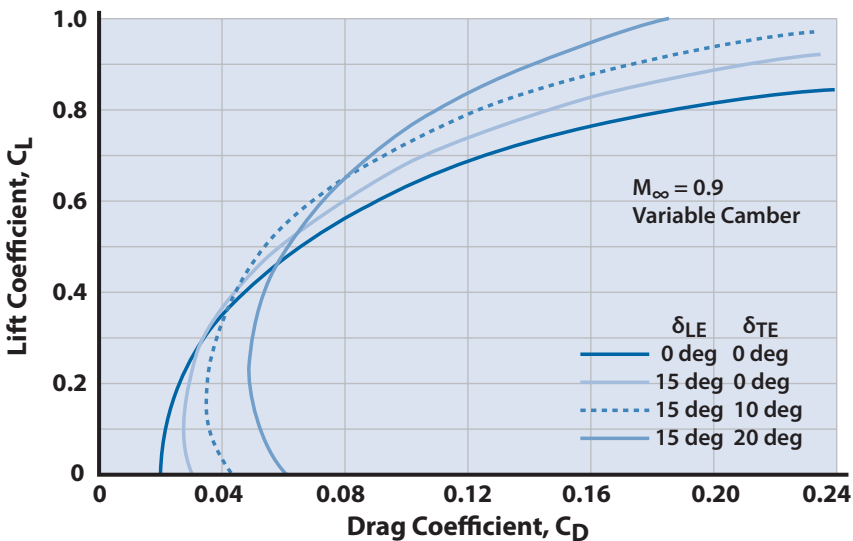
Positive camber gives an increase in section  $C_{\ell_{max}}$ . For example, a camber of 6 % of the chord at 30% chord gives an increase in  $C_{\ell_{max}}$  of about 0.4 over an equivalent symmetric section. This behavior should be obvious because a small flap deflection is equivalent to a positive increase in camber.

The effect of increasing camber on  $C_D$  is to translate the drag polar to higher values of  $C_{L_{min}}$  (i.e., that  $C_L$  for  $C_{D_{min}}$ ). This behavior is shown in Fig. 7.6 for the NACA 65<sub>3</sub>-X18 laminar flow airfoil sections and Fig. 7.7 for a complete aircraft. The designer should determine the lift coefficient that



**Figure 7.6** Drag characteristics of some NACA 65-series airfoil sections of 18% thickness with various amounts of camber,  $Re = 6 \times 10^6$  (data from [2]).

the aircraft requires during a critical mission phase, such as cruise. Then the camber is selected to give a  $C_{Lmin}$  (called the *design  $C_L$* ) close to the required  $C_L$ . Consider the USSR sailplane Antonov A-15, which has an aspect ratio of 26.4, a wing loading of 6 psf, and a best glide ratio of 40:1 at 54 kt. At 5000 feet the required  $C_L = 0.7$ . The Antonov A-15 uses the NACA



**Figure 7.7** Aircraft drag polar with variable-camber wing.

65<sub>3</sub>-618 airfoil at the root and NACA 65<sub>3</sub>-616 at the tip. From Fig. 7.6 the NACA 65<sub>3</sub>-618 has a design  $C_\ell = 0.6$  with a broad drag bucket for  $C_\ell$  excursions to either side of the design point (note: the subscript 3 denotes the range of  $C_\ell$  in tenths above and below the design  $C_\ell$  for the drag bucket).

Camber can be used effectively for high-subsonic cruise and transonic maneuvering. Figure 7.7 indicates the behavior of camber for a complete aircraft at Mach = 0.9. A range-dominated aircraft cruising at Mach = 0.8 would normally require a cruise  $C_L$  of 0.3–0.4 (see Fig. 3.9). Thus, the designer selects an airfoil to give a design  $C_L$  in this range. A fighter aircraft maneuvering transonically at high  $C_L$  (in the neighborhood of 0.8) would have a low-camber airfoil (the F-16 uses a 64-204 airfoil) but employs leading and trailing edge flaps (called *maneuver flaps* or *variable camber*) to reduce the level of drag-due-to-lift during combat. The designer must be careful in the selection of positive camber as it is accompanied by a negative  $C_{m_{a.c.}}$  and must be trimmed by a down aft tail load for statically stable aircraft. Camber is normally not used for supersonic flight because of the wave drag penalty associated with camber [see Eqs. (2.28) and (2.31), Chapter 2].

The airfoils used on high-altitude ISR aircraft are usually highly cambered because their optimum  $C_L$ s (the  $C_L$  for maximum endurance) are high, typically 0.7–1.0 (see Fig. G.4). The Lockheed Tier 3-minus “Darkstar” cruised at  $C_L = 0.53$  with its straight-wing tailless design, low levels of pitch control power, and flight altitude of less than 50,000 ft. By comparison the Boeing Condor started its loiter at a  $C_L = 1.33$ .

## 7.6 Effect of Planform: Aspect Ratio

This section discusses the effects of the planform aspect ratio on the design measures of merit. If the selected wing planform is a delta shape, the AR is related to the LE sweep by the expression

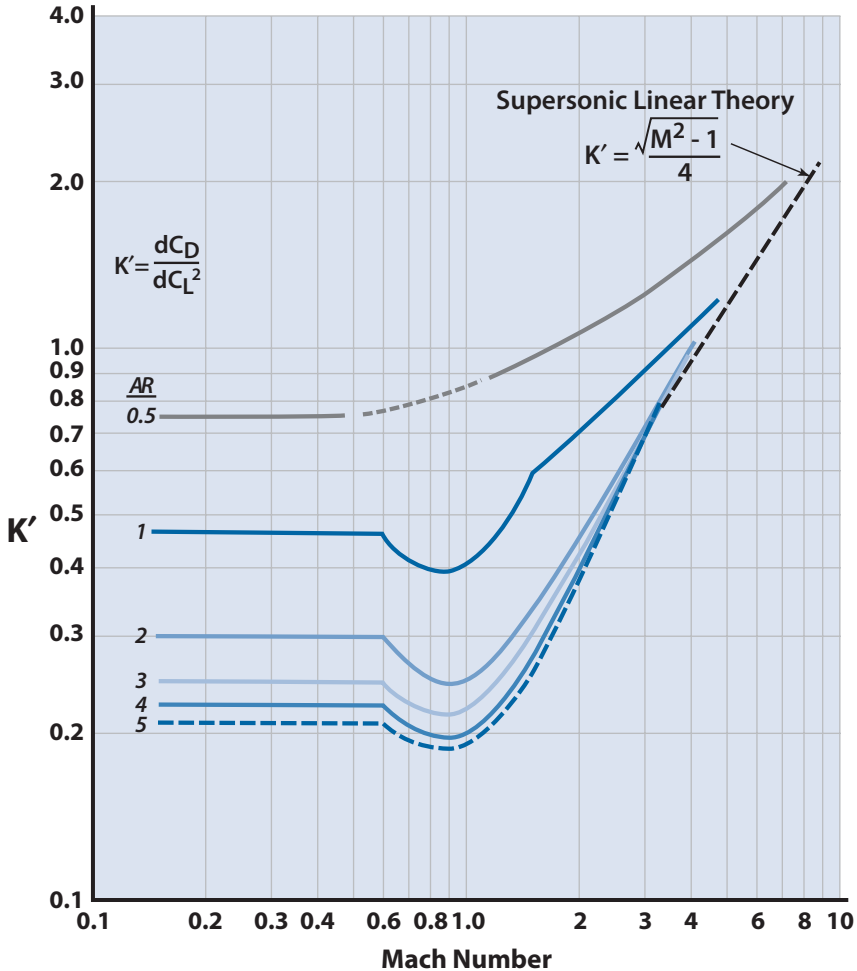
$$AR = 4 \cot \Delta \quad (7.4)$$

The aspect ratio is a major design parameter as it has a large influence on the wing lift curve slope [Eq. (2.13)] and the subsonic cruise efficiency through its relationship with the subsonic inviscid drag-due-to-lift factor  $K'$ ,

$$K' = \frac{1}{\pi AR e} \quad (2.18)$$

This relationship is shown in Fig. 7.8 for the wing–body combinations of Appendix H. Figure 7.8 also shows the reduction in  $K'$  through the tran-





**Figure 7.8** Inviscid drag-due-to-lift factor (based upon total planform area) for wing-body combinations with delta planforms and LE radius = 0.45%.

sonic region due to an increase in  $C_{L\alpha}$  and the reduced influence of AR on  $K'$  in the supersonic region.

The effect of AR on wing weight is shown quantitatively in Eqs. (20.1), (20.2), and (20.69) [and qualitatively in Fig. 7.10 (see Section 7.7)]; the effect on wing volume is shown qualitatively in Fig. 7.10].

For low-speed flight there is little effect of AR on  $C_{D0}$  as the drag is primarily skin friction and independent of planform shape. However, supersonically the  $C_{D0}$  increases with increasing AR as shown in Fig. H.6 and limits supersonic design to  $AR < 5$ .

## 7.7 Effect of Planform: Sweep

For the most part the effects of wing sweep are independent of whether the sweep is forward or aft. However, forward sweep does introduce the problem of *aeroelastic divergence*, which results from an increase in section angle-of-attack along the span (from root to tip) as the wing is deflected upward. As the forward-swept wing is loaded along the span the upward deflection increases the angle-of-attack of the tip section, which further loads the tip resulting in a divergent situation if the structural elastic restoring forces cannot halt the wing twist. One solution is to tailor the stiffness of the LE downward twist.

### Designing to Counter the Aeroelastic Effect

With its forward swept wing, the X-29 demonstrated excellent roll control up to 60 deg; however, this type of wing exhibits aeroelastic divergence, which can quickly lead to structural failure. Part of the technology goal while designing the X-29 was to demonstrate tailoring of the carbon fiber composite material to counter this aeroelastic effect without a large wing structure penalty. The tailoring of the advanced composite material was successfully demonstrated on the X-29 and later used on the forward swept wing Advanced Cruise Missile AGM-129 (see Fig. 12.22). The X-29 first flew December 1984; it demonstrated subsonic and supersonic high alpha maneuvering from 1985–1991. See an X-29 at the USAF Museum (Dayton, Ohio) or at the NASA Dryden Flight Research Center (Edwards AFB, California).

Although a forward-swept wing would weigh more than an aft-swept wing, the forward sweep offers several advantages. A forward-swept wing should offer improved area rule distribution, longer lever arm between the wing and tail mean aerodynamic chord ( $mac$ ), and reduced tip stall. This last advantage is quite important as it decreases stall-spin departure tendencies and gives lower landing speeds.

Essentially, the pressure distribution over a chordwise section of the wing is a function of the Mach number normal to the LE (Fig. 2.19). If the wing sweep results in a normal Mach number less than 1.0, the wing is said to have a subsonic LE at that freestream Mach number. If the normal Mach number is greater than 1.0, the wing has a supersonic LE (Fig. 2.24).

Wing sweep can delay and soften the transonic drag rise, as shown for a wing alone in Fig. 2.27 and for wing–body combinations in Fig. H.4. In Fig. H.4 the wing–body combinations represent wing sweeps of 0, 45, and 60 deg. Wing sweep permits subsonic aircraft to cruise at higher subsonic Mach numbers before encountering compressibility effects. Essentially the wing and fuselage drags are additive (plus some interference effects), with the fuselage  $C_{D_0}$  peaking at about Mach 1.2 (see Fig. 2.22).

At high subsonic speeds the effects of compressibility must be considered. The  $M_{CR}$  represents the onset of compressibility and the upper speed boundary for subsonic aircraft. As discussed earlier, it is desirable to keep  $M_{CR}$  as high as possible. The  $M_{CR}$  can be increased by increasing wing sweep, as shown in Fig. 7.9.

The peak wing  $C_{D0}$  occurs during the transonic regime. An unswept wing has its peak  $C_{D0}$  occur at a Mach number of about 1.1. The swept wing has its peak  $C_{D0}$  occur at approximately

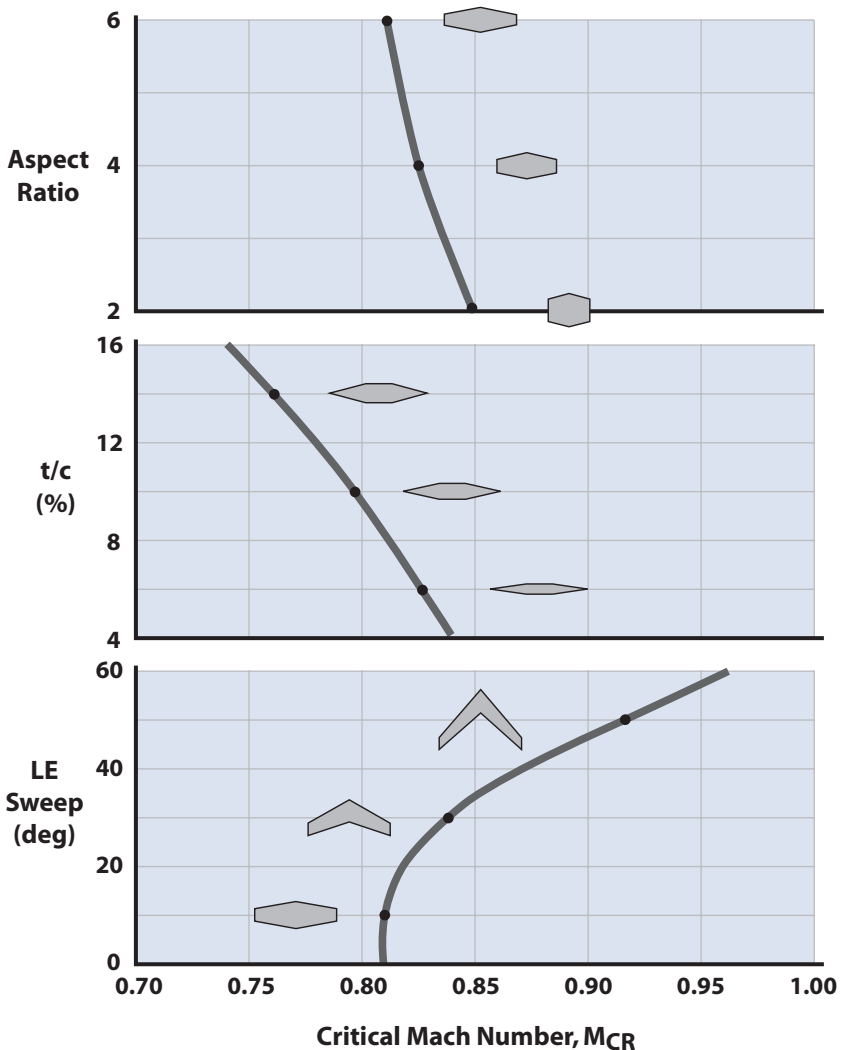


Figure 7.9 Effect of LE sweep,  $t/c$ , and AR on the critical Mach number.

$$M_{C_{D_{\text{peak}}}} = \frac{1.2}{\sqrt{\cos \Delta_{t/c}}} \quad (7.5)$$

where  $\Delta_{t/c}$  is the sweep of the maximum thickness line. The value of the peak  $C_{D_0}$  is decreased by sweep. This  $C_{D_0}$  softening is estimated by

$$C_{D_{\text{peak}\Delta_{t/c}}} = (\cos \Delta_{t/c})^{2.5} C_{D_{\text{peak}\Delta_{t/c}=0}} \quad (7.6)$$

For supersonic flight the designer must decide whether the leading edge will be subsonic or supersonic. The selection of the leading edge radius rests largely on this decision. Equation (7.2) indicates that increasing wing sweep and decreasing AR will give lower values for  $C_{D_{LE}}$ . However, the resulting wing has poor low-speed qualities. If the leading edge is to be subsonic, the sweep should be about 5 deg behind the Mach line. The rule is, “just enough sweep to do the job,” because of the disadvantages associated with high sweep and low AR at low speed.

Figure 2.29 shows the general influence of sweep on  $C_{D_0}$  for supersonic flight. The airfoil is the sharp LE double wedge in Table 2.1 so there is no drag due to LE bluntness.

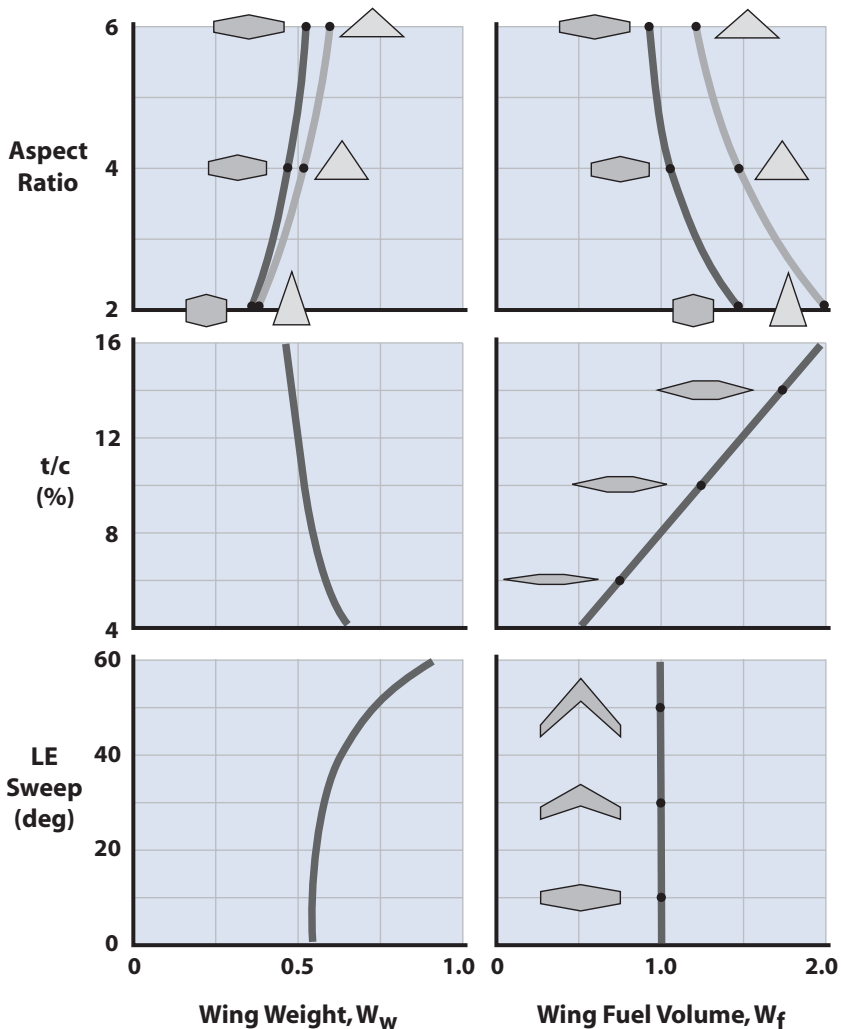
A disadvantage of wing sweep is the decrease in wing lift curve slope as given by Eq. (2.13) and shown in Fig. 2.21. This means that a swept-wing aircraft will have to land and take off at higher angles-of-attack than a straight-wing aircraft.

Other disadvantages to wing aft sweep are a reduction in  $C_{L_{\text{max}}}$  and tip stall. The early flow separation at the tip is due to the spanwise flow causing a thickening of the boundary layer near the tips and hastening flow separation. This can be troublesome during low-speed flight because the roll control surfaces (the ailerons) are located near the tips. A forward-swept wing will have the opposite situation in that the root will stall early but the ailerons will operate in high-energy attached flow. This premature tip or root stall can be controlled by twisting the wing tip or root.

The wing sweep and aspect ratio interact to influence the pitch-up tendency of the wing. As the tip region of a high-AR, aft-swept wing stalls, the center-of-pressure of the wing moves forward, producing a pitch-up. This behavior is undesirable as the aircraft tends to pitch up violently, with disastrous results. Several fighter aircraft (such as the F-101 Voodoo) had horns, buzzers, or stick shakers that would warn the pilot of entry into the wing stall region. Figure 21.14a shows a pitch-up boundary developed by NASA from extensive wind tunnel and flight test data. Planforms in Region I are pitch-up prone and should be avoided for fighter aircraft. If a Region I planform is used, then the aircraft must have an aft horizontal tail that is located outside the wake of the stalled wing in order to arrest the divergent

motion. Figure 21.14b illustrates four regions of horizontal tail location with general recommendations regarding pitch-up. Figure 21.14 can be used by the designer for general guidance in fighter aircraft planform selection and horizontal tail location.

The effect of wing aft sweep on wing weight is shown quantitatively in Eqs. (20.1), (20.2), and (20.69) and qualitatively in Fig. 7.10. The effect of forward sweep would be even greater because extra structure is added to stiffen the wing to arrest the aeroelastic divergence. The effect of wing sweep on wing volume is shown qualitatively in Fig. 7.10 to be negligible.



**Figure 7.10** Effect of LE sweep,  $t/c$ , and AR on wing weight and wing fuel volume.

Wing weight is dependent to a large degree on the weight that is required to take out the bending moment. For a given wing area and moment about the centerline, this weight is a function of the structural span divided by the root thickness. The structural span can be considered as twice the length of the line bisecting the leading and trailing edge angle. If our structural span is high, our weight is high. If wing root thickness is high, wing weight is low. In the first chart of Fig. 7.10, LE sweep is doing one thing. It is increasing the structural span for the wing in question, thus increasing wing weight. Notice in the chart how the projected span remains the same, but the structural weight increases. The weight shown in Fig. 7.10 is nondimensionalized but is relative to the fuel weight, which we will take up shortly. On the aspect ratio plot is shown the wing weight of a delta wing at the same  $t/c$  as the straight wing. Reducing AR involves increasing the LE sweep, but here structural span is also reduced, and the root maximum thickness is increased. There is very little difference between a delta-wing weight and a straight-wing weight at the same AR and  $t/c$ .

On any long-range vehicle, the wing is extremely important not only as a device for holding the vehicle in the air, but also for carrying fuel because the wing is physically large and has a considerable amount of usable volume. If AR and wing area remain constant, the volume and, thus, fuel weight will not be affected. Therefore, sweep will not affect volume (bottom-right chart of Fig. 7.10). The volume will vary linearly with our thickness ratio, and fuel volume will decrease as we increase aspect ratio.

## 7.8 Effect of Planform: Taper Ratio

Taper ratio (ratio of tip chord to root chord,  $\lambda = C_T/C_R$ ) has a fine-tuning effect on the wing performance. As the taper ratio increases from zero (a delta planform) toward 1.0 (a rectangular planform) it passes through a nearly elliptical lift distribution at  $\lambda = 0.35$ , which gives minimum finite-span downwash effects and minimum induced drag. For a given wing area and thickness ratio a delta wing planform will have a larger root chord than a rectangular planform, resulting in approximately 40% more volume available in the delta for fuel (see Fig. 7.10). From the wing weight equations of Chapter 20 it is observed that decreasing taper ratio from 1 to 0 gives a decrease in the wing weight due to the increased root depth and decreased tip loading.

## 7.9 Variable Geometry

The preceding discussions have pointed out that for good low-speed performance the aircraft should have low sweep and high AR, whereas, for good supersonic cruise the aircraft should have high sweep and low AR.

This conflict in design conditions is a real dilemma for the designer. For a fixed-wing aircraft there is no real solution. The design answer is one of compromise, trying to select the fixed-wing planform that will fit both ends of the performance spectrum with minimum degradation of the mission.

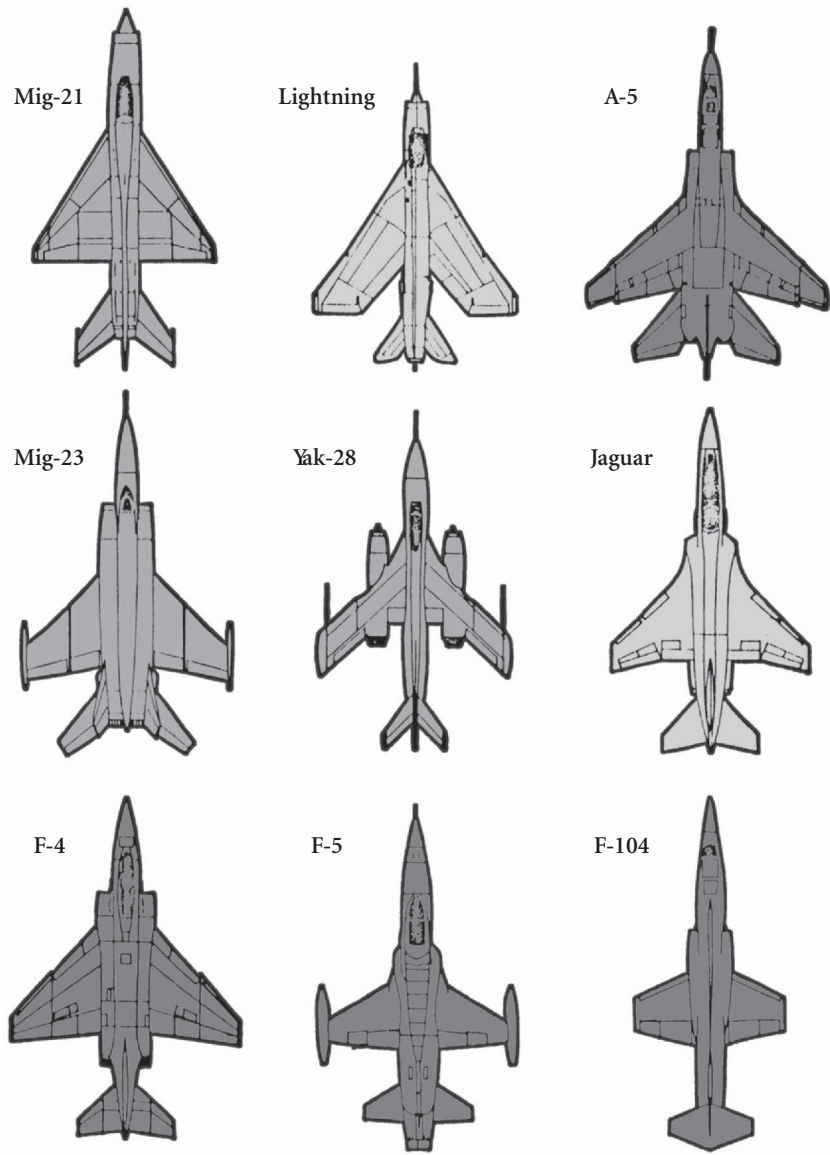
The key term here is “fixed wing” (see Fig. 7.11a). Why does the wing geometry have to be fixed? In fact, the wing geometry can be variable, capable of being adjusted to fit several different performance requirements. This is the idea behind the variable-geometry, or variable-sweep, wing.

The wing panels would be pivoted at the root so that each wing could swing from a low-sweep to a high-sweep condition. This idea is not new. The Bell X-5 and Grumman XF10F were early (1951–1952) research aircraft that demonstrated the versatility of high-speed and low-speed performance with variable sweep. Variable geometry is being used on current aircraft such as the Lockheed Martin (General Dynamics) F-111, Dassault Mirage IIIG, Sukhoi SU-7B, and the Mikoyan Flogger (see Fig. 7.11c).

The idea of variable geometry is a good one, but there are some disadvantages. The main disadvantage is weight. The variable-sweep wing, because of the wing pivot structure and associated machinery, is much heavier than a fixed-geometry wing. Estimates are that the variable-geometry wing weighs about 20% more than a comparable fixed wing. This 20% is significant. For example, the McDonnell F4C wing weighs 4600 lb for an aircraft gross weight of about 50,000 lb. A 20% increase in the wing weight would seriously cut into the aircraft performance.

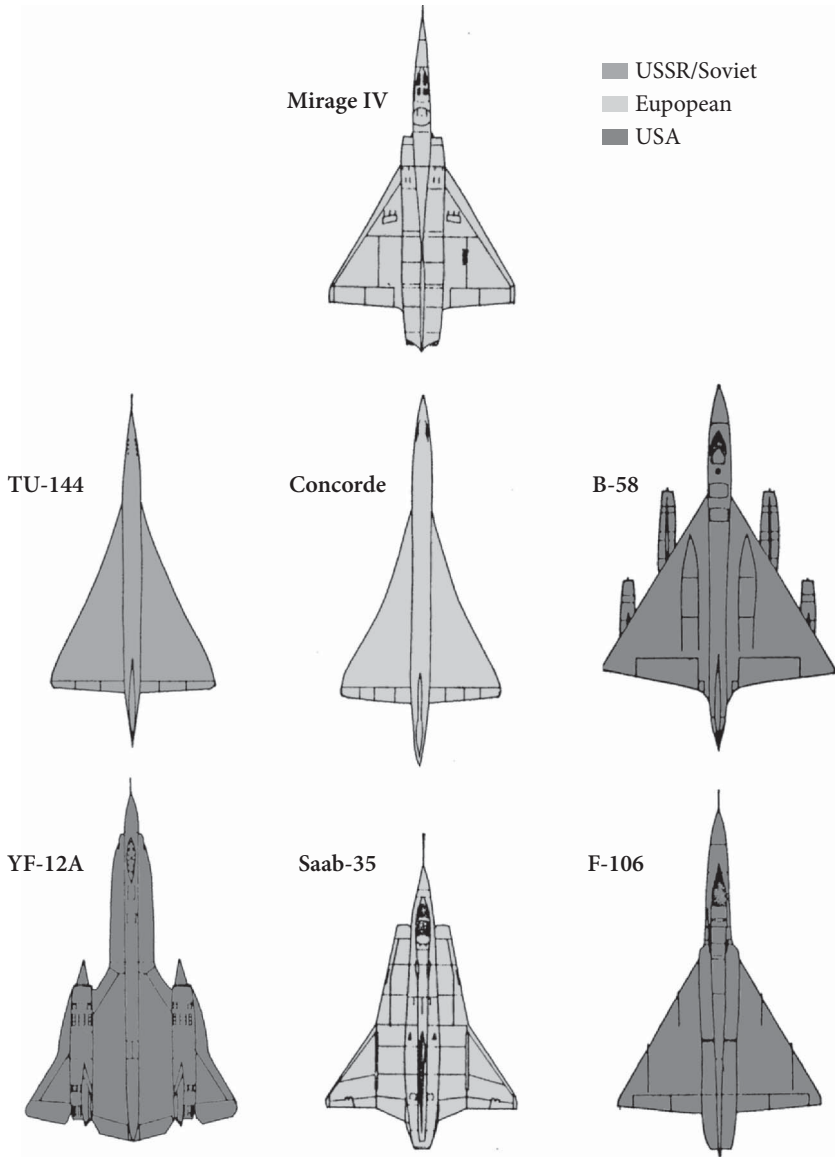
Another disadvantage is the large shift in the aircraft aerodynamic center as the wings are swept back. This causes large stability and control problems. The wing glove (fixed portion of wing at the root) helps to eliminate part of this aerodynamic-center shift but it is still a problem. Also, if external stores are carried on wing pylons, the wing pylons must be able to swivel the stores for zero yaw angle at all wing sweep angles. This swivel capability also means additional weight.

Variable geometry is a good design feature but not for all aircraft. If an advanced design has conflicting mission requirements that cannot be compromised, then variable geometry should be considered. If the performance gains from using variable geometry outweigh the disadvantages, then the variable geometry “buys its way” onto the airplane. A good example is the U.S. Navy F-14 Tomcat shown in Fig. 7.12. This aircraft required a 120-kt approach speed for carrier landings and a supersonic acceleration to Mach 2.5. These and other performance requirements drove the F-14 design to variable geometry. The F-14 is shown in three-view in Fig. 7.13. The Tomcat protected the Navy battle groups for four decades; it was retired in 2007.

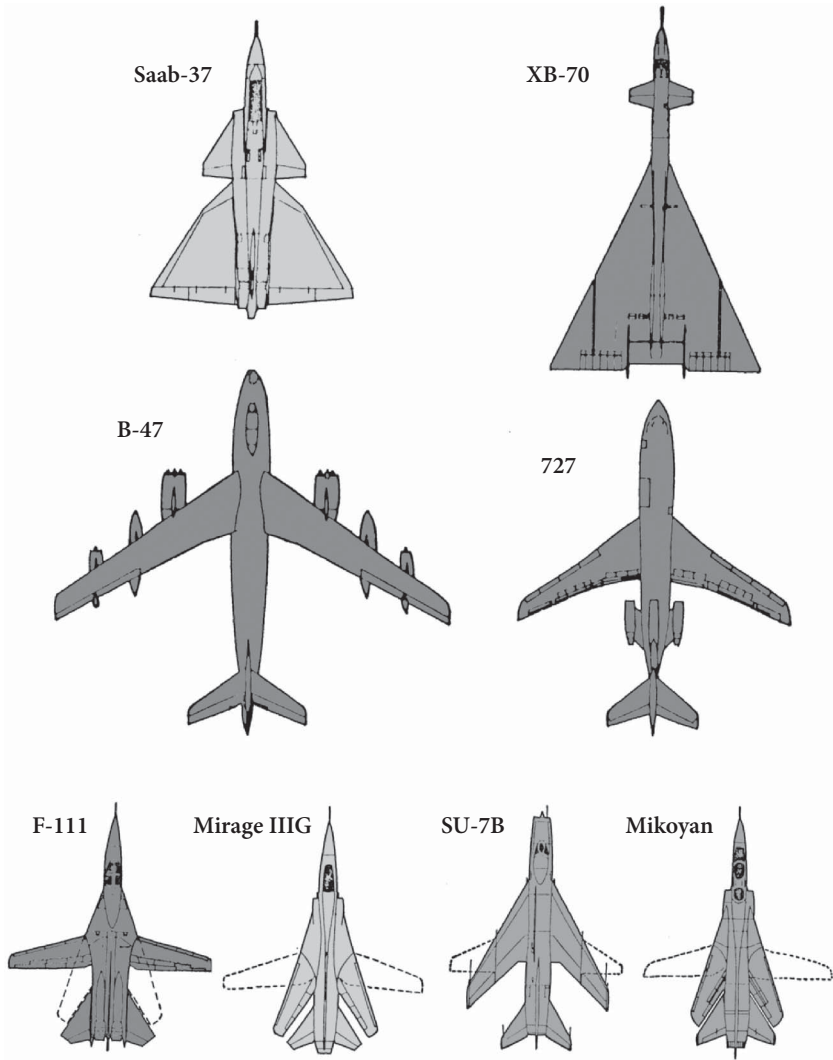


**Figure 7.11a** Typical wing planform shapes for fixed-wing, conventional-tail aircraft.





**Figure 7.11b** Typical wing planform shapes for tailless delta aircraft.



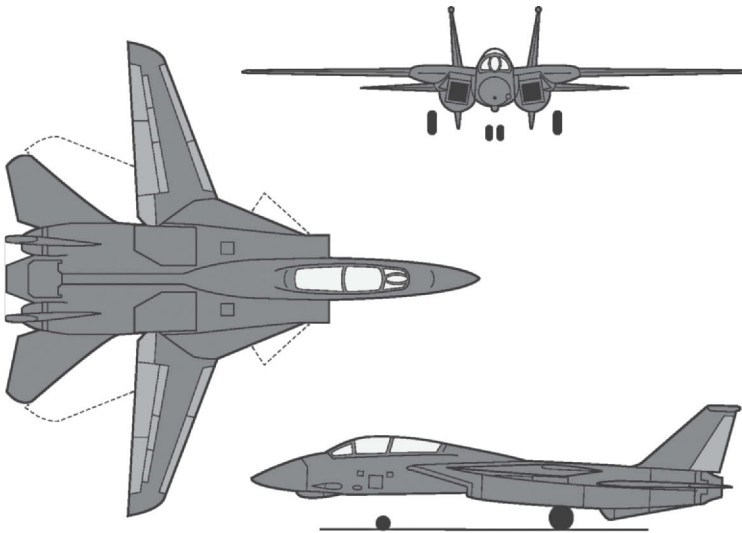
**Figure 7.11c** Typical wing planform shapes for canard, subsonic-cruise, and variable-sweep aircraft.

Another example of a current aircraft design that was forced into a variable-sweep wing is the Rockwell (North American) B-1 Lancer bomber shown in Fig. 7.14. The mission requirements called for an extended cruise range at Mach = 0.8, which dictated moderate sweep and high aspect ratio



**Figure 7.12** USN Grumman F-14 Tomcat.

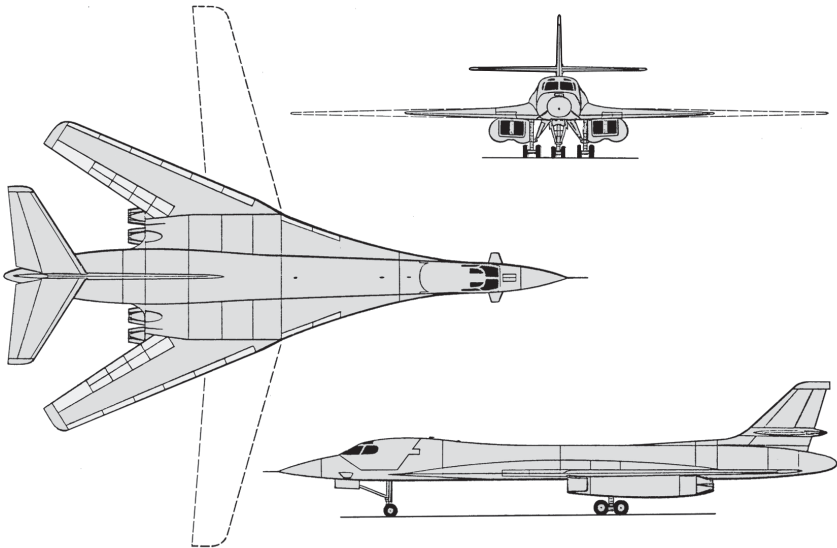
to give a good  $(L/D)_{\max}$ . In addition, the B-1 must “dash on the deck” at  $Mach = 0.9$  and be able to accelerate to  $Mach\ 2.2$  at altitude. These two requirements call for low aspect ratio and high sweep. The high sweep alleviates the aircraft gust response during the low-altitude dash and results in a much smoother ride. The B-1 is shown in 3-View on Fig. 7.15.



**Figure 7.13** Three-view of U.S. Navy Grumman F-14 Tomcat, a two-seat carrier-based swing-wing fighter ( $W_{TO} = 54,000$  lb, length = 62 ft, extended wing span = 64 ft, and sweep = 20–68 deg).



**Figure 7.14** USAF/Rockwell B-1 Lancer.



**Figure 7.15** Rockwell B-1 strategic bomber ( $W_{TO} = 400,000$  lb, length = 143 ft, extended wing span = 137 ft, and sweep = 15–65 deg).

**Table 7.1** Summary of Airfoil and Planform Effects

Increase In ↓ Changes →	$C_{D0}$		K	$C_{L\alpha}$	$C_{Lmax}$	Wing Wt	Wing Vol
	Subsonic	Supersonic					
Aspect Ratio	NO EFFECT	↑	↓	↑	↑	↑	↓
Wing Sweep	NO EFFECT	↓	↑	↓	Aft ↓ Fwd NO EFFECT	↑	NO EFFECT
Taper Ratio	NO EFFECT	NO EFFECT	↓ ↑	↑ ↓	NO EFFECT	↑	↓
Airfoil Thickness Ratio	NO EFFECT	↑	NO EFFECT	NO EFFECT	↑	↓	↑
Leading Edge Radius	NO EFFECT	↑	↓	NO EFFECT	↑	NO EFFECT	↑
Camber	↑	↑	↓	NO EFFECT	↑	NO EFFECT	NO EFFECT

## 7.10 Summary

Selecting the right airfoil and planform is a difficult task. Even experienced designers can be confused, but the point to remember is that there is no right answer—only a best answer at a point in time. And the best answer will involve making compromises in the measures of merit listed at the beginning of this chapter.

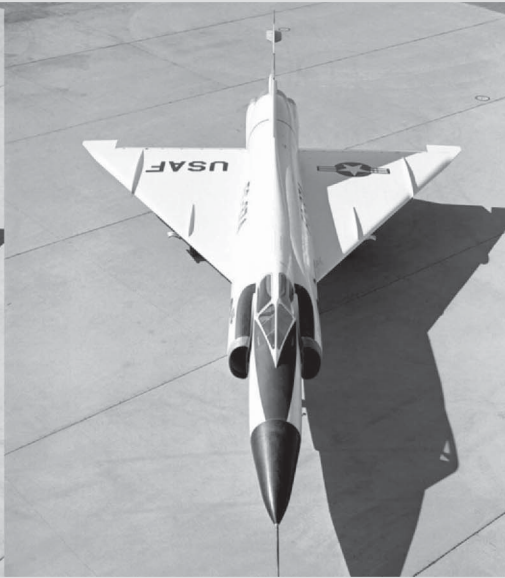
Table 7.1 is a summary of the airfoil and planform effects discussed in this chapter. The measures of merit are listed along the top and the airfoil–planform features are along the left-hand side. The table indicates the effect on the measure of merit if the airfoil or planform feature is *increased*.

## References

- [1] Abbott, I. H., and Von Doenhoff, A. E., *Theory of Wing Sections*, Dover, New York, 1959.
- [2] Abbott, I. H., Von Doenhoff, A. E., and Stivers, L., Jr., “Summary of Airfoil Data,” NACA TR-824, 1945.
- [3] Riegels, F. W., *Aerofoil Sections*, Butterworth, London, 1961.
- [4] *Evolution of Aircraft Wing Design Symposium*, AIAA, Reston, VA, 1980.
- [5] McCullough, G. B., and Gault, D. E., “Examples of Three Representative Types of Airfoil-Section Stall at Low Speed,” NACA TN-2502, 1951.
- [6] Simon, W. E., Ely, W. L., Niedling, L. G., and Voda, J. J., “Prediction of Aircraft Drag Due to Lift,” U.S. Air Force Flight Dynamics Laboratory AFFDL-TR-71-84, July 1971.

## Chapter 8

# Preliminary Fuselage Sizing and Design



- Passenger Seating
- Supersonic Area-Ruling
- Body Fineness Ratio
- Integrating Propulsion
- Integrating Crew
- Integrating Landing Gear
- Initial Fuselage Length
- Initial C.G. Location

The Convair F-102 Delta Dagger was built in the 1950s as part of the USAF's air defense. The prototype (left) could not go supersonic, but using area rule theory (see Section 8.4) to revise the aircraft design solves the problem and gives the fuselage a "Coke bottle" appearance at the wing/fuselage intersection (right).

*"I must do something" will always solve more problems than "Something must be done."*

The aircraft is now beginning to take shape. In Chapter 5 a preliminary estimate of the takeoff weight and fuel weight was established. The takeoff wing loading was also determined, in Chapter 6, so that the wing is sized. The airfoil section and planform shape derive from the work in Chapter 7. Designing and sizing the fuselage is the next step.

## 8.1 Fuselage Volume

Preliminary estimates of fuselage volume requirements are relatively easy to assess, provided the designer has decided upon its contents. The cutaway drawings in this chapter will help remind the designer of what is usually put into the fuselage. Reference [1, Vols. 3 and 4] is an excellent reference for fuselage design. This chapter focuses on two important design items: an initial fuselage length and the c.g. location. The following points should be considered when locating all equipment, payload, subsystems, fuel, and structure in the aircraft.

### Going Supersonic with Area Rule Theory

The Convair F-102 Delta Dagger was an interceptor aircraft built in the late 1950s as part of the USAF's air defense. Entering service in 1956, its main purpose was to intercept invading Soviet bomber fleets. The 1951 RFP called for a high-altitude, supersonic interceptor armed with guided missiles to replace the F-86 Saber Jet and the F-89 Scorpion.

Convair won the competition and developed the prototype YF-102 (see chapter opener art), which flew in 1954 and had dismal performance. Despite Convair's prediction, the airplane could not go supersonic. It could not even reach Mach = 1 because of excessive transonic drag [3]. To solve this problem of higher-than-expected transonic drag, Convair engineers employed an emerging NASA technology developed by Richard Whitcomb called *area ruling* (discussed in Section 8.4).

Area rule theory dictates that cross-sectional area distribution from nose to tail should be smooth and continuous to give low wave drag, meaning that the fuselage cross-sectional area in the vicinity of the wing should be reduced to accommodate the cross-sectional area of the wing.

These criteria gave the fuselage a "Coke bottle" appearance at the wing/fuselage intersection. The pinched-in waist of the redesigned Delta Dagger is typical of an area-ruled design. Once this design adjustment was made, the YF-102 accelerated out to Mach 1.22 at 53,000 feet. Convair went on to build 1000 Delta Daggers.



**Table 8.1** Passenger Compartment Requirements

	Long Range	Short Range
Seat width (in.)	17–22	16–18
Seat pitch (in.)	34–36	30–32
Headroom (in.)	>65	>65
Aisle width (in.)	18–20	>12
Aisle height (in.)	>76	>60
Passengers per attendant	31–36	<50

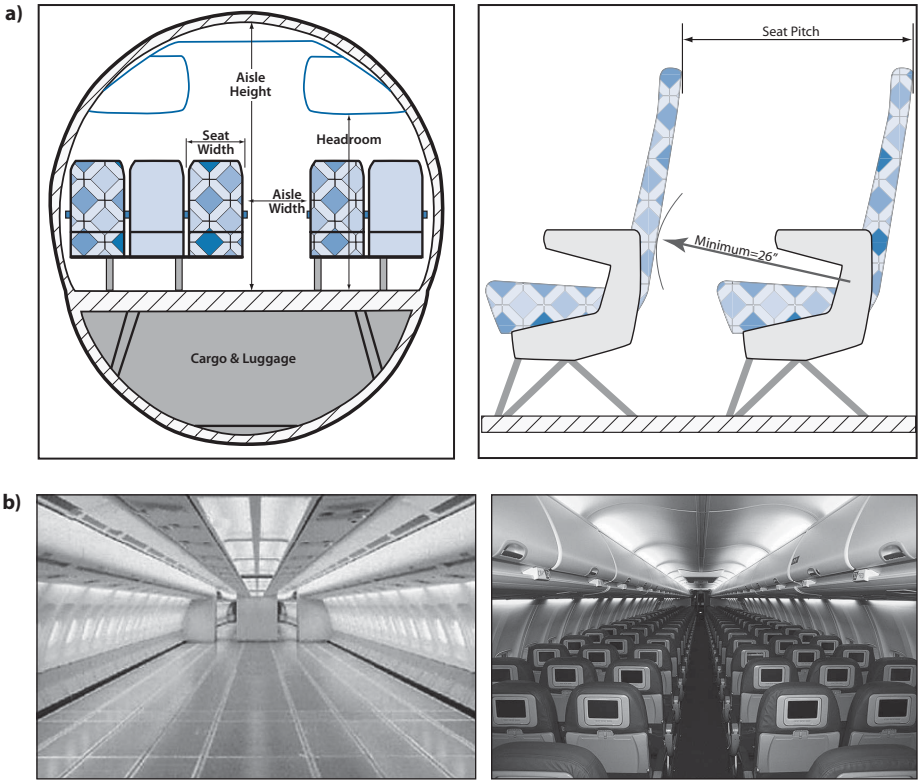
### 8.1.1 Passengers

The passenger seating in a transport aircraft varies depending upon whether the section is first class, business class, or coach. The first-class and business-class sections have no typical seating arrangement. The arrangement in these more expensive sections depends upon the airline's desire to attract a more affluent clientele. In long-range transports these sections often feature sleeper seats, lounges, and high attendant-to-passenger ratios. Typically these sections accommodate less than 10% of the total number of passengers because the revenue per volume (space required) used is much less than for the coach section.

The seating arrangement in the coach section is driven by a desire to have the most passengers per cubic foot of volume, while still maintaining passenger comfort. Each coach passenger should have the volume shown in Table 8.1 and Fig. 8.1a. Each passenger is assumed to weigh 180 lb (this includes an allowance for carry-on baggage). Each passenger is allowed ~40 lb of baggage (a volume of approximately 15 ft<sup>3</sup>) on domestic flights and 65 lb (approximately 25 ft<sup>3</sup>) on international flights. In the coach section the number of seats across depends on the size of the aircraft and the selection of a single or double aisle. Table 8.2 shows the numbers of passenger seats across the aircraft for current aircraft.

The passenger section of the aircraft usually has a round cross section because that is the most structurally efficient shape for a conventional metal structure. However, the most volumetrically efficient cross section is an oval, which is the shape of the Boeing 787 composite fuselage. The passengers are located in the upper half of the cross section; baggage and cargo, in the lower half.

The passenger and cargo sections are pressurized to 6500-ft pressure altitude. The pressure differential between 6500 ft and the typical operating altitude of 35,000–40,000 ft is a major factor in the structural and fatigue design criteria for the aircraft. For each row of seats it is desirable to



**Figure 8.1** Commercial transport seating arrangement: **a)** schematic; **b)** compare the empty cabin (left, courtesy of Sharam Sharifi) to the full interior (right, courtesy of Wikimedia Commons).

**Table 8.2** Aisle and Passenger Distributions for Various Commercial Transports

Aircraft	Aisle	No. Passengers on Sides	No. Passengers in Middle
Boeing 727	Single	3 and 3	0
Boeing 737	Single	3 and 3	0
Airbus 300	Double	2 and 2	4
Boeing 747	Double	3 and 3	4
Boeing 757	Single	3 and 3	0
Boeing 767	Double	2 and 2	3
Boeing 777	Double	2 and 2	5
Lockheed L-1011	Double	2 and 2	4
DC-10	Double	2 and 2	5
Boeing 787	Double	2 and 2	5

have a window that is as large as possible. Typical window spacing is 40 inches for 14 × 10 inch windows.

Reference [1, Vol. 3], has considerable information on passenger section layout for commercial transports.

### 8.1.2 Lavatories, Galleys, and Emergency Exits

The size of these items will vary depending on the aircraft and number of passengers. There should be one lavatory for approximately every 20 passengers. The number and type of emergency exits required for passenger transport aircraft is defined in the Federal Aviation Regulations (FAR Part 25.807) [2].

### 8.1.3 Passenger Cargo

The passenger luggage and revenue cargo for the aircraft listed in Table 8.2 is preloaded into standard-size cargo containers and carried beneath the passengers in the cargo compartment. Table 8.3 lists the dimensions for the most widely used cargo containers. Smaller, short-range aircraft do not use cargo containers, but rather have space only for bulk cargo with a volume that is based upon 6–8 ft<sup>3</sup> per passenger.

### 8.1.4 Military Cargo and Equipment

The military cargo is preloaded onto flat pallets, tied down and covered with a tarp. The most common is the 463L pallet which measures 108 × 88 inches. MIL-STD-1791 requires 6-in. clearance in all directions between the cargo and the aircraft interior. Military transports must have their cargo compartment floor approximately 4–5 feet off the ground to allow for direct loading and unloading of the cargo pallets from a truck bed at air bases without cargo-handling facilities.

**Table 8.3** Cargo Container Specifications

Type	Height (in.)	Width (in.)	Depth (in.)	Weight (lb)
LD-2 <sup>a</sup>	64	61.5	60.4	2700
LD-3 <sup>a</sup>	64	79	60.4	3500
LD-4	64	96	60.4	5400
LD-5	64	125	60.4	5400
LD-8 <sup>b</sup>	64	125	60.4	5400

<sup>a</sup>Lower corner chamfered 30 deg.

<sup>b</sup>Both lower corners chamfered 30 deg.

The military transports have the dimensions of their cargo compartments sized by the equipment they need to carry. Typical equipment includes jeeps, humvees, armored personnel carriers, special forces boats, and numbers of 463L pallets. The C-130 has a cargo bay that measures 10 ft 3 in. wide  $\times$  9 ft 2 in. high  $\times$  41 ft 5 in. long. The C-5 and C-17 were developed to carry “outsize” cargo such as M-60 tanks, helicopters, and large trucks. The C-5 has a cargo bay with dimensions of 19 ft wide  $\times$  13 ft 6 in. high  $\times$  121 ft long. These military transports need a ramp at the rear of the aircraft to load and unload the equipment.

### 8.1.5 Crew Compartment

The size of the crew compartment varies depending on the aircraft. For long-range military or commercial transports it is recommended that the crew compartment have a length approximately 150 inches for a crew of four, 130 inches for a crew of three, and 100 inches for a crew of two. This gives the crew room to get out of their seats and stretch their legs as well as room to store their map cases and flight bags.

The size of the cockpit for a fighter depends on the number of crew and whether the seating arrangement is tandem or side-by-side. The cockpit arrangement uses a typical 13-deg seatback angle, although angles up to 30 deg have been used (i.e., F-16) to provide better “g” tolerance for the pilot during air combat. Typical fighter single-seat crew station dimensions are 30 in. wide  $\times$  50 in. to the top of the canopy  $\times$  60 in. from the foot pedals to the back of the seat. An ejection seat is required for safe escape when flying at a dynamic pressure greater than 230 psf (equivalent to 260 knots at sea level). At speeds approaching Mach = 1 at sea level (dynamic pressure = 1480 psf), even an ejection seat is unsafe and an encapsulated seat or crew capsule must be used. The FB-111 and B-1A flew fast and low and used a separable crew capsule. The crew capsules were heavy and complex but gave the crew a chance of surviving a high- $q$  ejection. Reference [3] has an excellent chapter on fighter crew station design.

MIL-STD-850B defines the vision requirements for various classes of military aircraft in terms of over-nose and over-side vision angles. These angles are important during low-altitude maneuvering and allow the pilots to see the runway threshold during landing approach. Because all landing approaches are different and all aircraft have different approach angles-of-attack, the minimum over-nose angles shown in Table 8.4 are typical recommended values. An over-nose analysis would put the aircraft at the  $\alpha$  for  $0.8C_L$  max and an approach angle of 3 deg for commercial and U.S. Air Force aircraft, 4 deg for a carrier approach in a Navy or Marine aircraft, and 7 deg for a short takeoff and landing (STOL) aircraft. The supersonic transports Concorde and Russian TU-144 drooped the entire nose, as shown in Fig. 8.2, during landing to provide pilot vision.

**Table 8.4** Typical Minimum Over-Nose and Over-Side Pilot Viewing Angles

Aircraft	Over-Nose	Over-Side
Military transports and bombers	17 deg	35 deg
Commercial transport	11–20 deg	35 deg
Fighter	11–15 deg	40 deg
General aviation	5–10 deg	35 deg

### 8.1.6 Armament

The number and size of bombs must be determined and they must be located in or on the aircraft. Arrangements for storage, positioning, and release of missiles must be considered.

Guns or cannon can be carried in gun pods external to the aircraft or mounted internally. Armament carried external to the aircraft will provide lower fuselage volume requirements but will cause greater drag on the aircraft. Reference [1, Vol. 4] has an excellent discussion on armament integration and size–weight information on air-to-air and air-to-ground weapons.

### 8.1.7 Landing Gear

The size and location of the landing gear will vary depending on the aircraft. A good first estimate can be made by examining existing aircraft in the same weight class as you are designing. References [1,4] have good discussions on landing gear design.



**Figure 8.2** Concorde with nose drooped for landing (courtesy of Wikimedia Commons).

The main landing gear is located relative to the c.g. of the aircraft based upon the following two considerations:

1. The airplane should not fall on its tail or nose at any possible loading condition.
2. The moment to rotate the aircraft about the main gear to  $0.8C_L\max$  at  $V_{TO}$  and worst c.g. location should not size the horizontal tail (or canard or wing flaps).

Based upon these considerations the main gear wheel (with strut depressed) is located behind the most forward c.g., for a tricycle gear, and in front of the most aft c.g., for a tail dragger, by the angles shown in Table 8.5. For carrier-suitable Navy aircraft 15 deg behind c.g. is necessary based on the real possibility of a 5-deg pitching deck. This main gear–c.g. geometry is shown in Figs. 8.3 and 11.1.

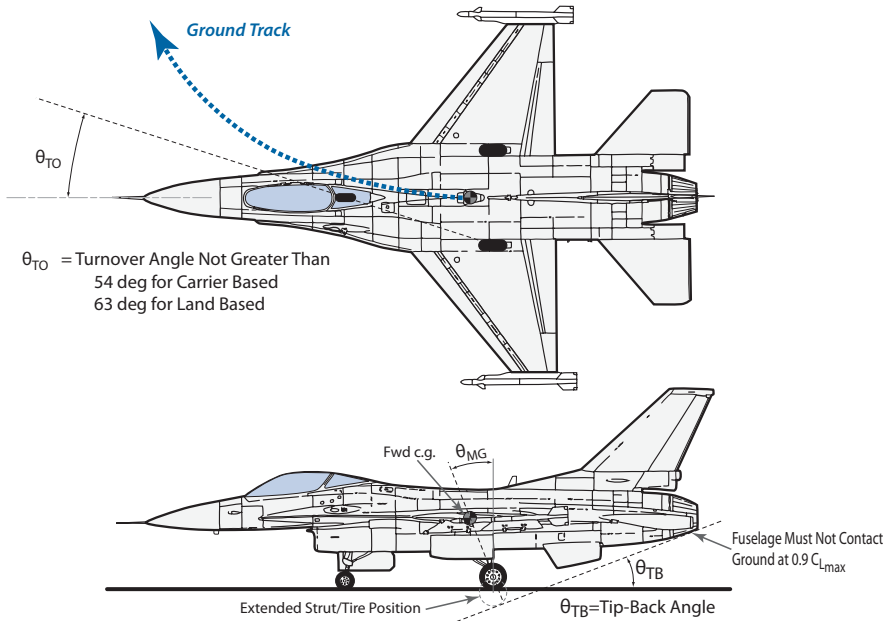
A good rule of thumb for the nose gear is to have 20% of the takeoff gross weight (TOGW) on the nose wheel for good nose-wheel steering. The nose gear is located so that the aircraft does not tip over during high-speed taxi turns. This tip-over geometry and typical tip-over angles are shown in Fig. 8.3.

As the aircraft rotates about the main gear for takeoff or touches down for a landing the aft end of the fuselage must not strike the ground. The angle between the main gear in an extended strut position and the aft end of the fuselage is called the *tip-back angle*, shown in Fig. 8.3. The tip-back angle is determined by rotating the aircraft to the  $\alpha$  for  $0.9C_L\max$  about the main gear in the extended strut position and observing if any part of the aft fuselage touches the static ground line (see Fig. 8.3). During normal takeoff and landing the aircraft is rotated to  $0.8C_L\max$ . The value  $0.9C_L\max$  is used in the tip-back analysis to account for pilot overshoot.

Aircraft typically have a 3-deg glide slope during approach and then flare over the threshold, giving a 10-ft/s sink rate at touchdown. The flare is an imprecise maneuver and results in considerable dispersion about the touchdown point and great variance in landing distance from one pilot to another. Carrier-suitable Navy and Marine aircraft approach the carrier at about 4 deg and not flare at touchdown (reducing the dispersion distance), giving a sink rate of 24 ft/s and a much heavier landing gear weight require-

**Table 8.5** Angles for Location of Main Landing Gear

Gear Type	Aircraft	Angle for Main Gear
Tail dragger	All	15 deg forward of c.g.
Tricycle	All	10 deg behind c.g.
Tricycle	Carrier suitable	15 deg behind c.g.



**Figure 8.3** Aircraft turnover and tip-back angle definitions.

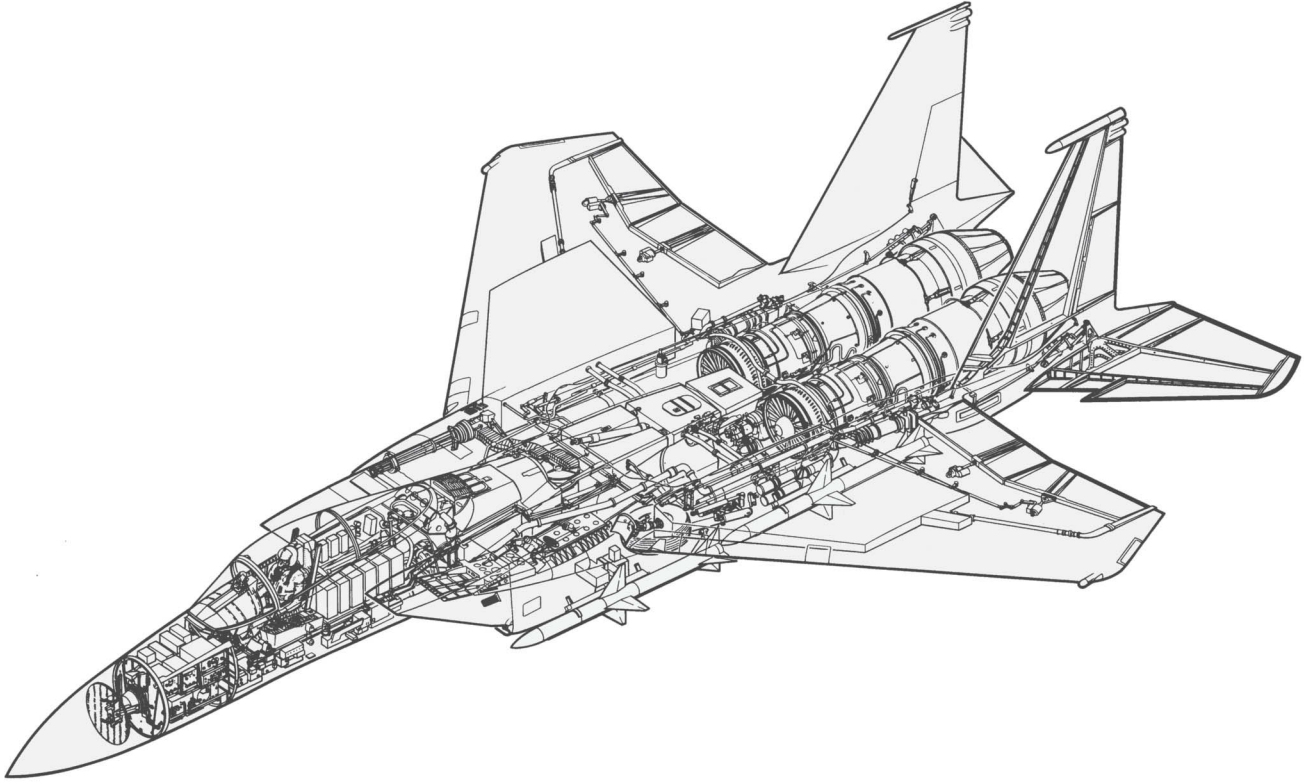
ment. Supporters of unmanned aerial vehicles (UAVs) argue that autonomous landing systems result in a highly consistent and low touchdown sink rate of 5 ft/s and should therefore have lighter landing gears.

### 8.1.8 Wing Carry-Through

Although not visible externally, volume must be made available for the wing carry-through. Because the wing is thickest at the root chord this will account for a considerable portion of the fuselage volume requirement. The carry-through may be either a straight carry-through of the wing center section or a ring-type construction following the fuselage cross section outer contour (see Figs. 8.4–8.10 and Figs. 19.1 and 19.2).

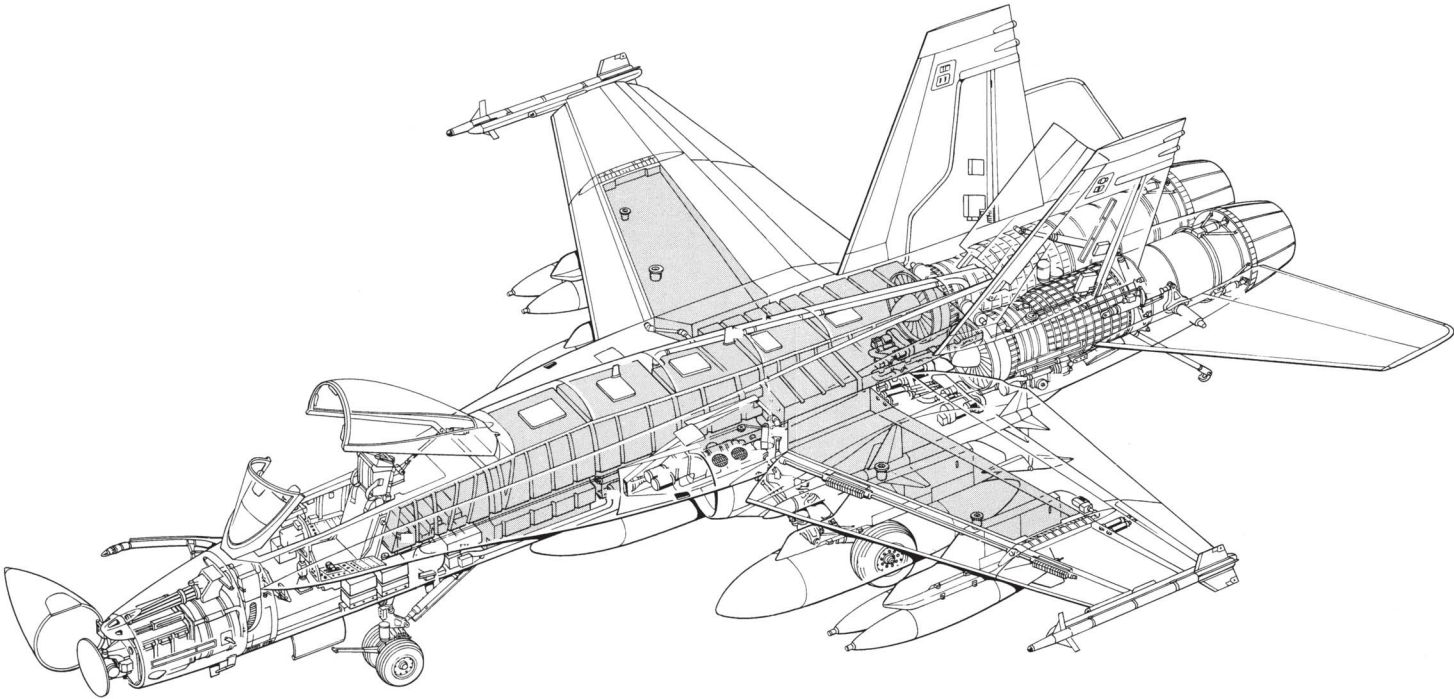
### 8.1.9 Propulsion Integration

Engines may be mounted internally as in the F-15 (Fig. 8.4) and F-18 (Fig. 8.5), partially embedded in the fuselage as with the F-4 (Fig. 8.6), or completely external as with the DC-9 (Fig. 8.7). The internal and partially internal arrangements are difficult to assess because engine size and number are not yet known. If the propulsion units will likely be internal, the designer should reserve some fuselage volume for the engines. First estimates can be

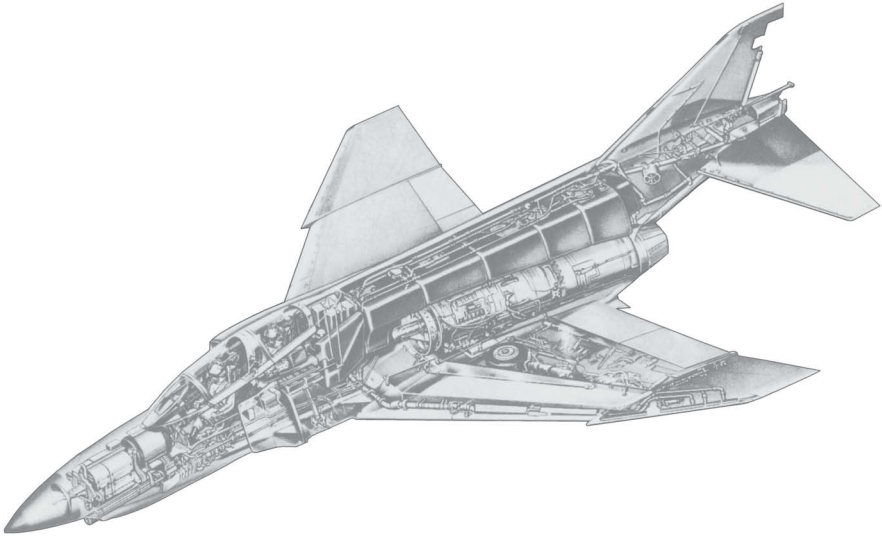


**Figure 8.4** Boeing F-15A Eagle internal arrangement ( $W_{TO} = 40,000$  lb,  $AR = 3$ ,  $W/S_{TO} = 66$  psf, two PW F-100 engines).  
(Courtesy of The Boeing Company.)





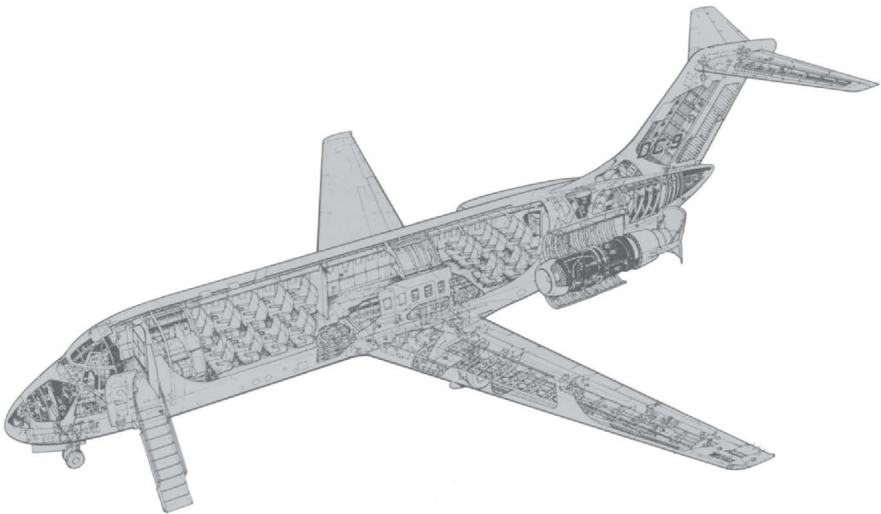
**Figure 8.5** Boeing F-18C Hornet internal arrangement ( $W_{T0} = 56,000$  lb,  $AR = 3.5$ ,  $W/S_{T0} = 140$  psf, two GE F404-400 turbofans).  
(Courtesy of The Boeing Company.)



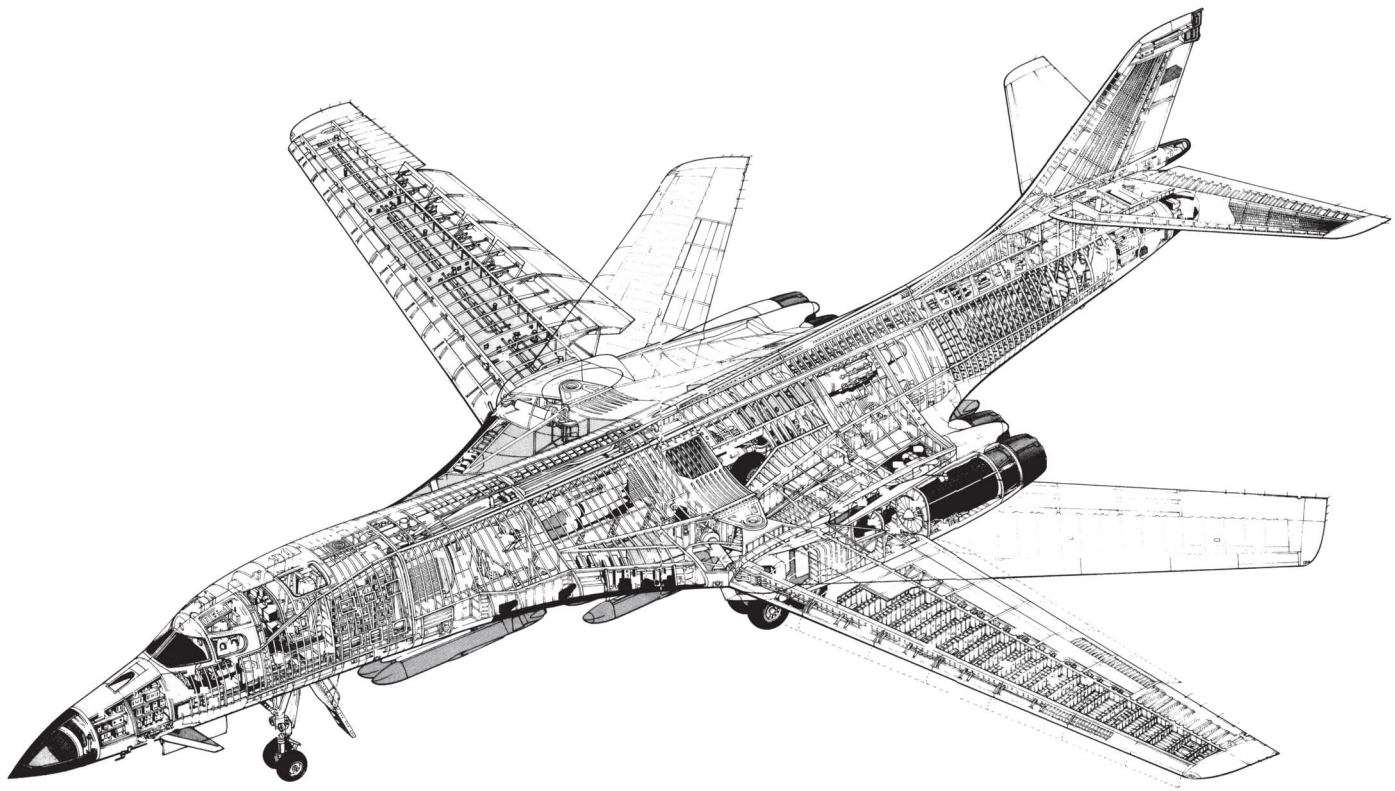
**Figure 8.6** F-4 Phantom II internal arrangement, a high-performance fighter-bomber ( $W_{TO} = 54,000$  lb, length = 58 ft, wing span = 38.5 ft, maximum Mach = 2.1). (Courtesy of The Boeing Company.)

made from Figs. 8.4 and 8.5. Internal arrangements for the B-1, F-16, and Piper Comanche are given as further examples in Figs. 8.8–8.10.

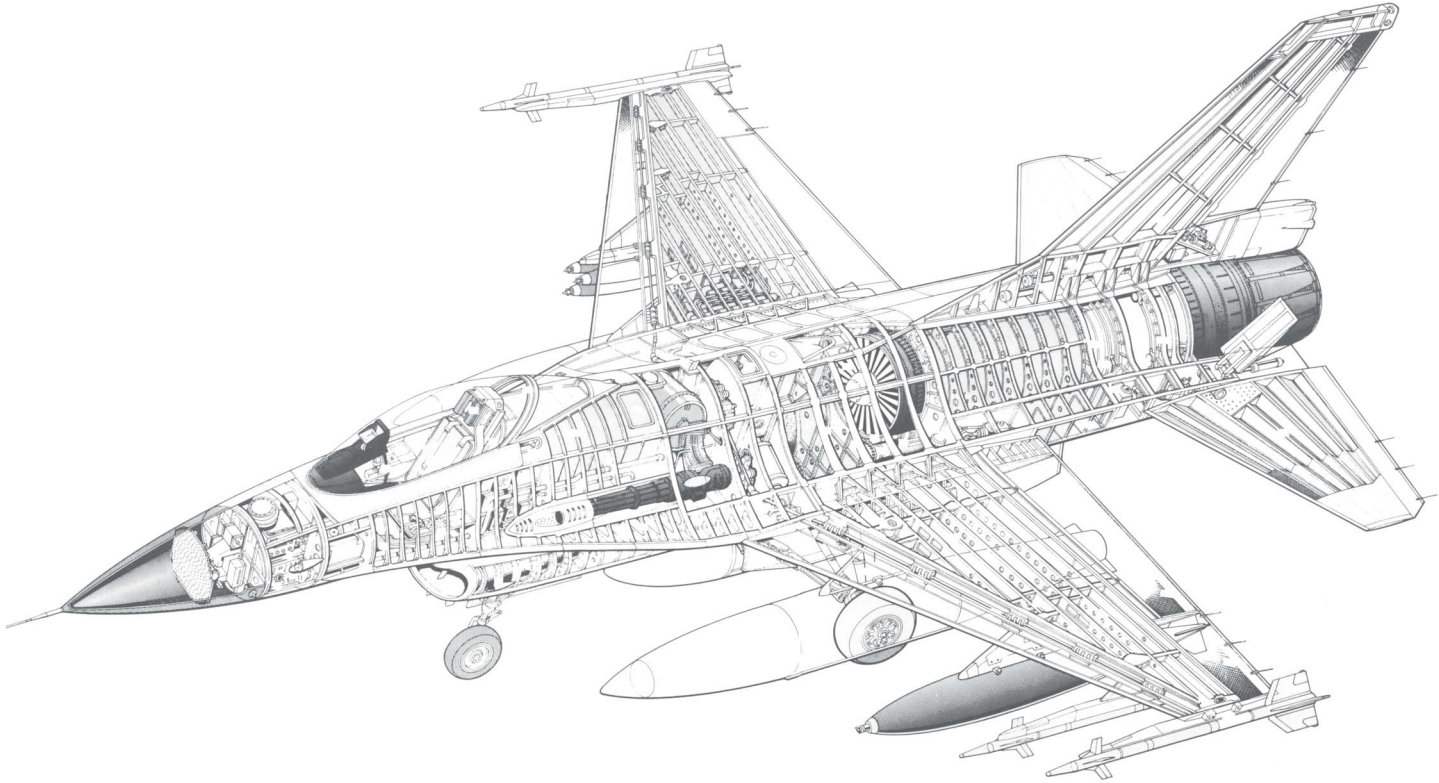
If jet engines are mounted in or partially within the fuselage, the volume required for the inlet must be reserved. A first estimate of the inlet volume



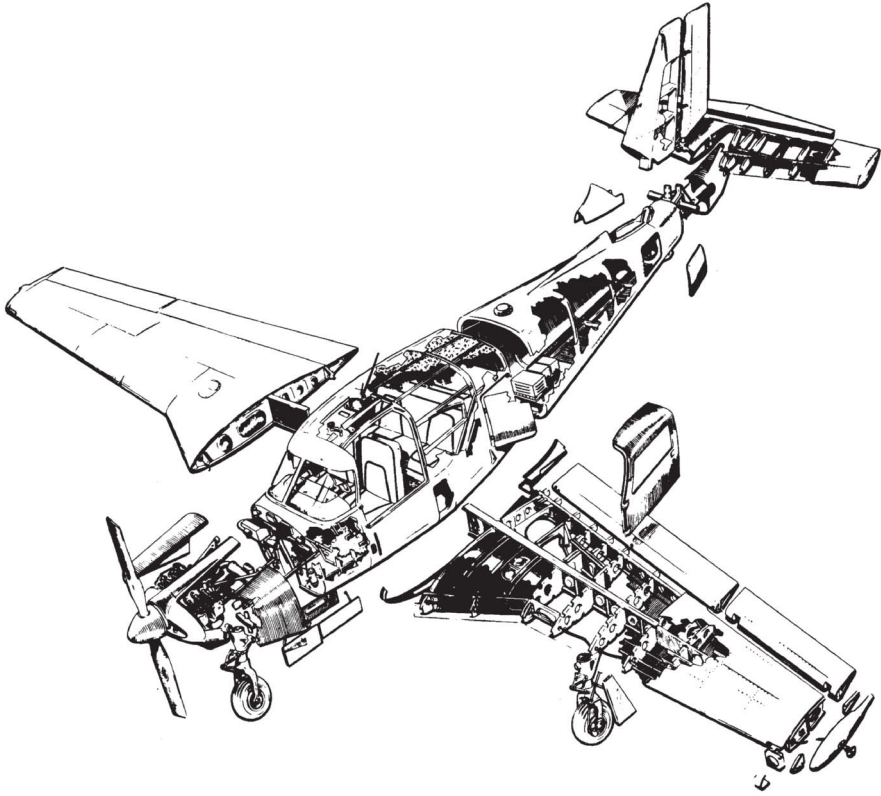
**Figure 8.7** DC-9 internal arrangement, a subsonic, short- to medium-range jet transport ( $W_{TO} = 114,000$  lb, 70–125 passengers, two JT8D turbofans). (Courtesy of The Boeing Company.)



**Figure 8.8** Boeing B-1B Lancer internal arrangement [ $W_{TO} = 477,000$  lb,  $AR(\text{ext}) = 9.6$ ,  $AR(\text{swept}) = 3.1$ , four GE F-101-102 turbofans]. (Courtesy of The Boeing Company.)



**Figure 8.9** Lockheed Martin F-16A Fighting Falcon internal arrangement ( $W_{TO} = 33,000$  lb, wing span = 32.8 ft, length = 49.3 ft, one PW F-100-100 turbofan).



**Figure 8.10** Piper Comanche internal arrangement, a four-place general aviation aircraft ( $W_{TO} = 2800$  lb,  $W_{empty} = 1600$  lb, length = 24.9 ft, wing span = 36 ft) (courtesy of Piper Aircraft Corp.).

required can be determined by using the diameter of the engine compressor face and a length equal to six-tenths of the engine length.

### 8.1.10 Fuel

The large quantity of fuel required for the mission will be carried within the fuselage, the wing structure, or both. The decision must be made about where to store fuel and how “wet” the wing structure will be. Final fuel placement will depend a great deal upon weight and balance requirements plus vulnerability to enemy fire. Use the fuel densities in Table 8.6 to determine the fuel volume requirements.

Locate the fuel around the c.g. with provision for pumping fuel to keep the c.g. envelope small. The wing is usually a good place to put the fuel as the wing is always located close to the c.g., resulting in a small c.g. movement as the fuel is burned. The fuel tank volume required to house the fuel

**Table 8.6** Fuel Densities

Fuel	Gallon Weighs (lb)	Cubic Foot Weighs (lb)
JP-4	6.5	48.6
JP-5	6.8	51.1
JP-8	6.7	50
Aviation gas	6.0	44.9

is determined using *packaging factors*, which account for the increased tank volume to accommodate structure, pumps, baffles, fuel lines, and general fuel tank inefficiencies:

$$\text{Tank volume} = (\text{fuel volume})/(\text{packaging factor})$$

When locating the fuel tanks in the aircraft, use the following packaging factors:

Tank Type and Location	Packaging Factor
<b>Integral tank</b>	
Shallow fuselage	0.8
Deep fuselage	0.85
Wing	0.75
<b>Bladder tank</b>	
Fuselage	0.75
Wing	0.65

### 8.1.11 Avionics

The *avionics equipment* consists of the communications and navigation gear, radar, fire control system, penetration aids, autopilot, and instrumentation. This equipment may be included in the mission specifications or left up to the designer. Table 8.7 lists current avionics weights and volumes for common avionics systems. If the weight of the avionics gear is known, the volume required can be estimated by assuming an avionics equipment density of 45 lb/ft<sup>3</sup>. If the power or volume requirements are known, the avionics equipment weights can be determined from Table 8.8.

Avionics equipment must be maintained frequently, so the equipment must be located for easy access by the ground crew. The equipment must not be stacked, which would require that a good piece of equipment be removed to get to the faulty piece. McDonnell did not adhere to this rule in the F-4 and located some avionics equipment under the rear ejection seat. U.S. Air Force maintenance records reported the rear ejection seat as a “high maintenance” item when in fact it was getting a bad rap: it

was being removed frequently only to get to the low-reliability avionics equipment [5].

In many cases the avionics equipment will need to be cooled, so make provision for good cooling by locating the items on cooling plates and separating the items for good air circulation.

**Table 8.7** Weights and Volumes for Common Avionics Equipment

Item <sup>a</sup>	Model Designation	Volume (ft <sup>3</sup> )	Weight (lb)
Intercom system	AIC-25	—	19.2
UHF communications	ARC-109	—	51.0
	ARC-150	0.21	11.0
UHF DF homing	705CA	—	5.0
Air-to-ground IFF	APX-64	—	53.0
	APX-92	0.11	13.0
TACAN	ARN-52	—	61.0
	ARN-100	1.1	46.0
ILS-VOR	ARN-584	—	27.0
	RCS-AVN-220	0.05	3.5
Gyrocompass	ASN-89	0.21	8.4
Inertial navigation system	AJQ-20	—	207.0
	LN-30	1.08	44.0
High-frequency radio	ARC-123	—	78.4
Autopilot system	—	—	168.5
Air data computer	AXC-710	0.5	14.0
Radar warning and homing	APS-109	—	182.0
	APR-41	0.17	22.0
ECM equipment	ALQ-103	—	637.0
Countermeasures dispensing set I	ALE-28	—	117.0
Countermeasures receiving set	ALR-23	—	94.0
Radar altimeter	APN-167	—	38.2
Attack radar	APQ-113	—	387.2
Range-only radar	SSR-1 (GE)	0.55	25.0
Terrain-following radar	APQ-110	—	249.0
Head-up display	TSP-2199	1.6	37.0
Gun camera	16-mm Telford	0.03	2.0
Lead computing optical sight	ASG-23	—	5.0
Flight data recorder	—	0.3	15.6

<sup>a</sup>Abbreviations: UHF, ultrahigh frequency; DF, direction finder; IFF, identification, friend or foe; TACAN, tactical air navigation; ILS-VOR, instrument landing system, very-high-frequency omnidirectional radio; ECM, electronic countermeasures.

**Table 8.8** Statistical Methods for Estimating Avionics Weight Given Volume or Power

<p><b>Radar Systems:</b>  <math>Wt = 0.431(\text{Power})^{0.777}</math>      <math>Wt = 38.21(\text{Volume})^{0.873}</math>                      for radar weight (less antenna) in pounds, power in watts, and volume (less antenna) in cubic feet</p>
<p><b>Doppler Navigation Systems:</b>  <math>Wt = 0.408(\text{Power})^{0.868}</math>      <math>Wt = 29.67(\text{Volume})^{0.662}</math>                      for weight in pounds, power in watts, and volume in cubic feet</p>
<p><b>Inertial Navigation Systems:</b>  <math>Wt = 0.465(\text{Power})^{0.848}</math>      <math>Wt = 51.85(\text{Volume})^{0.738}</math>                      for weight in pounds, power in watts, and volume in cubic feet</p>
<p><b>TACAN Systems:</b>  <math>Wt = 13.61 + 0.104(\text{Power})</math>      <math>Wt = 0.311(\text{Volume})^{0.704}</math>                      for weight in pounds, power in watts, and volume in cubic inches</p>
<p><b>Receiver Systems:</b>  <math>Wt = 6.3 + 0.17(\text{Power})</math>      <math>Wt = 44.5(\text{Volume})^{0.737}</math>                      for weight in pounds, power in watts, and volume in cubic feet</p>
<p><b>Transmitter Systems:</b>  <math>Wt = 0.73(\text{Power})^{0.610}</math>      <math>Wt = 6.4 + 40.2(\text{Volume})</math>                      for weight in pounds, power in watts, and volume in cubic feet</p>
<p><b>Identification Systems:</b>  <math>Wt = 0.607(\text{Power})^{0.724}</math>      <math>Wt = 0.069(\text{Volume})^{0.868}</math>                      for weight in pounds, power in watts, and volume in cubic inches</p>
<p><b>Computers:</b>  <math>Wt = 2.246(\text{Power})^{0.630}</math>      <math>Wt = 0.123(\text{Volume})^{0.817}</math>                      for weight in pounds, power in watts, and volume in cubic inches</p>
<p><b>Electronic Countermeasures (ECM):</b>  <math>Wt = 0.429(\text{Power})^{0.771}</math>      <math>Wt = 0.055(\text{Volume})^{0.912}</math>                      for weight in pounds, power in watts, and volume in cubic inches</p>

### 8.1.12 Wrap It Up

Once the required volume has been determined for each of the fuselage sections, the fuselage can be “packaged” (locating all the internal items in the fuselage) and the initial length determined. All equipment and subsystems should be designed for easy access. The rule for good “design for maintainability” is as follows:

- Place equipment one deep—do not stack or hide.
- Place equipment chest high—to minimize the need for stands and ladders on the flight line.



**Table 8.9** Initial Estimation of Empennage Weight

Aircraft Type	Empennage Area per Wing Area	Empennage Weight per Area
Jet transports	0.44	5.0
Business jets	0.43	4.3
General aviation		
Single engine	0.3	1.1
Twin engine	0.45	1.44
Intelligence, surveillance, and reconnaissance	0.2	3.0
Supersonic fighters		
Land based	0.39	7.0
Carrier based	0.48	6.0

- Make all replaceable equipment less than 40 lb—to minimize the need for more than one person or special equipment to remove or replace equipment (engines are exempt).

Consider the fuselage to be a cone-cylinder shape and assume a diameter. Then determine the length required for each of the fuselage sections. This will give the initial fuselage sizing requirement. The fuselage length and diameter can then be juggled to give the desired fuselage fineness ratio as discussed in Section 8.2.

Locate the tail at the aft end of the fuselage and estimate the empennage (horizontal plus vertical tails) weight from Table 8.9 (data from Appendix I).

Determine an initial c.g. location as follows: Assign a weight to every item of the aircraft except the fuselage, the wing, and any item on the wing (fuel, engines, weapons, etc.) and determine the c.g. of the ensemble. Chapter 20 contains weights of many of the minor items such as crew seats, passenger seats, galleys, and lavatories. The reason the fuselage is excluded is that the c.g. of the fuselage is typically about the c.g. of the aircraft, and the wing will be located at the c.g.

The wing is now located on the fuselage such that the c.g. is at approximately 30% of the wing mean aerodynamic chord. This location will be refined later as more becomes known about the airplane. The designer can now draw the complete airplane and locate the landing gear based on the guidelines in Section 8.1.7. The tip-back and tip-over angles discussed in Section 8.1.7 should be checked.

## 8.2 Fuselage Fineness Ratio

The *fuselage fineness ratio* is defined as the fuselage length divided by its diameter,  $l/d$ . The optimum  $l/d$  for the fuselage is different for subsonic and supersonic flow:

- **Subsonic flight.** The subsonic  $C_{D_0}$  for a fuselage is a compromise between skin friction drag coefficient  $C_F$  and the pressure drag coefficient due to viscous separation  $C_{D_{p_{\min}}}$ . The variation of subsonic  $C_{D_0}$  (based upon maximum cross-sectional area) with the inverse of fineness ratio,  $d/l$ , is shown in Fig. 8.11 [6]. A  $d/l = 1$  is a sphere and Fig. 8.11 shows that  $C_{D_0}$  is predominately viscous separation. The  $C_{D_0}$  has a minimum value at a  $d/l$  of approximately 0.33. Thus, a fineness ratio of 3 gives near-minimum  $C_{D_0}$  for subsonic flight.
- **Supersonic flight.** For supersonic flow the  $C_{D_0}$  on a streamlined body (i.e., no blunt base) is a compromise between skin friction  $C_F$  and wave drag  $C_{D_w}$ . The variation of supersonic  $C_{D_0}$  with  $d/l$  is shown in Fig. 8.11 [6]. From Fig. 8.11 the minimum  $C_{D_0}$  occurs for a fineness ratio of approximately 14.
- **Mixed subsonic and supersonic flight.** If the aircraft spends the majority of its flight at either subsonic or supersonic speeds, then the fineness ratios just discussed should be used. An SST is an aircraft that should have a fineness ratio of 14, for example. However, if the aircraft spends about half of its flight at subsonic and the other half at supersonic speeds, then the fuselage fineness ratio should be a compromise between the two conflicting criteria. The F-15 and other fighter aircraft should have a fineness ratio of 8–10 for minimum fuselage  $C_{D_0}$ .

## 8.3 Fuselage Shapes

The fuselage should be a streamlined shape with a tapered aft end. A blunt aft end would cause the flow to separate, with a large increase in  $C_{D_0}$  due to the afterbody separation drag (called *base drag* in supersonic flow). Some possible shapes for the fuselage are discussed in the following subsections.

### 8.3.1 Cone-cylinder

The  $C_{D_0}$  is easy to determine because subsonically it is primarily skin friction and supersonically  $C_{D_w} = C_p$ . The pressure coefficient  $C_p$  can be determined from the conical-shock charts in Appendix D.

### 8.3.2 Ogive-cylinder

The ogive is similar to a cone except its shape is formed by segments of arcs rather than by straight lines. It is better than a cone in that it has a greater volume for a given base diameter and length.

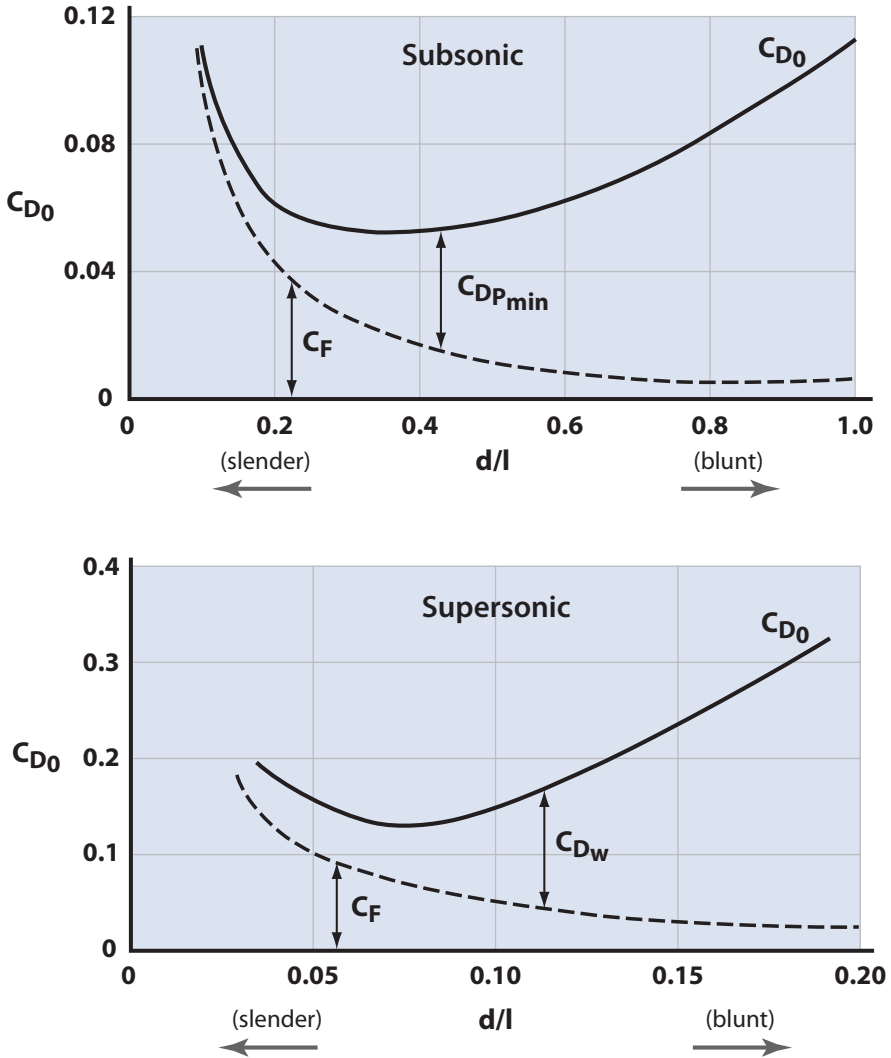


Figure 8.11 Subsonic and supersonic zero-lift drag for various fineness ratios.

### 8.3.3 Power Series-cylinder

The power series nose shapes are given by

$$\left( \frac{R}{d/2} \right) = \left( \frac{x}{\ell} \right)^n$$

where  $R$  is the radius at a given  $x$  location,  $d$  is the base diameter, and  $\ell$  is the length from nose to end of forebody. There is much data available in the literature for different values of  $n$ . An  $n = 3/4$  gives the minimum wave drag for this family. Notice that  $n = 1$  gives a cone.

### 8.3.4 Von Kármán Ogive

This is for a half-body of given length and diameter. The following results are from [7]:

$$\left(\frac{R}{R_{\max}}\right)^2 = \frac{1}{\pi} \left[ \frac{2x}{\ell} \sqrt{1 - \left(\frac{2x}{\ell}\right)^2} + \cos^{-1}\left(\frac{-2x}{\ell}\right) \right]$$

for  $-\ell/2 \leq x \leq \ell/2$ . The volume is  $(1/2)\ell S_{\max}$  and

$$C_{DW} = \frac{4S_{\max}}{\pi \ell^2}$$

### 8.3.5 Sears-Haack Body

This is for a complete body of given length and volume. The following results are from [7,8].

The area distribution is shown in Fig. 8.12 and is described by the equation

$$\left(\frac{R}{R_{\max}}\right)^2 = \left[ 1 - \left(\frac{2x}{\ell}\right)^2 \right]^{3/2} \quad \text{for } -\frac{\ell}{2} \leq x \leq \frac{\ell}{2}$$

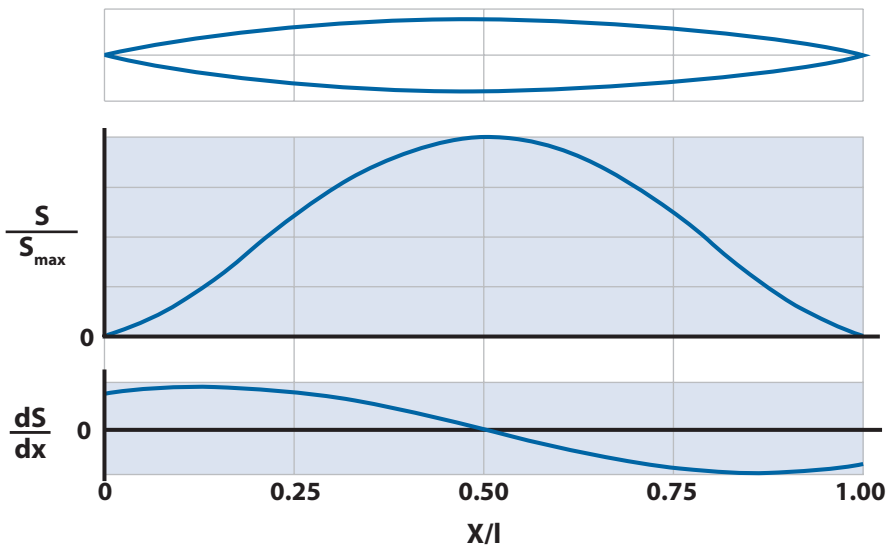


Figure 8.12 Sears-Haack body geometric characteristics.

The volume is  $(3/16)\ell S_{\max}$  and

$$C_{D_w} = \frac{9}{2} \frac{\pi}{\ell^2} S_{\max}$$

where the wave drag coefficient  $C_{D_w}$  is referenced to the maximum cross-sectional area  $S_{\max}$ . The wetted area =  $1.8667(\text{length} \times \text{volume})^{1/2}$ .

The designer should not worry too much about the entire fuselage shape at this point. The supersonic wave drag is dependent upon the cross-sectional area distribution of the fuselage plus wing together. Thus, the fuselage is often indented or bulged out to give a smooth wing-body cross-sectional area distribution. This practice is called *area-ruling* and is discussed in the next section.

## 8.4 Transonic and Supersonic Area-Ruling

Wave drag interference effects in the transonic and supersonic range are greater than those in the subsonic region because of the higher local velocities of the individual components and the greater propagation of these perturbations from this source. The most successful and by far the most systematic method for predicting the transonic and supersonic wave drag is the area-rule concept.

The *area-rule method* is based upon the supersonic slender body theory discussed in [7,9]. It can be assumed that at large distances from the body the disturbances are independent of the arrangement of the components and are only a function of the cross-sectional area distribution. This means that the drag of a wing-body combination can be calculated as though the combination were a body of revolution with equivalent-area cross sections. This is shown in Fig. 8.13 for  $Mach = 1$ .

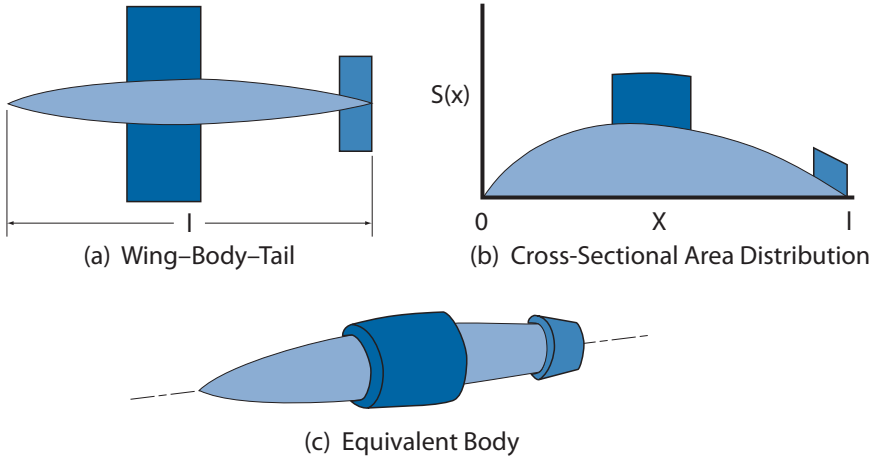
For  $Mach \geq 1.0$ , the cross-sectional areas  $S(x)$  are along planes inclined at the angle  $\mu = \arcsin(1/M_\infty)$  to the  $x$  axis. There is a different  $S(x)$  for each roll angle  $\phi$ . This is shown in Fig. 8.14.

Once the area distribution  $S(x)$  is determined [one  $S(x)$  for each  $\phi$  angle for  $M_\infty > 1$ ] the wave drag is calculated using the following expression [9] developed from supersonic slender body (linear) theory:

$$C_{D_w} = \frac{-1}{2\pi S_{\text{ref}}} \int_0^\ell \int_0^\ell \frac{d^2 S}{dx^2} \frac{d^2 S}{d\xi^2} \ln(x - \xi) dx d\xi \quad (8.1)$$

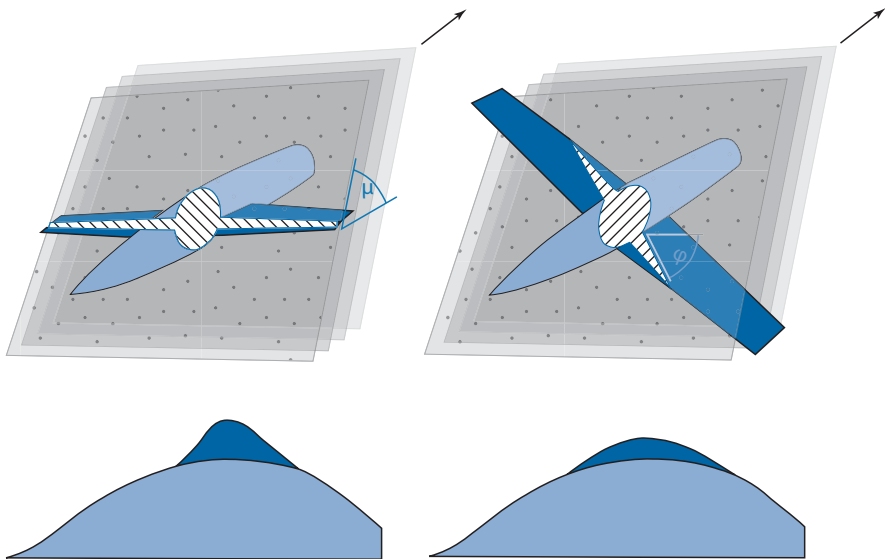
For  $M_\infty > 1$  the  $C_{D_w}$  is determined for each roll angle  $\phi$  and then averaged. Application of the area-rule method usually requires automatic computing equipment.

The area-rule method suggests the most desirable way to arrange the vehicle components for minimum wave drag at a particular  $M_\infty$ . A study of



**Figure 8.13** Equivalent body for a wing-body-tail combination at  $M_\infty = 1$ .

Eq. (8.1) indicates that at the very least it is desirable to have a smooth cross-sectional area distribution  $dS/dx$  as any discontinuities would give large values of  $d^2S/dx^2$  or  $d^2S/d\xi^2$ . The most common example of this is to indent or “coke bottle” the fuselage enough to permit the wing to be added without a sharp discontinuity appearing on the  $S(x)$  distribution. If the cross-sectional area distribution of a wing-body combination at a particular  $M_\infty$  is the same as a Sears-Haack distribution (see Fig. 8.12), the con-



**Figure 8.14** Area distribution given by intersection of Mach planes for  $M_\infty > 1$ .

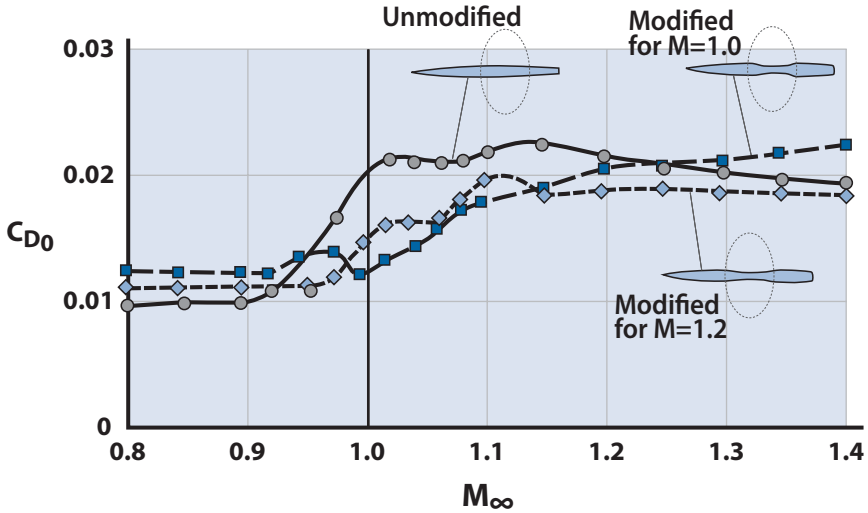


Figure 8.15 Wave drag of bodies with elliptic wings and with or without area-ruling.

figuration produces minimum wave drag at that  $M_\infty$ . Thus, a wing-body can be configured to give minimum wave drag at one Mach number but will usually aggravate the wave drag at other Mach numbers. Figure 8.15 demonstrates this (data from [10]).

An aircraft before area-ruling might have cross-sectional area distribution for  $M_\infty = 1$  as shown in Fig. 8.16 Aircraft are usually area-ruled for  $M_\infty$

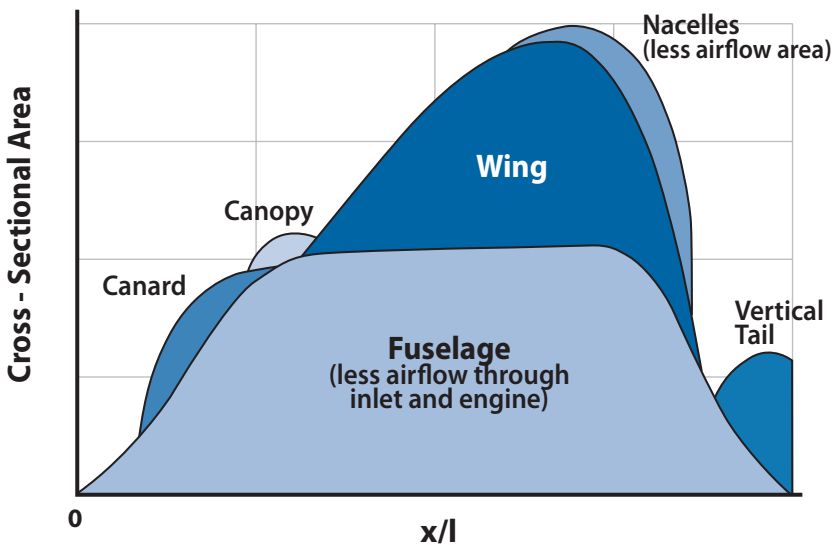


Figure 8.16 Typical cross-sectional area distribution for an aircraft before area-ruling.

= 1 because of the tendency for a “thrust pinch” at  $M_\infty = 1$ . However, if the aircraft will spend a major portion of its mission at  $M > 1$  (such as the Concorde) it should be area-ruled along planes inclined at the Mach angle as shown in Fig. 8.14. It should be pointed out that the cross-sectional area does not include the area of the air flow through the engine. The designer would take the area distribution of Fig. 8.16 and massage it until it is free of discontinuities and looks more like that of a Sears–Haack body than it originally did.

## References

- [1] Roskam, J., “Airplane Design,” Roskam Aviation and Engineering Corp., Ottawa, KS, 1989. [Available via [www.darcorp.com](http://www.darcorp.com) (accessed 31 Oct. 2009).]
- [2] “Airworthiness Standards: Part 25—Transport Category Airplanes,” *Federal Aviation Regulation*, Vol. 3, U.S. Department of Transportation, U.S. Government Printing Office, Washington, DC, 2009.
- [3] Whitford, R., *Design for Air Combat*, Jane’s Publ., New York, 1987.
- [4] Wood, K. D., *Aircraft Design*, Vol. 1, Johnson, Boulder, CO, 1966.
- [5] *Aerospace Daily*, Vol. 135, No. 15, Sep. 1985, p. 113.
- [6] Miele, A., *Flight Mechanics*, Vol. 1, Addison Wesley, Reading, MA, 1962.
- [7] Ashley, H., and Landahl, M., *Aerodynamics of Wings and Bodies*, Addison Wesley, Reading, MA, 1965.
- [8] Sears, W. R., “On Projectiles of Minimum Drag,” *Quarterly Mathematics Series*, Vol. 4, No. 4, 1947, p. 361.
- [9] Liepmann, H. W., and Roshko, A., *Elements of Gasdynamics*, Wiley, New York, 1957.
- [10] Nelson, R. L., and Walsh, C. J., “Some Examples of the Application of the Transonic and Supersonic Area Rules to the Prediction of Wave Drag,” NASA TN-D-446, Sept. 1960.



# Chapter 9 High-Lift Devices



- Mechanical High-Lift Devices
- Leading- & Trailing-Edge Flaps
- Slots & Slats
- Conversion of Airfoil to Wing Data
- Powered High-Lift Devices for STOL
- Powered High-Lift Devices for VTOL
- Vectored Thrust
- Lift Fan

The McDonnell Douglas YC-15 features externally blown flaps. This aircraft met Advanced Medium STOL Transport requirements but never saw production (see Section 9.6). One of the YC-15 prototypes is on display outside the main gate of Edwards AFB in California.

*Quality is never an accident; it is always the result of intelligent effort.*

John Ruskin

## 9.1 Introduction

To increase the lift of a wing, the suction on the upper surface must be increased relative to that on the lower surface (see Fig. 2.3) and separation delayed or prevented. The suction may be increased by increasing the wing angle-of-attack and by making the airfoil camber more positive in the region of the trailing edge (TE). A TE flap [and to a small extent a leading edge (LE) flap] effectively increases the airfoil camber and increases the air flow acceleration on the upper surface (and overall wing circulation) resulting in an increase in  $C_L$ . This increase in  $C_L$  is observed as an increase in the magnitude of the angle for zero lift,  $\alpha_{0L}$ . Separation is prevented by reducing the adverse pressure gradient over the top of the airfoil or by stabilizing the boundary layer using suction or blowing.

*High-lift devices* fall into two distinct categories: unpowered or mechanical high-lift devices and powered-lift devices. Mechanical high-lift devices are of two types: (1) TE flaps, which operate by increasing the camber of the airfoil, and (2) separation delay devices. The separation delay devices most commonly used are LE flaps, slats, or slots plus boundary layer control. This chapter considers mechanical high-lift devices in detail. The more practical powered-lift concepts are internal and external blown flaps, deflected slipstream and upper surface blowing, jet flap, lift-fan, tilt wing, direct jet lift, and augmentor wing. These powered-lift concepts are designed for application to *vertical or short takeoff and landing* (V/STOL) and are discussed briefly at the end of the chapter.

## 9.2 Mechanical High-Lift Devices: Trailing Edge Flaps

Trailing edge flaps operate by changing the camber of the airfoil section as shown in Fig. 9.1. The camber is made more positive in the region of the trailing edge, which has a powerful influence on making  $\alpha_{0L}$  more negative [1–3]. A camber change in the region of the leading edge has only a small influence on  $\alpha_{0L}$ . The section lift coefficient is expressed as

$$C_{\ell} = \frac{dC_{\ell}}{d\alpha}(\alpha - \alpha_{0L}) = C_{\ell\alpha}(\alpha - \alpha_{0L}) \quad (9.1)$$

where  $\alpha$  is the angle between the unflapped section chord line and the freestream velocity. The performance of trailing edge flaps is shown qualitatively on Fig. 9.2.

Figure 9.1 shows some typical TE high-lift devices. Notice that an aileron is nothing more than a plain flap that operates with both positive

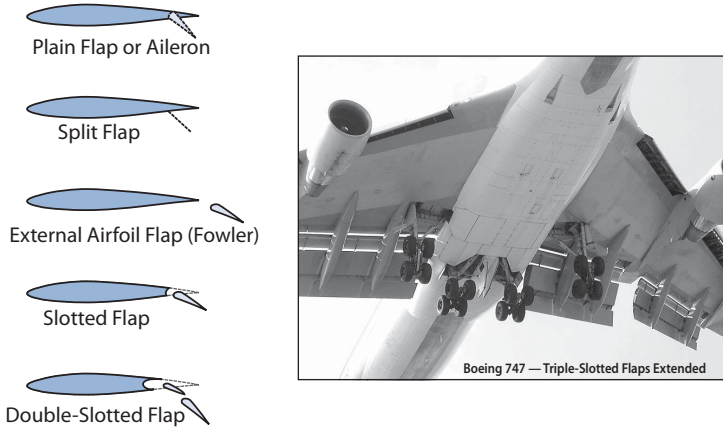


Figure 9.1 Typical TE high-lift devices.

and negative deflections. Also note that the effective area of the wing is increased slightly for Fowler or double-slotted flaps, but the  $C_{L_{max}}$  is referenced to the baseline unflapped wing reference area.

Trailing edge flaps do not prevent flow separation; in fact, they aggravate flow separation slightly (decrease  $\alpha_{stall}$  slightly as shown in Fig. 9.2) due to the increase in upwash at the leading edge due to increased circulation. Wing sweep promotes stall as discussed in Chapter 2. Thus, trailing edge flaps become less effective as the wing sweep is increased. (This effect is shown as a correction in Fig. 9.23.) Trailing edge flaps are very effective on wings swept up to about 35 deg.

### 9.3 Mechanical High-Lift Devices: Separation Delay Devices

Flow separation from the top of the airfoil, that is, stall, results from the loss of the kinetic energy in the boundary layer due to viscous shear and an

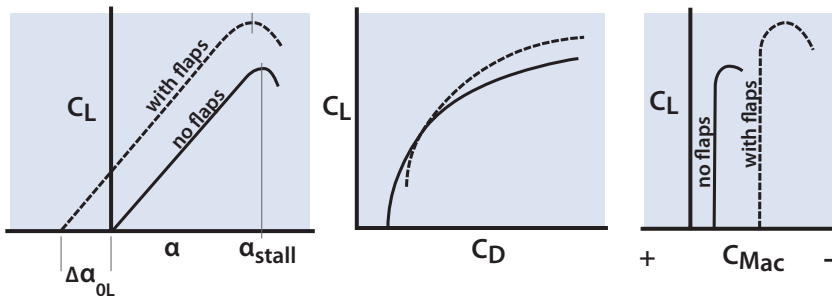


Figure 9.2 Characteristics of TE flaps.

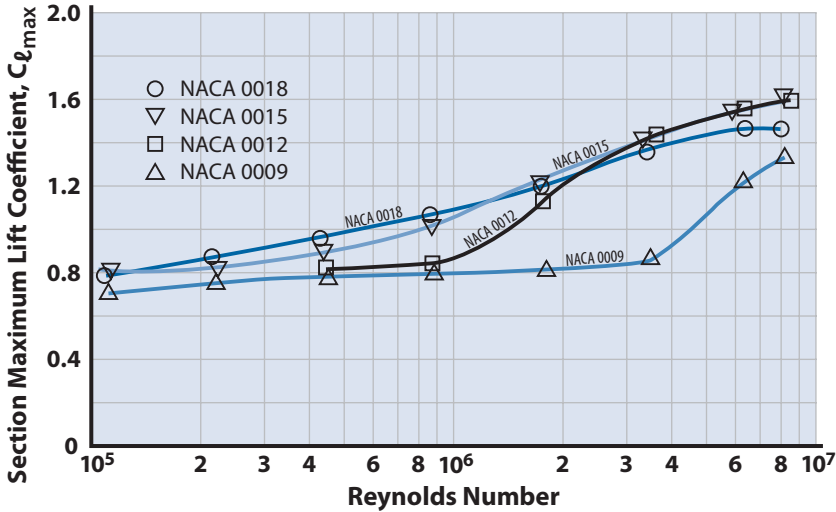


Figure 9.3 Variation of maximum section lift coefficient with Reynolds number.

adverse pressure gradient [4]. A turbulent boundary layer is better able to delay flow separation than a laminar boundary layer because of the higher energy associated with the turbulence. For this reason it is better to have a turbulent boundary layer over the airfoil for lift at high alpha. Vortex generators are put on the top surface of a wing for the purpose of forcing the early transition of the boundary layer from laminar to turbulent. The effect of Reynolds number on  $C_{l_{max}}$  is shown in Fig. 9.3. Remember that the boundary layer usually transitions from laminar to turbulent at  $Re$  of one million.

### 9.3.1 Boundary Layer Control

Boundary layer control (BLC) consists of energizing the boundary layer by either suction or blowing so that the boundary layer can “fight” the adverse pressure gradient with increased energy and thereby delay separation. Boundary layer control devices will not be discussed here because:

1. Numerous papers on this subject exist and are easily available.
2. Significant operational issues become a major part of the system, such as the following:
  - There are large power requirements for the pumps.
  - Much maintenance is needed to keep suction holes and slots free and open.
  - The suction holes and slots cause a rough surface and give large drag at high speeds (if the system is not operative).

### 9.3.2 Slots and Slats

A *slot* or *slat* (movable slot) operates as shown in Fig. 9.4. The LE shape in the slot or slat is more blunt such that the air flowing through the slot or slat is accelerated and moves farther toward the rear of the airfoil section before slowing down and separating from the surface. Operation of the slat is either manual or automatic. The automatic slat operates at high  $C_L$  by the suction in the vicinity of the the LE. The Douglas A-4 Skyhawk had automatic slats that worked quite well during high- $C_L$  maneuvering [5]. Occasionally during a tight turn the slat on one wing would pop out and the slat on the other wing would not. The result was a rapid roll and a surprised pilot. The slats on the A-4 could be manually locked in or out for landing and takeoff.

The principal disadvantage of slots and slats is that a high  $\alpha$  is required for  $C_{l_{\max}}$ . Also, it is hard to put slots or slats on very thin wings. They are best if used full span, but the main advantage is they protect the outboard wing by reducing tip stall. Slots and slats continue to give beneficial results for sweep greater than 45 deg because they reduce separation near the tip and thus reduce tip stall.

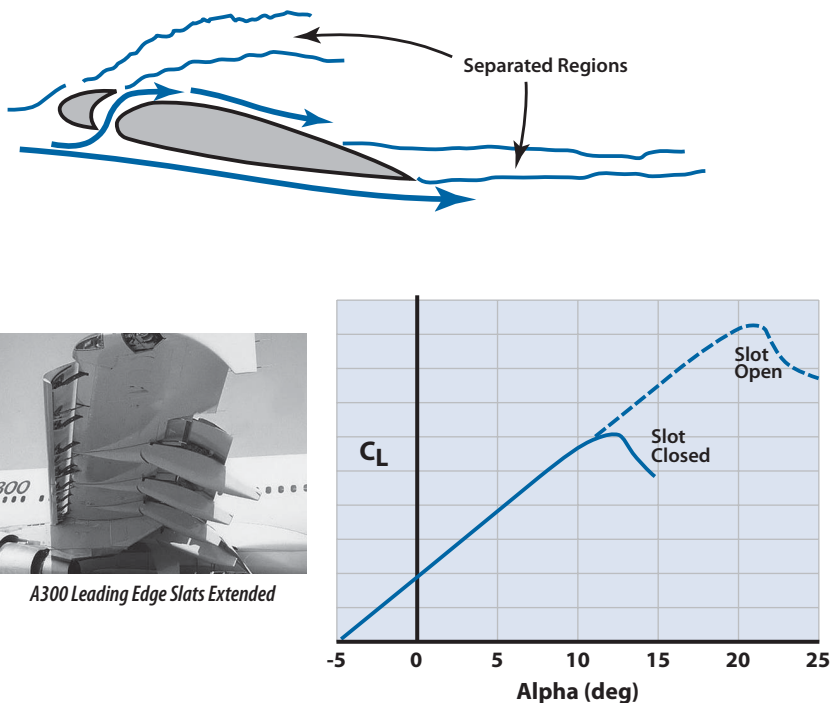


Figure 9.4 Characteristics of slots and slats.

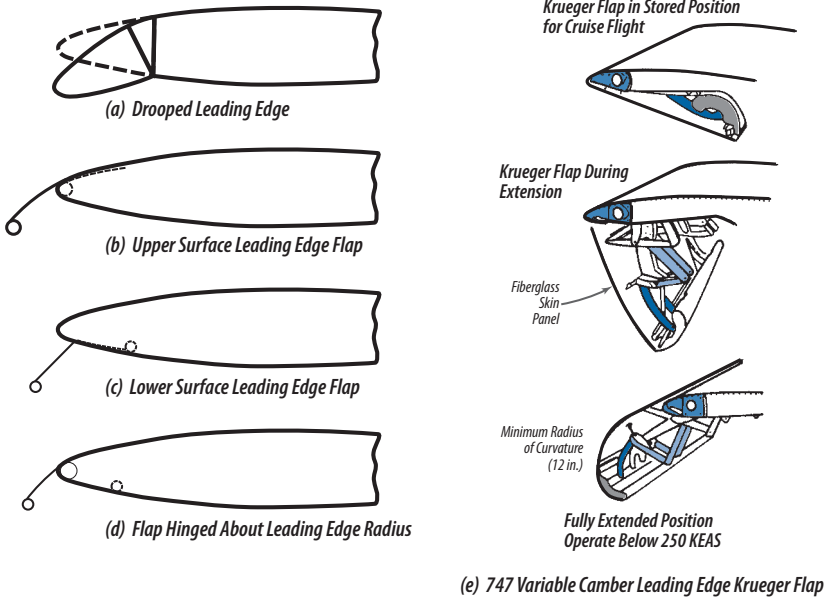


Figure 9.5 Various LE flap devices.

### 9.3.3 Leading Edge Flaps

Various types of LE flaps are shown in Fig. 9.5. They operate by making the leading edge more rounded and work well on sharp-nosed airfoil sections as shown in Fig. 7.6 of Chapter 7. Because LE flaps change the camber of the section there is a slight change in  $\alpha_{0L}$  as shown in Fig. 9.6. Leading edge flaps are more effective than slots on highly swept wings [6]. They are usually employed over the outer half-span to reduce tip stall. Typically, optimum flap deflections are between 30 and 40 deg.

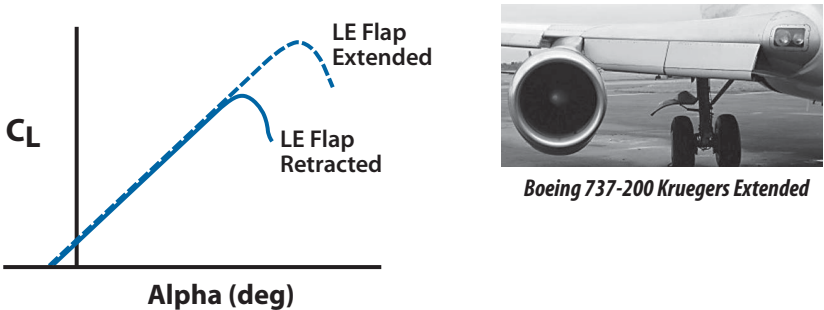


Figure 9.6 Characteristics of LE flaps.

### 9.3.4 Practical Mechanical High-Lift Systems

The mechanical high-lift devices just discussed are integrated into practical high-lift systems for aircraft to meet the requirements for takeoff, landing, and maneuvering. The low-speed  $C_{L_{\max}}$  is usually driven by takeoff and landing requirements to meet the runway length available at airports of interest. Remember that when designing the high-lift system for takeoff and landing the  $C_{L_{\max}}$  has to be usable. That means that the  $C_{L_{\max}}$  must be available within the limits of the aircraft over-nose vision angle and the tip-back angle (review Chapter 8, Table 8.4 and Fig. 8.3). A  $C_{L_{\max}}$  of 3.0 at an  $\alpha$  of 30 deg is of little value if the aircraft's aft fuselage strikes the ground at an  $\alpha$  of 16 deg. Typical limits for takeoff and landing angles-of-attack are 12–16 deg for fighter aircraft, 10–14 deg for transports, and 8–12 deg for general aviation (GA) aircraft due to tip-back angles and over-nose vision.

Fighter aircraft usually have a high  $T/W$  (typically  $> 0.5$ ) so that takeoff is not a problem and the landing distance establishes  $C_{L_{\max}}$ . Transport aircraft have lower  $T/W$  (typically  $< 0.35$ ) and either takeoff or landing will determine  $C_{L_{\max}}$ . General aviation aircraft with their low wing loadings do not need much  $C_{L_{\max}}$  to operate in and out of local airports with 3000-ft fields.

Typical measured data on slots, slats, LE flaps, and TE flaps is presented in Tables 9.1, 9.2, and 9.3. Figure 9.7 shows the practical low-speed  $C_{L_{\max}}$  limits for mechanical high-lift systems (note that the reference area remains the original wing area and does not change to reflect an increased area for an extended LE or TE flap). Increasing wing sweep and decreasing wing aspect ratio (AR) both decrease the efficiency of the high-lift system. The Airbus A321-200 with its double-slotted TE Fowler flaps and full span LE slats (see the photograph in Fig. 9.4) sets the standard for the transport community with a  $C_{L_{\max}}$  of 3.2. The A321 flap system was designed to operate from the shorter runways at regional hub airports. The transport aircraft typically have thick airfoil sections ( $\sim 10\%$  or greater) and can accommodate the internal machinery required for the more sophisticated high-lift systems. The fighter aircraft shown in Fig. 9.7 have thinner airfoil sections and incorporate the more simple high-lift devices such as split or plain TE flaps and drooped LE flaps. General aviation aircraft (such as the Piper PA-30 and Cessna 177 Cardinal) have takeoff wing loadings less than 20 psf and operate from short-field airports using simple plain flap systems. The U-2S with its takeoff  $T/W > 0.35$  and  $W/S < 40$  psf does not need a high  $C_{L_{\max}}$  to meet landing and takeoff requirements. The U-2S has a partial-span, simple hinged plain flap, giving it a  $C_{L_{\max}}$  of 1.2 at a 15-deg flap deflection. The U-2S has a unique bicycle landing gear and does not rotate for takeoff (same for the B-52 and B-47).

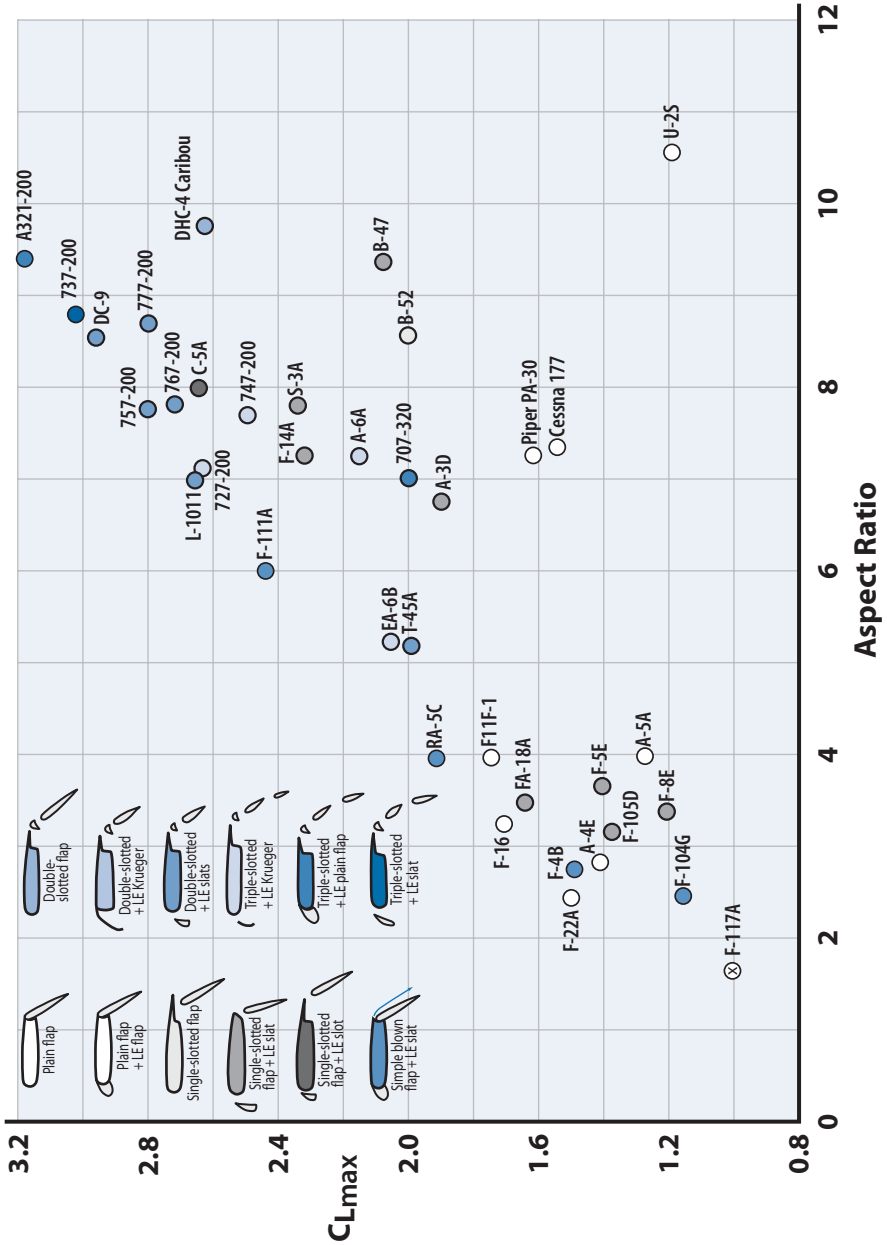


Figure 9.7 Practical low-speed  $C_{Lmax}$  limits for mechanical high-lift systems (data from [7]).



**Table 9.1** Mechanical High-Lift Systems and Maximum Lift Summary of Current Aircraft

<b>Current Aircraft Mechanical High-Lift Systems</b>				
<b>Aircraft</b>	<b>AR</b>	<b><math>C_{L_{max}}</math></b>	<b>Leading Edge</b>	<b>Trailing Edge</b>
707-320	7.0	2.0	Full-span plain flap	Triple-slotted Fowler
E-6A	7.0	2.16	Improved 707-320 system	
727-200	7.1	2.62	1/3 Krueger, 2/3 span slats	Triple-slotted Fowler
737-200	8.83	3.05	Krueger IB, slats OB <sup>a</sup>	Triple-slotted Fowler
747-400	7.7	2.5	Krueger IB, slats OB	Triple-slotted Fowler
757-200	7.77	2.8	Full-span slats	Double-slotted Fowler
767-200	7.9	2.75	Full-span slats	Double slot IB, single slot OB
777-200	8.7	2.8	Full-span slats	Double slot IB, single slot OB
787	Var.	NA	Krueger IB, slats OB	Triple-slotted Fowler+variable camber
A321-200	9.5	3.2	Full span slats	Double slotted Fowler+drooped ailerons
L-1011	6.95	2.65	Full-span slats	Double-slotted Fowler
S-3A	7.8	2.36	Slats OB of engine	Single-slotted Fowler
DC-9	8.5	2.96	Full-span slats	Full-span double-slotted flap
DHC-4	9.9	2.63	None	Full-span double-slotted flap
C-5A	8.0	2.64	Slots IB+slotted slats OB	Partial-span single-slotted Fowler
U-2S	10.6	1.21	None	Partial-span simple hinge flap
PA-30	7.3	1.6	None	Half-span plain flap
Cessna177	7.4	1.55	None	Half-span plain flap
B-47	9.42	2.05	Full-span slat	Partial-span Fowler
B-52G	8.56	2.0	None	Partial-span Fowler
F-16C	3.2	1.7	Full-span maneuver flap	Half-span plain flap
F-22A	2.36	1.48	Full-span maneuver flap	Full flaperon+drooped aileron
A-3D	6.75	1.9	Full-span slats	Partial-span single-slotted flap
F-4B	2.78	1.4	Full plain flap (blown)	Partial-span blown plain flap
A-4E	2.9	1.42	Automatic LE slats	1/2 split flap+drooped ailerons
RA-5C	4.0	1.9	Full-span plain flap	Partial-span plain flap (blown OB)
F-5E	3.7	1.4	Full-span plain flap	Partial-span single-slotted flap
A-6A	5.3	2.05	Full-span plain flaps	Partial-span Fowler flap
F-14A	7.25	2.35	Full-span LE slats	Full-span slotted flaps
F-111A	6.0	2.45	Full-span LE slats	Partial-span blown plain flap
F-117	1.65	0.95	None	None
F-18A	3.5	1.62	Full-span plain flap	Half-span single-slotted TE flap
F-105D	3.18	1.38	Full-span plain flap	Partial-span single-slotted flap
F-104G	2.45	1.12	Full-span plain flap	Blown flap+drooped aileron
T-45A	5.0	2.0	Full-span plain flap	2/3 span double-slotted flaps
F-8E	3.5	1.2	Full-span plain flap	2/3 plain flap+variable-incidence wing
F-11F	3.95	1.75	Full-span slats	Full-span plain flaps

<sup>a</sup>Abbreviations: IB, inboard; OB, outboard.

**Table 9.2** Summary of Maximum Lift Coefficient Obtained with Various Types of High-lift Devices (data from [5,8,9])

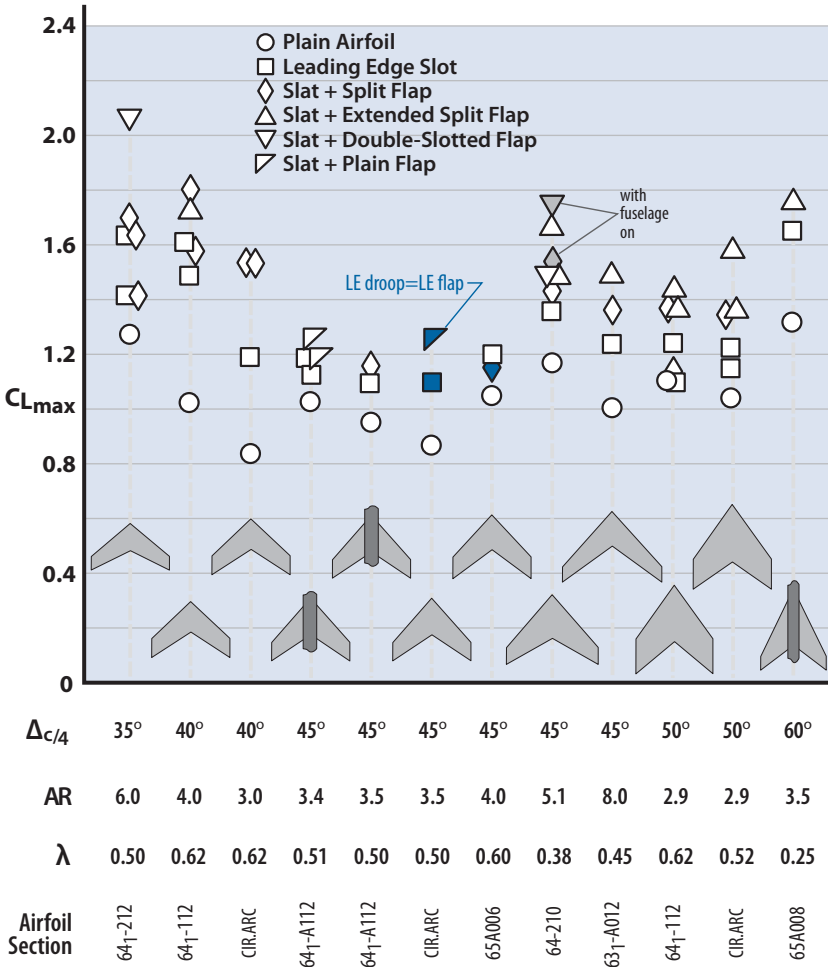


Figure 9.7 shows a trend of increasing  $C_{L_{max}}$  for increasing AR and flap system sophistication. The transport aircraft shown in Fig. 9.7 (i.e., the A321-200) represent the current practical limit in mechanical high-lift system sophistication.

### 9.4 Methods for Determining Maximum Subsonic $C_L$ of Mechanical Lift Devices

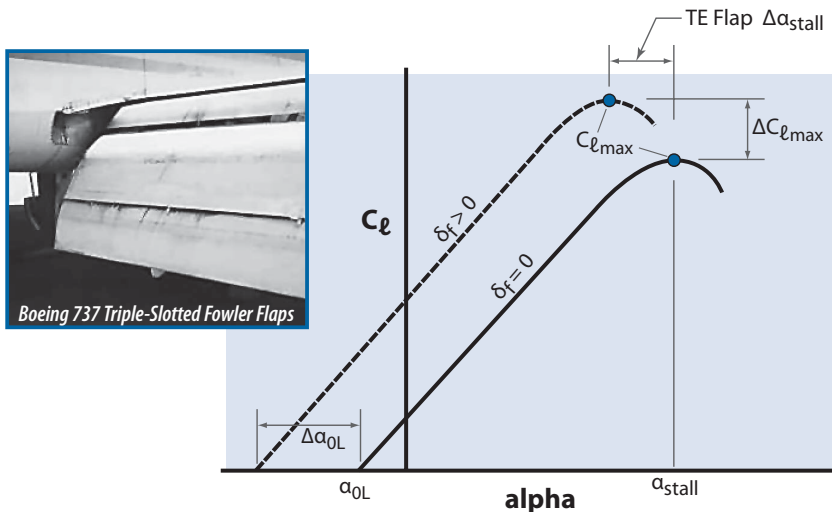
The method presented here is empirical and will give satisfactory results for the first iteration of the design loop [10]. The method involves determining the  $C_L$  vs  $\alpha$  curve for the basic wing and then correcting it for the effects of the mechanical high-lift devices.

**Table 9.3** Typical High-Lift Device Data

$\Delta = 35$ deg, $AR = 5.76$ , $\lambda = 0.54$		
Airfoil section: 10% symmetrical		
Arrangement	$C_{L_{max}}$	$\alpha_{stall}$
Plain wing	0.90	16
20% full-span split flap, $\delta f = 60$	1.45	10.6
20% full-span slat	1.38	23.6
20% full-span LE flap	1.49	26.5
20% full-span split flap + 20% full-span LE flap	2.01	19.7
$\Delta = 0$ deg, $AR = 4.0$ , $\lambda = 1.0$		
$Re = 10^5$		
Airfoil section: NACA 0010		
Arrangement	$C_{L_{max}}$	$\alpha_{stall}$
Plain wing	0.80	13
30% full-span split flap, $\delta f = 40$ deg	1.52	10
20% full-span slat	1.36	24

The airfoil section behavior with TE flaps is determined first. The construction of the  $C_\ell$  vs  $\alpha$  curve is shown in Fig. 9.8.

Values of  $\Delta\alpha_{0L}$ ,  $\Delta C_{\ell_{max}}$ , and  $\sim\Delta\alpha_{stall}$  are needed to complete the construction of Fig. 9.8. The first step is to obtain the section  $\alpha_{0L}$ ,  $C_{\ell_{\alpha'}}$ , and  $\alpha_{stall}$  from experimental data (i.e., Appendix F or [2,11,12]). If experimental data on



**Figure 9.8** Construction of section lift curves for TE flaps.

the selected airfoil section cannot be found, use  $C_{l\alpha} = 2\pi$  per radian and compute  $\alpha_{0L}$  using Eq. (2.4) of Chapter 2. Estimate  $C_{l_{max}}$  from Figs. 7.2 or 9.3, then use Eq. (9.1) to determine  $\alpha_{stall}$ .

Decide upon the type of TE flap, the flap-to-chord  $c_f/c$  ratio (see Fig. 9.9), and the flap deflection  $\delta_f$  (positive for downward deflection). The  $\Delta\alpha_{0L}$  is determined using the method outlined next (from [10]):

1. **Plain TE flaps.** Calculate the change in  $\alpha_{0L}$  for flap deflection  $\delta_f$ :

$$\Delta\alpha_{0L} = -\frac{dC_l}{d\delta_f} \frac{1}{C_{l\alpha}} \delta_f K'_f \tag{9.2}$$

where

$C_{l\alpha}$  = section lift curve slope (per radian) from Appendix F

$K'_f$  = correction for nonlinear effects, Fig. 9.9

$dC_l/d\delta_f$  = change in  $C_l$  for a change in  $\delta_f$ , Fig. 9.10

2. **Single-slotted flaps.**

$$\Delta\alpha_{0L} = -\frac{d\alpha}{d\delta_f} \delta_f \tag{9.3}$$

where  $d\alpha/d\delta_f$  is obtained from Fig. 9.11.

3. **Fowler flaps.** Use single-slotted flap method.

4. **Split flap.**

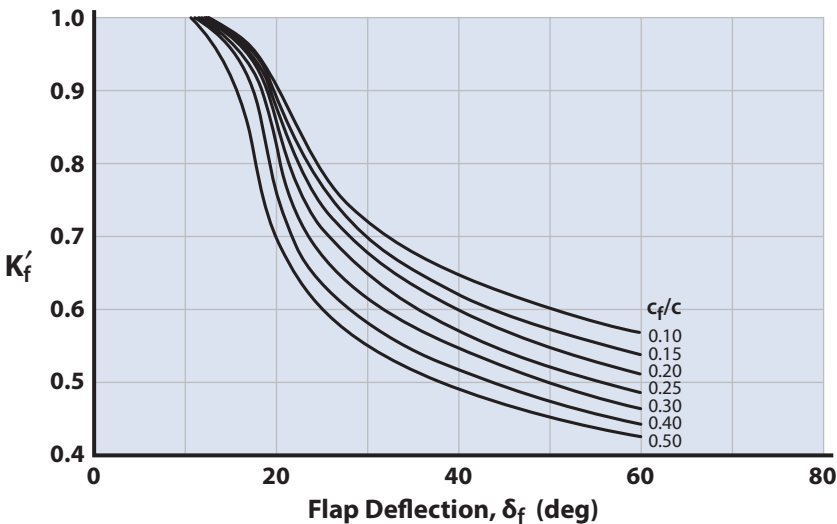


Figure 9.9 Nonlinear correction for plain TE flaps (adapted [10]).

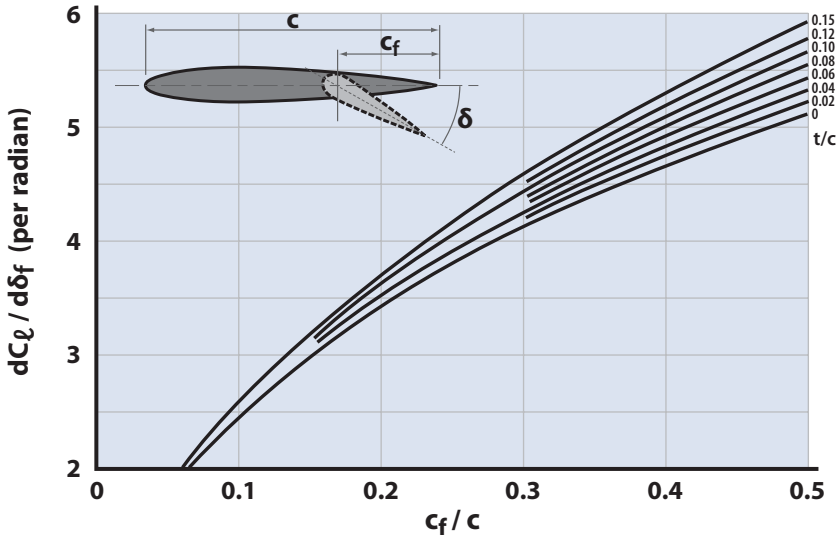


Figure 9.10 Variation of  $dC_{l_i}/d\delta_f$  with flap chord ratio (adapted [10]).

$$\Delta\alpha_{0L} = \frac{k}{C_{l\alpha}} (\Delta C_l)_{c_f/c=0.2}$$

where  $k$  and  $(\Delta C_l)_{c_f/c=0.2}$  are obtained from Fig. 9.12.

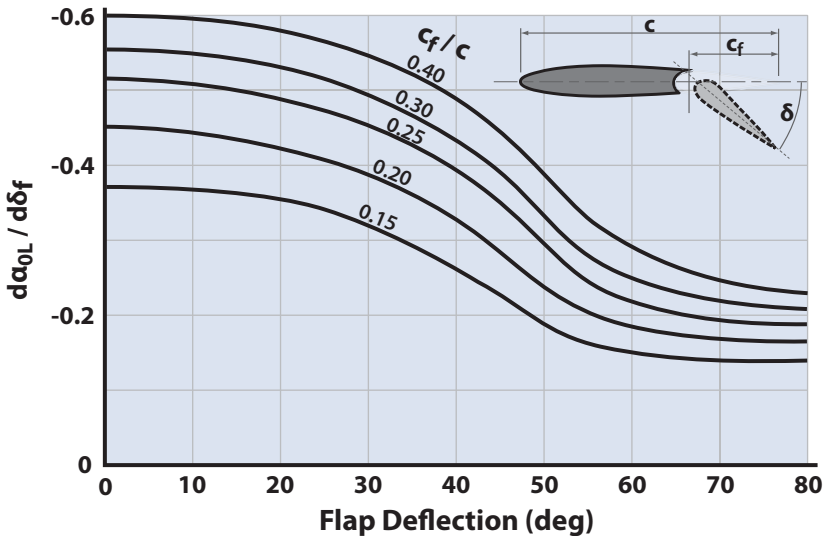


Figure 9.11 Section lift effectiveness parameter for single-slotted flaps (adapted [10]).

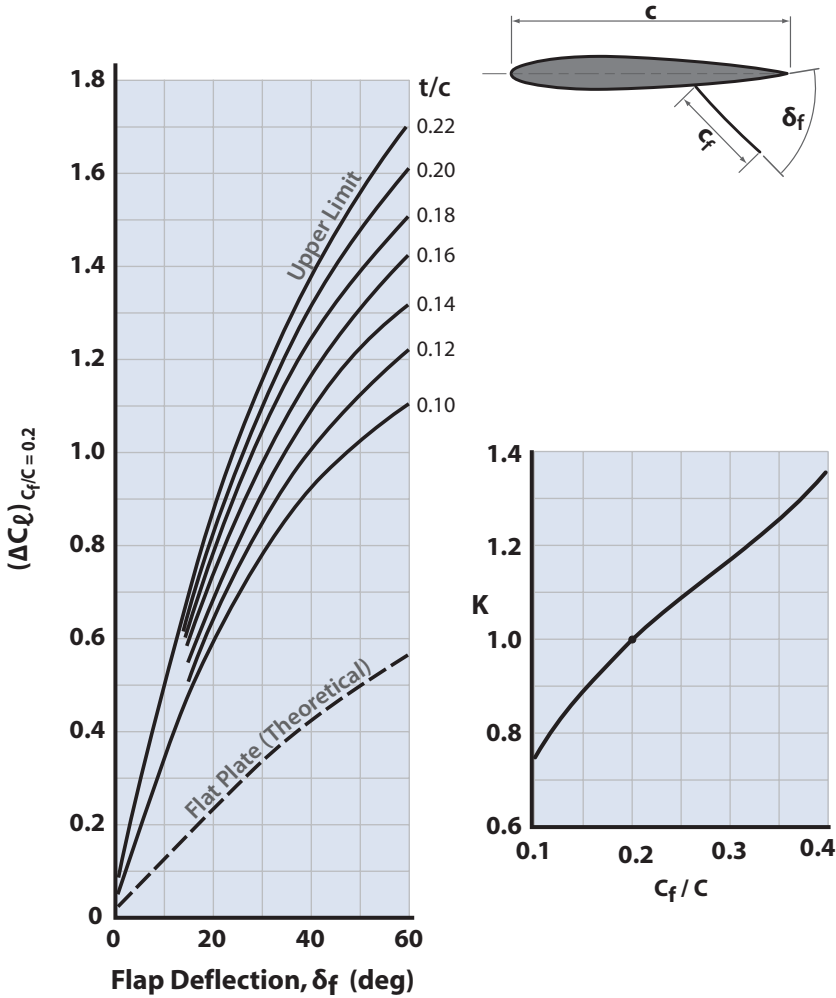


Figure 9.12 Empirical constants for split flap analysis (adapted [10]).

Now construct the  $C_\ell$  vs  $\alpha$  curve as shown in Fig. 9.8. The TE flaps aggravate separation slightly and the section  $\alpha_{\text{stall}}$  decreases. This  $\alpha_{\text{stall}}$  is obtained from Fig. 9.13. Estimate  $\Delta C_{\ell_{\text{max}}}$  from the completed curve.

At subsonic speeds a distinction is made between low- and high-AR wings. This is because two different sets of parameters are required to describe the wing characteristics in the two AR regimes. The  $C_{L_{\text{max}}}$  of a high-AR wing is determined by the properties of the airfoil section, whereas, the  $C_{L_{\text{max}}}$  of a low-AR wing is primarily dependent upon its planform shape. The high-AR wing is defined by

$$AR > \frac{4}{(C_1 + 1)\cos \Delta_{LE}} \tag{9.4a}$$

and the low-AR wing by

$$AR < \frac{4}{(C_1 + 1)\cos \Delta_{LE}} \tag{9.4b}$$

where  $C_1$  is a function of taper ratio and is obtained from Fig. 9.14.

For high-AR wings the  $C_{L_{max}}$  and  $\alpha_{stall}$  for the basic wing are determined from

$$C_{L_{max}} = \frac{C_{L_{max}}}{C_{\ell_{max}}} C_{\ell_{max}} \tag{9.5}$$

$$\alpha_{stall} = \frac{C_{L_{max}}}{C_{\ell_{\alpha}}} + \alpha_{0L} + \Delta\alpha_{C_{L_{max}}} \tag{9.6}$$

where

- $(C_{L_{max}}/C_{\ell_{max}})$  is obtained from Fig. 9.15
- $C_{L_{\alpha}}$  = the wing lift curve slope from Eq. (2.13) of Chapter 2
- $\alpha_{0L}$  = the section angle for zero lift
- $\Delta\alpha_{C_{L_{max}}}$  is obtained from Fig. 9.16
- $C_{\ell_{max}}$  = the unflapped section maximum lift coefficient from construction of Fig. 9.8

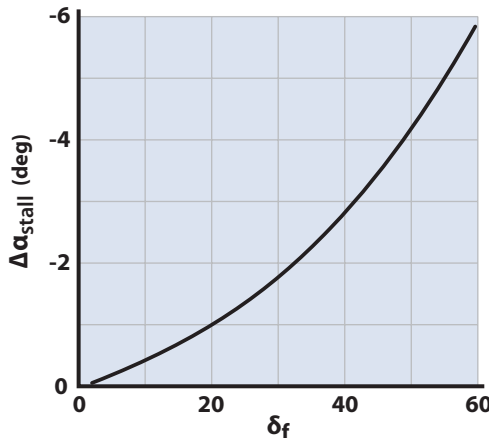


Figure 9.13 Decrease in stall angle with flap deflection (data from [2]).

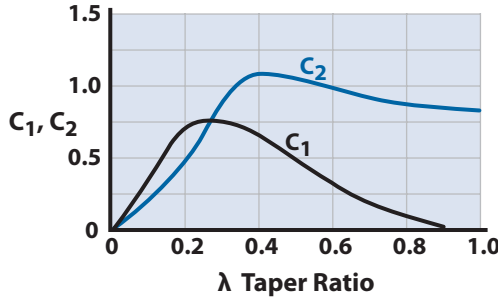


Figure 9.14 Taper ratio correction factors (adapted [10]).

Figures 9.15 and 9.16 make use of a  $\Delta y$ . This  $\Delta y$  is a leading edge sharpness parameter presented in Fig. 9.17.

For low-AR wings the  $C_{L_{max}}$  and  $\alpha_{stall}$  for the basic wing are determined from

$$C_{L_{max}} = (C_{L_{max}})_{base} + \Delta C_{L_{max}} \tag{9.7}$$

$$\alpha_{stall} = (\alpha_{C_{L_{max}}})_{base} + \Delta \alpha_{C_{L_{max}}} \tag{9.8}$$

where

$(C_{L_{max}})_{base}$  is obtained from Fig. 9.18

$\Delta C_{L_{max}}$  is obtained from Fig. 9.19

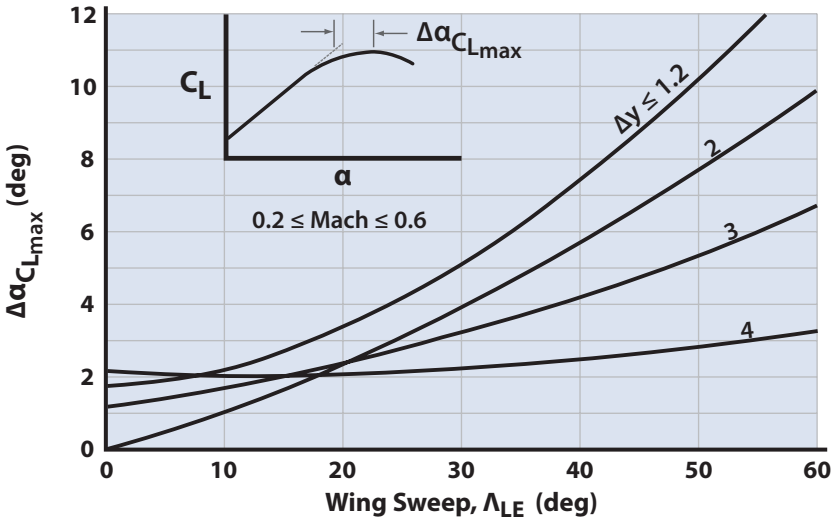
$(\alpha_{C_{L_{max}}})_{base}$  is from Fig. 9.20

$\Delta \alpha_{C_{L_{max}}}$  is from Fig. 9.21

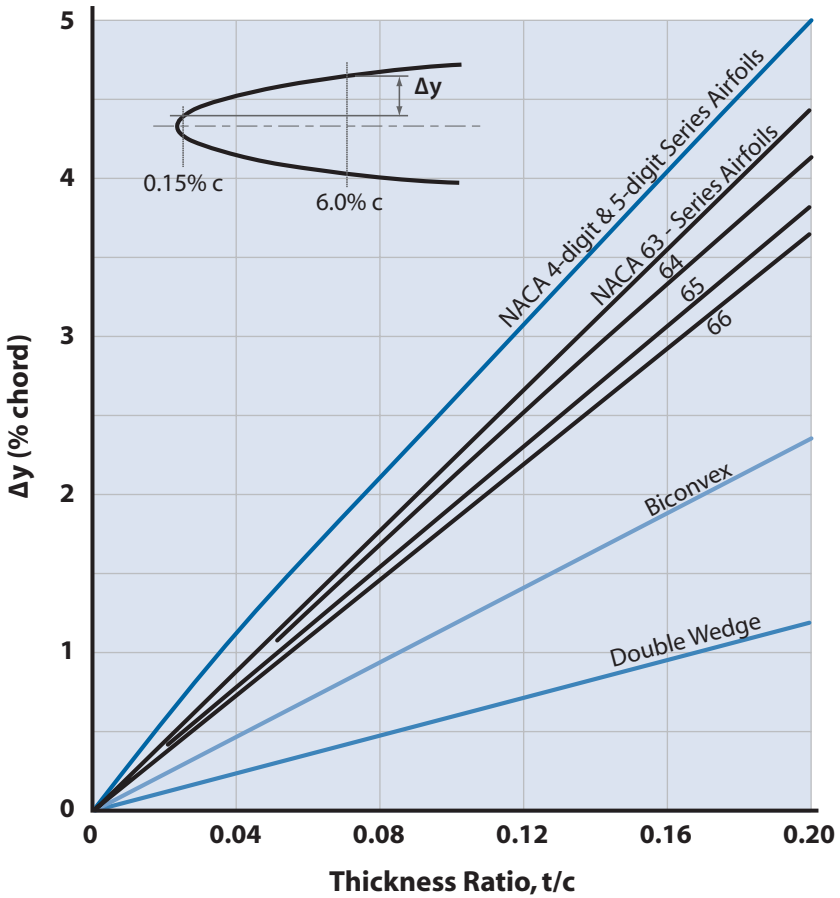


Figure 9.15 Subsonic maximum lift of high-AR wings (adapted [10]).





**Figure 9.16** Angle-of-attack increment for subsonic maximum lift of high-AR wings (adapted [10]).



**Figure 9.17** Variation of LE sharpness parameter with airfoil thickness ratio (adapted [10]).

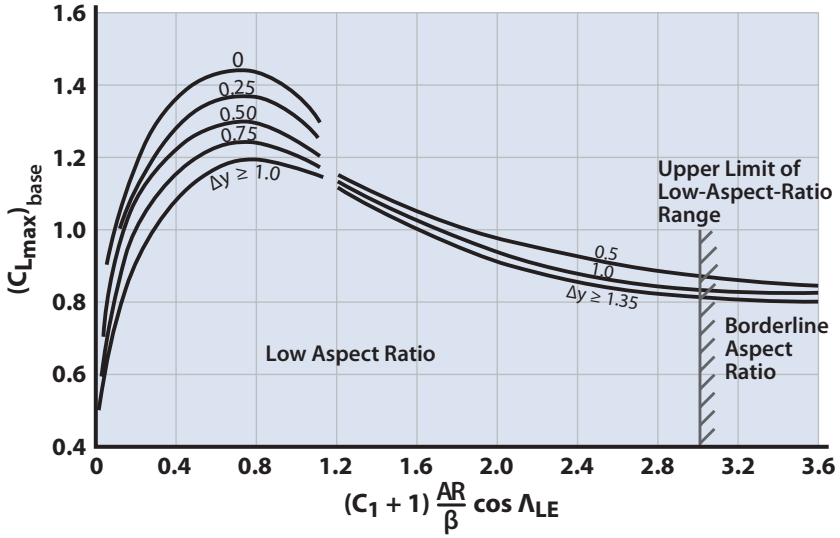


Figure 9.18 Subsonic maximum lift of low-AR wings (adapted [10]).

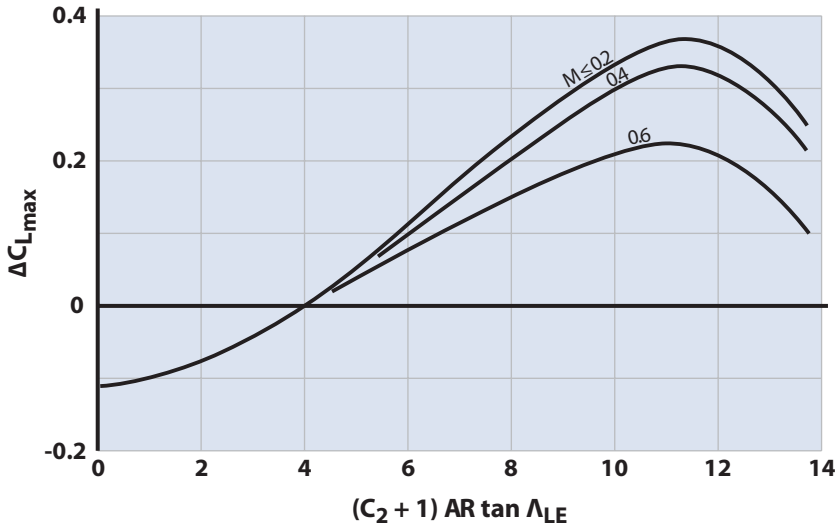


Figure 9.19 Subsonic maximum-lift increment for low-AR wings (adapted [10]).

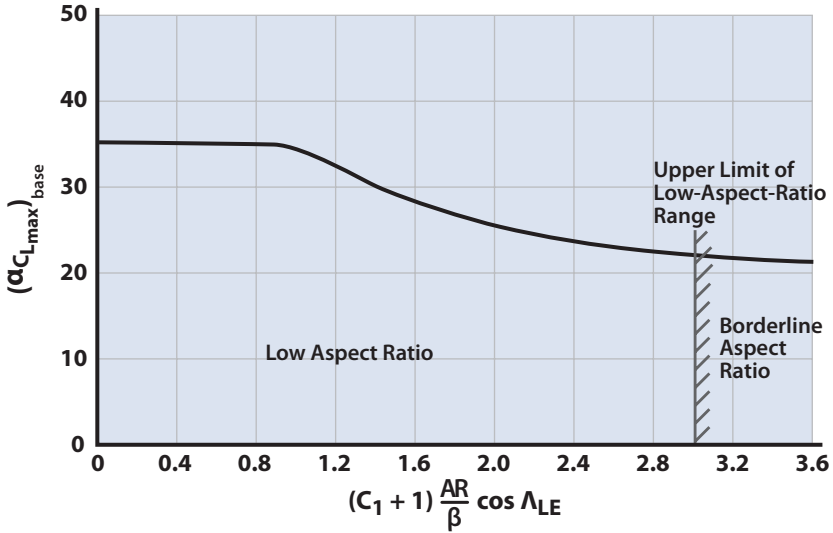


Figure 9.20 Angle-of-attack for subsonic maximum lift of low-AR wings.

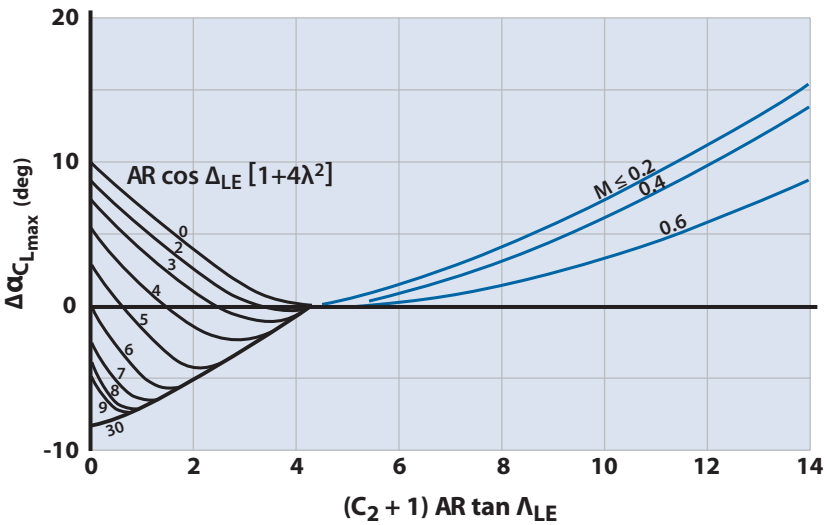


Figure 9.21 Angle-of-attack increment for subsonic maximum lift of low-AR wings.

Now the basic wing  $C_L$  vs  $\alpha$  chart can be constructed as illustrated in Fig. 9.22. The  $\alpha_{0L}$  for the wing is the same as for the airfoil section.

The finite wing increase in  $C_{L_{max}}$  due to a TE flap is obtained from (9.9),

$$\Delta C_{L_{max}} = \Delta C_{\ell_{max}} \frac{S_{WF}}{S_W} K_{\Delta} \tag{9.9}$$

where  $K_{\Delta}$  is an empirical sweep correction (Fig. 9.23),  $\Delta C_{L_{max}}$  is obtained from the construction of Fig. 9.8, and  $S_{WF}$  is defined in Fig. 9.24. The  $\Delta C_{L_{max}}$  is added to the basic (unflapped) wing  $C_{L_{max}}$  and the final flapped wing curve is drawn in Fig. 9.22. The  $\Delta\alpha_{0L}$  for the flapped wing is the same as for the flapped airfoil section determined earlier. Notice that TE flaps are not particularly effective on highly swept wings.

There is no method to predict the  $\Delta C_{L_{max}}$  for a wing with LE devices. Here the designer should use experimental data such as that presented in Tables 9.1 and 9.2 or Fig. 9.7. For example, for the wing in Table 9.1 a 20% full-span slat gives a  $\Delta C_{L_{max}} = 0.48$  and a 20% full-span LE flap gives a  $\Delta C_{L_{max}} = 0.59$ . These values can now be added to the  $C_{L_{max}}$  of similar wing shapes to give the  $C_{L_{max}}$  for a wing with LE flaps or slats. The  $\Delta\alpha_{stall}$  can be determined similarly.

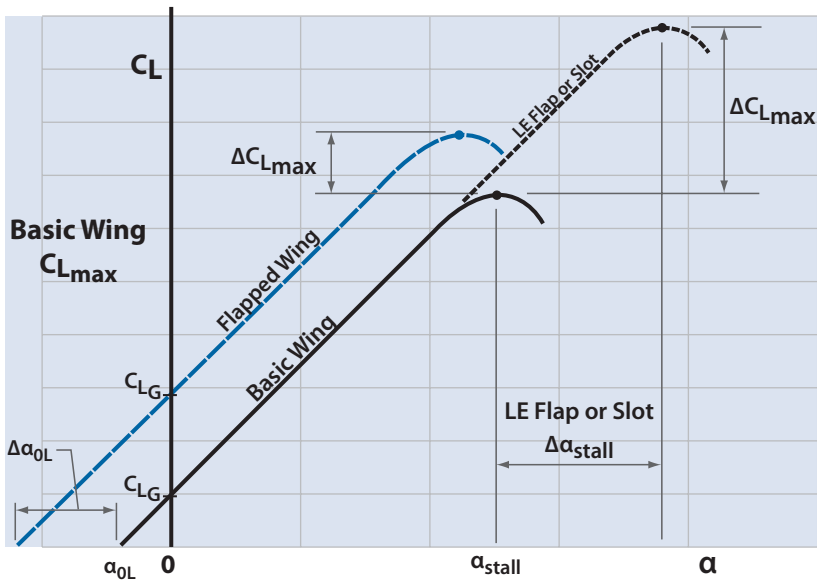


Figure 9.22 Construction of wing lift curves for mechanical high-lift devices.

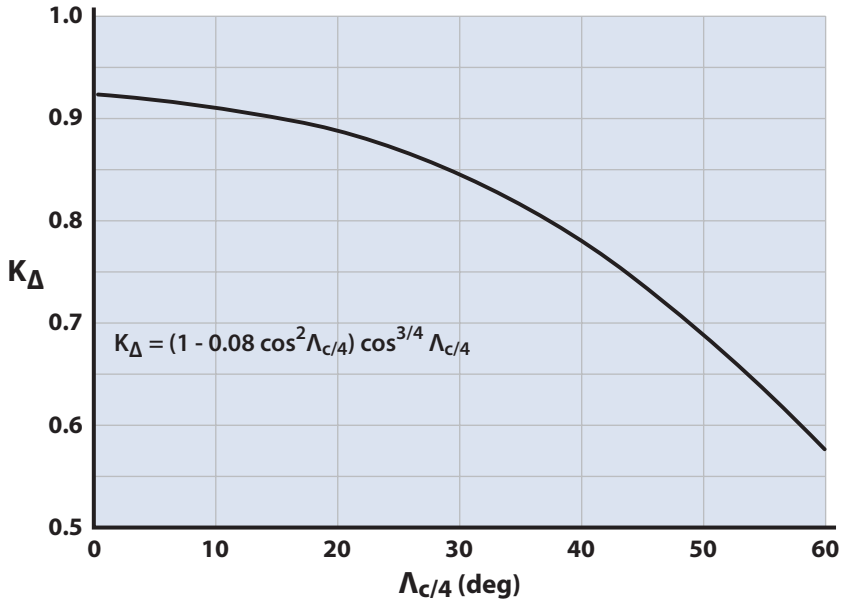


Figure 9.23 Planform correction factors for TE flaps (adapted [10]).

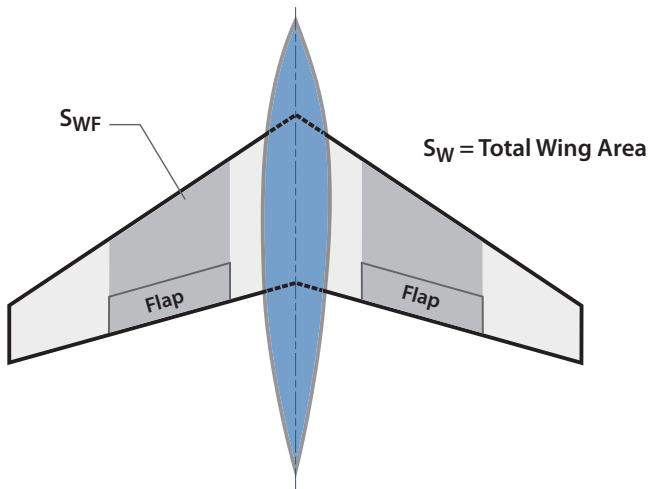


Figure 9.24 Schematic showing flapped wing area.

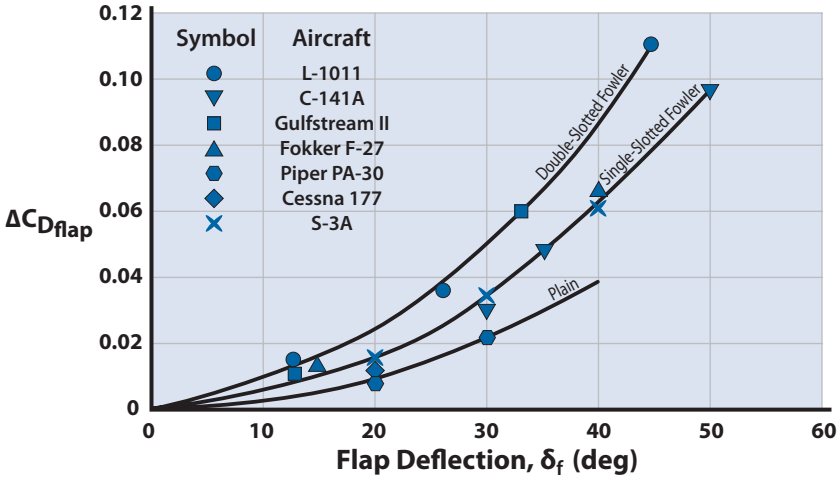


Figure 9.25 Trailing edge flap drag coefficient increment (referenced to wing area).

### 9.5 Subsonic Drag Due to Flap Deflection

The drag of the deflected flaps must be considered in the landing and takeoff analysis. The designer can get a first-order estimate for the drag of a slotted or plain flap from Fig. 9.25.

A more refined estimate of the drag coefficient for split, plain, and slotted flaps is given in [13]. The influence of the flap chord ratio and flap area ratio is determined as follows:

$$\Delta C_{D_{flap}} = k_1 k_2 \frac{S_{WF}}{S_W} \tag{9.10}$$

where  $k_1$  is a function of the ratio  $c_f/c$  and is obtained from Fig. 9.26;  $k_2$  is dependent upon  $\delta_f$  and is presented in Fig. 9.27; and  $S_{WF}/S_W$  is the ratio of the flapped wing area to the total wing area (see Fig. 9.24).

### 9.6 Powered High-Lift Devices for STOL

The characterization of a *short takeoff and landing* (STOL) aircraft is not well defined at present. However, it is generally agreed that the lower limit for a STOL aircraft would be a landing and takeoff distance, over a 50-ft obstacle, of 1000 ft (air distance + ground roll).

This 1000-ft restriction for landing means a steep descent (7 deg) over the obstacle to shorten the air distance and a low touchdown speed with high braking coefficients to keep the ground run short. The air distance

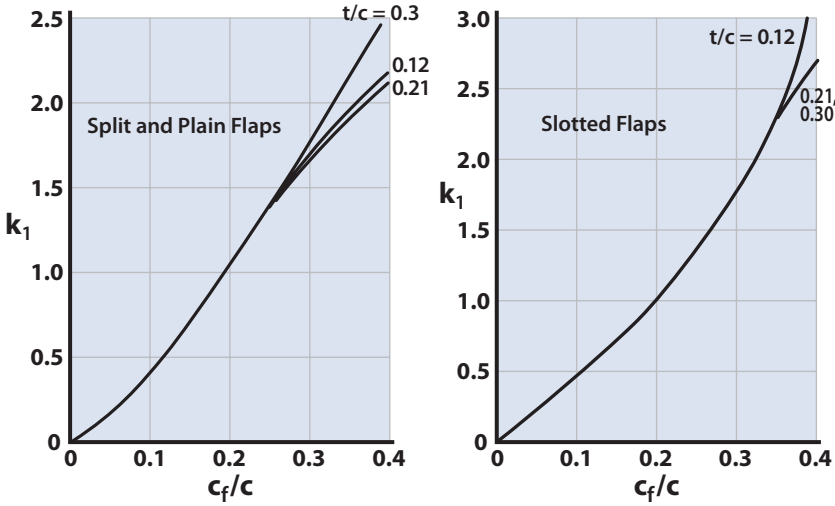


Figure 9.26 Factor  $k_1$  to calculate drag increment due to flaps (data from [13]).

over 50 ft for a 7-deg glide slope is  $\sim 400$  ft, leaving only 500 ft for the ground roll. The touchdown speed is defined as  $1.15V_{\text{stall}}$  and the approach speed over 50 ft as  $1.3V_{\text{stall}}$ . For takeoff the aircraft must accelerate to takeoff speed, which is  $1.2V_{\text{stall}}$ . Thus, the stall speed is the primary takeoff performance parameter for STOL aircraft.

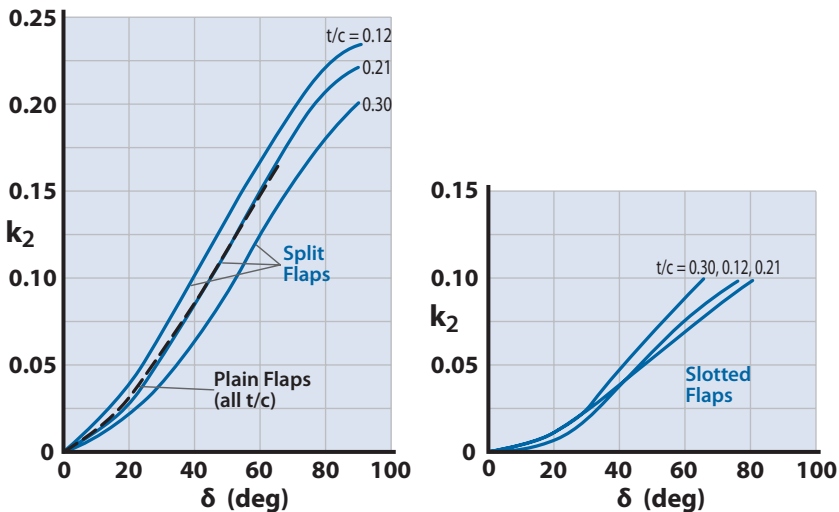


Figure 9.27 Factor  $k_2$  to calculate drag increment due to flaps.

**Example 9.1 Wing Loadings for STOL Aircraft**

Figure 6.5 (from [14]) indicates that routine landing in a 1000-ft field requires an approach speed of 50 kt, or 84.5 ft/s. Using the Federal Aviation Administration requirement for approach speed equal to 1.3 times the stall speed (Chapter 10) the stall speed is approximately 65 ft/s, which is the result of using the one-*g* lift expression at sea level ( $V_{\text{stall}} = 65 \text{ ft/s}$ ):

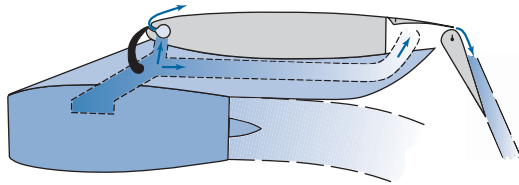
$$\frac{W}{S} \frac{1}{C_{L_{\max}}} = 5.0 \quad (9.11)$$

Using the practical upper limit of  $C_{L_{\max}}$  for mechanical lift devices of 4.0 (see Fig. 9.7), Eq. (9.11) indicates that the wing loading would have to be 20 psf! This is an appropriate wing loading for light utility aircraft but not for commercial short-haul STOL transports. Transport aircraft cannot operate economically at such a low wing loading (poor cruise efficiency), and passengers would not like the bumpy ride. The Breguet 941, a STOL commercial short-haul transport ( $W_{\text{TO}} = 48,000 \text{ lb}$ ), lands in 1000 ft with a wing loading of about 45 psf. The Breguet 941 employs the deflected slipstream concept, thrust reversers, and oversize brakes. The point here is that commercial STOL operation with field distances of 1000 ft must use powered-lift devices as well as aerodynamic high-lift devices.

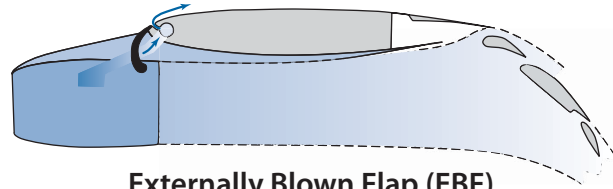
**9.6.1 Deflected Slipstream**

In a *deflected slipstream* system, lift is produced at low speed by deflecting the propeller slipstream or jet exhaust downward by a wing-flap arrangement (as used in the Breguet 941). The slipstream of the four propellers blows over the entire span of the wing and is deflected by slotted flaps at the trailing edge. A derivative of this system is the upper surface blowing (USB) employed on the Boeing Advanced Medium STOL Transport (AMST) YC-14 demonstrator in the 1970s. The effectiveness of a USB flap, shown schematically in Fig. 9.28, in turning a jet exhaust flow depends on a principle known as the *Coanda effect*, which describes how a jet airflow adheres to the outside of a convex curved surface. This phenomenon was first systematically investigated by Henri Coanda prior to WWII. He found that a high-velocity jet will adhere to an adjacent convex surface, provided that the jet depth is not large compared with the radius of the turn. In fact, blowing boundary layer control at the knee of a flap is a practical application of this principle. The YC-14 (Fig. 9.29a) locates its CF6-50 turbofan engines on top of the wing and bathes the inboard upper surface of the

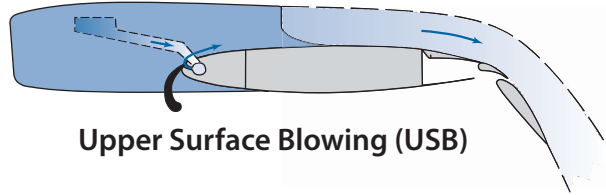




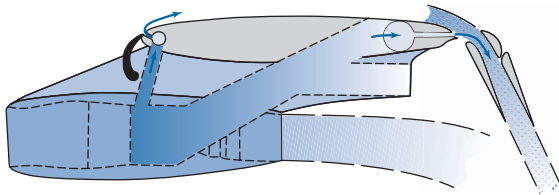
**Internally Blown Flap (IBF)**



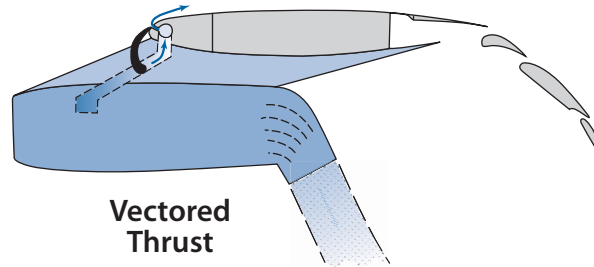
**Externally Blown Flap (EBF)**



**Upper Surface Blowing (USB)**

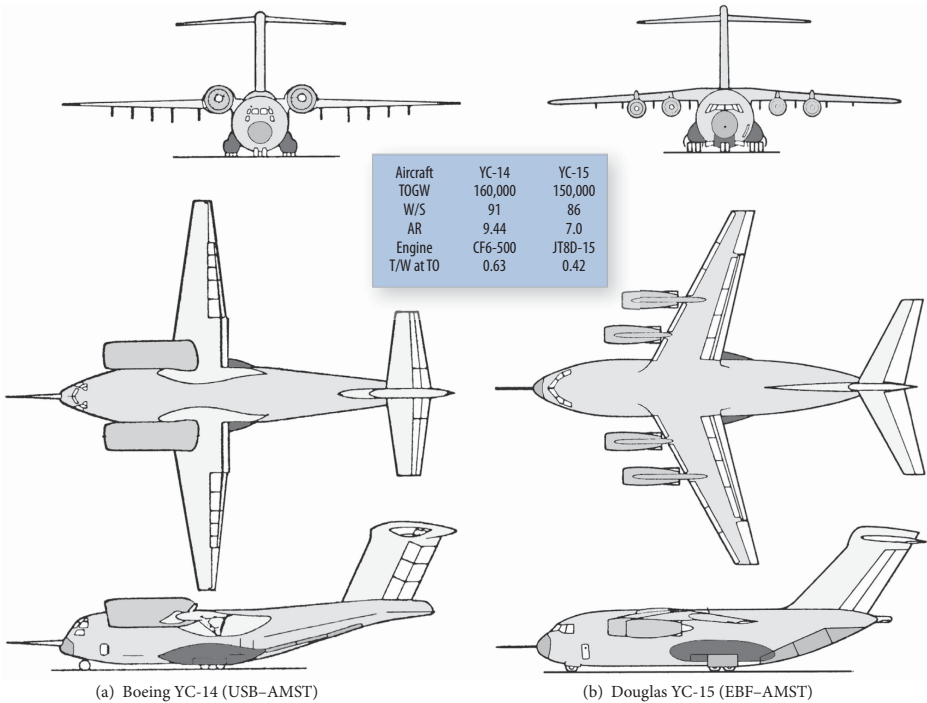


**Augmentor Wing**



**Vectored Thrust**

**Figure 9.28** Powered-lift STOL concepts.



**Figure 9.29** Prototype advanced medium STOL transports, AMST (data from [13,14]).

wing and TE flap with the jet exhaust. Performance of the YC-14 USB arrangement (Fig. 9.30) depends upon the jet coefficient

$$C_j = \frac{\text{Thrust}}{q S_{\text{ref}}} \tag{9.12}$$

Notice that the YC-14 also employs blowing of the LE flap. The amount of blowing is expressed by the blowing coefficient

$$C_\mu = \frac{\dot{m}_B V_e}{q S_{\text{ref}}} \tag{9.13}$$

where  $\dot{m}_B$  is the mass flow rate of the blowing device and  $V_e$  is the exhaust velocity of the blowing jet.

### 9.6.2 Externally or Internally Blown Flap

In the *internally blown flap* (IBF) and the *externally blown flap* (EBF), high-energy jet exhaust is blown over a slotted TE flap arrangement, providing both thrust vectoring and boundary layer control. In the IBF concept, jet exhaust (all or part) is ducted from the engine, through the wing, and

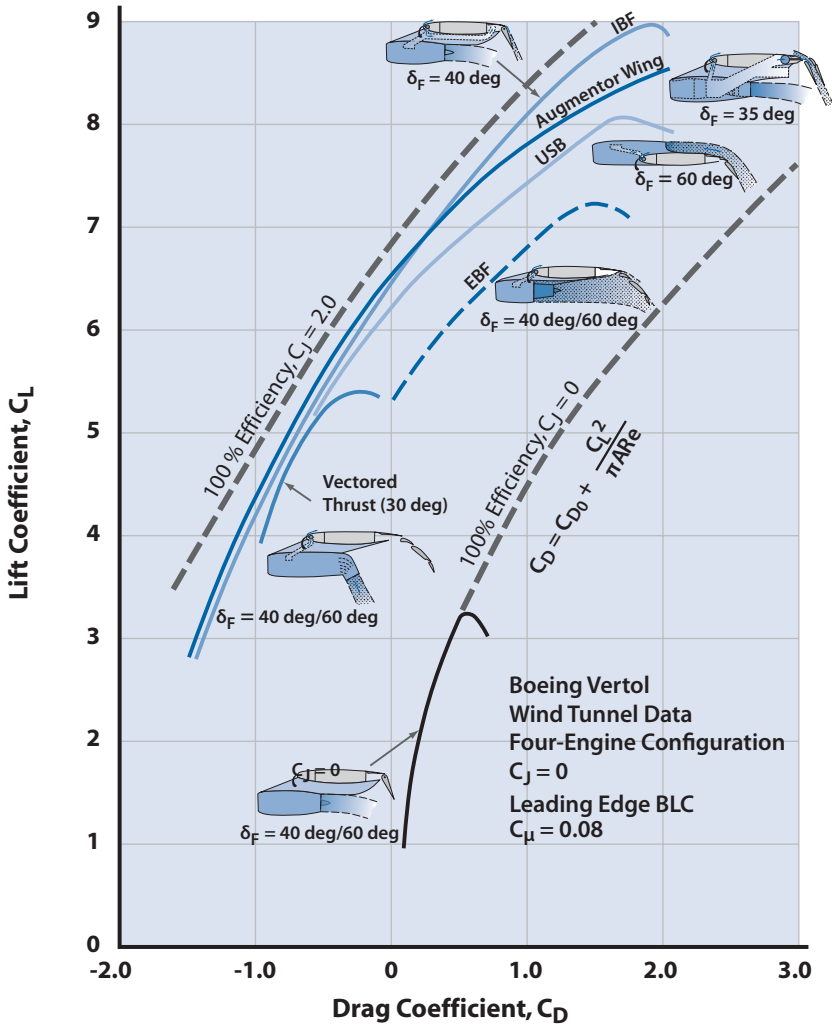


Figure 9.30 Low-speed drag polars for various powered-lift concepts.

exhausted over the TE flap as shown in Fig. 9.28. There is usually a cross-over ducting arrangement so that one engine can feed the flaps on both sides of the aircraft. This ducting is heavy and complicated but the arrangement solves the one-engine-out problem. The performance of the IBF is shown in Fig. 9.30.

The EBF concept is shown in Fig. 9.28 and has the principle advantage of being light and simple. No internal ducting or thrust deflection mechanisms are required other than the flap system itself. However, the flap system is subjected to severe temperature and load environments and one-engine-out is a major design problem. Despite these drawbacks, the EBF concept is popular and was employed on the YC-15 (see Fig. 9.29b) and the more recent USAF

C-17 transport. The performance of a typical EBF arrangement is shown in Fig. 9.30.

### 9.6.3 Jet Flap

The *jet flap* is simply a sheet of air blown downward from the trailing edge of the wing, providing increased circulation about the wing and a vectored thrust component. In contrast to the usual TE flap, there is no solid surface in the jet sheet to support a pressure distribution, hence no drag from the device. Drag is desirable during landing to reduce the air and ground distance; thus, this feature of the jet flap is not an advantage for landing. The jet flap does have an advantage over TE flaps during maneuvering flight at transonic speeds. Not only is there the absence of the flap drag but also the jet flap extends the low-pressure region on the wing upper surface in the TE region that moves the upper surface normal shock aft, which delays flow separation.

In 1972, the USAF started an AMST program that called for operating a 27,000-lb payload into a 2000-ft semi-prepared field. Boeing's YC-14 featuring USB competed with McDonnell Douglas's YC-15 featuring EBF. Both companies' prototypes met AMST requirements, but neither aircraft saw production. McDonnell Douglas, however, incorporated the YC-15 EBF into their winning C-17 design.

### 9.6.4 Augmentor Wing

The *augmentor wing* is similar to the IBF except that the ducted engine air is exhausted between two TE flap sections forming a diffuser section as shown in Fig. 9.28. The high-velocity engine air mixes with stagnant secondary air in the diffuser section, increasing the momentum of the mixture and decreasing the pressure. The decreased pressure causes more secondary air from the wing upper surface to be entrained and to move into the diffuser section. The result is an augmentation of the thrust from the primary engine exhaust by as much as a factor of 2.

## 9.7 Powered High-Lift Devices for V/STOL

The first thing to understand about V/STOL is that the high lift during vertical ascent or descent does not come from air flowing over a wing, because the "V" means zero air speed. The high lift comes from directing the force from a propulsion unit downward. A good rule of thumb is that you need a force of  $\sim 1.2$  times the weight of the aircraft directed downward to achieve VTOL. The extra 20% is needed for three-axis control and to overcome the "suck down" (suction is usually present beneath a VTOL aircraft). In addition to the three-axis control, there must be provision for fore and aft translation during hover.

The candidate V/STOL concepts are shown in Figs. 9.31 and 9.32. Figure 9.31 was generated by the McDonnell Aircraft Company in 1968

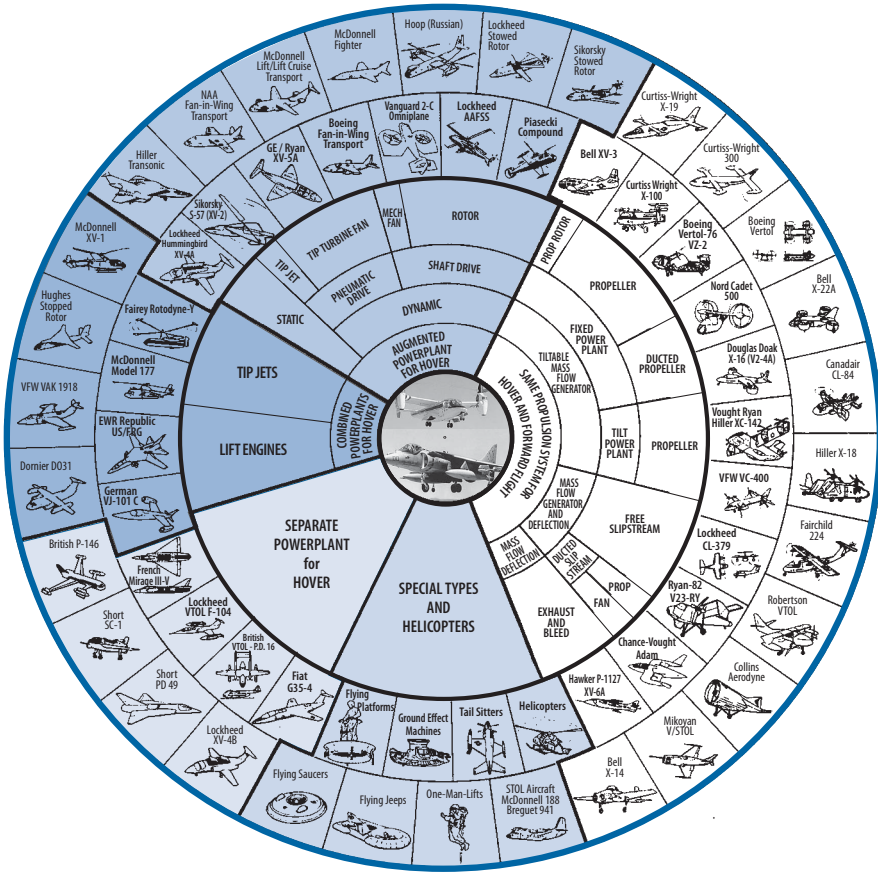


Figure 9.31 V/STOL aircraft summary (1970s).

and shows the state of the art at that time. Figure 9.31 is often called the Wheel of Misfortune because not every aircraft shown in the figure was actually built and flown, many of them crashed during testing, and only the P-1127/XV-6A saw production—as the Harrier. Figure 9.32 shows the more successful V/STOL aircraft up to the present. The only aircraft from Fig. 9.32 that have gone into production are the Yak-38 (lift + lift/cruise), V-22 (tilt rotor), AV-8 Harrier (vectored thrust), and F-35B (fuselage fan + vectored thrust). There is a good chance that a derivative of the XV-15 will be produced for the commercial sector as the Bell/Boeing 609 and for the Coast Guard as the Bell Eagle Eye UAV.

The augmentor (ejector) wing can be used as a VTOL device, for example, the Rockwell International XFV-12A (see [7]) for the U.S. Navy, using all the engine air or as a STOL device using only part of the engine air. The ejector concept was first used in the Lockheed Hummingbird XV-4A in the early 1960s, with limited success. The XV-4A had two 3300-lb thrust

PW JT 12A-3 turbojets that could be exhausted rearward for forward flight or diverted to feed the ejector system located in the fuselage. The fuselage ejector was replaced with lift engines in the XV-4B to demonstrate the lift plus lift–cruise concept. The XV-4B had four J85-19 turbojets in the fuselage to provide vertical lift only and two J85s in external engine pods that could be vectored for lift or forward thrust.

Tilt-wing concepts such as the XC-142 have propellers mounted on the wing and the entire wing is rotated up to 90 deg while keeping the fuselage horizontal. The major portion of the wing is immersed in the propeller slipstream and does not stall during the wing rotation. Several tilt-wing V/STOL prototypes can be seen in Fig. 9.32. In the tilt-rotor/propeller concept the wing is fixed and only the propeller or rotor tilts. The XV-15 was one of the more successful tilt-rotor prototypes due mainly to Bell’s 40 years of persistence and commitment to the concept. It will see military service as the V-22 and very likely commercial service.

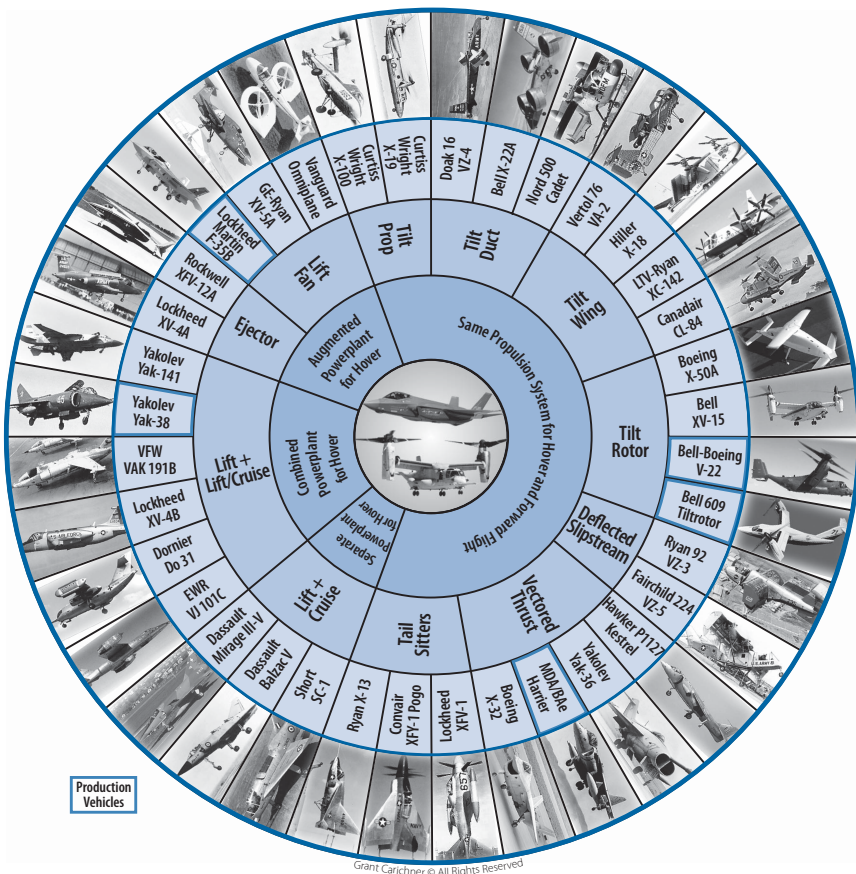
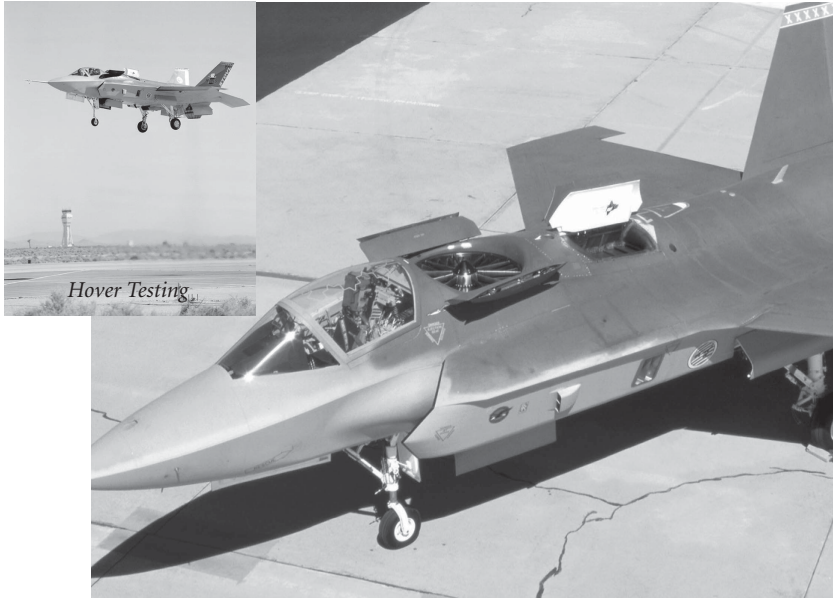


Figure 9.32 V/STOL aircraft summary (2008).

Some V/STOL designs use direct engine thrust to provide additional lift force during takeoff and landing. This direct engine thrust can come from dedicated lift engines, such as on the Lockheed XV-4B, or from cruise engines capable of vectoring their thrust such as on the AV-8B Harrier, or from a combination (called lift plus lift–cruise) such as the German VAK-191B and Russian Yak-38. The lift engine or vectored thrust concepts have the advantage of being mature, straightforward, low-risk concepts but suffer the disadvantage of producing a field of very hot gas beneath the aircraft that can be ingested by the engine thereby reducing its thrust.

Energy can be extracted from the cruise engine to power a lift fan. This energy extraction can be shaft power driving a lift fan or hot exhaust gas driving a tip-driven lift fan. In either case the lift fan exhausts downward with a lift force greater than the vectored thrust of the cruise engine. In other words, the lift fan is able to augment the thrust from the cruise engine. The lift-fan concept was demonstrated in the Ryan XV-5A in the 1960s. The XV-5A had two gas-driven lift fans in the wings and one in the nose of the aircraft. This arrangement gave the XV-5A three-axis control by modulating the nose fan thrust for pitch, modulating the wing fan thrust for roll, and deflecting the nose fan lift sideways for yaw control. Fore and aft translation was available by deflecting the wing fan thrust fore and aft. With the hot exhaust gas from the two J85-GE-5 turbojets (rated at 2650 lb static thrust each) driving the three lift fans, the XV-5A was able to generate 13,886 lb of vertical thrust, or an augmentation ratio of 2.62. The disadvantage of the gas-driven lift fan concept is the volume required for the hot gas ducting and the vulnerability of this ducting to small arms ground fire.

In 1996 the U.S. government awarded a contract to Boeing and Lockheed Martin to build two Joint Strike Fighter (JSF) prototypes each. The prototypes were to demonstrate three JSF variants, a conventional takeoff and landing variant for the U.S. Air Force, a carrier-suitable variant for the U.S. Navy, and a *short takeoff vertical landing* (STOVL) variant for the U.S. Marine Corps. The STOVL variant was the discriminating factor in the program. The JSF engine was the PWF119 afterburning turbofan engine with ~32,000 lb of vectored thrust available for VTOL. Boeing selected the low-risk vectored thrust concept for their X-32B demonstrator (see Fig. 1.11). Lockheed Martin selected the higher risk, but more capable *shaft-driven lift fan* (SDLF) plus vectored thrust concept, shown in Fig. 9.33 for their X-35B demonstrator. Most of the risk was in developing a gear box to drive the SDLF, a clutch and a functional, lightweight fan. The SDLF was located behind the cockpit. The 3 axes control arrangement modulates the lift fan thrust for pitch, deflects the lift fan thrust sideways for yaw, and uses wing tip mounted reaction control jets for roll. At sea level on a 75°F day the X-35B was able to generate 39,100 lb of vertical lift distributed as



**Figure 9.33** X-35B showing shaft-driven lift-fan (SDLF) and auxiliary inlet.

follows: 16,411 lb from the three bearing swivel nozzle, 3,607 lb from the wingtip roll control jets, and 19,082 lb from the lift fan. The lift fan achieved an augmentation ratio of about 1.6. The SDLF plus vectored thrust concept of the X-35B had considerable margin over the vectored thrust concept of the X-32B and won the JSF competition. The aircraft is now in production

### F-35 and the Joint Strike Fighter Program

The F-35 has three variants: the F-35A conventional TO and landing for the USAF, the F-35B STOVL for the U.S. Marine Corps, and the F-35C carrier suitable for the U.S. Navy. This aircraft has a single PWA F135 turbofan with 43,000 lb TSLS in afterburner. The specifications for the three variants are as follows:

	F-35A	F-35B	F-35C
Wing area (ft <sup>2</sup> )	460	460	668
Empty weight (lb)	29,300	32,000	34,800
Max TOGW (lb)	70,000	60,000	70,000
Range (nm)	1200	900	1400
Combat radius (nm)	610	500	640
Max speed (Mach)	1.67	1.67	1.67

The program is joined by eight international partners: the United Kingdom, Italy, the Netherlands, Canada, Turkey, Australia, Norway, and Denmark.



and will see service in the Air Force, Navy, and Marine Corps as the F-35. The F-35 Case Study in Volume 2 is recommended reading.

There are several excellent references on V/STOL aerodynamics and aircraft technology that are recommended to the reader. Reference [15] is a good text on the theoretical aspect of high-lift devices with supporting experimental data. Reference [16] is an excellent summary report on STOL aerodynamic technology, with [17] being a summary of the USAF Advanced Medium STOL Transport Program. Reference [18] is an excellent design text for V/STOL aircraft. Reference [7] is a superb historical account of VTOL military research aircraft.

## References

- [1] Kuethe, A. M., and Schetzer, J. D., *Foundations of Aerodynamics*, Wiley, New York, 1959.
- [2] Abbott, I. H., and von Doenhoff, A. E., *Theory of Wing Sections*, Dover, New York, 1959.
- [3] Furlong, G. C., and McHugh, J. G., "A Summary and Analysis of the Low-Speed Longitudinal Characteristics of Swept Wings at High Reynolds Number," NACA TR-1339, 1957.
- [4] Thomson, L. P., "A Review of Leading Edge High Lift Devices," Dept. of Supply, Army Research Laboratory Rept. A-77, 1951.
- [5] Gambucci, B. J., "Section Characteristics of the NACA 0006 Airfoil with Leading-Edge and Trailing-Edge Flaps," NACA TN-3797, 1956.
- [6] Menees, G. P., "Lift, Drag and Pitching Moment of an Aspect-Ratio-2 Triangular Wing with Leading-Edge Flaps Designed to Simulate Conical Camber," NASA Memo 10-5-58A, Dec. 1958.
- [7] Rogers, M. J., *VTOL Military Research Aircraft*, Orion Books, New York, 1989.
- [8] Nonweiler, T., "Flaps, Slots and Other High Lift Aids," *Aircraft Engineering*, Vol. 6, Sept. 1955, pp. 19–23.
- [9] Cahill, J. F., et al., "Aerodynamic Forces on a Symmetrical Circular Arc Airfoil with Plain LE and TE Flaps," NACA TR-1146, 1953.
- [10] Ellison, D. E., "USAF Stability and Control Handbook (DATCOM)," U.S. Air Force Flight Dynamics Laboratory, AFFDL/FDCC, Wright–Patterson AFB, OH, June 1969.
- [11] Abbott, I. H., Von Doenhoff, A. E., and Stivers, L., Jr., "Summary of Airfoil Data," NACA TR-824, 1945.
- [12] Riegels, F. W., *Aerofoil Section*, Butterworth, London, 1961.
- [13] Young, A. D., "The Aerodynamic Characteristics of Flaps," NACA Ames Research Center ARC R&M 2622, 1953.
- [14] Kuhn, R. E., "Takeoff and Landing Distance and Power Requirements of Propeller Driven STOL Aircraft," IAS Preprint 690, presented at 25th Annual Meeting, New York, 28–31 Jan. 1957.
- [15] McCormick, B. W., *Aerodynamics of V/STOL Flight*, Academic Press, New York, 1967.
- [16] May, F., and Widdison, C. A., "STOL High-Lift Design Study, Vol. 1, State-of-the-Art Review of STOL Aerodynamic Technology," U.S. Air Force Flight Dynamics Laboratory Rept. AFFDL-TR-71-26, Wright–Patterson AFB, OH, April 1971.
- [17] Oates, G. S., Brown, S., and Nicolai, L., "STOL Tactical Aircraft Investigation, Executive Summary," U.S. Air Force Flight Dynamics Laboratory, AFFDL TR-74-125, PTC, Wright–Patterson AFB, OH, July 1975.
- [18] Kohlman, D. L., "Introduction to V/STOL Airplanes," Iowa State Univ. Press, Ames, IA, 1981.

# Chapter 10

# Takeoff and Landing Analysis



- CTOL Takeoff & Landing Rules
- Ground Effects
- Takeoff & Landing Analysis
- Landing Gear Drag
- Stall, TO, & Touchdown Speed
- Balanced Field Length
- Comparison with L-1011 Flight Test

Landing the Lockheed L-1011 TriStar. The L-1011 with Rolls Royce RB 211 turbofans compared favorably with its competition. The high lift system of the L-1011 is discussed in Section 10.7.

*Creative people who know exactly what they are doing aren't creative people.*

## 10.1 Introduction

This chapter considers aircraft takeoff and landing performance in detail. The discussions of Chapter 6, Section 6.3, and of Chapter 9 addressed this performance aspect in general terms and provided initial estimates. This chapter assumes that the aircraft design is defined in fair detail and the designer is ready for a thorough takeoff and landing analysis.

The ground rules governing takeoff and landing are reported in MIL-C-5011A [1] for military aircraft and in the Federal Aviation Regulations (FAR) Parts 23 and 25 [2] for civil and commercial aircraft. The U.S. Navy uses AS-5263 [3] in lieu of MIL-C-5011. Before discussing these regulations it is useful to consider the following definitions for *conventional takeoff and landing* (CTOL):

$V_{\text{stall}} = V_S = 1 g$  stall speed out of ground effect (sometimes called *minimum flight speed* or *control speed*,  $V_{\text{min}}$ ) [Eq. (6.1)]

$V_{\text{TO}}$  = takeoff or liftoff speed

$V_{\text{CL}}$  = climb-out speed during takeoff

$V_{\text{EF}}$  = one-engine-failure speed

$V_1$  = decision speed (continue or brake)

$V_R$  = rotation speed (speed at which an aircraft is rotated, during the ground run)

$V_{\text{OBS}}$  = speed over the obstacle [obstacle height = 50 ft for military and 35 ft for Federal Aviation Administration (FAA) commercial] for takeoff

$V_{50}$  = speed over 50-ft obstacle during landing

$V_{\text{TD}}$  = speed at touchdown during landing

$V_{\text{app}}$  = approach speed for carrier aircraft (120 kt from [3])

A summary of CTOL ground rules for military and civil aircraft is shown in Tables 10.1 and 10.2. The reader should note that in all cases the speeds specified are minimum speeds.

The takeoff and landing analyses, in Sections 10.3 and 10.4 respectively, will assume realistic speeds compatible with these minimum speeds. There are no satisfactory military or civilian ground rules for STOL aircraft at present. STOL flying qualities are addressed in military specification MIL-F-83300 but this document is currently under revision and only alludes to STOL takeoff and landing ground rules. References [4,5] make recommendations for realistic STOL takeoff and landing ground rules. The analyses in Sections 10.3 and 10.4 are appropriate for STOL performance with consideration given to realistic speed ground rules and the features peculiar to STOL operation (for example, dirt-strip operation giving rolling  $\mu = 0.04$  and braking  $\mu = 0.30$ ).

**Table 10.1** Summary of CTOL Takeoff Rules

Item	MIL-C-5011C (Military)	FAR Part 23 (Civil)	FAR Part 25 (Commercial)
Speeds	$V_{T0} \geq 1.1 V_S$ $V_{CL} \geq 1.2 V_S$	$V_{T0} \geq 1.1 V_S$ $V_{CL} \geq 1.1 V_S$	$V_{T0} \geq 1.1 V_S$ $V_{CL} \geq 1.2 V_S$
Climb gradient <sup>a</sup>	Gear up: 500 fpm at SL (AEO) 100 fpm at SL (OEI)	Gear up: 300 fpm at SL (AEO)	Gear up: 3% at $V_{CL}$ (OEI) Gear down: 0.5% at $V_{T0}$
Rolling coefficient	$\mu = 0.025$	Not specified	Not specified
Field-length definition	Takeoff distance over 50 ft	Takeoff distance over 50 ft	115% of takeoff distance over 35 ft or critical field length (see Section 10.6)

<sup>a</sup>SL = sea level; AEO = all engines operating; OEI = one engine inoperative.

## 10.2 Ground Effects

As the aircraft flies close to the ground, the ground interferes with the horseshoe vortex system trailing behind the wing (see Section 2.3 and Fig. 10.1). Ground effects are often analyzed by putting an *image horseshoe vortex* system of equal but opposite strength at the same distance  $h$  below the ground that the wing is above the ground. This image vortex system effectively cancels the wing's induced velocities normal to the ground surface, the necessary boundary condition at the ground surface. This image vortex system induces velocities at the wing aerodynamic center (a.c.), which decreases the strength of the downwash at the wing a.c., thereby decreasing the induced angle-of-attack,  $\alpha_i$ . Thus, the wing  $C_L$  is increased (or more correctly, the lift curve slope increases, giving an increase in  $C_L$  for the same geometric angle-of-attack,  $\alpha$ ) and the induced drag is decreased. This influence of the ground effect is a function of how close the aircraft is to the ground and of the size of the wing. The effect of

**Table 10.2** Summary of CTOL Landing Rules

Item	MIL-C-5011C	FAR Part 23	FAR Part 25
Speeds	$V_{OBS} \geq 1.2 V_S$ $V_{TD} \geq 1.1 V_S$	$V_{OBS} \geq 1.3 V_S$ $V_{TD} \geq 1.15 V_S$	$V_{OBS} \geq 1.3 V_S$ $V_{TD} \geq 1.15 V_S$
Braking coefficient	0.30	Not specified	Not specified
Field-length definition	Landing distance over 50 ft	Landing distance over 50 ft	Landing distance over 50 ft divided by 0.6



**Figure 10.1** B-767 generates a strong trailing vortex system during a landing approach (courtesy of Ray Nicolai).

the proximity of the ground on the wing can be thought of as an increase in the wing geometric aspect ratio ( $AR$ ) to some effective aspect ratio  $AR_{\text{eff}}$ . Figure 10.2a shows the variation of  $AR/AR_{\text{eff}}$  with the nondimensional wing height parameter  $h/b$ , where  $h$  is the height of the wing above the ground and  $b$  is the wing span. Figure 10.2a can be used to obtain the effective aspect ratio  $AR_{\text{eff}}$ , which is then put into Eq. (2.13) of Chapter 2 to obtain the wing lift curve slope in ground effect.

Figure 10.2b shows the influence of ground effect on an  $AR = 4$  wing. Here, the nondimensional wing height parameter is  $h/\bar{c}$ , where  $\bar{c}$  is the wing mean aerodynamic chord. An  $(h/\bar{c})$  value of  $\infty$  means that the wing is out of ground effect or in free air. Notice that the wing lift curve slope increases as the ground is approached and the angle for zero lift,  $\alpha_{0L}$ , becomes less negative. Approaching the ground essentially decreases the effect of camber. Camber causes the circulation about the airfoil to increase, which introduces a curving upward of the flow streamlines as they approach the airfoil (an upwash ahead of the airfoil). The proximity of the ground straightens the flow streamlines (or the image vortex system decreases the upwash), thereby decreasing the magnitude of  $\alpha_{0L}$ . The  $C_L$  for  $\alpha = 0$  is approximately the same value for all values of  $h/\bar{c}$ . This fact should be used when generating a curve similar to Fig. 10.2b to determine the ground  $C_L$  during the takeoff and landing analysis.

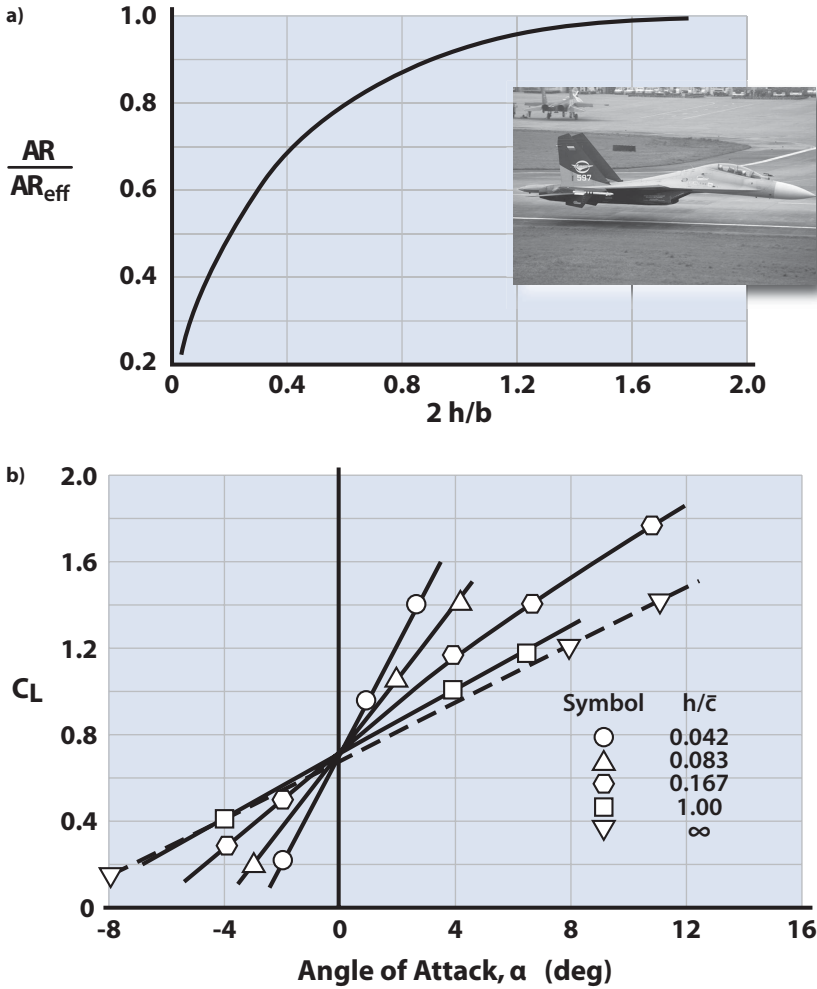


Figure 10.2 Influence of ground effects (data from [7]) on **a)** effective aspect ratio,  $AR_{eff}$ , and **b)** an  $AR = 4$  wing.

As the wing approaches the ground, the induced drag is decreased but the zero-lift drag is essentially unchanged. The reduction in induced drag of the aircraft in ground effect can be expressed as (from [6])

$$\Delta C_{Di} = -\sigma C_L^2 / (\pi AR)$$

where  $\sigma$  is defined as the ground influence coefficient. At values of  $h/b$  between 0.033 and 0.25,  $\sigma$  can be estimated from

$$\sigma = \frac{1 - 1.32 h/b}{1.05 + 7.4 h/b}$$

### 10.3 Takeoff Analysis

Takeoff is the distance required for an aircraft to accelerate from  $V = 0$  to takeoff speed and climb over a 35- or 50-ft obstacle. Figure 10.3 shows a schematic of the takeoff problem.

The takeoff distance is the sum of the ground distance ( $S_G$ ), rotation distance ( $S_R$ ), transition distance ( $S_{TR}$ ), and climb distance ( $S_{CL}$ ).

It is assumed that the aircraft accelerates to a takeoff velocity  $V_{TO} = 1.2V_{stall}$  and at that speed the aircraft is rotated to an angle-of-attack such that the  $C_L = 0.8C_{Lmax}$ . The aircraft then leaves the ground and transitions from horizontal to climbing flight over the distance  $S_{TR}$ .

#### 10.3.1 Ground Distance $S_G$

The *ground distance*  $S_G$  is defined as

$$S_G = \int_0^{V_{TO}} \frac{VdV}{a} = \frac{1}{2} \int_0^{V_{TO}} \frac{dV^2}{a} \tag{10.1}$$

where  $a$  is the acceleration during  $S_G$  and

$$V_{TO} = 1.2 V_{stall} = 1.2 \sqrt{\frac{W_{TO}}{S_{ref}} \frac{2}{\rho C_{Lmax}}} \tag{10.2}$$

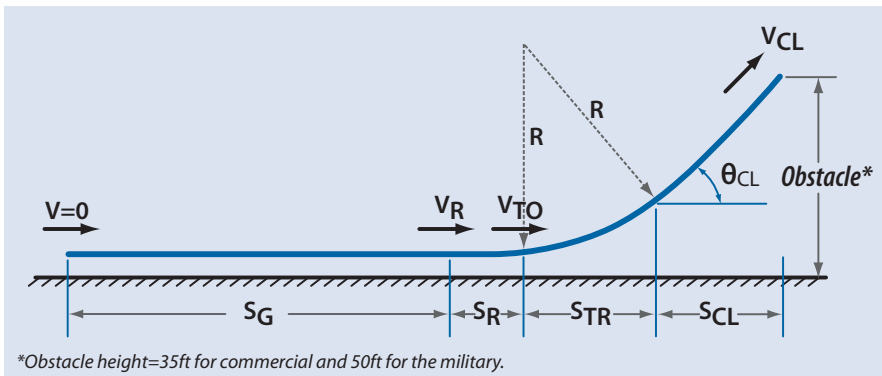


Figure 10.3 Schematic of an aircraft takeoff analysis.

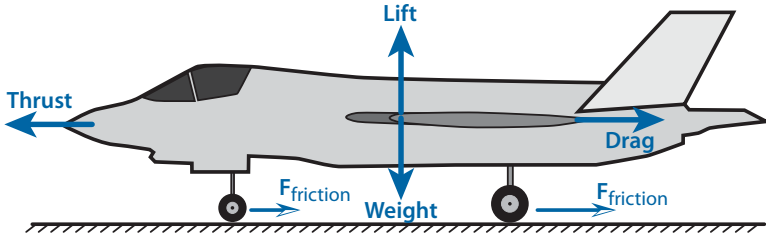


Figure 10.4 Force diagram during ground run.

and  $C_{L_{max}}$  is for a particular flap setting. The  $C_{L_{max}}$  is determined using the methods of Chapter 9.

From the force diagram shown in Fig. 10.4,

$$a = \frac{g}{W} [T - D - F_f] = \frac{g}{W} [T - D - \mu(W_{TO} - L)] \quad (10.3)$$

where  $\mu$  is the coefficient of friction for brakes off (see Table 10.3).

The lift and drag during the ground run are given by

$$D = (0.5)\rho V^2 S_{ref} [C_{D0} + \Delta C_{D_{flap}} + \Delta C_{D_{gear}} + KC_{LG}^2]$$

$$L = (0.5)\rho V^2 S_{ref} C_{LG}$$

where  $C_{LG}$  is the lift coefficient during the ground run for a particular flap setting (see Fig. 9.22, Chapter 9). There is a difference in the  $C_L$  vs  $\alpha$  curve

Table 10.3 Coefficients of Friction for Various Takeoff and Landing Surfaces

Type of Surface	Brakes Off, Average Ground Resistance Coefficient	Brakes Fully Applied, Average Wheel-Braking Coefficient
Concrete or macadam	0.015–0.04	0.3–0.6
Hard turf	0.05	0.4
Firm and dry dirt	0.04	0.30
Soft turf	0.07	0.5
Wet concrete	0.05	0.2
Wet grass	0.10	0.2
Snow- or ice-covered field	0.01	0.07–0.10



for an aircraft in ground effect (IGE) and out of ground effect (OGE). This difference is slight and will be ignored for the moment but is discussed in Section 10.7 for the L-1011. The  $\Delta C_{D_{flap}}$  is determined from data in Fig. 9.25 and  $\Delta C_{D_{gear}}$  from Fig. 10.5.

The *landing gear drag coefficient*  $\Delta C_{D_{gear}}$  is a difficult term to determine. The landing gear drag is dependant on the flap setting, the aircraft  $C_L$ , and sometimes the spoilers. It is a nightmare in computational fluid dynamics and is seldom attempted. Wind tunnel testing usually underestimates the  $\Delta C_{D_{gear}}$  because the full-scale landing gear is often not known at this point in the design and it is expensive to model all of the gear’s detail. Thus, determining the landing gear drag is usually delayed until flight testing, and then it is a low priority because the landing gear is already built and the aircraft is flying. Figure 10.5 and Table 10.4 present the landing gear drag coefficients of current aircraft. Based upon this discussion the data needs to be used carefully.

The landing gear is designed to be functional, reliable, and lightweight—but not low drag. The reason is that most landing gears are retracted inside the aircraft during up-and-away flight. If the gear is not to be retracted, it is streamlined by shaping the struts and fitting a fairing over the wheels (sometimes called *wheel pants*). During landing and takeoff the landing gear is extended and the drag must be accounted for. During takeoff the landing gear drag is a nuisance because it reduces the acceleration to  $V_{TO}$ .

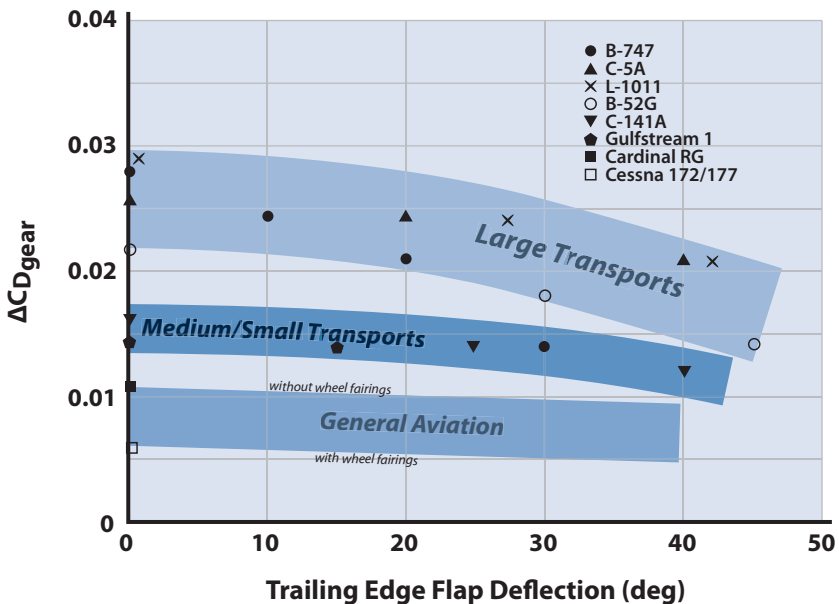


Figure 10.5 Drag of landing gear.

**Table 10.4** Landing Gear Drag Coefficients

Aircraft	Reference Area (ft <sup>2</sup> )	$\Delta C_{D_{gear}}$	Landing Gear Configuration <sup>a</sup>
<b>Fighters</b>			
A-7	375	0.028	Two-wheel NLG, two one-wheel MLG
F-104	196	0.035	One-wheel NLG, two one-wheel MLG
F-16A1B	300	0.0325	One-wheel NLG, two one-wheel MLG
F-22	840	0.014	One-wheel NLG, two one-wheel MLG
U-2S	1000	0.0045	One dual-wheel MLG, large tail wheel, and two wingtip pogos
<b>Large transports</b>			
L-1011	3456	0.028–0.0205	Two-wheel NLG, two four-wheel trucks MLG
C-5A	6200	0.0257–0.021	Four-wheel NLG, four four-wheel trucks MLG
B-747	5500	0.028–0.014	Two-wheel NLG, four four-wheel trucks MLG
B-52G	4000	0.024–0.0155	Quadricycle with wingtip gear, four dual-wheel MLG
<b>Medium transports</b>			
P-3	1300	0.020	Two-wheel NLG, two two-wheel MLG
L-1049 Connie	1650	0.024	Two-wheel NLG, two two-wheel MLG
B 727	1650	0.017	Two-wheel NLG, two two-wheel MLG
DC-8	2771	0.012	Two-wheel NLG, two four-wheel trucks MLG
C-141A	3228	0.0165–0.012	Two-wheel NLG, two four-wheel trucks MLG
<b>Small transports</b>			
S-3A	598	0.023	Two-wheel NLG, two one-wheel MLG
Gulfstream I	615	0.015	Two-wheel NLG, two one-wheel MLG
Fokker F-27	754	0.024	One-wheel NLG, two dual-wheel MLG
<b>General aviation</b>			
Cessna 172	226	0.006 <sup>b</sup>	One-wheel NLG, two one-wheel MLG
Cessna 177	174	0.006 <sup>b</sup>	One-wheel NLG, two one-wheel MLG
Cardinal RG	174	0.011	One-wheel NLG, two one-wheel MLG

<sup>a</sup>Abbreviations: NLG, nose landing gear; MLG, main landing gear.

<sup>b</sup>Fixed landing gear with wheel fairings.

However, during landing the landing gear drag is useful as it shortens the air distance and helps slow the aircraft down during braking.

The data in Fig. 10.5 and Table 10.4 reveal several interesting things. First, the drag coefficient due to the landing gear is huge: equal to or greater

than the  $C_{D_{min}}$  of the entire aircraft in most cases. Second, the  $\Delta C_{D_{gear}}$  decreases as the flaps are deflected. This is because the flap deflection increases the circulation about the wing, and the landing gear beneath the wing is in a lower dynamic pressure field than the rest of the aircraft. Figure 10.5 shows that this is more prevalent on transport aircraft, which typically have more sophisticated flap systems to achieve higher maximum  $C_L$  (see Fig. 9.7). Fighter and general aviation aircraft have simpler flap systems, have lower maximum  $C_L$ , and exhibit a fairly constant  $\Delta C_{D_{gear}}$ . The fixed gear on general aviation aircraft is typically a simple strut-and-wheel (with wheel pants) arrangement referenced to a large wing area (low  $W/S$ ) giving a relatively low  $\Delta C_{D_{gear}}$ . Fighter aircraft on the other hand have beefy retractable gear and small wing area (high  $W/S$ ) giving a relatively large value for  $\Delta C_{D_{gear}}$ .

The designer should pick a value for  $\Delta C_{D_{gear}}$  from Fig. 10.5 or Table 10.4 for their class of aircraft to use in the ground  $C_D$  build-up. Remember that the flaps are usually retracted during the braking ground run (landing) and set to the takeoff position for the acceleration ground run (takeoff).

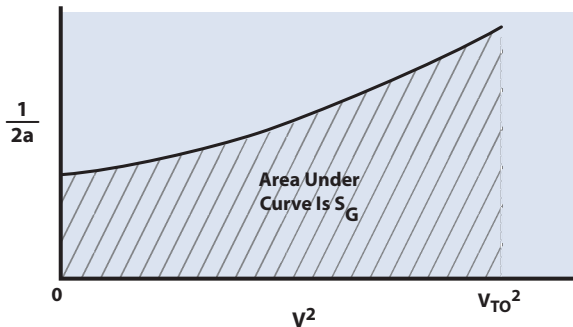
There are several ways to calculate  $S_G$ :

1. Approximate the integral, Eq. (10.1).
2. Assume the acceleration  $a$  is constant, equal to the value at  $V = 0.707 V_{TO}$ .

Then solve Eq. 10.3 for  $a$  at  $V = 0.707 V_{TO}$  and then

$$S_G = \frac{1}{2} \frac{V_{TO}^2}{a_{(at\ 0.707\ V_{TO})}} \tag{10.4a}$$

3. Stepwise integration of Eq. (10.1), that is, calculate  $a$  for values of  $V = 0, 20, 40, \dots, V_{TO}$  and then plot  $1/2a$  versus  $V^2$  as shown in Fig. 10.6. The value for  $S_G$  is the area under the curve. Putting Eq. (10.2) into Eq. (10.4a) gives



**Figure 10.6** Stepwise integration for ground roll distance  $S_G$ .

$$S_G = \frac{1.44(W/S_{\text{ref}})_{\text{TO}}}{g\rho C_{L_{\text{max}}} \left[ (T/W) - (D/W) - \mu(1 - L/W) \right]} \quad (10.4b)$$

where the lift, drag, and thrust terms are evaluated at a speed of  $0.707V_{\text{TO}}$ . From Eq. (10.4b) it can be seen that there are several factors the designer can influence to vary the takeoff ground run: that is, takeoff wing loading  $(W/S)_{\text{TO}}$ , takeoff thrust-to-weight ratio  $(T/W)$ , retardation force-to-weight ratio  $(D + F_f)/W$ , and maximum wing lift coefficient.

Low values of  $(W/S)_{\text{TO}}$  can shorten  $S_G$  but will result in poor riding qualities (due to sensitive gust response), less efficient cruise, and poor acceleration. Achieving a short takeoff through low wing loading is considered acceptable only when other performance requirements are lower priority.

A high thrust-to-weight ratio will shorten the takeoff roll but the engines should not be sized by the takeoff requirement alone. If the thrust is installed solely to expedite takeoff, cruise efficiency is likely to suffer. The  $(T/W)_{\text{TO}}$  must be selected by considering all the mission requirements (see Chapter 15).

An increase in  $C_{L_{\text{max}}}$  is the one method by which the designer can influence just the takeoff (or landing) performance. The idea is to obtain a large increase in  $C_{L_{\text{max}}}$  for a small increase in drag because the quantity  $\max(D + F_f)/W$  decreases the ground run acceleration. The  $C_{L_{\text{max}}}$  and aircraft  $C_D$  both increase with flap deflection. Thus, the  $\delta_f$  for minimum ground run is a compromise between lowering  $V_{\text{TO}}$  (by increasing  $C_{L_{\text{max}}}$ ) and lowering the ground run acceleration (by increasing  $C_D$ ). High  $C_{L_{\text{max}}}$  is the answer for STOL operation and is receiving considerable attention from government agencies and industry.

### 10.3.2 Rotation Distance, $S_R$

*Rotation distance* is the distance in which the aircraft (still on the ground) is rotated to that  $\alpha$  such that  $C_L = 0.8C_{L_{\text{max}}}$ . For the military this rotation takes two seconds, whereas for FAA–commercial aircraft this time is established during flight testing:

$$S_R = 2V_{\text{TO}} \quad (10.5)$$

(where  $V_{\text{TO}}$  is in feet per second). Note that the geometry of the aircraft should be checked to insure that the tail of the aircraft does not strike the ground during this rotation. For airplanes that are “geometry limited” during ground rotation the FAA applies different criteria for establishing the various takeoff speeds.

### 10.3.3 Transition Distance, $S_{TR}$

In the *transition distance* the aircraft flies a constant-velocity arc of radius  $R$  (see Fig. 10.3). The load factor on the aircraft is

$$n = 1 + \frac{V_{TO}^2}{Rg} = \frac{L}{W} = (0.8)(1.2)^2 = 1.15$$

and solving for

$$R = \frac{V_{TO}^2}{0.15g} \tag{10.6}$$

(in feet). The aircraft is assumed to be in an unaccelerated climb such that

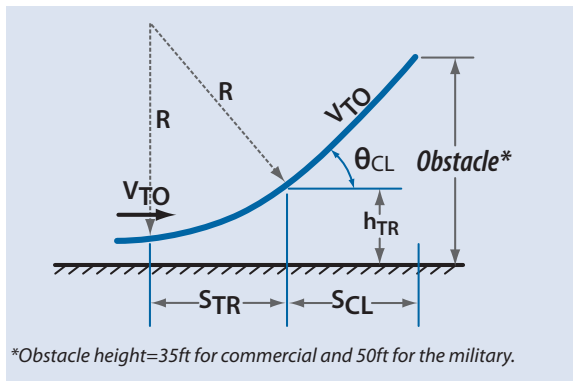
$$\text{Rate of climb} = V_{TO} \sin \theta_{CL} = \frac{V_{TO}(T - D)}{W}$$

and then becomes

$$\text{Rate of climb} = V_{TO} \sin \theta_{CL} = \frac{V_{TO}(T - D)}{W} \tag{10.7}$$

Now the transition distance is (see Fig. 10.7)

$$S_{TR} = R \sin \theta_{CL} \tag{10.8}$$



**Figure 10.7** Schematic for transition and climb distance.

### 10.3.4 Climb Distance, $S_{CL}$

The *climb distance* is

$$S_{CL} = \frac{50 - h_{TR}}{\tan \theta_{CL}} \quad (10.9)$$

where  $h_{TR}$  is shown in Fig. 10.7. If  $h_{TR} > 50$  ft, then  $S_{CL} = 0$ .

### 10.3.5 Time During Takeoff

Assume the ground run acceleration  $a$  is constant, equal to  $0.707V_{TO}$ . Then

$$\text{time (ground)} = t_g = \frac{1}{a} \int_0^{V_{TO}} dV = \frac{V_{TO}}{a}$$

The rotation time is assumed to be two seconds. The time for transition and climb can be approximated by

$$\text{time (transition)} = t_{TR} = \frac{S_{TR} + (S_{CL} / \cos \theta_{CL})}{V_{TO}}$$

## 10.4 Landing Analysis

The *landing distance* is the horizontal distance required to clear a 50-ft obstacle, free roll, and then brake to a complete stop. Figure 10.8 shows the schematic for the landing analysis.

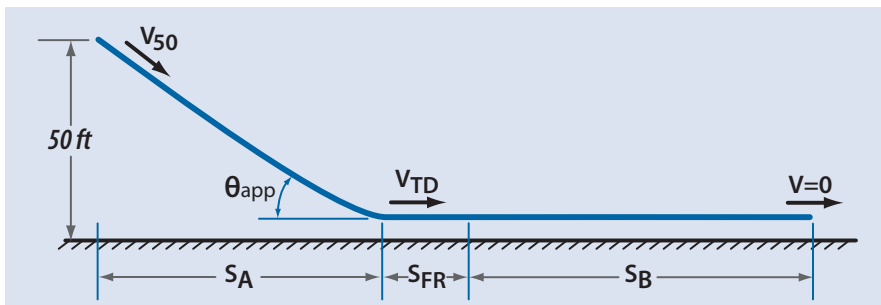


Figure 10.8 Schematic for landing analysis.

It is assumed that the velocity over the 50-ft obstacle  $V_{50} = 1.3V_S$  and the touchdown velocity  $V_{TD} = 1.15V_S$ . The  $V_S$  is for the aircraft in its landing configuration, that is,

$$W_L = \text{aircraft weight with 1/2 fuel remaining}$$

$$C_{L_{land}} = C_{L_{max}} \text{ for flaps in landing configuration}$$

The landing distance is the sum of the *air distance*  $S_A$ , the *free-roll distance*  $S_{FR}$ , and the *braking distance*  $S_B$ .

### 10.4.1 Air Distance $S_A$

The change in kinetic energy (KE) plus potential energy (PE) is

$$KE + PE = (\text{retarding force})S_A$$

Assume  $\theta_{app}$  to be small such that  $\cos\theta_{app} \approx 1$ . Then

$$\frac{W}{g} \left[ \frac{V_{50}^2}{2} + 50g - \frac{V_{TD}^2}{2} \right] = FS_A$$

$$S_A = \frac{W}{F} \left[ \frac{V_{50}^2 - V_{TD}^2}{2g} + 50 \right]$$

because  $W \approx L$  and  $F \approx D$

$$S_A = \frac{L}{D} \left[ \frac{V_{50}^2 - V_{TD}^2}{2g} + 50 \right] \tag{10.10}$$

or  $S_A = 50/\tan \theta_{app}$ , where  $\theta_{app}$  = approach glide slope (3 deg for typical CTOL, 7 deg for STOL) and where  $L = W_L$  and  $D = C_{Dq}S_{ref}$

$$C_D = C_{D0} + KC_{L_{max}}^2 + \Delta C_{D_{flaps}} + \Delta C_{D_{gear}} \tag{10.11}$$

### 10.4.2 Free Roll Distance $S_{FR}$

The *free-roll distance*  $S_{FR}$  is the distance covered while the pilot reduces the power to idle, retracts the flaps, deploys the spoilers, and applies the brakes. Free roll is *assumed* to be three seconds so that

$$S_{FR} = 3V_{TD} \tag{10.12}$$

### 10.4.3 Braking Distance $S_B$

Let  $a$  = deceleration. Then

$$S_B = \int ds = \int_{V_{TD}}^0 \frac{VdV}{a} = \frac{1}{2} \int_{V_{TD}}^0 \frac{d(V^2)}{a}$$

Using the force diagram in Diagram 10.1 yields

$$a = (1/m) [T - D - F_f - R]$$

where  $R$  is a reverse thrust during braking and  $T = 0$ . Also,  $F_f$  is the force of friction,  $F_f = \mu(W_L - L)$ , and  $\mu$  is given in Table 10.3.

Also,

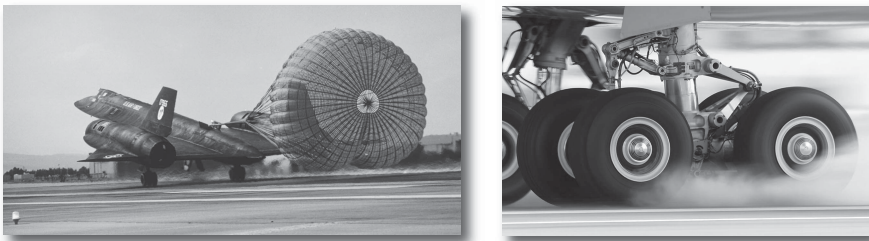
$$C_D = C_{D0} + KC_{LG}^2 + \Delta C_{Dflaps} + \Delta C_{Dgear} + \Delta C_{Dmisc} + \Delta C_{Dspoilers}$$

where

- $C_{LG}$  =  $C_L$  at the  $\alpha$  during braking (see Fig. 9.22).
- $\Delta C_{Dflaps}$  =  $\Delta C_D$  due to flaps (from Fig. 9.25). If flaps are retracted during braking,  $\Delta C_{Dflaps} = 0$  and  $C_{LG} \approx 0$
- $\Delta C_{Dspoilers}$  =  $\Delta C_D$  due to spoilers
- Use  $\Delta C_{Dspoilers} = 0.006 - 0.007$
- $\Delta C_{Dmisc}$  =  $\Delta C_D$  due to miscellaneous items such as a drag chute and high energy absorption brakes (Fig. 10.9)
- Use  $\Delta C_{Dmisc} = 1.4$  for drag chutes based upon their inflated frontal area [8].

By neglecting reverse thrust  $R$  and setting  $T = 0$ ,

$$-a = \frac{g}{W_L} (F_f + D) = \frac{g}{W_L} [\mu(W_L - L) + C_D q S_{ref}]$$



**Figure 10.9** Brakes in action: **left**) SR-71 during braking ground roll with drag chute deployed, and **right**) typical commercial transport main gear during heavy braking.



$$S_B = \frac{W}{2g} \int_{V_{TD}}^0 \frac{d(V^2)}{\mu W_L + (\rho/2) S_{ref} V^2 (C_D - \mu C_{LG})}$$

$$S_B = \frac{W_L}{g \mu \rho S_{ref} [(C_D/\mu) - C_{LG}]} \ln \left[ 1 + \frac{\rho}{2} \frac{S_{ref}}{W_L} \left( \frac{C_D}{\mu} - C_{LG} \right) V_{TD}^2 \right] \quad (10.13)$$

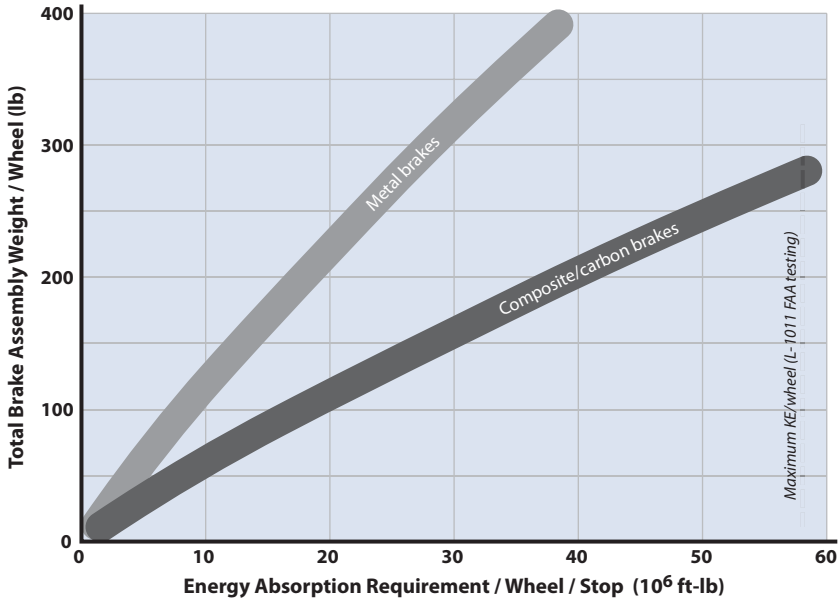
An examination of the landing analysis reveals that short landing distances require a low  $V_{stall}$  and a large retardation force (unlike the takeoff). A low  $V_{stall}$  is the result of a low wing loading at landing and a high  $C_L$ . Fortunately, the high  $C_L$  will also give a large drag. Thus, high  $C_{L_{max}}$  is extremely important for short landing distances.

## 10.5 Aircraft Retardation Devices

In designing an aircraft, the method selected to stop the vehicle on landing is dependent upon weight and maintenance penalties, and hence cost, that one is prepared to pay. To dissipate the kinetic energy the aircraft possesses at touchdown, the engineer may select to use mechanical means (wheel brakes or arresting gear), propulsive means (reverse thrust), aerodynamic means (drag chutes or speed brakes/spoilers), or some combination of these methods, but the ultimate decision must be based on a consideration of the overall weapon or transportation system and not just the airframe itself.

Wheel brakes have been the traditional means for halting landing rolls; no matter what other braking devices may be selected by the designer, all aircraft must have some wheel braking capability for use while taxiing and during ground maneuvering. For a given brake life, the weight of the brake assembly is a function of the energy that must be absorbed. The level of this energy can be calculated using the predicted landing weight and a touchdown velocity equal to  $1.15V_{stall}$  for that weight; the brake assembly weight can then be estimated using Fig. 10.10, from [9]. Notice the effect that brake lining life has on brake weight. Some tradeoff must be made between airframe cost–performance and maintenance (hence, total system) costs. A large aircraft requiring frequent full-stop landings and low maintenance, such as an airliner, could not depend on wheel brakes for its entire stopping capability without paying a penalty in payload capacity.

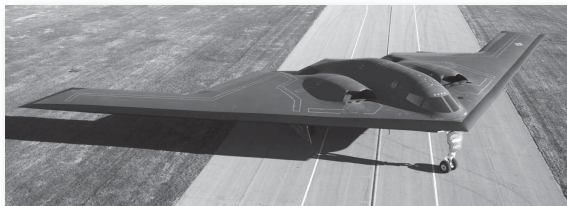
With the trends to higher landing weights and speeds of modern aircraft, energy dissipation requirements have become so large that the weight of a brake assembly that would provide the entire retardation effort would be prohibitive even for low-life brake linings. Some additional means of energy dissipation must be provided to supplement the wheel brakes, and aerodynamic and propulsive retardation devices provide this capability. A



**Figure 10.10** Weight of main gear wheel brakes based on maximum energy “rejected takeoff” (RTO).

secondary requirement for these devices has been generated by the desire to shorten landing distances by supplying some stopping force soon after touchdown, when velocities are still high and wheel brakes are least effective. Again, drag chutes and thrust reversers meet this need. However, the B-2 shown in Fig. 10.11 dissipates energy using its split ailerons. It has no drag chute.

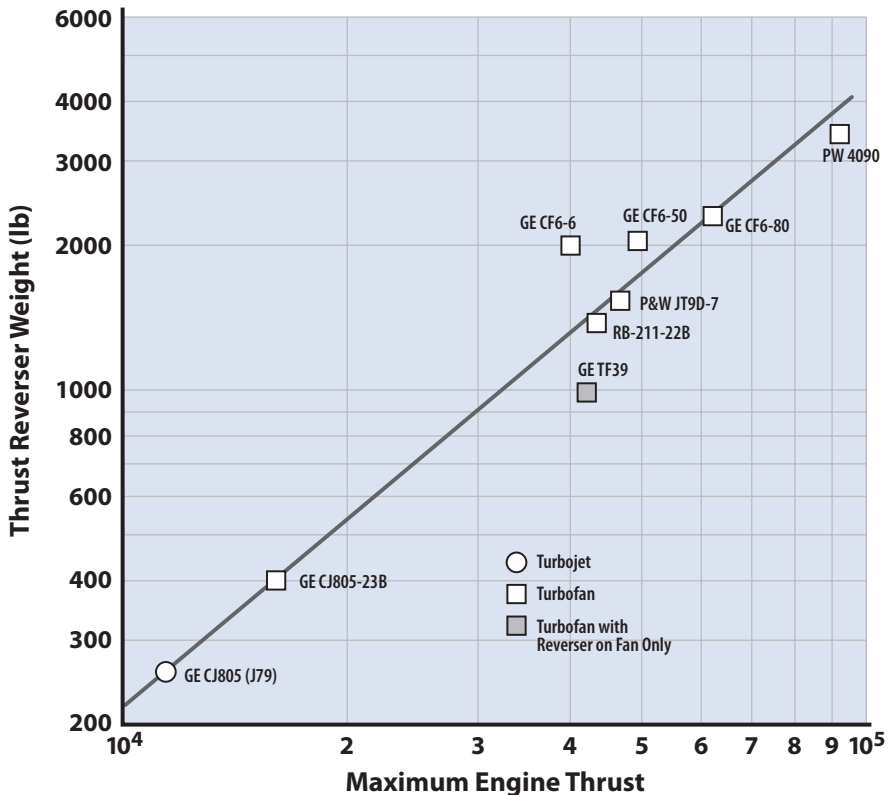
Thrust reversers on jet aircraft provide a significant ground deceleration force with high reliability and little additional maintenance with repeated application. On some transport aircraft (DC-8, C-5) the thrust reversers on inboard engines may be activated in flight to function as speed brakes. A jet or turbofan engine with thrust reversers is capable of providing up to approximately 40% of the rated takeoff thrust for braking.



**Figure 10.11** B-2 taxiing.

However, the relatively high weight of these devices has all but prohibited their use on combat aircraft. The major exception to this is the Swedish Viggen, a STOL fighter whose thrust reverser is activated automatically upon touchdown for rapid stopping. A thrust reverser may be designed by the engine manufacturer or may be provided by the airframe designer. The weight of a thrust reverser installation will vary with the rated thrust of the engine and may be estimated from Fig. 10.12, which has been compiled from both airframe and engine manufacturers' data.

The provision for reversible pitch on propeller aircraft is an inexpensive, lightweight method of retardation for this class of aircraft. Turboprop engine-propeller combinations have a capability of providing a reverse force of up to 60% of their rated static thrust, whereas reciprocating engines can provide a lower retardation force (approximately 40% of static thrust) and require a longer delay between touchdown and the actuation of full reverse thrust. Reversible propellers also give an aircraft the ability to taxi backward, an extremely useful asset in combat airlift operations.



**Figure 10.12** Turbojet and turbofan thrust reverser weight as a function of maximum engine thrust.

Drag chutes have received almost universal acceptance as landing retardation devices on high-performance combat aircraft (the F-117A used one). They are lightweight, reliable, and if one is willing to ignore the problems of repacking, relatively simple. Drag parachutes are most effective at higher velocities and, thus, nicely complement the capabilities of wheel brakes. Reference [8] gives an average drag coefficient based on projected (inflated) cross-sectional area of 1.4 for nylon or ribbon-type parachutes. The parachute weight (in pounds) can be predicted using the formula

$$W_p = 6.5 \times 10^{-2} (d_{\text{chute}})^2$$

where  $d_{\text{chute}}$  is the maximum chute diameter in feet. The weight of the entire chute and rigging is approximately 3–4 times this figure.

## 10.6 Critical Field Length (Balanced Field Length)

The *critical field length* (sometimes called *balanced field length*) is a balance between the distance required to accelerate to  $V_1$  and then either continue the takeoff over 35 ft with one engine inoperative or brake to a stop. The definition of takeoff field length for commercial transport aircraft is 115% of the distance over 35 ft with all engines operating or the critical field length, whichever is greater.

The analysis is one of selecting a failure recognition speed  $V_{\text{EF}}$  and then calculating two distances. The first distance, called LAB, is the distance required to accelerate to  $V_{\text{EF}}$ , free roll for 3 seconds at  $V_{\text{EF}}$ , and then brake to a full stop. The second distance, called LAC, is the distance required to accelerate to  $V_{\text{EF}}$  and then continue the takeoff over 35 ft with one engine out. During the one-engine-out phase, the thrust is reduced accordingly and the drag is increased to account for a windmilling engine. There is a unique value for  $V_{\text{EF}}$  such that LAB = LAC. This value for  $V_{\text{EF}}$  is also called the *refusal speed* and the distance LAB = LAC is called the *critical field length* or *balanced field length*. This analysis is shown in Fig. 10.13. If an engine should fail below  $V_{\text{EF}}$ , the pilot should brake to a stop; if one engine fails above the refusal speed, the pilot should continue the takeoff with one engine out. Figure 10.14 illustrates several high performance takeoffs.

## 10.7 Comparison of Analytical Estimates With L-1011 Flight Test

This section will determine the takeoff and landing distances for the L-1011 using the methods in this chapter and Chapter 6, and compare the results with flight test data.

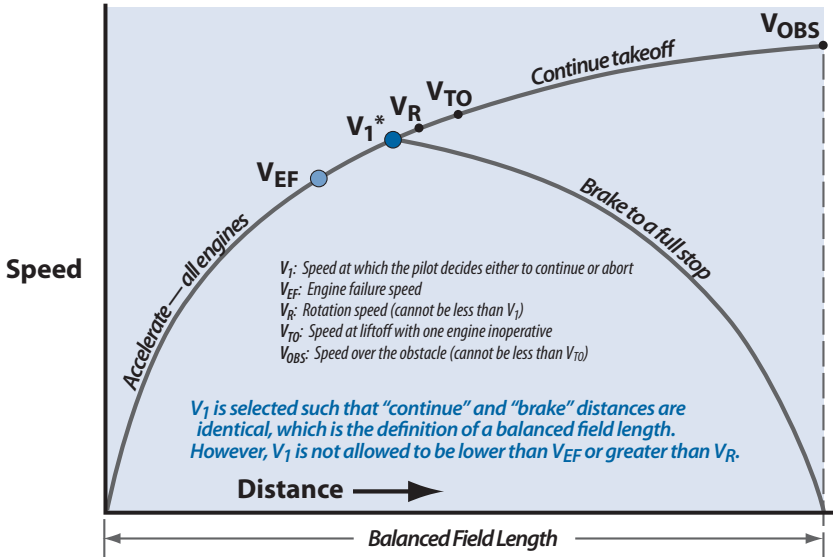


Figure 10.13 Schematic of balanced field length.

The Lockheed L-1011 TriStar is a subsonic wide-body commercial transport aircraft designed to operate over transcontinental, short- and medium-length airline routes with passenger payloads of up to 260 passengers in a 15/85 mixed seating and with passenger payloads of up to 345 in an all-economy-class seating. The L-1011 received FAA certification in April 1972. Lockheed produced 250 aircraft between 1968 and 1984. The airplane is powered by three Rolls Royce RB.211–22 high-bypass-ratio turbofan engines. Two engines are mounted in underwing pylons and the third engine is mounted in the fuselage aft body. Figure 10.15 shows the L-1011 with emphasis on the high-lift system, and Table 10.5 gives dimensions and geometry for the aircraft.

The high-lift system consists of double-slotted Fowler TE flaps and full-span LE slats. Slat and flap extension is manually controlled by the pilot using the flap handle on the center console. Fully extended, the three inboard slat panels deflect 28 deg and the four outboard slat panels deflect 30 deg.

The trailing edge flaps consist of four double-slotted Fowler-type flap surfaces on each wing. The following discrete flap positions may be selected for the corresponding takeoff, landing, or cruise segment:

- Flaps up, cruise
- Flaps down 4 deg, transition
- Flaps down 10 deg, takeoff and alternate approach

- Flaps down 18 deg, takeoff
- Flaps down 27.5 deg, takeoff
- Flaps down 33 deg, alternate landing
- Flaps down 42 deg, landing

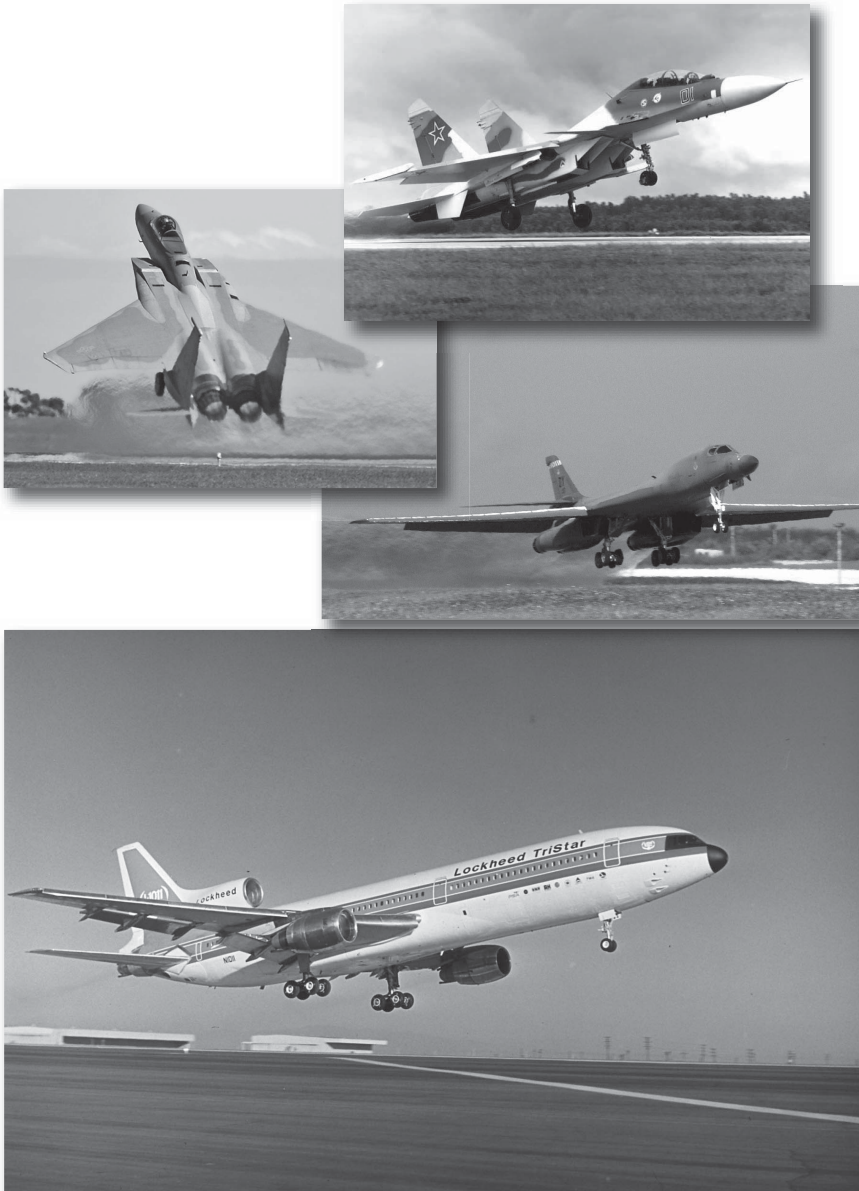


Figure 10.14 Mig 31, F-15, B-1B, and L1011 takeoffs.

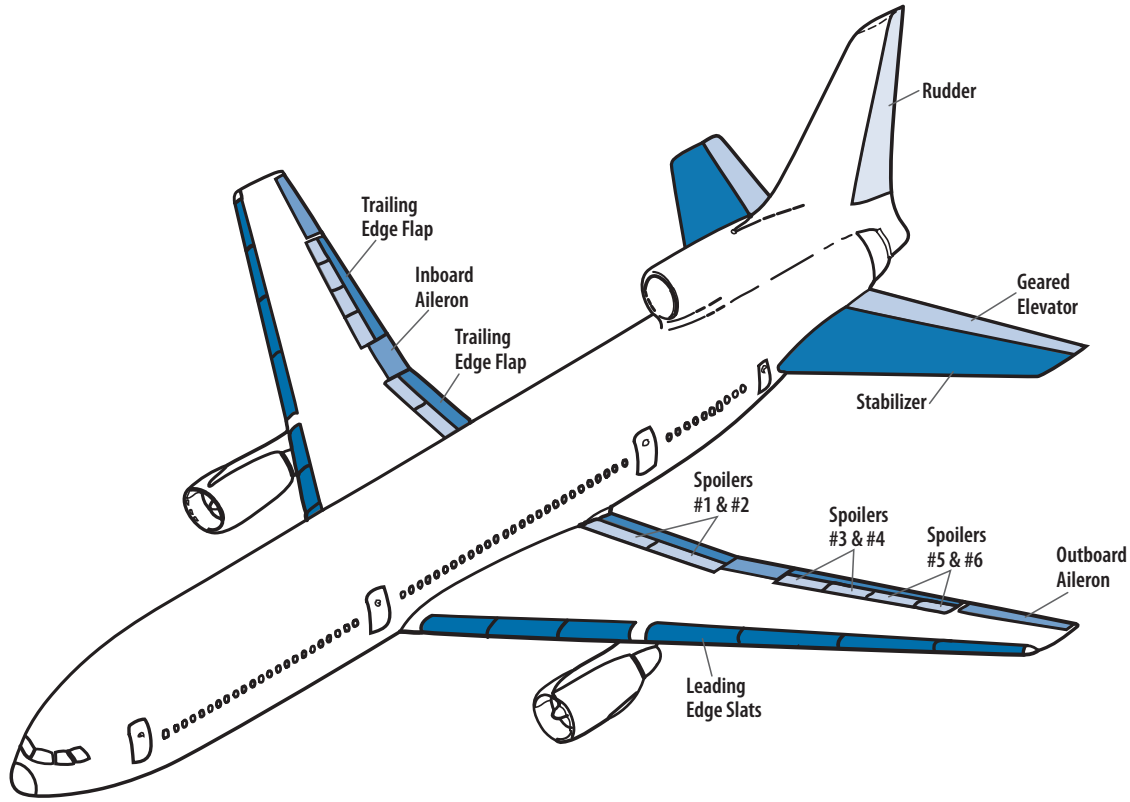


Figure 10.15 L-1011 control surfaces arrangement.

**Table 10.5** Summary of L-1011 Dimensions and Geometry

Geometry	Dimensions
Maximum takeoff weight (lb)	430,000
Maximum landing weight (lb)	358,000
Maximum fuel weight (lb)	159,560
Wing span (ft)	155.3
Wing area (ft <sup>2</sup> )	3456
Wing sweep (quarter-chord)	35 deg
Aspect ratio	6.95
Mean aerodynamic chord (mac; ft)	24.5
Location of mac leading edge	FS 1143
Spoiler area/span (each side ft <sup>2</sup> /ft)	
1	27/10
2	34/12
3	12/5
4	16/7
5	7/3
6	11/5
TE flap area/span/chord (each side ft <sup>2</sup> /ft/ft)	
Inboard	145/22/6.5
Outboard	123/22/30% chord
LE slat area/span (each side ft <sup>2</sup> /ft)	
Inboard	61.74/22
Outboard	118/38.67
Horizontal tail	
Area (ft <sup>2</sup> )	1282
Aspect ratio	4.0
Taper ratio	0.33
mac (ft)	19.5
Location of mac leading edge	FS 1885
Vertical tail	
Area (ft <sup>2</sup> )	550
Aspect ratio	1.6
Taper ratio	0.3
mac (ft)	20.3
Location of mac leading edge	FS 1924



The TriStar also has six pairs of spoilers on each wing to dump the load during landing to reduce the lift on the aircraft, thereby putting more weight on the wheels for greater braking. The spoilers are manually deflected up to 60 deg.

**Example 10.1 Takeoff Distance Comparison**

We calculate the takeoff distance using the method discussed in this chapter, with the following initial conditions:

Weight	358,000 lb
TE flap deflection	27.5 deg
Maximum $C_L$	2.0 (IGE at $\alpha = 16$ deg, limited by tail strike)
Rolling friction coefficient, $\mu$	0.015 (measured during flight test)
Ground $C_L, C_{LG}$	0.32 (value at $\alpha = 0$ deg and $\delta_f = 27.5$ deg from flight test)
Thrust, all three engines	100,022 lb
$\Delta C_{D_{flap}}$	0.042 (from Fig. 9.25)
$C_{D_{min}}$	0.0175 (from Fig. G.1)
$\Delta C_{D_{gear}}$	0.024 (from Fig. 10.5)
Air density, $\rho$	0.002378 slug/ft <sup>3</sup>
Ground run drag-due-to-lift factor, $K$	0.0468 (from flight test)

The value  $K = 0.0468$  can be estimated considering the drag-due-to-lift in the presence of ground effects. Using Fig. 10.2a and assuming the  $2h/b = 0.12$  during the ground run, the effective AR for the L-1011 is approximately 17. From Fig. G.9 the wing efficiency factor for this class of aircraft can be estimated to be  $e = \sim 0.4$ , giving  $K = 0.0468$ .

Assuming  $V_{TO} = 1.2V_S$  gives a takeoff speed of 250 ft/s, or 148 kt, which is under the flap and slat placard limit of 200 kt for the L-1011. The drag coefficient during the ground run is determined as follows:

$$C_{D_{ground}} = C_{D_{min}} + KC_{LG}^2 + \Delta C_{D_{flap}} + \Delta C_{D_{gear}} = 0.0883$$

The dynamic pressure at  $0.7V_{TO}$  is 36.4 psf, which gives  $L = 40,270$  lb and  $D = 11,107$  lb. Using Eq. (10.3) gives an acceleration at  $0.7V_{TO}$  of 7.57 ft/s<sup>2</sup> ( $\sim 1/4$  g) and, from Eq. (10.4), a ground run distance  $S_G = 4172$  ft.

At  $V_{TO}$  the aircraft rotates to an  $\alpha$  such that  $C_L = 0.8C_{L_{max}}$ . It is assumed that this rotation takes two seconds. The aircraft geometry should be checked to make sure the aircraft can rotate to this  $\alpha$  without striking the tail on the ground. Thus,  $S_R = 500$  ft.

**Table 10.6** Comparison of Takeoff Analysis

Phase	Eq. (10.4) Eq. (10.5) Eq. (10.8)	Eq. (6.3)	Flight Test (1972)
Ground run	4172	3867	3632
Rotate and transition	875	500	1225
Takeoff distance	5047	4367	4857

The transition distance analysis indicates that the L-1011 clears the 35-ft obstacle about midway through the transition phase to a steady-state climb rate of 61.6 ft/s. Thus, it is assumed that the L-1011 spends about 1.5 s in the transition phase and covers another 375 ft in distance. *The total takeoff distance for the L-1011 is 5047 ft.*

The comparison with the simplified method of Chapter 6 [Eq. (6.3)] and flight test results are shown in Table 10.6. It should be recognized that the actual takeoff distance depends on several factors, such as winds, runway characteristics, aircraft aerodynamic performance, and pilot technique. Equation (6.3) should be used for early analysis and sizing the wing loading. The analysis in this chapter should then be used to refine the takeoff analysis as more information is available on the aircraft design.

**Example 10.2 Landing Distance Comparison**

We calculate the landing distance using the method discussed in this chapter, with the following initial conditions:

Weight	345,100 lb
TE flap deflection	42 deg
Maximum $C_L$	2.63 (IGE from flight test)
Braking friction coefficient, $\mu$	0.32 (measured during flight test)
Ground $C_L, C_{L_G}$	-0.18 (value at $\alpha = 0$ deg, $\delta_r = 0$ deg, and spoilers deployed, from flight test)
$\Delta C_{D_{flap}}$	0.095 (from Fig. 9.25 during approach); 0 (flaps retracted during ground braking)
$C_{D_{min}}$	0.0175 (from Fig. G.1)
$\Delta C_{D_{gear}}$	0.021 (from Fig. 10.5 for $\delta_r = 42$ deg); 0.029 (from Fig. 10.5 for $\delta_r = 0$ deg)
$\Delta C_{D_{spoiler}}$	0.0065 (from [10])
Air density, $\rho$	0.002378
Average approach $L/D$	5.0 (IGE from flight test)
Drag-due-to-lift factor, $K$	0.057 (IGE from flight test)

Assuming  $V_{TD} = 1.15V_S$  gives a touchdown speed of 199 ft/s (124 kt), and  $V_{50} = 1.3V_S$  gives a speed over 50 ft of 225 fps (133 kt), which are both under the flap and slat placard limit of 164 kt for the L-1011.

The average approach  $K = 0.057$  can be estimated assuming an average value for  $2h/b = 0.32$ . From Fig. 10.2a the effective aspect ratio during approach is approximately 10.7. Estimating the wing efficiency factor using Fig. G.9 for this class of aircraft and  $AR = 10.7$  gives  $e \sim 0.52$  and  $K = 0.057$ .

The air-distance phase is one of the few times that drag is good. The larger the value of  $D/L$ , the steeper the glide slope and the shorter the air distance over the 50-ft obstacle. The drag coefficient on approach is

$$C_{D\text{Approach}} = C_{D\text{min}} + KC_{L\text{max}}^2 + \Delta C_{D\text{flap}} + \Delta C_{D\text{gear}} = 0.527$$

The value of  $L/D$  for the L-1011 during landing approach is 5.0. Using Eq. (10.10) gives an air distance of 1106 ft.

During the free-roll phase the L-1011 pilot is busy applying the brakes, putting the engines at idle, retracting the TE flaps, and deploying the spoilers. It is assumed that this takes three seconds, so that  $S_{FR} = 597$  ft. During the flight test of the L-1011 the test pilots routinely took under two seconds for this phase.

The drag coefficient during the ground braking phase is determined as follows:

$$C_{D\text{ground}} = C_{D\text{min}} + KC_{L_G}^2 + \Delta C_{D\text{flap}} + \Delta C_{D\text{gear}} + \Delta C_{D\text{spoiler}} = 0.0548$$

During ground braking the flaps are retracted and the spoilers deployed to dump the lift and put as much weight on the wheels as possible, to increase the friction force. The spoilers actually produce a small downward force coefficient of  $-0.18$ . Equation (10.13) is used to calculate a braking distance of 1778 ft. *The total landing distance is 3481 ft.*

The comparison with the simplified method of chapter 6 [Eq. (6.5)] and flight test results are shown in Table 10.7. The discussion for Table 10.7 is the same as that for Table 10.6 presented earlier. The dependence of the analysis on pilot technique is even more pronounced for landing because pilots (carrier pilots excluded) will flare the aircraft just prior to touchdown to give a soft landing and minimize tail strike. The distance covered during the flare varies significantly between pilots. The analysis in this chapter does not assume a flare.

**Table 10.7** Comparison of Landing Analysis

Phase	Eq. (10.10) Eq. (10.12) Eq. (10.13)	Eq. (6.5)	Flight Test (1972)
Air distance	1106	954	953
Free roll	597	Included below	315
Braking distance	1778	3014	1898
Landing distance	3481	3968	3166

The L-1011 compared favorably with its competition (the DC-10 and the Boeing 747), but a Rolls Royce bankruptcy in 1971 caused the L-1011 to arrive late in the marketplace and only 250 were built. Even so, the aircraft is a significant design achievement: The L-1011 is the first airplane to certify Category 3C landing capabilities using its spoilers to provide excellent control of lift during landing approach.

## 10.8 Airport Operations

Airport personnel have to be vigilant in maintaining safety of operations around airports. The presence of birds and wake turbulence can pose a real hazard to airport operations. Aircraft are especially vulnerable during the ATC (air traffic control) part of their mission as they are low and slow, high angle-of-attack, and the crew is in a high workload environment.

The vortex system generated by an aircraft during landing and takeoff (Fig. 10.1) is both beautiful (on a humid day) and dangerous. This vortex system is generated by a wing as it develops lift (see Section 2.6) and should not be confused with prop wash (the rotating air mass behind a propeller) or jet wash (the swirling hot gas from a jet engine exhaust), which are both of shorter duration and extent than the trailing vortex system. The trailing vortex generated by an aircraft wing (called wake turbulence) can cause a trailing aircraft in close proximity to the vortices to be flipped upside down. For this reason airports have landing and departure time intervals that gives the vortex system time to dissipate. The time intervals are dependant upon the temperature and wind conditions, and the relative size of the trailing aircraft to the lead aircraft that is generating the trailing vortices. A typical departure time interval is 3 minutes for a smaller aircraft taking off behind a larger aircraft. The landing time interval is in terms of separation distance. The separation for two aircraft of the same size (for example, two B 767s) is 4 nm and increases to 8 nm for a small aircraft landing behind a large aircraft (such as a Cessna Citation behind a B 747).

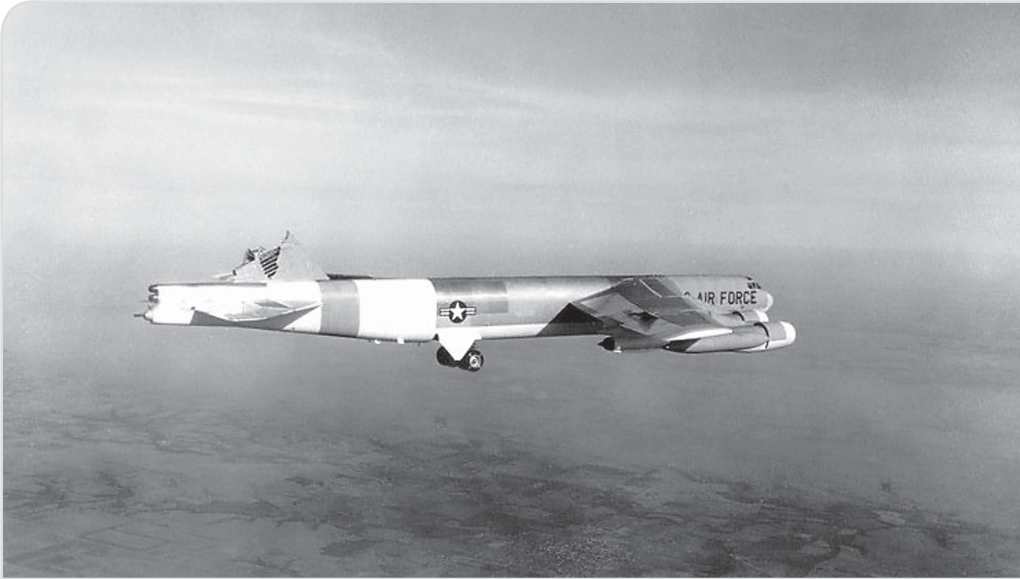
Birds around an airport are a problem as they can be ingested into a jet inlet or impact a propeller and shut down an engine. On January 15, 2009 an Airbus A320 struck a flock of Canadian Geese during departure from LaGuardia Airport, New York, which resulted in an immediate loss of thrust from both turbine engines. Due to the masterful piloting by the pilot the aircraft was ditched in the Hudson River with no loss of the 155 passengers and crew. Airports go to great lengths (scare crows, sound systems emanating shrill and annoying noise, and professional hunters) to discourage the bird population around airports.

## References

- [1] "Charts; Standard Aircraft Characteristics and Performance," Military Specification MIL-C-5011A, 14 Feb. 2003.
- [2] "Airworthiness Standards: Part 23—Normal, Utility and Acrobatic Category Airplanes; Part 25—Transport Category Airplanes," *Federal Aviation Regulation*, Vol. 3, U.S. Department of Transportation, U.S. Government Printing Office, Washington, DC, Dec. 1996.
- [3] "Guidelines for Preparation of Standard Aircraft Characteristics Charts and Performance Data of Piloted Aircraft (Fixed Wing)," AS-5263, Naval Air Systems Command, Patuxent River, MD, 23 Oct. 1986 (for Navy use in lieu of MIL-C-25011).
- [4] Davenport, F. J., Rengstorff, A. E., and Van Heyningen, V. E., "Takeoff and Landing Performance Ground Rules for Powered Lift STOL Transport Aircraft," U.S. Air Force Flight Dynamics Laboratory AFFDL-TR-73-19, Vol. 3, Wright-Patterson AFB, OH, May 1973.
- [5] Hebert, J., Moorehouse, D., and Richie, S., "STOL Takeoff and Landing Ground Rules," U.S. Air Force Flight Dynamics Laboratory AFFDL-TR-73-21, Vol. 3, Wright-Patterson AFB, OH, May 1973.
- [6] Carter, W. E., "Effect of Ground Proximity on the Aerodynamic Characteristics of Aspect Ratio I Wings with and without End Plates, II," NASA TN D-970, Langley Research Center, Oct. 1961.
- [7] Fink, M. P., and Lastinger, J. L., "Aerodynamic Characteristics of Low Aspect Ratio Wings in Close Proximity to the Ground," NASA TN D-926, Langley Research Center, July 1961.
- [8] Brown, W. D., *Parachutes*, Pitman, London, 1951.
- [9] Schaezler, G. B., "Synthesis of Ground Flotation Requirements and Estimation of Aircraft Running Gear Weight," Proc. 3rd Weight Prediction Workshop, Aeronautical Systems Division, Wright-Patterson AFB, OH, Oct. 23-27, 1967.
- [10] "FAA Type Certification Report, Model L-1011-385-1 with Rolls-Royce RB.211-22 Engines," Lockheed Rept. LR 25089, 14 July 1972.

## Chapter 11

# Preliminary Sizing of the Vertical and Horizontal Tails



- Tail Volume Coefficient Method
- Vertical Tail Sizing Criteria
- Horizontal Tail Sizing Criteria
- Location of Horizontal Tail Criteria
- Location of Vertical Tail Criteria

During flight this B-52 encountered severe CAT and lost most of its vertical tail. Yaw stability was lost, making the aircraft directionally unstable. Directional control was maintained through differential thrust from its four engines. The pilot was able to steer and land the airplane successfully!

*Good instincts usually tell you what to do long before your head has figured it out.*

Michael Burke

## 11.1 Tail Volume Coefficient Approach

At this point the aircraft has been sized [a takeoff gross weight (TOGW) has been estimated] and it has a wing–body configuration. Tails are now added to the configuration and their associated aerodynamics are determined. Before tail aerodynamics can be incorporated it is necessary to know the tail’s location (front, back, or no tail at all), shape, and size.

What the tails look like and where they are located is a design decision: The designer needs to decide what the tails will look like, determine their mean aerodynamic chord (mac), and decide where they will be located. Then the designer estimates the distance from the initial c.g. location (estimated in Chapter 8) to the macs of the vertical and horizontal tails (mac or  $\bar{c}_h$  and  $\bar{c}_v$ ). These distances are the moment arm length of the pitch and yaw stability and control devices and are shown in Fig. 11.1.

The sizing of the tail surfaces is a lot of work. It requires a precise knowledge of the c.g. location and is the subject of Chapters 21–23. Unfortunately, the c.g.’s location depends upon knowing the weight (size) of the tail surfaces. Thus, at this point the tail surfaces are sized using a shortcut technique called the *tail volume coefficient* approach. It is based on the observation that values of these volume coefficients are similar for like classes of existing aircraft [1–3].

## 11.2 Sizing the Vertical Tail

The vertical tail provides directional control and stability (motion about the Z axis). It may be sized by one or more of the following criteria (discussed in Chapter 23) [1,2]:

- 1. Landing and takeoff.** Low-speed one-engine-out or severe crosswind conditions.
- 2. Maneuverability.** The required maneuverability for a fighter aircraft may size the vertical tail.
- 3. Subsonic cruise directional stability.** Both MIL-HDBK-1797 and FAR Parts 23 and 25 require that the directional static stability derivative  $C_{n\beta} > 0$  for normal cruise. Typical  $C_{n\beta}$  values for business jets and commercial transports is 0.08–0.17 per radian at Mach = 0.8.
- 4. High-speed directional stability.** For high speed ( $M > 2.0$ ) the directional static stability derivative  $C_{n\beta}$  decreases so that the vertical tail might be sized to give a minimum value of  $C_{n\beta} = 0.08$  at high speed.

At this point in the design there is insufficient information to size the vertical tail by any of these four criteria. Tail size and c.g. location have to

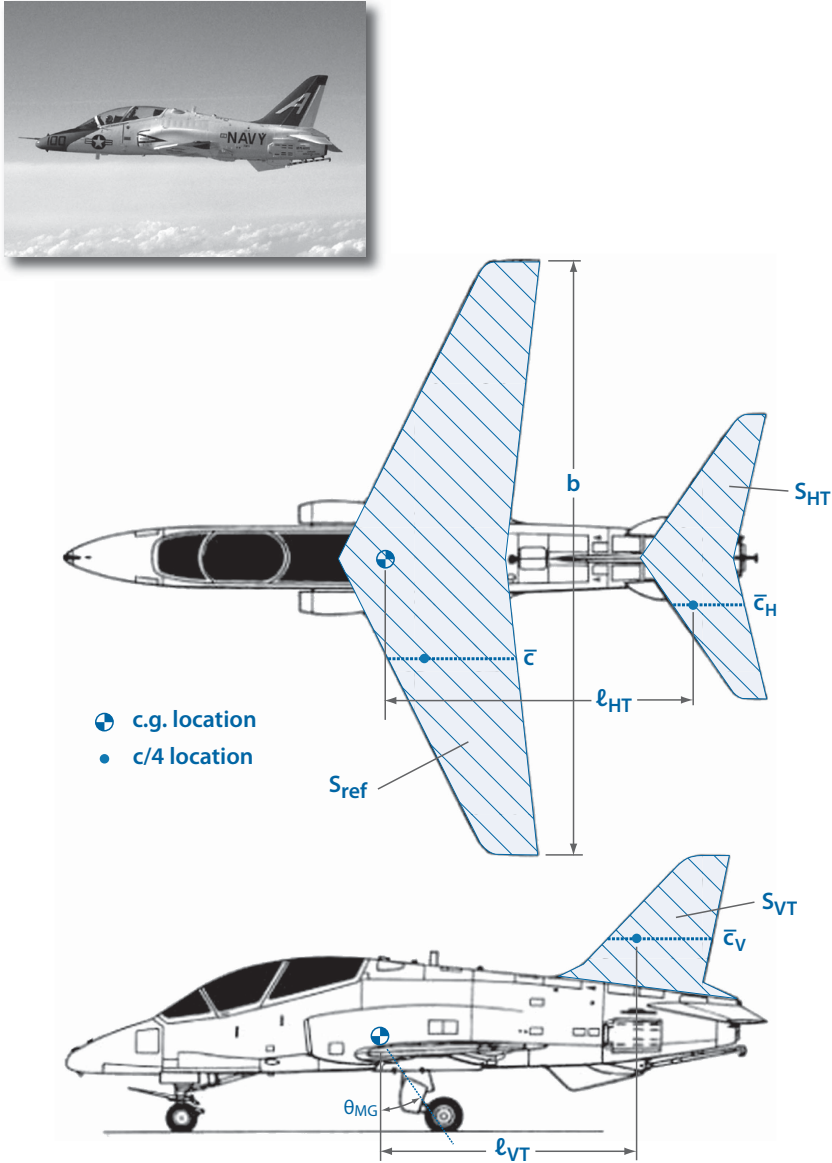


Figure 11.1 Illustration of reference geometry for tail sizing (inset is a T-45).

be realistic so that total aircraft drag can be determined. At this point historical trends determine the vertical tail area  $S_{VT}$ .

A convenient parameter to compare across classes of aircraft is the vertical tail volume coefficient:



$$C_{VT} = \frac{\ell_{VT} S_{VT}}{b S_{ref}} \quad (11.1)$$

where  $b$  is the wing span,  $S_{ref}$  is the reference wing area, and  $\ell_{VT}$  is the distance between the initial estimate of the c.g. and the quarter chord of the vertical tail mac.  $S_{VT}$  is the exposed side view area of the vertical tail as shown in Fig. 11.1.

Tables 11.1–11.7 show the  $C_{VT}$  for classes of existing aircraft. Table 11.8 lists typical volume coefficient values for preliminary tail sizing. The designer would select an appropriate value of  $C_{VT}$  for a similar class of aircraft and solve Eq. (11.1) for the  $S_{VT}$ .

### 11.3 Sizing the Horizontal Tail (Aft Tailplane)

The horizontal tail provides longitudinal stability and control. The horizontal tail (both aft tailplane and canard) may be sized by one or more of the following conditions (discussed in Chapter 23) [1,2]:

- 1. Static longitudinal stability.** The static longitudinal stability derivative  $C_{m\alpha}$  should be negative at all flight speeds as it represents the tendency of the aircraft to resist moving away from equilibrium flight. However, it cannot be too negative as the lift on the tail to trim the aircraft would

**Table 11.1** Tail Volume Coefficients for Light Reciprocating-Propeller Aircraft

Aircraft	No. Engines	$C_{HT}$	$C_{VT}$
Cessna Skywagon 207	1	0.92	0.046
Cessna Cardinal	1	0.60	0.038
Cessna Skylane	1	0.71	0.047
Piper Cherokee	1	0.61	0.037
Bellanca Skyrocket	1	0.61	0.037
Grumman Tiger	1	0.76	0.024
Cessna 310	2	0.95	0.063
Cessna 402	2	1.07	0.08
Cessna 414	2	0.93	0.071
Piper PA-31	2	0.84	0.056
Piper Chieftain	2	0.72	0.055
Piper Cheyenne I	2	0.85	0.045
Beech Duchess	2	0.67	0.053
Beech Duke B60	2	0.64	0.060

**Table 11.2** Tail Volume Coefficients for Turbofan (TF) and Turboprop (TP) Business Aircraft

Aircraft	Engines	$C_{HT}$	$C_{VT}$
Beech 1900	Turboprop	1.33	0.076
Beech B200	Turboprop	0.91	0.065
Cessna Conquest	Turboprop	0.91	0.071
DeHavilland DHC-6	Turboprop	0.91	0.077
DeHavilland DHC-7	Turboprop	1.11	0.076
DeHavilland DHC-8	Turboprop	1.47	0.121
BAE 31	Turboprop	1.22	0.120
Dassault Falcon 10/20/50	Turbofan	0.68	0.063
Cessna Citation 500	Turbofan	0.73	0.081
Cessna Citation II	Turbofan	0.64	0.062
Cessna citation III	Turbofan	0.99	0.086
Learjet 24	Turbofan	0.67	0.077
Learjet 35	Turbofan	0.65	0.066
Learjet 55	Turbofan	0.76	0.086
BAE 125	Turbofan	0.72	0.061

**Table 11.3** Tail Volume Coefficients for TF and TP Transports

Aircraft	Engines	$C_{HT}$	$C_{VT}$
Lockheed C-130E	Turboprop	0.94	0.053
Lockheed C-5A	Turbofan	0.62	0.079
Lockheed L-1011	Turbofan	0.83	0.055
Boeing 727-200	Turbofan	0.82	0.11
Boeing 737-200	Turbofan	1.28	0.10
Boeing 737-300	Turbofan	1.35	0.10
Boeing 747-200	Turbofan	0.74	0.079
Boeing 757-200	Turbofan	1.15	0.086
Boeing 767-200	Turbofan	0.94	0.067
DC-9/S 80	Turbofan	0.96	0.062
DC-10-30	Turbofan	0.90	0.060
Airbus A-300	Turbofan	1.12	0.094
Airbus A-310	Turbofan	1.09	0.098
BAE 146-200	Turbofan	1.48	0.12

**Table 11.4** Tail Volume Coefficients  
TF and TP Military Trainers

Aircraft	Engines	$C_{HT}$	$C_{VT}$
T-34	Turboprop	0.76	0.048
Aero L-39	Turbojet	0.58	0.083
Alphajet	Turbojet	0.43	0.084
Aermacchi MB-339	Turbojet	0.52	0.043
BAE Hawk/T-45	Turbojet	0.61	0.059
Cessna T-37	Turbojet	0.68	0.041

produce a large trim drag. Business jets and commercial transports have  $C_{m\alpha}$  values of  $-0.7$  to  $-1.5$  per radian.

- 2. Maneuverability.** Because fighter aircraft have to *maneuver* (move away from an equilibrium condition) their  $C_{m\alpha}$  values would be closer to 0 (neutral stability) or even positive (unstable—this requires a stability augmentation system as discussed in Chapter 23), which makes them maneuverable.
- 3. Landing and takeoff.** The horizontal tail must be powerful enough (large enough) to rotate the aircraft about the main gear at  $V_{TO}$  to  $\alpha_{TO}$  for takeoff. Also, the horizontal tail must be large enough to rotate the aircraft and trim it at low speed to  $C_L = 0.8C_{L_{max}}$  for landing approach.
- 4. Low trim drag.** The size of the horizontal tail should be such that the drag due to the trim load on the tail at cruise is less than 10% of the total aircraft drag. Otherwise the trim loads are too large and the associated trim drag degrades the aircraft’s performance.

**Table 11.5** Tail Volume Coefficients for  
Supersonic Transport and Bomber Aircraft

Aircraft	$C_{HT}$	$C_{VT}$	$C_C$
Rockwell XB-70	0	0.034	0.10
Tu-144	0	0.081	0
Tu-22M	1.11	0.087	0
Tu-22	0.44	0.059	0
Concorde	0	0.08	0
Rockwell B-1B	0.8	0.039	0
Convair B-58A	0	0.057	0
North American F-108	0	0.045	0.11

**Table 11.6** Tail Volume Coefficients for Fighter Aircraft

Aircraft	$C_{HT}$	$C_{VT}$
Convair F-106	0	0.075
Grumman A-6A	0.41	0.069
Grumman F-14A	0.46	0.06
North American F-86	0.203	0.0475
North American F-100	0.36	0.0584
Northrop F-5E	0.4	0.098
McDonnell Douglas F-4E	0.26	0.054
McDonnell Douglas F-15	0.2	0.098
General Dynamics F-111A	1.28	0.064
General Dynamics FB-111	0.75	0.054
General Dynamics F-16	0.3	0.094
Cessna A-37B	0.68	0.041
MIG-21	0.214	0.08
MIG-23	—	0.06
MIG-25	0.36	0.1
SU-7	0.4	0.1
Viggen	0	0.0834

Later the horizontal tail (aft tailplane or canard) will be sized to the preceding criteria. For now, however, use the historical trends of horizontal tail volume coefficients, which are defined as follows:

$$C_{HT} = \frac{\ell_{HT} S_{HT}}{\bar{c} S_{ref}} \tag{11.2}$$

where  $\bar{c}$  is the wing mean aerodynamic chord,  $\ell_{HT}$  is the distance from the initial estimate of the c.g. location to the quarter-chord of the horizontal tail mac,  $S_{ref}$  is the wing reference area, and  $S_{HT}$  is the total planform area

**Table 11.7** Tail Volume Coefficients for Intelligence, Surveillance, and Reconnaissance Aircraft

Aircraft	$C_{HT}$	$C_{VT}$
Lockheed Martin U-2S	0.34	0.014
Northrop Global Hawk	0.32	0.0186
Boeing Condor	0.53	0.012

**Table 11.8** Typical Values of Volume Coefficients for Preliminary Tail Sizing

Aircraft	$C_{HT}$	$C_{VT}$
Sailplane [3]	0.53	0.022
ISR	0.34	0.014
General aviation (one-engine propeller)	0.7	0.032
General aviation (two-engine propeller)	0.76	0.06
Business aircraft (two-engine)	0.91	0.09
Commercial jet transports	1.0	0.083
Military jet trainer	0.6	0.06
Jet fighter (all speeds)	0.5	0.076

of the horizontal tail (includes the aft fuselage carryover as shown in Fig. 11.1).

Tables 11.1–11.7 show the  $C_{HT}$  for various classes of existing aircraft. Table 11.8 lists typical volume coefficient values for preliminary tail sizing. The designer would select an appropriate value of  $C_{HT}$  for a similar class of aircraft and solve Eq. (11.2) for  $S_{HT}$ .

## 11.4 Horizontal Tail (Canard)

For the canard configuration, the wing aerodynamic center (a.c.) is behind the aircraft center of gravity and thus the wing is stabilizing (i.e., contributes a negative  $C_{m\alpha}$ ). The canard “pulls” the configuration a.c. (neutral point) forward; therefore, because the canard is destabilizing, it is not for stability but is for control. The contribution of the canard is statically destabilizing. However, the destabilizing nature of the canard can be helpful for supersonic speeds as it will help offset the aft movement of the a.c. from the wing. The canard  $S_C$  is sized by the same criteria as discussed for the aft tailplane in Section 11.3.

The canard volume coefficient is defined as

$$C_C = \frac{\ell_C S_C}{\bar{c} S_{\text{ref}}} \quad (11.3)$$

where  $\ell_C$  is the distance from the c.g. to the mac of the canard and  $S_C$  is the exposed top view area of the canard. A value of  $C_C = 0.10\text{--}0.11$  is suggested for preliminary canard sizing.

## 11.5 Tailless

For aircraft without a horizontal tail (i.e., F-106 and B-58)  $C_{HT} = 0$ . Previously suggested values for  $C_{VT}$  are appropriate for sizing the vertical tail.

Here the wing a.c. is behind the c.g. so that the wing is stabilizing.

The longitudinal control must come from the wing. The wing will have trailing edge surfaces (positive and negative deflection flaps) that can give the wing positive or negative camber to control the pitching moment.

## 11.6 Vertical Location of the Aft Horizontal Tail

The aft horizontal tail is initially located along the  $X$  axis based upon an initial estimate of the fuselage length. Then the horizontal tail is sized using historical tail volume coefficients. Final horizontal location will be established when the length of the propulsion system is known (Chapters 15 and 16). A refined weight estimate (Chapter 20) is performed along with the stability and control analysis discussed in Chapter 21. However, the vertical location of the horizontal tail is unknown. It is not essential that this vertical location is known at this time, unless the designer is anxious to close out the design.

Horizontal tails are located vertically for several reasons. One reason is to reduce their being blanked by the wake from the wing as it stalls, which results in a loss of pitch control as discussed in Section 21.7, Fig. 21.15. Another reason is to move them out of the hot gas exhaust of aft fuselage mounted engines (see Fig. 8.7). Also, of course, the overall appearance of the aircraft is an important consideration.

## 11.7 Horizontal Location of the Vertical Tail

A spin is a rotation about the  $Z$  axis with the aircraft in a 30–60 deg nose-down attitude from the horizontal. The rudder on the vertical tail is the main recovery surface for an aircraft in a spin. The procedure is to stop the spin by applying opposite rudder and then recover from the steep dive using the horizontal tail. For high-maneuvering aircraft (i.e., fighters and trainers) it is important that the rudder be located so that it is not blanked by the horizontal tail. The analysis is graphical, consisting of drawing two lines, one at 30 deg from the horizontal tail trailing edge and the other at 60 deg from the leading edge and positioning the rudder outside of this region. The F-15, F-16, F-18 and T-46 are good spin recovery aircraft.

## **References**

- [1] Roskam, J., *Airplane Design*, Pt. II, Roskam Aviation and Engineering Co., Ottawa, KS 66067, 1989. [Available via [www.darcorp.com](http://www.darcorp.com) (accessed 31 Oct. 2009).]
- [2] McCormick, B., *Aerodynamics, Aeronautics, and Flight Mechanics*, Wiley, New York, 1995.
- [3] Thomas, F., *Fundamentals of Sailplane Design*, College Park Press, College Park, MD, 1999.

## Chapter 12

# Designing for Survivability (Stealth)



- Vulnerability
- Susceptibility (Signature)
- RF/Radar (RCS)
- Shaping
- Absorption & Cancellation
- IR/Infrared
- Visual
- Acoustic

“Father of Stealth” Ben Rich with the F-117A stealth fighter. See “Father of Stealth Wins Big” in Section 12.4.

*What is my management style?  
I manage with charisma.*

Ben Rich



## 12.1 Putting Things in Perspective

All aircraft should be designed with survivability in mind. Commercial and private aircraft can be at risk to terrorists armed with inexpensive, easy-to-use surface-to-air missiles (SAMs). These SAMs are the man-portable missiles, with infrared (IR) sensors, called MANPADS. Military aircraft often encounter enemy MANPAD units and the more sophisticated integrated air defenses (IADs) with large, expensive SAMs and air-to-air interceptors.

When designing for survivability one should consider a hierarchy of actions. Hardening the aircraft or reducing the aircraft signature is not the first action to consider. This hierarchy consists of the following actions in order:

- **Mission planning.** Plan the mission to avoid the threat. Select the time of day and conditions to minimize the effectiveness of the threat.
- **Plan the mission profile.** Select conditions of speed, altitude, terrain following or terrain avoidance (TF/TA), and so on.
- **Use electronic countermeasures (ECM).** Integrate onboard and off-board ECMs into the aircraft such as flares, chaff, towed decoys, radio-frequency (RF) and IR missile warning systems, and countermeasure electronics (spoofers, jammers, etc.).
- **Defeat the end game.** Using onboard RF/IR missile warning systems a properly timed maneuver can cause the missile to miss.
- **Design-in survivability features.** These survivability features will involve weight, vehicle shape, and cost. These features will impose a lifetime performance penalty on the aircraft and should be considered as a last resort for survivability.

Survivability has two parts: susceptibility and vulnerability. *Susceptibility* is the probability that the aircraft will be detected, tracked, and fired upon:

$$P_{KS} = P_D \times P_T \times P_{\text{FIRE}}$$

*Vulnerability* is the probability that once a missile or bullet is fired it will fuse or hit the aircraft and, if it hits the aircraft, the probability that it will kill the aircraft:

F-117 Shoot Down: During the 1999 Kosovo air campaign the Yugoslav air defenses were able to locate, track, and shoot down an F-117 by intercepting its electronic emissions. The Yugoslavs' technique was crude and involved a lot of luck, but it worked, resulting in the only F-117 ever to be shot down. Russia bought the remains of the F-117 from Yugoslavia and used data from component testing to design improved SAMs. Given the faceted design and 1970s coating technology, it's an open question how much useful information was actually obtained [1].

$$P_{KV} = P_{F/H} \times P_{H/K}$$

Then the probability of a kill is  $P_K = P_{KS} \times P_{KV}$  and the probability of survival is  $P_S = 1 - P_K$ .

Reducing susceptibility and reducing vulnerability are two different strategies for high survivability and are shown in Fig. 12.1 for the A-10A and F-117A.

The A-10A (nicknamed the Warthog) was developed in the early 1970s as a close air support aircraft for low-intensity conflicts. It was designed for low-speed maneuvering and killing tanks with its GAU-8 seven-barrel 30-mm cannon. It also carried a vast array of air-to-surface missiles.

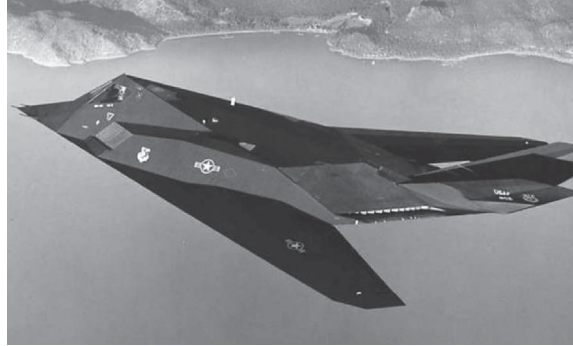
## 12.2 Designing for Reduced Vulnerability

Designing for *reduced vulnerability* is the strategy of letting the aircraft “take a licking but keep on ticking.” The vulnerability reduction concepts are as follows:

- **Critical component redundancy with separation.** Try to have redundancy (usually two) in the critical components and to separate them so that a missile warhead will not take both of them out. Examples are multiple engines, flight control computers, control surfaces, and fuel pumps.
- **Critical component location.** Locate the critical components so that they are not damaged by failure of another component, such as an engine fire or a thrown blade from a damaged compressor or turbine section.
- **Passive damage suppression.** Design critical structure to be damage tolerant or fail safe. Filling the fuel tanks with foam will minimize the voids in the tank and limit the fuel–air mixture leading to an explosion.
- **Active damage suppression.** Filling the fuel tank with an inert gas (such as nitrogen or HALON) as the fuel is consumed will limit the buildup of a fuel–air mixture and greatly reduce the probability of an explosion. The addition of fire detection and suppression systems, especially in the engine bay, has saved many aircraft.
- **Critical component shielding.** Try to shield critical components by deliberate shielding or by locating them so they are shielded by other components. Examples are the titanium “bathtub” surrounding the pilot and locating the two turbofan engines above the wing, providing shielding from ground fire, for the A-10A.
- **Critical component elimination.** If possible, eliminate critical components and replace their function some other way. An example is replacing the pilot on UAVs.



**Low Vulnerability (A-10A)**



**Low Susceptibility (F-117A)**



**Figure 12.1** Different strategies for high survivability.

These vulnerability concepts are shown in Fig. 12.2 and discussed in great detail in [2]. Figure 12.3 shows that the concepts worked for the A-10A (but they made the pilot nervous).

### 12.3 Designing for Reduced Susceptibility

Reducing an aircraft's susceptibility starts with reducing the ability of an enemy defense system sensor to detect the presence of the aircraft. The enemy defense system sensors are of five types:

- **RF/Radar.** The radar operates by transmitting RF energy, which reflects off the target aircraft and back to an RF sensor. This RF sensor is usually located at the transmitter. This reflected RF energy represents a radar cross section (RCS) return, or signature, to the sensor. This is the only active defense system. The RF frequencies of interest are 100 MHz to 16 GHz, which covers the Worldwide RF air defense systems. The lower frequency (VHF and UHF band) systems provide long-range detection, the midrange frequencies (L, S, and C bands) are for the tracking radars, and the high-frequency X band with its fine-resolution capability is for the fire control radars.
- **IR/Infrared.** The infrared system operates by sensing the emitted or reflected IR energy from the target aircraft minus the IR energy of the background. This IR signature is a contrast relative to the background and can be negative or positive. This is a passive system represented by a thermal-sensitive sensor in the 1- to 12-micron wavelength bands.
- **Visual.** The visual system operates by sensing the emitted or reflected visual energy from the target aircraft minus the visual energy of the background. An example of emitted visual energy would be a head lamp. The visual signature is a contrast relative to the background and can appear as a glint or a black hole. This is a passive system represented by electro-optical sensors and the human eyeball. The visible band is the 0.37–0.75 micron part of the electromagnetic spectrum.
- **Acoustic.** The acoustic system operates by sensing the emitted or reflected acoustic energy from the target aircraft minus the acoustic energy of the background. The acoustic energy of the target rarely contains any reflected energy. The acoustic signature of the target is a contrast relative to the background. This is a passive system represented by microphones or the human ear.
- **Electronic intelligence and signals intelligence (ELINT/SIGINT).** Aircraft will often emit electronic signals that can be used to locate

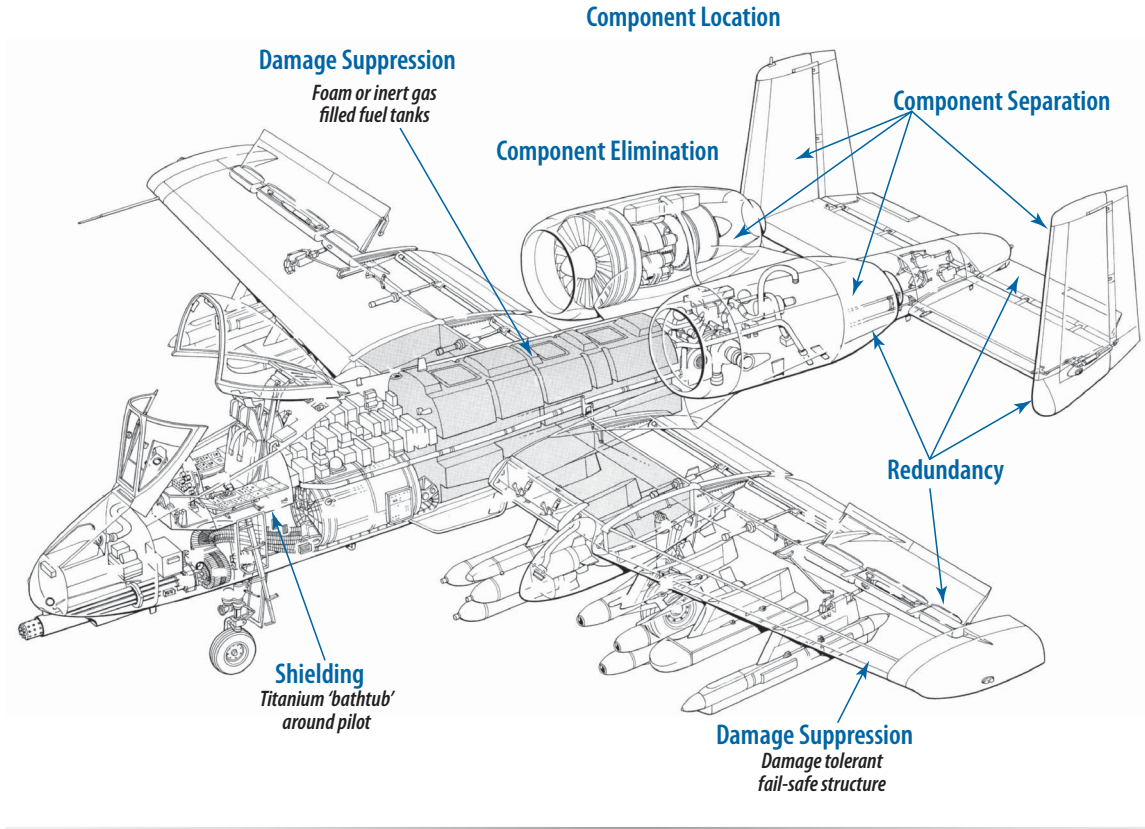
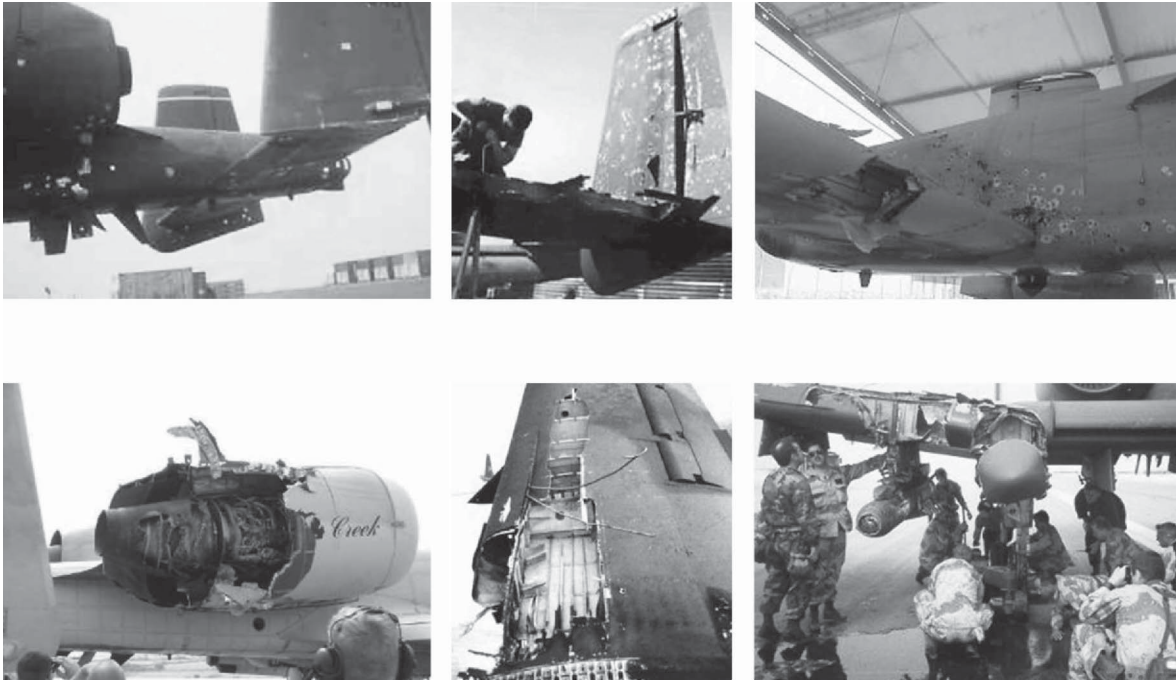


Figure 12.2 Design for low vulnerability.



**Figure 12.3** A-10 can tolerate severe damage and still survive. It has excellent vulnerability.

them. The intelligence community uses these electronic signals to locate ground targets and to gather electronic information on enemy weapon systems, both in development and fielded. The United States uses airborne platforms such as the EP-3, EC-130, and U-2 to gather this electronic intelligence.

This chapter discusses design features that reduce the RF, IR, visual, and acoustic signatures of aircraft.

## 12.4 Radar Cross Section (RCS) Signatures

An aircraft's RCS is measured relative to the radar return from a metal sphere with a cross section of one square meter. The common unit for RCS is decibels relative to a one square meter reference cross section (dBsm):

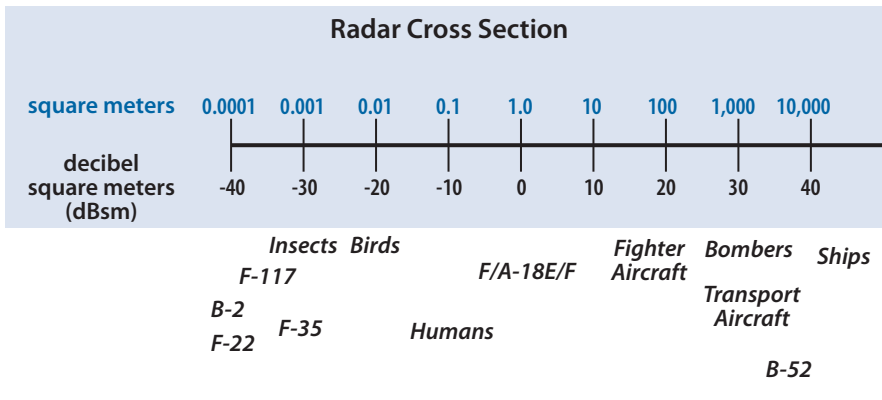
$$\text{RCS in dBsm} = 10 \log_{10} (\text{RCS in square meters}) \quad (12.1)$$

Figure 12.4 (from [3]) shows the RCS of typical aircraft.

### 12.4.1 Radar Scattering Phenomena

As the electromagnetic (EM) field generated by a radar washes over a target, the RF energy is reflected. This reflected energy is received by RF sensors as the target RCS. The strategy for reducing the target RCS is as follows [4–6]:

- **Shaping.** If the target surface is properly shaped, the reflected energy will not be received by the threat radar. This strategy controls the



**Figure 12.4** Definition of RCS used to assess the level of stealth (data from [3]).

direction of the reflected energy and works well provided the threat RF sensor is collocated with the radar. If the RF sensor is located somewhere else, the target vehicle RCS could actually be enhanced (note that this is the theory behind a bistatic radar defense).

- **Absorption.** If the EM energy interacts with high-resistance iron particles on the target surface, the energy is converted to thermal energy by ohmic heating. Ohmic heating is the temperature rise in a conducting material with electrical resistance when a current flows.
- **Cancellation.** If the target surface can reflect part of the EM energy with a 180-deg phase change, the EM energy will be canceled. Typically this is done passively with coatings on the target surface that have a judiciously chosen thickness to cause the cancellation. The thickness of the absorber depends upon the frequency or wavelength of the incident energy. The cancellation can also be done actively by an onboard electronic system that senses the time and direction of the incident EM energy and then transmits energy of equal strength and opposite phase to cancel the incident energy.

The EM energy is reflected at the target vehicle by the three scattering mechanisms shown in Fig. 12.5 [7,8].

- *Specular reflections* result when a radar wave is directly reflected from an object, similar to a flashlight shining on a mirror. The specular reflection angle is equal to the incidence angle of the radar wave. A normal surface reflects the specular energy right back to the radar, whereas an angled surface reflects the energy away from the radar. The specular reflection has a main lobe and side lobes as shown in Fig. 12.6. Specular reflections are controlled by shaping the aircraft to reflect the energy away from the radar.
- *Diffraction* occurs when the EM energy encounters a sudden discontinuity in surface slope or change in electrical impedance (material change). Everyday examples of diffraction are rainbows and reflections from glass prisms. Diffraction scattering is reduced by avoiding surface discontinuities (Fig. 12.5), cancellation, and absorption.

In the late 1970s, the Skunk Works was preparing for its first wind tunnel test of a stealth aircraft design by taking routine pictures of the model with a Polaroid camera. The photographer complained to the test engineers that all of the pictures were out of focus and that something was wrong with the Polaroid camera he was using. After a brief silence someone realized what the problem was. The cameras used a sonar-focusing device that depended on return reflections to adjust the focus length. Because stealth aircraft are designed to not directly return any impinging waves, the camera could not focus on it. It was clear to those in the room that stealth from shaping was going to work. Have Blue and the F-117A designs followed and the rest is history.



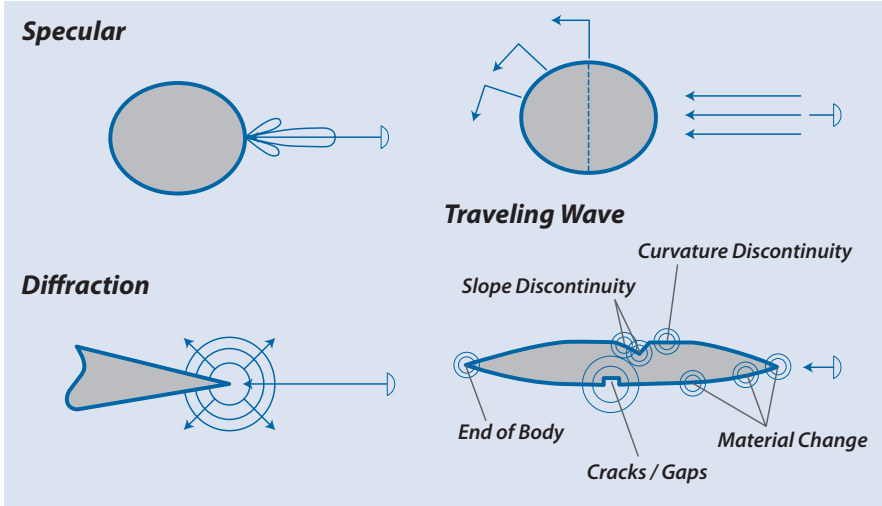


Figure 12.5 Electromagnetic (EM) scattering mechanisms.

- *Traveling waves* (or surface waves) occur as the EM field washes over the target and sets up electrical currents (induced by the incident EM energy) in the conducting surface of the aircraft. Traveling waves, like diffraction, will scatter when they encounter surface discontinuities. Traveling wave scattering is reduced in the same ways as diffraction.

The RCS of an aircraft is the vector sum of all reflected energy from all scattering sources and is dependant upon the orientation of the aircraft to

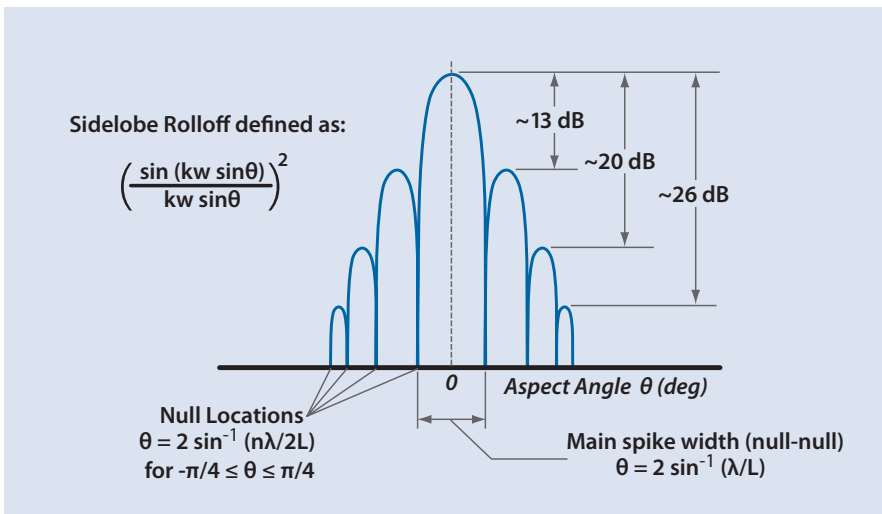


Figure 12.6 Electromagnetic wave backscatter geometry.

the radar and upon the wavelength and polarization of the EM wave. The wavelength of the EM wave is an important parameter in RCS reduction. The wavelength ( $\lambda$ ) depends on the frequency ( $f$ ) of the EM wave as follows:

$$\lambda \text{ (in inches)} = 11.8/f \quad (12.2)$$

where the frequency is in gigahertz. For example, the 170-MHz Tall King long-range detection radar has a wavelength of 66 inches and the 10-GHz Flap Lid fire control radar has a wavelength of a little over one inch. Every scattering source on the aircraft (i.e., wing leading edge length, vertical tail height, inlet lip radius, outer mold line (OML), gaps and cracks, skin surface imperfections, etc.) has a characteristic dimension  $L$  and a scattering size in wavelengths of  $L/\lambda$ . The primary scattering mechanisms (specular, diffraction, and traveling wave) vary depending upon the scattering source size in wavelengths as shown in Fig. 12.7. Figure 12.7 also shows that the technique for reducing the scattering mechanism varies depending upon the source size in wavelengths. Notice from Fig. 12.6 that the width of the specular main lobe, the null locations, and the sidelobe rolloff are all dependant on the parameter  $L/\lambda$ .

### Father of Stealth Wins Big

Ben Rich took over the Skunk Works from Kelly Johnson in early 1975 and maneuvered it, over Kelly Johnson's objection, into the DARPA XST program. By October Lockheed and Northrop were locked in a "winner take all" competition on the USAF's radar test range at White Sands, New Mexico. Each company built an RCS model of their "Have Blue" design.

Ben had ball bearings made with the same RCS as Lockheed's design. Ben then prowled the halls of the Pentagon, rolling a ball bearing across the desks of various generals and announcing "General, here's your new fighter airplane." The generals' eyes would bug out of their heads. Northrop yelled foul and Ben stopped approaching anyone not cleared into the DARPA program. Thanks to the creative genius of several Skunk Works engineers and Ben's rapport with the customer, the Skunk Works won the program with a design that later became the F-117A stealth fighter.

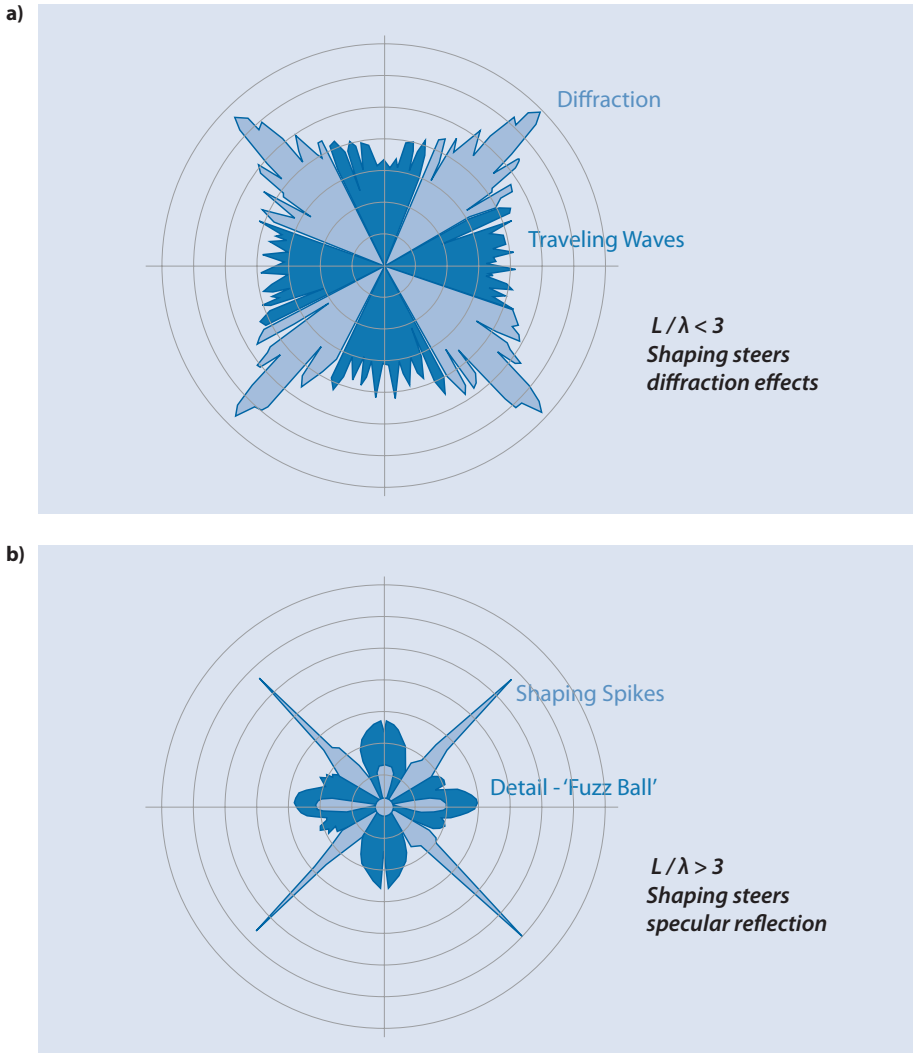
Ben was the chief Skunk until his retirement in 1991. Ben's management style was very different from Kelly's. Kelly ruled the Skunk Works by his bad temper ... Ben ruled by his bad jokes. Ben was a schmoozer, a glad hander, a cheer leader. He was well-liked and respected by his customers and his employees. Ben became the chief spokesman for the pursuit of stealth technology within the DOD and rightly earned the title of the "Father of Stealth."

		$L/\lambda < 3 \leftarrow \rightarrow L/\lambda > 3$			$L/\lambda \gg 3$	
		HF	VHF	UHF	Microwave	MMW
<b>Primary Scattering Sources</b>		Diffraction Traveling Waves Resonances			Specular Reflection Apertures Details	Details Diffuse Scattering
	<b>Scattering Reduction Techniques</b>	Radar Absorbers Nulling Techniques			Shaping Radar Absorbers Shielding	Radar Absorbers Tolerances
		<b>Design Approaches</b>	High-Power Computation with Optimization Experiment			Simple Computer Models Experiment

**Figure 12.7** Scattering for aircraft-size targets.

With this dependence on  $L/\lambda$  one would expect a different polar RCS pattern for the case of a small  $L/\lambda$  aircraft vs a large  $L/\lambda$ . This is indeed the case, as shown in Fig. 12.8 for a diamond-shaped metal (no coatings) aircraft. For the case of  $L/\lambda < 3$  shaping is not very effective although it does steer the diffraction scattering and the RCS pattern is a blob with no distinct spikes. The RCS reduction design would feature absorption and cancellation. For the  $L/\lambda > 3$  case the pattern is characterized by very distinct and narrow spikes and a fuzz ball (surface detail scattering). Here the RCS reduction design would feature shaping as well as absorption.

The history of current U.S. aircraft stealthy design is shown in Fig. 12.9. The basics of stealth have been known since the 1950s but the analytical techniques were experimental because computer power was lacking. In the 1970s computer power had increased to where the RCS of faceted vehicles could be estimated. This second-generation stealth capability led to the DARPA XST (Experimental Stealth Technology)/UASF Have Blue demonstrator program shown in Fig. 12.10. Even before the Have Blue flight test was completed, the U.S. Air Force ordered 59 F-117As. In the 1980s the United States entered the third generation of stealth due to increasing computer power that allowed the RCS of curved surface configurations to be analyzed. This led to the Northrop B-2 stealth bomber (the aircraft proved to be very expensive and only 21 were produced), the AGM-129 Advanced Cruise Missile (over 400 produced with nuclear warheads), the F-22, and the AGM-158 JASSM. The F-35 Joint Strike Fighter represents the fourth generation of stealth. Figure 12.11 shows a gallery of U.S. low-signature (stealthy) demonstrator vehicles and production aircraft.



**Figure 12.8** RCS pattern shaping and details for **a)** VHF and UHF, and **b)** microwave.

### 12.4.2 Vehicle Shaping

The RCS design starts by establishing a smooth conducting ground plane completely around the aircraft. The ground plane keeps the EM energy from penetrating into the interior of the aircraft and reflecting off all the structure and subsystems. Silver paint is a popular treatment with conductive films and fabrics used over gaps, cracks, and fasteners. The glass canopy and sensor lenses are made conducting by painting them with a thin film of indium tin oxide (ITO).

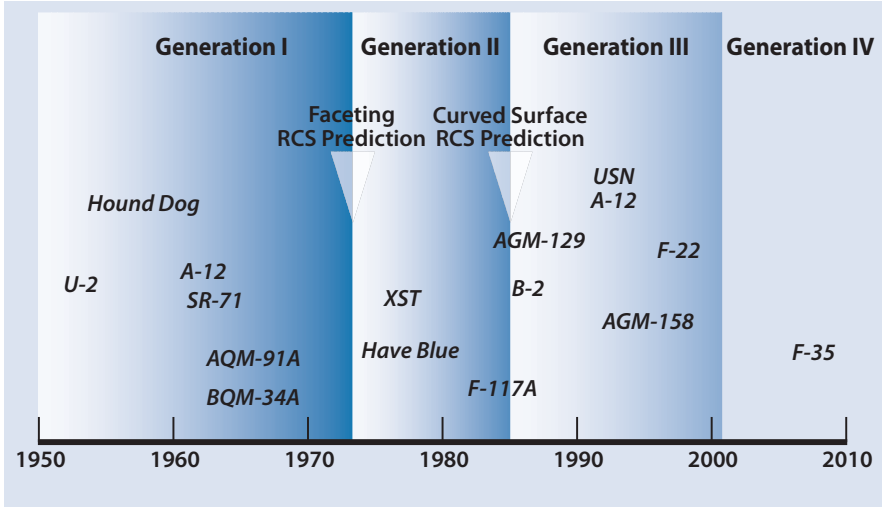


Figure 12.9 Definition of stealth generations.

The RCS design continues by controlling the direction of the reflected energy through shaping, then coatings are put on the surface to absorb and cancel the energy. Here it is assumed that there is intelligence information on how and where the threat radar is deployed and how many. It is necessary to know if the threat is above, below, co-altitude, in front, off to the side, or behind when it is encountered so that the reflected energy can be deflected away from the receiver.

Vehicle shaping works best for the case of an  $L/\lambda > 3$  target. This is because the reflected energy spikes are narrow and well defined. The sweep of the wing and tail leading edge (LE) and trailing edge (TE) establishes the basic spike structure for the target vehicle to defeat the threat. Then the

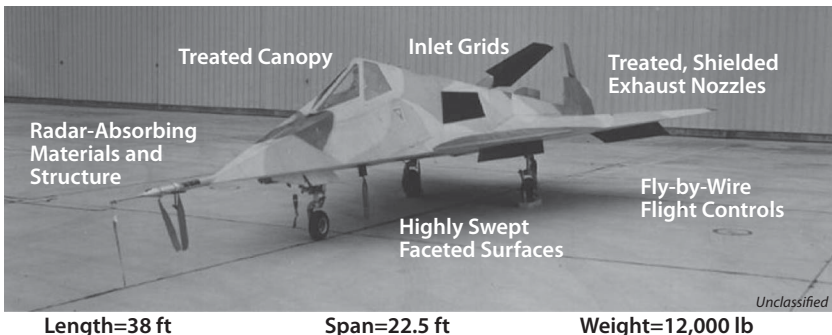
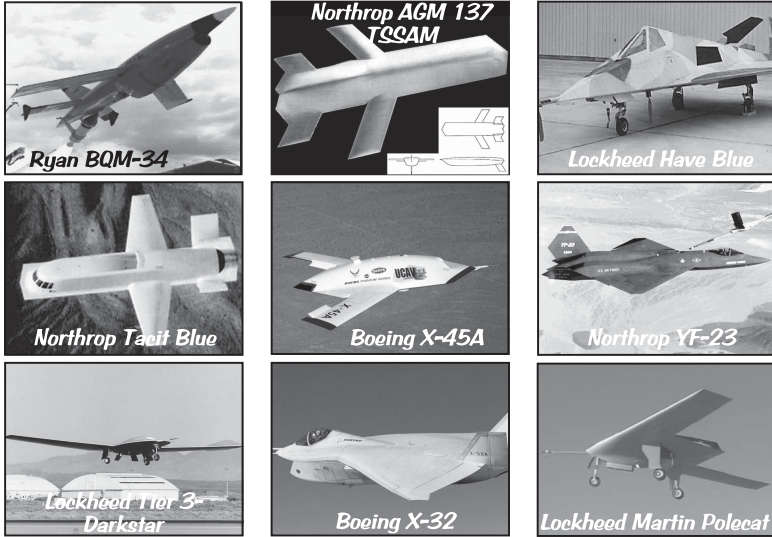


Figure 12.10 Have Blue low-observable technology demonstrator.

Development



Production

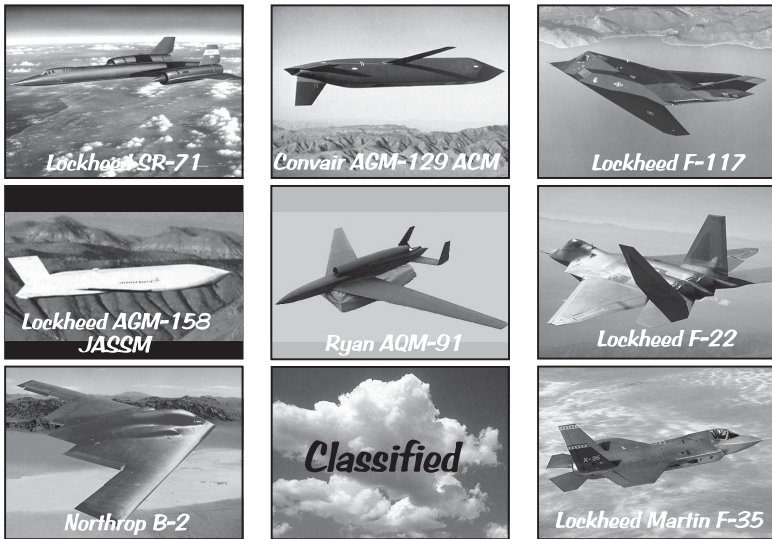
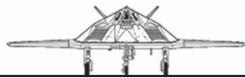
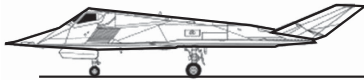
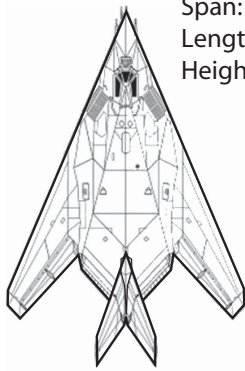


Figure 12.11 Gallery of low-observable aircraft.

scattering spikes from all other sources are aligned with this basic spike structure. This strategy is shown in Figs. 12.12 and 12.13. The F-117 and B-2 are termed four-spike designs, whereas the YF-22 and YF-23 are six-spike designs due to the fuselage side spikes. Notice how the inlet and nozzle apertures, and all the gaps and cracks from the bomb bay doors, landing gear doors, and control surface hinge lines are swept to line up with the wing or tail spikes. Typically the wing and tails are swept such that their

### Lockheed F-117A

Span: 43 ft 4 in.  
Length: 65 ft 11 in.  
Height: 12 ft 5 in.



### Northrop B-2A

Span: 172 ft 0 in.  
Length: 69 ft 0 in.  
Height: 17 ft 0 in.

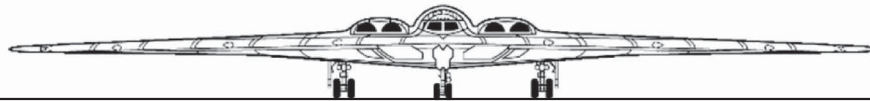
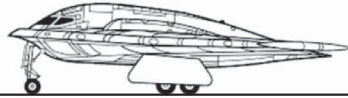
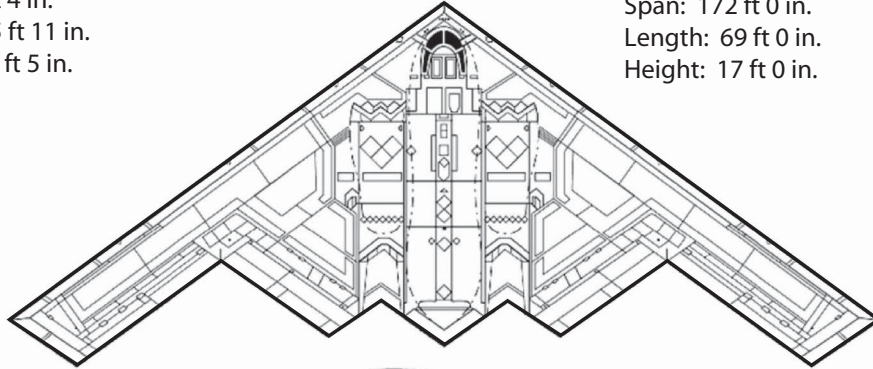
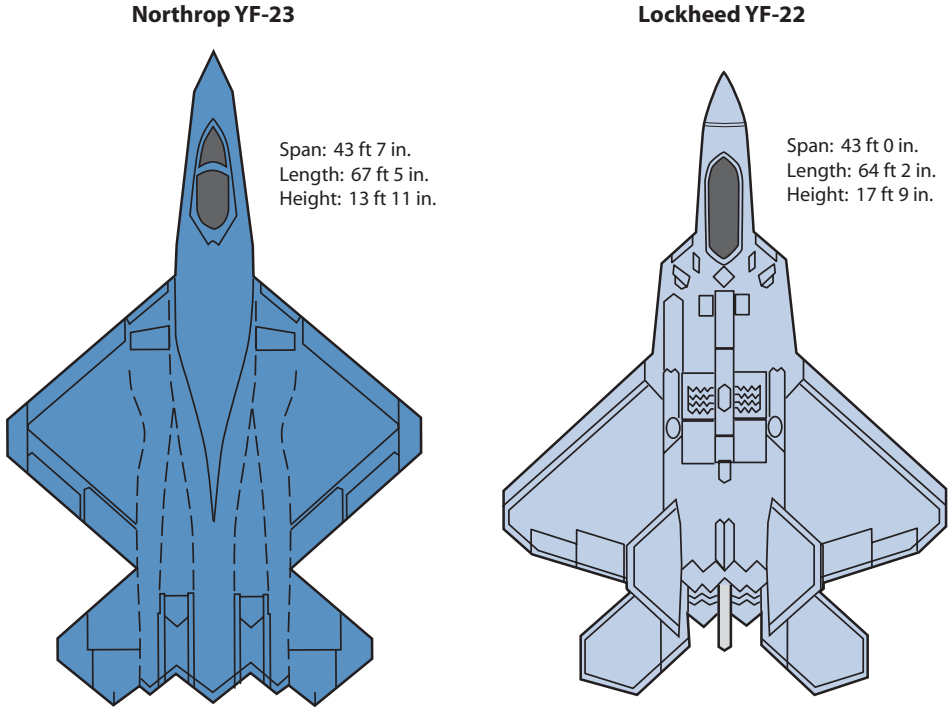


Figure 12.12 Planform shaping for low observables.



**Figure 12.13** Planform shaping for low observables (YF-23 vs YF-22).

LE and TE spikes are away from a threat directly in front of the aircraft (the Tier 3-Minus Dark Star was an exception).

Careful attention must be paid to the shaping of the vehicle surface so that there are not any surface discontinuities to trigger diffraction and travelling-wave scattering (see Fig. 12.5). This means continuous second derivatives (slope change gradient) everywhere. Certainly gaps, cracks, control surface hinge lines, and facet edges do not meet this criterion and must be swept to align their scattering with the basic spike structure of the aircraft.

### 12.4.3 Absorption and Cancellation

As mentioned earlier the EM energy can be absorbed by ohmic heating and in some cases can-

In 1975 the Lockheed Skunk Works was testing the Have Blue RCS model when range operators abruptly started to get large readings. Visual checks showed a small bird was now sitting on the model. After chasing the bird away measurements were still not consistent with previous data. A closer check of the model revealed that the bird had left droppings on the model. Once these were removed the new data agreed with the old. RCS measurements are very sensitive to many model irregularities.

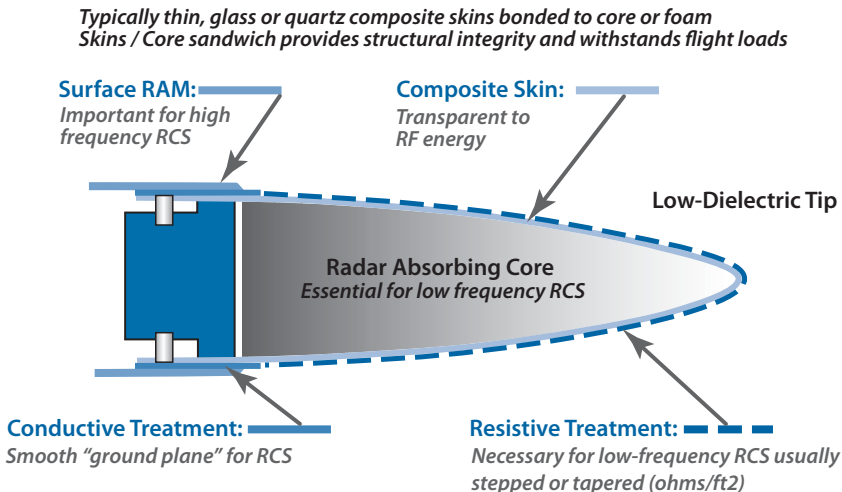


celled. This action all takes place in the coatings that are put on the surface of the aircraft. These coatings are usually of three types: radar absorbing structure (RAS, sometimes called loaded edge), radar absorbing material (RAM), and resistive sheet. These coatings are shown in Fig. 12.14 applied to a leading edge.

The RAS is the main treatment for low-frequency radars. It is an aerodynamic fairing made of a material that is transparent to the RF energy but can take flight loads. The fairing is reinforced with structural honeycomb core or foam that is impregnated with a resistive liquid (similar to printer's ink) that absorbs the penetrating EM energy through ohmic heating. The depth of the RAS edge should be  $0.38\lambda$  for maximum cancellation.

RAM is primarily a treatment for high-frequency radars. It absorbs the EM energy and provides cancellation when the thickness is one-quarter wavelength. RAM is very heavy and pretty much limited to high-frequency application because of the quarter-wavelength thickness criterion. The RAM is an iron powder held together in a binder. The iron powder is carbonyl iron (most common but oxidation is a problem), FeSi (excellent corrosion resistance), and FeAl or FeCoV for high-temperature applications. The following are binders for the iron particles:

- **Urethane.** This is the toughest, most common, lowest cost, fast curing, user friendly binder, and it adheres to most materials. It is commercially available as a paste and a spray. It has a good temperature range of  $-65^{\circ}\text{F}$  to  $250^{\circ}\text{F}$ .



**Figure 12.14** Low-observable materials selection and implementation—radar absorbing structure (RAS) edge construction.

- **Silicone.** The aircraft industry has over 40 years' experience with silicone RAM. It is available in sheet, paste, and spray forms. It has a very good temperature range of  $-65^{\circ}\text{F}$  to  $250^{\circ}\text{F}$ . The disadvantage of silicon RAM is that nothing bonds to it except silicone.
- **Ceramic.** Ceramic has an excellent temperature range of  $600^{\circ}\text{F}$  to  $2000^{\circ}\text{F}$  and is used in nozzle applications. It is made by loading thin ceramic tiles with the iron powder. It is also used in brick form for RAS.

The resistive sheet absorbs the surface currents traveling along the target vehicle surface through ohmic heating. It is also known as edge card or R-card and is available commercially as a thin decal or appliqué (resistive ink), resistive mat (resistive fibers suspended in a resin soluble sheet), metalized film (sputter or vapor deposit Nichrome or Nickel on Kapton film) or fabric (glass fabric with Nickel treatment).

The weights of these treatments are as follows:

- High-frequency RAM (quarter-wavelength thick),  $0.6\text{ lb/ft}^2$
- Resistive sheet,  $0.05\text{ lb/ft}^2$
- Low-frequency edge RAS—carbon loaded foam/core
  - VHF, 24-inch edge,  $6\text{ lb/ft}$
  - UHF, 12-inch edge,  $2\text{ lb/ft}$

#### 12.4.4 Inlet and Nozzle RCS Design

If not properly designed, the inlet or nozzle can drive the RCS of the entire vehicle in the front or rear sector. This is because the normal reflection from the compressor face or turbine blades bounces right back to the radar. A popular design trick is to block the line of sight (LOS) into the inlet or nozzle by giving the duct an “S” or serpentine shape. This causes the EM energy entering the duct to bounce off the duct walls, reflect off the compressor or turbine face, and then bounce off the duct walls again as it exits. If the duct walls are coated with RAM, each bounce reduces the reflected energy back to the radar.

Another popular design trick is to block the energy entering the inlet or nozzle cavity by a physical phenomenon called aperture cutoff. If the inlet or nozzle cavity dimension (normal to the polarization) is less than  $\lambda/2$  the EM wave cannot enter the cavity. This is why your car AM radio (530–1600 kHz,  $\lambda \sim 1000\text{ ft}$ ) will not work in a 60 ft diameter tunnel, but your FM radio (88–108 MHz,  $\lambda \sim 10\text{ ft}$ ) continues to work. The cavity appears as a black hole. The inlet or nozzle aperture is then swept to reflect the energy away from the radar. This design trick was used on the F-117A inlet by putting a grid into the inlet. The grid had a cell size of 0.6 in., which kept the EM energy of all frequencies below 10 GHz from entering. The inlet

aperture was highly swept so that the inlet contributed very little to the F-117A overall RCS. The disadvantage for the F-117 was a higher than normal inlet total pressure loss at cruise speed and ice buildup on the grid. This latter problem was solved by having a wiper blade sweep the ice off of the grid.

The F-117 flew at altitudes of 28,000 ft so that most threats were below it or co-altitude. The F-117 nozzle featured a high-AR, two-dimensional nozzle that provided aperture cutoff for low and middle frequencies. In addition the nozzle lower surface ramp blocked the LOS into the nozzle cavity for all co-altitude threats and below. Ceramic tile RAM was applied to the duct, and ceramic brick was used for the loaded edges.

Inlet and nozzle RCS design is summarized on Fig. 12.15. The front-rear frame referred to in Fig. 12.15 is a device that looks like a potato chip that prevents a normal reflection off of the compressor or turbine blades. Reference [9] is an excellent article on inlet design.

### 12.4.5 RCS Design Summary

Figure 12.16 shows a typical RCS design. The overall configuration should have as few spikes as possible (the minimum is a three-spike delta configuration) and their directions should be away from the threat sensors (usually located at the radars). All the scattering sources should align their individual spikes with the basic spike structure. Edges should be RAS for low-frequency threats and RAM-coated for high-frequency threats. Resistive sheet should be applied to reduce the travelling-wave scattering. All gaps, cracks, and hinge lines should be filled, treated, and swept. Inlets and nozzles should have LOS blockage to the compressor and turbine blades either by aperture cutoff, serpentine-shaped ducts, or front/rear frame. All ducts should be coated with RAM. The fuselage side slopes should direct

#### Line of Sight (LOS) blockage

Low frequency–cutoff frequency

Dimension  $< \lambda/2$  normal to polarization

Serpentine ducts

Need length/diameter (L/D)  $\sim 2.5$ – $3.5$ ; for nozzles

Need L/D  $\sim 4$ – $6$  for inlets

Front and Rear Frames (approx. one diameter in length)

Nozzle ramp angle

#### Absorb reflected energy

MagRAM on duct walls

Nozzle ducts need high-temperature RAM

#### Sweep inlet and nozzle lips

**Figure 12.15** Inlet and nozzle design guidelines for low-RCS configuration.

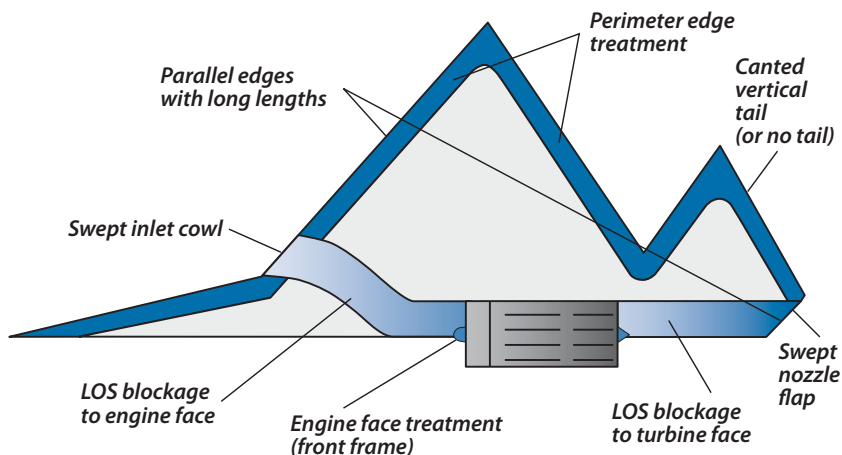


Figure 12.16 Typical low-observable design features (planview).

the reflected energy away from the threat and the side shape should have continuous second derivatives.

## 12.5 Infrared

Infrared and visual are contrast signatures. This means that they are observed relative to their background:

$$\text{Contrast} = E_T + E_R - \text{Background} \quad (12.3)$$

where

$E_T$  = target emissions

$E_R$  = emissions due to the reflections from the sun, earth, and sky (clouds)

For Contrast > 0: the target is brighter than the background and appears as a glint (need to reduce  $E$ ).

For Contrast < 0: the target is dimmer than background and appears as a black hole (need to add  $E$ ).

For Infrared:

$$I_{\text{Contrast}} = I_E + I_R - \text{Background} \quad (\text{W/sr}) \quad (12.4)$$

For Visual:

$$V_{\text{Contrast}} = V_E + V_R - \text{Background} \quad (\text{lm/sr}) \quad (12.5)$$

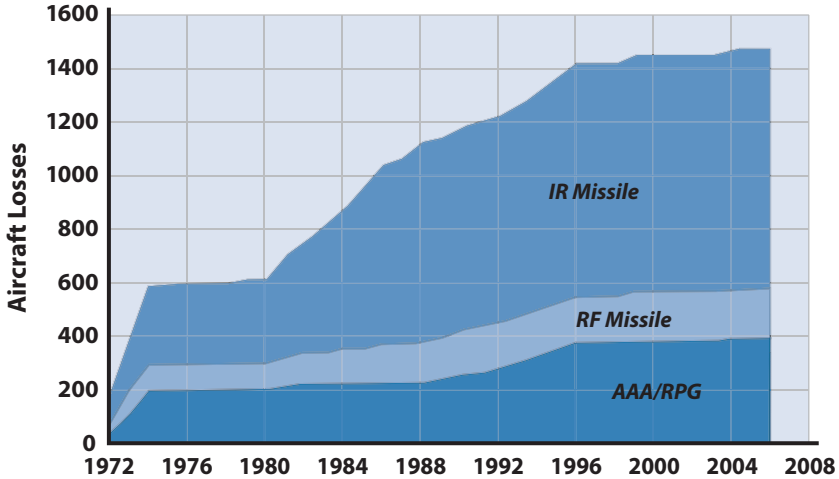


Figure 12.17 Combat aircraft losses (1972–2006).

IR signature reduction is a hard problem because the IR threats are passive (you do not know where a threat is) and the background varies with time of day, orientation, and weather. In addition most (over 60%) of the aircraft kills since 1972 have been from IR missiles (see Fig. 12.17). IR SAMs are the weapon of choice for downing aircraft by terrorist elements because they are user friendly, require minimum maintenance, and are much cheaper than RF SAMs.

### 12.5.1 Introduction to Infrared (IR 101)

The IR radiation sources are shown in Fig. 12.18. The IR signature is determined as follows:

$$I_{\text{Contrast}} = I_E + I_R - \text{Background} \quad (\text{W/sr}) \quad (12.4)$$

The aircraft emissions are

$$I_E = \sigma \epsilon f T^4 A_p \quad (12.6)$$

where

$\sigma$  = Stephan–Boltzmann constant =  $0.481 \times 10^{-12}$  Btu/ft<sup>2</sup>·s·°R

$\epsilon$  = Emissivity of emitting surface

$f$  = Distribution of IR energy in band of interest (i.e., SWIR, MWIR, or LWIR)

$T$  = Absolute temperature of emitter in °R

$A_p$  = Projected area

The

$$I_E = I_{\text{Hot Parts}} + I_{\text{Plume}} + I_{\text{Airframe}} \tag{12.7}$$

The following are some representative temperatures [10]:

- Turbine blades (usually cooled), 2300°F
- Nozzle exit (turbojet), 1800°F
- Nozzle exit (turbofan), 1100°F
- Plume (turbojet), 1000°F
- Plume (turbofan), 500°F
- Airframe aero heating at Mach 0.85, 122°F
- Airframe aero heating at Mach 3.2
  - LE stagnation point, 800°F
  - Surface, 550°F

The reflected IR energy is

$$IR = \left[ (1 - \epsilon) / \pi \right] \sum (E_{\text{sun}} F_{\text{sun}} + E_{\text{sky}} F_{\text{sky}} + E_{\text{earth}} F_{\text{earth}}). \tag{12.8}$$

Notice that the IR reflectance =  $(1 - \epsilon)$ , which poses a dilemma when the designer wants to select an IR paint that will reduce emissions and reflections at the same time.

The IR sensor bands are shown in Fig. 12.18:

- Fire control: SWIR (near IR) 1–3 microns and MWIR (middle IR) 3–6 microns
- Detection,IRST (IR search and track): LWIR (far IR) 6–12 microns

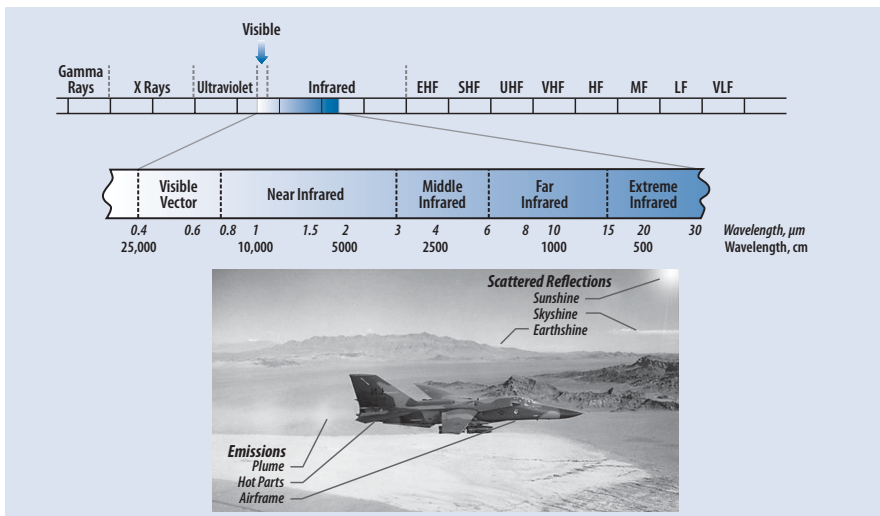


Figure 12.18 Aircraft infrared radiation sources.

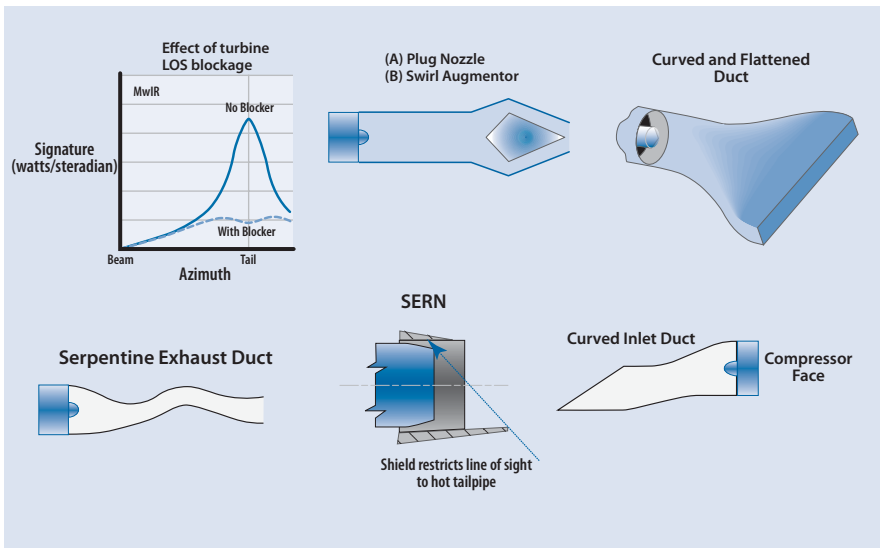
## 12.5.2 IR Design

The rule for reducing the hot-parts emissions is hide what you cannot cool and then coat it with low-emissivity paint. Figure 12.19 shows some concepts for blocking the LOS to the aircraft hot parts. The A-10A very carefully located the twin vertical tails so that they blocked the LOS into the engine cavities at most tail-on angles. The 2-D nozzle and lower surface nozzle ramp on the F-117A effectively shield the exhaust hot parts from co-altitude and below look angles. Changing from a turbojet to a medium bypass ratio (i.e., 1–2) turbofan reduces the engine hot parts and plume emissions significantly. Low-emittance (0.2) paints are available commercially.

The design rule for reducing the exhaust plume emissions is to use a high-bypass turbofan engine if possible and then promote aggressive mixing of the plume with the ambient air. The exhaust mixers on commercial transports to reduce noise do a very good job of reducing the plume temperature. Ejector nozzles also promote plume mixing.

Airframe emissions due to aerodynamic heating can be controlled by flying slower and using low-emissivity coatings. Most of the time the airframe emissions are small compared with the hot parts.

Once the aircraft is deployed its IR emissions are pretty much fixed. However, the aircraft can be repainted from time to time with different  $\epsilon$



**Figure 12.19** Hot parts blocking—IR design guidelines.

paints. From then on it is managing the reflections and background to drive the contrast to zero.

The strategy for managing the IR reflections is to tailor the mission in terms of time of day, background, and weather and in some cases to change the reflectance by changing the emissivity.

## 12.6 Visual Signature

The visual signature is

$$V_{\text{Contrast}} = V_E + V_R - \text{Background} \quad (\text{lm/sr}) \quad (12.5)$$

The  $V_E$  is usually zero; however, sometimes illumination can be added (positive  $V_E$  using a head lamp, for example) but illumination can never be taken away (negative  $V_E$ ).

The visual sensor is usually a human eyeball. Thus, the detection ranges are small—typically 5–8 n mile.

Once again the strategy needs to be to plan the mission and mission profile to avoid or minimize the threat before designing-in performance penalty features. For example, the visual signature can be eliminated by shielding the target from the sensor with terrain or by flying above 5 n mile and not contrailing. The visual signature can be minimized by flying at night.

If the target needs to fly at low altitudes and within visual range of the human eyeball, then the tradeoff between reflectance ( $1 - \epsilon$ ) and background must be considered. Figure 12.20 shows how the target reflectance needs to vary with a daytime background to reduce the detection range for a C-130-sized target. For a clear full-moon night background the same C-130 would need a reflectance of about 0.85 to fill in the black hole contrast.

## 12.7 Acoustic Signature

The acoustic sensor is the human ear and sometimes a microphone. The acoustic signature is a contrast between the emitted noise and the background:

For Acoustic:

$$A_{\text{Contrast}} = A_E + A_R - \text{Background} \quad (\text{EPNdB}) \quad (12.9)$$



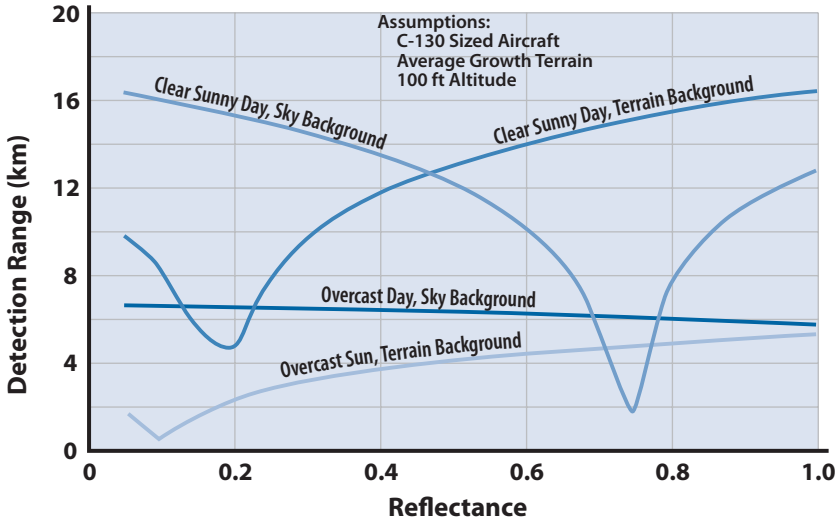


Figure 12.20 Daytime visual detection ranges.

where EPNdB is the effective perceived noise level in decibels and the reflected noise term  $A_R$  is usually zero.

Here a negative contrast (the background is more noisy than the target) is a good thing. If you are a special forces team, the best place to land your aircraft is in the middle of a noisy mall. The good news is that the locals will never hear you. The bad news is that you will probably be seen, with the result being the same as if they heard you.

Acoustic energy is absorbed by buildings, walls (e.g., the noise barriers between residential areas and freeways), humidity, and trees.

Figure 12.21 shows the noise source characteristics for an aircraft. Notice that the main sources of noise are the airframe (aircraft in a dirty

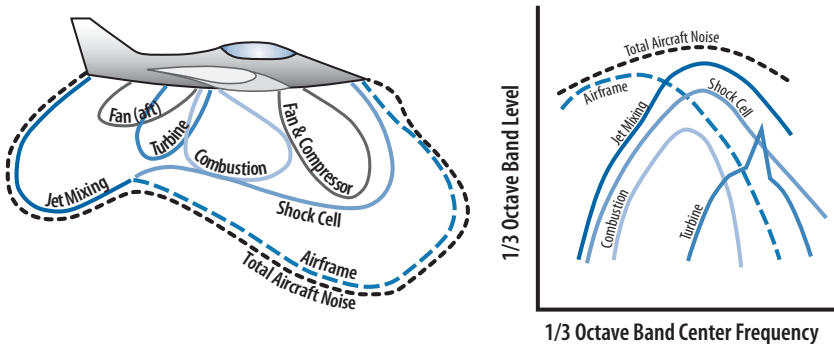


Figure 12.21 Noise source characteristics.

configuration with gear and flaps down) and the jet mixing. The reader is urged to return to Section 4.7 for more discussion of aircraft noise and its suppression. Another aircraft noise source is the sonic boom at speeds greater than Mach 1.0 (see Section 4.6). The main noise source for helicopters is the “slapping” of the rotor blades.

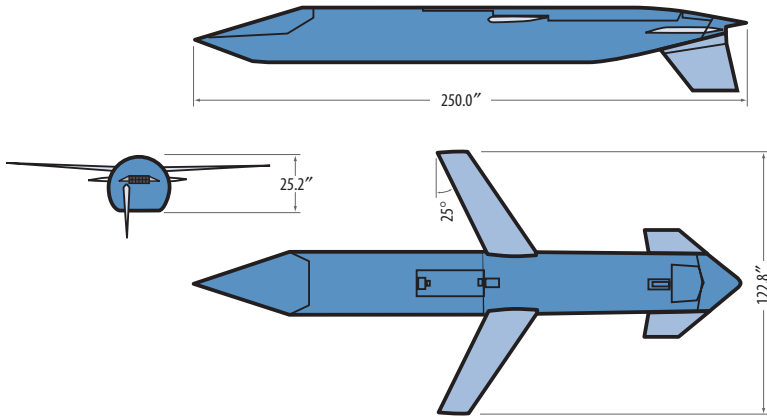
There are design features that can reduce the acoustic signature, such as nozzle noise suppressors, but the most effective approach is mission planning and tactics:

- Avoid acoustic sensors (human ears)
- Power down or slow down when possible
- Carefully select the background and environment

## 12.8 Case Study—AGM-129A Advanced Cruise Missile

In 1977 the U.S. Air Force was convinced (from the Have Blue program) that stealth could greatly increase the survivability of their strategic cruise missile fleet and issued the requirements for the Advanced Cruise Missile (ACM). The requirement was for a low-signature air-launched cruise missile that could deliver a nuclear weapon (W-80) against a high-value strategic target from a distance of 1900 n mile. Industry went to work, with Lockheed pursuing a medium-altitude design and Boeing a low-altitude design. Having started the Have Blue program with their XST program, DARPA was emotionally involved with the stealth technology and started their own ACM program called Teal Dawn. The first author was an Air Force colonel at DARPA and became the Teal Dawn program manager. Teal Dawn was selected for the ACM and entered development by the U.S. Air Force, with GD Convair as the contractor, in 1983. The ACM entered operation in 1991 with over 460 cruise missiles produced. The AGM-129A ACM is shown in Fig. 12.22.

Example 5.3 (Low-Altitude, Subsonic Cruise Missile) in Chapter 5 is essentially the AGM-129A ACM. The ACM requirement was pretty clear except for the mission profile: high altitude or low altitude. After much discussion, including intense interaction with the Defense Science Board, it was decided that Teal Dawn would fly a low-altitude TF/TA profile at Mach 0.7 similar to the AGM -86 ALCM and the AGM-109 Tomahawk. This meant that the RCS design against the low-frequency detection radars (Tall King and Spoon Rest) would be made easier because most of the flight would be below the radar horizon. The threats would be the short-range, high-frequency SAMs defending the high-value targets (located co-altitude and head-on) and the airborne interceptors (AIs, located above). The signature requirements were as follows:



**Figure 12.22** Three-view of Convair AGM-129A ACM.

- Very low RCS in the  $\pm 20$  deg front sector (X-band)
- No side or rear sector RCS requirement
- Low IR signature (top sector for the lookdown–shootdown AIs)

The TF/TA flight profile compounded the AI RF and IR detection problem because the ACM was operating in ground clutter, and the dense air (and possible clouds) increased the IR transmission losses. It was concluded that the TF/TA flight profile resulted in more relaxed signature requirements than a medium-altitude profile.

The RCS design was a sharp chisel nose shape and a flush inlet on the bottom of the fuselage. The wings were swept forward 25 deg for a more favorable packaging of the wing deployment mechanism. The wing LE spikes reflected off the fuselage and outside of the  $\pm 20$  deg front sector. The missile was treated with high-frequency RAM. The IR design was to use a Williams F 112 turbofan (derivative of the F107 turbofan) for a cool exhaust plume. The plume was cooled further using an aspect ratio 4, 2-D nozzle that enhanced the plume mixing with the ambient air. The exhaust cavity was shielded from RF and IR sensors by an upper surface nozzle ramp. Finally the missile was painted with a high-emissivity paint to reduce the sunshine and cloudshine IR reflections (because the ground background is dark).

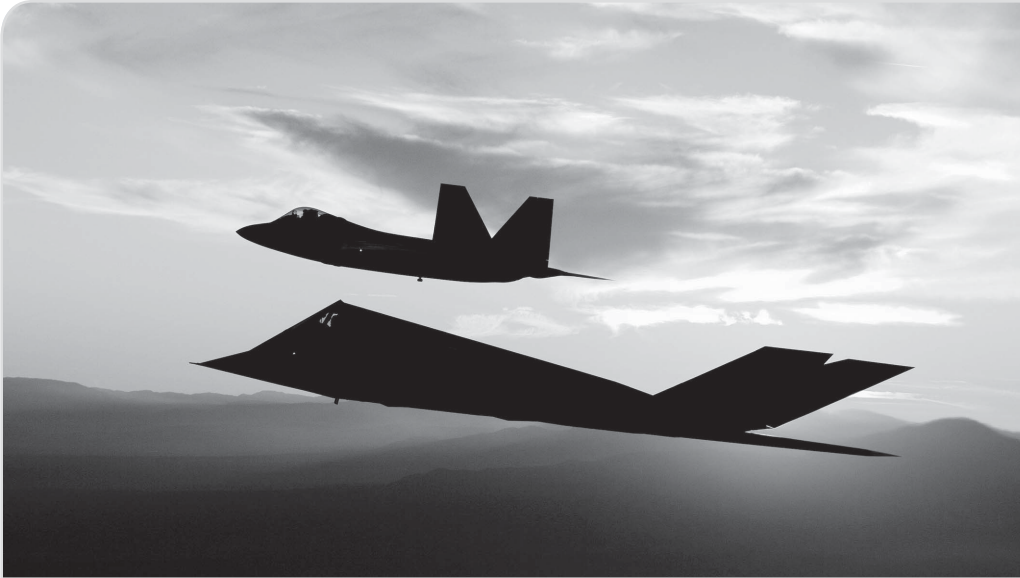
An AGM-129A has never been launched in anger!

## References

- [1] Rich, B. R., *Skunk Works*, Little, Brown, Toronto, 1994.
- [2] Ball, R. E., *The Fundamentals of Aircraft Combat Survivability Analysis and Design*, AIAA Education Series, AIAA, Reston, VA, 1985.

- [3] Fulghum, D. A., "Stealth Retains Value, but Its Monopoly Wanes," *Aviation Week and Space Technology*, 5 Feb. 2001, pp. 53–57.
- [4] Barrie, D., "LO and Behold," *Aviation Week and Space Technology*, 11 Aug. 2003, pp. 50–53.
- [5] Whitford, R., "Designing for Stealth in Fighter Aircraft (Stealth from the Aircraft Designer's Viewpoint)," Paper 965540, 1996 World Aviation Congress, 21–24 Oct., Los Angeles, CA (sponsored by AIAA and SAE).
- [6] Lynch, D., "How the Skunk Works Fielded Stealth," *Air Force Magazine*, Nov.1992, pp. 22–28.
- [7] Piccirillo, A. C., "The Have Blue Technology Demonstrator and Radar Cross Section Reduction," Paper 965538, 1996 World Aviation Congress, 21–24 Oct., Los Angeles, CA (sponsored by AIAA and SAE).
- [8] Aronstein, D. C., "The Development and Application of Aircraft RCS Prediction Methodology," Paper 965539, 1996 World Aviation Congress, 21–24 Oct., Los Angeles, CA (sponsored by AIAA and SAE).
- [9] Fulghum, D. A., "Stealth Engine Advances Revealed in JSF Designs," *Aviation Week and Space Technology*, 19 March 2001, pp. 53–57.
- [10] Varney, G. E., "IR Signature Measurement Techniques and Simulation Methods for Aircraft Survivability." Paper 79-1186, AIAA–Society of Automotive Engineers–American Society of Mechanical Engineers 15th Joint Propulsion Conf., 18–20 June 1979, Las Vegas, NV.

# Chapter 13 Estimating Wing-Body Aerodynamics



- Three-Dimensional Lift Curve Slope
- Inviscid Drag-Due-to-Lift (Induced)
- Viscous Drag-Due-to-Lift
- Skin Friction Drag
- Wing Sweep Effects
- Drag Divergence Mach Number
- Canopy & Boattail Drag
- Vehicle Aerodynamics

After 25 years of service with the U.S. Air Force, the F-117 (lower) was retired to the Tonopah Nevada test range. With its second-generation stealth, 64 F-117s were produced from 1982 to 1991. The F-22 (upper), with its third-generation stealth, replaced the F-117. The F-117 received the Collier trophy in 1989, as did the F-22 in 2006.

*If the aerodynamic estimates appear "too good to be true," they probably are. Always check estimates with real data.*

**A**t this point the design has matured to an aircraft wing–body–tail configuration. Next an aerodynamic analysis is performed to get a refined estimate of the lift and drag (and later the stability derivatives) to determine baseline takeoff and fuel weights. If the design does not close (i.e., the sum of the payload fraction plus the fuel fraction plus the empty-weight fraction does not equal 1.0), then go back to Chapter 5 and start over.

If this were an industry study, the design would be handed to the aerodynamics group and they would start modeling to input to computational fluid dynamics (CFD) codes. However, because this is more of a nonindustry–academic study, we employ well-respected rapid methods developed in the 1970s by the Air Force Flight Dynamics Laboratory [1], the National Advisory Committee for Aeronautics (NACA; now the National Aeronautics and Space Administration [NASA]), and others. The aerodynamic derivatives covered in this chapter are  $C_{L\alpha}$ ,  $K$ ,  $K'$ ,  $K''$ , and  $C_{D0}$ .

## Aircraft Big and Small

It is worth mentioning that the aero analysis and performance methods for a 6-ft wing span, 8-lb radio-controlled (R/C) model airplane are identical to those for a full-scale airplane such as a Cessna 172 (36-ft wing span, 2300 lb). Thus, the methods discussed in this text are applicable to aircraft big and small. The only differences between the R/C model and the full-scale airplane are the wing loading, the Reynolds number, and the moments of inertia.

The R/C model wing loading is one to two orders of magnitude less than a full-scale airplane (because of the “square–cube law”; see Appendix I). R/C models typically have wing loadings of 1–3 lb/ft<sup>2</sup> whereas full-scale airplanes have greater than 10 (Cessna 172 has 12.6 lb/ft<sup>2</sup>). The impact is lower stall speeds and shorter takeoff and landing distances.

The R/C model will typically have Reynolds numbers less than 500,000, which gives the wing a predominately laminar boundary layer. Full-scale airplanes have Reynolds number greater than one million and have turbulent boundary layer wings. The impact is that the full-scale airplanes have higher maximum lift coefficients due to the turbulent boundary layer delaying flow separation over the wing better than the laminar boundary layer. The R/C models and the full-scale airplanes are in a Reynolds number region where the drag coefficients are about the same.

The R/C model will have much smaller moments of inertia than the full-scale airplane. The impact is that the time-to-double-amplitude ( $t_2$ ) from a disturbance will be much shorter for the R/C model because  $t_2 = f(1/(\text{moment of inertia})^{1/2})$ . R/C pilots will have their hands full with a neutral or unstable model.

## 13.1 Linear Lift Curve Slope

The subsonic  $C_L$  vs  $\alpha$  curve for low aspect ratio wings ( $AR < 4$ ) has a linear and a nonlinear region as shown in Fig. 13.1 (see the  $C_{L\alpha}$  for  $AR = 2$  in Figs. H.2 and H.3).

The wing lift coefficient is given by the expression

$$C_L = (C_{L\alpha})(\alpha - \alpha_{0L}) + C_1\alpha^2 \quad (13.1)$$

where  $C_{L\alpha}$  is the linear lift curve slope and  $C_1$  is the nonlinear lift factor. The value of  $C_1$  is determined from Fig. 2.13. The value of  $C_1$  can be assumed zero for  $M_\infty > 1$  flight. Performance calculations of cruise range, climb-out, and acceleration to cruise Mach seldom require angles-of-attack in the nonlinear range. However, the nonlinear lift may be important for landing and takeoff.

### 13.1.1 Subsonic

The subsonic linear lift curve slope  $C_{L\alpha}$  per radian is given by Eq. (2.13) of Chapter 2:

$$\frac{dC_L}{d\alpha} = C_{L\alpha} = \frac{2\pi AR}{2 + \sqrt{4 + AR^2\beta^2(1 + [(\tan^2 \Delta t/c)/\beta^2])}} \quad (13.2)$$

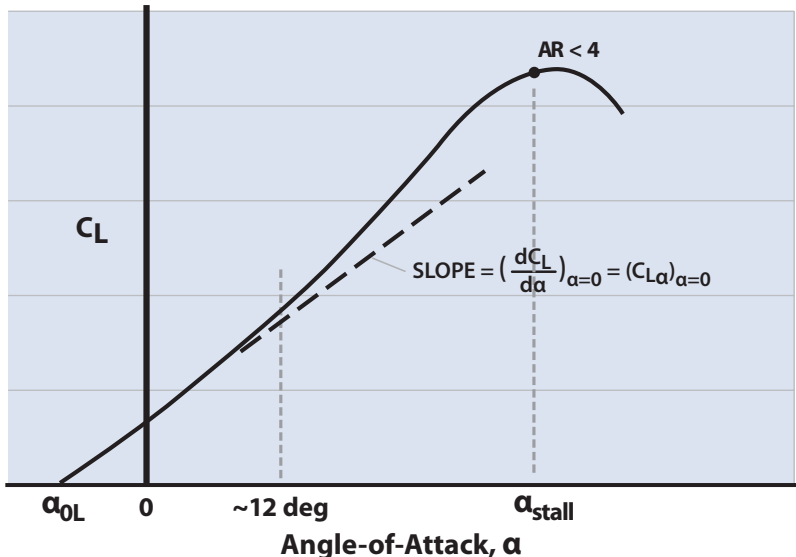


Figure 13.1 Wing  $C_L$ -vs- $\alpha$  curve showing nonlinear behavior for low-AR wings.

where

$$\beta = \sqrt{1 - M_\infty^2}$$

$\Delta t/c$  = sweep of maximum thickness line

Equation (13.2) is the  $C_{L\alpha}$  of the wing only and is therefore based upon the exposed wing planform area  $Se$ .

### 13.1.2 Supersonic

The method for estimating the wing supersonic lift curve slope is developed using supersonic linear theory corrected for three-dimensional flow effects. The wing  $C_{L\alpha}$  is determined using the charts in Fig. 13.2, where

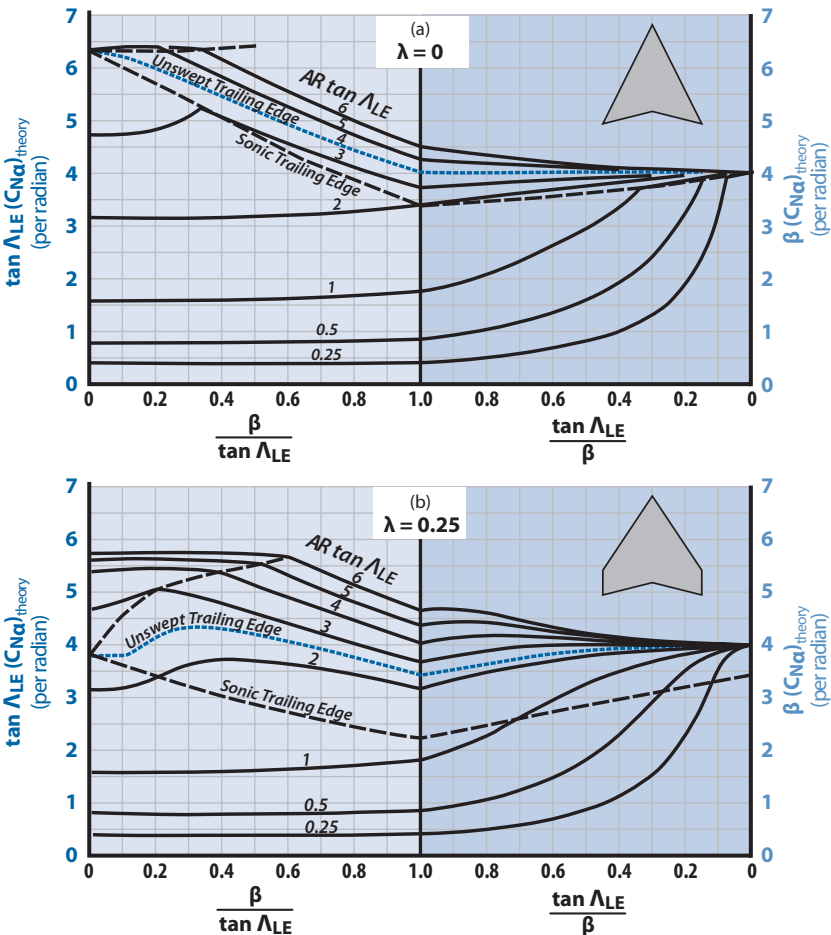


Figure 13.2 Theoretical wing lift curve slope (data from [2,3]).



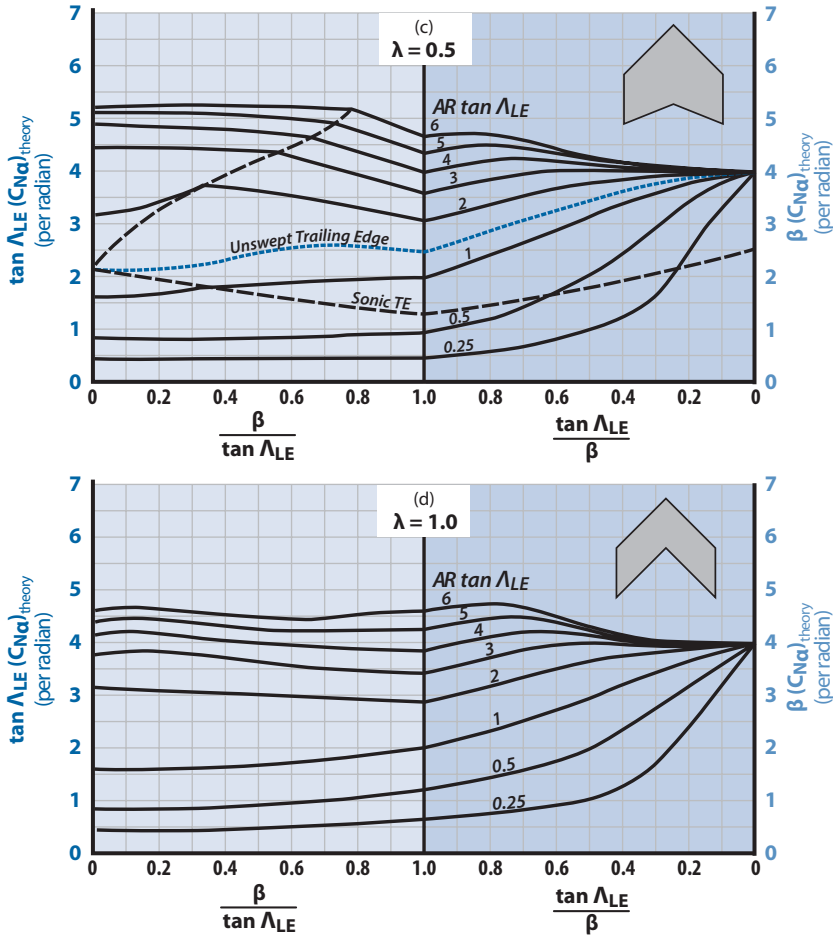


Figure 13.2 (continued) Theoretical wing lift curve slope (data from [2,3]).

$C_N$  is the normal force coefficient slope and is equal to  $C_L$  for small to moderate angles-of-attack. In Fig. 13.2,  $\beta = \sqrt{M_\infty^2 - 1}$ , AR is the wing aspect ratio, and lambda ( $\lambda$ ) is the taper ratio.

Here again  $C_{L\alpha}$  is based upon exposed wing planform area.

### 13.1.3 Transonic

There is no well-defined method for estimating transonic  $C_{L\alpha}$ . Reference [1] reports an empirical method that works reasonably well. The method is too complicated and cumbersome to present here, so an alternate method is suggested.

The  $C_{L\alpha}$  vs Mach number behavior will be as shown in Fig. 13.3a. Use the subsonic method up to about Mach 0.9 and extend the supersonic method down to about Mach 1.3. Then fair in a curve between Mach = 0.9 and 1.3 similar to the curves shown in Fig. 13.3a.

### 13.1.4 Wing-Body $C_{L\alpha}$

The lift characteristics of a wing and a body do not add directly to give the wing-body lift. Rather, there are interference effects of one component

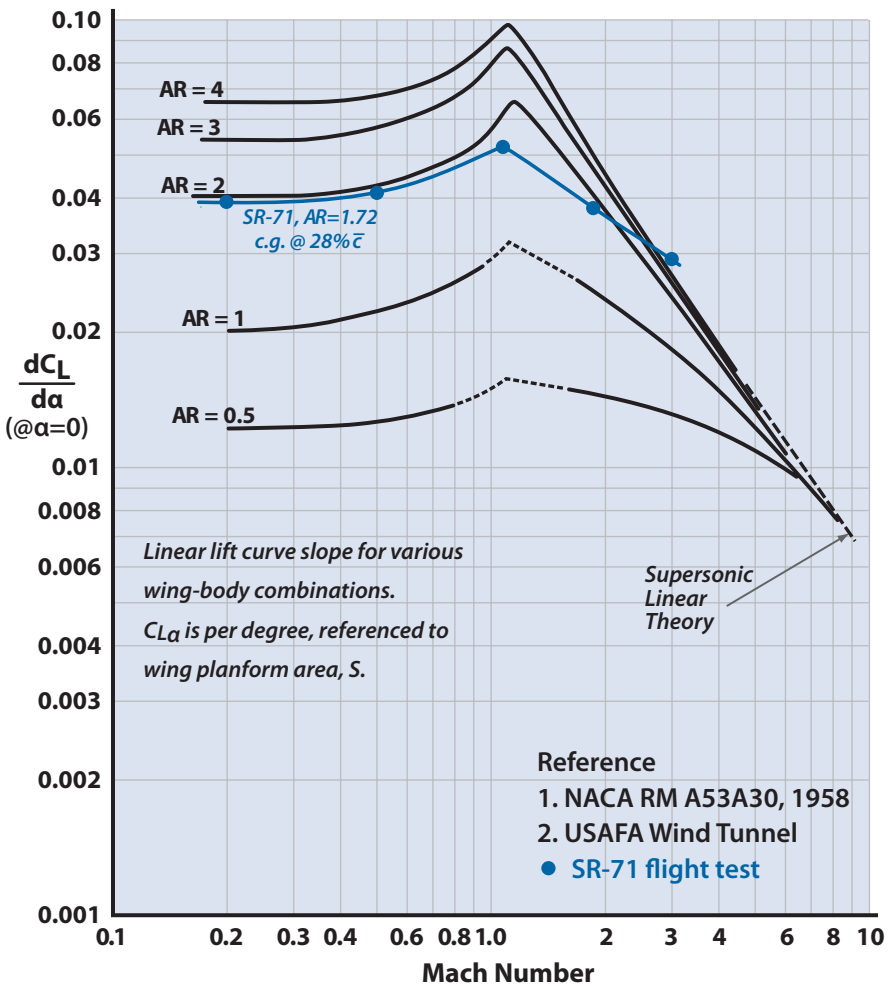
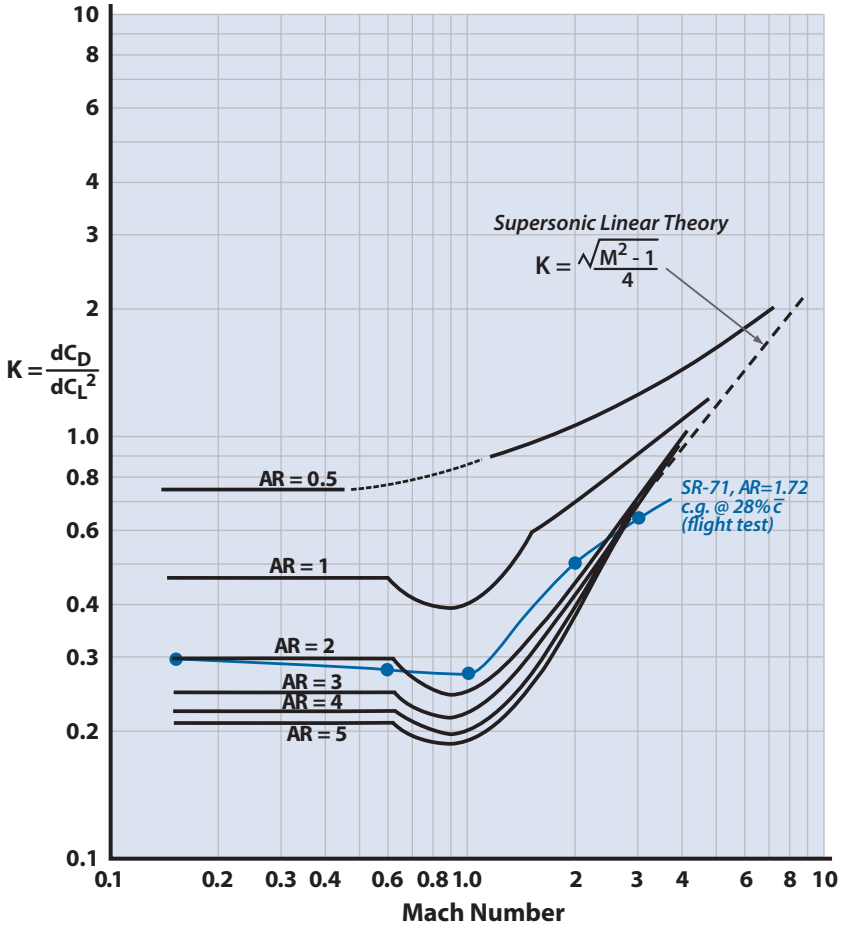


Figure 13.3a Linear lift curve slope for various wing-body combinations ( $C_{L\alpha}$  based on total planform area).



**Figure 13.3b** Drag-due-to-lift factor (based on total platform area) for uncambered wing-body combinations with delta planforms and LE radius of 0.045% chord.

on the other that make the wing-body lift greater than the sum of the individual components [4]. A method that gives good results for the wing-body linear lift curve slope is

$$(C_{L\alpha})_{WB} = F(C_{L\alpha})_W \tag{13.3}$$

where  $(C_{L\alpha})_W$  is the linear lift curve slope (based upon the exposed wing area) of the wing and  $F$  is the wing-body lift interference factor shown in

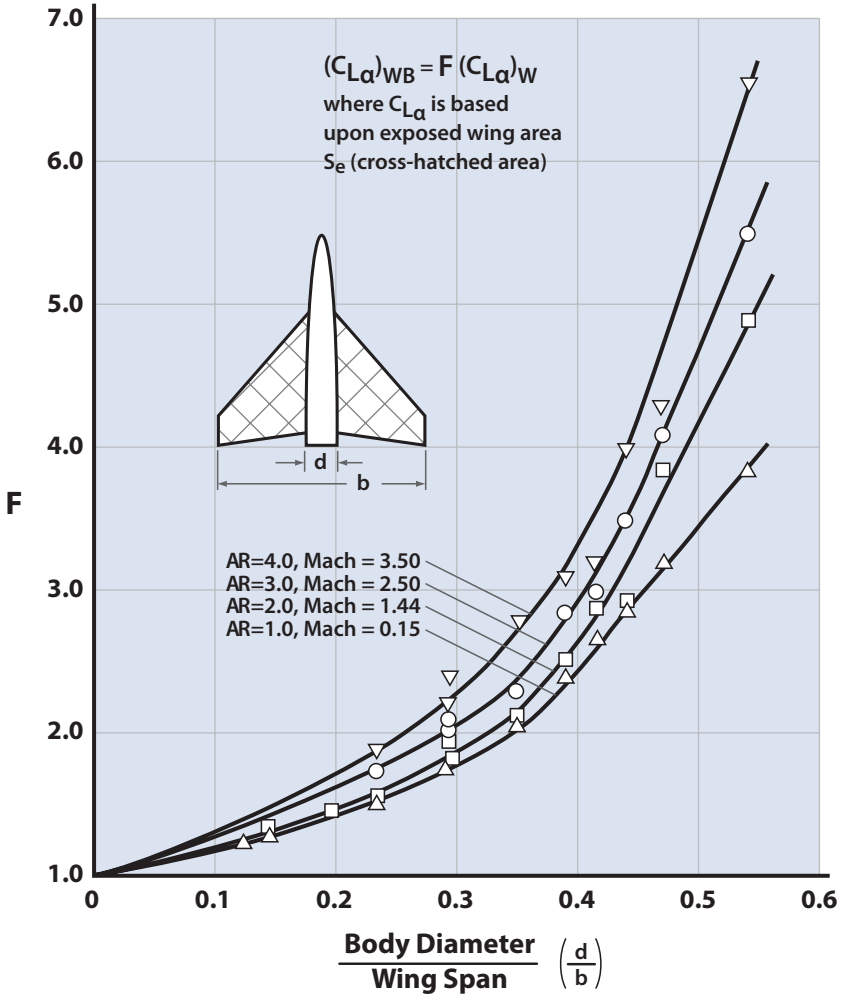


Figure 13.4 Wing-body interference factor (data from [5-7]).

Fig. 13.4. The  $(C_{L\alpha})_{WB}$  is the wing-body lift curve slope and is referenced to the exposed wing planform area  $S_e$ .

The final curve of wing-body  $C_{L\alpha}$  vs Mach number can be compared with the experimental data shown in Fig. 13.3a. Notice that the  $(C_{L\alpha})_{WB}$  presented in Fig. 13.3a are referenced to the total wing planform area  $S_W$ . The aircraft aerodynamic derivatives can be referenced to either  $S_e$  or  $S_W$  (see Fig. 7.1), but they must all be referenced to the same reference area. The total wing planform area  $S_W$  is more conventional and is recommended.

## 13.2 Drag-Due-to-Lift

The total drag coefficient for a wing-body combination is expressed as

$$C_D = (C_{D0})_{\text{wing}} + (C_{D0})_{\text{body}} + \Delta C_{D0} + C_{DL} \quad (13.4)$$

where  $\Delta C_{D0}$  is the zero-lift drag coefficient due to miscellaneous protuberances (canopy, pitot tube, etc.) and  $C_{DL}$  is the drag coefficient due to lift. Estimating the wing-body  $C_{DL}$  is difficult as discussed below; [3] calls it more of an art than a science. The wing-body  $C_{DL}$  is primarily due to the wing so that it is safe to assume

$$\text{wing-body } C_{DL} \approx \text{wing } C_{DL}$$

The methods for  $C_{DL}$  that follow use wing geometry primarily but represent the entire wing-body  $C_{DL}$  referenced to  $S_w$ .

### 13.2.1 Subsonic

In subsonic flow the total drag coefficient for the wing is expressed as

$$C_D = C_{D_{\min}} + K' C_L^2 + K'' (C_L - C_{L_{\min}})^2 \quad (13.5)$$

The terms containing  $K'$  and  $K''$  are collectively called the *drag-due-to-lift*. This parabolic behavior of  $C_D$  with  $C_L$  is shown in Figs. 2.16 and 2.17.

The  $K'$  term in Eq. (13.5) is the *inviscid* drag-due-to-lift called the *induced drag*. This drag results from the vortices trailing off a finite wing inducing a downwash at the wing aerodynamic center. The  $K''$  term is the *viscous* drag-due-to-lift caused by flow separation and increased skin friction. This drag results from the viscous nature of the fluid causing the separation point on the upper surface to move forward from the trailing edge as the wing rotates to higher angles-of-attack and the region of adverse pressure gradient spreads. There is also an increase in skin friction occurring in the leading edge region due to the local superelevations associated with increasing lift. The  $C_{L_{\min}}$  is the lift coefficient for minimum drag coefficient  $C_d$ . For cambered airfoils,  $C_{L_{\min}} \neq 0$  and is approximately equal to the  $C_l$  for  $\alpha = 0$ . For symmetric airfoils,  $C_{L_{\min}} = 0$  and Eq. (13.5) is expressed as

$$C_D = C_{D0} + K C_L^2 \quad (13.6)$$

where  $K = K' + K'' = dC_D/dC_L^2$  and is called the drag-due-to-lift factor. The variation of  $K$  with Mach number is shown in Fig. 13.3b for low-AR wing-bodies. The SR-71 is certainly a low AR aircraft ( $AR = 1.72$ ) and its  $K$  from flight test data agrees well with Fig. 13.3b. Figure G.9 shows the subsonic

$K = 1/\pi AR e$  for many real aircraft (symmetric and cambered). Figure G.9 is empirical and discussed in Appendix G. The  $C_{D_0}$  is called the zero-lift drag coefficient. It should be pointed out that  $C_{D_0} \approx C_{D_{\min}}$  for wings with cambered airfoils, and the terms  $C_{D_0}$  and  $C_{D_{\min}}$  are often used interchangeably. This text will use the term  $C_{D_0}$  to mean both  $C_{D_0}$  (for wings with symmetric airfoils) and  $C_{D_{\min}}$  (for wings with cambered airfoils). This is not done to confuse the reader but rather in keeping with convention.

Equations (13.5) and (13.6), which display the parabolic behavior of  $C_D$  with  $C_L$ , are valid only up through moderate values of  $C_L$ . At a  $C_L$  called the *break*  $C_L$ ,  $C_{LB}$ , the drag coefficient ceases to be parabolic with  $C_L$  as shown in Fig. 2.17. As the  $C_L$  increases past  $C_{LB}$  the drag-due-to-lift increases sharply from that expected from a parabolic behavior. The flow phenomenon involved here is not too well understood. However, it is connected with the onset of trailing edge separation spreading rapidly over the upper surface and/or the onset of leading edge separation spreading rapidly over the upper surface with no reattachment [8]. For  $C_L$ s above  $C_{LB}$  the expression for total drag coefficient is expressed as

$$C_D = C_{D_0} + K' C_L^2 + K'' (C_L - C_{l_{\min}})^2 + \Delta C_{DB} \tag{13.7}$$

where  $\Delta C_{DB}$  is the drag deviation from a parabolic behavior (see Fig. 2.17).

The prediction method for  $\Delta C_{DB}$  is complicated and will not be presented here. The method is presented in [8].

The viscous drag-due-to-lift factor  $K''$  is dependant primarily on LE radius, camber, and  $Re$ , and secondarily on taper ratio for sharp-edged airfoils. Determining  $K''$  is difficult as it is viscous-dominated. Reference [9] offers a method shown on Fig. 13.6. Fig. 13.6 is independent of camber and  $Re$ , and it tends to overestimate  $K''$ ; however, for symmetric or low camber airfoils, it offers a rapid estimate of  $K''$ .

A better method (and the one recommended) is to determine

$$K'' = \Delta(C_d - C_{d_{\min}}) / \Delta(C_l - C_{l_{\min}})^2$$

directly from airfoil polar data by plotting  $\Delta(C_d - C_{d_{\min}})$  vs  $\Delta(C_l - C_{l_{\min}})^2$  and determining the slope (see Section F.4).

The induced drag-due-to-lift factor  $K'$  is given as

$$K' = 1/\pi AR e \tag{13.8}$$

Where  $e$  is called the wing efficiency factor and corrects the finite wing theory result (see Chapter 2) for taper ratio, sweep and body effects on the span loading. The  $e$  factor is best determined from CFD using a vortex lattice method.

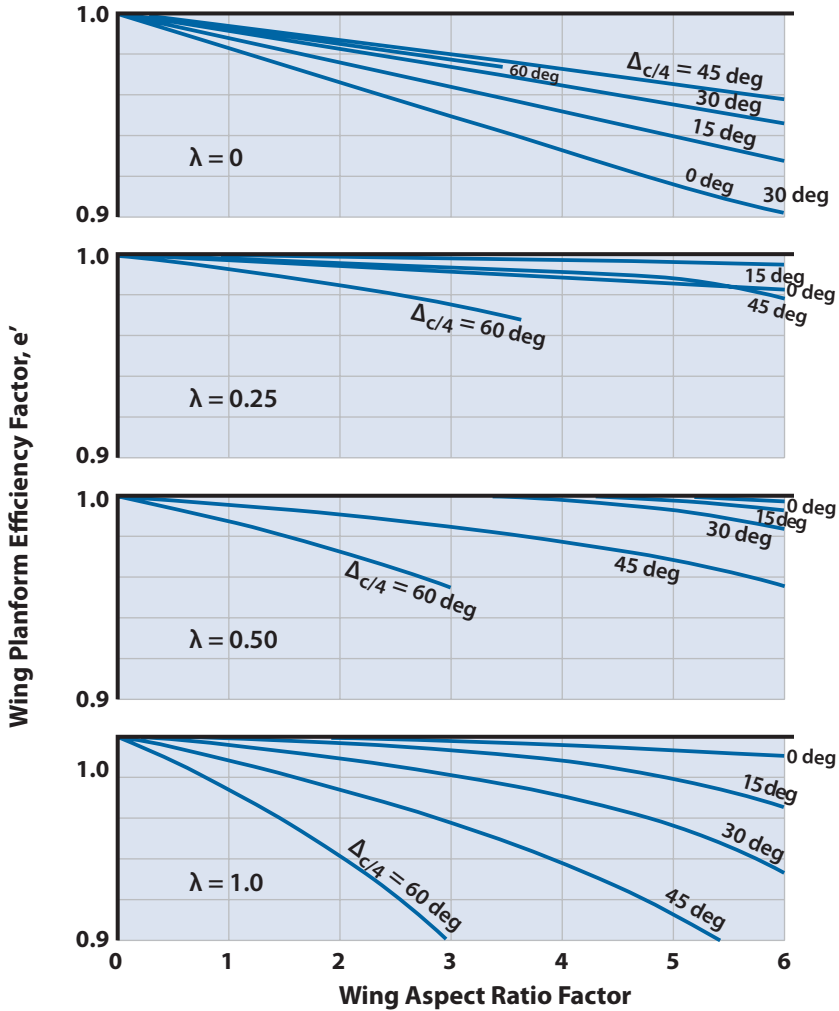


Figure 13.5 Weissinger wing planform efficiency factor (data from [1]).

The  $e$  factor can also be determined from

$$e = e' \left[ 1 - (d/b)^2 \right] \tag{13.9}$$

where  $d/b$  is the ratio of body diameter to wing span (see Fig. 13.4). The  $e'$  factor has been formulated by Weissinger in [10] and is presented in Fig 13.5. Figure 13.5 was developed for fighter type aircraft and tends to over-estimate the  $e$  for large aspect ratio configurations.

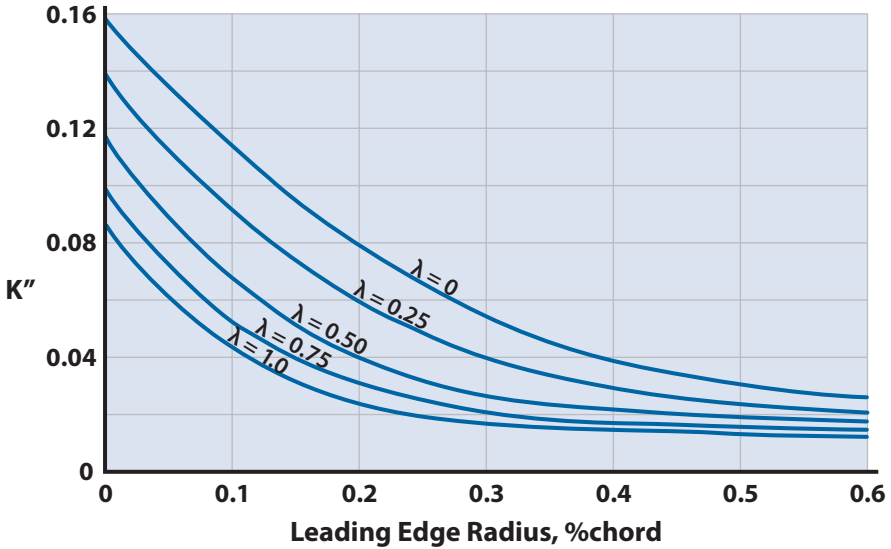


Figure 13.6 Viscous drag-due-to-lift factor  $K''$  (data from [9]); LE radius for NACA airfoils shown on Fig. F.2.

An alternate method (and the one recommended) is to estimate  $K$  from Fig. G.9 and determine  $K'$  from  $K' = K - K''$  as discussed in Section G.2.

### 13.2.2 Supersonic

The supersonic drag-due-to-lift is developed from supersonic linear theory (Chapter 2). For wings with supersonic leading edges the drag-due-to-lift factor  $K$  is given by

$$K = \frac{1}{C_{L\alpha}} \tag{13.10}$$

where  $C_{L\alpha}$  is the wing-body lift curve slope (per radian) referenced to  $S_{ref}$ . Using the  $C_{L\alpha} = 1.6$  per radian value for the SR-71 at Mach = 3.0 from Fig. 13.3a gives  $K = 0.62$ , which agrees well with the flight test data of Fig. 13.3b.

For wings with subsonic leading edges, the drag-due-to-lift is less than that given by Eq. (13.10) because of the suction of the leading edge. Thus, the general expression for supersonic drag-due-to-lift factor  $K$  is

$$K = \frac{1}{C_{L\alpha}} - \Delta N \tag{13.11}$$



where  $\Delta N$  is the leading edge suction parameter. The  $\Delta N$  parameter is determined from [8] as

$$\Delta N = \left( \frac{\Delta N}{\Delta N_{M=1.0}} \right) (\Delta N_{M=1.0}) \tag{13.12}$$

where  $(\Delta N/\Delta N_{M=1.0})$  is obtained from Fig. 13.7 and

$$\Delta N_{M=1.0} = \frac{1}{(C_{L\alpha})_{M=1.0}} - (K' + K'')$$

The  $K'$  and  $K''$  are the subsonic inviscid and viscous drag-due-to-lift factors already determined. The term  $(C_{L\alpha})_{M=1.0}$  is the wing-body lift curve slope at Mach = 1.0 (from Fig. 13.3a).

### 13.2.3 Transonic

There is no reliable method for estimating the transonic drag-due-to-lift factor. It is suggested that a curve be faired between the subsonic and supersonic K curves similar to the experimental data curves presented in Fig. 13.3b.

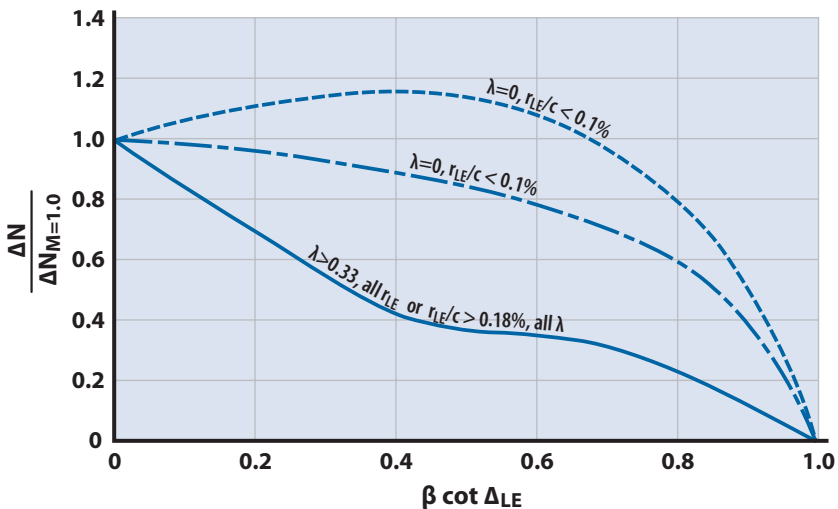


Figure 13.7 Values of LE suction parameter at supersonic speeds (data from [8]).

### 13.3 Zero-Lift Drag Coefficient

The total drag coefficient for a wing–body combination is given by Eq. (13.4) as

$$C_D = (C_{D0})_{\text{wing}} + (C_{D0})_{\text{body}} + \Delta C_{D0} + C_{DL} \quad (13.4)$$

where the  $C_{D0}$ s for the wing and the body are determined separately and then added together. Equation (13.4) implies that the individual drag coefficient terms are all referenced to the same reference area  $S_{\text{ref}}$ . This  $S_{\text{ref}}$  can be  $S_e$  or  $S_{\text{ref}}$  but must be the same for all.

The methods for predicting the fuselage and wing  $C_{D0}$  will be discussed separately. The wing methods are limited to wings with straight leading edges. For nonstraight wings, such as a double delta (Swedish SAAB-35, Draken) or an ogee (Anglo-French Concorde SST), the methods presented in [1] or [9] should be used.

#### 13.3.1 Wing: Subsonic

The subsonic wing  $C_{D0}$  is primarily skin friction. The expression for  $(C_{D0})_W$  based upon the reference area  $S_{\text{ref}}$  is given by

$$(C_{D0})_W = C_f \left[ 1 + L \left( \frac{t}{c} \right) + 100 \left( \frac{t}{c} \right)^4 \right] R \frac{S_{\text{wet}}}{S_{\text{ref}}} \quad (13.13)$$

where

$L$  = airfoil thickness location parameter

$L = 1.2$  for maximum  $t/c$  located at  $x \geq 0.3c$

$L = 2.0$  for maximum  $t/c$  located at  $x < 0.3c$

$t/c$  = maximum thickness ratio of the airfoil

$S_{\text{wet}}$  = wetted area of the wing ( $2S_e$ )

$R$  = lifting surface correlation factor obtained from Fig. 13.8

$C_f$  = turbulent flat plate skin friction coefficient

The effect of surface roughness on the skin friction values is determined using a cutoff Reynolds number. The type of surface is selected and the roughness height is determined from Table 13.1. The ratio  $\ell/k$  is computed and the cutoff Reynolds number,  $Re_\ell$ , determined from Fig. 13.9. The  $\ell$  is the mean aerodynamic chord  $\bar{c}$  of the wing (see Fig. 7.1). The wing flight Reynolds number,  $Re_e = \rho \bar{c} V/\mu$ , based upon  $\bar{c}$  is determined along a typical subsonic trajectory (see Chapter 4). Then the smaller of the two Reynolds numbers,  $Re_e$  or  $Re_\ell$ , is used to determine the  $C_f$  from Fig. 2.6.

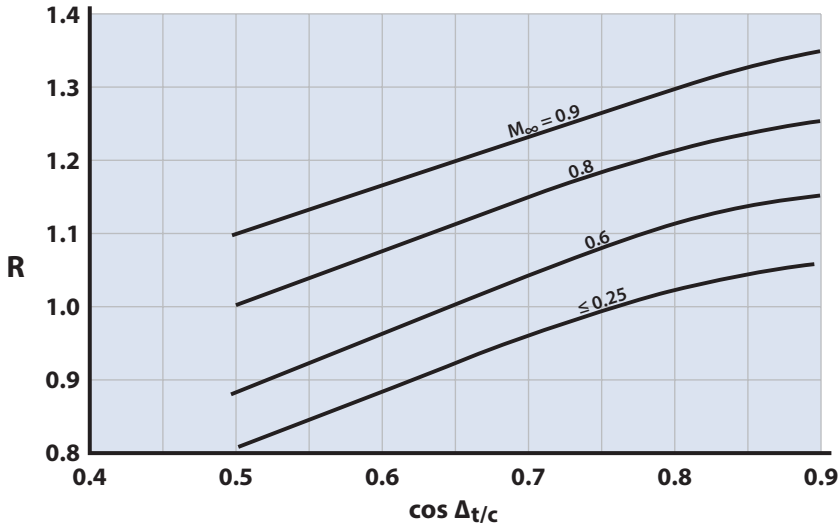


Figure 13.8 Lifting surface correlation factor for wing subsonic  $C_{D_0}$ .

### 13.3.2 Wing: Transonic

The transonic regime for the wing begins at  $M_{CR}$  but the drag rise is delayed slightly until the divergence Mach number,  $M_D$ . The divergence Mach number is defined as that Mach number where  $(\partial C_{D_0} / \partial M) = 0.1$ . The transonic wing  $C_{D_0}$  is expressed as

$$(C_{D_0})_W = C_{D_f} + C_{D_W} = C_f \left[ 1 + L \left( \frac{t}{c} \right) \right] \frac{S_{wet}}{S_{ref}} + C_{D_W}$$

Table 13.1 Roughness Height Values (in Equivalent Sand Roughness)

Type of Surface	$k$ (in.)
Aerodynamically smooth	0
Polished metal or wood	$0.02-0.08 \times 10^{-3}$
Natural sheet metal	$0.16 \times 10^{-3}$
Smooth matte paint, carefully applied	$0.25 \times 10^{-3}$
Standard camouflage paint, average	$0.40 \times 10^{-3}$ application
Camouflage paint, mass-production	$1.20 \times 10^{-3}$ spray
Dip-galvanized metal surface	$6 \times 10^{-3}$
Natural surface of cast iron	$10 \times 10^{-3}$

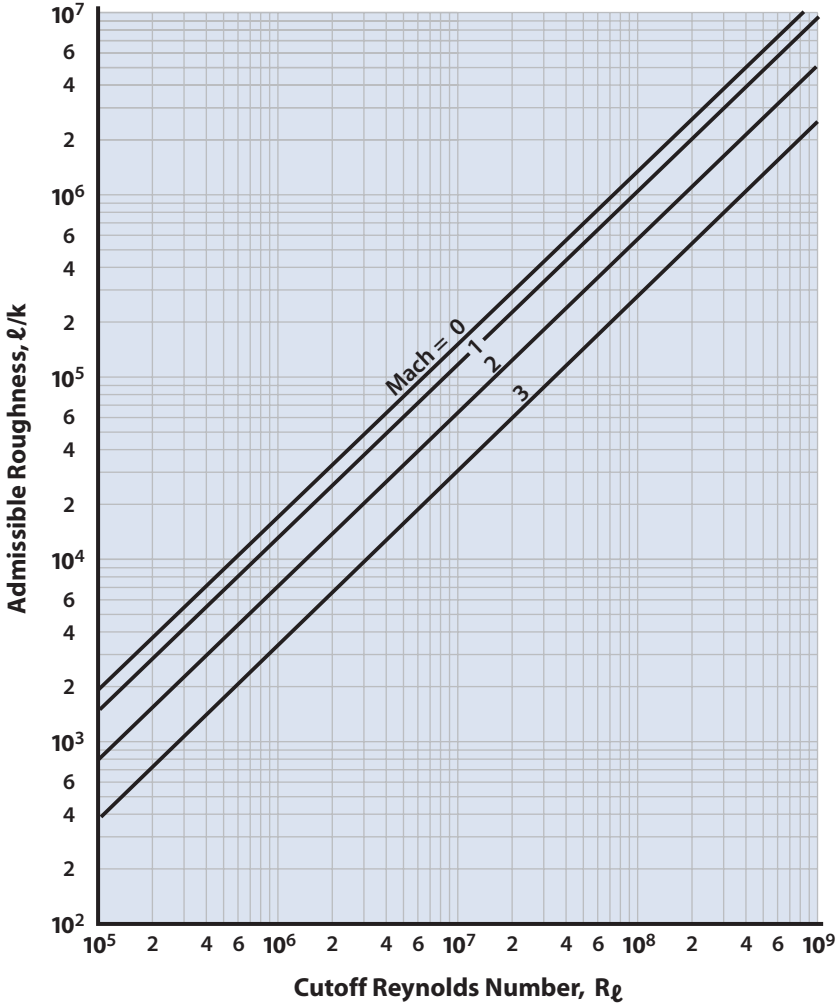


Figure 13.9 Cutoff Reynolds number (data from [1]).

The skin friction drag  $C_{D_f}$  is assumed to be a constant value throughout the transonic region. The value for  $C_{D_f}$  is the value at Mach = 0.6.

The task of constructing the wing transonic  $C_{D_w}$  curve is one of correcting experimental data for sweep, aspect ratio, and  $t/c$  using the von Kármán similarity laws for transonic flow. The transonic  $C_{D_w}$  curve for unswept wings is shown in Fig. 13.10. Table 13.2 presents useful values for  $t/c$ .

The Mach number for drag divergence,  $M_D$ , of the unswept wing is obtained by locating the point on the  $C_{D_w}$  vs Mach curve where the slope is 0.1. The values of peak  $C_{D_w}$ , Mach number for peak  $C_{D_w}$ , and  $M_D$  are corrected for sweep as follows:

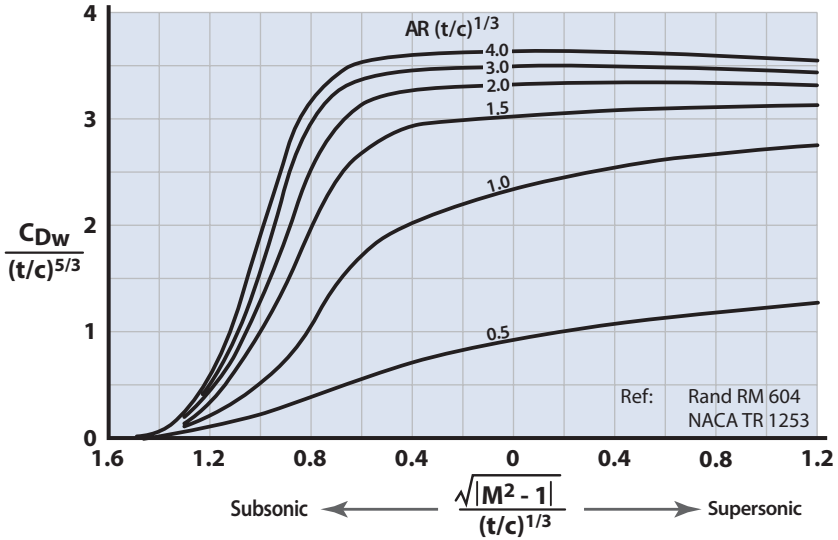


Figure 13.10 Transonic zero-lift wing wave drag for unswept wings.

Table 13.2 Unswept Wings (Values for  $t/c$ : Wave Drag)

$t/c$	$(t/c)^{1/3}$	$(t/c)^{5/3}$
0.12	0.493	0.0293
0.11	0.479	0.0254
0.10	0.464	0.0217
0.09	0.448	0.0181
0.08	0.431	0.0148
0.07	0.412	0.0118
0.06	0.392	0.0092
0.05	0.368	0.0068
0.04	0.342	0.00468
0.03	0.311	0.00292
0.02	0.271	0.00147

$$\text{Swept } M_D = [\text{Unswept } M_D] / (\cos \Lambda_{c/4})^{0.5} \tag{13.14}$$

$$\text{Swept } C_{DW_{\text{peak}}} = [\text{Unswept } C_{DW_{\text{peak}}}] / (\cos \Lambda_{c/4})^{2.5} \tag{13.15}$$

$$\text{Swept } M_{C_{DW_{\text{peak}}}} = [\text{Unswept } M_{C_{DW_{\text{peak}}}}] / (\cos \Lambda_{c/4})^{0.5} \tag{13.16}$$

where  $\Lambda_{c/4}$  = angle of wing quarter-chord.

**Example 13.1 Construction of the Transonic  $C_{D0}$  Curve**

Determine the construction of the transonic  $C_{D0}$  curve with sweep  $c/4 = 45$  deg:

Delta wing with AR	3
$t/c$	0.03
$C_{Df}$	0.006 at Mach 0.6
$(t/c)^{1/3}$	0.311
$(t/c)^{5/3}$	0.00292 (Table 13.2)
AR $(t/c)^{1/3}$	0.933
Unswept $C_{DW_{\text{peak}}}$	0.0082 (from Fig. 13.10)
Unswept $M_{C_{DW_{\text{peak}}}}$	1.09 (from Fig. 13.10)
Swept $C_{DW_{\text{peak}}}$	$(0.0082)(0.42) = 0.00344$
Swept $M_{C_{D_{\text{peak}}}}$	$1.09/0.841 = 1.3$

The construction of the wing transonic  $C_{D0}$  curve is shown on Fig. 13.11. The unswept  $M_D$  is located by finding the point where the slope is 0.1. The swept wing  $M_D$  is determined by Eq. (13.14). The swept wing  $C_D$  curve is then faired in as shown in Fig. 13.11.

**13.3.3 Wing: Supersonic**

The supersonic wing  $C_{D0}$  based upon  $S_{\text{ref}}$  is given by

$$(C_{D0})_W = C_{Df} + C_{DW}$$

The wing supersonic skin friction is expressed as

$$C_{Df} = C_f \frac{S_{\text{wet}}}{S_{\text{ref}}} \tag{13.17}$$

where  $C_f = (C_{f_c} / C_{f_i}) C_{f_i}$ . The ratio  $C_{f_c} / C_{f_i}$  is obtained from Fig. 13.12 and  $C_{f_i}$  is determined the same way as for subsonic flow using cutoff and flight Reynolds number comparison.

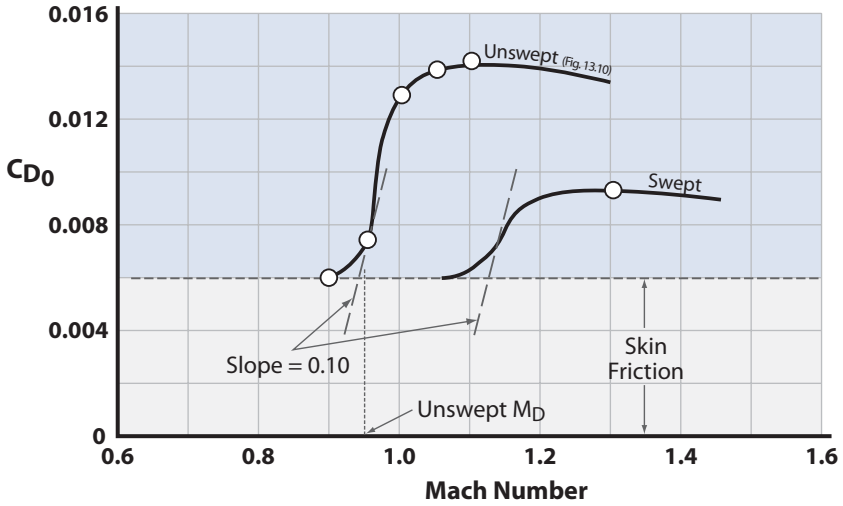


Figure 13.11 Construction of transonic wing  $C_{D0}$  for AR = 3 delta wing with  $t/c = 0.03$ .

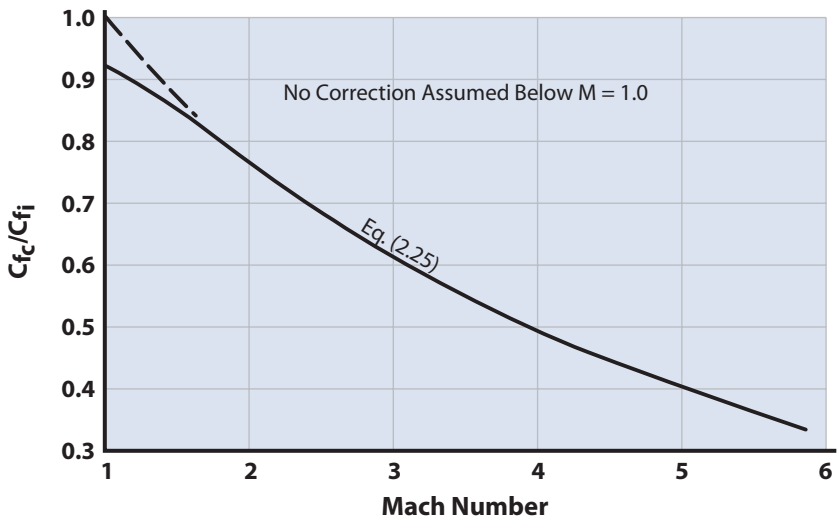


Figure 13.12 Compressibility effect on turbulent skin friction.

The method for predicting the wing supersonic wave drag coefficient is developed from supersonic linear theory. Wings with round leading edges will exhibit a detached bow wave, accompanied by an additional wave drag term due to leading edge bluntness.

For wings with sharp-nosed airfoil sections and the following:

1. Supersonic leading edge ( $\beta \cot \Lambda_{LE} \geq 1$ ), use

$$C_{Dw} = \frac{B}{\beta} \left( \frac{t}{c} \right)^2 \frac{S_e}{S_{ref}} \tag{13.18}$$

2. Subsonic leading edge ( $\beta \cot \Lambda_{LE} < 1$ ), use

$$C_{Dw} = B \cot \Delta_{LE} \left( \frac{t}{c} \right)^2 \frac{S_e}{S_{ref}} \tag{13.19}$$

where  $B$  is a constant factor for a given sharp-nosed airfoil.  $B$  factors for sharp-nosed airfoils are presented in Table 13.3.

For wings with round-nosed airfoil sections and the following:


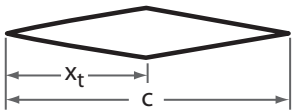
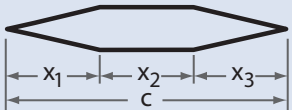
1. Supersonic leading edge ( $\beta \cot \Lambda_{LE} \geq 1$ ), use

$$C_{Dw} = C_{DLE} + \frac{16}{3\beta} \left( \frac{t}{c} \right)^2 \frac{S_e}{S_{ref}} \tag{13.20}$$

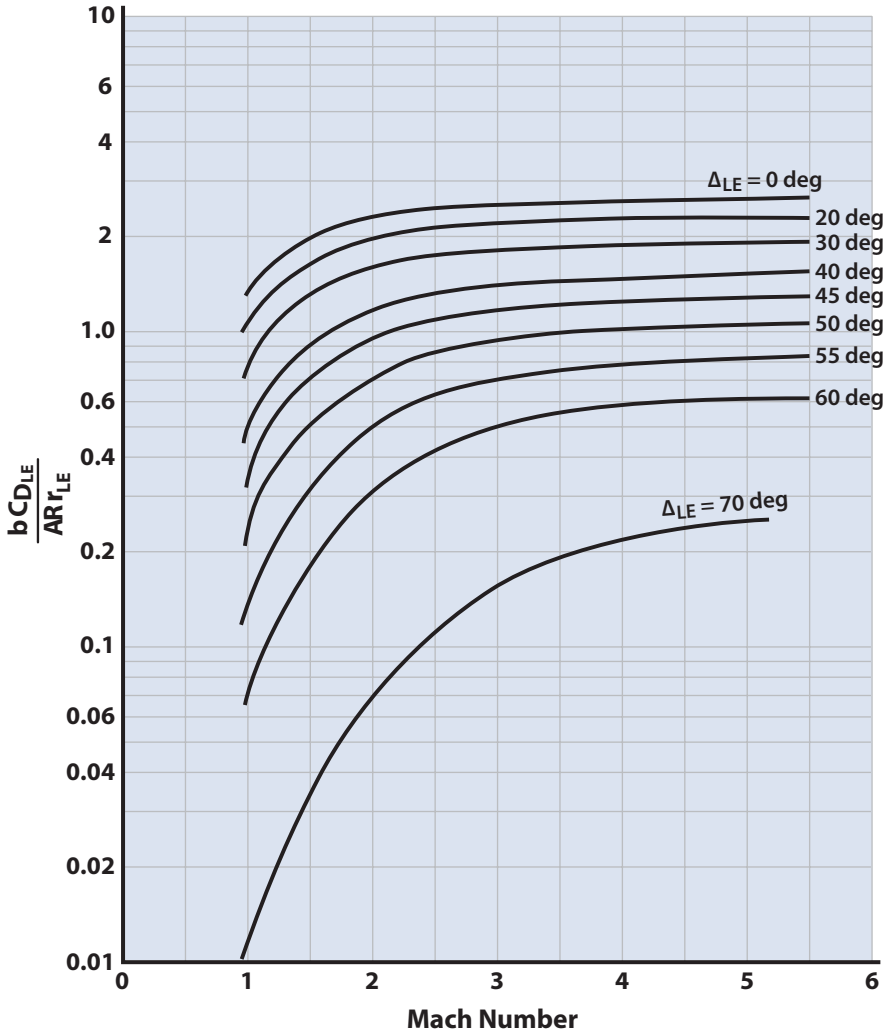
2. Subsonic leading edge ( $\beta \cot \Lambda_{LE} < 1$ ), use

$$C_{Dw} = C_{DLE} + \frac{16}{3} \cot \Delta_{LE} \left( \frac{t}{c} \right)^2 \frac{S_e}{S_{ref}} \tag{13.21}$$

**Table 13.3** B Factor for Sharp-Nosed Airfoils

Basic Wing Airfoil Section	B	Section
Biconvex	$\frac{16}{3}$	
Double wedge	$\frac{c/x_1}{1-x_1/c}$	
Hexagonal	$\frac{c(c-x_2)}{x_1x_3}$	





**Figure 13.13** Supersonic round LE blunt drag coefficient (data from [12]).

where the leading edge blunt term  $C_{D_{LE}}$  is determined from Fig. 13.13. In Fig. 13.13  $b$  is the wing span in feet and  $r_{LE}$  is the radius of the leading edge at the mean aerodynamic chord in feet.

Sometimes the  $C_{D_0}$  values determined in the transonic and supersonic regimes do not match so that it is difficult to fair a smooth curve through all the points. This is usually because the transonic method does not account for leading edge radius. In this event, average the data point values

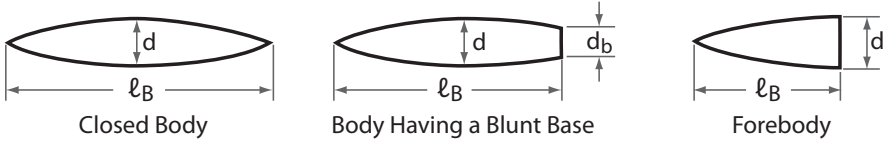


Figure 13.14 Body shapes and geometry.

until a smooth curve can be drawn. The peak  $C_{D_0}$  should occur at the Mach number given by Eq. (13.16).

### 13.3.4 Body: Subsonic

At subsonic speeds the body  $C_{D_0}$  of smooth slender bodies is primarily skin friction (Fig. 8.11). Figure 13.14 shows the body shapes considered. The body  $C_{D_0}$  referenced to the maximum cross-sectional area  $S_B$  is given as

$$(C_{D_0})_B = (C_{D_f})_B + C_{D_b}$$

where  $C_{D_f}$  is the skin friction coefficient and  $C_{D_b}$  is the base pressure coefficient. The body  $C_{D_f}$  is expressed as [13]

$$(C_{D_f})_B = C_f \left[ 1 + \frac{60}{(\ell_B/d)^3} + 0.0025 \left( \frac{\ell_B}{d} \right) \right] \frac{S_s}{S_B} \quad (13.22)$$

where  $S_s$  is the wetted area of the body surface and  $\ell_B/d$  is the body fineness ratio (see Fig. 13.14).

For noncircular bodies, the equivalent diameter should be used:

$$d_{\text{equiv}} = \sqrt{S_s / 0.7854}$$

The  $C_f$  is the turbulent skin friction coefficient and is determined in the same manner as the wing subsonic skin friction. The reference length is the body length  $\ell_B$ .

The base pressure coefficient is expressed in [14] as

$$C_{D_b} = 0.029 (d_b/d)^3 / \sqrt{(C_{D_f})_B} \quad (13.23)$$

The designer should avoid blunt-base bodies if at all possible because the  $C_{D_b}$  term can become quite large. If a jet engine exhaust completely fills the base region, then the base drag is zero.

### 13.3.5 Body: Transonic

The transonic body  $C_{D_0}$  is given as

$$(C_{D_0})_B = C_{D_f} + C_{D_p} + C_{D_b} + C_{D_W} \quad (13.24)$$

The  $C_{D_f} = C_f S_s / S_B$  is the skin friction drag coefficient, where  $C_f$  is the turbulent skin friction coefficient at Mach = 0.6. This value is assumed to be constant throughout the transonic region.

The pressure drag coefficient  $C_{D_p}$  is evaluated at Mach = 0.6 by

$$C_{D_p} = (C_f)_{M=0.6} \left[ \frac{60}{(\ell_B / d)^3} + 0.0025 \left( \frac{\ell_B}{d} \right) \right] \frac{S_S}{S_B} \quad (13.25)$$

The base drag term  $C_{D_b}$  is evaluated using

$$C_{D_b} = -C_{pb} \left( \frac{d_b}{d} \right)^2 \quad (13.26)$$

where the base pressure coefficient  $C_{pb}$  is obtained from the three-dimensional curve in Fig. 2.27.

The wave drag coefficient  $C_{D_W}$  is obtained from Fig. 13.15 (data from [15]).

The body transonic  $C_{D_0}$  curve is constructed by adding the four drag terms of Eq. (13.24). The divergence Mach number for bodies having fineness ratios of 4 and greater is about 0.95.

### 13.3.6 Body: Supersonic

The supersonic body  $C_{D_0}$  method presented in this section is taken from [11], which contains an excellent summary of the various supersonic theories compared with experimental data. The method presented here is restricted to nonblunt closed-nosed bodies of revolution. If the body is open nosed (such as the fuselage of the F-100 or MIG-21) or has significant nose bluntness, the method of [1] should be used.

The body supersonic  $C_{D_0}$  referenced to the maximum cross-sectional area  $S_B$  is expressed as

$$(C_{D_0})_B = C_f \frac{S_S}{S_B} + C_{D_{N2}} + C_{D_A} + C_{D_{A(NC)}} + C_{D_b} \quad (13.27)$$

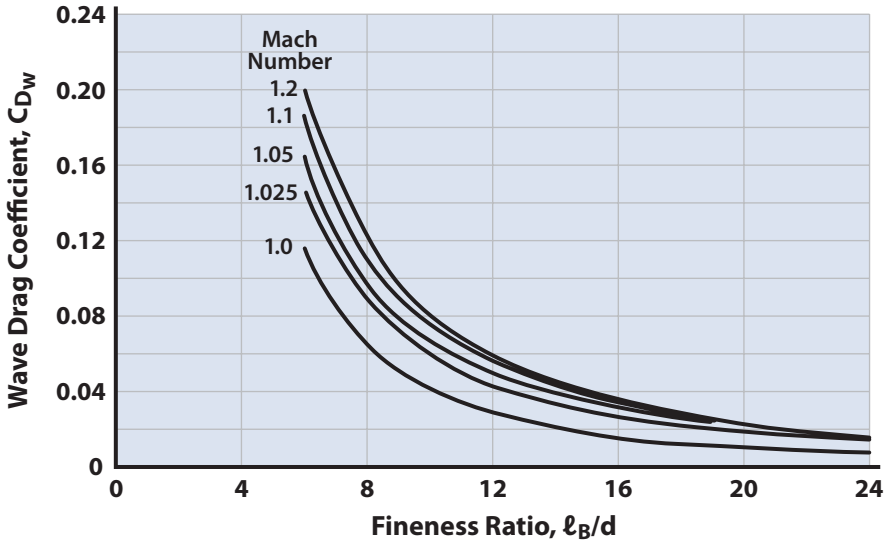


Figure 13.15 Wave drag for parabolic-type fuselage (data from [15]).

where the terms are defined as:

- $C_f$  = compressible turbulent skin friction determined in the same fashion as the supersonic wing skin friction
- $S_s$  = body wetted area
- $C_{D_{AN_2}}$  = interference drag coefficient acting on the afterbody due to the center body (cylindrical section) and the nose, obtained from Figs. 13.16 and 13.17
- $C_{D_{N_2}}$  = nose wave drag obtained from Figs. 13.18, 13.19, and 13.20, where  $f_N$  is nose fineness ratio  $l_N/d$  (see Fig. 13.16)
- $C_{D_A}$  = body afterbody wave drag obtained from Figs. 13.21 and 13.22, where  $f_A$  is the afterbody fineness ratio  $l_A/d$  (see Fig. 13.16)
- $C_{D_b}$  = base drag term given by Eq. (13.26);  $C_{p_b}$  is obtained from Fig. 2.27

### 13.3.7 Miscellaneous Drag Items

The designer should not neglect the drag of miscellaneous items such as external stores, the canopy, and other protuberances. The drag for these items is best obtained from experiment. Figure 13.23 shows the approximate  $C_{D_0}$  for a one-man canopy, typical protuberances (such as the pitot tube, antenna mounts, gun ports), and nozzle boattail. The nozzle-boattail approximate  $C_{D_0}$  shown in Fig. 13.23 is for a fuselage-mounted jet engine with a gentle afterbody taper down to the exhaust nozzle. This approximate

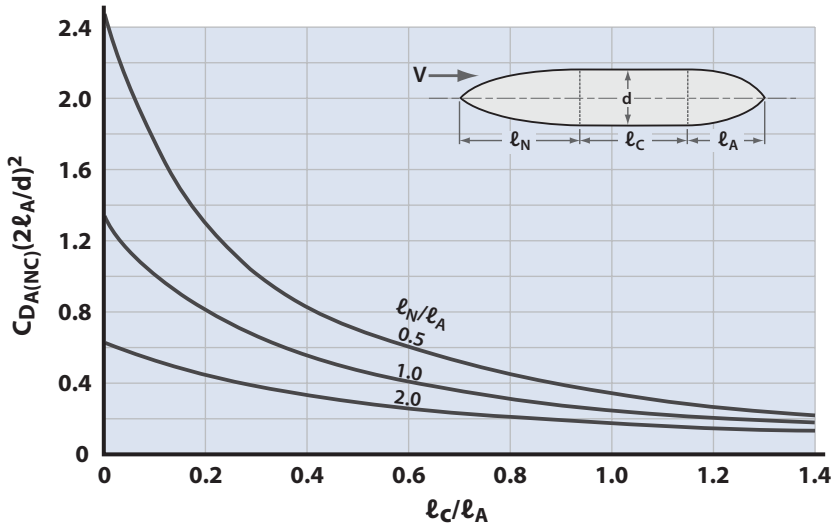


Figure 13.16 Interference drag for pointed bodies with parallel center section.

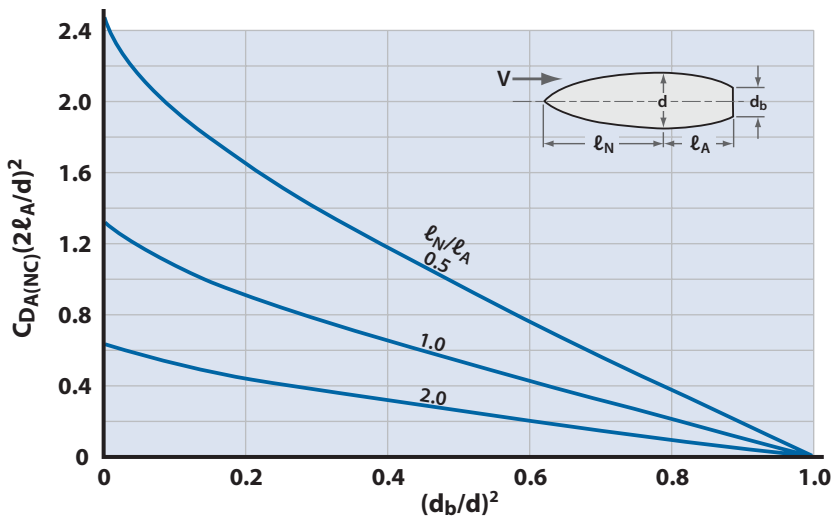


Figure 13.17 Interference drag of truncated afterbodies behind pointed forebodies with no parallel center section.

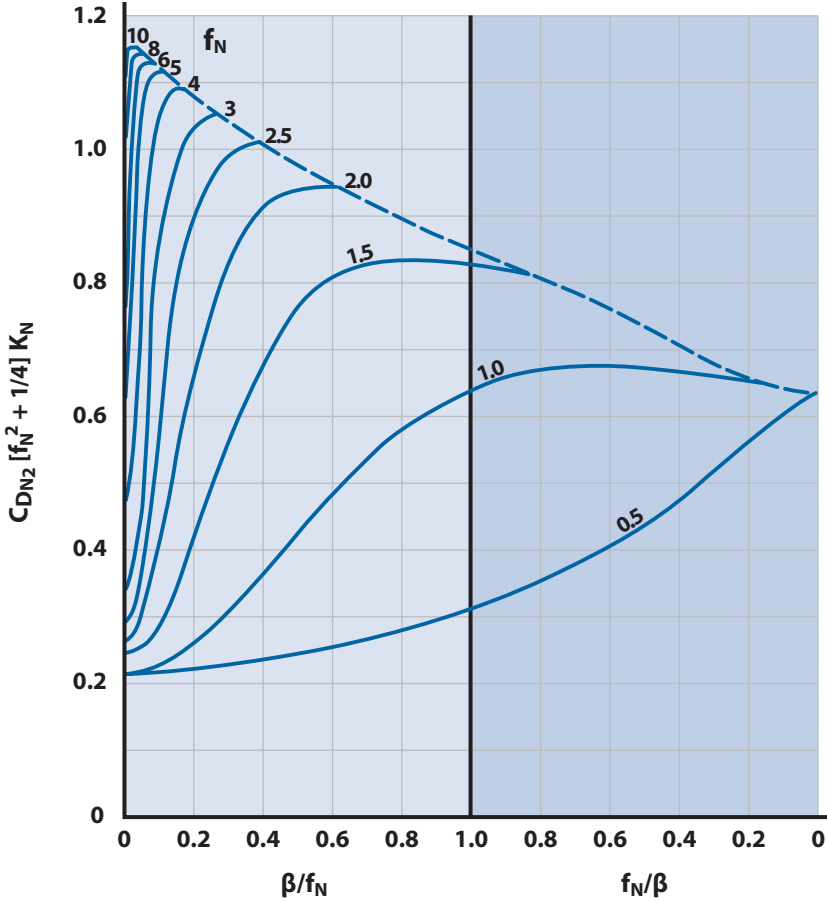


Figure 13.18 Supersonic pressure drag of ogive noses.

$C_{D_0}$  of the nozzle boattail would replace the afterbody and base drag terms mentioned earlier.

Figure 13.24 presents the approximate  $C_D$  for external stores.

The data in Figs. 13.23 and 13.24 is from [16] and is referenced to a wing area of 280 ft<sup>2</sup>. Thus, the data must be corrected for the appropriate  $S_{ref}$ . For example, the canopy drag coefficient at Mach = 1.0 would be

$$\text{Canopy } \Delta C_{D_0} = (0.004) \frac{280}{S_{ref}}$$

The  $\Delta C_{D_0}$  for a landing gear can be seen in Fig. 10.4.

### 13.3.8 Wing-Body $C_{D_0}$

The problem of estimating the wing-body combination  $C_{D_0}$  is one of properly accounting for the mutual interference effects of one component on the other. The problem is extremely complicated and requires a fairly accurate picture of the flow field interactions. This information is not available at this point in the design game. Correction studies have been

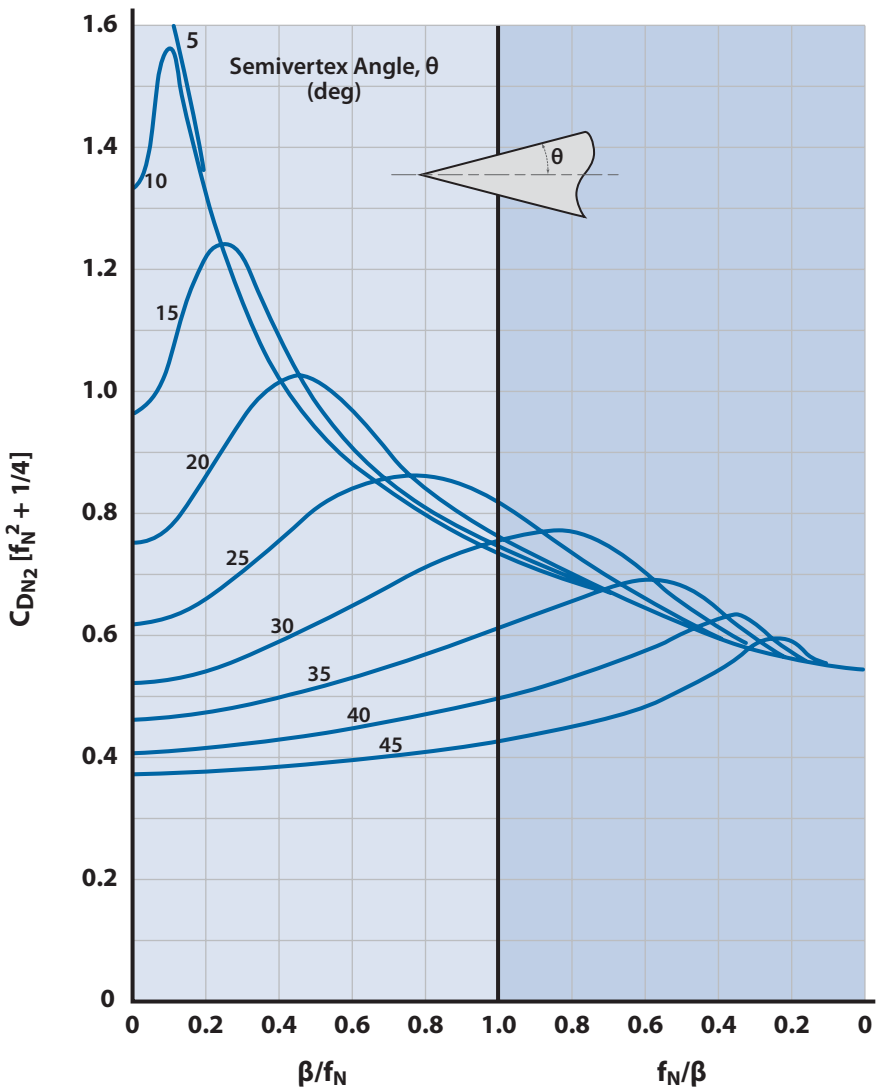


Figure 13.19 Supersonic pressure drag of conical noses.

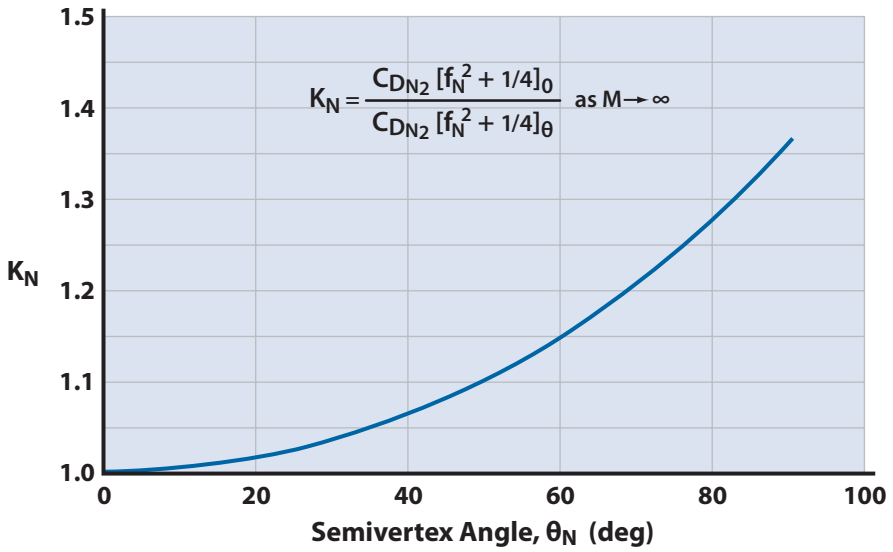


Figure 13.20 Correlation factor for pressure drag of ogive noses.

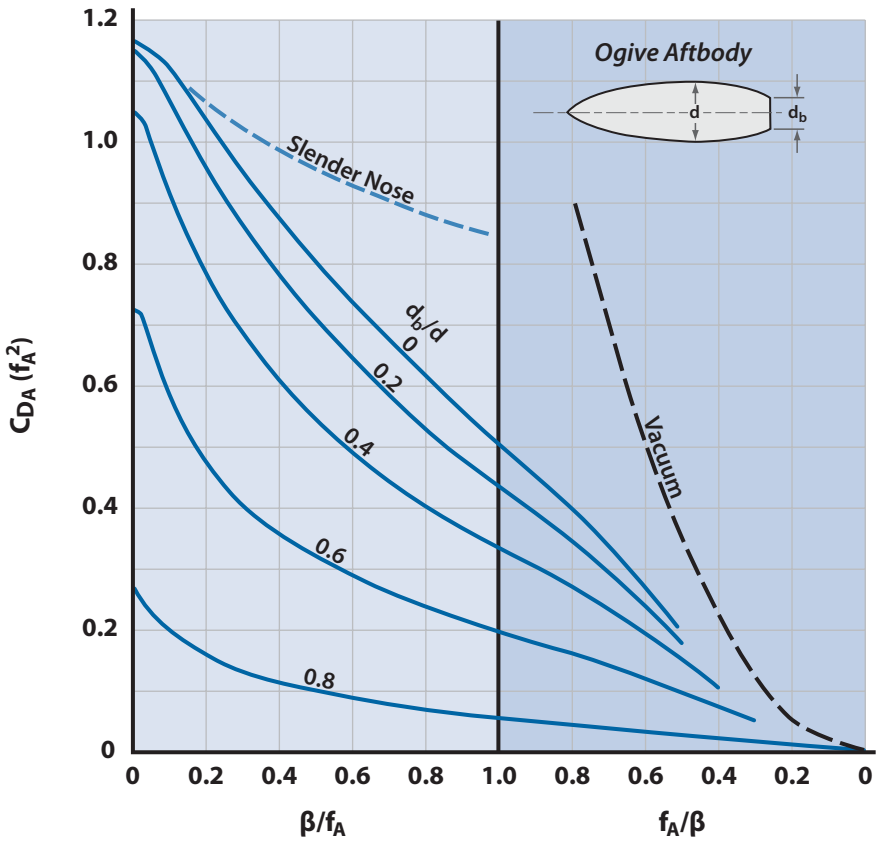


Figure 13.21 Supersonic pressure drag of ogive boattails (data from [11]).



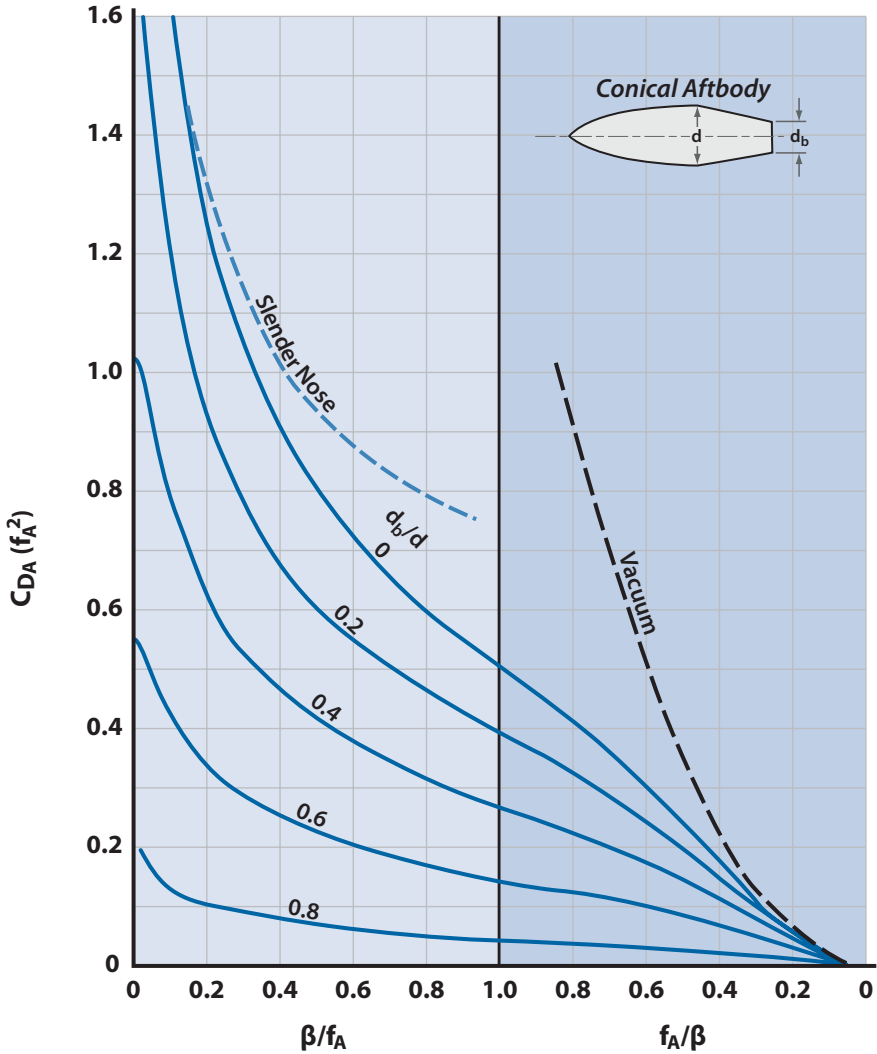


Figure 13.22 Supersonic pressure drag of conical boattails (data from [11]).

conducted on wing-body interference. The results [9] indicate that the wing-body interference effects amount to about  $\pm 5\%$  for subsonic flow with the generous use of fillets. It is hard to argue at this point that the  $C_{D0}$  of the components is accurate to within 5%. Thus, the wing-body subsonic  $C_{D0}$  will be assumed to be simply the sum of the components,

$$(C_{D0})_B = C_f \frac{S_S}{S_B} + C_{DN2} + C_{DA} + C_{DA(NC)} + C_{Db} \quad (13.27)$$

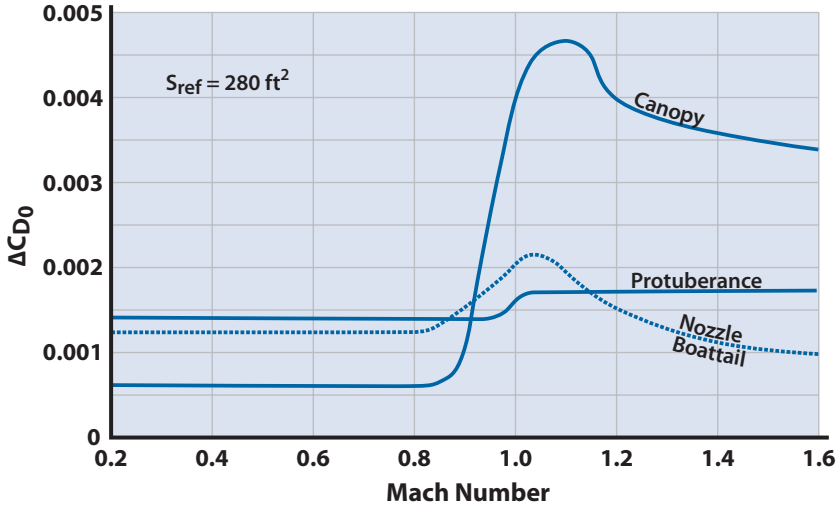


Figure 13.23 Incremental drag for miscellaneous items (data from [16]).

based upon the maximum cross-sectional area  $S_B$ . Then the wing-body  $C_{D0}$  referenced to  $S_{ref}$  is

$$(C_{D0})_{WB} = (C_{D0})_B \frac{S_B}{S_{Ref}} + (C_{D0})_W + \Delta C_{D0} \tag{13.28}$$

where  $\Delta C_{D0}$  is any miscellaneous drag items referenced to  $S_{ref}$ .

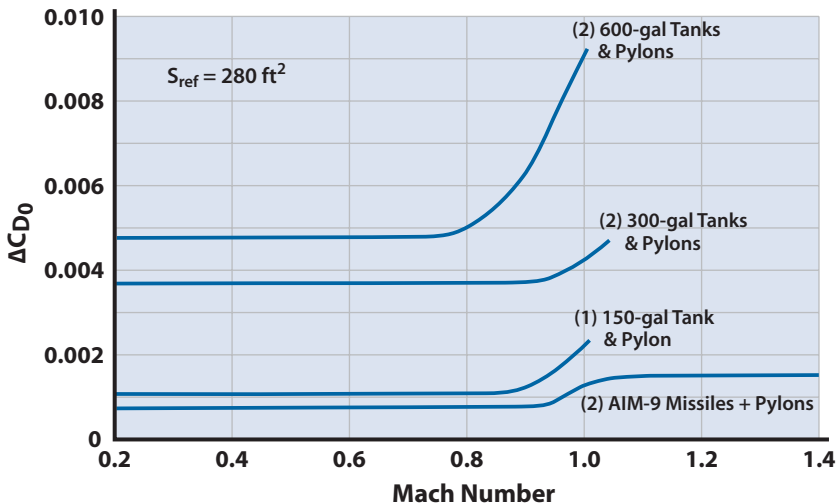


Figure 13.24 Incremental drag for external stores (data from [16]).

For transonic and supersonic flow the interference effects can be significant. The interference drag is usually positive for configurations not specifically contoured to reduce this drag component. However, for area-ruled configurations, this interference drag can be negative. It is recommended that aircraft designed for transonic and supersonic flight be area-ruled. Area-ruling is discussed in Chapter 8.

## 13.4 Combined Vehicle Aerodynamics

The complete aircraft aerodynamics can now be estimated. First tail surfaces ( $t/c$ , planform, symmetrical section) are designed based upon the preliminary estimates for tail size (from Chapter 11), then their individual aerodynamics are estimated and then combined with the wing-body aerodynamics. A popular trick at this point is to assume the tail surfaces to be miniature wings and nacelles to be miniature fuselages so that their aerodynamics are similar. This might appear as cheating, but it is appropriate for the first design loop. Our complete aircraft aerodynamics can be estimated as follows:

$$(C_{L\alpha})_{a/c} = (C_{L\alpha})_{W/B} \quad (13.29a)$$

$$(C_{l\alpha})_{a/c} = (C_{l\alpha})_{W/B} \quad (13.29b)$$

$$K_{a/c} = K_{W/B} \quad (13.30)$$

$$(C_{D0})_{a/c} = (C_{D0})_{W/B} + (C_{D0})_{wing} \frac{S_{VT} + S_{HT}}{S_{ref}} + (C_{D0})_{fuse} S_{nacelle} / S_{ref} \quad (13.31)$$

Remember to do a “sanity check” on your aerodynamic estimates. Compare your results with real aircraft data such as those found in Appendix G.

## References

- [1] Ellison, D. E., “USAF Stability and Control Handbook (DATCOM),” U.S. Air Force Flight Dynamics Laboratory, AFFDL/FDCC, Wright-Patterson AFB, OH, Aug. 1968.
- [2] Jones, R. T., “Properties of Low-Aspect-Ratio Pointed Wings at Speeds Below and Above the Speed of Sound,” NACA TR-835, 1946.
- [3] Mirels, H., “Aerodynamics of Slender Wings and Wing-Body Combinations Having Swept Trailing Edges,” NACA TN-3105, 1954.
- [4] Pitts, W. C., Nielsen, J. N., and Kaattari, P. J., “Lift and Center of Pressure of Wing-Body-Tail Combinations at Subsonic, Transonic and Supersonic Speeds,” NACA Rept. 1307, 1959.

- [5] Maher, R. J., and Bores, J. H., "Low Aspect Ratio Wing–Body Combination Lift Curve Slope Determination at Subsonic Speeds," Aero 350 Rept., U.S. Air Force Academy, CO, May 1970, pp. 13–36.
- [6] Sanchez, F., "Lift Curve Slope Interference Factor for Low Aspect Ratio Wing–Body Combinations," Aero 499 Rept., U.S. Air Force Academy, CO, May 1971.
- [7] Nicolai, L. M., and Sanchez, F., "Correlation of Wing–Body Combination Lift Data," *Journal of Aircraft*, Vol. 10, No. 2, Oct. 1973, pp. 126–128.
- [8] Simon, W. E., Ely, W. L., Niedling, L. G., and Voda, J. J., "Prediction of Aircraft Drag Due to Lift," U.S. Air Force Flight Dynamics Laboratory, AFFDL-TR-71-84, Wright–Patterson AFB, OH, June 1971.
- [9] Benepe, D. B., Kouri, B. G., Webb, J. B., "Aerodynamic Characteristics of Non-Straight Taper Wings," U.S. Air Force Flight Dynamics Laboratory, AFFDL-TR-66-73, Wright–Patterson AFB, OH, 1966.
- [10] Furlong, G. C., and McHugh, J. G., "A Summary and Analysis of the Low-Speed Longitudinal Characteristics of Swept Wings at High Reynolds Number," NACA RM L52D16, Aug. 1952.
- [11] Morris, D. N., "A Summary of the Supersonic Pressure Drag of Bodies of Revolution," *Journal of the Aeronautical Sciences*, Vol. 28, No.7, July 1961, pp. 516–521.
- [12] Crosthwait, E. L., "Drag of Two-Dimensional Cylindrical Leading Edges," General Dynamics, F /W Rept. AIM No. 50, 1966.
- [13] Blakeslee, D. J., Johnson, R. P., and Skavdahl, H., "A General Representation of the Subsonic Lift–Drag Relation for an Arbitrary Airplane Configuration," RAND RM 1593, 1955.
- [14] Hoerner, S. F., *Fluid-Dynamic Drag*, published by the author, 1958.
- [15] Gollos, W. W., "Transonic and Supersonic Pressure Drag for a Family of Parabolic Type Fuselages at Zero Angle of Attack," RAND Rept. RM 982, 1952.
- [16] Smith, C. W., "Aerospace Handbook," General Dynamics, Fort Worth, TX, FZA-381, March 1976.

# Chapter 14

# Propulsion System Fundamentals



- Propeller Systems (Reciprocal & Turbine)
- Turbine Engine Fundamentals
- Electric Aircraft System
- Solar Aircraft System
- Ramjet
- Rocket Engines
- Sir Frank Whittle & Hans von Ohain

Sir Frank Whittle (left) and Dr. Hans von Ohain (right) changed the propulsion world of aviation by inventing the jet turbine engine independently of each other. Their story is told at the end of this chapter.

*For any isolated system not in equilibrium the entropy will increase until that system attains equilibrium.*

Second law of thermodynamics

### 14.1 Introduction

The primary purpose of all aircraft propulsion devices is to impart a change in momentum to a mass of fluid. The fluid may be air, air and combustion products, or combustion products only. In the case of a watercraft the fluid would be water. Newton’s second law states that the force or thrust produced on a system is equal to the change in momentum of the system in unit time. This fundamental principle is shown in Fig. 14.1 for a stream tube of air [1]. The entrance conditions are denoted by the freestream symbol  $a$  and the exit conditions denoted by  $e$ . The mass flow rate of air through the stream tube is  $\rho AV$  and has units of slugs per second (slug/s). The stream tube boundaries are the fluid streamlines. The force or *net thrust* acting on the stream tube system is given by

The second law of thermodynamics traces its origin to the French physicist Sadi Carnot (1796–1832). In 1824, he published “Reflections on the Motive Power of Fire,” which presented the view that motive power (work) is due to the fall of fire (caloric heat) from a hot to a cold body (working substance). Simply stated it is an expression of the universal law of increasing entropy.

$$T_n = (\dot{m}_{air} + \dot{m}_{fuel})V_e - \dot{m}_{air}V_a + P_eA_e - P_aA_a \tag{14.1}$$

Notice that there may be a difference in the pressure and area at the entrance and exit such that a small pressure force would act on the system. Because the mass flow rate of the fuel added to the system is very small compared with the mass flow rate of the air, Eq. (14.1) is usually written

$$T_n = \dot{m}_{air}(V_e - V_a) + P_eA_e - P_aA_a \tag{14.2}$$

The principal types of propulsion devices accelerating the flow inside the stream tube are listed next and are shown qualitatively in Figs. 4.6 and 4.7:

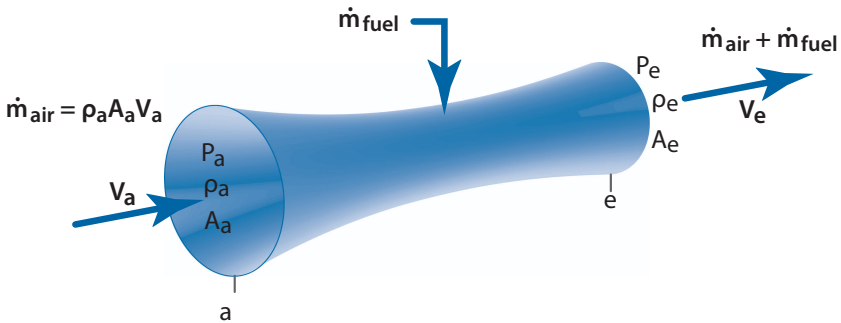


Figure 14.1 Momentum change on a fluid system.

- **Propellers.** Propellers are driven by reciprocating piston engines, gas turbines (turboprops), or electric motors. A propeller operates by producing a relatively small change in velocity of a relatively large mass of air. Propellers are limited to tip speeds less than sonic due to the formation of shocks and thus have a practical speed limit less than 500 kt (Mach = 0.75).
- **Gas turbines.** In the forms of simple jets (turbojets), afterburning turbojets, and turboprops, gas turbines accelerate a small mass of air to a large velocity change and can operate supersonically to about Mach 3.5.
- **Ramjets** (both subsonic and supersonic combustion)
- **Pulsejets**
- **Rockets.** Rockets carry their own oxidizer ( $m_{\text{air}} = 0$ ) and thus accelerate the very small (relative to turbines) combusted propellant products to very high velocities. The thrust equation for rockets becomes

$$T = \dot{m}_{\text{cp}} V_e + A_e (P_e - P_a) \tag{14.3}$$

where  $\dot{m}_{\text{cp}}$  is the mass flow per unit time of combusted propellant products.

## 14.2 Operation of Propeller Systems

The analysis and design of propellers is discussed in Chapter 17. This subsection will discuss the engines that drive the propeller. The engine provides a *thrust power available* equal to  $TV$ , which may be taken as the propeller output. The power input to the propeller from the engine shaft is the *engine brake horsepower*; thus, the *propeller efficiency* is

$$\eta_p = (\text{propeller thrust power}) / (\text{engine shaft brake horsepower})$$

In flight, the propeller accelerates a large mass of air rearward to a velocity only slightly greater than the flight speed, exhibiting efficiencies at normal flight speeds of between 85% and 90%. The lost horsepower appears mainly as unrecoverable kinetic energy of air in the slip stream.

The *horsepower required* for an aircraft to fly at a speed  $V$  is

$$\text{hp}_{\text{Req}} = DV / 550\eta_p \tag{14.4a}$$

where the  $1/550$  converts foot-pounds per second (ft·lb/s) to horsepower.

Using the equation for one-g drag  $D = W/(L/D)$  gives the useful equation

$$\text{hp}_{\text{Req}} = WV / (L/D) 550\eta_p \tag{14.4b}$$

## 14.2.1 Reciprocating Piston Engines

The aircraft *reciprocating piston engine* uses the well-known four-cycle Otto cycle [2]. An aircraft piston engine is similar to an automobile engine with a few differences. First, engine weight [given in horsepower per pound (hp/lb)] is a major performance parameter. Most aircraft engines are air cooled for this very reason. Second, reliability is very important because a malfunction at any altitude is a serious situation. The current piston engines are well developed to give high performance (hp/lb), low *brake specific fuel consumption* (BSFC) in pounds of fuel per hour per brake horsepower [(lb of fuel/h)/bhp], and high reliability.

Current piston and turboprop engines are shown in Fig. 14.2. The hp/lb for the current piston engines varies from about 0.6 for the small engines (less than 600 hp) to almost 1.0 for the larger engines. The BSFC for all the piston engines in Fig. 14.2 at sea level static (SLS) conditions varies from approximately 0.5 for the smaller engines (less than 400 bhp) to 0.42 for the larger engines. Most engines have a major overhaul recommended at 2000 hours. The engines have two spark plugs on each cylinder fired independently from engine-driven magnetos.

The power output from a piston engine depends primarily on two parameters: the engine rpm and the absolute pressure in the intake manifold. Maximum power is typically at 2800 rpm and SLS conditions of 59°F and 14.7 psia (30 in. of Hg).

Table 14.1 presents the specifications for the Lycoming 0–360-A aircraft engine. The 0–360-A (shown in Fig. 14.3) is in the Piper Cherokee 180 and represents a very typical general aviation piston engine. Notice that it is designed to cruise at 65%–75% of maximum power, which is a range of 2200–2450 rpm. The maximum throttle performance degradation with altitude is linear from 700 ft (180 hp at 2700 rpm and 28 in. of Hg) to 21,000 ft (76 hp at 2700 rpm). Cruise power is linear with altitude also.

A useful expression (from [1]) for the power loss (reduction in brake horsepower, Bhp) with altitude is

$$\text{Bhp} = \text{Bhp}_{\text{SL}} \left( \frac{\rho}{\rho_{\text{SL}}} - \frac{1 - \frac{\rho}{\rho_{\text{SL}}}}{7.75} \right) \quad (14.5)$$

Piston engines are sometimes supercharged to increase sea-level power for air racing or to increase the operating altitude. *Supercharging* involves compressing the air entering the intake manifold by means of a compressor. In earlier piston engines, this compressor was driven by a gear train from the engine crankshaft. The more modern supercharged engines employ a turbine-driven compressor powered by the engine's exhaust and



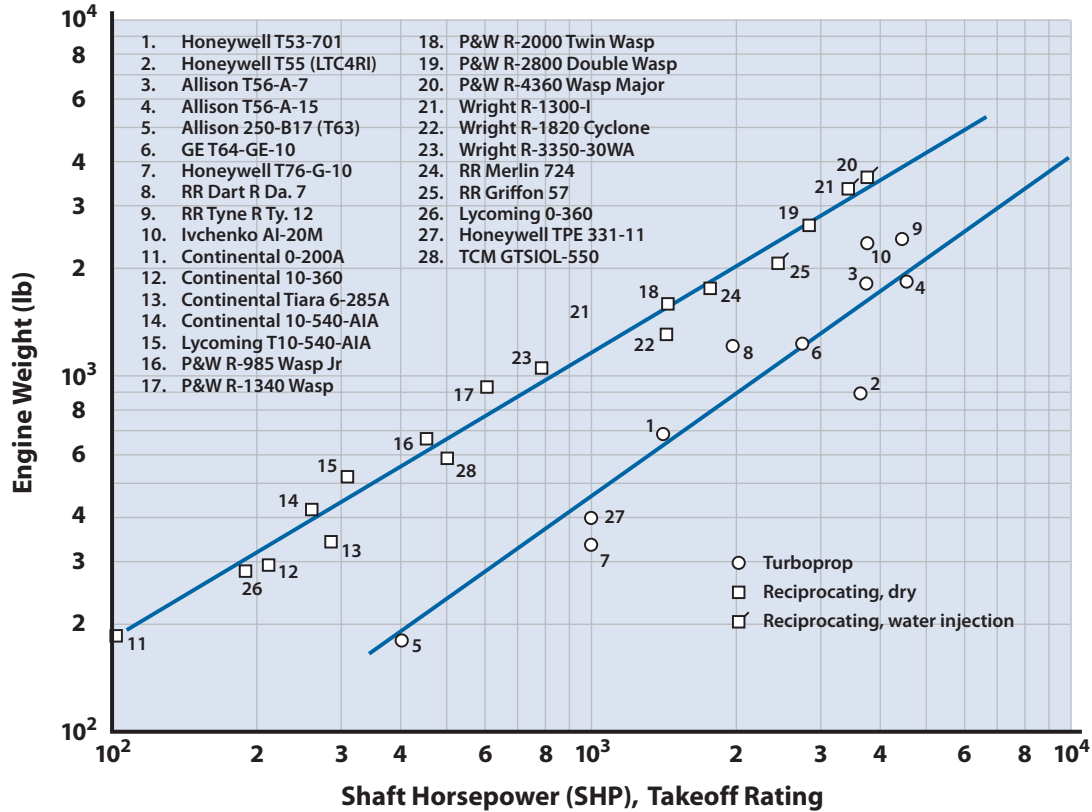
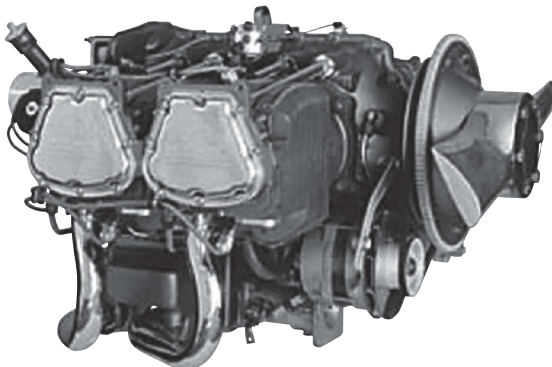


Figure 14.2 Weight vs shaft horsepower (SHP), for turboprop and piston aircraft engines.

**Table 14.1** Lycoming O-360-A Aircraft Engine Specifications and Description (data from [2])

<b>Type: Four-Cylinder, Direct Drive, Horizontally Opposed, Wet-Sump, Air-Cooled Engine</b>	
Weight, pounds	282
Bore, inches	5.125
Stroke, inches	4.375
Displacement, cubic inches	361
Compression ratio	8.5:1
Cylinder head temperature, max. °F	500
Cylinder base temperature, max. °F	325
Fuel: aviation grade, octane	100–130
<b>Performance, hp</b>	
Takeoff rating at SLS, hp	185 at 2900
Max. rated at 700 ft (28 in. of Hg), hp	180 at 2700
Max. rated at 7000 ft, hp	143 at 2700
Max. rated at 21,000 ft, hp	76 at 2700
Cruise rpm at 7000 ft, hp	135 at 2450
Cruise rpm at 21,000 ft, hp	74 at 2450
Cruise rpm at 7000 ft, hp	126 at 2200
Cruise rpm at 21,000 ft, hp	70 at 2200
Cruise BSFC, lb/bhp-h	0.47

are called *turbochargers*. The advantage of the turbocharger over the gear-driven supercharger is twofold. First, the compressor does not extract power from the engine, but uses exhaust energy that would normally be wasted. Second, the turbocharger is able to provide sea level rated power up to much higher altitudes than the gear-driven type.

**Figure 14.3** Lycoming O-360A aircraft engine.

An example of a turbocharger designed for high-altitude operation is the one on the Boeing/DARPA Condor. The Condor was designed to fly at 65,000 ft, where the freestream air pressure is 1/18 that of sea level. The Condor used two Continental GTSIOL-300 piston engines (175 hp, six cylinders, reduction gearing, spark ignition, fuel injected, liquid cooled) each weighing 289 lb. There were two stages of turbocharging, each boosting the pressure 4.2:1 and cooling the air. Each turbocharger weighed 560 lb. Each engine drove an 81-lb, three-bladed, 16-ft propeller geared down 3:1 from the 2700 rpm engine speed. The propeller efficiency was reported as 90%.

The HAARP aircraft (from Section 5.8) uses a three-stage turbocharger to boost the pressure of the air going into its piston engines to 93:1 for operation at 100,000 ft. The HAARP turbocharger is designed for 108:1, giving it a little margin to operate past 100,000 ft. The turbocharger was designed by Teledyne Continental (TCM) and is shown schematically in Fig. J.1.

The practical limit for pressure boost across a turbocharger stage is about 5:1 for current compressor design and materials. Thus, the Condor needed a two-stage and HAARP a three-stage turbocharger. The temperature of the air is increased through each compressor stage and needs to be cooled before going into the next stage. The cooling requirement for one HAARP engine and turbocharger is as follows:

- Engine coolant, heat load 3380 Btu/min
- Engine oil, heat load 1450 Btu/min
- Turbocharger intercoolers, heat load 9900 Btu/min
- Generator and gearbox, heat load 600 Btu/min

The cooling system for these items comprises ram air-cooled heat exchangers located in the leading edge of the wing that weigh 1147 lb total for the two sides. The ram drag for the cooling system is estimated to be equal to 25% of the aircraft  $C_{D_{\min}}$ . This greatly reduces the HAARP maximum  $L/D$  from 39 for a clean aircraft to the 27 reported in the example of Section 5.8.

Figure J.2 shows typical weights of the turbochargers, intercoolers, heat exchangers, and ducting as a function of maximum horsepower and altitude.

The engine for HAARP will be sized and selected in Chapter 18 (Section 18.10).

### 14.2.2 Turboprop Engines

The thermodynamics of the turboprop engine will be discussed in detail in the next section. This section discusses its characteristics as a propeller system.

The performance (hp/lb) of current turboprop engines is shown in Fig. 14.2. Turboprops are lighter than an equivalent piston engine with hp/lb of approximately 2.2–2.4 for all engines. The shaft on a turbine engine typically rotates at 10,000 rpm, a speed much too high for propeller operation. In most cases, the weights shown in Fig. 14.2 for the turboprop includes the weight of the reduction gearing required for a propeller speed of approximately 2000–2700 rpm. The BSFC is about 25% higher for turboprops than for a piston engine.

In a turboprop engine most of the power is extracted as shaft power to drive the propeller. However, there is a residual energy that is expanded through the nozzle as jet thrust  $T_j$ , which is not included in the listed shaft horsepower (SHP).

To account for the power produced by this jet thrust an *equivalent shaft horsepower* (ESHP) has been devised to account for the total power output of the engine. Using Eq. (14.4) the jet thrust is converted to a *thrust horsepower* by

$$\text{THP} = T_j V / (0.8)(550) \quad (14.6)$$

where the 0.8 accounts for a conventionally assumed 80% propeller efficiency. With this expression the ESHP may be written

$$\text{ESHP} = \text{SHP} + T_j V / (0.8)(550) \quad (14.7)$$

Notice that this relationship does not account for thrust horsepower under static conditions where  $V = 0$ . For such cases (and for  $V < 100$  kt) another convention has been adopted to equate a given thrust level per horsepower. Some European turboprop companies use 2.6 lb of thrust per horsepower, but the usual equivalence is 2.5 lb of thrust equals one horsepower. Thus, for  $V < 100$  kt,

$$\text{ESHP} = \text{SHP} + T_j / 2.5 \quad (14.8)$$

For example, the Honeywell (formerly Garrett) TPE 331–11 is rated statically at 1000 SHP and 1045 ESHP. This engine therefore produces a static thrust from the turbine exhaust of approximately 113 lb.

### 14.2.3 Electric Motors

*Electric motors* are simple and reliable (design life of 30,000 h when operated at ~60% rated power). They have a specific power of approx 0.27 hp/lb (0.2 kW/lb). Electric motors get their power from onboard auxiliary power units (APU; either piston or turboshaft engines driving

Table 14.2 Electric Aircraft System Data (2010)

Characteristic	Electric Motor	Solar Cell	Fuel Cell	Batteries
Specific energy (kW·h/lb)	0.2 <sup>a</sup>	NA	0.89 <sup>b,c</sup>	0.27 <sup>c,d</sup>
Design life	30,000 h	<sup>e</sup>	NA	300 <sup>f</sup>
Efficiency (%) <sup>g</sup>	97	28	55	90
Installed weight (lb/ft <sup>2</sup> )	NA	0.1	NA	NA

<sup>a</sup>Weight includes motor, controller, and propeller. Increase weight by 25% for installation.

<sup>b</sup>H<sub>2</sub>/O<sub>2</sub> regenerative fuel cell using proton exchange membrane technology.

<sup>c</sup>Specific power based on discharge time.

<sup>d</sup>Li-S batteries are projected to increase to 0.336 kWh/lb by 2015.

<sup>e</sup>Solar cells degrade about 1.5% of power output per year.

<sup>f</sup>300 full-depth discharges in 2010. Decreasing the discharge to 50% would increase number of recharges to approximately 1000.

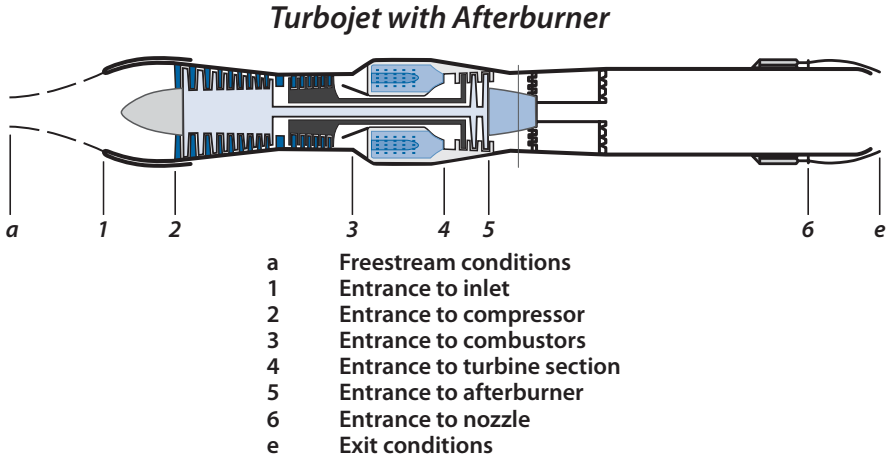
<sup>g</sup>Efficiency is energy out per energy in. Solar cell efficiency is projected to increase to 32% and fuel cell efficiency to 65% by 2015.

electric generators), batteries, fuel cells, or solar cells (photovoltaic cells that convert incident solar energy into electricity).

For missions having several day–night cycles the electric aircraft would need to be a solar-powered vehicle. It would collect solar energy from the sun during the day and convert it to electricity through the photovoltaic action of solar cells. It would need to store energy in batteries or fuel cells to power the vehicle during the night. The solar cells would then recharge the batteries or fuel cells for the next nighttime operation by collecting excess power during the day. Theoretically this cycle could go on forever; however, the batteries and fuel cells have finite recharging limits and their performance degrades over time [3]. Table 14.2 contains data on electric motors, solar cells, batteries, and fuel cells.

### 14.3 Operation of Turbine Systems

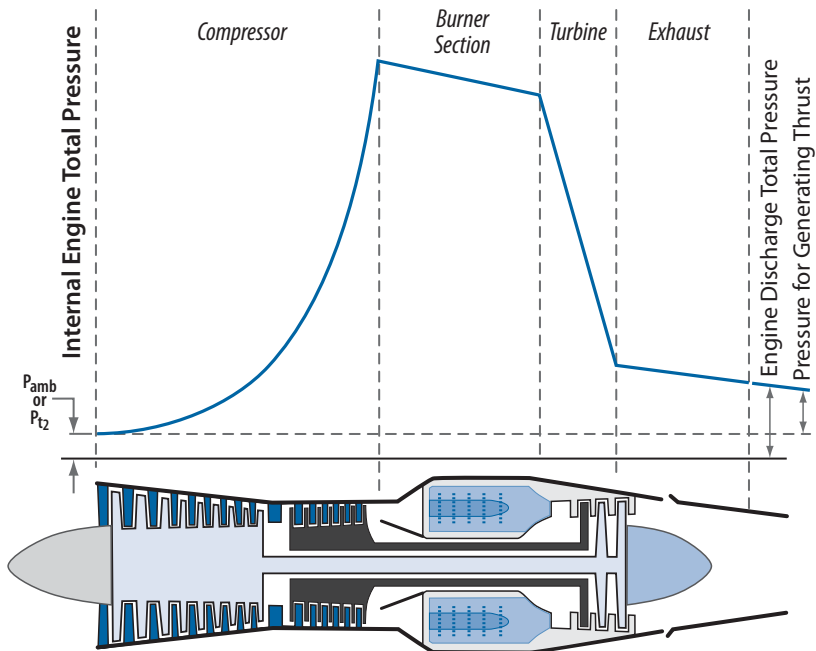
The *turbine engine* or *turbojet engine*, shown schematically in Fig. 14.4a, operates in a similar fashion to the other aircraft propulsion devices. Air is brought in the inlet and slowed down to approximately Mach = 0.4 at the face of the compressor. The air mass is compressed and pressure is built up (increasing pressure energy of fluid) as the air goes through the compressors with little change in velocity. The air is mixed with fuel in the combustor section, ignited, and burned, increasing the thermal energy of the air–fuel fluid mixture. The heated fluid expands in the turbine section, driving the turbines, which in turn powers the compressor section. The fluid is further expanded through the nozzle section to a high velocity (conversion of pressure and thermal energy into kinetic energy), thus increasing the



**Figure 14.4a** Schematic of typical turbojet with afterburner.

momentum of the fluid and producing a thrust. Figure 14.4b shows the internal pressure variations inside a typical turbojet engine.

The efficiency of the turbine engine as a propulsion device depends on many factors. One of the major factors is the *compression ratio* of the air through the compressor [overall pressure ratio (OPR)], which is a function of the number of compression stages and their stage efficiencies. The effi-



**Figure 14.4b** Typical turbojet engine, internal pressure variation.

ciency of the compressor and turbine stages depends upon the blade geometry (number and shape), the ratio of blade length to hub, and the ratio of blade length to tip clearance. The operating temperature of the combustor and turbine determines the amount of thermal energy in the gas available for power extraction and expansion to jet velocity.

The *net thrust* produced by a turbojet engine is given by [from Eq. (14.2) for  $A_a = A_e$ ]

$$T_n = \dot{m}_{\text{air}}(V_e - V_a) + (P_e - P_a)A_a \tag{14.9}$$

where

- $\dot{m}$  = mass flow of air, in slugs per second
- $V$  = velocity of air, in feet per second
- $P$  = static pressure, in pounds per square foot

and the subscripts correspond to the station locations of Fig. 14.4a. Notice that the mass flow of the fuel is not included in the  $\dot{m}$  term of Eq. (14.9). This is because the fuel flow is small compared to the air flow; also the weight of air leakage through the engine can be assumed to be approximately equivalent to the weight of the fuel consumed.

The *gross thrust* is defined as the product of the mass flow rate in the jet exhaust and the velocity attained by the jet after expanding to freestream static pressure

$$T_g = \dot{m}_{\text{air}} V_e$$

And the term  $\dot{m}_{\text{air}} V_a$  is called the *ram drag*. For static operation,  $T_g$  and  $T_n$  are equal.

To enable an accurate comparison to be made between turbine engines, fuel consumption is reduced to a common denominator, applicable to all types and sizes of turbine engines. The term used is *thrust specific fuel consumption* (TSFC) and is expressed as

$$C = \text{TSFC} = W_f / T_n \tag{14.10}$$

where  $W_f$  is the fuel weight flow in pounds per hour and  $T_n$  is the net thrust in pounds.

Frequently, a turbojet engine is equipped with an afterburner for increased thrust. Roughly, about 25% of the air entering the compressor and passing through the engine is used for combustion. Only this amount of air is required to attain the maximum temperature that can be tolerated by the metal parts. The balance of the air is needed primarily for cooling purposes. Essentially, an *afterburner* is simply a huge stovepipe, attached to the rear of the engine, through which all of the exhaust gases must pass.

Fuel is injected into the forward section of the afterburner and is ignited. Combustion is possible because 75% of the air that originally entered the engine still remains unburned. The result is, in effect, a tremendous blowtorch, which increases the total thrust produced by the engine by approximately 50%, or more. Although the total fuel consumption increases almost two-and-a-half times, the net result is profitable for short bursts of aircraft speed, climb, or acceleration. A turbojet aircraft with an afterburner can reach a given altitude with the use of less fuel by climbing rapidly in “afterburning” than by climbing much more slowly in “nonafterburning.” The weight and noise of an afterburner, which is used only occasionally on long flights, precludes the device being employed in present-day, transport-type aircraft.

The turbine engines shown in Fig. 14.5 are termed *two spool*. The shaft from the first stage of the turbine is hollow and drives the high-pressure stage of the compressor (called the *high spool*). The power shaft from the aft stages of the turbine runs through the hollow high spool shaft and drives the low-pressure stage of the compressor (called the *low spool*).

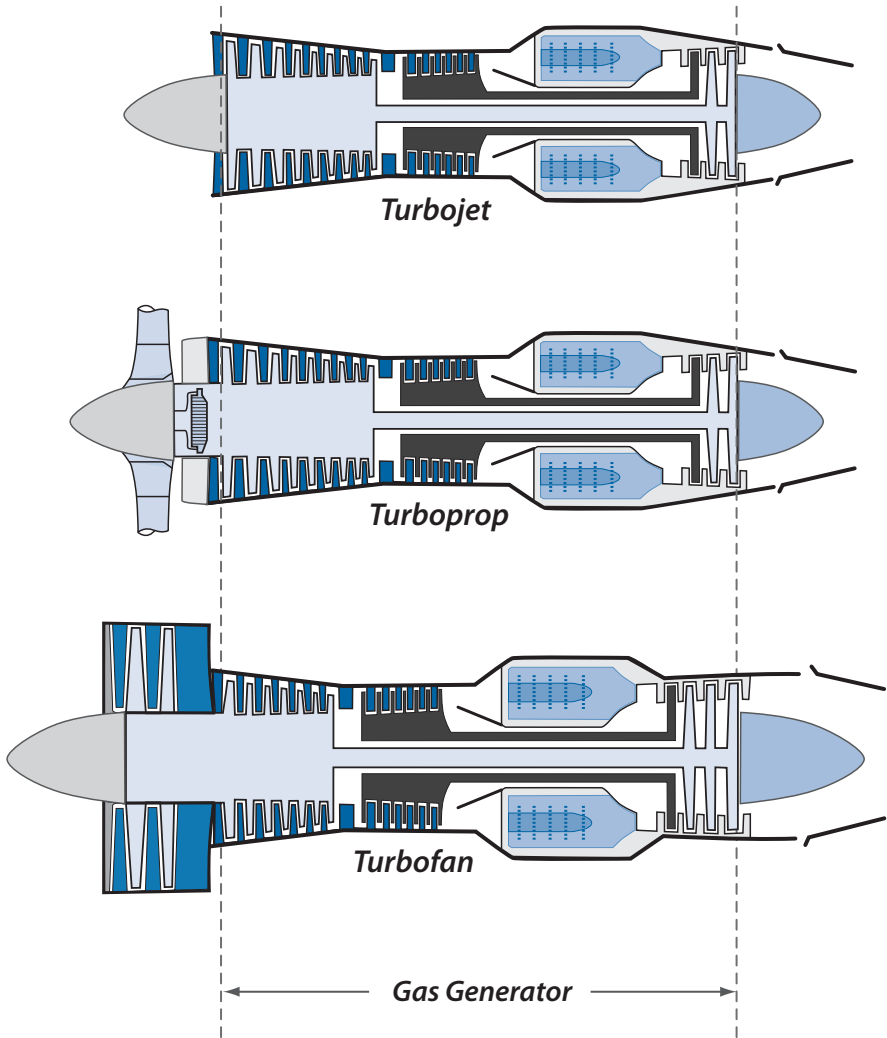
### 14.3.1 Turboprop

The *turboprop* (sometimes called a *turboshaft*) is essentially a turbojet designed to drive a propeller. The turboprop is shown schematically in Fig. 14.5 and uses the basic gas generator section of a turbine engine. The propeller operates from the same shaft as the low-spool compressor through reduction gearing. The hot gases are nearly fully expanded in the turbine first stage, which develops considerably more shaft power than required to drive the low-spool compressor and accessories. The excess power is used to drive a conventional propeller equipped with a speed-regulated pitch control. The remainder of the hot gases are expanded through the nozzle, providing a jet thrust as discussed in Section 14.2.2. This engine retains the advantage of having a light weight and low frontal area, together with the ease of installation that goes with turbojet engine design. In addition, it has a high efficiency at relatively low speeds. However, present propeller design limits the use of this type of powerplant to speeds below 500 kt (see Fig. 4.5 in Section 14.3.2).

### 14.3.2 Turbofan

The *turbofan* version of an aircraft gas turbine engine is shown in Fig. 14.5 and is the same as the turboprop, the geared propeller being replaced by a duct-enclosed fan driven at engine speed. One fundamental operational difference between the turbofan and the turboprop is that the airflow through the fan of the turbofan is unaffected by airspeed of the aircraft.





**Figure 14.5** Schematic of typical turbojet, turboprop, and turbofan engines showing basic gas generator core.

This eliminates the loss in operational efficiency at high airspeeds, which limited the air-speed capability of a turboprop engine. Also the total airflow through the turbofan engine is much less than that through the propeller of a turboprop. In the turbofan engine, 30% to 60% of the propulsive force is produced by the fan.

The *bypass ratio* (BPR) for a turbofan is defined as the ratio of the airflow through the fan to the airflow through the gas turbine core. Some modern turbofan engines have bypass ratios as high as  $BPR = 10$  (see Table J.1).

The turbofan engine offers several advantages over a turbojet, such as better takeoff thrust for the same-weight engine and lower TSFCs at high-subsonic speeds (see Fig. 14.6). This advantage comes about because the turbofan can accelerate a higher airflow  $\dot{m}_a$  to a lower jet velocity, giving a higher propulsive efficiency (see [1]) than a turbojet of equivalent weight and fuel flow. Figure 14.6 shows the influence of bypass ratio on the sea level static TSFC for current turbine engine technology. The turbofan's advantage decreases at high-subsonic and all supersonic speeds due to the higher drag associated with the larger frontal area.

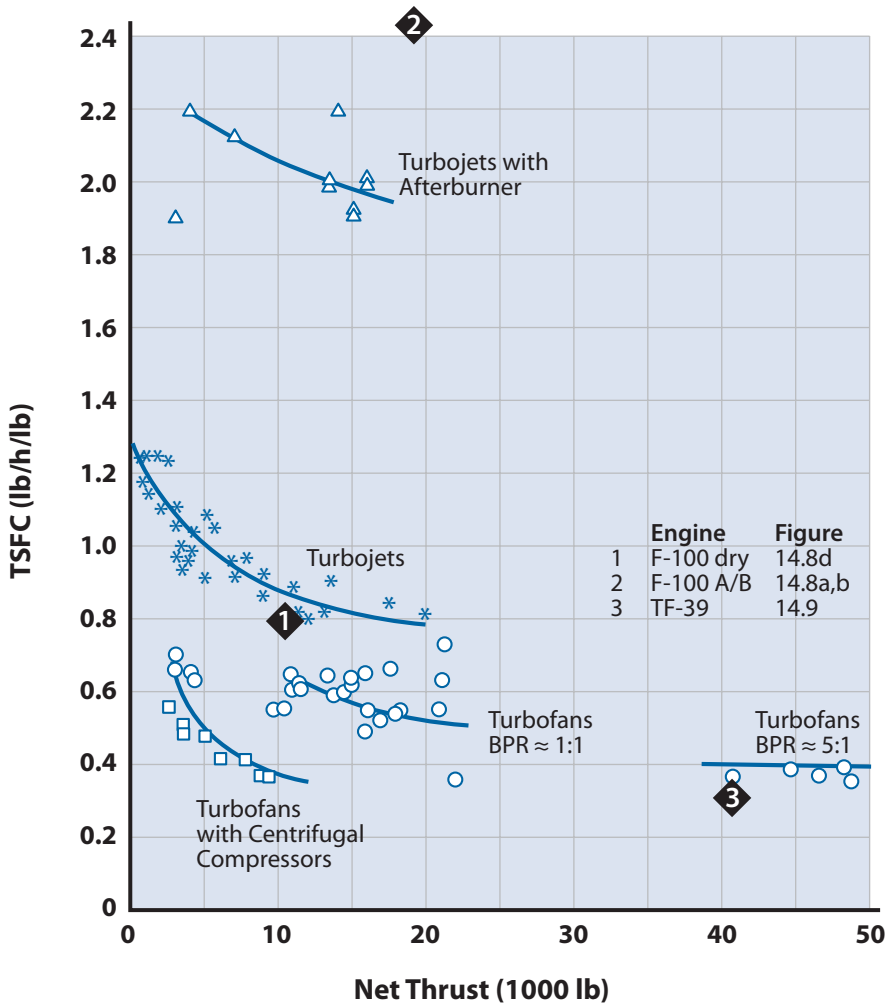


Figure 14.6 Sea level static (SLS) specific fuel consumption for turbojet and turbofan engines.

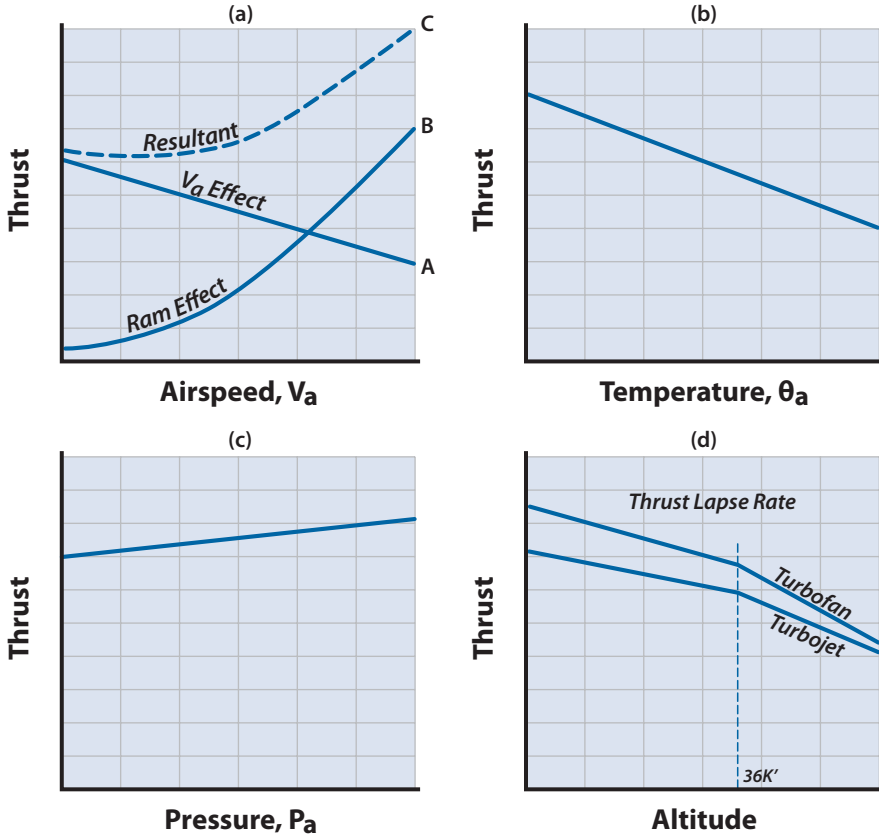


Figure 14.7 Variation of turbine engine thrust with airspeed, temperature, pressure, and altitude.

### 14.3.3 Factors Affecting Thrust and TSFC

As the aircraft increases its speed, the velocity of the air entering the engine,  $V_a$ , increases. The nozzle is usually close to a choked condition ( $V_e$  near the speed of sound, see [1]) such that  $V_e$  is relatively constant. Thus, the  $(V_e - V_a)$  term in Eq. (14.9) decreases with increasing airspeed and the result is a decrease in thrust as shown by curve (A) in Fig. 14.7a. However, as  $V_a$  increases, the airflow into the engine,  $\dot{m}_a = \text{density} \times \text{velocity} \times \text{capture area}$ , increases due to ram effect and the result is an increase in thrust as shown by curve (B) in Fig. 14.7a. The overall result of increasing airspeed is a combination of these two effects and is shown as curve (C) in Fig. 14.7a.

The ram effect is important, particularly in high-speed aircraft, because eventually, when airspeed becomes high enough, the ram effect will

produce a significant overall increase in engine thrust. At Mach numbers greater than 3.0 the ram effect can replace the compressor sections of turbine engines, resulting in a ramjet engine. At subsonic speeds the ram effect is not very large and does not greatly affect engine thrust. At supersonic speeds, however, ram can be a major factor in determining how much thrust an engine will produce.

The most significant variable in the thrust equation is mass airflow,  $\dot{m}_a$ . Because

$$\dot{m}_a = \rho VA$$

and

$$\rho = p / R'\theta$$

from the perfect gas relation ( $R'$  is the characteristic gas constant) it can be observed that an increase in temperature will result in a decrease in thrust as shown in Fig. 14.7b. Similarly, an increase in pressure  $p$  will give an increase in thrust as shown on Fig. 14.7c.

As the aircraft climbs in altitude, the temperature decreases until at the tropopause (36,000 ft) it remains constant (see Appendix B). The pressure decreases steadily with increasing altitude. The result of climbing in altitude is an interplay between the pressure and temperature variations giving a decreasing thrust (called the *thrust lapse rate*) as shown in Fig. 14.7d. The lapse rate is greater for a turbofan than a turbojet. The variation of thrust with altitude can be approximated by

$$T_n = (T_n)_{SL} (p / p_{SL}) (\theta_{SL} / \theta) \quad (14.11)$$

The TSFC for a turbine engine is given by Eq. (14.10), where the fuel flow to the engine is dependent on the throttle position. Thus, for a constant throttle setting (i.e., military continuous power) the TSFC varies with thrust.

The optimum altitude for subsonic cruise is that altitude where the TSFC is a minimum for a cruise power setting. For a turbine-powered aircraft cruising near Mach 0.8 the cruise power setting is around 80%–100% of normal rated thrust. The best altitude for cruise under these conditions is around 36,000 ft [4].

### 14.3.4 Turbine Engine Data

Appendix J contains information on the current stable of turbojet, turboprop, and turbofan engines. The engine characteristics in Table J.1 do

not reflect thrust losses and weights associated with installing the engines into aircraft. Turbine engine corrections for installation into aircraft are discussed in Chapter 16. Reference [5] is an excellent source of turbine engine data. It is published annually and is kept up to date.

Table 14.3 presents the characteristics for the Pratt and Whitney F-100-PW-100 afterburning turbofan. Figure 14.8 presents the variation of thrust and TSFC with altitude, airspeed, and throttle setting for the engine. The thrust shown in Fig. 14.8 is the installed thrust, which is the net thrust  $T_n$  from the basic engine corrected for inlet and nozzle losses, airflow bleed, and turbine power extraction. Figure 14.8g presents the mass airflow  $\dot{m}_a$  required for the F-100 in afterburner and military power.

Table 14.4 presents the characteristics for the General Electric TF-39-GE-1 turbofan. The installed engine data are shown in Figure 14.9 and are appropriate to a podded nacelle installation similar to that of the C-5A [6]. Figure 14.10 shows the GE CF-6 engine, which is a popular commercial engine. CF-6 engines were produced in many models providing power from DC-10s during the 1980s to today's Boeing 747/767/777.

**Table 14.3** Pratt and Whitney F-100-PW-100 Afterburning

<b>Turbofan Characteristics</b>	
Sea level static thrust	23,000 lb (uninstalled)
Sea level static TSFC	2.248
Bare engine weight	2737 lb
Sea level static airflow, $\dot{m}_a$	217 lbm/s
Engine length (including nozzle)	190 in.
Maximum diameter	44 in.
Compressor face diameter	40 in.
Bypass ratio	0.71
<b>Miscellaneous: Accessory Equipment Weight</b>	
Fuel system	433 lb
Engine controls	22 lb
Starting system	28 lb
The installed engine data of Fig. 14.8 reflects the following propulsion unit corrections: <ol style="list-style-type: none"> <li>1. Power extraction of 70 hp to drive electric generators and auxiliary equipment. This 70 hp is at all power settings and flight conditions.</li> <li>2. Normal shock inlet pressure recovery.</li> <li>3. Nozzle corrections at moderate pressure ratios.</li> <li>4. High-pressure bleed air extracted from compressor for operating environmental control system.</li> </ol> The bleed airflow rate is 0.4 lb/s.	

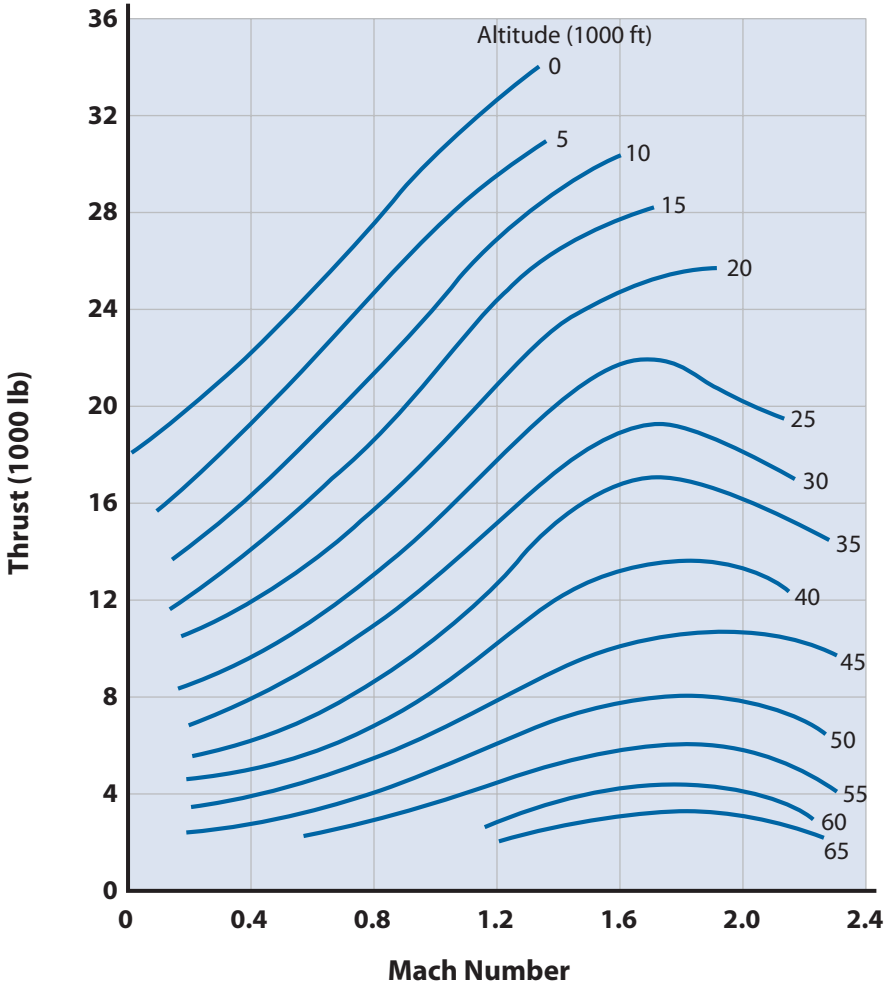


Figure 14.8a F-100 installed thrust, maximum afterburning.

Table 14.4 General Electric TF-39-GE-1 Turbofan Characteristics

Sea level static thrust (uninstalled)	41,100 lb
Sea level static TSFC	0.315
Sea level static airflow, $\dot{m}_o$	1541 lb/s
Bare engine weight	7026 in.
Engine length	271 in.
Engine diameter (maximum)	100 in.
Bypass ratio	8
Overall pressure ratio	26

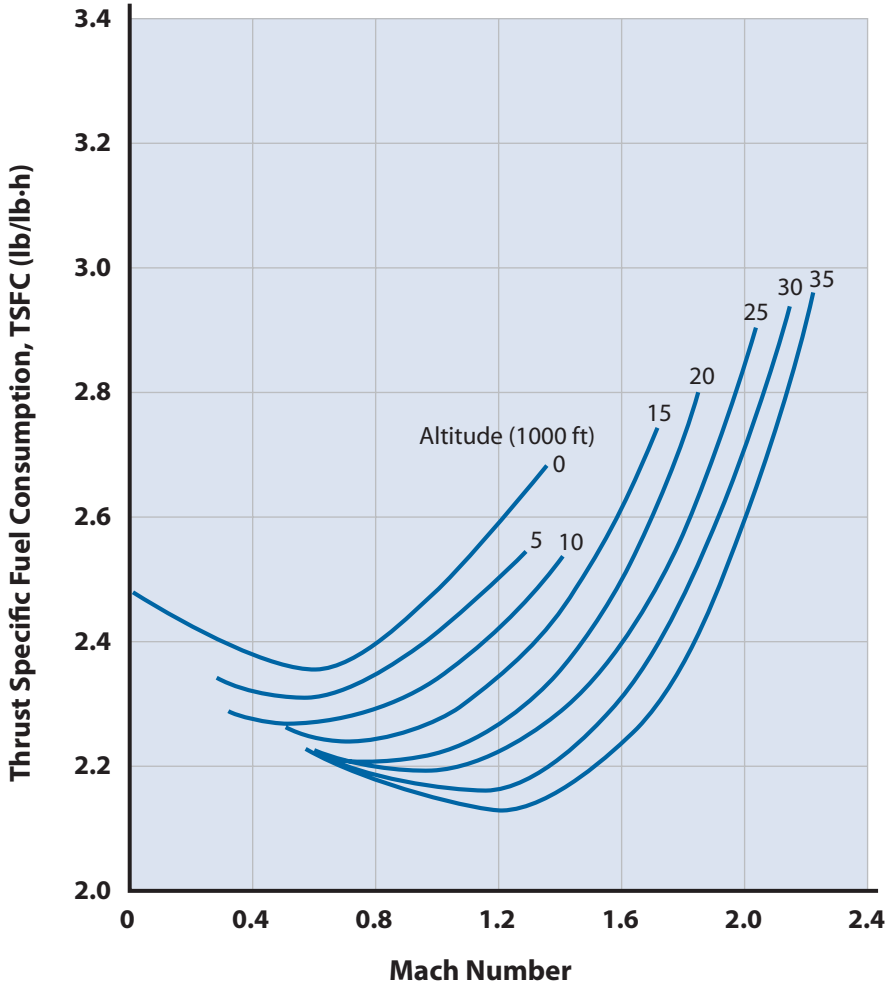
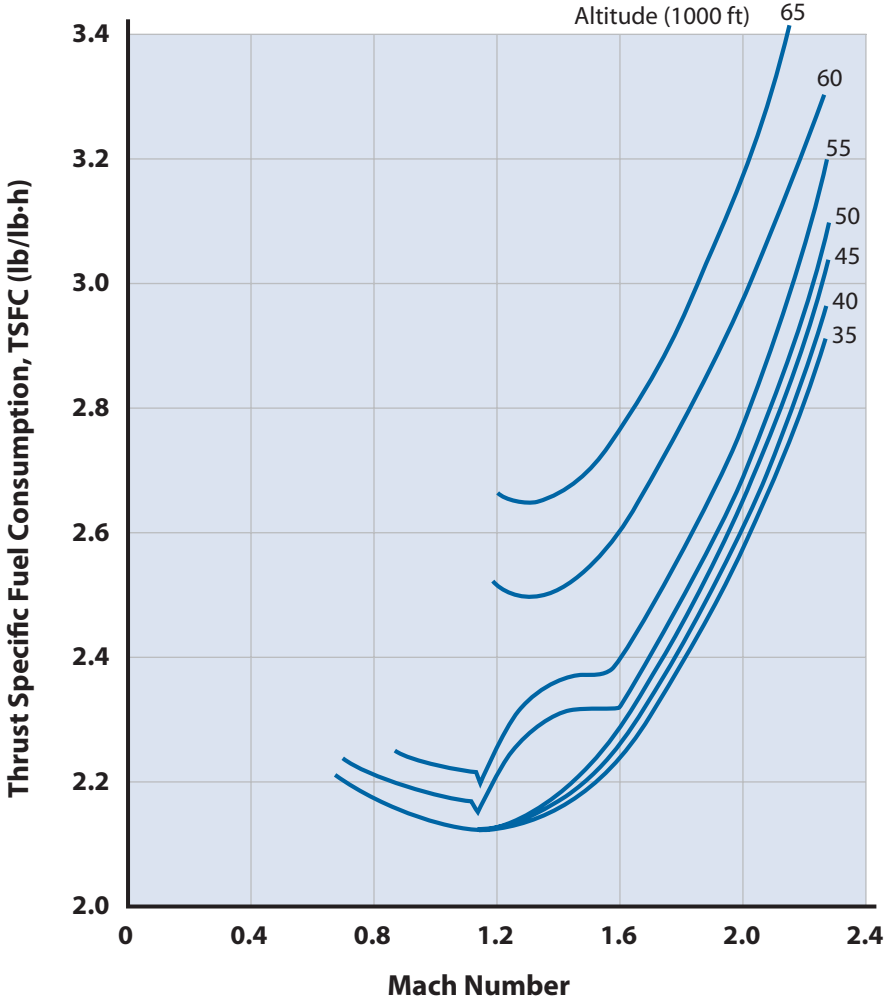


Figure 14.8b F-100 TSFC for maximum afterburning (low altitudes).

## 14.4 Ramjet Engine Operation

The *ramjet* operates on essentially the same gas cycle as the turbine. The ramjet is a very simple device and is shown schematically in Fig. 4.6. However, all the compression portion of the cycle occurs at the inlet and in the diffuser where the incoming air velocity is decreased producing a rise in static pressure. Fuel is burned and the mixture expanded to ambient through a nozzle. The ramjet is compared with other propulsion devices in Fig. 4.7.

At forward speeds of Mach  $\leq 1.0$  the ramjet is prohibitively expensive to operate because its low combustion efficiency results in a TSFC greater



**Figure 14.8c** F-100 TSFC for maximum afterburning (high altitudes).

than 6.0 (see Fig. 4.7c). At supersonic speeds a normal shock is located just ahead of the inlet. A normal shock compression, although not ideal is a practical substitute for a compressor. At Mach = 2.0 the shock compression ratio is about 4.5 and the ramjet TSFC is competitive with an afterburning turbojet. Above Mach = 2 the ramjet starts rivaling the dry turbojet. Thus, at Mach  $\geq 2$  the normal shock compression is an acceptable substitute for a mechanical compressor making the ramjet a very light and simple machine. Because no turbine is present the usable temperature limits are considerably higher than for a turbojet.

One of the major problems connected with the ramjet is the issue of flame stability. The high speed of the air through the duct tends to blow out the combustion. The art of the ramjet is in the design of a flame



holder that will stabilize the combustion but produce minimum resistance to the flow.

### 14.5 Rocket Operation

All of the propulsion devices considered thus far depend upon atmospheric air and, to some extent, forward speed for their operation. Rockets,

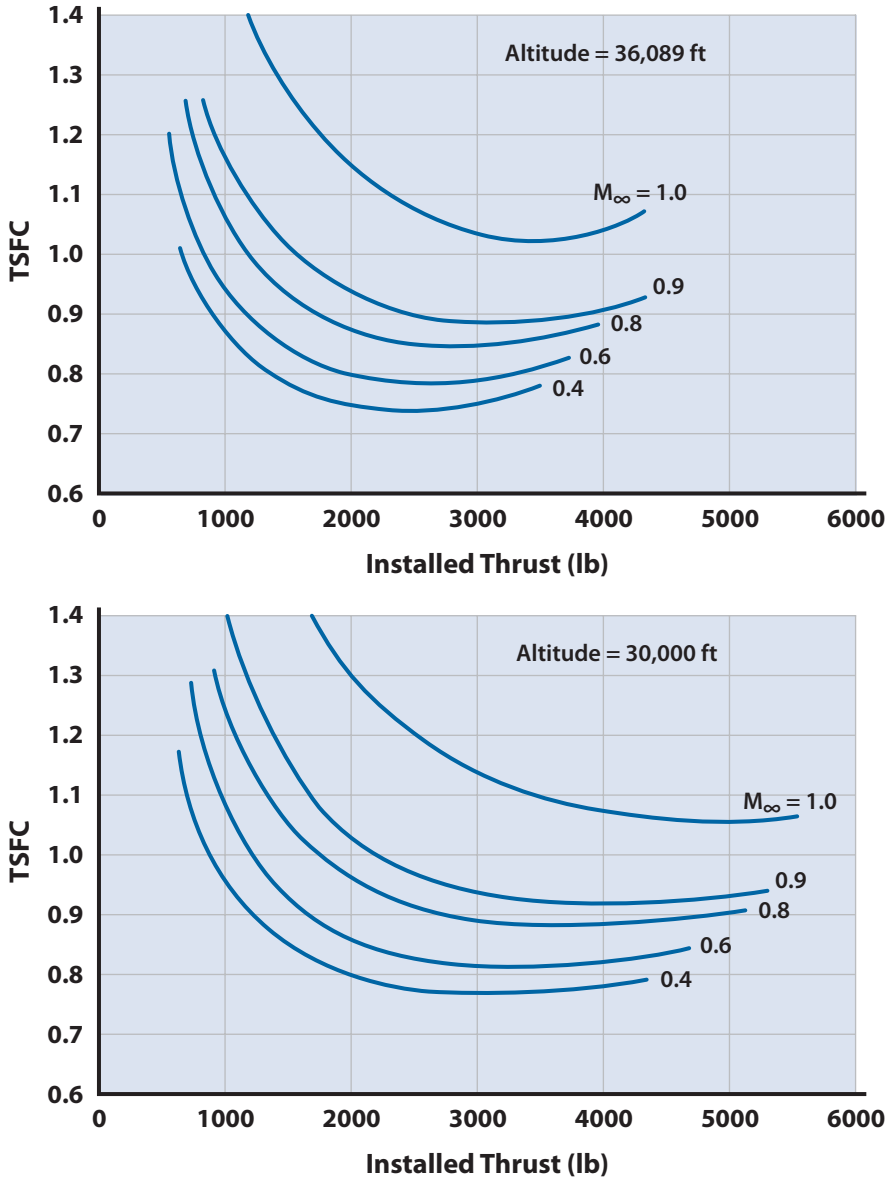
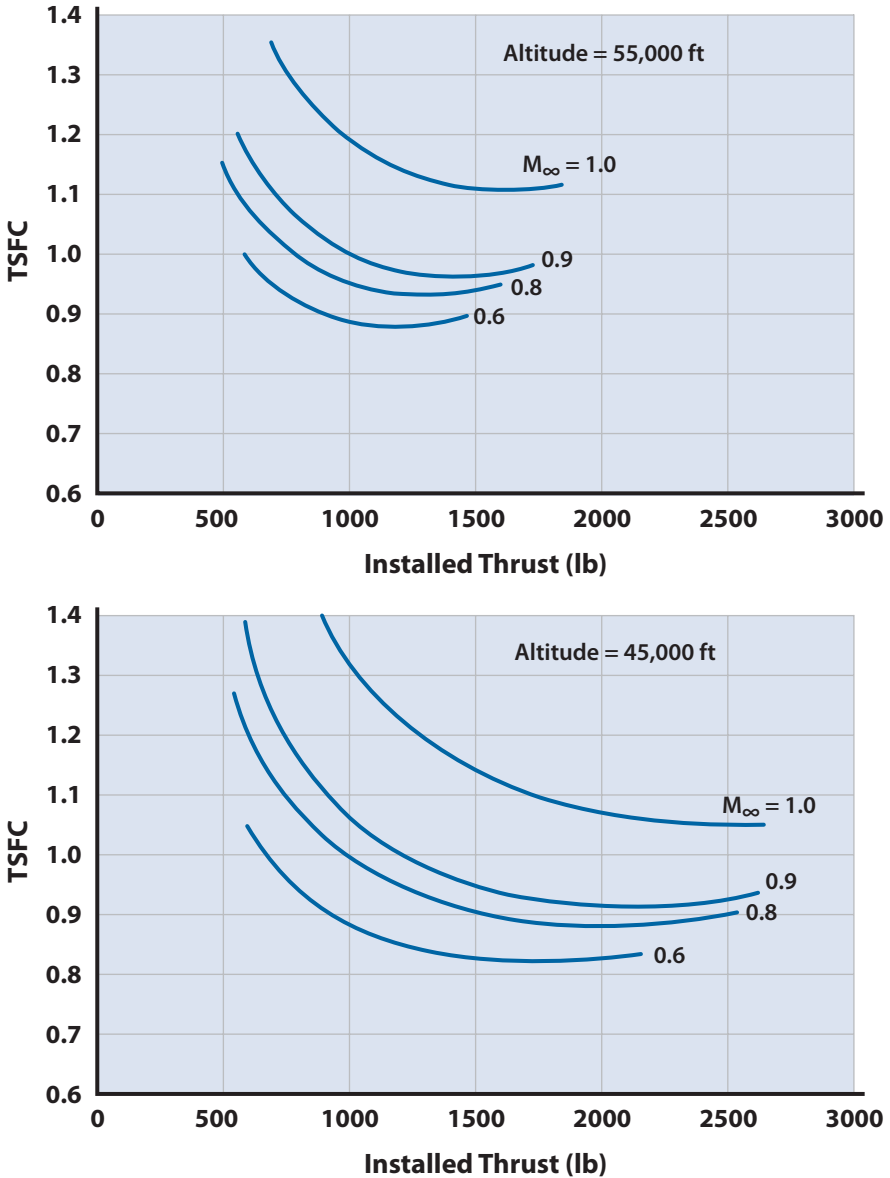


Figure 14.8d F-100 TSFC for partial power settings (nonafterburning).



**Figure 14.8e** F-100 TSFC for partial power settings (nonafterburning).

however, are independent of atmospheric air or forward speed. The atmospheric independence provides an advantage in that the rocket offers the only method of developing thrust outside of the earth's atmosphere. However, this independence is also a disadvantage in that all the mass creating the thrust must be carried in the rocket. Note that all of the propulsion

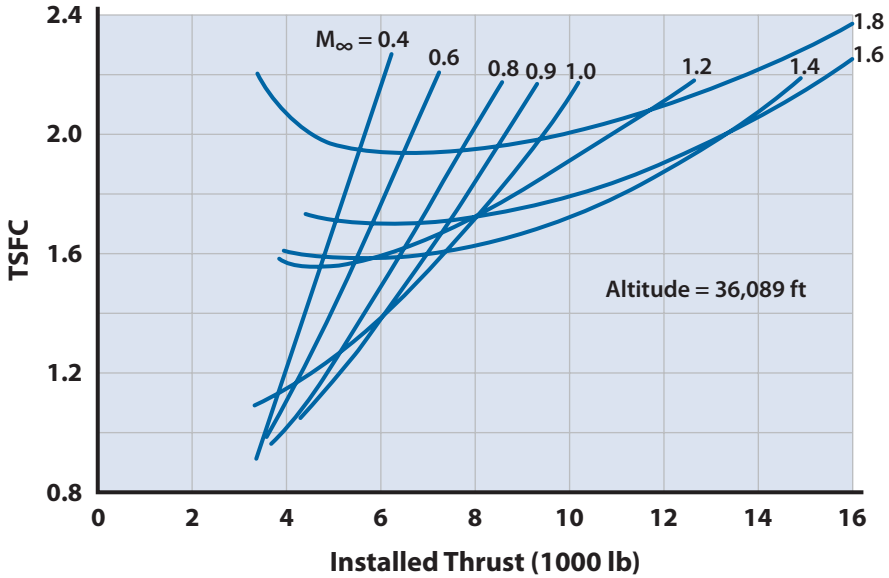


Figure 14.8f F-100 TSFC for partial afterburning.

devices discussed earlier carried only their fuel and that most of the mass accelerated rearward for thrust consisted of the ambient air.

The thrust of a rocket is expressed as

$$T = \dot{m}_{CP} V_e + A_e (P_e - P_a) \tag{14.3}$$

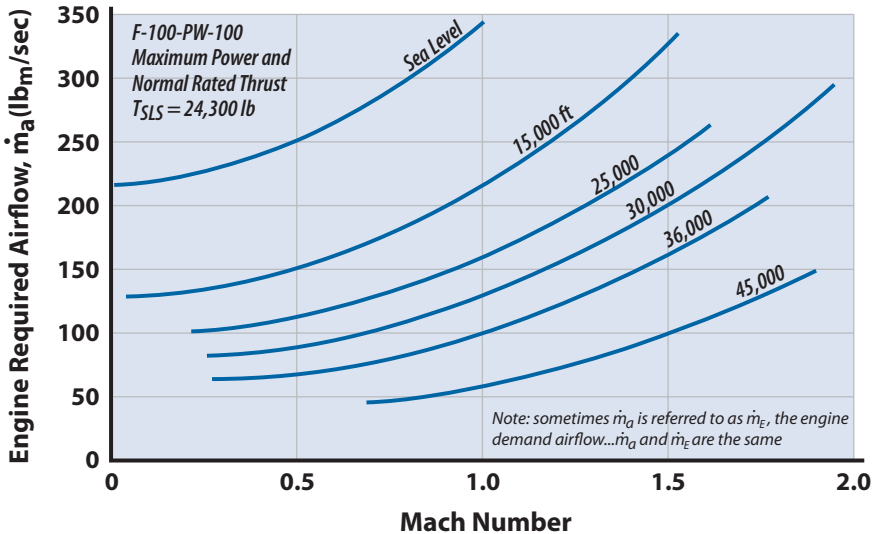


Figure 14.8g Required mass flow for PW F-100 turbofan engine at maximum power.

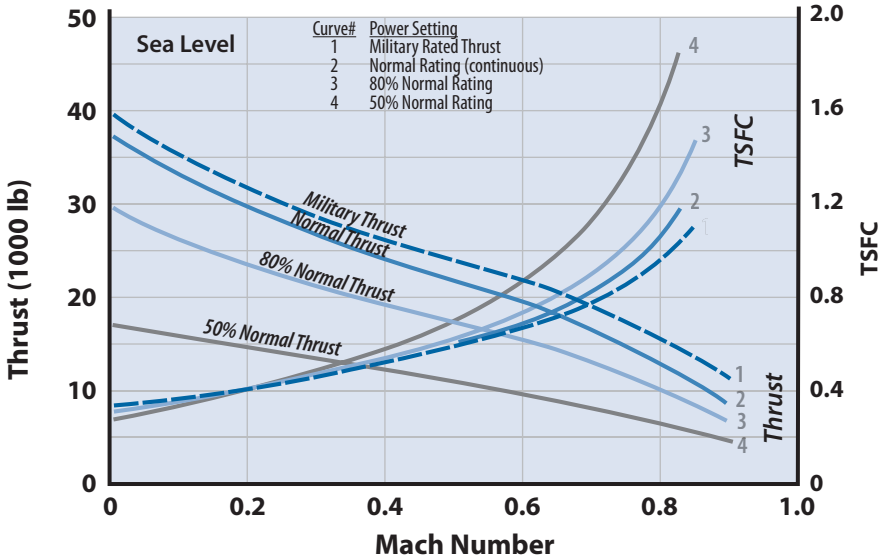


Figure 14.9a Installed thrust and TSFC for TF-39 turbofan engine (see Table 14.4).

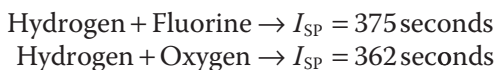
The exhaust velocity depends on the composition of the propellant, the design of the exhaust nozzle, and the ambient conditions. The thrust specific fuel consumption of a rocket is  $TSFC = \text{propellant weight flow (lb) per hour per thrust}$ . Rockets are very fuel inefficient compared to all other propulsion devices, as shown in Fig. 4.7c. The World of Rockets likes to use specific impulse  $I_{SP}$  as a measure of fuel consumption. Specific impulse is the reciprocal of TSFC, expressed in seconds and written as

$$I_{SP} = T / g \dot{m}_{CP} = 3600 / TSFC \tag{14.12}$$

In space (vacuum) for a perfectly designed nozzle (full expansion to zero pressure) the expression for specific impulse is

$$I_{SP} = V_e / g = V_e / 32.17 \tag{14.13}$$

The highest specific impulse values are obtained by using hydrogen as a fuel and burning it with either oxygen or fluorine. At sea level with a combustion chamber operating at 500 psia the specific values are



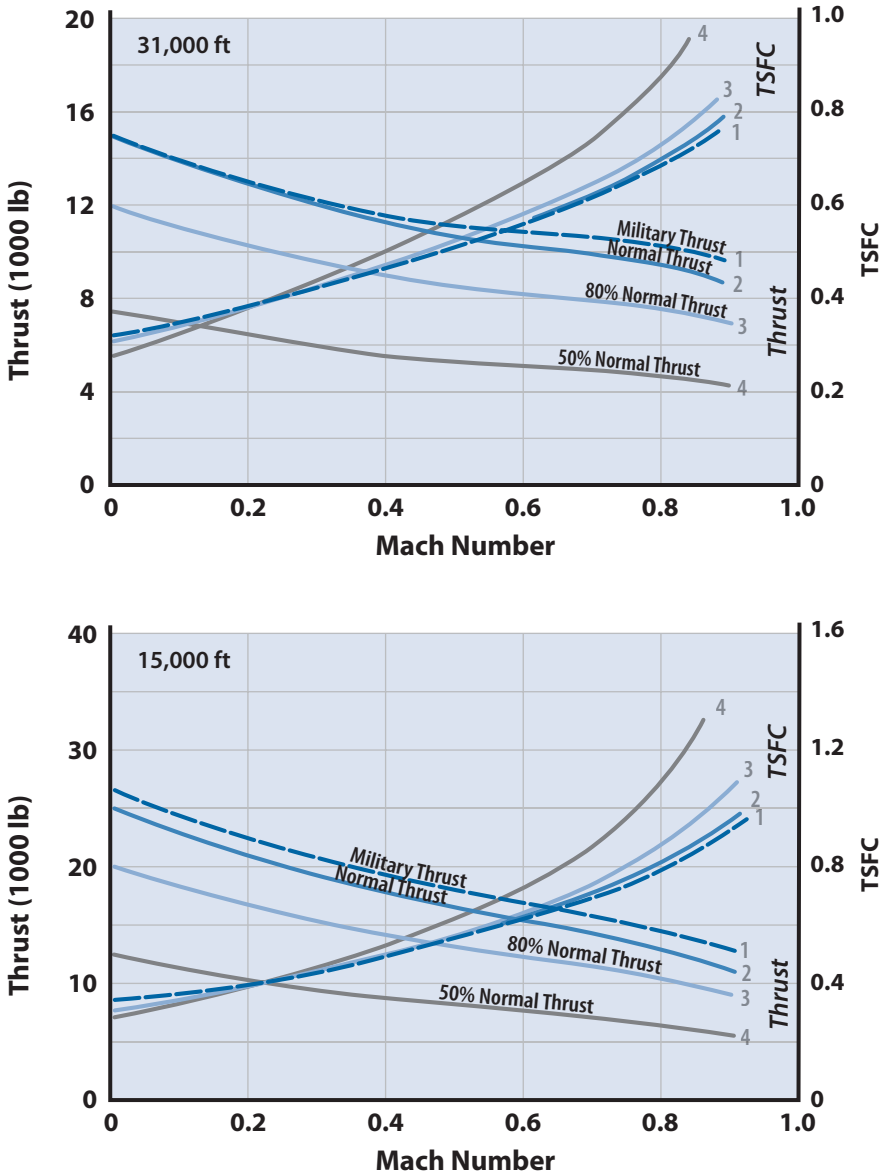


Figure 14.9b Installed thrust and TSFC for TF-39 turbofan engine (see Table 14.4).

The combinations of hydrogen and oxygen or fluorine are difficult to handle so that modern rockets use more modest fuel–oxidizer combinations, including solid propellants. The current space rockets have specific impulses at sea level of 200–300 seconds.

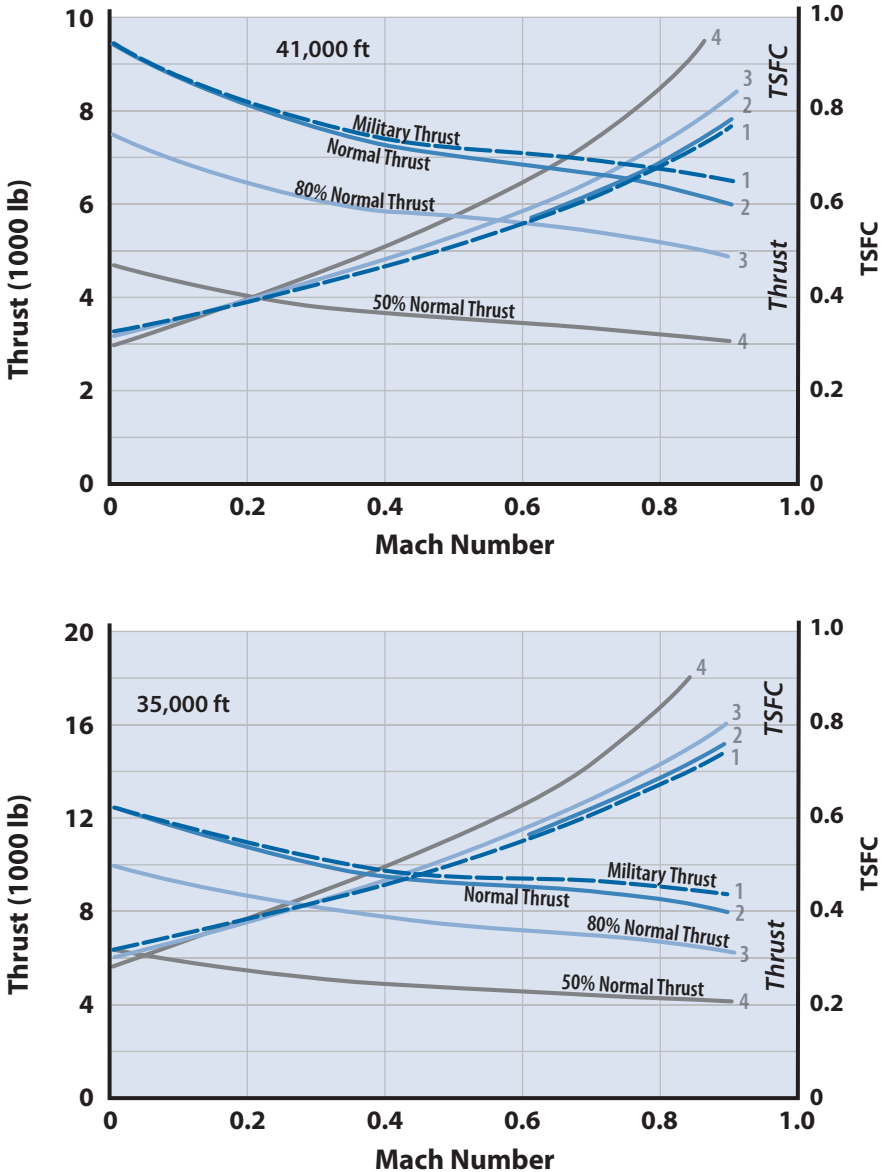
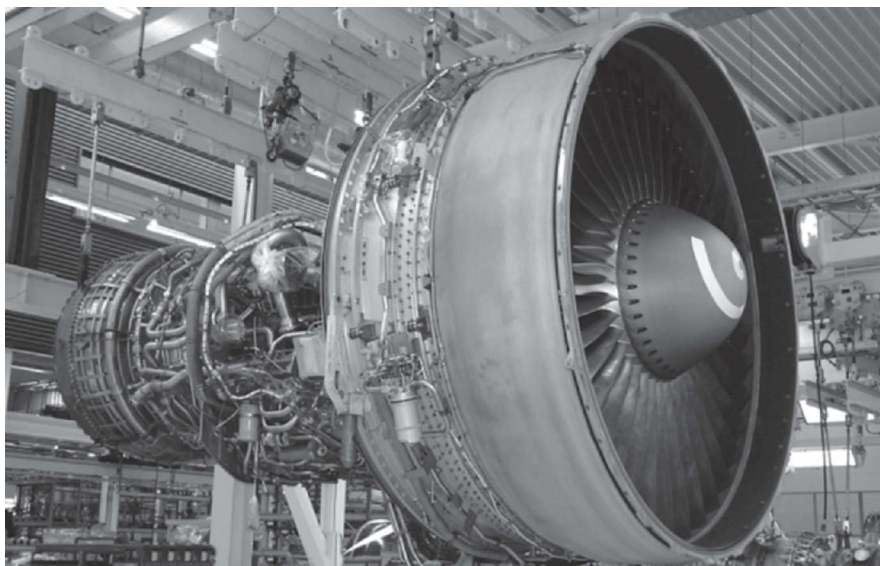


Figure 14.9c Installed thrust and TSFC for TF-39 turbofan engine (see Table 14.4).

### Whittle and von Ohain Change Aviation

Hans von Ohain and Frank Whittle developed the jet turbine engine about the same time in the 1930s but completely independent of one another—Ohain in Germany and Whittle in England. Whittle did his graduate work at



**Figure 14.10** CF-6 engine based on the TF-39 design.

Cranwell College as an RAF Flight Officer. His field of study was a new type of gas turbine and he was granted a patent in 1930. His RAF duties and lack of money prevented any serious development of the jet engine until 1937. The British Air Ministry was slow in recognizing the potential of the jet turbine but finally contracted with Whittle for an engine and with Gloster Aircraft for a jet engine powered aircraft in 1939. The Gloster E.28/39 flew on 15 May 1941 with Whittle's jet engine.

Hans von Ohain did his graduate work at the University of Göttingen and received a doctorate in physics and a patent for his jet engine concept in November 1935. Unlike Whittle, Hans was a man of means and hired a mechanic to build a working model of his concept. Ernst Heinkel (Heinkel Aircraft Co.) was impressed with the model and hired Hans in March 1936 to develop a jet turbine engine. A prototype jet engine was developed and ran successfully on hydrogen gas in March 1937. Heinkel was pleased with von Ohain's success and commissioned him to develop a flightworthy, kerosene-fueled engine to power the Heinkel He-178 aircraft shown in Fig. 14.11. Hans developed a jet engine with 992 lb of thrust; it flew in the He-178 on 27 August 1939 and changed the world forever.

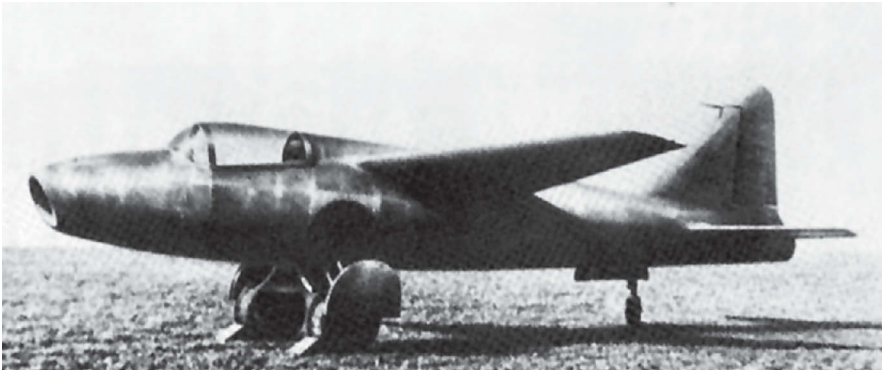
After World War II Whittle's engine was produced by several companies in England and the United States. Frank Whittle was knighted by King George VI of England in August 1948. He eventually immigrated to the United States, where he became a research professor at the U.S. Naval Academy in Annapolis, Maryland. He died on 9 August 1996.

(continued)

After World War II Hans came to the United States as part of Operation Paper Clip. He was assigned to Wright–Patterson AFB, Dayton, Ohio, as a propulsion consultant, then as Chief Scientist to the Propulsion Laboratory, and finally to the Aeronautical Research Laboratory. He retired from government service in 1979 and continued as a consultant to the University of Dayton Research Institute. He and his family settled in nicely in midwestern suburbia, living in Centerville (south of Dayton).

I met Hans in 1972 while on active duty at Wright–Patterson AFB, and our friendship flourished until his death in 1998. He was very gracious with his advice and was an annual visitor to my aircraft design short course in Dayton from 1975 to the mid-1990s. Hans and Sir Frank changed the aviation world with their invention of the jet engine. Hans was a technical giant, a true gentleman, and very humble.

*Leland Nicolai*



**Figure 14.11** Heinkel He-178 aircraft designed for the first jet engine.

## *References*

- [1] Hill, P. G., and Peterson, C. R., *Mechanics and Thermodynamics of Propulsion*, Addison Wesley, Reading, MA, 1965.
- [2] McCormick, B., *Aerodynamic, Aeronautics and Flight Mechanics*, Wiley, New York, 1995.
- [3] Mitlisky, F., Weisberg, A., and Myers, B., “Regenerative Fuel Cells,” Lawrence Livermore National Laboratory, UCRL-JC-134540, June 1999, paper prepared for the U.S. Department of Energy Hydrogen Program 1999 Annual Review Meeting, Lakewood, CO, 4–6 May 1999.
- [4] “The Aircraft Gas Turbine Engine and Its Operation, Pratt and Whitney Operating Instruction 200,” United Aircraft Corp., East Hartford, CT, Nov. 1960.
- [5] *Aviation Week and Space Technology, Annual Aerospace Source Book*, McGraw-Hill, New York (published annually in January).
- [6] Smith, P. R., “C-5A Aerodynamic Substantiating Data Based on Flight Test,” Rept. LGIC22-1-1, Lockheed-Georgia Co., Lockheed Aircraft Co., Marietta, GA, 16 Aug. 1971.



# Chapter 15 Turbine Engine Inlet Design



- Pitot or Normal Shock Inlet
- External Compression Inlet
- Mixed Compression Inlet
- SR-71 Inlet Operation
- Mass Flow Ratio
- Total Pressure Recovery
- Inlet Examples

The SR-71 mixed compression inlet (left) and the F-22 external compression inlet (right). The SR-71 inlet design and operation is discussed in detail in this chapter. See Example 15.1 for an external compression inlet design similar to the F-22.

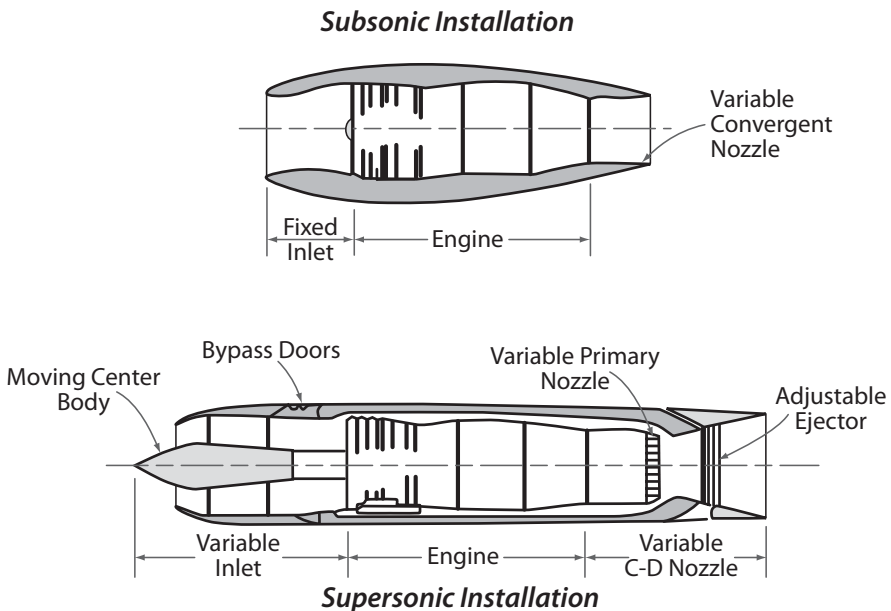
*The inlet messes up an otherwise clean design!*

An aerodynamicist

## 15.1 Introduction

The primary purpose of an inlet is to supply the correct quantity and quality of air to the compressor of the engine. The correct mass flow of air must be delivered to the compressor face at a Mach number of about 0.4. The mass flow must also be delivered with an acceptable velocity distribution across the engine face and with minimum loss in the total energy content of the air. In addition, the inlet is required to do this at all flight conditions and at least weight, cost, and drag. The installation of a turbine engine on an aircraft is a most challenging task.

A typical subsonic turbine engine installation consists of a high-compression engine with a short fixed inlet and probably a variable convergent nozzle. The supersonic installation, on the other hand, requires a powerplant with a sophisticated variable geometry inlet having its own automatic control system and a fully variable convergent–divergent (C–D) nozzle in order to extract the full performance from the engine throughout the speed range. A typical subsonic and supersonic installation is shown in Fig. 15.1. Notice that the supersonic inlet is more than two engine diameters in length as opposed to one diameter for the subsonic installation. The complications of the supersonic inlet and its influence on weight will be discussed in this chapter.



**Figure 15.1** Typical subsonic and supersonic powerplant installations.

The performance of the inlet is related to the following four characteristics:

- Total pressure recovery
- Quality of airflow—distortion and turbulence
- Drag
- Weight and cost

The overall value of an inlet must always be determined by simultaneously evaluating all four characteristics because the gain in one is often achieved at the expense of another. It should be kept in mind that the most serious aspect of the engine–inlet problem is concerned with off-design operation; none of the first three characteristics should deteriorate rapidly under conditions of varying power settings and angles-of-attack. As a result, in actual vehicles many compromises have to be made to achieve an acceptable performance throughout the variations in flight Mach number, angles-of-attack, and sideslip as well as variations in the properties of the atmosphere.

## 15.2 Pressure Recovery and Inlet Types

A supersonic airflow entering an inlet is decelerated through a shock wave or series of shock waves to a subsonic value. The flow is further decelerated in the subsonic diffuser (the diverging section of the inlet between the throat and the compressor face) to a value of about Mach = 0.4 at the compressor face.

The *total pressure recovery* of the inlet is defined as the ratio of the total pressure at the compressor face to that of the freestream:

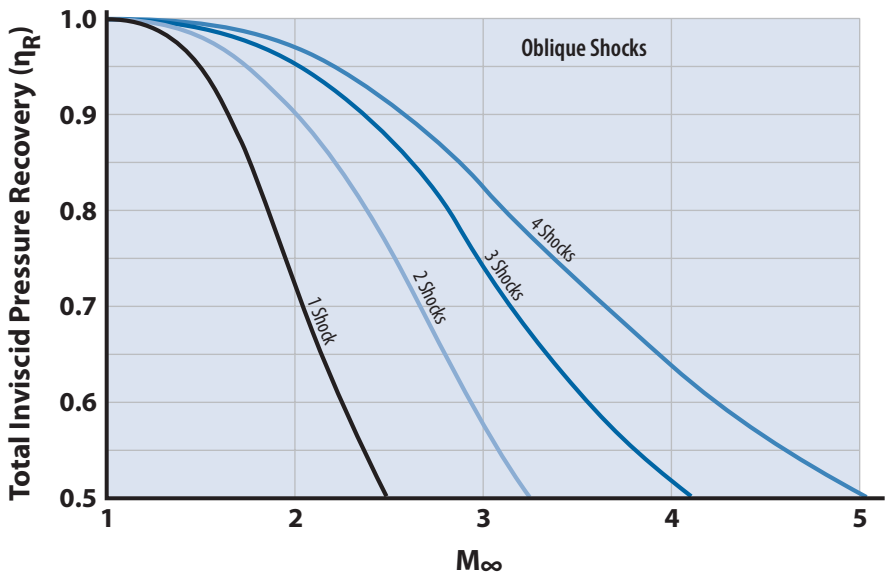
$$\eta_R = \text{total pressure recovery} = P_{0c} / P_{0\infty}$$

The total pressure recovery of the inlet is an important measure of the inlet performance. It is desired to recover as much of the total pressure at the compressor face as possible (high value of  $\eta_R$ ) because the total pressure of the freestream represents the available mechanical energy of the flow that can be converted into a static pressure increase as the flow is decelerated. A large static pressure is desirable at the compressor face because then the compressor section of the turbine engine does not have to be as large in order to compress the flow to the required pressure for combustion. Total pressure is lost due to the viscous dissipation (friction) in the shock waves, the boundary layer, and separated flow regions. The gradual deceleration of a supersonic stream to subsonic through a series of oblique (or conical) shocks prior to the final normal shock is less costly in terms of total pressure loss than a rapid deceleration through a normal shock. The

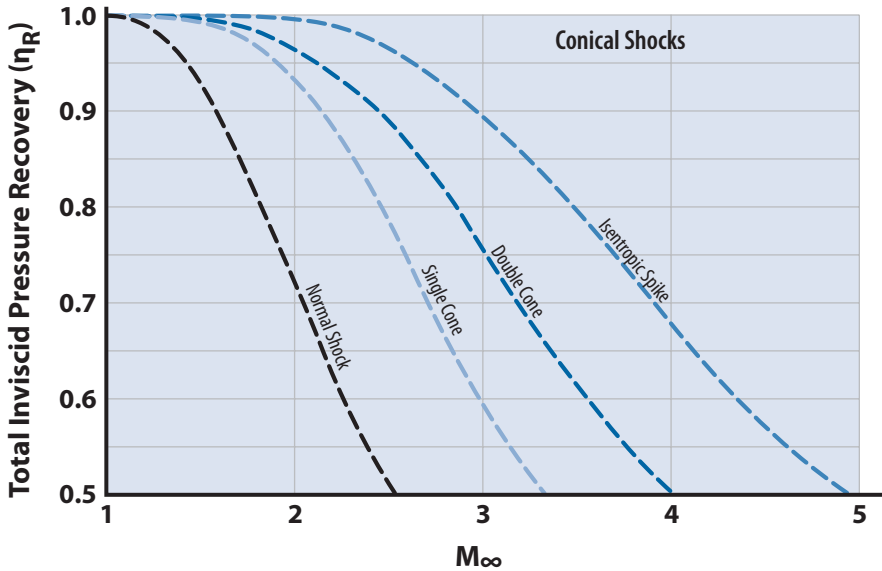
maximum total pressure recovery for different numbers of shocks in an optimum shock wave system is shown in Fig. 15.2. The curve for the single shock is from the normal shock data of Appendix D.

Inlets are of three types, characterized by their shock wave system: pitot or normal shock; external compression; and mixed compression. These three inlet types are shown in Fig. 15.3. The simplest type is the pitot inlet, with the supersonic compression being achieved through a normal shock and further compression carried out in the subsonic diffuser (Fig. 15.3a). The pitot inlet is simple, short, lightweight, and low cost. It gives tolerable total pressure recoveries up to about Mach 1.6. For aircraft having top speed requirements up to about Mach = 1.6, such as the F-16 and F-18 (and needless to say all subsonic aircraft), the pitot inlet is the best arrangement.

For speeds above Mach = 1.6, the flow needs to be decelerated gradually through one or more oblique shocks before the final deceleration through the normal shock. The external compression inlet, Fig. 15.3b, accomplishes the flow compression external to the inlet throat. The external ramp (with flow deflection angle  $\theta_R$ ) can be variable to put the oblique shock on the cowl lip for a variety of different Mach numbers. This “shock-on-lip” is called the *design condition* and will be discussed later. The desired operation is with the normal shock located at the inlet throat. This inlet provides tolerable pressure recoveries up to about Mach = 2.5.



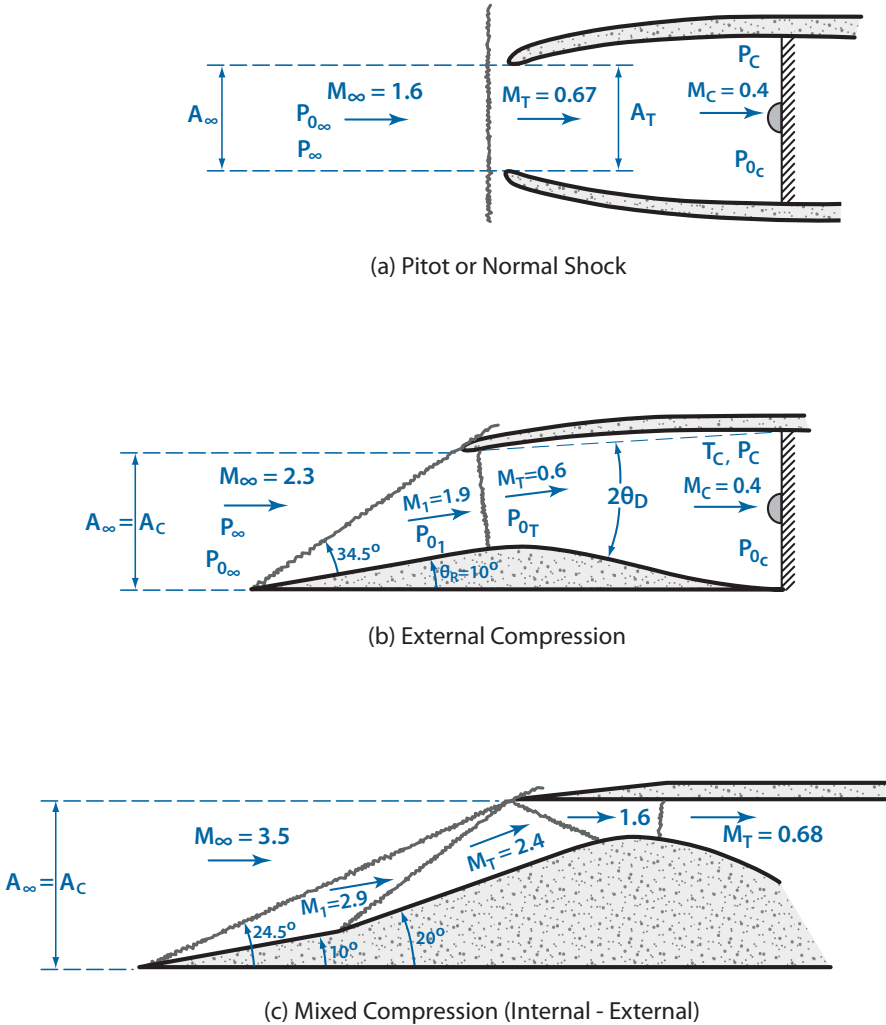
**Figure 15.2a** Maximum inviscid total pressure recovery—optimum oblique shock system.



**Figure 15.2b** Maximum inviscid total pressure recovery—optimum conical shock system.

At freestream Mach numbers above Mach = 2.5 the inlet must provide a multiple shock system and would be a *mixed compression inlet* (Fig. 15.3c). Here again the external ramp can be a series of ramps (or cones) providing a series of external oblique shocks. The shock system continues into the supersonic diffuser, with the normal shock located in the subsonic diffuser. The location of the normal shock is dependent upon the backpressure at the compressor face. The ideal location for the normal shock is just slightly downstream of the throat to minimize the strength of the normal shock and the total pressure loss across it. However, this position is very sensitive to the backpressure. Any perturbation downstream can cause the normal shock to “pop out” of the diffuser and move to a position forward of the inlet lip, “unstating” the inlet. The mixed compression inlets usually have bypass doors (see Fig. 15.6, Section 15.2.1) in the subsonic diffuser to control the backpressure and thereby the location of the normal shock. These vents can also be used to bypass the excess air in the inlet that cannot be accommodated by the engine. If this excess air is not bypassed it must be spilled ahead of the inlet, causing the mixed compression inlet to unstart.

The mixed compression inlet, sometimes called an *internal contraction inlet*, must have a variable geometry feature to obtain peak performance. The compression ramps must be able to collapse (fold down), giving a ratio of throat area  $A_T$  to cowl area  $A_c$  of about 0.8 in order to “swallow” the



**Figure 15.3** Types of inlets operating at supersonic “design” Mach numbers.

normal shock and locate it in the subsonic diffuser. Once the inlet is started, the throat area is decreased to an  $A_T/A_c$  of about 0.4 or less (dependent on Mach number, see [1]), which locates the normal shock just downstream of the throat for minimum total pressure loss.

Inlets can be *two-dimensional* with compression ramps as shown in Figs. 15.3b and 15.3c or *axisymmetric* with conical centerbodies as shown in Fig. 15.6 (Section 15.2.1). Axisymmetric inlets have a slight advantage over two-dimensional inlets in terms of weight and pressure recovery. Round ducts can usually be made lighter than rectangular ducts to take the

large internal pressures. Also, the total pressure loss across a conical shock is less than across an oblique shock for the same upstream Mach number and flow deflection angle.

The determination of the total pressure recovery for an inlet is accomplished by examining the shock wave system and subsonic diffuser separately. Each shock is considered independently, with its characteristics determined by the flow deflection angle and upstream Mach number. The characteristics for oblique and conical shocks are presented in Appendix E and for normal shocks in Appendix D. The total pressure recovery for the shock wave system is the product of the individual total pressure ratios across each shock. Appendix Figs. E.6 and E.7 present the pressure recovery for cone inlets and Appendix Figs. E.8 and E.9 for ramp inlets.

The total pressure loss in a subsonic diffuser is dependent upon the diffuser geometry, throat Mach number, and the presence of a normal shock ahead of the diffuser entrance. Figure 15.4 shows an empirically determined [2] diffuser loss coefficient,  $\epsilon$ , as a function of throat Mach number  $M_T$  and the ratio of diffuser length to throat height,  $L_D/H_T$ . The presence of a normal shock ahead of the diffuser entrance aggravates the boundary layer growth and tendency for the flow to separate, resulting in an increased diffuser loss coefficient. Figure 15.4 indicates that the designer should avoid short and long subsonic diffusers. Short diffusers,  $L_D/H_T$  of 4 or less, tend to cause flow separation, and long diffusers result in large friction losses. Long diffusers are heavy and should be avoided for that reason also. The ratio of the total pressure at the compressor face to that at the diffuser entrance,  $P_{0c}/P_{0T}$  is determined from Fig. 15.5.

### 15.2.1 SR-71 Mixed Compression Inlet Operation

The SR-71, shown on the Chapter 2 cover page, has two Pratt and Whitney J58 afterburning turbojet engines (34,000 lb SLS thrust). At this point the reader would be well served to review the SR-71 Case Study in Volume 2. The operating speed and altitude (Mach = 3.2 at 85,000 ft) of the SR-71 dictated a variable-geometry, mixed compression inlet. Figure 15.6 shows the axisymmetric mixed compression inlet on the SR-71. Figure 15.6b (from [3]) shows the position of the centerbody spike and bypass doors to locate the shock structure at four Mach numbers. This inlet design achieved a total pressure recovery of 78% at maximum speed and altitude.

The inlet control system operates to supply a flow of air, at correct pressure and velocity, to the engines throughout the flight envelope. The system includes the centerbody spikes, which are translated fore and aft to capture and retain the normal shock, and forward bypass doors, which operate to assist the spikes in positioning the normal shock. The system is normally

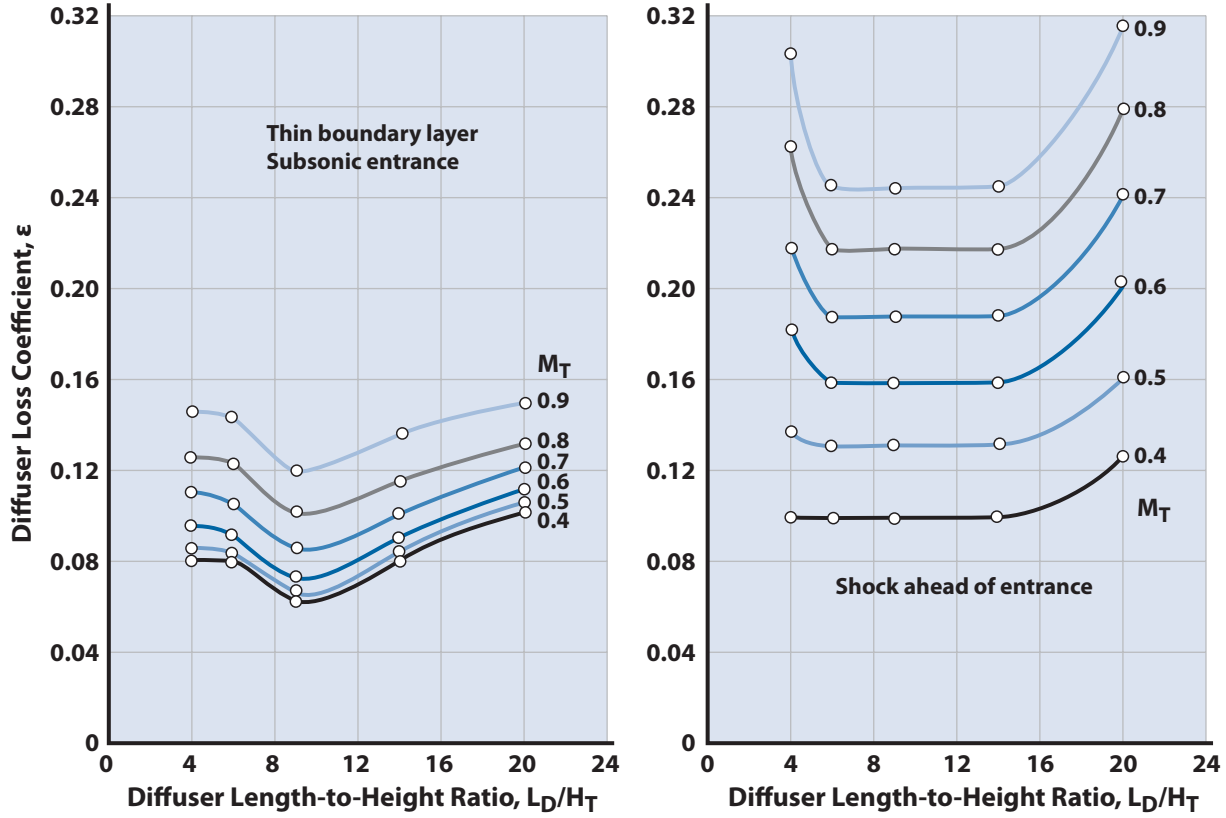


Figure 15.4 Effect of diffuser length on diffuser loss coefficient (data from [2]).



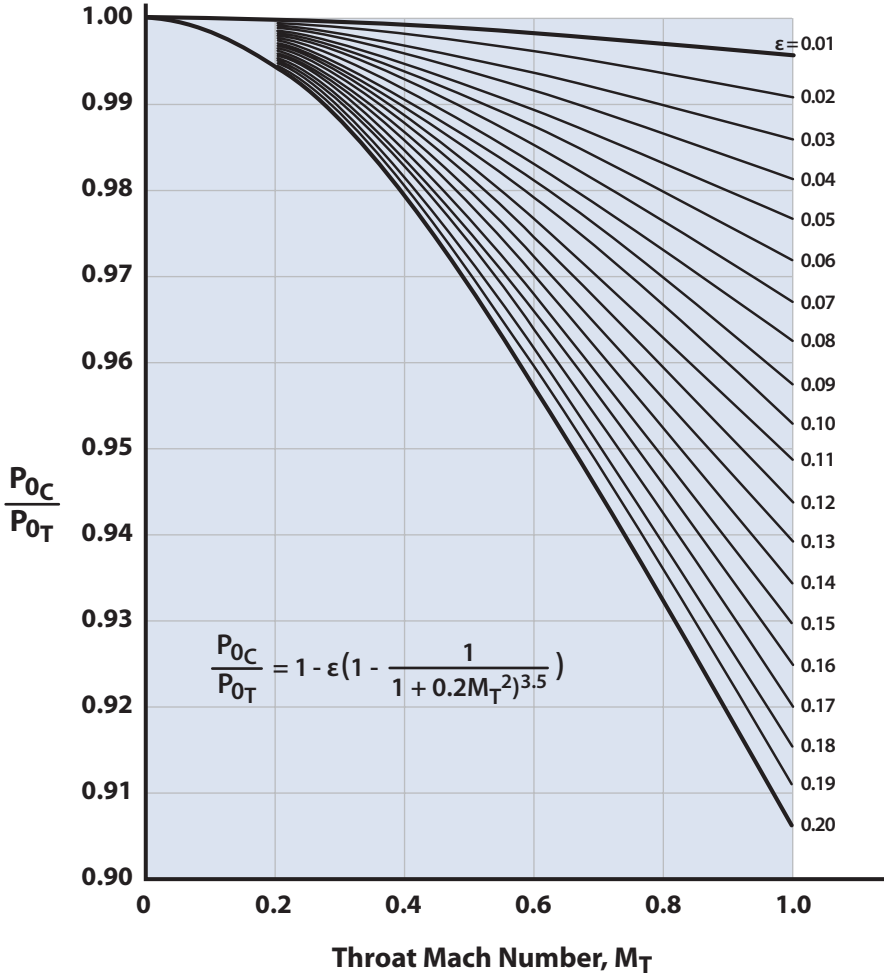
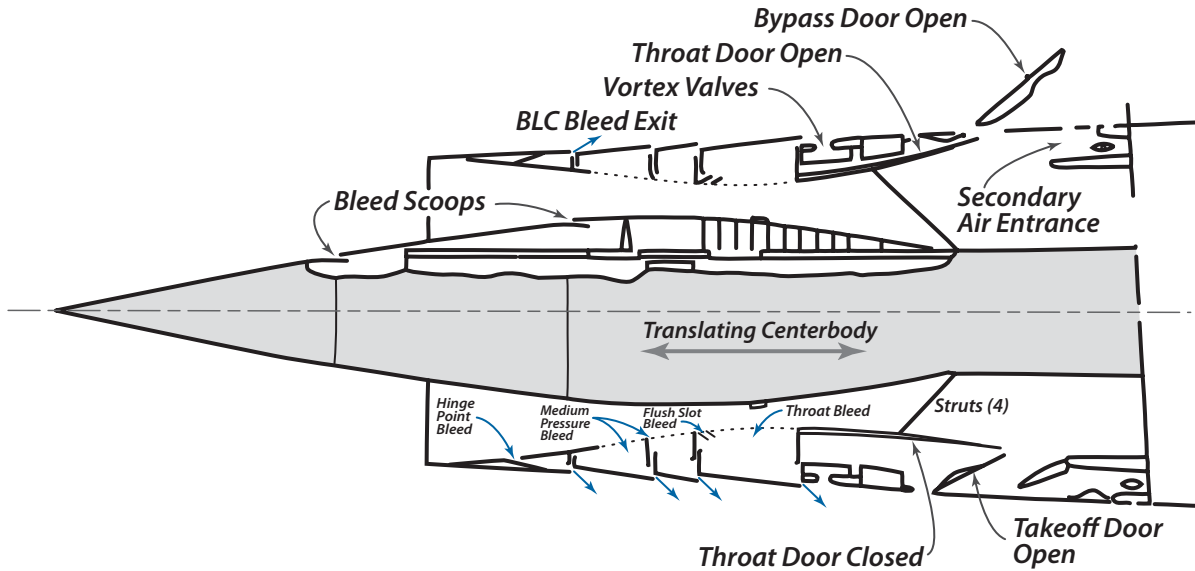


Figure 15.5 Total pressure recovery loss factors for subsonic diffuser.

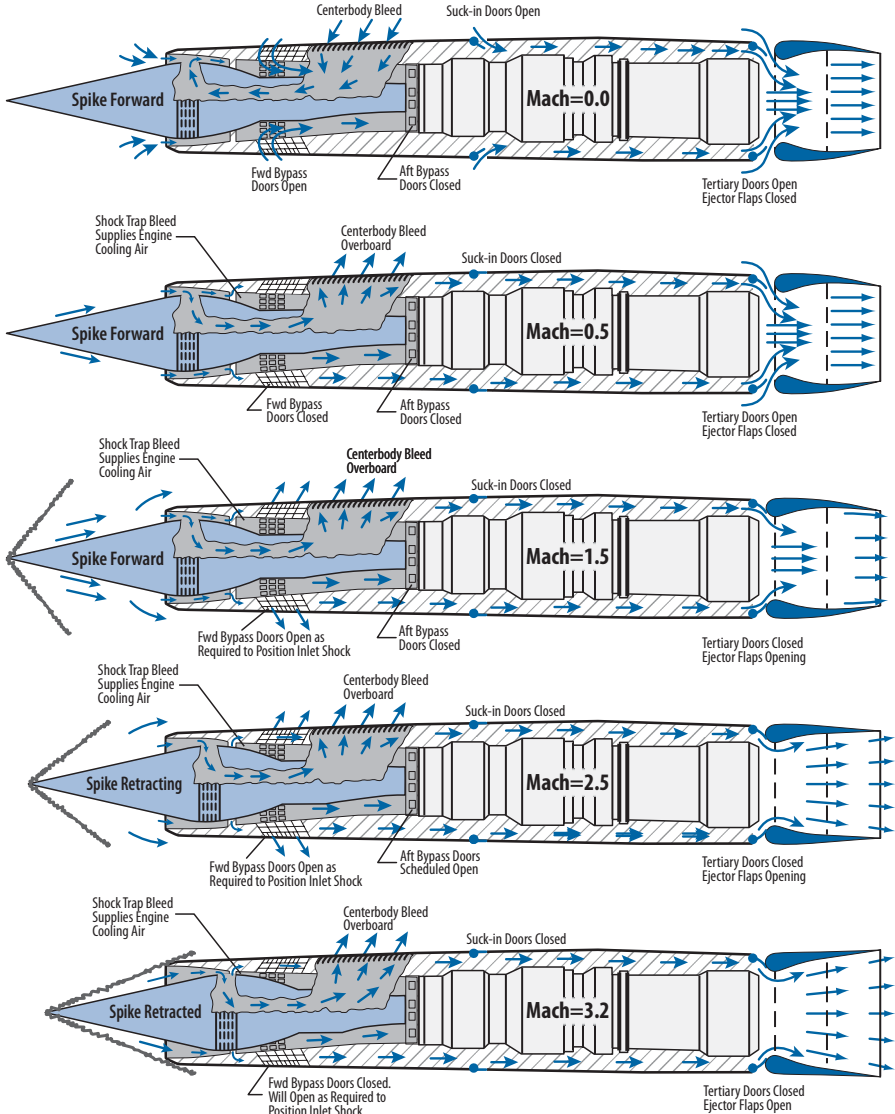
operated in the automatic mode; however, it can be manually controlled by the pilot.

In operation the spikes are moved forward and aft in the inlet duct as a function of Mach number, varying the size of the inlet throat area and position of the conical shockwaves and the single normal shock. The forward bypass doors are modulated to control inlet duct static pressure and therefore fine tune the location of the normal shock in the inlet throat. The doors operate to prevent excessive duct air pressure.

Operation of the spike and bypass doors, and the resulting airflow patterns, is shown in Fig. 15.6b. At altitudes below 30,000 ft and speeds less



**Figure 15.6a** Typical supersonic mixed compression axisymmetric inlet.



**Figure 15.6b** SR-71 mixed compression axisymmetric inlet airflows at various Mach numbers.

than Mach = 1.4, the spike is locked fully forward. At altitudes above 30,000 ft the spike begins to move aft as the speed increases above Mach 1.6. The spike is automatically scheduled aft as a function of Mach number biased by angle-of-attack, sideslip, and vertical acceleration. Aft movement of the spike properly positions the conical and normal shocks relative to the inlet and increases the inlet contraction ratio (inlet area versus throat area). At Mach = 3.2, the spike has moved 26 inches aft of its full forward

position and the captured stream tube area has increased 112%, from 8.7 to 18.5 ft<sup>2</sup>, and the throat area has closed down 54%, from 7.7 to 4.16 ft<sup>2</sup>. A peripheral “shock trap” bleed slot, around the inside of the inlet duct just forward of the throat, removes duct boundary layer air, which is ducted aft and exhausted through the ejector nozzle. Spike boundary layer air is removed at a porous bleed section in the spike surface at its maximum diameter. This air is ducted through the spike body and supporting struts to be exhausted overboard through nacelle louvers.

The forward bypass doors consist of two concentric, annular bands, located just aft of the inlet throat. The outer band is rotated slightly about the stationary inner band so that the rectangular openings in the two bands are shifted from doors fully open to fully closed. The doors are fully open when the landing gear is extended and fully closed when the gear is retracted. The doors remain closed until Mach = 1.5 is reached above 30,000 ft, at which point they modulate open or closed as a function of inlet pressure and a pressure ratio schedule to keep the normal shock near the inlet throat. The schedule is followed by comparing the ratio of internal duct pressures with external pressures sensed by pitot probes on the nacelle exterior surface. Any difference between the sensed pressure ratio and the pressure ratio schedule is used as a signal to drive the doors more open or closed.

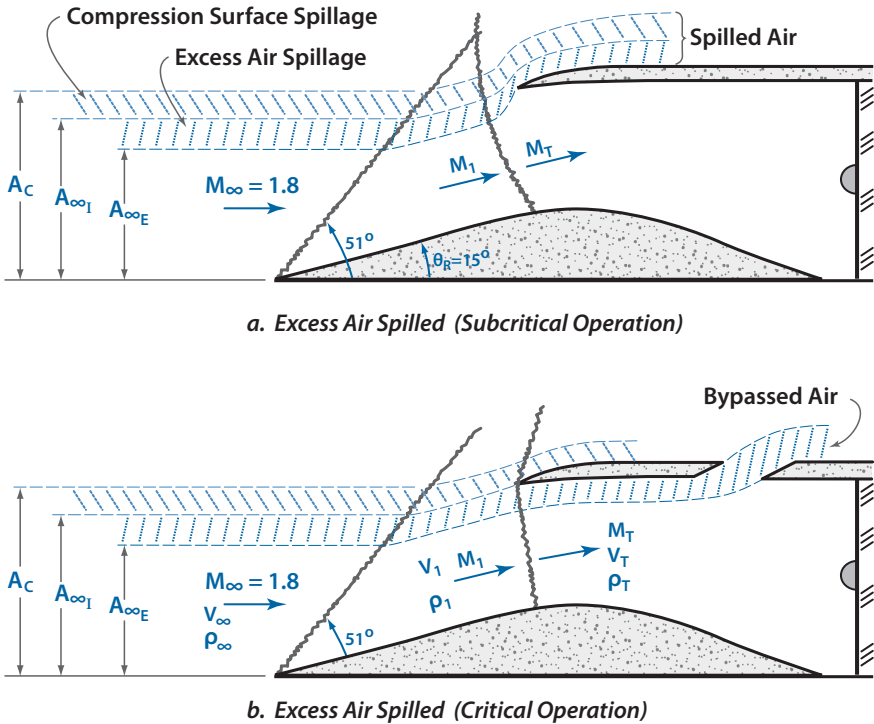
*Inlet unstart* is a sudden pressure change in the inlet that results in the normal shock moving forward from its controlled position just aft of the throat—or even expelled from the inlet entirely. This condition reduces the affected engine thrust significantly, causing an asymmetric thrust condition and a violent yaw. Pilots are often slammed against the side of the cockpit, causing their helmets to break.

An unstart causes a sudden decrease in the static pressure near the compressor face. The pressure change initiates an auto restart procedure that moves the spike forward and opens the forward bypass doors in about three seconds. The forward movement of the spike reduces the inlet throat contraction and opening the bypass doors reduces the backpressure, thereby accelerating the airflow and returning the normal shock to its desired position in the inlet throat. The spike and forward bypass doors slowly return to their scheduled positions over a period of 10 seconds. At speeds above Mach = 2.3, the restart operation is applied to both inlets even if a problem is sensed on only one side. This reduces the yaw due to the asymmetric thrust and also prevents a sympathetic unstart of the other inlet which oftentimes occurs during a severe yaw condition. Restart crosstie is not in effect below Mach = 2.3, allowing independent inlet restart operation at slower speed.

The SR-71 mixed compression inlet is truly spectacular—and the fact that it was developed in 1961 before the use of modern computers makes it even more so.

### 15.3 Capture-Area Ratio or Mass-Flow Ratio (Supersonic Flow)

In Fig. 15.7 the area  $A_c$  is the cross sectional area of the inlet and is called the *cowl capture area*. The area  $A_\infty$  is the cross-sectional area of the freestream tube of air entering the inlet. The cross-sectional areas  $A_{\infty I}$  and  $A_{\infty E}$  are defined on Fig. 15.7 and are equal to  $A_\infty$  under different conditions. When the engine demand for air,  $\dot{m}_E$ , and the inlet supply of air,  $\dot{m}_I$ , are equal,  $A_{\infty I} = A_{\infty E}$ , the engine and inlet are said to be *matched*. When the engine and inlet are not matched, the excess air can either spill around the



From Continuity:  $\dot{m} = \text{constant}$   
 For b:  $\rho_\infty V_\infty A_\infty = \rho_1 V_1 A_T = \rho_T V_T A_T$   
 Engine demand:  $\dot{m}_E = \rho_\infty V_\infty A_{\infty E} = \dot{m}_a$   
 Inlet supply:  $\dot{m}_I = \rho_\infty V_\infty A_{\infty I}$   
 Excess Air:  $\dot{m}_X = \dot{m}_I - \dot{m}_E$

Figure 15.7 Two schemes for inlet-engine flow matching.

cowl lips, expelling the normal shock from the inlet throat as shown in Fig. 15.7a, or the excess air can be bypassed through bypass doors in the subsonic diffuser as shown in Fig. 15.7b. When the excess air is spilled,  $A_\infty = A_{\infty E}$  and when the excess air is bypassed,  $A_\infty = A_{\infty I}$ . These definitions of  $A_{\infty I}$  and  $A_{\infty E}$  will be useful when discussing spillage drag and bypass drag.

The *capture area ratio* is defined as  $A_\infty/A_c$ . The ratio of the mass of air that enters the inlet to the maximum mass that could enter is called the *mass flow ratio*,

$$\frac{\dot{m}_\infty}{\dot{m}_c} = \frac{\rho_\infty V_\infty A_\infty}{\rho_\infty V_\infty A_c} = \frac{A_\infty}{A_c} \tag{15.1}$$

which is the same as the capture area ratio.

As the inlet mass flow ratio changes, the normal shock position and total pressure recovery ratio change, which is shown in Fig. 15.8. The inlet is designed to operate with the oblique shock crossing the lip of the inlet at the required mass flow of the engine (called the design mass flow) as shown in Figs. 15.3b, 15.3c, and 15.8b. At this condition (point B in Fig. 15.8) the normal shock is at the throat, giving a maximum value of mass flow and pressure recovery. This is referred to as the *critical condition*. As the engine demand for air becomes less (i.e., throttling the engine back for cruise) the normal shock is expelled forward to allow the excess air to be spilled over the outside of the lip (assuming no bypass facility). A portion of the air

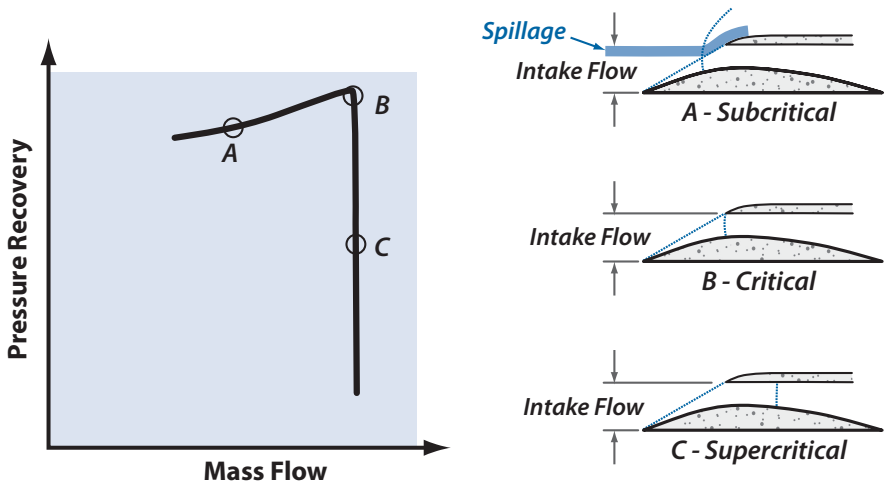


Figure 15.8 Mass flow–pressure recovery characteristic (data from [4]).

entering the inlet in this condition passes only through the single shock formed by the intersection of the normal and oblique shocks. As a result, this air enters the diffuser at a lower total pressure than the air that passes through the oblique and normal shocks. Therefore, there is a lower pressure recovery at this point. This condition is called *subcritical operation* and is point A on Fig. 15.8.

If the inlet is operating critically and the engine suddenly demands more airflow, the backpressure in the inlet is decreased and the normal shock moves back into the subsonic diffuser, becoming stronger as the Mach number in front of it increases. The mass flow cannot increase because the inlet is choked and the result is a reduction in pressure recovery to bring the engine airflow demand down to the inlet capacity. Because the engine cannot get all the airflow it needs, it is said to be *starved* and the inlet operation is termed *supercritical* (point C on Fig. 15.8).

## 15.4 Variable-Geometry Inlets

The *design Mach number*  $M_D$  is that flight vehicle speed that is critical in terms of mission performance. It might be the cruise speed, weapon delivery speed, or a maximum speed. The inlet is designed for this design Mach number to give high  $\eta_R$ , shock-on-lip operation, and  $A_{\infty I}$  matched to the engine demand so that spillage and bypass drag due to excess air are minimal. The performance of a fixed-geometry inlet deteriorates rapidly at Mach numbers other than  $M_D$ . For flight speeds above  $M_D$ , the engine demand airflow is usually greater than the supply airflow and the engine is starved. For flight speeds below  $M_D$  the shock is off the cowl lip ( $A_{\infty} < A_c$ ), giving rise to compression surface spillage of air (Fig. 15.7) and a resulting additive drag. Also, when the flight speed is off the design Mach the inlet throat area may not be sized properly for the incoming airflow.

Variable geometry can provide a resolution to some of these problems but at the expense of increased inlet complexity, weight, and cost. The designer must weigh the pros and cons of the variable-geometry inlet and decide the best compromise.

The inlet might incorporate a variable angle compression ramp or centerbody to keep the shock-on-the-lip at off-design Mach numbers. The ramp or centerbody can also translate to keep the shock-on-the-lip as well as providing a variable throat area. The inlet capture area  $A_C$  might also be varied through a hinged cowl lip to provide a better match of engine demand airflow with supply at a variety of flight speeds.

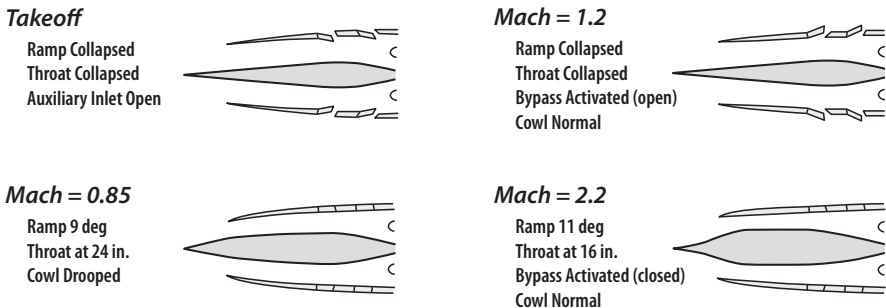
As an engine will accept only a certain amount of air, the excess air must be diverted to the freestream as efficiently as possible. This requires still further variation in geometry. One solution is to increase the compression

ramp angle,  $\theta_R$ , which moves the shock off the cowl lip, diverting the excess air over the lip of the cowl. This results in an additive drag (sometimes called *compression surface spillage* or *critical spillage drag*) but still lower losses than if the shock were left on the lip and the excess air permitted to back up in the inlet and spill around the lip (Fig. 15.7a). Another solution is to provide bypass vents or doors in the subsonic diffuser to bypass the excess air into the freestream (Fig. 15.7b). This approach will produce a bypass drag due to the pressure drag on the spill vents and the momentum change of the bypassed air between the inlet and the spill vent exit. Normally, facilities for both methods of getting rid of the excess air should be provided and compromise settings chosen that will result in a minimum drag for various flight Mach numbers. These two engine–inlet matching schemes are shown in Fig. 15.7.

The variable throat area feature of mixed compression inlets has already been discussed in Section 15.2.1. This variable throat area is necessary in order to swallow the normal shock in the case of an inlet unstart and then position the normal shock for best pressure recovery. The bypass doors are the main control over the normal shock location once the mixed compression inlet has started.

At low speed, most inlets do not have enough cowl area  $A_C$  to provide the required engine airflow. Auxiliary doors or suck-in doors are located in the subsonic diffuser to provide additional air during takeoff (see Fig. 15.6).

Figure 15.9 illustrates a two-dimensional variable-geometry inlet, designed for Mach = 2.2, in operation at different flight conditions. It should be clear to the reader that the mechanism details are a real design challenge.



**Figure 15.9** Mach 2.2 variable-geometry mixed-compression inlet operating at different flight conditions.



## 15.5 Quality of the Airflow—Distortion and Turbulence

Another characteristic of inlet performance is the quality of the airflow delivered to the engine compressor. It is important that the distortion and turbulence of the flow at the compression face be minimal, otherwise compressor stall and even engine flameout can result. The elements of distortion are swirl and uneven spatial distribution of total pressure, velocity, and temperature. *Turbulence* is a dynamic characteristic and results in a time variation of the distortion pattern. A poor velocity distribution at the compressor face can cause the compressor blades to pass through alternating high- and low-speed regions, which may cause vibration and possible blade failure. Local velocity variations may be interpreted as local variations in angle-of-attack of the compressor face flow. This variation in  $\alpha$  along the blade (i.e., radially) may be sufficient to cause the blade to stall, thereby stalling other blades and surging the engine. An often used measure of the flow quality or flow distortion is given by the distortion parameter.

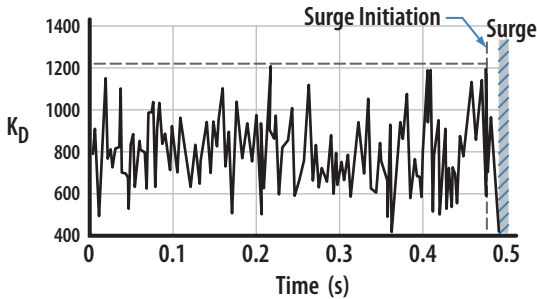
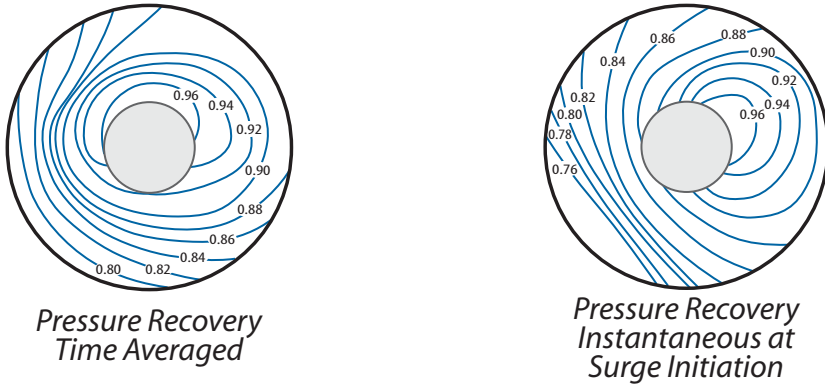
Figure 15.10 shows a comparison of average and instantaneous recovery maps with  $K_D$  for the F-111 at Mach = 0.9, 30,000 ft, and off-design spike position.

The main sources of distortion and turbulence are:

- Flow-field nonuniformity
- Ingestion of low-energy air
- Inlet shock system pressure gradients
- Shock/boundary layer interaction
- Cowl lip separation
- Duct pressure losses and flow separation
- Secondary duct flows

The location of the inlet on the vehicle is often determined by considerations of flow quality. The inlet should not be located in a region of separated or vortical (swirl) flow. Also, the vehicle boundary layer should not be permitted to interact with the inlet. Ingestion of the vehicle boundary layer can aggravate the inlet boundary layer and cause early separation. The inlet should be located out of the vehicle boundary layer by a boundary layer diverter as shown in Fig. 15.13b (in Section 15.7) for the Concorde, XB-70, and F-18. Also notice in this figure that the F-35 has a diverterless inlet.

The inlet boundary layer itself should be removed by boundary layer bleed. The inlet shock wave system interacting with the boundary layer can cause flow separation, resulting in greatly reduced total pressure recovery as well as poor quality flow at the compressor face. The amount of boundary layer that should be removed from within the inlet for satisfactory operation or performance is a function of the inlet type, shape, and shock



**Figure 15.10** Comparison of average and instantaneous recovery maps with  $K_D$ , F-111 flight conditions: Mach = 0.9 at 30,000 ft and off-design spike position.

wave system; the sensitivity of the engine to the flow distortion and turbulence at the compressor face and the relative sensitivity of vehicle performance to inlet pressure recovery and bleed drag.

External-compression inlet types normally require less bleed for satisfactory operation than mixed-compression inlets because they have fewer shocks interacting with the boundary layer and shorter compression surfaces on which the boundary layer is formed. Two-dimensional inlets usually require more bleed than axisymmetric inlets because of the tendency of the boundary layer to accumulate on the sidewalls and in the corners, and because of the greater amount of surface area usually present in the two-dimensional inlets. A recommended amount of boundary layer bleed is shown in Fig. 15.11. Boundary layer bleed ports should be located in the throat area and in the area of any sharp bends in the subsonic diffuser (see Figs. 15.6 and 15.14, Section 15.8). Angles of bends in ducts should not exceed 15 deg when the duct requires a high Mach number (e.g., 0.85) near the throat [5].

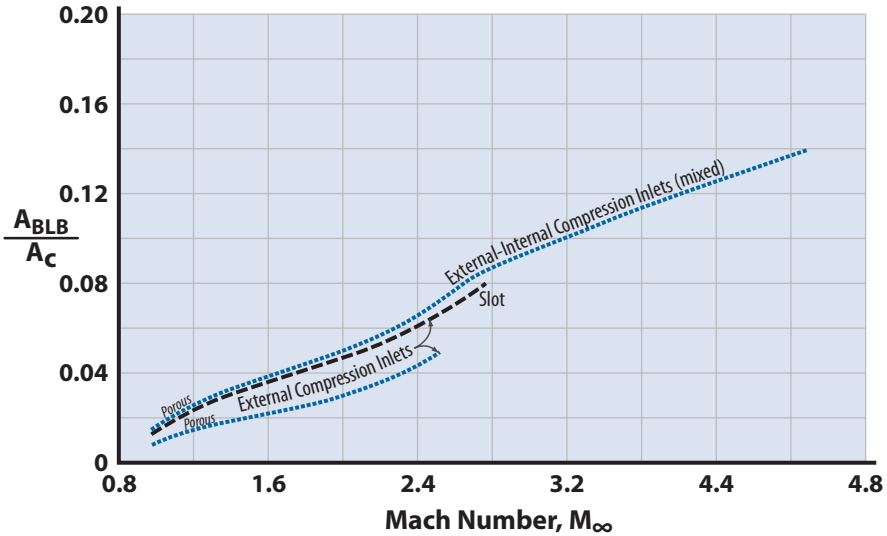


Figure 15.11 Recommended boundary layer bleed (data from [2]).

Podded engines, such as are used on the Boeing 747 and Lockheed C5, are good inlet designs from the standpoint of inlet flow quality. The inlet operates in undisturbed flow and the engine–airframe interactions are minimal. In addition, the podded engine offers good maintainability features such as easy access.

Low-slung inlets will initiate strong inlet vortices normal to the ground plane and with enough energy to scatter debris and to ingest objects. Where possible, the inlet lip should be more than two inlet diameters from the ground [5]. The locating of inlets in trail of the landing gear should be avoided to prevent picking up debris kicked up by the landing wheels.

## 15.6 Weight and Cost

Although high performance is desired from the inlet, it must be balanced by tolerable weight and cost. For example, an aircraft designed to operate at speeds up to Mach = 1.6 could have a normal shock inlet or a variable ramp external compression inlet. The designer must trade off the simple, low-weight, low-cost normal shock inlet with its shock  $\eta_R = 0.9$  at Mach = 1.6 against the more complicated, heavier, and costlier external compression inlet with its shock  $\eta_R \sim 0.97$ .

The question to be addressed is whether the improved total pressure recovery is worth the added weight and cost. It is not an easy question and one that should not be answered until all the tradeoff information is available. A nacelle weight comparison study reported in [6] showed that a

normal shock inlet, designed for low-subsonic flight, weighed 13% of the basic engine weight whereas a mixed compression inlet designed for Mach = 2.7 flight weighed 43% of the basic engine weight. The inlet weights are determined using the weight equations of Chapter 20.

## 15.7 Inlet Sizing and Design

This section discusses the general sizing and design of inlets and then follows with an example of a Mach = 2.3 inlet for the PW-F-100 engine. Reference [5] is an excellent report on the design of inlets and is recommended very highly to the reader. Many of the ideas of [5] are incorporated in this chapter.

The inlet should be sized to provide enough air to the engine at all flight conditions. It is rare that the inlet can provide exactly the right amount of air at all flight conditions, thus critical flight conditions are selected and the inlet is designed for these “design” conditions. There may be one or more design Mach numbers,  $M_D$ .

The engine demand cross-sectional area  $A_{1E}$  is determined for different Mach–altitude conditions using

$$A_{\infty E} = \frac{\dot{m}_E + \dot{m}_S}{32.17 \rho_{\infty} V_{\infty}} \quad (15.2)$$

where  $\dot{m}_E$  is the engine airflow in pounds mass per second (lbm/s) (a function of Mach, altitude, and power setting, see Fig. 14.8g) and  $\dot{m}_S$  is the secondary airflow required for engine oil cooling, ejector nozzle cooling, and so on. Typical values for secondary airflows are given in Table 15.1. The maximum value of  $A_{\infty E}$  is increased by the amount recommended for boundary layer bleed from Fig. 15.11 and the result set equal to the inlet capture area  $A_c$ . If the maximum  $A_{\infty E}$  occurs at takeoff, a lower value should be selected for  $A_c$  and the inlet provided with auxiliary takeoff doors, otherwise the inlet will be oversized for other parts of the mission resulting in

**Table 15.1** Typical Secondary Airflows (data from [5])

	$\dot{m}_S / \dot{m}_E$
Engine oil cooling	0–0.01
Engine nacelle cooling	0–0.04
Ejector nozzle secondary air	0.04–0.20
Hydraulic system cooling	0–0.01
Vehicle environmental control	0.02–0.05

large amounts of excess air. Usually the  $A_{\infty E}$  for cruise or maximum speed is selected for  $A_c$ .

Figure 15.16 (in Section 15.8) shows a typical *engine demand capture area ratio*,  $A_{\infty E} / A_c$ , for a supersonic aircraft. The inlet is now designed to give a capture area ratio of 1 at the flight condition of the selected  $A_c$ . This Mach number is termed the *design Mach number*  $M_D$ .

The type of inlet selected should be based upon the  $M_D$ . Figure 15.12 offers some good rules of thumb for inlet selection that are based primarily on tolerable total pressure recovery.

The inlet is now designed to match the *inlet supply capture area ratio*,  $A_{\infty I} / A_c$ , as closely as possible to the engine demand capture area ratio.

The inlet for subsonic and transonic aircraft will probably be the pitot inlet because of its simplicity and low weight and cost. Generally speaking, the inlets for these applications are sized for cruise altitude and Mach number and require very little (or no) variable geometry, bypass, boundary layer bleed, or control complexities to provide satisfactory operation [6]. They are usually characterized by generously rounded cowl lips and are either podded or blended into the fuselage in such a way that no appreciable low-energy air or vortex flows are likely to be ingested. Some designs have incorporated blow-in doors for low-speed, low-altitude flight, but when safety of flight is a prime consideration, the inlet cowl is usually sized

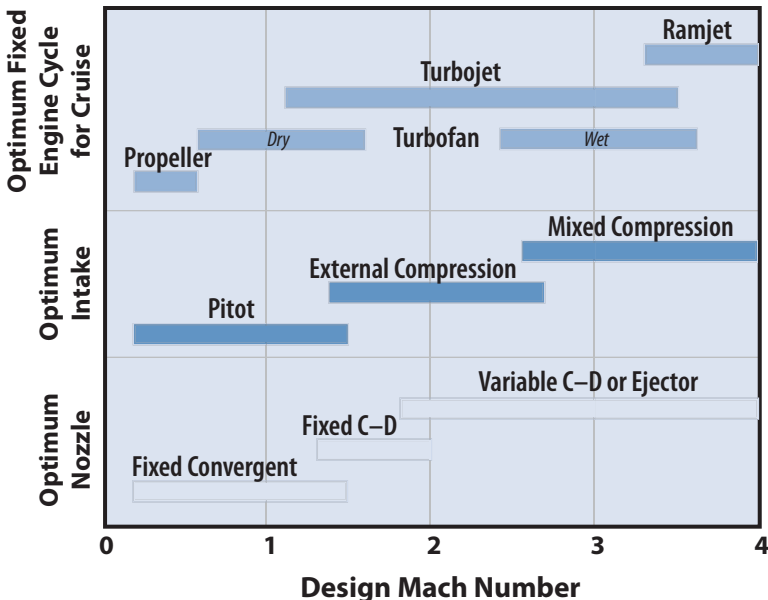


Figure 15.12 Effect of design Mach number on propulsion systems (data from [4]).

sufficiently large to avoid the added complexity of variable geometry. The pitot inlet gives  $A_{\infty I}/A_c = 1$  for Mach  $> 1.0$  and  $A_{\infty I}/A_c > 1$  for all subsonic Mach numbers. At Mach numbers  $< 1.10$  spillage is a better way of getting rid of excess inlet airflow because it has a lower drag penalty than bypassing at these Mach numbers. Above Mach = 1.10 the designer should examine the tradeoff between spillage and bypass drag and perhaps provide facilities for both.

At supersonic Mach numbers above Mach = 1.6 the inlets should be of the external compression or mixed compression type. For external compression and mixed compression inlets the designer has many decisions to make. Although the  $A_c$  is fixed by the airflow demand at  $M_D$ , there still remain the questions of two-dimensional vs axisymmetric, single vs multiple compression surfaces, compression surface angles, and fixed vs variable geometry. Axisymmetric inlets are slightly more efficient than two-dimensional inlets in terms of total pressure recovery and weight. However, if there is very much variable geometry, that is, translating or variable-angle compression surfaces, variable cowl area, and so on, the two-dimensional inlet could be less complicated and lighter. Multiple compression surfaces complicate the inlet design and always compound the off-design operation; however, high total pressure recovery at speeds greater than Mach = 2.3 require a multiple shock wave system. Appendix Figs. E.6, E.7, E.8, and E.9 can be used to select the cone or ramp angles to give desired total pressure recovery schedules. The fixed vs variable geometry question depends a lot on the matching of the supply to the demand airflow. These inlets should have boundary layer bleed control according to the schedule in Fig. 15.11 and the inlet supply must account for this. These inlets should also have provision for bypass because bypass is used not only for airflow matching, but for reduction of spillage drag and internal shock control as well.

Once the compression surfaces and angles are selected, the inlet supply capture area ratio  $A_{\infty I}/A_c$  as a function of Mach number is determined and compared with the engine demand capture area ratio  $A_{\infty E}/A_c$  (see Fig. 15.16 in Section 15.8).

This comparison readily illustrates the spillage and bypass requirements. The designer might choose to fine tune his inlet at this point to minimize the excess air schedule.

The throat area should be checked to insure that it is adequate to pass the supply air at all flight conditions. The *mass flow parameter* (MFP) of Appendix C is a useful parameter to make this quick check.

The subsonic diffuser must decelerate the flow to a Mach number  $\sim 0.4$  at the compressor face with minimum distortion and turbulence. This means a diverging duct with gentle bends. The ratio of the area at the diffuser exit to the throat area is given by

$$\frac{A_{\text{exit}}}{A_T} = \frac{\left(A/A^*\right)_{\text{exit}}}{\left(A/A^*\right)_T} \quad (15.3)$$

where both  $A/A^*$  are functions of the Mach numbers at the diffuser exit and throat, and they are determined from Appendix C. Usually  $A_T$  and  $M_T$  are fixed and  $A_{\text{exit}}$  is the area of the engine compressor face so that Eq. (15.3) can be used to find the Mach number at the compressor face.

The subsonic diffuser length  $L_D$  is usually determined by constraints imposed by acceptable locations for the inlet and engine on the vehicle. The necessity for locating the inlet in a favorable flow field and the engine at a good position for exhaust discharge or for favorable balancing of the vehicle will usually dictate the duct length. Figure 15.4 can be used to help select the subsonic diffuser length for good pressure recovery. A good rule of thumb is to keep the diffuser overall included expansion angle  $2\theta_D$  (see Fig. 15.3b) less than 10 deg [5]. There should be a short section of zero slope of one to three throat radii leading into the compressor to permit the flow to stabilize and even out the discharge velocity profile.

Figure 15.13 shows a few of the many inlet designs available to the propulsion engineer. Each aircraft has its own set of operating characteristics and the inlets are tailored to fit these “personalities.” For fixed-geometry subsonic operation it is hard to beat the axisymmetric pitot inlet for weight and performance. Most subsonic aircraft use the axisymmetric inlet in one form or another.

The variable-geometry features of the two-dimensional inlet are less complicated than on an axisymmetric inlet and have led to its selection on such supersonic aircraft as the Anglo-French Concorde, Soviet TU-144, B-1, MIG-23, RA5C, and F-15. Underwing location on the Concorde (Fig. 15.13b is a typical installation), the B-1 (Fig. 7.15), and the F-15 provides precompression and permits smaller capture areas than if the inlet were exposed to the freestream. Flow deflection by the wing also reduces the inflow angles at angle-of-attack.

Axisymmetric inlets have the advantage of efficient structural shape for low duct weight and also the lowest wetted area per unit of flow area. However, they require a cone-shaped spike, which presents certain problems. Translating the spike fore and aft to keep the shock-on-lip and collapsing the spike to provide a variable throat area represent design nightmares. The A-12 and SR-71 represent one successful circular inlet. The SR-71 has the inlet canted inboard and pointed down a few degrees to better align the spike with the local flow at cruise angles-of-attack.

The F-16 is not required to operate much past Mach = 1.6 and thus uses the simple, lightweight normal shock inlet mounted in a chin fashion.

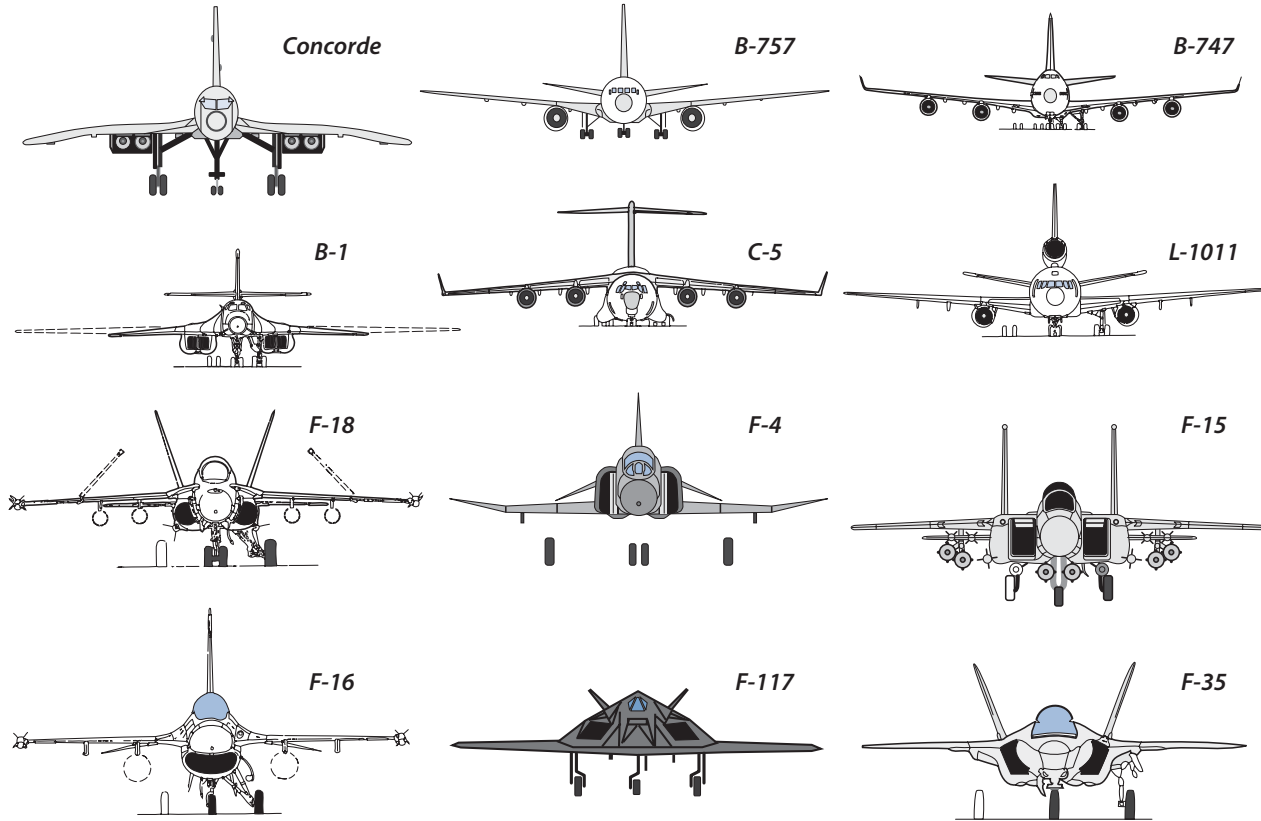
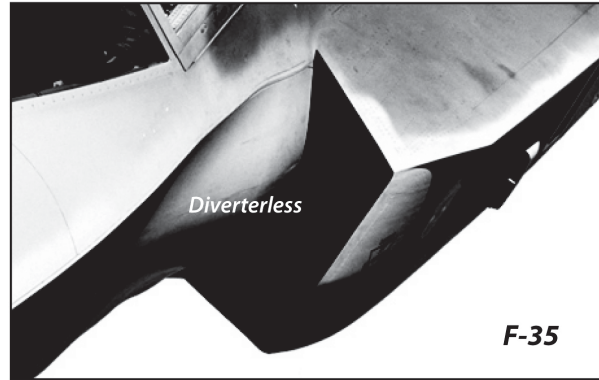
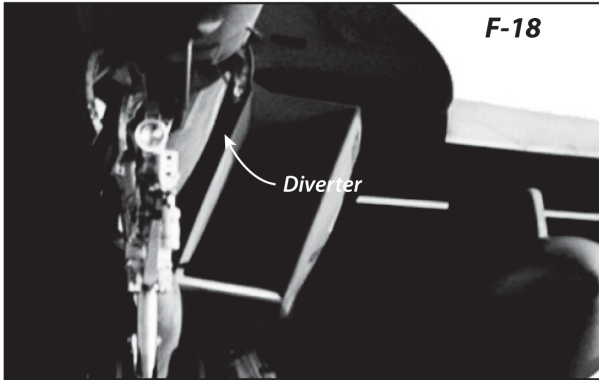
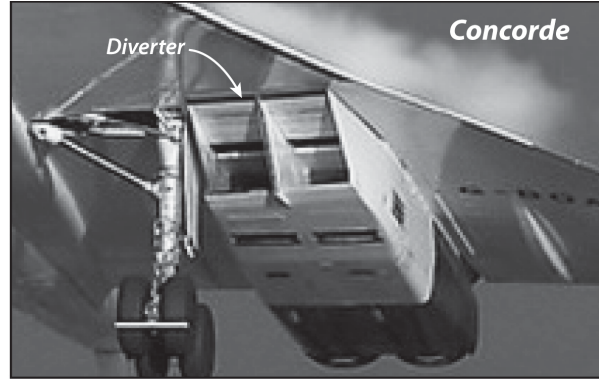
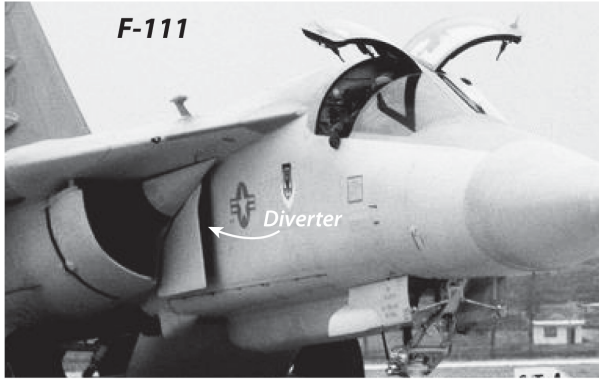


Figure 15.13a Typical inlet designs.





**Figure 15.13b** Inlet design examples.

Half-round inlets fit very nicely along the fuselage side and have been used on several Mach 2 class aircraft in the past. The F-104 uses this inlet design with a fixed half-round spike. The Mirage 3G uses this configuration located well forward on the fuselage. Also, with long, generous ducts, the system has been operating very well with early versions of the TF-30 engine that were a problem for the F-111.

Quarter-round inlets located in the wing–fuselage armpit, as on the F-111 (Fig. 15.13b), have very low external surface area and also low duct weight because of the short distance to the engine. In addition, the location offers some precompression from the wing shock and allows a smaller design capture area. On the F-111, a splitter plate is used to remove boundary layer air built up on the long forward fuselage. A pie-shaped subinlet is used to remove splitter plate boundary layer. Another pie inlet is used to remove boundary layer from the wing glove. In addition, bleed holes are used on the cone surface. Variable geometry includes both a variable second cone angle (diameter) and translation of the whole cone (fore and aft). As in all cone-type inlets, the cone cannot collapse enough to provide large subsonic flow area. This, plus the fact that the capture area was sized small initially, required the F-111 to employ large suck-in doors at low speed. Downstream of the throat the short subsonic diffuser makes an appreciable turn inboard to the engine. Due to its location, the inlet is sensitive to angle-of-attack as the boundary layer builds up between the fuselage and wing glove. The F-111 was plagued with engine–inlet problems during its flight test and motivated a great deal of activity in inlet distortion and turbulence research during the mid 1960s.

Many versions of the “D” inlet have been used successfully on Mach 2 class aircraft. The J-79-powered F-4 uses a “D” inlet with variable-geometry compression ramps. A slight downward tilt provides better flow alignment at angles of attack.

### **Example 15.1 External Compression Inlet for $M_D = 2.3$**

The sizing and design of a two-dimensional external compression inlet for the PW-F-100 turbofan engine is demonstrated. The design Mach number will be Mach = 2.3 at 30,000 ft. This example is representative of the inlet on the F-15.

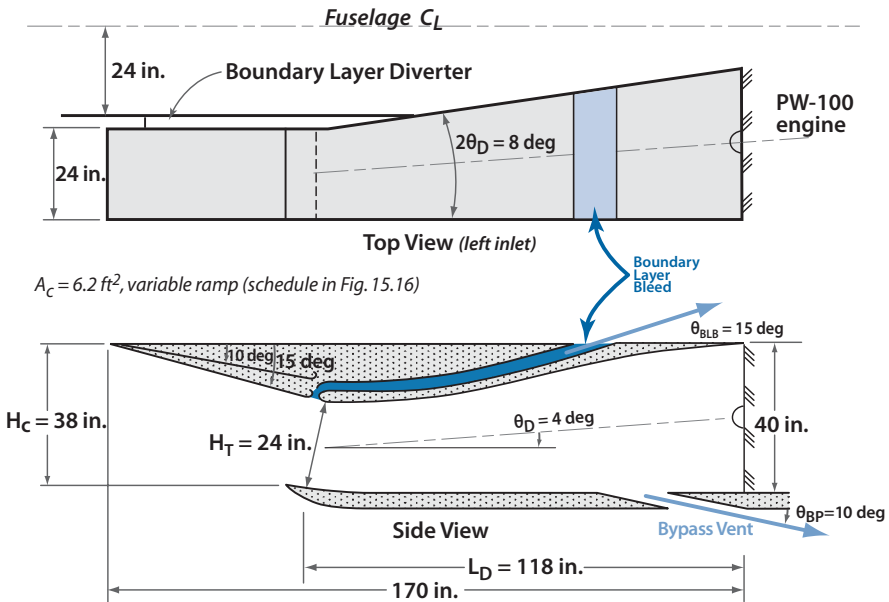
Table 15.2 presents the total pressure recovery data for the Mach 2.3 external compression inlet shown in Fig. 15.14. Notice that this two-dimensional inlet has a detached normal shock from Mach 1.0 to 1.5. Notice also that this inlet design has a short subsonic diffuser ( $L_D/H_T = 4.9$ ) and the resulting diffuser losses are as large as the losses across the shock wave system at most supersonic Mach numbers. This was a design compromise to give a lightweight (short) and reasonably efficient inlet at the design Mach number.

**Table 15.2** Total Pressure Recovery Data for Inlet in Fig. 15.14

$M_\infty$	$M_T$	$P_{0I}/P_{0\infty}$ <sup>(a)</sup>	$P_{0T}/P_{0I}$ <sup>(b)</sup>	$P_{0C}/P_{0T}$ <sup>(c)</sup>	$P_{0C}/P_{0\infty}$
0.4	0.4			0.99	0.99
0.6	0.6			0.977	0.977
0.8	0.8			0.955	0.955
1.0	1.0		1.0	0.925	0.925
1.2	0.84		0.993	0.905	0.90
1.4	0.74		0.958	0.927	0.89
1.6	0.91	0.972	0.999	0.875	0.85
1.8	0.81	0.958	0.986	0.91	0.86
2.0	0.72	0.953	0.942	0.933	0.84
2.3	0.63	0.942	0.84	0.957	0.76

<sup>a</sup>Across oblique shock.  
<sup>b</sup>Across normal shock.  
<sup>c</sup>Across subsonic diffuser.

The assumed trajectory and required engine and secondary airflows (from Fig. 14.8g) are shown in Table 15.3. Using Eq. (15.2) the  $A_{\infty E}$  is determined. The required engine capture area  $A_{\infty E}$  at  $M_D = 2.3$  is 5.92 ft<sup>2</sup>. The recommended bleed from Fig. 15.11 is 4%, which makes the design cowl area  $A_c = 6.2$  ft<sup>2</sup>. The demand capture area



**Figure 15.14** Mach = 2.3 two-dimensional external compression inlet.

**Table 15.3** Demand Capture Area for PW-F-100 Engine

		$\dot{m}_E + \dot{m}_S$	$A_{\infty E}$	$A_{\infty E}/A_C$
Mach	Altitude (1000 ft)	(lbm/s) <sup>(a)</sup>	(ft <sup>2</sup> )	<sup>(b)</sup>
0.25	2	205	10.9	1.76
0.5	4	220	5.9	0.95
0.75	5	245	4.53	0.73
1.0	30	130	4.56	0.74
1.2	30	154	4.53	0.734
1.4	30	183	4.62	0.749
1.6	30	217	4.76	0.77
1.8	30	257	5.01	0.81
2.0	30	300	5.26	0.853
2.3	30	388	5.92	0.96

<sup>a</sup> $\dot{m}_E$  and  $\dot{m}_S$  at maximum power from Fig. 14.8g and Table 15.1.

<sup>b</sup>Selected  $A_C = 6.2 \text{ ft}^2$ .

ratio  $A_{\infty}/A_C$  is plotted in Fig. 15.16 later in this section. The inlet will have auxiliary takeoff doors to augment the inlet area at takeoff.

The philosophy behind the inlet design, shown in Fig. 15.14, is a lightweight, low-cost inlet giving reasonably good efficiency at a maximum speed of Mach = 2.3. The primary mission of the aircraft is air superiority (similar to the F-15 Eagle), thus it is important that the inlet and engine be well matched in the transonic combat arena (Mach = 0.7–1.2 and 10,000–30,000 ft). The aircraft is designed around two PW-F-100 engines. The two-dimensional, single-ramp, external compression inlet shown in Fig. 15.14 was selected. The single ramp angle of 15 deg at Mach = 2.3 is a little on the high side for good pressure recovery; however, it gives a short inlet for shock-on-lip operation at this Mach number. The pressure recovery characteristics are shown in Table 15.2 and Fig. 15.15. The inlet features a variable ramp according to the schedule shown in Fig. 15.16. This ramp schedule was selected to keep the excess air during maximum power operation to a minimum. For Mach > 1.1 the excess air will be bypassed. Notice that the Mach = 2.3 pressure recovery is 75%, which is comparable with the 78% recovery for the SR-71 at Mach = 3.2.

The inlet supply capture area ratio is shown in Fig. 15.16 and provides a good match for the engine demand during maximum power operation. The maximum bypass requirement (for maximum power operation) above Mach = 1.1 is only 4% and this sized the spill vents

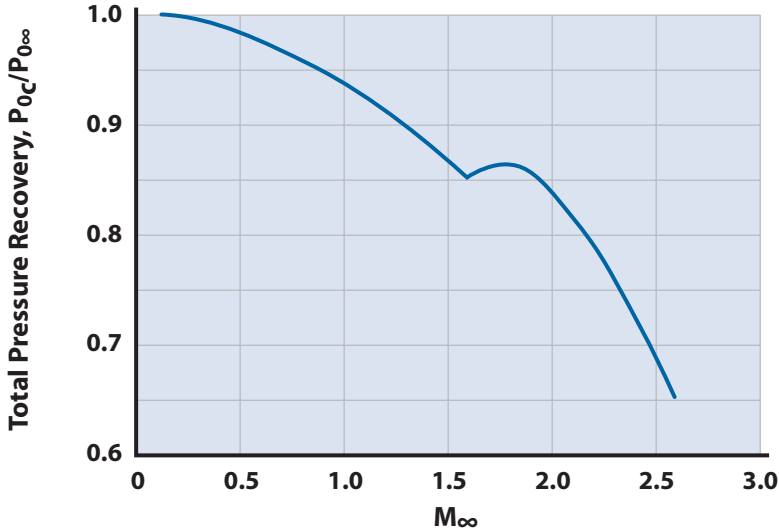


Figure 15.15 Total pressure recovery for inlet of Fig. 15.14.

(see Section 16.8). During cruise at Mach = 0.9, the required thrust is 70% of NRT which means the airflow requirement is approximately 70% [see Eq. (18.2)]. This cruise demand point at Mach = 0.9 is shown in Fig. 15.16 and indicates a spillage of about 27% of the supplied air.

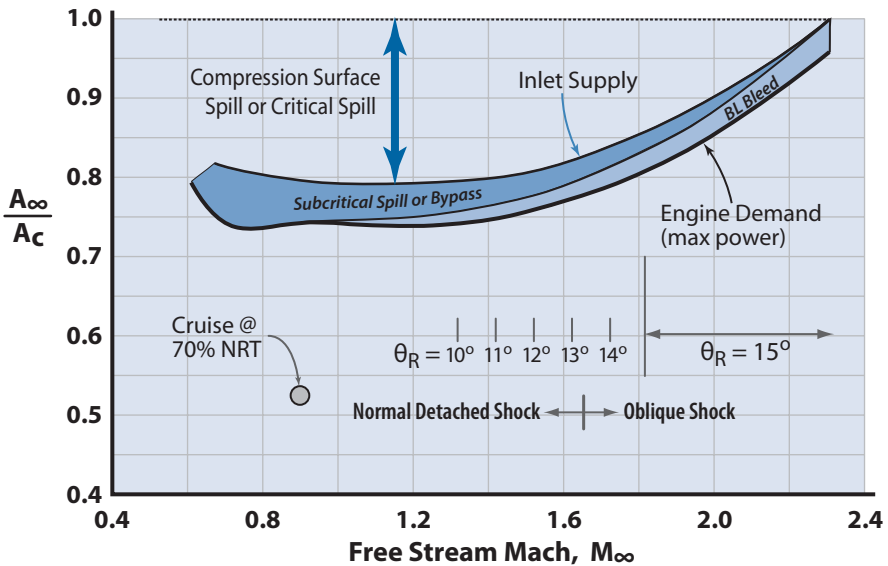


Figure 15.16 Engine-inlet flow matching for inlet of Fig. 15.14 and PW-F-100 engine.

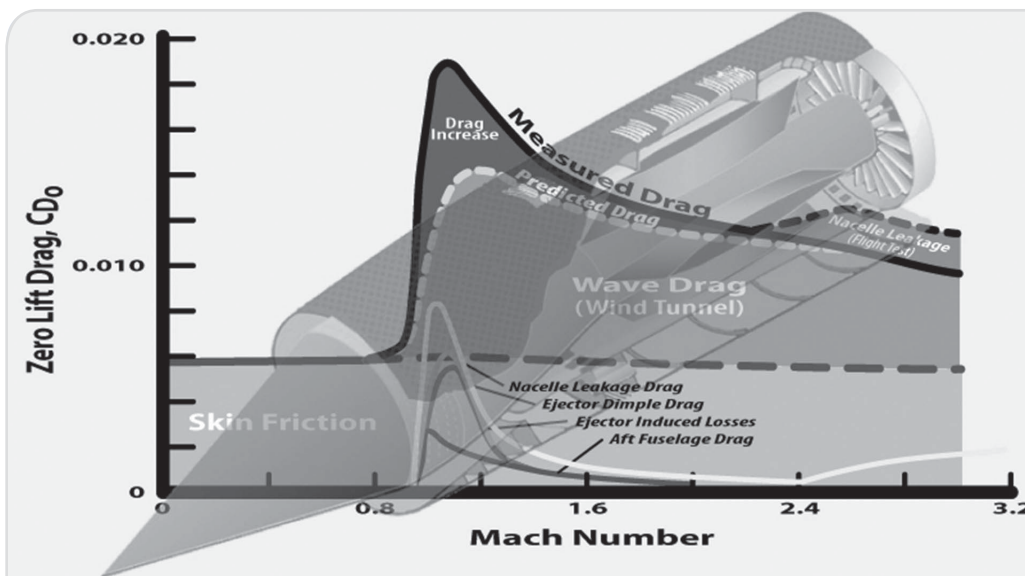
Fortunately, this is a subsonic spill and not too costly in terms of spillage drag (discussed in Chapter 16). This mismatch could have been relieved somewhat by a hinged cowl lip that would decrease the capture area at this cruise condition, but this feature would add weight and complexity (cost) and was not felt to be justified.

The subsonic diffuser was designed to be as short as possible (included diffuser angle  $2\theta_D$  of 8 deg for both side and top views) but still give tolerable pressure recovery and distortion levels. The subsonic diffuser total pressure recovery is lower than normal (see Table 15.2) due mainly to the high throat Mach numbers and the low diffuser length to height ratio,  $L_D/H_T = 4.9$ .

## References

- [1] Liepmann, H. W., and Roshko, A., *Elements of Gasdynamics*, Wiley, New York, 1957.
- [2] Ball, W. H., "Propulsion System Installation Corrections," U.S. Air Force Flight Dynamics Laboratory, AFFDL-TR-72-147, Wright-Patterson AFB, OH, Dec. 1972.
- [3] Urie, D., "Lockheed SR-71, a Supersonic/Hypersonic Research Facility," Lockheed Rept. SR-71-949, Lockheed Advanced Development Co., 1989.
- [4] Henshaw, J. T., *Supersonic Engineering*, Wiley, New York, 1962.
- [5] Crosthwait, E. L., Kennon, I. G., and Roland, H. L., "Preliminary Design Methodology for Air-Induction Systems," Technical Rept. SEG-TR-67-1, Wright-Patterson AFB, OH, Jan. 1967.
- [6] Antonatos, P. P., Surber, L. E., and Stava, D. J., "Inlet/Airplane Interference and Integration," AGARD Rept. LS-53, NASA, Report Distribution and Storage Unit, Langley Field, VA, May 1972.

## Chapter 16

Corrections for  
Turbine Engine  
Installation

- Total Pressure Recovery
- Additive or Spillage Drag
- Boundary Layer Diverter Drag
- Boundary Layer Bleed Drag
- Exit Flap Drag
- Bypass Drag
- Boattail Drag
- Nozzle Types

Flight test of the SR-71 revealed a higher transonic  $C_{D0}$  than predicted. Further testing showed this to be due to nacelle leakage, ejector-induced losses, ejector dimple drag, and aft fuselage drag. As a result the SR-71 routinely went into a dive maneuver to accelerate past Mach = 1.0.

*Those who ignore the mistakes of the past  
are destined to repeat them.*

## 16.1 Introduction

The engine thrust data provided by the engine manufacturer is termed *uninstalled* thrust. This uninstalled thrust data must now be corrected by the designer for airframe–engine integration effects.

These corrections to the propulsion system data are of three types:

1. **Installed engine thrust corrections.** Effects of inlet recovery and distortion, internal nozzle performance, engine bleed, and power extraction
2. **Inlet drag.** Effects of additive drag, cowl drag, boundary layer bleed drag, bypass drag, and boundary layer diverter drag
3. **Nozzle–afterbody drag.** Effects of nozzle–afterbody interference drag

## 16.2 Total Pressure Recovery

The *inlet* supplies air to the engine at a certain total pressure recovery schedule, and this schedule is very dependent upon the airframe–inlet design and flight condition. The engine manufacturer determines the thrust of the engine based upon a reference recovery schedule  $(P_{0c}/P_{0\infty})_{\text{Ref}}$ . There will be a percentage difference in the net thrust if the designer's inlet does not provide the same ram recovery schedule as that used by the manufacturer. The correction is

$$\text{Percent reduction in thrust} = C_R \left[ \left( \frac{P_{0c}}{P_{0\infty}} \right)_{\text{Ref}} - \left( \frac{P_{0c}}{P_{0\infty}} \right)_{\text{Design}} \right] \quad (16.1)$$

where  $C_R$  is the *ram recovery correction factor* and is a function of engine type, power setting, Mach number, altitude, and temperature conditions (i.e., cold, standard, or hot day). Figure 16.1 shows some typical data for standard day, maximum power operation at 45,000 ft [1]. Figure 16.1 is recommended for values of  $C_R$  at this point in the design.

The engine manufacturer's *reference ram recovery*  $(P_{0c}/P_{0\infty})_{\text{Ref}}$  should be reported in the engine data. Sometimes the engine manufacturer will use a constant recovery schedule of 1.0. Engine data supplied for military application will usually be based upon a standard military specification total pressure recovery schedule (MIL-E-5008B Ram Recovery is shown in Fig. 16.2).



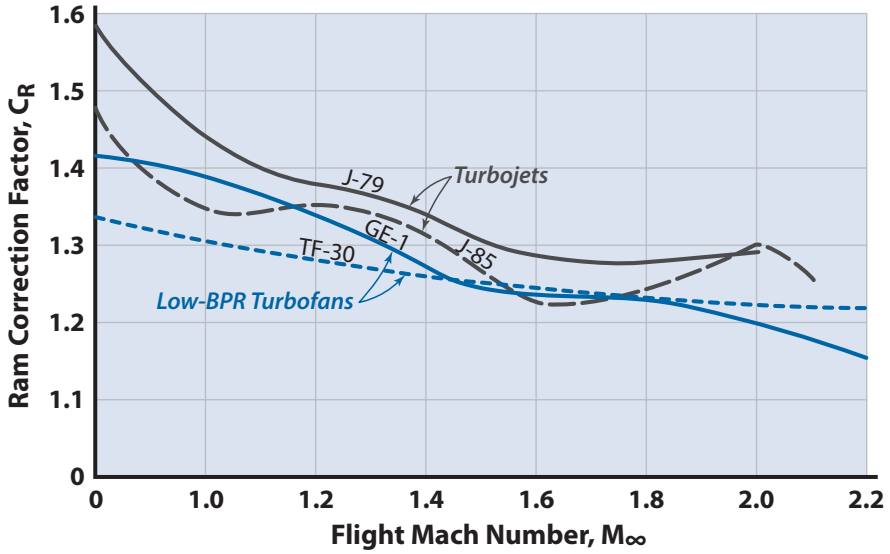


Figure 16.1 Ram correction factor for net thrust (data from [1]).

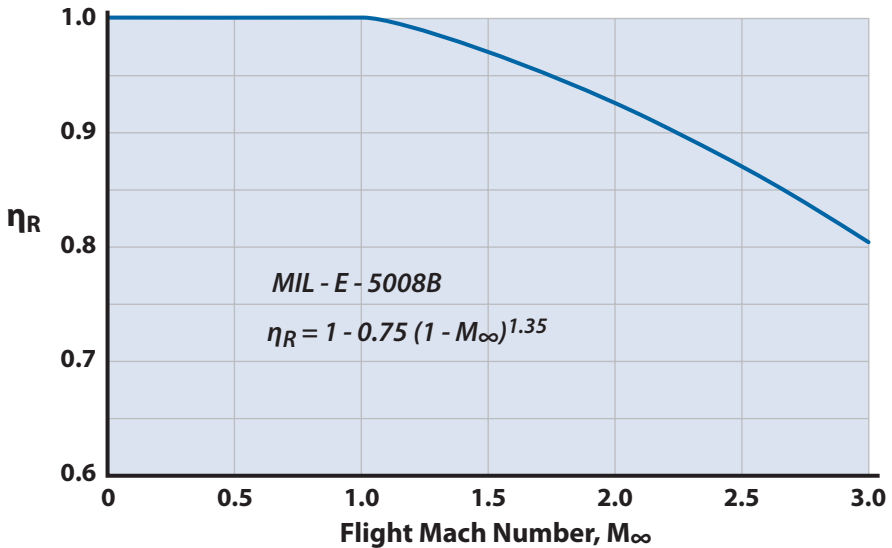


Figure 16.2 Mil-Spec total pressure recovery schedule.

### 16.3 Engine Bleed Requirements

*Airbleed* requirements (i.e., environmental control system, anti-icing, boundary layer control, etc.) from the engine compressor will reduce the thrust from the engine. This thrust reduction is estimated from

$$\text{Percent reduction in thrust} = C_B \left( \frac{\dot{m}_B}{\dot{m}_E} \right) \quad (16.2)$$

where  $\dot{m}_B$  is the bleed mass flow from the engine and  $\dot{m}_E$  is the engine demand mass flow. The bleed correction factor  $C_B$  may be assumed to be equal to 2.0 for design purposes. This bleed requirement is not to be confused with the secondary airflow requirement  $\dot{m}_S$  discussed in Section 15.7 (Table 15.1). The engine bleed  $\dot{m}_B$  seldom exceeds 5% as it has a significant effect on thrust.

### 16.4 Inlet Flow Distortion

*Inlet flow distortion* is actually a velocity distortion, but it has typically been expressed in terms of total pressure variations for the sake of simplicity. The most apparent effect of flow distortion on a turbine engine is a downward shift of the engine surge line [2]. This shift is due primarily to the fact that many of the compressor blades are operating closer to stall in the distorted flow. If the distortion is sufficient to alter the blades' effective angles-of-attack, operating line efficiency will be changed so that the distortion results in a shift along the engine operation line to a lower operating pressure. If surge margin loss due to flow distortion is greater than anticipated, the engine may have to be derated to allow sufficient margin for engine transients. The primary effect of inlet turbulence is to drop the surge line even closer to the operating line [1,2].

### 16.5 Inlet Drag

*Inlet drag* is usually defined as all drag associated with the captured streamtube of air and its variations with engine demand and/or aircraft operating conditions. The inlet drag is the responsibility of the propulsion group. The Chief Designer must check the drag bookkeeping to ensure that together the airframe and propulsion groups account for all of the aircraft drag and don't double bookkeep.

The elements of the inlet drag are shown in Fig. 16.3. *Additive drag* is the momentum loss of the streamtube of air defined by the capture area  $A_c$  that is diverted around the inlet. Some of this lost momentum may be recovered in lip suction as the diverted flow accelerates over the cowl, cre-

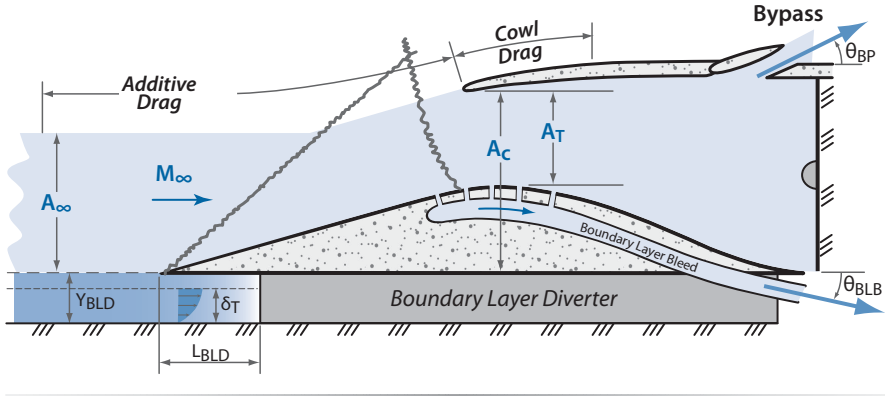


Figure 16.3 Elements of inlet drag.

ating a low-pressure region that acts in the thrust direction. Thus, as is shown later, cowl drag is not really a drag but a thrust force instead. The skin friction drag over the remainder of the inlet external surface, nacelle, or fuselage section is not charged as inlet drag but rather airframe drag, and the airframe group must account for it.

*Boundary layer bleed (BLB) drag* and *bypass drag* are defined as (1) combination of momentum lost by these flows from the time they are taken into the inlet until they exit the aircraft, and (2) the exit door pressure drags. *Boundary layer diverter drag* (usually included in inlet drag, but make sure someone accounts for it) is the momentum lost in the boundary layer that is turned away by the boundary layer diverter.

These drag elements will be discussed in the sections that follow. Methodology will be presented for estimating these inlet drag elements and in all cases the drag coefficients will be referenced to the cowl area  $A_c$ .

## 16.6 Additive (or Spillage) Drag

Additive drag is the momentum loss of the streamtube of air that is diverted around the inlet. For several reasons, not all of the air captured by the cowl (represented by  $A_c$ ) can enter the inlet and the extra air is diverted over the cowl lip. These several reasons are the presence of a compression surface and the engine airflow demand being less than the inlet supply. The air being diverted around the inlet can be thought of as being “spilled” and thus additive drag is often called *spillage drag*. Additive drag occurs any time  $A_\infty/A_c < 1.0$ .

Additive or spillage drag is made up of two parts as shown in Fig. 15.16. The first part is called *compression surface spill* or *critical spill* and is due to the physical turning (or deflection) of the flow streamlines by a compres-

sion surface [Fig. 15.7b]; the spilled air involved is the difference in airflow between  $A_c$  and  $A_{\infty}$ . This first part of additive drag is always accompanied by critical or supercritical inlet operation at supersonic Mach numbers.

The second part is called *subcritical spill* and is due to the excess air in the inlet (difference between inlet supply and engine demand) backing up and spilling around the lip as shown in Fig. 15.7a. It should be understood that if all of this excess air in the inlet is bypassed, then the subcritical spillage drag is zero. Thus, the designer can choose to trade off bypass drag for subcritical spillage drag. Subcritical spill is also accompanied by a decrease in pressure recovery as shown in Fig. 15.8.

For capture area ratios  $A_{\infty}/A_c$  much less than 1, the additive or spillage drag can be appreciable, easily amounting to 20% of the airplane drag. Fortunately in practice this entire penalty is seldom experienced. Proper contouring of the external cowl lip can result in appreciable lip suction effects due to the increased velocities and decreasing pressures on the forward portions of the cowl lip. The magnitude of the lip suction effects can result in the cancellation at subsonic and transonic speeds of up to 80% of the additive drag for subsonic inlets and up to 50% for supersonic inlets [1].

There are several methods to correct the additive drag for cowl lip suction. Reference [3] expresses the corrected additive drag  $C_{DA}$  as

$$C_{DA} = C_{DAdd} - C_{DLS}$$

where  $C_{DAdd}$  is the theoretical additive drag and  $C_{DLS}$  is the lip-suction term.

The method discussed in this section expresses the corrected additive drag as

$$C_{DA} = C_{DAdd} K_{Add} \quad (16.3)$$

where  $K_{Add}$  is less than 1 and accounts for the cowl effects. The factor  $K_{Add}$  is from experimental data and is shown in Fig. 16.4 (data from [1,3,4]). Figure 16.4 represents a first-order correction for the additive drag. Reference [3] presents a more refined method, accounting for more inlet lip geometry details than Fig. 16.4. Figure 16.4 is recommended for conceptual design and [3] for preliminary design.

Figure 16.5 shows the control volume for the theoretical additive drag analysis, where station infinity ( $\infty$ ) is freestream and station 1 is the entrance to the inlet. The angle  $\lambda$  is the angle of the flow velocity through station 1. The same schematic holds for subsonic flow, and the schematic for a pitot inlet is similar.

The  $A_{\infty}$  is the capture area of the flow streamtube entering the inlet and is expressed as

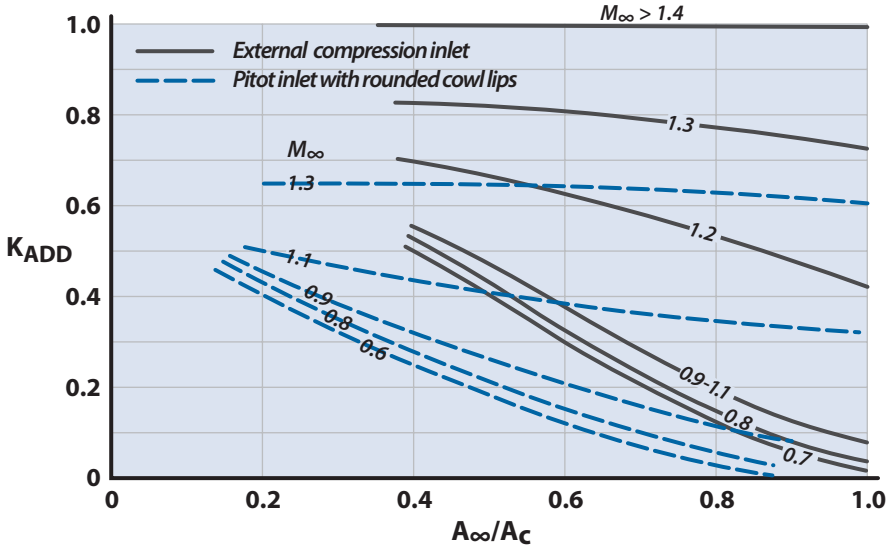


Figure 16.4 Additive drag correction factor for cowl lip suction effects.

$$A_{\infty} = \frac{\dot{m}_E + \dot{m}_{BP} + \dot{m}_{BLB} + \dot{m}_S}{32.17 \rho_{\infty} V_{\infty}} \tag{16.4}$$

where the mass flows in the numerator (in slugs per second) are the engine demand, bypass, boundary layer bleed, and secondary air, respectively. All other airflow is diverted over the inlet lip thus creating additive drag.

The additive drag is the summation of the pressure forces in the drag direction acting on the control volume surface  $BC$  in Fig. 16.5. This drag force, shown as  $D_A$  in Fig. 16.5, is expressed as (using gage pressures)

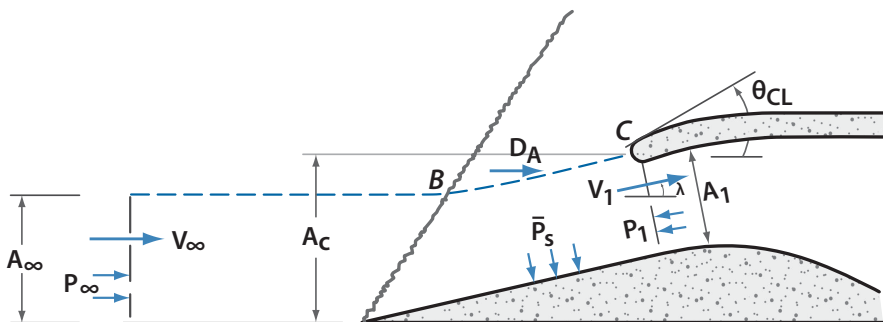


Figure 16.5 Schematic of control volume for additive drag analysis.

$$D_A = -\dot{m}_\infty V_\infty - (P_1 - P_\infty) A_\infty + \dot{m}_\infty V_1 \cos \lambda + (P_1 - P_\infty) A_1 \cos \lambda + (\bar{P}_S - P_\infty) A_S \quad (16.5)$$

where  $\bar{P}_S$  is the average surface pressure on the ramp or conical centerbody and  $A_S$  is the projected area in the drag direction of the ramp or centerbody (equal to zero for a pitot inlet). If there is an angle  $\alpha$  between the inlet centerline and the freestream, then  $D_A$  is multiplied by  $\cos \alpha$ .

The additive drag coefficient is

$$C_{DAdd} = \frac{D_A}{q_\infty A_c} = \left( \frac{P_\infty}{q_\infty} \right) \left( \frac{A_1}{A_c} \right) \cos \lambda \left[ \left( \frac{P_1}{P_\infty} \right) (1 + \gamma M_1^2) - 1 \right] - 2 \left( \frac{A_\infty}{A_c} \right) + \bar{C}_{PS} \left( \frac{A_S}{A_c} \right) \quad (16.6)$$

where

$$\bar{C}_{PS} = \frac{\bar{P}_S - P_\infty}{q_\infty} = \frac{2}{\gamma M_\infty^2} \left( \frac{\bar{P}_S}{P_\infty} - 1 \right) \quad (16.7)$$

Everything in Eq. (16.6) is known or can be determined at this point. If the flow is supersonic and the inlet is operating critically or supercritically (normal shock in throat or downstream of throat), then  $M_1 > 1$ . The  $M_1$  and  $P_1/P_\infty$  for two-dimensional ramp inlets are determined straightforwardly from the external shock structure using Fig. E.2. The  $M_1$  and  $P_1/P_\infty$  for an axisymmetric inlet with a centerbody is not straightforward due to the nonuniform flow region behind a conical shock. The  $M_1$  behind a conical shock wave is determined as follows. Obtain the cone surface Mach number  $M_s$  from Fig. E.5 and the cone shock wave angle  $\beta$  from Fig. E.3. Then determine the value of the Mach number behind an oblique shock having the same shock wave angle  $\beta$  as the conical shock (using Figs. E.1 and E.2). The  $M_1$  behind the conical shock is then estimated to be the average of these two Mach numbers.

$$(M_1)_{\text{cone}} = 0.5 (M_s + M_{1,\text{wedge}})$$

The pressure ratio  $P_1/P_\infty$  for an axisymmetric inlet is determined as follows:

$$\frac{P_1}{P_\infty} = \left( \frac{P_1}{P_{01}} \right) \left( \frac{P_{01}}{P_{0\infty}} \right) \left( \frac{P_{0\infty}}{P_\infty} \right) \quad (16.8)$$

where the static to total pressure ratios are functions of  $M_1$  and  $M_\infty$  (from Appendix C) and the  $P_{01}/P_{0\infty}$  is determined from

$$\left(\frac{P_{01}}{P_{0\infty}}\right) = \left(\frac{P_{0th}}{P_{0\infty}}\right) \left(\frac{P_{01}}{P_{0th}}\right) \quad (16.9)$$

The  $P_{0th}$  is from Figs. E.6 and E.7 and  $P_{01}/P_{0th}$  is the total pressure ratio across a normal shock (from Appendix D) with upstream Mach number  $M_1$ .

If  $M_\infty > 1$  but the shock is detached or the inlet is operating subcritically, then  $M_1 < 1$ . The  $M_1$  is found as follows:

$$(A/A^*)_{M_1} = (A/A^*)_{M_\infty} (A_1/A_c) (P_{01}/P_{0\infty}) (A_c/A_\infty) \quad (16.10)$$

and  $M_1$  is the Mach number for  $(A/A^*)_{M_1}$  as found from Appendix C. The pressure ratio  $P_1/P_\infty$  is found using Eq. (16.8), where

$$\left(\frac{P_{01}}{P_{0\infty}}\right) = \left(\frac{P_{0th}}{P_{0\infty}}\right)$$

For  $M_\infty < 1$  the  $M_1$  is found as follows:

$$\left(\frac{A_\infty}{A_1}\right) = \frac{(A/A^*)_{M_\infty}}{(A/A^*)_{M_1}} \quad (16.11a)$$

or

$$\left(\frac{A}{A^*}\right)_{M_1} = \frac{(A/A^*)_{M_\infty}}{(A_\infty/A_1)} \quad (16.11b)$$

where  $(A/A^*)_{M_\infty}$  is determined for  $M_\infty$  from Appendix C and  $A_\infty/A_1$  is known from geometry. The  $M_1$  is then found as a function of  $(A/A^*)_{M_1}$  from Appendix C. The pressure ratio is

$$P_1/P_\infty = (P_1/P_{01}) / (P_\infty/P_{0\infty}) \quad (16.12)$$

since  $P_{01} = P_{0\infty}$ .

The surface pressure coefficient (averaged for multiple compression surfaces)  $\bar{C}_{p_S}$  is determined from Figs. E.2 and E.10, for a ramp surface, and from Figs. E.4 and E.11, for a conical surface.

The theoretical additive drag coefficient is now determined from Eq. (16.6) and corrected for cowl lip effects using Eq. (16.3) and Fig. 16.4. Reference [3] is recommended for more refined estimates of  $K_{Add}$ . The  $C_D$  is referenced to the cowl area  $A_c$ .

## 16.7 Boundary Layer Bleed Drag

The methodology presented here (from [4]) estimates the drag produced by the removal and disposal of boundary layer air from the inlet. This air is normally removed to ensure satisfactory stability and uniformity of flow at the diffuser exit for good pressure recovery. Figure 15.11 shows recommended boundary layer bleed levels; however, the designer should choose the bleed mass flow after examining the tradeoff between inlet pressure recovery and boundary layer bleed drag.

The *bleed drag* is composed of two parts: (1) the change of momentum of the bleed air between the bleed system entrance and the exit to the freestream (FS), and (2) the pressure drag on the exit flap door.

The following symbols and definitions apply for the methodology:

- $M_\infty$  = freestream Mach numbers
- $M_E$  = Mach number at bleed exit
- $P_{0E}/P_{0\infty}$  = total pressure recovery of bleed airflow FS to bleed exit  
(use Fig. 16.6)
- $\theta_{BLB}$  = exit of bleed air relative to freestream (15 deg or less is desirable)
- $A_{BLB}/A_c$  = boundary layer bleed mass flow ratio (Fig. 15.11)
- $A_E$  = bleed nozzle exit area
- $A_T$  = bleed duct throat area

A bleed exit discharging at a low  $\theta_{BLB}$  into a region of low base pressure is desired. This type of exit will provide the highest exit momentum and will reduce base drag at the same time. A convergent discharge nozzle is satisfactory for nozzle pressure ratios up to about 4. At higher pressure ratios, a convergent–divergent nozzle is desired [3].

The methodology presented here will be for a convergent nozzle. The reader should examine [4] for a convergent–divergent nozzle.

The freestream Mach number that will give choked flow in the bleed duct is determined from



$$(M_\infty)_{Ch} = \left[ \frac{6}{(P_{0E}/P_{0\infty})^{0.286}} - 5 \right]^{1/2} \tag{16.13}$$

where  $P_{0E}/P_{0\infty}$  is determined from Fig. 16.6. Equation (16.13) is plotted in Fig. 16.7.

### 16.7.1 Choked Flow

If  $M_\infty > (M_\infty)_{Ch}$ , the nozzle throat is choked,  $M_E = M_T = 1.0$ , and  $P_E = P_\infty$ . The bleed duct throat area is calculated from

$$A_T = \frac{(A_{BLB}/A_c)A_c}{(A/A^*)_{M_\infty}(P_{0E}/P_{0\infty})} \tag{16.14}$$

where  $(A/A^*)_{M_\infty}$  is determined from Appendix C for  $M_\infty$ . The boundary layer bleed drag coefficient,  $C_{D_{BLB}}$  (referenced to  $A_c$ ) is given by

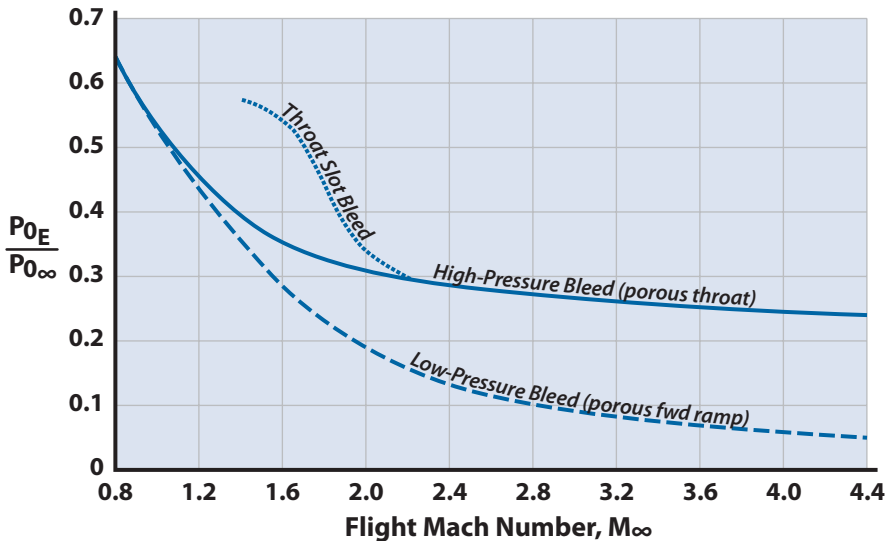


Figure 16.6 Total pressure recovery of bleed airflow (data from [4]).

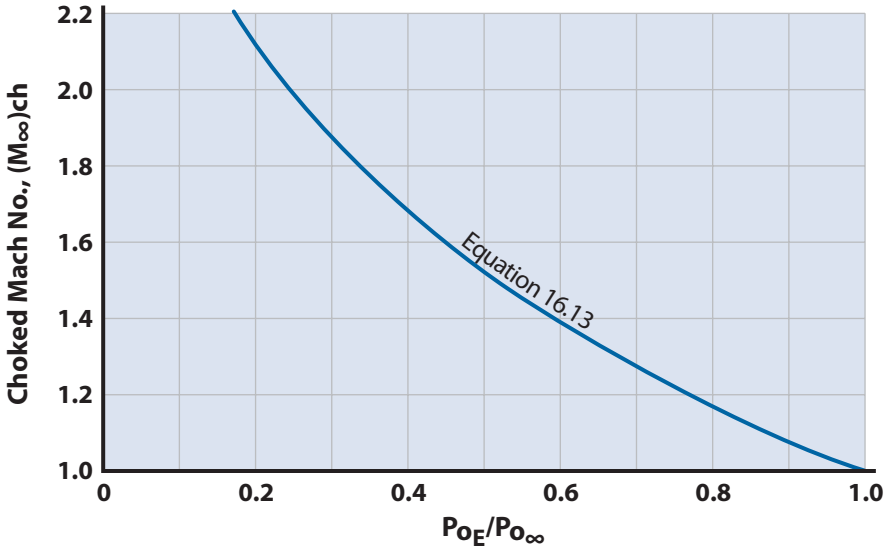


Figure 16.7 Freestream Mach number for choked flow in bleed and bypass ducts.

$$C_{D_{BLB}} = 2 \left( \frac{A_{BLB}}{A_c} \right) \left( 1 - \frac{\cos \theta_{BLB}}{M_\infty} \sqrt{0.833 + 0.167 M_\infty^2} \right) \times \left\{ 1.715 - \left[ \frac{0.715}{(P_{0E}/P_{0\infty})(0.833 + 0.167 M_\infty^2)^{3.5}} \right] \right\} \quad (16.15)$$

### 16.7.2 Unchoked Flow

If  $M_\infty < (M_\infty)_{Ch}$ , the static to total pressure ratio at the duct exit is

$$P_E/P_{0E} = (P_\infty/P_{0\infty}) / (P_{0E}/P_{0\infty}) \quad (16.16)$$

where  $P_\infty/P_{0\infty}$  is determined from Appendix C for  $M_\infty$ .

The Mach number at the exit,  $M_{E^*}$  is determined from Appendix C, corresponding to  $P_E/P_{0E}$ . The duct throat area is given by

$$A_T = \frac{(A_{BLB}/A_c) A_c (A/A^*)_{M_E}}{(A/A^*)_{M_\infty} (P_{0E}/P_{0\infty})} \quad (16.17)$$

where the area ratios  $A/A^*$  are determined from Appendix C for Mach numbers  $M_E$  and  $M_\infty$ . The bleed drag coefficient  $C_{D_{BLB}}$  (referenced to  $A_c$ ) is determined from

$$C_{D_{BLB}} = 2 \left( \frac{A_{BLB}}{A_c} \right) \left( 1 - \cos \theta_{BLB} \left[ \frac{5}{M_\infty^2} + 1 \right]^{1/2} \times \left[ 1 - \frac{1}{(1 + 0.2M_\infty^2)(P_{0E}/P_{0\infty})^{0.286}} \right] \right) \quad (16.18)$$

### 16.7.3 Exit Flap Drag

If there is a flap-type door over the exit of the boundary layer bleed duct, there will be a pressure drag on the flap. This *exit flap drag* can be omitted at this point but should be included later as the design is refined and fine tuned. The method of [4] is recommended. If the exit is a flush-type, there is no flap drag.

## 16.8 Bypass Drag

The methodology presented here (from [4]) estimates the drag of the airflow that enters the inlet but bypasses the engine for airflow matching, reduction of additive drag, or internal shock control.

The *bypass drag* is composed of two parts: (1) the change in momentum of the bypass air between the bypass exit and the freestream, and (2) the pressure drag on the bypass exit flap door.

The methodology for a bypass system with a convergent nozzle is identical to that presented in Section 16.7 for the boundary layer bleed drag, with values for the bypass system substituted for the bleed values. The total pressure recovery for the bypass airflow from freestream to bypass exit is approximated by  $0.85(P_{0c}/P_{0\infty})$ .

## 16.9 Boundary Layer Diverter Drag

The *boundary layer diverter* is a splitter plate arrangement that diverts the boundary layer, built up ahead of the inlet, away from the inlet. The reasons for the boundary layer diverter are discussed in Section 15.5. A boundary layer diverter is shown in Fig. 16.3 and locates the inlet out of the upstream boundary layer. The boundary layer diverter height  $Y_{BLD}$  should be at least twice the local turbulent boundary layer thickness given by

$$\delta_T = \frac{0.37x}{Re_x^{0.2}} \tag{16.19}$$

where  $x$  = distance from fuselage nose or wing leading edge to boundary layer diverter and the local Reynolds number is

$$Re_x = \frac{\rho_\infty V_\infty x}{\mu_\infty} \tag{16.20}$$

The boundary layer diverter is usually a compression ramp surface of flow deflection angle  $\theta_{BLD}$ . The drag of the boundary layer diverter is due primarily to the surface pressure on the compression ramp influenced by the presence of right-angle surfaces. The expression for the boundary layer drag coefficient (referenced to cowl area  $A_c$ ) is expressed as (from [3])

$$C_{DBLD} = (C_{DBLD}/2\theta_{BLD})(2.6\theta_{BLD})(A_{BLD}/A_c) \tag{16.21}$$

where the ratio  $C_{DBLD}/2\theta_{BLD}$  is obtained from Fig. 16.8, and the distance  $L$  in Fig. 16.8 is defined in Fig. 16.3 as  $L_{BLD}$ . The  $\theta_{BLD}$  is the diverter compression ramp angle in degrees and  $A_{BLD}$  is the projected surface area of the boundary layer diverter in the flow direction.

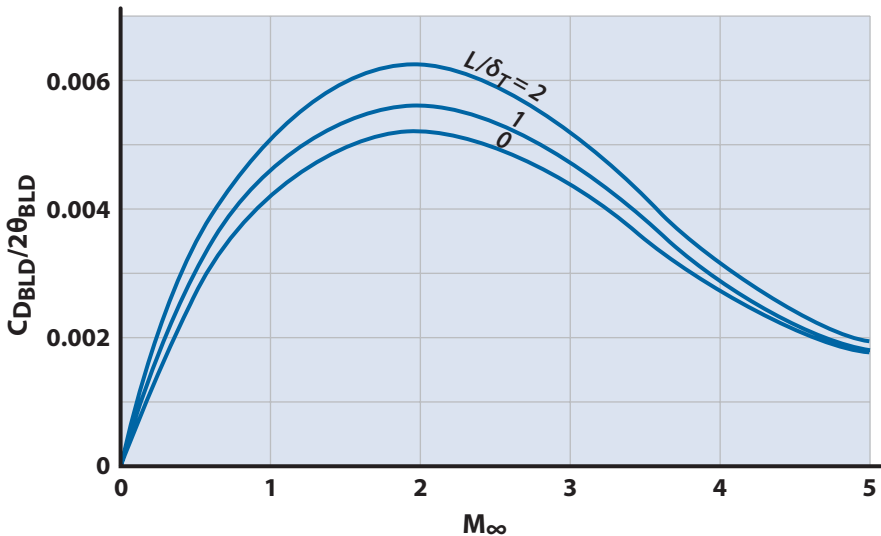


Figure 16.8 Boundary layer diverter drag variation with freestream Mach number.

## 16.10 Nozzle–Airframe Interference Effects

A jet exhausting from a nozzle has two effects on the surrounding flow field and hence the aircraft. First, the jet acts like a solid body (whose size and shape varies with power setting, nozzle setting, Mach number, and altitude) displacing the external flow; second, it normally entrains mass flow from the external stream. The jet contour affects the pressure distribution on the afterbody and nearby surfaces, which, in subsonic flow, transmits a strong upstream influence. In supersonic flight there is a limited upstream influence because any disturbance can only be propagated upstream through the subsonic part of the boundary layer. The shock system within the jet will continue through the jet boundary and may impinge on nearby surfaces. For aircraft configurations with two or more jet engines the mutual interference becomes even more complex. The influence of the elevated temperatures in the jet exhaust is another interference that must be considered but is not discussed here.

Computation methods available today are either not sufficiently accurate or fail completely to predict the complex afterbody flow field [5]. This is particularly true in subsonic flow incorporating boundary layer separation and strong upstream influences. Therefore, aircraft development relies heavily on wind tunnel tests with simulated jets. The aim of such jet effects testing is to obtain information on critical areas of nozzle–airframe interference. As mentioned in Chapter 1, this configuration fine tuning in the wind tunnel is done during the latter part of the preliminary design phase. At this point in the conceptual design phase only the gross features of the nozzle–airframe configuration will be considered.

The primary parameters influencing the nozzle–airframe interference are the nozzle type, the boattail angle, the base area, the nozzle spacing for multiengine aircraft, and the interfairing length between nozzles. The following subsections discuss each of these parameters briefly.

### 16.10.1 Nozzle Types

Figure 16.9 shows typical jet pressure ratios for turbojet and turbofan engines versus flight Mach number (the turbojet is the upper limit of the band). Two extreme engine operating conditions are shown. For cruise in the subsonic flight regime the nozzle pressure ratio is low, requiring little or no divergence. For maximum acceleration, that is, full afterburning, the throat area is increased by a factor of about 2 (depending on bypass ratio).

The required nozzle divergence increases gradually with increasing flight speed and reaches a value of  $A_e/A_t \sim 2.6$  at nozzle pressure ratios of 14.

Besides cruise and maximum acceleration all intermediate operating conditions are possible (military, partial afterburner). This requires in the

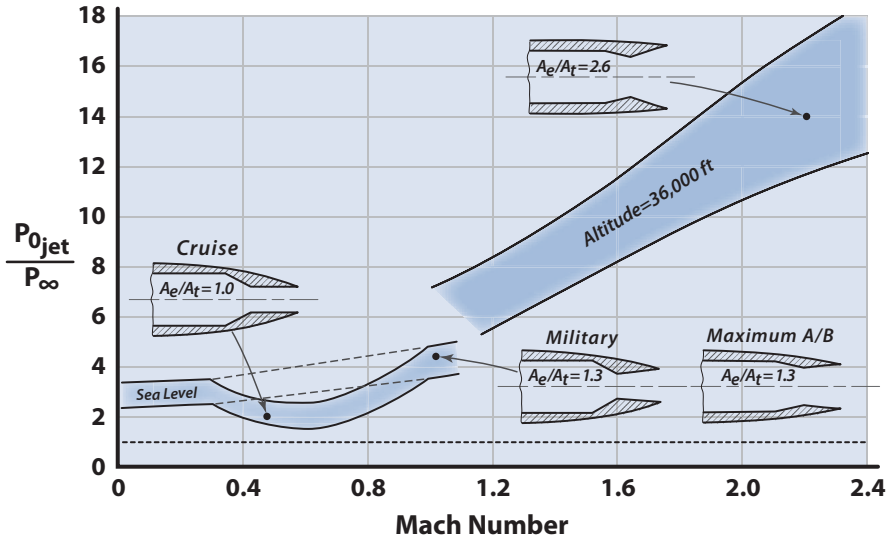
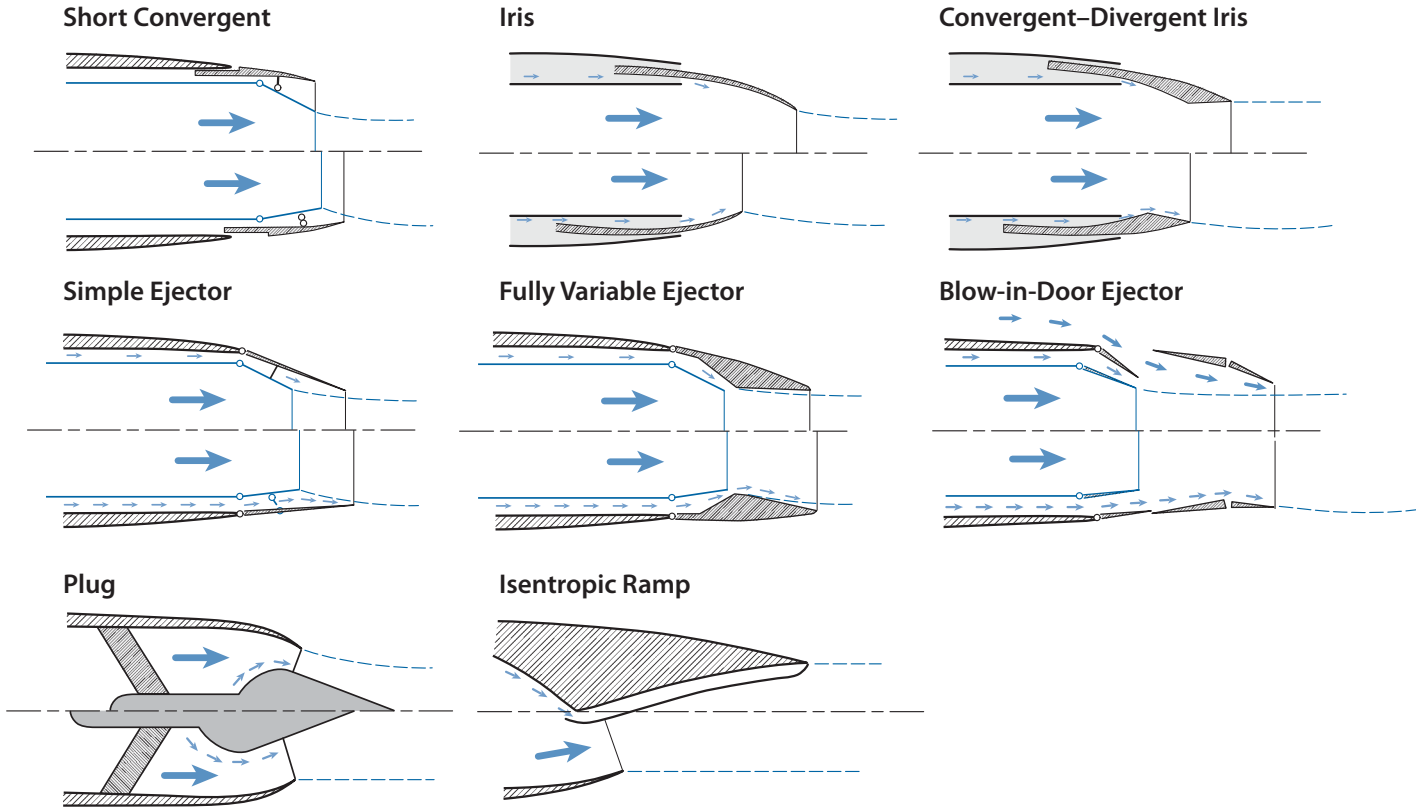


Figure 16.9 Required variation of nozzle geometry (data from [5]).

ideal case a fully variable nozzle with independent variation of throat size and divergence. In many practical cases more simple systems with either purely convergent nozzles or a fixed relation in throat-to-divergence are chosen as a compromise.

Figure 16.10 shows some typical nozzle concepts for afterburning engines. These nozzle types are discussed next (from [5]):

- **Short convergent nozzle.** This concept represents a mechanically simple lightweight nozzle. The major disadvantage from the aerodynamic point of view is the larger base in the closed position.
- **Iris-nozzle.** With the mechanically more complex iris nozzle, annular bases are avoided in all positions. As with the short convergent nozzle, large thrust losses occur at high pressure ratios because no divergence is provided.
- **Plug-nozzle.** The necessary variation in throat area is accomplished by variation of the plug position or geometry. As a consequence, a fixed lightweight shroud can be used. Large cooling air flows, however, are necessary for reheat operation.
- **C–D iris nozzle.** This provides some divergence in the reheat position. The variation in throat size and in divergence is coupled. Thus, the C–D iris is a compromise between the simple iris and a fully variable C–D nozzle.
- **Simple ejector.** This is a frequently chosen nozzle concept. Primary and secondary flaps are mechanically linked. Relatively large secondary airflows are required, associated with drag penalties.



**Figure 16.10** Typical nozzle concepts for afterburning engines (upper half of each sketch denotes dry power; lower half is maximum afterburning) [5].

- **Fully variable ejector.** This design yields near-optimum aerodynamic performance: throat area and divergence are independently variable; the required secondary mass flows can be kept low. High weights and complex design are associated with this nozzle concept.
- **Isentropic ramp.** This design is difficult to adapt to varying operating conditions, which normally results in undesirable changes in pitching moment.
- **Blow-in-door ejector.** This nozzle concept provides similarly good performance as the ordinary ejector in the reheat position. In the closed position, large quantities of tertiary air are taken aboard through spring-loaded flaps in order to fill the large annular base of the short primary nozzle. Large quantities of air, however, require careful handling to avoid losses in the sharp turnings of the secondary and tertiary flow passages. Especially this nozzle represents a highly integrated concept with respect to merging of internal and external flows. Peripheral nonuniformities (blockage) of the external flow may cause unfavorable interferences, which is particularly true with closely spaced twin jet installations.

Table 16.1 gives some incremental afterbody drag data for the nozzle concepts of Fig. 16.10. The drag data were taken from several sources and thus there is some scatter in the data.

### 16.10.2 Boattail Drag

The pressure and skin friction on the afterbody section surrounding the nozzle is called *boattail drag*. The boattail drag coefficient is shown in Fig. 16.11 as a function of Mach number and boattail angle  $\beta$ . For freestream Mach numbers greater than 1.0 the expression for  $C_D$  presented in Fig. 16.11 should be used. This  $C_{D\beta}$  is referenced to the maximum cross-sectional area.

**Table 16.1** Incremental Afterbody Drag

Nozzle Type	$\Delta C_D$
Short convergent	0.036–0.042
Blow-in-door ejector	0.025–0.035
Plug	0.015–0.02
Fully variable ejector	0.01–0.02
Iris	0.01–0.02
Ramp	0.01

$M_\infty = 0.8\text{--}0.9$   
 Nozzle pressure ratios = 2.5–3.0  
 $\Delta C_D$  referenced to fuselage maximum cross-sectional area



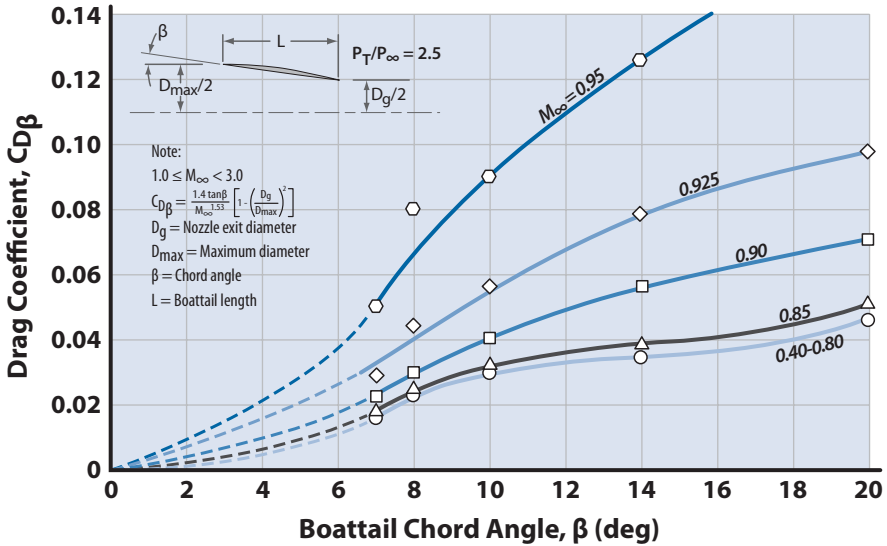


Figure 16.11 Nozzle boattail drag coefficients (data from [4]).

### 16.10.3 Base Area and Multiengine Installation

The designer should avoid any blunt-based areas as these regions result in large drag increases (Figs. 16.12 and 16.13). Figure 16.13 shows this behavior for blunt and tapered interfairings. Also, blunt-based areas upstream

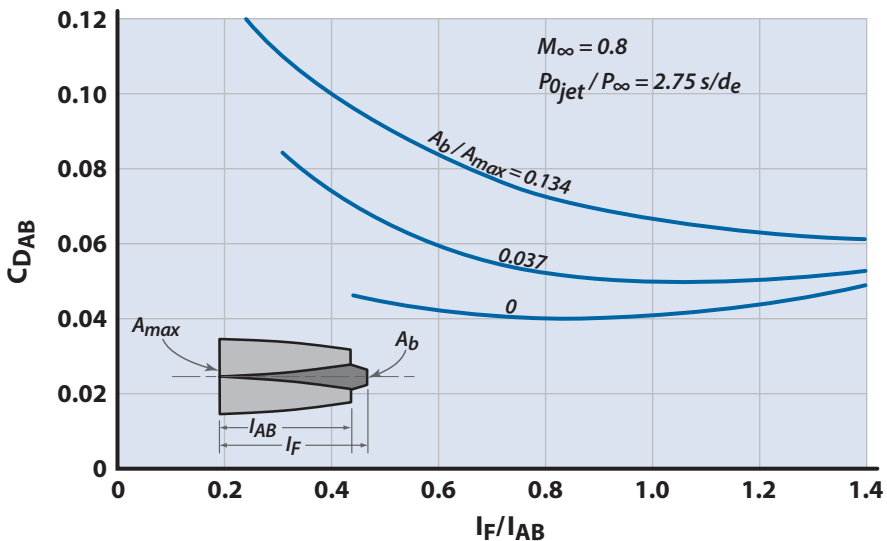
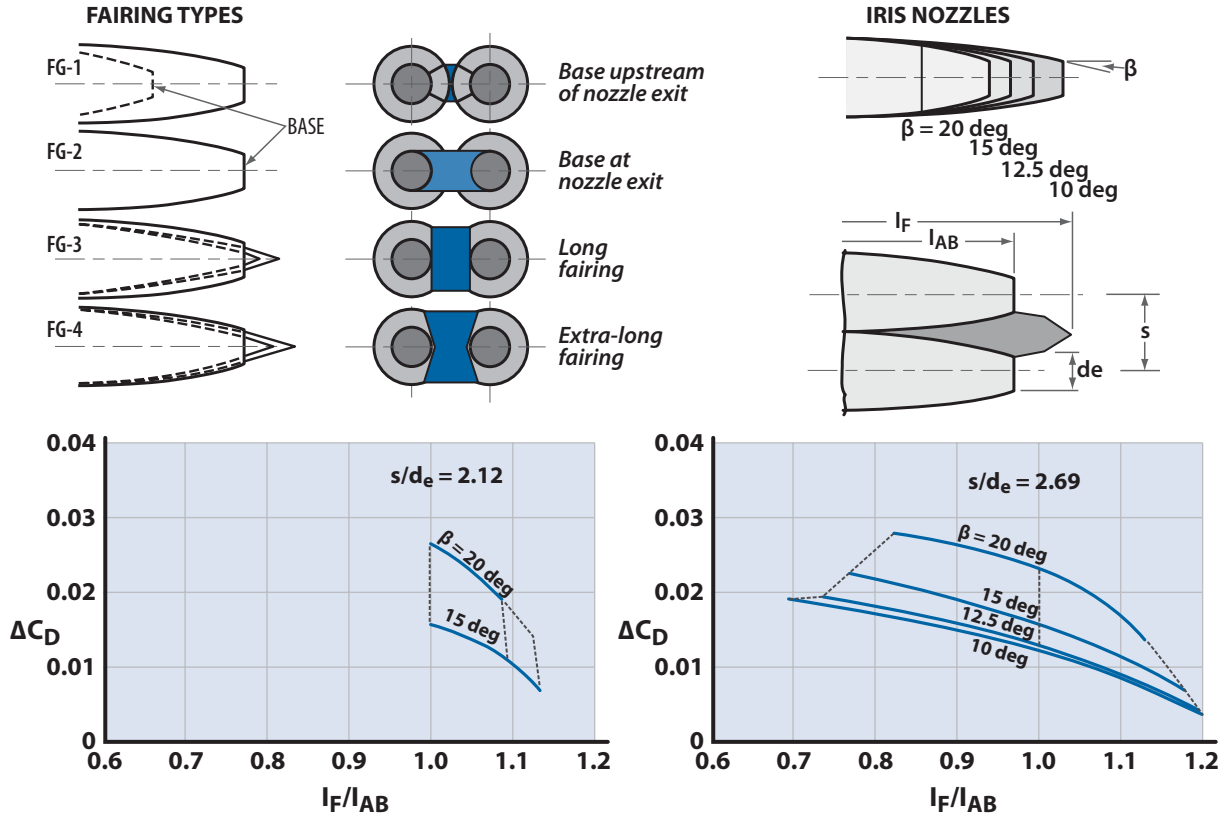


Figure 16.12 Effect of interfairing length on drag for constant-base areas (data from [5]).



**Figure 16.13** Effect of interfairing length on drag for two engine spacings,  $M_\infty = 0.9$  and  $P_{0_{jet}}/P_\infty = 2.5$  (data from [5]).

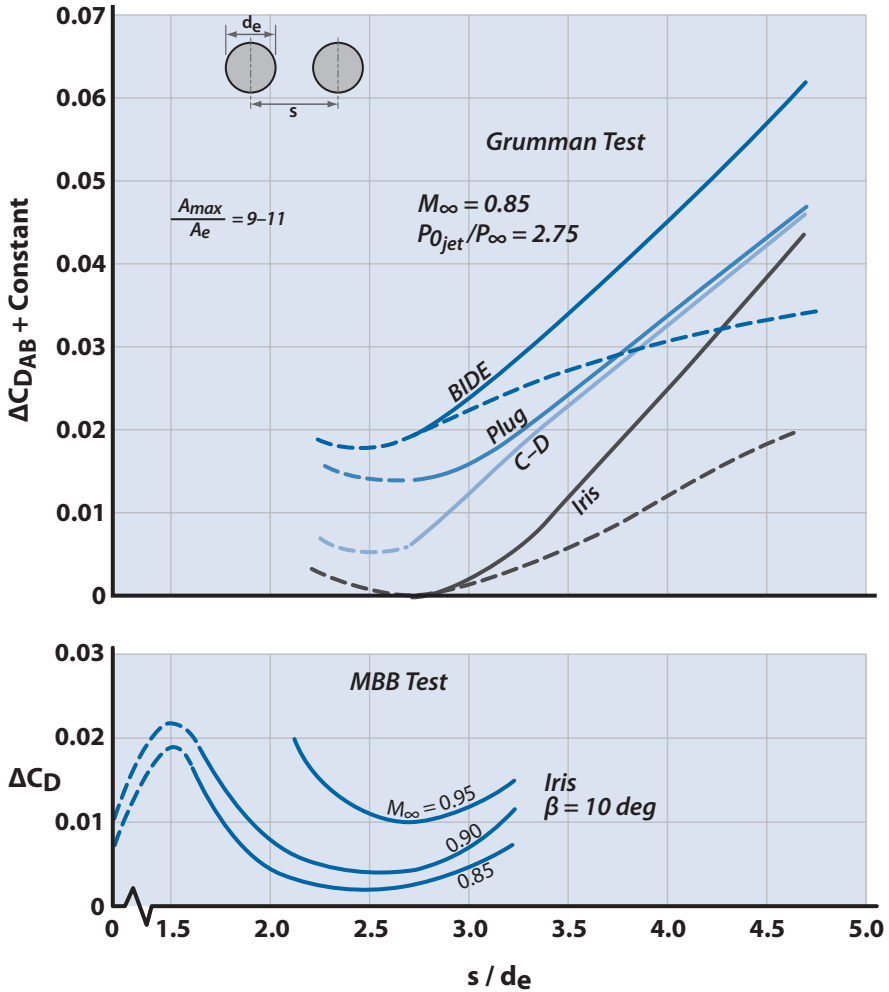


Figure 16.14 Optimization of engine spacing from two different investigations (data from [5]).

of the nozzle exit plane are worse than those downstream as shown in Figs. 16.12 and 16.13 by comparing the  $\Delta C_D$  for configurations FG-1 and FG-2. The drag due to a blunt base can be estimated using Fig. 2.27.

Fuselage-mounted multiengine installations should have a tapered interfairing between the engine nozzles. Figures 16.12 and 16.13 show the effect of interfairing location and length.

Engine nozzle spacing is a design parameter that needs to be negotiated between the configuration (layout) group and the propulsion group. Figure 16.14 shows the effect of engine spacing on  $\Delta C_D$  and indicates an optimum  $s/d_e$  of about 2.5 at high-subsonic speeds. However, this optimum  $s/d_e$

might aggravate some other feature of the design to the extent that a different  $s/d_e$  is warranted. This is another example of the compromise necessary between the design groups that was discussed in Chapter 1.

## *References*

- [1] Antonatos, P. P., Surber, L. E., and Stava, D. J., "Inlet/Airplane Interference and Integration," AGARD Rept. LS-53, NASA, Report Distribution and Storage Unit, Langley Field, VA, May 1972.
- [2] Zonars, D., "Dynamic Characteristics of Engine Inlets," AGARD Rept. LS-53, May 1972.
- [3] Crosthwait, E. L., Kennon, I. G., and Roland, H. L., "Preliminary Design Methodology for Air-Induction Systems," Technical Rept. SEG-TR-67-1, Wright-Patterson AFB, OH, Jan. 1967.
- [4] Ball, W. H., "Propulsion System Installation Corrections," U.S. Air Force Flight Dynamics Laboratory, Technical Rept. AFFDL-TR-72-147, Wright-Patterson AFB, OH, Dec. 1972.
- [5] Aulehla, F. and Lotter, K., "Nozzle/Airframe Interference and Integration," AGARD Rept. LS-53, May 1972.

# Chapter 17

# Propeller Propulsion Systems



- Why Propellers?
- Theories
- Power Coefficient
- Thrust Coefficient
- Advance Ratio
- Activity Factor
- Propulsive Efficiency
- Vendor Propeller Charts

Backdrop for the propeller used on a Wright Brothers 1908 aircraft. A propeller is best described as a rotating wing with all the complexity of aerodynamics, structures, materials, and control. Design pioneers confronted a situation aptly titled "Propellers and Mystery Are Synonymous" in a 1919 aircraft design textbook.

*Propellers and mystery are synonymous.*

## 17.1 Introduction

Despite the great deal of attention and fanfare that has been attached to the design of turbojet and turbofan aircraft since World War II, a large performance regime still exists that can be adequately filled only by propeller-driven aircraft. Certain STOL transport and long-endurance maritime reconnaissance missions lend themselves perfectly to turboprop power schemes, and the high cost of turbine powerplants guarantees that the reciprocating engine will play a major role in general aviation for decades to come. Indeed, one has only to look at the number and dollar value of light aircraft produced annually to realize that the propeller is alive and well in Wichita, Kansas, and in Lock Haven, Pennsylvania. Also, propellers are the only thing that make sense on the slow airships and solar-powered aircraft.

In this chapter we do the following:

- Discuss the theories of propeller performance
- Present a methodology for designing custom propellers
- Discuss the practical use of vendor-supplied propeller charts

## 17.2 Why Propellers?

The *open propeller*, or *airscrew*, offers an efficient means of propulsion in the low- to medium-subsonic speed range. Just as the turbofan engine is generally more efficient than a turbojet of the same thrust, a propeller–turbine engine combination is more efficient than either of them. The reason can be found from a brief look at Newton’s second law in the form that a propulsion engineer would use:

$$T_n = \dot{m}_{\text{air}}(V_e - V_a) \quad (14.2)$$

where, for this analysis, the pressure term is ignored and the resultant force is the thrust of the powerplant. A propeller achieves a specified level of thrust by giving a relatively small acceleration to a relatively large mass of air, whereas the turbofan and the turbojet each give a correspondingly higher acceleration to a correspondingly smaller mass of air. From energy considerations, the powerplant producing the smallest change in kinetic energy will require the smallest expenditure of fuel; thus, the propeller–shaft-engine powerplant provides the highest efficiency of the methods considered.

In 1908 the Wright brothers were conducting flight trials of their latest Wright Flyer design for the Army. The goal of the next flight was to demonstrate one hour at 40 mph with a passenger on board. Orville was the pilot and Lt. Selfridge was the passenger. Well into the flight one of the wooden propellers broke, sending it into the rigging and causing the aircraft to crash. Orville was badly injured but Lt. Selfridge died on the operating table, making him the first crash victim in a powered aircraft. Selfridge AFB in Michigan is named after him.

As will be shown, this argument breaks down at higher flight speeds, where compressibility effects cause additional and unacceptable blade losses.

The propeller offers an additional advantage to the designer of a multi-engine STOL aircraft by bathing large segments of the wing in its high-dynamic-pressure slipstream. This slipstream produces a significant amount of wing lift independently of any freestream dynamic pressure effects and provides an equivalent increase in wing lift coefficient.

High values of takeoff acceleration can be obtained by optimizing propeller design for static thrust conditions. However, this effort to improve STOL capability can only be made by compromising the cruise performance of the aircraft. As was mentioned in Chapter 10, the utilization of reversible-pitch propellers provides the designer with a high deceleration capability at little or no increase in weight or cost.

## 17.3 Theory

The analysis of propeller performance can be accomplished using one or more of the following theories: momentum theory, blade element theory, and vortex theory. Each method has its own distinct advantages as well as shortcomings, yet all play an important role in providing an understanding of airscrew performance. The following discussion is intended to convey a general working knowledge of the pertinent theory, but for deeper insight the reader is directed to [1–6].

### 17.3.1 Momentum Theory

Any aerodynamic propulsive device produces a thrust by imparting a change in momentum flux to a specified mass of air (Newton's second law). The basic momentum theory analyzes the effects of this change in momentum, the work done on the air, and the energy imparted to the air. Certain simplifying assumptions are made about the propeller and its surroundings in the development of this theory that divorce them from the real world, and yet the method remains a useful tool in calculating the maximum theoretical efficiency a propeller can obtain.

The first assumption made by momentum theory is that the propeller is replaced by an infinitesimally thin actuator disk that consists of an infinite number of blades. The disk is held to be uniformly loaded and is thus experiencing uniform flow and imparting a uniform acceleration to the air passing through it.

The actuator disk is further assumed to be surrounded by a sharply delineated streamtube that divides the flow passing through the propeller and the surrounding air. Far upstream and downstream from the disk the

walls of the streamtube are parallel, and the static pressure inside the streamtube at these points is equal to the freestream static pressure.

Momentum theory deals with a working fluid (air in this case) that is inviscid and incompressible. As a consequence, the propeller does not impart any rotation to the air, and any profile losses from the blades of the propeller are ignored.

To an observer moving with the actuator, the air far upstream will be moving with the freestream velocity  $V$  (Fig. 17.1). This air will be gradually accelerated until, at station 1, the actuator disk  $V_1 = V + v$ , where  $v$  is the induced velocity imparted to the air by the actuator. It can be shown at station 2, far downstream from the actuator disk, that  $V_2 = V + 2v$ . The net change in velocity through the control volume defined by the streamtube and planes perpendicular to the flow far upstream and far downstream is

$$(V + 2v) - V = 2v \tag{17.1}$$

and, from continuity considerations for an incompressible fluid,

$$A_1 = A = 2A_2 \tag{17.2}$$

For steady flow the mass flux will be constant across every plane of the streamtube that is perpendicular to the flow. Using the actuator disk as a reference plane,

$$\dot{m} = \rho A (V + v) \tag{17.3}$$

The thrust  $T$  produced by the actuator disk will be

$$T = \Delta \text{Momentum flux}$$

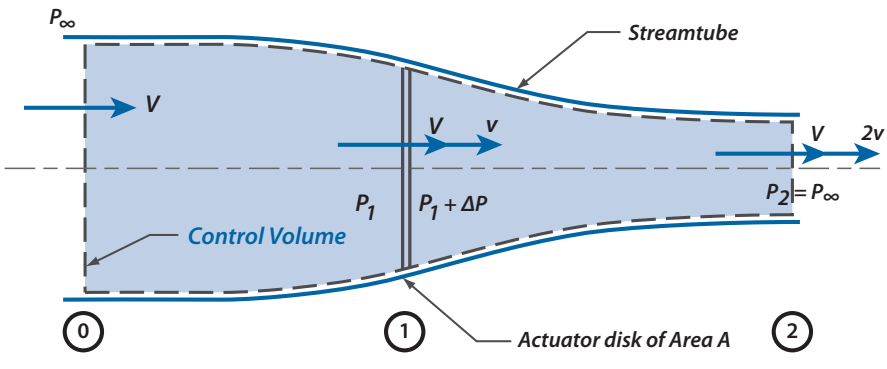


Figure 17.1 Propeller analysis by momentum theory.



$$T = \rho A(V + v)2v \quad (17.4)$$

To produce this level of thrust, the actuator (propeller) must supply energy to the slipstream. Because the theory ignores profile and rotational losses, this energy goes only to increasing the kinetic energy of the flow. The power required for this purpose, the induced power  $P_i$  will equal the change in kinetic energy flux through the control volume and may be shown to be simply the product of the resultant thrust and the velocity at which the thrust is applied, or

$$P_i = T(V + v) \quad (17.5)$$

Equation (17.5) indicates that, to minimize induced power requirements at a given thrust level and freestream velocity, the induced velocity must be kept as small as possible. Solving Eq. (17.4) for  $v$  (and remembering that  $v > 0$  for a propeller) yields

$$V = -\frac{V}{2} + \left( \frac{V^2}{4} + \frac{T}{2\rho A} \right)^{1/2} \quad (17.6)$$

Two important conclusions may be gleaned from this expression. To minimize  $V$  (hence,  $P_i$ ) at given values of  $T$  and  $A$ , the quantity  $T/A$ , the *disk loading*, must be minimized. Thus, within the limits of the assumptions made, it may be stated that the larger the propeller used to produce a given thrust, the smaller will be the power and energy requirements. The second result is that, for a given thrust as the freestream velocity increases, the induced velocity will decrease. This is not to imply, however, that the induced power requirement will decrease. For a given level of thrust,  $V$  will increase faster than  $v$  will decrease, and thus the required  $P_i$  will increase as freestream velocity increases. In practice, however, the thrust of a propeller will not remain constant with changing velocity, but the power of the engine turning it will, over moderate speed ranges, remain fixed. Because profile and rotational losses are being neglected,  $P_{\text{avail}}$  will remain constant and thrust will decrease with increasing velocity. This condition may be illustrated by combining Eqs. (17.5) and (17.6) to form an expression for  $P_i$  as a function of  $T$  and  $V$ . Solving for the static condition ( $V = 0$  as designated by the 0 subscript) and for the condition of  $V \neq 0$ , and assuming that  $P_i$  is constant for all  $V$ , gives

$$\frac{T}{T_0} = \frac{2}{(V/v_0) + \left[ (V/v_0)^2 + 4(T/T_0) \right]^{1/2}} \quad (17.7)$$

Although a general solution of this function  $T/T_0 = f(V/V_0)$  is not possible, the approximation

$$\frac{T}{T_0} \approx 1 - 0.32 \frac{V}{v_0} \quad (17.8)$$

will hold for  $V/v_0 \ll 1$ .

The theoretical power required by the propeller has been defined as the product  $T(V + v)$ . By defining the useful power output of the propeller as  $TV$ , it is possible to form an ideal efficiency

$$\eta_i = \frac{\text{Power Output (Useful Power)}}{\text{Power Input}}$$

$$\eta_i = \frac{TV}{T(V + v)} = \frac{V}{(V + v)} \quad (17.9)$$

Notice that the static ideal efficiency will be zero, but that  $\eta_i$  will increase with  $V$ . This concept of ideal efficiency is misleading for cases where  $V/v < 1$ . The use of the word “ideal” must again be emphasized as no real-world losses are included in its calculation.

The momentum theory does not provide a means to predict propeller losses due to blade skin friction, rotational motion, or mutual blade interference, nor does it account for any geometry parameters other than disk area. Although it is simple to apply, this theory must be combined with some other analytical tool to be of use to the designer.

### 17.3.2 Blade Element Theory

An aircraft propeller is nothing more than an airfoil rotating about a translating axis dividing a propeller blade into a number of chordwise strips. It is possible to analyze the performance of the entire propeller by summing the contributions of all segments on all blades of the airscrew. This is essentially what is done by the *blade element theory* (sometimes called *strip theory*).

In Fig. 17.2 a small element of the propeller blade is marked for consideration. This infinitesimal element is  $dr$  wide, has chord  $c$ , and is located a distance  $r$  from the axis of rotation. The entire blade has a radius of  $R$ . A cross section of the blade element is shown in Fig. 17.3. The airfoil shape can be clearly seen, and many of the angular and velocity notations are analogous to those used in wing theory.

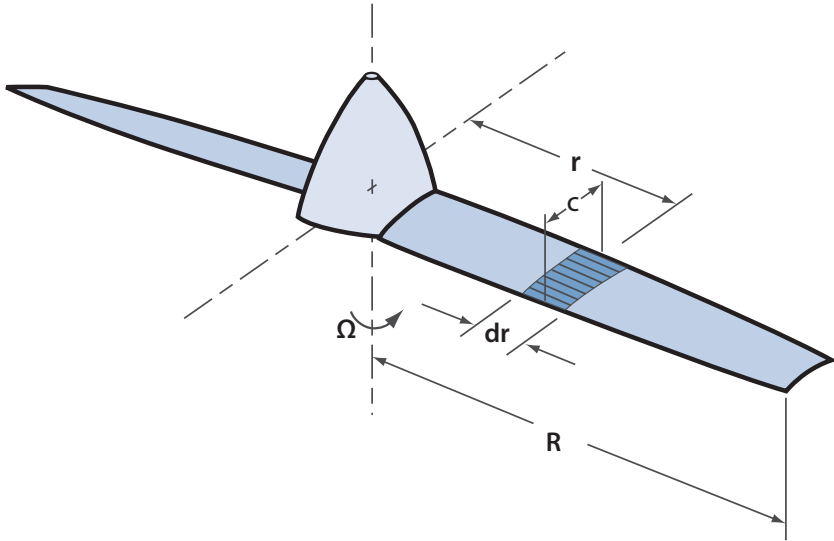
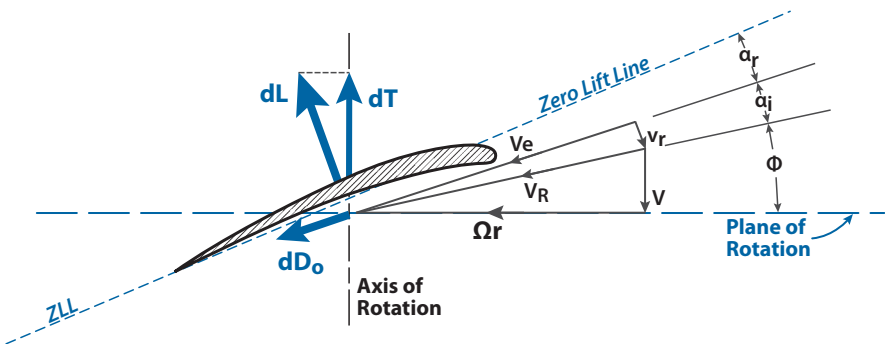


Figure 17.2 Propeller blade element.



- $\Omega r$  : Rotational velocity
- $V$  : Translational velocity (true airspeed)
- $V_R$  : Resultant velocity
- $V_e$  : Effective resultant velocity
- $V_r$  : Elemental induced velocity
- $\Phi$  : Effective pitch angle
- $\beta$  : Geometric pitch angle
- $\alpha_j$  : Elemental induced angle of attack
- $\alpha_r$  : Elemental angle of attack

Figure 17.3 Forces, velocities, and angles for a blade element.

To simplify the development of the blade element theory, it is assumed that each element is subjected to two-dimensional flow only and that each element is independent of its neighbors.

The aerodynamic lift force produced by the elemental lift  $dL$  will be perpendicular to the effective velocity  $V_e$  and will be inclined from the axis of rotation by the angle

$$\varphi + \alpha_i \approx \tan^{-1} \left( \frac{V + vr}{\Omega r} \right)$$

For freestream velocities up to the mid-subsonic range, it may be assumed that this angle is small, and

$$\sin(\varphi + \alpha_i) \approx \varphi + \alpha_i \quad (\text{in radians})$$

$$\tan(\varphi + \alpha_i) \approx \varphi + \alpha_i \quad (\text{in radians})$$

$$\cos(\varphi + \alpha_i) \approx 1$$

Thus, the elemental thrust is

$$|dT| = |dL| \cos(\varphi + \alpha_i) \approx |dL| \tag{17.10}$$

Similarly, the drag force opposing the rotation of the propeller element will consist of a drag component,  $dD_0$ , and a component due to the inclination of the lift force, the induced drag  $dD_i$ :

$$|dD| = |dD_0| \cos(\varphi + \alpha_i) + |dL| \sin(\varphi + \alpha_i)$$

$$|dD| \approx |dD_0| + |dL|(\varphi + \alpha_i) \tag{17.11}$$

It is now possible to express the thrust produced by a single element as

$$\begin{aligned} dT &\approx dL = \text{dynamic pressure} \times \text{area} \times \text{lift coefficient} \\ &= \left( \frac{1}{2} \rho V_e^2 \right) (c dr) c_l \end{aligned} \tag{17.12}$$

where  $c_l$  is the two-dimensional lift coefficient of the element. To determine the thrust of the propeller one must integrate this expression across the span of the blade and multiply by the number of blades  $b$ :

$$T = b \int_0^R 0.5 \rho V_e^2 c c_l dr \tag{17.13}$$

Practical propeller blades do not run to the axis of rotation because some allowance must be made for a mounting hub and, possibly, a pitch-changing mechanism. For this reason the inner limit of integration,  $r_i$ , is usually taken as  $0.1R$ . Similarly, some accounting must be made for losses caused by a decrease in effectiveness of outboard blade elements which results from the formation of a blade tip vortex. The outer integration limit is usually taken to  $BR$ , where the empirically determined tip-loss factor  $B \approx 0.96$ .

By ignoring compressibility effects, Eq. (17.13) becomes

$$T = 0.5\rho b \int_{r_i}^{BR} V_e^2 c c_\ell dr \quad (17.14)$$

where  $V_e$  will vary with  $r$ , and  $c$  and  $c_\ell$  may or may not be functions of radial position. Generally,  $c = c(r)$  is specified but, to calculate the propulsive thrust, one must know  $V_e = V_e(r)$  and  $c_\ell = c_\ell(r)$ .

From Fig. 17.3 it is obvious that

$$V_e \approx \left[ (V_r + V)^2 + (\Omega r)^2 \right]^{1/2} \quad (17.15)$$

and the two-dimensional lift coefficient may be expressed as

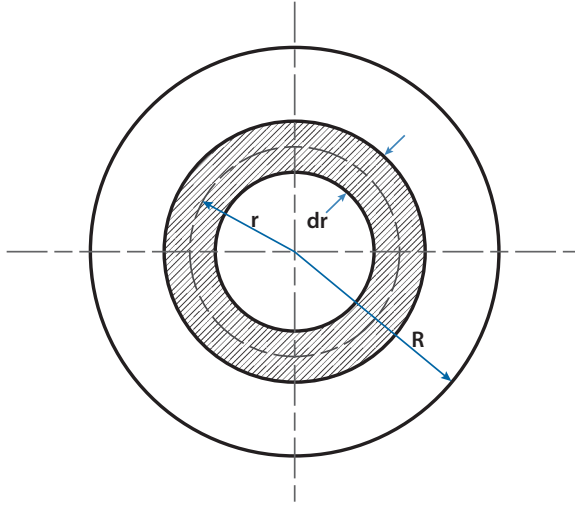
$$c_\ell = a\alpha_r = a \left[ \beta - (\varphi + \alpha_i) \right] \approx a \left[ \beta - \frac{V + vr}{\Omega r} \right] \quad (17.16)$$

where  $a = dc_\ell/d\alpha$ . Due to variations in local Mach number across the blade span,  $a$  will vary with  $r$ . However, with little loss of accuracy, it may be assumed that  $a$  is a constant with a value appropriate for the conditions at  $r = 0.75R$ .

Equations (17.15) and (17.16) still cannot produce the key to solving for the thrust of the propeller until the local induced velocity,  $v_r$ , is known at every blade location. An expression for  $v_r$  can be obtained by employing simple momentum theory in an elemental approach. Figure 17.4 shows an actuator disk upon which an annulus  $dr$  wide and located a distance  $r$  from the center has been using the same logic as was used to develop Eq. (17.4), the differential thrust produced by this annulus will be

$$dT = \rho(2\pi r dr)(V + v_r)2v_r \quad (17.17)$$

From blade element considerations, the thrust generated by this same annulus will be the product of the thrust produced by a single element located a distance  $r$  from the axis of rotation [Eq. (17.12)] and the number of blades  $b$ . With Eqs. (17.15) and (17.16) this becomes



**Figure 17.4** Annulus of an actuator disk.

$$dT = \frac{b}{2} \rho \left[ (v_r + V)^2 + (\Omega r)^2 \right] ca \left[ \beta - \frac{V + v_r}{\Omega r} \right] \quad (17.18)$$

By Eqs. (17.17) and (17.18) and solving for  $v_r$ :

$$v_r = \left( \frac{V}{2} + \frac{bca\Omega}{16\pi} \right) - 1 + \left[ 1 + \frac{2\Omega r \left( \beta - \frac{V}{\Omega r} \right)}{\frac{4\pi V^2}{bca\Omega} + V + \frac{bca\Omega}{16\pi}} \right]^{1/2} \quad (17.19)$$

which, within the limitations of the theory, will predict the induced velocity at a radial distance  $r$  of a propeller of known physical characteristics that is axially translating at a velocity  $V$ .

Theoretically, it would be possible to introduce Eq. (17.19) into (17.18) and integrate the latter expression between appropriate limits to calculate the thrust of a propeller of arbitrary twist distribution. In practice, however, the resulting expression would prove extremely difficult to handle. Satisfactory results can be obtained by dividing the blade into a finite number of stations, calculating  $v_r$  and  $dT$  at each station, and finally computing  $r$  total thrust via graphical integration or some numerical technique such as Simpson's rule.

The calculation of propeller thrust can be greatly simplified by the recognition that, as expressed by Eq. (17.19), the local induced velocity will be constant across the blade if the quantity  $2\Omega r[\beta - (V/\Omega r)]$  is also a constant.

(It can be shown [5] that constant  $v_r$  across the blade will require the minimum induced power for a given thrust and is thus desirable for reasons other than convenience of computation.) This may be accomplished by providing the blade with ideal twist such that, for any element located at  $r$ , the geometric pitch angle is defined by

$$\beta = \frac{\beta_t R}{r} \tag{17.20}$$

where  $\beta_t$  is the pitch of the tip section. This expression becomes unmanageable for  $r \rightarrow 0$  as a result of the *small-angle assumption*

$$(\varphi + \alpha_i) \tan^{-1} \left[ (V + v_r) / \Omega r \right]$$

Practically, as  $r \rightarrow 0$ ,  $\beta \rightarrow \pi/2$ . It must be noted that a unique twist distribution will be ideal only for a limited number of thrust and airspeed combinations. Because  $T = f(\beta_i)$  for a given  $V$ , varying thrust levels will require variable  $\beta_i$ . However, because  $\beta = \pi/2$  at  $r = 0$  for all cases, the ideal twist distribution must be optimized for a single thrust–airspeed combination.

The blade element theory furnishes a method for approximating the total power requirements of the propeller by providing insight into the profile losses of the blade. From Fig. 17.3 it can be seen that the power required to rotate the propeller (and thus generate thrust) will be the power needed to overcome the forces in the plane of rotation. For a single infinitesimal element this is

$$dP = \Omega r \, dD_0 \cos(\varphi + \alpha_i) + \Omega r \, dL \cos(\varphi + \alpha_i) \tag{17.21}$$

The term  $dD_0 = (1/2)\rho V_e^2 c c_{d_0} dr$  is the profile drag acting on the element, and thus the first series of terms in Eq. (17.21) may be thought of as the *elemental profile power*, whereas the second group is the *elemental induced power*. Then

$$dP = dP_0 + dP_i \tag{17.22}$$

It must be noted that the induced power requirements are directly associated with the production of propeller thrust, and when the expression for  $dP_i$  is integrated across the blade radius provisions must be made for the loss of thrust at the tips. Profile losses, however, are present across the entire exposed radius of the blade. Thus, each of the terms in Eq. (17.22) must be integrated between separate limits:

$$P = 0.5 \rho b \left[ \int_{r_i}^R (\Omega r)^2 V_e c c_{d_0} dr + \int_{r_i}^{BR} V_e c (\beta \Omega r - V - v_r)(V + v_r) dr \right] \quad (17.23)$$

This general equation is for modern high-speed propellers that employ ideal twist. Also, because most propellers are designed so that each section is operating at a low angle-of-attack, each element will also be functioning in the angle-of-attack region where the two-dimensional, incompressible profile drag coefficient  $c_{d_0}$  is approximately constant, and for low-speed application  $c_{d_0}$  may be removed from the integral. This last statement is certainly not true for high-speed propellers, however. As shown in Fig. 17.5, the resultant tip speed of a rotating blade is a function of rotational velocity and the true airspeed. At high flight speed and high propeller rpm (necessary for high thrust), the tip Mach number may approach or surpass the critical Mach number ( $\sim 0.9$ ) of the tip sections, and  $c_{d_0}$  will experience a drastic increase as  $r \rightarrow R$ . (For simplicity, skin friction, pressure, and wave drag effects are lumped together in  $c_{d_0}$ .)

Equation (17.23) provides a key to understanding the rationale behind the selection of a certain propeller geometry to fulfill given design requirements. For low-to-moderate airspeeds where  $c_{d_0}$  will be constant, power requirements may be reduced by minimizing the blade chord toward the tip where dynamic pressure is greatest. However, this high dynamic pressure in the blade tip region is also responsible for the lion's share of the

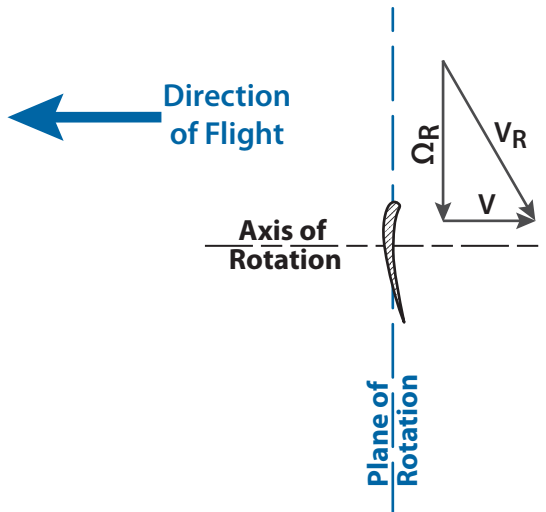


Figure 17.5 Resultant velocity at a propeller tip.



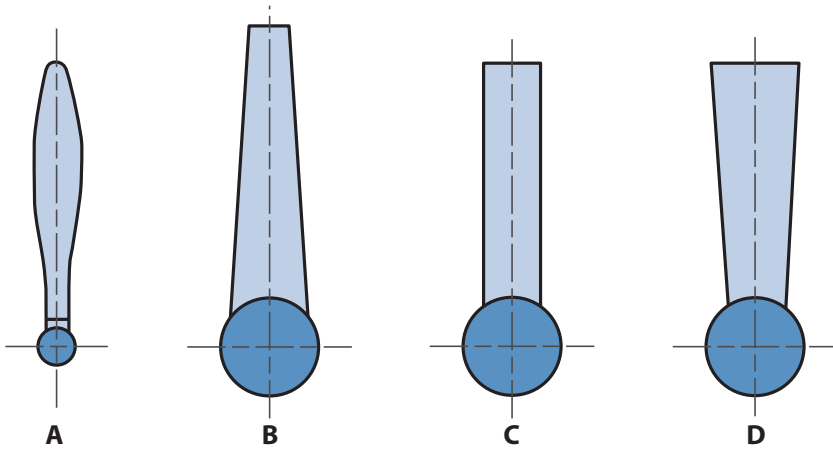


Figure 17.6 Typical propeller blade planforms.

resulting thrust, and larger tip chords would be desirable from this standpoint. Some compromise must be reached, and the results are planforms of the type shown in Fig. 17.6. Blade A is a type used on low-speed general aviation craft. It features a circular or elliptical root section developing into an 8%–12% thick section at the outer radii. Operating at rotational tip Mach numbers approaching 0.8, a propeller utilizing this blade can fly at airspeeds up to approximately  $Mach = 0.4$  before compressibility effects begin to be felt. Blade B exhibits a planform designed for use at high-subsonic Mach numbers and features thin sections and reduced chord at the tip. In this way the drag effects of transonic tip conditions can be minimized. This class of propeller blade has not found widespread application because the speed range for which it is designed ( $Mach = 0.6$ – $0.8$ ) can be more efficiently handled by turbofan engines.

A practical blade planform for the middle subsonic range is the “paddle blade” design, blade C, which was used on the original C-130 and Electra aircraft. The wide tip chord of this blade would seem to produce higher compressibility losses, but, as demonstrated in [7], the opposite is true. The blade with a large chord at the tip will be more efficient than a tapered blade producing the same thrust at the same operating conditions because the tip sections of the wider, untapered blade will be operating at a lower  $c_t$  and will have a higher critical Mach number. This argument would indicate that an even more efficient design would employ inverse taper as shown by blade D.

Although promising from an aerodynamic viewpoint, this approach has not been accorded wide acceptance because of structural difficulties.

### 17.3.3 Vortex Theory

Although providing a rapid method for the preliminary calculation of propeller performance, blade element theory does not provide the accuracy needed for detailed design work. Such factors as tip losses, three-dimensional effects, and mutual blade interference cannot be predicted by this method. For example, blade element theory indicates that a linear increase in thrust with no change in efficiency will result from adding blades to a propeller, whereas, in fact, the most efficient propeller consists of a single blade with efficiency decreasing as the number of blades increases.

The third major branch of propeller theory, vortex theory, overcomes many of the limitations of the previous two methods and offers the capability for great accuracy. The equations required to implement this theory satisfactorily, however, necessitate the use of large-capacity, high-speed computers. The details of the vortex theory are beyond the scope of this text and are more the tool of the propeller designer rather than the aircraft designer. The interested reader is referred to [1,3,4,8].

## 17.4 Preliminary Design

Although the previously discussed theoretical methods for propeller analysis provide convenient and relatively accurate schemes for predicting the performance of airscrews of known design, they would prove to be too cumbersome for preliminary design applications. To establish the propeller design parameters required by the preliminary design process, various semiempirical methods may be employed. Reference [9], for example, provides rapid performance calculations for light aircraft propellers driven by engines of up to 300 horsepower and at flight speeds ranging up to 200 kt. Propellers for larger and faster aircraft may be accurately analyzed through the methods and charts of [10]. The method developed here is based on [11] and is applicable for engine ratings over 300 horsepower and for flight Mach numbers up to 0.8.

The task of identifying the characteristics of a propeller to meet a given set of performance specifications is essentially a two-part problem attempting to relate the horsepower available to the thrust provided by the propeller in the takeoff mode and in the cruise mode. Each of these segments requires independent methodology, and the results must be faired together to provide a continuous picture of thrust output for a selected propeller from brake release up through the limits of the aircraft performance.

At this stage of the design loop the drag characteristics of the airframe should be well established and should include a rough approximation of nacelle drag for the selected number of engines. The major design parameters to be determined at a given flight condition are the propeller diameter

and the engine shaft horsepower required for that condition. All other parameters are defined by technology within rather narrow limits. If the propeller diameter is fixed by some structural consideration such as wing location or landing gear limitations, or by some aerodynamic consideration such as the ratio of propeller diameter to wing chord [12,13], then the resulting efficiency will be less than optimum, but the design process will be simplified as the required shaft horsepower can be calculated without iteration.

Certain definitions must be made at this point. As with most aerodynamic quantities, the thrust developed and power required by a propeller are conveniently expressed as nondimensional coefficients in the following forms:

Power Coefficient:

$$C_P = \frac{P}{\rho n^3 D^5} \quad (17.24)$$

Thrust Coefficient:

$$C_T = \frac{T}{\rho n^2 D^4} \quad (17.25)$$

where  $n$  is the *propeller rotational velocity* in revolutions per second (rps) and  $D$  is the diameter of the airscrew in feet. For generality, a third coefficient is defined to cover the torque  $Q$  generated by the propeller:

Torque Coefficient:

$$C_Q = \frac{Q}{n^2 D^5} = \frac{C_P}{2\pi} \quad (17.26)$$

The ideal efficiency  $\eta_i$  has been defined by Eq. (17.9) and should not be confused with another measure of effectiveness, the *propulsive* (or *propeller*) *efficiency*,

$$\eta = \frac{\text{Thrust Power Output}}{\text{Shaft Power Input}} = \frac{TV}{P} \quad (17.27)$$

This expression accounts for profile losses as well as induced losses and may be written as the product of an induced (or ideal) efficiency  $\eta_i$  and a *profile efficiency*  $\eta_0$ . Thus,

$$\eta = \eta_i \eta_0 \quad (17.28)$$

As with the ideal efficiency, the propeller efficiency will be zero under static condition.

Another useful parameter is the *rotational tip speed* of the propeller,  $V_{\text{tip}}$ , defined as

$$V_{\text{tip}} = \Omega R = \pi n D \quad (17.29)$$

The rotational tip speed has been given close consideration as a design point in recent years because of its importance in determining the operating noise level of the aircraft. Producing an aircraft with acceptable sideline noise levels is a major challenge to the designers of both civil and military STOL aircraft, and the reader is encouraged to consult [10,14–16] for further background on this problem. Suffice it to say that 700–800 ft/s is an upper limit on  $V_{\text{tip}}$ ; in light of the high sound levels created by the C-130 and Electra with their 720 ft/s tip speeds, even lower values might prove to be more realistic starting points.

The ratio of the true airspeed  $V$  to the tip speed has proven to be a powerful design variable in that it is related both to efficiency and to the aerodynamic coefficients. This ratio is most often expressed as the *proportional advance ratio*

$$J = V / n D \quad (17.30)$$

Two more parameters are needed to completely define the propeller and its operational conditions: one is to establish the blade planform and the other to set the sectional lift characteristics. The latter condition was defined in the section on blade element theory as a *two-dimensional lift coefficient*  $c_l$ , which could vary across the blade span. In practical propeller designs the sectional camber is defined by the *design lift coefficient*  $c_{l_d}$ , and the camber for the entire blade is designated by specifying  $c_{l_d}$  at  $r = 0.7R$ . Generally  $c_{l_d}$  at  $r = 0.7R$  will vary from 0.4 to 0.6, and minor excursions from the specified value at sections on either side of  $r = 0.7R$  will have a negligible effect on the propeller performance.

The blade planform is expressed by the *activity factor* (AF), which represents the rated power absorption capability of all blade elements. Equation (17.23) indicates that the power absorbed by a blade element will be proportional to the area of the element times the cube of the velocity. By assuming  $V_e \sim \Omega r$ , the power may be expressed as

$$dP \propto c(\Omega r)^3 dr \quad (17.31)$$

because at flight velocities  $dP_0 \gg dP_i$ . This expression has been nondimensionalized with  $V_{\text{tip}}$  and  $D$  to form a function of purely geometric properties

and yet one that reflects the relative ability of the blade to absorb power. The activity factor is conventionally defined as

$$\text{AF} = \frac{100,000}{16} \int_{0.15}^{1.0} \left( \frac{c}{D} \right) \left( \frac{r}{R} \right)^3 d \left( \frac{r}{R} \right) \quad (17.32)$$

for a single blade. The propeller AF is simply the blade AF times the number of blades  $b$ . Values for blade AF are usually constrained by structural considerations to values between 80 and 180. For example, the blade AF for the C-130 is 162.

The design process may be initiated with either the takeoff condition or the cruise condition, depending on the mission specifications. The designer must realize that the requirements for the two regimes may not be compatible and that a compromise solution most probably will be required. The following discussion assumes that the takeoff performance is not a driving consideration and that the aircraft design is being optimized for cruise.

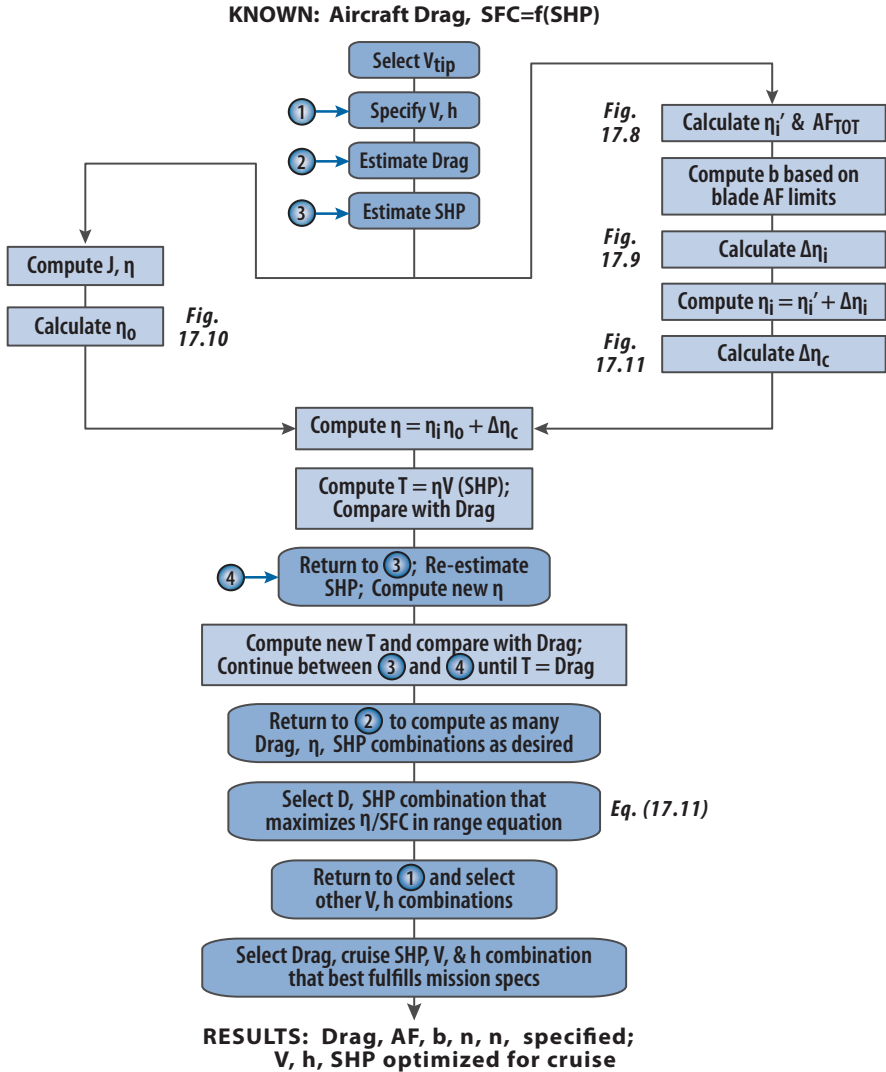
The general methodology for designing a propeller for cruise flight ( $J > 1.4$ ) is outlined in Fig. 17.7. Again, it is emphasized that only the drag characteristics of the airframe and the approximate specific fuel consumption (SFC) vs power setting and flight condition (speed and altitude) of the class of engine to be used need be known to begin the design procedure. All other parameters may be selected within the limitations previously discussed or calculated from the accompanying charts.

Figure 17.8 permits the computation of the propeller AF and a *basic induced efficiency*  $\eta'_i$ . Because this chart is based on a six-blade propeller and a  $C_\ell$  at  $r = 0.7R$  of 0.5, a correction must be made to  $\eta'_i$  to produce the induced efficiency  $\eta_i$ . The value specified for the representative lift coefficient is a reasonable value and may be used with good success for preliminary design purposes. However, changes to  $c_\ell$  at  $r = 0.7R$  within the acceptable 0.4–0.6 range will produce a negligible change in  $\eta$  and will produce thrust and power figures still well within the accuracy limitations required in initial aircraft design iterations. The basic induced efficiency should be corrected for number of blades and total activity factor using Fig. 17.9. With a value for  $\Delta\eta_i$ , the actual induced efficiency becomes

$$\eta_i = \eta'_i + \Delta\eta_i \quad (17.33)$$

The profile efficiency is obtained from Fig. 17.10 as a function of advance ratio  $J$  and flight Mach number. The total efficiency is then calculated using Eq. (17.28). This value of  $\eta$  may be corrected for compressibility effects with the addition of a term  $\Delta\eta_c$  from Fig. 17.11 [17].

A word of explanation should be given: the term *shaft horsepower* (SHP) used in this procedure is the engine output that is actually available to turn



**Figure 17.7** Propeller analysis procedure for cruise.

the propeller; it consists of the engine power at the given flight condition corrected for any bleed and auxiliary equipment losses and accounting for the inefficiency of the reduction gear.

This method applies to single-rotation propellers and does account for energy lost in the rotational motion of the slipstream. Approximately 60% of this lost rotational energy may be recovered through the use of dual counter-rotating propellers. The *rotational power expended* ( $P_R$ ) may be obtained from Fig. 17.12 in the ratio of  $P_R/R$ . The induced efficiency of a dual-rotation propeller may then be found using the expression

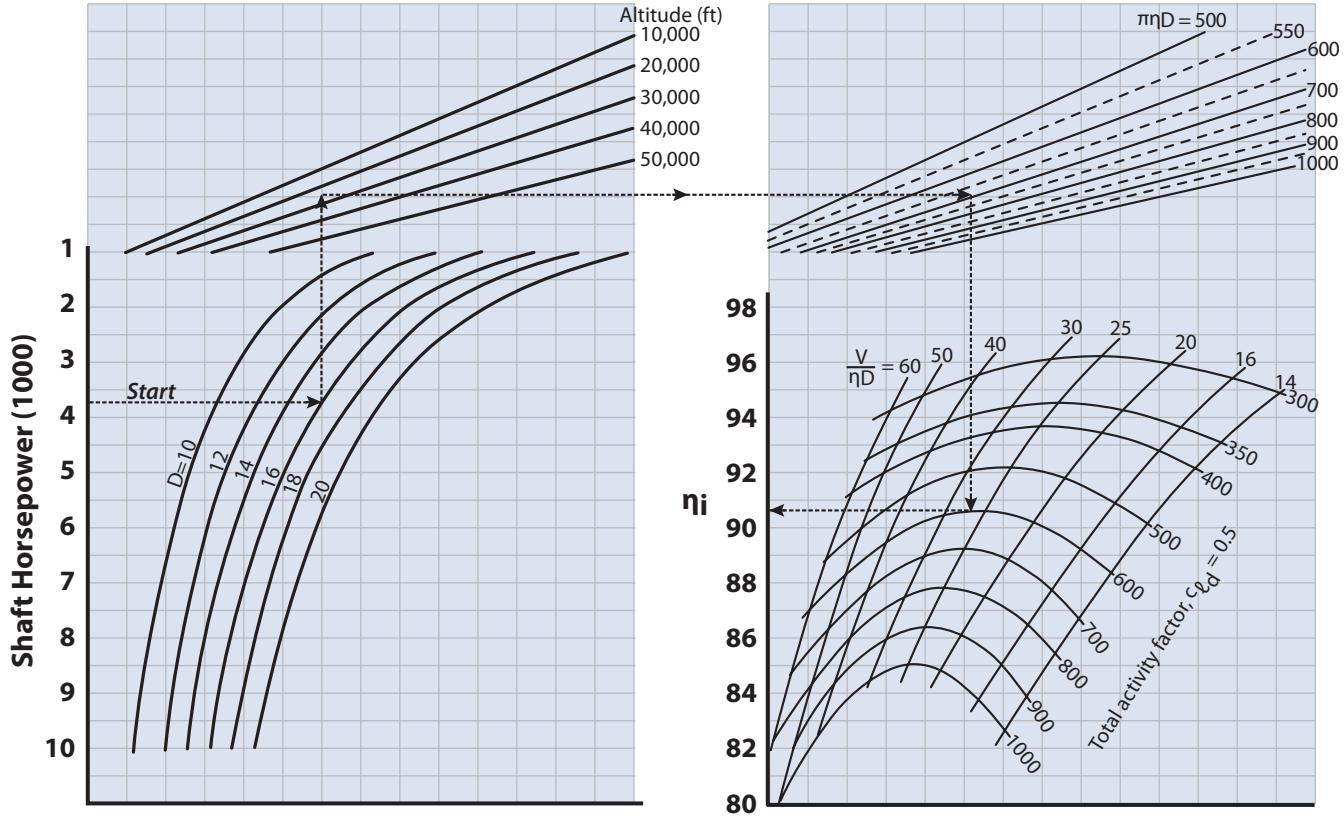


Figure 17.8 Propeller basic induced efficiency for cruise ( $b = 6$ ,  $c_{i,d} = 0.5$ ) (data from [11]).

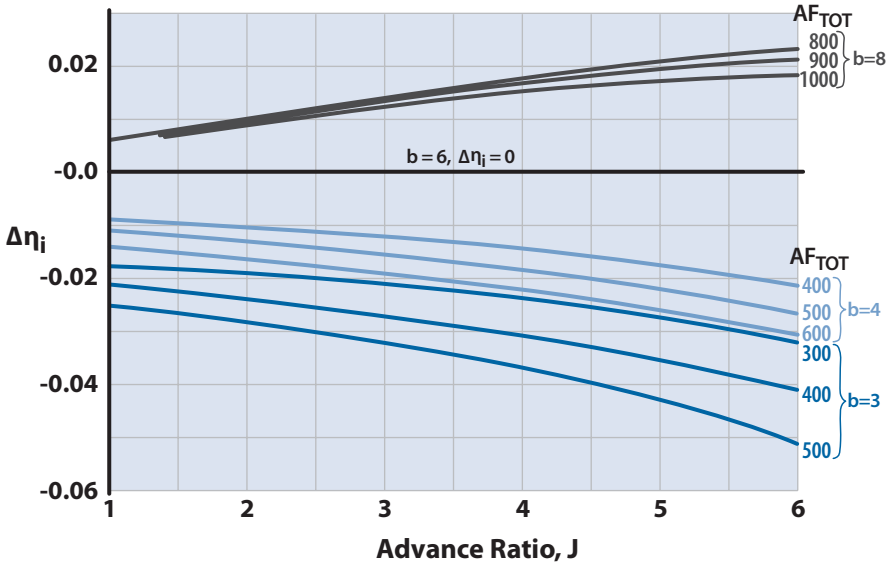


Figure 17.9 Blade number correction to basic induced efficiency.

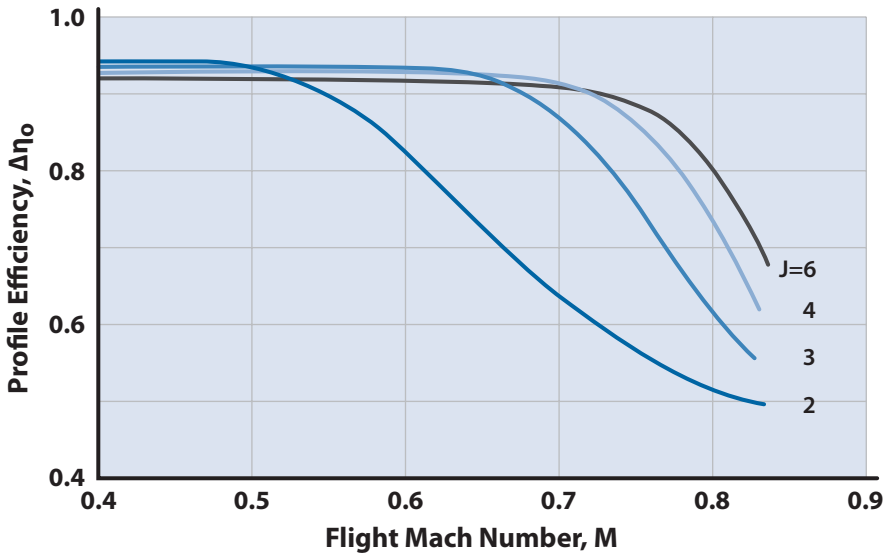


Figure 17.10 Estimated profile efficiency.



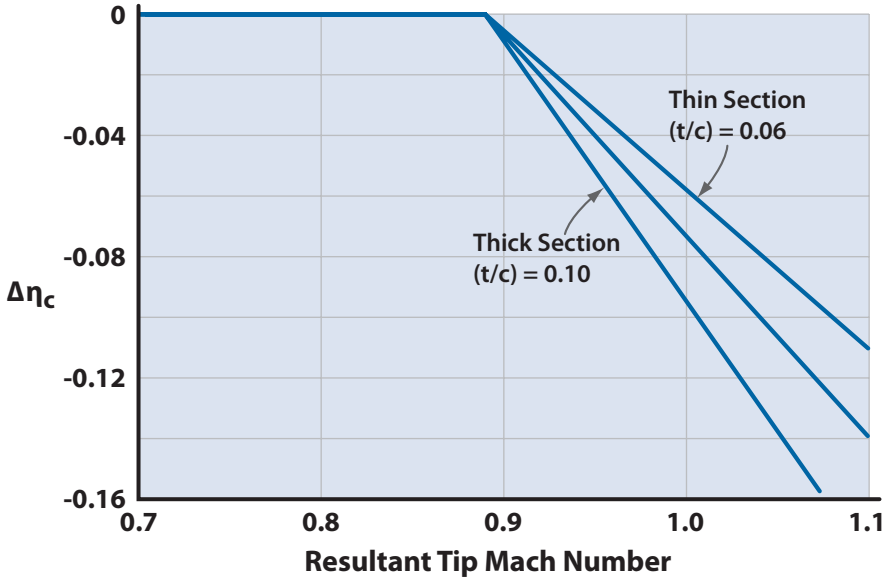


Figure 17.11 Compressibility correction to propeller efficiency.

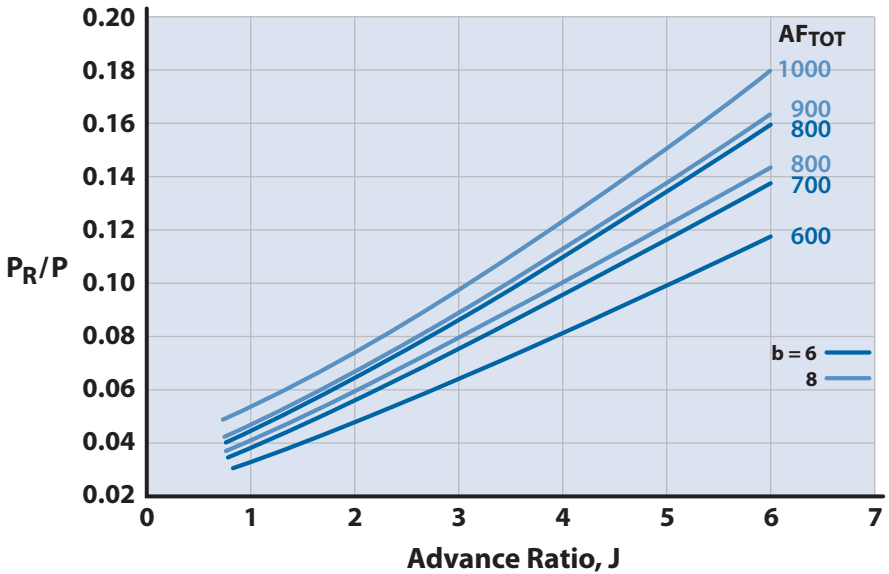


Figure 17.12 Efficiency correction for dual-rotation propellers.

$$\eta_i = \eta'_i + \Delta\eta_i + 0.6 \frac{P_R}{P} \quad (17.34)$$

Counter-rotating propellers offer a significant increase in efficiency, particularly for cases of high propeller activity factor and large numbers of blades ( $\geq 6$ ); however, they do require an increase in weight due to the associated gearing. Only the Soviet Union made extensive use of this feature on the An-22, Tu-95, and Tu-114.

The process of selecting or evaluating a propeller for takeoff conditions is generally simpler than a similar task for cruise flight because more information is known. For the case where the propeller has been optimized for cruise,  $AF$ ,  $D$ , and  $n$  have already been determined. Specification of SFC vs SHP in cruise will, for a given class of engines, establish the takeoff SHP, and the designer need only analyze the thrust produced by the propeller-engine combination for use in calculating the takeoff distance. If the propeller is to be optimized to meet a takeoff specification, a more complex iterative procedure must be utilized to pick the combination of propeller characteristics that will require the least power and, thus, the lowest engine weight.

The methodology for both of the preceding procedures is outlined in Fig. 17.13. In each case the takeoff velocity of the aircraft must be known (Chapter 10). Because the concept of propeller efficiency becomes meaningless for low airspeeds, the takeoff problem is one of finding the relationship between thrust produced and power required (or between  $C_T$  and  $C_P$ ). Figure 17.14 provides this relationship but it is expressed in terms of an *intermediate power coefficient*  $C_{P_x}$ , which is not corrected for variable activity factors. The correction to  $C_P$  may be obtained from Fig. 17.15, and the actual power coefficient may be computed from

$$C_P = X(C_{P_x}) \quad (17.35)$$

As with the calculation of cruise performance, the propeller tip speed is an important parameter for propeller analysis at takeoff. Noise criteria are especially critical during airfield operations, and the designer must make a difficult tradeoff between performance and sideline noise levels. Depending on the type of engine utilized, the tip speed in takeoff need not be the same as that in cruise, but generally

$$(V_{\text{tip}})_{\text{TO}} \geq (V_{\text{tip}})_{\text{cruise}}$$

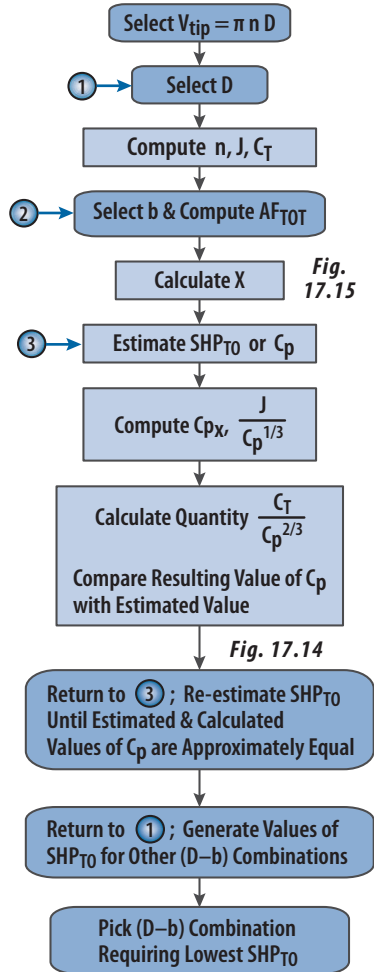
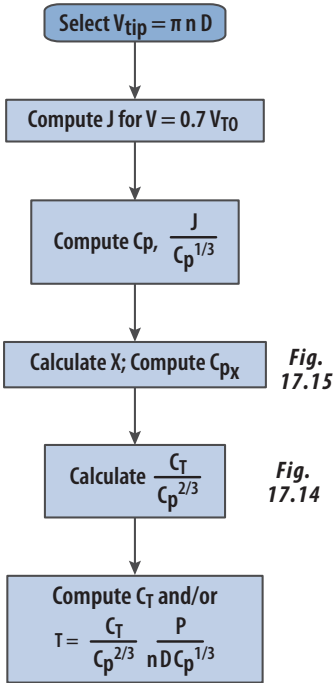
Once more it must be emphasized that the designer may have to accept a propeller that is optimized for neither takeoff nor cruise to produce an

**Propeller Optimized for Cruise**

**Propeller Optimized for Takeoff**

KNOWN: Propeller Characteristics,  $SHP_{T0}$

KNOWN:  $T_{REQ}$  at  $V = 0.7 V_{T0}$



**Figure 17.13** Propeller analysis procedure for cruise compared with takeoff.

acceptable performance level for both regimes. A propeller with high cruise efficiency would have blades with low-cambered sections, whereas the optimum blade for takeoff would have a highly cambered section. The solution to this dilemma is to design a propeller with variable-camber blades. Although such a propeller would increase weight and cost somewhat, it does permit very low tip speeds at takeoff to produce desirable noise signatures.

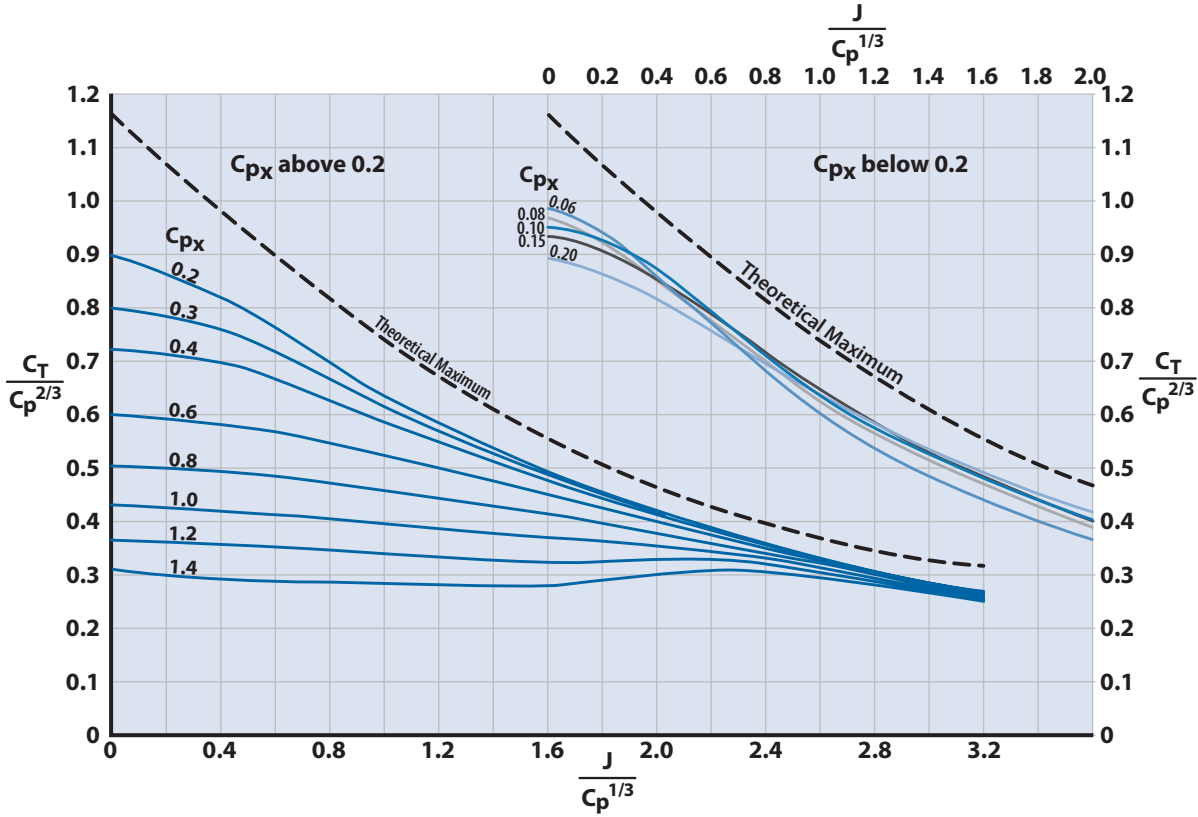


Figure 17.14 Propeller performance chart for takeoff (data from [11]).

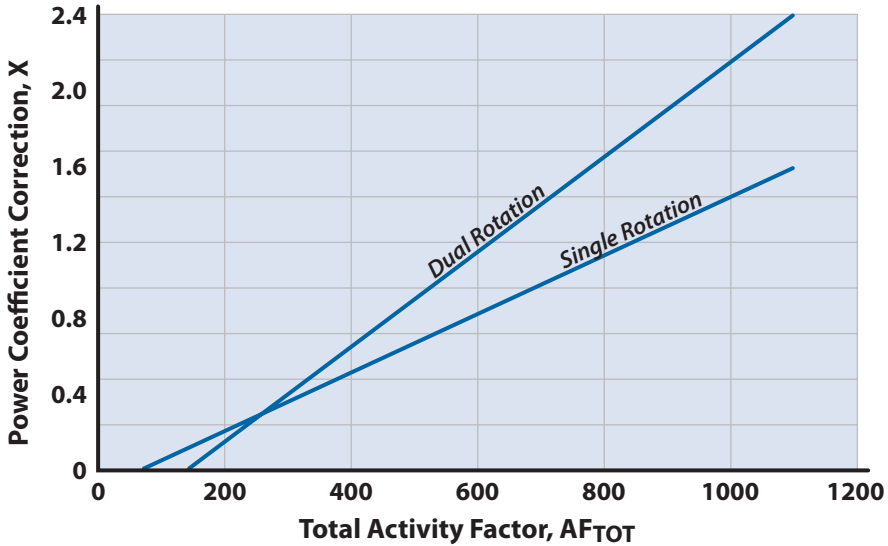


Figure 17.15 Power coefficient adjustment factor.

## 17.5 Shaft Engine Characteristics

In designing a propeller-driven aircraft, the designer must consider the propeller and its engine together. No discussion of propeller propulsion systems would be complete without some mention of the engine that will turn the airscrew.

Figure 14.2 shows the SHP-to-weight relationships for a spectrum of reciprocating and turboshaft engines. In most cases, the turbine engines include the weight of the reduction gearing required for their application as turboprop engines. The output of these engines is listed in terms of the shaft horsepower being produced to turn the propeller. This is not a complete picture of the capability of the turboprop powerplant because a certain amount of residual jet thrust  $T_j$  is also being generated (discussed in Section 14.2.2).

The propeller tip speed is a function of both propeller diameter and shaft speed  $n$ ; thus, the designer is concerned with the gear ratio between the power turbine and the output shaft. The Allison T56-A-15 (engine data in Appendix J, Fig. J.3) is designed to operate at a constant turbine speed of 13,820 rpm while the propeller shaft turns at a more reasonable 1021 rpm. Powerplant thrust changes are accomplished via simultaneous changes in fuel flow and propeller blade pitch. This same turbine engine could be designed to operate at a different output rpm with the attachment of a reworked gearbox. Each turboprop engine is evolved with a specific pro-

peller in mind, and thus the performance is based on the use of a standard reduction gear.

The performance of a turboprop is similar to a turbojet in that a performance gain is realized with increased velocity due to ram recovery up to about 400 kt, where the propeller losses start to dominate. For a reciprocating engine there is no power increase due to ram recovery; as the velocity increases the propeller efficiency decreases due to compressibility effects, and the drag due to cooling causes the thrust of the propeller–reciprocating-engine combination to drop off rapidly above 200 kt.

**Example 17.1 Use of Vendor Propeller Charts**

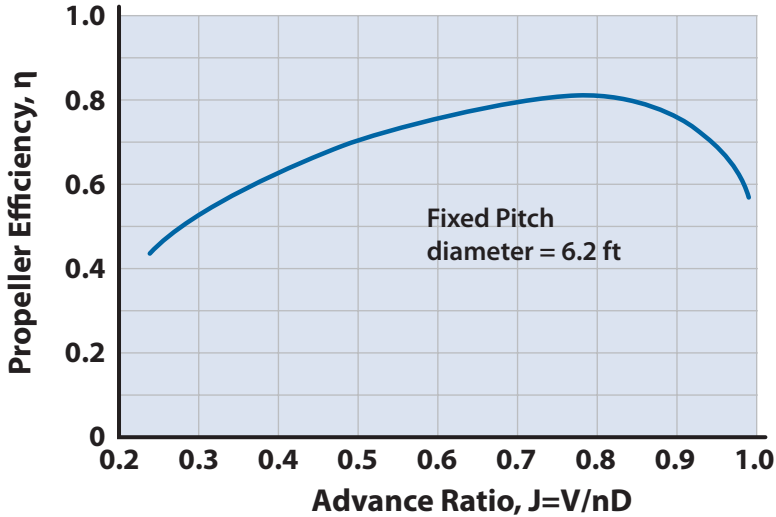
The designer will normally have available both engine and propeller operating charts supplied by the propeller and engine suppliers. This example uses the Piper PA-28–180 Cherokee Archer with a fixed-pitch propeller and the PA-28–200 Cherokee Arrow with a constant-speed, variable-pitch propeller. These two aircraft have the characteristics given in Table 17.1.

The Cherokee Archer at 7000 ft and 2450 rpm has 135 hp available (from Table 14.1). Using Eq. (17.31) the advance ratio at the 122-kt cruise speed is

$$J = V / nD = 206 / (40.8)(6.2) = 0.814$$

**Table 17.1** Comparison between the Cherokee Archer and Arrow

Aircraft	Cherokee Archer	Cherokee Arrow
Span (ft)	32	32
Wing area (ft <sup>2</sup> )	170	170
Aspect ratio	6.02	6.02
TOGW (lb)	2450	2650
W/S (lb/ft <sup>2</sup> )	14.4	15.6
Landing gear	Fixed	Retractable
Engine	Lycoming O-360-A	Lycoming IO-360-CIC
Maximum rated hp	185	200
Propeller	Sensenich fixed pitch	Hartzell variable pitch
Propeller diameter (ft)	6.2	6.2
Maximum speed (kt)	129	152
Cruise speed (kt)	122 at 7000 ft, 2450 rpm	143 at 7000 ft, 2450 rpm
Stall speed (kt)	53	57



**Figure 17.16** Estimated propeller efficiency for the Piper Cherokee Archer PA-28 (courtesy of Sensenich Propeller Manufacturing Co., Inc.).

From Fig. 17.16 the fixed propeller efficiency  $\eta = 0.8$ . Using Eq. (17.27) the propeller thrust  $T = \eta P/V = (0.8)(135)(550)/206 = 288$  lb. If the weight fraction for engine start and climb to 7000 ft is assumed to be 0.97, then the aircraft weight is 2376 lb and the  $L/D = 8.26$ . The aircraft  $C_D = 0.0435$  at the cruise condition.

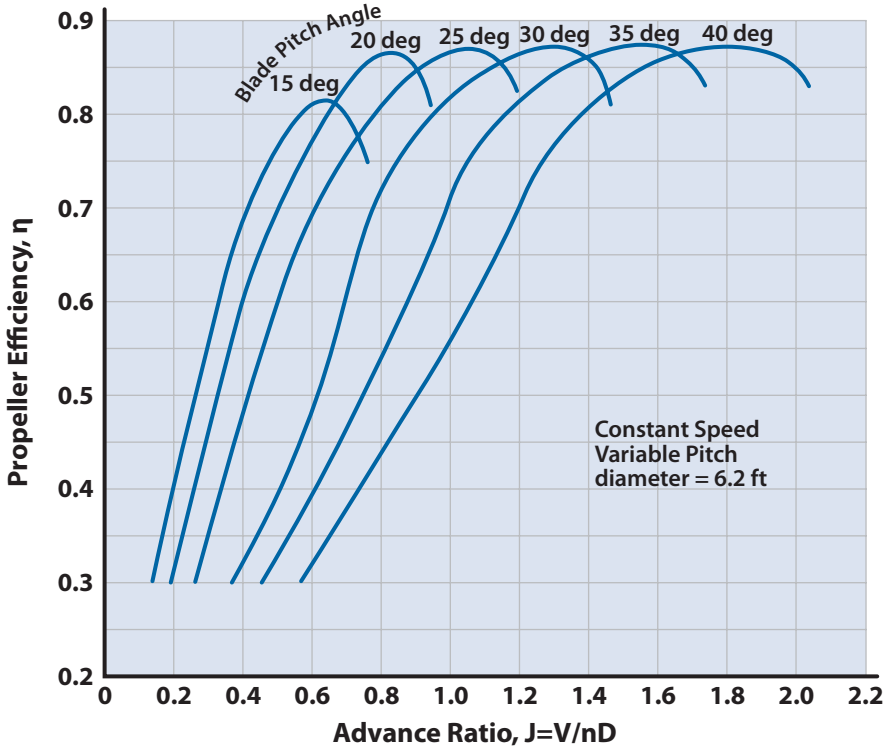
Using the published brake specific fuel consumption (BSFC) for the Lycoming O-360-A (from Table 14.1) of 0.47 lb/bhp·h, the fuel flow is 63.5 lb/h. For a trip of 400 n mile the Archer would burn about 208 lb of fuel.

For the Cherokee Arrow (Figs. 17.17 and 17.18) at 7000 ft and 2450 rpm the available power from its IO-360-CIC is 150 hp. At its cruise speed of 143 kt the propeller advance ratio is  $J = 0.95$ . Because the aircraft is equipped with a constant-speed propeller, use the blade-pitch data as shown in Fig. 17.18. Calculating the power coefficient using Eq. (17.24) gives

$$C_p = P(\text{ft} \cdot \text{lb}) / \rho n^3 D^5 = (150)(550) / (0.001927)(67917)(99161) = 0.069$$

Entering Fig. 17.18 with  $J = 0.95$  and  $C_p = 0.069$  gives a blade-pitch angle  $b \sim 27$  deg.

Figure 17.17 shows the estimated propeller efficiency for a variable-pitch propeller. The advantage of a variable-pitch propeller is



**Figure 17.17** Estimated propeller efficiency for the Piper Cherokee Arrow PA-28R (data courtesy of Hartzell Propeller Inc.).

that the blade angle can be adjusted to give a maximum propeller efficiency for different advance ratios and power loadings (horsepower per propeller area). Entering Fig. 17.17 with  $J = 0.95$  and  $b = 27$  deg gives a propeller efficiency  $\eta = 0.85$ . The propeller thrust is

$$T = \eta P / V = (0.85)(150)(550) / (241.5) = 290 \text{ lb}$$

Notice that the drag of the Arrow is only 2 lb more than the Archer but it is flying 21 kt faster. The lower drag for the Arrow is due to the retractable gear. The  $L/D = 8.85$  for the Arrow and its  $C_D = 0.0319$ . The Arrow for the same 400-n mile trip would burn 197 lb of gas, or 11 lb less than the Archer, and take almost 30 minutes less time.

At zero forward speed, the efficiency of a propeller is zero by definition, even though its thrust is not zero. In fact, for the same shaft power a variable-pitch propeller will produce the most thrust in zero forward velocity (i.e., its static thrust is greater than the thrust produced in forward flight). Figures 17.19 and 17.20 can be used to esti-



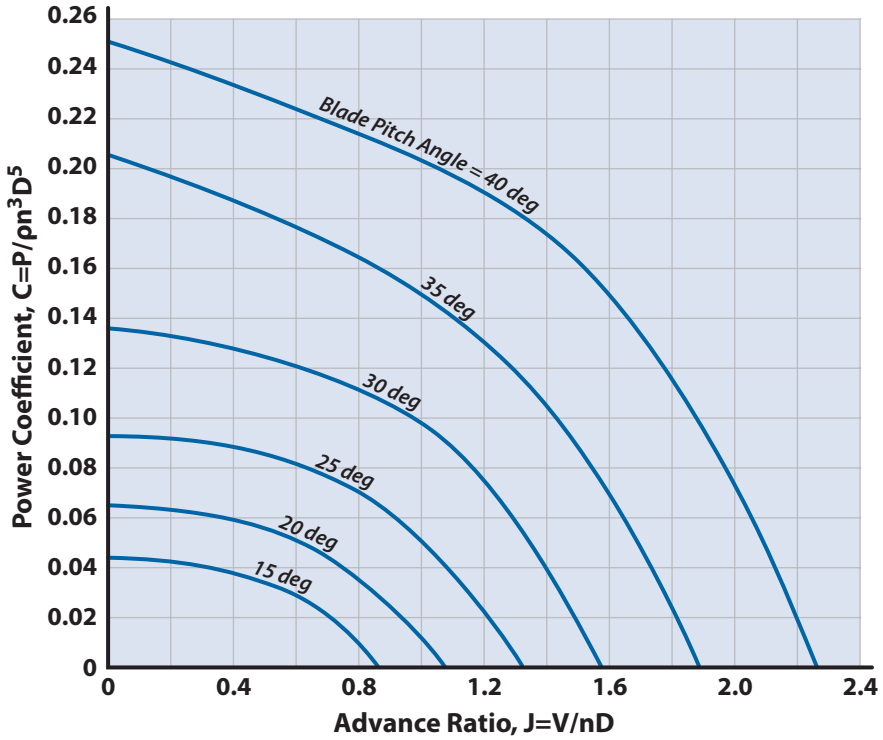


Figure 17.18 Estimated propeller power coefficients for the Piper Cherokee Arrow PA-28R (data courtesy of Hartzell Propeller Inc.).

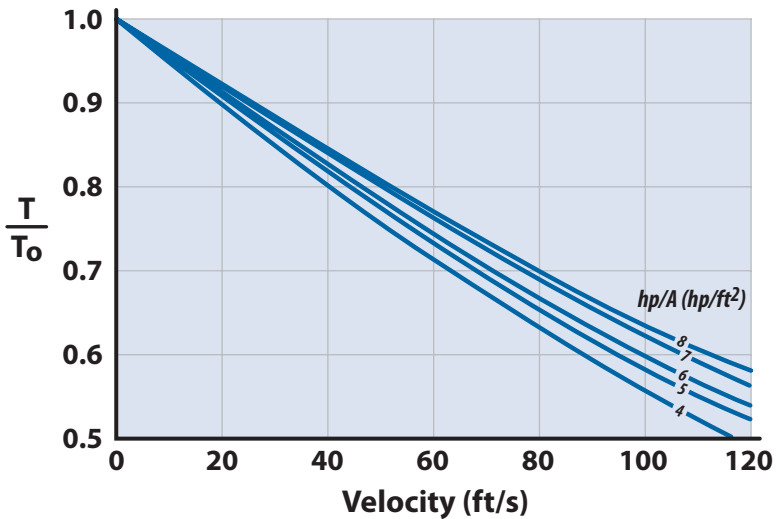
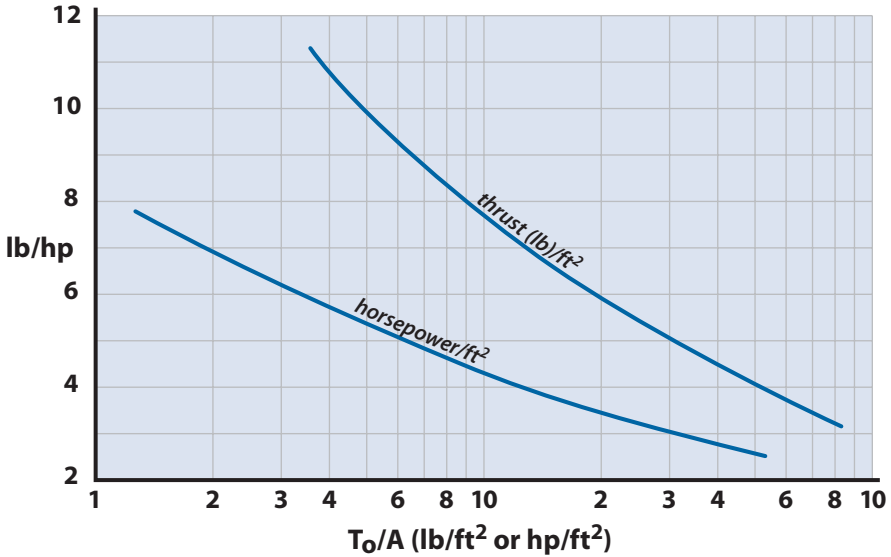


Figure 17.19 Decrease of thrust with velocity for different power loadings (data from [18]).



**Figure 17.20** Static thrust and power performance of propellers or rotors (data from [18]).

mate the thrust available from a variable-pitch propeller at low forward speeds. The static thrust is first obtained from Fig. 17.20 and then reduced by a factor from Fig. 17.19. These charts apply only to a constant-speed propeller, which allows the engine to develop its rated power regardless of the forward speed. These charts are used to estimate the static thrust for the Cherokee Arrow.

The Arrow at takeoff has 200 hp at 2700 rpm. This gives it a power loading (horsepower per propeller area) of 6.62 hp/ft<sup>2</sup>. From Fig. 17.20 the static thrust-level per horsepower (lb/hp) is 4.9, giving a static thrust of 980 lb. The takeoff analysis presented in Chapter 10 calculates the ground run acceleration for the thrust available at  $0.7V_{TO}$ , where  $V_{TO} = 1.2V_{Stall}$ . The stall speed for the Arrow is 57 kt, or 96 ft/s. So, use the thrust at 80 ft/s in the ground run analysis. From Fig. 17.19 the thrust at 80 ft/s is about 67.5% of the static thrust, or 662 lb. This is a respectable acceleration  $T/W$  of 0.25, giving a takeoff distance of about 1000 ft.

## References

- [1] McCormick, B. W., Jr., *Aerodynamics of V/STOL Flight*, Academic Press, New York, 1967.
- [2] Theodorsen, T., *Theory of Propellers*, McGraw-Hill, New York, 1948.

- [3] Dommasch, D. O., *Elements of Propeller and Helicopter Aerodynamics*, Pitman, New York, 1953.
- [4] Glauert, H., "Airplane Propellers," *Aerodynamic Theory*, Vol. 4, edited by William F. Durand, Dover, New York, 1963.
- [5] Gessow, A. and Myers, G. C., Jr., *Aerodynamics of the Helicopter*, Ungar, New York, 1952.
- [6] Stepniewski, W. Z., *Introduction to Helicopter Aerodynamics*, Rotorcraft Publishing Committee, Morton, PA, 1950.
- [7] Stack, J., Draley, E. C., Delano, J. B., and Feldman, L., "Investigation of the NACA 4-(3)(08)-045 Two-Blade Propellers at Forward Mach Numbers to 0.725 to Determine the Effects of Compressibility and Solidity on Performance," NACA TR-999, 1950.
- [8] Goldstein, S., "On the Vortex Theory of Screw Propellers," *Proceedings of the Royal Society, Series A: Mathematical and Physical Sciences*, Vol. 123, 1929.
- [9] Crigler, J. L., and Jaquis, R. E., "Propeller-Efficiency Charts for Light Airplanes," NACA TN 1338, 1947.
- [10] "Generalized Method of Propeller Performance Estimation," Hamilton Standard Div., Hamilton Standard Publ. PDB 6101A, United Aircraft Corp., 1963.
- [11] Gilman, J., Jr., "Propeller-Performance Charts for Transport Airplanes," NACA TN 2966, 1953.
- [12] Kuhn, R. E., and Draper, J. W., "Some Effects of Propeller Operation and Location on the Ability of a Wing with Plain Flaps to Deflect Propeller Slipstreams Downward for Vertical Takeoff," NACA TN 3360, 1955.
- [13] Spreeman, K. P., "Investigation of a Semi-Span Tilting-Propeller Configuration and Effects of Wing Chord to Propeller Diameter on Several Small-Chord Tilting-Wing Configurations," NASA TN D-1815, 1963.
- [14] Stepniewski, W. Z., and Schmitz, F. H., "Noise Implications for VTOL Development," Society of Automotive Engineers Paper 70-286, 1970.
- [15] Hubbard, H. H., "Propeller Noise Charts for Transport Airplanes," NACA TN 2968, 1953.
- [16] Rosen, G., and Rohrbach, C., "The Quiet Propeller—A New Potential," AIAA Paper No. 69-1038, 1969.
- [17] Perkins, C. D., and Hage, R. E., *Airplane Performance, Stability and Control*, Wiley, New York, 1949.
- [18] McCormick, B. W., *Aerodynamics, Aeronautics and Flight Mechanics*, Wiley, New York, 1995.

## Chapter 18

# Propulsion System Thrust Sizing



- Turbine Engine Thrust Sizing
- Turbine Engine Scaling
- Piston Engine Sizing
- Solar-Power Sizing
- Human-Power Sizing
- Rocket Engine Sizing

Formula One racing aircraft Nemesis rounding the pylon on its way to another win at the Reno National Championship Air Races. (Photograph courtesy of Jon Sharp.)

*Small deeds done are better than great deeds planned.*

Peter Marshall

## 18.1 Introduction

**A**t this point in the design game, the size of the fuselage is known, the general configuration has been established, and the first estimate of the aircraft aerodynamics is complete. Now the propulsion unit needs to be sized, that is, select the  $(T/W)_{TO}$  so that the aircraft performance can be determined and, in the case of a jet aircraft, the inlet sized and designed.

Sometimes the designer works with existing “off the shelf” engines, such as those reported in Appendix J. The designer would vary the number and type, finding the combination that gives the required vehicle performance at minimum weight, cost, and noise. Other times the designer might work with a nonexistent conceptual engine. In this case, the engine manufacturer would give the designer a “rubber” engine, that is, a paper engine that can be scaled up or down according to scaling laws established by the engine manufacturer. In the case of a jet engine, the designer would vary the engine thrust and perhaps the number of engines to fit the parametric study. The appropriate engine weight, diameter, and length would be determined from the engine scaling information. Occasionally, the designer might examine the influence of engine turbine temperature, overall pressure ratio, fan pressure ratio, and bypass ratio on aircraft design. However, this type of parametric study is usually performed by the engine manufacturer as part of the paper engine design.

The  $(T/W)_{TO}$  is usually sized by one or more of the following items:

1. Cruise/Loiter
2. Energy maneuverability (air combat)
3. Acceleration-time and fuel burned during acceleration
4. Takeoff
5. Maximum speed

These criteria are often in conflict with one another. The designer must consider the  $(T/W)_{TO}$  for these mission requirements, establish their priorities, and then decide upon an appropriate compromise, after looking at the entire mission. Table 18.1 indicates trends in  $(T/W)_{TO}$  based upon current aircraft.

The Nemesis was built and piloted by Jon Sharp, a research engineer at the Lockheed Martin Skunk Works. The 520-lb Nemesis with a stock 100-hp Continental piston engine won every Reno championship race from 1991 to 1995, plus 20 out of 22 races entered during the period. In 1993 Nemesis set a new Formula One A class (F1A) 3-km closed course speed record of 277.26 mph at Oshkosh, Wisconsin, and received the Bleriot Award.

## 18.2 Turbine Engine Scaling

Assume that the aircraft designer has selected the propulsion type, in terms of bypass ratio, turbine inlet temperature, and pressure ratio, and now desires to scale it up or down to get the proper  $T/W$ . The engine man-

Table 18.1 T/W Range for Various Aircraft Types

Dominant Mission Requirement	Range for $(T/W)_{T0}$ (uninstalled)
Long range	0.2–0.35
Short and intermediate range with moderate field length	0.3–0.45
STOL and utility transport	0.4–0.6
Fighter—close air support	0.4–0.6
Fighter—strike interdiction	0.45–0.7
Fighter—air-to-air	0.8–1.3
Fighter—interceptor	0.55–0.8

manufacturer provides a reference engine (either a paper engine or an existing engine) and the appropriate scaling information. The engine weight, diameter, and length scale according to the mass flow as follows:

$$W_{eng} = \left( \frac{\dot{m}}{\dot{m}_{REF}} \right)^n (W_{eng})_{REF} \tag{18.1}$$

where  $n = 0.8–1.3$  (usually about 1.0) and  $\dot{m}$  is sea level static (SLS) airflow required for the engine. From Chapter 14,

$$T = \dot{m}(V_e - V_a) + A_e(P_e - P_a) \tag{14.1}$$

and if constant nozzle velocity  $V_e$  is assumed for any thrust size, then

$$\left( \frac{T}{T_{REF}} \right) = \left( \frac{\dot{m}}{\dot{m}_{REF}} \right) \tag{18.2}$$

Equation (18.2) is usually a pretty good assumption and facilitates the engine scaling.

The engine diameter  $d$  and length  $\ell$  scale as follows:

$$d = \left( \frac{\dot{m}}{\dot{m}_{REF}} \right)^{1/2} d_{REF} \tag{18.3}$$

$$\ell = \left( \frac{\dot{m}}{\dot{m}_{REF}} \right)^{n-(1/2)} \ell_{REF} \tag{18.4}$$

### 18.3 Turbine Engines Sized for Cruise Efficiency

The turbine engine is sized by matching the thrust required (drag) during best cruise condition with the thrust available at the power setting

for minimum thrust specific fuel consumption (TSFC). This power setting for minimum TSFC varies from engine to engine. For example, the F-100 (Fig. 14.8d) at Mach = 0.8 and 36,089 ft has a minimum TSFC at 70% normal rated thrust (NRT) whereas the TF-39 (Fig. 14.9c) at Mach = 0.8 and 35,000 ft has a minimum at 100% NRT. The engine sizing should be checked at several points during the cruise, as the aircraft cruise climbs, to find the best sizing compromise.

**Example 18.1 Sizing for Optimum Cruise Performance**

Consider a four-engine long-range cruise transport using scaled TF-39 engines. Size the engines for optimum cruise performance.

Assume	
$W_{T0}$	500,000 lb
$(W/S)_{T0}$	120 psf
$W_{fuel}/W_{T0}$	0.40
$S_{ref}$	4167 ft <sup>2</sup>
$W/S$ at start of cruise	116 psf
Cruise at Mach	0.8
$C_{Dmin}$	0.018, $d/b = 0.1$
Wing, AR	8.0
$\Lambda$	30 deg
$\lambda$	0.37
Section	NACA 64 <sub>2</sub> -215 airfoil
Determine	
Cruise	from 31,000 ft to 41,000 ft
From Appendix F:	
$\alpha_{0L}$	2.6 deg
$r_{LE}$	1.1% chord
From Section 13.1.1:	
$C_{L\alpha}$	0.1 per degree
$C_{Lmin}$	0.26 (see Fig. F.5)
From Section 13.2.1 and Fig. G.9 ( $e = 0.65$ ):	
$K$	0.0606
$K'$	0.0406
$K''$	0.02
$(L/D)_{max}$	17.3 [from Eq. (3.10b), Chapter 3]
Drag and thrust required (start of cruise):	
$q$	269.5 psf at Mach = 0.8 and 31,000 ft
$C_L = W/q S_{ref}$	116/270 = 0.430
$C_D = C_{Dmin} + K' C_L^2 + K''(C_L - C_{Lmin})^2$	0.018 + 0.0081 = 0.0261

Cruise $L/D$	$0.43/0.0261 = 16.48$ [agrees well with result from Eq. (3.29)]
Drag	$C_D q S (0.0261) (269.5)(4167) = 29,308$ lb
Required thrust	7327 lb (each engine)

An examination of Fig. 14.9b for 31,000 ft indicates that the power setting for the TF-39 that gives the lowest TSFC in continuous operation is 100% NRT. Thus, for 100% NRT: thrust available each engine = 9460 lb. Therefore, use four TF-39 engines that are scaled: scaling factor =  $7327/9460 = 0.775$ .

The scaled engines will have 77.5% of the thrust and airflow (assume  $V_e$  to be the same) of the TF-39 engines:

Assume	
Engine weight	$(0.775)(7026) = 5442$ lb
Diameter	$\sqrt{(0.775)(100)} = 88$ inches
Bullet length	$\sqrt{(0.775)(271)} = 238.6$ inches for $n = 1.0$
$T_{SLS}$	$0.775 (41,100) = 31,853$ lb
$(T/W)_{TO}$	0.255
Check engine sizing for end of cruise	
At end of cruise	$W/S \sim 80$ psf
$q$	168 psf at Mach = 0.8 and 41,000 ft
$C_L$	0.477
$C_D$	$0.018 + 0.010 = 0.028$
Cruise $L/D$	16.93
Drag	19,568 lb
Thrust required each engine	4892 lb
Thrust available each engine	$(6400)(0.775) = 4960$ lb at 100% NRT (from Fig. 14.9c)

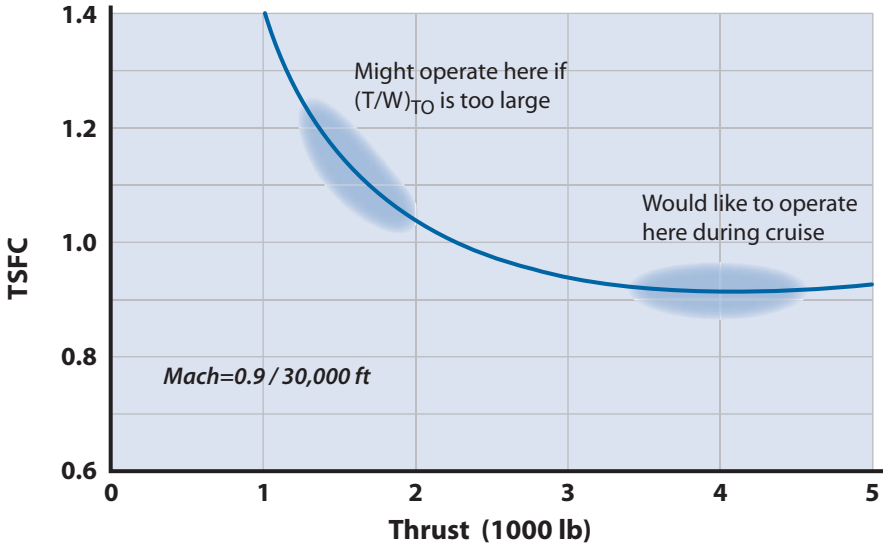
Thus, the 77.5% scaling of the TF-39 provides a good engine match at the beginning and end of cruise.

### 18.4 Energy Maneuverability (Air-to-Air Combat)

The performance of an aircraft in air combat at a point in velocity–altitude space is indicated by its value of *maximum sustained turn rate* (from Chapter 3):

$$\dot{\psi}_{MS} = \frac{g \sqrt{n_{MS}^2 - 1}}{V} \tag{3.32}$$





**Figure 18.1** F-100 TSFC for partial power setting at Mach = 0.9 and 30,000 ft (see Fig. 14.7).

where  $n_{MS}$  is the *maximum sustained load factor*. The  $n_{MS}$  can be expressed by

$$n_{MS} = \frac{q}{\sqrt{W/S}} \sqrt{\frac{1}{K} \left[ \frac{T}{W} \frac{1}{q} - \frac{C_{D0}}{W/S} \right]} \quad (18.5)$$

(from Section 3.9). Equation (18.5) indicates that large  $T/W$  gives improved combat maneuverability. However, as  $T/W$  increases the cruise situation worsens because the engine would have to be throttled back during cruise, which moves away from the minimum TSFC bucket as shown in Fig. 18.1.

Also, as  $T/W$  increases so does the propulsion weight. Thus, for a large  $T/W$  there would be a lot of extra weight that is used for only a portion of the mission (admittedly the most important part of the mission). Again it is emphasized to examine the entire mission fuel requirement before selecting the  $(T/W)_{TO}$ .

### 18.5 Engine Sizing for Acceleration

Acceleration can be examined very simply by looking at the ideal rocket equation

$$\Delta V = I'_{sp} g \ln \left( \frac{W_i}{W_f} \right) \quad (18.6)$$

where  $I'_{sp}$  is the effective  $I_{sp}$  available for accelerating the vehicle. The effective  $I_{sp}$  is defined as

$$I'_{sp} = I_{sp} \left( 1 - \frac{D}{T} \right) \quad (18.7)$$

where  $D$  is the drag,  $T$  is the thrust available, and  $I_{sp} = 3600/\text{TSFC}$  is the *engine specific impulse*. It is clear from Eqs. (18.6) and (18.7) that the thrust must be much larger than the drag; otherwise the  $I'_{sp}$  will be small and considerable fuel will be expended during a  $\Delta V$  acceleration. If  $\Delta V$  is a very large increment, the  $I'_{sp}$  must be an averaged value over the acceleration interval.

The acceleration performance of an aircraft improves as  $D/T$  decreases or  $(T/W)_{TO}$  is increased. The reason is that the excess thrust (i.e.,  $T - D$ ) increases, which decreases acceleration time and fuel burned. Absolute minimum intercept or acceleration time would mean  $(T/W)_{TO} \rightarrow \infty$ . A typical plot of time vs  $(T/W)_{TO}$  is shown in Fig. 18.2 and it is observed that after a certain  $(T/W)_{TO}$  the curve gets rather flat, resulting in a small improvement for additional  $(T/W)_{TO}$ . Equations (18.6) and (18.7) indicate that the fuel burned during an acceleration continues to decrease as  $(T/W)_{TO}$  increases. It is misleading to look solely at acceleration fuel burned because, as  $(T/W)_{TO}$  increases, the weight of the propulsion system increases. Thus, a better quantity to examine is the sum of engine weight plus fuel weight. This is shown plotted in Fig. 18.2 for a conceptual Advanced Manned Interceptor (AMI). Near-minimum acceleration time is certainly important for an interceptor; however, the designer must trade off decreased acceleration time with increasing engine-plus-fuel weight. Figure 18.2 shows the point design for the AMI at a  $(T/W)_{TO} = 0.586$  (two reference turbo-ramjet engines), which is a compromise between acceleration time and engine-plus-fuel weight. The AMI is also range dominated and the designer is reminded to examine the cruise efficiency also before making the final selection for  $(T/W)_{TO}$ .

## 18.6 Turbine Engine Sizing for Takeoff

If a short takeoff distance is a primary mission requirement, it should be considered in a fair amount of detail at this point because it may size the engines. The takeoff analysis is discussed in Chapter 10. It must be remembered that a short takeoff distance can be achieved using combinations of  $(T/W)_{TO}$ ,  $(W/S)_{TO}$ , and high-lift devices [see Fig. 6.3 and Equation (6.3)]. Thus, a short takeoff distance need not have a high  $(T/W)_{TO}$ .

### Example 18.2 Turbine Engine Sizing Dilemma

Figure 18.3a shows the mission profile for the Advanced Tactical Fighter (ATF) that became the F-22. The mission profile is very

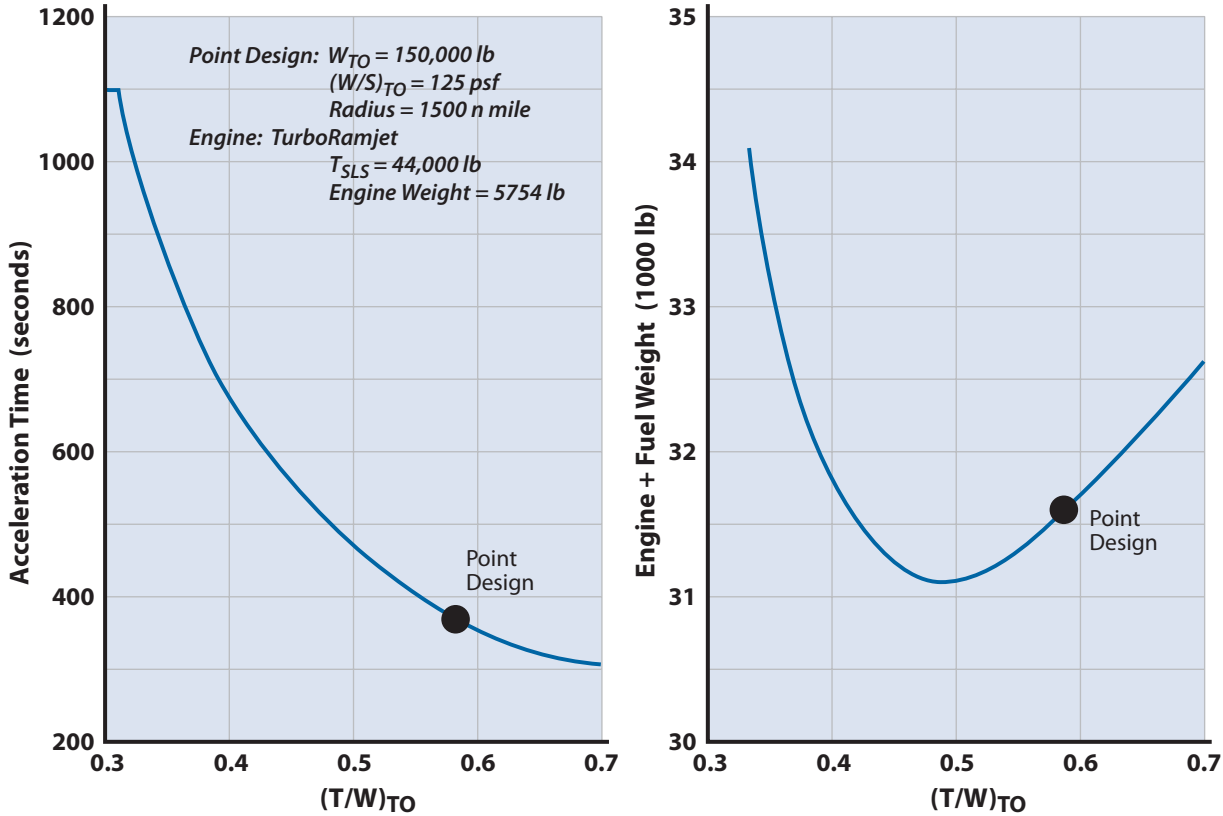


Figure 18.2 Acceleration performance of an Advanced Manned Interceptor (acceleration from 250 ft/s to Mach 4.5 at 75,000 ft).

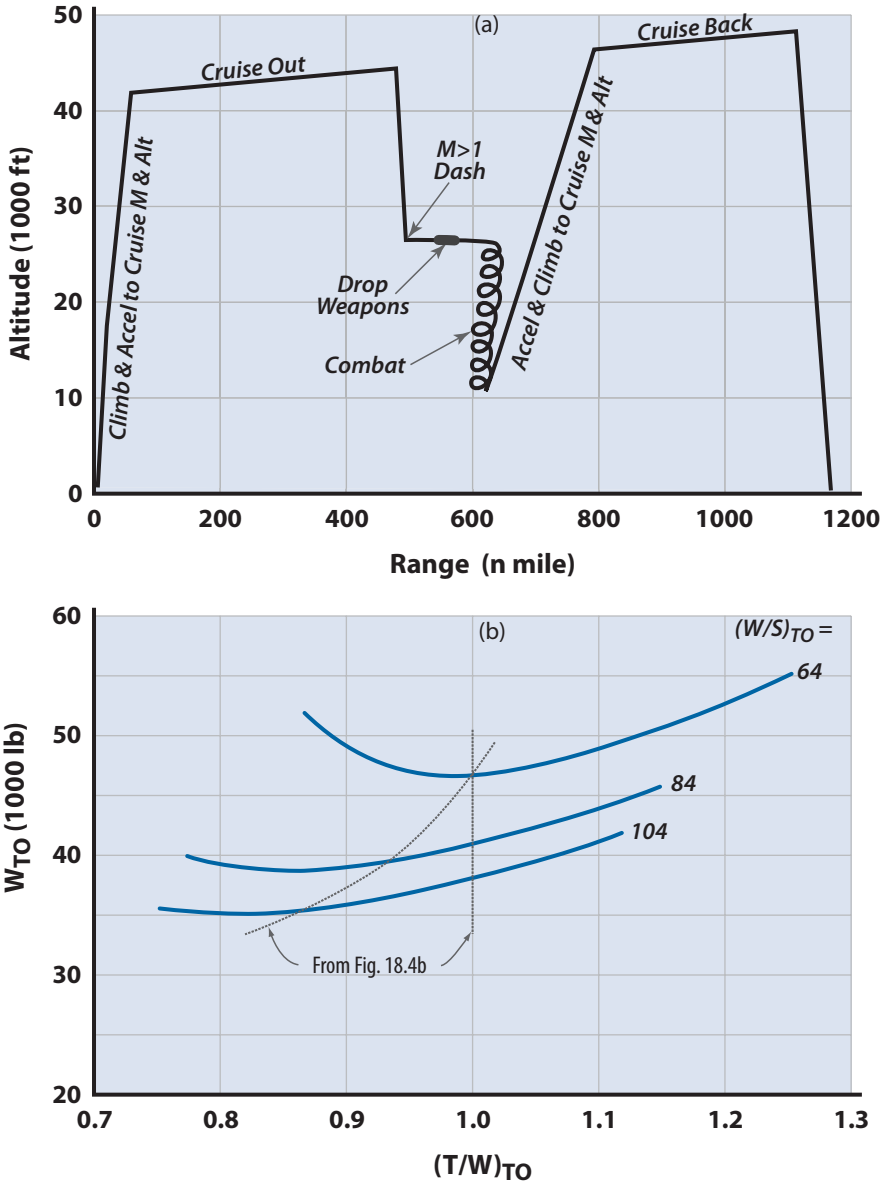


Figure 18.3 Typical tactical fighter mission profile and its associated  $(T/W)_{TO}$  variation.

demanding as it calls for a significant supersonic cruise phase, a supersonic dash, several acceleration phases, and air combat. The Air Force was asking for supercruise, supermaneuver, and superstealth—all in the same airplane. This example will bring out the dilemma

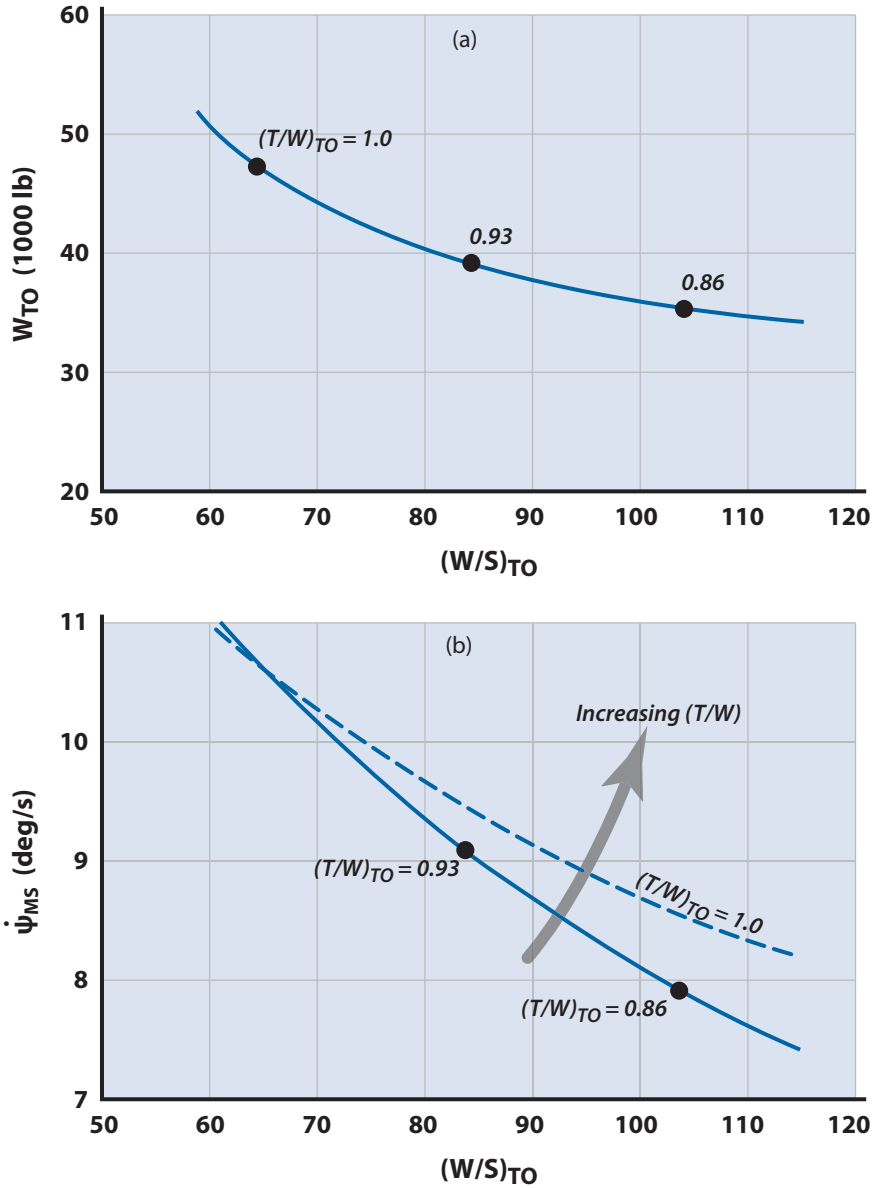


Figure 18.4  $(W/S)_{TO}$  variation for a typical tactical fighter on its basic mission.

facing the designer when selecting the  $(W/S)_{TO}$  and  $(T/W)_{TO}$  for an aircraft that is driven by several conflicting requirements.

Figures 18.3b and 18.4a show that the  $W_{TO}$  decreases for increasing  $(W/S)_{TO}$  and decreasing  $(T/W)_{TO}$ . The decreasing  $(W/S)_{TO}$  is understandable from the discussion in Chapter 6 and the fact that the level of air combat is not specified. The best  $(T/W)_{TO}$  from Figures

18.3b and 18.4a would be a compromise between the supercruise, supersonic dash, and acceleration requirements. When air combat is considered, Fig. 18.4b, the situation is reversed; the desire to have high  $\dot{\psi}_{MS}$  would drive the design to high  $(T/W)_{TO}$  and low  $(W/S)_{TO}$ . The designer has a dilemma and must compromise the design to give tolerable cruise performance, acceleration fuel, and air combat levels.

## 18.7 Solar Power

The sun is a source of unlimited energy during the day. Every day it bathes the outer edge of the earth's atmosphere with  $127 \text{ W/ft}^2$  of solar energy on average. The  $127 \text{ W/ft}^2$  is termed the *solar constant*. The amount of solar energy received anywhere on the earth at a point in time depends on the latitude  $\Phi$  of the surface, the tilt (inclination) of the earth's spin axis as it orbits around the sun, and its position relative to the sun (time of day).

This dependence is shown in Fig. 18.5. The inclination of the earth to the orbital plane varies between  $+23.5$  deg on 21 June and  $-23.5$  deg on 21 December and is the reason the earth has its four seasons. On 21 June the northern hemisphere is getting more solar energy and is enjoying summer while the southern hemisphere is getting less and is having winter. On 21 December the situation reverses. On 21 June the northern hemisphere has its longest day of the year and on 21 December the shortest.

The solar energy received on earth is converted to useful electrical energy by the photovoltaic action of solar cells. The electrical energy per unit area available from a horizontal solar cell of efficiency  $\eta_{SC}$  at an altitude  $H$  and solar elevation angle  $\theta$  is

$$P_{\text{Elect}} = P_{\text{Solar}} \eta_{SC} \sin \theta \quad (18.8)$$

where  $\theta$  is the elevation angle of the sun above the horizon and  $\sin \theta$  accounts for the presented area of the horizontal solar cell. The solar elevation angle is a complicated function of the latitude, inclination angle (time of year), and orientation to the sun (time of day) [1,2]. The best way to determine  $\theta$  is to go to the National Oceanic and Atmospheric Administration (NOAA) Web site and use their solar position indicator.

The quantity  $P_{\text{Solar}}$  is the average solar radiation at altitude  $H$  and solar elevation angle  $\theta$ . The earth's *atmospheric mass* (AM) has a significant effect on the value of  $P_{\text{Solar}}$ . The water and ozone in the atmosphere absorb and scatter the solar radiation:  $P_{\text{Solar}} = 127 \text{ W/ft}^2$  in space (outside the earth's atmosphere at an altitude of approximately 320,000 ft or 53 n mile), whereas  $P_{\text{Solar}} = 96.5 \text{ W/ft}^2$  on the earth's surface and  $\theta = 90$  deg, having suffered a 24% energy loss due to atmospheric attenuation. The space condition is termed AM0 and the condition on the earth's surface and  $\theta = 90$  deg is AM1.0. Values for  $P_{\text{Solar}}$  at altitude  $H$  and solar elevation angle  $\theta$  are given

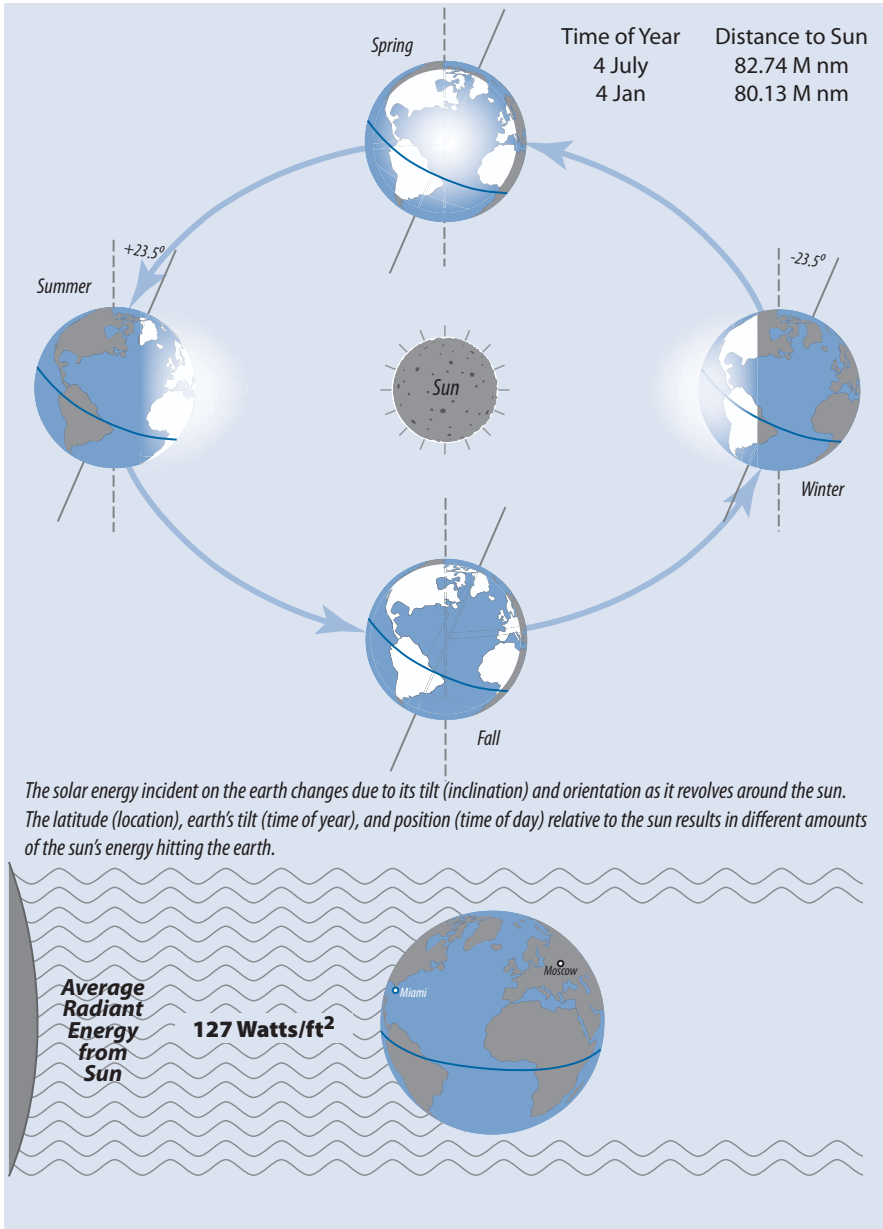


Figure 18.5 Solar energy radiated to earth during the year.

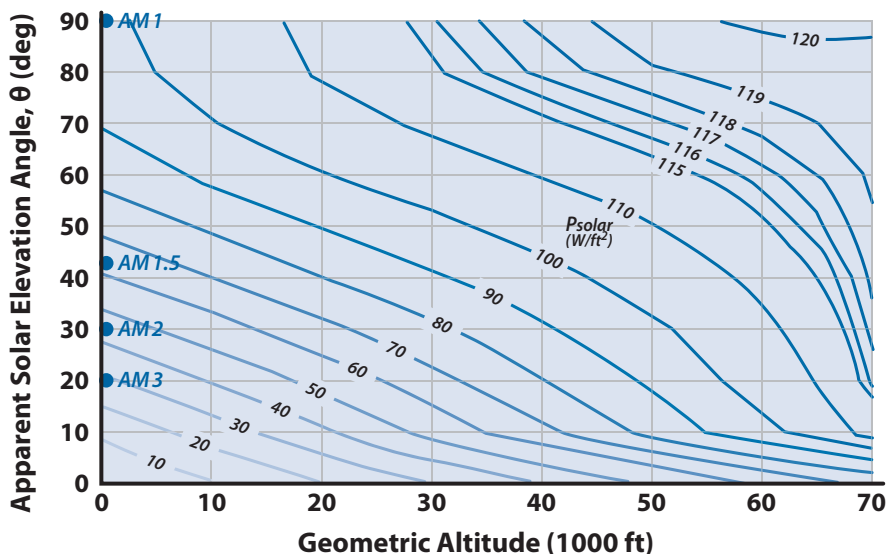


Figure 18.6 Direct clear-sky  $P_{\text{solar}}$  ( $\text{W}/\text{ft}^2$ ).

in Fig. 18.6 (essentially,  $H$  and  $\theta$  define the *slant range* through the atmosphere).

Even though the solar energy is limitless and free, it is small when compared with the energy available from burning hydrocarbon fuels (i.e., gasoline or kerosene). Because the power required increases by the cube of the speed and the available solar power is small, the speed of a solar aircraft will always be less than 30 KEAS (knots equivalent airspeed). This can be shown by setting power required = power available.

$$\begin{aligned} \text{Power required} &= (\text{Drag})(\text{Velocity}) / (\text{Propulsive efficiency}) \\ &= \left( \frac{1}{2} \rho C_D S_{\text{Wing}} V^2 \right) (V) / \eta_{\text{Prop}} \end{aligned} \quad (6.10)$$

$$\text{Power available} = P_{\text{Solar}} \eta_{\text{SC}} S_{\text{SC}} \sin \theta \quad (18.8)$$

Then assume typical values for the parameters and solve for  $V$  as follows:

Altitude = 60,000 ft	$\rho = 0.000224 \text{ slug}/\text{ft}^3$
$\theta = 90^\circ$ (optimistic)	$P_{\text{Solar}} = 120 \text{ W}/\text{ft}^2$ (Fig. 18.6)
$\eta_{\text{SC}} = 31\%$	35% in lab, 31% installed on wing
$\eta_{\text{Prop}} = 0.81$	Motor, propeller and line losses
$S_{\text{Wing}} = S_{\text{SC}}$	Reasonable and it makes the math simpler
$C_D = 0.0356$	Condor at best loiter condition (see Fig. G.11)
Payload and vehicle power = 0	Not realistic but makes the point



$V = 177 \text{ ft/sec} = 105 \text{ knots at } 60,000 \text{ ft} \sim 30 \text{ KEAS}$ , and this is the best it can do.

The electrical energy available from a solar cell of efficiency 28.7% at Miami, Florida (latitude  $\Phi = +25^\circ 46'$ ), and Moscow ( $\Phi = +55^\circ 45'$ ) is shown in Fig. 18.7 for 4 July and 5 January over a 24-hour period [1,2]. The area under the curves is the total electrical energy per unit area [watt-hours per square foot ( $\text{W}\cdot\text{h}/\text{ft}^2$ )] captured by horizontal solar cells during the daylight hours. Notice that Moscow and Miami have about the same total energy on 4 July even though Moscow is at a much higher latitude. The reason for this is that Moscow has more daylight hours than Miami (17 and 14 hours, respectively). This is not the case on 4 January.

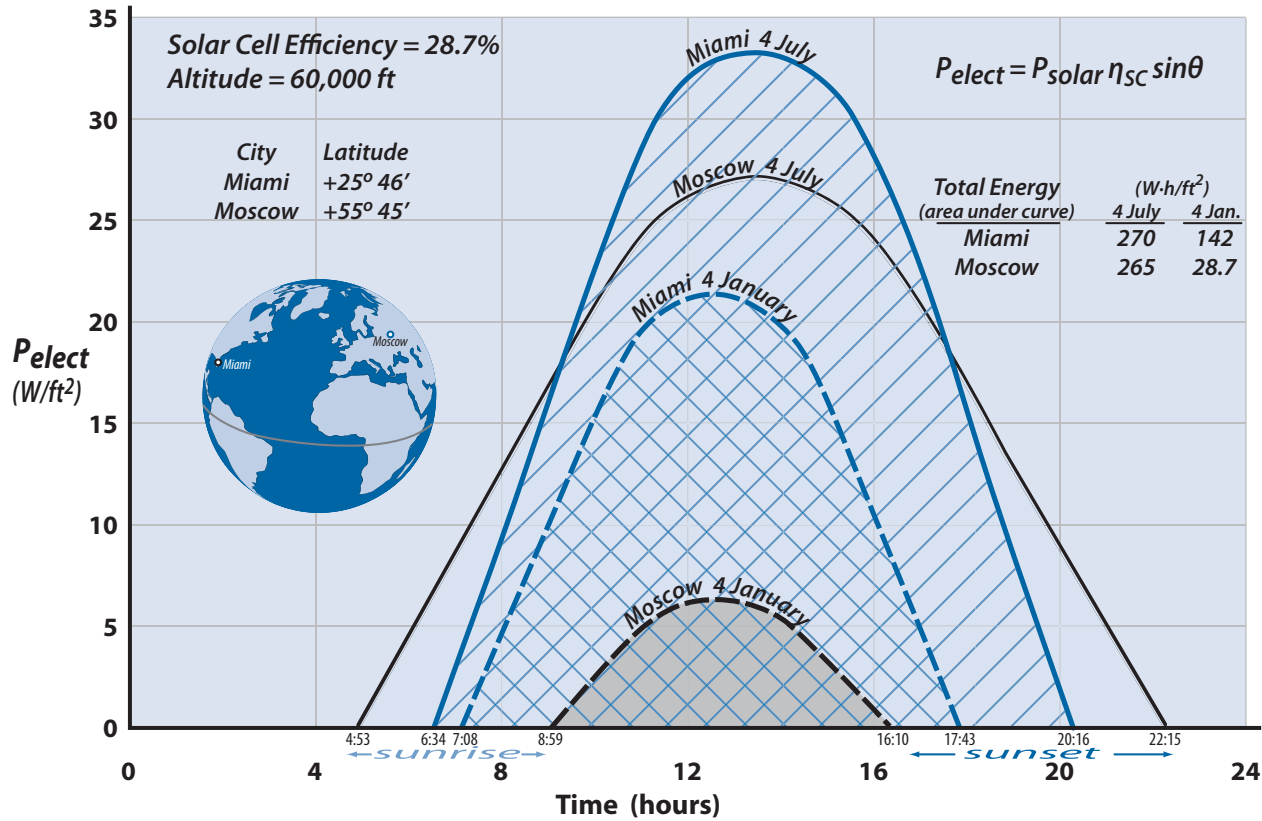
## 18.8 Sizing Solar-Powered Aircraft

It is time to return to the Solar Snooper, introduced in Chapter 6, and close the design shown in Fig. 6.8 by determining if the wing size  $S_w = 2793 \text{ ft}^2$  from Section 6.7 will provide enough solar-cell area to meet the power required. Then the design can be closed by developing a weight buildup to meet the assumed 4800 lb takeoff gross weight (TOGW).

The requirement for the Solar Snooper is to provide 4 weeks of “24/7” intelligence, surveillance, and reconnaissance (ISR) at 64,000 ft, in midlatitudes during the summer months. The payload is 500 lb, which requires 1 kW of power.

The goal is to design a solar-powered aircraft for operation over Miami and Moscow during the 4-week period starting 7 June and ending 4 July. Trade studies reveal that 4 July is the critical day during the 4-week interval in terms of energy available from the sun (longest distance to sun).

The analysis of Section 6.7 concluded that the total power required to operate at 68 kt at 64,000 ft at  $C_L = 1.33$  was a continuous 24 kW. Refer to the electric aircraft data base shown in Table 14.2 and assume a solar-cell efficiency of 32% (note, these will be multijunction cells and will be expensive). Also, assume that the energy for nighttime operation will be stored in batteries instead of fuel cells (this is an important trade study that needs to be conducted and is left as an exercise for the reader). The baseline round trip efficiency for the batteries is 0.9. However, there are line losses that need to be considered. First there is a transmission efficiency  $\eta_{\text{Trans}} = 0.98$  going in and coming out of the battery. Then there is a power control switch/step efficiency  $\eta_{\text{Switch}} = 0.90$  going in and coming out of the battery. Thus, the total round trip efficiency for the battery storage system is  $\eta_{\text{RT}} = (0.98)(0.98)(0.9)(0.9)(0.9) = 0.7$ . The continuous power that needs to be provided to the batteries is  $24/0.7 = 34.28 \text{ kW}$  for operating at night. The continuous required power loading for the batteries is  $P_{\text{Req}} = (34.28)(1000)/(2793) = 12.3 \text{ W}/\text{ft}^2$ , where the solar cell area is assumed to be the wing



**Figure 18.7** Comparison of electrical energy available for Miami and Moscow at 60,000 ft.

surface area. This  $P_{\text{Req}}$  will be balanced with the available energy collected by the solar cells.

Solar cells are assumed to have a laboratory efficiency of 32%. As mentioned, these are multijunction cells and will be expensive. Each solar cell generates 0.5 volt. The cells are connected together to form a blanket (typically 36 individual cells are connected together, generating 18 volts DC with a blanket packing efficiency of ~95%). The blankets are connected together to form a solar array with an array electronics efficiency of 95%. The solar arrays are glued onto the vehicle surface. If the cells are going to be in service for long periods, the environment will degrade the cell efficiency by about 1.5% per year (called *end-of-life efficiency*). The Solar Snooper cells will be in service for only 4 weeks so that this will not be a concern. Thus, the end-of-life efficiency for the solar cells will be  $(32)(0.95)(0.95) = 28.7\%$ .

The solar cells are put on the upper surface of the wing. However, the cells should not run right to the leading edge as their heat and contour disturbance will trip the boundary layer to turbulent and limit the laminar extent of the wing. The cells should start at about 15% chord, where the boundary layer thickness is large compared with the thickness of the solar cells. Similarly, there is about 5% of the trailing edge region that is not usable for the solar cells. Common practice initially sizes the horizontal tail to recover the 20% of the wing area lost for the solar cell installation (note, this initial tail sizing can be compared with the tail volume coefficient method of Chapter 11 later). Thus, the horizontal tail is  $S_{\text{HT}} = 558 \text{ ft}^2$  and the solar cell area is assumed to be  $2793 \text{ ft}^2$ . This assumption lets us now balance  $P_{\text{req}} = 12.3 \text{ W/ft}^2$  with the power available  $P_{\text{Elect}}$  shown in Fig. 18.7.

This power balance is shown in Fig. 18.8. The total electrical energy available on 4 July over Miami and Moscow is 270 and  $265 \text{ W} \cdot \text{h/ft}^2$  respectively. The total power required by the Solar Snooper is  $12.3 \text{ W/ft}^2$  continuous over the nighttime period and  $8.6 \text{ W/ft}^2$  continuous during the daytime (the difference is due to the round trip efficiency of the batteries).

During the daylight hours of 4 July the aircraft must collect an excess amount of power  $A_1$  that equals the storage power required ( $R_1 + R_2$ ). From Fig. 18.8 the power sizing results are (shown for Moscow)

Over Miami:

$$A_1 - (R_1 + R_2) = 167 - 154.6 = 12.4 \text{ W} \cdot \text{h/ft}^2 \text{ (8\% margin)}$$

Over Moscow:

$$A_1 - (R_1 + R_2) = 140 - 127.2 = 12.8 \text{ W} \cdot \text{h/ft}^2 \text{ (10\% margin)}$$

Because 4 July is the critical day (least total energy available) there will be excess energy collected on all other days in the 4-week surveillance

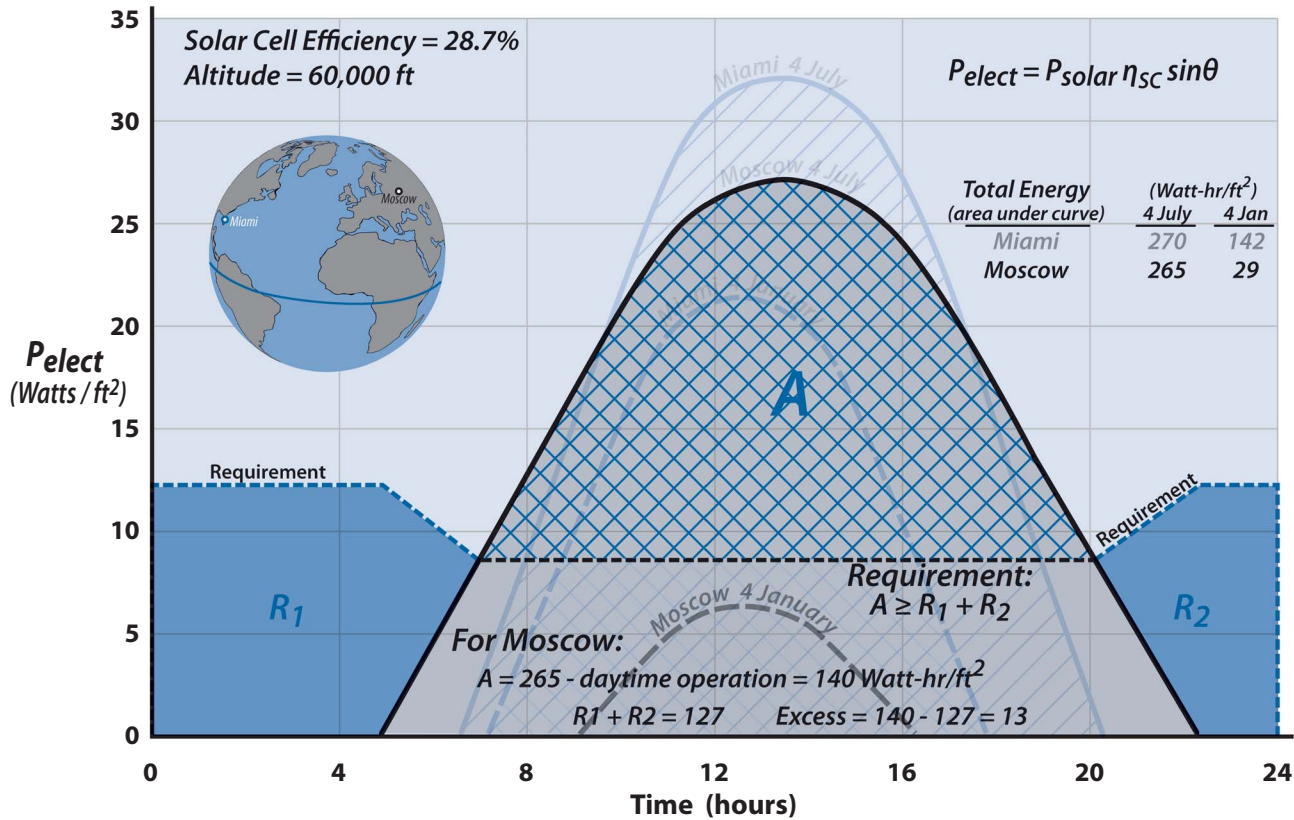


Figure 18.8 Diurnal energy balance example for stationkeeping over Moscow.

period. It is a good idea to carry at least a 10% margin during the conceptual design phase. A power balance closure for Miami and Moscow has been obtained.

The horizontal tail area should be checked by using the tail volume coefficient method of Chapter 11 to make sure there is adequate static pitch stability. From Table 11.8,  $C_{HT} = \ell_{HT} S_{HT}/S_W \bar{c} = 0.34$  for ISR aircraft. From Fig. 6.8,  $\ell_{HT} = 41$  ft and  $\bar{c} = 8$  ft so that  $S_{HT} = 185$  ft<sup>2</sup>. Observe that  $S_{HT}$  is sized not by static pitch stability but by the required solar cell area by a factor of 3. This results in a neutral point that is very far aft. Because the center of gravity should be located slightly forward of the neutral point (a static margin of approximately +5%  $\bar{c}$  as discussed in Chapter 22) to minimize trim drag, the location of the center of gravity can be changed by sliding the payload pod fore and aft.

The vertical tail area is determined by static yaw stability using the method of Chapter 11. From Table 11.8,  $C_{VT} = \ell_{VT} S_{VT}/S_W b = 0.014$  for ISR aircraft. From Fig. 6.8,  $\ell_{VT} = 55$  ft and  $b = 317$  ft so that  $S_{VT} = 225$  ft<sup>2</sup> for the two verticals.

Now it is time to re-examine the assumed TOGW = 4800 lb. Weight is estimated for electric motors, solar cells, and batteries using the data from Table 14.2. Estimating the weights of the wing, tails, landing gear, payload pod, and booms is a real challenge for a  $W/S < 5$  lb/ft<sup>2</sup> aircraft because the historical data base is almost nonexistent. The wing is the major structural component and its weight is estimated using Fig. 20.1. Chapter 19 will discuss this dilemma but it will remain a design weakness. The Solar Snoopers weight summary is shown in Table 18.2.

**Table 18.2** Solar Snoopers Weight Summary

Component	Weight (lb)	Reference
Wing	838	0.30 lb/ft <sup>2</sup> (Fig. 20.1) for $W/S = 1.72$
Pod and booms	341	Sailplane data [3]
Motor, propellers, install	188	0.2 kW/lb + 25% install factor (Table 14.2)
Solar cells	279	0.1 lb/ft <sup>2</sup> (Table 14.2)
Landing gear	96	2% of TOGW (sailplane data)
Tails	235	0.30 lb/ft <sup>2</sup> (Fig. 20.1)
Payload	575	Requirement (500 lb) + 15% for installation
Batteries	1524	34.3 kW for 12 hr at 3.7 lb/kW (Table 14.2)
Battery installation	230	15% installation factor
Avionics, actuators	100	Double that for Helios
Margin	393	8% (should carry at least a 6% margin)
<b>Total</b>	<b>4800</b>	

An interesting question at this point is “Is there a Solar Snooper design that could operate over Moscow on 4 January?” It is clear from Fig. 18.8 that the design shown in Fig. 6.8 will not work because the total available electrical energy of  $28.7 \text{ W}\cdot\text{h}/\text{ft}^2$  is nowhere close to the required nighttime  $R_1 + R_2 = 127.2 \text{ W}\cdot\text{h}/\text{ft}^2$ . Thus, the design must change considerably.

If it is assumed that the daytime continuous  $P_{\text{Req}} = 1 \text{ W}/\text{ft}^2$  over  $\sim 7 \text{ h}$  (or  $7 \text{ W}\cdot\text{h}/\text{ft}^2$ ), then the excess electrical energy  $A_1 = 28.7 - 7 = 21.7 \text{ W}\cdot\text{h}/\text{ft}^2$ . The required nighttime energy  $R_1 + R_2 = (1)(14)/0.7 = 20 \text{ W}\cdot\text{h}/\text{ft}^2$ , which gives a positive power balance with an 8.5% margin—so the design is “in the ballpark.”

However, the challenge is to decrease the daytime continuous  $P_{\text{Req}}$  from  $8.6 \text{ W}/\text{ft}^2$  for the current design to  $1.0 \text{ W}/\text{ft}^2$  for the new design. Some design changes to consider are the following:

- Decrease the payload and aircraft operation power required to 0.5 kW each.
- Decrease the  $W/S$  from 1.72 to  $1.0 \text{ lb}/\text{ft}^2$ . This would increase the wing area (more area for solar cells) and decrease the speed to about 90 ft/s. The increase in wing area would increase the TOGW (heavier wing and more solar cells) and drag, but the overall impact would be a lower propulsion power required.
- Increase the vertical tail area and cover it with solar cells. This would provide more electrical energy especially at the low solar elevation angles over Moscow in the winter. The flight path would have to be tailored to take advantage of the vertical solar cells.
- Finally, the solar cell efficiency could be increased within reason.

It remains as an exercise for the reader to determine if there is a design that closes. It should be obvious to the reader that the design of an aircraft powered by hydrocarbon fuels (i.e., gasoline, diesel, JP-4, etc.) is a much easier challenge than the design of a solar-powered aircraft. This is because the hydrocarbon-powered aircraft:

- Is not expected to have an endurance of more than about 3 days (72 hours).
- The size of the required propulsion unit is independent of latitude, time of year, and time of day.
- The size of the wing is independent of latitude, time of year, and time of day.
- If there is a thrust shortfall, get a bigger engine (do not have to resize the whole aircraft).
- And the list goes on!

## 18.9 Piston Engine Sizing—HAARP

From the discussion in Chapter 5 (Section 5.8) HAARP is required to fly at 100,000 feet and Mach 0.6 (594.7 ft/s). The design information for sizing the piston engine is as follows:

TOGW	16,000 lb
Weight at start of cruise	14,880 lb
$L/D$ at start of cruise	27
Drag at start of cruise	$14,880/27 = 551$ lb
High-altitude propeller (designed using ISES code):	
Diameter	24 ft
RPM	528
Efficiency $\eta_P$	0.85
Power required at start of cruise	$(\text{drag})(\text{speed})/550 \eta_P = 700$ hp

Teledyne Continental (TCM) had provided the engines and developed the two-stage turbochargers for the Boeing Condor. Discussions with TCM centered around their family of geared, liquid-cooled piston engines and their turbocharger experience. Their GTSIOL-550 piston engine was selected. The engine specifications were as follows:

Takeoff-climb power	500 hp
Continuous cruise maximum power	375 at BSFC = 0.42
94% maximum power	350 at BSFC = 0.40
Number of cylinders	6
Weights (total = 581 lb):	
Engine	445 lb
Ignition and plugs	30 lb
Exhaust manifold	12 lb
Starter	19 lb
Gearbox	75 lb

The HAARP configuration shown in Fig. 5.11 is a twin-engine pusher design. The engines are in wing pods. The propeller arrangement consists of an 8 ft diameter, four-blade propeller for takeoff, landing, and climb and a 24 ft diameter, two-blade propeller for high altitude. The small propeller would operate all the time whereas the large propeller would be clutched in at 45,000 ft. The two engines would be operated at maximum power (500 hp) for climb but throttled back to 94% (350 hp) for cruise at Mach = 0.6 at 100,000 ft.

The Lockheed Skunk Works submitted a proposal to NASA Dryden Flight Research Center in 1991 to build and operate two HAARP aircraft. NASA declined the offer and instead contracted with Aurora Flight Systems to build the Perseus aircraft (Fig. 18.9). The Perseus B exceeded 60,000 ft in 1998 with a three-stage turbocharged piston engine.



**Figure 18.9** The Aurora Flight Systems Perseus UAV developed for NASA high altitude ozone measurements.

A structural analysis and design will be conducted for the HAARP wing in Chapter 19 (Section 19.14).

## 18.10 Human-Powered Aircraft—Daedalus

The design of a human-powered aircraft starts with the description and performance of the propulsion system. The powerplant in this case is the human engine. Yale University investigated the limits of endurance and the power level of the human powerplant. Their research concluded that an endurance-trained athlete using a specially built recumbent ergometer (essentially a reclined bicycle) could produce a specific power of 3 W/kg (0.00183 hp/lb) for several hours [4,5]. For peak performance the athlete needed preloading with glycogen, controlled temperature, and adequate water supply.

Thus, the available power would be 0.2745 hp for a well-trained 150-lb athlete.

Because the power available is small the design approach is very similar to that of a solar-powered aircraft, such as the Perseus shown in Fig. 18.9 and the Solar Snooper discussed in Example 6.7. The aircraft speed will be low (less than 20 kt) and the wing loading less than 1 lb/ft<sup>2</sup>.

Previous human-powered projects have shown that the aircraft is about two-thirds the weight of the pilot. For our 150-lb pilot the aircraft weight would be about 100 lb. For the human-powered aircraft the payload is essentially the pilot so that the total aircraft weight would be approximately 250 lb.

If analysis methods from the early part of the book are used, then specifications can be estimated for the human-powered aircraft. Start by assuming the speed to be 12 kt and the propeller efficiency to be 0.85. The rationale is based upon observations with the Solar Snooper analysis. Then



the drag from the power required Eq. (6.10) is 6.25 lb. This means that the aircraft cruise  $L/D$  needs to be 40. From the Solar Snooper example the aspect ratio would be  $\sim 36$ .

The altitude will be less than 500 ft above ground level (AGL) because the aircraft would like to take advantage of ground effects. This gives us a Reynolds number per foot  $\rho V/\nu = 127,300$  per ft. If the  $W/S = 1$  lb/ft<sup>2</sup>, then  $S = 150$  ft<sup>2</sup> and the wing span = 73.5 ft. The average chord is 2.0 ft and the  $Re = 260,000$ . The cruise  $C_L = W/qS = 1.0/0.48 = 2.1$  for the  $W/S = 1.0$  lb/ft<sup>2</sup>. This is much too high for current low- $Re$  airfoils [6]. Because the aircraft cannot fly any faster than  $\sim 20$  ft/s the  $q$  is fixed at 0.48 lb/ft<sup>2</sup>. A cruise  $C_L = 1.0$  is more realistic. Thus, the wing loading needs to decrease to about 0.5 lb/ft<sup>2</sup> and the wing area increase to 300 ft<sup>2</sup>. Holding the aspect ratio constant gives a wing span of 104 ft. This is a good trade as it gives us a slightly larger average chord of 2.9 ft and a wing  $Re = 368,000$ .

The design specifications for our human-powered aircraft are as follows:

Power available	0.2745 hp
Pilot weight	150 lb
Aircraft weight	100 lb
Cruise speed	12 kt
Propeller efficiency	0.85
Cruise $L/D$	40
Wing aspect ratio	36
Wing span	104 ft
Wing average chord	2.9 ft
Wing area	300 ft <sup>2</sup>
Wing $Re$	368,000

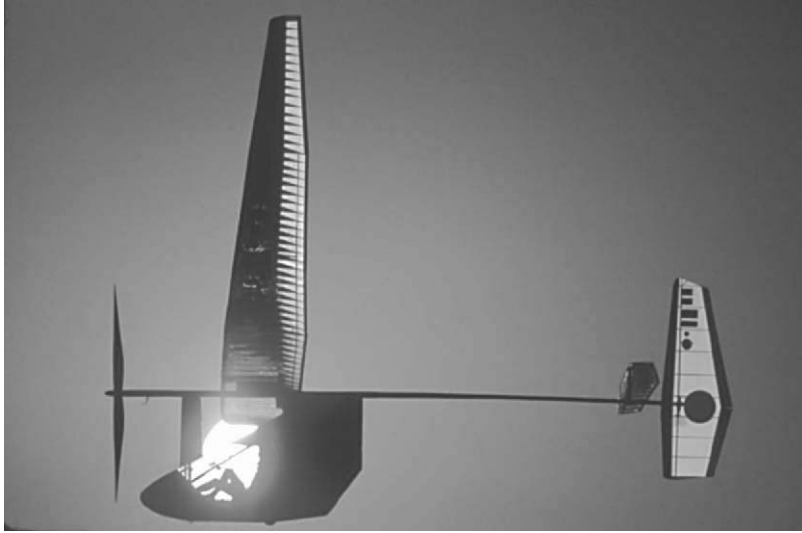
Readers are now requested to read the Daedalus case study in Volume 2. They should recognize the Daedalus specifications as being very similar to the preceding estimates. The case study will add substance and realism to the design analysis in this section.

Figure 18.10 shows the human-powered Daedalus at sunrise, at the start of its 3 h 54 min historic flight across the Sea of Crete on 23 April 1988 [7]. The Daedalus case study in Volume 2 was written by Harold Youngren, the chief engineer on the MIT project.

## 18.11 Rocket Engine Sizing

Rockets are sized for acceleration and burn-out speed. Acceleration is a function of the  $T/W$  of the rocket. A typical  $T/W$  is 1.4–2.0 so that the rocket accelerates quickly through the atmosphere in about 140 seconds.

The burn-out speed is determined by the amount of fuel carried by the rocket  $W_i/W_f$  as given by Eq. (18.6). The rocket sizing needs to account for the gravity and drag losses as the rocket exits the atmosphere. Gravity



**Figure 18.10** Human-powered Daedalus takes off on its historic flight across the Sea of Crete (courtesy of Charles O’Rear).

losses are insignificant for aircraft but significant for rockets as they usually are boosting vertically until outside of the atmosphere. Similarly the drag losses are small for a rocket because they accelerate through the atmosphere quickly. Instead of correcting the rocket  $I_{sp}$  for these losses as was done for jet aircraft in Eq. (18.7), the  $\Delta V$  will be increased to account for drag and gravity losses.

A low earth orbit (LEO) is defined as an orbit outside of the earth’s atmosphere where orbital decay of the spacecraft due to drag is not a problem. The edge of the atmosphere is approximately 90 miles up from the earth’s surface. The outer limit for a LEO is below the inner Van Allen radiation belt (about 1088 n mile). A geosynchronous orbit (GEO) is an orbit where a spacecraft would appear stationary over a point on the surface of the earth (would have a period of 24 h). A GEO orbital altitude would be 19,468 n mile above the earth’s surface.

The Daedalus was a project undertaken by the MIT Department of Aeronautics and Astronautics in 1985 to recreate the mythical escape of Daedalus from his tower cell on the island of Crete, across the Sea of Crete to the island of Santorini—a distance of almost 65 n mile [7]. According to Greek mythology Daedalus and his son Icarus escaped from their cell by gluing bird feathers onto their bodies with wax. Icarus flew too close to the sun and the wax melted, causing Icarus to plummet to his death. The older and wiser Daedalus stayed a safe distance from the sun and flew to freedom.

### Example 18.3 Rocket Sizing for a Low Earth Orbit

Size a rocket to put 1000 lb of payload into a 500,000 ft (82 n mile) LEO. The speed of the rocket at 500,000 ft needs to be 25,638 ft/s

tangent to the curve of the earth, balancing the centrifugal and gravitational forces. If the orbital direction is to the east at latitude  $\Phi^\circ$ , the rocket will get a  $\Delta V$  boost of  $1520 \cos \Phi$  ft/s due to the earth's rotation. If launching to the west, the rocket has to increase its  $\Delta V$  by the amount  $1520 \cos \Phi$  ft/s.

Assume the following launch conditions:

Launch location	Cape Canaveral, Florida ( $\Phi = 26^\circ$ latitude)
Launch direction	east
Earth rotation speed	1366 ft/s ( $1520 \cos \Phi$ )
Gravity losses during boost	3100 ft/s
Drag losses during boost	1200 ft/s
Rocket $I_{sp}$	330 s (kerosene/O <sub>2</sub> )

The  $\Delta V$  required from the rocket is  $\Delta V = 25,638 - 1366 + 3100 + 1200 = 28,572$  ft/s.

The rocket weight fraction using Eq. (18.6) is

$$W_i / W_f = \exp[\Delta V / g I_{sp}] = 14.7$$

which means that the payload, structure, and motor comprise 7% of the rocket and the fuel the remaining 93%. For a launch weight of 200,000 lb and a payload of 1000 lb, the fuel weighs 186,000 lb, leaving 13,000 lb for structure and motor. Fortunately, the motors are light (liquid propellant rockets have  $T/W_{\text{Motor}} \sim 55$ , and solid rockets are even better) and the structure is mostly a fuel tank. Using the  $T/W$  of 1.4–2.0 gives a rocket thrust of 280,000–400,000 lb.

## References

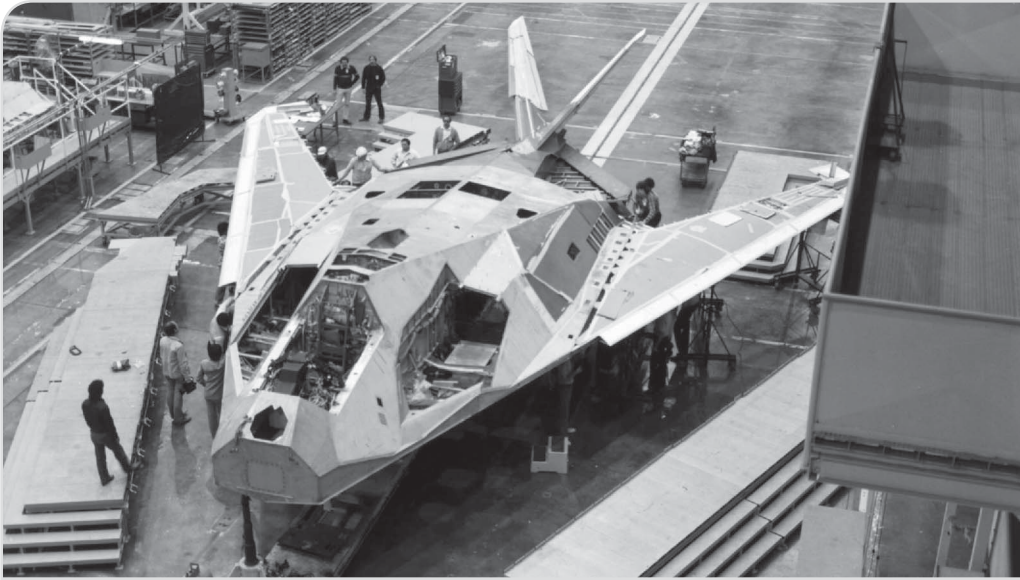
- [1] Youngblood, J. W., and Talay, T. A. "Solar Powered Airplane Design for Long Endurance, High Altitude Flight," AIAA Paper AIAA-82-0811, 18 May 1982.
- [2] Youngblood, J. W., Talay, T. A., and Pegg, R. J., "Design of Long Endurance Unmanned Airplanes Incorporating Solar and Fuel Cell Propulsion," AIAA Paper AIAA-84-1430, 13 June 1984.
- [3] Stender, W., "Sailplane Weight Estimation," OSTIV (International Scientific and Technical Gliding Organization), Elstree-Wassenaar, The Netherlands, 1969.
- [4] Wierwille, W. W., "Physiological Measures of Aircrew Workload," *Human Factors*, Vol. 21, No. 5, 1979, pp. 575–593.
- [5] Nadel, E. R., "Physiological Adaptations to Aerobic Training," *American Scientist*, Vol. 73, July–Aug. 1985.
- [6] Drela, M., "Low Reynolds Number Airfoil Design for the MIT Daedalus Prototype: A Case Study," *Journal of Aircraft*, Vol. 25, No. 6, 1988, pp. 724–732.
- [7] Lloyd, P., "Man's Greatest Flight," *Aeromodeller Magazine*, Aug. 1988 (Argus Specialist Publ., London).

# Chapter 19

# Structures and Materials

by Walter Franklin

Lockheed Martin Fellow in Structures and Materials



- Structural Design Criteria
- Strength vs Buckling Stability
- Finite Element Modeling
- Loads
- Stress Analysis
- Joints
- Material Selection
- Example

This F-117 was one of 64 built in total secrecy by Lockheed in Burbank, California. Completed aircraft were disassembled, put into a C-5A, flown to a secret base at Tonopah, Nevada, and reassembled. At base, they were kept in shelters during the day and flown for training only at night.

*One simple test can be worth a whole lot of analysis.*

## 19.1 Introduction

**A**ircraft structural design and analysis embodies a philosophy that is significantly different from the approach used for many civil engineering structures, such as bridges and buildings. Structural efficiency and minimum weight are of paramount importance for aircraft structure; and taking advantage of the inherent capability of thin-sheet structures to carry substantial load, even in a postbuckled state, is one of the key differences that separates aircraft structural design from other types of structural engineering. Since the Wright brothers' flight in 1903, the aircraft industry has developed a comprehensive body of design and analytical methods, based on extensive structural development testing combined with a wealth of lessons-learned from flight hardware, that make possible airframe structure that is safe, robust, and lightweight.

Aircraft structural engineering combines aspects of design, analysis, and manufacturing; and a basic knowledge in each of these areas is essential to the aircraft structural design process. The engineering disciplines that make up the Structures Group include the following:

1. External loads
2. Stress
3. Flutter and Dynamics
4. Mass properties
5. Materials and Processes
6. Structural testing

### Factor of Safety for Aircraft Structural Design

The ultimate factor-of-safety of 1.5 for aircraft structural design was first introduced in the early 1930s. Prior to this time, aircraft were designed to withstand, without failure, a certain load factor which was typically on the order of 6.0 *g*'s. The concept of limit load and ultimate load had not been developed at this time. Since aircraft structure designed in this manner did not show any widespread evidence of permanent yielding or structural failure, it was felt the existing load factor requirements must have included an inherent factor-of-safety. As aircraft speed and performance increased during this time period, it was felt necessary to define this factor-of-safety for future design efforts. The selection of 1.5, although somewhat arbitrary, was based in part on the ratio of ultimate strength to yield strength of the aluminum alloys that were being used at that time. Although a higher factor-of-safety could have been selected, there was also a desire to keep the resulting "limit load" as high as possible to not unduly penalize future aircraft designs.

*Professor F. R. Shanley, 1961*

The functions and responsibilities of each of these disciplines, and many of the technical challenges that each discipline encounters during the aircraft design and development process, are discussed in the following sections.

## 19.2 Structural Design Criteria and External Loads

The starting point for the design of airframe structure involves definition of the structural design criteria. The *structural design criteria* are the key parameters, such as design load factors, vehicle weights, speeds and altitudes, design life, factors-of-safety, and other operational considerations, that drive the design of the airframe. Although there are similarities in the structural design criteria among the various types of aircraft, many detailed requirements can vary greatly from one aircraft to another depending on a number of factors, including the agency that will grant flight certification (for example, commercial vs military certification), the particular class of aircraft (for example, fighter vs transport), and other requirements as dictated by the intended operator of the aircraft (for example, U.S. Air Force vs U.S. Navy requirements).

For military aircraft, the MIL-A-8860 series of documents provides a good starting point for defining structural design criteria. The various documents contained in the MIL-A-8860 series are summarized as follows:

1. MIL-A-8860, Aircraft Strength and Rigidity—General Specification
2. MIL-A-8861, Flight Loads
3. MIL-A-8862, Landplane Landing and Flight Handling Loads
4. MIL-A-8863, Ground Loads for Navy Procured Airplanes
5. MIL-A-8864, Water and Handling Loads for Seaplanes
6. MIL-A-8865, Miscellaneous Loads
7. MIL-A-8866, Reliability Requirements, Repeated Loads, and Fatigue
8. MIL-A-8867, Ground Tests
9. MIL-A-8868, Data and Reports

Similar design criteria for commercial and private aircraft are covered under the Federal Aviation Administration (FAA) guidelines contained in the Federal Aviation Regulation (FAR) documents.

Although the MIL-A-8860 documents are a valuable source of commonly used structural design requirements, new military aircraft development programs commonly employ “tailored” design criteria that are unique to the particular aircraft being developed. The “Joint Service Specification Guide—Aircraft Structures” (JSSG-2006) [1] provides a framework for developing such tailored design criteria. JSSG-2006 is one of eight Joint Service Specification Guides that were developed as part of acquisition reform by the U.S. government. These specification guides were developed

to provide the aerospace industry with a single, consistent approach for defining design requirements that would be common among the different military services [2]. JSSG-2006 is a comprehensive “fill-in-the-blank” type of template that covers a wide range of structural design requirements such as vehicle weight and center-of-gravity requirements, loading conditions, airframe construction parameters, aeroelastic requirements, material properties, and structural durability requirements. As such, it is an excellent resource to guide the development of a tailored set of design criteria to insure that all pertinent structural requirements are being addressed.

The Bell X-1, which in 1947 became the first aircraft to break the sound barrier, was designed to a vertical load factor ( $n_z$ ) of  $\pm 18 g$ , which was about 50% higher than the known  $g$  capability of any other aircraft being flown at that time.

A key design parameter contained in the structural design criteria is the flight envelope for the aircraft, commonly represented as a  $V-n$  diagram plotting aircraft speed in KEAS vs vertical load factor  $n_z$ , commonly expressed in  $g$ 's. Figure 19.1 shows a typical  $V-n$  diagram. Here, KEAS translates to *knots-equivalent airspeed*, which is the true airspeed corrected for the difference in density of the air at altitude compared with sea level (SL), as shown in the following expression:

$$V_e = \sqrt{\sigma} V_t$$

where

$V_e$  = equivalent airspeed (this is always written in knots as KEAS)

$\sigma = \rho_{alt} / \rho_{SL}$  (air density ratio)

$V_t$  = true airspeed

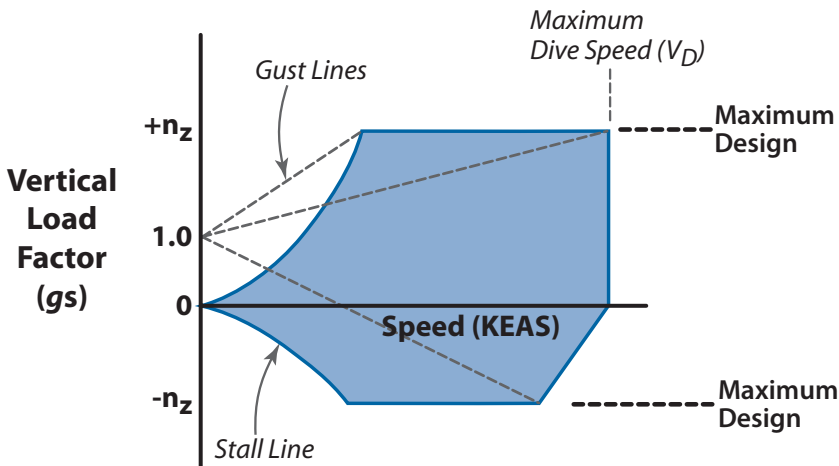


Figure 19.1 Typical  $V-n$  diagram used for airplane design.

Equivalent airspeed is often the measure of aircraft speed preferred by the Loads Engineer because it represents a speed with a constant dynamic pressure ( $q$ ), regardless of the aircraft's altitude.

The *vertical load factor*  $n_z$  is of particular interest because it is a key indicator of the critical flight loads that drive the design of the airframe structure, especially the wing structure. MIL-A-8861 provides guidance on the appropriate vertical load factors for different classes of aircraft. Maximum positive vertical load factors, as would be experienced during a pull-up maneuver, typically range from +3.0  $g$  for many transport-type aircraft to +7.5  $g$ , or more, for fighter-type aircraft. Maximum negative vertical load factors, as might occur during a push-over maneuver, commonly range from -1.0  $g$  for transport-type aircraft to -3.0  $g$  for fighter-type aircraft [3].

*Gust load factors*, which result from the aircraft flying through turbulent air, are also typically included on the  $V$ - $n$  diagram in the form of "gust lines." When an aircraft experiences a gust, the effect is an increase or decrease in the angle-of-attack, resulting in a change in lift and, consequently, a change in load factor. The load factor resulting from a gust can be estimated using the following *discrete gust relationship*:

$$n = 1 \pm \frac{K_g C_{L\alpha} U_e V_e}{498 W/S} \quad (19.1)$$

where

$C_{L\alpha}$  = lift curve slope (per radian) for the complete airplane

$U_e$  = equivalent gust velocity (ft/s)

$V_e$  = equivalent airspeed (KEAS)

$W/S$  = wing loading (lb/ft<sup>2</sup>)

$K_g$  = gust alleviation factor =  $0.88\mu/(5.3 + \mu)$  (subsonic aircraft)

where

$\mu$  =  $(2 W/S)/(\rho \bar{c} C_{L\alpha} g)$

$\rho$  = air density (slug/ft<sup>3</sup>)

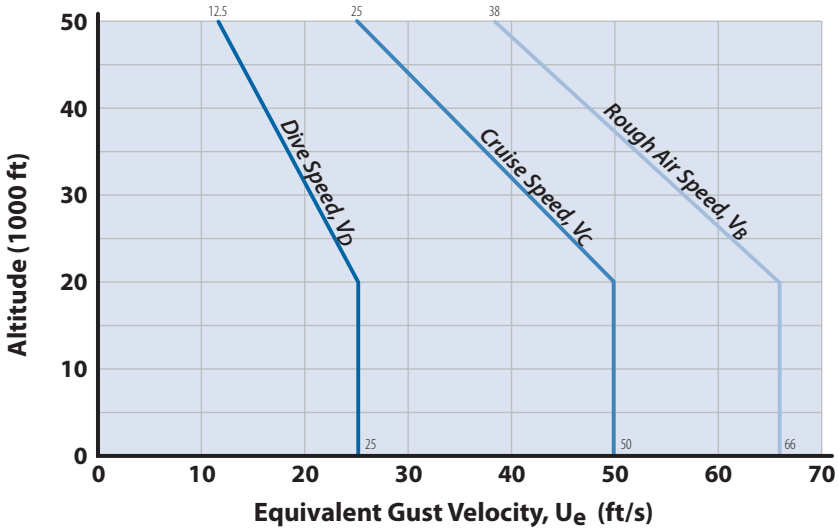
$\bar{c}$  = mean aerodynamic chord (ft)

$C_{L\alpha}$  = lift curve slope (per radian)

$g$  = acceleration due to gravity (ft/s<sup>2</sup>)

The *equivalent gust velocity*  $U_e$ , input into Eq. (19.1), is defined as a function of both aircraft speed and altitude. Consequently, there is a range of equivalent gust velocities used for aircraft design, as shown in Fig. 19.2. There is an inverse relationship between gust velocity and aircraft speed—as aircraft speed increases the gust velocity used for design decreases. This relationship is representative of customary aircraft operation in which a pilot will reduce speed consistent with the level of turbulence that is encountered [4].





**Figure 19.2** Equivalent gust velocity as a function of speed and altitude.

Load factors generated by gust conditions can be more critical than maneuver load factors depending on the speed, altitude, and wing loading ( $W/S$ ) of the aircraft. In general, aircraft with low wing loading are more susceptible to being designed by gust loads, and gust velocities are typically higher at altitudes less than 20,000 feet. Therefore, an aircraft with a lightly loaded wing that generally flies at lower altitudes is likely to be designed by gust conditions, not flight maneuver conditions. MIL-A-8861 and FAA FAR Part 25 provide additional guidance on defining gust loads for military and commercial aircraft.

The key task of the Loads Engineer is to develop a set of aerodynamic and inertia design loads based on the flight envelope and intended usage of the aircraft. Aerodynamic and inertia loads that are applied to the aircraft are referred to as *external loads* to differentiate them from the *internal loads* that are distributed within the airframe and carried internally by the various structural members. As illustrated in Fig. 19.3, there are a number of tools available to predict the external design loads, ranging from computational fluid dynamics (CFD) and other computational methods such as VORLAX (vortex lattice method), to wind tunnel testing in which the overall forces and moments applied to the vehicle, as well as surface pressure distributions, can be measured. A set of external load conditions must be defined that cover the range of flight weights and center-of-gravity locations for the vehicle, as well as all altitudes, speeds, and possible configurations of flight control surfaces such as ailerons, rudder, flaps, and spoilers. It is common to utilize all types of loads analysis tools in generating a full

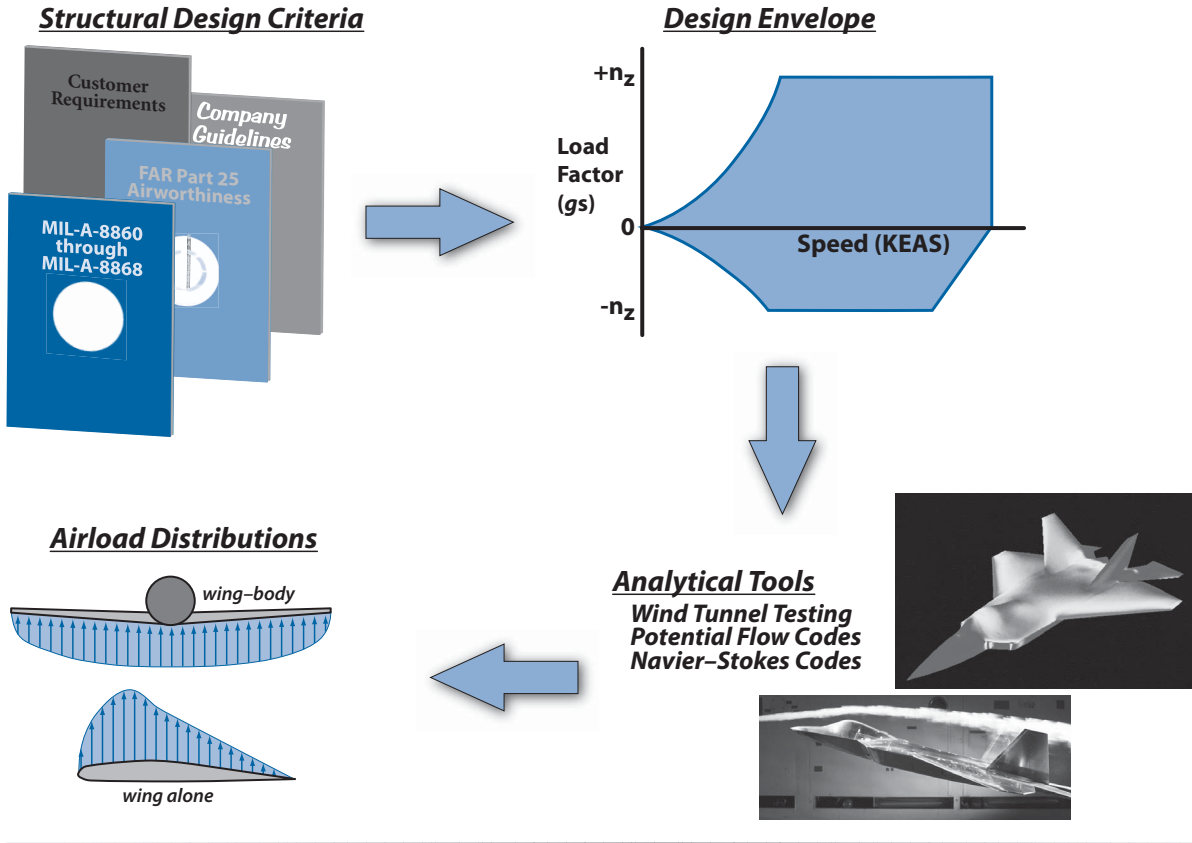


Figure 19.3 External loads definition process.

set of external design loads. Wind tunnel testing is commonly used to define and verify key design points within the flight envelope and it is often complemented by other analytical methods, such as CFD and VORLAX, to populate intermediate design points and off-design conditions.

In addition to the basic aerodynamic and inertia loads resulting from flight maneuvers, there are many other types of load conditions that must be considered in the design of an airframe. As shown in Fig. 19.4, these other types of design loads include landing and taxi loads, cabin and fuel pressures, crash loads, propulsion system loads, control surface loads, loads generated by cargo or stores, and loads associated with various ground handling activities such as jacking, hoisting, or towing of the aircraft. All of these types of design loads may not be applicable to all types of aircraft. Therefore, it is very important to document the pertinent load conditions and criteria to be used in the design of the aircraft in a Structural Design Criteria Document. The Structural Design Criteria Document serves as a single source of requirements that will keep all designers and structural analysts involved in an aircraft development effort working to a consistent set of requirements and focused on the same technical goals and objectives.

Although there are many powerful analytical tools and wind tunnel testing methods available to the Loads Engineer, a key ingredient that should always be used in generating design load conditions is sound reasoning and good judgment based on a thorough understanding of how the aircraft will be flown and operated. Ensuring safety-of-flight must always be of paramount importance. However, there are many second-tier design requirements, not directly related to safety-of-flight, that are often subject to interpretation. Many of these secondary requirements can be tailored to fit the specific mission requirements of the aircraft. An example involves the structural design requirements for low-observable (LO) aircraft. From a structural and signature standpoint, an important design requirement for LO aircraft involves the allowable step, gap, and waviness of the outer skin panels of the vehicle. Steps, gaps, and waviness can result from several sources, such as manufacturing tolerances, but the primary source is often structural deflections caused by in-flight maneuver loads. Meeting the surface smoothness criteria may be critical to the signature of the aircraft, but it is likely not a safety-of-flight issue per se, and satisfying very tight surface smoothness requirements can significantly increase the structural weight of the vehicle by requiring increased thickness of skins or tighter spacing of substructure frames and ribs. Therefore, it may be advantageous to specify a subset of the flight envelope where the surface smoothness requirements must be satisfied for maximum survivability with minimum weight impact. This concept is illustrated in Fig. 19.5 and highlights that the airframe must possess sufficient strength and structural integrity to

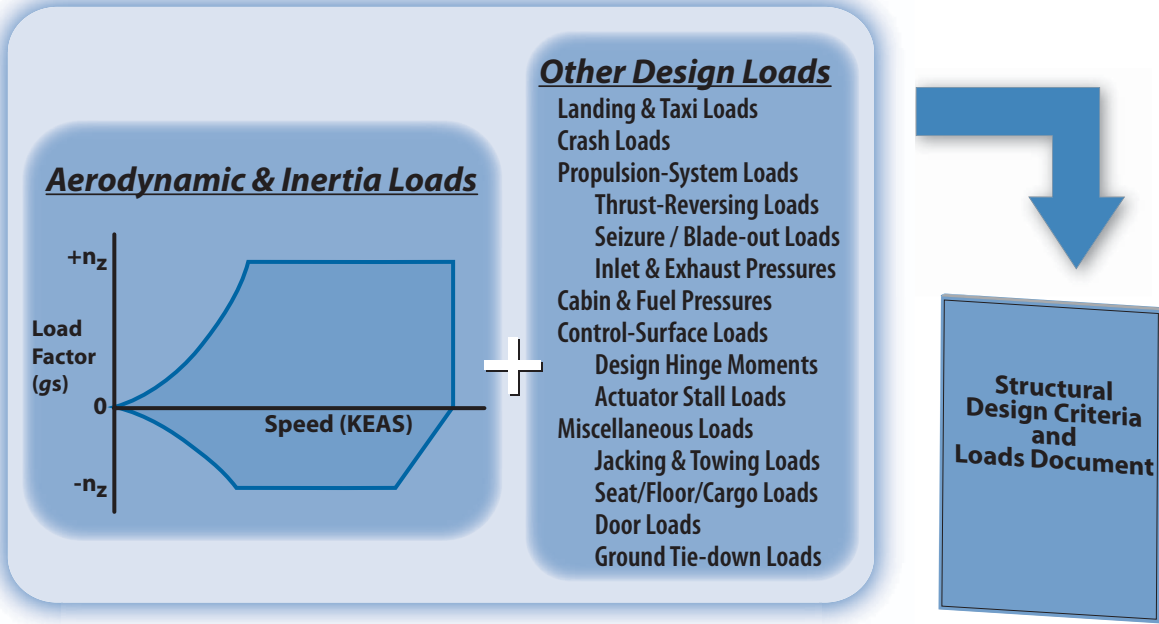
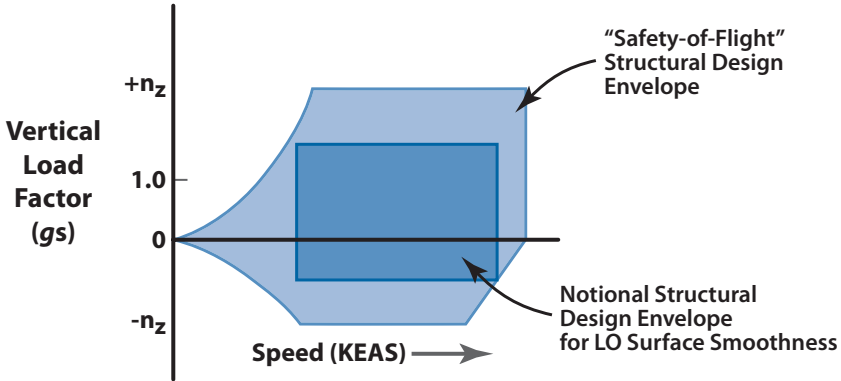


Figure 19.4 Example of design loads contained in Structural Design Criteria Document.



**Figure 19.5**  $V$ - $n$  diagram showing notional LO design envelope as a subset.

provide safe operation throughout the flight envelope, but the airframe weight does not need to be unduly penalized to meet surface smoothness requirements for relatively short duration excursions at the corners of the flight envelope where high- $g$  maneuvers are being performed, or for the low-speed portions of the flight envelope where deployment of flaps or wing leading edge (LE) devices might preclude meeting signature requirements regardless of the smoothness of the outer surface of the aircraft.

Although this example is specific to LO vehicles and the issue of surface smoothness, the same basic philosophy can be extended to other types of design requirements for all classes of aircraft. Structural design criteria dictated by safety-of-flight requirements, versus those driven by non-flight-critical considerations, should be evaluated carefully in this manner to avoid a “worst case on worst case” approach that can burden the vehicle with overly conservative design requirements resulting in unnecessary structural weight.

### 19.3 Stress Analysis

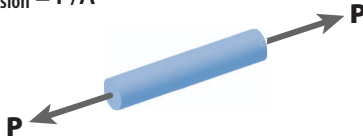
The primary objective of stress analysis is to insure that each structural member of the airframe is properly designed and sized to meet structural requirements with the lowest possible weight. These structural requirements typically include strength and buckling stability, but they can also include stiffness and deflection requirements, as well as durability and damage-tolerance analysis (DaDTA) considerations related to fatigue and crack growth.

*Stress* is simply force (load) per unit area, and it can result from four basic types of loading: tension, bending, shear, and compression. Figure 19.6 illustrates these four basic types of loading and provides the expres-

### **TENSION**

Stress = Force/Area

$$f_{\text{tension}} = P/A$$



*Failure Mode: Strength*

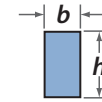
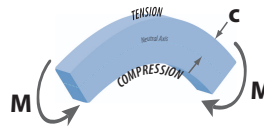
### **BENDING**

$$\text{Stress} = f_{\text{bending}} = Mc/I$$

$M$  = applied Moment

$c$  = distance to Neutral Axis

$I$  = Moment of Inertia



Rectangular  
Section  
 $I = bh^3/12$

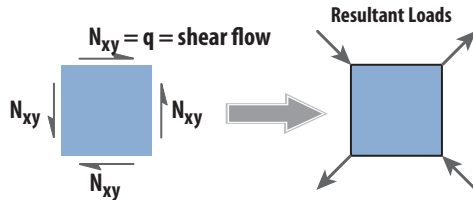
*Failure Mode:*

- Strength (tension side)

- Local Buckling Stability (compression side)

### **SHEAR (in-plane)**

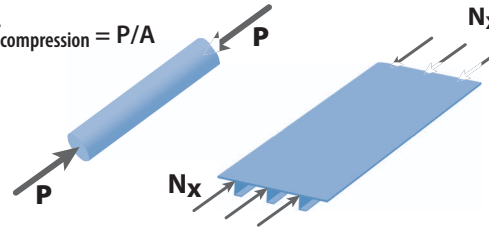
$$f_{\text{shear}} = N_{xy} / \text{thickness}$$



*Failure Mode: Buckling Stability  
(for thin sheet)*

### **COMPRESSION**

$$f_{\text{compression}} = P/A$$



*Failure Mode: Buckling Stability  
(for thin sheet structure and slender columns)*

Figure 19.6 Basic types of applied loads and stresses.

sion for calculating the resulting stress for each case. Any single structural member in an airframe will likely be subjected to some combination of these four types of loads for any single design condition. Therefore, the challenge of stress analysis is to understand the interaction of the different types of load, anticipate the potential failure modes of the structural member, design the structural member so that failure does not occur within a specified design envelope, and minimize the structural weight of the component.

The failure mode for tension loading is typically material strength, either tension ultimate strength or tension yield strength. For compression loading the failure mode is usually buckling instability, either global or local buckling instability. Bending results in both tension and compression stress, as shown in Fig. 19.6. Depending on the configuration of the structural member to which the bending moment is applied, the failure mode can be either strength (at the tension side) or local buckling instability (compression side). An in-plane shear load can also be resolved into tension and compression loads as shown in Fig. 19.6. Therefore, for a thin-sheet structure such as a wing or fuselage skin, the failure mode for in-plane shear loading is usually buckling instability caused by the resultant compression loads. The key point is that buckling instability, and not necessarily material strength, can be the governing failure mode for a significant amount of an airframe, especially if constructed of lightweight, thin-sheet structure. As an example, Fig. 19.7 lists the various failure modes, and the percentage of airframe structural weight driven by that failure mode, for the Lockheed Martin S-3A Viking aircraft [5]. This data illustrate that only 30% of the airframe structural weight for this particular aircraft is driven by tension strength, but over 40% of the weight is driven by buckling stability. These characteristics are typical of many other airframe designs.

The concept of limit load vs ultimate load is fundamental to understanding aircraft stress-and-loads analysis. *Limit load* is defined as the maximum load that an airframe will experience anytime during its service life. *Ultimate load* is simply limit load multiplied by a factor-of-safety. The *ultimate factor-of-safety* is typically 1.5 for manned aircraft and 1.25 for unmanned aircraft. However, there are many other factors that may be required depending on the type of structure and type of loading. For example, compartments subjected to internal pressure, such as pressurized passenger cabins or crew compartments, are usually required to be designed to withstand a *proof pressure* that is 1.33 times the maximum attainable pressure and a *burst pressure* that is 2.0 times the maximum attainable pressure. The MIL-8860 series of documents provides guidance on many of these other factors required for structural design.

For strength-critical components, stresses resulting from limit load and ultimate load are compared with the yield and ultimate strength of the par-

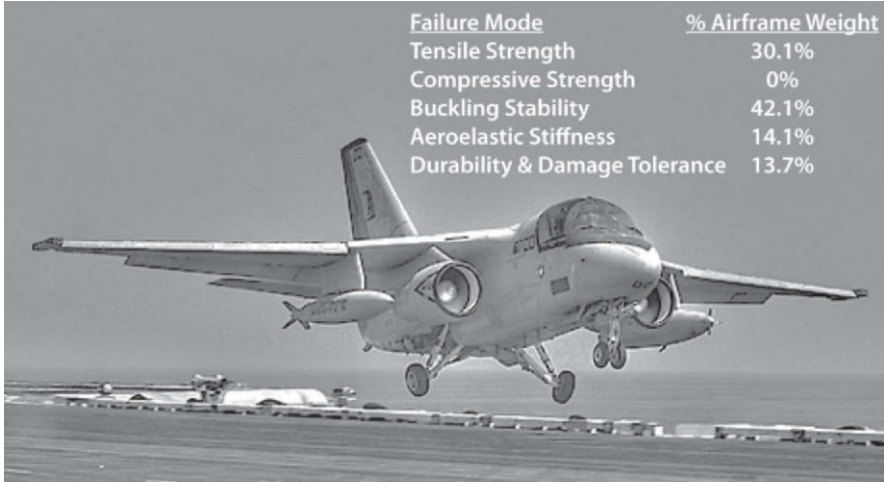


Figure 19.7 Airframe structural weight per failure mode for S-3A aircraft.

ticular material from which the component is constructed. Figure 19.8 shows a stress–strain curve for a typical ductile material. The *yield stress* is defined as the point on the stress–strain curve at which permanent deformation starts to occur (also called *plastic deformation*). Structural design criteria for most aircraft state that no detrimental permanent deformation

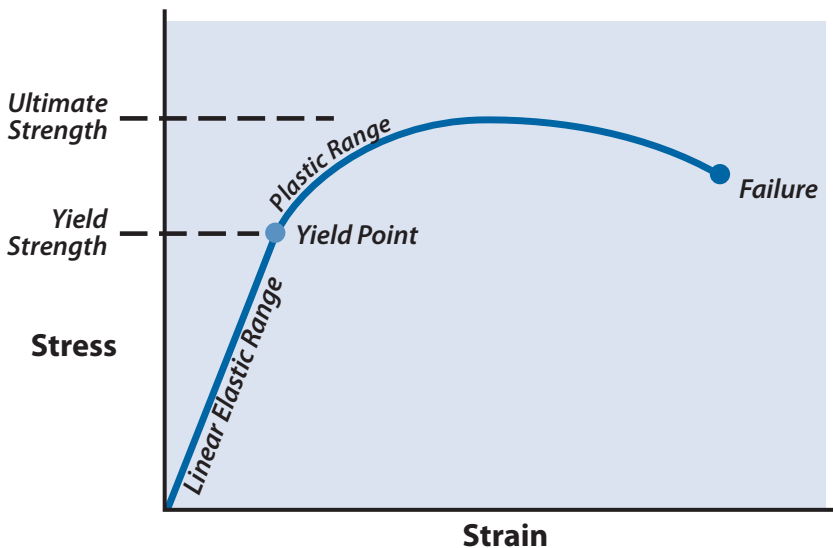


Figure 19.8 Engineering stress–strain curve for a ductile material.



is allowed at, or below, limit load and no failure at, or below, ultimate load [6]. This implies that yielding of the material may be allowed above limit load. However, some yielding may be allowed below limit load provided that the permanent deformation does not interfere with safe operation of the aircraft.

*Margin-of-safety* is a measure of how much capability a structural component possesses in excess of design requirements. For structural components, margin-of-safety is usually expressed in terms of a material *allowable* (for example, a material strength allowable such as ultimate strength or yield strength) compared against an applied stress:

$$\text{Margin-of-Safety (M.S.)} = \frac{\text{Allowable Stress}}{\text{Applied Stress}} - 1.0$$

Margin-of-safety should not be confused with factor-of-safety; the two quantities serve two distinctly different purposes.

### Example 19.1 Margin-of-Safety

Consider a rod with a 1.0-in.<sup>2</sup> cross section, loaded in tension with 40,000 lb, as shown in Fig. 19.9.

Limit load for this example is 40,000 lb and ultimate load is  $1.5 \times 40,000 \text{ lb} = 60,000 \text{ lb}$ . Based on these applied loads, the tension stress at limit load is calculated to be  $40,000 \text{ lb}/1.0 \text{ in.}^2 = 40,000 \text{ psi}$ , and the stress at ultimate load is  $60,000 \text{ lb}/1.0 \text{ in.}^2 = 60,000 \text{ psi}$ . The Structural Design Criteria state that permanent deformation is not allowed below limit load and failure is not allowed below ultimate load. Therefore, the two margins-of-safety are

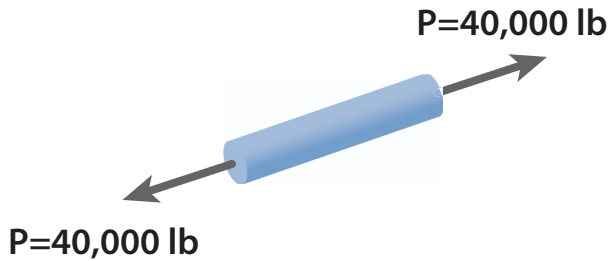
$$\text{M.S. (Yield Strength)} = \frac{48,000 \text{ psi}}{40,000 \text{ psi}} - 1.0 = +0.20$$

$$\text{M.S. (Ultimate Strength)} = \frac{63,000 \text{ psi}}{60,000 \text{ psi}} - 1.0 = +0.05$$

Yield strength is compared against applied limit stress, and ultimate strength is compared against applied ultimate stress, resulting in margins-of-safety of +20% and +5%. Unless specified otherwise in the Design Criteria, it is permissible to drive all margins as close to zero as possible for minimum weight. Therefore, the cross-sectional area of the rod could be reduced slightly from 1.0 in.<sup>2</sup> to 0.96 in.<sup>2</sup>, resulting in a margin of 0% at ultimate and +15% at limit. Additional reduction in cross-sectional area to bring the yield margin closer to zero would result in a negative margin at ultimate load, which is unacceptable in

Cross-Sectional Area =  $A = 1.0 \text{ in.}^2$

$$f_{\text{tension}} = P/A$$



#### Design Criteria

- Ultimate Factor-of-Safety = 1.5
- No Yielding at or Below Limit Load
- No Failure at or Below Ultimate Load

#### Material Design Allowables

- Tension Ultimate Strength =  $F_{tu} = 63 \text{ ksi}$
- Tension Yield Strength =  $F_{ty} = 48 \text{ ksi}$

Figure 19.9 Example of design criteria and allowables.

this example. In all cases, however, the ultimate factor-of-safety is unchanged at 1.5.

Example 19.1 illustrates several key points related to stress analysis and sizing of airframe structure: (1) There are usually multiple failure modes, and therefore multiple margins-of-safety, for every structural member. (2) It is desirable to drive the margins-of-safety to zero for minimum weight. (3) It is virtually impossible to drive all margins for all failure modes of a particular structural member to zero at the same time. Therefore, it is important to determine which margins drive the weight of the component and, therefore, warrant the highest priority for being minimized.

Material strength allowables for metallic materials commonly used in the aerospace industry can be found in the government handbook “Metallic Materials Properties Development and Standardization” or MMPDS [7]. Prior to 2004, the MMPDS was known as MIL-HDBK-5 “Metallic Materials and Elements for Aerospace Vehicle Structures.” The MMPDS is a source of metallic material and fastener allowables for aluminum, titanium, steel, and high-temperature alloys and is accepted by the Federal Aviation Administration (FAA), all departments and agencies of the Department of Defense (DoD), and the National Aeronautics and Space Administration (NASA).

An example of a typical material allowable data sheet found in the MMPDS is shown in Table 19.1. The headings “A” and “B” near the top of the MMPDS data sheet refer to the statistical basis used in generating the material design allowable. *A-basis allowables* are defined as those for which 99% of the material population is expected to equal or exceed the stated allowable with a 95% confidence level; *B-basis allowables* are defined as those for which 90% of the material population is expected to equal or exceed the allowable with 95% confidence. For most airframe primary and secondary structure, B-Basis allowables are used for design. However, A-basis allowables may be required for a single-load path, safety-of-flight structure, depending on customer requirements and company design policy.

Compared with strength analysis, determination of the buckling stability of a structure can entail a more-involved analysis. There are several forms of buckling instability, such as shear and compression buckling of thin skins or webs, local “crippling” buckling of beam flanges, torsional buckling of open-section columns, and Euler buckling of slender columns loaded in compression, and there are numerous analytical and empirical methods available for addressing each of these types of buckling instability. Unlike yield or ultimate strength, which is an inherent property of a material, the allowable buckling load is dependent on material properties (such as compression modulus  $E_c$  or shear modulus  $G$ ), the geometry of the structural member, and the boundary conditions of the member (usually

defined as fixed, simply supported, or free). Also, unlike strength analysis, where there is often a clear “not-to-exceed” strength allowable, it is possible for a structure to experience certain types of buckling and still carry 100% of the required load. Therefore, provided the buckling does not initiate a global instability leading to catastrophic structural failure, it may be permissible to allow buckling below ultimate or limit load. Understanding and taking advantage of this “postbuckled” capability to achieve minimum weight are key features that separate aircraft structural design philosophy from other forms of structural design.

## 19.4 Finite Element Modeling

Finite element modeling is arguably the most powerful analytical tool available to the stress engineer. The theory of finite element modeling is based on the fundamental mechanics-of-materials relationship:

$$\text{Force} = \text{Stiffness} \times \text{Displacement}$$

which can be expressed in matrix notation as

$$\{\mathbf{F}\} = [\mathbf{K}] \times \{\mathbf{d}\}$$

A *finite element model* (FEM) is a mathematical representation of the airframe structure in terms of a stiffness matrix  $[\mathbf{K}]$ . Once this stiffness matrix is defined, forces  $\{\mathbf{F}\}$  can be applied to the FEM (commonly in the form of external loads supplied by the Loads Group), and displacements  $\{\mathbf{d}\}$  can be solved. From displacements the stresses and loads in each individual structural member in the FEM can then be determined.

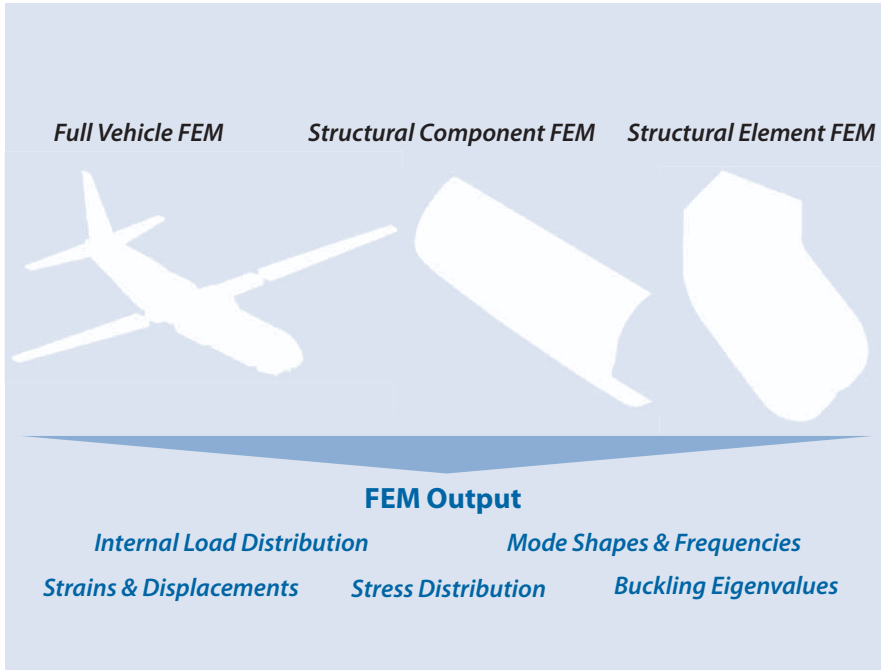
As with any analytical tool, the results of a FEM are only as accurate as the input data and the fidelity of the model itself. FEM results can be greatly affected by the types of elements used in the model, mesh density, and model boundary conditions. Therefore, it is always good practice to perform a first-order hand analysis of the problem being modeled to provide a sanity check of the FEM results.

Finite element models can range from a detailed model of a fitting to a complete airframe, as shown in Fig. 19.10. A full-vehicle FEM is typically used to determine the load distribution within the airframe and is commonly called an *internal loads model*. An internal loads FEM will include a set of external-loads cases (represented by the  $\{\mathbf{F}\}$  matrices) that cover all the critical conditions to which the airframe must be designed. These load conditions typically include symmetric and unsymmetric flight maneuvers, internal pressures (such as cabin pressures), propulsion system loads, landing loads, ground handling loads, and any other loading condition that

**Table 19.1** Design Mechanical and Physical Properties of Clad 2024 Aluminum Alloy Sheet and Plate

Specification	QQ-A-250/5																			
Form	Flat sheet and plate																			
Temper	T3				T351															
Thickness, in.	0.008–0.009		0.010–0.062		0.063–0.128		0.129–0.249		0.250–0.499		0.500–1.000		1.001–1.500		1.501–2.000		2.001–3.000		3.001–4.000	
Basis	A	B	A	B	A	B	A	B	A	B	A	B	A	B	A	B	A	B	A	B
<b>Mechanical Properties</b>																				
$F_{tu}$ , ksi																				
<i>L</i>	59	60	60	61	62	63	63	64	62	64	61	63	60	62	60	62	58	60	55	57
LT	58	59	59	60	61	62	62	63	62	64	61	63	60	62	60	62	58	60	55	57
ST	—	—	—	—	—	—	—	—	—	—	—	—	—	—	—	—	52	54	49	51
$F_{ty}$ , ksi																				
<i>L</i>	44	45	44	45	45	47	45	47	46	48	45	48	45	48	45	47	44	46	39	41
LT	39	40	39	40	40	42	40	42	40	42	40	42	40	42	40	42	40	42	39	41
ST	—	—	—	—	—	—	—	—	—	—	—	—	—	—	—	—	38	40	38	39
$F_{cy}$ , ksi																				
<i>L</i>	36	37	36	37	37	39	37	39	37	39	37	39	37	39	36	38	35	37	33	35
LT	42	43	42	43	43	45	43	45	43	45	42	45	42	44	42	44	41	43	39	41
ST	—	—	—	—	—	—	—	—	—	—	—	—	—	—	—	—	46	48	44	47
$F_{su}$ , ksi	37	37	37	38	38	39	39	40	37	38	36	37	35	37	35	37	34	35	32	34
$F_{bru}$ , ksi																				
( <i>e/D</i> ) = 1.5)	96	97	97	99	101	102	102	104	94	97	92	95	91	94	91	94	88	91	83	86
( <i>e/D</i> ) = 2.0)	119	121	121	123	125	127	127	129	115	119	113	117	111	115	111	115	107	111	102	106

Specification	QQ-A-250/5																			
Form	Flat sheet and plate																			
Temper	T3								T351											
Thickness, in.	0.008–0.009		0.010–0.062		0.063–0.128		0.129–0.249		0.250–0.499		0.500–1.000		1.001–1.500		1.501–2.000		2.001–3.000		3.001–4.000	
Basis	A	B	A	B	A	B	A	B	A	B	A	B	A	B	A	B	A	B	A	B
<b>Mechanical Properties</b>																				
$F_{br}$ , ksi																				
( $e/D$ ) = 1.5	68	70	68	70	70	73	70	73	69	72	69	72	69	72	69	72	69	72	67	70
( $e/D$ ) = 2.0	82	84	82	84	84	88	84	88	82	86	82	86	82	86	82	86	82	86	80	84
$e$ , percent (S-basis)																				
LT	10	—	—	—	15	—	15	—	12	—	8	—	7	—	6	—	4	—	4	—
$E$ , $10^3$ ksi																				
Primary	10.5								10.7											
Secondary	9.5				10.0				10.2											
$E_s$ , $10^3$ ksi																				
Primary	10.7								10.9											
Secondary	9.7				10.2				10.4											
$G$ , $10^3$ ksi																				
$\mu$											0.33									
<b>Physical Properties</b>																				
$\omega$ , lb/in <sup>3</sup>											0.101									
$C$ , $K$ , and $\alpha$											—									



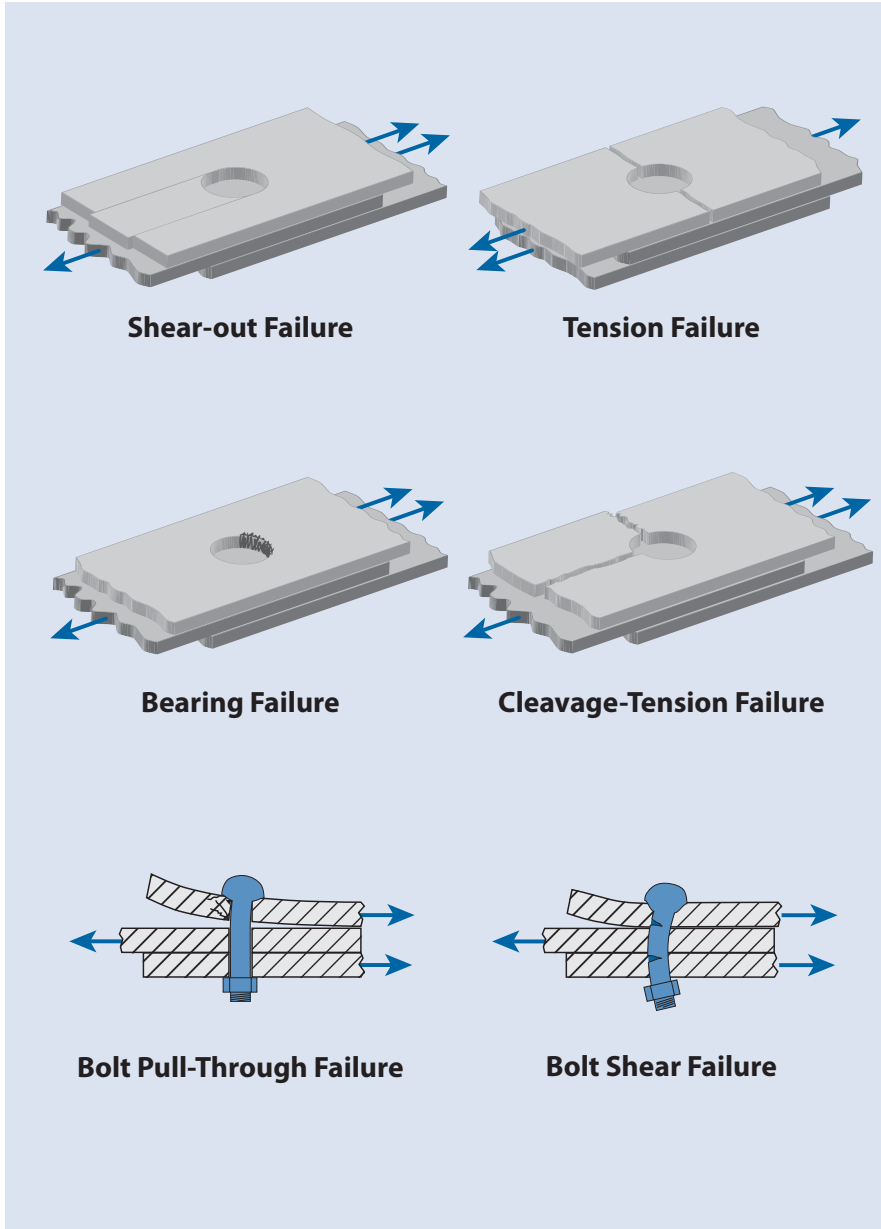
**Figure 19.10** Types of structural finite element models.

might drive the structural design of the airframe. The possible range of gross weights and c.g. locations for the aircraft are also commonly included in these FEM runs. Once the internal loads are defined, the stress engineer will use this information to calculate stresses and perform detailed stress analysis and sizing of structure.

## 19.5 Structural Joints

Sizing of major structural members such as skins, frames, bulkheads, and spars is a major focus of stress analysis, but proper design and analysis of structural joints is also of critical importance to the structural integrity of an airframe. A structure is only as good as its weakest link, and joints can be a common cause of structural failure if not addressed correctly. The majority of airframe structural joints fall into three primary categories: *mechanically fastened* joints, *adhesively bonded* joints, and *welded or brazed* joints. Although it is not uncommon for all three types of joints to be found in any particular aircraft, mechanically fastened and adhesively bonded are usually more prevalent in airframe primary structure.

Potential failure modes for mechanically fastened joints are illustrated in Fig. 19.11. Fastener shear failures can be precluded by selecting a



**Figure 19.11** Failure modes of mechanically fastened joints.

fastener of appropriate diameter and shear strength to carry the required loads. Bearing failures can be precluded by selecting a fastener of appropriate diameter and by maintaining sufficient thickness in the parts being joined together. Design guidelines regarding fastener minimum spacing,

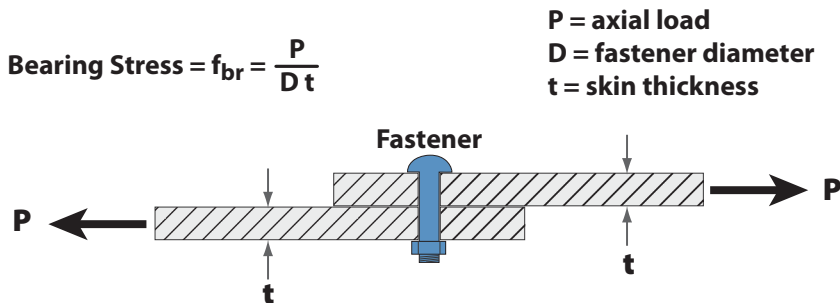


minimum edge distance, fastener type (for example, tension head vs shear head fasteners), and minimum sheet thickness for countersunk fasteners help guard against many of the other failure modes shown in Fig. 19.11, but it is the responsibility of the stress engineer to insure that the joint is analyzed and sized properly to preclude all possible failure modes.

*Bearing stress* results from the shank of the fastener compressing, or “bearing,” against the side of the hole as the fastener transmits load from one plate to the next. A *bearing failure* is a local compression-like failure of the plate or skin from this type of loading. It is normally good practice to design a fastened joint to be *bearing-critical*; that is, design the joint so that a bearing failure would occur first compared with the other possible failure modes. Figure 19.12 presents the equation used to calculate bearing stress for a single lap shear joint and shows that, for a given applied load, the two parameters that can be adjusted to determine bearing stress are the diameter of the fastener and the thickness of the parts being joined. A bearing-critical joint is preferred because it provides a degree of fail-safety in that the joint, even if inadvertently loaded beyond intended design levels, will remain intact and capable of transferring some amount of load until a repair can be implemented.

Bonded joints are usually preferred over fastened joints for laminated composite materials, such as graphite–epoxy composites, due to the relatively poor bearing strength of these materials. Poor bearing strength can necessitate a localized increase in the thickness of the parts being joined, as well as an increase in the diameter and number of fasteners. All of these factors tend to add weight. However, use of bonded joints in primary structure places an emphasis on strict adherence to proven manufacturing process specifications and use of nondestructive inspection (NDI) techniques to insure that the bond is structurally reliable.

Stress analysis of bonded joints focuses on the shear stress distribution in the adhesive layer. As shown in Fig. 19.13, this shear stress distribution



**Figure 19.12** Bearing stress equation for a single lap shear joint.

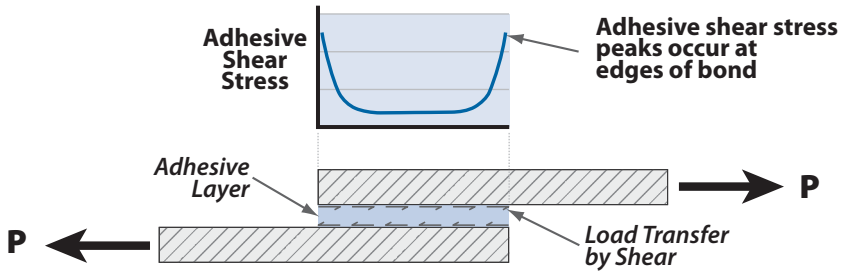


Figure 19.13 Bonded-joint shear stress distribution.

may not be uniform and can peak near each end of the bonded joint. As a result, simply increasing the bond area by increasing the overlap length of the joint may not be sufficient to reduce the peak shear stresses to within the adhesive shear strength allowable. Tailoring the stiffness of the bonded components, usually by tapering each end of the joint or by optimizing the composite layup, is often employed to reduce this peaking of shear stresses and minimize out-of-plane “peel” stresses that can lead to premature bondline failure.

Detailed design and analysis of structural joints is usually not performed in the Conceptual Design phase, but it is important to identify the basic types of joining methods that will be used in construction of the airframe as early as possible. Both bonded and fastened joints represent a source of structural inefficiency; therefore from a weight standpoint it is desirable to minimize the number of joints in the airframe. However, other considerations such as manufacturing constraints on part size, material limitations on maximum billet size, and maintainability considerations related to ease of replacing damaged structural components, may tend to increase the number and influence the location of major structural joints. These types of issues are appropriate topics for structural and manufacturing trade studies during the Conceptual Design phase. In addition, any joint design concepts that might be critical to the structural viability of the airframe design are likely candidates for component-level development testing during Preliminary Design. Planning for these tests, ordering of long-lead materials, and designing of test specimens may need to be accomplished during Conceptual Design in order to meet downstream program schedule milestones.

## 19.6 Durability and Damage Tolerance

*Durability and damage tolerance analysis* (DaDTA) addresses issues such as fatigue and other types of structural damage that may be incurred

during operation of the aircraft. For a demonstrator aircraft that might have a design life on the order of a hundred flight hours, the influence of fatigue considerations on the airframe design are likely to be minimal. However, for an operational aircraft with a design life of perhaps tens of thousands of flight hours, fatigue considerations can drive the selection of structural design concepts and materials and have a significant impact on structural weight.

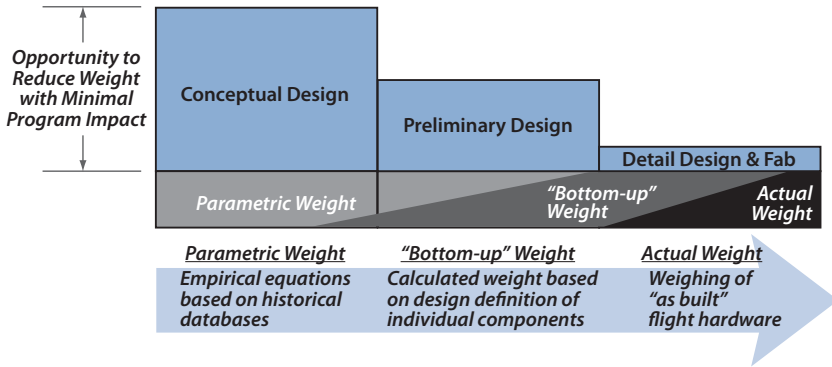
Two terms are important in determining the best design approach for satisfying DaDTA requirements: *fail safe* and *safe life*. The goal of the fail safe design philosophy is a structure that, even though damaged to a limited extent, is still capable of carrying a reasonable percentage of its design load to allow an emergency landing or return to base. Complete failure of any single structural member is made safe by providing alternate load paths. However, providing alternate load paths with redundant structure can entail a weight penalty. This weight penalty can be mitigated by applying the fail safe design philosophy to selected areas only, and not the entire airframe structure.

Safe life refers to a design approach that relies heavily on fatigue or crack growth analysis to show the airframe can meet design life requirements. This approach also involves implementation of inspection intervals to ensure that any premature fatigue damage is located and repaired before reaching critical proportions. Replacement of a structural component may be required once the predicted fatigue life is expended, even if the component shows no signs of fatigue damage. A safe life design is often a lighter approach than a fail safe design because it does not rely on redundant structure and multiple load paths. However, the safe life approach can be very analysis-intensive and typically requires detailed definition of the planned operational usage of the aircraft in order to develop the repeated loads spectrum required for crack growth analysis.

## 19.7 Mass Properties

The universal challenge for all aircraft development programs is achieving vehicle weight and performance while staying within program cost and schedule constraints. Achieving minimum weight structure is always a top priority for the Aircraft Structures engineer, and every decision made during the design process should be balanced with its potential impact on weight.

Several weight-prediction methods are used as a vehicle progresses through the design cycle, as illustrated in Fig. 19.14. During the Conceptual Design phase, the predominant method for predicting weight is based on parametric equations. Chapter 20, “Refined Weight Estimate,” contains a detailed discussion of parametric weight-estimating methods for both air-



**Figure 19.14** Weight-estimating methods utilized throughout the design cycle.

frame structure and subsystems, and provides parametric weight equations for wing, fuselage, and empennage structure as well as propulsion system components, surface controls and hydraulics, avionics, electrical system, and various furnishings such as seats, windows, and cargo-handling provisions.

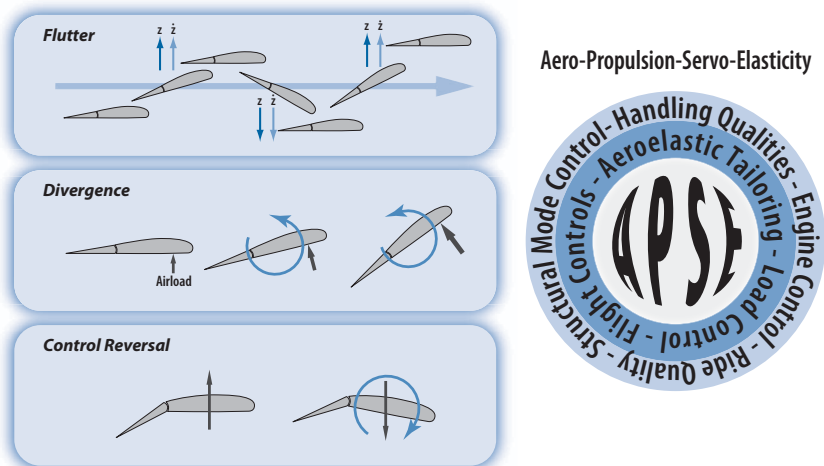
Because parametric weight equations are based on actual weights of previously developed aircraft, there is a risk these equations may not accurately predict the weight of a new, unconventional configuration that falls well outside the existing database of aircraft. In these cases, it is advisable to validate the parametrically estimated weight by performing a “bottom-up” weight analysis. A *structural bottom-up weight* is composed of calculated weights for each of the structural members (frames, spars, keelons, ribs, longerons, skins, etc.) based on a sufficient level of design definition for each member, supported by stress sizing. The weight for each of these components is then summed, resulting in a total weight comprising each of the individual pieces, in other words, a total weight derived from the bottom up.

Figure 19.14 also highlights that the opportunity for reducing weight without major impact to program cost and schedule decreases drastically as the design becomes more mature. Design decisions made during the early phases of a program often “lock in” the weight of the final product. A useful philosophy for controlling structural weight during these early design phases is to always strive to approach the airframe design from the “light side”—that is, initiate the design process with the minimum structural sizing (i.e., skin thickness, cap area, number of stiffeners, etc.) deemed necessary to satisfy requirements. As the configuration is matured through the design cycle, any additional structure or increase in sizing must “earn its way” onto the vehicle. This philosophy is in contrast to

the approach of starting with a structure that is overdesigned, and then presupposing weight will be reduced as the design matures. In effect, this is approaching weight from the “heavy side” and rarely leads to a true minimum weight design. Once a superfluous capability or design feature finds its way into a design, it can be very difficult to isolate that item during later design stages and reach consensus with all stakeholders that it can be eliminated.

## 19.8 Flutter and Dynamics

*Aeroelasticity* refers to the structural response of a flexible airframe when subjected to aerodynamic forces. As illustrated in Fig. 19.15, there are several types of aeroelastic phenomena that can occur, such as flutter, divergence, control reversal, and aero-propulsion-servo-elasticity (APSE). *Flutter* is a dynamic instability of an elastic structure in an airstream; it occurs when the phasing between motion and aerodynamic loading extracts an amount of energy from the airstream that is equal to the energy dissipated by damping within the structure. *Divergence* occurs when the torsional stiffness of a wing or aerosurface is not sufficient to maintain the structure in a statically stable position as the speed of the aircraft increases. *Control reversal* is also related to insufficient torsional stiffness and is characterized by movement that is opposite to the desired direction based on the control input. *APSE* is the coupling of the airframe aeroelastic response with the dynamic characteristics of the flight control and propulsion systems.



**Figure 19.15** Types of aeroelastic behavior.

Detailed evaluation of any of these aeroelastic phenomena requires a considerable amount of structural design definition, particularly the mass and stiffness distribution of the vehicle. As a result, the Conceptual Design phase, where this type of detailed structural definition is often not available, has historically contained a minimal amount of aeroelastic analysis. Not performing detailed aeroelastic analysis during the Conceptual Design phase probably introduces minimal program risk provided the aircraft configuration is similar to previous, flight-proven designs. However, for new aircraft with very unconventional design features, such as extremely thin wings, extremely slender fuselages, nontraditional control surfaces, or placement of large mass items (such as engines) in unconventional locations, it is imperative to perform at least a first-order aeroelastic analysis to provide confidence in the feasibility of the design and insure that any weight penalties for additional structural stiffness are captured. This first-order analysis typically involves evaluating the  $EI$  (bending stiffness) and  $GJ$  (torsional stiffness) of the wing, fuselage, and tail structure and may involve a simple “stick model” FEM that represents the wing, fuselage, and tail structure with simple beam elements.

*Structural dynamics* is concerned with the vibration, shock, and vibroacoustic environment of the vehicle structure and subsystems. As with aeroelastic analysis, there is usually little need to perform a great deal of dynamics analysis in the Conceptual Design phase as long as the vehicle configuration and flight environment are fairly conventional. The vibration and shock environment for the aircraft is usually more of a driver for the design and mounting of subsystem components such as avionics and electrical components. Although primary structure is rarely sized by the vibration or shock environment, high vibroacoustic levels can drive skin thickness and stiffener spacing, such as structure near the exhaust system. For unconventional configurations or operating environments, such as higher than normal acoustic levels resulting from a new propulsion concept, it may be necessary to perform a preliminary structural dynamics evaluation to insure the feasibility of the vehicle configuration and that all associated weight penalties are captured.

## 19.9 Structural Layout

Major load paths of an airframe are defined by a *structural layout drawing*, sometimes called a *structural “bones” drawing*. As the basic configuration of the vehicle is being developed, it is important to define these load paths to insure that adequate volume is reserved within the vehicle for primary structure such as frames, bulkheads, keelsons, spars, and ribs, and that major design features and subsystems such as engine, landing gear, and inlet-and-exhaust structure are successfully integrated into the design.

The structural layout philosophy used for different aircraft is varied, but there are several recurring themes that can be discerned for the wing and fuselage structure of many aircraft. Lessons-learned and optimization of airframe structure over many years have generated several basic structural layout approaches that have been demonstrated to achieve minimum weight with superior strength and stiffness.

### 19.9.1 Wing Structure

Wing structure can account for as much as half of the total structural weight of an aircraft. Therefore, selecting the most weight-efficient structural layout for the wing is always a high priority. For most conventional aircraft, two basic types of wing structural layout are most prevalent; the multi-rib wing and the multi-spar wing as shown in Fig. 19.16. The *multi-rib wing* typically features two spars (a forward spar and a rear spar, with a third intermediate spar sometimes present), upper and lower stiffened wing covers (or skins), and numerous ribs that are generally oriented in a chordwise direction. Taken together, this structural system of spars, ribs, and skins is called the *wing box*. The primary function of the spars is to carry vertical shear ( $P_z$ ) loads (carried in the spar webs) and a percentage of wing spanwise bending ( $M_x$ ) loads (carried in the spar caps). The wing upper and lower covers react the majority of the spanwise bending loads by carrying tension and compression loads. For example, a wing upbending moment would be reacted by compression loads in the upper skin and tension loads in the lower skin. The wing cover features a thin skin with discrete spanwise stiffeners to provide buckling stability. The primary function of the ribs is to support the wing skins to resist global buckling of these stiffened skins when loaded in compression. Torsional stiffness of the wing is provided by the wing box, which acts as a torque box and carries torsional ( $M_y$ ) loads as a shear load distributed around the periphery of the box structure.

Multi-rib wings are commonly found in transport-type aircraft that feature relatively high aspect ratio wings with generous thickness (i.e., relatively large wing thickness-to-chord ratios). These types of wings are usually subjected to moderate spanwise bending loads, as might be expected from a design vertical load factor ( $n_z$ ) of less than 6.0 *g*.

*Multi-spar wings*, on the other hand, are commonly found in high-speed or fighter aircraft that feature relatively thin, highly loaded wings. The upper and lower wing skins tend to be thicker than the covers of a multi-rib design and in many cases may not require any discrete stiffening other than the multiple spars. The tight spacing of the multiple spars combined with the thicker skins precludes the need for tightly spaced ribs to resist column buckling of the skins. However, some ribs may be present in

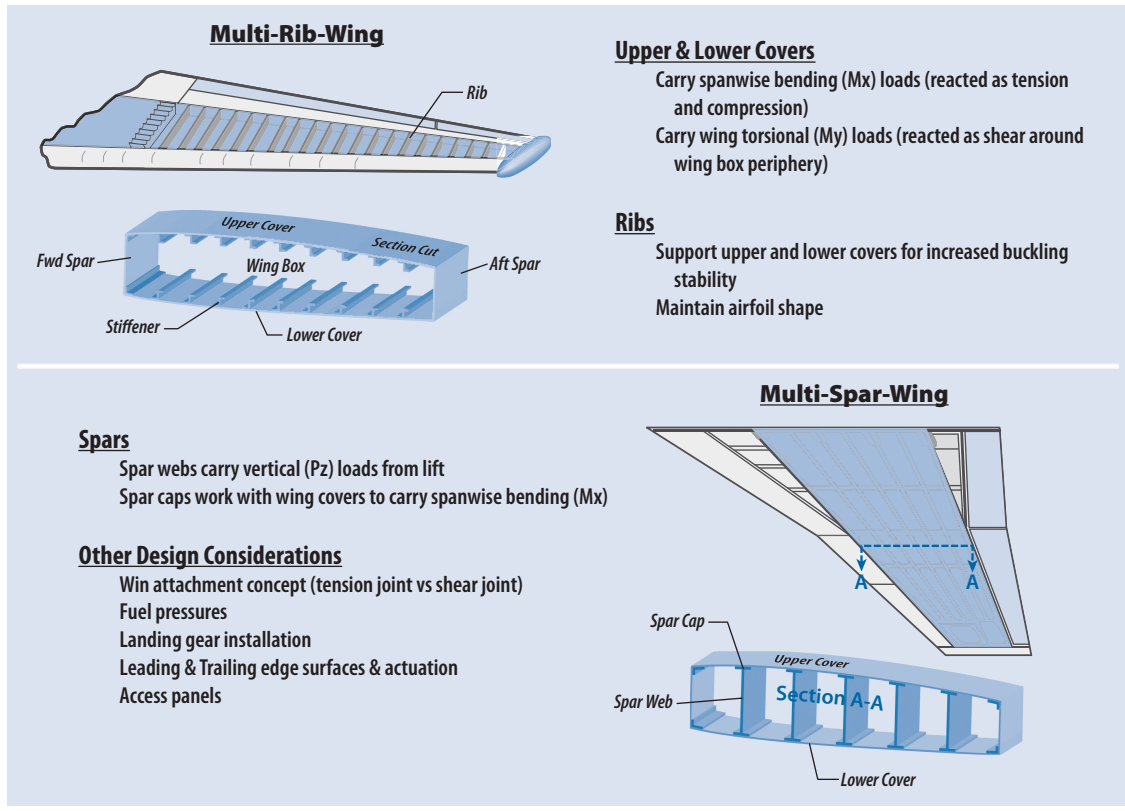


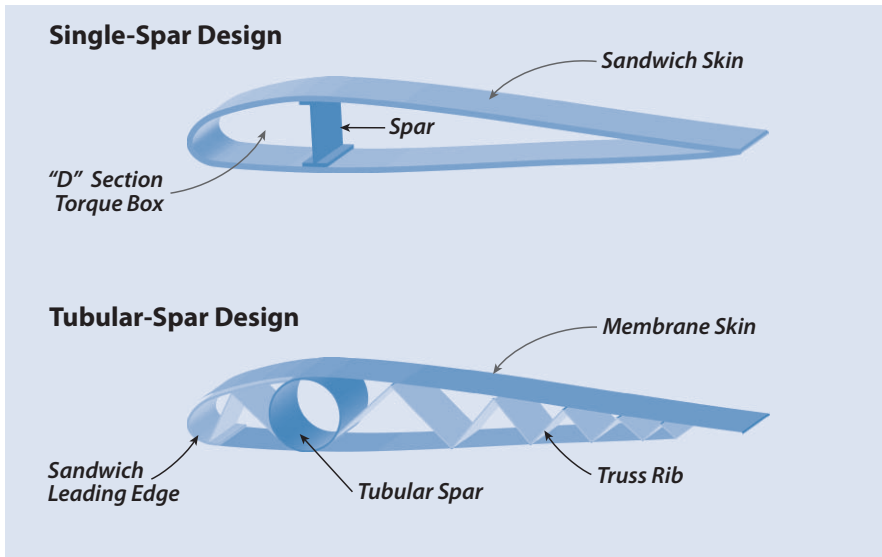
Figure 19.16 Wing structural configurations.



the multi-spar design to serve as attachment points for external stores or to provide back-up structure for attachment of leading or trailing edge control surfaces and actuation.

Cutaway drawings of many aircraft illustrate these two popular wing structural layouts, but notable exceptions can be found. Some aircraft feature a combination of the two concepts, using a multi-spar approach for thin outboard wing sections and a multi-rib approach for thicker inboard sections. Also, extremely lightweight aircraft such as sailplanes typically use a wing structural design that is neither multi-rib or multi-spar, but rather a single spar supporting sandwich wing covers requiring few, if any, ribs for buckling stability. Figure 19.17 shows a single spar wing typical of many sailplane designs. Extremely low wing structural weights have been achieved on high-altitude long-endurance (HALE) vehicles by using the tubular spar concept also shown in Fig. 19.17. Although somewhat similar in appearance to a multi-rib design, the wing skins in this concept act only as an aerodynamic covering, with all wing bending and torsional loads carried by the single tubular spar.

This type of wing structural approach is especially attractive for span-loader vehicle configurations such as the AeroVironment Centurion and Helios vehicles (see Chapter 20, Fig. 20.1) that distribute the vehicle mass across the entire wing span, which reduces wing spanwise bending ( $M_x$ ) moments.



**Figure 19.17** Ultralightweight wing structure concepts.

Although the various wing structural concepts presented here offer a good starting point for the design process, the final choice of wing structural layout for a particular aircraft should be supported by trade studies and weight optimization given the specific wing geometry and loads for that particular aircraft. In addition, other design issues related to integration of major subsystems into the wing, such as landing gear, propulsion system, and fuel system, can drive the preferred wing structural concept and must be considered.

### 19.9.2 Fuselage Structure

Fuselage structure also accounts for a significant percentage of airframe structural weight and can be subject to more demanding subsystem integration challenges than wing structure. This is especially true for densely packed fighter-type aircraft, where integration of inlet, cockpit, engine, internal stores, landing gear, and other subsystems can greatly affect the structural layout options that are available. As with wing structure, there are several recurring themes for fuselage structural layouts that are evident among the many different types of aircraft. Three of these design approaches (skin–stringer, frame–longeron, and sandwich-skin fuselage) are shown in Fig. 19.18.

The *skin–stringer approach* is typical of many commercial airliners. The longitudinal stringers, in conjunction with the skin, react fuselage bending ( $M_y$  and  $M_z$ ) loads. The primary function of the frames is to reduce the column length of the stringers for improved buckling resistance, as well as to maintain the overall shape of the fuselage. Fuselage torsional ( $M_x$ ) loads are reacted in the skin as shear, and internal cabin pressure loads are primarily carried in the skins in hoop tension (for fuselages with circular cross section).

The *frame–longeron approach* is very similar to the skin–stringer except that the axial-load carrying function of the numerous stringers is consolidated into discrete longerons. This design approach might be preferred for a number of reasons. For one, if the fuselage longitudinal bending loads are relatively low, it may be difficult to design and manufacture weight-efficient stringers due to material minimum gage limitations. Also, if the fuselage design features numerous cutouts for doors or windows, the frame–longeron approach may be advantageous because the longerons can be positioned either above or below the cutouts to provide an uninterrupted axial load path. It is interesting to note that the optimum frame spacing of the frame–longeron approach is typically less than the skin–stringer approach due to the skin between frames being less supported, thus requiring more closely spaced frames to achieve the same buckling load capability.

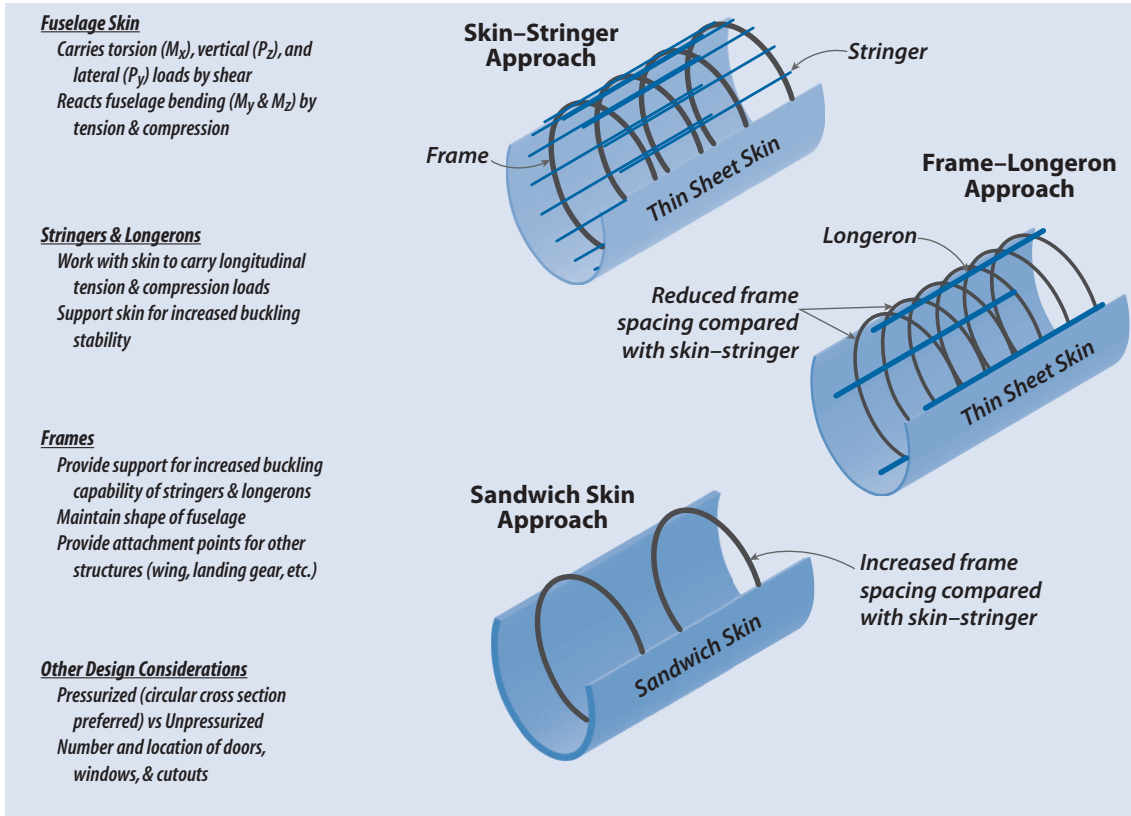


Figure 19.18 Fuselage structural configurations.

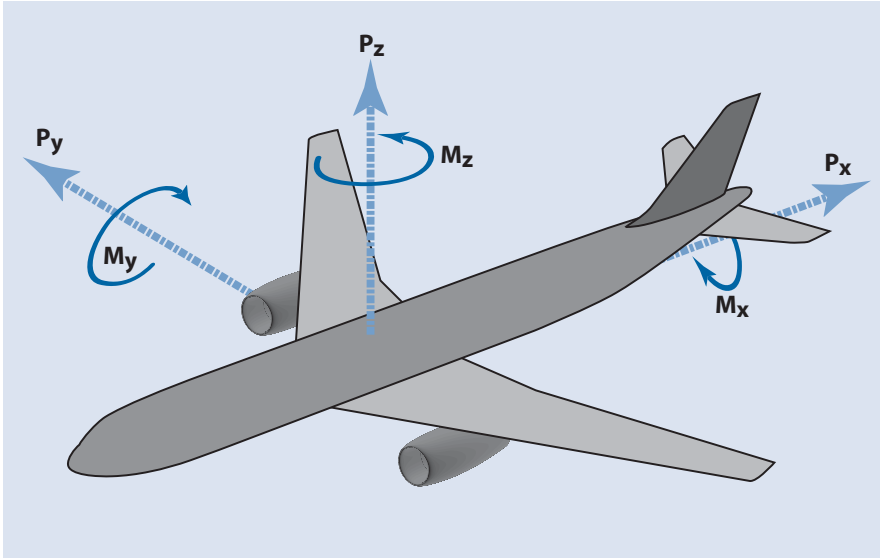
The *sandwich-skin approach* effectively eliminates the need for either stringers or longerons by utilizing the inherent compression buckling resistance of the sandwich skins. As might be expected, the optimum frame spacing for this configuration is usually increased compared with the other two concepts.

Selection of which fuselage structural configuration is optimum from a weight standpoint for a particular aircraft depends on a number of factors, including the following: fuselage geometry; number and location of design features such as doors and cutouts; magnitude of the fuselage bending, torsional, and shear loads; and material minimum gage limitations. As with wing structure, the fuselage structural concepts presented can provide a good starting point for analysis and trade studies to determine which particular design approach is preferred.

### 19.9.3 Structural Design Rules-of-Thumb

Regardless of the specific type of structural approach selected for the wing or fuselage, there are several basic rules-of-thumb that should always be considered:

- 1. Keep load paths simple and direct.** Simple load paths can result in a number of benefits. A structural layout with easily understood load paths is easier to design and analyze, often resulting in a lighter weight solution. Also, a simple design is often easier to fabricate and assemble, resulting in decreased manufacturing schedule and cost.
- 2. All six components of structural loading must be considered.** All structural members can be subjected to six components of loading, namely axial loads in the three principal axes ( $P_x$ ,  $P_y$ ,  $P_z$ ) and moments about the three axes ( $M_x$ ,  $M_y$ ,  $M_z$ ), as shown in Fig. 19.19. Although it is common for one or two of these loads or moments to dominate the design of any particular structural member, all six components of loading must be considered. For example, design of the root attachment joint for a wing may be dominated by the vertical shear ( $P_z$ ) load, resulting from lift, and the spanwise ( $M_x$ ) bending moment. However, the wing joint must also be capable of reacting the other four types of loading resulting from drag ( $P_x$ ), inboard–outboard loads ( $P_y$ ), wing torsion ( $M_y$ ), and fore–aft wing bending ( $M_z$ ).
- 3. A statically determinate structure is usually preferred for minimum weight.** A *statically determinate structure* is one where the reaction forces can be solved directly from the equations of equilibrium, namely, the sum of the forces equals zero and the sum of the moments equals zero. Therefore, for a given set of applied loads, there can be only one set of reaction forces with a determinate structure. Conversely, an *indeter-*



**Figure 19.19** Six components of structural loading.

*minate structure* can have multiple solutions for the reaction forces depending on the relative stiffness of the redundant load paths within the structure. A determinate structure, because it does not include redundant structure, usually represents the minimum amount of material required to carry a specific load and is often a lighter weight solution. Determinate structure is also typically easier to analyze and often easier to build, all leading to lighter weight. However, other design requirements, such as the fail safe requirements discussed in Section 19.6, might dictate that a statically indeterminate design is required.

4. **Each structural component should serve multiple functions.** A key philosophy for achieving minimum weight structure is to require that every major structural member serve multiple functions. For example, the primary function of a wing spar is to carry wing spanwise bending ( $M_x$ ) and vertical shear ( $P_z$ ) loads. However, with a well-thought-out structural layout, a main spar can also provide support structure for the main landing gear, serve as a fuel tank wall, and provide attachment points for the engine and external stores.
5. **Subsystems integration requirements must be considered early.** Subsystems integration and accessibility should be considered at the earliest stages of a structural layout, especially for tightly packed vehicles such as fighter aircraft. Location of doors, windows, and nonstructural access panels, as well as integration of major subsystems such as landing gear, engines, inlet and exhaust structure, flight crew stations, and

weapons bays can have a major impact on airframe weight and structural performance if not integrated in an intelligent and synergistic manner.

## 19.10 Material Selection

From a structures standpoint, one of the most important decisions made during the Conceptual Design phase is selecting the materials from which to build the airframe. Material selection can have far-reaching influence on a number of programmatic issues, including vehicle weight and performance, manufacturing cost and schedule, and the reliability and maintainability of the aircraft in operational service. Key parameters that should be considered in selecting airframe materials are the following:

- Specific strength
- Specific stiffness
- Usage environment
- Fracture toughness
- Manufacturability
- Minimum gage limitations
- Availability

*Specific strength* and *specific stiffness* are measures of the structural performance of a material per unit weight; specific strength is usually expressed as *ultimate tension strength* ( $F_{tu}$ ) divided by material density, and specific stiffness is expressed as Young's modulus ( $E$ ) divided by density. Table 19.2 compares the room-temperature specific values for a number of common airframe materials. Note that laminated composite materials, such as graphite–epoxy, show a wide range of specific strength and stiffness values depending on the specific orientation of the various plies. Table 19.2 also highlights that many metallic materials, while displaying wide variation in density, have very similar specific stiffness properties at room temperature.

In conjunction with specific strength and stiffness, a key discriminator for material selection is the usage environment, specifically, the operational temperatures that the structure will experience. Table 19.2 also lists the approximate maximum usage temperature and it is interesting to note that, for the materials listed, density increases as temperature capability increases. Specific strength and stiffness values for each material will change at different rates as the usage temperature increases, implying that a material that has a clear advantage in specific strength or stiffness at room temperature may not be the best choice at elevated temperature conditions. Therefore, candidate materials must be evaluated and compared throughout the range of expected operational temperatures.

**Table 19.2** Comparison of Material Specific Properties and Maximum Use Temperatures

Material	Density (lb/in. <sup>3</sup> )	Specific Ultimate Tension Strength at 70°F (ksi/lb/in. <sup>3</sup> )	Specific Stiffness at 70°F (msi/lb/in. <sup>3</sup> )	Maximum Usage Temperature (°F)
Composite	0.057	368 (quasi-iso layup) 1105 (all 0° layup)	61 (quasi-iso layup) 368 (all 0° layup)	~275
Aluminum (2024)	0.100	630	105	~300
Aluminum (7050)	0.102	745	101	~300
Titanium (6Al-4V)	0.160	812	100	~700
Carbon steel (4130)	0.283	336	102	~800
Stainless steel (301 Full Hard)	0.286	646	91	~1000
Inconel (718 STA)	0.297	606	99	~1200

*Fracture toughness*, denoted by the symbol  $K_{IC}$ , is the measure of the inherent capability of a material to resist crack growth, and it can be a very important material selection parameter for high-usage, long-life aircraft such as commercial airliners and military transports. Very brittle materials, such as ceramics and glass, typically have a very low fracture toughness, whereas more ductile materials have a higher fracture toughness. Material strength properties are often compromised to achieve increased fracture toughness; that is, an improvement in fracture toughness may correspond with a slight reduction in ultimate tension strength. Therefore, the tradeoff between strength and fracture toughness, and the resulting weight impact, is important to understand and quantify. For a fatigue-critical airframe with a design life of tens of thousands of hours, high fracture toughness can be more important than high specific strength.

*Manufacturability* addresses the ability to fabricate an end product from a particular material, and it is a selection criterion that should not be overlooked in the initial stages of the material selection process. Commonly used metallic materials such as aluminum, titanium, and steel alloys have a variety of manufacturing processes that can be utilized to make a final product starting from the initial sheet, plate, or billet stock. These processes include various forming and machining methods. Likewise, commonly used composite materials, such as graphite–epoxy systems, have a variety of material placement and curing methods. However, all manufacturing methods are not equally applicable to all materials. For example, aluminum alloys are easily cold-formed but many titanium alloys require hot-forming methods. Hot-forming usually involves more complex tooling and, therefore, can have an impact on program manufacturing cost

and schedule. Similarly for composites, out-of-autoclave processing using vacuum bag pressure and an oven cure may be perfectly acceptable for some airframe applications. However, if optimum material properties are required, an autoclave cure may be necessary. The increased pressure and temperature of an autoclave cure can drive tooling costs, and autoclave size limitations can restrict the overall dimensions of the part being cured, potentially resulting in additional assembly joints and structural weight. Therefore, it is important to consider the manufacturing impacts during the material selection process to make sure the material selected, and its associated manufacturing process, is compatible with program technical requirements, cost, and schedule.

*Minimum gage* refers to the minimum thickness to which a material can be produced. For a metallic material, this can be either the minimum thickness of the sheet stock or the minimum thickness that can be achieved by machining. For a laminated composite material, minimum gage can refer to the minimum thickness available for each individual ply. Minimum thickness limitations can have an impact on the structural design approach and weight of airframe structure. For example, if initial stress analysis indicates that a 0.020-in. thickness is required for a metallic skin in a particular region, but the material is only available in a minimum sheet thickness of 0.030 in., then there is an inherent weight inefficiency resulting from incompatibility between the selected material and the selected design concept. Fortunately, there can be possible solutions to this type of scenario, ranging from revising the structural layout so that a 0.030-in. skin is a more optimum solution, to employing chemical milling to reduce the thickness of the sheet stock.

Material availability can be a significant factor, especially for a demonstrator aircraft with a very aggressive development schedule. Many materials, both composite and metallic, can require from several months to well over a year for delivery of quantities sufficient to fabricate a full airframe. Large billets of the less commonly used metallic materials, such as titanium, Inconel, or other high-temperature alloys, can have especially long lead times. Although ordering of materials is rarely performed in the Conceptual Design phase, an early understanding of the lead times involved in procuring materials is important for developing an overall program schedule that progresses from Conceptual Design to Preliminary Design, Detail Design, Vehicle Assembly, and First Flight.

## 19.11 Composite Materials

Usage of composite materials in military aircraft has seen a steady increase over the past several decades. The benefits offered by composites are many, including reduced weight (see Chapter 20, Section 20.2.3), excel-

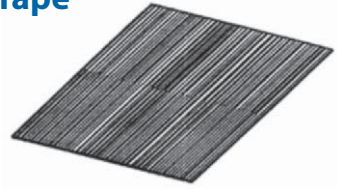
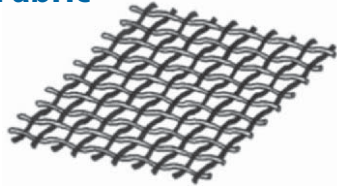


**Typical Reinforcement Materials**

*carbon (graphite) fibers*  
*glass fibers*  
*Boron fibers*  
*Kevlar fibers*  
*SiC fibers, whiskers, & particles*  
*Aluminum oxide (Al<sub>2</sub>O<sub>3</sub>) fibers, whiskers, and particles*

**Typical Matrix Materials**

*Epoxy resins*  
*Bismaleimide (BMI) resins*  
*Polyimide (PI) resins*  
*Thermoplastic resins*  
*Metals (Metal Matrix Composites)*  
*Ceramics (Ceramic Matrix Composites)*  
*Carbon (Carbon-Carbon Composites)*

**Tape****Fabric****Woven Preform**

**Figure 19.20** Common composite reinforcement and matrix materials.

lent fatigue performance, low coefficient of thermal expansion, corrosion resistance, and the ability to tailor the strength and stiffness properties of the material. Composite materials are composed of a reinforcement material and a matrix, and there are many combinations available, as shown in Fig. 19.20. The reinforcement material provides strength and stiffness to the composite and can be in the form of fibers, whiskers, or particles. The primary function of the matrix is to hold the reinforcement materials in place and distribute loads among the fibers, whiskers, or particles.

Fully realizing the benefits offered by composite materials requires a completely different mind-set for design, analysis, and manufacturing compared with metallic structures. This different way of thinking should be applied early in the design process to avoid the “black aluminum” mentality of designing with composites as if they were simply a different kind of metallic material. As an example, most laminated composites, such as graphite–epoxy tape and fabric laminates, have excellent in-plane strength properties but relatively poor out-of-plane (through-the-thickness) properties. This is in contrast to metallic materials, which are basically isotropic

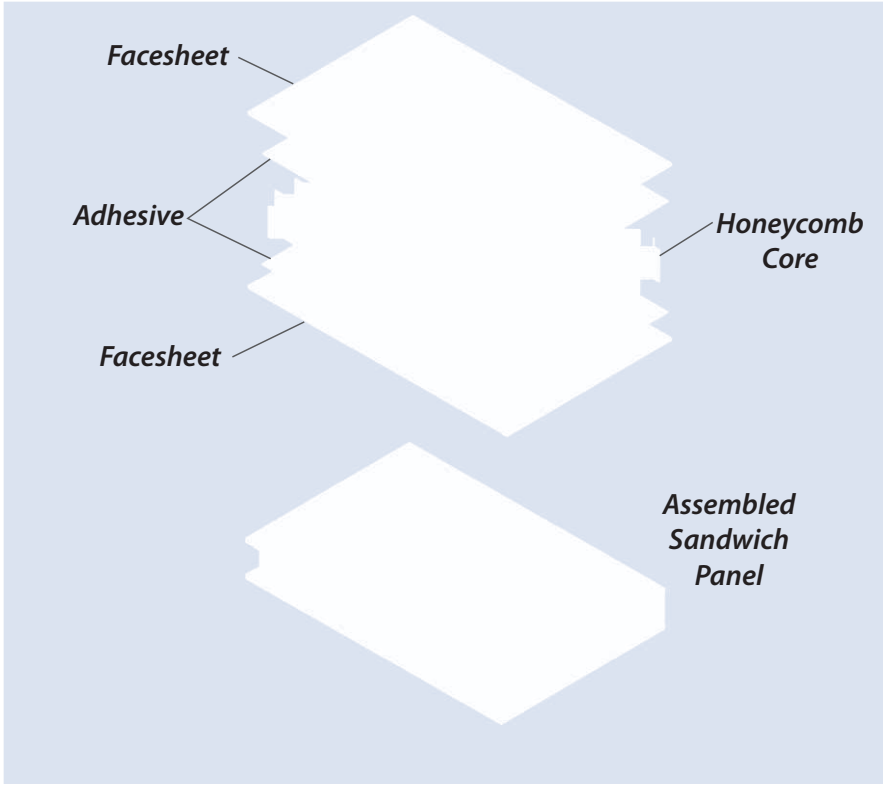
and have comparable properties in all three directions. Therefore, a good composite design should take these types of fundamental characteristics of composites into consideration and enhance the advantages of the material, not accentuate the weaknesses.

Unlike the metallic material design allowables contained in the MMPDS, there is no comprehensive, industry-wide source for composite design allowables. There are several reasons for this. Composite material mechanical properties are very dependant on the specific details of the cure cycle that is utilized (i.e., curing time, temperature, and pressure), and most manufacturers of composite structure have developed unique, and often proprietary, process specifications. Also, new and improved fiber and matrix materials are constantly being developed, and the number of possible combinations of fiber and resin is almost limitless. Therefore, a decision to utilize the “latest & greatest” composite material system may entail an extensive coupon testing program to develop design allowables. Vendor-supplied data may be suitable for early Conceptual Design trade studies, but these data commonly represent “best case” properties and do not include any statistical basis (such as A- or B-basis) or material property knockdowns for environmental exposure and damage tolerance effects. Therefore, vendor data are not normally used for Detail Design unless substantiated by independent tests.

The Vought XF5U-1 and XF6U-1 aircraft of the mid-1940s featured a sandwich construction called Metalite, which was a balsa wood core with bonded aluminum face sheets. The Metalite panels were formed in molds and cured in a large autoclave, similar to present day composite structures. The Metalite panels minimized the number of ribs or stiffeners required for a lightweight, efficient structure and provided an aerodynamically smooth exterior surface.

## 19.12 Sandwich Structure

There are many structural design concepts available for integration into airframe structure, but sandwich structure deserves special mention because it can be an extremely weight-efficient and cost-effective method for stiffening a skin or web to achieve increased buckling load capability. *Sandwich structure* is composed of a core material placed between two outer face sheets, as shown in Fig. 19.21. Sandwich core is typically in the form of honeycomb, although foam cores, made of various polymeric materials, and corrugated and truss cores, made of metallic and nonmetallic materials, are also used. Honeycomb core can be fabricated from metallic materials such as aluminum, titanium, and steel, as well as from nonmetallic materials such as Nomex, Fiberglass, and graphite. Similarly, face sheets can be metallic or nonmetallic, with aluminum, titanium, steel, graphite, and Fiberglass being commonly used materials.



**Figure 19.21** Construction of a honeycomb sandwich panel.

The function of the core material is to carry transverse (out-of-plane) shear loads, separate the face sheets for increased moment-of-inertia for reacting bending loads, provide support to the face sheets to prevent buckling, and provide shear continuity between the two face sheets so that the sandwich panel acts as a single structural entity. The primary function of the face sheets is to carry in-plane tension, compression, and shear loads. Panel bending is reacted as tension on one face sheet and compression on the other.

The connection between the face sheets and core is critical to the structural performance of a sandwich panel. In the case of composite or aluminum sandwich panels, this connection is usually made with an adhesive bond by using a film adhesive. For titanium and steel sandwich panels, the connection is usually formed by brazing or welding. When performing trade studies of sandwich panels against other stiffened skin designs, it is important to include the weight of the adhesive or braze material for each face sheet. Although adhesive and braze weights may seem insignificant on

a weight per unit area basis, the total adhesive or braze weight can be significant over a large acreage. In addition, the joint concept for attaching the sandwich panel to surrounding structure should be considered in any weight trades. Core ramp-downs, doublers, or core inserts may be required in joint areas, and all of these options have an associated weight penalty that can be significant.

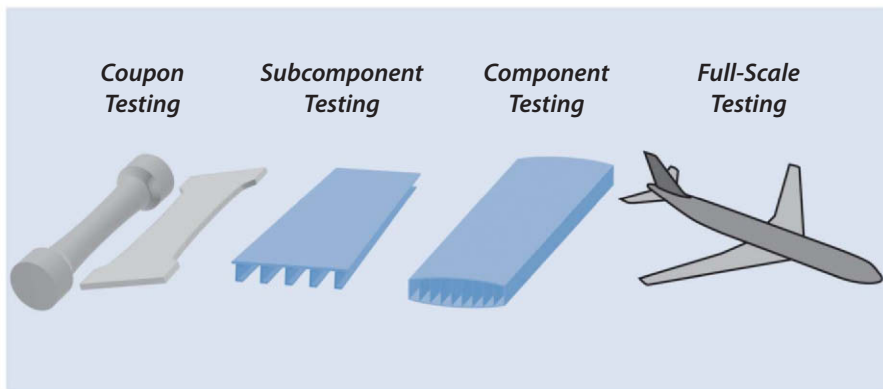
Sandwich construction has excellent stiffness-to-weight characteristics and, therefore, is a very attractive approach for achieving very lightweight airframe structure. However, sandwich construction does have some potential drawbacks that must be understood and addressed for actual design application. Sandwich panels can be subject to moisture entrapment where moisture passes through small pores or microcracks, in either the face sheets or the perimeter of a panel, and accumulates in the honeycomb core cells. Over time, this accumulation of moisture will increase the weight of the panel and can result in significant structural damage if the moisture freezes and expands at altitude, thereby causing the face-sheet-to-core bond to fail. In addition, the face sheets and core of a sandwich panel can be prone to impact damage, especially for lightly loaded sandwich structure where the face sheets can be extremely thin. However, these risks can be mitigated with proper design practices, and the weight reduction advantages often outweigh these potential drawbacks.

### 19.13 Structural Testing

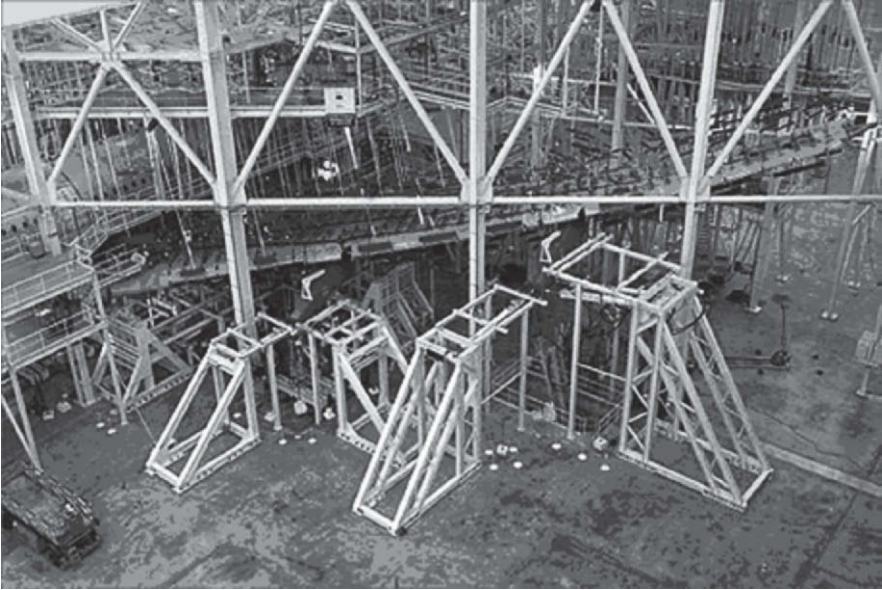
Although tremendous advances in structural analysis tools, such as finite element modeling, have been made over the last several decades, structural testing is still a very important part of the aircraft design and development process. There are two basic categories of structural testing: development testing, which is focused on generating data required to support detail design and drawing release; and verification testing, which is focused on demonstrating that the as-designed airframe meets structural requirements prior to flight. The bulk of these testing efforts normally occur in the Preliminary and Detail Design phases; however, it may be appropriate to perform “proof-of-concept” testing of new and unproven structural technologies (for example, a new material or innovative design concept) during Conceptual Design, especially if the success of the overall vehicle design hinges on the viability of that new technology. The structural testing philosophy and scope of testing that is envisioned for supporting vehicle development from Conceptual Design to First Flight can influence the airframe structural design approach, minimum margins-of-safety, material selection, and structural weight, as well as overall program cost and schedule. Therefore, it is important to have basic definition of the intended structural test plan and philosophy early in the design process.

Most structural test programs are composed of a series of tests that start at the coupon level, transition to subcomponent- and component-level specimens, and culminate in full-scale structural test articles, as depicted in Fig. 19.22. This progression in scope and complexity of tests is referred to as a *building block* testing approach [8]. Coupon-level testing is commonly focused on material characterization and generation of design allowables. If design allowables for the materials selected already exist in the MMPDS, coupon testing may not be required. However, if a new material is being utilized that has no existing database of design allowables, extensive coupon testing involving hundreds of specimens may be required for generating a full database of A-basis or B-basis design allowables. Subcomponent- and component-level testing typically includes testing of critical structural joints and other key design details. Component-level testing might include testing a section of fuselage or wing structure. In a world with unlimited program schedule and budget, these tests would be performed sequentially and the knowledge gained in each phase of testing would be applied to the next phase. For example, coupon testing would be completed before subcomponent testing is started, and the material data generated by the coupon testing would be used to design the subcomponent test articles. However, programs rarely have the schedule and budget to allow this sequential approach. Compression of the development testing schedule often results in significant overlap of the different levels of testing, with many tests being run in parallel. This places additional emphasis on defining a developing test program that is sufficiently flexible to accommodate test results, both good and bad, as they become available.

Verification testing usually involves static or fatigue testing of a full-scale, flightlike airframe. Figure 19.23 shows a full-scale static test of the Airbus A380 wing. The test article for a full-scale static test can be either an actual flight vehicle or an airframe of identical design to the flight vehicle



**Figure 19.22** Building-block structural testing approach.



**Figure 19.23** Airbus A380 full-scale static test (courtesy of Airbus Industrie).

but dedicated for ground testing only. Depending on the size of the aircraft and the scope of testing required, these full-scale tests can represent a substantial cost and schedule investment to the program. Therefore, the verification testing approach should be defined as early as possible in the design cycle, especially if test facilities must be modified or built. For prototype or demonstrator aircraft programs, where perhaps only one or two aircraft are being designed and built, it may not be desirable from a cost standpoint to perform extensive full-scale testing. In these cases, restriction of the flight test envelope or an increased minimum margin-of-safety imposed during the Detail Design phase is sometimes utilized in lieu of extensive full-scale static testing. Increased minimum margins can range from  $+0.20$  to  $+0.50$  instead of the  $0.00$  margin that is the normal goal for minimum weight structure. Different minimum margins can be required for different parts of the airframe, with the specific values selected dependent on a number of factors, such as the failure mode expected for each component (for example, strength vs stability failure) and the consequence of failure of the component. Any increased margin-of-safety requirement will impact vehicle weight and performance and, therefore, must be defined early in the design cycle. Most important, the overall structural flight certification approach,

The Republic XF-91 Thunderceptor, which first flew in 1949, featured a structurally challenging inverse taper wing in which the chord and thickness of the wing were greater at the tip than at the root. In addition, the entire wing could be tilted to vary the angle of incidence for improved takeoff and landing performance.

whether it includes increased minimum margins-of-safety or extensive structural testing, must be discussed with and agreed to by the customer and the flight certification agency, be consistent with company design policy, and provide a clear path for ensuring a flightworthy and safe design.

**Example 19.2 HAARP Wing Structural Analysis**

**Vehicle Description**

Consider the HAARP vehicle shown in Fig. 5.13 and discussed in Sections 5.8, 6.6.1, and 18.10. Vehicle dimensions, weights, and characteristics are as follows:

Wing span = $b$	269 ft
Wing area = $S$	2884 ft <sup>2</sup>
Wing aspect ratio = AR	25
Wing taper ratio = $\lambda$	0.35
$t/c$	12.2%
Wing structural weight	2708 lb [from Chapter 20, Eq. (20.2)]
Fuel weight in wing tanks	4800 lb (total both tanks)
Fuel tank structural weight + pumps	93 lb (total both tanks, scaled from U2-A, Table I.4)
Payload weight	578 lb (total both sides—located in engine or payload pods)
Heat exchanger weight	1147 lb (total both sides—located in wing LE, Section 14.2.1)
System weights in engine or payload pod (total both sides, Section 18.10):	
Propellers	400 lb (total weight of the two 8-ft and two 24-ft propellers)
Engine + turbocharger + accessories	2803 lb (from Section 18.10 and Fig. J.2)
Pod structural weight	290 lb (total for both sides)
Main landing gear	276 lb (U2-A bicycle gear + pogo, Table I.4)
Wing station for engine or payload pod	21.6 ft from centerline
Wing station for fuel tank	23.75 ft to 44.25 ft from centerline
Wing station for heat exchangers	7.6 ft to 28 ft from centerline
Vehicle takeoff gross weight (TOGW)	16,000 lb
Maximum airspeed	55 KEAS

The example problem will determine the spar cap sizing for the wing encountering a gust at 20,000 ft.

**Analysis Approach**

Part 1. Calculate the gust positive vertical load factor,  $+n_z$ , for the HAARP vehicle at the vehicle maximum airspeed and an altitude of

20,000 ft using the discrete gust formula. Assume an equivalent gust velocity of 66 ft/s, a lift curve slope of 0.1 per deg, and a total of 300 lb of fuel burned in reaching altitude.

The discrete gust formula is

$$n = 1 \pm \frac{K_g C_{L\alpha} U_e V_e}{498 W/S} \quad (19.1)$$

The gust alleviation factor  $K_g$  can be calculated for subsonic aircraft by using the expression

$$K_g = \frac{0.88\mu}{5.3 + \mu} \quad (19.2)$$

where  $\mu = 2(W/S)/\rho c a g$ .

The vehicle gross weight at altitude is  $W = 16,000 \text{ lb} - 300 \text{ lb} = 15,700 \text{ lb}$ . This gives a wing loading  $W/S = 15,700 \text{ lb}/2884 \text{ ft}^2 = 5.44 \text{ lb/ft}^2$ .

The air density  $\rho$  at an altitude of 20,000 ft can be obtained from a standard atmospheric table and is approximately  $12.67 \times 10^{-4} \text{ slug/ft}^3$ .

The acceleration of gravity is  $g = 32.2 \text{ ft/s}^2$ .

The lift curve slope  $a$  is given as 0.1 per degree, which must be expressed as 5.730 per radian for Eq. (19.2).

The mean chord of the wing,  $c$ , can be calculated from the wing area  $S$  and span  $b$ :

$$c = S/b = 2884 \text{ ft}^2/269 \text{ ft} = 10.72 \text{ ft}$$

Plugging these values into Eq. (19.2) for  $\mu$  gives  $\mu = 4.34$ . The gust alleviation factor can then be calculated to be  $K_g = 0.40$ .

The following values can then be input into the discrete gust formula:

$$\begin{aligned} K_g &= 0.40 \\ a &= 5.730 \text{ per radian} \\ V_e &= 55 \text{ KEAS} \\ U_e &= 66 \text{ ft/s} \\ W/S &= 5.44 \end{aligned}$$

This gives gust load factors of  $-2.1 g$  and  $+4.1 g$ . Therefore, the gust positive load factor (resulting in wing upbending) for this example is  $+4.1 g$ .

Part 2. Using the positive vertical gust load factor calculated in Part 1, calculate the lift distribution for the wing using Schrenk's approximation [9].

The first step in calculating the lift distribution is to divide the wing into a number of spanwise panels. Although the number and



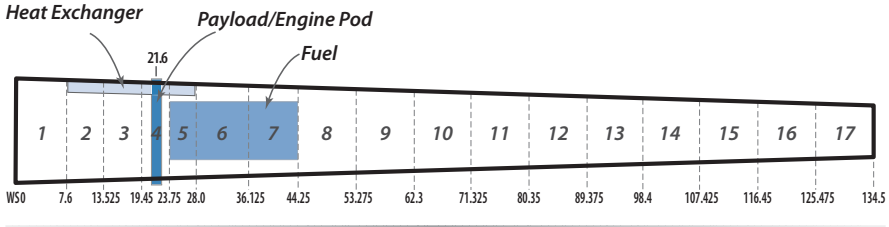


Figure 19.24 HAARP wing panel layout as used for analysis.

size of these panels is somewhat arbitrary, a sufficient number of panels should be used to insure the accuracy of the solution. In addition, subsequent parts of this example problem will involve calculating the inertia relief provided by the weight of the wing structure, fuel, and subsystems. Therefore, it is desirable to divide the wing into panels that match the location of various distributed and concentrated mass items in order to simplify subsequent calculations. For the solution presented here, the HAARP wing has been divided into 17 panels as shown in Fig. 19.24.

The lift distribution applied to the wing can be calculated using *Schrenk's approximation*. This method assumes that the spanwise lift distribution of an untwisted wing or tail is the average of the lift based on the actual trapezoidal wing shape and the lift based on an elliptical wing.

For a trapezoidal wing, lift can be expressed as a function of wing station  $y$  by using the following equation:

$$L^{\text{trap}}(y) = \frac{2L}{b(1+\lambda)} \left[ 1 - \frac{2y}{b}(1-\lambda) \right] \tag{19.3}$$

For an elliptical wing, the expression is

$$L^{\text{ellip}}(y) = \frac{4L}{\pi b} \sqrt{1 - \left[ \frac{2y}{b} \right]^2} \tag{19.4}$$

For the trapezoidal wing equation,  $\lambda$  is the wing taper ratio. In both equations,  $L$  is the total lift applied to the wing and  $b$  is the wing span. For the HAARP wing example under the prescribed vertical gust load,

$$L = (4.1 g)(15,700 \text{ lb}) = 64,370 \text{ lb (total)}$$

$$b = 269 \text{ ft}$$

$$\lambda = 0.35$$

The calculations for trapezoidal and elliptical lift as a function of wing station  $y$  are shown in the spreadsheet presented in Table 19.3. Because the wing lift distribution is the same for each side, or semi-span of the wing, the calculations are shown only from wing station 0 (WS0, the vehicle centerline) to wing station 134.5 ft (wingtip). In the far right column the total lift per panel, based on the average of the trapezoidal and elliptical lift distributions, is shown. As a check, the lift force for all panels is summed at the bottom of this column and shows a total wing lift of 32,215 lb per side, which is well within 1% of the expected answer of 32,185 lb per side ( $64,370 \text{ lb}/2 = 32,185 \text{ lb}$ ). Figure 19.25 plots the trapezoidal, elliptical, and average lift distributions as a function of wing station.

Part 3. Calculate the distribution of lift minus weight for the gust load calculated in Part 1 using the lift distribution derived in Part 2 and the given wing weights.

Table 19.4 shows the spreadsheet for calculating the weight for each of the 17 wing panels. Column F, the wing unit structural weight ( $0.939 \text{ lb}/\text{ft}^2$ ), is obtained by dividing the given total wing structural weight (2708 lb) by the wing planform area (2884  $\text{ft}^2$ ). Column G, the structural weight per panel, is obtained by multiplying this unit structural weight by the planform area of each panel, column E. Column H, the weight per span for each panel, is obtained by dividing each panel structural weight by the panel span.

The heat exchanger weight per span, column I, is obtained by dividing the total heat exchanger weight per side ( $1147 \text{ lb}/2 = 573.5 \text{ lb}/\text{side}$ ) by the spanwise length of each heat exchanger ( $28 \text{ ft} - 7.6 \text{ ft} = 20.4 \text{ ft}$ ), giving a value of  $573.5 \text{ lb}/20.4 \text{ ft} = 28.113 \text{ lb}/\text{ft}$ . The spanwise distributed weights for the fuel, column J, and fuel tanks and pumps, column K, are calculated in a similar manner. Columns H, I, J, and K are then added for each panel to give the total distributed weight per panel shown in column L.

Each side of the HAARP wing also contains a number of significant concentrated mass items located at WS 21.6 ft. Specifically, the weight of the payload, payload pod structure, propulsion system (propeller, engine, turbocharger, and accessories), and main landing gear are shown in columns M and N and are summed in column O.

Column P multiplies the total 1 g distributed weight per panel of column L by 4.1 g, and column Q multiplies the total concentrated weight at WS 21.6 (column O) by 4.1 g. The total 4.1 g distributed and concentrated weights are then summed for each panel in column R; they are totaled at the bottom of the column to serve as an interim check.

Table 19.5 shows the spreadsheet for calculating the (lift-minus-weight) for each of the 17 wing panels. Column F is the average wing

**Table 19.3** HAARP Wing Lift Distribution

			Elliptical Lift Distribution		Trapezoidal Lift Distribution			
Panel	Wing Station $y$ (ft)	Panel Span (ft)	$[(1 - (2y/b)^2)]^{1/2}$	Elliptical Lift ( $y$ ) at Midpanel (lb/ft)	$1 - (2y/b)(1 - \lambda)$	Trapezoidal Lift ( $y$ ) at Midpanel (lb/ft)	Avg. Lift (Ellip.+Trap.)/2 (lb/ft)	Lift per Panel (lb)
1	0.00	7.6	0.9996	304.6	0.9816	348.0	326.3	2479.7
	3.80							
	7.60							
2	10.56	5.925	0.9969	303.7	0.9490	336.4	320.1	1896.5
	13.53							
3	16.49	5.925	0.9925	302.4	0.9203	326.3	314.3	1862.4
	19.45							
4	21.60	4.3	0.9870	300.7	0.8956	317.5	309.1	1329.2
	23.75							
5	25.88	4.25	0.9813	299.0	0.8750	310.2	304.6	1294.5
	28.00							
6	32.06	8.125	0.9712	295.9	0.8451	299.6	297.8	2419.2
	36.13							
7	40.19	8.125	0.9543	290.8	0.8058	285.7	288.2	2341.7
	44.25							

8	48.76 53.28	9.025	0.9320	284.0	0.7643	271.0	277.5	2504.0
9	57.79 62.30	9.025	0.9030	275.1	0.7207	255.5	265.3	2394.4
10	66.81 71.33	9.025	0.8679	264.4	0.6771	240.0	252.2	2276.4
11	75.84 80.35	9.025	0.8259	251.6	0.6335	224.6	238.1	2148.9
12	84.86 89.38	9.025	0.7758	236.4	0.5899	209.1	222.7	2010.3
13	93.89 98.40	9.025	0.7161	218.2	0.5463	193.7	205.9	1858.5
14	102.91 107.43	9.025	0.6439	196.2	0.5027	178.2	187.2	1689.5
15	111.94 116.45	9.025	0.5544	168.9	0.4590	162.7	165.8	1496.5
16	120.96 125.48	9.025	0.4372	133.2	0.4154	147.3	140.2	1265.6
17	129.99 134.50	9.025	0.2569	78.3	0.3718	131.8	105.0	948.0
							<b>TOTAL</b>	<b>32,215.2</b>

**Table 19.4** Wing Weight Distribution Spreadsheet

							Distributed Structure, Fuel, and Systems Weight		
Panel	B Wing Station (y) (ft)	C Panel Span (ft)	D Panel Chord (ft)	E Panel Planform Area (ft <sup>2</sup> )	F Wing Unit Structural Weight (lb/ft <sup>2</sup> )	G Wing Structural Wt/Panel (lb)	H Wing Structural Wt/Span (lb/ft)	I Heat Exchanger Wt/Span (lb/ft)	J Fuel Wt/ Span (lb/ft)
	0.00								
1	3.80 7.60	7.60	15.6	118.5	0.939	111.3	14.64	0.00	0
2	10.56 13.53	5.93	15.1	89.3	0.939	83.9	14.15	28.11	0
3	16.49 19.45	5.93	14.6	86.6	0.939	81.3	13.73	28.11	0
4	21.60 23.75	4.30	14.2	61.2	0.939	57.4	13.36	28.11	0
5	25.88 28.00	4.25	13.9	59.1	0.939	55.5	13.05	28.11	109.8
6	32.06 36.13	8.13	13.4	109.1	0.939	102.4	12.60	0	109.8
7	40.19 44.25	8.13	12.8	104.0	0.939	97.6	12.02	0	109.8
8	48.76 53.28	9.03	12.1	109.6	0.939	102.9	11.40	0	0
9	57.79 62.30	9.03	11.4	103.3	0.939	97.0	10.75	0	0
10	66.81 71.33	9.03	10.8	97.1	0.939	91.1	10.10	0	0
11	75.84 80.35	9.03	10.1	90.8	0.939	85.3	9.45	0	0
12	84.86 89.38	9.03	9.4	84.6	0.939	79.4	8.80	0	0
13	93.89 98.40	9.03	8.7	78.3	0.939	73.3	8.12	0	0
14	102.91 107.43	9.03	8.0	72.1	0.939	67.7	7.50	0	0
15	111.94 116.45	9.03	7.3	65.8	0.939	61.8	6.85	0	0
16	120.96 125.48	9.03	6.6	59.5	0.939	55.9	6.20	0	0
17	129.99 134.50	9.03	5.9	53.3	0.939	50.0	5.55	0	0
				1442.0		1353.8			

		Concentrated Payload and Systems Weight			4.1 g Weight		
K Fuel Tank and Pump Wt/Span (lb/ft)	L Total Wing Dist. Wt/Span (lb/ft)	M 1 g POD Systems Weight (lb)	N 1 g POD Payload Weight (lb)	O 1 g POD Payload Weight (lb)	P Total 4.1 g Wing Dist. Wt/Span (lb/ft)	Q 4.1 g Concentrated Weight (lb)	R Total 4.1 g Wing Wt/Panel (lb)
0	14.64	0	0	0	60.0	0	456
0	42.27	0	0	0	173.3	0	1027
0	41.84	0	0	0	171.5	0	1016
0	41.47	1885	289	2174	170.0	8911	9642
2.27	153.19	0	0	0	628.1	0	2669
2.27	124.63	0	0	0	511.0	0	4152
2.27	124.04	0	0	0	508.6	0	4132
0	11.40	0	0	0	46.7	0	422
0	10.75	0	0	0	44.1	0	398
0	10.10	0	0	0	41.4	0	374
0	9.45	0	0	0	38.7	0	350
0	8.80	0	0	0	36.1	0	326
0	8.12	0	0	0	33.3	0	300
0	7.50	0	0	0	30.7	0	277
0	6.85	0	0	0	28.1	0	253
0	6.20	0	0	0	25.4	0	229
0	5.55	0	0	0	22.7	0	205
							26,229

**Table 19.5** HAARP Lift-Minus-Weight Distribution Spreadsheet

Panel	B Wing Station (y) (ft)	C Panel Span (ft)	D Panel Chord (ft)	E Panel Planform Area (ft <sup>2</sup> )	F 4.1 g Lift (Ellip.+Trap.)/2 (lb/ft)	G Total 4.1 g Wing Distr. Weight/Span (lb/ft)	H 4.1 g Lift Distributed Weight (lb/ft)	I 4.1 g Concentrated Weight (lb)
1	0 3.80 7.60	7.60	15.59	118.49	326.27	60.02	266.25	0
2	10.56 13.53	5.93	15.07	89.30	320.08	173.29	146.79	0
3	16.49 19.45	5.93	14.62	86.61	314.32	171.54	142.79	0
4	21.60 23.75	4.30	14.23	61.17	309.11	170.03	139.08	-8911
5	25.88 28.00	4.25	13.90	59.06	304.59	628.06	-323.48	0
6	32.06 36.13	8.13	13.42	109.05	297.75	510.97	-213.22	0
7	40.19 44.25	8.13	12.80	103.98	288.21	508.57	-220.36	0

8	48.76 53.28	9.03	12.14	109.56	277.46	46.74	230.72	0
9	57.79 62.30	9.03	11.45	103.31	265.31	44.07	221.24	0
10	66.81 71.33	9.03	10.76	97.06	252.23	41.41	210.83	0
11	75.84 80.35	9.03	10.06	90.81	238.11	38.74	199.37	0
12	84.86 89.38	9.03	9.37	84.56	222.75	36.07	186.68	0
13	93.89 98.40	9.03	8.68	78.30	205.92	33.30	172.63	0
14	102.91 107.43	9.03	7.98	72.06	187.20	30.74	156.46	0
15	111.94 116.45	9.03	7.29	65.80	165.82	28.07	137.75	0
16	120.96 125.48	9.03	6.60	59.55	140.23	25.40	114.83	0
17	129.99 134.50	9.03	5.91	53.29	105.04	22.73	82.31	0
			<b>TOTAL =</b>	<b>1442.0</b>				



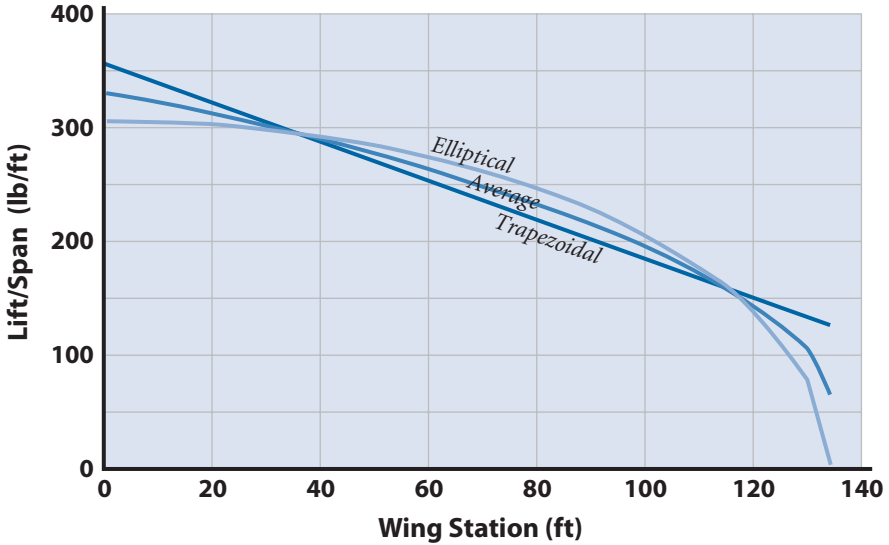


Figure 19.25 Trapezoidal, elliptical, and average wing lift distributions ( $n_z = +4.1 g$ ).

lift distribution at 4.1 g calculated in Part 2, and column G is the 4.1 g distributed weight that was previously calculated. Column H is obtained by subtracting the lift from the weight for each panel, and column I contains concentrated weight located at WS 21.6.

Figure 19.26 plots the 4.1 g (lift-minus-weight) distribution and 4.1 g concentrated weight located at WS 21.6.

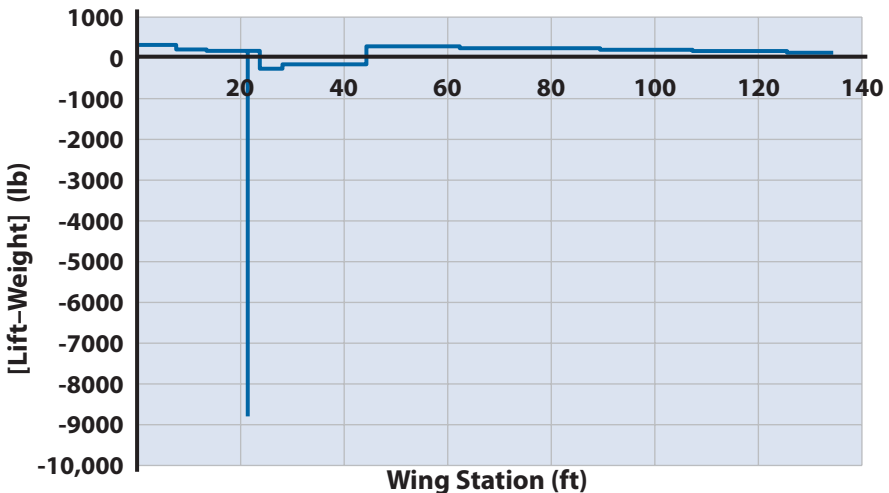


Figure 19.26 HAARP lift-minus-weight distribution.

Part 4. Using the lift-minus-weight distribution calculated in Part 3, calculate the net vertical shear load ( $P_z$ ) distribution and spanwise bending moment ( $M_x$ ) distribution for the HAARP wing for the gust condition.

Table 19.6 summarizes the lift-minus-weight distribution and concentrated mass items for the HAARP wing that have been calculated in Parts 1 through 3 of this example problem. Column F presents the net total load for each panel (assumed to act at the panel midpoint), which is derived from multiplying the lift-minus-weight (expressed in pounds per foot of panel span) by the panel span. Notice that the concentrated mass items located at WS 21.6 are handled separately and are not included in the load-per-panel calculations for column F. The vertical shear load ( $P_z$ ) applied to the wing (column G) is obtained by starting at the wingtip (panel 17) and summing the net load from each panel and progressing toward the wing root (panel 1). This shear load is plotted against wing station in Fig. 19.27 and illustrates the reduction in vertical shear loading resulting from the large mass items (fuel, heat exchanger, propulsion system, payload, etc.) located toward the inner span of the wing. This reduction in wing shear and bending loads due to mass items (both distributed and concentrated mass items) is referred to as *inertia relief*.

The spanwise bending moment ( $M_x$ ) is obtained by calculating the area under the shear curve. Starting at the wingtip (panel 17) the area under the shear curve is calculated for each panel and summed

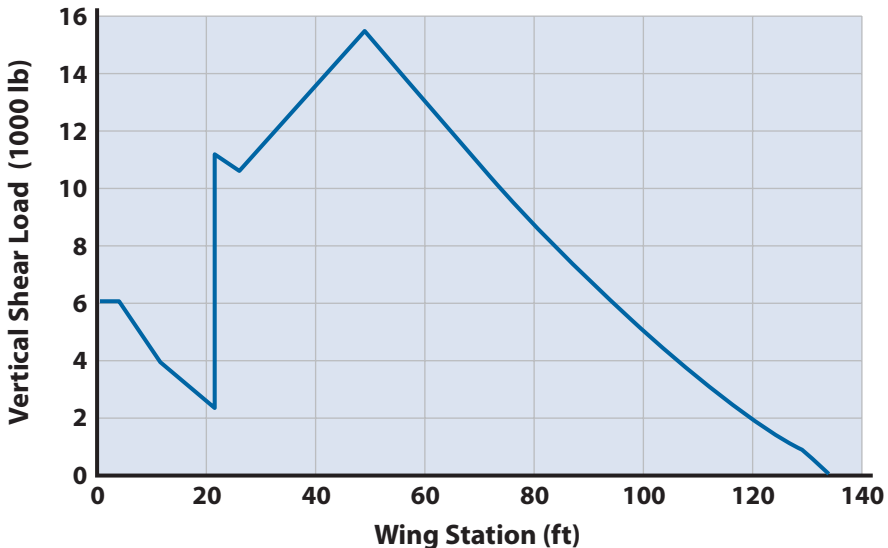
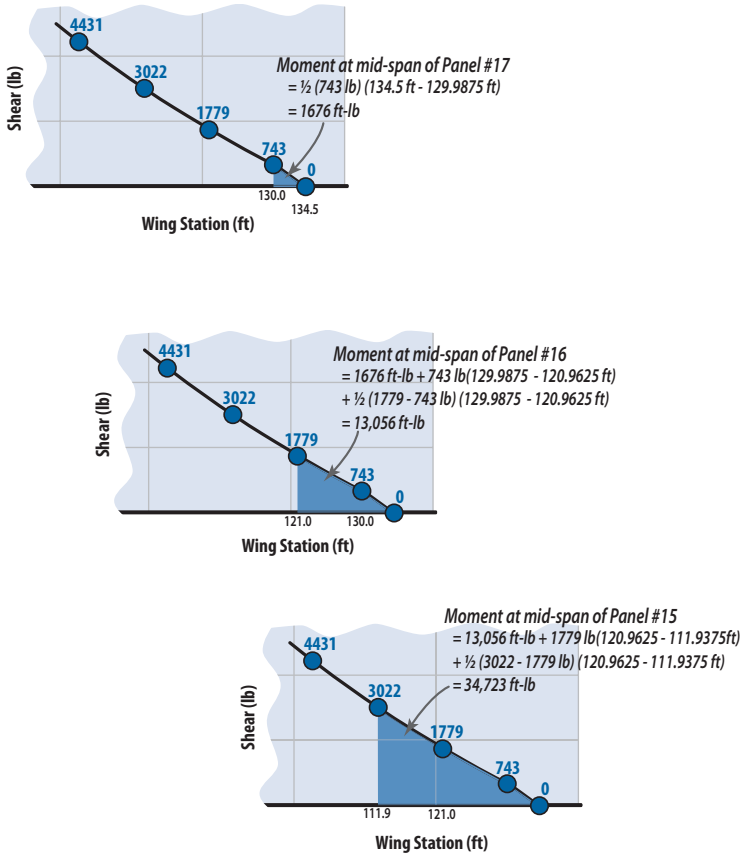


Figure 19.27 HAARP wing vertical shear ( $n_z = +4.1 g$ ).

**Table 19.6** HAARP Wing Vertical Shear Spreadsheet ( $n_z = +4.1 g$ )

Panel	B Wing Station (y) (ft)	C Panel Span (ft)	D 4.1 g Lift Distr. Weight (lb/ft)	E 4.1 g Concentrated Weight (lb)	F Total 4.1 g Load per Panel (lb)	G Shear Load (lb)
	0					
1	3.80 7.60	7.6	266.2	0	2023.5	5,986.4
2	10.56 13.53	5.925	146.8	0	869.7	3,962.9
3	16.49 19.45	5.925	142.8	0	846.0	3,093.1
4	21.60 23.75	4.3	139.1	-8911	598.0	2,247.1
5	25.88 28.00	4.25	-323.5	0	-1374.8	10,560.4
6	32.06 36.13	8.125	-213.2	0	-1732.4	11,935.2
7	40.19 44.25	8.125	-220.4	0	-1790.4	13,667.6
8	48.76 53.28	9.025	230.7	0	2082.2	15,458.0
9	57.79 62.30	9.025	221.2	0	1996.7	13,375.8
10	66.81 71.33	9.025	210.8	0	1902.7	11,379.1
11	75.84 80.35	9.025	199.4	0	1799.3	9,476.4
12	84.86 89.38	9.025	186.7	0	1684.8	7,677.1
13	93.89 98.40	9.025	172.6	0	1558.0	5,992.3
14	102.91 107.43	9.025	156.5	0	1412.0	4,434.4
15	111.94 116.45	9.025	137.7	0	1243.2	3,022.3
16	120.96 125.48	9.025	114.8	0	1036.3	1,779.1
17	129.99 134.50	9.025	82.3	0	742.8	742.8



**Figure 19.28** Example of method for calculating area under shear curve.

progressively working toward the wing root (panel 1), as illustrated in Fig. 19.28. Table 19.7 summarizes the calculation used to derive the spanwise bending moment based on the area under the shear curve, and Fig. 19.29 is the plot of the spanwise bending moment as a function of wing station.

Part 5. Using the wing moment distribution derived in Part 4, what is the spanwise bending moment at WS 40.2? Assuming the HAARP wing uses a single “I-beam” spar located at maximum  $t/c$  of the airfoil that reacts all of the spanwise bending load (i.e., wing skin is ineffective at carrying any load), and assuming that the centroids of the upper and lower spar caps are coincident with the outer surface of the wing skins, what are the spar cap loads at WS 40.2 resulting from the gust condition?

**Table 19.7** Spanwise Bending Moment Spreadsheet

Panel	Wing Station (y) (ft)	Panel Span (ft)	Vertical Shear Load (lb)	Delta Spanwise Bending Moment, $M_y$ (ft-lb)	Spanwise Bending Moment, $M_y$ (ft-lb)
1	0	7.60	5,986	22,748	1,027,053
	3.80		5,986	33,641	1,004,305
	7.60				
2	10.56	5.93	3,963	20,903	970,664
	13.53				
3	16.49	5.93	3,093	13,651	949,761
	19.45				
4	21.60	4.30	11,158	46,424	936,110
	23.75				
5	25.88	4.25	10,560	69,596	889,686
	28.00				
6	32.06	8.13	11,935	104,011	820,090
	36.13				
7	40.19	8.13	13,668	124,876	716,079
	44.25				
8	48.76	9.03	15,458	130,113	591,202
	53.28				
9	57.79	9.03	13,376	111,707	461,089
	62.30				
10	66.81	9.03	11,379	94,111	349,383
	71.33				
11	75.84	9.03	9,476	77,405	255,272
	80.35				
12	84.86	9.03	7,677	61,683	177,867
	89.38				
13	93.89	9.03	5,992	47,050	116,183
	98.40				
14	102.91	9.03	4,434	33,648	69,133
	107.43				
15	111.94	9.03	3,022	22,429	35,485
	116.45				
16	120.96	9.03	1,779	11,380	13,056
	125.48				
17	129.99	9.03	743	1,676	1,676
	134.50		0	0	0

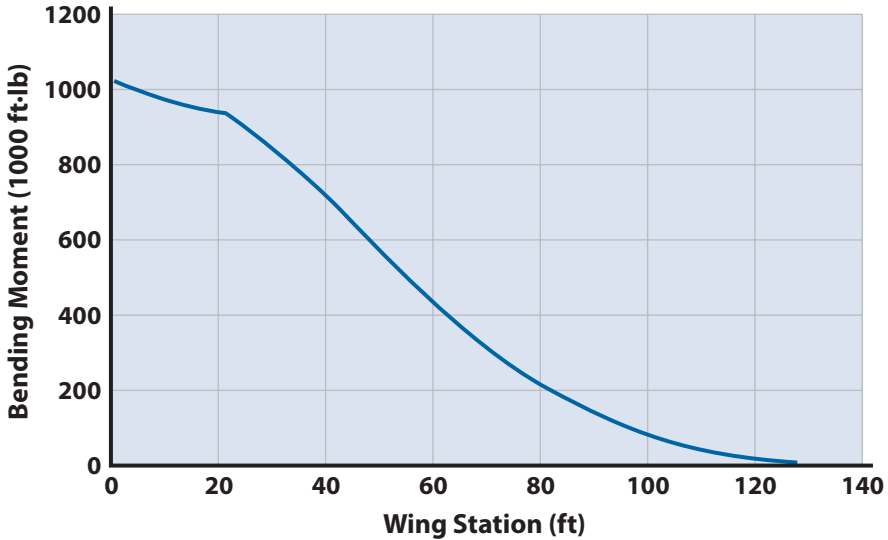


Figure 19.29 Wing bending moment.

The  $M_x$  moment at WS 40.2 is 716,079 ft-lb. The wing chord at WS 40.2 is 12.798 ft. Therefore, using a  $t/c = 12.2\%$ , the spar depth at WS 40.2 =  $(0.122)(12.798) = 1.56$  ft.

The wing bending moment is reacted by a couple load in the spar caps as shown in Fig. 19.30. These cap loads can be calculated by dividing the bending moment  $M$  by the spar depth  $d$ , which at WS 40.2 is  $716,079 \text{ ft-lb}/1.56 \text{ ft} = \pm 459,025 \text{ lb}$  (tension in the lower cap, and compression in the upper cap for the  $+4.1 g$  wing upbending condition).

Part 6. Assuming an ultimate factor-of-safety = 1.5, and assuming that the wing spar is constructed of a material with  $F_{ty} = 60 \text{ ksi}$  and  $F_{tu} = 75 \text{ ksi}$ , what cross-sectional area is required for the lower spar cap at WS 40.2 when subjected to the gust condition?

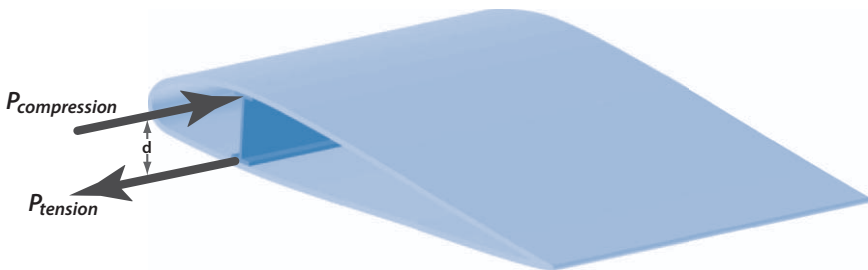


Figure 19.30 Wing spanwise bending moment reacted by couple load in the spar caps.

The lower spar is loaded in tension due to this gust condition, with a limit load of 459,025 lb and an ultimate load of  $(1.5)(459,025 \text{ lb}) = 688,538 \text{ lb}$ . The required lower cap area based on tension yield strength is

$$A_{\text{req-yield}} = 459,025 \text{ lb}/60,000 \text{ psi} = 7.7 \text{ in.}^2$$

The required lower cap area based on tension ultimate strength is

$$A_{\text{req-ult}} = 688,538 \text{ lb}/75,000 \text{ psi} = 9.2 \text{ in.}^2$$

Because the spar cap sizing must satisfy both the yield and ultimate strength criteria, the required cross-sectional area for the HAARP wing lower cap at WS 40.2 due to an  $n_z = +4.1 g$  is  $9.2 \text{ in.}^2$ .

## 19.14 Summary

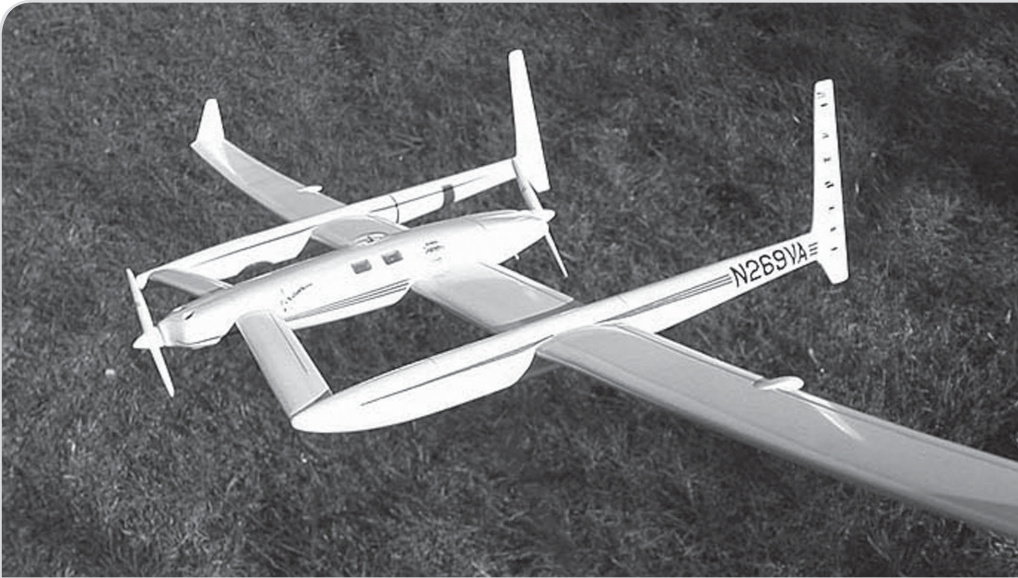
The world of aircraft structures involves many diverse technical disciplines related to design, analysis, materials, manufacturing, and testing. There are many options available to the Structures Engineer regarding design concepts, material selection, analysis approach, manufacturing methods, and test verification philosophy; accordingly, it is important to have a rational and objective decision-making process to determine which design options are optimal for satisfying a particular set of vehicle requirements. Although it is sometimes obvious which structural design options are best, there are often multiple paths to achieve the same end result, and most structural design decisions represent a complex balance between weight, risk, cost, and schedule.

## References

- [1] "Joint Service Specification Guide—Aircraft Structures," JSSG-2006, U.S. Department of Defense, 1998.
- [2] "Joint Service Specification Guide—Air Vehicle," JSSG-2001B, U.S. Department of Defense, 2004.
- [3] "Aircraft Strength and Rigidity—Flight Loads," MIL-A-8861B, Naval Air Systems Command, 1986.
- [4] Niu, M. C. Y., *Airframe Structural Design*, Technical Book Co., Los Angeles, CA, 1988.
- [5] Ekvall, J. S., Rhoades, J. E., and Wald, G. G., "Methodology for Evaluating Weight Savings from Basic Material Properties," Design of Fatigue and Fracture Resistant Structures, American Society for Testing and Materials ASTM STP 761, 1982.
- [6] "Aircraft Strength and Rigidity—General Specification," MIL-A-8860B, Naval Air Systems Command, 1987.
- [7] "Metallic Materials Properties Development and Standardization," MMPDS-04, Federal Aviation Administration, 2008.
- [8] "Aircraft Strength and Rigidity—Ground Tests," MIL-A-8867C, Naval Air Systems Command, 1987.
- [9] Raymer, D. P., *Aircraft Design: A Conceptual Approach*, AIAA Education Series, AIAA, Washington, DC, 1989.

## Chapter 20

# Refined Weight Estimate



- Military, Commercial, & GA WERs
- Adjustment for Advanced Composites
- Low Wing Loading ( $W/S < 5$ )
- Locating the C.G.
- Estimating Moments of Inertia

Estimating weights is critical in the design of an aircraft. This is especially true for weight-critical aircraft such as the Voyager designed by Burt Rutan (Scaled Composite Inc). Learn more about this aircraft in Section 20.2.4.

*Estimating the weight of an airplane or airship involves as much art as it does science.*



## 20.1 Introduction

**A**t this point the designer should do a detailed weight estimate of the aircraft. The original estimate of the aircraft empty weight (from Chapter 5) used the impersonal empty-weight trend curves of Appendix I. As such they were not able to capture the unique and innovative features of the conceptual aircraft. However, they were appropriate for that point in the design cycle when the aircraft information was sparse. Now there is considerable information available on the aircraft and the weights of all the aircraft components can be estimated to get a refined empty weight and center of gravity location. Component weights are determined in a large part through the use of empirical formulations that are conditioned upon the many different geometric properties of the components. A multiple regression analysis is used to determine the best curve-fit expression for the historical data.

The designer must be careful when applying these weight-estimate equations to new designs. If the new aircraft will be considerably different in performance and/or structural design than the aircraft used to develop the weight-estimate equations, then the weight equations might have to be altered. Weight-estimation methods for advanced systems are guarded very closely by aircraft companies as they represent their expertise in the design of advanced systems. The Aeronautical Systems Center at Wright-Patterson AFB, Ohio, served as a clearinghouse for the exchange of weights information in the 1960s and 1970s, hosting weight-prediction workshops. Currently, NAVAIR at Patuxent River, Maryland, serves as the government clearinghouse. The Society of Allied Weight Engineers (SAWE) also promotes the exchange of weight-estimating information.

The weight-estimating equations contained in this chapter have come from many sources. It is recommended that the equations be calibrated case-by-case, by comparing the estimated weights with real aircraft (Appendix I) and other sources (see [1–6]).

As discussed in Appendix I, estimating the empty weight of an aircraft is the most challenging part of the conceptual design process. Historical data are available to make credible weight estimates (estimating weight at the conceptual design level is an art and it will never be a science). Most design groups carry a weight margin through conceptual and preliminary design to account for the uncertainty in the weight estimates and the inevitable and dreaded “weights growth.” At the Lockheed Martin Skunk Works the margin on empty weight is 6%.

## 20.2 Weight-Estimation Methods

### 20.2.1 Conventional Metal Aircraft—Moderate Subsonic to Supersonic Performance

Credit for the following weight-estimation methods for conventional metal aircraft goes to many sources in the aerospace industry. The weight equations give the component weight in pounds.

#### 20.2.1.1 Structure

##### Wing

U.S. Air Force (USAF) Fighter Aircraft:

$$W_t = 3.08 \left( \frac{K_{PIV} N W_{TO}}{t/c} \left\{ \left[ \tan \Lambda_{LE} - \frac{2(1-\lambda)}{AR(1+\lambda)} \right]^2 + 1.0 \right\} \times 10^{-6} \right)^{0.593} \left[ (1+\lambda) AR \right]^{0.89} S_w^{0.741} \quad (20.1a)$$

U.S. Navy (USN) Fighter Aircraft:

$$W_t = 19.29 \left( \frac{K_{PIV} N W_{TO}}{t/c} \left\{ \left[ \tan \Lambda_{LE} - \frac{2(1-\lambda)}{AR(1+\lambda)} \right]^2 + 1.0 \right\} \times 10^{-6} \right)^{0.464} \left[ (1+\lambda) AR \right]^{0.70} S_w^{0.58} \quad (20.1b)$$

where

$K_{PIV}$  = wing variable-sweep structural factor

= 1.00 for fixed wings

= 1.175 for variable-sweep wings

$t/c$  = maximum thickness ratio

$W_{TO}$  = takeoff weight, in pounds (lb)

$\Lambda_{LE}$  = leading edge sweep

$\lambda$  = taper ratio

AR = wing aspect ratio

$S_w$  = wing area, in square feet (ft<sup>2</sup>)

$N$  = ultimate load factor

= 13.5 for fighter aircraft (based on a design limit load factor of +9.0 and a margin of safety of 1.5)

= 4.5 for bomber and transport aircraft (based on a design limit load factor of +3.0)

Subsonic Aircraft (Military and Commercial):

$$Wt = 0.00428 (S_w)^{0.48} \frac{AR^{1.0} (M_0)^{0.43} (W_{TO} N)^{0.84} (\lambda)^{0.14}}{(100 t/c)^{0.76} (\cos \Lambda_{1/2})^{1.54}} \quad (20.2)$$

where

$M_0$  = maximum Mach number at sea level

$\Lambda_{1/2}$  = sweep of half-chord

$t/c$  = maximum thickness ratio

This wing weight equation is valid for an  $M_0$  range of 0.4–0.8, a  $t/c$  range of 0.08–0.15, and an aspect ratio (AR) range of 4–12.

### Horizontal and Vertical Tail

Horizontal Tail:

$$Wt = 0.0034 \gamma^{0.915} \quad (20.3a)$$

where

$\gamma = (W_{TO} N)^{0.813} (S_{HT})^{0.584} (b_{HT}/t_{RHT})^{0.033} (\bar{c}_{wing}/L_t)^{0.28}$

$N$  = ultimate load factor

$S_{HT}$  = horizontal tail total planform area (include fuselage carry-through), in square feet (ft<sup>2</sup>)

$t_{RHT}$  = thickness of the horizontal tail at the root, in feet

$\bar{c}_{wing}$  = mac of the wing, in feet

$L_t$  = tail moment arm, in feet; distance from one-fourth wing mac to one-fourth tail mac. For canard surfaces, use distance from 0.4 wing mac to one-fourth canard mac

$b_{HT}$  = span of horizontal tail, in feet

Vertical Tail:

$$Wt = 0.19 \gamma^{1.014} \quad (20.3b)$$

where

$$\gamma = (1 + h_T/h_V)^{0.5} (W_{TO} N)^{0.363} (S_{VT})^{1.089} M_0^{0.601} (L_t)^{-0.726} (1 + S_r/S_{VT})^{0.217} \times (AR_{VT})^{0.337} (1 + \lambda_V)^{0.363} (\cos \Lambda_{VT})^{-0.484}$$

$h_T/h_V$  = ratio of horizontal tail height to vertical tail height. For a “T” tail this ratio is 1.0; for a fuselage-mounted horizontal tail this ratio is 0

- $S_{VT}$  = area of vertical tail, in square feet (ft<sup>2</sup>)
- $M_0$  = maximum Mach number at sea level
- $L_t$  = tail moment arm, in feet; distance from one-fourth wing mac to one-fourth tail mac
- $S_r$  = rudder area, in square feet. If unknown, use  $S_r/S_V = 0.3$
- $AR_{VT}$  = aspect ratio of vertical tail
- $\lambda_V$  = taper ratio of vertical tail
- $\Lambda_{VT}$  = sweep of vertical tail quarter-chord

### Fuselage

USAF and Commercial:

$$Wt = 10.43 (K_{INL})^{1.42} (q \times 10^{-2})^{0.283} (W_{TO} \times 10^{-3})^{0.95} (L/H)^{0.71} \quad (20.4)$$

USN:

$$Wt = 11.03 (K_{INL})^{1.23} (q \times 10^{-2})^{0.245} (W_{TO} \times 10^{-3})^{0.98} (L/H)^{0.61} \quad (20.5)$$

where

- $q$  = maximum dynamic pressure, in pounds per square foot (lb/ft<sup>2</sup>)
- $L$  = fuselage length, in feet (ft)
- $H$  = maximum fuselage height, in feet
- $K_{INL} = 1.25$  for inlets on fuselage
- $= 1.0$  for inlets in wing root or elsewhere

### Landing Gear

USAF and Commercial:

$$Wt = 62.21 (W_{TO} \times 10^{-3})^{0.84} \quad (20.6)$$

USN:

$$Wt = 129.1 (W_{TO} \times 10^{-3})^{0.66} \quad (20.7)$$

## 20.2.1.2 Propulsion

### Engine

Engine weights should be based upon the engine manufacturer's data and scaling factors. Assume the exhaust, cooling, turbo-supercharger, and lubrication systems weights are included in the engine weight.

### Propulsion Subsystems

Propulsion subsystem items are the air induction system, fuel system, engine controls, and starting system.

### Air Induction System

The parameters used in determining air induction system weights are defined as follows:

- $A_i$  = capture area per inlet, in square feet (ft<sup>2</sup>)
- $N_i$  = number of inlets, vehicle configuration
- $L_d$  = subsonic duct length, per inlet, in feet (ft)
- $L_r$  = ramp length forward of throat, per inlet, in feet
- $K_{\text{GEO}}$  = duct shape factor; use  $K = 1.33$  if duct has two or more relatively flat sides; use  $K = 1.0$  if duct is round or has one flat side
- $P_2$  = maximum static pressure at engine compressor face, in pounds per square inch absolute (psia)
- $K_{\text{TE}}$  = temperature correction factor
  - = 1 for  $M_D$  less than 3.0
  - =  $(M_D + 2)/5$  for  $M_D$  between 3.0 and 6.0, where design Mach number  $M_D$  is the maximum Mach number
- $K_M$  = duct material factor, use  $K = 1.0$  for  $M_D < 1.4$ ; use  $K = 1.5$  for  $M_D \geq 1.4$

Duct Provisions:

$$\text{Wt} = 0.32 (N_i)(L_d)(A_i)^{0.65} (P_2)^{0.6} \quad (20.8)$$

This equation accounts for the duct support structure and should only be used for internal installations. Duct provisions are normally included with the weight, but they have been separated out for this discussion to complete the total air-induction system weight.

Internal Duct Weight:

$$\text{Wt} = 1.735 \left[ (N_i)(L_d)(A_i)^{0.5} (P_2)(K_{\text{GEO}})(K_M) \right]^{0.7331} \quad (20.9)$$

This equation accounts for the duct structure from the inlet lip to the engine compressor face, and it should only be used for internal engine installations.

Variable-Geometry Ramps, Actuators, and Control Weights:

$$\text{Wt} = 4.079 \left[ (N_i)(L_r)(A_i)^{0.5} (K_{\text{TE}}) \right]^{1.201} \quad (20.10)$$

This equation should only be used for internal installations. Variable-geometry ramps are normally used with rectangular inlets.

Half-Round Fixed Spike Weight:

$$W_{\text{HFS}} = 12.53 (N_i)(A_i) \quad (20.11)$$

This equation should only be used for internal installations.

Full-Round Translating Spike Weight:

$$W_t = 15.65 (N_i)(A_i) \quad (20.12)$$

This equation can be used for either internal or external (podded) engine installations.

Translating and Expanding Spike Weight:

$$W_{\text{TES}} = 51.8 (N_i)(A_i) \quad (20.13)$$

This equation can be used for either internal or external engine installations.

External Turbojet Cowl and Duct Weight:

$$W_t = 3.00 (N_i) \left[ (A_i)^{0.5} (L_d)(P_2) \right]^{0.731} \quad (20.14)$$

This equation accounts for the exterior cowl or cover panels, ducting, and substructure such as rings, frames, stiffeners, and longerons, from the inlet lip to the engine compressor face, and should only be used for external engine installations.

External Turbofan Cowl and Duct Weight:

$$W_{\text{DTF}} = 7.435 (N_i) \left[ (L_d)(A_i)^{0.5} (P_2) \right]^{0.731} \quad (20.15)$$

This equation accounts for cowl panels, substructure, and the basic engine duct and the fan duct, and it should only be used for external engine installations.

## Fuel System

Self-Sealing Bladder Cells:

$$W_t = 41.6 \left[ (F_{\text{GW}} + F_{\text{GF}}) \times 10^{-2} \right]^{0.818} \quad (20.16)$$

where  $F_{\text{GW}}$  = total wing fuel in gallons and  $F_{\text{GF}}$  = total fuselage fuel in gallons.

Non-Self-Sealing Bladder Cells:

$$Wt = 23.10 \left[ (F_{GW} + F_{GF}) \times 10^{-2} \right]^{0.758} \quad (20.17)$$

Fuel System Bladder Cell Backing and Supports (Both Self-Sealing and Non-Self-Sealing):

$$Wt = 7.91 \left[ (F_{GW} + F_{GF}) \times 10^{-2} \right]^{0.854} \quad (20.18)$$

In-Flight Refuel System:

$$Wt = 13.64 \left[ (F_{GW} + F_{GF}) \times 10^{-2} \right]^{0.392} \quad (20.19)$$

Dump-and-Drain System:

$$Wt = 7.38 \left[ (F_{GW} + F_{GF}) \times 10^{-2} \right]^{0.458} \quad (20.20)$$

C.G. Control System (Transfer Pumps and Monitor):

$$Wt = 28.38 \left[ (F_{GW} + F_{GF}) \times 10^{-2} \right]^{0.442} \quad (20.21)$$

### Engine Controls

Body- or Wing-Root-Mounted Jet:

$$Wt = K_{ECO} (L_f N_E)^{0.792} \quad (20.22)$$

where

$L_f$  = fuselage length, in feet (ft)

$N_E$  = number of engines (per airplane)

$K_{ECO}$  = engine control engine-type coefficient

= 0.686, nonafterburning engines

= 1.080, afterburning (A/B) engines

Wing-Mounted Turbojet and Turbofan:

$$Wt = 88.46 \left[ (L_f + b) N_E \times 10^{-2} \right]^{0.294} \quad (20.23)$$

Wing-Mounted Turboprop:

$$Wt = 56.84 \left[ (L_f + b) N_E \times 10^{-2} \right]^{0.514} \quad (20.24)$$

Wing-Mounted Reciprocating:

$$Wt = 60.27 \left[ (L_f + b) N_E \times 10^{-2} \right]^{0.724} \quad (20.25)$$

where  $b$  = wing span, in feet.

### Starting Systems

One or Two Jet Engines—Cartridge and Pneumatic:

$$Wt = 9.33 \left( N_E W_{ENG} \times 10^{-3} \right)^{1.078} \quad (20.26)$$

where  $N_E$  = number of engines per airplane, and  $W_{ENG}$  = engine weight, in pounds per engine.

One or Two Jet Engines—Electrical:

$$Wt = 38.93 \left( N_E W_{ENG} \times 10^{-3} \right)^{0.918} \quad (20.27)$$

Four or More Jet Engines—Pneumatic:

$$Wt = 49.19 \left( N_E W_{ENG} \times 10^{-3} \right)^{0.541} \quad (20.28)$$

Turboprop Engines—Pneumatic:

$$Wt = 12.05 \left( N_E W_{ENG} \times 10^{-3} \right)^{1.458} \quad (20.29)$$

Reciprocating Engines—Electric:

$$Wt = 50.38 \left( N_E W_{ENG} \times 10^{-3} \right)^{0.459} \quad (20.30)$$

### Propeller Systems

Propellers:

$$Wt = K_p N_p (N_{BL})^{0.391} \left( d_p \times HP \times 10^{-3} \right)^{0.782} \quad (20.31)$$

where

$N_p$  = number of propellers per airplane

$N_{BL}$  = number of blades per propeller

$d_p$  = propeller diameter, in feet per propeller

HP = rated engine shaft horsepower

$K_p$  = propeller-engine coefficient

= 24.00 for turboprop above 1500 shaft horsepower

= 31.92 for reciprocating engine at all horsepower and turboprop below 1500 shaft horsepower



Propeller Controls—Turboprop Engines:

$$Wt = 0.322 (N_{BL})^{0.589} (N_p d_p \text{ HP} \times 10^{-3})^{1.178} \quad (20.32)$$

Propeller Controls—Reciprocating Engines:

$$Wt = 4.552 (N_{BL})^{0.379} (N_p d_p \text{ HP} \times 10^{-3})^{0.759} \quad (20.33)$$

### 20.2.1.3 Surface Controls Plus Hydraulics and Pneumatics

Fighters—USAF:

$$Wt = K_{SC} (W_{TO} \times 10^{-3})^{0.581} \quad (20.34)$$

where

- $K_{SC}$  = surface control coefficient
- = 106.10 for elevon without horizontal tail
- = 138.18 for horizontal tail
- = 167.48 for variable-sweep wing

Fighter and Attack—USN:

$$Wt = 23.77 (W_{TO} \times 10^{-3})^{1.10} \quad (20.35)$$

Executive and Commercial Passenger Transports:

$$Wt = 56.01 (W_{TO} \times q \times 10^{-5})^{0.576} \quad (20.36)$$

where  $q$  = maximum dynamic pressure, in pounds per square foot (lb/ft<sup>2</sup>).

Commercial and Military Cargo—Troop Transports:

$$Wt = 15.96 (W_{TO} \times q \times 10^{-5})^{0.815} \quad (20.37)$$

Bombers:

$$Wt = 1.049 (S_{TOT} \times q \times 10^{-3})^{1.21} \quad (20.38)$$

where  $S_{TOT}$  = total surface control area, in square feet (ft<sup>2</sup>).

### 20.2.1.4 Instruments

Flight Instrument Indicators

$$Wt = N_{PIL} \left[ 15.0 + 0.032 (W_{TO} \times 10^{-3}) \right] \quad (20.39)$$

where  $N_{PIL}$  = number of pilots.

Engine Instrument Indicators

Turbine Engines:

$$Wt = N_E \left[ 4.80 + 0.006 (W_{TO} \times 10^{-3}) \right] \quad (20.40)$$

where  $N_E$  = number of engines.

Reciprocating Engines:

$$Wt = N_E \left[ 7.40 + 0.046 (W_{TO} \times 10^{-3}) \right] \quad (20.41)$$

Miscellaneous Indicators:

$$Wt = 0.15 (W_{TO} \times 10^{-3}) \quad (20.42)$$

### 20.2.1.5 Electrical System

The weight prediction relationships are expressed in terms of the total weight of the fuel system plus the total weight of the electronics system, the prime users of electrical power on most aircraft.

USAF Fighters:

$$Wt = 426.17 \left[ (W_{FS} \times W_{TRON}) \times 10^{-3} \right]^{0.510} \quad (20.43)$$

where

$W_{FS}$  = weight of fuel system, in pounds (lb)

$W_{TRON}$  = weight of electronics system, in pounds (lb)

USN Fighters and Attack:

$$Wt = 346.98 \left[ (W_{FS} \times W_{TRON}) \times 10^{-3} \right]^{0.509} \quad (20.44)$$

Bombers:

$$Wt = 185.46 \left[ (W_{FS} \times W_{TRON}) \times 10^{-3} \right]^{1.286} \quad (20.45)$$

Transports:

$$Wt = 1162.66 \left[ (W_{FS} \times W_{TRON}) \times 10^{-3} \right]^{0.506} \quad (20.46)$$

### 20.2.1.6 Furnishings

Fighter and Attack Aircraft

Ejection Seats:

$$Wt = 22.89 \left( N_{CR} \times q \times 10^{-2} \right)^{0.743} \quad (20.47)$$

where

$N_{CR}$  = number of crew

$q$  = maximum dynamic pressure, in pounds per square foot (lb/ft<sup>2</sup>)

Miscellaneous and Emergency Equipment:

$$Wt = 106.61 \left( N_{CR} W_{TO} \times 10^{-5} \right)^{0.585} \quad (20.48)$$

Bomber and Observation Aircraft

Seats:

$$\textit{Fixed: } Wt = 83.23 \left( N_{CR} \right)^{0.726} \quad (20.49)$$

$$\textit{Ejection: } Wt = K_{SEA} \left( N_{CR} \right)^{1.20} \quad (20.50)$$

where

$K_{SEA}$  = ejection seat coefficient

= 149.12 with survival kit

= 99.54 without survival kit

Oxygen System:

$$Wt = 16.89 \left( N_{CR} \right)^{1.494} \quad (20.51)$$

Crew Bunks:

$$Wt = 12.18 \left( N_{BU} \right)^{1.085} \quad (20.52)$$

where  $N_{BU}$  = number of crew bunks

Transport Aircraft

Flight Deck Seats—Executive and Commercial:

$$Wt = 54.99 \left( N_{FDS} \right) \quad (20.53)$$

where  $N_{FDS}$  = number of flight deck stations

Passenger Seats—Executive and Commercial:

$$Wt = 32.03 (N_{PASS}) \quad (20.54)$$

where  $N_{PASS}$  = number of passengers.

Troop Seats—Troop Transports:

$$Wt = 11.17 (N_{TRO}) \quad (20.55)$$

where  $N_{TRO}$  = number of troops.

Lavatories and Water Provisions—Executive and Commercial:

$$Wt = K_{LAV} (N_{PASS})^{1.33} \quad (20.56)$$

where

- $K_{LAV} = 3.90$  for executive
- $= 1.11$  for long-range commercial passenger
- $= 0.31$  for short-range commercial passenger

Lavatories and Water Provisions—Military Transport:

$$Wt = 1.11 (N_{PASS})^{1.33} \quad (20.57)$$

Food Provisions—Executive and Commercial:

$$Wt = K_{BUF} (N_{PASS})^{1.12} \quad (20.58)$$

where

- $K_{BUF} = 5.68$  for long-range (707, 990, 737, 747, 757, 767, 777, etc.)
- $= 1.02$  for short-range (340, 202, Citation, Learjet, King Air, Jetstream, etc.)

Oxygen System:

$$Wt = 7.00 (N_{CR} + N_{PASS} + N_{ATT})^{0.702} \quad (20.59)$$

where  $N_{ATT}$  = number of attendants

Cabin Windows—Executive and Commercial:

$$Wt = 109.33 \left[ N_{PASS} (1 + P_C) \times 10^{-2} \right]^{0.505} \quad (20.60)$$

where  $P_C$  = ultimate cabin pressure, in pounds per square inch (lb/in<sup>2</sup>)

Baggage and Cargo Handling Provisions:

$$Wt = K_{CBC} (N_{PASS})^{1.456} \quad (20.61)$$

where

$K_{CBC} = 0.0646$  without preload provisions  
 $= 0.316$  with preload provisions

Miscellaneous Furnishings and Equipment

Executive and Commercial:

$$Wt = 0.771 (W_{TO} \times 10^{-3}) \quad (20.62)$$

Military Passenger:

$$Wt = 0.771 (W_{TO} \times 10^{-3}) \quad (20.63)$$

Military Troop–Cargo:

$$Wt = 0.618 (W_{TO} \times 10^{-3})^{0.839} \quad (20.64)$$

### 20.2.1.7 Air Conditioning and Anti-Icing

Fighters

High Subsonic and Supersonic:

$$Wt = 210.66 \left[ (W_{TRON} \times 200 N_{CR}) \times 10^{-3} \right]^{0.735} \quad (20.65)$$

where

$W_{TRON}$  = weight of electronics system, in pounds (lb)  
 $N_{CR}$  = number of crew

Subsonic (Below Approximately  $M = 0.50$ ):

$$Wt = K_{ACAI} \left[ (W_{TRON} \times 200 N_{CR}) \times 10^{-3} \right]^{0.538} \quad (20.66)$$

where

$K_{ACAI}$  = air conditioning and anti-icing coefficient  
 $= 108.64$ , no wing or tail anti-icing  
 $= 212.00$ , wing and tail anti-icing

Bombers and Military Troop–Cargo–Passenger Transports

$$Wt = K_{ACAI} [V_{PR} \times 10^{-2}]^{0.242} \quad (20.67)$$

where

- $V_{PR}$  = pressurized or occupied volume, in cubic feet (ft<sup>3</sup>)
- $K_{ACAI}$  = air conditioning and anti-ice coefficient
  - = 887.25, bomber and military transport with wing and tail anti-icing
  - = 748.15, bomber and military transport without wing and tail anti-icing, supersonic to  $M = 2.50$
  - = 610.56, bomber and military transport without wing or tail anti-icing, subsonic

### Executive and Commercial Passenger-Cargo Transports

$$Wt = 469.30 \left[ V_{PR} (N_{CR} + N_{ATT} + N_{PASS}) \times 10^{-4} \right]^{0.419} \quad (20.68)$$

where

- $V_{PR}$  = pressurized or occupied volume, in cubic feet (ft<sup>3</sup>)
- $N_{ATT}$  = number of attendants
- $N_{PASS}$  = number of passengers

#### 20.2.1.8 Electronics (Avionics)

Usually requirements will specify the avionics gear for the aircraft. The weight of the avionics can then be determined using Table 8.6 of Chapter 8 or manufacturer information on the particular electronics equipment.

If the electronics gear is not specified, estimates of the weight can be made using the statistical methods of Table 8.7.

#### 20.2.1.9 Landing Retardation Devices

The weight of landing retardation devices (brakes, thrust reversers, and drag chutes) can be determined using the information in Chapter 10. The designer should examine the engine information to see if the thrust reverser is included in the basic engine weight.

### 20.2.2 Conventional Metal Aircraft—Light Utility Aircraft

The weight equations of Section 20.2.1 predict unrealistic component weights for light utility aircraft such as those reported in Table I.3 in Appendix I. The following equations are recommended for the low-to-moderate performance (up to about 300 kt) light utility aircraft. The weight equations give the component weight in pounds.

### 20.2.2.1 Structure

#### Wing

$$W_t = 96.948 \left[ \left( \frac{W_{TO} N}{10^5} \right)^{0.65} \left( \frac{AR}{\cos \Lambda_{1/4}} \right)^{0.57} \left( \frac{S_w}{100} \right)^{0.61} \left( \frac{1 + \lambda}{2t/c} \right)^{0.36} \left( 1 + \frac{V_e}{500} \right)^{0.5} \right]^{0.993} \quad (20.69)$$

where

$W_{TO}$  = takeoff weight, in pounds (lb)

$N$  = ultimate load factor ( $1.5 \times$  limit load factor)

$AR$  = wing aspect ratio

$\Lambda_{1/4}$  = wing quarter-chord sweep

$S_w$  = wing area in square feet ( $ft^2$ )

$\lambda$  = wing taper ratio

$t/c$  = maximum wing thickness ratio

$V_e$  = equivalent maximum airspeed at sea level, in knots

#### Fuselage

$$W_t = 200 \left[ \left( \frac{W_{TO} N}{10^5} \right)^{0.286} \left( \frac{L}{10} \right)^{0.857} \left( \frac{W + D}{10} \right) \left( \frac{V_e}{100} \right)^{0.338} \right]^{1.1} \quad (20.70)$$

where

$L$  = fuselage length, in feet

$W$  = fuselage maximum width, in feet

$D$  = fuselage maximum depth, in feet

#### Horizontal Tail

$$W_t = 127 \left[ \left( \frac{W_{TO} N}{10^5} \right)^{0.87} \left( \frac{S_H}{100} \right)^{1.2} \left( \frac{\ell_T}{10} \right)^{0.483} \left( \frac{b_H}{t_{HR}} \right)^{0.5} \right]^{0.458} \quad (20.71)$$

where

$S_H$  = horizontal tail area, in square feet ( $ft^2$ )

$\ell_T$  = distance from wing one-fourth mac to tail one-fourth mac

$b_H$  = horizontal tail span, in feet

$t_{HR}$  = horizontal tail maximum root thickness, in inches

### Vertical Tail

$$W_t = 98.5 \left[ \left( \frac{W_{TO} N}{10^5} \right)^{0.87} \left( \frac{S_V}{100} \right)^{1.2} \left( \frac{b_V}{t_{VR}} \right)^{0.5} \right] \quad (20.72)$$

where

$S_V$  = vertical tail area, in square feet (ft<sup>2</sup>)

$b_V$  = vertical tail span, in feet

$t_{VR}$  = vertical tail maximum root thickness, in inches

### Landing Gear

$$W_t = 0.054 (L_{LG})^{0.501} (W_{LAND} N_{LAND})^{0.684} \quad (20.73)$$

where

$L_{LG}$  = length of main landing gear strut, in inches

$W_{LAND}$  = landing weight (if unknown, use  $W_{TO}$  minus 60% fuel)

$N_{LAND}$  = ultimate load factor at  $W_{LAND}$

### 20.2.2.2 Propulsion

#### Total Installed Propulsion Unit Weight Less Fuel System

This includes mounting and air induction weight:

$$W_t = 2.575 (W_{ENG})^{0.922} N_E \quad (20.74)$$

where

$W_{ENG}$  = bare engine weight

$N_E$  = number of engines

### Fuel System

This includes fuel pumps, lines, and tanks:

$$W_t = 2.49 \left[ (F_G)^{0.6} \left( \frac{1}{1 + \text{Int}} \right)^{0.3} (N_T)^{0.2} (N_E)^{0.13} \right]^{1.21} \quad (20.75)$$

where

$F_G$  = total fuel, in gallons

Int = percentage of fuel tanks that are integral

$N_T$  = number of separate fuel tanks



### 20.2.2.3 Surface Controls

For powered surface control systems, use

$$Wt = 1.08 (W_{TO})^{0.7} \quad (20.76)$$

For unpowered surface control systems, use

$$Wt = 1.066 (W_{TO})^{0.626} \quad (20.77)$$

### 20.2.2.4 Electrical System

The weight-prediction relationships are expressed in terms of the total weight of the fuel system and the electronics system, the primary users of electrical power on the aircraft:

$$Wt = 426 \left( \frac{W_{FS} + W_{TRON}}{1000} \right)^{0.51} \quad (20.78)$$

where

$W_{FS}$  = fuel system weight, in pounds, Eq. (20.75)

$W_{TRON}$  = weight of installed electronics, in pounds, Eq. (20.81)

### 20.2.2.5 Furnishings

The weight expression for the crew seats is

$$Wt = 34.5 (N_{CR}) (q)^{0.25} \quad (20.79)$$

where

$N_{CR}$  = number of crew

$q$  = maximum dynamic pressure, in pounds per square foot (lb/ft<sup>2</sup>)

The weight of the passenger seats is determined from Eq. (20.54) and a weight allowance for miscellaneous furnishings from Eq. (20.62). If the aircraft is pressurized, an additional weight allowance should be considered using Eq. (20.60).

### 20.2.2.6 Air Conditioning and Anti-Icing

If the aircraft has air conditioning and anti-icing, the following expression can be used to estimate the weight of this equipment:

$$Wt = 0.265 (W_{TO})^{0.52} (N_{CR} + N_{PASS})^{0.68} (W_{TRON})^{0.17} (M_E)^{0.08} \quad (20.80)$$

where

$N_{PASS}$  = number of passengers

$N_{CR}$  = number of crew

$W_{TRON}$  = weight of installed electronics in pounds, see Eq. (20.81)

$M_E$  = equivalent maximum Mach number at sea level

### 20.2.2.7 Electronics (Avionics)

The total installed weight of the avionics equipment is

$$W_{\text{TRON}} = 2.117 (W_{\text{AU}})^{0.933} \quad (20.81)$$

where  $W_{\text{AU}}$  = bare avionics equipment weight (uninstalled)

## 20.2.3 Advanced-Composites Aircraft

The high strength-to-weight and stiffness-to-weight ratios associated with advanced composite materials can significantly reduce aircraft structural weight. The blending of high-strength fibers such as graphite, boron, Kevlar 49, and glass in epoxy, polyimide, or metallic matrices (as discussed in Chapter 19) offers new opportunities for the creative structural engineer to tailor the material to exploit innovative structural designs. The full potential of advanced composites in realizing structural weight reductions (and airframe cost reductions) has not been demonstrated yet; however, there is no question that it will be significant. The designer should review the discussion in Appendix I.

The results of many advanced composites development programs and aircraft conceptual studies indicate that the material can decrease the weight of primary and secondary structural elements by about 25% and 40%, respectively. The conceptual complete aircraft studies indicate that an aircraft should not be 100% composite materials because there are many places where it is more cost effective to use metals, honeycomb, and other materials. Some of the places where it is not cost effective or practical to use advanced composites are canopies, tires, seats, seals, mechanisms, radomes, latches, hinges, and clamps. The optimum composite utilization appears to be about 55% in terms of most cost and weight effectiveness.

Based upon a composite utilization by weight of about 55%, the following methodology is recommended for estimating the aircraft component weights, at this point in the conceptual design:

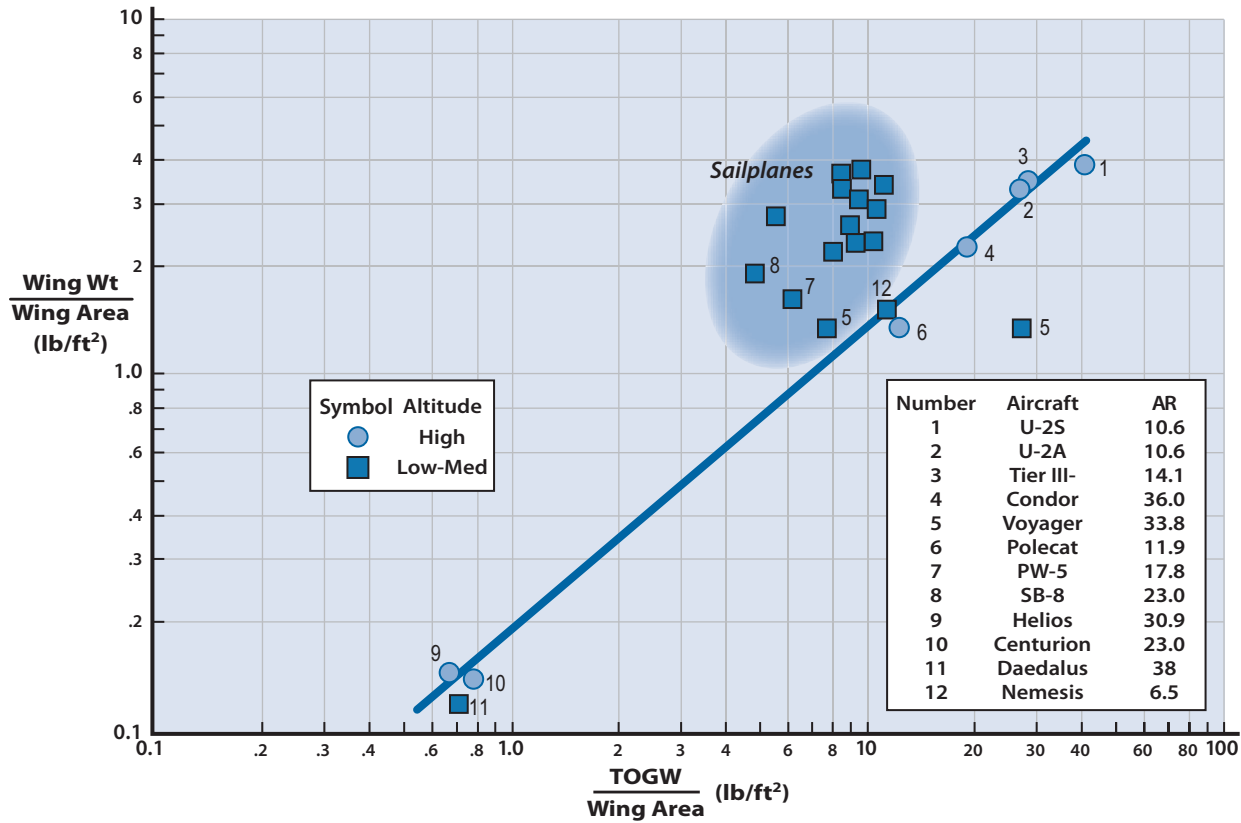
1. Estimate the weight of the component using the metal weight equations of Sections 20.2.1 or 20.2.2.
2. Reduce the metal weights by the following amounts:
  - Wing, 20%
  - Tail, 25%
  - Fuselage, fighter, 10%
  - Fuselage, transport, 25%
  - Secondary (flaps, slats, access panels, etc.), 40%
  - Landing gear, 8%
  - Air induction, 30%

## 20.2.4 Low Wing Loading Aircraft

Aircraft in this class are characterized by  $W/S \leq 2 \text{ lb/ft}^2$  and are powered by solar or human energy. Solar or human energy is puny compared to the more traditional sources of energy for aircraft (i.e., turbine, piston, and rocket). Because power required is dependent on speed, this aircraft class will typically have flight speeds less than 30 KEAS. Human-powered aircraft cruise at speeds of 16 KEAS or less (current distance record was established by the MIT Daedalus at 74 miles in 3 hr 54 min, in 1988) and solar-powered at 23 KEAS (typical maximum speed for Helios at 1000 ft), both flying at wing loadings of between 0.6 and 1.0 lb/ft<sup>2</sup>. The Solar Snooper solar-powered aircraft of Sections 6.7 and 18.9 had a  $W/S = 1.86 \text{ lb/ft}^2$ .

Estimating weights for this class of aircraft is very challenging because the historical data base is almost nonexistent. The large data base for sailplanes is not much help because their wing loadings range from about 5 to 12 lb/ft<sup>2</sup>. Sailplanes are designed for aggressive maneuvering as they chase a thermal and high speed for wind penetration. The structural criteria and design of an aircraft with  $W/S = 1 \text{ lb/ft}^2$  are very much different than for one with  $W/S = 10 \text{ lb/ft}^2$ . Solar-powered aircraft would have design limit load factors of 2.0 whereas sailplanes would have a limit of 6.0. The patent for the AeroVironment Centurion contains a good discussion of structural design for this class of aircraft [7]. The wing weight (weight per wing area) for existing aircraft and sailplanes with wing loadings ranging between 0.6 and 40 lb/ft<sup>2</sup> is shown in Fig. 20.1.

The construction materials for the wings shown in Fig. 20.1 vary significantly as the wing loading decreases. The U-2A, U-2S, and Boeing Condor wings are conventional built-up metal structures. The Lockheed Martin Tier III-Minus Darkstar wing was made from graphite composites with an aluminum carry-through spar. The Scaled Composites Voyager wing is also made from high-strength composites. Figure 20.1 shows two wing loadings for the Voyager (26.8 to 7.5 lb/ft<sup>2</sup>) because its 72% fuel fraction is uncommonly large. The Lockheed Martin Polecats features sandwich structures, water-jet cut ribs and keel, and simplified sandwich skins using LTM45 carbon fiber prepreg. The sailplane group is constructed from Fiberglass and graphite composites. The Helios, Centurion, and Daedalus wings use a hollow carbon tube spar with polystyrene sheet ribs with leading edge and trailing edge members wrapped in a clear plastic Mylar skin covering that is one-half mil thick.



**Figure 20.1** Wing weight vs wing loading for various high-AR, low wing loading aircraft.

## Weights Rule!

Estimating weights is critical in the design of an aircraft (remember the weights rule). This is especially true for weight-critical aircraft such as the Voyager, designed by Burt Rutan (Scaled Composite Inc). It had to have a fuel fraction of 72 percent in order to fly 22,912 nm around the world nonstop. The Voyager, piloted by Dick Rutan (Burt's brother) and Jeana Yeager, took off from Edwards AFB in California on December 14, 1986 and returned 9 days later—making this unique aircraft the first to complete the first nonstop, nonfueled flight around the world.

The airframe, largely made of fiberglass, carbon fiber, and Kevlar, weighed 939 lb when empty, which gave it a weight fraction of 9.7 percent. The aircraft weighed 9695 lb at takeoff, 2250 lb empty, 534 lb for payload (including the pilots) and 7010 lb of fuel. The Voyager had a wing span of 110 ft, 8 inches and an aspect ratio of 33.8, giving the aircraft a maximum L/D of 27. The takeoff wing loading was 26.8 psf and 7.5 psf at landing (with 3 gallons of fuel remaining in the tanks).

The team behind the Voyager's flight, including designer Rutan, were awarded the Collier Trophy for their record-breaking flight. The Voyager is hanging in the Smithsonian Air and Space Museum in Washington, D.C.

### 20.3 Determining Center of Gravity and Moments of Inertia

The following component weights are summed to give the aircraft empty weight:

- Structure (wing, fuselage, tail, and landing gear)
- Propulsion (engine, inlet, fuel system, starting system, engine controls, and thrust reversers)
- Surface controls plus hydraulics and pneumatics
- Instruments
- Electrical system
- Furnishings (ejection seats and crew equipment)
- Air conditioning and anti-icing
- Electronics (avionics)
- Miscellaneous (drag chutes, etc.)

Adding the fuel weight and fixed weights (crew and payload) gives the aircraft takeoff weight.

Next, it is important to determine the location for each of the components to determine the center of gravity (c.g.) of the aircraft. Many of the component weight locations will be self-evident, such as the pilot, fire control system, and landing gear. Other components, such as fuel cells,

Table 20.1 Weight and Moment Summary

Component	Weight (lb)	Distance from Aircraft Nose (ft)	Moment (ft-lb)
Fuselage			
Wing			
Main gear			
Vertical tail			
Horizontal tail			
etc.			
	$\Sigma Wt$	Total moment =	$\Sigma M$

navigation equipment, bombs, and baggage, can be shifted around to a certain extent to influence the c.g. location.

A weight and moment summary in tabular form is shown in Table 20.1. This serves to provide the designer with a refined estimate of the aircraft c.g. as a function of component placement. Chapter 23 discusses the desired c.g. location to give good flying qualities.

The longitudinal position of the c.g. may now be determined as

$$X_{c.g.} = \text{Total Moment} / \Sigma Wt$$

This center of gravity should be expressed as distance from the nose of the aircraft and percentage of the mean aerodynamic chord. The designer should determine an  $X$  location of c.g. for both a full and an empty aircraft as shown in Fig. 23.3 (the c.g. envelope). Figure 23.3 shows the most forward and most aft c.g. locations. It would be embarrassing to have a tricycle-gear aircraft fall on its tail in one of these extreme loading conditions.

The aircraft body axes are defined according to Fig. 2.2 or 21.1. The aircraft moments of inertia are defined as follows:

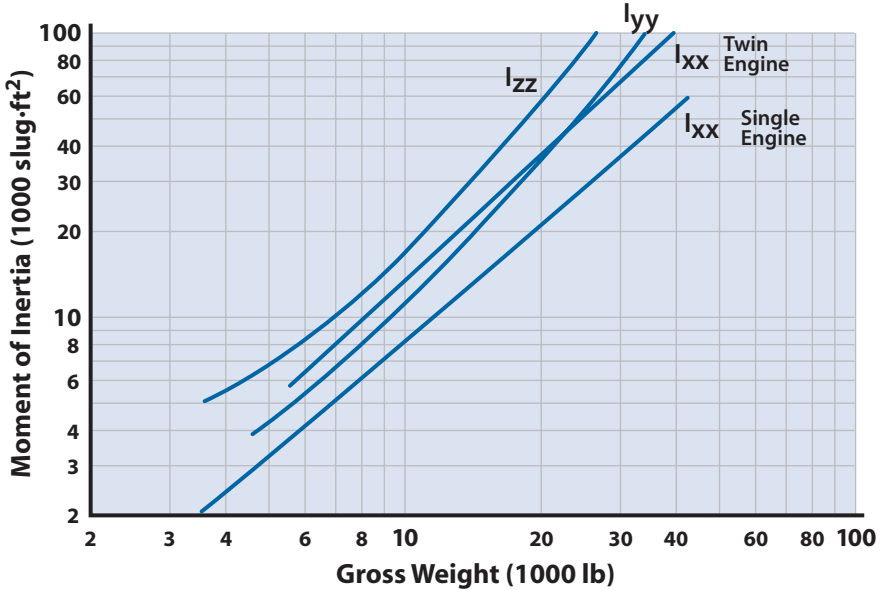
$$I_{xx} = \int (y^2 + z^2) dm$$

$$I_{yy} = \int (x^2 + z^2) dm$$

$$I_{zz} = \int (x^2 + y^2) dm$$

where  $dm$  is an incremental mass element of aircraft. The products of inertia are defined as

$$I_{xy} = \int (xy) dm$$



**Figure 20.2** Aircraft moments of inertia as a function of gross weight.

and so on. The moments of inertia can be estimated at this point in the design process using Figure 20.2, which is based upon historical data from many existing aircraft.

## References

- [1] Torenbeek, E., *Synthesis of Subsonic Aircraft Design*, Delft Univ. Press, The Netherlands, 1976.
- [2] Roskam, J., *Aircraft Design*, Pt. 5, Roskam Aviation and Engineering Corp., Ottawa, KS, 1985. [Available via [www.darcorp.com](http://www.darcorp.com) (accessed 31 Oct. 2009).]
- [3] Raymer, D. P., *Aircraft Design: A Conceptual Approach*, AIAA Education Series, AIAA, Reston, VA, 2006.
- [4] Thomas, F., *Fundamentals of Sailplane Design*, College Park Press, College Park, MD, 1999.
- [5] Stender, W., "Sailplane Weight Estimation," OSTIV (International Scientific and Technical Gliding Organization), Elstree-Wassenaar, The Netherlands, 1969.
- [6] Adams, D. F., "High Performance Composite Material Airframe Weight and Cost Estimating Relations," *Journal of Aircraft*, Vol. 11, No. 12, Dec. 1974.
- [7] Hibbs, B. D., Lissaman, P. B. S., Morgan, W. R., and Radkey, R. L., "Solar Rechargeable Unmanned Aircraft," U.S. Patent No. 5,810,284, 22 Sept. 1998 (patent for the AeroVironment Centurion).

# Chapter 21

# Static Stability and Control



- Static & Dynamic Stability Modes
- Federal Regulations
- Static S&C Considerations
- Static Longitudinal S&C
- Static Lateral S&C
- Static Directional S&C

The Sopwith Camel was statically unstable (as was the Wright Flyer), giving it a quickness in maneuvering. It was a wonderful machine in combat (it had more aerial victories than any other allied WWI airplane), but it killed many a pilot who was not paying close attention to its deadly lack of stability.

*Take your hand off the stick and it would rear right up with a terrific jerk and stand on its tail.*

Pilot report on the Sopwith Camel

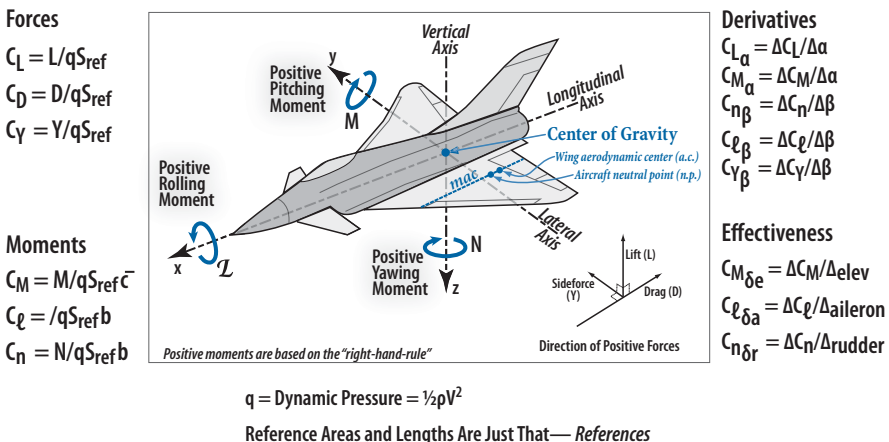


## 21.1 Introduction

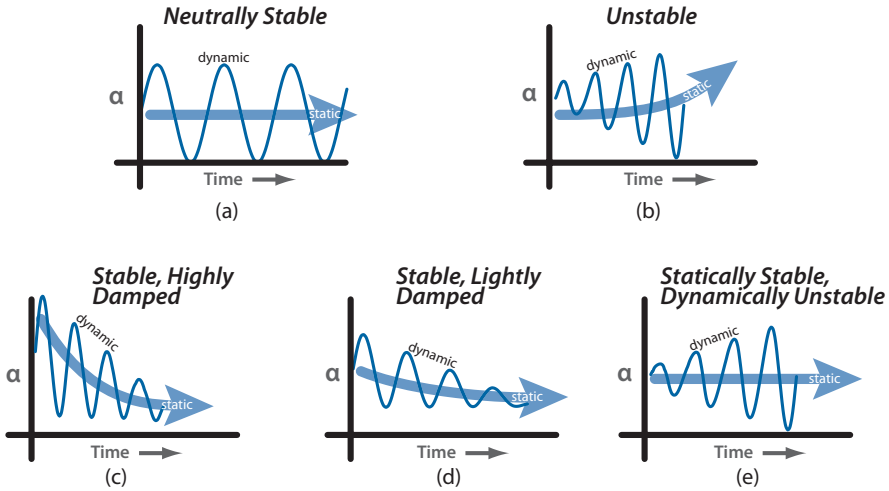
The discussion in the next three chapters assumes some familiarity with aircraft static *stability and control* (S&C). If not, review this subject in outside texts such as [1–4] for a fundamental understanding of static stability and control. Reference [3] is especially recommended as a companion to this text as it has a very complete discussion of aircraft stability and control.

The axis system for the S&C discussion is shown in Fig. 21.1. An aircraft is in equilibrium if the summation of moments about the three axes is zero. The aircraft is said to be *stable* if it returns to equilibrium about the pitch, roll, and yaw axes when disturbed. The aircraft has *static stability* if it “tends” to return to equilibrium by itself. In other words, the resulting forces and moments from the disturbance push the aircraft toward its original equilibrium state. This static stability will fight the disturbance, making it difficult to move away from the equilibrium condition. Thus, a high degree of static stability will make it hard to maneuver the aircraft. The aircraft has *dynamic stability* if the actual motion of the unsteady forces and moments returns the aircraft (eventually) to its original equilibrium condition.

Figure 21.2 shows an aircraft system disturbed in pitch. In Fig. 21.2a the aircraft has neutral stability and remains at whatever  $\alpha$  the disturbance produces. Figure 21.2b shows an unstable system because the tendency of the system is to diverge. In Fig. 21.2c the aircraft has static stability with very high damping, giving it dynamic stability as well. The aircraft slowly returns to its original  $\alpha$  without any overshoot. Figure 21.2d shows a more



**Figure 21.1** Major nondimensional aerodynamic parameters and sign convention.



**Figure 21.2** Static and dynamic stability about the pitch axis.

typical aircraft response. The aircraft returns to its original state, but experiences overshoot with a converging oscillation. This is acceptable behavior, provided the time to converge is reasonable. In Fig. 21.2e the restoring forces and moments are in the right direction so the aircraft is statically stable. However, the restoring forces and moments are high and the damping is low, so the aircraft overshoots the original equilibrium condition. These restoring forces and moments then push the nose back up, overshooting again, but with increasing amplitude. The pitch oscillations continue to increase in amplitude until the system diverges into an uncontrollable flight mode. It should be obvious that static stability is a necessary but not sufficient condition for dynamic stability.

The degree of dynamic instability is the “time to double amplitude ( $t_2$ )” for the system. If the  $t_2$  is large compared with the reaction of the control system, then the aircraft would have acceptable flying qualities. The 1903 Wright Flyer had a  $t_2$  of about 30 seconds for the pitch axis, which permitted Wilbur and Orville to arrest the divergent motion with a pitch control input and fly the aircraft safely. Most aircraft have an unstable lateral mode, the *spiral divergence*. This divergence mode is so slow that the pilot has ample time to make the minor roll correction needed to prevent it.

The strategy of modern flight control systems is to design for low static stability (in fact near neutral stability) and then augment the stability of the aircraft by electronic systems. The *stability augmentation system* (SAS) consists of sensors (rate gyros and accelerometers to sense the movement away from equilibrium), computers (to analyze the aircraft motion and determine the correct control input to counter the aircraft motion), and servos (to input the control deflection to the control surface). These active

controls control the aircraft's rapid perturbations from an equilibrium position and make possible the practicality of the unstable aircraft.

A dynamically unstable aircraft would be a very maneuverable aircraft. This was indeed the case for the WWI-era Sopwith Camel (a 1917 British biplane, pictured on the first page of this chapter) as recorded by V. M. Yeates in his "Winged Victory":

But it was just this instability that gave [Sopwith] Camels their good qualities of quickness in manoeuvre. A stable machine had a predilection for normal flying positions and this had to be overcome every time you wanted to do anything, whereas a Camel had to be held in flying position all the time, and was out of it in a flash. It was nose light, having a rotary engine weighing next to nothing per horsepower, and was rigged tail heavy so that you had to be holding her down all the time. Take your hand off the stick and it would rear right up with a terrific jerk and stand on its tail. Moreover, only having dihedral on the bottom plane gave a Camel a very characteristic elevation. You could tell one five miles off. ... With these unorthodox features, a Camel was a wonderful machine in a scrap. If only it had been 50% faster! There was the rub. A Camel could neither catch anything except by surprise, nor hurry away from an awkward situation, and seldom had the option of accepting or declining combat. But what of it? You couldn't have everything.

## 21.2 Federal Regulations

Aircraft operating in the United States must conform to regulations. Commercial aircraft must follow the following federally mandated regulations:

1. **FAR 23.** Airworthiness standards for small airplanes in the normal, utility, and acrobatic categories that have passenger seating of nine seats or fewer  
Paragraph 23.171—The airplane must be longitudinally, directionally, and laterally stable. In addition, the airplane must show suitable stability and control "feel" (static stability) in any condition normally encountered in service.
2. **FAR 25.** Airworthiness standards for transport category airplanes  
Paragraph 25.171—The airplane must be longitudinally, directionally, and laterally stable. In addition, the airplane must show suitable stability and control "feel" (static stability) in any condition normally encountered in service.

Military aircraft must follow the following specifications and standards:

1. **MIL-F-8785C (1980).** Flying Qualities of Piloted Airplanes. (Inactive 1996 for new design and no longer used)  
Although inactive the document contains much good design data, theories, and information on aircraft handling and flying qualities [5].

2. **MIL-HDBK-1797 (1997)**. Flying Qualities of Piloted Aircraft  
This document replaced MIL-F-8785C and MIL-STD-1797. It contains requirements for qualitative and quantitative flying qualities for all military aircraft, latest theories, and information relating to pilot opinion. In addition to requirements for handling qualities, it also specifies other requirements that an aircraft must meet, such as operational missions, external stores, configurations, and flight envelopes. This handbook also applies to piloted transatmospheric flight when flight depends upon aerodynamic lift and/or air-breathing propulsion systems.
3. **MIL-F-9490**. Flight Control Systems—Design, Installation and Test for Piloted Aircraft
4. **MIL-F-1873**. Flight Control Systems—Design, Installation and Test for Aircraft
5. **MIL-C-18244**. Control and Stabilization Systems, Automatic for Piloted Aircraft
6. **MIL-F-83300**. Flying Qualities of Piloted V/STOL Aircraft
7. **MIL-H-850**. Flying Qualities of Military Rotorcraft

All of these documents require dynamically stable aircraft—either inherently stable (passive) or augmented with an SAS.

### 21.3 Static Stability and Control Considerations

The purpose of the next three chapters is to size and design the aircraft control surfaces and to determine the trim drags. The criteria and methodology presented will be based upon static considerations only. Dynamic stability and control analysis is usually reserved for the preliminary design phase because it requires information about the design that is not available during the conceptual design phase. For example, the moments of inertia introduced in Chapter 20 require knowledge of the aircraft mass distribution on all three axes. These are design details that are not generally known at this point.

Static stability and control considerations will permit the designer to assess the configuration layout and balance of his design and size the surfaces for adequate stability and control margins. The dynamic analysis in the preliminary design phase will fine tune the configuration.

The discussions of longitudinal, directional, and lateral motion will center about the body axes shown in Fig. 21.1.

The mean aerodynamic chord of a wing, denoted by  $\bar{c}$  or  $mac$ , represents an average chord that, when multiplied by the average section moment coefficient, dynamic pressure, and reference wing area, gives the moment for the entire wing. The  $mac$  for wings of constant taper and sweep is given by

$$\bar{c} = \frac{2}{3} c_r \left[ \frac{1 + \lambda + \lambda^2}{1 + \lambda} \right]$$

where  $c_r$  is the root chord and  $\lambda$  is the wing taper ratio.

The aerodynamic center (a.c.) is that point on an aircraft, wing, or airfoil section about which the pitching moment is independent of angle-of-attack. The aerodynamic center is the most convenient place to locate the lift, drag, and moment of an aircraft wing or airfoil section. This is obvious from stability considerations because  $dC_{m_{a.c.}}/d\alpha = 0$  and it is one less term to worry about.

For most aircraft, the body contributes a small amount of lift compared with the wing, resulting in the total aircraft a.c. location being very close to the wing a.c. This is not the case for missiles (where the body is large relative to the wing) and contribution of the body pressure distribution must be considered in locating the missile a.c.

The theoretical position of the aerodynamic center on the mean aerodynamic chord is presented in Fig. 21.3. Notice that at low speed the a.c. is approximately at the quarter-chord and moves aft for supersonic flight. Figures H.8 and H.9 of Appendix H present experimental data on the a.c. location as a function of Mach number for many different low aspect ratio (AR) wing-body combinations.

## 21.4 Static Longitudinal Stability and Control

The forces and moments acting on an aircraft are shown in Fig. 21.4. The lift and drag are by definition always perpendicular and parallel to  $V_\infty$ , respectively. It is, therefore, inconvenient to use these forces to obtain moments because their moment arms relative to the center of gravity vary with angle-of-attack  $\alpha$ . For this reason, all forces are resolved into normal,  $N$ , and chordwise,  $C$ , forces whose axes remain fixed with the aircraft and whose arms are, therefore, constant:

$$N = L \cos \alpha + D \sin \alpha$$

$$C = D \cos \alpha - L \sin \alpha$$

For small  $\alpha$ ,  $N \approx L$  and  $C \approx D$ . For this discussion consider  $\alpha$  to be small and use  $L$  and  $D$  in the development of stability and trim equations.

The moments are summed about the center of gravity for each aircraft. The horizontal tail or canard is usually a symmetric section so that  $M_{a.c.c} = 0$  and  $M_{a.c.T} = 0$  for  $\delta_e = 0$ . In Fig. 21.4a, b, and c moments have been neglected due to the fuselage and engine nacelles.

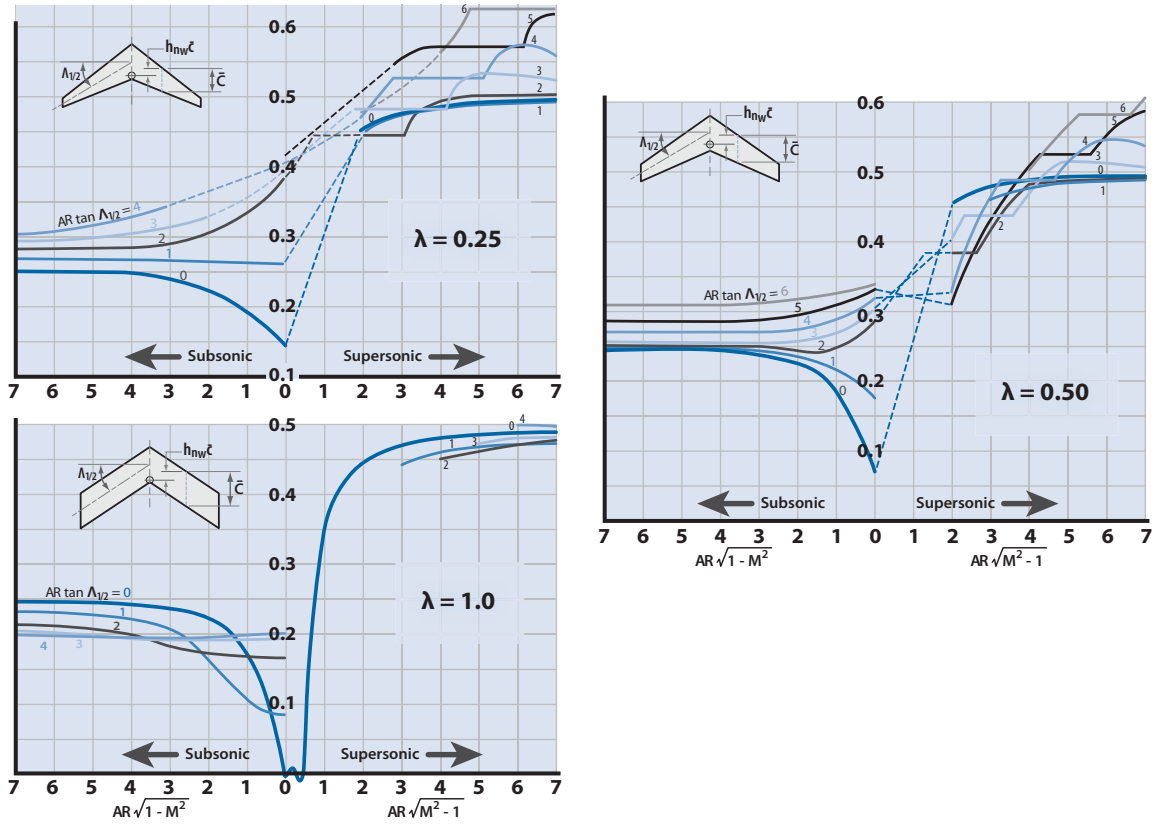
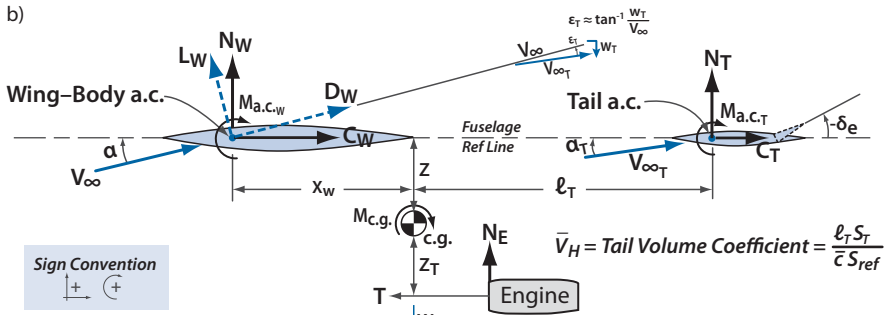
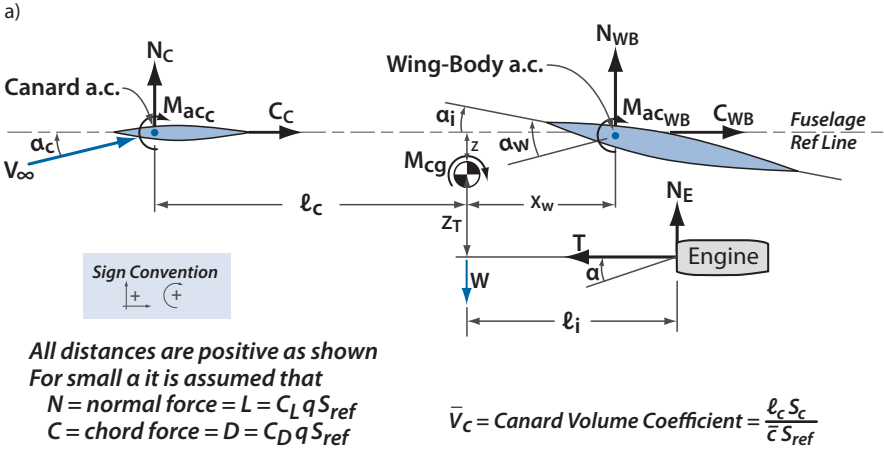
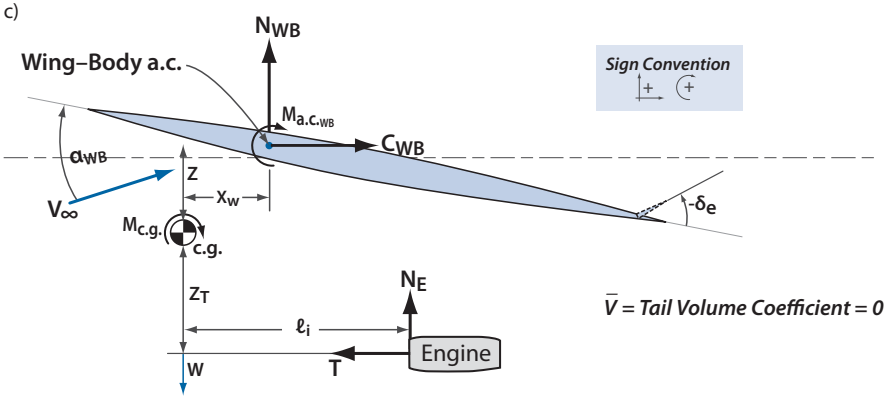


Figure 21.3 Theoretical chordwise position of the aerodynamic center (data from [6]).



**Note:** Wing and tail chord lines are parallel to fuselage reference line



*All distances are positive as shown*  
 $\epsilon_T = \text{tail downwash angle due to wing downwash } w_T \text{ at the tail a.c.}$   
*For small  $\alpha$  we can assume*  
 $N = \text{normal force} = L = C_L q S_{ref}$   
 $C = \text{chord force} = D = C_D q S_{ref}$

**Figure 21.4** Forces and moments acting on **a)** an aircraft with a canard tail, **b)** an aircraft with an aft tail, and **c)** a tailless aircraft.

The moment or trim equations are usually placed in coefficient form by dividing through by  $(q_\infty S_{\text{ref}} \bar{c})$ , where  $q_\infty$  is the dynamic pressure ( $\frac{1}{2}\rho V^2$ ),  $S_{\text{ref}}$  is the wing reference area, and  $\bar{c}$  is the mac of the wing. Now, replace the wing by its mac and locate the lift, drag, and moment of the wing at the aerodynamic center a.c.

Trim equations for the three aircraft types shown in Fig. 21.4a–c are as follows:

Aft Tail:

$$C_{M_{c.g.}} = C_L \frac{x_w}{\bar{c}} + C_D \frac{z}{\bar{c}} + C_{M_{a.c.w}} + \frac{Tz_T}{q_\infty S_{\text{ref}} \bar{c}} - c_{LT} \bar{V}_H \eta_T - C_{M_{c.g. \text{inlet}}} \quad (21.1)$$

Canard:

$$C_{M_{c.g.}} = -C_L \frac{x_w}{\bar{c}} + C_D \frac{z}{\bar{c}} + C_{M_{a.c.w}} + \frac{Tz_T}{q_\infty S_{\text{ref}} \bar{c}} + c_{LC} \bar{V}_C - C_{M_{c.g. \text{inlet}}} \quad (21.2)$$

Tailless:

$$C_{M_{c.g.}} = -C_L \frac{x_w}{\bar{c}} + C_D \frac{z}{\bar{c}} + C_{M_{a.c.w}} + \frac{Tz_T}{q_\infty S_{\text{ref}} \bar{c}} - C_{M_{c.g. \text{inlet}}} \quad (21.3)$$

In these equations the moment due to the aft tail or canard drag is much smaller than the wing counterpart and was neglected. The term  $q_{\infty T}/q_\infty$  is called the *tail efficiency factor*  $\eta_T$  and comes about because of the influence of the wing on the freestream velocity striking the tail. The wing induces a downwash  $w_T$  (due to trailing vortices) at the a.c. of the aft tail (see Fig. 21.4b). Notice that  $\eta_T = 1.0$  for the canard. The term  $(C_{M_{c.g.}})_{\text{inlet}}$  comes about because of the momentum change in turning the air into the inlet. At small  $\alpha$ , this term can be neglected.

Often,  $z \ll c$  so that the wing–body drag moment can be neglected. Also, if  $z_T$  is small, the thrust term is negligible.

The aircraft must be able to set the trim equation equal to zero for any attitude or flight condition and all thrust levels. The wing primarily establishes the load factor for the aircraft and the aft tail or canard balances the aircraft. If the aircraft is tailless, the moments about the aircraft c.g. are balanced by changing the wing camber (flap deflection), which changes the moment about the wing a.c. The horizontal tail (aft tail and canard) is movable, either all movable (all flying aft tail or canard) or a portion (called the *elevator* on an aft tail) is movable, so that  $L_T$  or  $L_c$  can be changed independently of the aircraft angle-of-attack. In this way, the horizontal tail can



cause the aircraft to rotate from one equilibrium (trimmed) condition to another (i.e., change angle-of-attack  $\alpha$ ).

If the horizontal aft tail is an all-flying-tail (such as the B-52, 727, and L1011), then the expression for  $C_{L_T}$  is

$$C_{L_T} = m_T(\alpha_T + \alpha_{cs}) = m_T \left[ (1 - d\varepsilon/d\alpha)\alpha + \alpha_{cs} \right]$$

where  $\alpha_{cs}$  is the deflection angle that the pilot initiates by moving the control stick, and  $d\varepsilon/d\alpha$  is the change in downwash angle  $\varepsilon$  for a change in  $\alpha$ . The  $m_T$  is the horizontal tail lift curve slope,  $(C_{L_\alpha})_T$ .

If the horizontal tail is a stationary stabilizer–movable elevator arrangement, then the expression for  $C_{L_T}$  is

$$C_{L_T} = m_T \left[ (1 - d\varepsilon/d\alpha)\alpha - \alpha_{0LT} \right]$$

where  $\alpha_{0LT}$  is the tail angle for zero lift (see Fig. 2.1a or Table F.1) and is dependent upon the elevator deflection  $\delta_e$  (note, same as for a flapped airfoil).

If the trim equations (21.1), (21.2), and (21.3) are differentiated with respect to  $\alpha$ , the results are as follows:

Aft Tail:

$$\frac{dC_{M_{c.g.}}}{d\alpha} = C_{M\alpha} = m_w \frac{x_w}{c} - m_T \left( 1 - \frac{d\varepsilon}{d\alpha} \right) \bar{V}_H \eta_T + C_{M\alpha I} \quad (21.4)$$

Canard:

$$C_{M\alpha} = \bar{V}_c m_c - \frac{x_w}{c} m_w + C_{M\alpha I} \quad (21.5)$$

Tailless:

$$C_{M\alpha} = -\frac{x_w}{c} m_w + C_{M\alpha I} \quad (21.6)$$

where  $m_w = (C_{L_\alpha})_w$  is the wing–body lift curve slope,  $m_c = (C_{L_\alpha})_c$  is the canard lift curve slope (based upon canard surface area,  $S_c$ ),  $m_T = (C_{L_\alpha})_T$  is the aft tail lift curve slope (based upon aft tail area,  $S_T$ ) and  $(C_{M\alpha})_I$  is the change in inlet moment due to  $\alpha$ . In Eqs. (21.4), (21.5), and (21.6) the term

due to the wing–body has been neglected. The thrust term disappears because the thrust is not (at least to a first-order approximation) a function of  $\alpha$ .

The criterion for static stability in an aircraft is that its value of  $C_{M\alpha}$  be negative. This means that if an aircraft with  $C_{M\alpha} < 0$  is in equilibrium (trimmed) at a positive  $\alpha$  and suddenly  $\alpha$  is increased (e.g., wind gust), the aircraft will generate a negative moment to push the nose down toward the original equilibrium  $\alpha$ .

The inlet term in the trim and stability equation comes about because of the moment generated about the center of gravity when the freestream air is turned at the inlet lip into the engine. The force diagram is shown schematically in Fig. 21.5.

The inlet force  $N_E$  can be expressed as

$$N_E = \dot{m}_0 \Delta V = \dot{m}_0 V_\infty \tan \beta \approx \dot{m}_0 V_\infty \beta$$

where  $\dot{m}_0$  is the mass flow of air into the inlet in slugs per second and  $\beta$  is the flow turning angle in radians shown in Fig. 21.5. The moment about the center of gravity is  $\ell_i N_E$  and is positive for the aircraft in Fig. 21.5. The moment and stability contribution from the inlet is finally expressed as

$$C_{M_{c.g.inlet}} = \frac{N_E \ell_i}{q_\infty S_{ref} \bar{c}} \approx \frac{2 \dot{m}_0 \beta \ell_i}{\rho V_\infty S_{ref} \bar{c}} \tag{21.7}$$

$$\left( \frac{dC_M}{d\alpha} \right)_I = C_{M_{\alpha inlet}} \approx \frac{2 \dot{m}_0 \beta \ell_i}{\rho V_\infty S_{ref} \bar{c}} \frac{d\beta}{d\alpha} \quad (\text{per radian}) \tag{21.8}$$

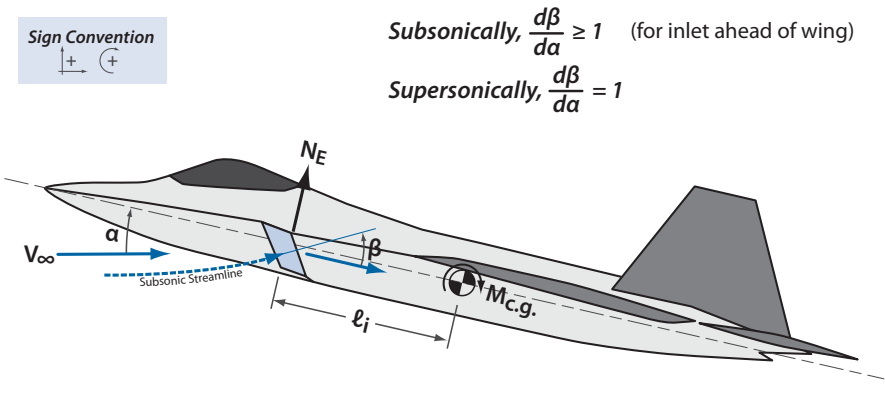


Figure 21.5 Schematic of inlet force on aircraft.



**Figure 21.6** Lockheed Jetstar with inlet behind the wing.

where

- $\dot{m}_0$  = mass flow rate of air accepted by the inlet (slug/s)
- $\bar{c}$  = mean aerodynamic chord (ft)
- $\rho$  = air density (slug/ft<sup>3</sup>)
- $V_\infty$  = freestream velocity (ft/s)
- $S_{\text{ref}}$  = wing area (ft<sup>2</sup>)
- $\ell_i$  = distance of the inlet face ahead of the aircraft c.g. (ft)
- $d\beta/d\alpha$  = change in flow direction into the inlet due to upwash of the wing

Note the following:

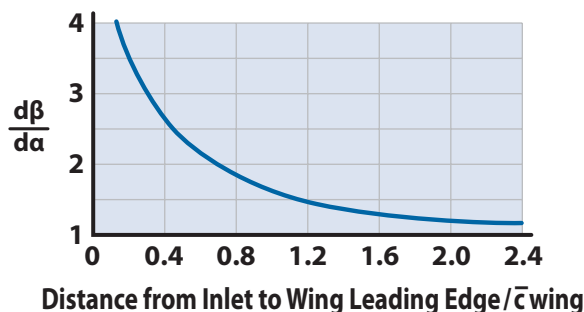
1. If the inlet is under the wing as for the F-18, the wing turns the airflow into the inlet and there is no inlet moment. For this inlet location use  $\beta = 0$  and  $d\beta/d\alpha = 0$ .
2. For inlets behind the wing trailing edge (such as the JetStar in Fig. 21.6)  $d\beta/d\alpha$ , may be analyzed as

$$\left(1 - \frac{d\varepsilon}{d\alpha}\right) \frac{x_i}{\ell_h}$$

where  $x_i$  is the distance from the wing trailing edge to the inlet and  $\ell_h$  is the length from the wing trailing edge to the horizontal tail mean aerodynamic chord.

3. For inlets ahead of the wing leading edge  $d\beta/d\alpha = 1$  for supersonic flight and may be determined from Fig. 21.7 for subsonic speeds.

The tail downwash term for an aft-tail aircraft,  $(1 - d\varepsilon/d\alpha)$ , depends largely on the location of the tail with respect to the wing and the position of the horizontal tail with respect to the wing wake. If the horizontal tail is positioned so that it lies either close to or inside the wing wake, large changes in downwash occur, as well as reduced tail efficiency and unpleas-



**Figure 21.7** Change in flow direction into the inlet due to upwash of the wing (data from [7]).

ant tail buffeting. In the usual design the horizontal tail is kept high enough (or low enough) to avoid the wing wake at all lift coefficients. If this is done, a simplified empirical method, developed from [8], is available to estimate the change of downwash with  $\alpha$  at the aft horizontal tail. The method is shown in Fig. 21.8. If increased accuracy is desired, the methods in [9] should be used.

## 21.5 Static Lateral Stability and Control

The lateral motion for an aircraft is the rolling motion about the fuselage centerline. This lateral motion is shown in Fig. 21.9 with the rolling moment  $\mathcal{L}$  being defined as positive for the right wing down. The rolling moment coefficient is  $C_\ell$  (forgive the confusion with section lift coefficient) and is defined as

$$C_\ell = \frac{\mathcal{L}}{qS_{\text{ref}}b} \quad (21.9)$$

where  $b$  is the aircraft wing span.

The static lateral stability derivative is

$$\frac{dC_\ell}{d\beta} = C_{\ell\beta}$$

which gives the change of rolling moment coefficient with respect to sideslip angle  $\beta$ . A negative  $C_{\ell\beta}$  will cause the right wing to come up for a positive sideslip and is the requirement for lateral static stability. Static lateral stability by itself does not guarantee dynamic lateral stability, but it is a necessary condition. The stability derivative  $C_{\ell\beta}$  is influenced by the wing, the vertical stabilizer, and the wing–fuselage interaction.  $C_{\ell\beta}$  can be expressed as

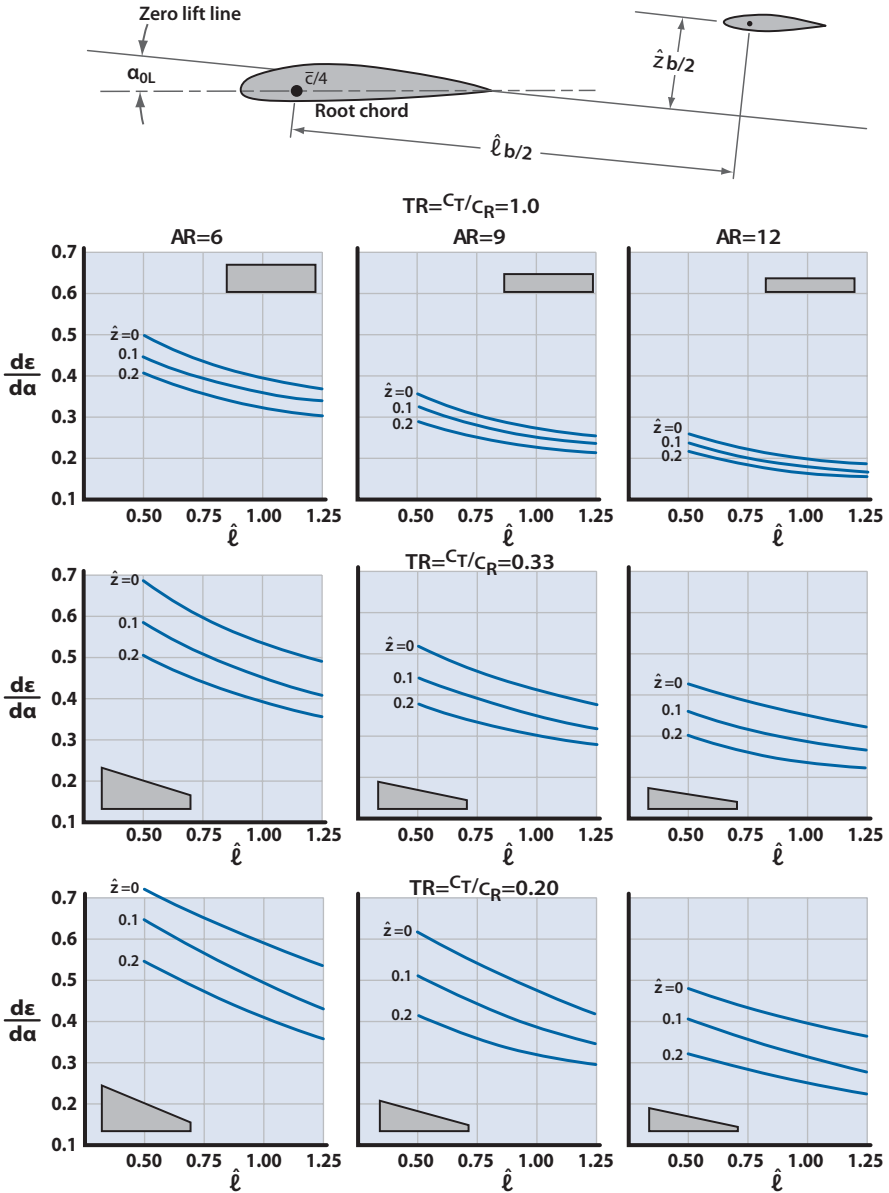
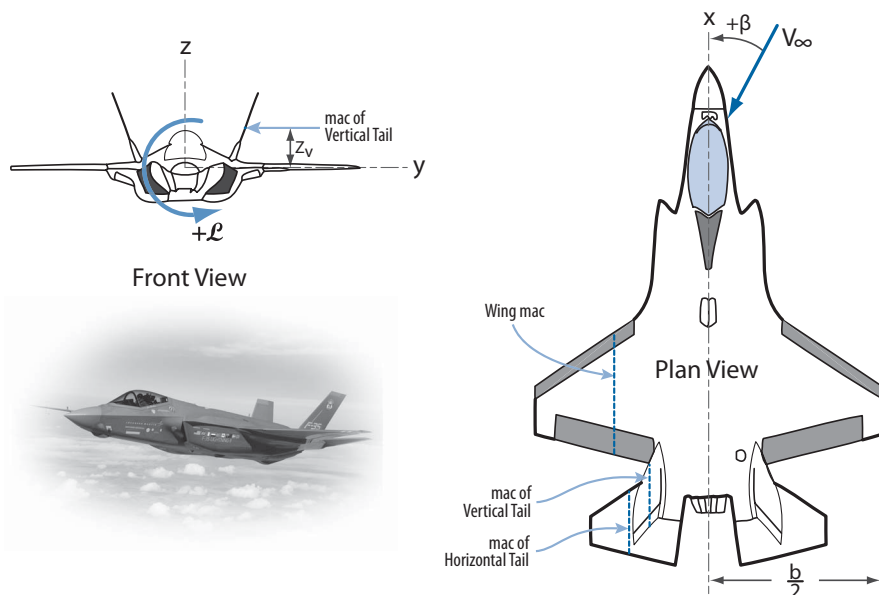


Figure 21.8 Downwash charts for various taper ratios (TR) (data from [8]).



**Figure 21.9** Lateral motion of an aircraft and notation for lateral analysis.

$$C_{\ell\beta} = C_{\ell\beta\text{wing}} + C_{\ell\beta\text{vertical stabilizer}} + C_{\ell\beta\text{wing-fuselage}} \quad (21.10)$$

Now consider the contribution of each component separately.

First, the wing contribution  $C_{\ell\beta\text{wing}}$  has three components: the basic wing planform, the sweepback, and the dihedral,

$$C_{\ell\beta\text{wing}} = C_{\ell\beta\text{basic}} + C_{\ell\beta\Delta} + C_{\ell\beta\Gamma} \quad (21.11)$$

The wing contribution due to the basic wing and sweepback is presented on Fig. 21.10. Notice that the contribution is negative (i.e., stabilizing) and dependent upon the flight  $C_L$ . Extrapolate the data on Fig. 21.10 for a delta wing (i.e.,  $\lambda = 0$ ).

The wing contribution due to dihedral is stabilizing for positive dihedral and its use is the most common way of controlling lateral stability. The expression for the dihedral contribution is given as (from [9])

$$\left(C_{\ell\beta}\right)_{\Gamma} = -0.25C_{L\alpha}\Gamma \left[ \frac{2(1+2\lambda)}{3(1+\lambda)} \right] \quad (21.12)$$

where the lift curve slope  $C_{L\alpha}$  is per radian and  $\Gamma$  is in radians.

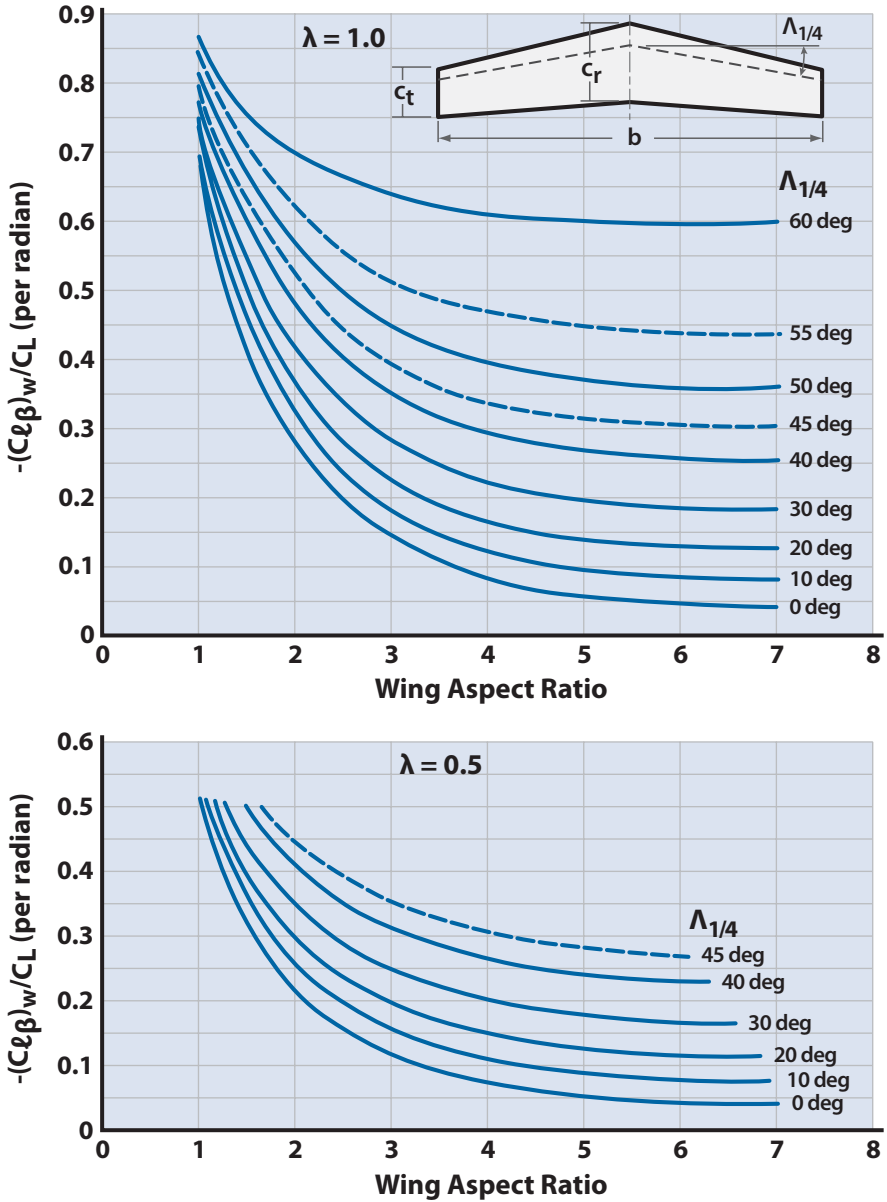


Figure 21.10 The  $C_{\ell\beta}$  of straight tapered wings with zero dihedral.

In actual practice, the dihedral angle is usually not set from analytical considerations, because of the large errors involved. Most designers set the wing dihedral only after careful analysis of wind tunnel test data, in which the effects of angle-of-attack, power, and flap settings are carefully analyzed.

Consideration might also be given to using [9, Section 5.1.2.1–1] in determining  $C_{\ell\beta_{wing}}$ . This reference combines both the dihedral and sweep-back effects to provide an empirical method for obtaining the desired stability derivative.

Second,  $C_{\ell\beta_{wing-fus}}$  is obtained empirically from [2] and is found to be a function of wing vertical placement on the fuselage:

$$\begin{aligned} \text{High wing } C_{\ell\beta_{wing-fus}} &\approx -0.0344/\text{rad} \\ \text{Middle wing } C_{\ell\beta_{wing-fus}} &\approx 0 \\ \text{Low wing } C_{\ell\beta_{wing-fus}} &\approx +0.0458/\text{rad} \end{aligned} \tag{21.13}$$

Third,  $(C_{\ell\beta})_{\text{vertical stabilizer}}$ : the force on a conventional vertical stabilizer, which is generated as an aircraft sideslips, provides a restoring moment by acting through a moment arm to the aircraft c.g. projection. The opposite is of course true for the ventral fin because it is destabilizing. One may estimate this contribution as

$$(C_{\ell\beta})_{VT} = -C_{L\alpha_{VT}} \left( 1 + \frac{d\sigma}{d\beta} \right) \frac{q_{VT}}{q} \frac{S_{VT}}{S_{ref}} \frac{z_v}{b} \tag{21.14}$$

Terms in Eq. (21.14) are defined as follows:

- $(C_{L\alpha})_{VT}$  = lift curve slope of vertical stabilizer, which is based on an effective aspect ratio that is 1.55 times the actual ratio and is based on the vertical stabilizer area
- $S_{VT}$  = planform area of the vertical stabilizer
- $S_{ref}$  = wing planform area
- $z_v$  = distance from mean aerodynamic chord of vertical stabilizer to aircraft vertical c.g. projection (see Fig. 21.9)

The quantity

$$\left( 1 + \frac{d\sigma}{d\beta} \right) \frac{q_{VT}}{q}$$

is a difficult parameter to determine. Reference [9, Section 5.4] presents what appears to be the best analytical method for finding this term:

$$\left( 1 + \frac{d\sigma}{d\beta} \right) \frac{q_{VT}}{q} = 0.724 + \frac{3.06(S'_{VT}/S_{ref})}{1 + \cos\Lambda_{c/4}} + 0.4 \frac{z_w}{d} + 0.009 \text{ AR} \tag{21.15}$$



where

$S'_{VT}$  = vertical stabilizer area with this area extended to fuselage centerline

$z_w$  = distance along aircraft  $z$  axis from the wing root chord to the fuselage centerline

$d$  = maximum fuselage depth

AR = wing aspect ratio

The maximum effect of the vertical stabilizer is greatest as Mach number approaches unity because  $(C_{L\alpha})_{VT}$  increases toward that speed condition.

Too large a lateral stability aggravates the condition of Dutch roll (a dynamic lateral response) and does not lend itself to a desirable flight condition. A first approximation to determining the desired amount of lateral stability is suggested as

$$C_{l\beta} = -C_{n\beta} \text{ at Mach} = 1.0 \tag{21.16}$$

Too large a value of  $C_{l\beta}$  will also result in slow reaction from ailerons and/or spoilers in trying to roll the aircraft.

The lateral control of the aircraft is achieved using ailerons and/or spoilers. As the ailerons deflect, the aircraft begins to roll about the fuselage centerline. If the ailerons remain deflected, the roll rate will increase until the rolling moment due to aileron deflection is balanced by the damping in roll moment. This steady state roll rate condition is given by

$$C_l = 0 = C_{l_p} \left( \frac{Pb}{2V} \right) + C_{l_{\delta_a \delta_a}} \tag{21.17a}$$

where

$C_{l_p} = dC_l/d(Pb/2V)$  is the damping in roll coefficient (determined from Fig. 21.11)

$C_{l_{\delta_a}} = dC_l/d\delta_a$  is the aileron control power derivative

$P$  = roll rate in radians per second

$\delta_a$  = aileron deflection

Rearranging Eq. (21.17a) to solve for the roll rate yields

$$P = -\frac{2V}{b} \frac{C_{l_{\delta_a}}}{C_{l_p}} \delta_a \tag{21.17b}$$

The flying qualities in military specification MIL-HDBK-1797 suggest a 90-deg roll in one second for fighter aircraft (discussed further in Section 23.5).

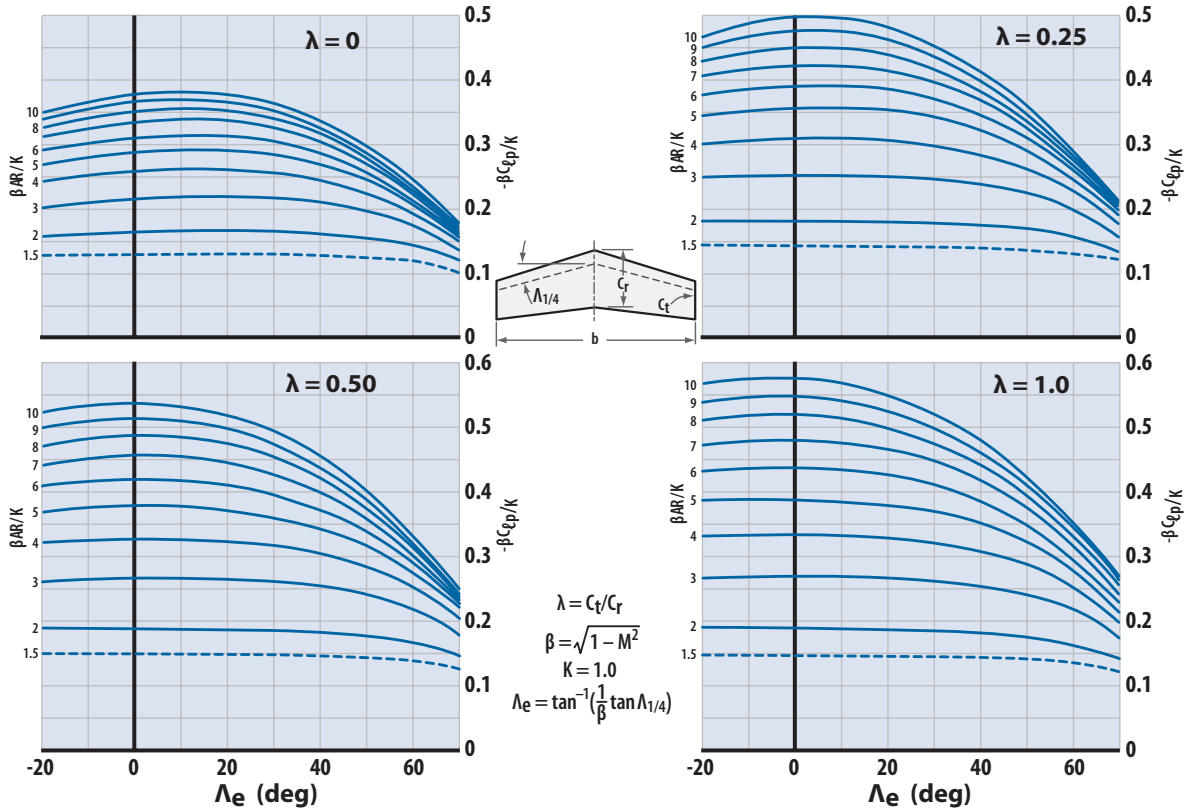


Figure 21.11  $C_{dp}$  for straight wings (data from [6]).

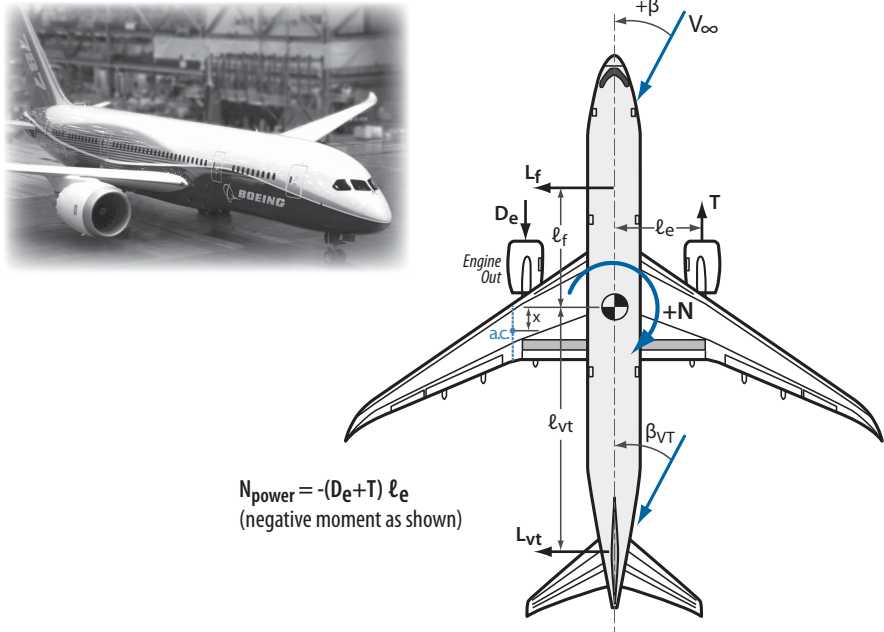
The  $C_{l_{\delta_a}}$  depends upon the amount of aileron area or spoiler area and their locations. Reference [9, Section 6.2.1] or [3] is recommended for determining  $C_{l_{\delta_a}}$ .

## 21.6 Static Directional (Weathercock) Stability and Control

The *directional motion* of an aircraft is a rotation about the vertical axis of the aircraft. Figure 21.12 shows a schematic of the forces on an aircraft for directional motion. The directional moment is denoted by  $N$  and is positive for the right wing back (clockwise motion). The moment  $N$  about the c.g. is (from Fig. 21.12)

$$N = l_f L_f + l_{VT} L_{VT} + N_{power} + N_{wing} \tag{21.18}$$

where  $L_f$  is the side force on the fuselage,  $N_{power}$  is the moment due to asymmetric power effects (Fig. 21.12 shows this as a one-engine-out condition), and  $N_{wing}$  is the moment due to the wing. If ailerons are deflected, there is a differential lift and drag on each wing and hence an additional moment.



**Figure 21.12** Forces on aircraft for directional motion (photograph courtesy of The Boeing Company).

The directional moment coefficient is

$$C_n = \frac{N}{q_\infty S_{\text{ref}} b}$$

$$C_n = -\frac{\ell_f L_f}{q_\infty S_{\text{ref}} b} + \frac{\ell_{\text{VT}} S_{\text{VT}}}{b S_{\text{ref}}} \frac{q_{\text{VT}}}{q_\infty} C_{L\alpha_{\text{VT}}} \beta_{\text{VT}} + \frac{N_{\text{power}}}{q_\infty S_{\text{ref}} b} + \frac{N_{\text{wing}}}{q_\infty S_{\text{ref}} b} \quad (21.19)$$

where  $\beta_{\text{VT}} = (1 + d\sigma/d\beta)\beta$  and accounts for the fuselage sidewash on the vertical tail.

The directional stability derivative is expressed as

$$\frac{dC_n}{d\beta} = C_{n\beta} = C_{n\beta_{\text{fus}}} + C_{n\beta_{\text{wing}}} + \bar{V}_{\text{VT}} C_{L\alpha_{\text{VT}}} \left(1 + \frac{d\sigma}{d\beta}\right) \frac{q_{\text{VT}}}{q_\infty} \quad (21.20)$$

where  $\bar{V}_{\text{VT}} = (\ell_{\text{VT}} S_{\text{VT}} / b S_{\text{ref}})$  is the vertical tail volume coefficient. Power effects are usually not dependent on sideslip angle  $\beta$  so that  $C_{n\beta_{\text{power}}}$  is neglected.

The directional stability derivative  $C_{n\beta}$  must be positive for static directional stability. A  $C_{n\beta} > 0$  will insure that moments will be generated, for a positive sideslip to rotate the aircraft so that  $\beta$  is reduced.

The vertical tail contribution is stabilizing for vertical tails (or ventral fins) aft of the center of gravity:

$$C_{n\beta_{\text{VT}}} = \bar{V}_{\text{VT}} C_{L\alpha_{\text{VT}}} (1 + d\sigma/d\beta) (q_{\text{VT}}/q) \quad (21.21)$$

where  $C_{L\alpha_{\text{VT}}}$  is the lift curve slope of the vertical tail based upon the vertical tail planform area and an effective aspect ratio 1.55 times that of the geometric aspect ratio (the fuselage acts as a large tip plate). The term

$$\left(1 + \frac{d\sigma}{d\beta}\right) \frac{q_{\text{VT}}}{q}$$

is determined from Eq. (21.15).

The  $C_{n\beta}$  wing is due to the asymmetrical drag and lift distributions on the different wing panels undergoing sideslip. Wing sweep adds to the weathercock stability of the aircraft. An expression for the wing subsonic contribution is (from [9])

$$C_{n\beta_{\text{wing}}} = C_L^2 \left[ \frac{1}{4\pi AR} - \frac{\tan\Lambda_{c/4}}{\pi AR (AR + 4\cos\Lambda_{c/4})} \right. \\ \left. \left( \cos\Lambda_{c/4} - \frac{AR}{2} - \frac{AR^2}{8\cos\Lambda_{c/4}} + \frac{6x}{\bar{c}} \frac{\sin\Lambda_{c/4}}{AR} \right) \right] \quad (21.22)$$

per radian, where  $x$  is the distance (positive rearward) from the aircraft c.g. to the wing aerodynamic center.

The fuselage at a sideslip angle  $\beta$  behaves like a lifting body. The sideslip derivative of the fuselage is usually destabilizing because the fuselage n.p. is usually ahead of the vehicle c.g. and the effect is very significant. The fuselage yawing moment is easier to calculate than the pitching moment due to  $\Delta\beta$ . The reason is that longitudinally the lift on the fuselage is very much affected by the wing (upwash and downwash) but directionally it can be assumed that the wing has very little effect. The several references used to find a general formula providing a first-order estimate of this contribution have led to the following form:

$$C_{n\beta_{\text{fuselage}}} = -1.3 \frac{\text{Vol } h}{S_{\text{ref}} b w} \quad (21.23)$$

per radian, where

Vol = fuselage volume

$(h/w)$  = ratio of mean fuselage depth to mean fuselage width

$b$  = wing span

$S_{\text{ref}}$  = wing planform area

The desirable level of directional stability in terms of  $C_{n\beta}$  is very difficult to express in general terms. Chapter 23 lists some desired values for  $C_{n\beta}$  that have been shown to give pleasant flying qualities. The vertical tail area is sized such that Eq. (21.20) gives desired values for  $C_{n\beta}$ . The rudder is sized to meet certain low-speed directional control criteria.

The contributions of the wing and fuselage are essentially independent of Mach number. However, the tail  $C_{n\beta}$  increases then decreases with increasing Mach number due to the variation in  $C_{L\alpha VT}$ . Because the wing contributes little stability, the vertical tail is the main component offsetting the destabilizing contribution of the fuselage. Because  $C_{L\alpha VT}$  can decrease by a factor of 3 from subsonic to Mach = 3, the static directional stability decreases at high Mach. Some vehicles need extra vertical surfaces at high Mach numbers to give adequate directional stability. The XB-70 did this by folding its wingtips downward (see Fig. 21.13).

The requirements for adequate directional control (discussed in Chapter 23) are that the rudder be powerful enough to hold  $\beta = 0$  for a one-engine-out (asymmetric power) flight condition at  $1.2V_{TO}$ , hold a straight ground path landing and takeoff in a crosswind up to  $0.2V_{TO}$  and overcome the adverse yaw associated with abrupt aileron rolls at  $V_{TO}$ .

The asymmetric power condition would be (from Fig. 21.12)

$$C_n = 0 = -\frac{(T + D_e)}{q_\infty S_{\text{ref}} b} + C_{n\delta_r} \delta_r \quad (21.24)$$

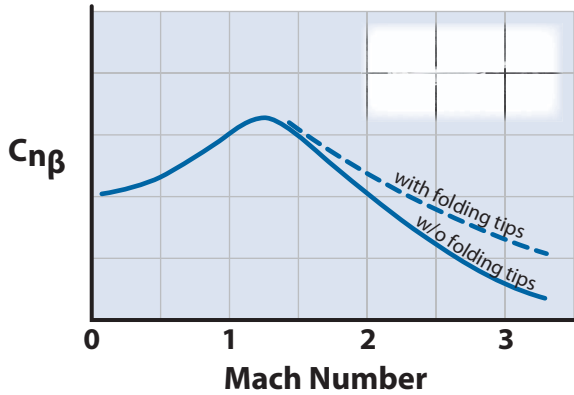


Figure 21.13 Typical  $C_{n\beta}$  variation with Mach number.

where  $C_{n\delta_r} = dC_n/d\delta_r$  is the rudder control power and  $\delta_r$  is the rudder deflection angle.

The crosswind condition is

$$C_n = 0 = C_{n\beta}\beta + C_{n\delta_r}\delta_r \quad (21.25)$$

where  $\beta = 11.5$  deg for a  $0.2V_{TO}$  crosswind. In both cases maximum rudder deflection is  $\pm 20$  deg.

The rudder control power can be estimated from

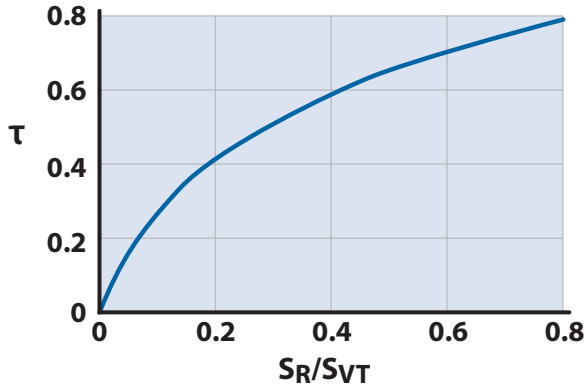
$$C_{n\delta_r} \approx 0.9C_{L\alpha_{VT}}\bar{V}_{VT}\tau \quad (21.26)$$

where  $\tau = d\alpha_{OL}/d\delta_r$ , and is shown in Fig. 21.14.

The required rudder area  $S_R$  for adequate directional control is determined by solving Eqs. (21.24), (21.25), and (21.26) for the maximum value of  $\tau$  and then going to Fig. 21.14.

## 21.7 Aft Tail Location for Reduced Pitch-Up

Pitch-up is the longitudinal instability at high lift that results in an aircraft having a positive pitching moment as the wing begins to stall. It is due to the forward shift of the wing center of pressure as the wingtip region stalls and/or the blanking of the aft horizontal tail by the separated wing wake. It is a very undesirable phenomenon as the aircraft tends to pitch up violently with disastrous results at high subsonic speeds. Many of the fighter aircraft (such as the McDonnell F-101 Voodoo) had horns, buzzers,



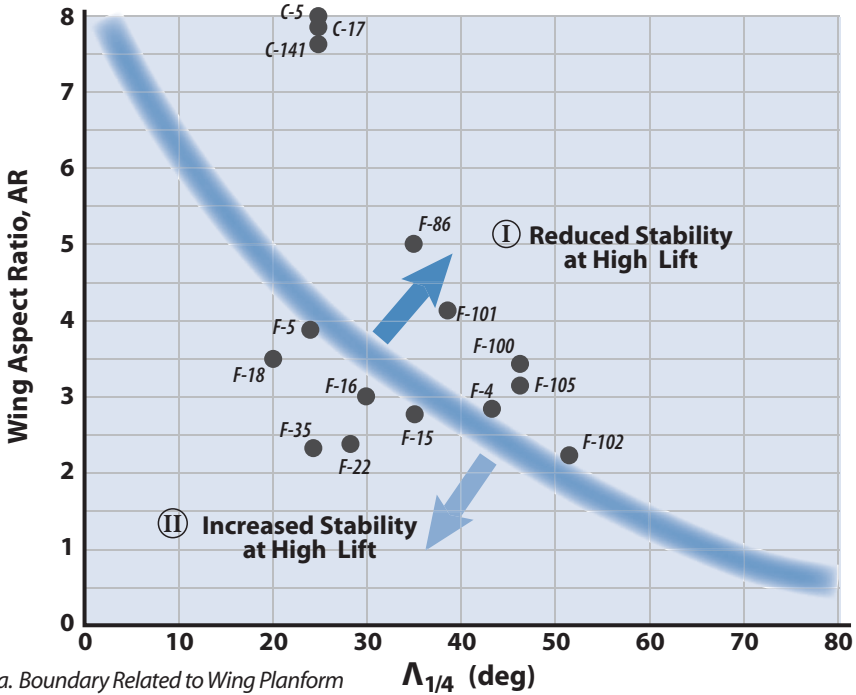
**Figure 21.14** Rudder effectiveness chart (from data in Fig. 9.10).

or stick shakers that would warn the pilot about entry into the wing-stall region.

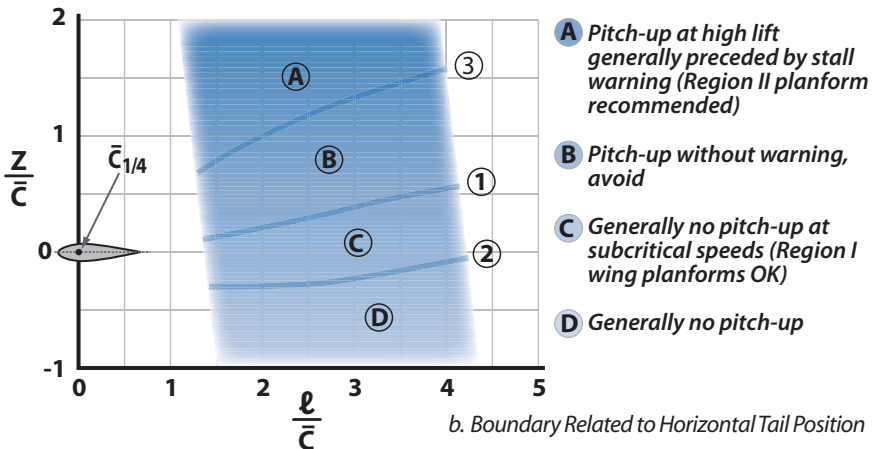
Sometimes the aircraft will pitch up gradually to a high angle-of-attack and the horizontal tail will lose the control power to push the nose down. This situation is termed *pitch hang-up*. If the wing is stalled, it can lead to an unrecoverable deep stall. One design solution is to locate the horizontal tail outside of the wing wake by mounting it on top of the vertical tail in a “T-tail” arrangement. In 1963 the aviation transport world was troubled by several accidents of the newly produced “T-tail” aircraft, including the BAC-111 and the Trident. These accidents were the result of an unrecoverable deep stall, which is a condition marked by softening of the horizontal tail control power at poststall angles-of-attack. Transport aircraft do not normally get to these high angles-of-attack so it is not a problem. However, STOL transports need special features such as stick shakers, stall limiters, and T-tails to stay out of trouble. The Lockheed C-5 had all three features and flew trouble free for over three decades. In 2005 the C-5 was re-engined with the more powerful CF6-80C2 turbofans. Because the engine thrust line was below the c.g. (giving a pitch-up moment) the nose-down pitch authority was reduced, giving the possibility of an unrecoverable deep stall. The solution was to bias the stall limiter to lower angles-of-attack and train the crews in aggressive stall recovery techniques. The C-17 has similar features to those of the C-5. The initial F-16As had a pitch hang-up problem above 35-deg angle-of-attack, and the horizontal tail area was increased on subsequent aircraft.

Reference [10] presents some design guidelines for aircraft planforms and aft tail location for minimizing the possibility of pitch-up at high

subsonic speeds. Figure 21.15a presents a boundary for AR–sweep combinations for tailless aircraft. Aspect ratio and sweep combinations in region I (to the right of the boundary) display a tendency to pitch-up at high  $C_L$ . Notice that the more modern air-to-air fighters all have region II wings and the high subsonic transports all have region I wings.



a. Boundary Related to Wing Planform



b. Boundary Related to Horizontal Tail Position

**Figure 21.15** Guidelines for wing design and aft tail location for minimal pitch-up at high-subsonic speeds (data from [10]).



Figure 21.15b presents design information on aft tail location for reducing pitch-up tendencies at high-subsonic speeds. The point is to locate the tail out of the high- $C_L$  wing wake so that the tail continues to be effective in providing longitudinal control. Figure 21.8 can be used to locate the wing downwash (wake) behind the wing. Region B of Fig. 21.15b is to be avoided. Region A, although not recommended for aircraft, is permissible provided a region II planform (from Fig. 21.15a) is used.

Most of the aircraft with region I wings have horns and stick shakers, and many have T-tails. The F-4 with a clear region I wing has dihedral on the wing tips and anhedral on the horizontal tail to locate the tail outside of the wing wake.

## References

- [1] McCormick, B., *Aerodynamics, Aeronautics and Flight Mechanics*, Wiley, New York, 1995.
- [2] Etkin, B., *Dynamics of Atmospheric Flight*, Wiley, New York, 1972.
- [3] Roskam, J., *Flight Dynamics of Rigid and Elastic Airplanes*, Univ. of Kansas, Lawrence, KS, 1972. [Available via [www.darcorp.com](http://www.darcorp.com) (accessed 31 Oct. 2009).]
- [4] Roskam, J., *Airplane Design, Part VII: Determination of Stability, Control and Performance Characteristics: FAR and Military Requirements*, Univ. of Kansas, Lawrence, KS, 1988. [Available via [www.darcorp.com](http://www.darcorp.com) (accessed 31 Oct. 2009).]
- [5] Chalk, C. R., "Background Information and User Guide for MIL-F-8785, Military Specification—Flying Qualities of Piloted Airplanes," U.S. Air Force Flight Dynamics Laboratory, AFFDL-TR-69-72, Wright-Patterson AFB, Dayton, OH, Aug. 1969.
- [6] Data sheets, Royal Aeronautical Society, London, UK.
- [7] Multhopp, R., "Aerodynamics of the Fuselage," NACA TM-1036, 1942.
- [8] Silverstein, A., and Katzoff, S., "Design Charts for Predicting Downwash Angles and Wake Characteristics Behind Plain and Flapped Wings," NACA TR-648, 1939.
- [9] Ellison, D. E., "USAF Stability and Control Handbook (DATCOM)," U.S. Air Force Flight Dynamics Laboratory, AFFDL/FDCC, Wright-Patterson AFB, Dayton, OH, Aug. 1968.
- [10] Spreemann, K. P., "Design Guide for Pitch-up Evaluation and Investigation at High Subsonic Speeds of Possible Limitations Due to Wing-Aspect-Ratio Variations," NASA TM-X-26, NASA Langley Research Center, Langley, VA, Aug. 1959.

## Chapter 22

Trim Drag and  
Maneuvering  
Flight

- Neutral Point
- Static Margin
- Aft Trim  $C_L$
- Canard Trim  $C_L$
- Tailless Aircraft Control
- Pitch Damping Coefficient
- Tail & Canard Control Power

An A-10A Thunderbolt II in a tight turn rolling in on a target. Notice the TE up deflection in the horizontal tail. The A-10A's survivability strategy was low vulnerability as it could "take a lickin' and keep on tickin'" (see Figs. 12.2 and 12.3).

*Of times the most successful test is the one that failed.  
Most learning comes from failure.  
Do not fear failure but keep the cost of failure low.*

## 22.1 Neutral Point and Static Margin

The aircraft *stick fixed neutral point* is defined as that center of gravity position where  $C_{M\alpha} = 0$ . It is determined by setting Eq. (21.4), (21.5), or (21.6) of Chapter 21 equal to zero and solving for  $X_w$ . The  $X_w$  then gives the neutral point location relative to the wing-body aerodynamic center (see Fig. 21.4a, b, and c). Notice that the neutral point for a tailless aircraft is at the wing-body aerodynamic center location when the inlet stability term is zero. With the center of gravity at the neutral point the aircraft is neutrally stable. The stick fixed neutral point is essentially the total aircraft aerodynamic center.

A convenient way to remember the location of the *neutral point* (n.p.) relative to the wing-body *aerodynamic center* (a.c.) is that the n.p. and a.c. are coincident for a tailless aircraft; then, as you add an aft tail or canard, the n.p. moves in the direction of the horizontal control surface. Thus, the n.p. is behind the a.c. for an aft tail and ahead of the a.c. for a canard.

The *static margin* (SM) is defined as follows:

$$SM = \frac{X_{n.p.} - X_{c.g.}}{\bar{c}} \quad (22.1)$$

where  $X_{n.p.}$  and  $X_{c.g.}$  are the locations of the neutral point and aircraft center of gravity, respectively. When the neutral point is ahead of the center of gravity the SM is negative and the aircraft is statically unstable. The condition of negative SM is termed *relaxed static margin* and means that, if the aircraft is perturbed from equilibrium, the moments generated will tend to rotate the aircraft further from equilibrium. The aircraft would be extremely sensitive as it would have the tendency to maneuver away from equilibrium. The pilot would have a very maneuverable aircraft and would have to be controlling it all the time; he could not relax for a second. The Sopwith Camel of Chapter 21 was such an aircraft.

The static margin and the longitudinal stability derivative are related as follows:

$$C_{M\alpha} = -SM C_{L\alpha WB} \quad (22.2)$$

where  $C_{L\alpha WB}$  is the wing-body linear lift curve slope,  $m_w$ .

Canard is the French word for hoax. When French airplane designers first saw pictures of the Wright brothers' airplane they thought it was a hoax because they knew that the forward control surface makes the airplane unstable and unflyable. The Wrights knew this was unstable but they also knew the pilot could easily control it. Forward control surfaces have been referred to as canards ever since.

## 22.2 Aft Tail Deflection to Trim $n = 1$ Flight

For the aft tail aircraft set the trim equation [Eq. (21.1) of Chapter 21] equal to zero:

$$0 = C_L \frac{x_w}{\bar{c}} + C_D \frac{z}{\bar{c}} + C_{M_{a.c.w}} + \frac{Tz_T}{q_\infty S_{ref} \bar{c}} - C_{LT} \bar{V}_H \eta_T - C_{M_{c.g.inlet}} \quad (22.3)$$

where the  $C_L$  is the required wing-body  $C_L$  for  $n = 1$ . Equation (22.3) is solved for the trim load coefficient  $C_{LT}$  of the tail, where  $C_{LT}$  is referenced to tail area  $S_T$ .

For statically stable aircraft (positive SM), this  $C_{LT}$  is usually negative, that is, the tail trim load is downward. Recalling that

$$n = \frac{\text{Lift}}{\text{Weight}} = \frac{q(C_L S_{ref} + \eta_T C_{LT} S_T)}{W} \quad (22.4)$$

the  $C_L$  of the wing-body will have to be increased to counter the down load on the tail in order to cruise at  $n = 1$ . Equation (22.3) may have to be iterated several times with different values of  $C_L$  to satisfy Eq. (22.4).

The *trim drag* for  $n = 1$  flight is expressed as

$$D_{trim} = \eta_T q_\infty S_T K_T C_{LT}^2 \quad (22.5)$$

The trim drag is only the drag-due-to-lift of the tail because the zero-lift tail drag coefficient is included in the total aircraft  $C_{D_0}$ . If the trim is too large, that is, greater than 10% of the aircraft drag, the designer should take steps to reduce the value of  $C_{LT}$ . This can be accomplished by the following:

1. Moving the c.g. aft (closer to the neutral point)
2. Increasing the tail volume coefficient  $\bar{V}_H$  by increasing  $S_T$  and/or  $\ell_T$  (see Fig. 21.2), both of which will also move the c.g. aft
3. Increasing  $C_{L_{\alpha T}}$  by increasing tail aspect ratio (AR)

Figure 22.1 shows a typical variation of  $C_{LT}$  with wing-body  $C_L$  for different c.g. locations. As the c.g. moves aft and the aircraft becomes less stable and then unstable, the tail trim load reverses from a down load to an up load. Figure 22.1 is for a composite Light Weight Fighter (LWF) at Mach = 0.9 and 30,000 ft. Figure 22.2 shows the behavior of the total aircraft cruise drag, wing-body  $C_L$ , and aft tail trim coefficient  $C_{LT}$  for different c.g. locations. The advantage of negative static margin is clearly evident in Fig. 22.2 as the total aircraft drag decreases to a minimum at an SM of about -8%. As the SM is decreased past -8% the aircraft drag starts to increase

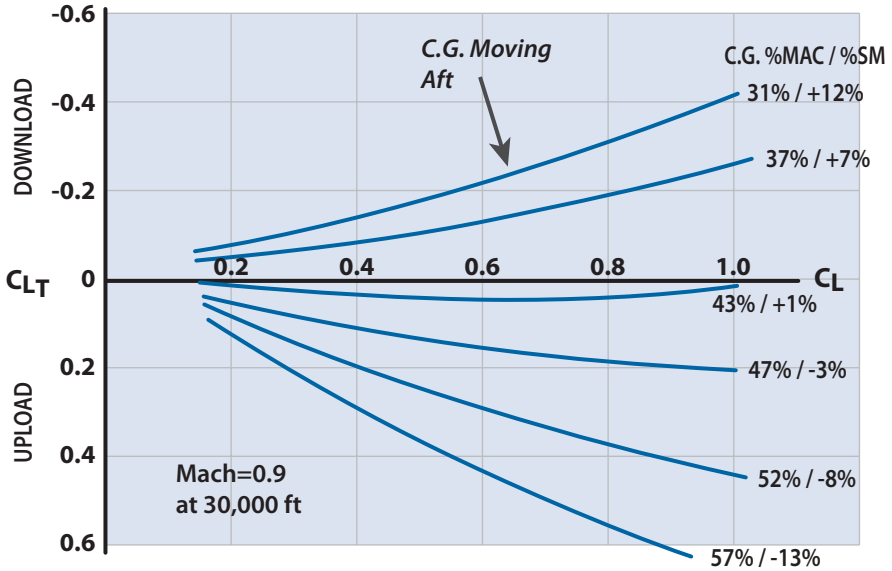


Figure 22.1 Variation of aft tail trim  $C_{LT}$  with aircraft  $C_L$  and c.g. (composite LWF).

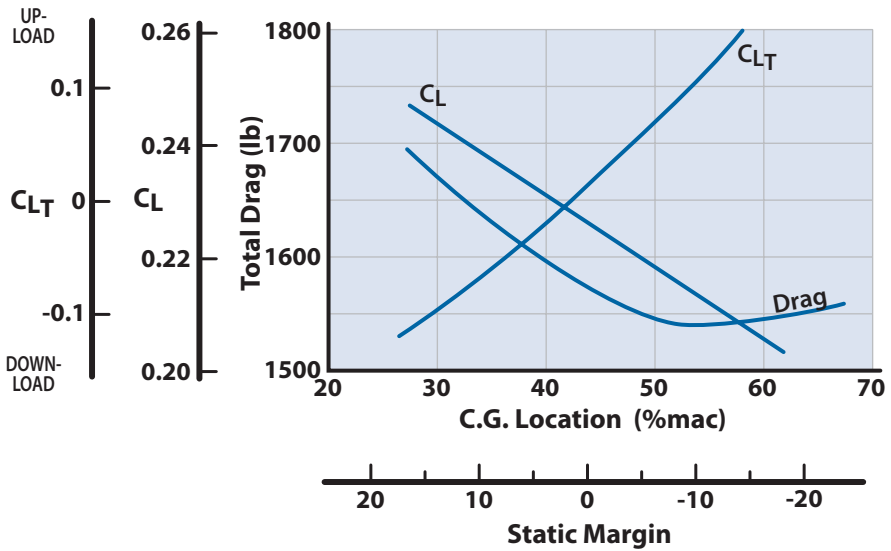


Figure 22.2 Variation of aircraft drag,  $C_L$ , and  $C_{LT}$  for LWF at  $n = 1$  (cruise), Mach = 0.9, and 45,000 ft.

because the trim drag is increasing faster than the wing–body drag–due-to-lift is decreasing, that is,

$$\text{Drag} = qS_{\text{ref}} \left( C_{D_0} + K C_L^2 \right) + D_{\text{trim}} \quad (22.6)$$

Normally, aircraft fly at an SM of about +3% to +10%. Figure 22.2 indicates a cruise drag reduction of about 3% by relaxing the SM from +5% to –8%. The overall payoff depends upon the comparison of the decreased aircraft weight due to reduced cruise fuel through relaxed SM with the cost and weight increase of the stability augmentation system. In the case of the F-16 there was a payoff for the relaxed SM and it flies at a –6% SM during its Mach = 0.9 cruise.

The tail deflection depends upon the type of aft tail being used. As discussed in Chapter 21 the aft tail can be a stabilizer–elevator arrangement or an all flying tail. If the aft tail is an all flying tail, the expression for  $C_{LT}$  is

$$C_{LT} = \left( \frac{dC_L}{d\alpha} \right)_T (\alpha_T + \alpha_{cs}) = \left( \frac{dC_L}{d\alpha} \right)_T \left[ \left( 1 - \frac{d\varepsilon}{d\alpha} \right) \alpha + \alpha_{cs} \right] \quad (22.7)$$

where  $\alpha$  is the aircraft angle-of-attack and  $\alpha_{cs}$  is the deflection angle for the tail. The term  $(1 - d\varepsilon/d\alpha)$  is the downwash term and can be determined from Fig. 21.8. The all flying tail is a miniature wing, and the quantity  $|\alpha_T + \alpha_{cs}|$  should not exceed the stall angle for the section.

If the horizontal tail is a stabilizer–elevator arrangement, the expression for  $C_{LT}$  is

$$C_{LT} = \left( \frac{dC_L}{d\alpha} \right)_T \left[ \left( 1 - \frac{d\varepsilon}{d\alpha} \right) \alpha + \alpha_{0L} \right] = \left( \frac{dC_L}{d\alpha} \right)_T \left[ \left( 1 - \frac{d\varepsilon}{d\alpha} \right) \alpha + \frac{d\alpha_{0L}}{d\delta_e} \delta_e \right] \quad (22.8)$$

where  $\alpha_{0L}$  is the zero-lift angle for the aft tail and is similar to a flapped wing. The term  $d\alpha_{0L}/d\delta_e$  is the same as the  $\tau$  of Fig. 21.14, Chapter 21. When using Fig. 21.14 for  $d\alpha_{0L}/d\delta_e$ , replace  $S_R/S_{VT}$  by  $S_e/S_T$ , where  $S_e$  is the elevator area and  $S_T$  is the total horizontal tail area.

Equation (21.1) can also be expressed as

$$C_M = C_{M_0} + C_{M_\alpha} \alpha + C_{M_\delta} (\delta_e, \alpha_{cs}) \quad (22.9)$$

where  $C_{M_\delta}$  is called the *horizontal tail power* and, for an all flying tail,

$$C_{M_\delta} = -\bar{V}_H \eta_T C_{L\alpha_T} \quad (22.10a)$$

and, for an elevator–stabilizer arrangement,

$$C_{M\delta} = -\bar{V}_H \eta_T C_{L\alpha T} \frac{d\alpha_{0L}}{d\delta_e} \tag{22.10b}$$

and  $C_{M0}$ , the moment coefficient at zero  $\alpha$  and control deflection, is given by

$$C_{M0} = C_{M_{a.c.w}} + C_{D0} \frac{z}{\bar{c}} \frac{Tz_T}{q_\infty S_{ref} \bar{c}} \tag{22.11}$$

Using Eqs. (22.9) and (22.2), the expression for the control deflection for trimming the aircraft is

$$\alpha_{cs}, \delta_e = \frac{-C_{M0} + (SM)C_L}{C_{M\delta}} \tag{22.12}$$

Figure 22.3 shows a typical variation of the control surface deflection required to trim the aircraft. Notice that the most forward c.g. location is fixed by the maximum control surface deflection (usually  $\pm 20$  deg). Figure 21.4b shows the sign convention for elevator deflection.

The static longitudinal stability changes with increasing Mach number. The most pronounced Mach number effect is the rearward shift of the wing-body aerodynamic center to about the 50% mac location for supersonic flight. This results in an aftward shift of the neutral point and

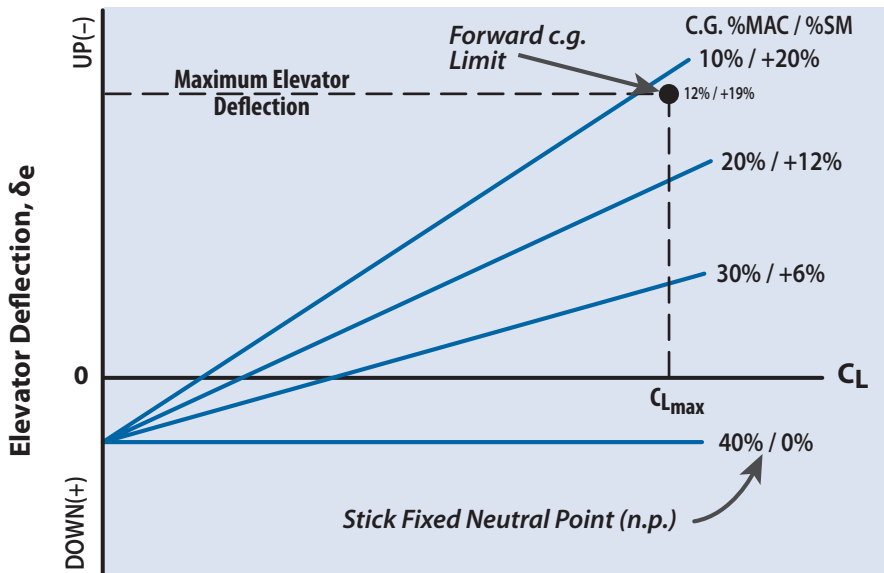


Figure 22.3 Trim  $C_L$  vs elevator deflection.

a resulting increase in the SM and aircraft stability. The designer should check the trim drag at this increased stability condition. Sometimes the c.g. is shifted aft by fuel transfer during supersonic flight to reduce the trim drag (see Chapter 23). Another effect is the increase of  $(C_{L\alpha})_T$  at transonic speeds and then its decrease at supersonic speeds (see Fig. 13.3a). This changes the horizontal tail effectiveness and will make the aircraft more stable in the transonic regime and less stable supersonically. At supersonic speeds there is also a decrease in the downwash at the tail.

### 22.3 Canard Deflection for Trim at $n = 1$

For the canard, set the trim equation [Eq. (21.4a)] equal to zero:

$$0 = C_{M_{a.c.w}} - \frac{x_w}{\bar{c}} C_L + \frac{z}{\bar{c}} C_D + C_{L_c} \bar{V}_c + \frac{Tz_T}{q_\infty S_{\text{ref}} \bar{c}} - C_{M_{c.g.\text{inlet}}} \quad (22.13)$$

Equation (22.13) is solved for the canard lift coefficient  $C_{L_c}$  and the resulting trim drag is

$$D_{\text{trim}} = q_\infty S_c K_c C_{L_c}^2 \quad (22.14)$$

Because the aircraft  $\alpha$  for cruise is usually small assume that nonlinear lift is negligible and

$$C_{L_c} = \left( \frac{dC_L}{d\alpha} \right)_c (\alpha - \alpha_{0L} + \alpha_c) = \left( \frac{dC_L}{d\alpha} \right)_c (\alpha + \alpha_c) \quad (22.15)$$

The canard is usually symmetric so that  $\alpha_{0L} = 0$ .

The trim equation can be expressed in a form similar to Eq. (22.9) as

$$C_M = C_{M_0} + C_{M_\alpha} \alpha + C_{M_{\alpha_c}} \alpha_c \quad (22.16)$$

where  $C_{M_{\alpha_c}}$  is the canard control power

$$C_{M_{\alpha_c}} = \bar{V}_c C_{L_{\alpha_c}} \quad (22.17)$$

and

$$C_{M_0} = C_{M_{a.c.w}} + C_{D_0} \frac{z}{\bar{c}} + \frac{Tz_T}{q_\infty S_{\text{ref}} \bar{c}} \quad (22.18)$$

The canard deflection for trimming the aircraft is expressed as [from Eqs. (22.18) and (22.2)]



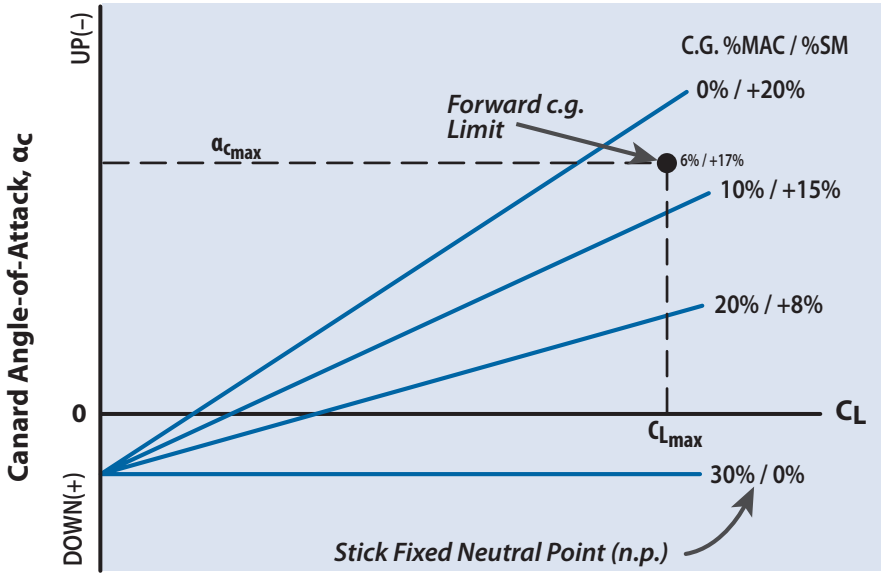


Figure 22.4 Variation of canard angle-of-attack with wing-body  $C_L$  and c.g. location.

$$\alpha_c = \frac{-C_{M0} + (SM)C_L}{C_{M\alpha_c}} \tag{22.19}$$

Equation (22.19) indicates that the canard trim load is up for positive SM and reverses to a down trim load as the c.g. moves aft and the SM decreases to zero and then becomes negative. This behavior is shown on Fig. 22.4. Thus, the canard acts opposite to an aft tail. A down trim load works against the wing-body lift and is undesirable, so that relaxed static margin is not as attractive for a wing-canard arrangement as it is for a wing-aft tail configuration.

## 22.4 Control of a Tailless Aircraft at $n = 1$

As mentioned earlier, the neutral point for a tailless aircraft is located at the wing-body aerodynamic center. Thus, the tailless aircraft must have the center of gravity ahead of the wing-body a.c. for static stability. This is shown on Fig. 22.5. Because the tailless aircraft does not have any horizontal control surfaces (aft tail or canard), the moment to trim the aircraft must come from the wing moment about the a.c.  $C_{M\alpha_c}$ ,  $C_M$  about the a.c., is changed by deflecting the wing flaps (called *elevons*) up and down, effecting a positive or negative camber change. Figure 22.5 illustrates this. The

upsweep of the trailing edge (called *reflex camber*) produces a positive  $C_{M_{\alpha c}}$  and balances the aircraft at positive  $C_L$ .

For the tailless aircraft set the trim equation (neglecting the moment due to wing drag and inlet) equal to zero:

$$0 = C_{M_{a.c.w}} - \frac{x_w}{\bar{c}} C_L + \frac{Tz_T}{q_\infty S_{ref} \bar{c}} \quad (22.20)$$

As the elevon is deflected the wing lift coefficient  $C_L$  changes and  $C_{M_{a.c.w}}$  changes. Equation (22.20) can be rewritten as

$$0 = \left( \frac{dC_{M_{a.c.}}}{d\delta_e} \right) \delta_e - \frac{x_w}{\bar{c}} \left[ \left( \frac{dC_L}{d\alpha} \right)_w \alpha + \left( \frac{dC_L}{d\delta_e} \right) \delta_e \right] + \frac{Tz_T}{q_\infty S_{ref} \bar{c}}$$

and the elevon deflection is expressed as

$$\delta_e = \frac{(x_w / \bar{c})(dC_L / d\alpha)_w \alpha - (Tz_T / q_\infty S_{ref} \bar{c})}{-(x_w / \bar{c})C_{L_\delta} + C_{M_\delta}} \quad (22.21)$$

The denominator is referred to as the *elevon control power* and [1, Sections 6.1.1–6.1.5; 2], can be used to estimate  $C_{L_\delta}$  and  $C_{M_\delta}$ .

The trim drag for a tailless aircraft is much different than for an aft tail or canard aircraft. A tailless aircraft trims itself by changing the camber of

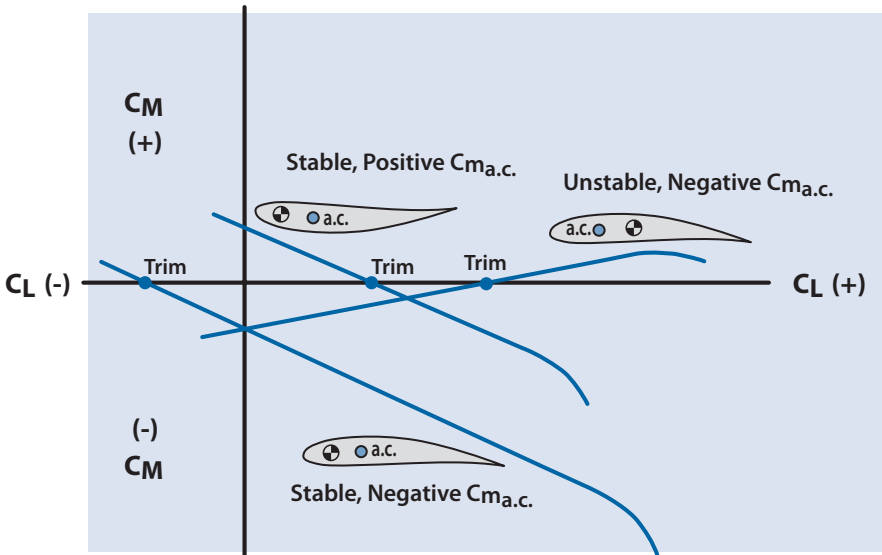


Figure 22.5 Control of a tailless aircraft by camber change.

the wing. Subsonically, this results in a small change in the wing separation drag and can be determined using the method of Section 9.5.

Supersonically the elevon deflection results in a change in the wave drag. From linear theory

$$C_{Dw} = \frac{4}{\sqrt{M^2 - 1}} \left[ \alpha^2 + \left( \frac{dh}{dx} \right)^2 + \overline{\alpha_c^2} \right]$$

and by deflecting the elevon  $\alpha$  and  $\alpha_c^2$  are also changed. The result is

$$\frac{(C_{Dwave})_{\delta_e}}{(C_{Dwave})_{\delta_e=0}} = \left[ 1 - \frac{c_e}{c} \right] + \frac{c_e}{c} \frac{(\alpha + \delta_e)^2}{\alpha^2} \tag{22.22}$$

where  $c_e$  is the elevon chord and  $c$  is the wing chord (including elevon).

## 22.5 Aft Tail Deflection for Maneuvering Flight—Pull-Up Maneuver

In a pull-up or loop maneuver the weight of the aircraft always opposes the lift vector. The aft tail deflection,  $\delta_e$  or  $\alpha_{cs}$ , for a pull-up maneuver is greater than  $n - 1$  times the trim deflection for  $n = 1$  flight because of the inertial loading and pitch damping of the aircraft.

The increase in  $\delta_e$  or  $\alpha_{cs}$  for a pull-up maneuver of  $n$  gs is given by

$$\left( \Delta\alpha_{cs}, \Delta\delta_e \right)_{\text{maneuver}} = - \frac{[-SM + (\rho S_{\text{ref}} \bar{c} / 4m) C_{Mq}]}{C_{M\delta}} (n-1) C_{L_{n=1}} \tag{22.23}$$

where  $m$  is the mass of the aircraft in slugs,  $\rho$  is the density in slugs per cubic foot (slug/ft<sup>3</sup>), and  $C_{L_n} = 1$  is the  $C_L$  required for  $n = 1$  flight. The  $C_{Mq}$  is the pitch damping derivative and is determined from

$$C_{Mq} = \frac{dC_M}{d(q\bar{c}/2V)} = -2.2\eta_T \bar{V}_H C_{L\alpha_T} \frac{\ell_T}{\bar{c}} \tag{22.24}$$

The  $C_{M\delta}$  for Eq. (22.23) is determined from Eq. (22.10a) for an all flying tail and Eq. (22.10b) for an elevator–stabilizer arrangement. The total aft tail deflection is determined by adding the value from Eq. (22.23) to the value for  $n = 1$  from Eq. (22.12). The  $C_{L_T}$  is determined from Eq. (22.7) or (22.8) and the trim from Eq. (22.5).

## 22.6 Canard Deflection for Maneuvering Flight—Pull-Up Maneuver

The additional canard deflection to pull  $n$  gs may be found from

$$(\Delta\alpha_c)_{\text{maneuver}} = -\frac{[-SM + (\rho S_{\text{ref}} \bar{c} / 4m) C_{Mq}](n-1)C_{L_{n=1}}}{\bar{V}_c C_{L_{\alpha c}}} \quad (22.25)$$

where the denominator is the canard control power  $C_{M_{\delta c}}$  [Eq. (22.17)] and the pitch damping term

$$C_{Mq} = -2.2\bar{V}_c C_{L_{\alpha c}} \frac{\ell_c}{\bar{c}}$$

## 22.7 Elevon Deflection for a Tailless Aircraft in Maneuvering Flight—Pull-Up Maneuver

For the tailless aircraft the damping in pitch is very small compared with an aircraft with an aft tail or canard. As a first approximation set  $C_{Mq} = 0$ . This makes the maneuver point coincide with the neutral point, which coincides with the aerodynamic center.

Thus,

$$(\Delta\delta_e)_{\text{maneuver}} = -\frac{SM(n-1)C_{L_{n=1}}}{-(x_w / \bar{c})C_{L_{\delta}} + C_{M_{\delta}}} \quad (22.26a)$$

$$\Delta\delta_e(\text{maneuver}) = (n-1)\delta_{e_{n=1}} \quad (22.26b)$$

or

$$\Delta\delta_e(\text{total}) = n\delta_{e_{n=1}} \quad (22.26c)$$

where  $\delta_{e_{n=1}}$  is the elevon deflection for  $n = 1$  flight as given by Eq. (22.21).

## 22.8 Control Deflection for Level Turn Maneuvering Flight

The previous discussion of maneuvering flight (i.e., Sections 22.5, 22.6, and 22.7) was for a pull-up or loop maneuver where the weight of the aircraft always opposed the lift vector. For a level turn only a component of the lift is equal to the weight (see Section 3.7) and thus the control deflection equations are slightly different from those for a loop.

The increased control deflection for a level turn is given by the following:  
Aft Tail:

$$\left(\Delta\alpha_{cs}, \Delta\delta_e\right)_{\text{levelturn}} = -\frac{\left[-SM(n-1) + C_{Mq}(\rho S_{\text{ref}}\bar{c}/4m)(n-(1/n))\right]C_{L_{n=1}}}{C_{M\delta}} \quad (22.27)$$

where  $n = 1/\cos \varphi$  for a level turn,  $\varphi$  is the bank angle (from Fig. 3.11),  $C_{Mq}$  is given by Eq. (22.24), and  $C_{M\delta}$  is given by Eq. (22.10).

Canard:

$$\left(\Delta\alpha_c\right)_{\text{levelturn}} = -\frac{\left[-SM(n-1) + C_{Mq}(\rho S_{\text{ref}}\bar{c}/4m)(n-(1/n))\right]C_{L_{n=1}}}{\bar{V}_c C_{L\alpha_c}} \quad (22.28)$$

where

$$C_{Mq} = -2.2\bar{V}_c C_{L\alpha_c} \frac{\ell_c}{\bar{c}}$$

Tailless: Because the damping in pitch is negligible, the control deflection for a tailless aircraft in a level turn is the same as Eq. (22.26).

## References

- [1] Ellison, D. E., "USAF Stability and Control Handbook (DATCOM)," U.S. Air Force Flight Dynamics Laboratory, AFFDL/FDCC, Wright-Patterson AFB, OH, Aug. 1968.
- [2] Roskam, J., *Flight Dynamics of Rigid and Elastic Airplanes*, Univ. of Kansas, Lawrence, KS, 1972. [Available via [www.darcorp.com](http://www.darcorp.com) (accessed 31 Oct. 2009).]

# Chapter 23

# Control Surface Sizing Criteria



- Typical Values for S&C
- Recommended  $C_{M\alpha}$  Values
- Lateral Control Spin Parameter
- Recommended  $C_{n\beta}$  Values
- $C_{n\beta}$  Dynamic
- C.G. Travel
- Aileron Sizing Criteria

Two Canada geese coming in for a STOL landing. Mother Nature (the ultimate designer) did a superb job of sizing the geese's control surfaces for this high angle-of-attack, low-speed, low-power approach condition. It is too bad she didn't write a design text.

*If it looks good, it flies good.*

Clarence "Kelly" Johnson

## 23.1 Government Regulations Require Static Stability

The Federal Aviation Regulations, Parts 23 and 25 [1] are more abbreviated and qualitative than MIL-HDBK-1797 with regard to stability and control requirements and handling qualities. The FARs require the aircraft to be stable in the longitudinal, directional, and lateral modes. The civilian regulations in their current form do not contain guidelines that are sufficiently detailed for use in design.

Both MIL-HDBK-1797 and FAR Parts 23 and 25 require that the elevator fixed neutral point be aft of the center of gravity for all loading conditions for aft tail configurations. This insures that

$$C_{M\alpha} < 0$$

for all c.g. positions. It is interesting to note that the British Civil Airworthiness Requirements [2, Paragraph 2.1] specify a maximum allowable negative stick fixed static margin of  $-0.05$ .

Both MIL-HDBK-1797 and FAR Parts 23 and 25 require static directional stability, that is,

$$C_{n\beta} > 0$$

in terms of characteristics involving rudder position and rudder force.

*Roll damping* is an important handling-qualities parameter, particularly in roll maneuvers and in Dutch roll. The government regulations do not specify minimum values for the roll damping derivative  $C_{\ell_p}$  directly. However, to meet the roll-handling requirements of [3,4] it is necessary that

$$C_{\ell_p} < 0$$

Similarly, the government regulations do not give minimum values for the pitch-damping derivative  $C_{M_q}$ . However, to meet the short-period damping requirement of [5] it is necessary that

$$C_{M_q} < 0$$

MIL-HDBK-1797 requires that left aileron force be generated for left sideslip. For conventional control arrangements this can be shown to imply that the lateral stability parameter

$$C_{\ell\beta} < 0$$

Table 23.1 Typical Aircraft Stability and Control Data

	Learjet	B-727	T-38	Cherokee 180 Archer
Takeoff weight (lb)	13,500	152,000	11,250	2450
Empty weight (lb)	7,252	88,000	7,370	1390
Wing area (ft <sup>2</sup> )	232	1,560	170	156
Span (ft)	34.2	106	25.25	30
Aspect ratio	5.02	7.2	3.75	5.71
Wing sweep c/4 (deg)	0	35	24	0
mac (ft)	7.04	15	7.73	5.25
Vertical tail area (ft <sup>2</sup> )	37.4	15,356	7.73	11.4
Horizontal tail area (ft <sup>2</sup> )	54.0	376	59.0	25
Derivatives at Mach = 0.8				At Mach = 0.19
C.G. location (% mac)	32	25	19	19
$C_{M0}$	0.06	-0.042	—	-0.07
$C_{L\delta\theta}$ (per radian)	0.6	0.4	—	—
$C_{M\alpha}$ (per radian)	-0.7	-1.5	-0.16	-0.32
$C_{M\delta\theta}$ (per radian)	-1.6	-1.3	-0.13	-1.1
$C_{L\delta\sigma}$ (per radian)	0.015	—	—	—
$C_{L\delta r}$ at $C_L = 1.1$ (per radian)	0.007	0.017	—	—
$C_{n\beta}$ (per radian)	0.12	0.08	0.28	0.092
$C_{n\delta r}$ (per radian)	-0.074	-0.098	—	-0.06
$C_{Mq}$ (per radian)	-14	-24	-8.4	-12
$C_{ip}$ (per radian)	-0.5	-0.30	-0.35	-0.47
$C_{i\beta}$ (per radian)	-0.1	-0.13	-0.075	-0.107
$I_{xx}$ (10 <sup>4</sup> ) (slug·ft <sup>2</sup> )	3	92	1.48	0.107
$I_{yy}$ (10 <sup>4</sup> ) (slug·ft <sup>2</sup> )	1.9	300	2.82	0.1249
$I_{zz}$ (10 <sup>4</sup> ) (slug·ft <sup>2</sup> )	5	380	2.9	0.2312

This condition is also necessary to keep the spiral mode from being divergent.

Over the years, all of the aircraft companies have developed their own flying-qualities criteria to supplement the government regulations. These criteria are reflected in the stability and control characteristics of the current inventory of aircraft. Table 23.1 lists the static stability and control characteristics of a representative small general aviation aircraft, FAR 23 business jet, FAR 25 transport, and a fighter-class aircraft.

### 23.2 Center of Gravity Location

The designer should not leave the c.g. location to chance, but rather force its location by judicious placement of components, including the



wing. The c.g. is the most important element in the stability and control of an aircraft. It should be located so that the tail size (if it has a tail) is not unduly large and the trim drags are acceptable.

Current regulations require a statically stable aircraft,  $C_{M\alpha} < 0$ . Figure 23.1 shows some recommended  $C_{M\alpha}$  values for general aviation, FAR 23 business jet, FAR 25 transport, and fighter aircraft. Transport aircraft should be more stable than fighters because of the comfort of the passengers. Fighter aircraft on the other hand need lower values of  $C_{M\alpha}$  because of their maneuverability requirements. A good rule of thumb is an SM of +4% to +7% for transport aircraft and neutral to +3% for fighter aircraft. Larger static margins lead to trim drags that become intolerable. The recommended curves of  $C_{M\alpha}$  on Fig. 23.1 are based on this range of SM and the expression

$$C_{M\alpha} = -(SM)(C_{L\alpha})_{WB} \tag{23.1}$$

At this point the designer has a wing-body configuration and thus the wing-body a.c. location can be determined (Fig. 21.3). The usual aft tail or canard will move the n.p. about 5% mac behind or ahead of the a.c., respectively (Table 23.2). If an SM of +5% mac is desired, c.g. locations can be determined using Eq. (22.1).

$$SM = (x_{n.p.} - x_{c.g.}) / \bar{c} \tag{22.1}$$

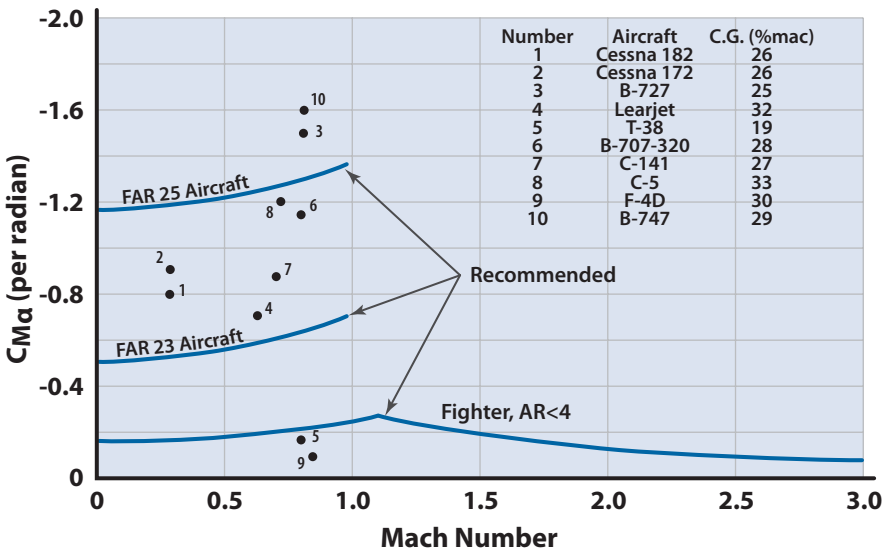


Figure 23.1  $C_{M\alpha}$  values for current aircraft.

**Table 23.2** Approximate N.P. and C.G. Locations

<b>Subsonic: Assume A.C. at 35% mac</b>		
<b>Type</b>	<b>Approximate N.P. Location (% mac)</b>	<b>Approximate C.G. Location (% mac)</b>
Aft tail	40	35
Tailless	35	30
Canard	30	25
<b>Supersonic: Assume A.C. at 50% mac</b>		
<b>Type</b>	<b>Approximate N.P. Location (% mac)</b>	<b>Approximate C.G. Location (% mac)</b>
Aft tail	55	50
Tailless	50	45
Canard	45	40

The c.g. moves around as fuel is burned, ordnance expended, cargo or passengers unloaded and loaded, and so on. The c.g. travel must be watched very closely as it can be costly in terms of excessive trim drag and aircraft safety-of-flight. The designer must allow for all possible c.g. locations, which may require system events (such as fuel transfer) so that the c.g. shift is within tolerable limits. Usually a c.g. shift of less than 10% mac for subsonic aircraft is tolerable; however, it varies from aircraft to aircraft. If the aircraft is scheduled to spend much of its mission at supersonic speeds, there should be some provision for shifting the c.g. aft (such as fuel sequencing) to follow the a.c. shift and keep the SM at a desired level.

Fuel sequencing or transfer is imperative for most aircraft. Here the fuel is located in fuel tanks distributed throughout the fuselage and wing. Fuel is then taken from these tanks in a definite schedule so that fuel is transferred from tank to tank to keep the c.g. located properly. Fuel is also sequenced so that when the weapons are dropped the c.g. shift is within limits. Figure 23.2 shows an example of this scheduling for the Boeing/McDonnell F-4D. This part of the preliminary design is not easy but it is essential to keep the c.g. shift within acceptable limits; otherwise performance benefits of the aircraft can be negated by excessive trim drags.

Finally, the aircraft should be unloaded completely ahead of the c.g. to insure that the aircraft does not fall back on its tail. Aircraft can, as a last resort, have a placard that dictates the load distribution while it is parked.

The designer should try very hard to get the c.g. close to the predetermined location. Payload, subsystems, and fuel can be shifted around, within fuselage constraints, to locate the c.g. at a desired position. Shifting the wing back and forth has a large effect on c.g. location because the

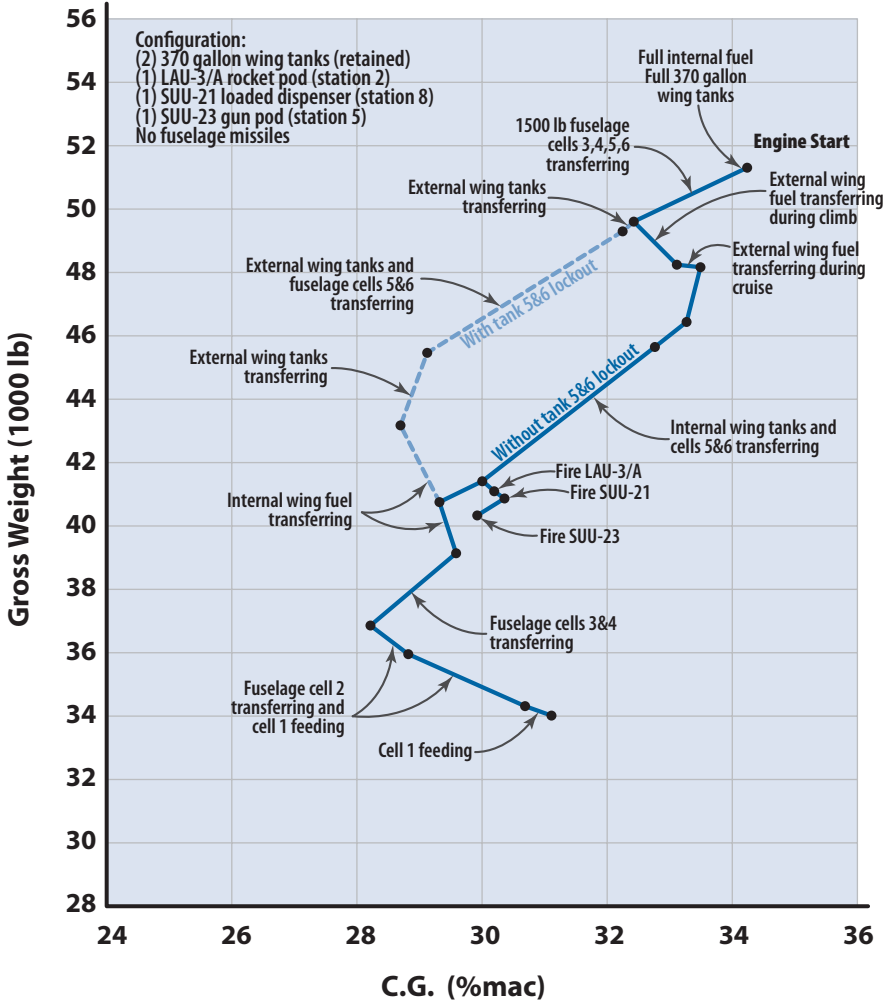


Figure 23.2 Center of gravity travel due to fuel consumption, "potato curve" (F-4D).

mac and a.c. move directly. Shifting the wing should be considered as a last resort because of its effect on inlet location and area-ruling.

### 23.3 Sizing the Horizontal Surface

The horizontal surface (aft tail or canard) is used for longitudinal stability and control. The designer should recognize at this point that stability and control are two independent functions. The horizontal surface is sized separately for each and the larger of the areas selected.

The designer should locate the horizontal surface on the aircraft and estimate a general planform shape (i.e., aspect ratio, taper ratio, and sweep).

### 23.3.1 Static Longitudinal Stability

The desired level of stability,  $C_{M_{\alpha^2}}$  is determined from Fig. 23.1, and then Eq. (21.4) or (21.5) is used to solve for  $S_T$  or  $S_C$ . Several Mach numbers should be examined and the largest area for all design conditions is then selected.

### 23.3.2 Longitudinal Control

The horizontal surface is now sized for adequate longitudinal control. The horizontal control surface can be an elevator (with deflection  $\delta_e$ ), an all flying stabilizer (with control surface angle-of-attack  $\alpha_{cs}$ ), or an all flying canard (with canard angle-of-attack  $\alpha_c$ ). The  $\delta_e$ ,  $\alpha_{cs}$ , or  $\alpha_c$  is usually limited to about  $\pm 20$  deg.

There are several critical conditions for longitudinal control that should be examined:

1. **Trim drag.** The trim drag during cruise should be less than 10% of the total aircraft drag. Many designers reduce this limit to 5% for range-dominated vehicles.
2. **High-g maneuver.** If the aircraft is a fighter, the horizontal control surface should be checked to insure that there is sufficient control power to trim the high-g condition.
3. **Takeoff rotation.** The takeoff rotation to climb  $C_L$  (see Chapter 10) should be checked. The horizontal control surface must have enough control power to rotate the aircraft about the main landing gear to the takeoff attitude. This problem is shown schematically in Fig. 23.3. Attention paid to the recommended angle between the center of

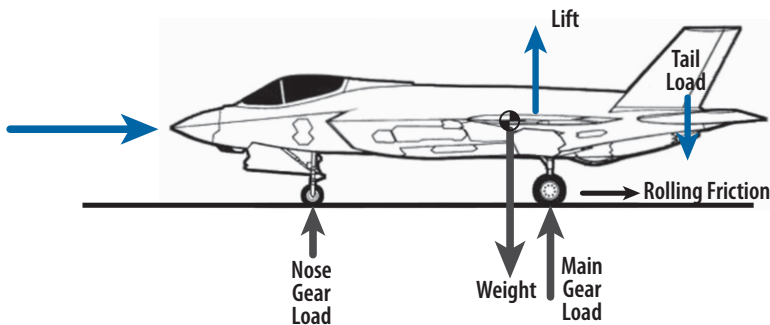


Figure 23.3 Takeoff control schematic.

gravity and the main gear wheel as shown in Table 8.5 will insure that the size of the horizontal tail will be acceptable.

4. **High  $\alpha$ , low speed.** The condition of low-speed approach for landing with power at idle, flaps down, and high angle-of-attack is often a critical condition for sizing control surfaces. This condition often determines the most forward c.g. position as shown in Figs. 22.3 and 22.4. Ground effects must be considered as this condition increases the aircraft stability and compounds the control problem.

## 23.4 Sizing the Vertical Tail

### 23.4.1 Static Directional Stability

The vertical tail is sized to give adequate static directional stability. Desired values of  $C_{n\beta}$  are put into Eq. (21.20) and the vertical tail area,  $S_{VT}$ , is determined. Figure 23.4 gives some recommended values for  $C_{n\beta}$ .

### 23.4.2 Fighter Aircraft Spin Resistance

The degree of susceptibility to spin during hard turns with and without rolling inputs has a significant impact on the dogfighting capability of air superiority aircraft. Reference [5] reports two simple parameters that have been related to spin resistance margin and provide a good approximation of the relative resistance of aircraft to spin departure.

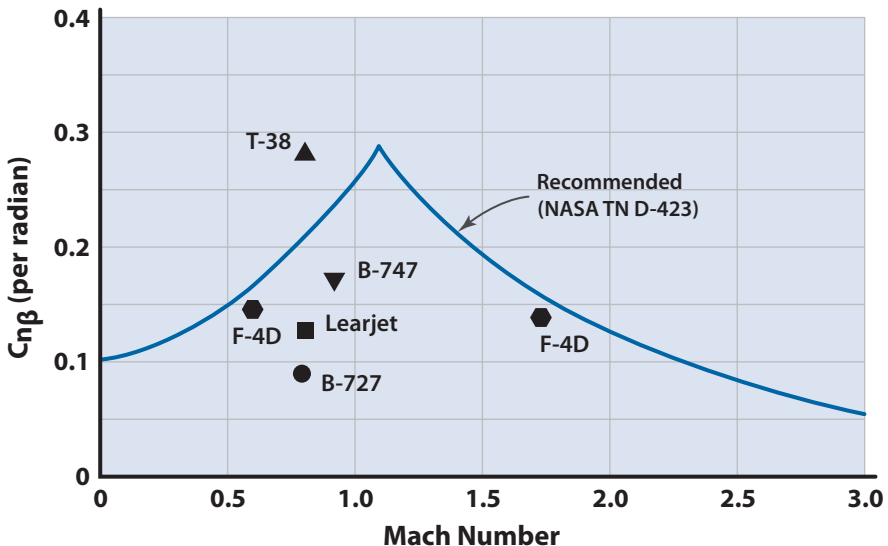


Figure 23.4 Recommended  $C_{n\beta}$  values.

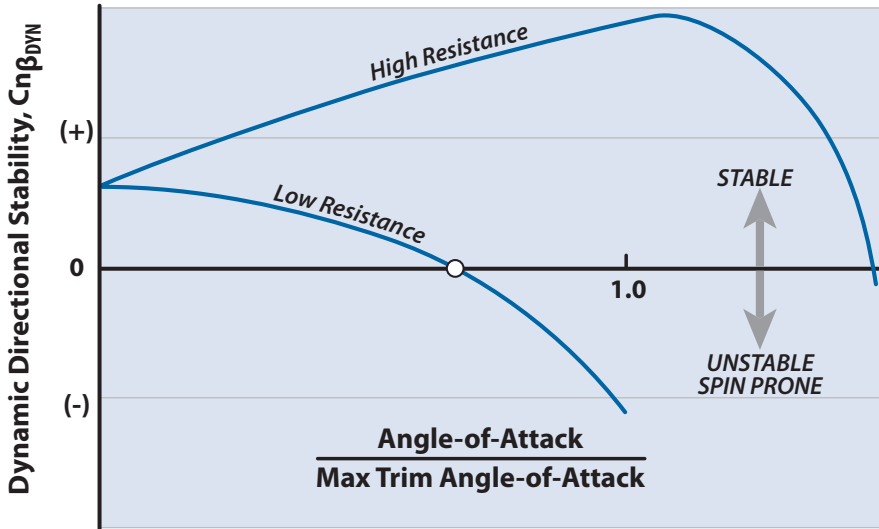


Figure 23.5 Measure of spin resistance (turning without rolling).

The angle-of-attack region of spin susceptibility for nonrolling turning maneuvers without lateral or directional inputs has been correlated with the dynamic directional stability parameter

$$C_{n\beta_{dyn}} = C_{n\beta} - C_{l\beta} \frac{I_{zz}}{I_{xx}} \tan \alpha \tag{23.2}$$

Figure 20.2 can be used to estimate the moments of inertia  $I_{xx}$  and  $I_{zz}$ . Unless the  $C_{n\beta_{dyn}}$  is positive throughout the possible operating angle-of-attack range as illustrated in Fig. 23.5, the aircraft will be susceptible to spin in hard nonrolling turns.

For assessing the spin susceptibility in turning maneuvers where lateral control inputs are introduced, it has been found that the angle-of-attack at which the roll reverses due to sideslip opposing the aileron correlates very closely with the region of spin susceptibility of a number of current fighter aircraft. The dominant parameters influencing roll reversal are the yaw due to aileron  $C_{n\delta_a}$  and the directional stability  $C_{n\beta}$ .

High adverse yaw and low directional stability are detrimental. A *lateral control spin parameter* (LCSP) is defined by

$$LCSP = C_{n\beta} - C_{l\beta} \frac{C_{n\delta_a}}{C_{l\delta_a}} \tag{23.3}$$

where  $C_{l\beta}$  and  $C_{l\delta_a}$  were introduced in Chapter 21 and  $C_{n\delta_a}$  can be estimated from [6] or [7]. Roll reversal occurs at the point where this parameter

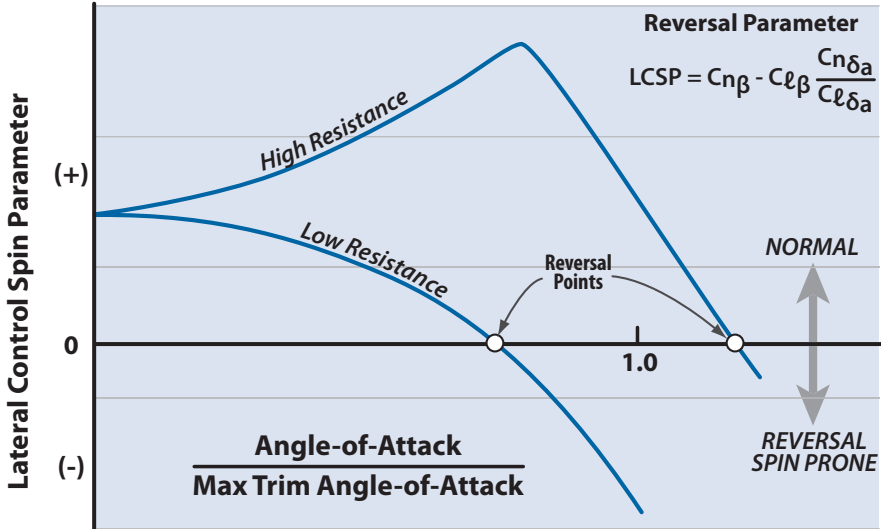


Figure 23.6 Measure of spin resistance (combined turning and rolling maneuvers).

equals zero. Figure 23.6 illustrates the variation of the LCSP vs angle-of-attack normalized to maximum angle.

### 23.4.3 Static Directional Control Requirements

The requirements on the rudder for adequate static directional control are as follows:

1. **Crosswind landing.** The rudder must be powerful enough to maintain a straight ground path during normal takeoff and landing in 90-deg crosswinds up to velocities of  $0.2V_{TO}$ . This means adequate rudder power to hold a sideslip of  $\beta = 11.5$  deg at approach speeds. The analysis was discussed in Section 21.6.
2. **Antisymmetric power.** The rudder must be powerful enough to hold zero sideslip ( $\beta = 0$ ) in straight flight at all speeds above  $1.2V_{stall}$  with gear down, flaps in best setting, thrust on one outboard engine equal to zero (with associated drag), and all other engines developing full thrust. This condition was discussed in Section 21.6.
3. **Adverse yaw.** When an airplane is rolled into a turn, yawing moments are often produced that require rudder deflection to maintain zero sideslip, that is, coordinate the turn. For example, when initiating a roll to the right, aileron deflection may cause yaw to the left. This is termed *adverse yaw* and a rudder deflection is required to eliminate the sideslip. Because adverse yaw will be greatest at high  $C_L$  and full deflection of the ailerons, steep turns at low speed may produce a critical requirement for rudder control power.

## 23.5 Sizing the Ailerons

The *lateral control surface* is the aileron. As discussed in Chapter 21, this lateral control surface has no effect on the lateral stability of the aircraft. The lateral stability derivative is  $C_{\ell\beta}$  and is influenced by the wing (independent of the ailerons), the vertical tail, and the wing–fuselage. The regulations require  $C_{\ell\beta}$  to be negative. Typical values are given in Table 23.1.

MIL-HDBK-1797 places all aircraft in one of the following classifications, Class I, Class II, Class III, Class IVA, Class IVB, or Class IVC:

### Class I

Small, light airplanes such as

- Light utility
- Primary trainer
- Light observation

### Class II

Medium-weight, low-to-medium maneuverability airplanes such as

- Heavy utility or search and rescue
- Light or medium transport, cargo, or tanker
- Early warning, electronic countermeasures, or airborne command, control, or communications relay
- Antisubmarine
- Assault transport
- Reconnaissance
- Tactical bomber
- Heavy attack
- Trainer for Class II

### Class III

Large, heavy, low-to-medium maneuverability airplanes such as

- Heavy transport, cargo, or tanker
- Heavy bomber
- Patrol, early warning, electronic countermeasures, or airborne command, control, or communications relay
- Trainer for Class III

### Class IVA

High-maneuverability airplanes such as

- Fighter–interceptor
- Attack
- Tactical reconnaissance



**Table 23.3** MIL-HDBK-1797 Roll Requirements

Class	Roll Performance
I	600 in 1.3 s
II	450 in 1.4 s
III	300 in 1.5 s
IVA	900 in 1.3 s
IVB	900 in 1.0 s
IVB	3600 in 2.8 s
IVC	900 in 1.7 s

- Observation
- Trainer for Class IV

### Class IVB

Air-to-air fighter

### Class IVC

Air-to-ground fighter with external stores

The ailerons should be sized to provide the roll performance listed in Table 23.3 for the appropriate class of aircraft under consideration. The roll rate  $P$  in radians per second is given by Eq. (21.17b):

$$P = -\frac{2V}{b} \frac{C_{\ell\delta_a}}{C_{\ell_p}} \delta_a \quad (21.17b)$$

where  $V$  is speed in feet per second,  $C_{\ell\delta_a}$  is the aileron control power, and  $C_{\ell_p}$  is the roll-damping coefficient.

## References

- [1] "Airworthiness Standards: Part 23—Normal, Utility and Acrobatic Category Airplanes; Part 25—Transport Category Airplanes," *Federal Aviation Regulation*, Vol. 3, U.S. Department of Transportation, U.S. Government Printing Office, Washington, DC, Dec. 1996.
- [2] "British Civil Airworthiness Requirements," Sec. D, Air Registration England, 15 Nov. 1991.
- [3] "Military Specification—Flying Qualities of Piloted Aircraft," MIL-F-8785C, Nov. 1980.
- [4] "Flying Qualities of Piloted Aircraft," MIL-HDBK-1797, Dec. 1997.
- [5] Chambers, J. R., and Anglin, E. L., "Analysis of Lateral-Directional Stability Characteristics of a Twin-Jet Fighter Airplane at High Angles of Attack," NASA TN D-5361, 1969.
- [6] Ellison, D. E., "USAF Stability and Control Handbook (DATCOM)," U.S. Air Force Flight Dynamics Laboratory, Wright-Patterson AFB, OH, Aug. 1968.
- [7] Roskam, J., *Flight Dynamics of Rigid and Elastic Airplanes*, Univ. of Kansas, Lawrence, KS, 1972. [Available via [www.darcorp.com](http://www.darcorp.com) (accessed 31 Oct. 2009).]

# Chapter 24 Life Cycle Cost



- Cost-Estimating Equations
- Economic Escalation Factors
- Design for Reduced O&M
- Cost-Estimating Charts
- UCAV vs Manned Aircraft O&S
- Design for Production

The Boeing 777 transport or “Triple 7” was developed in the 1990s to compete head-on with the Airbus 340 and the MD-11/12. Boeing has delivered over twice as many “Triple 7s” as Airbus has A-340s. (McDonnell Douglas dropped out of this market.) Example 24.1 uses the Triple 7 to estimate development and acquisition cost. (Photograph courtesy of Singapore Airlines.)

*A billion here, a billion there—  
pretty soon it adds up to real money!*

Everett McKinley Dirksen

## 24.1 Life Cycle Cost

The *life cycle cost* (LCC) of a military aircraft is the total cost to transition the aircraft from “cradle to grave.” It includes the following phases (as shown in Fig. 1.16):

- Research
- Development, Test, and Evaluation (DT&E)
- Acquisition (production, ground equipment, initial spares, training aids, etc.)
- Operations and Maintenance (O&M)

The *research phase* involves the basic research and the exploratory and advanced development efforts required to mature those technologies that are essential to the successful operation of the aircraft. This phase can include technology demonstrator aircraft, testbeds, and prototypes. An example of this phase would be the effort expended in researching the integration of the shaft-driven lift fan into the Joint Strike Fighter short takeoff, vertical landing (STOVL) prototype X-35B. This phase is important because, without it, advanced technologies would not find their way onto new aircraft systems. In many cases, a commercial aircraft will build upon technology that was developed for a military aircraft program, thereby reducing the research cost for the commercial program. The research phase is a difficult cost item to estimate because of the uncertainty inherent in a research and technology development program. Also, the research phase is a mixture of contractor funding and government funding.

The *development, test, and evaluation cost* is that cost required to engineer, develop, fabricate, and flight test a number  $Q_D$  of aircraft prior to committing to production. The DT&E aircraft might number as few as 2 or as many as 10. The DT&E phase is usually government funded. The cost elements charged to DT&E are as follows:

- Airframe engineering
- Development support
- Flight test aircraft
  - Engine and avionics
  - Manufacturing labor
  - Material and equipment
  - Tooling
  - Quality control
- Flight test operations
- Test facilities
- Profit

The *acquisition cost* includes the cumulative cost of  $Q_p$  production aircraft, associated ground equipment (such as starting carts and special

equipment for maintenance and operation), initial spares, and training aids (simulators, manuals, etc.). The cost elements charged to production are as follows:

- Engines and avionics
- Manufacturing labor
- Material and equipment
- Airframe engineering (sustaining)
- Tooling
- Quality control
- Manufacturing facilities
- Profit

The *operations costs* comprise the fuel and oil (POL), including storage and delivery, salaries of operating and support personnel, day-to-day (direct) maintenance, depot and overhaul, spares, depreciation of equipment, and indirect costs.

For a military aircraft the breakdown of O&M costs (sometimes called O&S, operations and support) is as follows:

- **Spares.** Initial, replenishment, engines, war reserve material (WRM)
- **Maintenance.** Both on-equipment and off-equipment
- **Management personnel.** System and item managers
- **Training.** Ground and flight training
- **Operations.** Crew, commander, staff, and operations personnel
- **Support.** Base operating support (the care and feeding of all squadron personnel)
- **POL.** Fuel, oil, and lubricants
- **Modifications.** Hardware modifications
- **Munitions and missiles.** Training
- **Personnel.** Permanent change of station (PCS)
- **Attrition**
- **New facilities**

For commercial aircraft the LCC phases are similar to those of a military aircraft except that the research, development, test, and evaluation (RDT&E) phase is all privately funded. This phase ends with the type certification of the aircraft by the Federal Aviation Administration (FAA). As discussed in Chapter 1, this phase is shorter for a commercial aircraft than for a military aircraft.

The acquisition phase for a commercial aircraft is termed the *production phase*.

For commercial operations the cost breakdown is as follows:

- Flight operations—crew, POL, airport fees, insurance
- Station and ground

- Ticketing, sales, and promotion
- Maintenance and overhaul
- Flight equipment depreciation
- Passenger services
- General administration and taxes

The O&M phase costs are the largest element of the LCC because most aircraft are operational for several decades: the commercial aircraft flying 24/7 revenue flights [1] and the military manned aircraft doing peacetime training. Figures 24.1 and 24.2 show the LCC for the B-52 and the F-111, respectively—two military aircraft whose operational life was more than three decades. The B-52 LCC shown in Fig. 24.1 is typical of the military LCC history, where the RDT&E is small relative to the acquisition and operations phases and precedes the acquisition phase with only a small overlap. The F-111, Fig. 24.2, on the other hand, had technical problems during the latter part of the flight test and early operations phase, which resulted in an overlapping RDT&E phase and significant increase in RDT&E cost. The F-111 history was more the exception than the rule, involving several new technologies and occurring during a semiwartime situation. However, it points out the importance of being careful and thorough during the RDT&E phase and committing to production only after completed test and evaluation.

In both the commercial and military O&M phase, direct personnel costs are more than one-third of the costs. This points out the huge impact

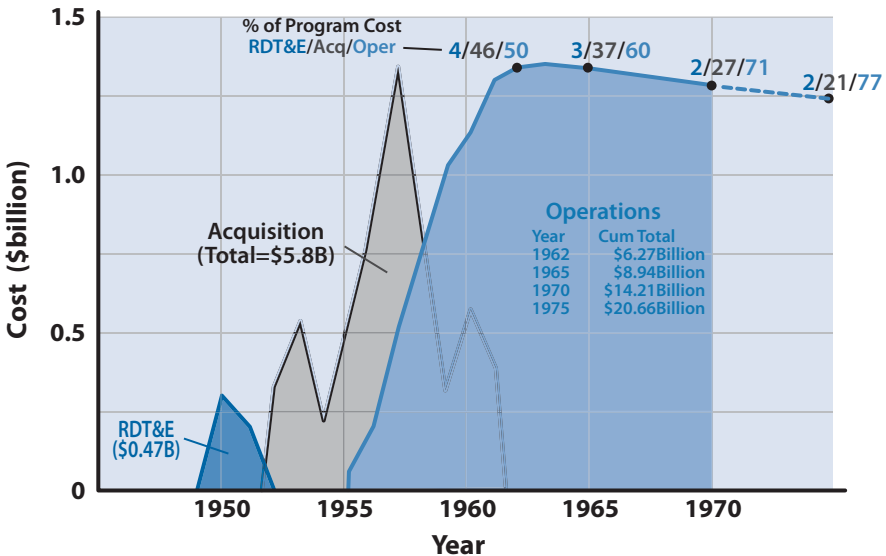


Figure 24.1 B-52 life cycle cost (LCC) (data from [2]).

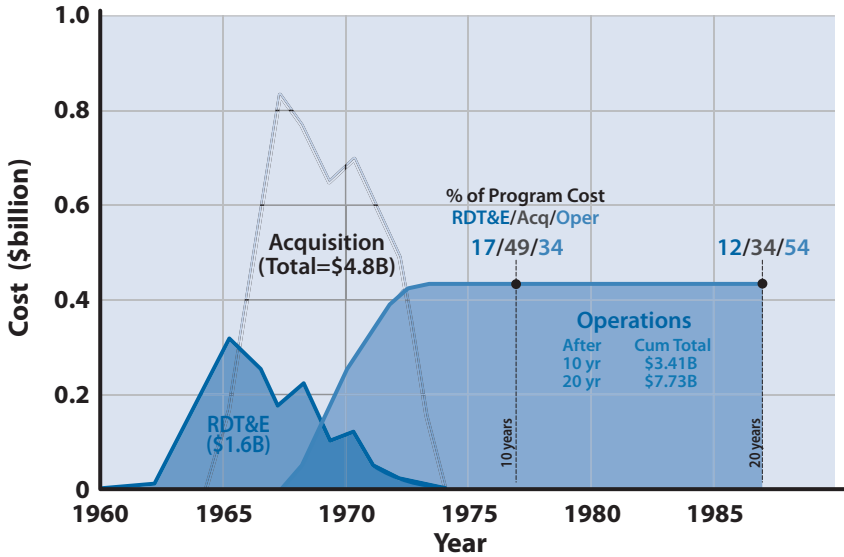


Figure 24.2 F-111 life cycle cost (data from [3]).

that the human element has on aircraft O&M and makes a good argument for military UAVs [this will be examined later in an example comparing squadron O&M costs for the F-16 and an unmanned combat aerial vehicle (UCAV)].

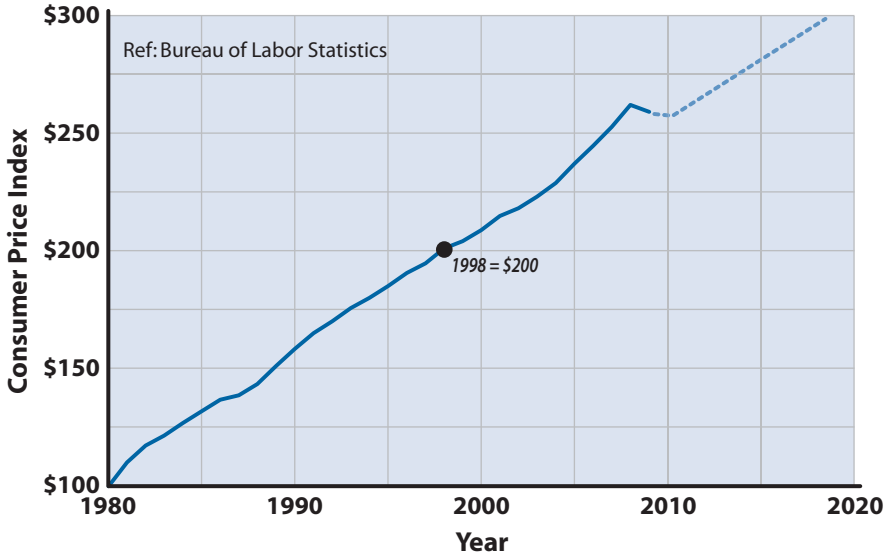
## 24.2 DT&E and Acquisition-Production Costs

The methodology presented in this section is very preliminary but is adequate for the economic analysis appropriate to this level of design. There are more-refined LCC methods available but they require information that is normally not available at the conceptual design.

Methodology for estimating the research phase costs is not available as this is a very nebulous effort and very much dependent upon the individual aircraft program. The designer should examine the design for the development status of the technologies being used, then talk with the technology community relative to the schedule and funds appropriate to these technologies.

Methodology for estimating costs for the remaining three LCC phases will be discussed in the following sections. In many cases the costs will be estimated in terms of 1998 U.S. dollars. Figure 24.3 can be used to convert the 1998 dollar costs to “now year” costs by multiplying the 1998 dollars by the economic escalation factor [Consumer Price Index (CPI)].

The *cost-estimating relationships* (CERs) for the military DT&E and production phases will be based upon the methodology developed by the



**Figure 24.3** Economic escalation factors (CPI).

Rand Corporation in 1986 and presented in [4]. This was preceded by [5] in 1971; it examined 29 aircraft built between 1945 and 1970. Reference [4] added the following 13 more modern aircraft to the data base:

- **Attack.** A-6, A-7, A-10, S-3
- **Fighter.** F-111, F-4, F-14, F-15, F-16, F-18
- **Transport.** C-141, C-5
- **Utility.** T-39

The Rand study of the DT&E and production costs for aircraft built between 1945 and 1986 concluded that the primary characteristics driving these costs were as follows:

1.  $W$ , empty weight in pounds (discussed in the next section)
2.  $S$ , maximum speed in knots
3.  $Q$ , quantity of aircraft produced during DT&E and production

All other aircraft characteristics appeared to be second order.

It is worth bringing to the attention of the reader that the weight influencing the cost of the aircraft is more correctly the weight according to the American Manufacturers Planning Report (the *AMPR weight*), which is the empty weight of the aircraft minus the procured items (such as engines, wheels, instruments, and electrical equipment). To determine the AMPR weight the designer needs a detailed weight summary, which is often not available during the conceptual design phase. Typically, the AMPR weight

is approximately 62% of the empty weight. In the cost methodology that follows (from [4]) the always-available empty weight is used and the 62% has been absorbed into the coefficients. Reference [5] used AMPR weight.

The reader will observe that the direct labor hours to produce an item (such as engineering, assembly, or tooling) will decrease as the cumulative number of items produced ( $Q$ ) increases. The basis for this is that the personnel involved in producing the item get smarter as they produce more items. This improvement is called the learning curve. Early CERs were built upon an 80% learning curve, where the labor hours reduced by 20% every time the quantity produced doubled. Thus, the second-unit labor cost was 80% of that for the first unit, the fourth was 80% of the second, the eighth was 80% of the fourth, and soon. When large quantities of the same item are produced, the rate of improvement with respect to time may be so small as to go unnoticed. For example, if 1000 units have been produced and the production rate is 250 units per year, four years will be required to reach 2000 units: four years to double the quantity and attain a 20% reduction in labor hours. It should be noticed, however, that the 2000th unit would require 8.7% of the labor hours needed for the first unit. Thus, production runs are necessary to drive the unit costs down. If Ford only produced 50 automobiles each year, no one could afford them. It is only through mass production that could put “a car in every garage.”

Reference [4] examined the cost–quantity relationship and found it to vary for the different cost elements. Thus, the CERs presented in the next sections will have different values of the cost–quantity curve slope (or exponent for  $Q$ ) for each cost element. The learning curve is close to 80 for only a few of the cost elements.

### 24.2.1 Airframe Engineering (DT&E and Production)

The engineering activities involved in the DT&E are as follows:

1. Design studies and integration
2. Engineering for wind tunnel models, mock-ups, and engine tests
3. Test engineering, laboratory work on subsystems and static test items, and development testing
4. Release and maintenance of drawings and specifications
5. Shop and vendor liaison (\*)
6. Analysis and incorporation of changes (\*)
7. Materials and process specifications (\*)
8. Reliability (\*)

The starred items (\*) are also part of the sustaining engineering effort production. Engineering hours not directly related to airframe design and



development are not included here. For example, test engineering, ground handling equipment design and development, mobile training units, and publications are not charged to airframe engineering.

The cumulative total *airframe engineering hours*  $E$  can be estimated using the following expression (from [4]):

$$E = 4.86 W^{0.777} S^{0.894} Q^{0.163} \quad (24.1)$$

where

$W$  = empty weight in pounds

$S$  = maximum speed (kt) at best altitude

$Q$  = cumulative quantity produced

=  $Q_D$  for DT&E phase (number of development flight test aircraft)

=  $Q_D + Q_P$  for production phase

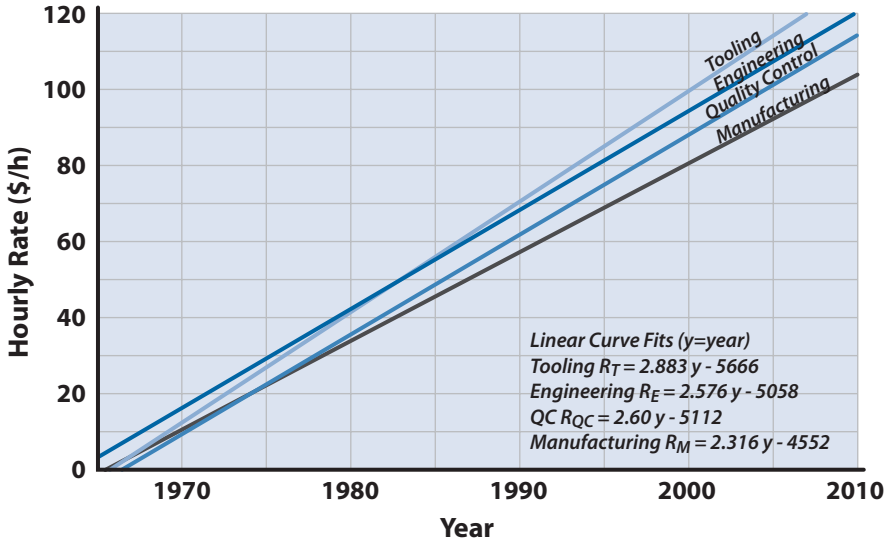
The empty weight  $W$  is defined as the takeoff gross weight (TOGW) minus the fuel and payload. Said another way, the empty weight of the aircraft is the sum of the (1) airframe structure and canopy, (2) wheels, brakes, and tires, (3) engines and accessories, (4) cooling fluid, (5) rubber or nylon bladder type fuel cells, (6) crew seats and instruments, (7) batteries, electrical power supply, and conversion-conditioning equipment, (8) electronic and avionics equipment, (9) armament and fire-control system, (10) air conditioning units and fluid, (11) onboard power plant unit, and (12) trapped fuel and oil.

Equation (24.1) gives the total engineering hours for either DT&E or production. For the DT&E phase the quantity  $Q$  is equal to the number of flight test aircraft  $Q_D$  and the engineering hours are just for DT&E. For the production phase, the quantity  $Q$  is the total produced ( $Q_D$  plus the  $Q_P$  production aircraft). The production phase sustaining engineering hours are the hours from Eq. (24.1) minus the DT&E engineering hours (see Section 24.3.9 for an example).

The hours from Eq. (24.1) are then multiplied by an appropriate engineering dollar rate for the year of interest. This rate includes direct labor, overhead, general and administrative expense, and miscellaneous direct charges. Figure 24.4 presents historical data on average hourly rates, created with data from the U.S. Department of Labor. These labor rates can be estimated from the consumer price index (CPI), which is available from the U.S. Department of Labor, Bureau of Labor Statistics Web site.

### **24.2.2 Development Support (DT&E)**

*Development support* is defined as the nonrecurring manufacturing effort undertaken in support of engineering during the DT&E phase of an



**Figure 24.4** Trends in hourly rates in aircraft construction for engineering, tooling, manufacturing, and quality control.

aircraft program. The cost of the development support is the cost of manufacturing labor and material required to produce mock-ups, test parts, static test items, and other items of hardware that are needed for airframe design and development work. The level of this effort is largely dependent upon the extent that new technologies figure into the aircraft program. If the aircraft design involves new and untried concepts, then the development support cost can be high. For example, the KC-135 was largely a derivative of the Boeing 707, and the development support cost was \$(1957)37 million, whereas the F-111A incorporated several new and untried technologies and its development support cost was \$(1965)178 million.

The development support cost can be estimated using (from [4])

$$D = 66 W^{0.63} S^{1.3} \tag{24.2}$$

where

$D$  = development support cost in 1998 constant dollars

$W$  = empty weight, in pounds (lb)

$S$  = maximum speed, in knots (kt), at best altitude

### 24.2.3 Flight Test Operations (DT&E)

The *flight test operations* cost element includes all costs incurred by the aircraft builder to carry out flight tests except the cost of the flight test

aircraft. It includes flight test engineering planning and data reduction, manufacturing support, instrumentation, spares, fuel and oil, pilot's pay, facilities rental, and insurance. The flight test establishes the operating envelope of the aircraft, its flying and handling qualities, general airworthiness, initial maintainability features, and compatibility with ground support equipment. Civil and commercial aircraft are establishing the aircraft's compliance with the FARs for airworthiness certification. Military aircraft are demonstrating compliance with government specifications and regulations, such as Air Force Regulation 80–14.

The cost for flight test operations can be estimated using (from [4])

$$F = 1852 W^{0.325} S^{0.822} Q_D^{1.21} \quad (24.3)$$

where  $F$  is the flight test operations cost in 1998 constant dollars and  $W$ ,  $S$ , and  $Q_D$  are as defined in Eq. (24.1).

#### 24.2.4 Tooling (DT&E and Production)

*Tools* are the jigs, fixtures, dies, and special equipment used in the fabrication of an aircraft. *Tooling hours* are defined as the hours charged for tool design, tool planning, tool fabrication, production test equipment, checkout of tools, maintenance of tooling, normal changes, and production planning. Tooling hours are dependent upon a new variable called *production rate*. Tools designed for low production rates do not have to be as well engineered as tools for high production rates. Sometimes tools are destroyed during the fabrication process (called *soft tooling*) and have to be rebuilt for each aircraft. Tooling can be as simple as  $2 \times 4$ s or as complicated and costly as matched metal dies of stainless steel accurate to one ten-thousandth of an inch (1/10,000 in.).

The tooling hours can be estimated using the following expression (from [4]):

$$T = 5.99 W^{0.777} S^{0.696} Q^{0.263} \quad (24.4)$$

where

- $T$  = cumulative tooling hours
- $Q$  = cumulative quantity,  $Q_D + Q_P$
- $Q_D$  = DT&E
- $Q_P$  = production

The *total tooling cost* is the tooling hours multiplied by an appropriate tooling hourly rate. Figure 24.4 shows some historical data on average hourly tooling rates.

Equation (24.4) gives the total tooling hours for either DT&E or production. For the DT&E phase tooling hours, the quantity  $Q$  is  $Q_D$ . For the production phase, the quantity  $Q$  is  $Q_D$  plus the  $Q_P$  production aircraft and the tooling hours are the hours from Eq. (24.4) minus the DT&E tooling hours.

### 24.2.5 Manufacturing Labor (DT&E and Production)

Manufacturing labor hours include those hours necessary to fabricate, process, and assemble the major structure of an aircraft, and to install purchased parts, government furnished equipment (GFE), and off-site manufactured assemblies (i.e., subcontract components). Airframe structure direct manufacturing man-hours also include effort on those parts that, because of their configuration or weight characteristics, are design controlled for the basic aircraft. These normally represent significant proportions of the airframe weight and manufacturing effort, and they are included regardless of their method of acquisition. Such parts specifically include [4] the following:

1. Actuating hydraulic cylinders
2. Radomes, canopies, and ducts
3. Passenger and crew seats
4. Fixed external tanks

The manufacturing labor hours can be estimated using the expression (from [4])

$$L = 7.37 W^{0.82} S^{0.484} Q^{0.641} \quad (24.5)$$

where  $L$  is cumulative total manufacturing hours, and  $W$ ,  $S$ , and  $Q$  are defined in Eq. (24.1). The manufacturing labor hours for DT&E and for production are determined separately as discussed in Sections 24.2.1 and 24.2.4. The cumulative manufacturing cost is obtained by multiplying the manufacturing labor hours  $L$  by a representative hourly rate. Figure 24.4 gives representative average hourly rates for manufacturing.

### 24.2.6 Quality Control

*Quality control* (QC) is the task of inspecting fabricated and purchased parts, subassemblies, and assembled items against material and process

standards, drawings, and/or specifications. Quality control is an extremely important activity in the manufacture of aircraft because of their complexity. Government specifications and standards require close inspection of all facets of fabrication. Quality control is closely related to direct manufacturing labor and is considered to be a percentage of the labor hours. The quality control hours can be estimated as follows (from [4]):

$$QC = 0.076 L \text{ for cargo and transport aircraft} \quad (24.6a)$$

$$QC = 0.13 L \text{ for all other aircraft} \quad (24.6b)$$

The total cost for quality control is obtained by multiplying the man-hours from Eq. (24.6) by the representative manufacturing hourly rate.

### **24.2.7 Manufacturing Material and Equipment (DT&E and Production)**

The *material and equipment list* (sometimes called the BOM, bill of materials) includes the raw material, hardware, and purchased parts required for the fabrication and assembly of the airframe. All airframe equipment except engines and avionics are included in this cost item. Specific items in the material and equipment cost are as follows:

1. Raw materials in sheets, plates, bars, rods, and so on
2. Raw castings and forgings
3. Wires, cables, fabrics, tubing, windshield glass and canopies, and so on
4. Fasteners, clamps, bushings, and so on
5. Hydraulic and plumbing fittings, valves, and fixtures
6. Standard electrical products such as motors, transformers, inverters, alternators, voltage regulators, switches, controls, generators, batteries, and auxiliary power units (APUs)
7. Pumps for fuel, hydraulic, water, and so on
8. Environmental systems, air conditioning, and oxygen equipment
9. Crew furnishings, seats, instruments, bunks, and so on
10. Bladder-type fuel tanks

The manufacturing material and equipment costs can be estimated from the following expression [4]:

$$M = 16.39 W^{0.921} S^{0.621} Q^{0.799} \quad (24.7)$$

where  $M$  = cumulative total manufacturing material and equipment cost in 1998 dollars and  $W$ ,  $S$ , and  $Q$  are defined in Eq. (24.1). The costs for DT&E

and production are determined separately using development  $Q = Q_D$  and production  $Q = Q_P$  (see example in Section 24.3).

### 24.2.8 Engine and Avionics Costs

The engine and avionics will be assumed to be off-the-shelf items so that DT&E costs of these subsystems will not be considered. Only production unit costs are considered.

Costs in 1998 dollars for current turbine engines are shown in Fig. 24.5. Figure 24.5 shows quite a bit of scatter in the data. This scatter is explained by the fact that the engines represent different types, levels of technology, and production quantities. More refined propulsion cost methodology would take these variables into consideration [6]. However, at this point in the design, the data from Fig. 24.5 or the following expression is adequate:

$$P = 2306 [0.043 T_{\text{SLS}} + 243.3 M_{\text{max}} + 0.969 T_R - 2228] \quad (24.8)$$

where

$P$  = production engine unit cost in 1998 dollars

$T_{\text{SLS}}$  = sea level maximum thrust in pounds

$M_{\text{max}}$  = maximum Mach number

$T_R$  = turbine inlet temperature in degrees absolute (Rankine)

Avionics equipment is so varied that space will not be taken here to list avionics gear and associated costs. The designer is referred to the avionics vendors for prices of selected avionics equipment.

Figure 24.6 presents unit prices [\$(1993)] for existing fighters, bombers, transports, bizjets, cruise missiles, and targets. The charts confirm that aircraft are bought by the pound. The prices can be adjusted to reflect any year by ratioing the escalation factors from Fig. 24.3.

Unit prices are not the only thing taken into account when determining an aircraft's selling price. Often the selling price will include initial spares for initial fleet operation, data and publications, and flight training for the pilots and maintenance training for the ground crews. These "extras" can easily be 10% of the selling price.

The cost-estimating relations presented in Sections 24.2.1 through 24.2.8 will be demonstrated by estimating the cost for the Boeing 777-200LR. This will be a good checkout for the CERs as they were developed from a military aircraft data base.

Note the cost numbers in this example: it is a major decision for a company to commit to an \$8 billion DT&E cost for a new aircraft line.

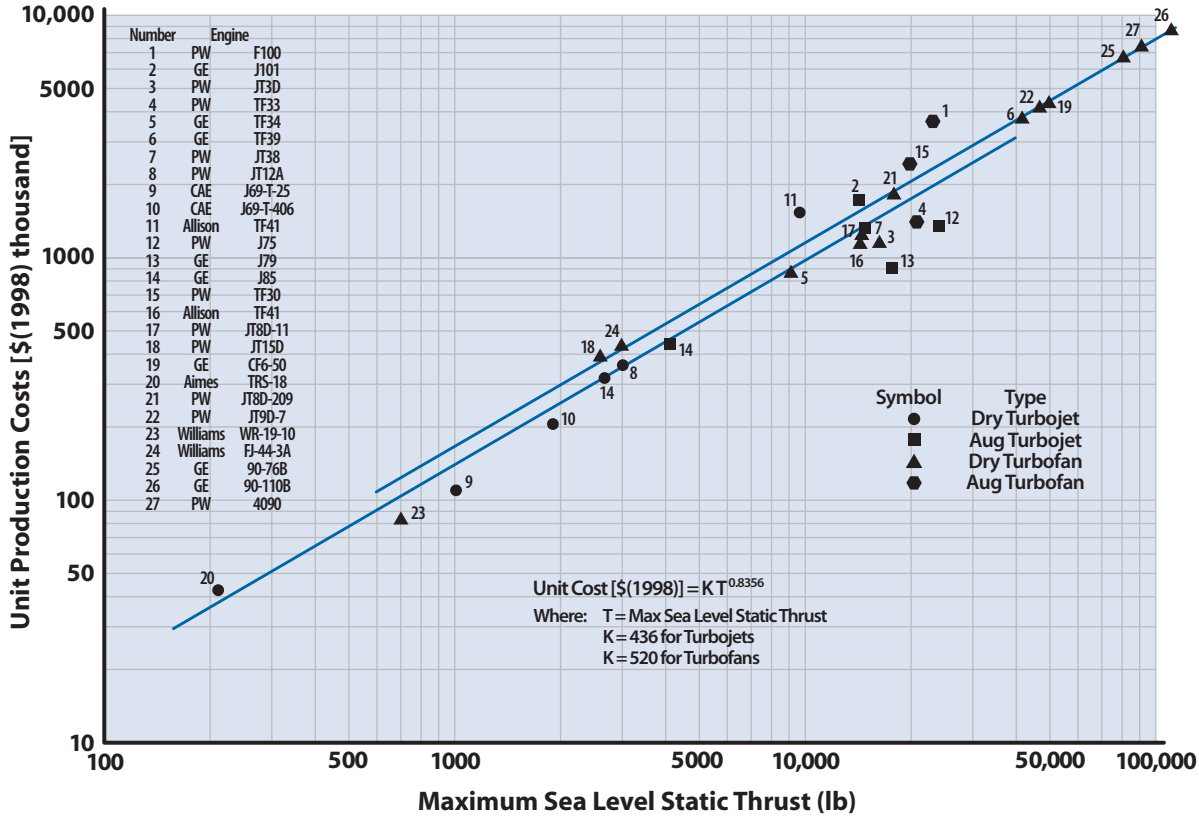


Figure 24.5 Engine production unit costs in 1998 dollars.

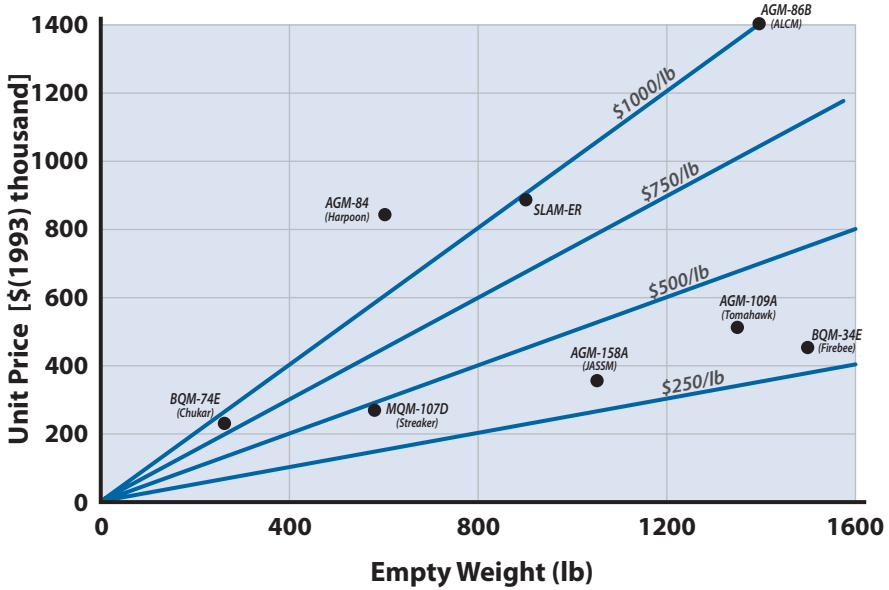


Figure 24.6a Unit prices for target and cruise missiles.

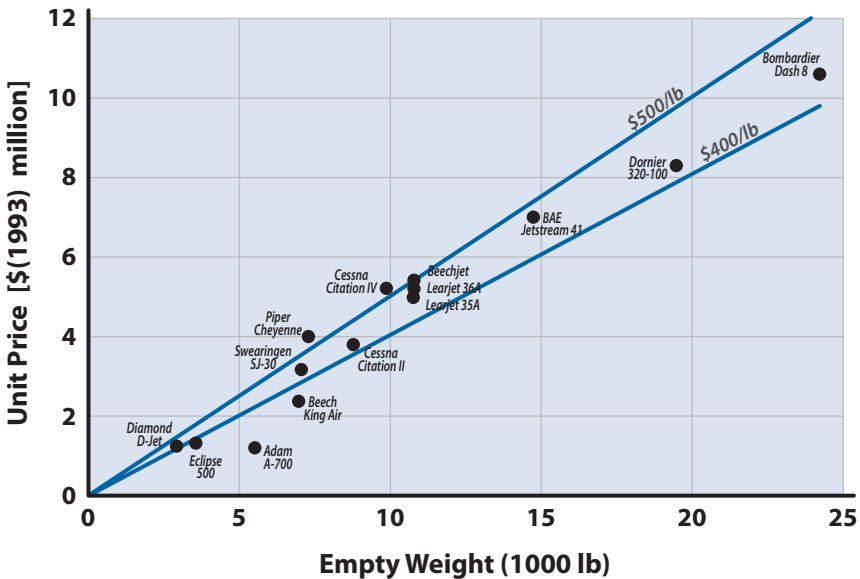


Figure 24.6b Unit prices for light bizjets and turboprop aircraft.



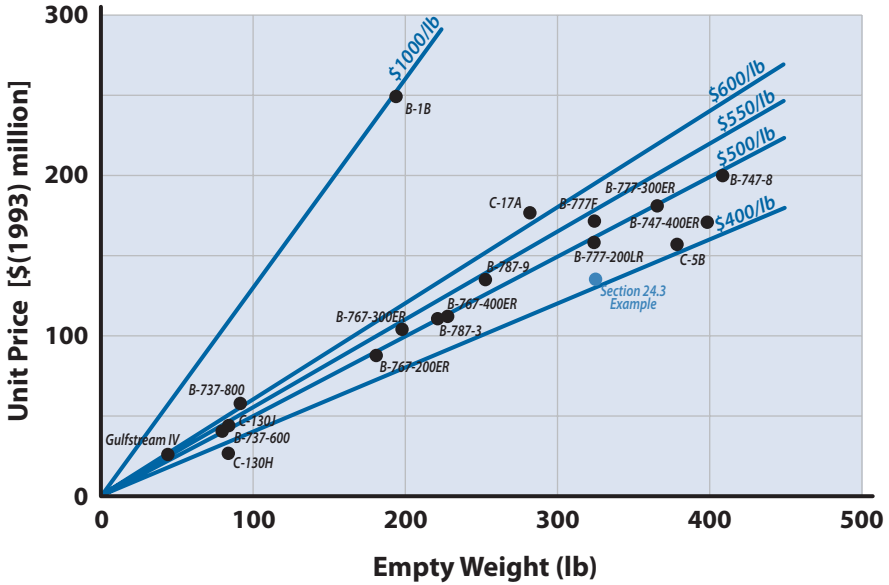


Figure 24.6c Unit prices for medium and large transports and bombers.

**Example 24.1 DT&E and Acquisition Cost of the Boeing 777**

Estimate the cost of the Boeing 777 (called the triple seven). It was designed and developed between October 1990 and October 1994. The first flight of the 777-200 was June 1994 and the aircraft became

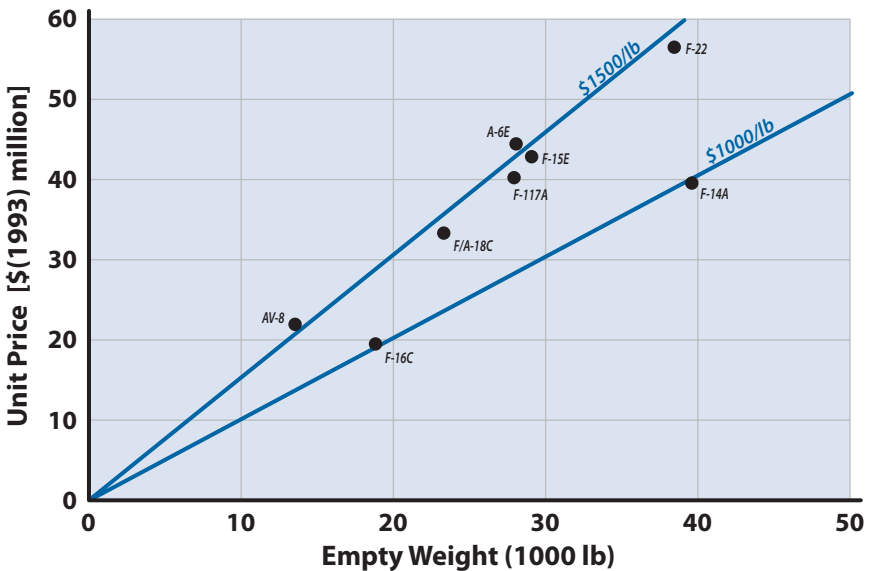


Figure 24.6d Unit prices for fighter aircraft.

operational with United Airlines in June 1995. The aircraft received its FAA and Joint Aviation Authority (JAA, the European FAA) certificates in April 1995.

The 777-200LR (LR for longer range) became the world’s longest unrefueled range commercial airliner when it entered service in 2006. In November 2005, a 777-200LR flew 11,664 n mile on a special flight from Hong Kong to London, a new world record. The aircraft can carry 440 passengers in an economy-class arrangement. The 777 family features a digital fly-by-wire flight control system, a supercritical airfoil on a wing swept 31.6 deg, 9% of the structural weight is composite materials, and the largest landing gear and tires ever used on a commercial aircraft. The aircraft was designed entirely on a computer. All design drawings were created on 3-D CAD software system known as CATIA. The aircraft was entirely “paperless.” As of November 2009 Boeing had delivered 816 aircraft in all models.

The information needed for developing the selling price for the 777-200LR is as follows (at this point it is recommended that the reader review the Boeing 777 case study in Volume 2):

Time frame for costing	1998
TOGW	766,000 lb
Empty weight	326,000 lb
Maximum speed	510 kt (Mach 0.89)
Engines	two GE 90–110B ( $T_{SLS} = 110,000$ lb)
Avionics cost	\$250,000 (estimated)
Flight test aircraft number	9
Production quantity for costing	500 units
Labor rates, dollars per hour (\$/h) for 1998	
Engineering $R_E$	\$88.85
Tooling $R_T$	\$94.23
Manufacturing $R_M$	\$75.37
Quality control $R_{QC}$	\$82.80

Engineering hours	
	$E = 4.86 W^{0.777} S^{0.894} Q^{0.163}$ (24.1)
Development	$Q_D = 9$ $E_D = 35,201,600$ h
Cost	\$3,127,664,790
Production	$Q_P = 500 + 9 = 509$ $E_P = 67,909,467 - 35,201,600 = 32,707,867$ h
Cost	\$2,906,093,988

Development support	
	$D = 66 W^{0.63} S^{1.3}$ (24.2) $D = \$666,235,760$
Flight test operations	
	$F = 1852 W^{0.325} S^{0.822} Q_D^{1.21}$ (24.3) $F = \$275,407,260$
Tooling	
Development	$T = 5.99 W^{0.777} S^{0.696} Q^{0.263}$ (24.4) $Q_D = 9$ $T_D = 15,718,000$ h
Cost	\$1,481,107,000
Production	$Q_P = 9 + 500 = 509$ $T_P = 45,419,128 - 15,718,000 = 29,707,000$ h
Cost	\$2,799,324,000
Manufacturing labor	
Development	$L = 7.37 W^{0.82} S^{0.484} Q^{0.641}$ (24.5) $Q_D = 9$ $L_D = 20,437,778$ h
Cost	\$1,540,395,000
Production	$Q_P = 9 + 500 = 509$ $L_P = 271,521,328 - 20,437,778 = 251,062,540$ h
Cost	\$18,922,583,650
Quality control	
Development	$QC = 0.13 L$ (24.6b) $Q_{CD} = 2,657,000$ h
Cost	\$219,992,000
Production	$Q_{CP} = 32,638,000$ h
Cost	\$2,702,431,000
Material and equipment, in 1998 dollars [\$(1998)]	
Development	$M = 16.39 W^{0.921} S^{0.621} Q^{0.799}$ (24.7) $Q_D = 9$ $M_D = \$544,418,700$
Production	$Q_P = 500$ $M_P = \$13,682,352,500$
Engine cost [\$(1998)]	
Engines	Maximum $T_{SLS} = 110,000$ lb
Unit cost	\$8,483,800 (from Fig. 24.5)
Development	Assume three per aircraft
Cost	\$229,041,000
Production	two per aircraft
Cost	\$8,483,000,000

<b>Avionics cost [\$(1998)]: \$250,000</b>	
Development	Cost = \$2,250,000
Production	Cost = \$125,000,000
<b>Total DT&amp;E cost [\$(1998)]</b>	
Airframe engineering	\$3,127,665,000
Development support	\$666,236,000
Flight test aircraft	\$4,017,204,000
Engines	\$229,041,000
Avionics	\$2,250,000
Manufacturing labor	\$1,540,395,000
Material and equipment	\$544,418,700
Tooling	\$1,481,107,000
Quality control	\$219,992,000
Flight test operations	\$275,407,000
Test facilities	\$0
Subtotal	\$8,086,512,000

If this were a contracted effort there would be a profit added onto the DT&E cost. Because this is a private company project there is no profit. Assume no special test facilities were built for this program.

This DT&E cost is amortized over some number of units. Assume it to be amortized over 250 units so that the price per aircraft will be increased by \$32,346,000.

<b>Total production and unit cost [in \$(1998)]</b>	
Engines	\$8,483,000,000
Avionics	\$125,000,000
Manufacturing labor	\$18,922,584,000
Material and equipment	\$13,682,353,000
Sustaining engineering	\$2,906,094,000
Tooling	\$2,199,324,000
Quality control	\$2,702,786,000
Manufacturing facilities	0
Subtotal for 500 aircraft	\$49,020,786,000

Assume for this discussion that there were no new manufacturing facilities needed for the production of the 777-200LR. This was not the case, as new facilities were built for the 777 family—but this information was not available for this example.

The unit cost is the total production cost divided by 500 aircraft plus the amortized cost: The unit cost = \$130.4 million.

The unit price is the unit cost plus the profit on each aircraft. Assuming a 15% profit the unit selling price is \$(1998)150 million. Boeing quotes a 2008 selling price for the 777-200LR of \$237.5 million. Adjusting our estimated selling price to 2008 dollars (using the economic escalation factors on Fig. 24.3) gives  $(260/200) = \$194$  million, or a 22% cost difference. In the world of cost estimating a difference of 22% is considered quite close.

### 24.3 Operations and Maintenance Phase

The O&M costs are based upon a period of operation, usually 10 years. A fleet size and number of flying hours (FH) per year are estimated.

The aircraft operating characteristics are known at this point so that an average fuel flow per hour, in gallons per hour, can be determined. At the time of this writing the fuel prices were in a state of random motion. The designer should obtain current and projected fuel prices from petroleum vendors and then determine the operating fuel costs. The oil and lubricant costs are less than 0.5% of the operating fuel costs and could be neglected in the total POL costs.

Each fleet of aircraft has a crew ratio that varies with the type of aircraft and the utilization rate. Table 24.1 gives information on crew ratios for different aircraft and annual flying rates. Salaries for these personnel are estimated and the aircrew costs determined.

The direct maintenance personnel costs are best determined using the *maintenance-man-hours per flying-hour* (MMH/FH). Table 24.2 gives MMH/FH for current aircraft. This ratio varies with the type of aircraft, the mission or sortie length, the utilization rate, and the years-in-service of the aircraft. The MMH/FH decreases with increased sortie length because the takeoffs and landings are harder on the aircraft than cruising flight. In addition, maintenance cannot be performed on a failed item until the aircraft lands; when the aircraft is flying it continues to accumulate flying hours.

**Table 24.1** Crew Ratio for LCC Planning

Aircraft Type	Flying Hours	Ratio
Transport	Less than 1200	1.5
Transport	1200–2400	2.5
Transport	2400–3600	3.5
Bomber	500	1.5
Fighter	500	1.1

Table 24.2 LCC Planning Data

Aircraft	Average Annual FH per Aircraft	MMH/FH	Year
Cessna 150/172		0.3	1974
Cessna Skywagon		0.5	1974
Beech Kingair		1.0	1974
Citation II		3.0	1988
T-37		7.8	1981
T-38	400	10	1981
T-39	600	9.8	1974
T-43	700	10	1974
F-5E	410	17	1981
A-7D	300	25	1974
A-10A	300	13	1984
F-14	314	48	1988
F-15C	302	22	1998
F-16C	346	19	1998
F-18C	360	18	1988
F-4E	302	33	1981
F-105G	316	58	1974
F-111D	280	40	1974
F-117A	—	113	1983 (IOC)
F-117A	—	45	2003
F-22A	316	10.5	2009
B-2A	—	124	1997 (IOC)
B-2A	—	51	2002
B-2A	—	32	2004
C-17	780	24	2005
C-17	780	20	2007
C-17	780	16	2008
C-5B	716	58	2005
C-5B	716	41	2007
C-5B	716	33	2008
C-130E	720	20	1974
C-141B	1080	21	1981
B-52D	424	37	1981
B-52G	516	49	1981
B-58A	430	54	1974
KC-135	377	27	1974
L1011	1870	14.1	1981

(continued)

Aircraft	Average Annual FH per Aircraft	MMH/FH	Year
DC-10-10	2450	11	1981
B727-100	2670	8	1974
B727-200	2800	6.5	1974
B737-200	2200	6.6	1974
B747	3525	14.5	1981
B757	3010	9.1	1998
B767	3010	11.4	1998
B777	3010	10.2	1998
SR-71	260	~400	1981

Data sources:

General Aviation—Cessna and Beech Aircraft

Military—AFM-173-10, 3M data and U.S. Air Force and U.S. Navy maintenance records

Commercial—CAB Form 41, Boeing Airplane Co.

Blackbird—Lockheed SR-71 Researcher's Handbook

Notice the big difference in annual flying hours for the military and commercial. This is because the commercial aircraft are losing money when they are sitting on the ground. Thus, the commercial aircraft average about 14 hours in the air each day for the long-range transports and 10–12 hours for the shorter route aircraft. In the military each pilot needs about 260 flying hours per year to stay proficient. Using the crew ratios from Table 24.1, this gives about 300 h for fighters and 400 h for bombers per year, or about one hour per day.

The *utilization rate* (flying hours per period of time) also affects the MMH/FH. This reduction in man-hour requirement with increased utilization can be explained as follows. Aircraft systems, used daily, normally receive better upkeep and experience fewer failures per flight hour. Also, aircraft that fly frequently are on the ground less time and require maintenance to be accomplished in a limited amount of time. Because of this pressure, maintenance is accomplished more efficiently and frequently by personnel with higher skill level. Maintenance personnel can more easily retain knowledge of failures and maintenance accomplished the day before, hence there is better continuity between maintenance tasks [3].

The MMH/FH are not static but vary with the point in the aircraft's service life. The MMH/FH decreases from the initial deployment to a point where the aircraft is a mature, well-understood member of the fleet and then starts increasing as the aircraft begins to wear out. Two good examples are the F-117A and B-2A. Both aircraft had a very high MMH/FH at initial operational capability (IOC) due largely to the new stealth technolo-

gies on the aircraft. As the maintenance crews became familiar with the aircraft and the new low-observable (LO) materials the MMH/FH dropped dramatically.

The data in Table 24.2 are for typical sortie lengths and several years-in-service. The maintenance personnel costs are determined from an estimated MMH/FH, the maintenance personnel hourly rates and the annual flying hours.

## 24.4 O&M Costs

The elimination of peacetime flying (or at most minimal flying) would result in a large O&M cost saving for a UCAV relative to a manned fighter squadron. The following example is notional and is used to develop values for the various O&M cost elements. The example indicates that the cost savings in annual O&M for the UCAV could be greater than 80%. This O&M cost saving needs to be quantified with a careful and thorough study that examines the peacetime training (of both operators and ground crew) and the design impact of long-term flyable storage.

### Example 24.2 Comparison of O&M Costs for Manned and Unmanned Tactical Fighter Squadrons

Manning of a 24-aircraft UCAV squadron is shown in Table 24.3 and compared with a 24-aircraft F-16C squadron. Both squadrons are air-to-ground strike/SEAD (suppression of enemy air defenses) units. The costs shown are annual O&M during peacetime. The number of officers (primarily pilots or remote operators) is about the same for the two squadrons, but the number of enlisted personnel doing maintenance and support is very much less for the UCAV squadron. The UCAVs would be stored in a humidity-controlled, flyable storage facility. To ensure readiness, four UCAVs would be taken out of storage each year and flown for manned aircraft interface and maintenance–support crew training. The total squadron flying hours would be about 140. In contrast, a 24-unit F-16 squadron would fly about 8300 h each year. The composition of the enlisted personnel are 15 ground support crew (6 weapons handlers, 7 vehicle support, 1 chief, and 1 administration), 10 technicians (ground control station and associated avionics maintenance), and 7 administration and support. During wartime the active duty ground support crew would be augmented by 4 reserve crews to support a tempo of four sorties per day for 30 days. During peacetime the active-duty ground support crew would train the 4 reserve crews, support the limited UCAV flying, and maintain the aircraft in flyable storage.



**Table 24.3** UCAV Peacetime O&S Cost Compared with an F-16C Squadron  
[\$(2002)Million]

F-16C Annual O&S (per AFI 65–503)		UCAV Annual O&S (per modified AFI 65–503)	
Unit personnel (42 off./307 enl.)	\$15.7M	Unit personnel (30 off./32 enl.)	\$3.6M
Fuel for 8300 flying hours	5.5M	Fuel for 140 flying hours	0.09M
Base support personnel	10.1M	Base support personnel	1.4M
Depot maintenance	6.7M		
Training and personnel acquisition	5.3M	Training and personnel acquisition	0.69M
Replenish spares	6.6M		
System support and mods.	4.3M	System support and mods.	0.66M
Munitions and missiles	1.2M		
<b>Total</b>	<b>\$55.4M</b>		<b>\$6.44M</b>

## 24.5 Design for Reduced Cost

The designer must recognize and appreciate the fact that he has a powerful influence over the life cycle cost of an aircraft system. The major portion of the LCC is locked in at the conceptual and early preliminary design phases, because it is during these early design phases that the aircraft is taking on its shape and size. Once the design is in preliminary design, details are being fine tuned and all the gross features, good and bad, are already locked in. This argument was presented in Fig. 1.16 and will be developed in the following paragraphs.

The designer influences the RDT&E costs directly by the choice of new technologies to be incorporated in the new design. The selection of new technologies that are not quite mature (i.e., ready for system application) can cause this cost to skyrocket. The F-111 is an example of incorporating new technologies that needed more research before moving them into the DT&E phase. The F 111A cost for development support and engineering was more than any other U.S. Air Force production fighter. The technologies should be fully demonstrated and validated before putting them on a new aircraft.

### 24.5.1 Design for Production

The key to reducing production costs is to reduce the “touch labor.” The designer has more influence over this than any other person. Some design guidelines for reducing production costs are as follows:

1. Minimize the part count; this in turn reduces the tooling, fabrication, and assembly time, which reduces touch labor.
2. Standardize left and right tooling; this is another way to keep the part count down. Examples would be interchangeable right and left ailerons, main landing gears, and horizontal tails.
3. Require structural parts to perform multiple functions. An example would be the main landing gear mounted to the wing carry-through structure.
4. Use large unitary pieces of structure rather than build up the structure from many smaller pieces. This reduces touch labor and is oftentimes the rationale for using composites (large co-cured pieces) rather than metal built-up parts.
5. Minimize complex checkout.
6. Combine engineering and quality testing.
7. Use simple curvature shapes; the use of compound curvature surfaces greatly increases the tooling and fabrication time.
8. Use simple and common parts; use parts that are common to other aircraft such as landing gears, crew furnishings, and equipment.
9. Use state-of-the-art materials and structures design; this means the use of technology demonstrators during the research phase to fully develop and validate materials and structural concepts before committing them to the aircraft.
10. Use proven engines and inlet–nozzle configurations.

The overall design rule is “Keep It Simple.”

### 24.5.2 Design for O&M

The best thing that a designer can do for reduced O&M costs is to design for quick and easy access to everything. This is difficult and it means a far from optimum packaging in the fuselage and wings. However, a slightly larger and roomier fuselage, although weighing more and giving lower performance, will pay for itself in reduced MMH/FH. The MMH/FH is a direct function of accessibility (getting to the faulty or suspicious item), complexity of the system, and ease of component removal. The designer should recognize that

- Avionics equipment is always going to need attention
- Hydraulic systems are going to leak
- Fasteners are going to “unfasten”
- Mechanisms are going to wear out and/or need adjusting

so design for the situation. The location of most of the components and the roominess of the equipment bays are locked-in by the conceptual and early preliminary design.

The early McDonnell F-4s had some communications avionics located beneath the rear seat. Every time the communications gear needed adjusting (which was about every 3 sorties) the rear ejection seat needed to be removed and then replaced. This poor design added 2.3 maintenance hours just to gain access to the avionics equipment [7]. A tightly packed fuselage might be elegant from a design viewpoint but it is a nightmare for the ground crew as they often have to remove good equipment just to gain access to a faulty piece of equipment. A good design rule is to only package equipment “one deep.”

The McDonnell F-4 and F-15 are aircraft of similar size and weight. The F-15, designed in the early 1970s, emphasized reduced MMH/FH. The primary design solution was to improve the accessibility of the F-15 over that of the F-4. The result was 570 ft<sup>2</sup> of access doors and panels on the F-15 compared with 55 ft<sup>2</sup> on the F-4. This feature was largely responsible for the MMH/FH being reduced from 33 for the F-4 to 22 for the F-15.

The painful compromise that a designer must make between performance and cost must surely be evident by now. It is paramount that the designer appreciate the importance of cost, otherwise Calvin Coolidge’s recommendation of “buy one aircraft and let the aviators take turns flying it” may someday become a reality.

## References

- [1] “LCC Breakdown,” *Aviation Week and Space Technology*, 22 Oct. 2007, p. 23.
- [2] Reel, R. E., Totey, C. E., and Johnson, W. L., “Weapon System Support Cost Reduction Study (U),” Aeronautical Systems Div., Deputy for Development Plans, ASD /XR Rept. 72-49, Wright-Patterson AFB, OH, June 1972.
- [3] Johnson, W. L., and Reel, R. E., “Maintainability/Reliability Impact on System Support Costs,” U.S. Air Force Flight Dynamics Laboratory, AFFDL/PTC, AFFDL-TR-73-152, Wright-Patterson AFB, OH, Dec. 1973.
- [4] Hess, R. W., and Romanoff, H. P., “Cost-Estimating Relationships for Aircraft Airframes,” Rand Rept. R-3255-AF, Rand Corporation, Santa Monica, CA, Dec. 1987.
- [5] Levenson, G. S., Boren, H. E., Tihansky, D. P., and Timson, F., “Cost Estimating Relationships for Aircraft Airframes,” Rand Rept. R-761-PR, Rand Corp., Santa Monica, CA, Dec. 1971.
- [6] Large, J. P., “Estimating Aircraft Turbine Engine Costs,” Rand Corp. Rept. RM-6384/1-PR, Sept. 1970.
- [7] “R&M Proof,” *Aerospace Daily*, Vol. 135, No. 15, 23 Sept. 1985, p. 113.

# Chapter 25 Trade Studies and Sizing



- Trade Studies
- Carpet Plots
- Knothole Plots
- Risk Assessment
- Risk Mitigation
- Kelly's 14 Rules

Kelly Johnson was perhaps the greatest airplane designer of the 20th century. His legendary designs included among many others the P-38, XF-90, F-94, F-104, F-117A, C-130, U-2, SR-71, and D-21 drone. His famous 14 rules of management were the forerunners of "concurrent engineering" and are summarized at the end of this chapter.

*Be quick, be quiet, and be on time!*

Clarence "Kelly" Johnson

## 25.1 Introduction

**A**re we done yet? The answer is No. We have essentially completed one iteration for a baseline configuration as shown in Fig. 25.1. The design may meet the mission requirements, or exceed some and fall short on others. In any event the designer, being very close to the design, has definite feelings on what should be changed to make the design better. The designer is now ready to start another iteration, hoping to make the estimates of aerodynamics, weight, propulsion data, and performance more refined.

There are three major trade studies shown in Fig. 25.1 that the designer needs to conduct:

1. **Design.** Helps the designer select the best combination of design features to meet the measures of merit (MoM)
2. **Mission.** Indicates the sensitivity of the baseline design to changes in the mission requirements
3. **Technology.** Indicates the sensitivity of the baseline design to the selected technologies and forms the basis for the risk assessment

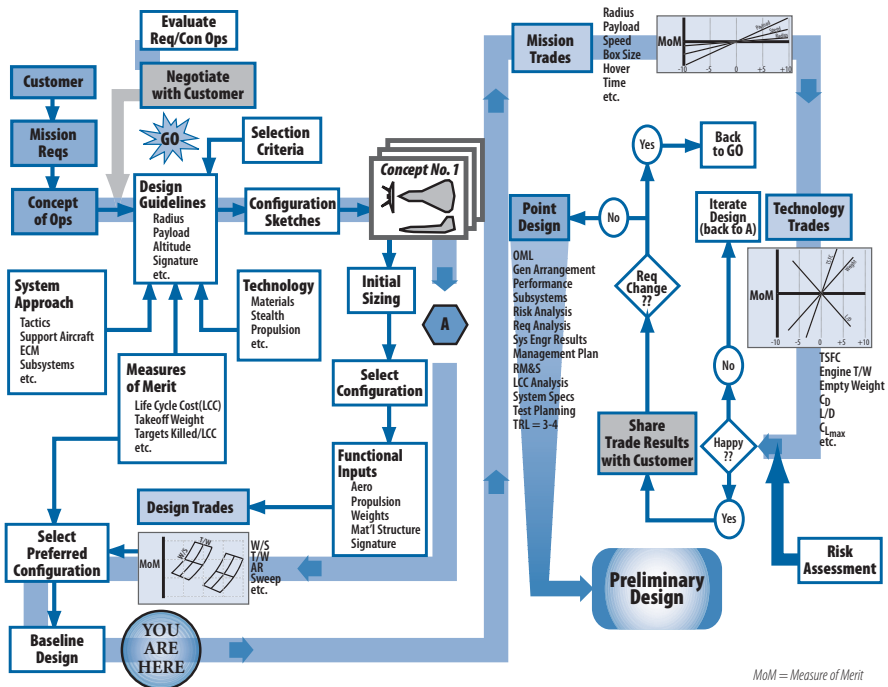


Figure 25.1 What happens after the first design iteration?

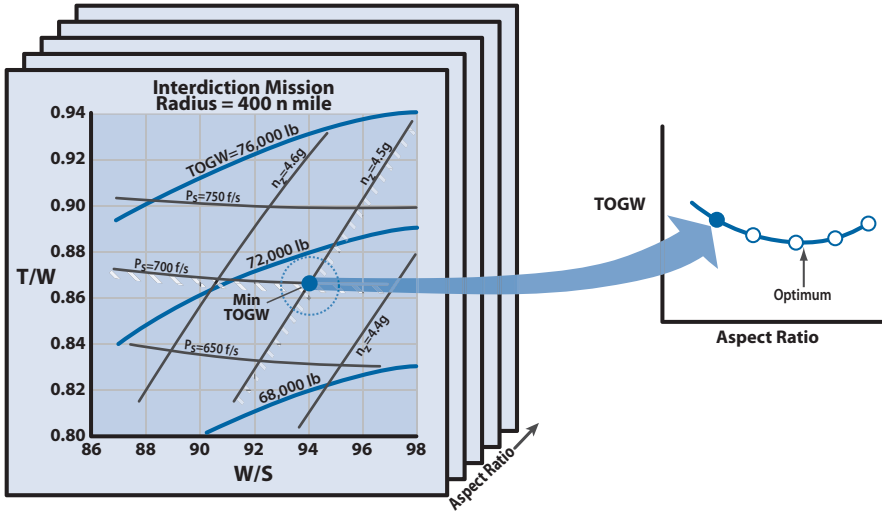
The results of the trade studies are extremely important as they indicate the sensitivity of some measure of merit to changes in the design parameters, mission requirements, and technologies. These measures of merit are usually one or more of the following:

- **Takeoff weight.** Indicates the general vehicle size and hence cost and energy requirements
- **Cost.** The total life cycle cost (LCC) over a fixed period such as 10 years; tradeoff between RDT&E, acquisition, and O&M costs
- **Energy.** Total fuel required for mission
- **System effectiveness.** Some parameter that combines performance, cost, and/or energy, such as the following:
  - Return on investment (ROI)
  - Bombs on target per hour per dollar
  - Kill ratio per aircraft dollar
  - Survivability
  - Transport direct operating cost (DOC)
  - Energy effectiveness parameter

## 25.2 Carpet Plots and Knotholes

The number of variables that might be considered in a tradeoff study may be less than 10 or more than 50. The designer has the difficult task of sorting through all combinations in a systematic fashion to find the best combination. These data should also be used to visually explain why certain design decisions were made so internal and external managers understand why the final design looks the way it does. Sometimes the designer might want to display several parameters on the trade study charts.

Figure 25.2 shows an example of examining the three design variables  $T/W$ ,  $W/S$ , and aspect ratio (AR). The mission requirement calls for a deep strike interdiction fighter with a payload of 4500 lb and a mission radius of 400 n mile. The fighter also has the acceleration requirement of  $P_5 = 700$  fps at  $M = 1.6/35,000$  ft and a maximum sustained maneuver load factor of  $4.5 g$  at  $M = 0.9/20,000$  ft. The takeoff gross weight (TOGW) is the measure of merit for this example. The AR is held constant and the  $T/W$  and  $W/S$  are iterated to give the minimum TOGW vehicle that just meets the mission. The design cycle is then repeated for other values of AR. The minimum TOGW for each AR is then plotted versus AR to find the best AR for the interdiction fighter. Admittedly, the computer must be used to perform the design iterations; however, the designer is in the loop to assess the results and make the final design selection. The computer cannot be asked to select the final design as some measures of merit are qualitative and will often change with time. The designer must be aware of this and

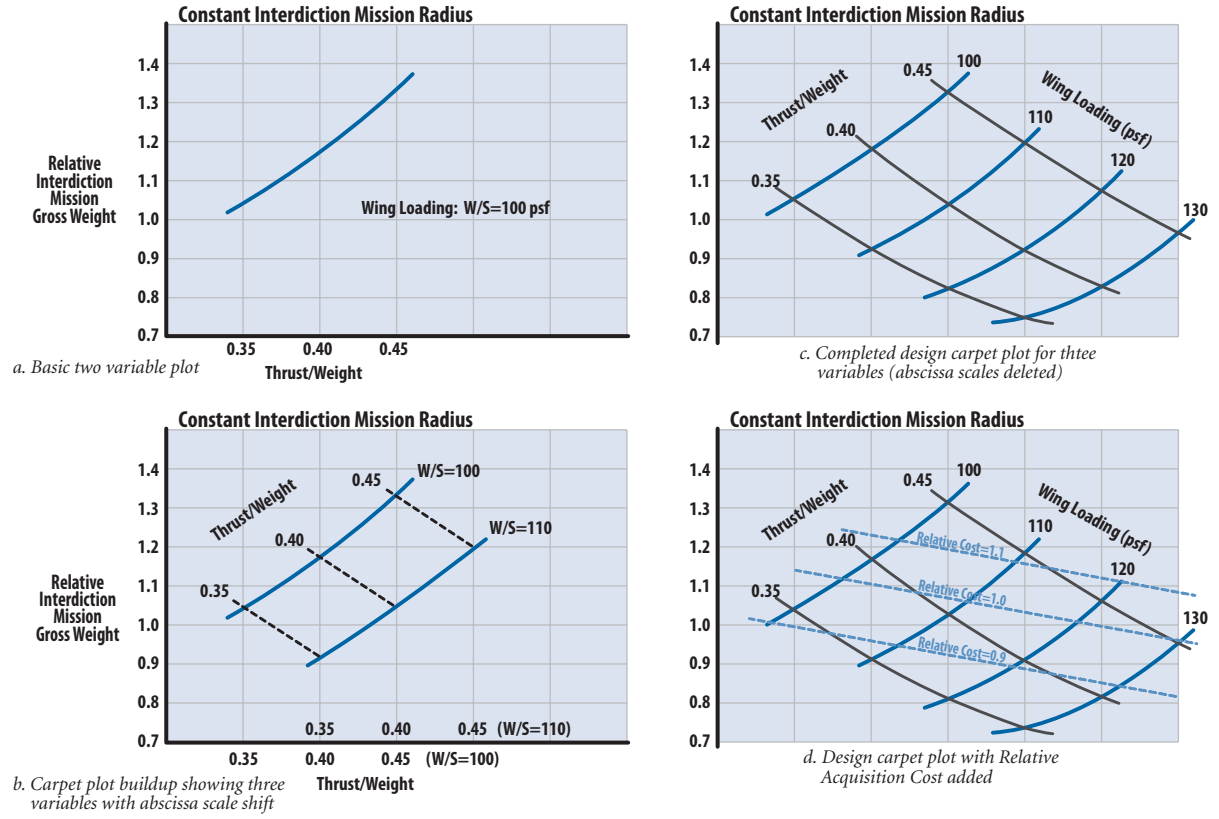


**Figure 25.2** Parametric tradeoff showing a three-variable example of wing loading, thrust-to-weight ratio, and aspect ratio.

project into the future as best as he can. Alan Mullaly (Project Manager for the Boeing 777 and later Boeing CEO) said it best: “Planes are made by people not computers [1].”

Sometimes during a parametric trade study, the data on the charts become dense and tend to overlap. This makes interpolation difficult. One way of spreading the data of more than two variables apart for better visibility and still providing direct interpolation is to present the data on *design carpet plots*. A design carpet plot buildup is demonstrated in Fig. 25.3 using a Navy multimission fighter–attack aircraft.

Figure 25.3a shows the relative interdiction mission gross weight required to fly the desired radius with a constant  $W/S$  of 100 psf, with  $T/W$  varying from 0.35 to 0.45. The relative gross weights required to fly this constant radius interdiction mission at other wing loadings can be presented by shifting the abscissa and plotting a second wing loading on the new shifted scale as shown in Fig. 25.3b. Additional wing loadings can be added in the same manner and points of constant  $T/W$  are connected to form a final design carpet plot as shown in Fig. 25.3c, where the abscissa scales have been eliminated. By interpolation between the curves the relative interdiction mission gross weight can be determined for any combination of  $W/S$  and  $T/W$ . Other information could be presented in Fig. 25.3c by superimposing lines of constant design characteristics. For example, Fig. 25.3d shows lines of constant relative acquisition cost. Other design constraint lines can be added such as approach speed, takeoff field length, and airport noise.



**Figure 25.3** Example of design carpet plot buildup for a Navy multimission fighter.



The trade space data just discussed can also be presented in a format that is capable of illustrating an entire trade study on a single plot. This plot is called a *knothole* based on its usual form. Figures 25.4 and 25.5 summarize the entire process used to create a complete “knothole” for a commercial transport. The benefits of putting the data in this format are that it clearly communicates where the optimum design point is and what constraints are preventing the optimum from being selected. The extra work

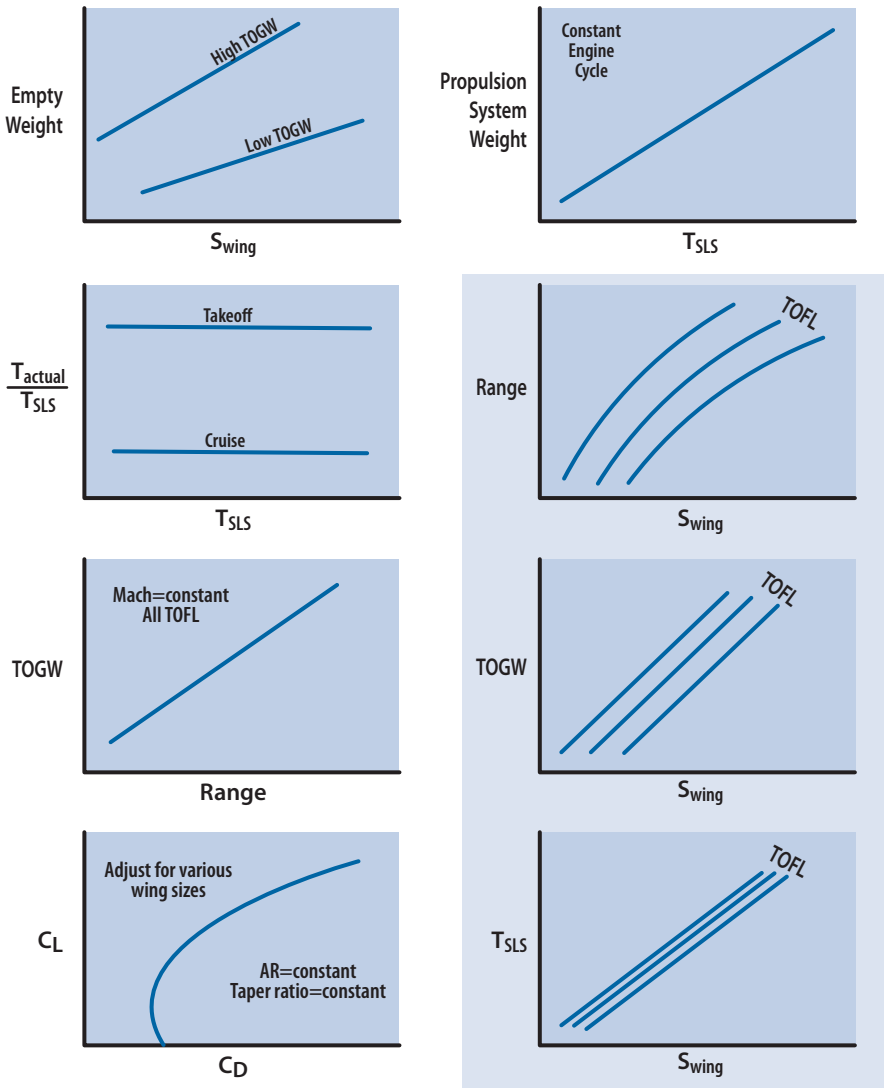
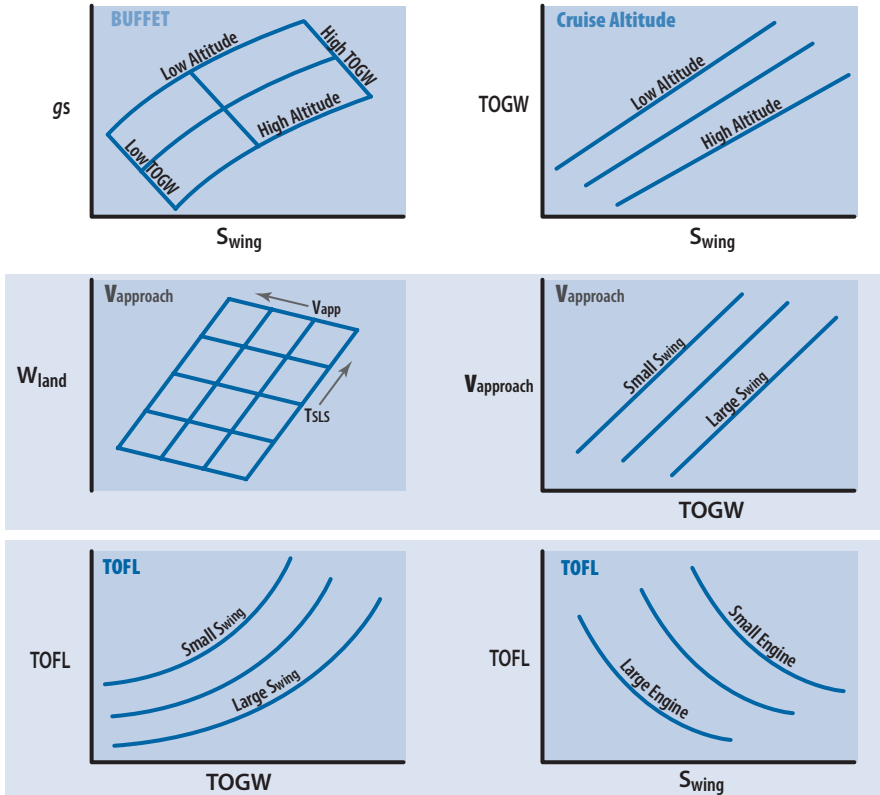


Figure 25.4a Performance trade results used to construct “knotholes.”



**Figure 25.4b** Performance results needed to draw constraint lines on “knotholes.”

involved to generate this plot is repaid many times over because it distills numerous technical issues into a form that is easily understandable by customers, management, and nontechnical program personnel.

The included example is for defining an optimum large-scale commercial transport that has a size somewhere between an L-1011 and a B-747. Figures 25.4a and 25.4b summarize all of the data that must be accumulated. This data is a mix of experimental, analytical, and sometimes “best guess” information. The data plots are unique to a commercial transport and differ significantly from that of a military fighter or bomber. Here the constraints were noise, buffet, approach speed, and takeoff and landing field lengths. The final knotholes are shown in Fig. 25.5 and present that data in two different ways. One plot holds range constant and shows rings of constant TOGW. The other is for a constant TOGW and shows rings of constant range. This entire study assumed a constant wing aspect ratio of 8.0.

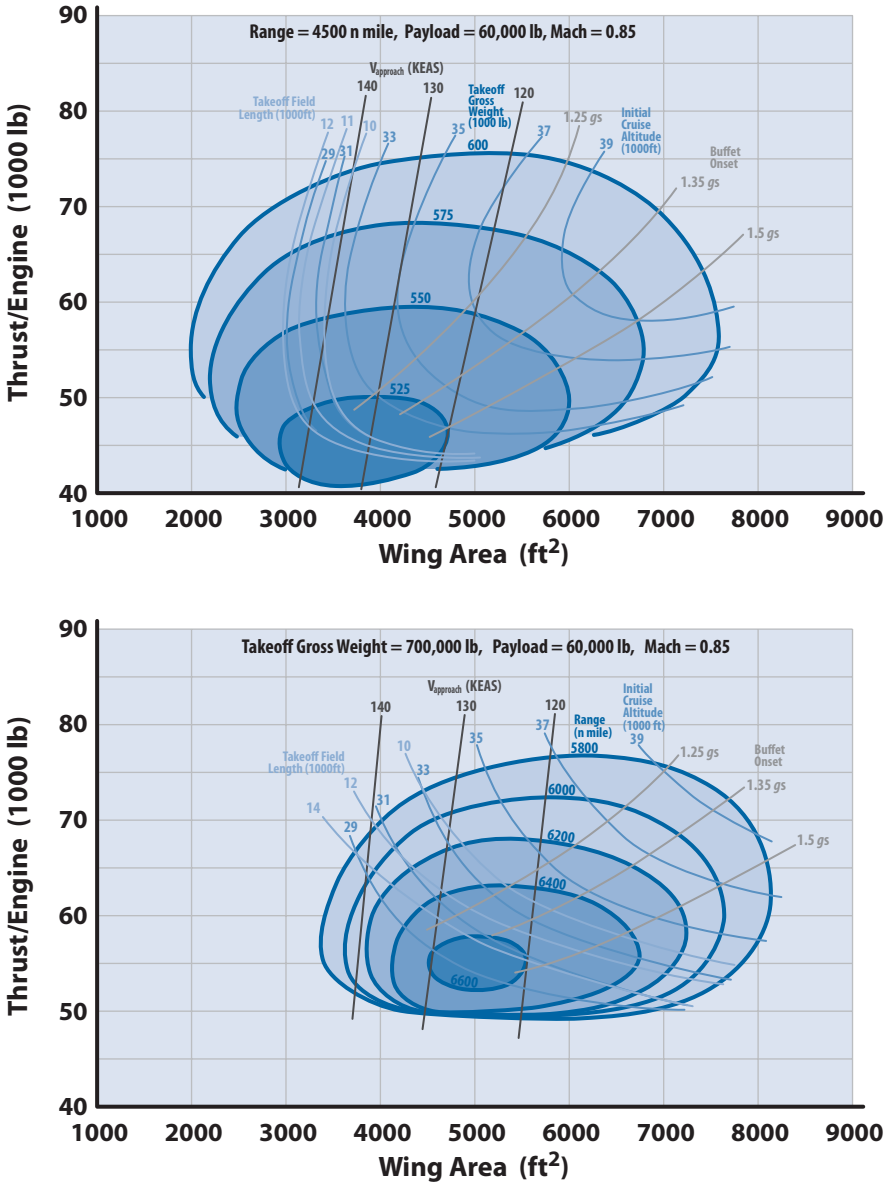


Figure 25.5 Parametric trade study results presented as “knotholes” (commercial transport).

These knotholes used  $T/W$  and  $W/S$  for the axes, but for studies where the engine is known and the wing planform is also known the axes will become  $T$  (thrust) and  $S$  (wing area). The process is identical.

Some words of caution when generating knotholes are appropriate at this point. First, knotholes take extra time to generate so they must be

useful for communicating outside the technical study group. If the results are only going to be used by technical groups, then the carpet plots in Fig. 25.2 will likely suffice. Second, drawing the entire ring can be difficult particularly on the low wing loading and low thrust/weight edges. Solutions will blow up for very slight changes, making a little “artistic license” necessary for the final shapes. In the end knotholes offer a means to concisely summarize large amounts of carpet-plotted data in an easily understood form.

To illustrate that knotholes can look vastly different depending on the type of air vehicle that is being studied, Figure 25.6 is presented without discussion but represents a small autonomous UAV that has a portable ground control station. It is similar yet very different from the commercial transport knothole in Fig. 25.5.

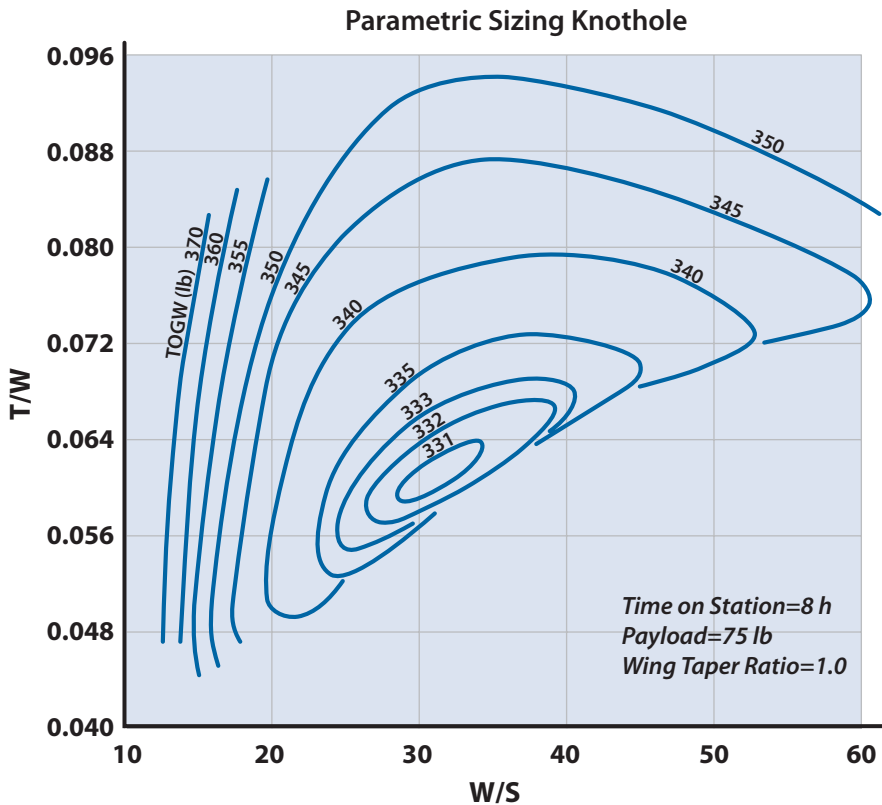


Figure 25.6 Parametric sizing study for Class III UAV.

## 25.3 Design Trades

The tradeoff information is used to select the proper combination of design features to achieve the most efficient vehicle relative to the measure of merit criteria. Some of the design parameters that are often varied during a parametric study are the following:

- Body shape (fineness ratio, nose shape, cross-sectional area distribution)
- Wing size and wing loading
- Wing shape (sweep, aspect ratio, taper ratio, thickness ratio, variable versus fixed geometry)
- High-lift devices (mechanical vs powered)
- Tail configuration (aft tail, canard, or tailless)
- Stability level (degree of static margin)
- Engine [ $T/W$ , number of engines, bypass ratio, fan pressure ratio, overall pressure ratio, turbine temperature, propulsion concept (turboprop, turbofan, turbojet, etc.)]
- Inlet or nozzle (location, type of inlet, type of nozzle)
- Materials (metals vs composites)

Figures 25.3–25.6 show examples of design trades.

## 25.4 Mission Trades

Mission requirements are usually fixed by the customer; however, they should be considered negotiable and forcefully challenged when they distort the design. The designer has the responsibility of pointing out the

### Nontechnical Issues Can Drive Technical Decisions

Sometimes technical decisions are made based on nontechnical events. In 1987 the YF-22 design team (Lockheed, Boeing, and General Dynamics) was conducting design trades to select the best wing (planform, sweep, aspect ratio, and span) for their advanced tactical fighter (ATF) prototype. The clipped diamond planform won out over the swept trapezoidal planform (even though the “trap” wing had more aspect ratio) because it offered more wing area at a lighter structural weight (more root chord). The 48 deg LE wing sweep was a compromise between supersonic drag and subsonic aero performance. The 43-ft wing span was selected (even though it had a low aspect ratio of 2.2) because the width of the door on the TAB-V aircraft shelters was 45 ft. The wing span on the production F-22A was increased to 44.5 ft and sweep decreased to 42 deg to increase the aspect ratio to 2.4.

sensitivity of the aircraft design to the mission requirements. If one mission requirement, such as range, is driving the aircraft design to large takeoff weights (and hence high cost) the designer should advise the customer of this situation. The customer might choose to back off on the performance requirement to bring the cost down to an affordable level. The designer should provide mission requirement tradeoff information to the decision makers to permit the best compromise between performance and cost. Thus, the mission requirements of range, payload, turning performance, field length, and so on are typical candidates for the mission requirements trade study.

This trade is briefly discussed in Chapter 5, where the composite Light-weight Fighter (LWF) was sized.

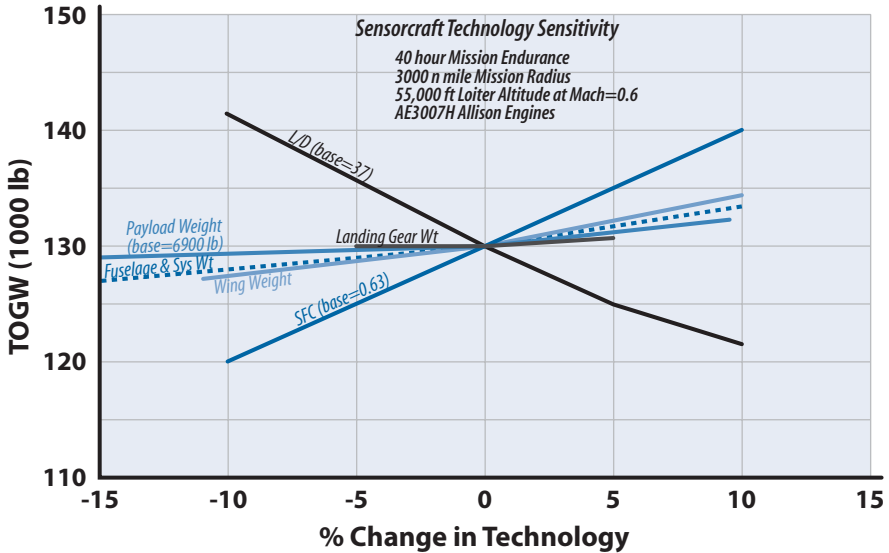
## 25.5 Technology Trades

The results of a technology trade are used in two different ways by different groups:

1. The results are used by the program community to form the basis for a risk analysis as it answers two very important questions: What is the consequence (on the MoM) of the technology failing to perform as expected and what is the probability of the technology not performing as expected?
2. The results are used by the technology planners to form the basis for technology investment decisions as they show the payoff for spending research dollars on maturing the technology.

An example of a technology trade is shown in Fig. 25.7. The example is an intelligence, surveillance, and reconnaissance (ISR) aircraft (called SensorCraft) with the mission requirements shown on the chart. SensorCraft uses the off-the-shelf (OTS) engines AE 3007H and the aircraft TOGW is 130,000 lb using state-of-the-art technologies. The technologies are allowed to improve or degrade and the sensitivity of TOGW is determined. The change in the TOGW is the consequence of failure (or success) of the technology. The technology community would be asked to assess the probability of technology failure (or success).

The technology trade study shows that aircraft  $L/D$  and engine thrust specific fuel consumption (TSFC) have the most impact on the aircraft TOGW: both have a  $\Delta\text{TOGW}/\Delta\%$  change =  $-1000$ . Getting a +5% improvement in TSFC is probably expensive, otherwise Allison (Rolls Royce) would have done it long ago. Similarly the TSFC is not likely to degrade because the AE 3007H is a mature engine in the Global Hawk. Thus, it is probably unwise to invest dollars in the AE 3007H. Likewise, there is little concern about the TSFC degrading (low probability of failure). On the other hand



**Figure 25.7** ISR aircraft technology trade results.

dollars might be invested in improving the  $L/D$  (more laminar flow, winglet, and airfoil research) and be concerned about degraded  $L/D$  (high probability of failure) due to losing laminar extent on the wing. The trade study shows that reducing aircraft structural and system weight has less impact on TOGW and the technology community would probably agree that it is harder to achieve.

## 25.6 Risk Analysis

Risk is an increasingly popular topic in the aerospace industry because there is risk in every decision that is made [2]. Choosing between configurations that have similar performance could prove to be easy if their respective risks were quite different. Folding in risk to conceptual and preliminary design efforts adds another element to consider when making engineering choices. Understanding potential risks early in the program is important but there needs to be an objective means of assigning risk to unfavorable program events. Assigning risk allows customers and management to better understand how the engineering group plans on maturing technologies that are part of a selected design and the priorities of each risk.

Quantifying risk uses relationships from probability and set theory as its mathematical basis (see [3]). Risk is simply defined mathematically as the union of failures and impacts or the probability of occurrence of unfa-

favorable events. A *failure* is an unfavorable event and an *impact* is an unfavorable event that follows a failure; an impact may also be a failure. Risk has two major components. The first is the probability that the item will fail (Pf) (or likelihood that the failure will occur, Lo) and the second is the consequence (impact) of that failure, Cf (or the consequence of occurrence, Co). The terms Pf and Cf are considered to be too negative and so, popular usage has replaced them with their equivalents Lo and Co. These two parameters are mathematically combined (based on set theory) in Eq. (25.3) to yield a single number, generally referred to as the *risk index*, that represents the total risk of that item. Generally, Co is broken into its three parts representing (technical, schedule, and cost). Scoring the three components of Co can be combined using the same set theory mathematics to yield a single value for Co ([see Eq. (25.2)]. Once Co is calculated then Eq. (25.3) can be used to obtain the *Risk Index*. Both equations depend on Eq. (25.1) realistically representing the risk of any system. Table 25.1 shows a sample calculation of the total system risk based on the individual risks of each of its components. Notice how high the total risk index is. Managers and engineers often underestimate the aggregate risk of numerous items when assigning a total system risk:

$$\text{Risk(Overall)} = A \cup B - A \cap B = Lo \cup Co - Lo \cap Co \tag{25.1}$$

$$\text{Risk(Consequences, Co)} = P(C_T) \cup P(C_S) \cup P(C_C) \tag{25.2}$$

where

$P(C_T)$  = probability of the consequence from technical failure

$P(C_S)$  = probability of the consequence from schedule failure

$P(C_C)$  = probability of the consequence from cost failure

$$\text{Risk Index (RI)} = Lo + Co - Lo \cdot Co \tag{25.3}$$

**Table 25.1** Sample Risk Calculation

Component No.	Lo	Co	Risk Index
1	0.3	0.2	0.44
2	0.2	0.2	0.36
3	0.4	0.3	0.58
4	0.6	0.1	0.64
5	0.1	0.4	0.45
<b>TOTAL =</b>	<b>0.879</b>	<b>0.758</b>	<b>0.971</b>



Although the mathematics is appealing and objective, many system engineers assess risk in other ways. However, any other mathematical technique is clearly inferior to the set theory approach. Many engineers use a nonmathematical technique that ultimately ends up with risk simply having a value of low, moderate, or high. This approach will be discussed next.

In the non-mathematical approach a risk matrix is used to determine the overall Risk Index value. Although this matrix can vary from user to user, Fig. 25.8 is a good representative of this matrix. The 5 ratings of Lo and Co must have agreed-upon definitions (see Fig. 25.9) so that they are consistent across the program and independent of the person(s) giving the rating. Once Lo and Co (remember Lo and Co are probabilities with values from 0 to 1) ratings have been assigned they are located on the matrix and will end up in the low, moderate, or high category. General rules state that any item that is high risk must have a mitigation plan and a backup plan in case the original plan fails. Any item that has moderate risk must have a mitigation plan. Items that are low risk are just watched to make sure their risk does not change over the course of the program. Some managers will also use the results of risk assessment to allocate resources. Obviously, there is a relationship between the amount of risk (i.e., difficulty) and the cost of mitigating or maturing that risk.

The final result of these risk identification and assessment processes becomes a risk mitigation chart (waterfall chart) that shows the amount of risk reduction (mitigation) as a function of time. Figure 25.10 illustrates the relationship between risk assessment and risk mitigation.

It is a good time to reflect on how individuals assign risk to systems containing numerous components. Which system has more risk, (1) a

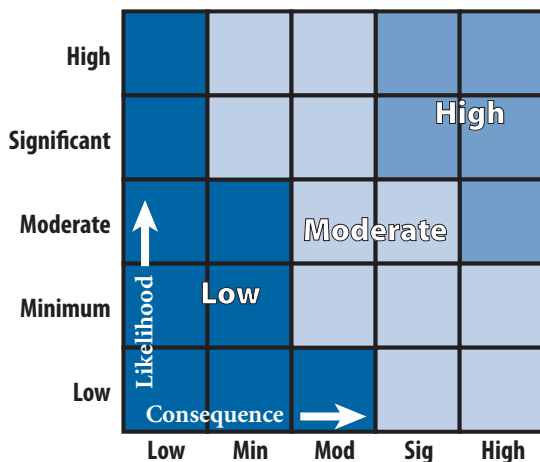


Figure 25.8 Risk assessment matrix.

Risk Assessment Template—Performance				
Likelihood of Occurrence—Lo				
Low	Minor	Moderate	Significant	High
Off the shelf	Flight Test	Element test complete	Partial test mixed with mostly analysis	Analysis only
Consequence of Occurrence—Co				
Low	Minor	Moderate	Significant	High
Negligible cost impact	Minor cost impact on functional area No cost impact on overall program	Minor cost impact on the program	Significant cost impact on the program	Major cost impact on the program
Schedule				
Low	Minor	Moderate	Significant	High
Negligible impact on program success	Could impact noncritical path milestones No impact on program critical path	Minor impact on program critical path milestones Workaround will likely maintain schedule	Moderate impact on program critical path milestones	Major impact on program schedule (>4 month slip)
Technical				
Low	Minor	Moderate	Significant	High
Negligible impact on mission performance No impact on program success Can accept degradation	Minor impact on mission performance No impact on program success Can accept degradation	Minor impact on mission performance Minor impact on program success Acceptable workaround available	Degrades mission performance Impacts program success Expedited resolution required	Significantly impacts mission performance Endangers program success Must be fixed prior to aircraft delivery

Figure 25.9 Example of risk assessment template (performance).

system that has one high-risk item and one low-risk item or (2) a system that has one moderate-risk item and two low-risk items? There is no single right answer and answers will vary with individuals. Although the mathematical technique (Eq. 25.1) can consistently calculate relative risks regardless of the number of components, managers will often substitute subjective values for the mathematical values.

## 25.7 Now We Are Done

There is no set rule on how many iterations and parametric tradeoffs are necessary for a design—it depends upon the skill and thoroughness of the designer and the design team and upon the time and budget available for the conceptual phase. The conceptual phase usually continues until the decision is made to move the most promising design into the preliminary design phase or to terminate the design effort.

## 25.8 Kelly Johnson’s 14 Rules of Management

1. The Skunk Works manager must be delegated practically complete control of his program in all aspects. He should report to a division president or higher.
2. Strong but small project offices must be provided by both the military and industry.

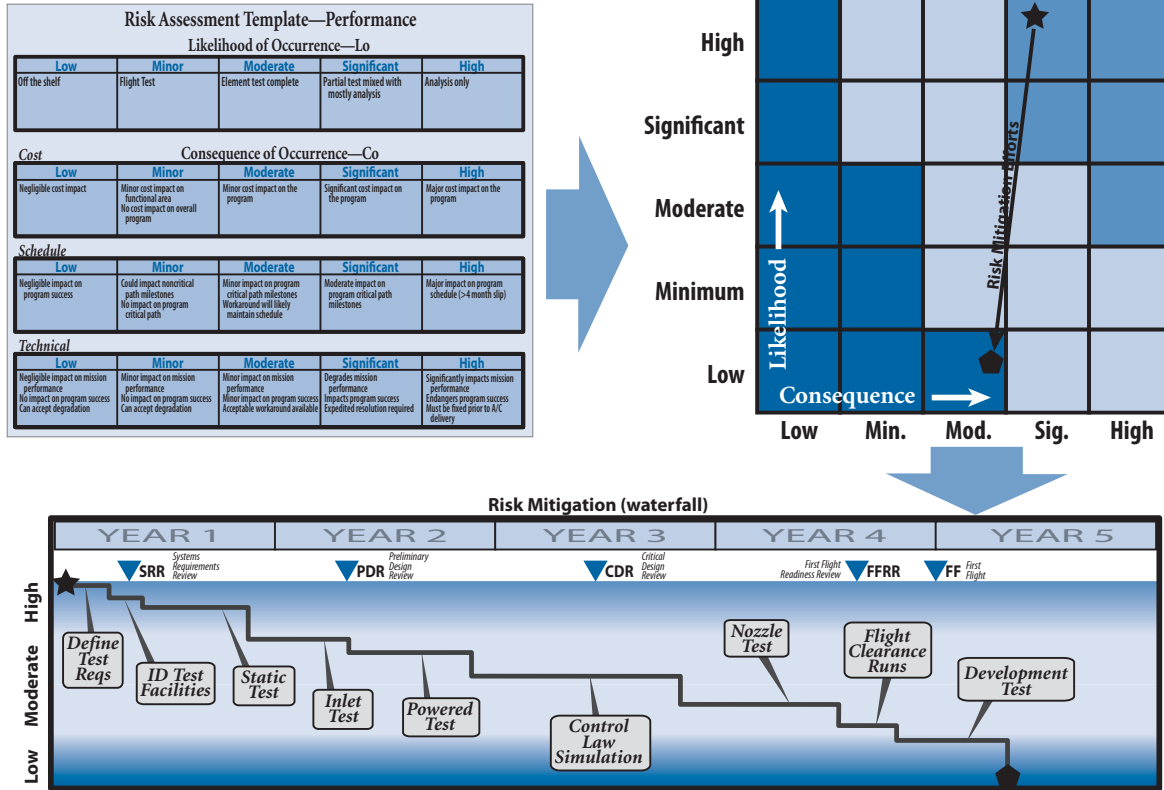


Figure 25.10 Assessing and mitigating risk.

3. The number of people having any connection with the project must be restricted in an almost vicious manner. Use a small number of good people (10% to 25% compared with the so-called normal systems).
4. A very simple drawing and drawing release system with great flexibility for making changes must be provided.
5. There must be a minimum number of reports required, but important work must be recorded thoroughly.
6. There must be a monthly cost review covering not only what has been spent and committed but also projected costs to the conclusion of the program. Don't have the books 90 days late, and don't surprise the customer with sudden overruns.
7. The contractor must be delegated and must assume more than normal responsibility to get good vendor bids for subcontract on the project. Commercial bid procedures are very often better than military ones.
8. The inspection system as currently used by the Skunk Works, which has been approved by both the Air Force and Navy, meets the intent of existing military requirements and should be used on new projects. Push more basic inspection responsibility back to subcontractors and vendors. Don't duplicate so much inspection.
9. The contractor must be delegated the authority to test his final product in flight. He can and must test it in the initial stages. If he doesn't, he rapidly loses his competency to design other vehicles.
10. The specifications applying to the hardware must be agreed to well in advance of contracting. The Skunk Works practice of having a specification section stating clearly which important military specification items will not knowingly be complied with and reasons therefore is highly recommended.
11. Funding a program must be timely so that the contractor doesn't have to keep running to the bank to support government projects.
12. There must be mutual trust between the military project organization and the contractor with very close cooperation and liaison on a day-to-day basis. This cuts down misunderstanding and correspondence to an absolute minimum.
13. Access by outsiders to the project and its personnel must be strictly controlled by appropriate security measures.
14. Because only a few people will be used in engineering and most other areas, ways must be provided to reward good performance by pay not based on the number of personnel supervised.

## Kelly Johnson and Lulu Belle

Axis Germany's Messerschmitt Me 262 was the first operational jet fighter, becoming operational during the summer of 1944. It instantly raised the bar for fighter aircraft, having a 100-mph advantage over every WWII Allied fighter.

The US Army Air Force had commissioned Bell aircraft in September 1941 to build a jet fighter—the P-59 Airacomet using a British jet engine with the Whittle design. The YP-59 had its first flight in October 1942, but from the beginning its performance was disappointing. On June 21, 1943 the US Army gave Lockheed a contract to build one prototype of a jet fighter using the British Goblin jet engine. The contract was for \$642,000 with a delivery date of November 1943 (180 days).

The project lead was given to a young engineer named Clarence “Kelly” Johnson. The Lockheed Advanced Development Projects (ADP, better known as the Skunk Works) was born. Kelly set up a super-secret operation with about 20 engineers and 80 shop men working 10 hour days, 6 days a week (Sunday was a day of rest ... no matter what). Kelly shaped his 14 rules of management during this mission-critical project.

Four days early on November 17, 1943, the XP-80, dubbed “Lulu Belle,” (see the first page of Appendix K) rolled out with the Goblin engine installed and ready for systems check-out. Problems with engine/inlet integration delayed first flight until January 8, 1944. Lulu Belle made two flights that day and reached 490 mph on the second flight—50 mph more than the maximum speed of the fastest Allied aircraft, the P-38. The XP-80 led to the P-80 Shooting Star, which eventually reached 600 mph. Kelly Johnson and his team's implementation of his 14 rules of management led to the Skunk Works' success: Lockheed built 1,715 aircraft for the USAF and Navy.

## References

- [1] Sabbagh, Karl, “21st Century Jet-The Making of the Boeing 777,” MacMillan General Books, London, UK, 1995.
- [2] Bernstein, P. L., *Against the Gods, The Remarkable Story of Risk*, Wiley, New York, 1998.
- [3] Blanchard, B. S., *System Engineering Management*, 3rd ed., Wiley, New York, 2004.

# Appendix A Conversions



- Unit Conversions
- Temperature Conversions
- Gases and Liquids

USAF/Northrop B-2 Spirit stealth bomber being refueled by a KC-10 tanker. The B-2 was designed to penetrate dense anti-aircraft defenses and deliver both conventional and nuclear weapons. The program has been controversial because of the high unit and O&S costs, and Northrop has only built 21 aircraft to date.

*A scientist discovers that which exists.  
An engineer creates that which never was.*

Theodore von Kármán

**A.1 Unit Conversions****A.1.1 Length**

<b>Multiply</b>	<b>By</b>	<b>To Obtain</b>
Centimeter (cm)	$3.281 \times 10^{-2}$	Feet
	$3.938 \times 10^{-1}$	Inches
	$1.000 \times 10^{-5}$	Kilometers
	$1.000 \times 10^{-2}$	Meters
	$1.094 \times 10^{-2}$	Yards
Foot (ft)	30.48	Centimeters
	12.00	Inches
	$3.048 \times 10^{-4}$	Kilometers
	$3.048 \times 10^{-1}$	Meters
	$1.894 \times 10^{-4}$	Miles
	$3.333 \times 10^{-1}$	Yards
Inch (in.)	2.540	Centimeters
	$8.333 \times 10^{-2}$	Feet
	$2.540 \times 10^{-2}$	Meters
	$2.778 \times 10^{-2}$	Yards
	$1.000 \times 10^{-3}$	Miles
Meter (m)	$1.000 \times 10^2$	Centimeters
	3.281	Feet
	39.37	Inches
	$1.000 \times 10^{-3}$	Kilometers
	$6.214 \times 10^{-4}$	Miles
	1.094	Yards
	Statute mile (mile or mi)	$5.280 \times 10^3$
1.609		Kilometers
$1.760 \times 10^3$		Yards
0.868976		Nautical miles
Nautical mile (n mile)	$6.076 \times 10^3$	Feet
	$1.852 \times 10^3$	Meters
	1.15078	Miles
Yard (yd)	91.44	Centimeters
	3.000	Feet
	36.00	Inches
	$9.144 \times 10^{-1}$	Meters
	$5.682 \times 10^{-4}$	Miles

### A.1.2 Area

Multiply	By	To Obtain
Acre	$4.356 \times 10^4$	Square feet
	$4.047 \times 10^3$	Square meters
	$1.562 \times 10^{-3}$	Square miles
Square centimeter (cm <sup>2</sup> )	$1.076 \times 10^{-3}$	Square feet
	$1.550 \times 10^{-1}$	Square inches
	$1.000 \times 10^{-4}$	Square meters
	$1.000 \times 10^2$	Square millimeters
Square foot (ft <sup>2</sup> )	$2.296 \times 10^{-5}$	Acres
	$1.440 \times 10^2$	Square inches
	$9.290 \times 10^{-2}$	Square meters
	$3.587 \times 10^{-8}$	Square miles
	$1.111 \times 10^{-1}$	Square yards
Square inch (in. <sup>2</sup> )	6.4516	Square Centimeters
	$6.944 \times 10^{-3}$	Square feet
	$6.452 \times 10^{-4}$	Square meters
Square kilometer (km <sup>2</sup> )	$2.471 \times 10^2$	Acres
	$1.076 \times 10^7$	Square feet
	$3.861 \times 10^{-1}$	Square miles
Square meter (m <sup>2</sup> )	$2.471 \times 10^{-4}$	Acres
	$1.000 \times 10^4$	Square centimeters
	10.76	Square feet
	$1.550 \times 10^3$	Square inches
	$3.861 \times 10^{-7}$	Square miles
Square mile	$6.40 \times 10^2$	Acres
	$2.778 \times 10^7$	Square feet
	2.590	Square kilometers
	$2.590 \times 10^6$	Square meters
	$3.0976 \times 10^6$	Square yards



### A.1.3 Volume

Multiply	By	To Obtain
Cubic centimeter (cm <sup>3</sup> )	$3.531 \times 10^{-5}$	Cubic feet
	$6.1024 \times 10^{-2}$	Cubic inches
	$1.000 \times 10^{-6}$	Cubic meters
	$1.308 \times 10^{-6}$	Cubic yards
	$3.381 \times 10^{-2}$	Fluid ounce
Cubic foot (ft <sup>3</sup> )	$2.832 \times 10^4$	Cubic centimeters
	$1.728 \times 10^3$	Cubic inches
	$2.832 \times 10^{-2}$	Cubic meters
	28.317	Liters
	7.481	Gallons
Cubic inch (in. <sup>3</sup> )	16.39	Cubic centimeters
	$5.787 \times 10^{-4}$	Cubic feet
	$1.639 \times 10^{-5}$	Cubic meters
Cubic meter (m <sup>3</sup> )	$1.000 \times 10^6$	Cubic centimeters
	35.31	Cubic feet
	$6.102 \times 10^4$	Cubic inches
	1.308	Cubic yards
Gallon (U.S.) (gal)	$1.3368 \times 10^{-1}$	Cubic feet
	3.78542	Liters
	$3.785 \times 10^{-3}$	Cubic meters
	231	Cubic inches
	128	Fluid ounces
	8.000	Pints
Imperial gallon	$2.774 \times 10^2$	Cubic inches
	1.201	Gallons (U.S.)
	4.546	Liters
Liter	$3.532 \times 10^{-2}$	Cubic feet
	0.2642	Gallons
	$1.000 \times 10^{-3}$	Cubic meters
	2.113	Pints
	1.05669	Quarts
	33.8142	Fluid ounces
Pint (U.S.) (pt)	$1.671 \times 10^{-2}$	Cubic feet
	$1.250 \times 10^{-1}$	Gallons
	$4.732 \times 10^{-1}$	Liters
	0.5	Quarts
	28.875	Cubic inches
	16	Fluid ounces
Quart (U.S.) (qt)	$3.342 \times 10^{-2}$	Cubic feet
	$2.500 \times 10^{-1}$	Gallons
	$9.463 \times 10^{-1}$	Liters
	2	Pints

### A.1.4 Velocity

Multiply	By	To Obtain
Centimeter per second (cm/s)	$3.281 \times 10^{-2}$ $3.937 \times 10^{-1}$ $1.000 \times 10^{-2}$	Feet per second Inches per second Meters per second
Foot per second (fps or ft/s)	30.48 1.097 $5.921 \times 10^{-1}$ $3.048 \times 10^{-1}$ $6.818 \times 10^{-1}$	Centimeters per second Kilometers per hour Knots Meters per second Miles per hour
Inch per second (ips)	$8.333 \times 10^{-2}$ 2.540	Feet per second Centimeters per second
Kilometer per hour (km/h)	$9.113 \times 10^{-1}$ $5.396 \times 10^{-1}$ $6.214 \times 10^{-1}$	Feet per second Knots Miles per hour
Knot (kt)	1.689 1.151 1.000 1.852	Feet per second Miles per hour Nautical miles per hour Kilometers per hour
Meter per second (m/s)	3.281 3.600 1.943 2.237	Feet per second Kilometers per hour Knots Miles per hour
Mile per hour (mph)	1.467 1.609 0.8684 0.4470	Feet per second Kilometers per hour Knots Meters per second

### A.1.5 Acceleration

Feet per second <sup>2</sup> (ft/s <sup>2</sup> )	30.48 0.6818	Centimeters per second <sup>2</sup> Miles per hour-second
---------------------------------------------------	-----------------	--------------------------------------------------------------

### A.1.6 Angular Rate and Frequency

Multiply	By	To Obtain
Radians per second (rad/s)	0.1592 9.549 57.296	Revolutions per second Revolutions per minute Degrees per second
Revolutions per minute (rpm)	0.01667 0.10472 6	Revolutions per second Radians per second Degrees per second
Cycle per second (cps)	1.000 $2\pi$	Hertz Radians per second

### A.1.7 Mass

Multiply	By	To Obtain
Kilogram (kg)	$1.000 \times 10^3$	Grams
	$6.854 \times 10^{-2}$	Slugs
Slug	$1.459 \times 10^4$	Grams
	14.59	Kilograms

### A.1.8 Weight

Multiply	By	To Obtain
Gram (g)	$3.528 \times 10^{-2}$	Ounces
	$2.205 \times 10^{-3}$	Pounds
Pound (lb)	$4.536 \times 10^2$	Grams
	16	Ounces
Short ton	2000	Pounds
	907.185	Kilograms
Metric tonne	2205	Pounds
	1000	Kilograms

### A.1.9 Force

Multiply	By	To Obtain
Dyne	$1.020 \times 10^{-3}$	Grams
	$1.000 \times 10^{-5}$	Newtons
	$2.248 \times 10^{-6}$	Pounds
Gram (g)	$3.528 \times 10^{-2}$	Ounces
	$2.205 \times 10^{-3}$	Pounds
	$9.807 \times 10^2$	Dynes
	$9.807 \times 10^{-3}$	Newtons
Kilogram (kg)	2.205	Pounds
	9.807	Newtons
	70.93	Poundals
Pound (lb)	$4.536 \times 10^{-1}$	Kilograms
	4.448	Newtons
	32.17	Poundals
Poundal	$1.410 \times 10^{-2}$	Kilograms
	$1.383 \times 10^{-1}$	Newtons
	$3.108 \times 10^{-2}$	Pounds

**A.1.10 Pressure**

Multiply	By	To Obtain
Atmosphere (atm)	29.92	Inches of mercury (0°C)
	760	Millimeters of mercury (0°C)
	1.0133	Bars
	14.70	Pounds per square inch
	$1.01325 \times 10^6$	Dynes per centimeter
	$1.01325 \times 10^5$	Newtons per meter
Bar	$9.870 \times 10^{-7}$	Atmospheres
	1.000	Dyne per square centimeter
	$1.0 \times 10^5$	Newtons per square meter
	$7.501 \times 10^2$	Millimeters of mercury (0°C)
	$1.451 \times 10^{-5}$	Pounds per square inch
Dyne per square centimeter (dyne/cm <sup>2</sup> )	$2.952 \times 10^{-5}$	Inches of mercury (0°C)
	$1.020 \times 10^{-2}$	Kilograms per square meter
	$7.501 \times 10^{-4}$	Millimeters of mercury (0°C)
	$1.450 \times 10^{-5}$	Pounds per square inch
Inch of mercury (in. Hg)	$3.342 \times 10^{-2}$	Atmospheres (0°C)
	$3.388 \times 10^{-2}$	Bars
	$3.388 \times 10^3$	Dynes per square centimeter
	13.60	Inches of water
	25.40	Millimeters of mercury
	$3.388 \times 10^3$	Newtons per square meter
	70.73	Pounds per square foot
	$4.912 \times 10^{-1}$	Pounds per square inch
Inch of water (in. H <sub>2</sub> O) (4°C)	$2.458 \times 10^{-3}$	Atmospheres
	$7.355 \times 10^{-2}$	Inches of mercury
	1.868	Millimeters of mercury
	$2.491 \times 10^2$	Newtons per square meter
	$3.613 \times 10^{-2}$	Pounds per square inch
	5.203	Pounds per square foot
Kilogram per square meter (kg/m <sup>2</sup> )	$9.678 \times 10^{-5}$	Atmospheres
	98.07	Bars
	$2.896 \times 10^{-3}$	Inches of mercury
	9.807	Newtons per square meter
	6.588	Poundals per square foot
	$2.048 \times 10^{-1}$	Pounds per square foot
	$1.422 \times 10^{-3}$	Pounds per square inch

(continued)

Multiply	By	To Obtain
Millimeter of mercury (0°C) (torr or mm Hg)	$1.333 \times 10^3$	Dynes per square centimeter
	$3.937 \times 10^{-2}$	Inches of mercury
	$5.354 \times 10^{-1}$	Inches of water
	$1.333 \times 10^2$	Newtons per square meter
	$1.934 \times 10^{-2}$	Pounds per square inch
Newton per square meter [pascal (Pa)] (N/m <sup>2</sup> )	$9.869 \times 10^{-6}$	Atmospheres
	10	Dynes per square centimeter
	$2.953 \times 10^{-4}$	Inches of mercury
	$1.020 \times 10^{-1}$	Kilograms per square meter
	$2.089 \times 10^{-2}$	Pounds per square foot
	$1.450 \times 10^{-4}$	Pounds per square inch
Pound per square foot (psf)	$4.725 \times 10^{-4}$	Atmospheres
	$4.788 \times 10^{-4}$	Bars
	$4.788 \times 10^2$	Dynes per square centimeter
	$1.414 \times 10^{-2}$	Inches of mercury
	4.882	Kilograms per square meter
	47.88	Newtons per square meter
	$6.944 \times 10^{-3}$	Pounds per square inch
Pound per square inch (psi)	$6.804 \times 10^{-2}$	Atmospheres
	$6.895 \times 10^4$	Dynes per square centimeter
	2.036	Inches of mercury
	$7.031 \times 10^{-2}$	Kilograms per square meter
	$6.895 \times 10^3$	Newtons per square meter
	$1.44 \times 10^2$	Pounds per square foot

### A.1.11 Density

Multiply	By	To Obtain
Pound per cubic foot (lb/ft <sup>3</sup> )	$5.787 \times 10^{-4}$	Pounds per cubic inch
	16.018	Kilograms per cubic meter
	$1.6018 \times 10^{-2}$	Grams per cubic centimeter

### A.1.12 Work and Energy

Multiply	By	To Obtain
British thermal unit (Btu)	$2.530 \times 10^2$	Calories
	$7.783 \times 10^2$	Foot pounds
	$3.927 \times 10^{-4}$	Horsepower hours
	$1.055 \times 10^3$	Joules
	$1.055 \times 10^3$	Newton meters
	$2.930 \times 10^{-4}$	Kilowatt hours
	$1.055 \times 10^3$	Watt seconds
Foot pound (ft·lb)	$1.285 \times 10^{-3}$	British thermal units
	$5.050 \times 10^{-7}$	Horsepower hours
	1.356	Joules
	$3.766 \times 10^{-7}$	Kilowatt hours
	1.356	Newton meters
Horsepower hour (hp·h)	$2.545 \times 10^3$	British thermal units
	$1.980 \times 10^6$	Foot pounds
	$2.684 \times 10^6$	Joules
	$7.457 \times 10^{-1}$	Kilowatt hours
Joule	$9.486 \times 10^{-4}$	British thermal units
	$2.389 \times 10^{-1}$	Calories
	$1.000 \times 10^7$	Dyne centimeters (ergs)
	$7.376 \times 10^{-1}$	Foot pounds
	1.000	Newton meter
	1.000	Watt second
Kilowatt hour (kWh)	$3.415 \times 10^3$	British thermal units
	$2.655 \times 10^6$	Foot pounds
	1.341	Horsepower hours
	$3.600 \times 10^6$	Joules
	$3.670 \times 10^5$	Kilogram meters
	$3.600 \times 10^6$	Watt seconds
Dyne centimeter	$7.3756 \times 10^{-8}$	Foot pounds
	$1.000 \times 10^{-7}$	Newton meters

### A.1.13 Power

Multiply	By	To Obtain
British thermal unit per minute (BTU/min)	$3.969 \times 10^6$	Calories per second
	12.97	Foot-pounds per second
	$2.357 \times 10^{-2}$	Horsepower
	17.58	Joules per second
	$2.987 \times 10^{-2}$	Kilogram meters per second
Foot-pound per second (ft·lb/s)	$7.713 \times 10^{-2}$	British thermal units per minute
	$3.239 \times 10^{-1}$	Calories per second
	$1.818 \times 10^{-3}$	Horsepower
	1.356	Joules per second
	$1.383 \times 10^{-1}$	Kilogram meters per second
Horsepower (hp)	42.42	British thermal units per minute
	550	Foot-pounds per second
	33,000	Foot-pounds per minute
	$7.457 \times 10^2$	Joules per second
	76.04	Kilogram-meters per second
Kilogram-meter per second	$7.457 \times 10^2$	Watts
	33.47	British Thermal Units per minute
Watt (joule per second) (W)	7.233	Foot-pounds per second
	$5.689 \times 10^{-2}$	British thermal units per minute
	$2.388 \times 10^{-1}$	Calories per second
	$7.376 \times 10^{-1}$	Foot-pounds per second
	$1.341 \times 10^{-3}$	Horsepower
	$1.020 \times 10^{-1}$	Kilogram-meters per second

## A.2 Temperature Conversions

- $T(^{\circ}\text{C}) = (5/9) [T(^{\circ}\text{F}) - 32]$
- $T(^{\circ}\text{C}) = (5/9) [T(^{\circ}\text{R}) - 491.67]$
- $T(^{\circ}\text{C}) = T(^{\circ}\text{K}) - 273.15$
- $T(^{\circ}\text{F}) = (9/5) T(^{\circ}\text{C}) + 32$
- $T(^{\circ}\text{F}) = (9/5) [T(^{\circ}\text{K}) - 273.15] + 32$
- $T(^{\circ}\text{F}) = T(^{\circ}\text{R}) - 459.67$

## A.3 Gases and Liquids

### A.3.1 Standard Values for Air at Sea Level

- $p_0 = 2116.22 \text{ psi} = 1.01325 \times 10^5 \text{ N/m}^2 = 29.92 \text{ in. Hg} = 760 \text{ mm Hg}$
- $T_0 = 518.67^\circ\text{R} = 59.0^\circ\text{F} = 288.15^\circ\text{K} = 15.0^\circ\text{C}$
- $g_0 = 32.174 \text{ ft/s}^2 = 9.80665 \text{ m/s}^2$
- $\rho_0 = 0.002377 \text{ slug/ft}^3 = 0.12492 \text{ kg}\cdot\text{s}^2/\text{m}^4$
- $\nu_0 = 1.5723 \times 10^{-4} \text{ ft}^2/\text{s} = 1.4607 \times 10^{-5} \text{ m}^2/\text{s}$
- $\mu_0 = 1.2024 \times 10^{-5} \text{ lb/ft}\cdot\text{s} = 1.7894 \times 10^{-5} \text{ kg/m}\cdot\text{s}$
- $\mu_0 = 3.737 \times 10^{-7} \text{ slug}/(\text{ft}\cdot\text{s})$

### A.3.2 Specific Weights of Other Gases at One Atmosphere and 0°C

- Carbon dioxide = 0.12341 lb/ft<sup>3</sup>
- Helium = 0.01114 lb/ft<sup>3</sup>
- Hydrogen = 0.005611 lb/ft<sup>3</sup>
- Nitrogen = 0.07807 lb/ft<sup>3</sup>
- Oxygen = 0.089212 lb/ft<sup>3</sup>

### A.3.3 Specific Weights (Specific Gravity) of Some Liquids at 0°C

- Alcohol (methyl) = 50.5 lb/ft<sup>3</sup> (0.810)
- Gasoline = 44.9 lb/ft<sup>3</sup> (0.72)
- JP1 = 49.7 lb/ft<sup>3</sup> (0.80)
- JP3 = 48.2 lb/ft<sup>3</sup> (0.775)
- JP4 = 49.0 lb/ft<sup>3</sup> (0.785)
- JP5 = 51.1 lb/ft<sup>3</sup> (0.817)
- JP7 = 48.6–50.3 lb/ft<sup>3</sup> (0.779–0.806)
- JP8 = 55.81 lb/ft<sup>3</sup> (0.894)
- JP10 = 58.62 lb/ft<sup>3</sup> (0.939)
- Kerosene = 51.2 lb/ft<sup>3</sup> (0.82)
- Sea water = 63.99 lb/ft<sup>3</sup> (1.025)
- Water = 62.43 lb/ft<sup>3</sup> (1.000)



# INDEX

---

Note: Page numbers in *italics* refer to figures (*cp* for color plate) those in **bold** to tables.

## Index Terms

## Links

### A

A-4 Skyhawk	225			
A-10A Thunderbolt II 4	295	601		
A-12/SR-71, <i>see</i> SR-71				
absorption	311			
Abbot, Ira (NACA Report No. 824)	717			
a.c. (aerodynamic center)	36	257	580	602
acceleration, in air-to-air combat	163			
activity factor (AF)	450	452		
actuator disk	437	443		
Advanced Manned Interceptor (AMI)	473			
Advanced Tactical Fighter (ATF)	13	473	660	
AE 3007H	661			
aerodynamic center (a.c.)	36	257	580	602
aerodynamics				
complete body	353			
configuration	29			
wing-body	353			
<i>see also</i> stability; subsonic; supersonic				
aeroelasticity	104	516		
divergence	182			
Aeronautical Systems Center (Wright- Patterson AFB, Ohio)	552			
aeronautics, forces in flight mechanics	2			

## Index Terms

## Links

Aero-Propulsion-Servo-Elasticity (APSE)	516			
AeroVironment Centurion	520	570		
AeroVironment Helios solar-powered UAV	<i>cp14</i>	168		
afterburner	365	<b>371</b>		
afterburner operation	120			
aft tailplane	291			
AGM-86 ALCM	319			
AGM-109 Tomahawk	319			
AGM-129A Advanced Cruise Missile	304	320	782	
AGM-137 TSSAM	5	14		
AGM-158 JASSM	15	304	777	
ailerons	222	624		
airbleed requirements	416			
airborne interceptor (AI)	319			
Airbus A380 wing	532			
aircraft				
acrobatic	21			
design	30			
growth factor	139			
man-powered (Daedalus)	<i>cp23</i>	488	570	
military	23			
range/payload dominated	146			
solar-powered	<i>cp14</i>	168	363	572
structural design	550			
composites	529			
criteria and external loads	500			
durability and damage tolerance analysis	513			
finite element modeling	510			
flutter and dynamics	517			
fuselage structure	523			

This page has been reformatted by Knovel to provide easier navigation.

## Index Terms

## Links

### aircraft

#### structural design (*Cont.*)

mass properties	516			
material selection	527			
rules of thumb	525			
sandwich structure	531			
stress analysis	507			
structural joints	513			
structural layout	517			
testing	534			
wing structure	<i>cp24</i>	521		
utility	21			

aircraft companies, *see specific names of companies*

### aircraft types

advanced composites	569			
bombers	<b>125</b>	<b>263</b>	561	562
	564	<b>644</b>		
fighter and attack	<b>153</b>	561	562	
human powered	487	489	570	
ISR	<b>153</b>	165	<b>290</b>	661
solar powered (worked example)	165			
worked example	156	165		
low-wing loading	570			
sailplanes	69	<b>153</b>	520	570
transport	<b>125</b>	143	197	227
	230	244	246	<b>263</b>
	<b>287</b>	<b>644</b>		
UAV	16	<b>17</b>	659	

*see also* unmanned aerial vehicle

*see also specific models of aircraft*

## Index Terms

## Links

airfoil	29	172	<b>193</b>	715
B factor for	<b>342</b>			
effect of	180			
Liebeck LD-17A	741			
NACA 64, 65, and 66 series	174			
NACA nomenclature and characteristics	717	718		
section	34			
selection considerations	729			
subsonic	40	43	54	
supersonic	65			
supercritical	56	59		
thickness ratio	56			
Air Force Regulation 80-14	634			
airports				
capital cities	<b>838</b>			
locations of	<b>841</b>			
names of	<b>841</b>			
operations of	281			
aisle distribution	<b>198</b>			
Allison (Rolls Royce)	661			
Allison T56-A-15	459			
American Manufacturers Planning Report	630			
Ames Aeronautical Laboratory (Moffett Field, CA)	716			
AMI, <i>see</i> Advanced Manned Interceptor				
AMST, YC-14	244			
angle-of-attack	36	257		
anti-symmetric power	622			
Antonov A-15	179			
aperture cut-off	311			
area rule theory	196	220		

## Index Terms

## Links

armament	201			
AS-5263	256			
aspect ratio	<i>cp20</i>	<i>cp21</i>	172	180
	258	619		
asymmetric power condition	596			
atmospheric				
mass (AM)	477			
nonstandard	<b>685</b>			
standard	<b>682</b>			
temperature profile	688			
auxiliary power unit (APU)	362			
AV-8 Harrier	<i>cp9</i>	249	251	
aviation pioneers, <i>see specific names of individuals</i>				
avionics	<b>212</b>			
Avro Vulcan B-1	151			
high cruise <i>L/D</i> (worked example)	155			
<b>B</b>				
B-1 Lancer bomber	<i>cp15</i>	190	200	206
	405			
B-2A Spirit (stealth bomber)	304	307	646	
B-47 Stratojet	151			
high cruise <i>L/D</i> (worked example)	155			
B-52 Stratofortress	628	741		
B-58 Hustler supersonic bomber	174	178		
B-767	<i>cp2</i>			
BAC-111	598			
balanced field length (critical field length)	273			
Beech Starship	777			

This page has been reformatted by Knovel to provide easier navigation.

## Index Terms

## Links

Bell/Boeing	609	249		
Bell Eagle Eye UAV	249			
Bell X-1	494			
Bell X-5	187			
bending	502			
bending stiffness ( <i>EI</i> )	571			
Bernoulli, Daniel	3			
Bernoulli Principle	3			
bill of materials	26	636		
black aluminum	528			
blade element theory	448			
Boeing 707	59	633		
Boeing 737	227			
Boeing 747	<b>142</b>	401		
Boeing 777–200	637			
costs (worked example)	640			
Boeing 787 Dreamliner	197	782		
Boeing Condor	146	180	361	486
	570			
subsonic drag polar (worked example)	741			
Boeing/McDonnell F-4D	617			
Boeing X-32	15			
boom, sonic	108			
boundary layers	38			
bleed	65	371		
control	224			
laminar	38	39		
thickness ( $\delta$ )	38	425	482	
turbulent	38	39		
Boyd, John	96	134		

This page has been reformatted by Knovel to provide easier navigation.

## Index Terms

## Links

BQM-34A Firebee	777			
BQM-167 Skeeter	782			
brake specific fuel consumption (BSFC)	129			
Breguet				
endurance equation	78			
condition for $C_L$ at maximum endurance	99			
glider or sailplane	99			
propeller aircraft	82			
turbine aircraft	80			
range equation	83			
condition for $C_L$ at max range	99			
glider or sailplane	98			
propeller aircraft	88			
turbine aircraft	84			
Breguet, Louis Charles	83			
British Civil Airworthiness Requirements	614			
buckling	502	506		
buffet	103			
bypass ratio, engine	367			
<b>C</b>				
C-5 Galaxy	<b>145</b>	200	271	598
C-17A	200	248	598	
C-130	200	317	450	651
C-141A	50			
CAIV (cost as an independent variable)	5	7		
camber, wing	2	178	258	

## Index Terms

## Links

canard	291	580	583	602
	618			
lift curve slope	584			
volume coefficient	290			
cancellation, wave	311			
capture-area ratio	397			
cargo containers	<b>199</b>			
Carnot, Sadi	356			
carpet plot	660			
CATIA	641			
Cayley, Sir George	2			
ceiling, absolute	104			
ceiling, operational	104			
centerbody	397			
center of gravity (c.g.)	29	213	574	<b>617</b>
	618			
center of pressure	184	597		
Cessna 172 Skyhawk	<i>cp4</i>	733		
Cessna 177 Cardinal	227			
CF6-50 turbofan engines	244			
CF6-80C2 turbofan	598			
Chanute, Octave	2			
Chief Designer	3			
climb and descent rate	100			
Coanda effect	244			
Coanda, Henri	244			
coefficient				
$C_d$ (section drag coefficient 2-D)	42	55	179	
$C_D$ (drag)	<i>cp17</i>	48	<b>129</b>	
$CD_0$ (zero lift)	353			



## Index Terms

## Links

coefficient (*Cont.*)

$C_l$				
rolling moment	587			
section lift, 2-D	41	42	179	
$C_L$				
wing lift	265			
for maximum $L/D$	76	<b>99</b>		
$C_{l\beta}$ (lateral stability derivative)	623			
$C_n$ (directional moment, yaw)	595			
$C_{n\beta}$ (directional stability derivative, yaw)	595			
$C_{n\delta r}$ (rudder control power)	597			
$C_p$				
power	449			
pressure	35			
$C_Q$ (torque)	449			
$C_T$ (thrust)	449			
$C_{VT}$ (vertical tail coefficient)	<b>286</b>			
compressibility	43	183	437	
compression, ramp	502	530		
compression modulus ( $E_c$ )	506			
compression, surface spillage	398			
computational fluid dynamics (CFD)	324	496		
computers	212			
Concept of Operations (ConOps)	12			
Concorde SST	<i>cp6</i>	108	200	220
	336	405		
concurrent engineering	651			
Condor	146	180	361	486
	570	741		
ConOps (Concept of Operations)	12			

This page has been reformatted by Knovel to provide easier navigation.

## Index Terms

## Links

Continental GTSIOL-300 piston engine	361			
consequence of failure (Cf)	663			
consequence of occurrence (Co)	663	665	666	
constant energy contours, altitudes for	<b>119</b>			
contrast signatures	313			
control reversal	516			
control surface, sizing	624			
Convair	319			
conventional takeoff and landing (CTOL)	7	158	256	<b>257</b>
conversion of				
temperature	678			
unit	<b>670</b>			
Corning, G.	30			
correction for lift curve slope ( $C_{L\alpha}$ )				
compressibility	43			
combined effects	46			
finite wing	43			
sweep	44			
cost as an independent variable (CAIV)	5	7		
cost estimating relationship	631			
cowl capture area	395			
crew compartment	200			
fighter	200			
long range military/commercial transports	200			
crew ratio	<b>644</b>			
critical component				
elimination	295			
location	295			
redundancy with separation	295			
shielding	295			

## Index Terms

## Links

critical condition	396	397
critical field length (balanced field length)	273	
cross-section, volumetrically efficient	197	
crosswind condition	597	
crosswind landing	622	
cruise climb schedule	85	
cruise efficiency	152	156
cruise missile	153	
AGM-129A, case study	319	
air launched (worked example)	153	
worked example	144	153
cruise turbine	129	152
$C_{VT}$ (vertical tail coefficient)	<b>286</b>	

## **D**

D-21(supersonic drone)	651		
DaDTA, <i>see</i> durability and damage tolerance analysis			
Daedalus	<i>cp23</i>	488	570
Darkstar (Tier 3-)	180		
Dassault Mirage IIIG	187		
da Vinci, Leonardo	2		
DC-1	13		
DC-2	13		
DC-3	<i>cp4</i>	13	722
DC-8	271		
defense system sensors	297		
acoustic	297	317	
ELINT/SIGINT	297		
IR/infrared	297	317	

This page has been reformatted by Knovel to provide easier navigation.

## Index Terms

## Links

defense system sensors ( <i>Cont.</i> )		
RF/radar	297	
visual	297	317
deformation, permanent (or plastic)	503	
delta (leading edge sweep)	172	
density		
gas	<b>826</b>	
liquid	<b>827</b>	
Department of Defense 5000.1	5	26
Department of Defense Specifications and Standards System (DODSSS)	21	<b>22</b>
design		
closing	324	
guidelines	24	
maintainability and	212	649
materials and properties	<b>526</b>	
phases of aircraft	27	
production and	648	
reduced cost and	648	
takeoff weight	124	
trade studies	25	
development support	632	
diesel	485	
diffraction	301	
dihedral, wing	589	
directional moment coefficient, yaw ( $C_n$ )	595	
directional stability derivative, yaw ( $C_{n\beta}$ )	595	
discrete gust relationship	495	

## Index Terms

## Links

distance				
air	268			
braking	269			
climb	267			
free roll	268			
rotation	265			
takeoff factors	279			
transition	266			
distortion, airflow	401			
diurnal cycle energy balance	<i>cp15</i>	483		
divergence	182	185	516	
dividing streamline	34			
Douglas Aircraft Company	13			
Douglas, Donald	13			
drag	2	37	580	
additive	414	416	422	
afterbody	<b>430</b>			
afterbody separation	214			
base	38	214		
boattail	430			
boundary layer				
bleed	414	417	423	
diverter	414	417	426	
bucket	180	472		
bypass	396	398	414	417
	425			
chute (or speed brakes/spoilers)	270	273		
coefficient ( $C_D$ )	<i>cp17</i>	<b>263</b>		
subsonic	331			
supersonic	334			

## Index Terms

## Links

drag

coefficient ( $C_D$ ) (*Cont.*)

transonic 335

for uncambered wing 77

zero lift ( $C_{D0}$ ) 353

subsonic 336 344

supersonic 344 346

transonic 340 345

cooling 38

cowl 414 417

cruise 605

deflected flap 242 248 413 425

divergence 56

due to lift 336

excrescence 38

exit flap 425

form 37

induced 37 331

inlet *cp7* 414 417

interference 37 353

inviscid 331 741

inviscid-due-to-lift 37 43

landing gear 262 **263**

lift correlation curve *cp20*

minimum 73 74 75 76

78 88 161 331

398

miscellaneous items 349

nacelle 448

nozzle/afterbody interference 414

## Index Terms

## Links

drag (*Cont.*)

polars	<i>cp18</i>	734		
subsonic	735			
swept wing tailless	735			
pressure	37	<b>106</b>	398	
profile	37			
ram	38	361		
rise	56			
skin friction	37	40	63	417
spillage	396	422		
compression surface	417			
critical	398	417		
subcritical	418			
tail trim load	288			
trim	37	603	607	609
	619			
viscous	331	741		
viscous-due-to-lift	37			
wave	38	<b>65</b>	66	174
wing separation	610			

Draken

336

durability and damage tolerance analysis

(DaDTA)

500 513

Dutch roll

592 614

## **E**

EC-130

300

$E_c$  (compression modulus)

506

ECM, *see* electronic counter measures

Economic Escalation Factor

629

This page has been reformatted by Knovel to provide easier navigation.

## Index Terms

## Links

edge card ( or R-card)	311		
effective perceived noise level in decibels (EPNdB)	108		
<i>EI</i> (bending stiffness)	517		
ejection seat	200		
Electra	450		
electric motors	363		
electrical systems	561		
electronic counter measures (ECM)	212		
elevon	608	609	
elements	<b>828</b>		
emergency exits	199		
empennage	<b>213</b>		
empty weight ( $W_{\text{empty}}$ )	124	<b>125</b>	
endurance	78		
jet equation	82	131	
propeller aircraft equation	131		
range and	100		
energy	91		
solar	<i>cp14</i>	480	486
specific	91		
total	91		
energy maneuverability (EM)	100		
energy–state approximation	100	112	120
engine			
liquid rocket	112		
piston	486	487	
podded	401	782	
ramjet	112	373	

*see also* F100-PW-100



## Index Terms

## Links

engine ( <i>Cont.</i> )				
reciprocating/propeller	112	361		
rocket	488	490		
rubber	468			
scramjet & pulse detonation	112			
turbine				
acceleration	473			
axisymmetric	388	400	404	405
external compression	386	400	412	
internal contraction	387			
mixed compression	386	387	389	
	395	400		
pitot (normal) shock	386			
pressure recovery	389			
two-dimensional	388	400	404	412
cruise economy	471			
inlet design	<i>cp6</i>	412		
installation corrections	434			
maneuverability	471			
scaling	468			
sizing (worked example)	473			
subsonic	384			
supersonic	384			
takeoff	473			
turbine (or turbojet)	366	370		
turbofan	112	366	436	
turbojet	436			
turboprop	112	362	366	459
turbo-ramjet	112			
turboshaft	459			

## Index Terms

## Links

engines, aircraft	2			
envelope				
flight	102			
operating	121			
EP-3	300			
equilibrium	576			
equivalent gust velocity ( $U_e$ )	495			
equivalent shaft horsepower	362			
ergometer, recumbent	487			
Eta glider	<i>cp23</i>	759	<b>783</b>	
Euler, Leonhard	3			
exhaust plume emissions	316			
Experimental Stealth Technology (XST)	304			
externally blown flap (EBF)	246			
$E$ (Young's modulus)	525			
<b>F</b>				
F-4, <i>see</i> McDonnell F-4 Phantom II				
F-5A	95			
F-5E	95			
F-14 Tomcat	<i>cp3</i>	187		
F-15 Eagle	<i>cp15</i>	13	52	405
	410	650		
F-16 Fighting Falcon	<i>cp9</i>	200	206	405
	598	600	<b>648</b>	
F-18	<i>cp3</i>	<i>cp6</i>		
F-20A Tigershark	49			
F-22	<i>cp3</i>	<i>cp12</i>	304	
F-35 Lightning II	<i>cp6</i>	<i>cp11</i>	252	304
F-94	651			

This page has been reformatted by Knovel to provide easier navigation.

## Index Terms

## Links

F-100	345			
F-100-PW-100 afterburning turbofan	371	408		
F-104	177	408	651	
F-104G	92	115		
F-111A	<i>cp6</i>	63	187	408
	628	633	648	
F-117A Nighthawk	<i>cp12</i>	<i>cp13</i>	273	294
	301	304	307	311
	646	651		
facesheets	530			
factor-of-safety (FS)	19	492	502	504
fail safe	514			
failure	663			
failure recognition speed ( $V_{EF}$ )	273			
Fairchild Republic A-10A	102	601	681	
FB-111	200			
Federal Aviation Regulations (FAR)				
FAR 21	578			
FAR 23	256	284	578	614
FAR 25	199	256	284	578
	614			
FAR 36	108	109		
finite element mode	507	531		
flame stability	374			
flaps				
area ratio	242			
chord ratio	242			
deflection	264			
Fowler	223	227	232	274
jet	248			

## Index Terms

## Links

flaps ( <i>Cont.</i> )			
leading edge	222		
single slotted	232		
split	232		
trailing edge	222		
flight level, unaccelerated	72		
flight envelope	494		
flight test operations	633		
flow			
choked	423		
sonic	54		
subsonic	3		
transonic	54		
unchoked	424		
fluid mechanics	2		
flutter	516		
Fokker F-10A	12		
fore-aft wing bending ( $M_z$ )	521	523	
forward control surface	602		
463L pallet	199		
fracture toughness	526		
frame-longeron approach	521		
FS, <i>see</i> factor-of-safety			
$F_{tu}$ (ultimate tension strength)	505	506	525
fuel	210		
brake-specific consumption	129		
combat	131		
density	<b>210</b>		
fraction	126		
reserve	132		

## Index Terms

## Links

fuel (*Cont.*)

sequencing 617  
thrust-specific consumption 128

fuselage

fineness ratio ( $l/d$ ), defined 29 213  
mixed subsonic and supersonic 214  
subsonic 214  
supersonic 214

sandwich skin 521

shapes 217

cone-cylinder 214  
ogive-cylinder 214  
power series-cylinder 215

Sears–Haack body 216 220 746

side spikes 307

sizing and design 220

volume requirements 196

## **G**

gas, density of **826**

gas turbines 357

gasoline 485

GAU-8 cannon 295

geosynchronous orbit 489

$GJ$  (torsional stiffness) 517

glider  $c_{p23}$  2

Global Hawk 140 165 175 661

worked example 156

gross thrust ( $T_g$ ) 365

ground effects 260

This page has been reformatted by Knovel to provide easier navigation.

## Index Terms

## Links

Grumman XF10F	187			
$G$ (shear modulus)	506			
gust load factors	495			
<b>H</b>				
Hage, R. E.	30			
HAARP, <i>see</i> high altitude atmospheric research platform				
Have Blue	12	304	309	319
heating				
aerodynamic	105	178		
lower surface	106			
ohmic	301	309	311	
rate	106			
stagnation point	106			
Heinkel, Ernst	381			
Heinkel He-178	381			
helicopters	21	83		
Helios	<i>cp14</i>	520	570	
high altitude				
long endurance aircraft	165	168		
reconnaissance aircraft	163			
high altitude atmospheric research platform (HAARP)	149	164	361	487
	<b>538</b>	<b>542</b>	550	
requirements (worked example)	146			
wing structure (worked example)	534			
high altitude long endurance vehicles	520			
“High Flight” (Magee)	<i>cp1</i>			
high-g maneuver	619			

This page has been reformatted by Knovel to provide easier navigation.

## Index Terms

## Links

high lift devices	159	221	<b>231</b>	
flaps	226			
leading edge	226			
maximum lift coefficient	<b>230</b>			
mechanical	222	<b>229</b>	248	
subsonic	242			
powered, for V/STOL	<i>cp8</i>	<i>cp10</i>	<i>cp11</i>	253
practical	230			
slats and slots	225	225	227	<b>229</b>
trailing edge	176	223	232	
high lift system	274			
horizontal surface, sizing	618			
horseshoe vortex	257			
Hughes, Howard	8			
Hydrodynamica	3			

## I

IAD, <i>see</i> integrated air defense	
IBF, <i>see</i> internally blown flap	
ICAO Annex 16	111
Iccarus	489
identification systems	212
IGE, <i>see</i> in-ground-effect	
impact	663
inboard–outboard loads ( $P_y$ )	523
indium tin oxide	305
in-ground-effect (IGE)	262

## Index Terms

## Links

inlet			
area ratio	395	403	
axisymmetric	420		
capture area	395		
D-shaped inlet	408		
diverterless	<i>cp6</i>	399	
drag	417		
external compression (worked example)	408		
flow distortion	416		
moment and stability contribution	585		
operation, supercritical	397		
pitot	386	418	420
RCS design	<i>cp6</i>	312	
sizing	402		
stability	602		
static pressures	<b>106</b>		
total pressure	<b>409</b>		
variable geometry	397		
weight and cost	401		
integrated air defense (IAD)	294		
internally blown flap (IBF)	246		
IO-360-CIC	461		
isentropic compressible flow	<b>692</b>		
equations	690		
ISR (SensorCraft) aircraft	661		
<b>J</b>			
J85-19 turbojets	250		
J85-GE-5 turbojets	251		
J85-GE-21 turbojet	97		



## Index Terms

## Links

JASSM (Joint Air-to-Surface Standoff Missile, AGM 158)	14	15	
Johnson, Kelly	651	667	
Joint Strike Fighter (JSF)	251		
competition	<i>cp5</i>	15	
F-35, variants of	252		
joints			
bearing-critical	512		
bonded	512		
categories	510		
mechanically fastened	510		
JP-4	485		
JSF, <i>see</i> Joint Strike Fighter			
JSSG-2006 (Joint Service Specification Guide-Aircraft Structures)	493		
JW 1416 airfoil	35	175	
<b>K</b>			
Kármán, Theodore von	2		
KC-135	633		
KEAS (knots-equivalent airspeed)	494		
kinetic energy (KE)	91		
kites	21		
Kitty Hawk	1		
knothole	660		
Kutta condition	34	715	716

## Index Terms

## Links

### L

L-1011	<i>cp15</i>	273	<b>277</b>	282
flight test, analytical estimates		273		
landing				
analysis	267		<b>281</b>	
distance (worked example)	279			
gear	203	262		
parameter	158			
performance	282			
<i>see also</i> short takeoff and landing; vertical takeoff and landing				
Langley Aeronautical Laboratory (Langley Field, Virginia)	716			
Langley, Samuel	2			
lateral control spin parameter	621			
lateral stability derivative ( $C_{l\beta}$ )	623			
lavatories	199			
leading edge sweep (delta)	172			
LEO, <i>see</i> low earth orbit				
level turn constant velocity	89			
level turn maneuvering flight	612			
Lewis Flight Propulsion Laboratory (Cleveland, Ohio)	716			
life cycle cost (LCC)	5	27	30	650
phases	626			
acquisition	626	627		
development, test, and evaluation	626	<b>644</b>		
operations and maintenance	626	627	628	650
planning data	<b>645</b>			

## Index Terms

## Links

lift	<i>cp17</i>	<i>cp20</i>	2	36
	46	49	580	
<i>see also</i> maximum <i>L/D</i>				
lightweight fighter (LWF)	<b>80</b>	<b>81</b>	140	603
competition	5	123		
speed of (worked example)	86			
weight of (worked example)	134			
likelihood of occurrence (Lo)	663	<i>665</i>	<i>666</i>	
Liebeck, Robert	730			
Lilienthal, Otto	2	28		
limits				
noise	108			
pollution	108			
propulsion	112			
line of sight (LOS)	311			
linear lift curve slope ( $C_{L\alpha}$ )	325			
subsonic	325			
supersonic	326			
transonic	327			
wing–body	329			
<i>l/d, see</i> fuselage fineness ratio				
<i>L/D, see</i> lift; maximum <i>L/D</i>				
<i>see also</i> drag				
<i>L</i> (manufacturing labor hour)	635			
load				
factor	77	130	162	583
maximum sustained ( $n_{MS}$ )	472			
vertical ( $n_z$ )	494			
limit	502			
ultimate	502			

## Index Terms

## Links

load (*Cont.*)

*see also* wing

Lockheed C-5 Galaxy	401	598		
Lockheed Martin	14			
Polecat	<i>cp13</i>	175	570	729
S-3A Viking	502			
Tier III- (Darkstar)	309	570		
X-35	15			
Lockheed SR-71, <i>see</i> SR-71				
Lockheed Skunk Works	vii	13	146	303
	665	668		
loiter	78	130	131	156
long range strike vehicle (LRSV)	19			
long range subsonic transport	154			
longitudinal control	619			
low altitude, ride quality	168			
low earth orbit (LEO)	489			
rocket sizing (worked example)	489			
Low-observable (LO) aircraft	498			
LRN 1015 airfoil	175			
LRSV, <i>see</i> long range strike vehicle				
LWF, <i>see</i> lightweight fighter				
Lycoming 0-360-A engine	358	461		

## **M**

*Mach*

angle	62
cone	62

## Index Terms

## Links

### *Mach (Cont.)*

number	<i>cp19</i>	37	54	56
	84	337		
wave	62			
Magee, John Gillespie, Jr.	<i>cp1</i>			
maintenance man hours per flight hour (MMH/FH)	7	644	<b>645</b>	649
maneuverability, combat	93			
maneuver limit load factor	19			
MANPAD (man portable missile with IR sensor)	294			
manufacturing labor hour ( <i>L</i> )	635			
margin-of-safety (worked example)	504			
mass airflow	370			
mass flow parameter	404	690		
mass flow ratio	397			
material and equipment list (MEL)	636			
maximum <i>L/D</i> , equation for	75			
cambered wing aircraft	76			
$C_L$ for maximum <i>L/D</i>	76			
uncambered wing aircraft	76			
McCormick, Barnes	70	463		
McDonnell Douglas F-15	204	408		
McDonnell F-4 Phantom II	51	187	206	210
	408	618	650	741
McDonnell F-101 Voodoo	597			
mean aerodynamic chord ( <i>mac</i> )	284	579		
mean flight time between unscheduled maintenance actions (MFTBUMA)	20			
Measure of Merit (MoM)	15	172	653	660
“Metalite”	529			

## Index Terms

## Links

Metallic Materials Properties Development and Standardization, <i>see</i> MMPDS				
Metals, properties of, at room temperature	<b>107</b>			
Mig-21	345			
Mig-23	405			
Mig-31	<i>cp16</i>			
Mikoyan Flogger	187			
MIL-A-8860	493			
MIL-A-8861	495	496		
MIL-C-5011A	256			
MIL-C-18244	579			
MIL-E-5008B Ram Recovery	414			
MIL-F-8587C	284	578		
MIL-F-9490D	169	579		
MIL-F-18732	579			
MIL-F-83300	256	579		
MIL-H-8501	579			
MIL-HDBK-5 (Metallic Materials and Elements for Aerospace Vehicle Structures)	506			
MIL HDBK-516B	22			
MIL-HDBK-1797 (Flying Qualities of Piloted Airplanes)	23	579	592	614
	<b>624</b>			
MIL-STD-850B	200			
MIL-STD-1791	199			
minimum drag	73	74	75	76
	78	88	161	331
	398			
Mirage 3G	408			

## Index Terms

## Links

mission requirements	172			
MMH/FH (maintenance man hours per flight hour)	7	644	<b>645</b>	649
MMPDS (Metallic Materials Properties Development and Standardization)	506			
model airplane, radio control	324			
moment of inertia	324	574		
moment, and weight summary	<b>573</b>			
Momentum theory	440			
Mullaly, Alan	654			
$M_x$ (spanwise bending)	518	520	523	524
	545	<b>548</b>		
$M_y$ (torsional loads)	518	523		
$M_z$ (fore-aft wing bending)	521	523		
<b>N</b>				
National Advisory Committee for Aeronautics (NACA)	716			
Report No. 824 (1945)	717			
RM A53A30	746			
64A series section	59			
National Aeronautics and Space Administration (NASA)	716			
NAVAIR (Patuxent River, Md)	552			
navigation systems	212			
Doppler	212			
inertial	212			
Nemesis	cp22	467		
net thrust ( $T_n$ )	365			
neutral point (n.p.), location of	602	<b>617</b>		
Newberry, C. F.	30			

This page has been reformatted by Knovel to provide easier navigation.

## Index Terms

## Links

noise	111
regulations	109
turbo-machinery	111
non-destructive inspection techniques	512
North American Rockwell	10
Northrop F-20A Tigershark	49
Northrop-Grumman	7
nozzle	
airframe interference effects	427
types	430
blow-in-door	430
C-D iris	428
fully variable ejector	430
isentropic ramp	430
plug	428
short convergent	428
simple ejector	428
nozzle RCS design	312
n.p. (neutral point), location of	602
$n_z$ (vertical load factor)	518
<b>O</b>	
Otto cycle	358
out of ground effect (OGE)	262
overall pressure ratio (OPR)	364
over-nose viewing angles	<b>201</b>
overpressure	108



## Index Terms

## Links

### P

P-38	651			
PA-28-180 Cherokee Archer	286	358	464	
PA-28-200 Cherokee Arrow	464			
packaging equipment, one deep	650			
packaging factors	210			
parametric study	660			
passenger compartment requirements	<b>197</b>	<b>198</b>		
payload ( $W_{\text{fixed}}$ )	124			
worked example	141			
performance				
accelerated	100			
aircraft	3			
optimum cruise (worked example)	470			
steady-state (cruise)	100			
Periodic Table	<b>828</b>			
Perkins, C. D.	30			
Perseus	486			
physical constants	<b>825</b>			
Pilot's Prayer	<i>cp1</i>			
Piper Comanche	206			
Piper PA-30	227			
planform	29	447	589	619
airfoil	194			
defined	172			
effects of	<b>193</b>	194		
parameters, defined	172			
wing	330			

## Index Terms

## Links

Polecat	<i>cp13</i>	175	570
airfoil (worked example)	729		
pollution, regulations	111		
potential energy	91		
power coefficient ( $C_p$ )	449		
Powers, Gary	20		
Prandtl–Glauret transformation	43		
Prandtl, Ludwig	2		
pressure			
coefficient ( $C_p$ )	35		
dynamic			
maximum limit	104		
minimum	103		
free stream total	104		
static	105		
pressurization	197		
production rate	634		
propeller(s)	357	435	
activity factor	450	456	
actuators	443	<b>484</b>	
disk loading	439		
efficiency	357	449	
open (or airscrew)	436		
operating charts (worked example)	460		
power efficient	449		
power required for	73	82	
rotational velocity	449		
section	459		
thrust coefficient	449		
tip speed	456	459	

## Index Terms

## Links

propeller(s) ( <i>Cont.</i> )				
torque coefficient	449			
variable pitch	460			
propulsion integration	203			
propulsion systems	379			
limits	112			
purpose	356			
thrust sizing	468	490		
propulsive efficiency	449			
pull up or loop maneuver				
aft tail	610			
canard	611			
tailless elevon deflection	611			
PW-F-100 demand capture area	<b>410</b>			
PW F119 afterburning turbofan engine	251			
PW JT 12A-3 turbojets	250			
$P_y$ (inboard–outboard loads)	523			
$P_z$ (vertical shear)	518	523	524	545
<b>Q</b>				
quality control	635			
<b>R</b>				
RA-5C	405			
radar	212			
10 Ghz Flap Lid fire control	303			
170 Mhz Tall King long range detection	303			
bistatic	301			

## Index Terms

## Links

radar ( <i>Cont.</i> )			
scattering phenomenon	304		
absorption	301		
cancelation	301		
shaping	300		
radar absorbing material	310	320	
radar cross-sections signature	300	305	312
ram drag	365		
ram effect	369		
ramjets	357		
ram recovery	460		
Rand Corporation	630		
range			
Breguet equation	83		
efficiency			
propeller aircraft	152		
endurance	100		
factor	84		
specific	83		
total	83		
vehicle	156		
Raymer, D. P.	30		
RB.211-22 high bypass ratio turbofan engines	274		
receivers	212		
reflection			
angle	301		
specular	301		
“Reflections on the Motive Power of Fire”	356		
refusal speed	273		
Republic XF-91 Thunderceptor	533		

## Index Terms

## Links

request for proposal (RFP)	26			
requirements				
cost	7			
critical	28			
defining	6			
maintenance and support	7			
mission	6			
pull	8			
scheduling	7			
technology push	12			
resistive sheet	310	311		
retardation devices	273			
retardation force-to-weight ratio	265			
revenue flight	20			
revenue per volume	197			
reverse thrust	270			
reversible pitch	272			
Reynolds Analogy	106			
Reynolds number	37	38	224	324
	336	488	746	
Rich, Ben	<i>cp12</i>	293	303	
risk				
analysis	665			
defined	662			
index	663			
rockets	357	382		
Rockne, Knute	12			
roll damping	614			
rolling moment coefficient	587			
Roskam, Jan	30			

## Index Terms

## Links

rotational power (RP)	452		
rotational tip speed	450		
roughness height values	<b>337</b>		
RQ-4A Global Hawk, <i>see</i> Global Hawk			
rudder	622		
rudder control power ( $C_{n\dot{r}}$ )	597		
Russian TU-144	200		
<b>S</b>			
S-3A Viking	502		
SAAB-35	336		
Sabreliner	10		
safe life	514		
sailplanes	570	741	
SAM, <i>see</i> surface-to-air missile			
SAS, <i>see</i> stability augmentation system			
Scaled Composites Voyager	570		
Schrenk's Approximation	535		
S&C (stability and control)	600	<b>615</b>	
SEAD, <i>see</i> suppression of enemy air defenses			
Sears–Haack body			
fuselage	216	220	746
shapes	216	220	
seating, passenger	199		
secondary airflows	<b>402</b>		
section drag coefficient 2-D ( $C_d$ )	42	55	179
section lift coefficient 2-D ( $C_l$ )	41	42	179
section pitching moment coefficient 2-D	174		
separation delay devices	222	223	
shaft driven lift fan	251		

This page has been reformatted by Knovel to provide easier navigation.

## Index Terms

## Links

shaft engine characteristics	460			
shaft horsepower	451			
shaping	309			
Sharp, Jon	468			
shear	506			
shear modulus ( $G$ )	506			
shock	517			
condensation	$cp3$			
conical	420	707		
normal	698	704		
oblique	704			
shock-on-lip	386			
shock wave system	389			
short takeoff and landing (STOL)	$cp8$	$cp10$	$cp11$	7
	159	242	256	
wing loading (worked example)	224			
short takeoff vertical landing (STOVL)	251			
sideslip	622			
signature				
acoustic	7			
infrared	7			
radar cross section	7			
visual	7			
six degrees of freedom (6-DOF)	25			
sizing				
engines	29			
fuselage	29			
initial aircraft	28			
inlets	29			
tail	29			

## Index Terms

## Links

skin-stringer approach	521			
Skunk Works, <i>see</i> Lockheed Skunk Works				
slipstream	244	437		
slot and slat	225			
Society of Allied Weight Engineers (SAWE)	552			
soft tooling	634			
Solar Constant	477			
solar power	<i>cp14</i>	480	486	
Solar Snooper	486	479	<b>484</b>	487
(worked example)	165			
Sopwith Camel	<i>cp22</i>	575	578	
Specification	486	8		
spike	394			
spin resistance margin	620	621		
spin susceptibility	620			
spoilers	278			
Spoon Rest	319			
square-cube law	324	784		
SR-71	<i>cp7</i>	47	71	73
	270	383	651	
AR	331			
flight hours	<b>646</b>			
flight test data	328	329	334	413
mixed compression inlet	389	393	405	
weight	127	<b>770</b>	779	
stability	25	576		
control data	600	<b>615</b>		
dynamic	578	579		



## Index Terms

## Links

stability ( <i>Cont.</i> )				
static	578	615		
control analysis	30			
directional (weathercock)	597			
federal regulations	579			
lateral	587			
longitudinal	580	619		
pitch hang-up	598			
pitch-up	600			
roll	109	182	217	225
	242	251	256	257
yaw	187	251	283	284
	394	484	576	596
	621	622		
stability augmentation system (SAS)	577			
stagnation point	34			
stall	103			
stall speed ( $V_{\text{stall}}$ )	157			
standards, military, <i>see</i> MIL entries				
static, <i>see</i> aerodynamics; stability				
static directional control	622			
static margin (SM)	602			
stealth, designing for	320			
Stephan–Boltzmann constant	106			
Stinton, D.	30			
STOL, <i>see</i> short takeoff and landing				
STOVL, <i>see</i> short takeoff vertical landing				
streamlines	38			
streamtube	437			
stress	500	503		

## Index Terms

## Links

stress–strain curve	503	
strip theory	448	
structural bones	517	
structural design		
composites	525	<b>526</b>
criteria and external loads	493	
durability and damage tolerance analysis	513	
finite element modeling	507	
flutter and dynamics	516	
fuselage structure	521	
mass properties	514	
material selection	525	
rules of thumb	523	
sandwich structure	529	
stress analysis	500	
structural joints	510	
structural layout	517	
testing	531	
wing structure	cp24	521
Structural Design Criteria Document	498	
structural dynamics	cp24	517
Structural Layout Drawing	517	
subsonic	3	48
compressibility corrections	43	
cruise	128	
diffuser	385	
drag-due-to-lift	331	
fuselage fineness ratio ( $l/d$ )	213	
installation	384	
leading edge	63	

## Index Terms

## Links

subsonic ( <i>Cont.</i> )			
lift slope, equation for	45		
linear left curve slope	325		
long-range transport (worked example)	154		
propulsion limits	112		
thin airfoil theory	40		
total aircraft	54		
weight estimation	553		
zero-lift drag coefficient	336		
Sukhoi SU-7B	187		
supercharging	358		
supersonic			
airflow	54		
area rule theory	196		
conical shock	707		
drag-due-to-lift	334		
inlet	385	418	
installation	384		
leading edge	63	178	
lift and wave drag	64	174	217
linear left curve slope	326		
linear theory	342		
Mach number effect	606		
maximum thickness ratio	173		
sonic boom	108		
weight estimation	553		
wing thickness ratio	56		
zero-lift drag coefficient	340		
suppression	295		
suppression of enemy air defenses (SEAD)	19		

## Index Terms

## Links

surface-to-air missile (SAM)	294	314	
survivability			
designing for	320		
hierarchy	294		
susceptibility	294	300	
vulnerability	294	295	
sweep, wing	186	187	619
sweepback, wing	57	589	

## **T**

TACAN systems	212		
tail			
aerodynamics	292		
canard	290		
efficiency factor	583		
sizing	284		
horizontal (aft tailplane)	289		
vertical	286		
tailless aircraft	291		
volume coefficient	284		
takeoff			
analysis	260	<b>279</b>	
distance (worked example)	278		
field length	273		
noise	109		
performance	282		
rotation	619		
thrust-to-weight ratio	265		
time during	267		

## Index Terms

## Links

takeoff ( <i>Cont.</i> )			
weight	132	149	<b>211</b>
wing loading	<b>153</b>	<b>155</b>	265
takeoff gross weight (TOGW)	202	653	
takeoff parameter (TOP)	157		
takeoff weight ( $W_{TO}$ )	132	149	
tail volume coefficients	<b>287</b>	<b>288</b>	<b>289</b>
Tall King (radar)	319		
taper ratio ( $\lambda$ )	172	186	619
Teal Dawn (DARPA, ACM)	319		
technology push	12		
temperature, conversion of	678		
TF-30	408		
TF 39-GE-1 turbofan	<b>11</b>	371	<b>372</b>
“Theory of Wing Sections”	717	731	
thermodynamics, second law of	356		
Thomas, Fred	30		
thrust	2	104	
boundary	104		
gross	365		
limit line	104		
net ( $T_n$ )	365		
rocket	377		
TSFC factors influencing	370		
uninstalled	414		
thrust coefficient ( $C_T$ )	449		
thrust pinch point	73		
thrust reversers	159	271	

## Index Terms

## Links

thrust specific fuel consumption (TSFC)	128	365	
<i>C</i> , definition of	131		
factors affecting	369		
Tier 3- (Dark Star)	309	570	
Tigershark (F-20A)	49		
TOGW, <i>see</i> takeoff gross weight			
TOP, <i>see</i> takeoff parameter			
tooling	634		
Torenbeek, E.	30		
torque coefficient ( $C_Q$ )	449		
torsional loads( $M_y$ )	518	523	
torsional stiffness ( $GJ$ )	517		
total pressure recovery	414		
touch labor	648		
TPE 331-11 engine	362		
trades			
design	139	652	660
mission	139	661	652
sizing	668		
studies	139		
technology	139	652	661
trailing edge reflexed	178		
trailing vortices	$cp2$	$cp3$	43
trajectory			
minimal fuel	120		
minimum time	120		
optimal	112		
transmitters	212		
Trident	598		
trim drag	619		

## Index Terms

## Links

trim equation				
aft tail	607			
canard	608			
tropopause	370			
TSFC, <i>see</i> thrust specific fuel consumption				
TU-144	108	405		
turbocharging	361			
turbofan	<b>287</b>			
turbojets				
J85-19	250			
J85-GE-5	251			
J85-GE-21	97			
turboprop	<b>287</b>			
turbulence				
airflow quality	399			
buffet	103			
inlet	416			
wake	43	281		
T/W range	<b>469</b>			
TWA (Transcontinental and Western Air Inc)	12			
Twin Jet Aircraft (UTX)	8			
<b>U</b>				
U-2	146	227	300	570
	651	741		
UAV, <i>see</i> unmanned aerial vehicle				
UCAV (Unmanned Combat Air Vehicle)	<b>648</b>			
$U_e$ (equivalent gust velocity)	495			
ultimate tension strength ( $F_{tw}$ )	504	<b>505</b>	525	

## Index Terms

## Links

unmanned aerial vehicle	16	<b>17</b>	258
composite structure	777		
control system	659		
cost (worked example)	647		
empty weight	780	781	
landing gears	<b>202</b>	203	
Persus	487		
solar-powered Helios	168		
tactical fighter (worked example)	647		
takeoff conditions	<b>788</b>		
XV-15 derivative	249		
US Air Force Regulation 80-14	634		
US Air Force T-39 Trainer	10	<b>11</b>	
US Navy A-12 aircraft (Navy)	5		
unit conversion tables	<b>670</b>		
utilization rate	646		
<b>V</b>			
V-22	249	250	
VAK-191B	251		
Van Allen radiation belt	489		
variable angle compression ramp	397		
$V_{EF}$ (engine failure recognition speed)	273		
vertical load factor ( $n_z$ )	495	518	
vertical shear ( $P_z$ )	518	523	524 545
vertical takeoff and landing (VTOL)	7		
vibration	517		
vibroacoustic environment	517		
viewing angles	<b>201</b>		
Viggen	272		



## Index Terms

## Links

<i>V-n</i> diagram	494	500	
von Doenhoff (NACA Report No. 824)	717		
von Kármán similarity laws	338		
von Ohain, Hans	<b>355</b>	380	
vortex	43		
vortex generators	224		
Vortex Lattice Method (VORLAX)	496		
vortex theory	448		
Vought XF-5U-1	529		
$V_{\text{stall}}$ (stall speed)	157		
V/STOL Aircraft Summary	<i>cp8</i>	<i>cp10</i>	<i>cp11</i>
VTOL, <i>see</i> vertical takeoff and landing			

## **W**

wake turbulence	43	281	
war reserve material (WRM)	627		
Warthog (A-10A)	295		
waterfall chart	664		
wave drag, <i>see</i> drag			
waves, traveling or surface	302		
weight	2		
analysis, bottom-up	514		
empty	124		
estimate			
advanced composite aircraft	570		
air-conditioning and anti-icing	565	568	
conventional metal light-utility aircraft	569		
electrical systems	562	568	
surface control	568		
electronics (avionics)	<b>212</b>	565	569

## Index Terms

## Links

weight

estimate (*Cont.*)

engine

body or wing root-mounted jet 558

reciprocating 559

turbojet and turbofan 558

turboprop 558

fuel system 567

bladder cell backing and support 558

dump and drain 558

in-flight refuel 558

non-self-sealing bladder cells 558

self-sealing bladder cells 557

transfer pumps and monitor 558

furnishings 564 568

instruments

engine indicators 561

flight indicators 561

miscellaneous 561

landing retardation 565 567

low wing loading aircraft 572

propeller systems 559 560

propulsion

air induction system 556

duct provisions 556

engine 555 567

expanding spike 557

external turbofan cowl and duct 557

external turbojet cowl and duct 557

full-round translating spike 557

## Index Terms

## Links

weight				
estimate				
propulsion ( <i>Cont.</i> )				
half-round fixed spike	557			
variable-geometry ramps, actuators				
and controls	556			
refining	574			
starting systems				
four or more jet engines	559			
one- and two-jet engines	559			
reciprocating	559			
turbo-prop	559			
structure				
fuselage	555	566		
landing gear	555			
tail	555	566		
wing	cp24	554	566	
fixed	124			
fraction, for acceleration	130			
fuel	132			
margin	552			
sensitivity ratio	139			
takeoff	149			
weight estimating relationships (WER)	764			
weight fractions	2	6	8	10
	11	13	16	18
	24	127	137	138
	153	166	168	196
$W_{\text{empty}}$ (empty weight)	124			
$W_{\text{fixed}}$ (payload)	124			

## Index Terms

## Links

wheel brakes (or arresting gear)	270			
“Wheel of Misfortune” (VTOL/VSTOL)	249			
Whittle, Frank	<b>355</b>	380		
Williams F 112 turbofan	320			
wind tunnel parametric testing	25			
wing(s)				
angle-of-attack	222			
takeoff and landing	227			
area of	28	34	46	61
	145	156	156	162
	164	166		
augmentor	248	249		
-body combinations for transonic flight	61			
double delta	336			
efficiency factor	<i>cp21</i>	130	278	280
	332			
high aspect ratio	<i>cp21</i>	234		
leading edge	63			
lift coefficient ( $C_L$ )	265			
loading	324			
air-to-air (worked example)	162			
fighter (worked example)	161			
STOL (worked example)	224			
low aspect ratio	<i>cp21</i>	235		
ogee	336			
planform shapes	48	188	189	190
reference area	172			
subsonic drag coefficient ( $C_D$ )	<i>cp17</i>	48		
supercritical	59			
structural configurations	<i>cp24</i>			

This page has been reformatted by Knovel to provide easier navigation.

## Index Terms

## Links

wing(s) ( <i>Cont.</i> )				
swept	57	340		
taper ratio	67	171	534	536
	566	580		
transonic $C_{D0}$ (worked example)	340			
thickness ratio	56			
unswept	338			
weight distribution	<b>540</b>			
wing carry through	203			
wing chord line (WCL)	72			
<i>Winged Victory</i> (Yeates)	578			
Wood, K. D.	30			
work breakdown structure (WBS)	26			
Wright Brothers	1	2	8	10
	435	436		
Wright Flyer	9	10	436	575
	577			
WRM, <i>see</i> war reserve material				
$W_{TO}$ (takeoff weight)	132	149		
<b>X</b>				
X-32B	<i>cp5</i>	251		
X-35	<i>cp5</i>	15		
XB-70	596			
XC-142	250			
XF6U-1	529			
XF-90	651			
XFV-12A	249			
XP-80	12	668	823	
XST (Experimental Stealth Technology)	304			

This page has been reformatted by Knovel to provide easier navigation.

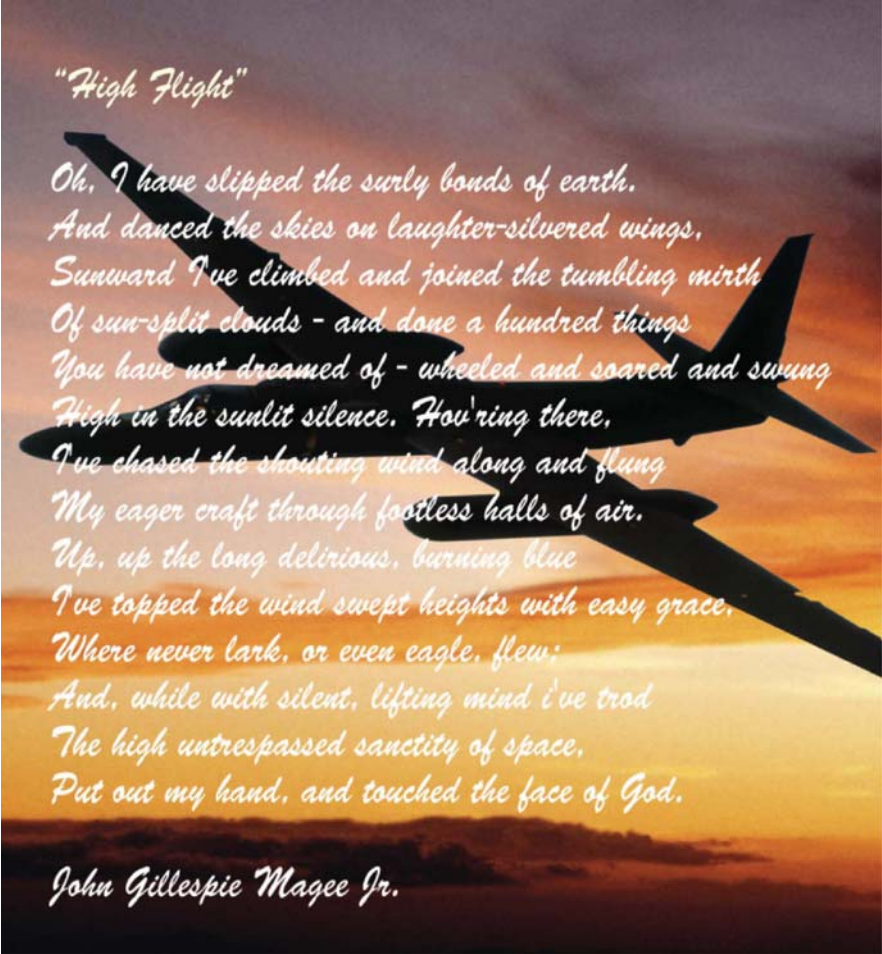
## Index Terms

## Links

XV-4A	249			
XV-4B	251			
XV-5A	251			
XV-6A	249			
XV-15	249	250		
<b>Y</b>				
Yak-38	249	251		
YAL-1/ABL	12			
yaw	187	251	283	284
	394	484	576	596
	621			
adverse	622			
Yeates, V. M.	578			
YF-16	<i>cp9</i>			
YF-17	<i>cp9</i>			
YF-22	<i>cp5</i>	14	16	660
YF-23	<i>cp5</i>	14	16	
yield strength	504			
yield stress	503			
Youngren, Harold	488			
Young's modulus	525			
<b>Z</b>				
zone of activity	62			
zone of silence	62			

## ***SUPPORTING MATERIALS***

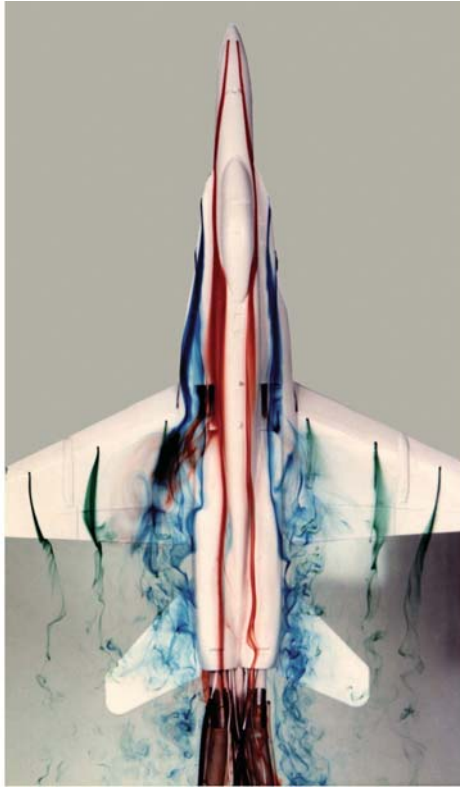
Many of the topics introduced in this book are discussed in more detail in other AIAA publications. For a complete listing of titles in the AIAA Education Series, as well as other AIAA publications, please visit <http://www.aiaa.org>.

*"High Flight"*

*Oh, I have slipped the surly bonds of earth,  
And danced the skies on laughter-silvered wings,  
Sunward I've climbed and joined the tumbling mirth  
Of sun-split clouds - and done a hundred things  
You have not dreamed of - wheeled and soared and swung  
High in the sunlit silence. Hov'ring there,  
I've chased the shouting wind along and flung  
My eager craft through footless halls of air.  
Up, up the long delirious, burning blue  
I've topped the wind swept heights with easy grace,  
Where never lark, or even eagle, flew;  
And, while with silent, lifting mind I've trod  
The high untrespassed sanctity of space,  
Put out my hand, and touched the face of God.*

*John Gillespie Magee Jr.*





F-18 Vortices (NASA, Dryden Water Tunnel Facility)



**Fig. 10.1** B-767 with Trailing Vortices (courtesy of Ray Nicolai)



**Fig. 2.14** Vortices Shedding from F-18 LEX and F-22 Wing Leading Edge



**Ch. 2** F-14 with Shock Condensation @  $M = 0.9$



**Fig. 1.8** DC-3—Timeless Elegance



**Appen. G.** Cessna 172 Skyhawk—Classic Design



**Ch. 5** YF-16 and YF-17—LWF Competition Finalists



**Fig. 1.9** YF-22 and YF-23—ATF Competitors



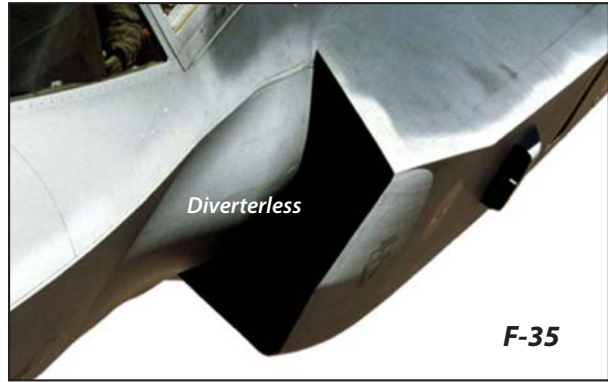
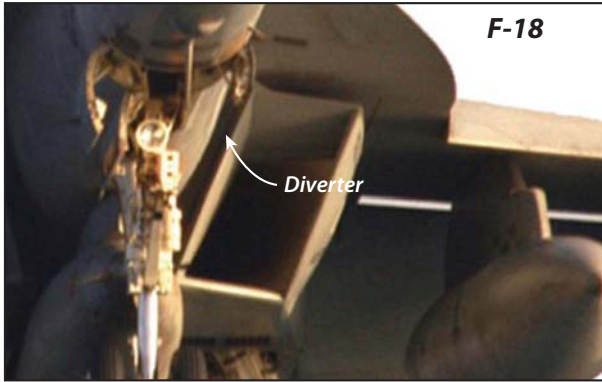
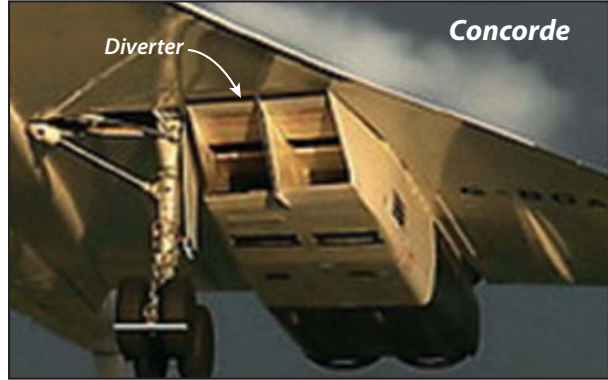
**Fig. 1.11** X-32 and X-35—JSF Competitors



**Appen. H** F-16 Fighting Falcon—Configured for Air-to-air Mission



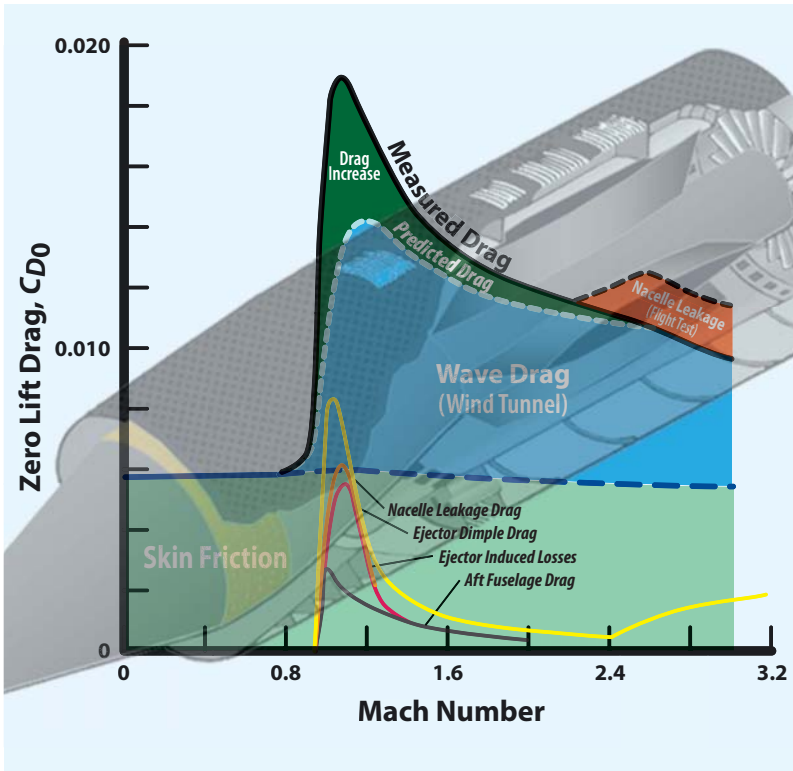
F-18—Powered Approach to Aircraft Carrier (courtesy of John Stratton)



**Fig. 15.13b** A Variety of Inlet Designs for Supersonic Missions



Ch. 3 SR-71—Kelly Johnson’s Crowning Achievement



Ch. 16 Transonic  $C_{D0}$  of the SR-71—A Surprise when Compared to Predictions

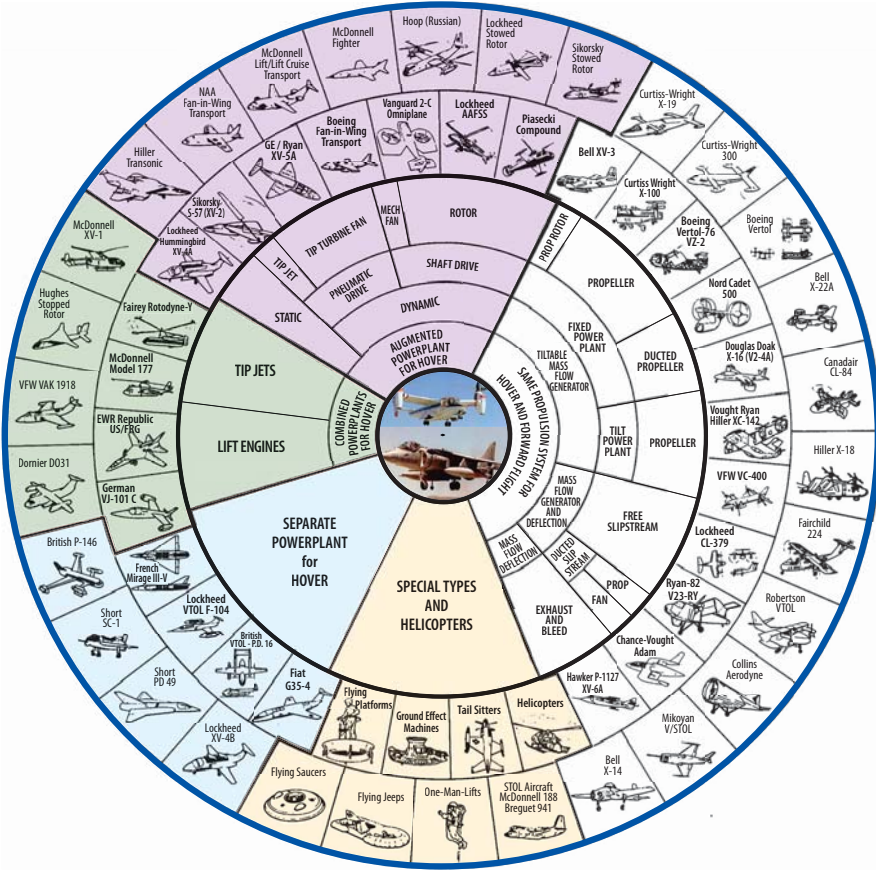
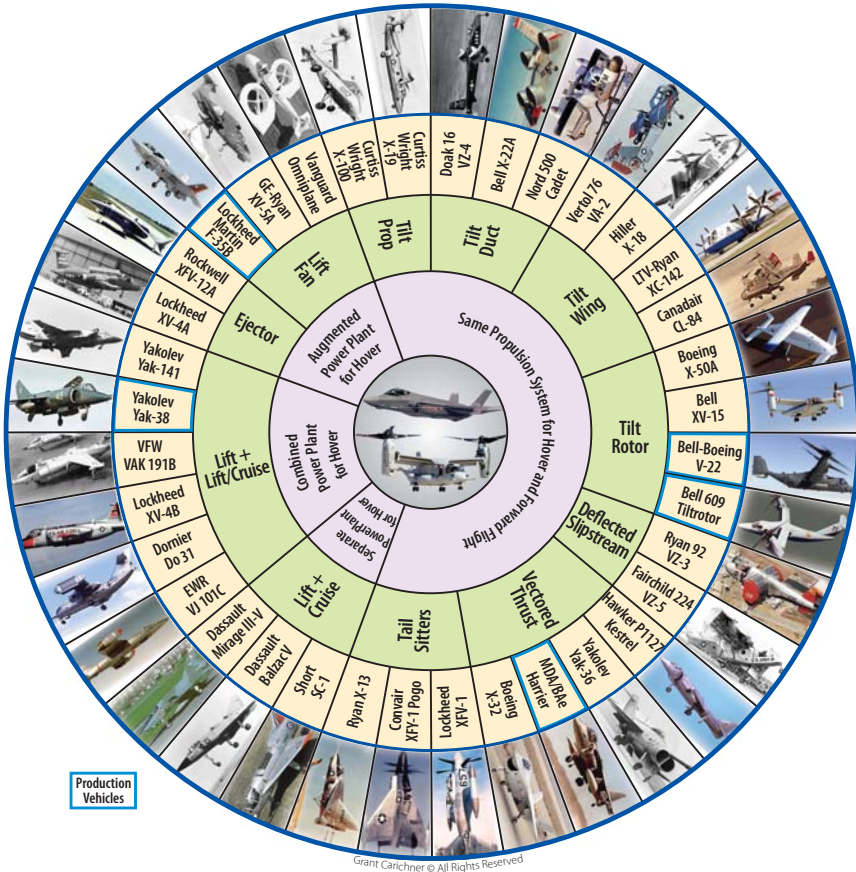


Fig. 9.31 V/STOL Aircraft Summary (1970s)



AV-8B Harrier Performs a Hover Maneuver





**Fig. 9.32** V/STOL Aircraft Summary (2008)



F-35B Transitions from Level Flight to Vertical Mode



**Ch. 23** Canadian Geese Make STOL Landing



**Appen. C** F-35B Lightning II Prepares for Vertical Landing



---

**Ch. 12** F-117A and the “Father of Stealth” Ben Rich



---

**Ch. 13** F-22 and F-117—Two Generations of Stealth